Proceedings of the 20th European Frequency and Time Forum

27-30 March 2006
Braunschweig, Germany

ACKNOWLEDGMENTS

The local organizing committee gratefully acknowledges help and support from the following institutions:

- Helmholtz-Fonds e.V.
- Deutsche Forschungsgemeinschaft
- The City of Braunschweig

ISBN 3-9805741-8-0

EFTF 2006 Local Organizing Committee
at Physikalisch-Technische Bundesanstalt, Braunschweig

Fritz Riehle, General Chair
Andreas Bauch, Technical Program Chair
Martina Bäumler
Eva-Maria Berber
Eberhard Claus
Andre Grote
Christine Haubold
Ingrid Herrmann
Ekkehard Peik
Dirk Piester
Carl-Otto Weiß
Robert Wynands

EFTF Executive Committee

Claude Audoin, France
Elio Bava, INRIM, Italy
Raymond Besson, Laboratoire de Chronométrie Electronique Piézoélectricité, France
Marcel Ecabert, FSRM, Switzerland
Vincent Giordano, CNRS Lab. de Physique et de Métrologie des Oscillateurs, France
Lute Maleki, Jet Propulsion Laboratory, USA
Fritz Riehle, Physikalisch-Technische Bundesanstalt, Germany
Giorgio Santarelli, LNE-SYRTE, France
Bernard Schlueter, FSRM, Switzerland
Pierre Thomann, Observatoire Cantonal de Neuchâtel, Switzerland
Michael Underhill, University of Surrey, UK

EFTF Scientific Committee

Jean-Pierre Aubry, Oscilloquartz SA, Switzerland
Claude Audoin, France
Andreas Bauch, Physikalisch-Technische Bundesanstalt, Germany
Elio Bava, INRIM, Italy
Laurent-Guy Bernier, METAS, Switzerland
Raymond Besson, Laboratoire de Chronométrie Electronique Piézoélectricité, France
Emmanuel Bigler, Laboratoire de Chronométrie Electronique Piézoélectricité, France
Jean-Simon Boulanger, National Research Council of Canada, Canada
Roger Bourquin, Laboratoire de Chronométrie Electronique Piézoélectricité, France
Michel Brunet, CNES, France
Giovanni Busca, Switzerland
André Clairon, LNE-SYRTE, France
Gerrit De Jong, NMI Van Swinden Laboratory, The Netherlands
Andrea De Marchi, Politecnico di Torino, Italy
Pascale Defraigne, Observatoire Royal de Belgique
Noël Dimarcq, LNE-SYRTE, France
Bernard Dulmet, Laboratoire de Chronométrie Electronique Piézoélectricité, France
Marcel Ecabert, FSRM, Switzerland
Christopher Ekstrom, US Naval Observatory, USA
Pekka Eskelinen, Helsinki University of Technology, Finland
Jeremy Everard, University of York, UK
Steve Feltham, European Space Agency ESTEC, The Netherlands
Michael Garvey, Symmetricom TRC, USA
Patrick Gill, National Physical Laboratory, UK
Vincent Giordano, CNRS - LPMO, France
Aldo Godone, INRIM, Italy
Philippe Guillemot, Centre National d'Etudes Spatiales, France
Jörg Hahn, European Space Agency ESTEC, The Netherlands
Jens Hammesfahr, DLR IKN, Germany
Daniel Hauden, LPMO - CNRS, France
Kurt Hilty, METAS, Switzerland
Carl Hruska, York University, Canada
Masami Kihara, College of Science and Technology, Nihon University, Japan
Peter Krempl, AVL List GmbH, Austria
Pierre Lemonde, LNE-SYRTE, France
Luca Lorini, INRIM, Italy
Eric Luvisutto, CNES, France
Lute Maleki, Jet Propulsion Laboratory, USA
Demetrios Matsakis, US Naval Observatory, USA
Bernd Neubig, Axtal, Germany
Rodriguez Juan Palacio, Real Instituto y Observatorio de la Armada, Spain
Ulrich Peier, Dr. U. R. Peier Engineering, Switzerland

Ekkehard Peik, Physikalisch-Technische Bundesanstalt, Germany
Dirk Piester, Physikalisch-Technische Bundesanstalt, Germany
Fritz Riehle, Physikalisch-Technische Bundesanstalt, Germany
Christophe Salomon, Ecole Normale Supérieure, France
Giorgio Santarelli, LNE-SYRTE, France
Bernard Schlueter, FSRM, Switzerland
Wolfgang Schlüter, Institut für angewandte Geodäsie, Germany
Patrizia Tavella, INRIM, Italy
Pierre Thomann, Observatoire Cantonal de Neuchâtel, Switzerland
Dmitry Tsarapkin, MPEI (TU), Russia
Philip Tuckey, LNE-SYRTE, France
Pierre Uhrich, LNE-SYRTE, France
Michael Underhill, University of Surrey, UK
Rainer Unverdross, Unverdross Technik, Germany
Jacques Vanier, Canada
Peter Wolf, BIPM, France
Walter Zingg, Rolex SA, Switzerland

Foreword of the Chairman of the Local Organizing Committee
Dr. Fritz Riehle

On behalf of the Local Organizing Committee of the 20th European Frequency and Time Forum (EFTF) I had the pleasure of welcoming more than 270 attendees from more than 30 countries to this year's EFTF in Braunschweig from 27th to 30th March. For two decades now, the EFTF as an international conference and exhibition has been providing information on recent advances and trends of scientific research and industrial development in the fields of Frequency and Time.

At its 20th anniversary the EFTF came to Germany for the second time after 1994 when it was held in Weihenstephan near Munich in the south of Germany. Braunschweig, located in the north of Germany, is the city of the duke Henry the Lion who lived here in the eleventh century and reigned over a large fraction of Germany. Most of the attendees of the EFTF used the guided tour on Monday evening to catch a glimpse of medieval Braunschweig. By the way, the fact that Henry the Lion also founded the city of Munich links the locations of the 1994 and 2006 meetings of the EFTF in Germany.

My first thanks go to the members of the Scientific Committee under the chairmanship of Dr. Andreas Bauch who selected the scientific contributions of 68 oral presentations and the 91 poster contributions. The Scientific Committee also selected the two special topics for this year's EFTF, namely *Time Scales for Satellite Navigation Systems* and *Optical Clocks*. These topics were so well received by the participants, including the contributors to the industrial exhibition, that they might become more regular topics in future EFTFs.

Next, I would like to thank the City of Braunschweig for supporting the banquet in the old town hall, the so-called Dornse, which sometimes is referred to as Braunschweig's noble living room. On this occasion, the EFTF Frequency and Time Award and the EFTF Young Scientist Award have been awarded by Professor Ernst-Otto Göbel, President of the International Committee for Weights and Measures and President of the Physikalisch-Technische Bundesanstalt. The awards for 2006 were sponsored by the Helmholtz Fonds for the advancement of science and research on the field of physical and technical precision measurements.

The proverb "In Braunschweig wird die Zeit gemacht" which means "Time is made in Braunschweig" refers to the fact that the Physikalisch-Technische Bundesanstalt with its atomic clocks is located in Braunschweig. PTB is the successor of the former PTR which was established in 1887 as a result of a strong recommendation and the invaluable support of Werner von Siemens. It is Germany's National Metrology Institute and is responsible for the realisation and dissemination of legal time in Germany. I am particularly thankful to PTB for its invaluable support of the EFTF and also for arranging the laboratory visits on its premises during the last day of the EFTF 2006.

Last but not least my sincerest thanks go to the Deutsche Forschungsgemeinschaft for its financial support and to all the participants for their contributions which are now available with these Proceedings for all the attendees of the EFTF 2006 and also for the scientific community.

Fritz Riehle

European Frequency and Time Award

The European Frequency and Time Award has been awarded since 1993, with the goal of recognizing outstanding contributions in all fields covered by the EFTF.

The Prize for 2006 was awarded to **Professor Dr. Raymond Besson** from the Laboratoire de Chronométrie Electronique Piézoélectricité, Besançon for his outstanding scientific research on the design and development of the BVA resonator as a prerequisite to the success of clocks on ground and in space and for his invaluable contributions to the existence and the success of the European Frequency and Time Forum.

The Award was presented to Professor Besson on the occasion of the 20th European Time and Frequency Forum at Braunschweig on 28 March 2006 by Professor Ernst O. Göbel, President of the International Committee on Weights and Measures, President of the Physikalisch-Technische Bundesanstalt and President of the Helmholtz Fonds. The 2006 Award was sponsored by the Helmholtz Fonds e.V. for the advancement of science and research on the field of physical and technical precision measurements.

Young Scientist Award of the European Frequency and Time Forum

The EFTF Young Scientist Award is conferred in recognition of a personal contribution that demonstrated a high degree of initiative and creativity and lead to already established or easily foreseeable outstanding advances in the field of time and frequency metrology. The award honors a person under the age of 40 at the date of the opening session of the EFTF conference.

The 2006 EFTF Young Scientist Award was awarded to **Dr. Pierre Lemonde** from the LNE-SYRTE, Paris in recognition of his outstanding contributions to the first transportable Cs fountain clock and to the space clock PHARAO and for his contributions to novel optical clocks based on neutral atoms.

The Award was presented to Dr. Lemonde on the occasion of the 20th European Time and Frequency Forum at Braunschweig on 28 March 2006 by Professor Ernst O. Göbel, President of the International Committee on Weights and Measures, President of the Physikalisch-Technische Bundesanstalt and President of the Helmholtz Fonds. The 2006 Award was sponsored by the Helmholtz Fonds e.V. for the advancement of science and research on the field of physical and technical precision measurements.

Table of Contents

Atomic Fountain Clocks

Microwave Atomic Clocks

Optical Clocks with Trapped Ions

Clocks in Space Projects

TAI Time Links

Time Scales and Distribution

Time and Frequency Transfer

Proceedings of the 20th EFTF, 2006

General Design Technique for High Q-factor Bragg Reflector Resonators

Jean-Michel le Floch*[1,2], Michael E. Tobar[1], Dominique Cros[2], Jerzy Krupka
[1]*School of Physics, The University of Western Australia, 35 Stirling Hwy, Crawley, WA, 6009, Australia*
[2] *XLIM - UMR CNRS n°6172 - 123, avenue Albert Thomas - 87060 LIMOGES CEDEX, France*
[3] *Institute of Microelectronics and Optoelectronics, Warsaw University of Technology, Koszykowa 75, Warsaw, Poland*
**Electronic address: lefloch@cyllene.uwa.edu.au*

The Bragg reflection technique improves the Q-factor of a resonator by reducing conductor and dielectric losses by concentrating the field in the inner area of the cavity. In this paper, we present a general way of designing a high Q-factor Bragg resonator, using a simple model of non-Maxwellian equations. The method is a more general method, which allows us to design resonators of cylindrical geometry and arbitrary thicknesses for either the horizontal or cylindrical dielectric reflectors, which is often imposed by the manufacturer. In this work, we only consider cylindrical symmetric resonators operating in transverse electric mode ($TE_{0,n,p}$), which only has the E_θ component made from low-loss single crystal dielectrics. The horizontal plates are of thickness 2.75mm and radius 24.3 mm, and the rings are 31.8 mm high and of the same radius. The size of the cavity to obtain Bragg reflection may be calculated using the simple model, which is verified with rigorous Method of Lines analysis. When we fix the number of variation of E_θ, in r and z directions to the minimum (fundamental mode) we obtained an unloaded Q-factor of order 2×10^5 at 9.7 GHz in a single crystal sapphire resonator. Two other cavities were built to investigate Bragg confinement of higher order modes in the sapphire structure at 12.4 GHz with unloaded Q-factors of order 10^5. We also illustrate the general designing principles of a Bragg reflector with dielectric layers of arbitrary thicknesses using the simple model, with verification using the Method of Lines.

1. INTRODUCTION

We have designed some Bragg reflector resonators [1, 2], using a simple model of non-Maxwellian equations. Previous work only calculated dimensions for plates that were necessarily quarter wavelength ($\lambda/4$) thick [3], while in this work we present a more general method, which allows us to design Bragg reflectors of cylindrical geometry and arbitrary thicknesses (not $\lambda/4$ thick) for either the horizontal or cylindrical dielectric reflectors, which is often imposed by the manufacturer. We only consider cylindrical symmetric resonators necessarily operating in Transverse Electric (TE) mode with only has the $E_{\square}$ component.

The work is generalized to include higher order Bragg confined modes with more than one variation in the inner resonator region and the outer-layered anti-resonant region where the Bragg reflectors are situated. We introduce the notation, $TE^{q,s}_{m,n,p}$ to describe the mode confined by Bragg reflection. Here the azimuthal mode number, m, is usually zero for the mode to be pure TE, the radial and axial mode number in the resonance region internal to the Bragg reflectors is n and p respectively, while the radial and axial mode number within the Bragg reflector region is q and s respectively. First we consider the horizontal layers along the cylindrical axis, and then the radial direction. Examples verifying the techniques are presented and confirmed using the Method of Lines (MoL) [3] [4] and by our experimental designs.

II. BRAGG REFLECTORS ALONG THE CYLINDRICAL AXIS

In this section we calculate general formulas based on the simple model to obtain the Bragg reflection condition of dielectric Bragg reflectors along the cylindrical axis. We also generalize the work to include higher order Bragg confined modes with more than one variation in the inner resonator region and the outer layered anti-resonant region where the Bragg reflectors are situated. The simple model is verified by simulating resonators using the Method of Lines (MoL). The resonators were designed using standard substrates of MGO of 0.5 mm thickness.

A schematic of the resonator is shown in Fig. 1. The origin is selected at the center, where the resonator exhibits symmetry in both the r and z directions. The structure can be divided into distinct regions, the main resonance region of thickness t_0 (region 0), and the Bragg reflector region. One Bragg reflector pair has 2-layers, and can be divided into two regions of different permittivity and thickness t_1 and t_2 as shown in figure 1 (region 1 and 2 respectively).

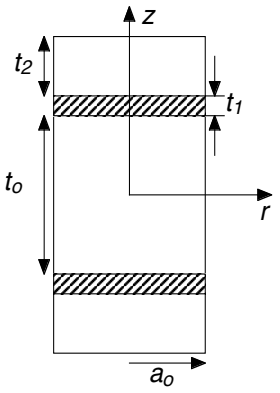

Fig. 1. Schematic of the z - r plane of the DBR resonator with 1 pair of reflectors (above and below) along the z-axis of the resonator.

Implicit in this analysis, we assume separation of variables is valid in cylindrical co-ordinates, and assume the TE (Transverse Electric) field distribution (E_ϕ) has a sinusoidal dependence in the z direction and Bessel function dependence in the r direction. The Bragg reflector region and the main resonance regions are considered separately, with the boundary condition matched at the interface. In this case the derivative is not matched and the field is piecewise sinusoidal, a schematic of the assumed magnitude of the field along the z-axis is shown in Fig. 2.

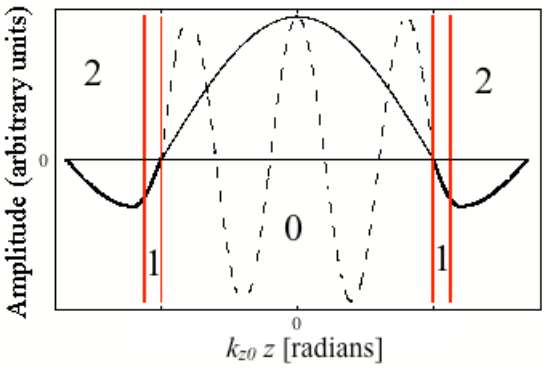

Fig. 2. The form of the E_ϕ field along the axis of the resonator for the $TE^{0,1}_{0,1,1}$ and the $TE^{0,1}_{0,1,5}$ mode in the structure of fig. 1, assuming the simple non-Maxwellian model in regions 0, 1 and 2. The amplitude is given in arbitrary units and the field along the axis is plotted with respect to distance, z.

The simplest Bragg reflection or anti-resonance condition requires E_ϕ to go to zero at $z = \frac{t_0}{2} + t_1 + t_2$ and $z = \frac{t_0}{2}$, and to accommodate an odd number of half wavelengths ($\lambda/2, 3\lambda/2, 5\lambda/2 \ldots$) within the total reflector of thickness $t_1 + t_2$ [3]. Thus, combined with our definitions of the mode nomenclature, $TE^{q,s}_{m,n,p}$ we obtain the following general equations that satisfy the required conditions:

$$k_{z2} t_2 = (1-\alpha)\pi(2s-1) \quad (1a)$$

$$k_{z1} t_1 = \alpha\pi(2s-1) \quad (1b)$$

$$k_{z0} . t_0 = p\pi \quad (1c)$$

Here k_{z0} is the wave number in the z direction in region 0, k_{z1} is the effective wave number in region 1, k_{z2} is the effective wave number in region 2 and α is a number between 0 and 1, which represents the proportion of the odd number of half wavelengths within region 1 and 2, so if α = ½, t_1 and t_2 are both reflectors of $\lambda/4$ thick, while in the extreme case when α = 1 the Bragg reflector is a single dielectric of $\lambda/2$ thick, which will confine the mode but usually does not improve the Q-factor [5]. Note that even though both region 0 and 2 could both be free-space, for this solution we can not assume $k_{z0} = k_{z2}$ as region 1 and 2 form an anti-resonant structure, which must depend on the radius of the resonator and thus the aspect ratio. Thus, we define a coefficient, γ [3] that relates the two effective wave vectors, such that;

$$k_{z2} = \gamma . k_{z0} \quad (2)$$

The following relationships between the effective wave numbers in (1) and the free space wave number, k_0, using the simple model have been shown previously to be [3]:

$$k_{z0} = k_0 / \gamma \quad (3a)$$

$$k_{z1} = k_0 / \sqrt{\varepsilon_r} \quad (3b)$$

$$k_{z2} = k_0 \quad (3c)$$

Here ε_r is the permittivity of the dielectric layer of region1. Thus, combining (3) and (1) we obtain the following;

$$t_2 = \frac{(1-\alpha)\pi(2s-1)}{k_0} \quad (4a)$$

$$t_1 = \frac{\alpha\pi(2s-1)}{k_0\sqrt{\varepsilon_r}} \quad (4b)$$

$$t_0 = \frac{\gamma\pi p}{k_0} \quad (4c)$$

The thickness of the resonant regime, t_0, depends on the value of γ, which is determined by the aspect ratio [3]. In the limiting case where the radius tends to infinity the structure approaches a set of parallel plates, γ-> 1 as expected. In all other cases the value of γ depends of the radial dimensions, which is determine in the following.

Since the form of the E_ϕ field distribution, in the radial direction is chosen to be a Bessel function, $J_1(k_r.r)$, in the simple model, we can use the boundary condition that the field must go to zero at the cavity walls. To

calculate the radius of the structure, a_0, we consider the radial wave number in the main resonance structure, k_{r0}, which is given by;

$$k_{r0} \cdot a_0 = \chi_{1n} \tag{5}$$

where, χ_{1n} is the n^{th} root of the Bessel function $J_1(\chi)$. Also the dispersion relation in region 0 must be satisfied.

$$k_{r0} = \sqrt{k_0^2 - k_{z0}^2} \tag{6}$$

Thus, by combining (7), (9) and (10) the value of the radius can be determined to be;

$$a_0 = \frac{\gamma \cdot \chi_{1n}}{k_0 \sqrt{\gamma^2 - 1}} \tag{7}$$

Thus, by combining (4) and (7) the aspect ratio, AR, of the resonator can be calculated as;

$$AR = \frac{t_0/2 + t_1 + t_2}{a_0} = \frac{\pi p}{2\chi_{1n}} \cdot \sqrt{\gamma^2 - 1} \cdot \left(1 + \frac{2(2s-1)}{\gamma p}\left(1 - \alpha + \frac{\alpha}{\sqrt{\varepsilon_r}}\right)\right) \tag{8}$$

When s and p = 1 and α = ½ (8) reduces the formula previously derived for the fundamental mode with Bragg reflectors of λ/4 thick [3]. Now we have all the formulas necessary to design the structure. For example, we may first choose the aspect ratio of the resonator and the dielectric material to determine the permittivity. Equation (8) then uniquely defines the coefficient, γ, required to obtain the anti-resonance condition of the Bragg reflector. To calculate the dimensions of the resonator the frequency must be defined so k_0 may be calculated. Then (7), and (4) can be solved to uniquely calculate the dimensions of the resonator.

A. Example using standard MGO substrates

In this subsection we confirm the equations of the simple model by simulating resonators of the form in fig. 1 using MoL. The resonators implement standard crystalline magnesium oxide (MGO) substrates of 0.5 mm thickness (i.e. t_1 = 0.5 mm) and a permittivity at room temperature of 9.6. First we fix the fundamental $TE_{0,1,1}^{1,1}$ mode to have a frequency of 10 GHz according to the simple model, with the aspect ratio of region 0 set to unity. These constraints fixes the following parameters of the resonator, $t_0/2 = a_0$ = 19.759 mm, which leaves t_2 as the only free parameter. Frequency and filling factor of various modes are plotted as a function of t_2 in Fig. 3. The Bragg confinement regions are quite broad, however we define the condition when the electrical energy filling factor in region 0, Pe_0, is a maximum (and energy in the Bragg reflector layers is minimum).

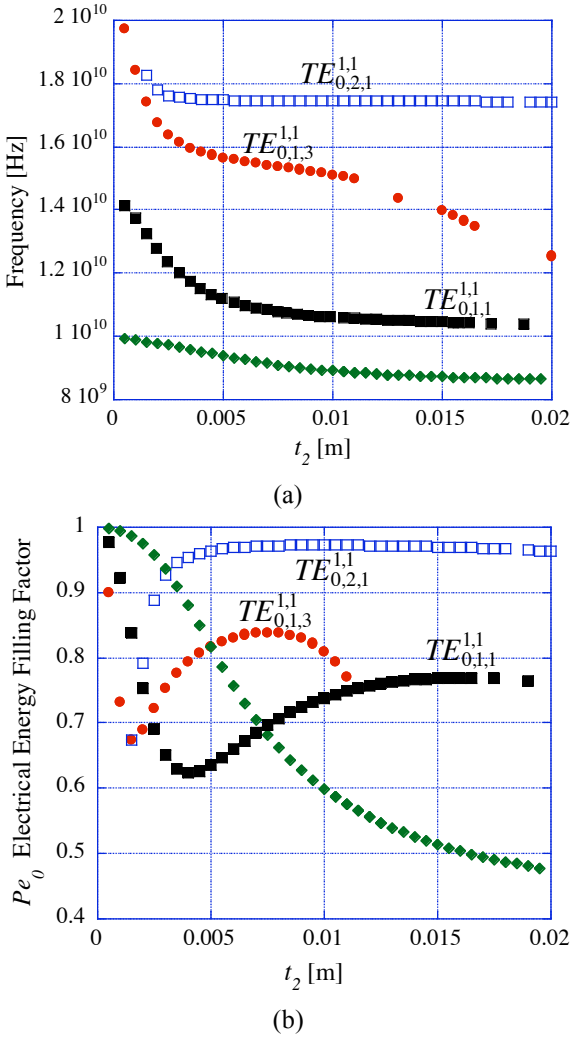

Fig. 3. (a) Frequency versus t_2 for various modes in the MGO resonator as calculated using MoL. (b) Electrical energy filling factor in region 0 for various modes in the MGO resonator as calculated using MoL.

Results in fig. 3 and table 1 show that the simple model provides a good first iteration for designing a Bragg reflector resonator. Because the Bragg confined regions are very broad, the calculated values of Pe_0 are very close at the values of $t_{2,SM}$ and $t_{2,MoL}$, in section IV it is shown that Q-factors are very close to the optimum (also see [3]). The main drawback with the simple model is the inaccuracy of the calculated frequency, which can be up to 5% out. If accuracy is required either a proportional scaling of the structure may be undertaken, or a rigours technique may be used to iterate the solution by changing slightly some but not all of the dimensions.

A similar technique may be applied to the radial direction, but for the sake of brevity is only introduced in the next section where we discuss the general multi-layer structure.

Table 1. Comparison for some parameters calculated using the Simple Model and the MoL for various Bragg confined modes as shown in Fig. 3.

Mode	f_{SM} [GHz]	f_{MoL} [GHz]	$t_{2,SM}$ [mm]	Pe_0 @$t_{2,SM}$	$t_{2,MoL}$ [mm]	Pe_0 @$t_{2,MoL}$	α
$TE^{1,1}_{0,1,1}$	10.00	10.43	13.44	0.764	16.09	0.769	0.103
$TE^{1,1}_{0,1,3}$	14.67	15.38	8.67	0.834	7.52	0.839	0.152
$TE^{1,1}_{0,2,1}$	17.36	17.44	7.09	0.971	10.10	0.972	0.179

III. THE GENERAL MULTI-LAYER DISTRIBUTED BRAGG REFLECTOR STRUCTURE

In this section the general multi-layer structure is solved for, with n_b Bragg reflector layers in the axial direction and m_b layers in the radial direction as shown in fig. 4.

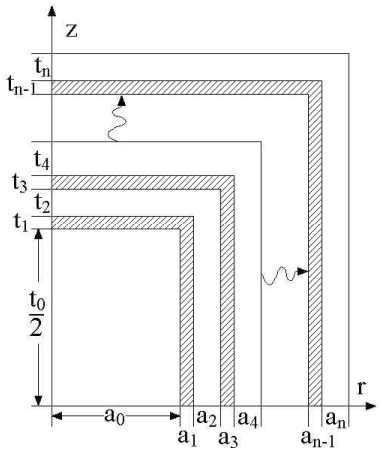

Fig. 4. Schematic of a quarter of the cylindrical structure, with n dielectric and free-space Bragg reflector layers, which are placed above the central free-space cavity along the z direction and axial direction. In this case $n = m$, but in general we solve for the case when n and m are not necessarily equal.

For the general multi-layer structure where the layers are not necessarily $\lambda/4$ thick, all the horizontal Bragg reflector layers will not automatically have the same thickness as given by (4) if the values of α, s or ε_r are different in each layer. Thus, equation (4) may be generalized to;

$$t_{2i} = \frac{(1-\alpha_i)\pi(2s_i-1)}{k_0}$$

for i = 1 to $n_b/2$ where $n_b \geq 2$ and even (9a)

$$t_{2i-1} = \frac{\alpha_i \pi(2s_i-1)}{k_0\sqrt{\varepsilon_i}}$$

for i = 1 to $n_b/2$ where $n_b \geq 2$ and even (9b)

$$t_0 = \frac{\gamma\pi p}{k_0} \quad (9c)$$

Where the value of α_i, s_i ($s = \sum s_i$) or ε_i may in general be different for each Bragg reflector pair (labelled for i = 1 to $n_b/2$ where $n_b \geq 2$ and even).

Along the radial direction, the dimensions of the vertical layers (concentric cylinders) may be determined by the roots of the first order Bessel function, $J_1(\chi)$, and its derivative, and by combining with the dispersion relations [3]. This is equivalent to choosing the dielectric layers in an analogous way to the axial "fraction of a quarter wavelength" condition using (4). Assuming m_b-layers the radial thickness of the concentric radial Bragg reflectors may be shown to be;

$$a_{2i} = \frac{\gamma(1-\rho_i)}{k_0\sqrt{\gamma^2-1}} \cdot \left(\chi_{1,i+n+2q_i-2} - \chi_{1,i+n-1}\right)$$

for i = 1 to $m_b/2$ where $m_b \geq 2$ and even (10a)

$$a_{2i-1} = \frac{\gamma\rho}{k_0\sqrt{\varepsilon_i\gamma^2-1}} \cdot \left(\chi_{1,i+n+2q_i-2} - \chi_{1,i+n-1}\right)$$

for i = 1 to $m_b/2$ where $m_b \geq 2$ and even (10b)

$$a_0 = \frac{\gamma \cdot \chi_{1n_i}}{k_0\sqrt{\gamma^2-1}} \quad (10c)$$

where the value of ρ_i, q_i ($q = \sum q_i$) or ε_i may in general be different for each Bragg reflector pair (labelled for i = 1 to $m_b/2$ where $m_b \geq 2$ and even). Here, ρ_i is a number between 0 and 1, which represents the proportion of the odd number of effective half wavelengths within the dielectric layer of the i^{th} Bragg reflector pair, so if ρ_i = ½, the dielectric and free-space layers are both reflectors of $\lambda/4$ thick, while in the extreme case when ρ_i = 1 the Bragg reflector is a single dielectric of $\lambda/2$ thick.

Now it is straightforward to combine (4) and (10) and in the process eliminate k_0 and calculate the relationship between the aspect ratio, $AR_{n_b m_b}$, and γ for the general multi-layer case, with a bit of manipulation we obtain;

$$AR_{n_b m_b}(\gamma,\varepsilon_r) = \frac{L/2}{a} = \frac{\frac{t_0}{2} + \sum_{j=1}^{n_b} t_j}{\sum_{j=0}^{m_b} a_j} = \frac{\pi p\sqrt{\gamma^2-1}}{2\chi_{1n}} \times \left(\frac{\left(1 + \sum_{j=1}^{n_b/2} \frac{2(2s_i-1)}{\gamma p}\left(1-\alpha_i + \frac{\alpha_i}{\sqrt{\varepsilon_i}}\right)\right)}{1 + \frac{1}{\chi_{1n}} \sum_{i=1}^{m_b/2} (1-\rho_i)\left(\chi_{1,i+n+2q_i-2} - \chi_{1,i+n-1}\right) + \rho_i \sqrt{\frac{\gamma^2-1}{\varepsilon_i\gamma^2-1}}\left(\chi_{1,i+n+2q_i-2} - \chi_{1,i+n-1}\right)} \right) \quad (11)$$

Here L is the total length of the resonator, a is the total radius. Now we have all the formulas necessary to design the multi-layer structure of n_b-layers along the z-axis and m_b-layers along the radial axis by solving (9), (10) and (11) simultaneously. Because the method is approximate it is expected that the comparisons will degrade for large values of mode number in the Bragg reflector (s_i and q_i see [3]). However, in practice the best results at microwave frequencies are obtained when s_i and $q_i = 1$ (as shown in the next section).

IV. SAPPHIRE BRAGG REFLECTOR RESONATOR: DESIGN MEASURMENT AND PROPERTIES

From a single set of sapphire rings and plates (which were initially implemented in another structure [6]) with $m_b = n_b = 2$, the simple model was implemented to design some resonant structures by loading the same dielectric in different size cavities as calculated by the simple model. A photo of the cavity designed with p, n, s_i and $q_i = 1$ is shown in fig. 5.

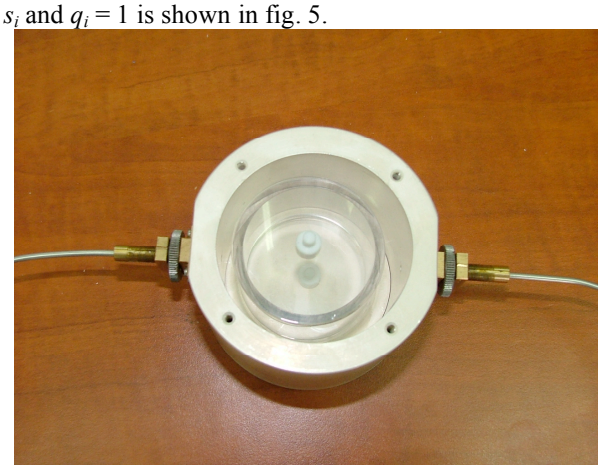

Fig. 5. Top view of a hollow sapphire cylinder supported by Teflon supports inside a silver plated copper cavity. An adjustable probe mechanism is attached on opposite sides of the resonator so the probes may be under-coupled and measured in transmission to obtain the unloaded Q-factor.

Three modes were chosen (see Table II and Fig. 6), with a_0 =21 mm a_1 = 3.3 mm t_0 = 31.8 mm and t_1 = 2.75 mm set by the dimensions of the sapphire rings and plates, and the permittivity [7] [8] and loss tangent [9] of sapphire perpendicular to the c-axis at room temperature taken to be 9.394 and $1.3\times10^{-6}f^{0.84}$ respectively, where f is in the unit of GHz. The calculated parameters using the simple model are given in table II. The rigorous MoL technique was then implemented to calculate the frequency and Q-factors of the resonator to compare with experiment (see table III). Electric field density plots of the modes are shown in fig. 6. To support the structure small Teflon pieces with low permittivity (2.06) and loss tangent ($1.6\ 10^{-4}$) are used [10] as shown in Fig. 5, and have minimal effect on the measured parameters.

Table II. Calculated parameters using the simple model.

Mode	α	ρ	t_2 [mm]	d_2 [mm]	f_{SM} [GHz]
$TE^{1,1}_{0,1,1}$	0.557	0.651	6.7	6.1	9.9
$TE^{1,1}_{0,2,1}$	0.722	0.829	3.2	3.0	12.8
$TE^{1,2}_{0,2,1}$	0.240	0.829	26.6	3.0	12.8

The Q-factor is calculated by calculating the filling factors and G-factors of the cavity using MoL and using the known loss tangent (tanδ) and the measure surface resistance (R_s):

$$Q^{-1} = Pe_{sapph}\tan\delta_{sapph} + Pe_{teflon}\tan\delta_{teflon} + R_S/G \quad (12)$$

The surface resistance was determined by measuring the Q-factor of the $TE_{0,1,1}$ in the empty cavity shown in fig. 5, and was determined to be, $R_S = 0.058\sqrt{f}$. Experiments and calculation are compared in table III.

The application of the simple model to describe various Bragg-confined modes is verified by comparing the model with rigorous analysis and experiment. Quite clearly the higher order modes suffer from higher spurious mode density and degraded Q-factor with respect to the fundamental. The properties of the fundamental mode have a similar Q-factor to Whispering Gallery modes [11] [7] [9], with a lower spurious mode density, and thus have application for low noise oscillator design. In fact it has been shown using MoL that Q-factors of greater than 300,000 may be obtained if plate and ring thickness are closer to λ/4 [3], however these results are the first experimental confirmation of this model.

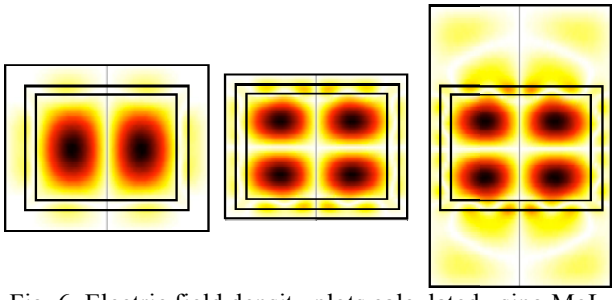

Fig. 6. Electric field density plots calculated using MoL of the three different Bragg modes: $TE^{1,1}_{0,1,1}$, $TE^{1,1}_{0,2,1}$ and $TE^{1,2}_{0,2,1}$ respectively.

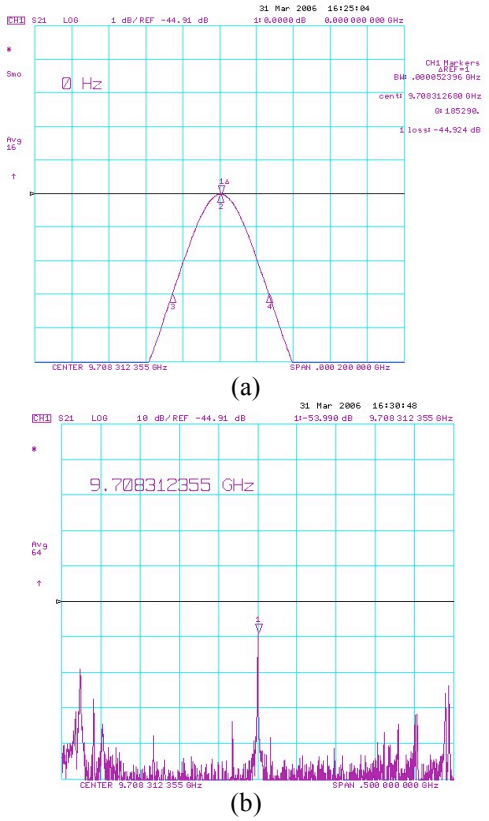

(a)

(b)

Fig. 7. Transmission measurements of the fundamental $TE^{1,1}_{0,1,1}$ mode at 9.7 GHz: (a) Measured Q-factor of 185,000: (b) Measured mode density over a 500 MHz span.

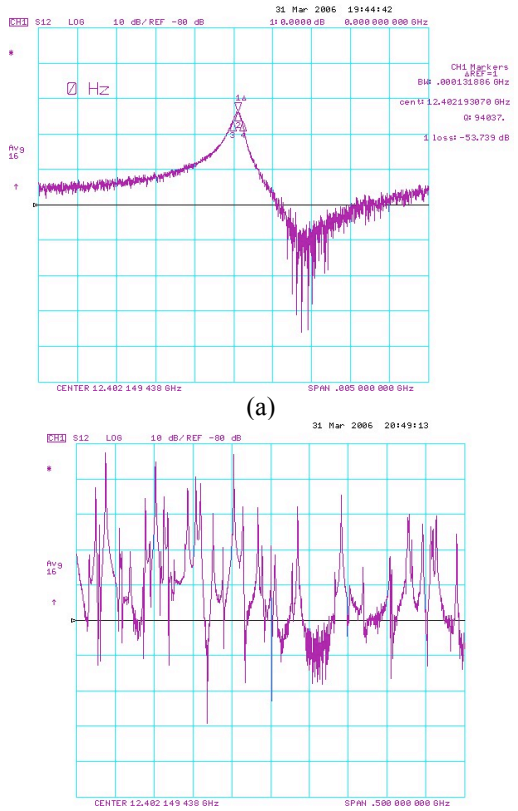

(a)

(b)

Fig. 8. Transmission measurements of the higher order $TE^{1,2}_{0,2,1}$ mode at 12.4 GHz: (a) Measured Q-factor of 94,000: (b) Measured mode density over a 500 MHz span.

Table III Calculation using MoL and comparison with experiment, with (*) and without the Teflon support.

Mode	f_{MOL}[GHz]	f_{EXP} [GHz]	$Q_{0\ MOL}$	$Q_{0\ EXP}$	Pe_{sapph}	Pe_{teflon}	G [Ω]
$TE^{1,1}_{0,1,1}$	9.7268	_____	229,100	_____	0.167	_____	9,353
$TE^{1,1}_{0,1,1}$ *	9.7266	9.7083	228,500	185,300	0.167	6.18×10^{-5}	9,347
$TE^{1,1}_{0,2,1}$	12.4397	_____	123,500	_____	0.226	_____	5,413
$TE^{1,1}_{0,2,1}$ *	12.4386	12.4562	122,400	128,300	0.225	3.78×10^{-4}	5,391
$TE^{1,2}_{0,2,1}$	12.2149	_____	96,900	_____	0.390	_____	4,969
$TE^{1,2}_{0,2,1}$ *	12.2090	12.4021	94,200	94,000	0.386	2.17×10^{-3}	4,969

V. CONCLUSION

A general technique to design Bragg reflector resonators of cylindrical geometry has been presented. In this work the dielectric rings and plates do not necessarily need to be approximately λ/4 thick, and the method has been generalised to higher order Bragg reflector modes. Using this model resonators at microwave frequencies were designed with Q-factors greater than 10^5. Recently some similar types of Bragg reflector resonators of spherical geometry have been designed and can achieve a similar Q-factor [12] [13]. The reflectors in these resonators were approximately λ/4 thick, it would also be straightforward to apply this technique to such resonators to loosen this constraint

Acknowledgements

This work was funded by the Australian Research Council.

REFERENCES

[1] Flory, C.A. and R.C. Taber, *High performance distributed Bragg reflector microwave resonator.* IEEE Trans on UFFC, 1997. **44**(2, March): p. 486-495.
[2] Flory, C.A. and H.L. Ko, *Microwave oscillators incorporating high performance distributed Bragg reflector microwave resonators.* IEEE Trans. on UFFC, 1998. **45**(3, May): p. 824-829.
[3] Tobar, M.E., et al., *Distributed Bragg reflector resonators with cylindrical symmetry and extremely high Q-factors*. IEEE Trans. UFFC, 2005. **52**(1): p. 17-26.
[4] Piquet, O., et al. *Application of the method of lines for high-Q resonant structures*. in *EUMC 2002*. 2002. Milan, EU.
[5] Tobar, M.E., et al., *Compact high-Q $TE_{01\delta}$ sapphire-rutile microwave Bragg resonator.* IEEE Trans. UFFC, 2001. **48**(3): p. 821-829.
[6] Piquet, O., et al., *High-Q sapphire resonator with distributed Bragg reflectors*. Electron. Lett., 2003. **39**(25): p. 1791-2.
[7] Krupka, J., et al., *Use of whispering gallery modes for complex permittivity determinations of ultra-low-loss dielectric materials*. IEEE Trans. on MTT, 1999. **47**(6): p. 752-759.
[8] Krupka, J., et al., *Complex permittivity of some ultralow loss dielectric crystals at cryogenic temperatures.* Meas. Sci. Technol., 1999. **10**(4): p. 387-392.
[9] Hartnett, J.G., et al., *Room Temperature Measurement of the Anisotropic Loss Tangent of Sapphire Using the Whispering Gallery Mode Technique.* IEEE Trans. UFFC, 2006. **53**(1): p. 34-38.
[10] Riddle, B., J. Baker-Jarvis, and J. Krupka, *Complex permittivity measurement of common plastics over variable temperatures.* IEEE Trans. MTT, 2003. **51**: p. 727-733.
[11] Tobar, M.E. and A.G. Mann, *Resonant frequencies of high order modes in cylindrical anisotropic dielectric resonators*. IEEE Trans. on MTT, 1991. **39**(12): p. 2077-2083.
[12] Tobar, M.E., et al., *Spherical Bragg Reflector Resonators*. IEEE Trans. UFFC, 2004. **51**(9): p. 1054-1059.
[13] Krupka, J., et al., *Extremely High-Q Factor Dielectric Resonators for Millimeter-Wave Applications.* IEEE Trans. MTT, 2005. **53**(2): p. 702-712.

Proceedings of the 20th EFTF, 2006

Piezoelectric thin film micromachined resonator at MHz applications

* T. T. Le[a,b], L. Valbin[b], F. Verjus[a] and T. Bourouina[b]
[a]*Philips Semiconductors, SiP Program, 14079 Caen, France.*
[b]*ESIEE-ESYCOM, 93160 Noisy-le-Grand, France.*
**Electronic address:* let@esiee.fr

This work investigates the Thin Film Bulk Acoustic Resonator operating at low frequencies. This study aims to substitute quartz resonators in the 4-27 MHz band and to fabricate selective filter for frequencies lower than 250MHz with quality factor higher than 10000 within Philips. In this paper, we present the design and fabrication of two different types of resonator. It consists of aluminum nitride film sandwiched between two aluminum electrodes. The first resonator is made by clamped edge beam and the second one is a free-free beam construction anchored in the middle of the cantilever. A demonstrator was achieved and the resonators are manufactured on a silicon substrate; AlN and Al layers were deposited on silicon using standard DC sputtering technology. Only the first types of resonator have been tested and they operate in extensional mode and the thicknesses of each of the materials are lower than 1µm. ANSYS, a Finite Element Analysis software, has been performed to simulate the static, modal and harmonic behaviour. The simulation has been used, on the one hand, to determine the resonators length so as to reach the desired frequency range, on the other hand, to compare theoretical and experimental frequency values. First resonant frequencies between 2 and 10MHz were measured for resonators with dimensions of 20-40µm wide and 200-1000µm long and were found close to theory. Quality factor up to 3000 operating in air has been achieved. These results confirm that such an integrated solution will replace Quartz oscillators and/or Surface Acoustic Wave filters in very compact applications.

1. INTRODUCTION

Since few years, the MEMS technology for microwave applications has grown up with the potential to improve the circuits and device performances. Several components were designed and demonstrated an important reduction of loss and a higher linearity than their main counterparts: the semi-conductor components. Currently, we can distinguish several categories of components and circuits resulting from this technology, for example: micro-switches, variable capacitors, and circuits on dielectric diaphragms, micromachined inductors and resonators. Very compact and with high-performance, these devices have a strong potential. They form a new generation of radio frequencies components (RF). They will increase the performances of the systems to which they will be embedded. In the literature, there exists a lot of Film Bulk Acoustic Resonators (FBAR) functioning in the Giga-Hertz frequency range. This work investigates the Thin Film Bulk Acoustic Resonator (TFBAR) operating at Mega-Hertz frequency band. The purpose of this study is to substitute quartz resonators in the 4-27 MHz band and to achieve selective filter for frequencies lower than 250MHz with quality factor higher than 10000. TFBAR has advantages of small size, low power, low insertion loss, band pass filter with high frequency, and wide and selective bandwidth [1-4].
In this paper, we address the design and fabrication of two different types of micro machined piezoelectric bulk acoustic resonator, and only the first types of resonator have been tested. They consist of an AlN film sandwiched between two Al electrodes on a silicon substrate.

II. DESIGN RULE, MODELING AND ANALYSIS

The commonly available piezoelectric materials for Bulk Acoustic Wave (BAW) devices are lead zirconate titanate (PZT), aluminum nitride (AlN) and zinc oxide (ZnO). AlN, especially, does not have lead, which performs the recombination centre of the carriers such as zinc of ZnO. Hence, AlN is attractive for the CMOS integration and moreover it is an excellent material for small to medium bandwidth filters (bandwidth <5%) [5]. In addition, AlN film has several other advantages such as high breakdown voltages and low dielectric loss.
Two types of resonator were fabricated by using 2 mask designs: the first resonator (figure 1) is made by clamped edge beam and the second one (figure 2) is a free-free beam construction anchored in the middle of

the cantilever. Each beam is made by multilayers: Al / AlN / Al.

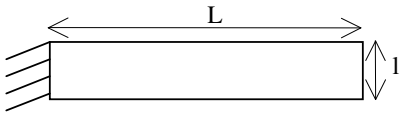

Figure 1: Schematic top view (configuration 1)

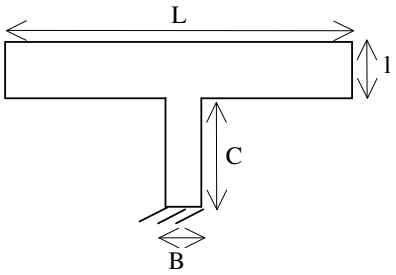

Figure 2: Schematic top view (configuration 2)

Dimensions of the masks (top electrode) and thin film thickness are respectively given in table 1 and table 2. Indeed, the design rules impose alignment errors of 3 µm between 2 layers.

Dimensions (µm)	Configuration 1	Configuration 2
l	20-400	20
L	50-1000	50-350
C		34
B		10

Table 1: Top layer dimensions of resonators

Thickness (µm)	Configuration 1			Configuration 2	
	a	b	c	a	b
AlN	0.8	0.8	0.9	0.8	0.8
Top electrode (Al)	0.2 or 0.24	0.2 or 0.24	1	0.2 or 0.24	0.2 or 0.24
Bottom electrode (Al)	0.2	0.2 + 0.78	0.2	0.2	0.2 + 0.78

Table 2: Materials thickness used for the manufacturing of the resonators (according to simulations)

A finite element static analysis of the structures was started in ANSYS. The model consists of the resonator beam, which is constituted by aluminum nitride sandwiched between 2 aluminum electrodes. ANSYS version 8.1 (ANSYS, Inc., Canonsburg, PA) was used to perform the necessary 3-dimensional (3D) finite element simulations. The 3D simulations made use of the 8-node, hexahedral, linear, coupled-field element SOLID5 supplied in ANSYS for the piezoelectric materials and the 8-node, linear, structural element SOLID45 for the non-piezoelectric materials.

The material properties used in the model are listed in table 3. The modal analysis supplied the eigen modes and the harmonic analysis provided the electric resonance of the resonators. Simulations showed for obtaining the desired frequency band for the selected dimensions of the resonators, it was necessary to work in extensional mode and not in flexional mode. Indeed, in flexional mode, the resonators had a resonant frequency below the MHz (around a hundred of KHz). So, in our study, the resonators work in extensional mode (figure 3).

Materials	Coefficients		Units
AlN	Elasticity	c_{11}	345 GPa
		c_{12}	125 GPa
		c_{13}	120 GPa
		c_{33}	395 GPa
		c_{44}	118 GPa
		c_{66}	110 GPa
	Piezoelectric	e_{31}	-0.58 C/m^2
		e_{33}	1.55 C/m^2
		e_{24}	-0.48 C/m^2
	Relative permittivity	ε_{11}	8
		ε_{33}	9.5
	Density	ρ	3260 kg/m^3
Al	Young modulus	E	70.3 GPa
	Poisson's ratio	υ	0.345
	Density	ρ	2690 kg/m^3

Table 3: Materials properties of aluminum nitride [6] and aluminum [7] used in the ANSYS model

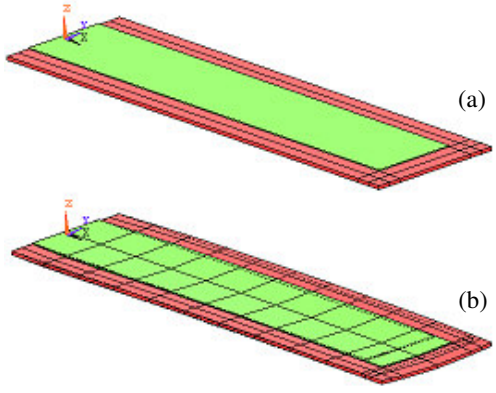

Figure 3: Configuration 1
a) initial state
b) deformed state

Since the design rules impose the geometry of the lower layer always higher than the upper layer, the resonators will behave like a bimetallic strip and thus will bend downwards. According to simulations, in order to enhance the extensional mode, it is necessary that the thickness of AlN is larger than the thickness of the electrodes and it is equally important to compensate the thickness of the top electrode compared with the bottom electrode. The selected values are indicated in table 2.
Resonant frequency values obtained from the harmonic analysis give the plot of first resonant frequency versus length of resonator for configuration 1. From the obtained curve, resulting equation has been written, which will help in approximate dimensioning of the resonators at the time of their fabrication.
Figure 4 represents the plot of resonance frequency versus the reciprocal length of the resonator obtained with ANSYS. The electrode width is fixed at 20 µm, the AlN thickness at 0.8 µm, the top and bottom electrodes thickness are 0.24 and 0.2 µm respectively, and the length varies from 50 to 500 µm.

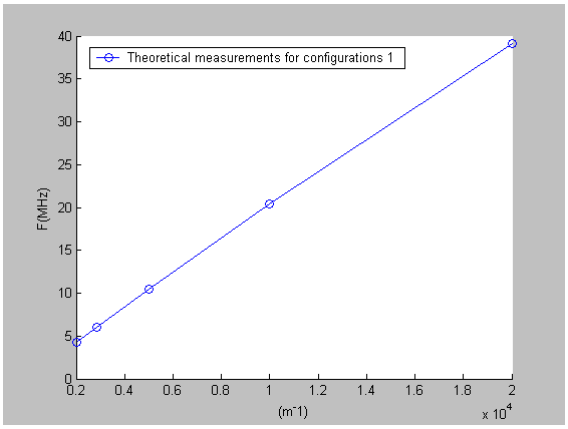

Figure 4: Resonant frequency versus reciprocal length of resonator

From figure 4, the equation relating the frequency and length of the resonators has been written and the following relation has been deduced:

$$f_1 = 1{,}9.10^{-3}\left(\frac{1}{L}\right) + 810.10^{-3} \quad (MHz) \qquad (1)$$

With f in MHz and L in µm.

This theoretical model gives dimensions of the resonators for obtaining the desired resonant frequencies. Devices working between 4 and 27MHz, and above can be realized.

Electrical analysis using ANSYS has been performed. Figure 5 shows current depending on electrical frequency for a constant electrical polarization. Electrical resonant frequency corresponding to mechanical one has been demonstrated.

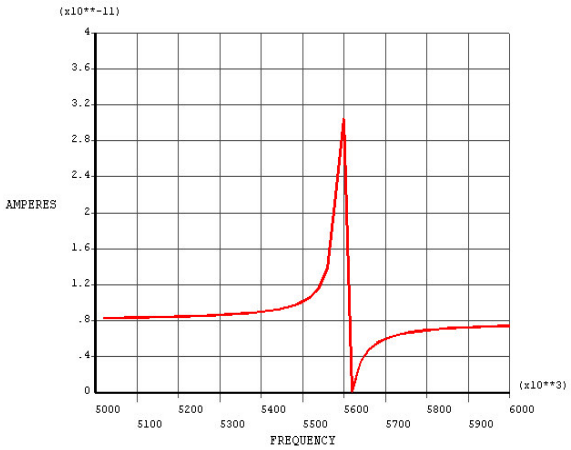

Figure 5: Theoretical response of 350 µm long resonator with ANSYS (configuration 1c).

At resonant frequency, resonator can be represented by the equivalent electrical circuit as shown in figure 6.

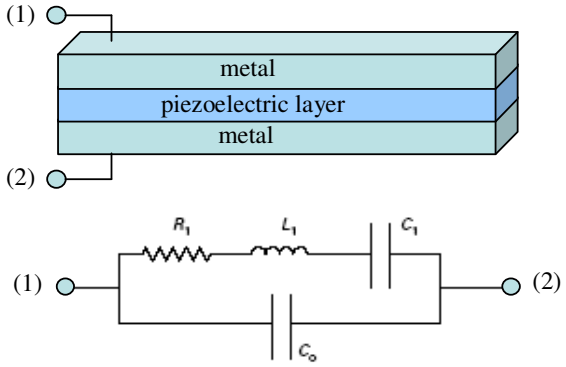

Figure 6: Schematic resonator and equivalent electrical circuit at resonant frequency.

- C_0 represents the static capacitance of the piezoelectric layer,
- C_1 and L_1 depend on the geometry and the parameters of the materials constituting the resonator,
- R_1 represents the mechanical losses of the resonator.

III. FABRICATION

Micromachined demonstrators were achieved and they were fabricated on oxidized silicon (Si) substrate. AlN and Al layers were deposited on silicon using DC sputtering technology.

Micromachined resonators using Al / AlN / Al cantilever were fabricated. Double-side polished, 100 mm in diameter by 500 µm thick wafers were used. Wafers were oxidized and back side oxide was removed. To minimize resistance access and to fabricate asymmetric and symmetric cantilever, first metal layer (0.8 µm Al) was deposited by DC sputtering and patterned by photolithography. Bottom electrode (0.2 µm Al) was deposited by DC sputtering and patterned by photolithography. Piezoelectric layer (0.9 µm AlN) was deposited by DC reactive sputtering and patterned by photolithography. Top electrode (0.2 µm Al) was deposited by DC sputtering and patterned by photolithography. Al was deposited on back side and patterned by photolithography then silicon back side is etched by deep reactive ion etching (Bosch process, etch rate: 7.5 µm/min). Then oxide was etched by Buffered HF / acetic acid mixed solution.
Figure 7 shows SEM view of resonator with the probe contact pads. Figure 8 shows the major fabrication steps to form the resonators.

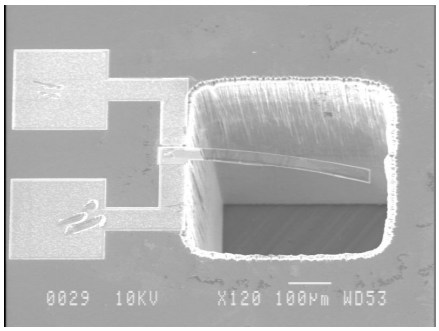

Figure 7: SEM view of resonator (Configuration 1)

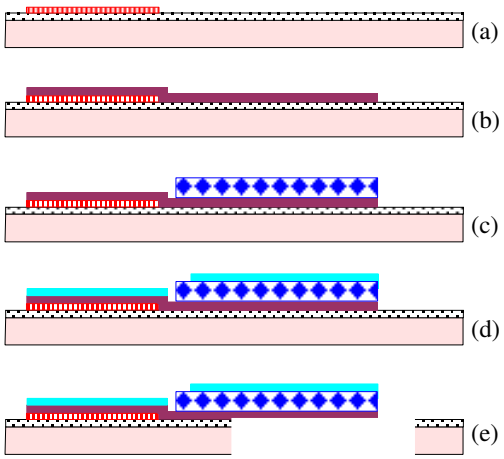

Figure 8: Fabrication process flow for the resonators on Si substrate.

(a).Patterning of the access lines and contact pads by photolithography and dry etching of Al.

(b).Patterning of the bottom electrode by photolithography and dry etching of Al.

(c).Patterning of AlN by photolithography and wet etching of AlN.

(d).Patterning of the top electrode by photolithography and dry etching of Al.

(e).Backside DRIE of Si and SiO_2 wet etching.

IV. EXPERIMENTAL RESULTS

Admittance of micromachined resonators (configuration 1) was measured in air, using an HP4194A LCR-meter and the experimental curves were plotted using LabVIEW 6.1 via GPIB bus (or IEEE 488 bus). Resonant frequencies between 2 MHz and 10 MHz and quality factors up to 3000 in air were observed.
Figure 9 shows the module and phase of admittance taken from LabVIEW for a 350 µm long, 20 µm wide clamped edge beam resonator (configuration 1c). This MEMS resonator has a resonant frequency of 5.137 MHz, anti-resonant frequency of 5.154 MHz, a quality factor of 97 in air and an electromechanical coupling of 0.8%. Low Q factor is due to high resistance value due to low AlN crystallinity.
Table 4 shows the equivalent electrical circuit values for resonator measured in figure 9.

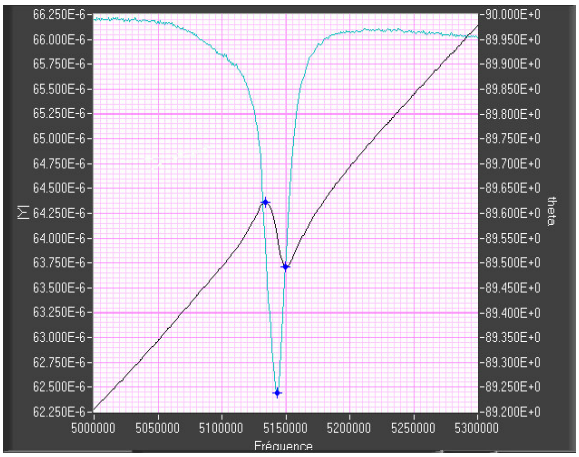

Figure 9: Measured admittance of 350 µm long resonator in air

(f_r =5.137 MHz, f_a =5.154 MHz, Q =97, K^2 = 0.8%)

Elements	Values
R_1 (KΩ)	879
L_1 (H)	2.63
C_1 (aF)	363
C_0 (pF)	2.03

Table 4: Equivalent electrical circuit values

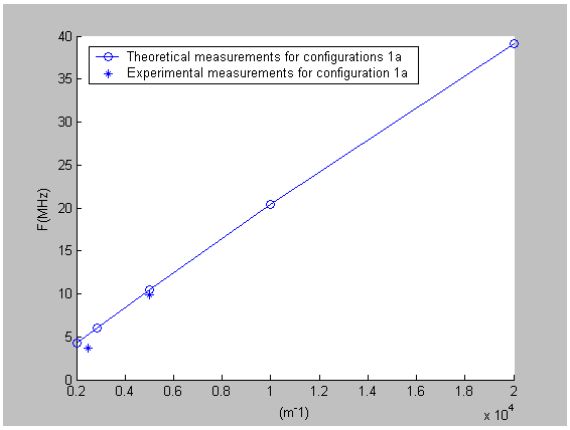

Figure 10: Resonant frequency versus reciprocal length of resonator (configuration 1a)

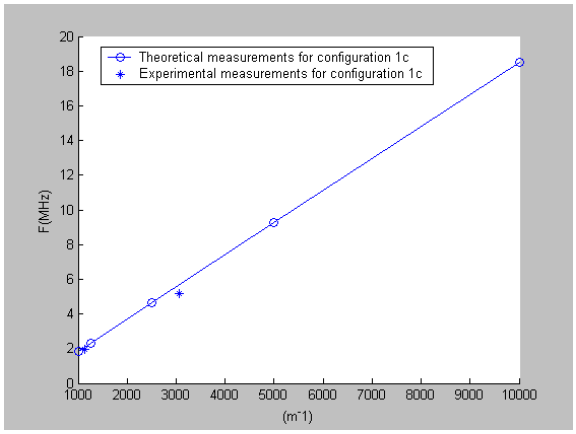

Figure 11: Resonant frequency versus reciprocal length of resonator (configuration 1c)

Figures 10 and 11 show the measured and theoretical resonant frequencies versus reciprocal beam length. Well match between theory and measurement has been found.

The first measurements using a laser Doppler vibrometer (Politec OFV 3001) have shown flexural mode for our resonators, but these modes don't induce electrical resonant frequencies. Some works are in hand to determine the reason of this phenomenon.

V. CONCLUSION

Bulk micromachined piezoelectric resonators employing AlN active films with clamped edge beam geometries and free-free beam construction anchored in the middle of the cantilever geometries have been designed and fabricated. In this study, only devices for configuration 1 have been measured. Resonant frequencies ranging from 2 MHz to 10 MHz were observed, and the overall performance of the resonators was lower than expected, with quality factors up to 3000 in air and with a phase lag ranging of 1° to 12° only. Resonant frequencies higher than 15 MHz were not observed due to the frequency limitation of the HP4194A LCR-meter.

By using the laser Doppler vibrometer (Politec OFV 3001) we have observed flexural mode and some works are in hand to determine why they didn't induce electrical resonant frequencies.

Process has to be improved to increase resonator quality factor by changing DC sputtering parameters for AlN deposition to improve its crystallinity and decrease mechanical and electrical losses.

However, the first measurements have shown that experimental resonant frequencies are close to modeled predictions, so the theoretical analysis can predict the dimensions of the resonators for obtaining the desired frequency.

First results show that bulk acoustic resonator in MHz range has been performed, working in plane extensional mode.

Acknowledgements

We would like to thank Frederic Marty from ESIEE-SMM for DRIE process.

REFERENCES

[1] K.M. Lakin, Modeling of thin film resonators and filters. Microwave Symposium Digest, IEEE MTT-S International, p.149–152, 1992.
[2] K.M. Lakin, G.R. Kline, K.T. McCarron. High-Q microwave acoustic resonators and filters. IEEE Trans Microwave Theory Tech; vol.41 (12): p.2139–2146, 1993.
[3] K.M. Lakin, G.R. Kline, K.T. McCarron. Development of miniature filters for wireless applications. IEEE Trans Microwave Theory Tech; vol.43 (12): p.2933–2939, 1995.
[4] S. Horwitz, C. Milton. Application of film bulk acoustic resonators. Microwave Symposium Digest, IEEE MTT-S International, vol.1: p.165-168, 1992.
[5] IEEE Standard on Piezoelectricity, American Institute of Standards Std., p.176, 1987.
[6] L. Valbin, Elaboration de couches minces de nitrure d'aluminum par pulvérisation cathodique pour la réalisation de micro-transducteurs ultrasonores, Ph.D. thesis, Université de Paris VII, 2004.
[7] ANSYS 8.1 program examples, VM176 input listing.

Proceedings of the 20th EFTF, 2006

HIGH FREQUENCY BULK ACOUSTIC WAVE RESONATOR USING THINNED MONOCRYSTALLINE LITHIUM NIOBATE

D. GACHON,* G. LENGAIGNE, S. BENCHABANE, H. MAJJAD, S. BALLANDRAS, and V. LAUDE
FEMTO-ST Institute 32, avenue de l'Observatoire 25044 Besançon France

During the last years, bulk acoustic waves excited in thin piezoelectric films have revealed their capabilities for addressing the problem of high frequency RF filters (above 1 GHz). Sputtered films such as aluminum nitride (AlN) or zinc oxyde (ZnO) are generally used in that purpose. In this paper, we propose an alternative to thin film deposition in which single crystal wafers bonded on a substrate (for instance silicon or glass) are thinned, allowing for a plate thickness close to 10μm. This can be achieved on 4 inches wafers and significantly allows for an accurate selection of the wave characteristics. Furthermore, the properties of the piezoelectric material are found to agree with tabulated values, enabling one to reliably design filters and more generally any passive signal processing device.

I. INTRODUCTION

Thin film bulk acoustic wave resonator (FBAR) [1] is a promising modern technology for the production of radio frequency (RF) resonators and filters [2]. FBARs exploit the thickness-extensional vibration modes of thin piezoelectric films with thicknesses of a few microns, yielding fundamental resonance frequencies in the GHz range. The piezoelectric thin films used to excite and detect waves are generally deposited by sputtering with their C axis normal to the wafer surface. This fabrication process results in limited Q factors, usually on the order of a few hundreds, which in turn sets limitations on their use as resonators for time and frequency applications. In view of improving over the Q factor of thin films, it is desirable to use single-crystal piezoelectric materials such as lithium niobate, lithium tantalate, langasite or quartz. This also will allow for the selection of any kind of polarization (longitudinal or shear modes) with properties adapted to the application (for instance, low thermal sensitivity).

This paper describes a new fabrication method to achieve high frequency acoustoelectric resonators. It is well known that the intrinsic losses of single crystal materials are much smaller than those of sputtered thin films. In addition, the material cut can be chosen to optimize such parameters as the coupling factor or the temperature dependence. Single-crystal piezoelectric materials however are not usually available under the form of thin wafers (i.e. with thicknesses smaller than 100 μm). We have developed a process for the fabrication of high quality piezoelectric films of intermediate thickness (between 50 and 10 μm) for bulk acoustic wave (BAW) resonator and filter applications. A piezoelectric wafer first is bonded onto a substrate (glass or silicon) using a thin resist layer (SU8) with a thickness of 5 to 1 microns using a dedicated facility. It is subsequently thinned by lapping and micro-polishing to control the final thickness. The final resonator thickness ranges between 10 to 20 microns at the end of the process. The fundamental frequency is then above 200 MHz but higher harmonics can be used thanks to the high coupling factor of the fundamental mode on (YXl)/36° lithium niobate cut.

In the first section of the paper, the typical longitudinal mode properties on (YXl)/36° lithium niobate are summarized, and the fabrication process is detailed. The second part of the paper discusses electrical measurements of the resonators and characterization results, with a particular emphasis on the electromechanical coupling and the Q factor of the different harmonics. As a conclusion, we propose some directions for improving our devices and to achieve thinner devices.

II. DESIGN AND FABRICATION

Lithium niobate was chosen because of its strong piezoelectric coupling properties. The (YXl)/36° lithium niobate orientation is well-known from the acoustic transducers community because of the very large electromechanical coupling factor for the longitudinal mode, compatible with acoustic imaging purposes [3]. Moreover, only this mode is coupled on this particular cut, yielding no parasitic signals due to unwanted shear wave excitation. The exploited mode then corresponds to a purely longitudinal polarization with a wave velocity of 7338 m.s^1 and an electromechanical coupling factor K_s^2 in the vicinity of 23%, i.e. largely above what can be obtained with sputtered films (6 to 8% are usually obtained with ZnO or AlN in the best cases [4]).

The resonator consists in a simple air backed structure, with the piezoelectric plate metallized on both sides. It is a square shaped membrane with typical length of 700 μm. To avoid machining the niobate plate after the thinning process to access the backside electrode, we have chosen a serial resonator architecture in which the backside electrode is at a floating

*Electronic address: dorian.gachon@femto-st.fr

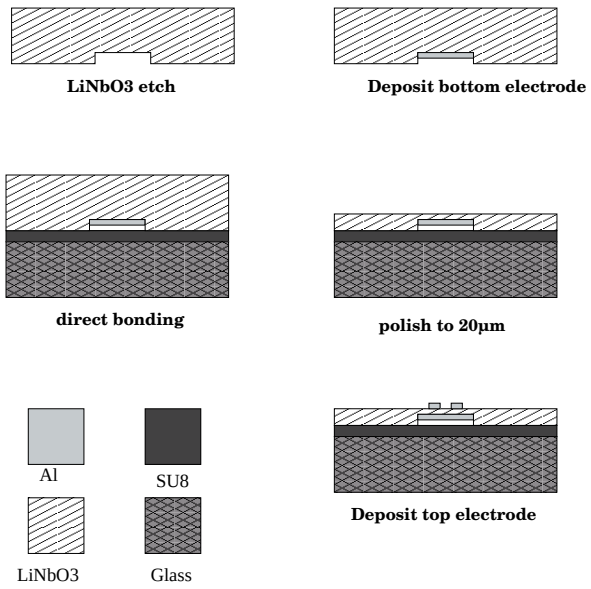

FIG. 1: Micro fabrication process flow.

potential and contacts can be taken at the upper surface. Different locations and shapes of the top electrodes have been tested to try and evaluate the influence of unwanted flexural modes. Figure 1 shows the flow chart developed for the fabrication of the resonators.

Since the lithium niobate plate is bonded onto a glass substrate, the backside air gap must be manufactured first. We start by etching the back side of a (YXl)/36° lithium niobate wafer using a reactive ion etching (RIE) process along a depth of 10 microns. To achieve a high etching selectivity, we use an electroplated Nickel mask, allowing for thick masking layers which exhibit a good robustness to the etching process. Aluminum electrodes are then deposited at the bottom of the etched hole. The lithium niobate wafer is then bonded onto a glass substrate using a thin resist layer (SU8) with a thickness of 5 to 1 microns (the thickness is controlled by the spin speed and by the initial viscosity of the resist) into an EVG wafer bonding machine. During the bonding process, we heat the material stack at a temperature of 60 K and we apply a pressure of 10 kg.cm^{-2} to the whole contact surface. This process yields an homogeneous and high quality bond as shown in Figure2(a). It is subsequently thinned by a lapping step to an overall thickness of 20 to 30 microns. It is then followed by a micro-polishing step, yielding a final $LiNbO_3$ thickness ranging between 10 to 20 microns. Figure 2(b) shows a detail of one membrane close to its embedment on the glass wafer, emphasizing the quality of the gap (no bond defect can be observed at the membranes bounds). The niobate plate still could be lowered by a second RIE etching of the whole top side of wafer. Finally, the two topside Aluminum electrodes

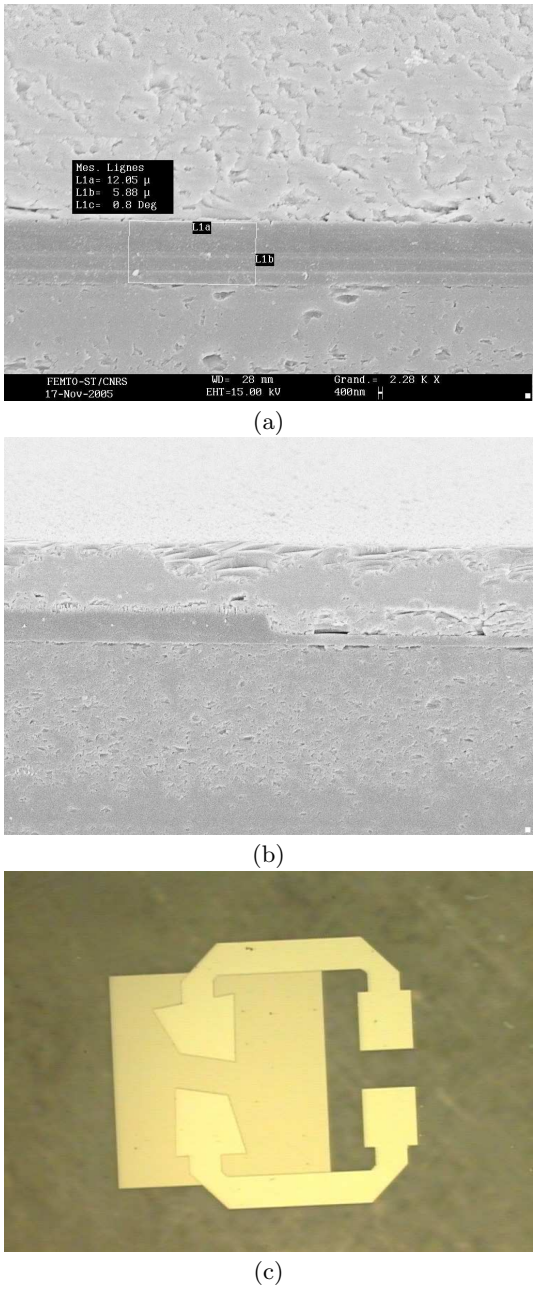

(a)

(b)

(c)

FIG. 2: (a) Detail of the SU-8 bond between glass and lithium niobate. (b) View of the membrane close to its embedment (no bond defects or unwanted gap filling can be observed). (c) One set of electrodes atop the LiNbO3 membrane (the backside electrode can be viewed by transparence).

are deposited on the LiNbO3 membranes as shown in Figure 2(c) to achieve two series-connected resonators for test.

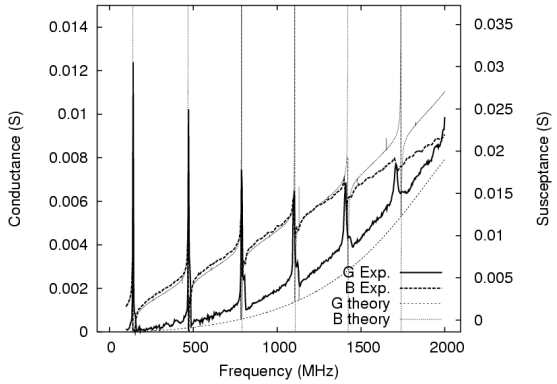

FIG. 3: Comparison of an experimental measurement with the theoretical prediction of the electrical response of the resonator.

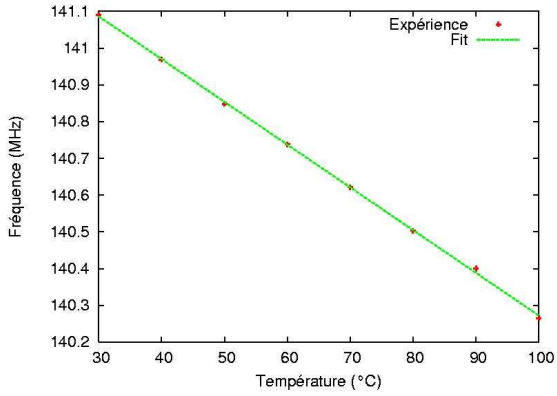

FIG. 4: The drift thermal is linear for the fundamental mode with a slope around 85 ppm/K.

III. EXPERIMENTAL RESULTS

The admittance of the resonators was measured for different membrane thickness in the vicinity of 20μm. A Süss Microtec PM-5 RF prober combined with a Rhode Schwarz ZVC network analyzer were used to characterize the devices. A typical example of a resonator response is plotted in Figure 3, showing the dynamics of the resonance and more particularly the capability of the resonator to provide well defined high order harmonics contributions. This characteristics is mainly due to the very high electromechanical coupling of the fundamental mode.

Harmonics order up to ♯11 can be excited and measured. The experimental electromechanical coupling factors of the three first contribution (fundamental, harmonics ♯3 and ♯5, respectively) have been found to equal 18%, 5% and 1%. The theoretical predictions are in good agreemen with these results (20%, 3% and 0.9% are expected theoretically for the fundamental, harmonics ♯3 and ♯5, respectively).

A finer analysis of the harmonics ♯3 makes it possible to verify that a rather large quality factor (Q=6770) is found together with a large electromechanical coupling factor K_s^2=5%. These characteristics compare well in terms of quality factor with those that are classically observed with resonators operating at higher harmonic modes (HBAR or overmoded FBAR), but with an increased electromechanical coupling factor. Clearly, it will be important to modify the electrodes design of the resonators to try and benefit fully from material quality factors higher than that of aluminum nitride. Lastly, we characterized the temperature sensitivity of the fundamental mode of the resonators (thickness 25μm, fundamental at 140 MHz). We found a thermal drift around 85 ppm/K (see Figure 6), in coherence with the data published on longitudinal bulk waves in lithium niobate. This rather strong drift encourages to seek temperature compensation solutions in applications. Let us finally note that the higher harmonic modes follow the same frequency-temperature law as the fundamental mode.

IV. CONCLUSION

This paper has presented a new design aspect for Film Bulk Acoustic Resonators fabrication. The wafer bonding with SU8 layer and the micropolishing offers a pratical mean of performing high frequency resonators. The results show the capability of the resonator to provide well defined high order harmonics contribution.

Acknowledgments

This work is supported by the Centre National d'Etudes Spatiales (CNES) under grant ♯04/$CNES$/1941/00−DCT094, and by the Direction Générale de l'Armement under grant 05.34.016.

[1] K. M. Lakin, G. R. Kline, R .S. Ketcham, A. R. Landin, W. A. Burkland, K. T. McCarron, S. D. Braymen, and S. G Burns, "Thin film resonator technology," IEEE International Frequency Control Symposium, 371 (1987).

[2] G. J. Coussot, "Bulk wave resonator for the 100-300 MHz frequency range," IEEE Ultrasonics and Frequency Control Symposium, 590 (1974).

[3] M. I. Grace, R. W. Kedzie, M. Kestigian, and A. B. Smith, "Elastic Wave Attenuation In Lithium Niobate," Applied Physics Letters **9** (4), 155 (1966).

[4] M.-A. Dubois, "Thin film bulk acoustic resonators: a technology overview," fourth workshop on MEMS for millimeter wave communications (2003).

Proceedings of the 20th EFTF, 2006

Semi Analytical Modelling of Thermosensitive Strip Resonators

B. Dulmet[1],* Yu. Lazarov, and L. Spassov [2]
[1] *FEMTO-ST, Dpt LCEP, ENSMM 26 Chemin de l'Epitaphe, 25000 Besançon cedex, France*
[2] *ISSP-BAS, AELab, 72 Tzarigradsko Blvd., Sofia, Bulgaria*

The goal of this research is to provide some tools to approximately determine the main parameters and the operating range of resonant sensors relying on strip resonators, and thereby to help in guiding associated and still necessary FEA analysis.

First, recent improvements of a previously presented two-dimensional semi-analytical model for strip resonators are presented. They namely consist of extending the number of branches used in the variational treatment of boundary conditions at the edges of the narrow strip, and of introducing piezoelectricity into the determination of the dispersion curves in the (x_1, x_2) cross section of strip. Thereafter, the paper briefly proposes an extension of this model in 3-D whereas its final section discusses issues concerning further improvements such as accuracy refinements and the introduction of Lagrangian formalism to take temperature sensitivity into account.

I. INTRODUCTION

The development of new miniature quartz thermometers consisting of strip-resonators in NLC-cut, which was performed during QxSens EU contract from program GROWTH [1], has shown that optimal dimensions of resonators must be theoretically estimated to achieve good electrical parameters and to control the occurrence of activity dips over the desired temperature range, namely 4.5-400K. Although this requirement was fulfilled by finite element analysis, it was found extremely useful to associate accurate but time–consuming FEA simulations with a specific analytical model. This permits to quickly determine the minimal mesh density along the width of strip to grant convergence of FEA for the targeted resonant modes. Moreover, since the results of FEA simulations are not self–explanatory, an additional work of a different nature is clearly welcome to provide with a more definite identification and understanding of the spurious modes which must be kept away from the main one throughout the whole desired temperature range.

First, we present latest improvements achieved in the develoment of our two–dimensional semi–analytical approach of moderately narrow strip resonators. In that case, the resonant modes which are actually usable for metrological application are combinations of guided waves belonging to separate branches of the dispersion curves in the (x_1, x_2) sagittal plane. As a rule, the weights of the combination are determined from a variational procedure which derives from Hamilton's principle and is applied to the treatment of boundary conditions at the edges of resonators. Such branches can be accurately determined in any crystal cut. This analysis holds if we put aside the x_3 behavior of modes, due to the expectedly small value of x_3 component of wave vector as a result of the specific geometry of resonator. Clearly, this approach leads to approximate solutions of the rigorous and complete two–dimensional equations. At this stage it has to be shown that an approximate three–dimensional analysis can be established from that starting point. Such an extension seems much easier whenever that some separation of variables along x_2 and x_3 is a sensible assumption for the resonant modes of strip. Here–proposed approach essentially differs from Mindlin's method [2], largely used in that field, since the latter one eliminates the x_3 variable by means of an expansion of three–dimensional equations into an infinite series of two–dimensional plate equations, which may lost their completion because of the necessary series truncation.

Immediate improvements are achieved by introducing piezoelectric effect and by adding imaginary branches of the dispersion curves into the treatment. Since there are an infinity of imaginary branches, it is necessary to determine how the number of incorporated branches impacts onto the results of the 2-D analysis.

Thereafter, we shortly present the ongoing work aimed to extend the semi analytical approach in three–dimensional to account for the trapped energy behavior of the essentially thickness shear component of the resonant modes along the length of the strip resonator. Thus, we show the basics of a three–dimensional semi–analytic model of strip resonators in terms of well established geometric and material parameters. Such model is intended as an alternative to the previous model of Tiersten and Sham [3] which essentially relies on Mindlin's plate theory.

Further improvements to embed static temperature dependence into the model are highly desirable and can be achieved by including the use of Lagrangian material constants in the approach. Related issues are shortly discussed in the last section of paper.

*Electronic address: bernard.dulmet@en2m.fr

II. THE NLC-CUT STRIP RESONATOR

The NLC–cut chosen for the thermosensitive strip sensors is a $Y+\theta$ singly–roated cut with $\theta = -31.5$.

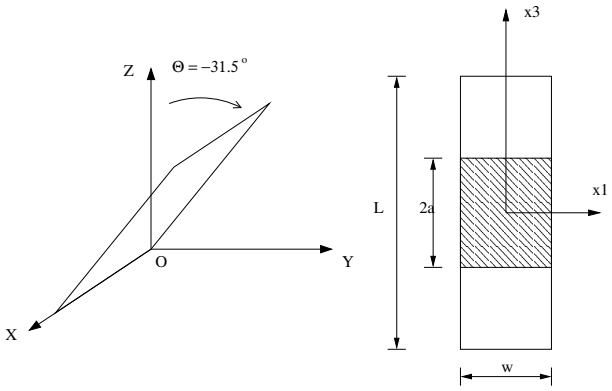

FIG. 1: Basic configuration of NLC strip resonator.

Unless otherwise specified, we take the following default values of parameters in this paper :

- thickness $t = 2h = 82\,\mu m$,
- electrode length $2a = 2\,mm$,
- electrode thickness $160\,nm$ (silver).
- width to thickness ratio $w/t \approx 24.808$,
- length of strip $L = 5\,mm$.

III. GUIDED AND STEADY STATE WAVES IN (x_1, x_2) CROSS SECTION

Since the theory is rather well–known and was extensively used in Refs. [1], we just summarize it before giving details about recent improvements. The basic step consists in determining so–called branches of dispersion curves, satisfying the elasticity equations as well as the boundary conditions on supposedly free major surfaces of the plate, located at $x_2 = \pm h$, under the assumption $\partial/\partial x_3 \equiv 0$. The branches of interest for here–considered problems take the following form

$$\begin{aligned} u_1 &= \left(\textstyle\sum_{n=1}^{3} C_n \alpha_1^n \sin \eta_n x_2\right) \cos \xi x_1 e^{-i\omega t} \\ u_2 &= \left(\textstyle\sum_{n=1}^{3} C_n \alpha_2^n \cos \eta_n x_2\right) \cos \xi x_1 e^{-i\omega t} \\ u_3 &= \left(\textstyle\sum_{n=1}^{3} C_n \alpha_3^n \cos \eta_n x_2\right) \cos \xi x_1 e^{-i\omega t} \end{aligned} \qquad (1)$$

The products represent partial waves, characterized by a vertical wavenumber η_n which can be determined as a function of the lateral wavenumber ξ and ω. Then, all amplitude factor α_k^n can be computed and put in a normalized form. The respective weights of partial waves for a given branch are given by the C_n constants which can be determined (also in a normalized form) from the boundary conditions :

$$T_{2j}(x_2 = \pm h) = 0, \qquad \forall j \in [1-3]$$

Then the basic dispersion curves of Fig. 2 are obtained in terms of dimensionless variables :

$$\Omega = \frac{\omega}{\omega^0_{B_1}} \quad \text{and} \quad \gamma = \frac{\xi}{\eta^0_{B_1}}$$

where the subscript B_1 indicates values for the fundamental branch of pure shear u_1 obtained as B mode in NLC-cut, and the superscript ^{0} indicates a zero value of lateral wavenumber ξ.

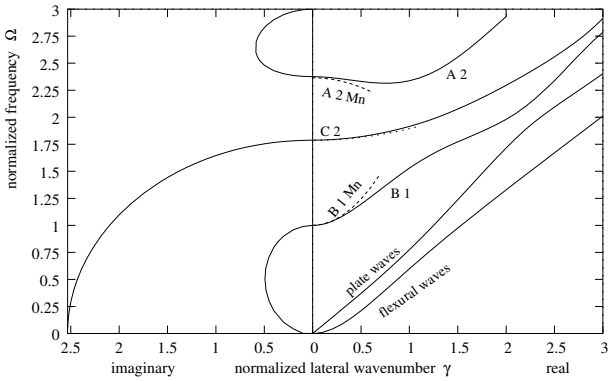

FIG. 2: Basic dispersion curves $\Omega(\gamma)$ in (x_1, x_2) cross section.

The edge boundary conditions are treated in the next step [1] by using a variational formulation in strong form consistent with Hamilton's principle [5] :

$$\int_{t_0}^{t_1} \left\{ \int_V (T_{ij,j} - \rho \ddot{u}_j)\, \delta u_j \, dV - \int_S (f_i - n_j T_{ij})\, \delta u_i dS \right\} dt = 0 \qquad (2)$$

although the principle is more often presented in the so–called weak form, for instance in the development of FEA method.

The general solution of problem is searched as a combination of branches of the dispersion curves, and one uses the variational equation to find the better combination to minimize the error in the part of surface integral in (2) which corresponds to the edges at $x_1 = \pm w/2$. By the way, all other integral terms vanish since the branch exactly satisfies elasticity equations and the boundary conditions on major surfaces at $x_2 = \pm h$. It has been shown in [1] how the variational equation turns into a system of which the unknowns are the weights of each branch into the combination. By zeroing the determinant of that system, one obtains discrete roots in terms of ω and all necessary quantities to describe the solution of problem. Since there is only one ω in the resonator, the coupling

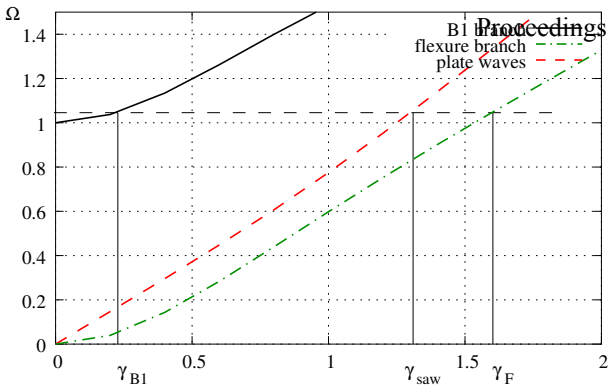

FIG. 3: Influence of ν_{B_1} onto the edge boundary conditions at $x_1 = \pm w/2$.

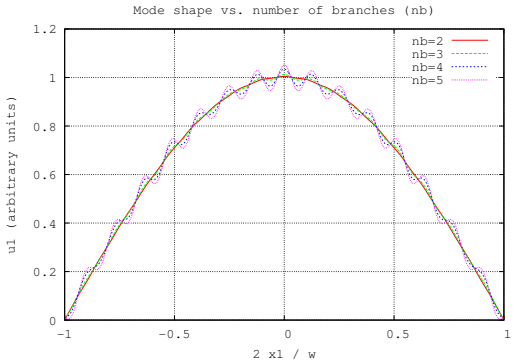

FIG. 4: Amplitude distribution along cross section for $w/t = 24.808$, (from 2 to 5 branches).

mechanism between B_1 branch and other branches illustrated by Fig. 3 results into u_1 amplitude distributions such as the ones represented onto Fig. 4. The rate of modulation reveals the contribution of branches other than quasi–thickness shear, and strip resonators usable for metrological use are obtained by chosing $w/2h$ ratios which minimize the contribution of the other branches.

Nevertheless, in some cases, the model predicted amplitude distributions much smoother (almost no modulation) in comparison with FEA–predicted results. As a matter of fact, the earlier work [1] limited to 3 the number of branches, *i.e.* the branch B_1 for fundamental thickness shear, the flexural branch and the branch above flexure, which corresponds to surface waves in a semi–infinite medium, and which we denote here as "plate waves" branch. General plate waves degenerate into Lamb waves when their polarization remains in the sagittal plane, which does not happen in the present case. Performing some additonal programming effort, we could increase the number of branches up to 5, by taking into account the imaginary branches C_2, quite visible on Fig. 2, and C_4, not reproduced on Fig. 2, but nevertheless easily obtained. Since we observe a real wavenumber for essential branch B_1 in normal conditions of design, a circumstance which implies $\Omega > 1$, it is pointless to take into account the imaginary branch closest to the origin. Fig. 4 shows the influence of the number of branches onto the predicted mode shape. It is worth remarking that the number of imaginary branches is not limited in principle.

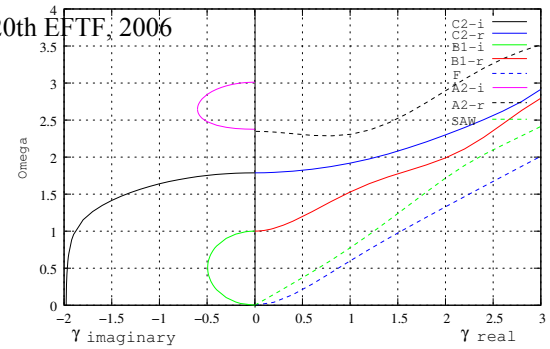

FIG. 5: NLC-cut dispersion curves in plane (x_1, x_2) with piezoelectric effect.

We have recently determined the dispersion curves with piezoelectric effect for this configuration. They are presented on Fig. 5. Their influence on the form of the curves is significant only for one imaginary branch, while it has the effect to lower the junction of essentially thickness branches with the Ω axis. However, the piezoelectric effect is not used in the further developments, otherwise than in analytical correction factors. However, we plan to take piezoelectric effect into account in further developments of here–presented model.

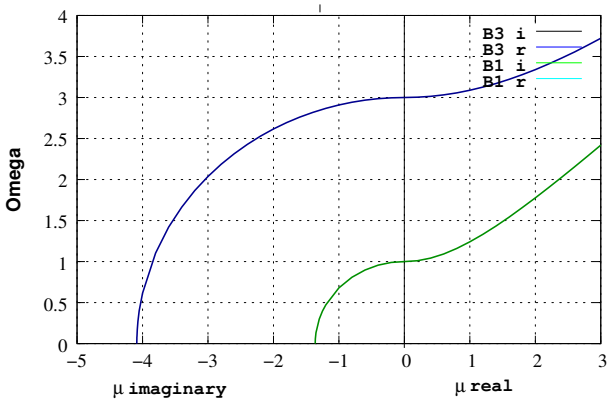

FIG. 6: Dispersion curve for B_1 and B_3 branches in (x_3, x_2) cross section.

IV. GUIDED AND STEADY STATE WAVES IN (x_3, x_2) CROSS SECTION

Let us investigate the behavior of the fundamental overtone modes of essentially thickness shear B_1 in case of propagation along x_3, under the assumption that $\partial/\partial x_1 \equiv 0$. Then, one can obtain the corresponding dispersion curves following an approach similar to the one of previous section. Nevertheless, there are some differences. Due to the particular symmetry level of $Y + \Theta$ cuts, u_1 for one hand, and (u_2, u_3) for another hand, are uncouples in the partial derivatives and boundary conditions on the major surfaces. Then, two problems can be solved independently. The first one concerns the shear horizontal SH waves, associated with the following kind of elementary waves :

$$\begin{aligned} u_1 &= \left(\sum_{n=1}^{2} A_n \cos \eta_n x_2 + B_n \sin \eta_n x_2 \right) e^{i\nu x_3}\, e^{-i\omega t} \\ \eta_2 &= \eta_1 + \frac{2c_{56}}{c_{66}}\,\nu, \quad A_2 = iB_2, \quad \text{and } A_1 = -iB_1 \\ u_2 &= u_3 = 0 \end{aligned} \tag{3}$$

while the second problem requires the following elementary waves polarized in the sagittal plane :

$$\begin{aligned} u_1 &= 0 \\ u_2 &= \left[\sum_{n=1}^{2} \beta_2^n \left(C_n \cos \eta_n x_2 + E_n \sin \eta_n x_2 \right) \right] e^{i\nu x_3}\, e^{-i\omega t} \\ u_3 &= \left[\sum_{n=1}^{2} \beta_3^n \left(D_n \cos \eta_n x_2 + F_n \sin \eta_n x_2 \right) \right] e^{i\nu x_3} e^{-i\omega t} \end{aligned} \tag{4}$$

where the weights of the partial waves in a given branch are fixed by the set of constants $(A_n, B_b, C_n, D_n$ and E_n while the normalized amplitude factors β_k^n give the respective weights of u_2 and u_3 in a given partial wave. The dispersion curves for branch B_1 and B_3 shown on Fig. 6 were obtained by repetition of the same procedure as in the previous section. On the figure, μ is the normalized lateral wavenumber along x_3 :

$$\mu = \frac{\nu}{\eta_{B_1}^0} \tag{5}$$

Still assuming $\partial/\partial x_1 \equiv 0$, a possible energy trapping behavior of the B_1 branch, arising from electrode mass loading and the field effect under the electrodes can readily be described in an analytical way. For the fundamental of B mode with transverse wave number $\xi = 0$, the resonant frequency can be easily obtained :

$$\rho \left(\omega_1^e\right)^2 \approx \frac{\pi^2 \bar{c}_{66}}{4h^2} \left(1 - \frac{8{k_{26}}^2}{\pi^2} - \frac{4\rho' h'}{\rho h} \right) = \frac{\pi^2 \hat{c}_{66}}{4h^2} \tag{6}$$

under the electrodes, and

$$\rho \left(\omega_1^f\right)^2 = \frac{\pi^2 \bar{c}_{66}}{4h^2} \tag{7}$$

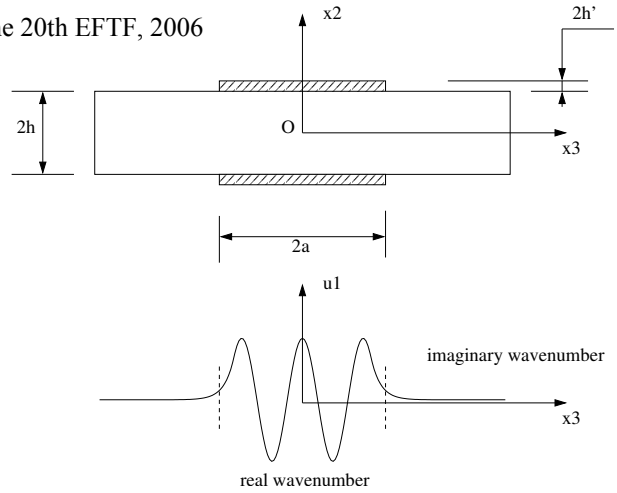

FIG. 7: Mechanism of energy trapping in (x_3, x_2) cross section.

outside them. The dispersion curves for electroded and unelectroded plates are quasi identical in the region $\nu \to 0$ and exhibit a parabolic behavior so that the B_1 branch can be accurately approximated by the following expansions

$$\left.\begin{aligned} \rho\omega^2 &= \rho \left(\omega_1^e\right)^2 + P_1 \nu^2 \text{ shortcut electrodes} \\ \rho\omega^2 &= \rho \left(\omega_1^f\right)^2 - P_1 \bar{\nu}^2 \qquad \text{outside them} \end{aligned}\right\} \tag{8}$$

where ν and $\bar{\nu}$ are both real and P_1 is a constant which can be either numerically derived by a fit of the branch at the junction with the Ω axis, or analytically obtained from Tiersten *et al.* well known papers [6, 7] of which other essential aspects will also be recalled in the next section. Then, we have

$$\left.\begin{aligned} u_1 &\approx A \cos(\nu x_3)\, \sin \frac{\pi x_2}{2h}\, e^{-i\omega t} \text{ under electrodes} \\ u_1 &\approx B \exp(-\bar{\nu} x_3)\, \sin \frac{\pi x_2}{2h}\, e^{-i\omega t} \quad \text{outside them} \end{aligned}\right\} \tag{9}$$

and we may limit the analysis to $x_3 > 0$ for simplicity : for $x_3 < 0$, we would have taken

$$u_1 \approx B \exp(+\nu \bar{x}_3) \sin \frac{\pi x_2}{2h} e^{-i\omega t}$$

outside electrodes. Thus, one can easily determine the distribution of vibration along x_3 shown on the Fig. 7. The frontier between electroded and unelectroded regions is located at $x_3 = a$. The displacement u_1 must be continuous $\forall x_2$ on that frontier because it must actually be continuous everywhere. The most important stress term concerned by the continuity is $T_5 = c_{55} u_{1,3} + c_{56} u_{1,2}$ if u_2 and u_3 are negligible w.r.t u_1 for that branch at small lateral wavenumbers, so that the continuity of T_6 and T_3 can be ignored in a first approximation. The continuity of $u_{1,2}$ at the border crossing automaticaly comes from the continuity

of u_1 since the same $\sin \pi x_2/2h$ thickness distribution is found on both sides of the border. As a consequence, the only stress continuity which one has to check out across the border is the one of $T_1 \approx c_{55} u_{1,3}$. In other words, u_1 and $u_{1,3}$ must be continuous across the border, which results into the following homogeneous system

$$A\cos(\nu a) - B\exp(-\bar{\nu} a) = 0$$

$$A\nu\sin(\nu a) - B\bar{\nu}\exp(-\bar{\nu} a) = 0$$

Equating to zero the determinant, one obtains a simple transcendental equation :

$$\nu \tan \nu a = \bar{\nu}$$

But ν and $\bar{\nu}$ are not independent since they are related by the two dispersion equations (8) respectively valid inside and outside the electroded region, where ω must be the same. After some algebric manipulations, one obtains

$$\nu \tan \nu a = \sqrt{\frac{\rho}{P_1}\left[(\omega_1^f)^2 - (\omega_1^e)^2\right] - \nu^2} \qquad (10)$$

or, equivalently by substituting (6) :

$$\nu \tan \nu a = \sqrt{\frac{1}{h^2}\left(2{k_{26}}^2 + \frac{\pi^2 \rho' h'}{\rho h}\right)\frac{\bar{c}_{66}}{P_1} - \nu^2} \qquad (11)$$

which can nearly instantaneously be solved numerically and leads to the determination of the resonant frequencies of anharmonic modes and of the corresponding u_1 amplitude distributions, such as the one schematically represented on Fig. 7.

V. AN APPROXIMATE THREE-DIMENSIONAL ANALYSIS

The developments of the two preceding sections are indeed mutually independent and can be used separately if the vibration is characterized by $\partial/\partial x_3 \equiv 0$ (Sec. III) or by $\partial/\partial x_1 \equiv 0$ (Sec. IV). In the circumstance, the 'or' has an exclusive meaning. Nevertheless, we can benefit from the work of Stevens and Tiersten [6], who have demonstrated that, for a cut of arbitrary symmetry, a general combination of partial waves of the following kind :

$$\begin{aligned} u_1 &= (A\sin\eta x_2 + B\cos\eta x_2)\, e^{-\bar{\xi} x_1} e^{-\bar{\nu} x_3} e^{-i\omega t} \\ u_2 &= (C\sin\eta x_2 + D\cos\eta x_2)\, e^{-\bar{\xi} x_1} e^{-\bar{\nu} x_3} e^{-i\omega t} \\ u_3 &= (E\sin\eta x_2 + F\cos\eta x_2)\, e^{-\bar{\xi} x_1} e^{-\bar{\nu} x_3} e^{-i\omega t} \end{aligned} \qquad (12)$$

leads to the asymptotic equation of dispersion :

$$M_n \bar{\xi}^2 + Q_n \bar{\xi}\bar{\nu} + P_n \bar{\nu}^2 - \frac{n^2\pi^2\bar{c}}{4h^2} + \rho\omega^2 = 0 \qquad (13)$$

when $2h\xi \to 0$ and $2h\nu \to 0$. Here, n is the thickness overtone number and $\bar{c}$ is the eigenvalue corresponding to the pure thickness propagation. Above result accurately expresses the asymptotic behavior of essentially thickness modes at small lateral wavenumbers, and the dispersion constants M_n Q_n and B_n can be determined in closed from for any kind of thickness modes (A, B or C) and for any type of crystal and any cut orientation.

In a trapped energy resonator Eq. (13) holds outside the electroded region, whereas, inside the electroded region, the partial waves which are the basic elements entering the combination which defines a given branch of the dispersion curves in 2-D (or surfaces in 3-D) take the following form

$$\begin{aligned} u_1 &= (A\sin\eta x_2 + B\cos\bar{\eta} x_2)\, e^{i\xi x_1} e^{i\nu x_3} e^{-i\omega t} \\ u_2 &= (C\sin\eta x_2 + D\cos\bar{\eta} x_2)\, e^{i\xi x_1} e^{i\nu x_3} e^{-i\omega t} \\ u_3 &= (E\sin\bar{\eta} x_2 + F\cos\bar{\eta} x_2)\, e^{i\xi x_1} e^{i\nu x_3} e^{-i\omega t} \end{aligned} \qquad (14)$$

and the dispersion equation becomes :

$$M_n \xi^2 + Q_n \xi\nu + P_n \nu^2 + \frac{n^2\pi^2\hat{c}}{4h^2} - \rho\omega^2 = 0 \qquad (15)$$

In here–studied problem, where only the fundamental branch of thickness shear is involved, we have :

$$\hat{c} \approx \bar{c}_{66}\left(1 - \frac{8{k_{26}}^2}{\pi^2} - \frac{4\rho' h'}{\rho h}\right) \qquad (16)$$

which is consistent with (6).

In the special case of singly rotated cut $Y+\theta$ such as NLC, Q_n is strictly equal to zero, and it is possible to consider partial waves with a dedicated parity along x_2, for instance $B = C = E = 0$ both in (12) and (14). Then, one falls back onto the results of previous model issued for $Y + \theta$ cuts [7], whereas the only branch of essentially thickness modes of interest in a NLC–cut strip resonator is the branch B_1. With $\theta = -31.5^o$, one obtains :

$$M_{B_1} = 118.264\, GPa \quad \text{and} \quad P_{B_1} = 32.781\, GPa \qquad (17)$$

Moreover, one readily check that the two independent models separately described in Sec. III and IV are consistent with that theory. As a consequence, the developments of Secs. III and IV can be seen as two special case of a single more general model, of which the starting point are partial waves dominated by essential terms of the following form :

$$\begin{aligned} u_1 &= A\sin\eta x_2 \cos\xi x_1 e^{i\nu x_3} e^{-i\omega t} \\ u_2 &= B\cos\eta x_2 \cos\xi x_1 e^{i\nu x_3} e^{-i\omega t} \\ u_3 &= C\cos\eta x_2 \cos\xi x_1 e^{i\nu x_3} e^{-i\omega t} \end{aligned} \qquad (18)$$

which must be combined to satisfy the boundary conditions on major surfaces of the plate, thereby defining branches of dispersion *surfaces* which can be established either in a dimensionless way as $\Omega(\gamma, \mu)$, or

with physical dimensions as $\omega(\xi,\nu)$, at will, and so on .... Such surfaces are continuous and, in the electroded region, the equation of the surface for branch B_1 n NLC–cut can be approximated by :

$$M_{B_1}\xi^2 + P_{B_1}\nu^2 + \frac{n^2\pi^2\hat{c}}{4h^2} - \rho\omega^2 = 0 \qquad (19)$$

with excellent precision whenever $h\xi$ and $h\nu$ remain small w.r.t $\pi/2$.

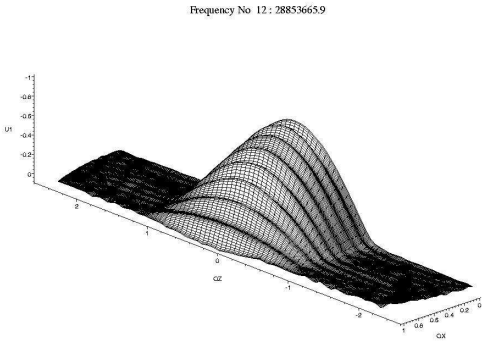

FIG. 8: u_1 FEA–predicted amplitude distribution of mode in strip resonator (only half width represented, due to symmetry).

One of the greatest ideas of Harry Tiersten certainly consisted in substituting the wavenumbers as differential operators

$$\begin{aligned} \bar{\xi}^2 &= \frac{\partial^2}{\partial x_1^2}, \qquad \xi^2 = -\frac{\partial^2}{\partial x_1^2} \\ \bar{\nu}^2 &= \frac{\partial^2}{\partial x_3^2}, \qquad \nu^2 = -\frac{\partial^2}{\partial x_3^2} \end{aligned} \qquad (20)$$

into above Eqs. (13,15), which resulted into a major improvement of previous models for energy trapping modes in plane–parallel [8] and plano–convex plates [9], respectively. Basically, the behavior of strip resonators pertains to the descriptions of Sec. III for what concerns the x_1 dependence, and of Sec. IV for what concerns the x_3 dependence of the dominant components of vibrations. The main difference between the two independent approaches of the preceeding sections is that several branches are necessary for the description of problem in (x_1, x_2) cross–section, while only one branch appears in the description of the problem in (x_3, x_2) cross–section. If we carefully analyze high precision FEA–predicted amplitude distributions such as the one represented of Fig. 8, one can observe a separation of variables x_1 and x_3 in the mode shape, and clearly one wave number, be it real or imaginary, is sufficient to describe the variation of amplitude u_1 along x_3, while at least two wavenumbers are needed to represent the variation of amplitude along x_1, to account for the modulation along the width. This feature remains true when considering u_2 and u_3 components of the mode patterns.

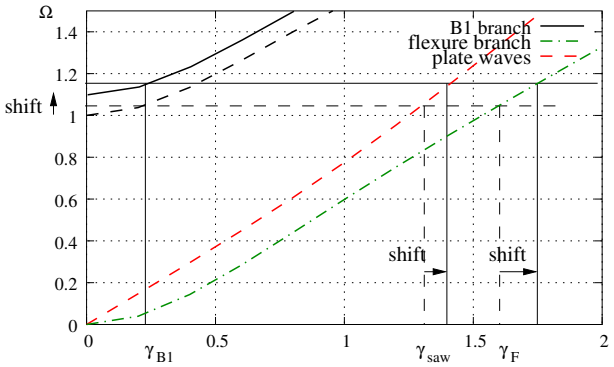

FIG. 9: Influence of ν_{B_1} onto the edge boundary conditions at $x_1 = \pm w/2$.

In the well known paper [6], the authors take advantage of (20) to efficiently replace the complex problem of establishing the modal analysis of plane–parallel and contoured resonators by a single partial derivative equation. Of course, this approach is valid only if a single branch (surface) contributes to the investigated problem, but the expansion of branches at their junction with Ω axis remains valid *per se*, so that Eq. (19) still rigorously governs the behavior of branch B_1 even in the more complex case where other branches (surfaces) have to be taken into account in the analysis. From another hand, the value of ξ lateral wavenumber for the flexural branch in $(x1, x2)$ plane in the frequency range of strip operation is much higher than the value of ν which is commensurable to ξ_{B_1}. Then the description of flexural branch and plate waves branches previously obtained with $\nu = 0$ can be used in, say, a "zero order" 3-D model, which can be improved later if necessary.

If only the B_1 branch is necessary to describe the behavior of strip along its length, according to (19), the frequency equations of Sect. IV must be replaced by

$$\begin{aligned} \rho\omega^2 - M_1\xi^2 &= \rho\left(\omega_1^e\right)^2 + P_1\nu^2 \text{ electrodes} \\ \rho\omega^2 - M_1\xi^2 &= \rho\left(\omega_1^f\right)^2 - P_1\bar{\nu}^2 \text{ free region} \end{aligned} \qquad (21)$$

at given real ξ_{B_1}, but the transcendental equation (10) arising from continuity conditions for u_1 remains unchanged because the terms $M_1\xi^2$ are identical and cancel out in above relations.

Solving (10) in terms of ν in the electroded region immediately provides with $\bar{\nu}$ outside it. Then, according to (19), one immediately obtains a frequency shift

$$\delta\left(\omega^2\right) = \frac{\nu^2 P_1}{\rho} \;\Rightarrow\; \delta\Omega = \frac{\delta\omega}{\omega_{B_1}^0} \approx \frac{\mu^2 P_1}{2\bar{c}_{66}} \qquad (22)$$

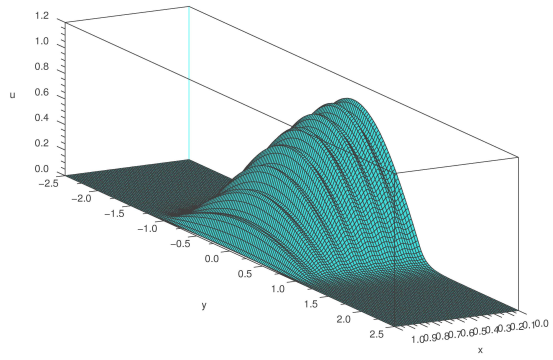

FIG. 10: 3-D semi-analytical simulation of u_1 displacement (half of resonator).

of the branch B_1 of Fig. 9, representing the dispersion curves when $\nu \neq 0$, whereas the effect of other branches remain approximately unchanged since there is no essential system of standing waves established along the length of strip for flexure and STW/plate waves. Then, for values of γ_{B_1} similar to the ones considered in the 2-D analysis of Sect. III, one readily observes that the existence of $\nu \neq 0$ shifts the wavenumbers of other real branches involved into the combination to upper values. This is a simple effect which is the first coupling mechanism between the (x_1, x_2) and (x_3, x_2) separate 2-D analyses previously established. Fig 8 shows a simulation obtained with such rather phenomelogical model. One observe that the model accurately describe the topology of FEA–predicted amplitude distribution of Fig. 8.

VI. FURTHER ISSUES

In its present above–described state, the model suffers from several flaws :

- if only ν in the electroded region is used to determine above–mentionned upshift of ω, then elasticity equations are not rigorously fulfilled in the unelectroded region, since the damping factor $\bar{\nu}$ in the latter region implies a different position of characteristic shown on Fig. 9 for the electroded region.

- Although we assume that there is no specific x_3–dependence of the standing wave regime of lower branches, $\nu \neq 0$ and $\bar{\nu} \neq 0$ should slightly affect the shape of the lower branches, not only the relative position of B_1 surface with respect to them.

The first issue can be solved by means of the variational principle (2). In principle, there are two possibilities :

- one can use the variational form in order that ω^2 adapts itself to minimize the effect of the residue of elasticity equation in the unelectroded region (volume error), while keeping the same assumption of mode shape as in the previous section,

- one can use the $\bar{\nu}$ exponential decay governing the x_3–dependence of assumed mode shape in the unelectroded region. Then, the variational form will account for the discontinuity surface at the frontier between electroded and unelectroded regions. This is a mode–matching type of approach.

Although the suggested treatments are left for the future, here–presented model already exhibits a clear advantage in comparison with FEA : the u_1 amplitude distribution at the crystal–electrodes interface is a relatively simple combination of trigonometric functions, which should give way to a straightforward computation of series capacitance C_1.

The temperature dependence is a big issue in the determination of the operating range of the use of strip resonators as sensors : due to the compound nature of the vibration, the various terms involved in the combinations which actually make the resonant modes have different dependences. Then, over large temperature intervals, one can expect that the wavenumbers of the lower branches enter significant changes, in a manner which is intrinsically similar to the mechanism at the origin of activity dips, although it may also manifest itself in a smoother form as well. This is a justification of this research, because the determination of temperature behavior of strips by FEA is still an intensive computing task (costly, in the literal sense), even if our previous research in the field showed its accuracy. The lagrangian formalism developped in [10] for the temperature dependence of resonators in material with small piezoelectric coupling can be readily incorporated in the writing of the model. At the present time, ourcomputer program to determine the effect of edge boundary conditions by the variational approach makes use of initial guesses of the dispersion curves, because it is technically difficult to optimize all root finding tasks in a proper without such a guess. Then, it may be necessary to update the accurate determinationof the dispersion curves along temperature variations, a task which is difficult to make altogether quick and safely automatic (i.e. without human checking). Ways to solve this issue will be investigated in the near future.

Acknowledgments

This joint research is presently supported as a CNRS/BAS bilateral cooperation project intitled “Resonant piezoelectric micro-sensors at cryogenic temperature” number 18803.

The European Commission within the GROWTH shared cost RTD funding scheme (RTD Project QxSens No. GRD1-2001-41816, Contract No. G6RD-CT-2002-00648) recently supported an international cooperation which created a favorable context for here–presented research.

[1] B. Dulmet, L. Spassov, R. Bourquin, A. Ivan, Ts. Angelov, Yu. Lazarov, Design of a new miniature resonant temperature sensor in NLC-cut of quartz, Proc. E.F.T.F., (2005).

[2] R.D. Mindlin, High Frequency Vibrations of Crystal Plates, Quarterly of Applied Mathematics, April 1961, n1, pp. 51–61(1961).

[3] H. F. Tiersten and T. L. Sham, A calculation of the resonant frequencies and motional capacitance for the fundamental family of modes of AT-cut quartz strip resonators, Proc. IEEE Intl. Freq. Ctrl. Symp., pp 947–955, (1998).

[4] L. Spassov, E. Yossiffov, V. Georgiev, L. Vergov, A rotated Y-cut quartz resonator with a linear temperature-frequency characteristic, Sensors & Actuators, A58, pp.185–189, (1997).

[5] H. F. Tiersten, Natural boundary conditions and initial conditions from a modification of Hamilton's principle, J. Math. Phys., **9**, n9, pp 1445–1450, sept. 1968.

[6] D. S. Stevens, H. F. Tiersten, An Analysis of doubly–rotated Quartz Resonators utilizing essentially Thickness Modes with Transverse Variations, J. Ac. Soc. Am., V 79, n6, pp 1811–1826, (1986).

[7] H. F. Tiersten, R. C. Smythe, An Analysis of Trapped Energy Resonators Operating in Overtones of Coupled Thickness Shear and Thickness Twist, J. Ac. Soc. Am., V 59, pp 879 sq, (197).

[8] W. Shockley, D. Curran, D. Koneval, Energy Trapping and Related Studies of Multiple Electrodes Filter crystals, Proc. IEEE Ann. Freq. Ctrl. Symp., pp 88-126, (1963).

[9] C. Wilson, Vibration Modes of AT cut Convex Quartz Resonators, J. Phys. D: Appl; Phtys., (**7**), pp 2449 sq., (1974).

[10] B. Dulmet, R. Bourquin, Lagrangian effective material constants for the modeling of thermal behavio of acoustic waves in piezoelectric crystals, part I. Theory, J. Acoust. Soc. Am. **110** (4), pp 1792–1799, October 2001.

Proceedings of the 20th EFTF, 2006

New sets of data for the thermal sensitivity of elastic coefficients of langasite and langatate

R.Bourquin and B.Dulmet
FEMTO-ST, Dep. LCEP, ENSMM,Besançon, France
**Electronic address: rbourquin@ens2m.fr*

Abstract: Thermal coefficients of elastic constants of LGS and LGT crystals have been determined from frequency-temperature curves of contoured resonators operating in thickness modes. Effect of the trapping of the vibration has been taking into account in order to improve the accuracy. In a first step, thermal sensitivity of stiffness coefficients in lagrangian description are obtained. Thermal sensitivity of usual elastic constants are further deduced.

I. INTRODUCTION

There exist several sets of published values of thermal coefficients of elastic constants of Langasite LGS[1-8] and Langatate LGT crystals. [5].These sets exhibit significant deviations of numerical values, even for the first order coefficients [6]. The determination of these coefficients can be made by measuring the variation, with respect of temperature, of the times of propagation of acoustic waves along particular direction in the crystal [9], or from the frequency-temperature curves of resonators of various cut angles [10]. We have retained this last way.

To obtain resonators of high quality factor, it is necessary to trap the vibration. At frequencies in the range 5 to 15 MHz, this is achieved by using plano-convex resonators. It is known that the resonant frequencies of such resonators exhibit a shift from the theoretical frequencies of an the infinite plate with flat parallel faces. Further the resonant frequencies are also function of piezoelectric coefficient trough the piezoelectric coupling factor. To reduce errors coming from these facts, we have retained the following features:

- Only overtones modes of rank equal or higher to 3 are used.
- Only resonators with good trapping of the vibration have been retained, the behaviour of which obeys the model of Tiersten [11]
- The sensitivities of the frequencies of modes to the elastic coefficients (partial derivatives with respect to the independent elastic coefficients), necessary to calculate the thermal sensitivities, are computed by taking into account the trapping of vibration.

In addition the change of the cut angles of resonators of arbitrary orientation with temperature is taken into account by using the lagrangian description of the vibration [12-14]. The use of this formalism offers also the advantage to simplify the computation of the sensitivities of the frequencies of modes to the elastic coefficients. So, in a first step, temperature sensitivities of effective elastic coefficients used in this description, are computed. Temperature sensitivities of usual stiffness coefficients and compliances are then deduced from the formers.

II. METHOD

In lagangian description [12], the stress-strain relations are expressed as:

$$P_{ij} = G_{ijkl} u_{l,k}$$

where effective elastic coefficients G_{ijkl} introduced in theses relations have the same values than usual elastic coefficients but exhibit different thermal sensitivities. P_{ij} is the first Piola-Kirchoff stress tensor and the derivatives of the mechanical displacement u_l are with respect to the coordinates of a material point referenced at the room temperature.

The resonant frequencies of a contoured resonator are given by [11]:

$$f_{nmp}^2 = f_n^2\left[1+\frac{1}{n\pi}\sqrt{\frac{2h_0}{R_0}}\left(\sqrt{\frac{M'_n}{G_e}}(2m+1)\right)+\sqrt{\frac{P'_n}{G_e}}(2p+1)\right)\right]$$

$$f_n^2 = \frac{n^2}{4h_0^2}\frac{G_e}{\rho_0}\left(1-8\frac{k_\alpha^2}{n^2\pi^2}\right)$$

In this expression the dimensions (thickeness 2 ho and radius of contour Ro) and mass per unit volume ρo are those at the reference temperature To (room temperature). Ge is the elastic coefficicient for the propagation of a thickness mode along the direction parallel to the normal of the resonator, and M'n and P'n are dispersion constants which govern the trappping of

the vibration in the resonator [11,15,16]. n is the overtone number. M'n, P'n, as well as Ge, are functions of the effective elastic coefficients, the orientation of the resonator (angle Φ, θ) and the overtone number n.
fn is the resonant frequency for the infinite plate with plane parallel faces. As stated in the introduction, since the piezoelectric coefficients and their thermal sensitivities of are not known with a good accurarcy, we neglect the term in the bracket in the expression of f_n containing the coupling factot k_α. In order to reduce the error coming from this fact, we don't use fundamental modes (n=1).

The effective elastic coefficients G_{ijkl} have a lover symmetry with respect to the indices than usual coefficients [12,13]. When compressing the indices by following the rule:

11	22	33	23	31	12	32	13	21
1	2	3	4	5	6	7	8	9

the resulting matrix is a 9 by 9 matrix:

G_{11}	G_{12}	G_{13}	G_{14}	0	0	G_{17}	0	0
G_{12}	G_{11}	G_{13}	$-G_{14}$	0	0	$-G_{17}$	0	0
G_{13}	G_{13}	G_{33}	0	0	0	0	0	0
G_{14}	$-G_{14}$	0	G_{44}	0	0	G_{47}	0	0
0	0	0	0	G_{55}	G_{17}	0	G_{47}	G_{17}
0	0	0	0	G_{17}	G_{66}	0	G_{14}	G_{66}
G_{17}	$-G_{17}$	0	G_{47}	0	0	G_{55}	0	0
0	0	0	0	G_{47}	G_{14}	0	G_{44}	G_{14}
0	0	0	0	G_{17}	G_{66}	0	G_{14}	G_{66}

$$G_{66} = \frac{1}{2}(G_{11} - G_{12})$$

The coefficients of temperature

$$T^{(n)}G_{ij} = \frac{1}{n!}\frac{\partial G_{ij}}{\partial T},$$

n = 1,2,3, are computed from the coefficients of temperature $T^{(n)}f_{nmp} = \frac{1}{n!}\frac{d f_{nmp}}{d T}$ of experimental frequency temperature curves. For that, it is necessary to compute numerically the partial derivatives $M^{(n)}_{ij}$ of the frequencies f_{nmp} with respect to the elastic coefficients G_{ij}
If the $T^{(n)}f$ are stored in a vector **Y**, the $T^{(n)}G_{ij}$ in a second vector **G** and the $M^{(n)}_{ij}$ in a matrix **M**, the following relations hold:

$$Y_i^{(1)} = M_{ij}^{(1)} G_j^{(1)}$$

$$Y_i^{(2)} = M_{ij}^{(1)} G_j^{(2)} + \frac{1}{2} M_{ijk}^{(2)} G_j^{(1)} G_k^{(1)}$$

$$Y_i^{(33)} = M_{ij}^{(1)} G_j^{(3)} + M_{ijk}^{(2)} G_j^{(1)} G_k^{(1)} + \frac{1}{6} M_{ijkl}^{(2)} G_j^{(1)} G_k^{(1)} G_l^{(1)}$$

The numerical computation is done by using the values of elastic coefficients in ref [17] for LGS and [18] for LGT
Since the number of relations is greater than the unknowns, the above system is solved by a least square method [19]. The first order coefficients are directly obtained by solving the system:

$$\left(\left[M^{(1)}\right]^T \bullet \left[M^{(1)}\right]\right) \bullet G^{(1)} = \left[M^{(1)^T}\right] \bullet Y^{(1)}$$

The higher order coefficients are then obtained recursively.
Once the $T^{(n)}G_{ij}$ known, the temperature sensitivity of usual elastic coefficients are computed by using the relations between the two families of coefficients [12]. These relations involve the thermal expansion coefficients The values used are those in ref.[20]. In a last step, the thermal sensitivities of compliances are obtained by inverting the matrix.

III. LANGASITE

The annex I summarises the characteristics of resonators and the experimental temperature coefficients of frequencies.

$$f_{nmp}(T) = f_{nmp}(T0)\left(1 + \sum_{j=1}^{3} T^{(j)} f\right)$$

The modes are labelled by the family (A,B or C), the overtone number n and the rank of anharmonic (m,p). The orientations of resonators (Y,ϕ,θ) is according the IEEE-std 176-1987 convention. The precision of measurement of angles is within plus or minus 2'.The reference temperature is To = 20°C. The thickness of most of the resonators is about 800µm. For each resonator the value is determined in order to obtain a resonant frequency equal to the experimental value.
Crystals are supplied by FOMOS (Russia) except for the resonators labelled S2 to S4 which are fabricated in a crystal supplied by Saint-Gobain (France). No significant changes have been observed for the thermal behaviour of Y cut made from crystals of different sources.

The lagrangian formalism allows to treat the problem of thermal behaviour of a resonator without the use of the thermal expansion coefficients. In this case we have to determined the values of the 8 independent elastic coefficients. (instead of 6 elastic coefficients plus to thermal expansion coefficients in classical formulation)
In the results given in this paper, we have only considered 6 independent effective coefficients and used to additional relations for the last two coefficients [12].This way simplify the treatment but is submitted to the reliability of values of thermal coefficients. We have

checked that the removing a resonator from the data base doesn't change the standard error.

The temperature coefficients of effective elastic coefficient, in lagrangian description, are summarised in table I.
Only the first and second order are given because the great variance of computed third order coefficients.

	First order (in 10^{-6})	Second order(in 10^{-9})
G11	-50.5	-70.1
G12	514.3	57.2
G13	-67.4	-59.9
G14	-347	213
G17	-345	216
G33	-94.0	-55.6
G44	-62.0	-72.0
G47	-60.4	-69.2
G55	-58.8	-66.3
G66	11.6	-128

Table I Thermal sensitivities of Gij effective coefficients for LGS

From the above data, temperature sensitivities of usual elastic coefficients can be computed (Table II)

	First order (in 10^{-6})	Second order(in 10^{-9})
C11	-54.6	-72.3
C12	-104.6	-25.2
C13	-73.1	-64.9
C14	-351.0	212
C33	-101.3	-63.2
C44	-66.1	-74.2
C66	7.51	-131

Table II Thermal sensitivities of Cij coefficients for LGS

By inverting the matrix of elastic coefficients, we have deducted the temperature sensitivities of compliances (Table III)

	First order (in 10^{-6})	Second order(in 10^{-9})
S11	-31.0	167
S12	-149	281
S13	109	62.3
S14	-355	492
S33	110.0	71.8
S44	3.91	148
S66	-69.7	205

Table III Thermal sensitivities of Sij compliances for LGS

IV. LANGATATE

Material has been supplied by FOMOS. The same number of resonators has been initially fabricated than for LGS. But instead of LGS case, we have found that by removing certain resonators, the standard error is significantly increased. So, we have not retained these crystals. Finally the data base consists of 48 curves, a number slightly inferior than for LGS (60 curves)

Temperature coefficients of effective elastic coefficients, in lagrangian description, are summarised in table IV.

	First order (in 10^{-6})	Second order(in 10^{-9})
G11	-68.9	-74
G12	-135	-0.50
G13	-76.6	-92
G14	-394	286
G17	-391	285
G33	-109	-72.7
G44	23.6	-195
G47	25.9	-195.3
G55	28.2	-195.5
G66	20.7	-172

Table IV Thermal sensitivities of Gij effective coefficients for LGT

The standard error resulting from the computation of coefficients is in this case $0.9.10^{-6.}$, a value of the same order of magnitude then for the LGS coefficients for which the standard error is $1.7\ 10^{-6}$but with a slightly higher number of data.

From the above data, temperature sensitivities of usual elastic coefficients are computed (Table V)

	First order (in 10^{-6})	Second order(in 10^{-9})
C11	-72.7	-79
C12	-140	-5.0
C13	-82.6	-96
C14	-398	282
C33	-117	-76
C44	19.8	-200
C66	16.8	-178

Table V Thermal sensitivities of Cij coefficients for LGT

As for langasite, we have computed the temperature sensitivities of compliances (Table VI)

	First order (in 10^{-6})	Second order(in 10^{-9})
S11	-43.3	231
S12	-209	428
S13	151	29.2
S14	-515	827
S33	136	70.2
S44	-101	318
S66	-97.7	296

Table VI Thermal sensitivities of Sij compliances for LGT

V ACKNOLEDGEMENTS

The authors would like to thank Mr. J.P. Romand for his help in manufacturing the resonators and the french DGA agency for his support under contract .03.34.020

VI. REFERENCES

[1] Present stage of La3Ga5SiO14 research , I.M.Silvestrova, P.A.Senyushenkov, Y.V .Pisarevsky, V.V.Bezdelkin, ASFC, p. 348-350, (1993)

[2] Stress induced optical activity in piezoelectric crystals and internal stresses method of control in quartz, langasite, lithium niobate crystals V.S.Naumov, I.I.Kalashnikova, S.S.Spassov, ASFC, p. 40-42, (1994)

[3] New data on temperature stability and acoustical losses of langasite crystals S.Sakharov, A.V.Medvedev, V.Lider, Y.Pisarevsky, P.A.Senushencov ASFC, p. 647-652, (1995)

[4] Influence of static electric field , mechanical pressure and temperature on the propagation of acoustic waves in La3Ga5SiO14 piezoelectric single crystal, B.P.Sorokin, P.P.Turchin, S.I.Burkov, D.A.Glushkov, K.S.Aleksandrov, IFCS, p. 161-169, (1996)

[5] Recent measurement of materials constants versus temperature of langate, langanite and langasite D.C.Malocha, E.Adler, S.Frederick, M.Chou, M.P. de Cunha, R.C.Smythe, R.Humbold, Y.S.Zhou IFCS p. 200-205, (2000)

[6] Langasite : what temperature coeffficients of material are correct ? ; R.M.Taziev, IFCS-EFTF joint meeting, 1999, p. 835-842,(1999)

[7] Investigation of technology of (La1-xNdx)Ga5SiO14 crystals Spectral laser and electron chemical properties. A.A.Kaminskii, I.M.Silvestrova, S.E.Sarkisov, G.A.Denisenko, Phys. Stat. Sol. (A), p. 607-620 (1983)

[8] Temperature dependence of electromechanical properties of LGS crystals, A.B.Ilyev, B.S.Umarov, L.A.Shabanova, M.F.Dubovic, Physica. Status. Solidi. (A98) Vol 190, p.K109-K114,(1986)

[9] Determination of complete fully consistent data set of the fundamental properties of high purity synthetic quartz, B.James, 5th EFTS, p. 221-223, (1991)

[10] Higher-order temperature coefficients of the elastic stiffnesses and compliances of alpha quartz, R.Bechman, A.Ballato, K.Lukasek, Proc. I.R.E.**50** p.1812-1821, (1962)

[11]An analysis of doubly-rotated quartz resonators utilising essentially thickness modes with transverse variation, D.S.Stevens, H.F.Tiersten, J.A.S.A.,Vol.79, N°6, p..1811-1826, (1986)

[12]Lagrangian effective material constants for the modelling of thermal behaviour of acoustic waves in piezoelectric crystals, Part I Theory B.Dulmet, R.Bourquin, J.A.S.A., Vol.110, N°4, p.1792-1799, (2001); Part II.Applications and numerical values for quartz, B.Dulmet, R.Bourquin, E.Bigler, S.Ballandras, J.A.S.A., Vol.110, N°4, p.1800-1807, (2001)

[13] Influence of the definition of material constants in the study of crystal plates thermal behaviour, B.Dulmet, R.Bourquin, 3rd. E.F.T.F.,Proc. p.305-312,(1989)

[14] R.N.Thurston,Waves in Solids, in Mechanics of solids IV, S.Flügge and C.Truesdell ed. Spinger-Verlag, Berlin,(1974)

[15]Analysis of thickness modes of contoured doubly rotated quartz resonators, Errol P.EerNisse, IEEE Trans. UFFC, vol.48, N°5, p.1351-1361, (2001)

[16]Doubly rotated contoured quartz resonators, Bikash K.Sinha, IEEE Trans. UFFC, vol.48, N°5, p.1162-1180, (2001)

[17] A review of langasite material constants from BAW and SAW data ; toward an improved data set J.A.Kosinski, R.A.Pastore, E.Bigler, M.P. da Cunha, D.C.Malocha, J.Detaint, IFCS, p278-286, (2001)

[18] Recent measurement of materials constants versus temperature of langatate, langanite and langasite, D.C.Malocha, E.L.Adler, D.Puccio, K.Knapp, M.P. de Cunha, Proc .IFCS, p.219-22, (2001)

[19] Elastic moduli of quartz versus hydrostatic pressure at 25°C and –195.8°C,H.J. Mc Skimin, P. Andreatch, R.N.Thurston, J. App. Phys. Vol.36, N°5, p.1624-1632,(Mai 1965)

[20]Measurements of LGS, LGN and LGT thermal coefficients of expansion and density, D.C.Malocha, H.Françcois-Saint Cyr, K.Richardson, R.Helmold, IEEE-UFFC, vol 49, N°3, p 350-355, March 2002

ANNEX I Experimental data for LGS

resonator	ϕ	θ	Ro (mm)	mode	fnmp (To) (Hz)	T(1)f	T(2)f	T(3)f
Y_1	-1'	-1'	700	C300	6970460	6,400E-06	-6,259E-08	9,64E-12
Y_2	0	-1'	700	C300	5341790	6,200E-06	-6,305E-08	2,80E-11
S2	-1'30"	35"	350	C300	5493630	6,172E-06	-5,849E-08	2,23E-11
S3	5'10"	20"	350	C300	5459430	3,135E-06	-6,249E-08	1,12E-11
S3	5'10"	20"	350	C500	9044720	6,986E-06	-6,244E-08	3,24E-10
S4	2'30"	-2'40"	350	C300	5424850	5,968E-06	-6,387E-08	4,86E-11
S4	2'30"	-2'40"	350	C320	5459010	3,128E-06	-6,246E-08	4,54E-11
S4	2'30"	-2'40"	350	C302	5478210	5,858E-06	-6,382E-08	4,90E-11
S4	2'30"	-2'40"	350	C500	9045210	6,959E-06	-6,312E-08	4,96E-11
S4	2'30"	-2'40"	350	C502	9094730	7,009E-06	-6,321E-08	4,94E-11
S4	2'30"	-2'40"	350	C520	9117450	5,095E-06	-6,161E-08	4,75E-11
S4	2'30"	-2'40"	350	C700	12657300	6,588E-06	-6,268E-08	5,25E-11
S4	2'30"	-2'40"	350	C702	12710100	6,402E-06	-6,246E-08	5,17E-11
S4	2'30"	-2'40"	350	C720	12740900	3,264E-06	-6,009E-08	5,01E-11
X_1	-90°02'	3'	500	A300	11212600	-2,459E-05	-3,573E-08	-7,51E-12
X_1	-90°02'	3'	500	A320	11288800	-2,374E-05	-3,681E-08	-4,66E-12
X_1	-90°02'	3'	500	A302	11327500	-2,563E-05	-3,518E-08	-7,97E-12
X_2	-90°02'	3'	500	A300	12019000	-2,478E-05	-4,276E-08	-1,40E-12
Y-60_1	-1'	-60°0	300	C300	4751030	2,736E-05	-7,627E-08	-4,49E-11
Y-60_2	0'	-60°0'	300	C300	4741160	2,701E-05	-7,510E-08	-3,02E-11
X+30_1	-89°58'	30°02'	500	C300	4978310	2,230E-06	-7,028E-08	4,14E-11
X+30_1	-89°58'	30°02'	500	C500	8292670	1,331E-06	-6,820E-08	2,31E-11
X+30_1	-89°58'	30°02'	500	A300	10749400	-3,057E-05	-1,377E-08	-2,60E-10
X+30_1	-89°58'	30°02'	500	A500	17827500	-3,488E-05	-3,659E-08	-6,45E-11
X+30_2	-89°58"	30°02'	500	C300	4973560	2,314E-06	-7,082E-08	4,06E-11
X+30_2	-89°58"	30°02'	500	C500	8284580	1,408E-06	-6,978E-08	1,78E-11
X+30_2	-89°58"	30°02'	500	A300	10740800	-3,157E-05	-2,889E-08	7,39E-11
X+30_2	-89°58"	30°02'	500	A500	17726970	-3,600E-05	-2,788E-08	-9,82E-11
X+30_2	-89°58"	30°02'	500	A500	17726800	-3,597E-05	-3,805E-08	-7,84E-11
X+45_1	-90°01'	45°00'	700	A300	11272600	-3,524E-05	-3,670E-08	4,19E-11
X+45_1	-90°01'	45°00'	700	C300	5081820	7,339E-06	-6,566E-08	-4,15E-13
X+45_1	-90°01'	45°00'	700	C500	8463930	3,927E-06	-6,959E-08	4,32E-12
X+45_2	-89°59'	44°59'	700	C500	8606340	3,613E-06	-6,990E-08	2,20E-11
X+45_2	-89°59'	44°59'	700	C300	5167980	4,364E-06	-6,657E-08	-2,17E-13
X+45_2	-89°59'	44°59'	700	A300	11438200	-3,694E-05	-3,642E-08	2,25E-11
X+75_1	-90°01'	75°00'	500	C300	5624730	-5,006E-06	-5,855E-08	7,87E-12
X+75_1	-90°01'	75°00'	500	C500	9362350	-5,199E-06	-5,735E-08	6,27E-12
X+75_2	-90°02'	75°00'	500	C300	5663430	-4,999E-06	-5,928E-08	1,49E-11
X+75_2	-90°02'	75°00'	500	C500	9426740	-5,201E-06	-5,831E-08	1,88E-11
Y+15-45_1	15°03'	-45°04'	400	C300	4716250	3,604E-05	-8,605E-08	4,76E-12
Y+15-45_1	15°03'	-45°04'	400	B500	10340900	-4,238E-05	-3,297E-08	6,05E-12
Y+15-45_1	15°03'	-45°04'	400	C700	10955400	3,774E-05	-9,230E-08	4,08E-11
Y+15-45_1	15°03'	-45°04'	400	A300	11647800	-4,144E-05	-3,024E-08	1,49E-12
Y+15+30_1	15°03'	29°59'	300	A300	10628600	-2,254E-05	-3,157E-08	-5,01E-11
Y+15+30_1	15°03'	29°59'	300	B700	14573300	-4,282E-05	-2,501E-08	3,90E-11
Y+15+30_1	15°03'	29°59'	300	A500	17678700	-2,207E-05	-4,016E-08	1,39E-11
Y+15-30_1	15°01'	-30°00'	300	C300	4646420	3,802E-05	-8,994E-08	4,22E-11
Y+15-30_1	15°01'	-30°00'	300	B500	9724160	-2,578E-05	-4,340E-08	1,89E-11

Y+15-30_1	15°01'	-30°00'	300	A300	11282300	-3,815E-05	-3,285E-08	7,94E-12
Y+15-30_1	15°01'	-30°00'	300	B700	13583900	-2,639E-05	-4,352E-08	1,52E-11
Y+15-30_1	15°01'	-30°00'	300	A500	18787800	-3,753E-05	-2,499E-08	-5,64E-11
Y+15-45_2	15°00'	-45°03'	400	A300	11163360	-4,333E-05	-2,407E-08	-2,83E-11
Y+15-45_2	15°00'	-45°03'	400	B500	10325400	-4,251E-05	-2,455E-08	-3,31E-11
Y+15-45_2	15°00'	-45°03'	400	C300	4706510	3,691E-05	-1,383E-07	4,46E-10
Y+15-45_2	15°00'	-45°03'	400	C700	10931400	3,797E-05	-9,906E-08	1,04E-10
Y+15+30_2	15°04'	29°59'	300	A300	10534500	-2,264E-05	-2,848E-08	-1,60E-10
Y+15+30_2	15°04'	29°59'	300	A500	17522100	-2,233E-05	-4,159E-08	2,34E-12
Y+15+30_2	15°04'	29°59'	300	B700	14448300	-4,314E-05	-3,070E-08	-4,05E-11
Y+15-30_2	15°01'	-30°01'	300	A300	11267500	-3,890E-05	-2,883E-08	3,76E-12
Y+15-30_2	15°01'	-30°01'	300	B500	9713190	-2,634E-05	-4,103E-08	1,23E-11
Y+15-30_2	15°01'	-30°01'	300	C300	4640060	3,870E-05	-1,003E-07	9,68E-11

ANNEX II Experimental data for LGT

resonator	ϕ	θ	Ro (mm)	mode	fnmp (To) (Hz)	T(1)f	T(2)f	T(3)f
T1	-0°2'	0°0'	500	C300	5153610	9,727E-06	-8,391E-08	7,15E-11
T1	-0°2'	0°0'	500	C500	8595270	9,886E-06	-8,481E-08	7,76E-11
T1	-0°2'	0°0'	500	C502	8640280	1,095E-05	-8,666E-08	7,96E-11
T1	-0°2'	0°0'	500	C520	8664760	8,760E-06	-8,365E-08	7,42E-11
T2	0°0'	0°0'	500	C300	5142740	9,713E-06	-8,373E-08	6,74E-11
T2	0°0'	0°0'	500	C320	5174040	8,289E-06	-8,281E-08	6,59E-11
T2	0°0'	0°0'	500	C302	5191620	1,082E-05	-8,532E-08	6,85E-11
T2	0°0'	0°0'	500	C500	8577090	9,856E-06	-8,445E-08	7,95E-11
T2	0°0'	0°0'	500	C502	8621660	1,089E-05	-8,618E-08	8,23E-11
T2	0°0'	0°0'	500	C520	8645000	8,737E-06	-8,315E-08	7,69E-11
T3	0°1'	0°0'35"	500	C300	5143100	9,740E-06	-8,528E-08	9,68E-11
T3	0°1'	0°0'35"	500	C500	8577890	9,824E-06	-8,491E-08	9,58E-11
T3	0°1'	0°0'35"	500	C502	8622130	1,083E-05	-8,536E-08	8,52E-11
Y+45_1	0°0'	45°0'	300	C100	1978850	-3,621E-05	-3,727E-08	1,33E-10
Y+45_2	0°0'	45°0'	300	C100	1974690	-3,595E-05	-3,099E-08	8,25E-11
Y-45_1	0°0'	45°0'	300	C300	4206070	1,010E-04	-2,345E-07	5,85E-10
Y-45_1	0°0'	45°0'	300	C300	4206020	9,796E-05	-1,855E-07	1,32E-10
Y-45_2	0°0'	45°0'	300	C300	4210820	9,685E-05	-1,709E-07	-1,16E-11
Y-45_2	0°0'	45°0'	300	C500	6988170	9,667E-05	-1,697E-07	-9,03E-11
Y-45_2	0°0'	45°0'	300	C700	9774040	9,813E-05	-1,750E-07	-2,28E-11
X+0_1	-90°5'	0°1'	500	A300	10213600	-3,370E-05	-2,626E-08	-1,62E-12
X+0_1	-90°5'	0°1'	500	A500	17000200	-3,435E-05	-4,008E-08	8,18E-11
X+0_1	-90°5'	0°1'	500	A500	16999800	-3,266E-05	-3,274E-08	-4,64E-11
X+0_2	-90°5'	0°1'	500	A300	10223000	-3,469E-05	-3,854E-08	3,27E-11
X+0_2	-90°5'	0°1'	500	A500	17016600	-3,458E-05	-4,172E-08	8,13E-11
X+30_1	-90°2'	30°7'	500	C300	4755790	2,211E-05	-1,017E-07	-2,48E-11
X+30_1	-90°2	30°7'	500	A300	10469500	-3,016E-05	-5,086E-08	1,71E-10
X+30_2	-90°0'	30°7'	500	C300	4753280	2,226E-05	-1,007E-07	6,84E-11
X+30_2	-90°0'	30°7'	500	A300	10471100	-3,004E-05	-4,819E-08	1,70E-10
Y+15-45_1	15°1'	-45°6'	300	C300	4392230	7,742E-05	-1,916E-07	5,65E-11
Y+15-45_1	15°1'	-45°6'	300	C700	10191500	7,485E-05	-1,737E-07	2,56E-10
Y+15-45_1	15°1'	-45°6'	300	A300	11103900	-3,839E-05	-2,858E-08	-8,12E-12
Y+15-45_1	15°1'	-45°6'	300	B500	9711240	-5,274E-05	-4,372E-08	4,59E-11
Y+15-45_2	14°59'	-45°5'	300	C300	4385140	6,682E-05	-1,735E-07	1,48E-10

Y+15-45_2	14°59'	-45°5'	300	C700	10175400	7,450E-05	-1,752E-07	2,66E-10
Y+15-45_2	14°59'	-45°5'	300	A300	11077500	-3,839E-05	-2,759E-08	-9,03E-12
Y+15-45_2	14°59'	-45°5'	300	B500	9689740	-5,264E-05	-3,931E-08	6,71E-11
Y+15+30_1	14°58'	30°1'	300	C500	8743640	-1,569E-05	-6,196E-08	1,13E-10
Y+15+30_1	14°58'	30°1'	300	C520	8776990	-1,230E-05	-6,566E-08	9,79E-11
Y+15+30_1	14°58'	30°1'	300	C502	8805620	-1,578E-05	-6,128E-08	1,07E-10
Y+15+30_1	14°58'	30°1'	300	A500	16874500	-1,818E-05	-6,266E-08	1,22E-10
Y+15+30_1	14°58'	30°1'	300	A520	16998400	-1,865E-05	-6,198E-08	1,16E-10
Y+15+30_1	14°58'	30°1'	300	A502	17037200	-1,942E-05	-6,154E-08	1,18E-10
Y+15+30_2	14°58'	30°1'	300	C500	8743580	-1,553E-05	-5,730E-08	9,38E-11
Y+15+30_2	14°58'	30°1'	300	C520	8815620	-1,229E-05	-6,245E-08	7,49E-11
Y+15+30_2	14°58'	30°1'	300	C502	8843120	-1,537E-05	-6,929E-08	1,74E-10
Y+15+30_2	14°58'	30°1'	300	A300	10141800	-1,816E-05	-5,751E-08	3,52E-12
Y+15+30_2	14°58'	30°1'	300	A500	16829000	-1,776E-05	-8,308E-08	-4,84E-10
Y+15-30_1	14°59'	-30°0'	300	C300	4328930	6,636E-05	-1,669E-07	2,518E-10
Y+15-30_1	14°59'	-30°0'	300	B500	9109340	-2,718E-05	-5,326E-08	3,14E-11
Y+15-30_2	15°0'	-30°0'	300	C300	4327110	6,619E-05	-1,671E-07	2,61E-10
Y+15-30_2	15°0'	-30°0'	300	B500	9107130	-2,730E-05	-5,326E-08	3,33E-10

Proceedings of the 20th EFTF, 2006

Localization of acoustic bulk modes due to negative refraction in crystal resonators

A. V. Kozlov and V. G. Mozhaev
Faculty of Physics, Moscow State University, 119992 GSP-2, Moscow, Russia
**Electronic addresses:* vgmozhaev@mail.ru and av_kozlov@inbox.ru

A new possibility is suggested in this paper to create crystal resonators of bulk acoustic waves with focusing and mode localization due to negative refraction at a planar interface between single-crystal layers. Local concavities of the slowness surface of crystals are considered to be the reason for negative refraction. The parabolic equations are derived to describe the spatial distribution of the focused fields. These equations correspond to: (i) three bulk modes propagating close to the crystallographic axes in orthorhombic crystals, (ii) pure shear mode propagating in the vicinity of the X-axis in orthorhombic piezoelectric crystal of potassium niobate, (iii) radially polarized quasi-shear mode propagating nearly in the direction of the Z-axis in hexagonal crystals. It is found that azimuthally symmetric beams of quasi-shear waves in hexagonal crystals have a ring-like structure of the wave field with zero radial displacement on the Z-axis, so there is no focusing on the beam axis in this case. The solutions to the parabolic equations are then used to construct focused modes of the travelling-wave type in periodic crystal layers and localized vibration in layered crystal resonators. A unique feature of this type of focusing is the absence of a fixed focusing axis in the uniform layered structures, that is, local and relatively long-lived vibration might be excited at an arbitrary point on the surface of planar crystal resonators. Therefore, such localized resonances could be used both as virtual keys for keyless keyboards and as movable pixels for imaging in touchscreen panels and graphics sensors.

I. INTRODUCTION

The wave properties of media exhibiting negative refraction of wave rays became one of the current research topics in physics after publication of the paper by Smith *et al.* in 2000 [1]. This paper reports about a new composite medium with negative values of effective permeability and permittivity that produces the effect of negative refraction for electromagnetic waves. The meaning of the term „negative refraction“ is illustrated in Fig. 1.

One of the most exciting consequences of this effect is that it offers a possibility of focusing the wave rays, spreading from a point source, after their refraction at a completely planar interface (Fig. 2).

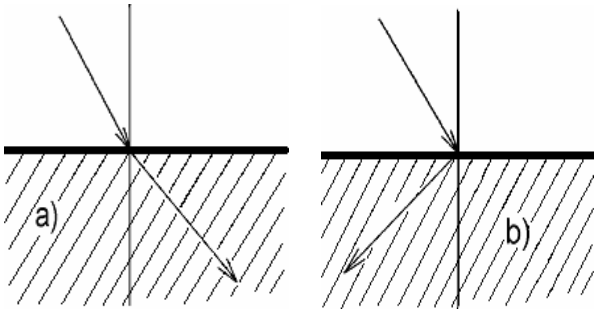

Fig. 1. a) Normal and b) negative refraction of wave ray

Strongly anisotropic media, such as plasma [2], may exhibit negative refraction for electromagnetic waves because of local concavities in the slowness surface, that is, due to anisotropy, rather than negative values of permeability and permittivity. By analogy with the case of plasma, Mason suggested in 1973 [3] that acoustic waves might be focused using negative refraction in crystals with a local concavity in the acoustic slowness surface. This suggestion was made in one of the concluding sentences of paper [3], and it seems that other researchers did not notice it. So the first study of such kind of focusing was done only recently in theoretical paper [4]. The results of paper [4] were obtained using a ray approximation to the focused field and finite element method and they are restricted by the

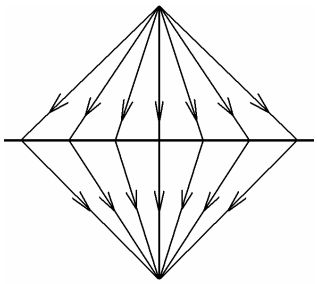

Fig. 2. Focusing due to negative refraction

wave field distribution on the focusing axis only. In the present study the same and similar problems are treated using another approach based on the parabolic equation that allows us to describe analytically the full 3-dimensional structure of the focused fields. Such analytical description serves as a basis for understanding the polarization features and restrictions of this focusing effect. The solution to anisotropic parabolic equation derived in the present study is then used to construct new spatially localized acoustic modes in a periodic multi-layered structure, containing crystal layers with negative refraction. Analysis of the wavefront shape for these modes reveals an opportunity to create layered crystal resonators for bulk acoustic waves with focusing and mode localization due to negative refraction at the interfaces between crystal layers. This makes possible new and promising practical applications of both the phenomenon of negative refraction itself and acoustic crystal resonators of the suggested type.

II. PARAXIAL WAVE EQUATIONS AND PARABOLIC EQUATIONS

The method of parabolic equation is widely used for solving various wave problems. Nevertheless, as it follows from the analysis of the literature, this method was previously applied to acoustics of crystals only in the case of quasi-longitudinal waves [5]. However, the waves of transverse or quasi-transverse polarization are of particular interest for the wave focusing due to negative refraction, since namely for these waves the needed concavities in the acoustic slowness surface are quite common for anisotropic solids. The following is a simple procedure suggested by us to derive approximate paraxial wave equations and parabolic equations applicable to waves of both mentioned polarizations. The procedure is outlined here in the case of wave propagation in the vicinity of the crystallographic axes in orthorhombic and hexagonal crystals although there is no principal restriction for its extension to the lower symmetries. The equations of motion for orthorhombic crystals are of the form

$$\rho \ddot{u}_1 = c_{11}\frac{\partial^2 u_1}{\partial x_1^2} + c_{66}\frac{\partial^2 u_1}{\partial x_2^2} + c_{55}\frac{\partial^2 u_1}{\partial x_3^2} + \\ + (c_{12}+c_{66})\frac{\partial^2 u_2}{\partial x_1 \partial x_2} + (c_{13}+c_{55})\frac{\partial^2 u_3}{\partial x_1 \partial x_3}, \quad (1)$$

$$\rho \ddot{u}_2 = c_{66}\frac{\partial^2 u_2}{\partial x_1^2} + c_{22}\frac{\partial^2 u_2}{\partial x_2^2} + c_{44}\frac{\partial^2 u_2}{\partial x_3^2} + \\ + (c_{12}+c_{66})\frac{\partial^2 u_1}{\partial x_1 \partial x_2} + (c_{23}+c_{44})\frac{\partial^2 u_3}{\partial x_2 \partial x_3}, \quad (2)$$

$$\rho \ddot{u}_3 = c_{55}\frac{\partial^2 u_3}{\partial x_1^2} + c_{44}\frac{\partial^2 u_3}{\partial x_2^2} + c_{33}\frac{\partial^2 u_3}{\partial x_3^2} + \\ + (c_{13}+c_{55})\frac{\partial^2 u_1}{\partial x_1 \partial x_3} + (c_{23}+c_{44})\frac{\partial^2 u_2}{\partial x_2 \partial x_3}. \quad (3)$$

Here ρ is the mass density of the crystal, c_{IJ} are the elastic constants ($I,J = 1 \div 6$), u_i are the particle displacement components ($i = 1 \div 3$). Let us first consider quasi-shear waves propagating in the vicinity of the Z axis and polarized predominantly along the X axis. This means that u_1 is the main displacement component. The minor displacement components u_2 and u_3, as well as the derivatives of displacements with respect to the x_1 and x_2 coordinates, are assumed to be proportional to a small parameter ε. With these assumptions, one can consider that all displacement components obey the following approximate relation

$$\rho \ddot{u}_i \approx c_{55}\frac{\partial^2 u_i}{\partial x_3^2}. \quad (4)$$

Let us now estimate the order of different terms in Eq. (1) with respect to the small parameter ε. The term containing the displacement u_2 is of the third order in ε, and so it should be ignored in the parabolic approximation. The term containing the displacement u_3 is of the second order in ε. Since this term includes the minor derivative with respect to the x_1 coordinate, the displacement u_3 in this term may be expressed via u_1 ignoring the corrections of higher than the first order in ε. To find this relation, the left-hand side of Eq. (3) is replaced by Eq. (4), and two first terms and the last one in the right-hand side of Eq. (3) are omitted as terms of higher order in ε than the remaining ones. Integrating the resulting equation over x_3 gives

$$c_{55}\frac{\partial u_3}{\partial x_3} \approx c_{33}\frac{\partial u_3}{\partial x_3} + (c_{13}+c_{55})\frac{\partial u_1}{\partial x_1}. \quad (5)$$

The constant of integration is equal to zero due to vanishing of waves in the far field of the source. Substituting Eq. (5) into Eq. (1) with omitted term containing component u_2 results in the following paraxial wave equation

$$\rho \ddot{u}_i = C_1\frac{\partial^2 u_i}{\partial x_1^2} + C_2\frac{\partial^2 u_i}{\partial x_2^2} + C_3\frac{\partial^2 u_i}{\partial x_3^2}. \quad (6)$$

The variables involved in Eq. (6) are defined below. The same procedure, applied to the other acoustic modes propagating in the vicinity of the Z axis and to

the other propagation directions close to the crystallographic axes, leads to the same paraxial wave equation, Eq. (6), but with other expressions for the involved coefficients. Summary results are the following.

Case 1. Quasi-shear waves polarized nearly along the X-axis, propagation in the vicinity of the Z-axis:

$$C_1 = c_{11} - (c_{13} + c_{55})^2 / (c_{33} - c_{55}),$$

$$C_2 = c_{66},\ C_3 = c_{55},\ u_i = u_1.$$

Case 2. Quasi-shear waves polarized nearly along the Y-axis, propagation in the vicinity of the Z-axis:

$$C_1 = c_{66},\ C_2 = c_{22} - (c_{23} + c_{44})^2 / (c_{33} - c_{44}),$$

$$C_3 = c_{44},\ u_i = u_2.$$

Case 3. Quasi-longitudinal waves propagating in the vicinity of the Z-axis:

$$C_1 = c_{55} + (c_{13} + c_{55})^2 / (c_{33} - c_{55}),$$

$$C_2 = c_{44} + (c_{23} + c_{44})^2 / (c_{33} - c_{44}),$$

$$C_3 = c_{33},\ u_i = u_3.$$

Case 4. Quasi-shear waves polarized nearly along the X-axis, propagation in the vicinity of the Y-axis:

$$C_1 = c_{11} - (c_{12} + c_{66})^2 / (c_{22} - c_{66}),$$

$$C_2 = c_{66},\ C_3 = c_{55},\ u_i = u_1.$$

Case 5. Quasi-longitudinal waves propagating in the vicinity of the Y-axis:

$$C_1 = c_{66} + (c_{12} + c_{66})^2 / (c_{22} - c_{66}),$$

$$C_2 = c_{22},\ u_i = u_2,$$

$$C_3 = c_{44} + (c_{23} + c_{44})^2 / (c_{22} - c_{44}).$$

Case 6. Quasi-shear waves polarized nearly along the Z-axis, propagation in the vicinity of the Y-axis:

$$C_1 = c_{55},\ C_2 = c_{44},\ u_i = u_3,$$

$$C_3 = c_{33} - (c_{23} + c_{44})^2 / (c_{22} - c_{44}).$$

Case 7. Quasi-longitudinal waves propagating in the vicinity of the X-axis:

$$C_1 = c_{11},\ u_i = u_1,$$

$$C_2 = c_{66} + (c_{12} + c_{66})^2 / (c_{11} - c_{66}),$$

$$C_3 = c_{55} + (c_{13} + c_{55})^2 / (c_{11} - c_{55}).$$

Case 8. Quasi-shear waves polarized nearly along the Y-axis, propagation in the vicinity of the X-axis:

$$C_1 = c_{66},\ C_2 = c_{22} - (c_{12} + c_{66})^2 / (c_{11} - c_{66}),$$

$$C_3 = c_{44},\ u_i = u_2.$$

Case 9. Quasi-shear waves polarized nearly along the Z-axis, propagation in the vicinity of the X-axis:

$$C_1 = c_{55},\ C_2 = c_{44},\ u_i = u_3,$$

$$C_3 = c_{33} - (c_{13} + c_{55})^2 / (c_{11} - c_{55}).$$

In isotropic limit $C_1 = C_2 = C_3 = \lambda + 2\mu$ for longitudinal waves, and $C_1 = C_2 = C_3 = \mu$ for shear waves, where λ and μ are the Lame constants. The anisotropy can make one of the coefficients C_i to be negative. The change of sign of such coefficients coincides with a transition from convex contours of the slowness surface to concave ones in the cross-sections by the proper planes. Although such a transition has a threshold with respect to the strength of elastic anisotropy, this does not impose strong restrictions on the search for crystals with required properties. There are many crystals applicable in practice, which have concavities in the acoustic slowness surface. Three examples of them are given in the next section.

Search for solutions to Eq. (6) in the form of a wave beam propagating along the x_3-axis

$$u_i = A(x_1, x_2, x_3)\exp(ikx_3 - i\omega t),$$

where $k^2 = \rho\omega^2 / C_3$, and the assumption that amplitude A is a slowly varying function of the x_3-coordinate, that allows us to neglect its second x_3 derivative, leads to the following parabolic equation

$$C_1 \frac{\partial^2 A}{\partial x_1^2} + C_2 \frac{\partial^2 A}{\partial x_2^2} + 2C_3 ik \frac{\partial A}{\partial x_3} = 0, \qquad (7)$$

If the coefficients C_1 and C_2 are equal to each other, Eq. (7) is reduced to a simpler form

$$\alpha \Delta_\perp A + 2ik\partial A / \partial x_3 = 0, \qquad (8)$$

where

$$\Delta_\perp = \frac{\partial^2}{\partial x_1^2} + \frac{\partial^2}{\partial x_2^2} = \frac{\partial^2}{\partial r^2} + \frac{1}{r}\frac{\partial}{\partial r} + \frac{1}{r^2}\frac{\partial^2}{\partial \phi^2},$$

$r = \sqrt{x_1^2 + x_2^2}$, $\tan\phi = x_2 / x_1$, $\alpha = C_1 / C_3$. The same transformation of Eq. (7) to Eq. (8) in the case of different values of coefficients C_1 and C_2 may be done by a change of the scale of the transverse coordinates x_1, x_2.

The remarkable property of the parabolic equation is the existence of its simple analytic solutions describing 3-dimensional structure of the wave beams. These are Hermite-Gaussian beams defined in Cartesian coordinates and Laguerre-Gaussian beams defined in cylindrical coordinates. The simplest known solution to Eq. (8) is a Gaussian beam

$$A = \frac{A(0)}{(1+iD)} \exp\left[-\frac{r^2}{a^2(1+iD)} \right], \qquad (9)$$

where $D = 2\alpha x_3 /(ka^2)$, $A(0)$ and a are arbitrary parameters, $A(0)$ determines the wave amplitude, a determines the minimum width of the wave beam which occurs at the point $x_3 = 0$. This point is a focus for the beams described by Eq. (9) and so the parameter a determines the transverse size of the focus spot. In contrast to the known expression, coefficient α in D is not equal to 1. This results in the following surprizing feature of wave properties, when α becomes negative. In this case the beams with convex wavefronts are convergent rather than spreading as in the common isotropic or quasi-isotropic case and vice versa for the beams with concave wavefronts. This unusual property takes place in the sectors of wave vectors in which the slowness surface is concave. The layered structures consisting from combination of alternating planar crystal layers with concave and convex parts of the slowness surfaces near the normal to the layers' interfaces, as shown in sections VI and VII, may support new spatially localized acoustic modes and vibrations.

III. CONCAVE SLOWNESS SURFACES

To attain the correct focusing of rays, propagating from a point source, one needs to use a planar lens with transverse isotropy in the plane of its surface. Plates of hexagonal crystals with Z axis normal to the surface possess such a property. The acoustic slowness surface for a hexagonal crystal can be concave in the vicinity of the Z axis, but only for quasi-shear waves. This is the case, in particular, for zinc crystal, in which the focusing due to negative refraction was studied in paper [4]. Fig. 3 shows the cross-section of the slowness surface for the quasi-shear waves in the XZ plane of this crystal. The values of elastic constants used to calculate this curve are the same as given in [4].

The useful property of the slowness surface is that its normal coincides with direction of the group velocity. The surface of the group velocities V_g, that is, the wave surface, which shows the form of the wavefronts radiated from a point source, is calculated from Fig. 3 on the basis of indicated property. The results of calculations are presented in Fig. 4.

The focusing effect via anisotropic negative refraction may occur only for concave parts of the acoustic slowness surface. Such concavities in zinc crystal, according to Fig. 4, are located in a cone of ray angles

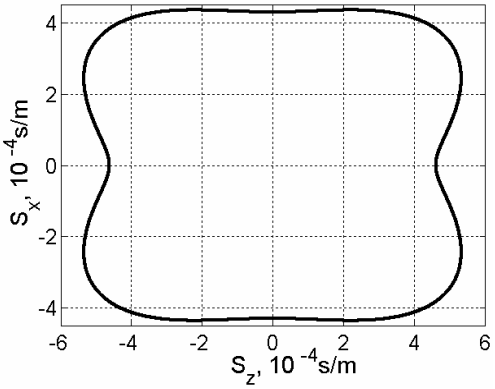

Fig. 3. Slowness S in the XZ-plane for zinc crystal

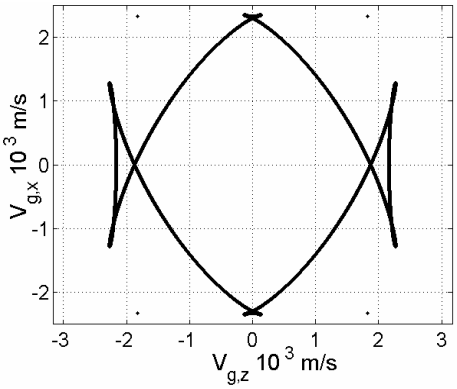

Fig. 4. Cross-section of the wave surface in the XZ-plane for zinc crystal

about $\pm 30^o$ from the Z axis and in an annular sector of ray angles about $\pm 5^o$ from the plane perpendicular to the Z axis. These ranges determine the maximum size of the angular aperture of the planar lenses from zinc crystal.

The slowness curves for pure shear waves in nonpiezoelectic crystals are elliptic and so they are always convex. Piezoelectricity deforms these contours and, in principle, it can produce concavities but only in an exceptional case of extremely strong piezoelectrics. The calculation of the slowness curve presented in Fig. 5 shows that crystals of potassium niobate have such an unusual property. This demonstrates an opportunity to achieve the focusing effect due to negative refraction for pure shear waves in similar superstrong piezoelectric crystals.

The cross-section of the wave surface corresponding to the slowness curve for pure shear waves in Fig. 5 is given in Fig. 6. The values of material constants of potassium niobate for these calculations are taken from Ref. [6].

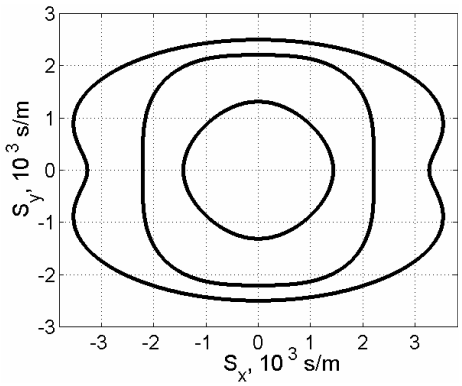

Fig. 5. Slowness curves in the XY-plane for potassium niobate crystal

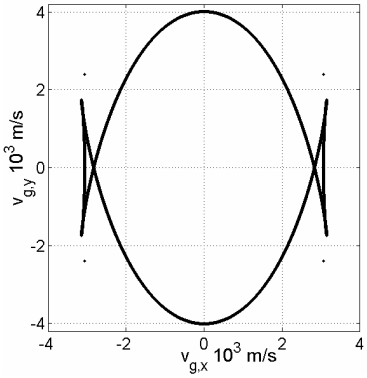

Fig. 6. Cross-section of the wave surface in the XY-plane for potassium niobate crystal

The concavities in the slowness curve for pure shear waves in potassium niobate are solely the result of influence of piezoelectricity, but the piezoelectric effect is not taken into account in the derivation of the paraxial wave equation and parabolic equation presented in the previous section. Therefore, in the next section the procedure described above is extended to the case of pure shear waves in orthorhombic piezoelectric crystals of $2mm$ class, to which potassium niobate belongs.

IV. PIEZOELECTRIC SHEAR WAVES

The equation of motion and the Laplace equation for pure shear waves in piezoelectric orthorhombic crystals of $2mm$ class are the following:

$$\rho\,\ddot{u} = \frac{\partial^2 (c_{55}u + e_{31}\varphi)}{\partial x_1^2} + \frac{\partial^2 (c_{44}u + e_{32}\varphi)}{\partial x_2^2}, \quad (10)$$

$$\frac{\partial^2 (\varepsilon_{11}\varphi - e_{31}u)}{\partial x_1^2} + \frac{\partial^2 (\varepsilon_{22}\varphi - e_{32}u)}{\partial x_2^2} = 0, \quad (11)$$

where $u = u_3$, φ is the electric potential, e_{iJ} are the piezoelectric constants, ε_{ij} are the permittivities. For the X-propagation these equations give

$$\rho\,\ddot{u} = (c_{55} + e_{31}^2/\varepsilon_{11})\frac{\partial^2 u}{\partial x_1^2}, \quad (12)$$

$$\varphi = (e_{31}/\varepsilon_{11})u. \quad (13)$$

In the case of small deviations of the propagation direction from the X-axis, there is a single small parameter in Eqs. (10)-(11) corresponding to the second derivative with respect to the x_2-coordinate. The estimation of order of different terms in Eqs. (10)-(11) with respect to the mentioned small parameter allows us to suggest the following procedure to derive the paraxial wave equation in this case. The last term in Eq. (10) can be replaced using Eq. (13). In order to transform the remaining term with electrical potential in Eq. (10), it is necessary to find an extension of Eq. (13) to include the effects of small parameter. For that, it is sufficient to replace the term $\varepsilon_{22}\varphi$ in Eq. (11) using Eq. (13) and then to find the required relation between φ and u

$$\varepsilon_{11}\frac{\partial^2 \varphi}{\partial x_1^2} = e_{31}\frac{\partial^2 u}{\partial x_1^2} + \left(e_{32} - e_{31}\varepsilon_{22}/\varepsilon_{11}\right)\frac{\partial^2 u}{\partial x_2^2}.$$

Using this relation, one can find the proper paraxial wave equation

$$\rho\,\ddot{u} = C_1\frac{\partial^2 u}{\partial x_1^2} + C_2\frac{\partial^2 u}{\partial x_2^2}, \quad (14)$$

where $C_1 = c_{55} + e_{31}^2/\varepsilon_{11}$,

$$C_2 = c_{44} + 2e_{31}e_{32}/\varepsilon_{11} - \varepsilon_{22}e_{31}^2/\varepsilon_{11}^2.$$

Then using Eq. (14), it is easy to derive a 2-dimensional (2D) parabolic equation similar to Eq. (8) with $\alpha = C_2/C_1$ to describe 2D focusing of pure shear waves propagating in the vicinity of the X-axis. For potassium niobate crystal $\alpha = -7.63$.

V. HEXAGONAL CRYSTALS

The procedure described above is not applicable directly to the case of wave propagation in the vicinity of acoustic axes of crystals. The problem in this case is to select correctly the proper sheet of the slowness surface among two contacting sheets in the direction of acoustic axis. Another problem, as shown further in this section, might be to determine the correct variable of the wave field to describe the spatial distribution of the focused beams. To solve these problems, it is convenient to use cylindrical coordinates. The equations of motion for hexagonal crystals in these coordinates in the axisymmetric case are [7]:

$$\rho \ddot{u}_r = c_{11} \frac{\partial}{\partial r}\left[\frac{1}{r}\frac{\partial}{\partial r}(ru_r)\right] + c_{44}\frac{\partial^2 u_r}{\partial z^2} + (c_{13}+c_{44})\frac{\partial^2 u_z}{\partial r \partial z}, \quad (15)$$

$$\rho \ddot{u}_z = c_{44}\frac{1}{r}\frac{\partial}{\partial r}\left[r\frac{\partial u_z}{\partial r}\right] + c_{33}\frac{\partial^2 u_z}{\partial z^2} + (c_{13}+c_{44})\frac{\partial}{\partial z}\left[\frac{1}{r}\frac{\partial}{\partial r}(ru_r)\right]. \quad (16)$$

The uncoupled equation for pure shear waves polarized along the angular coordinate ϕ is not used here, since the slowness surface for these waves has no concavities. Using the same arguments as above, the left-hand side of Eq. (16) is replaced by $c_{44}\partial^2 u_z / \partial z^2$, and the first term in the right-hand side of Eq. (16) is ignored. The resulting equation after integration over z becomes

$$\frac{\partial u_z}{\partial z} = -\frac{(c_{13}+c_{44})}{(c_{33}-c_{44})}\frac{1}{r}\frac{\partial}{\partial r}(ru_r). \quad (17)$$

Substituting Eq. (17) into Eq. (15) gives

$$\rho \ddot{u}_r = C_r \frac{\partial}{\partial r}\left[\frac{1}{r}\frac{\partial}{\partial r}(ru_r)\right] + C_z \frac{\partial^2 u_r}{\partial z^2}, \quad (18)$$

$$C_r = c_{11} - (c_{13}+c_{44})^2/(c_{33}-c_{44}),\ C_z = c_{44}.$$

The expansions of solutions to the relevant secular equations for plane bulk acoustic waves in a power series in a small angle of deviation from the basic directions give the same expressions for the angular dependences of the wave vectors as those following from Eqs. (6), (14), and (18). This agreement confirms the correctness of the derived equations. However, such an expansion does not give a reliable specification of the wave functions to be used as amplitudes in the parabolic equations in contrast to the present approach. The present approach leads to the following. By the change of variables

$$u_r = (\partial A/\partial r)\exp(ikx_3 - i\omega t), \quad (19)$$

where $k^2 = \rho\omega^2/c_{44}$, $x_3 = z$, and $\alpha = C_r/C_z$, (for zinc crystal $\alpha = -4.63$), Eq. (18) is reduced to Eq. (8). Thus, it turns out that the radial gradient of the solution to the axisymmetric parabolic equation determines the amplitude distribution of radial displacements in the axisymmetric beams. Hence, there is no focusing of radial displacements on the axis of beams under consideration. Indeed, the solutions to Eq. (8) are axisymmetric Laguerre-Gaussian beams [8] with amplitude maximum on the axis. The radial derivative for such field distribution is equal to zero at the center of beams. Therefore, the radial displacement in the axisymmetric beams of quasi-shear waves propagating

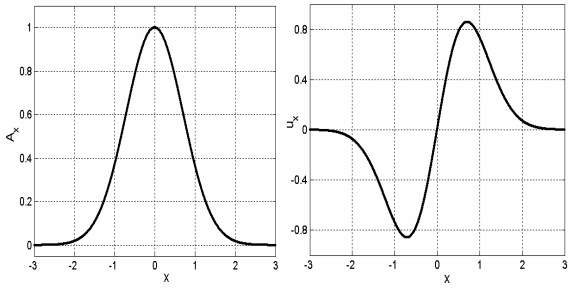

a) b)

Fig. 7. Profiles of beams in hexagonal crystals:
a) Gaussian beam in 2D case,
b) axisymmetric zero-order beam

along the axis of transverse isotropy in hexagonal crystals should have a null at any point on the beam axis. As illustration of this property, the Gaussian beam profile and its radial derivative are represented in Fig. 7. The Gaussian profile shown in this figure may correspond to the distribution of shear displacements in the beams of quasi-shear waves focused in 2 dimensions, while its transverse derivative shown in the same figure describes the profile of radial displacements for axisymmetric zero-order beam of quasi-shear waves, that coresponds to focusing in 3D case. The revealed property of zero radial displacement at the center of the beams is easy to understand with the aid of Fig. 8a. This figure shows how radial displacements might be distributed in the cross-section of the axisymetric beam. It is clear from this figure that non-zero radial displacements at the center would produce the violation of continuity of the solid medium and so they are impossible in this kind of beams.

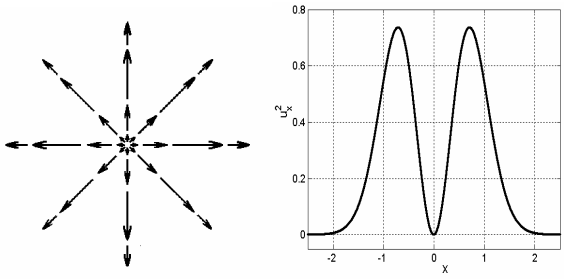

a) b)

Fig. 8. Axisymmetric zero-order beam in hexagonal crystals: a) transverse structure of radial displacements, b) profile of intensity

The intensity profile at the focus is proportional to the square of the radial displacement amplitude, shown in Fig. 8b for the studied axisymmetric beam. It follows from the figure that the cross-section of the intensity profile in this case looks like a ring with zero on the beam axis. Although the focusing on the beam axis (that is, focusing with respect to the main radial displacement) is impossible in the case of axisymmetric

beams, nevertheless, it becomes admissible if the beams have no axial symmetry.

VI. LENS MODES OF PERIODIC LAYERS

It is known that spatially localized traveling-wave-type modes can arise in a periodic array of lenses due to alternating focusing and spreading of wave beams. One would expect that a similar phenomenon might occur in a periodic system of two alternating layers with negative refraction at their interfaces. In this section, the solutions to the parabolic equations in the form of Eq. (9) are used to explore such a possibility. For simplicity let us consider a 2D case. In this case r in Eq. (9) is replaced by one of Cartesian coordinates, say x. To describe the wave fields in the layers using Eq. (9), it is necessary to distinguish the parameters $A(0)$, a and k involved in this equation for every layer. This is done using subscripts 1 and 2 on these parameters. Besides, it is necessary that a focus of wave energy is located in every layer (Fig. 9). In order to satisfy the last requirement, it is sufficient to replace x_3 by $z - f_n$ in Eq. (9), where z is a coordinate normal to the interface between the layers, f_n is the position of focus in the layer with number n, n is the individual number of the layers.

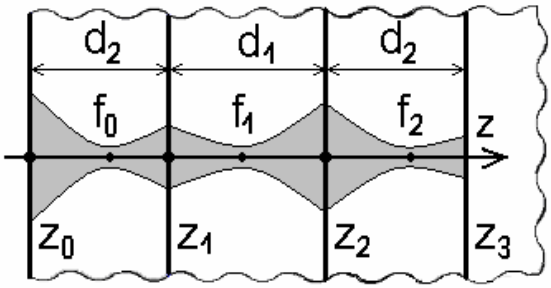

Fig. 9. Spatial distribution of the wave fields for a localized mode in two periodically alternating layers

An approximate solution to the problem may be found imposing the boundary conditions only on the dominant displacement component. Then it is sufficient to use the following two conditions. One of them is the continuity of the displacement at the interface between two adjacent layers, say at $z = z_2$. The other one following from the periodicity of the structure is the coincidence of the wave field distributions on the outer boundaries of two adjacent layers, i.e. at $z = z_1$ and $z = z_3$ for layers with the mutual boundary at $z = z_2$. These distributions are to be equivalent to within a constant factor, equal to the product of two transmission coefficients into these layers. At first, the dependences of transmission coefficients on the angle of incidence are ignored. Note that the deviation of the coefficients from unity is a measure of loss for the studied localized mode.

The formulated boundary conditions are fulfilled everywhere on the boundary planes only in the case when the arguments of the exponentials, corresponding to the wave fields in different layers, coincide with each other. This gives $a_1 = a_2$ and

$$\alpha_1(z_2 - f_1)/k_1 = \alpha_2(z_2 - f_2)/k_2, \qquad (20)$$

$$\alpha_1(z_1 - f_1)/k_1 = \alpha_2(z_3 - f_2)/k_2. \qquad (21)$$

Subtracting Eq. (21) from Eq. (20) results in

$$d_1/d_2 = -\alpha_2 k_1/(\alpha_1 k_2), \qquad (22)$$

where $d_1 = z_2 - z_1$ and $d_2 = z_3 - z_2$ are the thicknesses of the layers. Eq. (22) is the condition for the existence of localized modes of the travelling-wave type in periodic crystal layers. It shows that the coefficients α_1 and α_2 must be of different signs, that is, the slowness curve in the plane of Fig. 9 for one of two alternating layers should be concave while for the other layer it should be convex. The ratio of the thicknesses of the layers is not arbitrary but is instead circumscribed by Eq. (22). The account, in parabolic approximation, of the angular dependences of the transmission coefficients leads to a small shift in value of the thickness ratio defined by Eq. (22).

In the 2D focusing case under study, it is sufficient to use only two alternating layers with parameters prescribed by Eq. (22). In the case of 3D focusing by alternating layers which have no transverse isotropy, an additional third layer is required to correct the difference in curvature ratios in orthogonal directions on the slowness surfaces. This difference is present because there is no correlation between these ratios for different crystals used as layers.

VII. LOCALIZED RESONANCES

The solution for the localized mode in the layered structure considered in the previous section describes the wave beams with curved wavefronts in general case. The wavefronts become planar in the plane of minimal beamwidth. It means that a reflective surface in this plane would produce reflected beams without distortion of their structure. We suggest using this property to create a resonator with spatially localized acoustic modes. It follows from Eq. (20) that the thickness ratio of the layers required for the mode localization in 2-layer resonator is the same as that given by Eq. (22) for the periodic layered structure but with a different

definition of layer thicknesses $\tilde{d}_1$ and $\tilde{d}_2$: $\tilde{d}_1 = (z_2 - f_1)$ and $\tilde{d}_2 = (f_2 - z_2)$.

The spatial localization of vibrations due to focusing, as it is known, can occur in plano-concave resonators. However, the localization region of vibrations in such resonators is fixed by the design geometry and so it is unchangeable in the case of custom-made devices. A unique feature of the type of focusing studied in the present work is the absence of a fixed focusing axis in the uniform layered structures, that is, local and long-lived vibration might be excited at an arbitrary point on the surface of planar crystal resonators. For that, it is necessary to create a spatial distribution of exciting forces on the surface corresponding to the desired location of an excited resonant mode. The arbitrary mode localization allows us to consider this layered structure as a possible matrix for creation of arrays of uncoupled or weakly coupled resonators (Fig. 10). Such arrays may serve as sensors for measuring various parameters and they may be used for 2D imaging of spatial distribution of these parameters. In particular, the arrays of localized resonances under discussion could be used both as virtual keys for keyless keyboards and as movable pixels for imaging in touchscreen panels and graphics sensors. The excitation of such pixel resonances might be done using various scanning methods, in particular, laser beams or external electric or magnetic fields.

Besides these new opportunities, the advantage of the planar resonators is that they employ fabrication techniques, which are more suitable for mass production than those used for plano-convex resonators. On the other hand, the energy losses due to reflections at the interface of layers decrease the quality factor of the layered resonators. Obviously, this is a disadvantage in applications, for which high-quality-factor resonators are required. However, if the losses are not too high, they have no importance for the mentioned possible applications, related to the use of resonances with not so long lifetime. Thus, the suggested layered crystal resonators possess a unique property of free displacement of the region of excited localized resonances that offers new opportunities of their applications, which are absent for resonators of the previously known types.

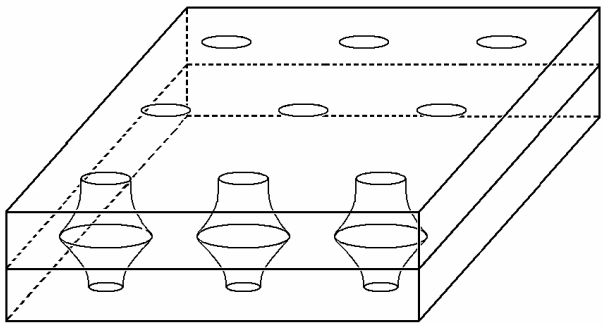

Fig. 10. Localized resonance modes as pixels for touchscreen panels and graphics sensors

VIII. CONCLUSIONS

The results of this study may be summarized as follows:

1. Parabolic equations are derived for quasi-shear and quasi-longitudinal acoustic waves in hexagonal and orthorhombic crystals. These equations are applicable to describe the effects of negative refraction due to local concavity in the slowness surface.
2. Analysis of the parabolic equation shows that efficient 3D focusing due to negative refraction is impossible in hexagonal crystals because of polarization restrictions. However, ring-like beams may occur in such crystals.
3. Solution to the parabolic equation is used to construct localized acoustic modes in periodic layered structure including crystal layers with negative refraction. The thickness ratio of the layers required for the mode localization is determined.
4. A new possibility is suggested to create crystal resonators of bulk acoustic waves with focusing and mode localization due to negative refraction at a planar interface between single-crystal layers. A unique feature of this type of focusing is that the focusing axis is defined by the source of mode excitation rather than the geometry of the structure. Therefore these resonances may be used as movable pixels in imaging for touchscreen panels and graphics sensors.

REFERENCES

[1] D. R. Smith, W. J. Padilla, D. C. Vier, S. C. Nemat-Nasser, and S. Schultz, Phys. Rev. Lett. **84**, 4184 (2000)
[2] L. B. Felsen, IEEE Trans. **AP-12**, 624 (1964)
[3] I. M. Mason, J. Acoust. Soc. Am. **53**, 1123 (1973)
[4] K. Imamura and S. Tamura, Phys. Rev. B **70**, 174308 (2004)
[5] B. C. Daly, T. B. Norris, J. Chen, and J. B. Khurgin, Phys. Rev. B **70**, 214307 (2004)
[6] M. Zgonic, R. Schlesser, I. Biaggio, E. Voit, J. Tscherry, P. Gunter, J. Appl. Phys. **74**, 1287(1993)
[7] R. W. Morse, J. Acoust. Soc. Am. **26**, 1018 (1954).
[8] H. Kogelnik and T. Li, Proc. IEEE **54**, 1312 (1966)

Proceedings of the 20th EFTF, 2006

The investigation of the mass-loading influence on the electrical parameters of AT-cut $GaPO_4$ resonators

I. Mateescu*, F. Krispel**, C. Bran*
[1]*National Institute of Materials Physics, P.O.Box MG-7, Bucharest, Romania*
[2]*Piezocryst Advanced Sensorics, Hans-List-Platz 1, 8020 Graz, Austria*
E-mail: imate@infim.ro

The results of the experimental investigations of the mass-loading effect and the influence of the thermal treatment and of the crystal plates finishing degree on the electrical parameters of AT-cut $GaPO_4$ resonators are presented. A comparison of these results with the results obtained previously for AT-cut quartz and Y-cut langasite resonators is performed. The conclusion of this study is that the mass-loading influence on the AT-cut $GaPO_4$ resonator characteristics is much smaller than that of the AT-cut quartz resonators, being almost the same as that of Y-cut langasite resonators.

I. INTRODUCTION

Many applications domains of piezoelectric devices are now requiring new characteristics for these devices to enhance the achievable system performances or simply to allow the implementation of new systems. Among them the most important are the recent and the future land mobile and space digital radio-communication systems. They require filtering devices with much larger bandwidth and increased centre frequencies i. e. resonators with larger coupling coefficient and better thermal stabilities. For these applications, a drastic reduction of the volume of the devices allowing the decrease of the equipments size is desirable [1].

The new piezoelectric materials of class 32 have very interesting complementary properties that can cover a very broad range of applications for frequency generation and filtering. The new materials belonging to this crystal class can surpass quartz for all the applications requiring a high coupling coefficient, and for many other applications demanding a new level of performances regarding other characteristics (lower losses or reduced phase noise, much reduced dimensions, lower impedance level, high temperature operations, etc.). They are particularly adapted for filtering and frequency generation in telecommunication equipments which requires a high performance level.

Among these new materials, Gallium Phosphate ($GaPO_4$), due to its properties, is a promising piezoelectric material for high tech applications such as high temperature pressure sensors, viscosimeters, microbalances for chemical sensors, etc. [2]. $GaPO_4$ [1] has a structure similar to α-quartz and presents improved physical properties compared with the quartz crystal. It belongs to point group 32 and its structure is homeotypic to quartz, the silicon atoms from SiO_2 being replaced alternately with phosphorus and gallium. Since there is no α-β phase transition, $GaPO_4$ can be used up to 970ºC. At this temperature occurs a phase transition to a cristobalite-like structure. The $GaPO_4$ crystal extends at high temperatures the good properties of the quartz for sensor applications (no pyroelectric effect, high insulation resistance). The high density of this material (3570 kg/m^3) leads to a lower acoustic velocity and, thus, to a lower thickness of a resonator working at the same frequency. The high piezoelectric coefficient (double, compared to quartz) leads to a higher electromechanical coupling coefficient of $GaPO_4$ resonators with better results in SAW and BAW devices. First measurements on $GaPO_4$ resonators were published 1989, and due to the poor material quality the results were modest. Since then, much effort has been done to improve the material quality and the manufacture process of the $GaPO_4$ resonators.

In the last time, the resonators suitable for BAW filters and oscillators, in the form of the rotated Y-cuts vibrating in the thickness-shear mode, have similar properties as the quartz resonators [3,4,5].

Previous investigations of the mass-loading effect in thickness-shear AT-cut quartz and Y-cut langasite resonators have shown that the resonators characteristics are influenced by the electrodes due to the non-uniformity of the vibration motion in the electrodes area [6,7]. The study of the mass-loading effect on the electrical characteristics of resonators is based on the Ballato's transmission-line analogs of the trapped-energy resonators vibrating in thickness-shear mode, that can evidence the electrical parameters behavior on fundamental frequency and harmonics [8,9,10].

As suggested in [10], the non-uniform distribution of motion is associated with the coupling of the thickness-shear and the thickness-twist modes, as well with the stress at the interface electrodes-piezoelectric substrate. In order to take into account the non-uniform distribution of motion found in practice for the plate resonators, a correction of the mass-loading and coupling coefficient relations was performed [10] using the Tiersten's

analysis [11] of the trapped-energy resonators vibrating in coupled thickness-shear and thickness-twist modes.
The experimental results regarding mass-loading effects on quartz resonator characteristics [12,13] pointed out that the harmonic dependence of the motional inductance for large thickness of electrodes, small electrode diameters and high frequencies could be ascribed to stress effects. In the case of small electrode thickness, large electrode diameter and low frequencies, the inductance behavior could be explained by the coupling of thickness-shear with thickness-twist modes.
Experimental investigations of the mass-loading effect on plan-parallel Y-cut langasite resonators, with various electrode diameters and thickness, were performed [14,15]. The comparison between the results of the measurements on AT-cut quartz and Y-cut langasite resonators has shown that the maximum variation of the effective mass-loading, effective coupling coefficient and motional inductance with overtones are significantly lower for Y-cut langasite resonators than for AT-cut quartz resonators.
In this paper are performed investigation of the mass-loading effect on electrical parameters of AT-cut $GaPO_4$ resonators and the influence of the thermal treatment and finishing degree of the plates on harmonic dependence of electrical characteristics. A comparison of the results with those previously obtained for Y-cut langasite resonators and AT-cut quartz resonators is given.

II. EXPERIMENTAL

Plan-parallel $GaPO_4$ AT-cut (Y-15.5^0) blanks of 14mm diameter and 5MHz fundamental resonant frequency, prepared from crystal grown by hydrothermal method in Piezocryst Advanced Sensorics, Graz, Austria, have been used in experiments. Four groups of $GaPO_4$ plates have been investigated: a) lapped (NN); b) polished (PN); c) lapped and thermal treated (NT); d) polished and thermal treated (PT). The crystal plates were lapped with abrasive powder $A1_2O_3$ (grain size 1μm) and part of them were polished using polishing pads. The thermal treatment of the samples was realized for 10 hours at 370ºC and a slow cooling down (9 hours). Ag electrodes with 7mm diameter and 80, 150, 200nm thicknesses have been deposited on the blanks by vacuum evaporation.
The resonance and anti-resonance frequencies and series resistances of the resonators function of the fundamental, 3rd, 5th and 7th overtones have been measured after every two pairs of electrode depositions. Using the relations for transmission-line equivalent electrical circuit of the resonator vibrating in thickness-shear mode, the effective mass-loading, piezoelectric coupling coefficient, motional inductance, motional capacitance and quality factor have been calculated. In our study we used the most relevant parameters: effective mass-loading, motional inductance and quality factor.

III. RESULTS AND DISCUSSION

The previous studies of the mass-loading influence on quartz and langasite resonators have shown that the harmonic dependence of electrical parameters is influenced by the electrodes due to the interfacial stress and to the coupling of the thickness-shear and thickness-twist modes. Taking into account the interesting properties and large application area of $GaPO_4$ crystal, in this paper has been performed an investigation of the mass-loading effect on the characteristics of AT-cut $GaPO_4$ resonators.
The most significant resonator parameters i. e. effective mass-loading, motional inductance and quality factor, were analyzed.
To compare the influence of the electrodes on AT-cut $GaPO_4$ resonators with that on AT-cut quartz and Y-cut langasite resonators, all these resonators, which vibrate in thickness-shear mode, have the fundamental resonant frequency of 5MHz. On these blanks have been deposited by vacuum evaporation Ag electrodes with 7mm diameter and 75, 150, and 200nm thicknesses.
The experimental results show that the maximum variations of the effective mass-loading, motional inductance and quality factor with overtones, for various electrode thicknesses, are influenced by the thermal treatment and by the finishing degree of the plates.
Figure 1 presents the effective mass-loading variation with harmonic order of AT-cut $GaPO_4$ resonators produced from the four types of plates (NN, NT, PN, PT) deposited with Ag electrodes of 150nm thickness. In figure 2 are presented the same resonators but with 200 nm electrode thickness.
These figures reveal that the effective mass-loading decreases with harmonic order for all types of resonators and all electrode thicknesses.

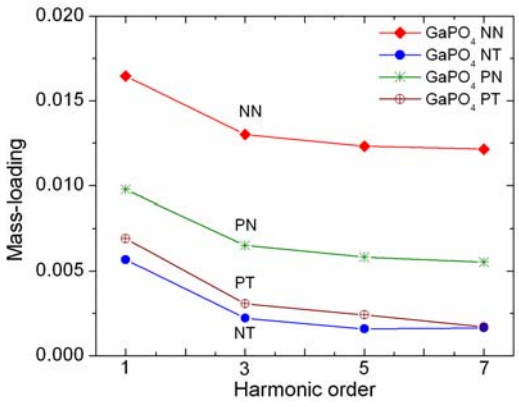

Fig.1 Harmonic dependence of mass-loading effect for resonators NN, NT, PN, PT with 150nm electrode thickness

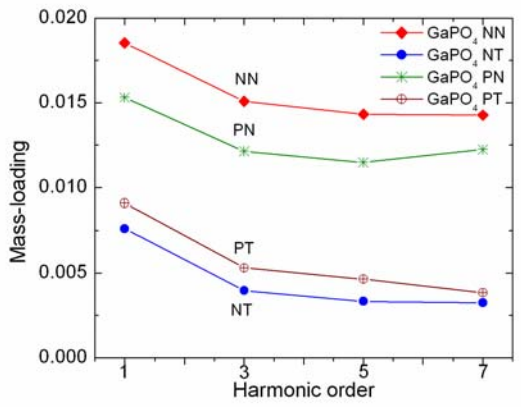

Fig.2. Harmonic dependence of mass-loading effect for NN, NT, PN, PT resonators with 200nm electrode thickness

This behavior is similar to that of Y-cut langasite resonators but is different to the dependence of AT-cut quartz resonators.

The extent of the changes of the effective mass-loading produced by the thermal treatment of $GaPO_4$ plates depends on surface state of resonators. In figure 1 (150 nm electrode thickness) is shown that, by thermal treatment of unpolished samples, the effective mass-loading decreases ~2.9 times, while for polished resonators the decrease of the mass-loading is only 1.6 times. The similar change of the effective mass-loading behavior by thermal treatment is shown in figure 2. Due to thicker electrodes (200nm), the mass-loading decrease 2.4 times in the case of unpolished plates and 1.2 times for polished plates.

A possible explanation of the effective mass-loading change by thermal treatment could be the diminution of the internal stress in $GaPO_4$ plates appeared during of the crystal growth and/or by the plates processing (cutting, lapping, polishing)

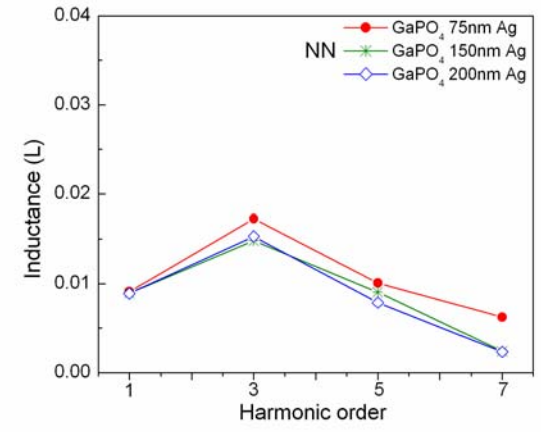

Fig.3. Harmonic dependence of inductance for NN resonators

In figure 3 is shown the inductance variation with harmonic order for NN type resonators (unpolished and no thermal treated) for three electrode thicknesses.

The inductance variation with harmonic order presents a maximum value on third overtone for all types of resonators (NN, NT, PN, PT) regardless the electrode thicknesses. The change of the inductance with electrode thickness is very small for all resonators. This behavior is similar to that of Y-cut langasite resonators.

By polishing and/or thermal treatment the inductance dependence on harmonic order is not significantly changed.

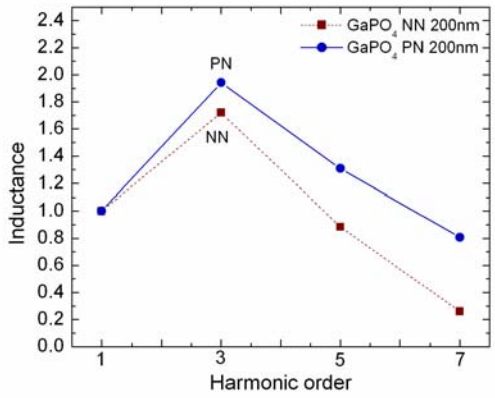

Fig. 4. Harmonic dependence of inductance of NN and PN resonators with 200nm electrode thickness.

In figure 4 is presented the variation with harmonics of the normalized inductance of resonators constructed from polished and unpolished substrates with 200nm electrodes. As in the case of AT-cut quartz resonators [7], the inductance values of polished resonators are higher than those of unpolished resonators: 1.13 times for third harmonic, 1.48 for fifth harmonic and 3.1 times for seventh harmonic. By polishing and by thermal treatment the inductance values increase on fifth overtone ~1.4 times (Figure 5).

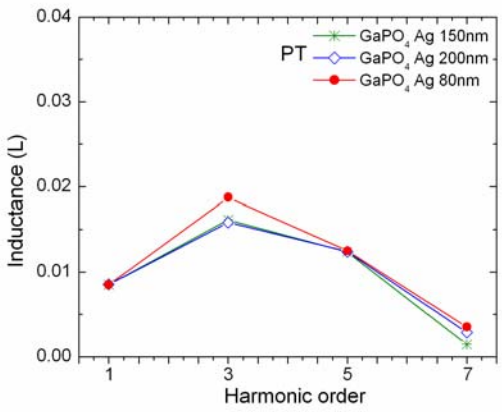

Fig.5. Harmonic dependence of inductance for PT resonators

The experimental results show that for $GaPO_4$ resonators the influence of the thermal treatment and finishing degree of the plates is more important for the quality factor than for the effective mass-loading and inductance. In figures 6-9 is presented the harmonic dependence of the quality factor for all types of resonators.

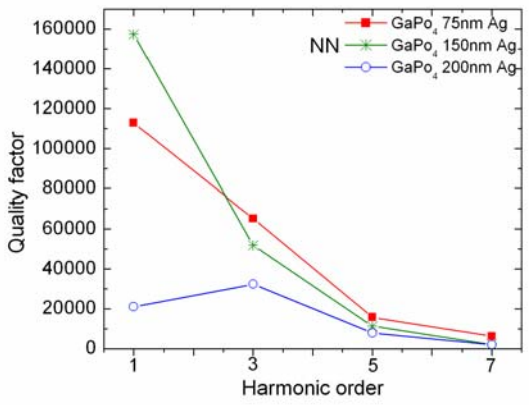

Fig.6. Harmonic dependence of quality factor for NN plates

Figure 6 shows that the maximum value of the quality factor (~160000) for resonators using unpolished and no treated plates is obtained on fundamental frequency for 150nm electrodes. For thin electrodes (80nm) the maximum Q value is obtained for the fundamental frequency, while for thick electrodes (200nm) the maximum Q value is obtained for the third harmonic and is much smaller (~32300).
The polishing and/or thermal treatment of the plates changes the position of the maximum quality factor from the fundamental frequency to the third harmonic.

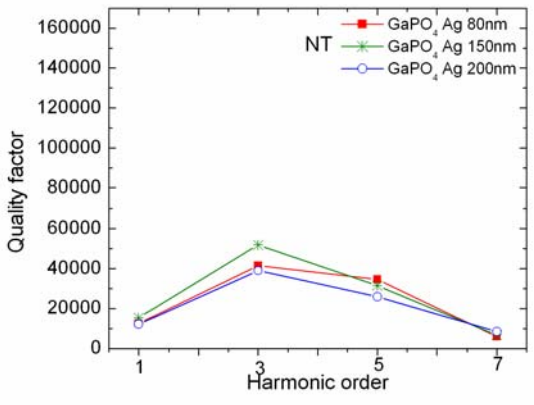

Fig.7. Harmonic dependence of quality factor for NT plates

In figure 7 is presented the variation of the quality factor with the harmonic order for all three electrode thickness of resonators produced from unpolished and thermal treated plates. By thermal treatment the maximum quality factor values is reduced (~51900 for 150nm electrode thickness) and is situated on third harmonic for all electrode thickness. In this case (NT plates) small differences between quality factors corresponding to various electrode thicknesses are observed.
Figure 8 reveals the quality factor dependence on harmonics and electrode thickness in the case of resonators with polished substrate. By polishing, the maximum quality factor is obtained on the third harmonic and his value increases comparing with that of unpolished resonators. As example for polished resonators with 80nm electrode thickness was obtained the maximum quality factor (~65950).

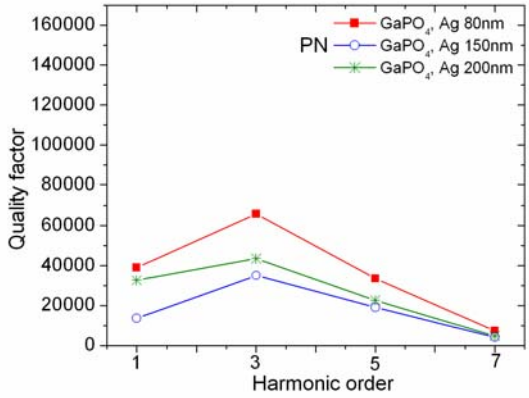

Fig.8. Harmonic dependence of the quality factor for PN plates

In the case of polished and thermal treated resonators (Figure 9) maximum quality factor value increases 1.6 times (~105700) for thin electrodes (80nm).

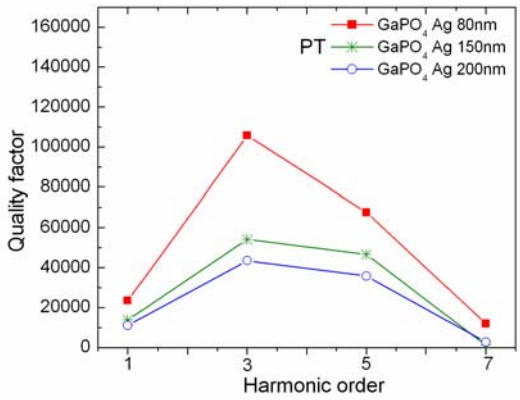

Fig.9. Harmonic dependence of quality factor for PT plates

As a conclusion, the highest value of the quality factor of $GaPO_4$ AT-cut resonators is obtained on fundamental frequency for 150nm electrode thickness (NN plates) or on the third harmonic for polished and thermal treated plates (PT) with 80nm electrodes.

To choose the optimum conditions for a specific application, the quality factor values for all electrode thickness and all resonator types (NN, PN, PT, NT) for the fundamental frequency (Figure 10) and for the third harmonic (Figure 11) have been presented.

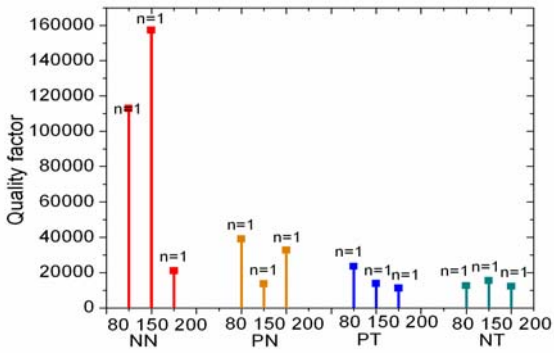

Fig. 10. Quality factor values for the fundamental frequency for all types of resonator and all electrode thickness.

Figure 10 shows that the resonator working on fundamental frequency has the maximum quality factor for unpolished $GaPO_4$ resonators with 150 nm electrode thickness.

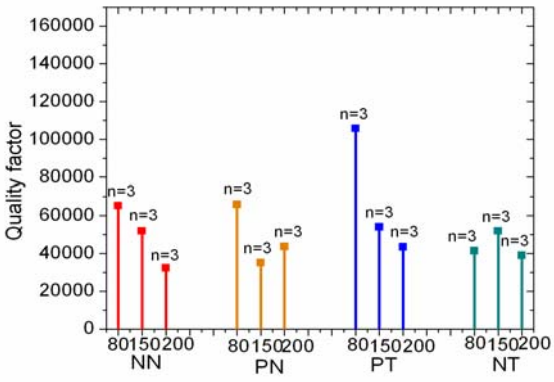

Fig.11. Quality factor for the third harmonic for all types of resonators and all electrode thickness

If the resonator is working on third harmonic the best quality factor is obtained using the polished and thermal treated plates with electrodes of 80nm thickness.

IV. COMPARISON OF AT-CUT QUARTZ, Y-CUT LANGASITE PARAMETERS WITH AT-CUT $GaPO_4$ RESONATORS

In the next figures (12,13,14) are presented the harmonic dependencies of the effective mass-loading, motional inductance and quality factor of AT-cut quartz, Y-cut langasite and AT-cut $GaPO_4$ resonators. All these resonators vibrate in thickness-shear mode on ~5MHz fundamental frequency, the crystal substrate (14mm diameter) is polished and no thermal treated. The vacuum deposited Ag electrodes have 150nm thickness.

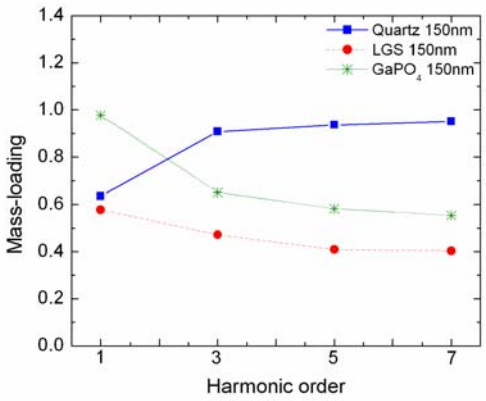

Fig. 12. Harmonic dependence of the effective mass-loading of AT-cut quartz, Y-cut LGS and AT-cut $GaPO_4$ resonators

Effective mass-loading behavior of AT-cut $GaPO_4$ resonators is similar to that of Y-cut langasite resonators and opposite to AT-cut quartz resonators (Figure 12).

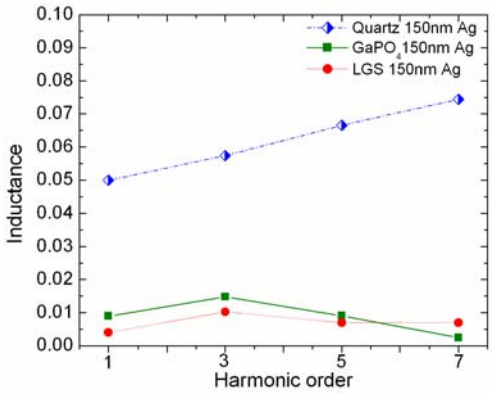

Fig. 13. Harmonic dependence of inductance for AT-cut quartz, Y-cut LGS and AT-cut $GaPO_4$ resonators

The mass-loading influence on motional inductance of AT-cut quartz resonators is much important than for Y-cut langasite and $GaPO_4$ resonators. It is possible that AT-cut of $GaPO_4$ and Y-cut of LGS crystals to be a stress-compensated cuts as SC-cut in quartz resonators. The previous results [7,13,14] concerning the mass-loading effect on the characteristics of AT-cut quartz resonators pointed out that, due to the internal stress at the interface substrate-electrode, the inductance changes with harmonic order and electrode thickness.
The quality factors of the polished and no thermal treated resonators obtained from these three crystals, have maximum values on the third harmonic.
This comparison reveals a new property of the gallium phosphate resonators: small mass-loading effect on resonator characteristics on fundamental frequency and harmonics for various electrode thicknesses.

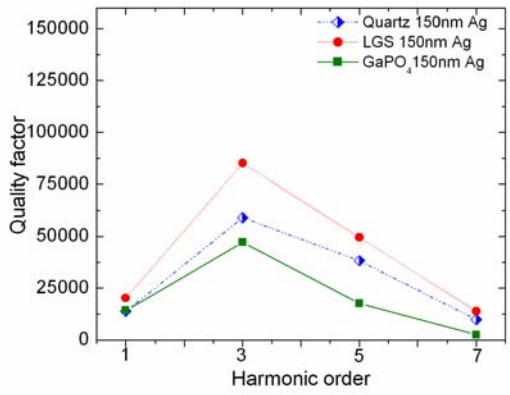

Fig. 14. Quality factor dependence on harmonic order for AT-quartz, Y-cut LGS and AT-cut $GaPO_4$ resonators.

V. CONCLUSIONS

The mass-loading influence on the parameters of AT-cut Gallium Phosphate resonators is much smaller than that previously reported for AT-cut quartz resonators, while being almost the same with that corresponding to Y-cut langasite resonators.

The harmonic dependence of the effective mass-loading is similar with that of Y-cut langasite resonators and opposite with that of AT-cut quartz resonators.

Influence of the thermal treatment on effective mass-loading is dependent on the surface state of the resonator substrate: stronger for unpolished resonators and weaker for polished resonators.

The change of harmonic dependence of inductance with electrode thickness is very small for all resonator types (NN, NT, PN, PT). The inductance variation with harmonic order of AT-cut $GaPO_4$ resonators is similar with that of Y-cut langasite (almost constant with harmonics) and different from AT-cut quartz resonators behavior. The thermal treatment does not significantly change the inductance behavior.

Thermal and mechanical treatments of the substrate influences the quality factor to a greater extent than the effective mass-loading and inductance.

The highest quality factor of the AT-cut Gallium Phosphate resonators is obtained on fundamental frequency with 150nm electrode thickness using the NN type of plate. For resonators with polished and thermally treated substrates, the maximum of the quality factor is obtained on the third harmonic and for 80nm electrode thickness.

Acknowledgements

This paper is the result of the scientific cooperation between the National Institute of Materials Physics, Bucharest, Romania and Piezocryst Advanced Sensorics, Graz, Austria.

REFERENCES

[1] J.Detaint, J.Schwartzel, A.Zarka, B.Capelle, J.P.Denis, E.Philippot, Proc.IEEE Int. Frequency Control Symposium, USA, 58 (1994)

[2] N.Prud'homme, P.Papet, Cachau-Herreillat, O.Cambon, J. Phys. IV France, **126,** 107 (2005)

[3] F.Krispel, H.Thanner, P.W.Krempl, C.Reiter, P.M.Worsch, W.Wallnofer, Proc.IEEE Int. Frequency Control Symposium, USA, 342 (2002)

[4] F. Krispel, C. Reiter, J. Neubig, P. W. Krempl, F. Lenzenhuber, W.Wallnofer, P.M.Worsch, Proc. IEEE Int. Frequency Control Symposium & European Frequency and Time Forum, USA, 668 (2003)

[5] J.Nosek, J.Zelenka, Proc. IEEE Int. Frequency Control Symposium, USA, 287 (2001)

[6] I.Mateescu, E.Candet, Proc. IEEE Int. Frequency Control Symposium, USA, 561 (1992)

[7] I.Mateescu, I.V.Mateescu, Proc. European Frequency and Time Forum, Switzerland, 63 (1993)

[8] A.Ballato, Proc. 26th Annual Symposium of Frequency Control, USA, 86 (1972)

[9] J.Kosinski, A.Ballato, S.Mallikarjun, Proc. 43rd Annual Symposium of Frequency Control, USA, 365 (1989)

[10] J.Kosinski, A.Ballato, I.Mateescu, I.V.Mateescu, Proc. IEEE Int. Frequency Control Symposium, USA, 229 (1994)

[11] H.F.Tiersten, Journal of the Acoustical Society of America, **59,** 879 (1976)

[12] I.Mateescu, J.Zelenka, I.V.Mateescu, Proc.IEEE Int.Frequency Control Symposium, USA, 405 (1996)

[13] I.Mateescu, I.V.Mateescu, G.Pop, Proc.Int. Piezoelectric Conference, Poland, 14 (1996)

[14] I.Mateescu, G.Johnson, A.Manea, Proc.European Frequency and Time Forum, Italy, 234 (2000)

[15] I.Mateescu, B.Capelle, J.Detaint, G.Johnson, L.Dumitrache, C.Bran, Proc. IEEE Int. Ultrasonics, Ferroelectrics and Frequency Control, Canada, 579 (2004)

Proceedings of the 20th EFTF, 2006

Chemical etching of LGS. Evidence for anisotropy

M. Akil, C.R. Tellier* and T.G. Leblois
Institute FEMTO-ST, Dept. LCEP, 26 chemin de l'épitaphe
25030 Besançon cédex, France
**Electronic address:* ctellier@ens2m.fr

The etching behaviour of differently oriented LGS plates in aqueous H_2SO_4 solution was studied. Variations of the etch rate of Y+θ plates with the angle of cut θ have been determined. Orientation effects in out-of-roundness profiles related to various LGS crystalline plates have been analysed in terms of crystal symmetry. Changes in surface texture of etched plates with orientation have been investigated. All the experimental results call for a dissolution process governed by orientation. However the observed anisotropy is different to that related to crystalline quartz.

I. INTRODUCTION

Up to now the quartz crystal remains the reference material for resonators with high stability. This crystal can also be used to fabricate MEMS devices by wet micromachining in HF or $NH_4F.HF$ solutions [1-3]. In the past few years interest in LGS crystal as an alternative material to quartz has been revived because LGS offers higher coupling coefficients [4,5]. However to our knowledge only few studies on the chemical etching of LGS were reported in literature [6-9]. Most of these studies were devoted to chemical polishing in acidic solutions. But micromachining is generally performed on crystalline plates for which the chemical etching is strongly anisotropic as for quartz [1-3] and for silicon [10-12]. So it is essential to determine if the chemical dissolution of LGS crystal is limited by diffusion or by orientation. This study replies to this lack and focuses on etch rates and on 2D shapes generated by chemical etching such as out-of-roundness profiles and surface profilometry traces.

II. EXPERIMENTAL DETAILS

Thin circular plates (1500 µm thick) were cut from a LGS ingot. Six orientations (as defined in [13]) were selected (Table 1). The angles of cut were determined using a double X-ray goniometer that offers an accuracy of about 30 s. The circular contour and one of the two faces of LGS plates were lapped and then mechanically polished. The other face is only lapped in order to initiate rapidly the development of dissolution figures.
The enchant is a H_2SO_4:H_2O solution with composition 2:1. Plates were etched at a constant temperature of 353 K. The temperature was controlled with an accuracy of about ± 1 K. Before and after etching thickness of etched plates was measured using a "Palmer" instrument that provides an accuracy of about ± 1 µm. Etched surfaces were examined by scanning electron microscopy (SEM). The surface topography was also investigated using a computer-based mechanical profilometer. The diamond tip of the stylus has a finite size of about 2 µm. Magnifications of profilometry traces allow us to recognize easily the etched shape of surface profiles. The changes in shape of the starting circular section of plates were studied using a Talyrond® analyser that generates the out-of-roundness profile at a magnified scale with the superimposed least mean square circle.

Cut	*X+0*	*X+45*	*Y+0*	*Y–45*	*Y+45*	*Y+90*
φ (°)	90	90	0	0	0	0
θ (°)	0	45	0	– 45	45	90

Table 1: Values of angles for the various cuts. Note that X+0, Y+0 and Y+90 plates correspond to X, Y and Z cuts respectively.

III. ETCH RATES

According to the IEEE standard [13] the Y+θ plates correspond to singly rotated plates with respect to X axis whereas the X+θ are doubly rotated plates with a second rotation about the Y axis. For a crystal belonging to class 32 the X axis is a two-fold axis and as a consequence the two faces of a Y+θ plate etch similarly. Then the etch rate R can be easily evaluated from the decrement in thickness Δd. But the two faces of a X+θ plate can suffer different chemical attacks so that measurements of Δd do not allow us to determine etch rates related to these two faces. It is the reason why experimental values of Δd/Δt rather than those of etch rates are collected in table 2. This table reveals that the Z cut etches more slowly than the Y-cut that is just the behaviour contrary to that observed for quartz crystal [1-3].

Cut	*X+0*	*X+45*	*Y+0*	*Y–45*	*Y+45*	*Y+90*
Δd/ Δt	0.54	0.82	0.41	0.16	0.34	0.24

Table 2: Experimental values of Δd/ Δt in µm/min.

IV. OUT-OF-ROUNDNESS PROFILES

Out-of-roundness profiles (ORP) displayed in Figures 1 and 2 are drawn after a first stage of etching. The duration Δt of etching is equal to one hour.

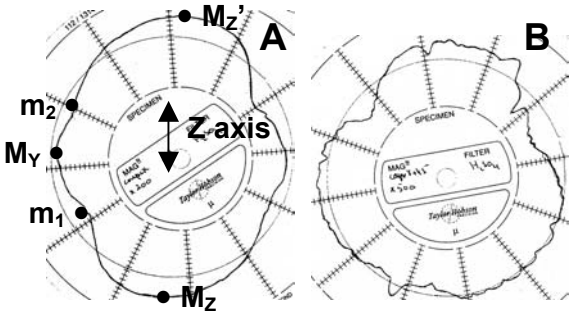

Figure 1: Out-of-roundness profiles related to X+θ plates. ORP **A** and **B** are for θ = 0°and θ = 45° respectively.

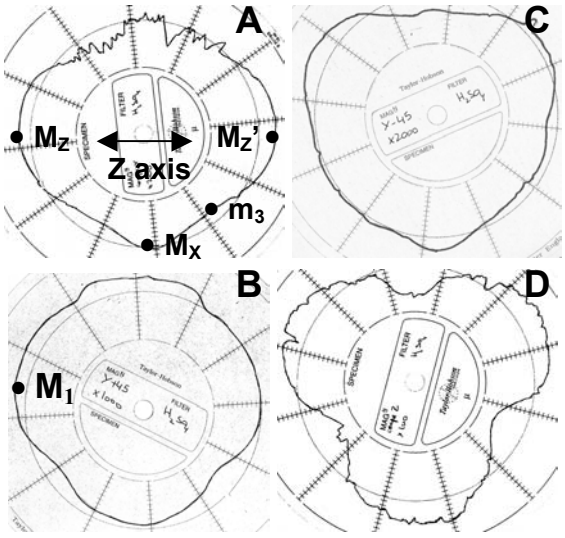

Figure 2: Out-of-roundness profiles related to some Y+θ plates. ORP **A**, **B**, **C** and **D** are for θ = 0°,θ = 45°,θ = –45° and θ = 90° respectively.

A visual inspection of cross-sectional ORP reveals several features:

(i) The final shape of ORP depends on the angles of cut. In particular the angular position of peaks and valleys in ORP is characteristic of the orientation.

(ii) Changes in ORP shape with orientation seem to be very progressive. Clearly the peaks and valleys are connected with maxima and minima in corresponding polar plots of the dissolution slowness [14, 15]. Consequently we infer that the representative surface of the dissolution slowness is certainly composed of few protuberances. Moreover Figures 1A and 2A call for more accentuated protuberances (M_Z and M_Z') corresponding to the two faces of the Z cut.

(iii) As expected for a dissolution process governed by orientation some ORP shown in figures 1 and 2 verify the symmetry specific to the class 32. The ORP related to the X cut (Figure 1A) shows the two-fold symmetry about the X axis. The ORP of the Z cut (Figure 2D) satisfies the three-fold symmetry about the Z axis. Moreover all the ORP corresponding to Y+θ sections exhibit a false mirror symmetry that in fact is associated to the two-fold X axis that lies in the section (The X axis is vertical in all ORP of Figure 2).

V. GEOMETRICAL SURFACE FEATURES

If the dissolution process is anisotropic and if we start with mechanically lapped surfaces the etching induces the formation of dissolution figures that cover entirely etched surfaces. The dissolution figures are characteristic of the cut and depending on the orientation more or less elongated pits or hillocks develop [14]. Linearly textured surfaces can be also observed for some specific orientations. The variety of dissolution figures is a consequence of anisotropy and thus it is essential to investigate the surface topography of etched surfaces. Figures 3 to 5 show SEM images of lapped surface after one hour of etching. At this point it is important to note that subsequent etchings do not modify the geometrical features of dissolution figures. In fact a prolonged etching causes only an enlargement of the dissolution figures.

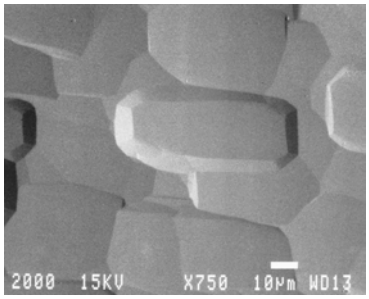

Figure 3: The surface texture of face 1 of the X+θ plate with θ = 0° (X cut)

The SEM images of Figures 3 to 5 give clearly evidence of a dissolution process mainly limited by orientation. Different dissolution figures are formed on the two faces of the X+θ plate with θ = 45° because this orientation has no symmetry elements. Depending on the angles of cut pits or hillocks develop on etched surfaces. The main features of the dissolution figures

that covered the various surfaces are listed in table 3. This table reveals that the etching of some Y+θ plates induces the formation of dissolution figures that are aligned along the X axis. This property is certainly correlated with the two-fold symmetry of the X axis. Kinematic models for the anisotropic etching establish without ambiguity that the dissolution figures result from the intersection of surface elements with diverging trajectories. In this condition dissolution figures must be composed of some curved portions. However it remains difficult on the SEM images to distinguish the concave portions from the convex portions. A method to overcome this difficulty is to perform a surface profilometry study.

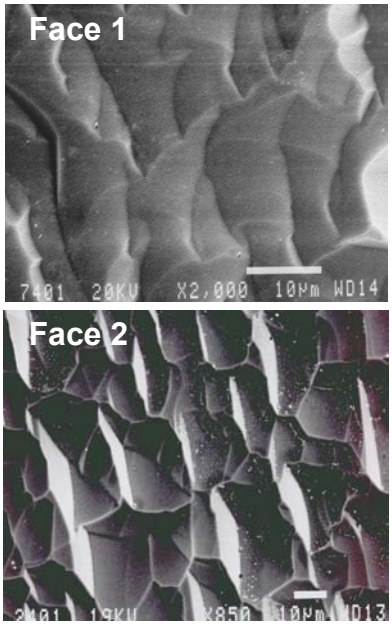

Figure 4: The surface texture of the two faces of the X+θ plate with θ = 45°.

φ, θ	*Geometrical features as viewed by SEM*
90°, 0°	Face 1 : Flat pits fitted into each other
90°, 45°	Face 1: Bumpy hillocks Face 2 : concave pits that overlap
0°, 0°	Relatively flat pits aligned along the X axis
0°, 45°	Bumpy hillocks aligned along the X axis
0°, – 45°	Elongated pits aligned along the X axis
0°, 90°	Pits with somewhat "circular" contours

Table 3: Geometrical features of dissolution figures as revealed by SEM examination.

VI. SURFACE PROFILOMETRY TRACES

Clearly profilometry traces must show directional effects. Hence we have chosen two perpendicular directions for the traces. For the four Y+θ plates one of the direction coincides with the X axis and the other trace corresponds to the rotated Z' axis (i.e. to the Z and Y axes for the Y and Z cuts respectively). In the case of X+θ plates the first trace is along the Y axis and the other along the rotated Z' axis.

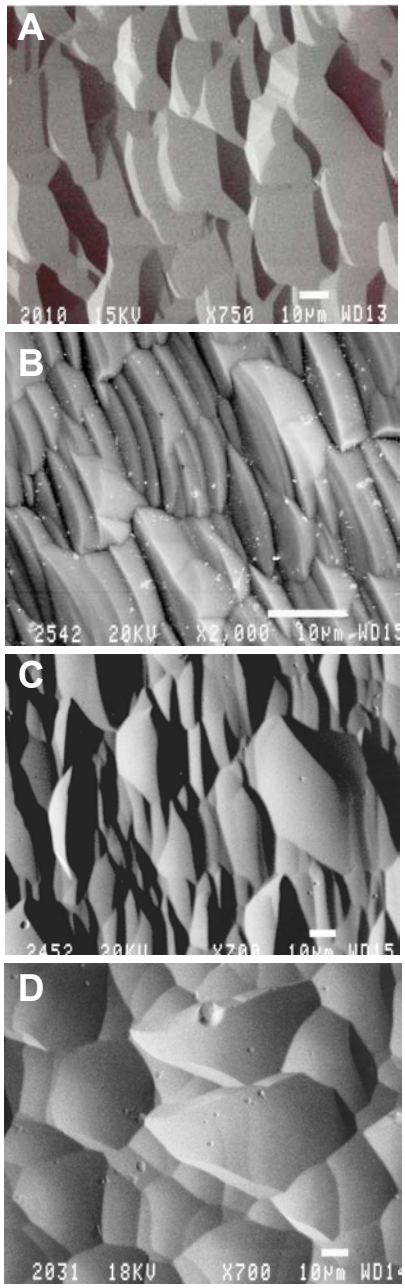

Figure 5: SEM profiles related to some Y+θ plates. ORP **A**, **B**, **C** and **D** are for θ = 0°,θ = 45°,θ = –45° and θ = 90° respectively.

Figures 6, 7 and 8 that collect the various profilometry traces allow us to identify the characteristic shape of these traces. In fact all traces are composed of curved elements. Let us for example examine the Z trace made

on the X cut (Figure 6 B). This trace shows clearly a "symmetrical concave" (Cc) background where a quite similar concavity affects portions of profile with positive and with negative slopes. A background of converse nature that is to say a convex (Cv) background associated to bumpy pits is observed (Figure 7 B) for the Z' trace made on the face 1 of the X+45 plate. But for some orientations the etching causes also the development of surface profiles with alternate concave-convex (or convex-concave) shapes. Figures 7a, $8B_2$ and $8B_3$ bear evidence of the formation of such traces with alternate shape. These traces allow us to describe schematically in tables 4 and 5 the main features of the various surface profiles.

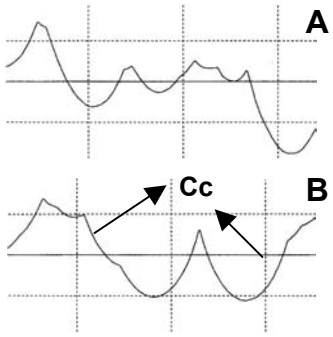

Figure 6: Profilometry traces made on the X+θ plate with θ = 0° (X cut). A and B are for Y and Z traces respectively.

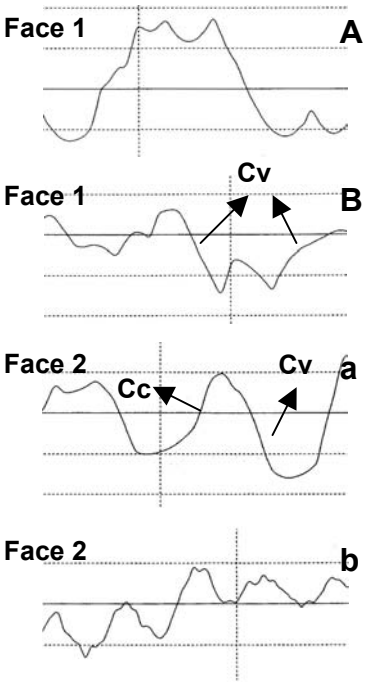

Figure 7: Profilometry traces made on the two faces of a X+θ plate with θ = 45°. **A**, **a** and **B**, **b** are for Y and Z' traces respectively.

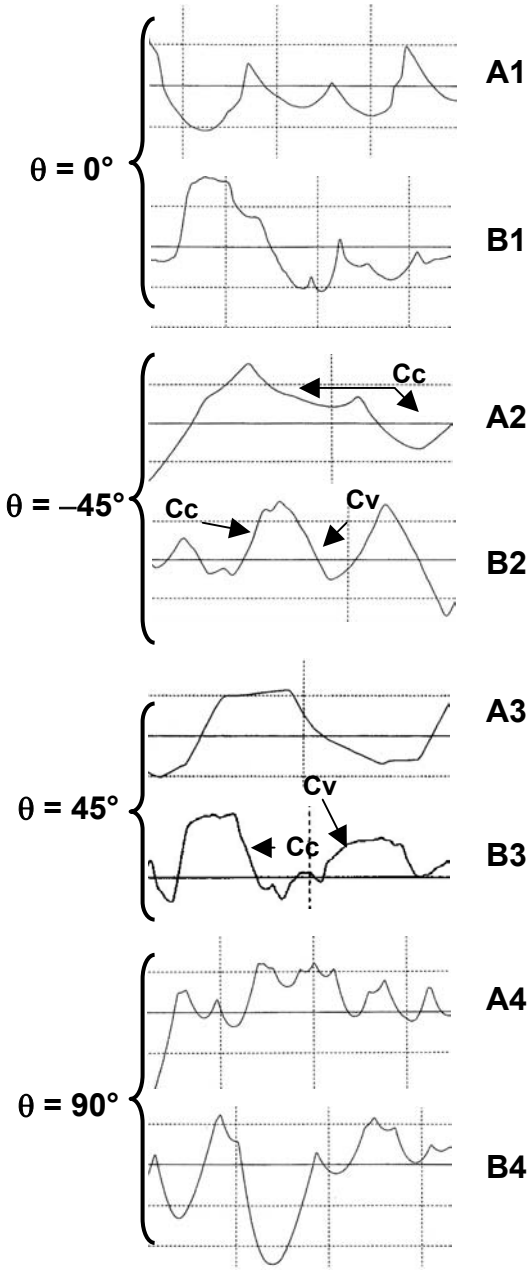

Figure 8: Profilometry traces made on various Y+θ plates. Profiles $\mathbf{A_j}$ and $\mathbf{B_j}$ with j =1, 2, 3 or 4 are for X and Z' traces respectively. Note that the peak to valley height R_{PV} remains smaller than 4 µm for all Y+θ plates other than the Y+45 plates where the R_{PV} reaches 4 µm.

Figures 6, 7, 8 and Tables 4, 5 demonstrate that only profiles elements with diverging trajectories participate to final etched surface profiles. Effectively diverging trajectories result in the formation of profilometry traces that necessary are only composed of curved elements. This behaviour is specific to a dissolution process governed by orientation.

Angles φ, θ	*Y trace*	*Z' trace*
90°, 0° Face 1	Concave and symmetrical	Concave and symmetrical
90°, 45° Face 1	Concave and symmetrical	Convex and nearly symmetrical
90°, 45° Face 2	Alternate concave-convex shape	With somewhat constant slopes

Table 4: Geometrical features of traces made on X+θ plates.

Angles φ, θ	*X trace*	*Z' trace*
0°, 0°	Concave and symmetrical	Concave and symmetrical
0°, - 45°	Concave and rather symmetrical	Alternate convex-concave shape
0°, 45°	Rather alternate convex-concave shape	Alternate shape with predominance of convex portions
0°, 90°	Concave and symmetrical	Concave and symmetrical

Table 5: Geometrical features of traces made on Y+θ plates.

VII. DISCUSSION AND CONCLUSION

All experimental etching shapes presented in this study give evidence for an orientation dependent dissolution process. The anisotropy of etching shapes can thus be conveniently described in terms of kinematic models [15-17]. The kinematic and tensorial model (KT model) for the anisotropic etching proposed by C.R. Tellier [17] is particularly convenient to understood observed 2D etching shapes such as out-of-roundness profiles and surface profilometry traces. Let us recall that in the KT model we associate at a surface element of orientation (φ,θ) (i.e. φ and θ are the angles of cut) a dissolution slowness vector **L** that characterises the anisotropy of the dissolution process. The vector **L** is related to parameters that can be determined experimentally in such a way [17] that is magnitude L (φ,θ) is equal to the reciprocal of the etch rate R (φ,θ) and that its direction coincides with that of the unit inward normal **n** to the surface element (Fig. 1). So when the orientation of the surface element varies the extremity of the vector **L** describes in space a representative surface called the dissolution slowness surface. Moreover the trajectory of a surface element within the crystal during the dissolution follows a straight line so that we can associate a displacement vector **P** to the surface element. This displacement vector lies perpendicular to the plane tangent to the dissolution slowness surface at the point of corresponding orientation. The interest of the KT model is that it is possible firstly, to determine the displacement **P** from the equation of the dissolution slowness surface and secondly, to construct numerically etching shapes. When we are concerned with a 2D etching shape we work with a particular cross-section of the dissolution slowness surface and consequently we have only to consider a polar graph of the dissolution slowness vector **L**. It is easy to show that depending on the concave (or convex) nature of the starting 2D shape displacements of profile elements diverge around a maximum (or a minimum) of the polar graph. More pronounced is the extremum of the dissolution slowness more accentuated is the divergence of trajectories. In the case of profilometry traces it thus appears that a concave (or a convex) background occurs when the polar graph present a maximum (or a minimum) for an orientation corresponding to the reference surface. In fact characteristic shapes of profilometry traces are correlated to the number and to the nature (maximum, minimum) of extrema of the dissolution slowness lying in an angular sector (–α°, +α°) centred on the reference dissolution slowness. For a starting lapped surface this angular sector is estimated to be (–20°, +20°). Table 6 lists the resulting shapes for the different cases that can be met in practice.

Number	*Nature*	*Shape of trace*
1	maximum	Concave
1	minimum	Convex
2	A maximum and a minimum	Alternate concave- convex shape
3	A minimum near α= 0° between two maxima	Concave -concave with constant average slopes
3	A maximum near α= 0° between two minima	Convex –convex with constant average slopes

Table 6: Expected geometrical features of traces with respect to number and nature of extrema present in the starting angular sector (–α°, +α°).

Moreover in terms of kinematic models out-of-roundness profiles constitute crude images of polar plots of the dissolution slowness lying in the corresponding cross sectional planes. Effectively the starting circular section is convex thus the etched section is mainly composed of profiles elements in the vicinity of minima in the cross-sectional polar plot. Moreover elements connected to minima have largest extents. As a consequence valleys in the ORP correspond to minima in polar graphs. But in practice peaks in ORP occur for orientations that at are found to be associated to maxima in polar graphs with departures of ±2° [14] that remain in experimental range. Owing to the properties predicted by kinematic models a tentative is made in the following to use the resemblance between polar graphs of the dissolution slowness and ORP to understand experimental etching shapes.

φ, θ	*Type of extrema*	*Expected shape of Z' trace*
0°, 0°	Maximum M_Y	Concave
0°, 45°	Minimum m_1	Mainly convex
0°, – 45°	Minimum m_2	Partly convex
0°, 90°	Maximum M_Z	Concave
90°, 0°	Maximum M_X	Concave
90°, 45° Face 1	Minimum m_3	Convex

Table 7: Expected geometrical features of Z' traces with respect to valleys (minima) and to peaks (maxima) present in the corresponding ORP.

Let us consider the Z' trace made on a given Y+θ plate. This trace lies in the plane (Y, Z) and the dissolution slowness $\mathbf{L}_{ref}$ (θ) of the reference Y+θ surface is directed in the rotated –Y' direction. Consequently the characteristic shape of Z' traces can be for Y+θ plates determined from the ORP related to the X cut (Figure 1A). Note that owing to the two-fold axis X the choice of the face is irrelevant for Y+θ plates. A similar analysis for the Z' traces related to X+θ leads to the conclusion that the ORP associated with the Y cut (Figure 2A) must be used to derive the characteristic shape of traces. Apparent minima and maxima situated in the angular sector centred on $\mathbf{L}_{ref}(\theta)$ are indicated in Table 7. Conclusions drawn from these observations are also collected in this table. These conclusions agree with experimental traces. Indeed Table 7 predicts:

(i) The formation of concave and nearly symmetrical Z' profiles for X, Y and Z cuts for which $\mathbf{L}_{ref}(\theta)$ coincides without ambiguity with a maximum (denoted respectively M_X, M_Y and M_Z on the ORP of Figures 2A and 1A).

(ii) The development of a convex Z' profile for the face 1 of the X+45 plate due to the minimum m_3 (Figure 2A).

(iii) The predominance of convex portions in the Z' trace made on the Y+45 plate. This predominance is caused by the minimum m_1 (Figure 1A) that is in the vicinity (7±1°) of the reference orientation.

In the case of the Z' profile related to the Y+θ plate with θ = – 45° the polar plot of **L** (and thus the X cut ORP) must fulfil one of the two following conditions to explain the observed alternate shape:

(1) Only the minimum m_2 that lies at about –15±2° of the reference orientation is present in the starting angular sector so the alternate shape is produced by changes in the curvature (from concave to convex) in the L(α) plot occurring when α takes positive values.

(2) A small maximum is also present in the angular sector that induces the formation a very slight protuberance that cannot be distinguished on the ORP. Note that his assumption implies also the existence of a third minimum between m_2 and M'_Z.

Taking into account that the identification of very small perturbations on ORP is problematic it is difficult to conclude with sureness. However to our opinion the first hypothesis remains the most probable.

φ, θ (Y+θ plane)	*Y+θ* cross-section*
0°, 0° (Y cut)	θ* = 90° (Z cut)
0°, 45° (Y+45 plane)	θ* = 135° or θ* = –45° (Y–45 plane)
0°, –45° (Y–45 plane)	θ* = 45° (Y+45 plane)
0°, 90° (Z cut)	θ* = 180° or θ* = 0° (Y cut)

Table 8: Identification of the cross-sectional plane Y+θ* for the various Y+θ plates.

Let us now turn attention on an X profile and on a given Y+θ cut. Elements of the starting profile stands in the Y+θ* plane with θ*= θ+90°. Hence to study the various X profiles we have to consider a part of the polar plot lying in cross-sectional planes listed in Table 8. The reference dissolution slowness $\mathbf{L}_{ref}(\theta)$ that in the reference system associated with the Y+θ plate is parallel to the rotated Y' axis lies now parallel to the Z'axis related to cross sectional Y+θ* plane. More precisely on Figure 2 $\mathbf{L}_{ref}(\theta)$ is parallel to the horizontal axis. Table 9 summarizes the position of $\mathbf{L}_{ref}(\theta)$ with respect to peaks and valleys that may be effective in determining final etching shapes of X traces.

φ, θ	*Position of $\mathbf{L}_{ref}(\theta)$*	*Expected shape*
0°, 0°	Between a minimum m_5 and a maximum M_2	Alternate shape convex-concave
0°, –45°	Near a maximum M_1	concave
0°,45°	No distinguishable extremum	No prediction
0°, 90°	Maximum M_Z	Concave

Table 9: Expected geometrical features of X traces with respect to valleys (minima) and to peaks (maxima) present in the corresponding ORP.

From comparison of Tables 5 and 9 we see that the theoretical analysis leads to correct results for Y+θ cuts with θ = 0°, 45° and 90°. In the case of the Y cut the fact that the concave portion of the X trace is important can be attributed to an abrupt change of curvature in the **L**(α) plot that certainly occurs in the vicinity of α = 0°. But it turns out that the analysis fails in the case of the Y+45 plate essentially because it is not possible to detect extrema with certainty on the Y–45 ORP.

Since LGS constitutes an alternative material to the quartz crystal it is justifiable to undertake a comparison of etching shapes encountered during anisotropic

chemical attacks of these two crystals. The comparison for quartz is undertaken for the $NH_4F.HF$: H_2O etchant [18]. Tables 10 and 11 give the main results of the comparison.

φ, θ	*LGS*	*Quartz*
0°, 45°	≈ 0.93	≈ 10
0°, – 45°	≈ 0.56	≈ 3.3
0°, 90°	≈ 0.12- 0.1	≈ 30

Table 10: Reduced anisotropy R(Y+θ)/R(Y cut)

φ, θ	*LGS*	*Quartz*
0°, 0°	Relatively flat pits	Somewhat triangular pits
0°, 45°	Mainly convex hillocks	Mainly concave pits
0°, – 45°	Concave pits	Elongated and flat hillocks
0°, 90°	Concave pits	Pyramidal hillocks

Table 11: Comparison of geometrical features of etched surfaces.

These tables emphasize the following main differences:
(i) Extrema of converse nature occur for the Z cut. We observe a large maximum of the dissolution slowness for the LGS crystal whereas it is commonly reported in literature [1-3,18] that in the case of the quartz crystal the Z cut corresponds to the smallest minimum.
(ii) In contrary to quartz the two faces of the X plate etch more rapidly than the Z surface in the case of LGS.
(iii) For a plate of a given orientation features of etched surfaces may be different for these two crystals. A good example of marked difference is furnished by the Z cut.
In conclusion the present work on the chemical etching of various LGS plates reveals three important points:
(1) Etching shapes are found to be orientation dependent.
(2) Kinematic models that outline the significant role played by extrema in the dissolution slowness can be conveniently used to determine final 2D etching shapes.
(3) The anisotropy of the dissolution process that affects LGS plates is different to that observed for quartz plates.
Hence it is important now to investigate the micromachining of 3D LGS structures in order to confirm the angular positions of peaks and valleys in the dissolution slowness surface. The subsequent step will be the determination of the dissolution constants that are involved in the analytical equation for the dissolution slowness surface. Accuracy in values of the dissolution constants is necessary to derive numerically etching shapes of 3D structures. This considerable work will be reported in a future paper.

Acknowledgements

We would like to thank the Direction General de l'Armement (DGA), Paris, France for its financial support.

REFERENCES

[1] G. Delapierre, Integrated Micro-Motion systems-Micromachining, Control and Applications, (Elsevier Science Publishers, 1990), pp 117-133
[2] C.R. Tellier, T.G.Leblois, *IEEE International frequency Control Symposium*, April 13-16, 1998, Besançon, France, (IEEE 1999) pp 847-850
[3] C.R. Tellier, T. Messaoudi, T.G. Leblois, S. Durand, *11th European Frequency and Time Forum*, March 8-11, 1997, Neuchâtel, Switzerland (FSRM Publisher, Neuchâtel, 1997), pp 386-390
[4] D.C. Malocha, M.P. Da Cunha, E. Adler, R.C. Smythe, S. Frederick, M. Chou, R. Helmbold, Y.Z. Zhou, *IEEE International frequency Control Symposium, 2000,* pp 200-205
[5] M. Sato, K. Moroishi, S. Ishigami, *IEEE International frequency Control Symposium, 1996,* pp 379-383
[6] S. Laffey, M. Hendricson, J.R. Vig, , *IEEE Int. Frequency Control Symposium, 1994*, (IEEE,1994) pp 245-250
[7] J. Bohm, R.B. Heimann, M. Hengst, R. Roewer, J. Schindler, J. Cryst. Growth **204**,128 (1999)
[8] H. Hyoung, K.B. Shim, K.H. Auh, T. Fukuda, Materials Lett., **46**, 354 (2000)
[9] H. Takeda, S. Okamura, T. Shiozaki,, J. Mater. Sci., **21**, 1117 (2002)
[10] C.R. Tellier, J. Mater. Sci. **33**, 117 (1998)
[11] A.R. Charbonnieras, C.R. Tellier, Sensors and Actuators A, **77**, 81 (1999)
[12] U. Schnakenberg, , W. Benecke, , B. Lochel, , Sensors and Actuators A, **21-23**, 1031 (1990)
[13] IEEE Standard on Piezoelectricity, (IEEE, New York, 1978) p 15
[14] C.R. Tellier, A. Brahim-Bounab, J. Mater. Sci., **29**, 6354 (1994)
[15] C.R. Tellier, J.Y. Amaudrut, A. Brahim-Bounab, J. Mater. Sci., **26**, 5595 (1991)
[16] K. Sangwal, *Etching of Crystals,* (North-holland, Amsterdam, 1987)
[17] A. Brahim-Bounab, J.Y. Amaudrut, C.R. Tellier, J. Mater. Sci., **26**, 5585 (1991)
[18] C.R. Tellier, *Technical report DRET, Convention 85.34.099.470.75.01*, (1988), 169 pp

Proceedings of the 20th EFTF, 2006

Balanced wideband tapered three-transducer low-loss SAW filters with impedance conversion

S. Doberstein
ONIIP, 231 Maslennikov str., Omsk, 644009, Russia
Electronic address: info@oniip.ru

This paper presents the balanced three-transducer SAW filters using tapered IDTs on YZ $LiNbO_3$ with impedance conversion as 1:2.6 from the input to output in a wide fractional bandwidth of 6-28%. The filters have shown an insertion loss of 4-6 dB, passband ripple of 0.5-2 dB, shape factor of 1.3-2.5, stopband attenuation of 20-35 dB in a center frequency of 35 MHz. Matching the filters with the loads was provided by LC-elements. Withdrawal weighting is used in order to improve the filter selectivity.

I. INTRODUCTION

The tapered single phase unidirectional transducers are widely used in the SAW filters for obtaining the fractional bandwidth over 10 % and reducing an insertion loss [1]. But sufficiently large insertion losses of 8-10 dB and narrow λ/8 or λ/6 width electrodes limit the application of these filters (λ is the SAW wavelength at the central frequency of the filter). In this connection the use of a three-transducer structure containing the conventional tapered input interdigital transducer (IDT) and two output IDTs placed symmetrically around the input IDT is very perspective [2]. Theoretically an insertion loss of the three-transducer structure with full matching is 3 dB. Because this structure has the conventional λ/4 electrodes it may be used readily in the frequency range up to 1 GHz. A passband ripple of the tapered three-transducer structure is controlled by an inclination of the output IDTs and may be about 1 dB [2]. In this structure a symmetrical connection of the tapered input and output IDTs to the loads is possible. Moreover this structure allows to increase the output impedance in sufficiently large limits. Consequently, the tapered three-transducer SAW filter can be the balanced/unbalanced structure with an impedance conversion in the wide frequency range. The balanced operation allows to combine the SAW filters with the modern balanced ICs of the amplifiers, mixers without using cumbersome baluns. The low impedance conversion to high impedance is highly suitable for matching the low impedance RF cascades with high impedance RF cascades for the wideband signal processing. This paper presents the new balanced low-loss SAW filters with impedance conversion as 1:2.6 from the input to output in a wide fractional bandwidth of 6-28%. The tapered three-transducer SAW filters are used for this purpose.

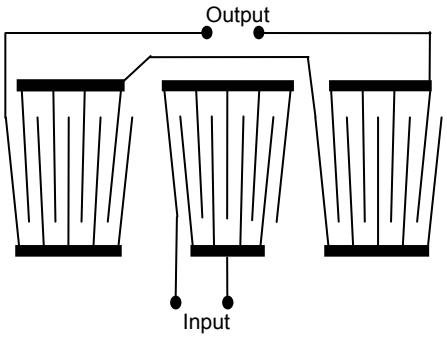

Fig.1. Balanced tapered three-transducer SAW filter with impedance conversion

II. BALANCED OPERATION AND IMPEDANCE CONVERSION IN THE TAPERED THREE-TRANSDUCER LOW-LOSS SAW FILTERS

For a fractional bandwidth of better then 5% we used wideband tapered three-transducer SAW filters [2] (Fig. 1). As will be seen from Fig. 1 in the three-transducer filter the input and output tapered IDTs connected in series/parallel have not a common grounded bus bar. So a symmetrical connection of the input and two output IDTs to the loads is possible. Consequently the tapered three-transducer filter can be both the balanced/ unbalanced structure similar to the conventional three-transducer SAW filter. This construction allows to increase the output impedance in sufficiently large limits by a series connection of the out IDTs (Fig. 1). In this case as a simulation shows in the tapered three-transducer filter the impedance conversion as 1:2 in achievable if all IDTs are identical.

III. EXPERIMENTAL RESULTS

The several tapered three-transducer SAW filters with a different fractional bandwidth of 6-28% have been designed on YZ $LiNbO_3$. The circuit used in the measurements is shown in Fig. 2. The parallel inductors Lc are used for the compensating of the IDTs static capacity. Measurements were carried out by a network analyzer and balanced transformers. The losses of the balanced transformers were eliminated from the measured insertion loss of the filter.

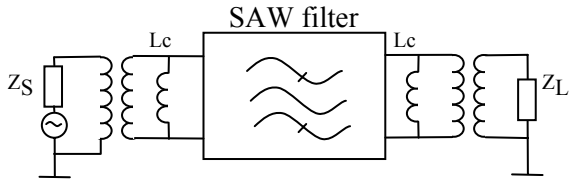

Fig.2. Circuit used in measurements

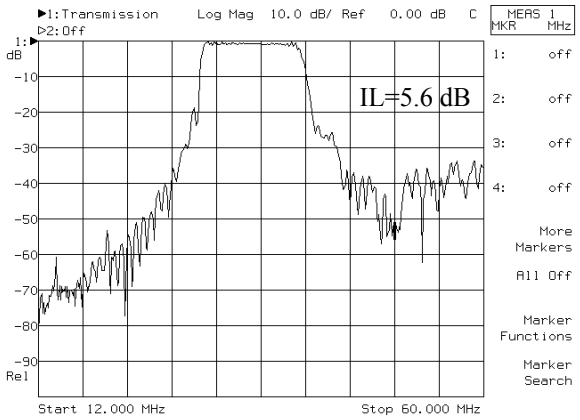

Fig. 3. Normalized frequency response of the filter with the 28% fractional bandwidth in a wide range

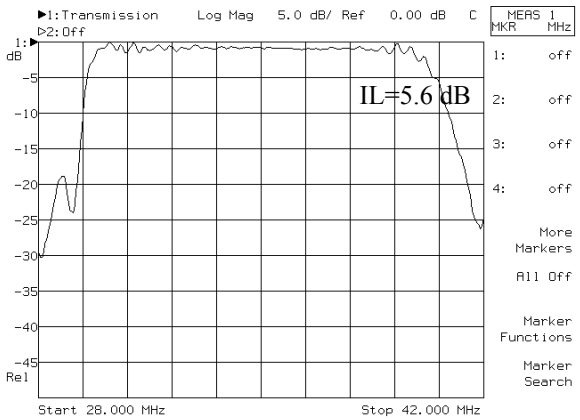

Fig. 4. Normalized frequency response of the filter with the 28% fractional bandwidth in the passband

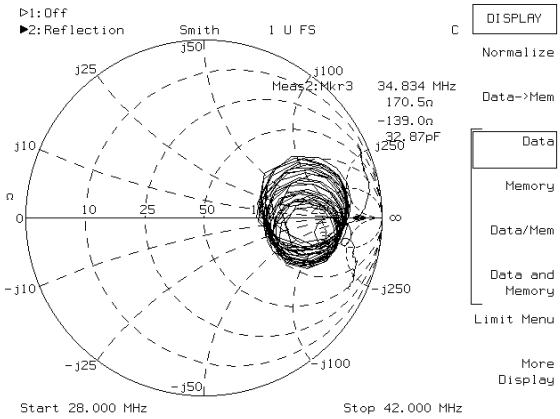

Fig. 5. Input impedance characteristic of the tapered three-transducer filter

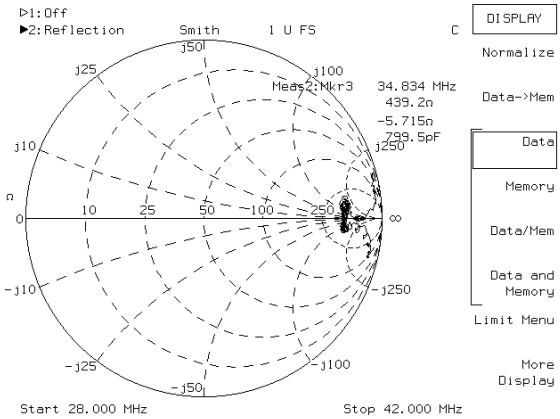

Fig. 6. Output impedance characteristic of the tapered three-transducer filter

The normalized measured frequency response of the filter with the fractional bandwidth of 28% is shown in Fig. 3,4. The filter has been symmetrically connected to a 170-Ω input load and to a 440-Ω output load. At the 34.83 MHz the filter has shown an insertion loss of 5.6 dB, low ripple of 0.5 dB, shape factor of 1.6 and stopband attenuation around 30 dB. An aperture of the filter was 36 λ. The input and output IDTs were 30 λ long. A measured input impedance characteristic of the filter with the parallel compensating inductor is shown in Fig. 5. As will be seen from Fig. 5 at the center frequency of 34.83 MHz the input impedance of the filter is close to real value of 170 Ω. A measured output characteristic of the filter is shown in Fig. 6. As will be seen from Fig. 6 at the center frequency of 34.83 MHz the output impedance of the filter is close to real value of 440 Ω. Thus the impedance conversion from 170 Ω to 440 Ω was obtained experimentally in the low-loss SAW tapered three-transducer filter with series connection of the output IDTs.

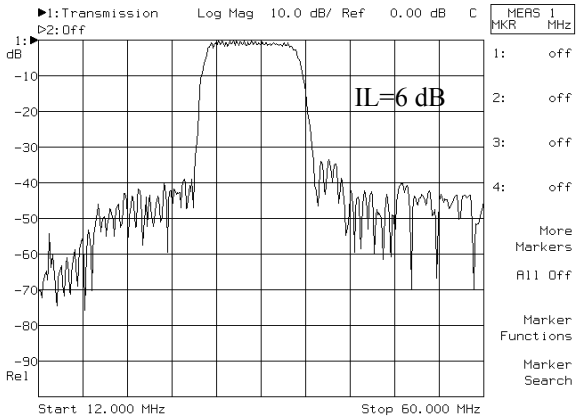

Fig. 7. Normalized frequency response of the filter with the withdrawal weighting in a wide range

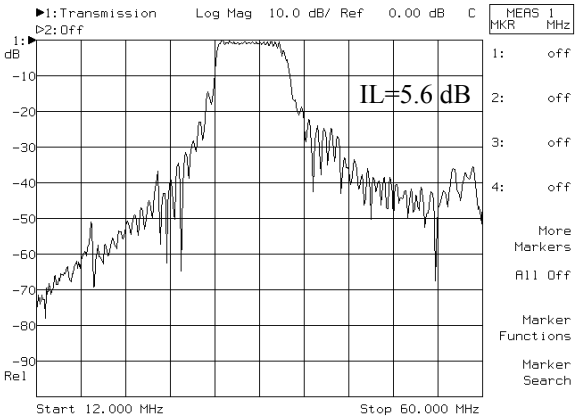

Fig. 9. Normalized frequency response of the filter with the 20% fractional bandwidth in a wide range

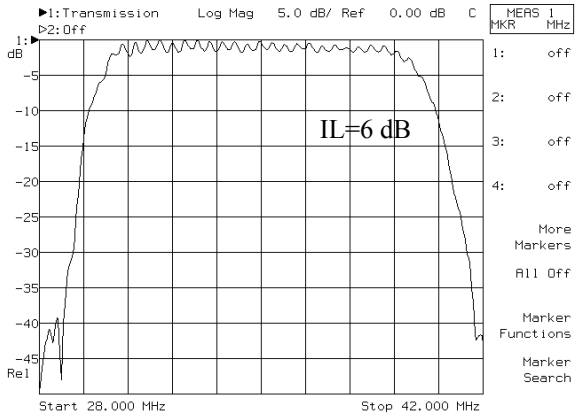

Fig. 8. Normalized frequency response of the filter with the withdrawal weighting in the passband

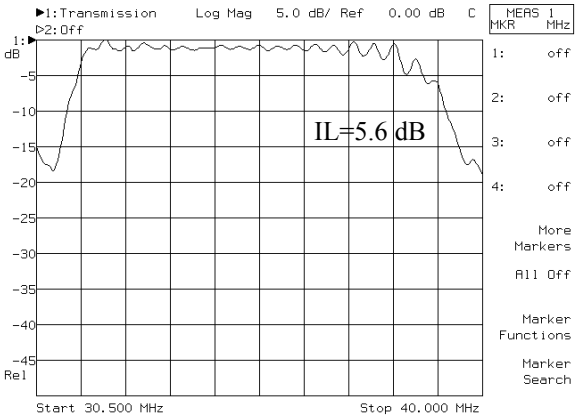

Fig. 10. Normalized frequency response of the filter with the 20% fractional bandwidth in the passband

To increase the stopband attenuation we can use the withdrawal weighting in the input IDT balanced tapered three-transducer filter. Fig. 7, 8 show the normalized frequency response of the filter with the withdrawal weighted central IDT. At the 34.83 MHz the filter has shown an insertion loss of around 6 dB, 3-dB fractional bandwidth of 28% with low ripple of 1 dB, stopband attenuation of 35-40 dB, shape factor of 1.3 in a symmetrical 250-Ω – 520-Ω system. The normalized frequency response of the filter with the 3-dB fractional bandwidth of 20% is presented in Fig. 9, 10. The filter has shown an insertion loss of 5.6 dB, low ripple of 0.5 dB, shape factor of 1.6 and stopband attenuation around 30 dB in a symmetrical 170-Ω – 440-Ω system. The amplitude ripples at the ends of the passband, shape factor will be enhanced when the fractional bandwidth is reduced (the slope of the IDT electrodes is reduced). Fig 11, 12 show the normalized frequency response of the filter with 6-dB fractional bandwidth of 10%. The filter has shown an insertion loss of 4.3 dB, ripple of 1.5 dB and 5 dB in the fractional bandwidth of 6% and 10% respectively, shape factor of 1.9, stopband attenuation of 20-30 dB in a symmetrical 100-Ω – 250-Ω system. The normalized frequency response of the filter with 6-dB fractional bandwidth of 6% is presented in Fig. 13, 14. The filter was provided an insertion loss of 3.8-4 dB, ripple of 2 dB and 5 dB in the fractional bandwidth of 3.6% and 6% respectively, stopband attenuation of 20-30 dB, shape factor of 2.5 in a symmetrical 50-Ω – 250-Ω system. Attempts at the reduction of the 6-10% fractional bandwidth ripple by the inclination of the output IDT according to method [2] have not been successful, even a deep minimum within the passband is appeared. Apparently this is depended on the phase responses of the inclined tapered structure. The further investigations associated with finding more precise inclination of the tapered IDT, curvatured [3] or stepped electrodes [4] of the tapered IDT are needed.

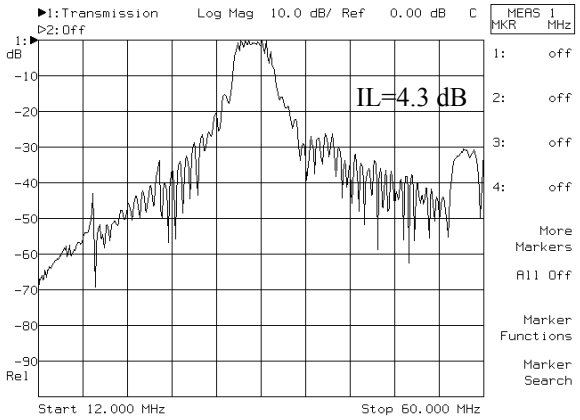

Fig. 11. Normalized frequency response of the filter with the 10% fractional bandwidth in a wide range

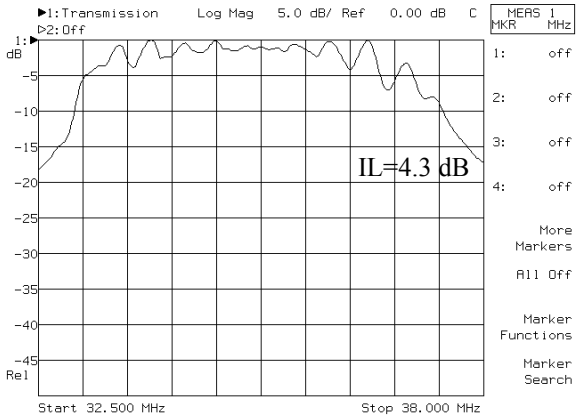

Fig. 12. Normalized frequency response of the filter with the 10% fractional bandwidth in the passband

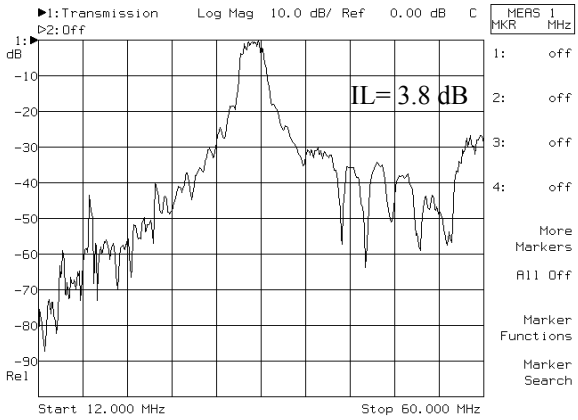

Fig. 13. Normalized frequency response of the filter with the 6% fractional bandwidth in a wide range

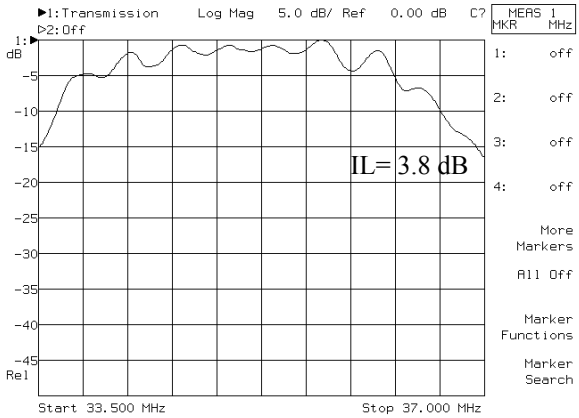

Fig. 14. Normalized frequency response of the filter with the 6% fractional bandwidth in the passband

IV. CONCLUSION

Developed the tapered three-trancducer filters have demonstrated the low insertion loss of 4-6 dB, balanced operation and impedance conversion in a wide fractional bandwidth of 6-28%. These filters have the wider functionalities than their much used prototypes and they are very promising for high frequencies because they have the conventional λ/4 width electrodes.

Acknowledgements

We would like to thank Mr. D. M. Gilfand for photomask design, valuable discussions and reduction work on manuscript.

REFERENCES

[1] L.Solie, Proc. IEEE Ultrason. Symp., pp. 27-37 (1998)
[2] M.Tsukamoto, J.Appl. Phys., v**. 50**, № **5**, pp. 3146-3152 (1979)
[3] C. K. Campbell, Y. Ye, and J. J. Sferrazza Papa, IEEE Trans. Sonics Ultrason., v**. SU-29**, pp. 224-228 (1982)
[4] G. Martin, B. Steiner, IEEE Trans. on Ultrason., Ferroelect., Freq. Contr., v**. 50**, №1, pp. 94-98 (2003)

Proceedings of the 20th EFTF, 2006

Single Point Calibration and Investigations of Thermosensitivity, Thermal Response Time and Long Term Stability of Quartz Temperature Sensors

*V.Gadjanova[1], R.Velcheva[1], L.Spassov[1], Y.Lazarov[1], L.Vergov[1], B.Dulmet[2]

[1]*Institute of Solid State Physics-Bulgarian Academy of Sciences*
72 Tzarigradsko chaussee blvd., 1784 Sofia, Bulgaria
viki_g@issp.bas.bg

[2]*Ecole Nationale Superieure de Mecanique et des Microtechniques, LCEP*
25030 Besancon, France

This paper presents the obtained results from the investigations of thermosensitivity; thermal response time and long-term stability of new miniaturized designs of thermosensitive quartz resonators with NLC-cut at fundamental frequency 29,3 *MHz,* used as high sensitive quartz temperature sensors (QTS). The comparison between thermal response time of the two types QTS01 (with plane parallel piezoelement) and QTS02 (with strip piezoelement) shows that QTS02 has shorter response time because of the smaller dimensions of the resonators. The frequency change does not exceed $3{,}5.10^{-7}$ after the 40th day of aging. This guarantees the reliable function of the sensor without additional recalibration in the next several years.

Special attention is given to the methodology and equipment for single point calibration of QTS. The QTS are calibrated at ice point according to the requirements of ITS-90. Knowing the thermosensitivity the frequency-temperature dependence in the interval from minus 20*°C* to 120*°C* is approximated. Thermosensitivity in this range is calculated as 1125 *Hz/°C*. The expanded uncertainty, obtained by multiplying the standard uncertainty by a coverage factor *k=2*, in the temperature range from minus 20*°C* to 120*°C* is estimated as 0,24*°C*. This value could be in an order lower if a correction of the non-linearity is taken into account at every defined temperature point.

I. INTRODUCTION

Thermo-sensitive quartz resonators became more attractive as high sensitive temperature sensors. The advantages of these sensors are: high sensitivity and dynamic range [1], independence from strong electric, magnetic and radiation fields [2] and a frequency output signal ideally suitable for digital processing. The thermosensitive quartz resonators are used in cryogenic techniques as temperature sensors for measurements at wide temperature range – from 4.2 *K* to 450 *K* [1,3]. Because of the attractive features of quartz crystal sensors (high sensitivity and accuracy) they are successfully used for calorimetric flow measurement of gaseous helium [4]. Such type of flow meters is more precise and convenient in comparison with other methods.

Precision, accuracy and reliability of the measurement strongly depend on calibration methodology and long-term stability of sensors.

This paper presents the obtained results from the investigations of thermosensitivity; thermal response time and long-term stability of new miniaturized designs of thermosensitive quartz resonators with NLC-cut at fundamental frequency 29,3 *MHz,* used as high sensitive quartz temperature sensors (QTS). Single point calibration methodology of QTS is proposed for some applications, where low cost calibrated sensors are necessary.

II. QUARTZ TEMPERATURE SENSORS QTS01 AND QTS02

The QTS01 type is the plan parallel circuit (ppc) resonator. They operate on resonant frequency 29,3 *MHz* on fundamental frequency. Resonators are housed in HC49-C enclosure with nitrogen or helium gas. The design of the resonators is shown on the Fig.1.

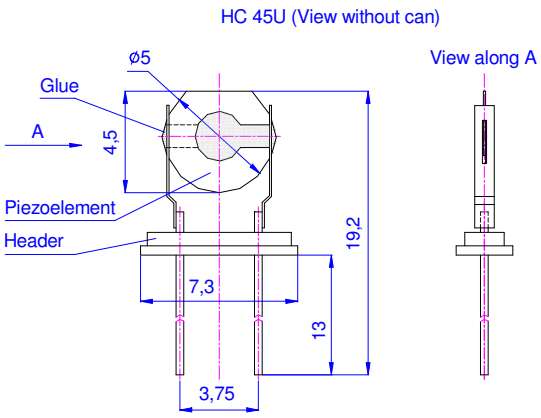

Fig.1. The QTS01 design

The QTS02 are the strip-type resonators. They operate on resonant frequency 29,3 *MHz* on fundamental frequency.

Resonators are housed in TU-39 enclosure with nitrogen or helium gas. The design of the resonators is shown on the Fig.2

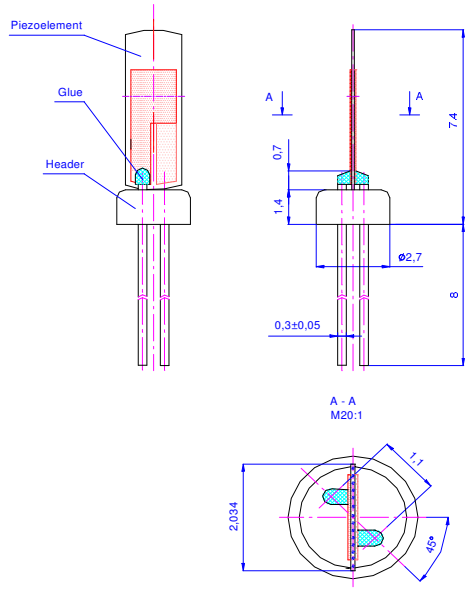

Fig.2. The QTS02 design

The typical value of the motional resistance for both series is 14 Ohm. The value of Q-factor is over 50000.

As it was mentioned in the previous reports [1,5], the QTS work in temperature range from minus 269℃ (4,2*K*) to 150℃ (430*K*) (fig.3). The temperature-frequency characteristic can be described by a polynomial of third order, but in the temperature range from minus 140℃ to 150℃ it has a linear character. Thermosensitivity is 2*Hz/*℃ at temperature minus 269℃ (4,2*K*) and becomes 1000 *Hz/*℃ at room temperature.

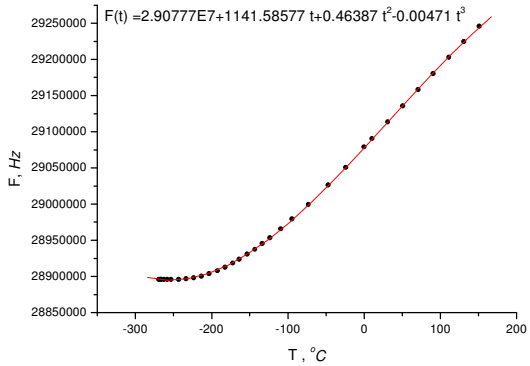

Fig.3.Temperature-frequency characteristic of QTS

III. SINGLE POINT CALIBRATION

III.1. Calibration setup

Figure 4 shows the block diagram of single point calibration setup.

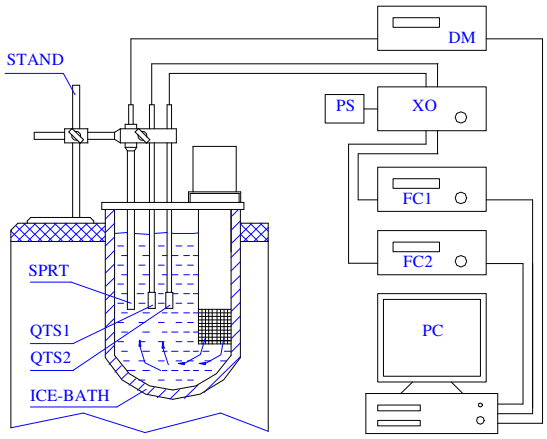

Fig.4. Setup for single point calibration
QTS1, QTS2 - Quartz thermo-sensors, SPRT – Standard Platinum Resistance Thermometer, PC – Personal computer, FC1, FC2 – Frequency counter 1 and 2, XO – Oscillator sours, PS – Power supply, DM – Digital multimeter

The comparison method of calibration is used. It involves comparing a QTS to Standard Platinum Resistance Thermometer (SPRT).

According to the requirements of the measurement traceability, several measurement devices have been calibrated, especially the frequency counters and the standard thermo sensor. The LabVIEW-program takes the readings from SPRT and QTS every 2 seconds and records them into a file..

III.2. Results and discussion

The expression "thermosensitivity of the quartz resonator" usually means the dependence of its resonant frequency versus temperature". Thermosensitivity is quantitatively measured by the thermosensitivity coefficient C_t determined at a fixed temperature t_0 (usually 25℃ or 0°*C*), which is equal to the derivative of the frequency *F* in regard to the temperature:

$$C_t = \frac{\partial F}{\partial t}\Big|_{t=t_0} \quad (1)$$

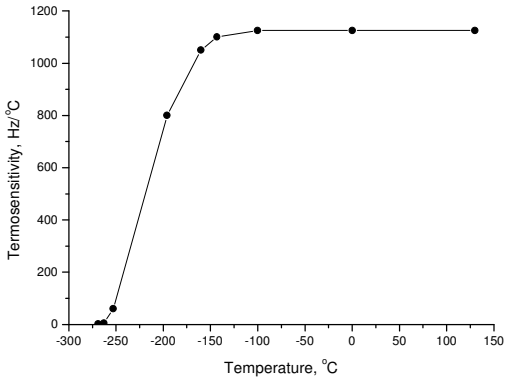

Fig.5. Thermosensitivity of QTS

The non-linearity is the smallest one (≤0,2 ℃) in the interval from minus 20 ℃ to 120 ℃. One can see, that the thermosensitivity is constant in the same interval too (fig 5).

The calibration of QTS by scanning in the whole interval is a very expensive procedure, which takes a lot of time. So this way, the QTS becomes expensive and the market too limited. Consequently, we have figured out that the single point calibration methodology of QTS for some applications is the best option. This is in the case where the low cost calibrated sensors are necessary. We consider that, if we have already found the thermo sensitivity (C_t) of the QTS we should be able to find the frequency temperature dependence in the all range from minus 20 ℃ to 120 ℃ according the equation:

$$F(T) = F_0 + C_t.T \qquad (2),$$

where

F_o is the resonant frequency in Hz at temperature 0 ℃,
C_t is the thermosensitivity in the range from minus 20 ℃ to 120 ℃,
T is the temperature in ℃.

The F_o is obtained from experimental measurement of resonant frequency at ice point (temperature 0 ℃). The measured thermosensitivity of the series TS01(which consists 50 of resonators) varies from 1114*Hz/℃* to 1154*Hz/℃*. In the series TS01 the drift of the C_t is 40*Hz*, which should be taken into account in uncertainty evaluation. The calculated average thermosensitivity is 1125*Hz/℃*. Next the frequency of QTS at the any desired temperature can be found and temperature-frequency characteristic can be drown as it is shown on Fig.6.

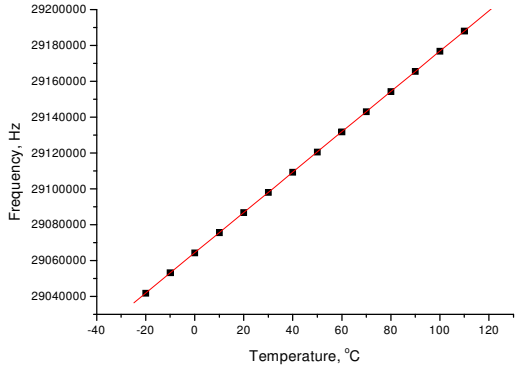

Fig.6. Temperature-frequency characteristic in temperature range from minus 20°C to 120°C.

Calibration of the QTS should be always connected to the evaluation of the uncertainties. The attainable uncertainty for temperature measurement system depends on a number of variables: statistical standard uncertainty, drift of thermosensitivity, non-linearity, instability and gradient of temperature, uncertainty of the measurement equipment. Expanded uncertainty, obtained by multiplying the standard uncertainty by a coverage factor *k=2*, in temperature range from minus 20 ℃ to 120 ℃ is estimated as 0,24 ℃. This value could be lower by one order of magnitude if a correction of the non-linearity is taken into account at every defined temperature point.

IV.THERMAL RESPONSE TIME

IV.1. Experimental setup

Using samples of QTS01 and QTS02 series, we measured the response time of the transducers for a temperature change from 100 ℃ to 0 ℃ in liquid medium. The experimental setup for measurement at 0 ℃ is shown on fig. 4. For measurement at 100 ℃ the ice bath is replaced by water vapor thermostat.

The frequency alteration is automatically registered by Lab VIEW program every 2 seconds. A standard quartz thermometer Hewlett Packard 2804A with sensitivity 10^{-4} ℃ detects the permanent static temperatures.

IV.2. Results and discussion

The thermal response time is the time interval necessary for reaching the temperature of the surrounding environment with a precision of up to 1 ℃, 0,1 ℃ and 0,001 ℃ when the transducer is removed from a medium with temperature 100 ℃ to a medium with temperature 0 ℃.

The typical thermal response time at cyclical temperature change from 100 ℃ to 0 ℃ within 1000sec. interval is shown on figure 7. The thermal response time

within 30 seconds for both QTS01 and QTS02 is shown on figure 8.

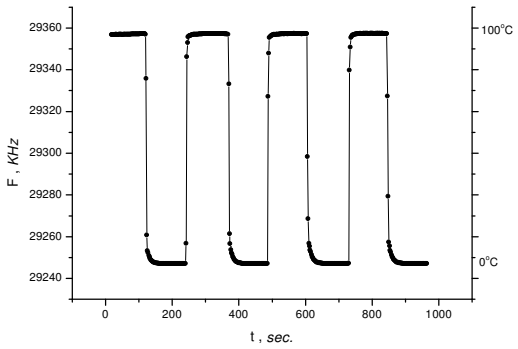

Fig.7. Typical thermal response time at cyclical temperature change from $100^{o}C$ to $0^{o}C$ of QTS02 sensor

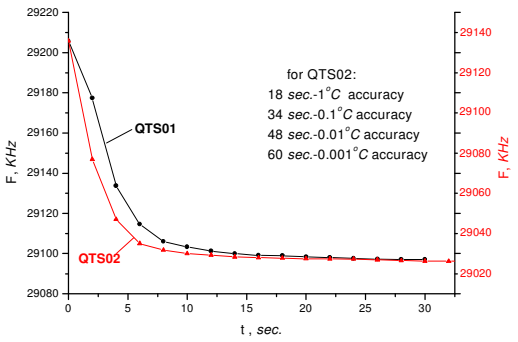

Fig. 8. Thermal response time within 30 seconds for both series

The results from the experiments carried out, show that the therma
l response time of the strip-type resonator is better compare to the thermal response time of the ppc resonator.

V. LONG-TERM STABILITY (AGING)

Long-term stability (aging) is the systematic change in frequency with time. Usually aging is stated as deviation in frequency, typically in part per million (ppm) over the time [6]. The aging of quartz crystal resonator has been identified as one of the most important quality control problems. The mechanisms that can cause aging are very complex:

- mass transfer to or from the resonator's surfaces due to adsorption or desorption of contamination inside the resonators enclosure;
- stress relief in the resonators-stress strain effects in the resonator blank, quartz defect, mounting and bounding structure effects, changes in the electrodes;
- other effects- package leaks and outgassing, chemical reaction effect. [7]

Manufacturing process, selection of electrode material, holder, seal-type and internal atmosphere can be optimised to produce resonators with minimum aging.

The long-term stability has been examined at room temperature $25^{o}C$. The purpose is to find the aging degree of the resonators under normal conditions in the storage. Sixty resonators have been kept in the storage at temperature about $25^{o}C$. The measurement period increases by 5, 10, 15, 30 and 90 days. Periodical frequency measurement is performed at supporting temperature $0^{o}C$ in an ice bath.

The temperature is registered by calibrated standard quartz thermometer Hewlett Packard 2804A. Frequency-measurement device for resonators frequency measurement consist of precise, calibrated frequency counter Ч3-64 type and two-channel crystal oscillator unit. The extended uncertainty is $\pm$ 0.059 °C. It includes uncertainty of frequency, uncertainty of oscillator and connecting cables, temperature gradient of the ice bath, temperature stability, uncertainty of the standard thermometer.

Experimental results prove that the aging can be positive or negative. The first part of the aging curve is sometimes referred as "initial" or "stabilization period".

Examples of aging behaviour are shown on figure 9.

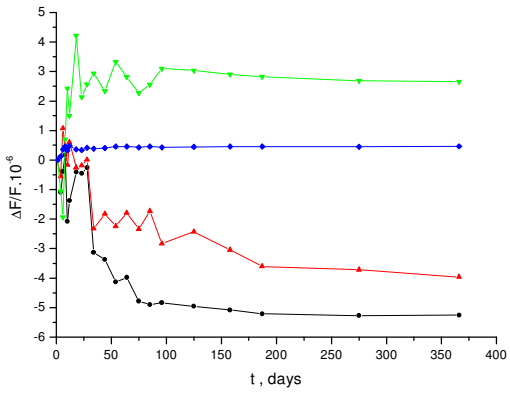

Fig. 9. Different aging behaviours

The typical changes of dependence $\Delta F / F$ in one year at $25^{o}C$ storage are shown on figure 10.

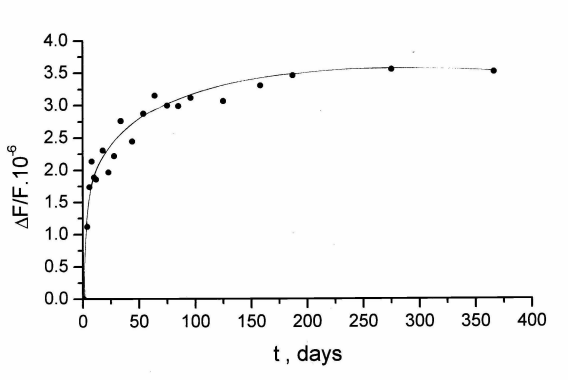

Fig.10. Typical aging characteristic at 25^oC storage.

The analysis shows that, the frequency change with the time is the most significant at the first forty days at 25^oC storage. The frequency change does not exceed $3{,}5.10^{-7}$ after the 40th day. This guarantees the reliable function of the sensor without additional recalibration in the next few years.

These changes are mainly due to relaxations of the crystal cell's intensity.

In order to decrease the aging, stabilizing processes are necessary. Such process could be the high temperature vacuum annealing at temperature about 200^oC at the end of the technological cycle before enclose the resonators.

In the next step of investigation, we are planning to carry out the characterization of aging at higher storage temperature of QTS.

VI. CONCLUSION

The QTS are calibrated at ice point according to the requirements of ITS-90. Knowing the thermosensitivity the frequency-temperature dependence in the interval from minus 20℃ to 120℃ is approximated. Thermosensitivity in this range is calculated as 1125*Hz/℃*. Calibration of the QTS should be always connect the evaluation of the uncertainties.. Expanded uncertainty, obtained by multiplying the standard uncertainty by a coverage factor *k=2*, in temperature range from minus 20℃ to 120°C is estimated as 0,24℃. This value could be in order lower if a correction of the non-linearity is taken into account at every defined temperature point.

The comparison between thermal response time of QTS01 and QTS 02 shows that it is better for QTS02 because of the smaller dimensions of the resonators.

When the transducer is removed from a medium with temperature 100℃ the time for reaching the medium with temperature 0℃ can be measured with a precision of up to 1℃ is 18 *sec*, 0,1℃ is 34 *sec* and 0,001℃ is 48 *sec*.

The frequency change does not exceed $3{,}5.10^{-7}$ after the 40th day of aging in storage at 25^o *C*. This guarantees the reliable operation of the sensor without additional recalibration in the next few years.

Aknowledgements

The European Commission within the GROWTH shared cost RTD funding scheme supported this work.
Project *QxSens* No. GRD1-2001-41816,
Contract No. G6RD-CT-2002-00648

REFERENCES

[1] L.Spassov, R.Velcheva et al., "Investigation of Thermosensitive Quartz Resonators NLC-cut at Cryogenic Temperatures", *16th European Frequency and Time Forum, 12-14 March, St.Peterburg, Russia, p. D037-D041 (2002);*

[2] R.Velcheva, L.Spassov, Yu. Filippov, E. Kulagin, V. Miklayev, Thermosensitive Quartz Resonators under gamma rays and Fast Neutrons", *Bulgarian Journal of Physics, vol.29(30), 2003;*

[3] L.Spassov, "Piezoelectric Quartz Resonators as Highly Sensitive Temperature Sensors", *Sensors&Actuators (A30), p.67-72 (1992)*

[4] LHE Internal Report, JINR, *Dubna, Russia (2005)*

[5] L.Spassov, E.Yossiffov, V.Georgiev, L.Vergov,"A rotated Y-cut Quartz Resonator with a Linear Temperature-FrequencyCharacteristic", *Sensor&Actuators A58(1997), p.185-189*

[6] J.R. Vig , T.R.Meeker, "The Aging of Bulk Acoustic Wave Resonators, Filters and Oscillators", *Proc. of 45 Ann. Freq. Control Symp. P.77-101, (1991) ;*

[7] A.Asiz, W.Zhang, Y.Xi, "Analysis of Aging of Piezoelectric Crystal Resonators", *IEEE Transaction on Ultrasonic, Ferroelectric and Frequency Control, vol.50, No12, (2003)*

Proceedings of the 20th EFTF, 2006

AUTODYNE MICROWAVE THERMOSENSOR UNDER VIBRODISTURBANCE INFLUENCE

Boloznev V.V., Safonova E.V., Sultanov F.I., Stanchenkov M.A., Mirsaitov F.N.
Kazan State Technical University, Kul-Gali str., 7 "a", 15apt, Kazan-420141, Tatarstan, Russia.
ksafonova@yandex.ru

1. INTRODUCTION

Our main goal is monitoring of flame parameters such as electron density and temperature with autodyne sensors, which operating principle is based on antenna's resistance dependence from these parameters. As estimating and optimization criterion of the quality control quantity of information, extracted by the sensor in a unit of time, has been chosen. Procedure of this quantity estimation, which has been called information productivity, includes spectral densities of controlled parameter and disturbance effect comparison by the Shannon method.

In the work [1] has been noted that autodyne sensors of combustion process in thermal power engine (TPE) chambers are subjected to the influence of many factors. Just one these factors (electron density or temperature) forms a monitoring signal. Other factors such as vibrations, different types of erosions, soot deposition on the firing surface, antenna's influence and etc. are disturbances. Preliminary quantitative estimations have been received under the assumption that listed factors are mutually independent; sensor's transfer characteristics are linear.

Actually in the TPE all the factors mentioned above, have been generated by one technological process. Their interconnection is indubitable, but not well known. With a fuel feeding growth not only power or traction are changing, but the temperature, pressure, vibrations and acoustic noise are growing too.

From the auto-oscillations theory point of view autodyne sensor's response both to monitoring parameter and to disturbance is equivalent to frequency destabilization. Destabilizing influence correlation (also including the one, appeared during response forming, because of this operation nonlinearity) has an effect on spectral envelope shape of the monitoring signal. It plays an important role in estimation of monitoring accuracy.

In a subject of our investigations there are two microwave autodyne sensors. One is the autodyne sensor of electron density in flame N_eAS [2, 3]. Another one (which is close to the first one by its circuit and construction) is an autodyne sensor of the temperature T in a wall area of combustion chamber - TAS.

Purpose of this work: quantitative estimation of the transfer characteristics nonlinear influence and correlation of actuating factors at the accuracy of monitoring. Accuracy measure as in [4] is an information productivity has been chosen.

Taking into account mentioned above features and pointed earlier [4] non-uniformity of the initial spectrums, goal achievement includes five stages:

- Finding a distribution law of monitoring signal;
- Determination of the correlation function (CF), spectral density (SD) of monitoring signal as a products of probe oscillation modulation by the influences aggregate;
- Finding of total and conditional entropies of monitoring signal; also their difference, which earlier has been called an information density;
- Monitoring signal band estimation taking into account an effective band of actuating factors and spectrum spreading under nonlinear transformation;
- Information density integration in this frequency band.
- As we see, such order of operations although has been provided by Shannon, but don't come to the well known example.

Because of the limited article size, we are going to present just part of received estimations, dedicated to the influence of:

- Nonlinearity - only for N_eAS;
- Correlation- only for TAS;
- Just one, but most essential for each AS disturbance factor. For TAS - only narrow band vibro-influence.

In the second situation only heat noise has been considered qualitatively.

2. CORRELATION FUNCTION AND SPECTRAL DENSITY OF THE SIGNAL

Under electron density N_e control the most powerful disturbance has been generated by fluctuating heating of antenna, which aperture coincides with N_eAS firing surface. Both influences are stationary, (except emergency situations) and have spectral densities and correlation functions

$$S_{N,T}(\Omega) = A_{N,T}\Omega^{-\gamma},$$

$$R_{N,T} = \frac{A_{N,T}}{\pi}\Gamma(1-\gamma)\sin\frac{\pi\gamma}{2}|\tau|^{\gamma-1} = B_{N,T}|\tau|^{\gamma-1} \quad (1)$$

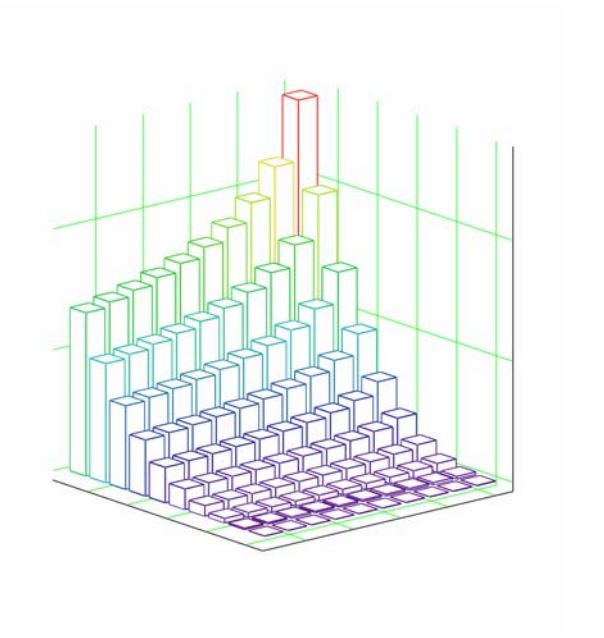

Fig. 1 Correlation function of stochastic process on the exit of NAS.

In linear approximation autodyne response in a sum with the sensor heating is:

$$x(N,T,t) = \Delta\omega(N,T,t)/\omega_0 = m_N\Delta_N + m_T\Delta_T = \\ = m_N(\Delta_N + \mu\Delta_T), \qquad (2)$$

where $\Delta_{N,T}$ - electron density and temperature increments, normalized by average values N_a, T_a.

Both spectrum responses are summarizing and the information density is estimating by the classical ratio [5]. Actually in the process of measuring transformation response's multiplication takes place because of nonlinearity $x(N,T,t)$ and dependence of m_N from the temperature. Simplifying the task and generalizing both cases, let's approximate response by polynomial:

$$y(N,T,t) = a_0 + a_1x + a_2x^2 + a_3x^3, \qquad (3)$$

where $x = x(N,T,t)$.

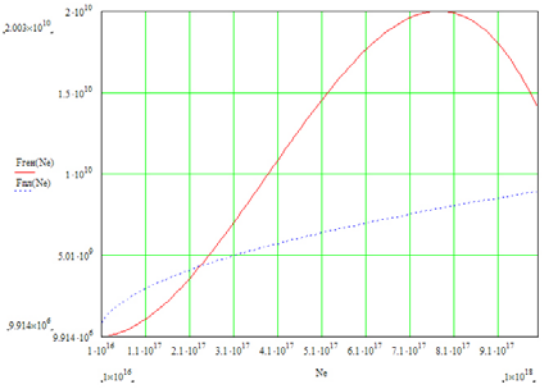

Fig. 2 Transfer function of NAS approximated by power polynomial and limited by plasma's frequency.

By the mentioned reasons polynomial coefficients are not the same like in Taylor's decomposition of the autodyne response. $x(N,T,t)$ stays as weighted sum (2), but with a different μ value.

Basing on a standard expression of the normal distribution law, attaching $x_1(t_1)$ and $x_2(t_2)$ values to the $x(N,T,t)$ function, let's calculate correlation function and spectral density of the monitoring signal:

$$R_\omega(\tau) = \sum_{n=0}^{n=3} b_n m_N^2 B_C^n |\tau|^{(1-\gamma)n},$$

$$S_{\omega N}(\omega) = \frac{b_0}{\omega} + \sum_{n=1}^{3}\left\{ b_n\cdot\left[\frac{A}{\pi}\cdot\Gamma(1-\gamma)\cdot\sin\left(\frac{\pi\gamma}{2}\right)\cdot\frac{1}{\sigma_x^2}\right]^n \times \right.$$

$$\left. \times\cos\left[\frac{\pi}{2}(\gamma-1)n+1\right]\cdot\frac{\Gamma(\gamma-1)n+1}{|\omega|^{(\gamma-1)n+1}}\right\}, \qquad (4)$$

where $B_C = (B_N + \mu^2 B_T)$, $b_n = b_n(a_n, M_{1,2})$, $M_{1,2}$ - mathematical expectations, corresponding to the electron density N_a and temperature T_a values in TPE nominal conditions.

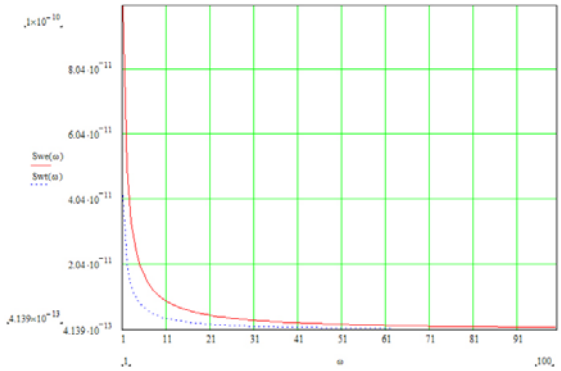

Fig. 3 Spectral densities of the frequency fluctuation caused by electron density and temperature values variation.

In a general case expressions (4) are bulky. However when $\mu^2 B_T \ll B_N$, $m_N = m_1(1+\mu\Delta_T)$ and under limitation of monitoring signal range from "bellow" (i.e. under $a_0 = 0$), polynomial (3) turns into

$$y(N,T,t) \approx m_1(\Delta_N + \mu\Delta_T) + m_1\mu\Delta_N\Delta_T + \\ + a_2\cdot(\Delta_N^2 + \Delta_N^2\Delta_T).$$

In this case expressions for correlation function and spectral density are simplifying.

3. SPECTRUM OF TAS SIGNAL

Operation principles of N_eAS and TAS are similar. Antenna plays the main role in the temperature response forming; its spectrum response is close to the $S_T(\Omega)$ spectrum. Due to autodyne frequency choice and antenna's construction features

N_e influence at the monitoring signal frequency is much less $\left(K_N\left\langle\Delta N\right\rangle \ll K_T\left\langle\Delta T\right\rangle\right)$. It considers like a noise. Influence mechanism of such disturbance and its result are clear from the previous part of the work. It is important also that neither controlled parameter T nor disturbance N don't cause nonlinear effects.

The main disturbance forms by combustion chamber vibration (in this work it is narrowband). Its influence mechanism consists in amplitude modulation of the monitoring signal. Moreover, resonator and oscillating diode heating exert influence on the amplitude. This process spectrum is much narrower than $S_T\left(\Omega\right)$.

Vibration spectrum is

$$S_V\left(\Omega\right)=\frac{A_V}{1+\left[2\left(\Omega_V-\Omega\right)/\Pi_V\right]^2}\cdot S_T\left(\Omega\right) \qquad (5)$$

It reflects not the direct temperature influence on vibrator (for example on the chamber wall), but their – vibration and temperature – common dependence from physicochemical effects in flame. $\Pi_V=\Omega_V/Q_V \ll \Omega_V$, Ω_V, Q_V - central frequency and Q-factor of vibrator.

Similar from the point of view of the fluctuation theory in active oscillators situation is also the same with considered in [5]. Following traditions, lets present spectral densities of amplitude (index α), frequency (υ) and joint fluctuations (even $\alpha\upsilon$ and odd $\alpha\upsilon^*$) for one sideband of the monitoring signal (following terms of the [5] it is a wing of the spectral line).

$$S_\alpha\left(\Omega\right)=A_T\frac{\Pi^2}{\Omega^{2+\gamma}}\left[\frac{K_V^2}{1+\left[\frac{2\left(\Omega_V-\Omega\right)}{\Pi_V}\right]^2}+K_d^2\left(\Omega\right)\right]$$

;

$$S_\upsilon=\frac{\left(K_A\cdot\Pi\right)^2}{2\Omega^\gamma}A_T\,;$$

$$S_{\alpha\upsilon}\left(\Omega\right)=K_A\cdot K_V\cdot A_T\frac{\rho\Pi+\Omega^2}{\Omega^{2+\gamma}}\,;$$

$$S^*_{\alpha\upsilon}\left(\Omega\right)=-K_A\cdot K_V\cdot A_T\frac{\Pi}{\Omega^{1+\gamma}}\,. \qquad (6)$$

Here K_V, K_A, K_d are influence coefficients of vibration, antenna's heating and resonator with a diode on the corresponding spectral densities. $\Pi=\omega/Q$ - resonator range and its Q-factor; $\rho=\omega\left(1+R_d/R_r\right)$ - where R_d, R_r - diode ($R_d<0$) and resonator resistances ; $\gamma<1$. Entire spectrum of the monitoring signal forms by $S_\alpha\left(\Omega\right)$, S_υ, $S_{\alpha\upsilon}\left(\Omega\right)$, $S^*_{\alpha\upsilon}\left(\Omega\right)$ magnitudes summation, where $S_{\alpha\upsilon}\left(\Omega\right)$ gets into "right" wing, $S^*_{\alpha\upsilon}\left(\Omega\right)$ - into "left", that causes spectrum asymmetry [5].

Spectral components presented on the figures

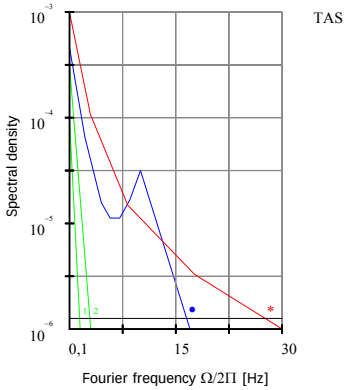

Fig. 4 Spectral densities of the sensor's responce (*), amplitude fluctuations (•), caused by the temperature and narrow-band vibration interferences.

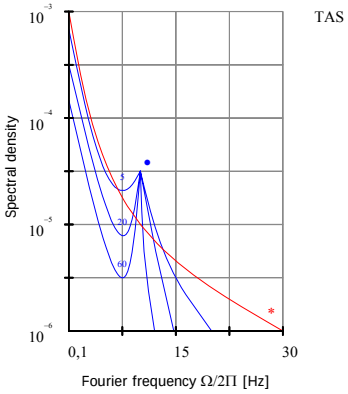

Fig. 5 Spectral densities of the sensor's responce (*), amplitude fluctuations (•), caused by narrow-band vibration interference with a different Q-factor.

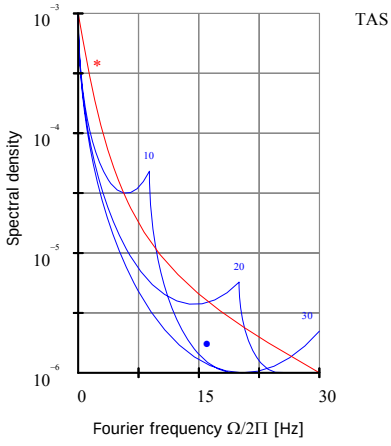

Fig. 6 Spectral densities of the sensor's responce (*), amplitude fluctuations (•), caused by narrow-band vibration interference with central frequencies: 10, 20, 30 Hz.

4. INFORMATION PRODUCTIVITY

According to the algorithm, which was described in the beginning of the article, information productivity estimation is

$$W = \int_0^{\Omega_V} \left[\log_2(S_{MS}+S_{\Pi}) - \log_2 S_{\Pi}\right] d\Omega \qquad (7)$$

where Ω_V - band boundary of the monitoring system.

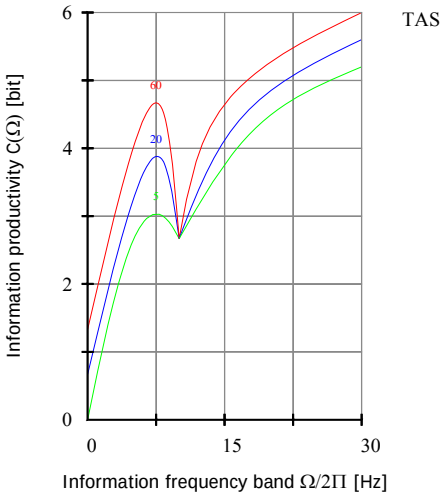

Fig. 7 Information productivity of the sensor under vibration interferences with a different Q-factor.

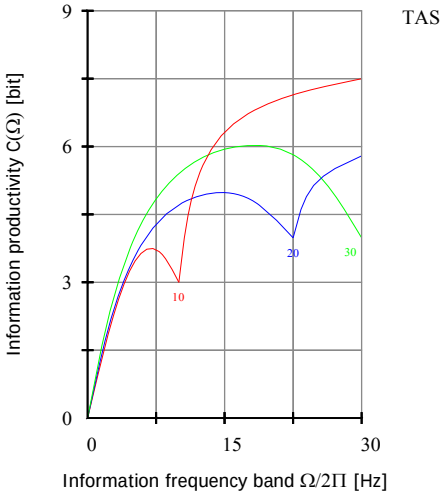

Fig. 8 Information productivity of the sensor under vibration interferences with central frequencies: 10, 20, 30 Hz.

All spectral densities, which were found for all types of the sensors, as summands get into the first term of subintegral expression; those which form conditional entropy get into second term.

It is complicated and ambiguous to relate spectral densities calculated components to the one of two aggregates S_{MS} or S_{Π}. It happens, because most of the calculated spectral densities more or less contain information about the monitoring parameter - N_e for the $N_e AS$ and T for the TAS. Let's restrict possible variants. Under the most hard restriction S_{MS} contains only undistorted monitoring signal, i.e. linear term for $N_e AS$ and S_{υ} for TAS, the rest components form disturbance. Under the mild restriction S_{Π} contains only those spectral densities, which are non-connected with monitoring parameter. It means that under the monitoring signal reprocessing quantity of information (in comparison with a hard variant) can be increased.

Formulas comparison (6) and especially (3) with integral (7) gives an idea about bulky structure of final expressions for information density. Because of that, results are presented only graphically on the figures.

Under drawing the graphs hard restriction variant has been accepted. Additive noises and heat noise (to avoid an information density growth outside the effective bandwidth of the monitoring signal) have been qualitatively considered.

5. DISCUSSION

Signal spectrums of both sensors, which have been constructed in accordance with traditions, existing in research of self-oscillators frequency instability are represented on the pictures ( ). These traditions are based on consideration of the single sideband envelope (usually right) of HF spectrum, which is assumed as identical to detected signal's form. In our case, there are some distinguishing moments, thus, so spectrums do not represent neither result of detection, nor single sideband of HF oscillation. Reasons are: coupling of factors, necessity to detect AM and FM oscillations in different ways, absence of phase ratio's account; that's why HF spectrum dissymmetry takes place.

The most evident result of non-linear transformation in $N_e AS$, as it was expected, is monitoring signal spectrum widening with some information loss in the main frequency band domain. This phenomenon occurs because of both decreasing of monitoring signal's spectral density and disturbance growth. The working point ($M_{1,2}$) choice is quite important, but it is not reflected in our pictures. A little bit unexpected was relative spectrums narrowing. Actually, they are disturbance, correlated with the monitoring signal. That's why they are worst under the monitoring signal reprocessing.

Formation of monitoring signal's spectrum in TAS in many respects is similar to the well known frequency modulation process in radio transmitters, accompanied by incidental amplitude modulation. Appearing cross correlation has a weak influence at the information productivity, because of cross-spectrums bandlimitedness. This is especially

important because the main task of *TAS* is fast temperature fluctuations control. Under the amplitude-independent frequency detecting of the monitoring signal vibration splash in spectrum, in fact, reduces. It is the result of known phase ratios for two modulation types.

It doesn't mean that for *TAS* vibroprotection is not required. First of all, real autodyne response is non-linear; consequences of that are well seen in the ratio expressions of the fourth part of the article (4. Information productivity). On the other hand, further processing of the monitoring signal includes non-linear operations. It is surely interesting to have a look on dependences of information productivity on frequency and Q-factor of vibrator (a little controversy from the point of view of thermal protection). The last phenomenon gives an idea of *TAS* constructing from elastic materials.

6. CONCLUSIONS

In this work the feature of information productivity estimation is stipulated by the condition that sensors working band $\Pi = \omega / Q$ in tens to hundreds times exceeds the band of useful signal and noise impacts. That's why in case of nonwhite spectrum information productivity significantly less in comparison with potential capacity of the sensor (the famous notice of Shannon about nonwhite spectrum is valid for only noise). Taking into consideration non-linearity and side amplitude modulation makes the picture worse.

On the other hand, it is possible to compare received spectral-correlated characteristics with a set of scientific works, but none of comparisons about information productivity can be done. Thus, we will come nothing more than coarse estimation of response rate, which is tens of millisecond (there no such results for compact sensors of flame had been obtained before).

Correlation reprocessing of the measuring signal, particularly at an independent disturbance control (for example, comparison of *TAS* and $N_e AS$ signals), we hope, will improve informational indexes of the sensors.

REFERENCE

1) Boloznev V.V., Safonova E.V. Proc. of 13-th IEEE Int. Frequency and Time Forum, France, Besancon, 1999
2) Safonova E.V., Stanchenkov M.A. "Temperature sensor of the flame", abstracts of Wave Electronics and its Applications in the Information and Telecommunication Systems, p.92-93, St.Petersburg, Russia, September 2005
3) Boloznev V.V., Sultanov F.I., "Estimation of an information content of an autodyne sensor signal", abstracts of Wave Electronics and its Applications in the Information and Telecommunication Systems, p.92-93, St.Petersburg, Russia, September 2005
4) Boloznev V.V., Safonova E.V., Sultanov F.I., Stanchenkov M.A. "Signal processing principal in a microwave autodyne sensor", abstracts and proceedings of the 19th European Frequency and Time Forum, p.69, Besancon, France, March 2005.
5) Malakhov A.N. "Fluctuations in self-oscillating systems" – M.[in Russian] Science, 1969, 690.

Proceedings of the 20th EFTF, 2006

Latest developments in ultra-stable microwave oscillators at Femto-ST Institute

V. Giordano,* Y. Gruson, N. Boubekeur, R. Boudot, K. Benmessaï, S. Cordier, C. Rocher, N. Bazin, E. Rubiola, P.Y. Bourgeois, and Y. Kersalé
Institut FEMTO–ST, Dpt. LPMO, UMR 6174 CNRS-Université de Franche-Comté 32 av. de l'Observatoire, 25044 Besançon Cedex, France

A growing number of scientific or technical applications requires very high frequency stability oscillators. Thus a frequency stability of the order of 1×10^{-14} at short term is now required for metrology, future space programs and some tests of fundamental physics. Besides any reduction in oscillators phase noise will improve radar systems and phase noise measurement sensitivity. These new requirements impose to surpass the performances of the state-of-the-art quartz crystal oscillators. Such a breakthough can today be effectively achieved by the Sapphire Whispering Gallery Mode Resonator technology. In this paper the new advances achieved in our laboratory, related to this technology, are presented.

I. INTRODUCTION

A growing number of scientific or technical applications requires very high frequency stability oscillators. Thus a frequency stability of the order of 1×10^{-14} for integration time between 1 and 10^4 s is now required for metrology, future space programs and some tests of fundamental physics [1–3]. Besides any reduction in oscillators phase noise will improve radar systems and phase noise measurement sensitivity. These new requirements impose to surpass the performances of the state-of-the-art quartz crystal oscillators whose short term frequency stability is limited to around 1×10^{-13}. Such a breakthough can today be effectively achieved by the Sapphire Whispering Gallery Mode Resonator technology. The aim of this paper is to present the new advances achieved in our laboratory, related to this technology. It summarizes about ten years of research and technical works and constitutes the continuation of a preceeding paper [4]. These developments have been mainly supported by the french national space and metrology agencies (CNES and BNM).

In the first section we review the main phenomena affecting the frequency stability of an electronic oscillator. The performances of classical RF and microwave sources are then compared to the new requirements in term of frequency stability and phase noise. The principle and the main characteristics of the Whispering Gallery Mode Sapphire Resonator are recalled in the section III. The main part of this paper (sections IV, V and VI) is devoted to present the different ultra-stable oscillators we have implemented and tested in our laboratory. The last section VII relates to a new avenue: a whispering gallery mode cryogenic MASER which presents very high potential to achieve ultra-high frequency stabilities.

*Electronic address: giordano@femto-st.fr

II. LIMITATIONS IN THE OSCILLATOR FREQUENCY STABILITY

A. Leeson formula

Basically, an electronic oscillator consists of a frequency reference, i.e. the resonator, inserted in the positive feedback loop of an electronic amplifier (see figure 1). The resonator is characterized by its resonance frequency ν_0 and its loaded Q–factor Q_L whereas the loop amplifier has a power gain G and a noise figure F.

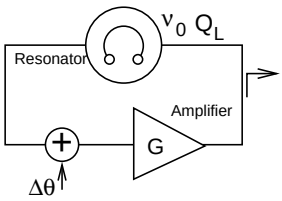

FIG. 1: Basic electronic oscillator

The signal output frequency fluctuations can arise from any phase noise source present in the loop circuit. Assume a phase variation $\Delta\theta$ arising at a given point of the circuit. As the oscillation condition imposes a constant phase along a round trip, oscillation frequency adjusts itself automatically to compensate these phase variations:

$$\frac{\Delta\nu}{\nu} = \frac{\Delta\theta}{2Q_L} \tag{1}$$

Obviously, this phase–to–frequency conversion also takes place with random fluctuations of any part of the loop, whereat higher Q–factor yield better frequency stability. This phenomena can be described by the well–known Leeson model [5] which expresses the power spectrum density (PSD) of output signal phase fluctuations $S_\varphi(f)$ as a function of the PSD of internal phase fluctuations $S_\theta(f)$:

$$S_\varphi(f) = \left(1 + \frac{\nu_0^2}{4Q_L^2}\frac{1}{f^2}\right) S_\theta(f) \tag{2}$$

An extensive discussion is available in reference [6].

B. Thermal noise

The fundamental limitation in the oscillator frequency stability can be derived by neglecting any internal noise source but the thermal noise. If T is the absolute temperature of the circuit and P the signal power at the amplifier input port, the PSD of the internal phase fluctuations is $S_{\theta_{th}}(f) = FkT/P$ where k_B is the Boltzmann constant. From equation (2) and for Fourier frequencies lower than the resonator bandwidth ($f < \nu_0/2Q_L$), the output signal PSD is:

$$S_{\varphi_{th}}(f) = \frac{\nu_0^2}{f^2}\frac{FkT}{4PQ_l^2} \tag{3}$$

In presence of such a white frequency noise, the oscillator frequency stability will improve as the square root of the integration time τ. Expressed as the square root of the Allan variance the frequency stability is:

$$\sigma_{y_{th}}(\tau) = \frac{1}{2}\sqrt{\frac{FkT}{2PQ_L^2\tau}} \tag{4}$$

This limitation is of the order of $2\times10^{-15}/\sqrt{\tau}$ at 1s for a 5MHz quartz oscillator and lower than $5\times10^{-18}/\sqrt{\tau}$ for a microwave oscillator based on a high–Q cryogenic resonator. Actual oscillators show frequency instability well above these limits and then additional noise sources have to be taken into account.

C. Amplifier flicker noise

In most cases, the intrinsic phase noise of the loop amplifier is the relevant noise source which limits the oscillator frequency stability at short term. For low Fourier frequencies the PSD $S_\theta(f)$ generally presents a flicker component resulting from the up–conversion of DC bias flicker [7]:

$$S_\theta(f) = (1 + f_c/f)FkT/P \tag{5}$$

where f_c depends on the amplifier technology. Combining equations 2 and 5, we get the oscillator phase noise for low Fourier frequencies:

$$S_\varphi(f) = \frac{\nu_0^2 f_c}{f^3}\frac{FkT}{4PQ_l^2} \tag{6}$$

$S_\varphi(f)$ appears now limited by a $1/f^3$ component leading in the time domain to a frequency instability independent of the integration time:

$$\sigma_y(\tau) = 0.59\sqrt{\frac{f_c FkT}{2PQ_L^2}} \tag{7}$$

D. Intrinsic noise, environmental sensitivity and resonator aging

Additional frequency fluctuations of the output signal can arise from the resonance frequency fluctuations of the resonator itself. Intrinsic flicker frequency fluctuations leading to a frequency instability of the order of $0.5-1\times10^{-13}$ have been measured on high quality quartz resonators [8]. Moreover, the resonator frequency is determined by its geometry and by the wave velocity inside the resonator medium. These physical characteristics are generally affected by the environmental parameters such as the temperature, the magnetic field, the level of radiation, etc ... The sensitivity to these external parameters limits the oscillator long term frequency stability. Random fluctuations in the environmental parameters lead to an oscillator stability with a $\tau^{1/2}$ slope in the Allan deviation curve.

The resonator medium properties vary with time. For example the stresses induced during the resonator mounting relaxe with a long time constant. As stresses induce a change of the wave velocity in the resonator medium, the oscillator frequency drifts. These phenomena are responsible for frequency stability degradation in the long term. This aging is generally characterized in the time domain by an Allan standard deviation increasing proportionally with the integration time τ.

E. Frequency stability requirements

Figure 2 represents the new requirements for a 10GHz carrier in term of phase noise for new applications in the fields of metrology, fundamental physic tests and radar systems. In the same figure the typical performance of available sources based on a quartz X-tal oscillator reference is shown. In term of frequency stability, metrology and physic experiments need secondary reference source presenting a standard deviation $\sigma_y(\tau) \leq 1\times10^{-14}$ over integration times ranging from 1 to typically 10.000 s.

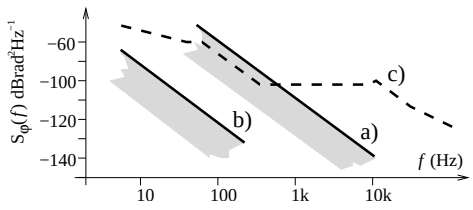

FIG. 2: Phase noise requirements (carrier frequency 10GHz): a) for Radar systems, b) for metrology and fondamental physic. c) Classical 10 GHz low noise synthetized source using 5MHz quartz reference.

It is obvious that these new requirements can not be fulfilled by classical quartz oscillators. This situation has motivated since about ten years a lot of researches and developments in the field of sapphire resonator based microwave oscillators which have the potential to surpass the quartz X-tal performances.

III. WHISPERING GALLERY MODE RESONATOR

The sapphire resonator consists of a cylindrical resonator machined in a low defect Al_2O_3 monocrystal. The use of particular resonance modes called Whispering Gallery (WG) modes allows to concentrate almost all the electromagnetic energy inside the sapphire cylinder. The latter has a typical diameter of 30–50mm and a high of 10–30mm for X-band operation . The Q–factor, essentially limited by the sapphire dielectric loss, is 200,000 at the ambient temperature, higher than 10 millions at 77K and up to 10^9 at the liquid helium temperature. This type of resonator constitutes an excellent frequency reference that can be implemented in an oscillator loop.

In practice the sapphire cylinder is placed in the center of a metallic cavity to prevent radiation losses. Two coupling probes consisting of small magnetic loops or straight antenna protude in the walls of the cavity and permit to excite the WG mode. In all the experiments described in the following, the sapphire resonators operate on quasi-transverse magnetic whispering gallery modes (or WGH modes). As the WG modes are high order modes, they can be perturbed by a number of low-Q spurious modes that have to be suppressed in order to get oscillation on the right resonance. We developed two different modal selection techniques enabling to operate the oscillator without the need of sharp bandpass filter in the loop [9]. The first method consists in the deposition of thin metallic lines on the flat surface of the sapphire cylinder. This technique can be applied at room temperature as well as at 77K [10]. At lower temperature and especially around 4.2K this method induces a strong decrease in the resonator Q-factor and then is not convenient. To address this issue we developed the opened cavity technique (see section VI).

One problem with sapphire WG mode resonator is the high sensitivity to thermal fluctuations. This sensitivity arises from the strong dependence of the sapphire permittivity with temperature. Temperature stabilization and thermal compensation techniques have been then developped.

IV. ROOM TEMPERATURE OSCILLATORS

A. Phase noise

At ambient temperature, the sapphire resonator shows a Q–factor at least 10 times higher than classical microwave dielectric ceramic resonators. As expected from the Leeson formula (see equation 2), our room temperature oscillators show a phase noise 20dB lower than that of ceramic resonators-oscillators with similar amplifier (Figure 4–a) [4].

New generation of microwave SiGe heterostructure transistors have been tested in collaboration with the LAAS (Laboratoire d'Analyse et d'Architecture des Systèmes - Toulouse) to achieve better phase noise (see figure 4–b) [11]. For lower noise the system has to be made more complex. A noise degeneration system can be implemented as suggested firsty by Galani [12] and improved later by Ivanov et al. [13]. In such a system the intrinsic noise of the amplifier is measured thanks to an interferometric phase noise detector that uses the sapphire resonator as phase reference (see figure 3). The signal reflected by the resonator consists of the carrier surperimposed to the phase noise modulation sidebands generated by the sustaining amplifier. A bridge comprising a variable attenuator l and a variable phase shifter γ is used to suppress the carrier. The noise sidebands are amplified and then detected with a properly pumped microwave mixer. This mixer finally delivers an error signal that is fed in a voltage controlled phase shifter (VCPS) to correct the amplifier phase noise. The interferometric technique provides in real time and with a high sensitivity a low frequency voltage proportional to the phase fluctuations induced by the amplifier [14]. Typical gain at low Fourier frequencies ($f \leq$ 1kHz) is of the order of 40dB [15].

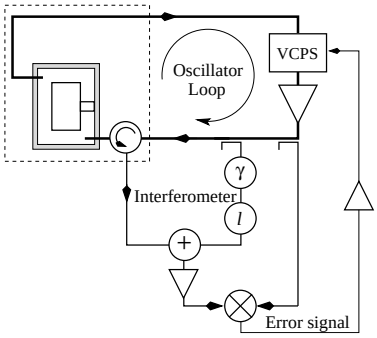

FIG. 3: WG mode sapphire resonator-oscillator with interferometric correction.

The figure 4 represents the phase noise for a 10 GHz carrier we obtained with the different versions of the room temperature sapphire resonator-oscillator.

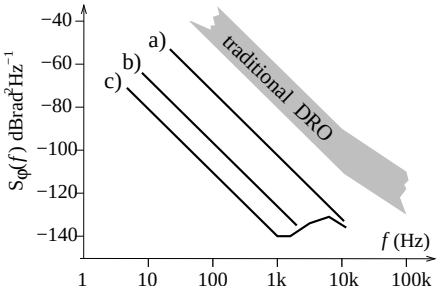

FIG. 4: Phase noise of ambient temperature 10 GHz sapphire resonator oscillators. *a*: Sapphire resonator and classical AsGa microwave transistor. *b*: Sapphire resonator and SiGe heterostructure microwave transistor. *c*: Sapphire resonator and interferometric correction.

B. Long term frequency stability

At room temperature the WG resonator suffers from a high sensitivity (-70ppm/K) to the temperature fluctua-

tions. It results in poor frequency stability for integration times higher than few tenth of second. A high efficiency thermal regulation has to be implemented to minimize the effect of the ambient temperature changes on the oscillator frequency. To solve this issue, we recently developed a special cavity design completed with a high-resolution thermal control [16]. The main idea is to ensure as perfect the best symmetry of the thermal paths with respect to the electromagnetic fields configuration inside the sapphire resonator. In this condition we demonstrated that the oscillator frequency stability remains limited by the intrinsic noise of the loop amplifier up to an integration time higher than 10s (Figure 5). At long integration time the oscillator frequency sensitivity to room temperature variation is reduced to -0.05ppm/K.

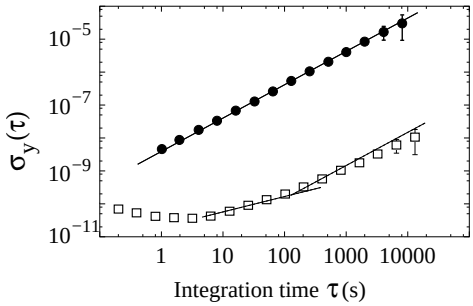

FIG. 5: Frequency stability of a room temperature WG sapphire resonator oscillator : (•) non thermally controlled, (⊡) thermally controlled.

V. THERMALLY COMPENSATED RESONATORS

The oscillators described above provide high spectral purity but are not at all suited for applications requiring a high frequency stability over integration times higher than few tenth of second. Indeed the frequency stability of these oscillators is drastically limited by the resonator sensitivity to the thermal fluctuations. This sensitivity decreases slowly with temperature but remains of the order of few ppm at cryogenic temperatures. Considering the temperature can be hardly stabilized within a few 10μK, there results in a frequency stability worst than 10^{-11} which cannot compete with the quartz oscillator.

The resonator structure has then to be modified to introduce some perturbation which will compensate the sapphire permittivity thermal sensitivity. If the compensating perturbation is well designed, the resonator shows a turnover temperature T_0 at which the thermal sensitivity nulls at the first order. The higher is the turnover temperature, the stronger is the perturbation. As the perturbation inevitably induces a degradation of the resonator Q–factor, the turnover temperature is in practice limited to $T_0 \leq 80$K. Few compensation technics have been tested in our laboratory.

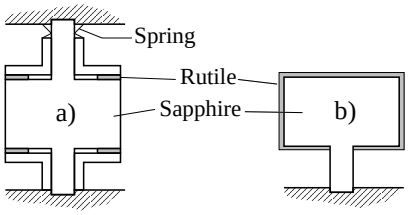

FIG. 6: Principle of dielectric compensation for cryogenic sapphire resonators. *a*): Two rings of rutile are placed on the two flat surfaces of the sapphire puck and maintained by the strength of a spring. *b*): A rutile thin film is directly deposited on the entire sapphire resonator surface.

A. Thermomechanical compensation

The principle of the thermo–mechanical compensation has been firstly proposed by J. Dick [17]. The sapphire resonator consists of two disks separated by a small gap. The height of this gap depends on the length of a piece made in copper or silver. For a WGH mode the electric field is essentially axial. The dilatation coefficient of the copper is stronger than those of the sapphire and any increase of the resonator temperature induces an increase of the relative height of the gap. The mean value of the relative permittivity seen by the electric field then decreases which is just opposite to the natural sapphire relative permittivity variation. Depending on the height of the copper piece the turnover temperature can be adjusted between 40 to 90K. We designed a compensated resonator presenting a turnover temperature of 88K and a Q-factor of 2 millions [18].

B. Dielectric compensation

The sapphire shows a positive temperature coefficient of permittivity (TCP). Thermal compensation is obtained by combining sapphire with another dielectric having a negative TCP as rutile (TiO_2). Low dielectric loss rutile monocrystal can be used. The compensated resonator is a sapphire disk on which two thin rutile rings are maintained thanks to a delicat mechanical assembly. The structure we tested in our lab was designed by two other groups [19, 20] and presents a turnover temperature of 53K and a Q–factor of the order of 10^7.

We also developed another technique consisting of the deposition of a rutile film (1–2μm thick) by using a sol–gel method on the overall surface of the sapphire disk [21, 22]. The main advantage of this technique is compactness, intrinsic immunity to mechanical vibration and low cost. Nevertheless, as the deposited rutile film is not a perfect crystal, the resonator Q–factor remains limited to 2 millions. Studies on the material and on other depositions techniques are currently under development aimed to improve the crystallographic characteristic of the deposited layer.

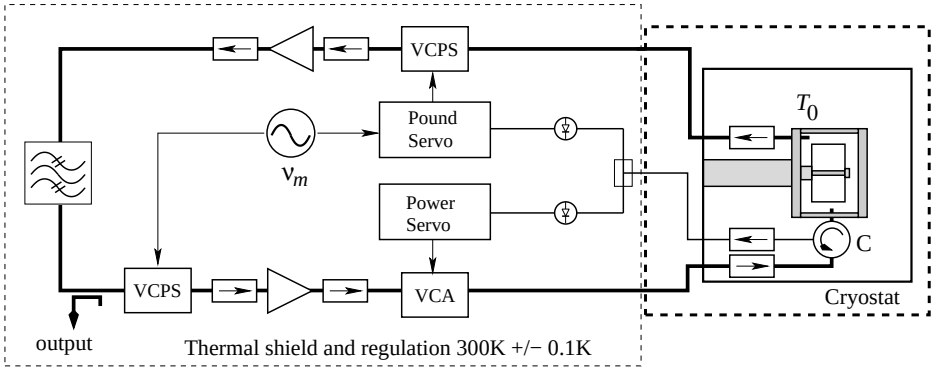

FIG. 7: Scheme of the oscillator circuit. The bold line are the oscillator loop. The thin lines refer to the electronic controls required to get a high frequency stability.

C. Paramagnetic compensation

Another type of thermal compensation is obtained by doping the sapphire crystal with paramagnetic Ti^{3+} ions. The magnetic susceptibility resulting from Ti^{3+} ions depends on temperature. Its effect on the resonator frequency is opposed to those due to the sapphire permittivity sensitivity. With a 0.1% by weight Ti^{3+} ions concentration, the turnover temperature is in the range of 20–77K, depending on the WG mode[23]. In collaboration with UWA (University of Western Australia, Perth) which provides the crystal, we tested in an oscillator loop a 25mm diameter, 20mm hight doped sapphire resonator excited in the $WGH_{8,0,0}$ mode at 12.7 GHz. For this mode the turnover temperature is 34.286K and the unloaded Q-factor is 1.6×10^6.

D. Oscillator loop and additional control

All the above thermal compensation techniques require to cool the sapphire resonator at a cryogenic temperature. The resonator can be immersed in a liquid nitrogen or helium bath or can be mounted in a closed-cycle cryocooler. The resonator is thermally connected to the cold source and stabilized at its turnover temperature.

With a special design the sustaining amplifier can be placed in the cryogenic environment [24]. This solution yields to difficult technological issues: thermal dissipation of the microwave amplifier, final adjustment of the round-trip phase and of the overall gain in the loop. Moreover, to get high frequency stability the power injected in the resonator as well as the phase of the oscillating loop have to be controlled. These controls are difficult to implement in the cryogenic environment. Generally only the resonator is cooled while the sustaining circuit is outside the cryostat. This hybrid solution permits more flexibility in the choice of the WG mode and in the oscillator parameters, as power, gain etc...Figure 7 shows the typical circuit implemented in our oscillators.

Two semi-rigid coaxial cables link the resonator to the oscillator circuit at room temperature. The coaxial cables undergo large temperature gradients. Their electrical length fluctuates due to the cryogenic fluid evaporation or to room temperature fluctuations. There results in a large phase drift along the oscillator loop which has to be compensated. This is realized thanks to a Pound servo which ensures the oscillation frequency to be equal to the resonator frequency [25]. The loop signal is phase modulated by a voltage phase shifter inserted in the loop. The modulation frequency ν_m is higher than the resonator bandwidth. A circulator placed at the resonator input port enables to derive the signal reflected by the resonator which is sent to a tunnel diode operating as a quadratic detector. The latter delivers a voltage which is synchronously demodulated at ν_m in a locking amplifier. Let's assume that the resonator input port coupling is adjusted to the unity, i.e. $\beta_1 = 1$. The reflected signal contains the residual carrier at ν_{osc} and two sidebands at $\nu_{osc} - \nu_m$ and $\nu_{osc} + \nu_m$. When the oscillating frequency ν_{osc} is just equal to the resonator frequency ν_0, the residual carrier is absorbed by the resonator and only the two sidebands subsist. These sidebands are mixed in the diode which delivers a voltage whose a.c. component is at the frequency $2\nu_m$. The demodulated signal is then equal to zero. If $\nu_{osc} \neq \nu_0$, the diode voltage is modulated at ν_m and the demodulated signal is proportional to $\nu_{osc} - \nu_0$. The locking amplifer output signal is integrated and sent back to the bias stage of the voltage controlled phase shifter. The phase fluctuations arising in the loop are corrected in real time in the loop bandwidth. The condition $\beta_1 = 1$ is required to optimize the Pound servo operation otherwise the slope of the frequency discriminator is decreased. In practice the adjustment of the resonator coupling coefficients is a difficult task. Indeed as the coupling coefficients increase as the Q-factor β_1 is almost 100 times higher at cryogenic temperature than at 300K. At room temperature, the resonator input port reflexion coefficient is hardly measurable with a network analyzer. Multiple cooldown are generally needed to get a proper value for β_1.

The sapphire resonator is also sensitive to the injected power. This sensitivity arises from two effects: the microwave power dissipation and the radiation pressure inside the resonator [26]. In our experiments we stabilized the power injected in the resonator by a classical power

control using a quadratic detector as the sensor and a voltage controlled attenuator (VCA) in the loop.

Finally all the room temperature electronics are stabilized at 300K$\pm$0.1K.

E. Performances

The different compensated sapphire resonators described above have been tested alone and in actual oscillators. The performances are given in Figure 8.

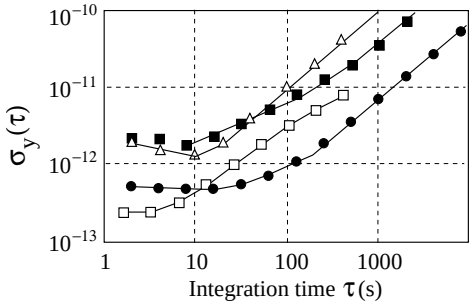

FIG. 8: Frequency stability obtained with the compensated resonators. (△): thermomechanical compensated resonator $T_0 = 87K$. those of(■): Dielectric compensation with sol–gel deposited thin film of rutile $T_0 = 47K$. (□): Dielectric compensation with mechanical assembly of monocrystal rutile rings on sapphire. (●): Ti^{3+} doped sapphire resonator.

These oscillators provide an improvement as compared to the non–compensated oscillators. Nevertheless, for integration time higher than few seconds, frequency drift phenomena occur, limiting the interest for these structures. The frequency drift causes have still not been clearly identified. Few phenomena can induce such long term variations, as stress or thermal gradient relaxation. Although the performances are still not sufficient, these structures are alternative solutions for the next–generation of low noise oscillators.

VI. LOW TEMPERATURE RESONATOR OSCILLATOR

A. *Natural* thermal compensation

In order to obtain ultra-high frequency stability, the sapphire resonator must be cooled near the liquid helium temperature, where the Q-factor of the WG modes can reach 10^9. Moreover the resonator shows a turnover temperature near 6K. Fortunatly even high quality crystals contain a small concentration ($\lesssim$ 1ppm in weight) of paramagnetic impurities as Mo^{3+} ions as the consequence of the growth process. There results a natural thermal compensation at random turning point between 4K and 10K, depending on the actual impurities and on the mode[27]. Figure 9 shows the frequency variation of the $WGH_{16,0,0}$ resonance

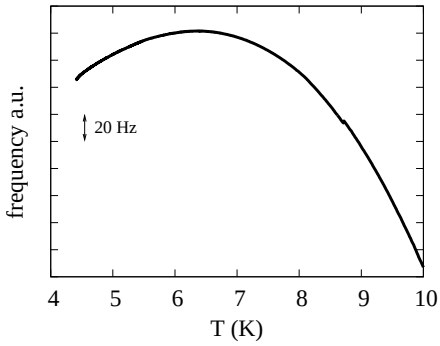

FIG. 9: $WGH_{16,0,0}$ resonant frequency as a function of temperature. The turning point occurs at 11.565051341 GHz.

FIG. 10: Picture of the opened cavity WG resonator.

of a 50x20 mm HEMEX sapphire resonator between 4 and 10K. The thermal sensitivity is zero at about 6K.

B. Opened cavity concept

It is a common pratice to enclose the sapphire in a Nb or Cu cylindrical cavity. This cavity prevents radiation losses and improve thermal stability. The main drawback of this configuration is the presence of a number of low–Q empty cavity modes perturbed by the sapphire resonator. These spurious modes induce Q-factor degradation and enhance of the thermal sensitivity [28]. To suppress these spurious modes we have used an opened cavity structure [29]. Only the metal caps remain while the cylinder is replaced with microwave absorber (Figure 10). This assembly is inserted in a vacuum chamber whose internal walls are covered with microwave absorber.

In this configuration the spurious resonances are no longer confined, for they are completely eliminated from the spectrum. Conversely, the high order whispering gallery modes are almost unaffected by the absorber. The measured Q-factor of these modes is still higher than 2×10^8 which is sufficient for a frequency stability of 1×10^{-14}. Figure 11 shows the frequency stability obtained with the resonator operating on the $WGH_{15,0,0}$ mode at 10.959 GHz with a Q-factor of 4.3×10^8. This measurement has been made by comparing the cryogenic oscillator frequency with a microwave synthetizer (Agilent 8254A) driven by a hydrogen maser.

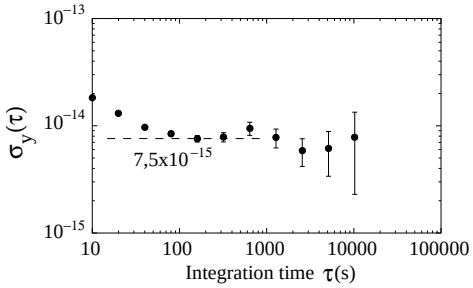

FIG. 11: Frequency stability of the cryogenic resonator-oscillator operating at 10.959 GHz.

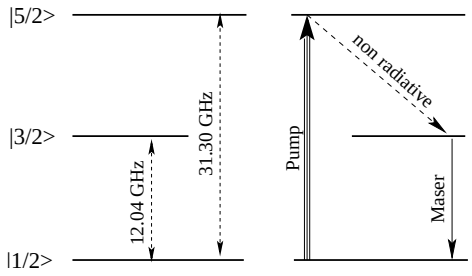

FIG. 12: Energy levels of Fe^{3+} ion in sapphire at zero dc magnetic field.

At short term, the measured stability is limited by the noise of the reference. The cryogenic oscillator instability shows up at $\tau > 100$s. The flicker floor is of the order of 7×10^{-15}. Interstingly, no drift is observed (up to 2×10^{-14}/day) [30], while similar oscillators implemented by other groups are affected by frequency drift of the order of 1×10^{-13}/day. The cause of this fortunate outcome is still not known. Nevertheless, we believe that it results from the opened cavity. In fact, all other oscillators are based on a sapphire resonator in a closed metallic cavity. The useful mode is in this case embedded by number of spurious modes. The latter can increase the reference mode senstivity to mechanical creeps or to thermal drift. Forthcoming experiments should permit to understand these phenomena.

VII. ZERO–FIELD FE^{3+} MASER

In the ultra-stable oscillator described above, the resonator and the sustaining amplifier are spatially separated and the oscillator requires appropriate microwave coupling and a frequency control loop. The overall system is therefore complex and need difficult adjustments. In this classical configuration the cryogenic resonator is simply a linear two-port system that provides a sharp resonance.

We have demonstrated that the sapphire resonator can be used in a different way [31]. Among the different paramagnetic impurities that can be found in high purity sapphire crystal there is the Fe^{3+} ion. The Fe^{3+} energy levels at zero dc magnetic field are shown in Figure 12. Near the liquid helium temperature, there are significant differences in the populations of these levels. Transitions between any of these levels are allowed and their linewidths are of a few tens of MHz. A 31.3 GHz pump signal causes a net transfert of Fe^{3+} ions from the $|1/2\rangle$ level to the $|5/2\rangle$ level. In turn non-radiative transitions $|5/2\rangle \mapsto |3/2\rangle$ create a negative population difference between the two lower states, making possible the amplification of a 12.04 GHz signal.

Our whispering-gallery-mode maser is represented in Figure 13. It is based on sapphire resonator whose $WGH_{17,0,0}$ mode frequency coincides with the $|1/2\rangle \mapsto |3/2\rangle$ frequency, i.e. 12.04 GHz. This resonator has a number of resonances near the pump frequency. After some attemps, we observed that a 2dBm pump signal at 31.34 GHz is sufficient to obtain a -56dBm maser signal, available outside of the cryostat. The output Maser signal was directly amplified by 70dB and mixed with the signal of a microwave synthesizer (Wiltron 69137A) driven by a hydrogen Maser. The 200kHz beatnote is sent to a high resolution frequency counter (HP 53132A). We slowly increased the resonator temperature and recorded the beatnote frequency. We determined experimentaly that the maser frequency has a turn-over point at 7.9K. Finally we stabilized the resonator temperature at the turning point and we measured the Allan deviation σ_y of the fractionnal frequency (Fig. 14).

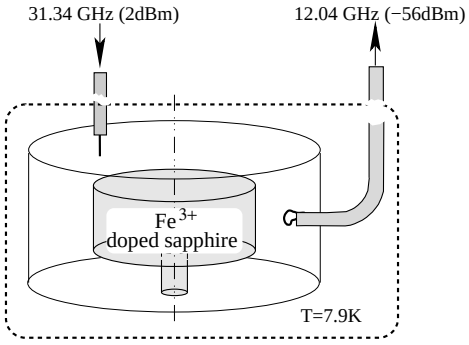

FIG. 13: Principle of the whispering gallery mode maser oscillator.

At short integration times, $\tau < 100$s, the WG maser exhibits a frequency stability better than 4×10^{-14}. The cause of the long term degradation has still not been determined. Although the system is not optimized, this preliminary result is encouraging. For instance, the two lines linking the cryogenic resonator to the outside do not include isolators. Fluctuations in the standing wave pattern could thus induce significant drift on the maser frequency. We have to evaluate the resonator sensitivity to experimental parameters as the pump power and frequency, the resonator coupling, the reflexion coefficient of feedthrough and cables, magnetic field, etc ...

The WG maser shows several advantages versus the classical oscillator: (i) there are fewer critical components, (ii) it is simpler and more compact, (iii) the number and the complexity of auxiliary controls is reduced, and (iv) the resonator coupling is far less critical.

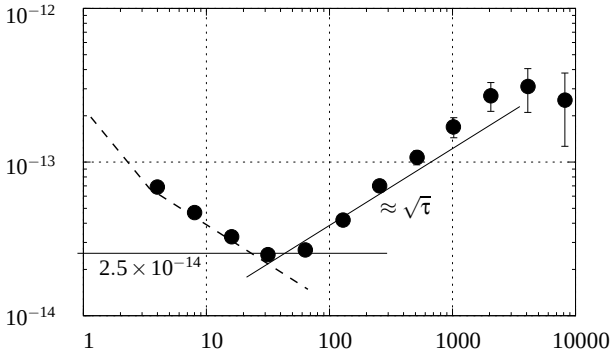

FIG. 14: *Preliminary result on frequency stability of the whispering gallery mode maser. The dashed line is the noise floor of the measurement system.*

VIII. CONCLUSION

The technology of the Sapphire Whispering Gallery Mode Resonator permits to surpass the frequency stability of traditional ultra-stable oscillators, and then can be exploited in number of applications requiring a high frequency stability. The main difficulties, i.e. thermal sensitivity and spurious modes, associated with such a type of frequency reference have been solved by means of original techniques. It has also been demonstrated that at liquid helium temperature the sapphire–resonator–oscillator shows a stability of 7.5×10^{-15} at short term and better than 5×10^{-14} over one day. Finally, we have demonstrated the maser operation of a Fe^{3+} doped sapphire. Engineering work is still needed in order to make a usefull frequency standard out of our maser.

[1] A.G. Mann and G. Santarelli and S. Chang and A. N. Luiten and P. Laurent and C. Salomon and D. G. Blair and A. Clairon, in *Proc. IEEE International Frequency Control Symposium* (Pasadena, CA., 1998), pp. 13–17.

[2] P. Wolf, S. Bize, A. Clairon, A. N. Luiten, G. Santarelli, and M. E. Tobar, Physical Review Letters **90**, 060402 (2003).

[3] V. Candelier, P. Canzian, J. Lamboley, M. Brunet, and G. Santarelli, in *Proc. IEEE International Frequency Control Symposium* (Tampa, FL, USA, 2003), pp. 575–582.

[4] V. Giordano, Y. Kersalé, O. Di Monaco, and M. Chaubet., European Physical Journal - Applied Physics **8**, 269 (1999).

[5] D. B. Leeson, Proceedings IEEE **54**, 329 (1966).

[6] E. Rubiola, arXiv:physics/0502143v1 (2005).

[7] D. Halford, A. E. Wainwright, and J. A. Barnes, in *Proc. of the Frequency Control Symposium* (1968), pp. 340–341.

[8] E. Rubiola, J. Groslambert, M. Brunet, and V. Giordano, IEEE Transactions on Ultrasonics, Ferroelectrics and Frequency Control **47**, 361 (2000), ISSN 0885-3010.

[9] O. Di Monaco, W. Daniau, I. Lajoie, Y. Gruson, M. Chaubet, and V. Giordano, Electronics Letters **32**, 669 (1996).

[10] O. Di Monaco, Y. Kersalé, and V. Giordano, IEEE Microwave and Guided Wave Letters **10**, 368 (2000).

[11] G. Cibiel, M. Régis, O. Llopis, A. Rennane, L. Bary, R. Plana, Y. Kersalé, and V. Giordano., IEEE Transactions on Ultrasonics, Ferroelectrics and Frequency Control **51** (2004).

[12] Z. Galani and M. Bianchini, IEEE Transactions on Microwave Theory and Techniques **32**, 1556 (1984).

[13] E. N. Ivanov, M. E. Tobar, and R. A. Woode, IEEE Transactions on Ultrasonics, Ferroelectrics and Frequency Control **45**, 1526 (1998).

[14] E. Rubiola and V. Giordano, Review of Scientific Instruments **71**, 3085 (2000), ISSN 0034-6748.

[15] Y. Gruson, Y. Kersalé, E. Rubiola, C. Rocher, M. Chaubet, and V. Giordano, in *Actes des 13eme Journées Nationales Microondes (JNM 2003)* (Lille, 2003), pp. 4C2–2.

[16] R. Boudot, C. Rocher, N. Bazin, S. Galliou, V. Giordano, and O. Llopis, in *Proc. 19th European Frequency and Time Forum* (Besançon, France, 2005), pp. 393–398.

[17] G. Dick, D. Santiago, and R. Wang, IEEE Transactions on Ultrasonics, Ferroelectrics and Frequency Control **42**, 812 (1995).

[18] Y. Kersalé, F. Ladret-Vieudrin, M. Chaubet, and V. Giordano., IEEE Transactions on Ultrasonics, Ferroelectrics and Frequency Control **47**, 427 (2000).

[19] M. E. Tobar, J. G. Hartnett, E. N. Ivanov, D. Cros, P. Blondy, and P. Guillon, IEEE Transactions on Microwave Theory and Techniques **48**, 1265 (2000).

[20] J. G. Hartnett, P. Y. Bourgeois, J. D. Anstie, M. E. Tobar, N. Bazin, E. N. Ivanov, D. Cros, V. Giordano, and Y. Kersalé, Electronics Letters **40** (2004).

[21] Y.Kersalé, O. Vallet, S. Vives, C. Meunier, and V. Giordano., Electronics Letters **37** (2001).

[22] Y. Kersalé, N. Boubekeur, P. Bourgeois, N. Bazin, S. Vives, C. Meunier, and V. Giordano., in *Proc. of the 2003 IEEE International Frequency Control Symposium.* (2003).

[23] J. G. Hartnett, M. Tobar, A. Mann, J. Krupka, and E. Ivanov, Electronics Letters **34**, 195 (1998).

[24] S. Vitusevich, K. Schieber, I. Ghosh, N. Klein, and M. Spinnler, IEEE Transactions on Microwave Theory and Techniques **51**, 163 (2003).

[25] A. Luiten, A. G. Mann, A. Giles, and D. Blair, IEEE Transactions on Instrumentation and Measurement **42**, 439 (1993).

[26] S. Chang, A. G. Mann, A. N. Luiten, and D. G. Blair, Physical Review Letters **79**, 2141 (1997).

[27] A. N. Luiten, A. Mann, and D. Blair, J. Phys. D: Appl. Phys. **29**, 2082 (1996).

[28] M. Tobar, J. Phys. D. Appl. Phys. **26**, 2022 (1993).

[29] P. Y. Bourgeois, Y. Kersalé, N. Bazin, M. Chaubet, and V. Giordano., IEEE Transactions on Ultrasonics, Ferroelectrics and Frequency Control **51** (2004).

[30] P. Y. Bourgeois, F. Ladret-Vieudrin, Y. Kersalé, N. Bazin, M. Chaubet, and V. Giordano, Electronics Letters **40** (2004).

[31] P. Bourgeois, M. Oxborrow, N. Bazin, Y. Kersalé, and V. Giordano., in *Proc. 19th European Frequency and Time Forum* (Besançon, France, 2005), pp. 134–137.

Proceedings of the 20th EFTF, 2006

Measurement of Short-Term Frequency Stability of Controlled Oscillators

M. Puranen[1]* and P. Eskelinen[2]
[1] *Helsinki University of Technology, Metrology Research Institute, Otakaari 5 A, FI-02150 Espoo, Finland*
[2] *Helsinki University of Technology, Applied Electronics Laboratory, Otakaari 5 A, FI-02150 Espoo, Finland*

A method for measuring the frequency of a controlled oscillator as a function of time is described. Sometimes it is necessary to detect and measure small but fast frequency changes. This method can also be used to measure frequency-hopping radio transmitters or radar pulses. In these cases suggested measurement tools, e.g. spectrum analyzers or frequency counters cannot be used.

The performance of the system depends mostly on the multimeter, whose accuracy, noise and speed set the limits for the measurements. So far we have been able to measure frequency changes of 5 Hz with sampling speed of 100 000 s^{-1}. The observed uncertainty is less than 2 Hz. With some further noise reduction better results are expected.

I. INTRODUCTION

Crystal oscillators provide nowadays a very accurate timebase. There are, however, some factors that may cause instability of the frequency. These are, e.g. temperature, humidity or pressure changes, acceleration or changes in their external load [1]. On the other hand, the frequency of the oscillator can also be changed intentionally, for example in voltage or oven controlled crystal oscillators (VCXO, OCXO)[2].

Sometimes it is necessary to measure fast frequency changes, caused by either external factors or intentional tuning, for example, in pulsed or chirped radars or in frequency hopping radios. Radar pulses are typically very short, so a predefined amount of measurements must be done during short time period. Frequency deviation during pulse may be hard to detect.

In chirped radars, the pulse is longer but has a frequency shift. In frequency hopping radios, frequency is changed typically in several millisecond intervals, but the change in frequency is significant and therefore easier to measure than radar pulses.

The primary target of this research is, however, to measure the frequency of controlled oscillators during the adjustment, when a frequency counter is too slow and domain-type analyzers are too inaccurate. This setup is also used to measure nonlinearities of controlled oscillators [3]. The goal of this research was to reach an uncertainty of less than 5 Hz and a measurement rate better than 20 000 s^{-1}.

Frequency counters provide accurate results, but can not be used for fast measurements, because a short gate time decreases accuracy too much. The data transfer rate of the communications bus may also be a factor that limits the measurement rate. A modulation domain analyzer was also used, but when measurement time was shortened, accuracy dropped substantially.

Characterization of frequency stability is discussed more in [4] and [5], for example.

*Electronic address: mikko.puranen@tkk.fi

II. MEASUREMENT SETUP

Block diagram of the setup is presented in Figure 1. It consists of a power splitter, coaxial delay line, mixer, attenuator, low-pass filter, DC-amplifier and a $8\frac{1}{2}$-digit multimeter. The output of the oscillator under test is connected to the splitter, whose first output goes straight to the RF-input of a mixer. The second signal from the splitter is delayed and connected to the LO-port. Because of the delay, there's a phase difference between two signals in mixer's inputs.

When the frequencies in the RF-port and LO-port are equal, a DC-voltage is present in the output of the mixer, proportional to the phase difference ϕ. In an idealized case, output voltage $v(t)$ of the mixer is

$$v(t) = A_1 \sin(\omega t) \cdot A_2 \sin(\omega t + \phi) = \frac{A_1 A_2}{2}(\cos(\phi) - \cos(2\omega t + \phi)). \quad (1)$$

The length of the delay line was tuned to generate a phase difference of 90° with measured frequency. With this arrangement output voltage is 0 V, as stated in Equation 1, and the response of the measurement system is linear as a function of frequency.

High-frequency components are filtered using a low-pass filter. An attenuator is used between mixer and filter to ensure proper impedance matching. The filtered signal, which now consists only of DC-voltage, is amplified using a low-noise operational amplifier, whose gain is 100. The amplifier is battery powered to reduce unintentional noise.

The DC-voltage is measured using a fast bus-controlled multimeter (digital voltmeter, DVM). The speed and accuracy of the multimeter defines also the sampling speed and accuracy of the frequency measurement. The uncertainty of the voltage measurement is defined by calibrating the multimeter using the same integration time and measurement range as in the actual frequency measurement.

The multimeter used in this setup was Agilent 3458A, which was calibrated using Keithley model 263 calibrator. The multimeter was connected to a PC via

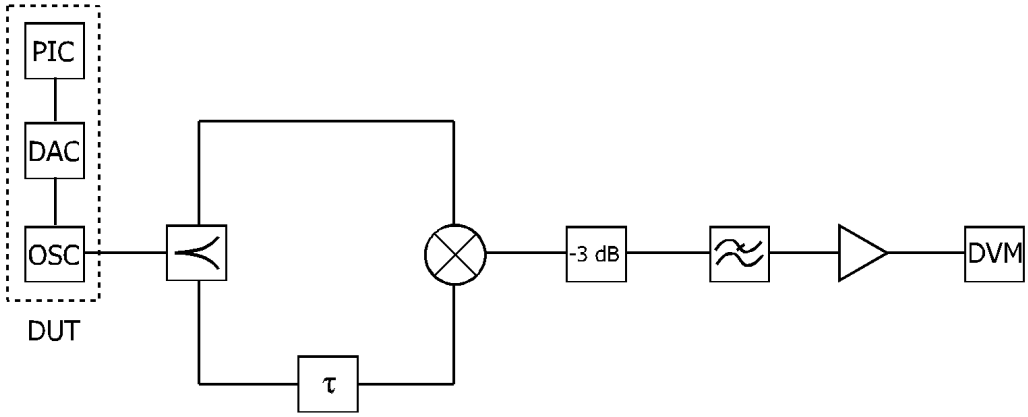

FIG. 1: Block diagram of the setup. PIC microcontroller drives the digital to analog-converter (DAC), which supplies the control voltage for the voltage controlled oscillator (VCXO), marked in the figure as OSC. Signal from the oscillator is split, and splitter's first output goes straight to the mixer. The second signal from the splitter is delayed and connected to the LO-port of the mixer. Mixer's output signal is attenuated and filtered using low-pass filter. The remaining DC-component is amplified and voltage is measured using digital voltmeter (DVM).

GPIB-bus. LabView-software was used to control the multimeter and to save the results.

The input impedance of the multimeter is very high, over 10 GΩ. Because a DC amplifier is used, the input impendace can be reduced to minimize noise. In this setup, 1 kΩ precision resistor was connected to the input terminals of the DVM.

A precise controller for voltage controlled oscillator (VCXO) was also needed. It is used to supply wanted waveform for desired frequency modulation, but it is also needed in defining the frequency scale. We used Microchip's PIC microcontroller, which is connected to 16 bit digital to analog-converter (DAC). DAC has parallel data bus and current output. It drives a low-noise operational amplifier, which was used as current to voltage converter.

PIC was programmed to produce a waveform that creates a linear frequency sweep (sweep measured with the modulation domain analyzer can be seen in Figure 2). Program also allowed us to measure a number of stable frequencies, which were used in defining the measurement scale of the setup.

Similar frequency measurement methods based on the phase detector and phase shifter have been presented before [6, 7], but an important difference is, that in this setup no reference oscillator is used. Measured frequency is compared to itself, and possible frequency fluctuations of the reference oscillator do not affect the results. Therefore the absolute frequency is not known, but only the differential frequency change, which in this research was the focus.

III. RESULTS

The output voltage of the setup was measured as a function of frequency. Eight different control voltages,

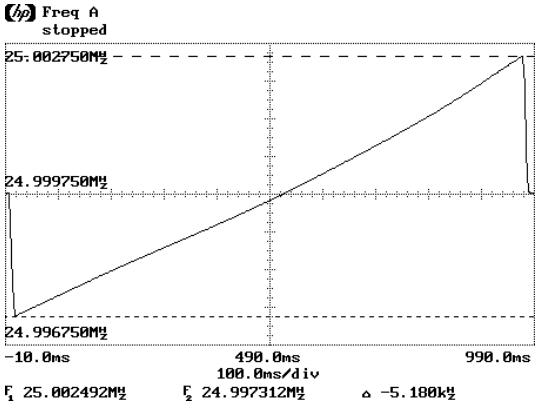

FIG. 2: Frequency of the VCXO in function of time measured with Agilent 53310A modulation domain analyzer. Center frequency ic ca. 25 MHz, frequency change is 5,18 kHz and sweep duration is 1 second.

which covered the whole tuning range of the measured VCXO, were used. VCXO output requencies were measured with frequency counter, and output voltages of the setup were measured respectively. Results are presented in figure 4; sensitivity is 0,139 mV/Hz.

Since the length of the delay line is tuned to generate a phase difference of about 90°, the output voltage is near 0 V and the response is linear.

The multimeter used in the setup was calibrated using the same settings as in frequency measurements. To achieve best possible measurement rate, averaging was not used, and the integration time was set to 0. The measurement range was 1 volt, and single precision was used to transfer results to the computer. With single precision, each result is transferred using two bytes.

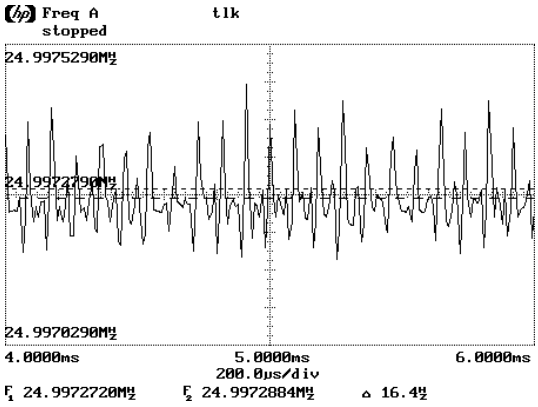

FIG. 3: The requency deviation of tested oscillator measured using modulation domain analyzer. Frequency deviation of 300 Hz shown in the figure is not plausible.

The multimeter was calibrated using Keithley model 263 calibrator. Triaxial cable was used to connect calibrator to the multimeter. Calibration was done with 0 V, 1 V and -1 V voltages. Observed voltage measurement uncertainty was 0,22 mV.

Using double precision in data transfer (4 bytes/result) did not provide lower uncertainty. Because averaging was not used, uncertainty was considerably higher than normally. The noise of the DC-amplifier was also measured, but it's contribution to the overall uncertainty was minimal.

When integration time is set to 0, the measurement speed of Agilent 3458A is 100 000 s^{-1}. Results are stored temporarily in DVM's internal memory, and transferred to the PC when the measurement is finished. The capacity of the internal memory is ca. 75 000 results, and if memory runs out, measurement rate drops dramatically. Therefore, the longest usable measurement time is about 0,75 seconds.

An example of the measurement done using described setup can be seen in Figure 5. The measured worst case frequency fluctuation between two samples was 5 Hz. The measured oscillator was Axtal Axis 10, with nominal frequency of 25 MHz. The measurement duration was 500 μs and it was done during a frequency sweep, shown in Figure 2.

When a modulation domain analyzer was used to measure same oscillator using more accurate time scale, frequency deviation of over 300 Hz was observed (Figure 3). With a shorter measurement time deviation increased. This kind of result is not plausible, and our method can be considered better in such precise measurements.

IV. CONCLUSIONS

A simple and cheap setup for measuring small differential frequency changes was presented. Measurement rate is 100 000 s^{-1} and the observed uncertainty is 1,6 Hz. The described setup is very flexible, it can be modified for even more precise frequency measurements by using longer delay line. A drawback is that the linear frequency range decreases. On the other hand, with shorter delay useful frequency range can be very wide.

Our results show, that using this kind of setup, fast frequency changes can be measured with greater measurement rate than with frequency counter, and far more accurately than with modulation domain analyzer.

In near future, better results may be obtained if noise is further reduced. It may be done by improving either the voltage supply used to control the VCXO or the DC-amplifier.

Since the performance of the setup depens mostly on the performance of the multimeter, high-quality instruments must be used. Calibration is also necessary, because normal calibrations are done using longer integration times.

The described setup can also be used in long-term stability measurements. Software, that controls the multimeter, provides possibility to measure output voltage of the setup with longer intervals (e.g. 1 second . . . 10 minutes)

[1] Fred L. Walls and John R. Vig, "Fundamental limits on the frequency stabilities of crystal oscillators", *IEEE Transactions on ultrasonics, ferroelectrics, and frequency control*, Vol. 42, No. 4, July 1995

[2] "Fundamentals of crystal oscillators", Application note 200-2, Hewlett Packard Co.

[3] "Measuring linearity of VCO's from 10 Hz to 23 GHz", Application note 181-1, Hewlett Packard Co.

[4] Jaques Rutman and Fred L. Walls, "Characterization of frequency stability in precision frequency sources", *Proceedings of the IEEE*, Vol. 79, No. 6, June 1991

[5] P Y Bourgeois, Y Kersale, N Bazin, V Giordano and M Chaubet, "Measurement of short-term stability of ultra-stable oscillators", *Proceedings of 18th European Frequency and Time Forum (EFTF '04)*, Guildford, U.K., 5-7 April, 2004

[6] Fred L. Walls and Arthur E. Wainwright, "Measurement of the short-term stability of quartz crystal resonators and the implications of crystal oscillator design and applications", *IEEE transactions on instrumentation and measurement*, Vol. IM-24, No. 1, March 1975

[7] Bernd Neubig and Wolfgang Briese, *Das groβe Quarzkochbuch*, Franzis-Verlag, 1997

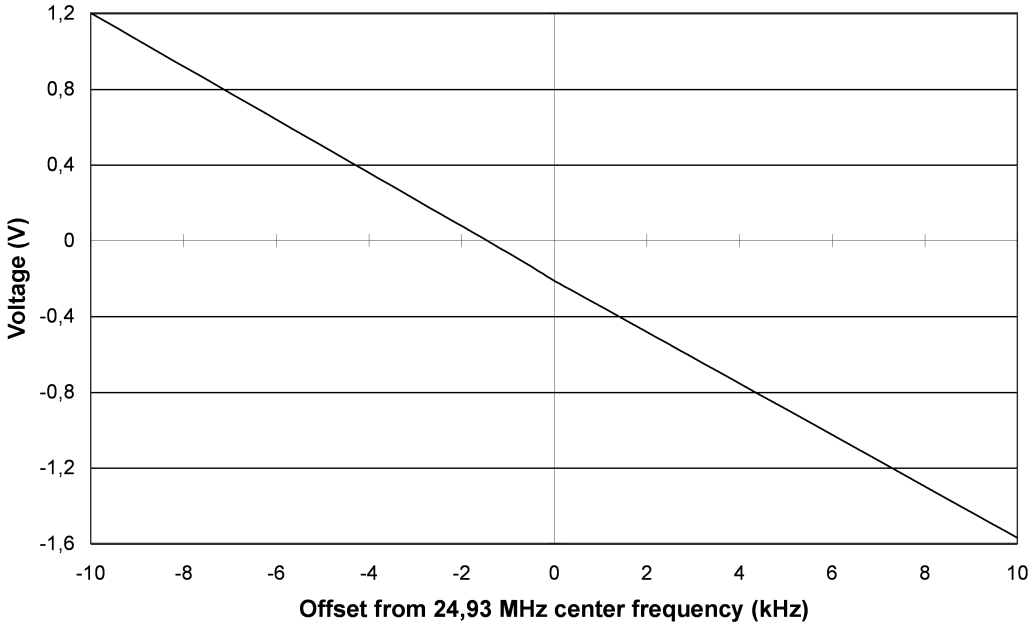

FIG. 4: Measured frequency scale. Microcontroller and digital to analog converter were used to feed stable control voltage to the VCXO. A number of stable frequencies were measured using frequency counter and output voltages of the setup were measured respectively. The response of the setup is linear in the whole measurement region, and sensitivity is 0,139 mV/Hz.

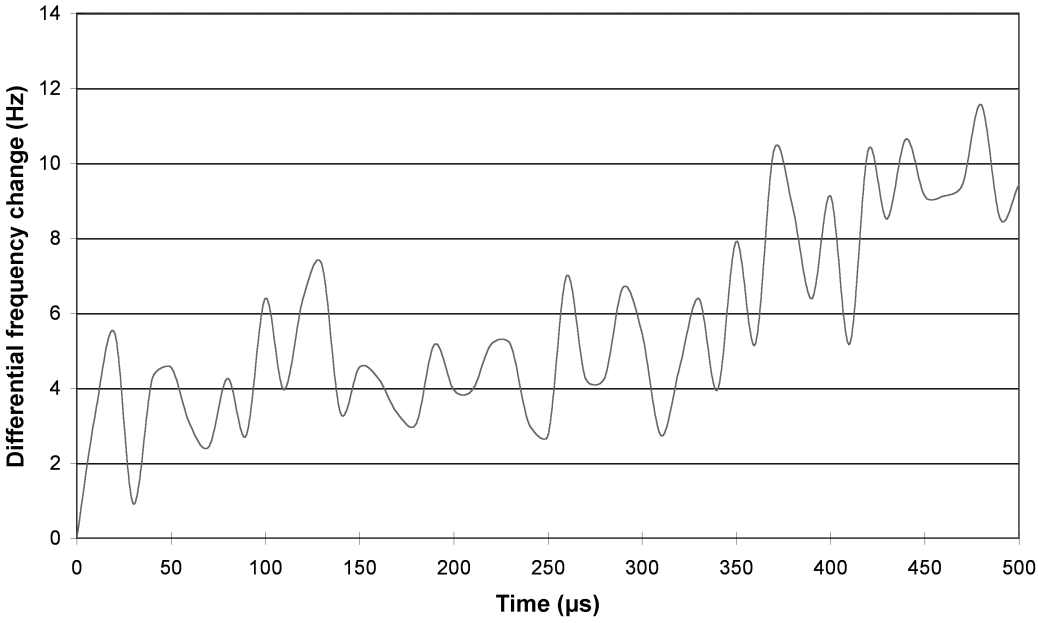

FIG. 5: The differential frequency fluctuation of the measured oscillator. Measurement time is 500 μs, measurement rate is 100 000 s^{-1} and measured frequency deviation is less than 5 Hz. Frequency is rising because the time period shown in this figure is part of longer frequency sweep (see Figure 2), where frequency changes over 5 kHz.

Proceedings of the 20th EFTF, 2006

Frequency flicker in ultra-stable quartz oscillators

Enrico Rubiola* and Vincent Giordano†
FEMTO-ST Institute, Dept. LPMO
UMR 6174 CNRS-Université de Franche-Comté, Besançon France

The frequency flicker of an oscillator, which appears as a $1/f^3$ line in the phase noise spectral density, and as a floor on the Allan variance plot, originates from two basic phenomena, namely: (1) the $1/f$ phase noise turned into $1/f$ frequency noise via the Leeson effect, and (2) the $1/f$ fluctuation of the resonator natural frequency. The discussion on which is the dominant effect, thus on how to improve the stability of the oscillator, has been going on for years without giving a clear answer. This article tackles the question by analyzing the phase noise spectrum of several commercial oscillators and laboratory prototypes, and demonstrates that the fluctuation of the resonator natural frequency is the dominant effect. The investigation method starts from reverse engineering the oscillator phase noise in order to show that if the Leeson effect was dominant, the resonator merit factor Q would be too low as compared to the available technology.

I. INTRODUCTION AND SUMMARY

In the domain of ultra-stable quartz oscillators used in the most demanding applications, like space and atomic fountain clocks, we notice that the frequency flicker is often the most critical parameter. The required stability is sometimes in the upper 10^{-14} (Allan deviation) at 1–30 s or so, which can only be achieved in the lower HF band (5–10 MHz), and after selection. In such cases, identifying the dominant flicker mechanism is far from being trivial. Whereas some authors strongly suggest that the amplifier noise can be the parameter that limit the frequency stability, rather than the flickering of the resonator natural frequency [1, 2], the general literature seems not to give a clear answer. This conclusion results from a set of selected articles, which includes the measurement of the frequency stability [3, 4] and the interpretation of the flicker noise of crystal resonators [5, 6]; the design fundamentals of the nowadays BVA resonators [7]; some pioneering works on the low-frequency noise in quartz oscillators [8, 9]; more recent articles focusing on specific design solutions for ultra-stable oscillators [10–14]; and, as a complement, a thorough review of the SiO_2 crystal for the resonator fabrication is found in [15]. Conversely, in everyday-life oscillators, which span from the low-cost XOs to the OCXOs used in telecommunications and instrumentation, the relative simplicity of the low-noise electronics required indicates that the frequency flicker is chiefly the $1/f$ fluctuation of the resonator.

In a previous work [16], now extended to more commercial products and laboratory prototypes, we have analyzed the phase noise spectrum of some oscillators, aiming at understanding the internal mechanisms and parameters. We look at the phase-noise spectrum from the right hand to the left, hence from the higher Fourier frequencies to the lower, matching theory, technology and physical insight. In this way we get information on the sustaining amplifier on the output buffer, on the Leeson effect and on the resonator.

In this article we first explain the phase noise mechanisms in amplifiers. Then we introduce the Leeson effect, which consists of the phase-to-frequency conversion of noise below the resonator cutoff (Leeson) frequency $f_L = \frac{\nu_0}{2Q}$. Finally, we analyze the phase noise spectral density $S_\varphi(f)$ of a few oscillators. The conclusion that the resonator natural frequency is the main cause of frequency flickering is based on experimental facts. After taking away the effect of the output buffer, we calculate the frequency f_L'' at which the oscillator f^{-3} line crosses the f^{-1} line of the sustaining amplifier. Provisionally assuming that f_L'' is the the Leeson frequency, we observe that the resonator merit factor $Q_s = \frac{\nu_0}{2f_L''}$ thereby calculated is far too low for a high-tech resonator. Conversely, under any reasonable assumption about the true merit factor, the Leeson effect is found at a frequency $f_L \ll f_L''$. Therefore the Leeson f^{-3} line on the $S_\varphi(f)$ plot is well hidden below the resonator fluctuation.

II. PHASE NOISE FUNDAMENTALS

Let the quasi-perfect oscillator sinusoidal signal of frequency ν_0

$$v(t) = V_0[1 + \alpha(t)]\cos[2\pi\nu_0 t + \varphi(t)] \ . \qquad (1)$$

where $\alpha(t)$ is the fractional amplitude noise, and $\varphi(t)$ is the phase noise. The AM noise is not essential to this work. The phase noise is best described in terms of $S_\varphi(f)$, i.e., the one-sided power spectral density of $\varphi(t)$, as a function of the Fourier frequency f. In addition to f, we use the angular frequency ω for both carrier-related frequencies ($\omega = 2\pi\nu$), and Fourier frequencies ($\omega = 2\pi f$) without need of introducing it, and the normalized frequency fluctuation $y = \frac{\nu - \nu_0}{\nu_0}$. The quantities ν, f and y refer to one-sided trans-

*Electronic address: rubiola@femto-st.fr; URL: http://rubiola.org
†Electronic address: giordano@femto-st.fr

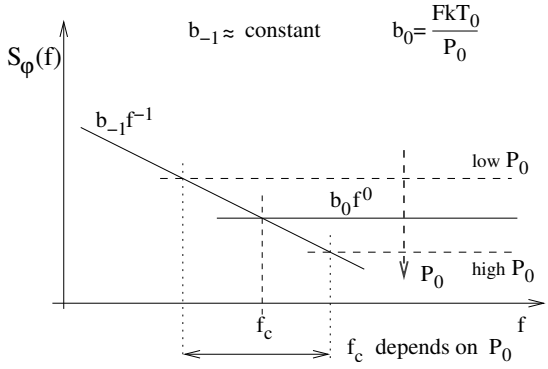

FIG. 1: Typical phase noise of an amplifier.

forms, ω to two-sided transforms. Frequency fluctuations are described in terms of $S_y(f)$, related to $S_\varphi(f)$ by

$$S_y(f) = \frac{f^2}{\nu_0^2}\, S_\varphi(f) \ . \tag{2}$$

A model that has been found useful in describing the oscillator noise spectra is the power-law

$$S_y(f) = \sum_{i=-2}^{2} h_i f^i \quad \Leftrightarrow \quad S_\varphi(f) = \sum_{i=-4}^{0} b_i f^i \ . \tag{3}$$

Our main concern is the frequency flickering term $b_{-3}f^{-3}$, which is related to the Allan variance by

$$\sigma_y^2 \ = \ 2\ln(2)\, h_{-1} \ = \ 2\ln(2)\, \frac{b_{-3}}{\nu_0^2} \ , \tag{4}$$

constant, i.e., independent of the measurement time.

Finally, the general background on phase noise and frequency stability is available from numerous references, among which we prefer [17], [18], [19], and [20, Vol. 1, Chapter 2]. A IEEE standard is also available [21].

III. PHASE NOISE IN RF (AND MICROWAVE) AMPLIFIERS

a. White noise. The equivalent noise spectrum density at the amplifier input is $N = FkT_0$, where F is the noise figure and kT_0 is the thermal energy. This type of noise is additive. In the presence of a carrier of power P_0, the phase noise spectral density is

$$S_\varphi(f) = b_0 f^0 \ \text{(constant)} \tag{5}$$

with

$$b_0 = \frac{FkT_0}{P_0} \ . \tag{6}$$

When amplifiers are cascaded, the noise contribution of each stage is divided by the gain of all the preceding stages (Friis formula [22]). Accordingly, in most practical cases the total noise is chiefly the noise of the first stage. Of course, this also holds for phase noise.

b. Flicker noise. Understanding the close-in noise starts from the bare observation that the output spectrum is of the white type—flat in a wide frequency range—when the carrier power is zero, and that noise shows up close to the carrier only when a sufficiently large carrier power is present at the amplifier output. The obvious consequence is that the close-in flickering results from a parametric effect by which the near-dc flicker noise modulates the carrier in amplitude and phase.

The simplest way to understand the noise upconversion is to model the amplifier signal as a nonlinear function truncated to the 2nd order

$$v_o(t) = a_1 v_i(t) + a_2 v_i^2(t) + \dots \ , \tag{7}$$

in which the complex input signal

$$v_i(t) = V_i\, e^{j\omega_0 t} + n'(t) + jn''(t) \tag{8}$$

contains the carrier and the internally generated near-dc noise $n(t) = n'(t) + jn''(t)$. Rather than being an easy-to-identify voltage or current, $n(t)$ is an abstract random signal that also accounts for the efficiency of the modulation process. Combining (7) and (8) and selecting the terms close to the carrier frequency ω_0, we get

$$v_o(t) = V_i\Big\{a_1 + 2a_2\big[n'(t) + jn''(t)\big]\Big\}e^{j\omega_0 t} \ . \tag{9}$$

Hence, the random fluctuations are

$$\alpha(t) = 2\,\frac{a_2}{a_1}\, n'(t) \quad \text{and} \quad \varphi(t) = 2\,\frac{a_2}{a_1}\, n''(t) \ . \tag{10}$$

Deriving Eq. (10), the statistical properties of $n'(t)$ and $n''(t)$ are not affected by the carrier power. This accounts for the experimental observation that the amplifier phase noise given in rad^2/Hz is about independent of power in a wide range [23–25]. Thus

$$S_\varphi(f) = b_{-1} f^{-1} \qquad b_{-1} \approx \text{constant} \ . \tag{11}$$

Of course, some dependence on P_0 remains. We ascribe it to terms of order higher than 2 in (7), and to the effect of the large signal regime on the dc bias. In the case of bipolar amplifiers used in HF/VHF amplifiers, b_{-1} is in the range of 10^{-12} to 10^{-14} rad^2/Hz (-120 to -140 dBrad^2/Hz).

When m amplifiers are cascaded, the The Friis formula does not apply. Instead, the phase noise barely adds

$$(b_{-1})_{\text{cascade}} = \sum_{i=1}^{m} (b_{-1})_i \ . \tag{12}$$

This occurs because the $1/f$ phase noise is about independent of power. Of course, the amplifiers are supposed independent.

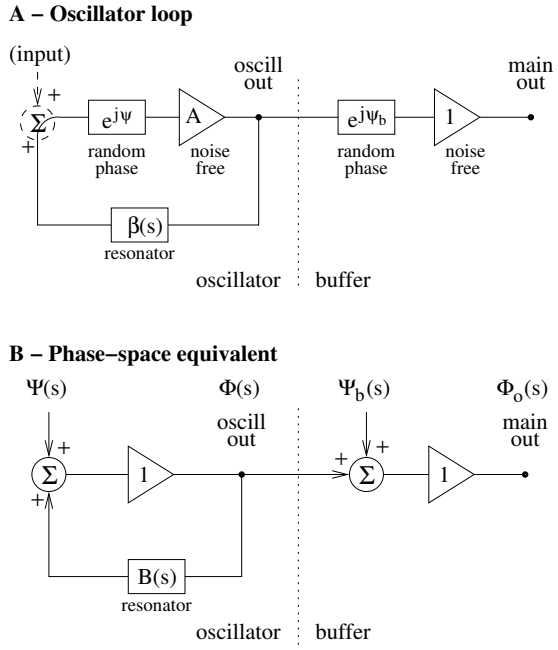

FIG. 2: Oscillator model and its phase-space equivalent. For the sake of simplicity all the dependence on s is moved to $\beta(s)$, hence the gain A is assumed constant. The scheme emphasizes the amplifier phase noise. Amplitude noise is not considered.

c. Phase noise spectrum. Combining white noise [Eq. (5)] and flicker noise [Eq. (11)], there results the spectral density $S_\varphi(f)$ shown in Fig. 1. It is important to understand that the white noise term $b_0 f^0$ depends on the carrier power P_0, while the flicker term $b_{-1}f^{-1}$ does not. Accordingly, the corner frequency f_c at which $b_{-1}f^{-1} = b_0$ is a function of P_0, thus f_c should *not* be used to describe noise. The parameters b_{-1}, F, and P_0 should be used instead.

IV. PHASE NOISE IN OSCILLATORS

A. The Leeson effect

Figure 2 shows a model for the feedback oscillator, and its equivalent in the phase space. All signals are the Laplace transform of the time-domain quantities, as a function of the complex frequency $s = \sigma + j\omega$. The oscillator transfer function is derived from Fig. 2 A according to the basic rules of linear systems

$$H(s) = \frac{1}{\beta(s)} \frac{1}{\frac{1}{A\beta(s)} - 1} = \frac{A}{1 - A\beta(s)} \qquad (13)$$

Stationary oscillation occurs at the angular frequency ω_0 at which $A\beta(j\omega) = 1$, thus $|A\beta(j\omega)| = 1$ and $\arg[A\beta(j\omega)] = 0$. This is known as the Barkhausen condition for oscillation. At $s = j\omega_0$ the denominator of $H(s)$ is zero, hence oscillation is sustained with zero input signal. Oscillation starts from noise or from the switch-on transient if $\Re\{A\beta(s)|_{s=j\omega_0}\} > 1$ (yet only slightly greater than 1 for practical reasons). When the oscillation reaches a threshold amplitude, the loop gain is reduced to 1 by saturation. The excess power is pushed into harmonics multiple of ω_0, and blocked by the resonator. For this reason, at ω_0 the oscillator operates in *quasi-linear* regime.

In most quartz oscillators, the sustaining amplifier takes the form of a negative resistance that compensates for the resonator loss. Such negative resistance is interpreted (and implemented) as a transconductance amplifier that senses the voltage across the input and feeds a current back to it. Therefore, the negative-resistance oscillator loop is fully equivalent to that shown in Fig. 2.

In 1966, D. B. Leeson [26] suggested that the oscillator phase noise is described by

$$S_\varphi(f) = \left[1 + \frac{1}{f^2}\frac{\nu_0^2}{4Q^2}\right] S_\psi(f) \qquad \text{(Leeson)}\,, \qquad (14)$$

This formula calls for the phase-space representation of Fig. 2 B, which deserves the following comments.

The Laplace transform of the phase of a sinusoid is probably the most common mathematical tool in the domain of PLLs [27–30]. Yet it is unusual in the analysis of oscillators. The phase-space representation is interesting in that *the phase noise turns into additive noise, and the system becomes linear.* The noise-free amplifier barely repeats the input phase, for it shows a gain exactly equal to one, with no error. The resonator transfer function, i.e., the Laplace transform of the impulse response, is

$$B(s) = \frac{1}{1 + s\tau} \qquad \tau = \frac{2Q}{\omega_0}\,. \qquad (15)$$

The inverse time constant is the low-pass cutoff angular frequency of the resonator

$$\omega_L = \frac{1}{\tau} = \frac{\omega_0}{2Q}\,. \qquad (16)$$

The corresponding frequency

$$f_L = \frac{\omega_L}{2\pi} = \frac{1}{2\pi\tau} = \frac{\nu_0}{2Q} \qquad (17)$$

is known as the Leeson frequency. Equation (15) is proved in two steps:

1. Feed a Heaviside step function $\kappa U(t)$ in the argument of the resonator input sinusoid. The latter becomes $\cos[\omega_0 t + \kappa U(t)]$.

2. Linearize the system for $\kappa \to 0$. This is correct in low phase noise conditions, which is certainly our case. Accordingly, the input signal becomes $\cos(\omega_0 t) - \kappa \sin(\omega_0 t) U(t)$.

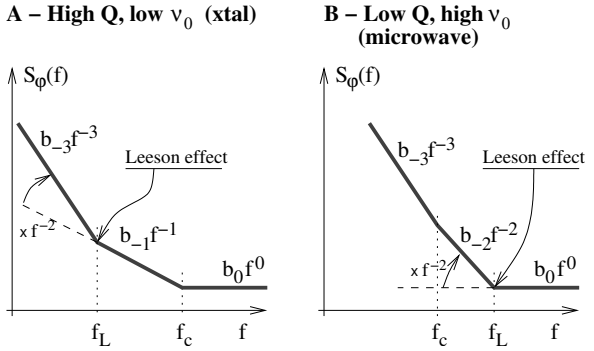

FIG. 3: Oscillator phase noise, not accounting for the output buffer.

3. Calculate the Laplace transform of the step response, and use the property that the Laplace transform maps the time-domain derivative into a multiplication by the complex frequency s. The Dirac function $\delta(t)$ is the derivative of $U(t)$.

The full mathematical details of the proof are available in [16, Chapter 3].

Applying the basic rules of linear systems to Fig. 2 B, we find the transfer function

$$\mathcal{H}(s) = \frac{\Phi(s)}{\Psi(s)} = \frac{1}{1 - B(s)} = \frac{1 + s\tau}{s\tau} , \qquad (18)$$

thus

$$|\mathcal{H}(j\omega)|^2 = \frac{1 + \omega^2\tau^2}{\omega^2\tau^2} . \qquad (19)$$

The Leeson formula (14) derives from Eq. (19) by replacing

$$\omega = 2\pi f \quad \text{and} \quad \tau = \frac{Q}{\pi\nu_0} . \qquad (20)$$

The transfer function $\mathcal{H}(s)$ has a pole in the origin (pure integrator), which explains the Leeson effect, i.e., the phase-to-frequency noise conversion at low Fourier frequencies. At high Fourier frequencies it holds that $\mathcal{H}(j\omega) = 1$. In this region, the oscillator noise is barely the noise of the sustaining amplifier.

The amplifier phase noise spectrum contains flicker and white noise, i.e., $S_\psi(f) = (b_{-1})_{\text{ampli}}\, f^{-1} + (b_0)_{\text{ampli}}$. Feeding such $S_\psi(f)$ into the Leeson formula (14), the oscillator $S_\varphi(f)$ can only be one of those shown in Fig. 3. Denoting with f_c the corner frequency at which flicker noise equals white noise, we often find $f_L < f_c$ in HF/VHF high-Q oscillators, and $f_L > f_c$ in microwave oscillators. In ultra-stable HF quartz oscillators (5–10 MHz), the spectrum is always of the type A ($f_L < f_c$).

B. Output buffer

The phase noise $S_{\psi\,b}(f)$ of the output buffer barely adds to the oscillator phase noise

$$S_{\varphi\,o}(f) = \left[1 + \frac{1}{f^2}\,\frac{\nu_0^2}{4Q^2}\right] S_\psi(f) + S_{\psi\,b}(f) . \qquad (21)$$

This a consequence of the flicker noise mechanism explained Section III 0 b, and inherent in the model of Fig. 2 B.

C. Resonator stability

The oscillator frequency follows the random fluctuation of the resonator natural frequency. However complex or tedious the formal proof for this statement can be, the experimentalist is familiar with the fact that the quartz oscillator can be frequency-modulated by a signal of frequency far higher than the Leeson frequency. For example, a 5 MHz oscillator based on a $Q = 2{\times}10^6$ resonator shows a Leeson frequency of 1.25 Hz (see Table I), while it can be modulated by a signal in the kHz region. Additionally, as a matter of fact, the modulation index does not change law from below to beyond the Leeson frequency. This occurs because the modulation input acts on a varactor in series to the quartz, whose capacitance is a part of the motional parameters.

D. Other effects

The sustaining amplifier of a quartz oscillator always includes some kind of feedback; often the feedback is used to implement a negative resistance that makes the resonator oscillate by nulling its internal resistance. The input admittance Y_i seen at the amplifier input can be represented as

$$Y_i = Y_i^{(v)} + Y_i^{(r)} , \qquad (22)$$

that is, the sum of a virtual term (v) plus a real term (r). The difference between 'virtual' and 'real' is that in the case of the virtual admittance the input current flows into the feedback path, while in the case of the real admittance the input current flows through a grounded dipole. This is exactly the same concept of virtual impedance routinely used in the domain of analog circuits [31, Chapter 1]. The admittance $Y_i^{(r)}$ also includes the the effect of the pulling capacitance in series to the resonator, and the stray capacitances of the electrical layout. As a consequence, the fluctuation $\delta Y_i^{(v)}$ is already accounted for in the amplifier noise, hence in the model of Fig. 2, while the fluctuation $\delta Y_i^{(r)}$ is not. On the other hand, $Y_i^{(r)}$ interacts with the resonator parameters, thus $\delta Y_i^{(r)}$ yields frequency fluctuations not included in the Leeson effect.

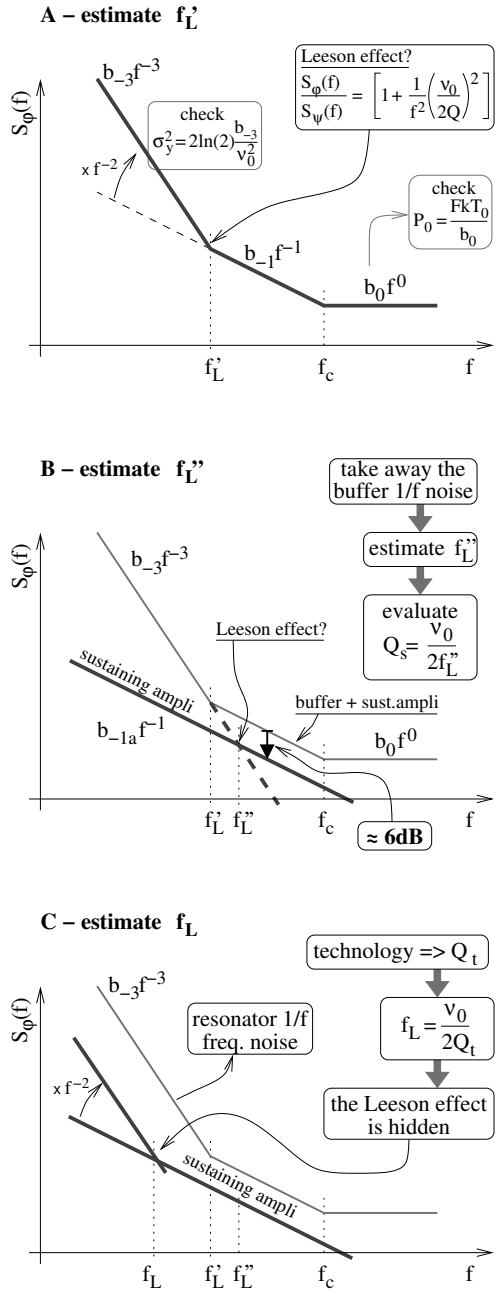

FIG. 4: Interpretation of the oscillator phase noise.

The hard assumption is made in our analysis, that $|\delta Y_i^{(r)}|^2 \ll |\delta Y_i^{(v)}|^2$. In words, we assume that the fluctuation of the electronics are chiefly due to the gain mechanism of the amplifier. Whereas the variety of circuits is such that we can not provide a proof for this hypothesis, common sense suggests that electronics works in this way.

V. ANALYSIS OF THE OSCILLATOR NOISE

This section address the core question, wether the $1/f^3$ noise observed on the oscillator $S_\varphi(f)$ plot is due to the Leeson effect, or it originates in the resonator. The interpretation method is shown in Fig. 4, and discussed below.

1. We start from the spectrum, measured or taken from the oscillator specifications. The first step is to remove the residual of the mains (50 or 60 Hz and multiples) and other stray signals, and to fit the spectrum with the power-law [Eq. (3)]. This process is called parametric estimation of the spectrum. With a pinch of experience, sliding old-fashion squares on a A4-size plot gives unexpectedly good results. Otherwise, the mathematical methods explained in [38, 39] are useful. After this, the spectrum looks like that of Fig. 4 A,

2. The term $b_0 f^0$ is chiefly due to the sustaining amplifier, hence the amplifier input power can be calculated using Eq. (6)
$$P_0 = \frac{FkT_0}{b_0} \ . \qquad (23)$$
In the absence of information, it is wise to take $F = 1.26$ (1 dB). To the extent of our analysis, estimating P_0 is only a check of plausibility.

3. Feeding the oscillator b_{-3} term into Eq. (4), we calculate the floor of the Allan deviation σ_y. We check on the consistency between calculated value and specifications or measures, if available.

4. At first sight, the cutoff frequency f_L' (Fig. 4 A) can be taken for the Leeson frequency because there the slope changes from f^{-3} to f^{-1}. Yet the term $b_{-1} f^{-1}$ contains the flicker of the sustaining amplifier and of the output buffer, which add [Equations (12) and (21)]. For this reason, f_L' can not be the Leeson frequency.

5. Actual oscillators have 2–4 buffer stages, the main purpose of which is to isolate the feedback loop from the environment in order to ensure frequency stability and to prevent injection locking. Owing to the Leeson effect, a wise designer will spend the lowest-noise technology in the sustaining amplifier, rather than in the buffer. Thus, we assume that the buffer contributes 3/4 of the total noise, and that sustaining amplifier contributes 1/4 (−6 dB). Accordingly, we plot the line $b_{-1\,a}\, f^{-1}$ in Fig. 4 B, 6 dB below the total flicker.

6. After taking away the buffer noise, the continuation of the $b_{-3} f^{-3}$ line meets the $b_{-1\,a} f^{-1}$ line at $f = f_L''$. The latter is a new candidate for the Leeson frequency. Feeding f_L'' into Eq. (17), we calculate the resonator merit factor Q_s (the subscript s stands for 'spectrum')
$$Q_s = \frac{\nu_0}{2 f_L''} \ . \qquad (24)$$

TABLE I: Estimated Parameters of some Ultra-Stable Oscillators.

Oscillator	ν_0	$(b_{-3})_{\rm tot}$	$(b_{-1})_{\rm tot}$	$(b_{-1})_{\rm amp}$	f'_L	f''_L	Q_s	Q_t	f_L	$(b_{-3})_{\rm L}$	R	Note	References
Oscilloquartz 8600	5	−124.0	−131.0	−137.0	2.24	4.5	5.6×10^5	1.8×10^6	1.4	−134.1	10.1	(1)	[14, 32]
Oscilloquartz 8607	5	−128.5	−132.5	−138.5	1.6	3.2	7.9×10^5	2×10^6	1.25	−136.5	8.1	(1)	[14, 32]
CMAC Pharao	5	−132.0	−135.5	−141.1	1.5	3	8.4×10^5	2×10^6	1.25	−139.6	7.6	(2)	[12, 13, 33]
FEMTO-ST LD protot.	10	−116.6	−130.0	−136.0	4.7	9.3	5.4×10^5	1.15×10^6	4.3	−123.2	6.6	(3)	[34]
Agilent 10811	10	−103.0	−131.0	−137.0	25	50	1×10^5	7×10^5	7.1	−119.9	16.9	(4)	[35]
Agilent prototype	10	−102.0	−126.0	−132.0	16	32	1.6×10^5	7×10^5	7.1	−114.9	12.9	(5)	[36]
Wenzel 501-04623	100	−67.0	−132 ?	−138 ?	1800	3500	1.4×10^4	8×10^4	625	−79.1	15.1	(6)	[37]
unit	MHz	dB rad^2/Hz	dB rad^2/Hz	dB rad^2/Hz	Hz	Hz	(none)	(none)	Hz	dB rad^2/Hz	dB		

Notes
(1) Data are from specifications, full options about low noise and high stability.
(2) Measured by CMAC on a sample. CMAC confirmed that $2\times10^6 < Q < 2.2\times10^6$ in actual conditions. See Fig. 5.
(3) LD cut, built and measured in our lab, yet by a different team. All design parameters are known, hence Q_t.
(4) Measured by Hewlett Packard (now Agilent) on a sample.
(5) Implements a bridge scheme for the degeneration of the amplifier noise. Same resonator of the Agilent 10811.
(6) Data are from specifications. See Fig. 7.

7. Technology suggests a merit factor Q_t (the subscript t stands for 'technology') significantly larger than Q_s, even in actual load conditions. Feeding Q_t into Eq. (17), we calculate f_L based on the actual merit factor

$$f_L = \frac{\nu_0}{2Q_t} \ , \qquad (25)$$

as shown in Fig. 4 C. There follows a phase noise term $(b_{-3})_L$, which account for the Leeson effect alone.

8. Given $Q_t \gg Q_s$, thus $f_L \ll f''_L$, the Leeson effect is hidden. Consequently, the oscillator f^{-3} phase noise is chiefly due to the fluctuation of the resonator natural frequency.

We introduce the stability ratio R, defined as

$$R = \frac{(\sigma_y)_{\rm oscill}}{(\sigma_y)_{\rm Leeson}} \qquad \text{(floor)}, \qquad (26)$$

and related to the other oscillator parameters by

$$R \ = \ \sqrt{\frac{(b_{-3})_{\rm tot}}{(b_{-3})_L}} \ = \ \frac{Q_t}{Q_s} \ = \ \frac{f''_L}{f_L} \ . \qquad (27)$$

This can be demonstrated from the b_{-3} term of the Leeson formula (14), using Equations (4) and (17). The parameter R states how bad is the actual oscillator, as compared to the same oscillator governed only by the Leeson effect, with the resonator fluctuations removed. Thus, $R = 1$ (0 dB) indicates that the oscillator f^{-3} phase noise comes from the Leeson effect. Equal contribution of resonator and Leeson effect yield $R = \sqrt{2}$ (3 dB), while $R \gg \sqrt{2}$ is found when resonator instability is the main cause of f^{-3} phase noise. In all cases we have analyzed, discussed in the next Section, we find R of the order of 10 dB, with a minimum of 6.6 dB. This means that the Leeson effect is hidden below the frequency fluctuation of the resonator.

Coming back to the estimation of the $1/f$ noise of the sustaining amplifier it is to be remarked that if the $1/f$ noise of this is lower than 1/4 of the total flicker, f''_L is further pushed on the right hand on Fig. 4 B-C, which reinforces the conclusion that the resonator is the main cause of frequency fluctuation.

VI. EXPERIMENTAL DATA AND DISCUSSION

Figure 5 shows the phase noise spectrum of a 5 MHz oscillator, out of a small series intended as the flywheel for the space Cesium fountain clock Pharao [40, 41]. On this plot, the reader can follow the interpretation process explained in Section V, and illustrated in Fig. 4. Guessing on technology, the merit factor was estimated to be 2×10^6. Afterwards, the manufacturer confirmed [42] that Q_t is between 2×10^6 and 2.2×10^6 in actual load conditions for that series of oscillators,

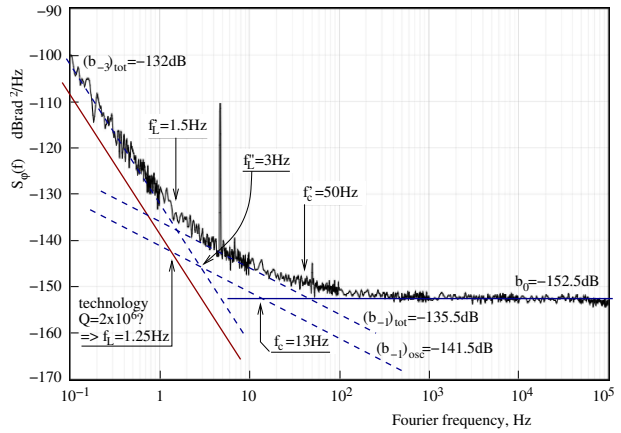

FIG. 5: Phase noise of the CMAC Pharao 5 MHz quartz OCXO. Courtesy of CMAC. Interpretation and mistakes are of the authors.

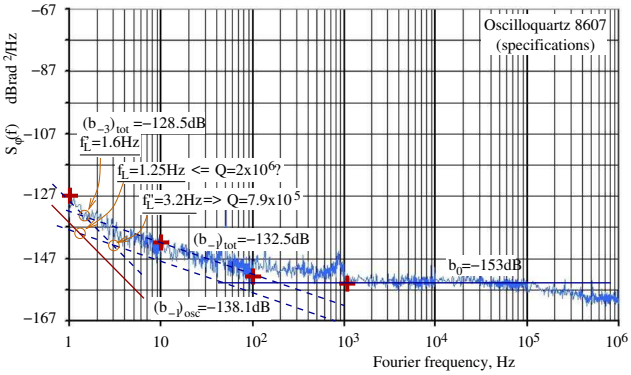

FIG. 6: Phase noise of the Oscilloquartz 8607 5 MHz quartz OCXO. Courtesy of Oscilloquartz. Interpretation and mistakes are of the authors.

and that the flicker noise of the sustaining amplifier is less than 1/4 (−6 dB) of the total flickering. This validates our conclusions.

Table I shows the results of our analysis on some oscillators. The ability to estimate the resonator merit factor is necessary to understand the oscillator inside. Experience indicates that the product $\nu_0 Q$ is a technical constant of the piezoelectric quartz resonator, in the range from 1×10^{13} to 2×10^{13}. As a matter of fact, the highest values are found in the 5 MHz resonators. In load conditions, the resonator merit factor is somewhat lower. The actual value depends on frequency, on the designer skill, and on the budget for implementation. A bunch of data are available from [1, 6, 43], and from our early attempts to measure the resonator frequency stability [4]. The oscillators we have analyzed exhibit the highest available stability, for we are confident about published data. The Agilent 10811 (hence the Agilent prototype) is closer to the routine production, and probably closer to the cost-performance tradeoff, as compared to the other ones, thus understanding oscillator the inside is more difficult. Nonetheless, in this case the value of Q_s is

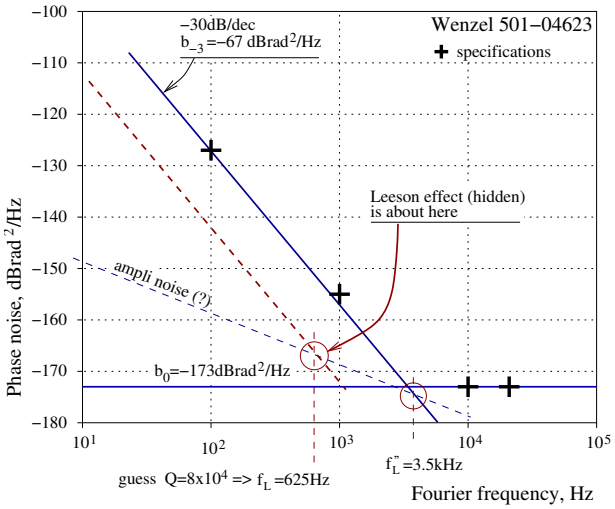

FIG. 7: Phase noise of the Wenzel 100 MHz OCXO [37].

so low that there is no doubt that it can not be the resonator merit factor.

In the case of the Oscilloquartz 8607 (Fig. 6), the f^{-3} noise is too low for it to be extracted from the $S_\varphi(f)$ spectrum available on data sheet, which starts from 1 Hz. Yet, we can use the device specifications $S_\varphi(f)|_{1\,\mathrm{Hz}} = -127$ dBrad²/Hz, $S_\varphi(f)|_{10\,\mathrm{Hz}} = -142$ dBrad²/Hz, and $S_\varphi(f)|_{1\,\mathrm{kHz}} = -153$ dBrad²/Hz. In fact, looking at the spectrum and at the Allan variance it is clear that at $f = 1$ Hz and $f = 10$ Hz the terms $b_{-3}f^{-3}$ and $b_{-1}f^{-1}$ determine $S_\varphi(f)$, with at most a minor contribution of b_0. It is also clear that $S_\varphi(f)|_{1\,\mathrm{kHz}} \simeq b_0$. Thus b_{-3} and b_{-1} are obtained by solving a system of two equations like $S_\varphi(f) = b_{-3}f^{-3} + b_{-1}f^{-1} + b_0$, at 1 Hz and 10 Hz.

In the case of the Wenzel 501-04623 oscillator (Fig. 7), the specifications available on the manufacturer web site consist of a few points, while the whole spectrum is not published. Experience indicates that in the case of 100 MHz oscillators the f^{-1} line tends to be hidden by the frequency flickering. That said, we can only guess that the f^{-1} noise of the sustaining amplifier is similar to that of other oscillators. This is sufficient to estimate f_L'', and to notice that the merit factor Q_s is far too low as compared to the state of the technology, and to conclude that the f^{-3} phase noise is due to the fluctuation of the resonator natural frequency. It is to be remarked that the power at the amplifier input is of the order of 10–20 μW in all other cases, and of 1 mW here. In addition, the 100 MHz resonator is smaller in size than the other resonator. A relatively high frequency flicker is therefore not surprising.

The examples shown above indicate that, under the assumption of Sections III–IV, the oscillator frequency flickering is chiefly due to the fluctuation of the resonator natural frequency.

Acknowledgements

We are indebted to Jean-Pierre Aubry (Oscilloquartz, Switzerland), and Vincent Candelier (CMAC, France) for providing spectra and support. Jacques Grolambert (FEMTO-ST, retired) set up the methods and the knowledge on oscillator measurement in our laboratory. Rémi Brendel (FEMTO-ST), Giorgio Brida (INRIM, Italy), Lute Maleki and G. John Dick (JPL, USA) helped us with several discussions. Rémi Brendel has taken a personal interest in our work and has offered a wealth of suggestions and constructive criticism; we owe him special thanks.

[1] F. L. Walls, in *Proc. Europ. Freq. Time Forum* (Besançon, France, 1995), pp. 227–243.
[2] R. J. Besson, M. Mourey, S. Galliou, F. Marionnet, F. Gonzalez, P. Guillemot, R. Tjoelker, W. Diener, and A. Kirk, in *Proc. Europ. Freq. Time Forum and Freq. Control Symp. Joint Meeting* (Besançon (France), 1999), pp. 326–330.
[3] F. L. Walls and A. E. Wanwright, IEEE Trans. Instrum. Meas. **24**, 15 (1975).
[4] E. Rubiola, J. Groslambert, M. Brunet, and V. Giordano, IEEE Trans. Ultras. Ferroelec. and Freq. Contr. **47**, 361 (2000), ISSN 0885-3010.
[5] V. F. Kroupa, IEEE Trans. Ultras. Ferroelec. and Freq. Contr. **35**, 406 (1998).
[6] V. F. Kroupa, Phys. Lett. A pp. 126–132 (2005).
[7] R. J. Besson, in *Proc. Freq. Control Symp.* (Fort Monmouth, NJ, USA, 1977), pp. 147–152.
[8] R. Brendel, M. Olivier, and G. Marianneau, IEEE Trans. Instrum. Meas. **22**, 160 (1975).
[9] M. M. Driscoll, IEEE Trans. Instrum. Meas. **24**, 21 (1975).
[10] J. R. Norton, in *Proc. Freq. Control Symp.* (Los Angeles, CA, USA, 1991), pp. 426–430.
[11] J. R. Norton, in *Proc. Freq. Control Symp.* (San Francisco, CA, USA, 1996), pp. 614–619.
[12] V. Candelier, J. Chauvin, C. Gellé, G. Marotel, M. Brunet, and R. Petit, in *Proc. Europ. Freq. Time Forum* (Warszawa, Poland, 1998), pp. 345–351.
[13] V. Candelier, P. Canzian, J. Lamboley, M. Brunet, and G. Santarelli, in *Proc. Europ. Freq. Time Forum and Freq. Control Symp. Joint Meeting* (Tampa, FL, USA, 2003), pp. 575–582.
[14] K. K. Thladhar, G. Jenni, and J. Aubry, in *Proc. Europ. Freq. Time Forum* (Neuchâtel, Switzerland, 1997), pp. 273–280.
[15] J. C. Brice, Rev. Mod. Phys. **57**, 105 (1985).
[16] E. Rubiola, *The Leeson effect*, arXiv:physics/0502143v1, web site arxiv.org (2005).
[17] J. Rutman, Proc. IEEE **66**, 1048 (1978).
[18] CCIR Study Group VII, in *Standard Frequencies and Time Signals* (International Telecommunication Union (ITU), Geneva, Switzerland, 1990), vol. VII (annex) of *Recommendations and Reports of the CCIR*, pp. 160–171.
[19] V. F. Kroupa, ed., *Frequency Stability: Fundamentals and Measurement* (IEEE Press, New York, 1983), ISBN 0-87942-171-1.
[20] J. Vanier and C. Audoin, *The Quantum Physics of Atomic Frequency Standards* (Adam Hilger, Bristol, UK, 1989), ISBN 0-85274-434-X.
[21] J. R. Vig (chair.), *IEEE Standard Definitions of Physical Quantities for Fundamental Frequency and Time Metrology–Random Instabilities (IEEE Standard 1139-1999)*, IEEE, New York (1999).
[22] H. T. Friis, Proc. IRE **32**, 419 (1944).
[23] D. Halford, A. E. Wainwright, and J. A. Barnes, in *Proc. Freq. Control Symp.* (1968), pp. 340–341, abstract only is published.
[24] F. L. Walls, E. S. Ferre-Pikal, and S. R. Jefferts, IEEE Trans. Ultras. Ferroelec. and Freq. Contr. **44**, 326 (1997).
[25] A. Hati, D. Howe, D. Walker, and F. Walls, in *Proc. Europ. Freq. Time Forum and Freq. Control Symp. Joint Meeting* (2003).
[26] D. B. Leeson, Proc. IEEE **54**, 329 (1966).
[27] J. Klapper and J. T. Frankle, *Phase-Locked and Frequency-Feedback Systems* (Academic Press, New York, 1972).
[28] F. M. Gardner, *Phaselock Techniques* (Wiley, New York, 1979), ISBN 0-471-04294-3.
[29] R. Best, *Phase-Locked Loops* (McGraw Hill, 1999).
[30] W. F. Egan, *Phase-Lock Basics* (Wiley, 1998).
[31] S. Franco, *Design with Operational Amplifiers and Analog Integrated Circuits* (McGraw Hill, Singapore, 1997), 2nd ed., ISBN 0-07-021857-9.
[32] oscilloquartz.com, `http://www.oscilloquartz.com/`.
[33] cmac.com, `http://www.cmac.com/`.
[34] S. Galliou, F. Sthal, J. Jacques Boy, and M. Mourey, in *Proc. Ultrason. Ferroelec. Freq. Contr. Joint Conf.* (IEEE, New York, 2004, Montréal, Canada, 2004), pp. 475–477.
[35] J. R. Burgoon and R. L. Wilson, Hewlett Packard J. pp. 20–29 (1981).
[36] R. K. Karlquist, IEEE Trans. Ultras. Ferroelec. and Freq. Contr. **47**, 390 (2000).
[37] wenzel.com, `http://www.wenzel.com/`.
[38] G. M. Jenkins and D. G. Watts, *Spectral Analysis and its Applications* (Holden Day, San Francisco, CA, 1968).
[39] D. B. Percival and A. T. Walden, *Spectral Analysis for Physical Applications* (Cambridge, Cambridge, UK, 1998), ISBN 0-521-43541-2.
[40] P. Lemonde, P. Laurent, G. Santarelli, M. Abgrall, Y. Sortais, S. Bize, C. Nicolas, S. Zhang, A. Clairon, N. Dimarcq, et al., in *Frequency Measurement and Control*, edited by A. N. Luiten (Springer, Berlin, D, 2001), Topics in Applied Physics, pp. 131–152.
[41] S. Bize, P. Laurent, M. Abgrall, H. Marion, I. Maksimovic, L. Cacciapuoti, J. Grünert, C. Vian, F. Pereira dos Santos, P. Rosenbusch, et al., C. R. Physique **5**, 829 (2004).
[42] Candelier (unpublished), V. Candelier (CMAC), personal communication.
[43] E. A. Gerber and A. Ballato, *Precision Frequency Control (2 vol.)* (Academic Press, London, 1985).

Proceedings of the 20th EFTF, 2006

A study of the paramagnetic properties of Fe^{3+} ions in sapphire towards realizing an ultra-stable cryogenic Maser oscillator

K. Benmessaï,* P.Y. Bourgeois, M. Oxborrow†, N. Bazin, Y. Kersalé, and V. Giordano
Institut FEMTO–ST, Dpt. LPMO,
UMR 6174 CNRS-Université de Franche-Comté 32 av. de l'Observatoire,
25044 Besançon Cedex, France
† *National Physical Laboratory*
Queens Road, Teddington,Middlesex, TW11 0LW, UK.

In a preceding publication, we reported the experimental demonstration of maser oscillation at 12.04 GHz in a cryogenic sapphire whispering-gallery-mode resonator, where the resonator's dielectric ring contained a low concentration of paramagnetic Fe^{3+} ions within its monocrystalline sapphire lattice. Our preliminary measurements revealed a frequency stability of the order of 2.5×10^{-14} in a non-optimized design. In this paper, we report new measurements made on this same resonator to determine more precisely the main parameters affecting the dynamics of the Fe^{3+} ions when exposed to a microwave signal within their ESR bandwidth.

I. INTRODUCTION

The search for a flywheel oscillator presenting frequency stability better than 1×10^{-14} at short term concerns a growing number of scientific or technical as future space programs, metrology and tests of fundamental physicss [1–3]. The best solution achieved today consists in an oscillators based on a whispering gallery mode sapphire resonator cooled at 4,2K. Nevertheless the few units build in some laboratories around the world are exceedingly complex systems. Among all the difficulties to run such a system, the resonator adjustment is certainly the most critical task. To get the proper values of the resonator couplings at low temperature needs skill, training and above all a lot of luck. Moreover the sapphire whispering gallery mode resonator oscillator is a spatially extended system; at least two microwave lines, each typically > 1 m in length, are required to connect the cryogenic resonator to the room-temperature section of the oscillator's loop. To achieve stabilities at the 1×10^{-14} level, several auxiliary cables and sensors, supporting the control of the resonator's temperature, the Pound servo, loop-power regulation[4], ... all need to be wired into the cryostat.

We have demonstrated that the sapphire resonator can be used in a different way [5, 6] allowing noticeable simplification of the system. Among the different paramagnetic impurities that can be found in high purity sapphire crystal there is the Fe^{3+} ion presenting at zero dc magnetic field three levels: $|1/2\rangle$, $|3/2\rangle$ and $|5/2\rangle$. Near the liquid helium temperature, there are significant differences in the populations of these levels. Transitions between any of these levels are allowed and their linewidths are of a few tens of MHz. A 31.3 GHz pump signal causes a net transfert of Fe^{3+} ions from the $|1/2\rangle$ level to the $|5/2\rangle$ level. In turn non-radiative transitions $|5/2\rangle \mapsto |3/2\rangle$ create a negative population difference between the two lower states, making possible maser oscillation at 12.04 GHz if the resonator presents a high-Q mode at this frequency. The principle of our first whispering-gallery-mode maser oscillator (WhigMO) is represented in Figure 1. It is based on sapphire resonator whose $WGH_{17,0,0}$ mode frequency coincides with the $|1/2\rangle \mapsto |3/2\rangle$ frequency, i.e. 12.04 GHz. Another WG mode at 31.3 GHz is used to pump the cristal. A 2mW pump signal generated by a microwave synthetizer is sufficient to obtain a -56dBm maser signal, available outside of the cryostat. The frequency stability measured in e very preliminary experiment is better than 4×10^{-14} for $\tau \leq 100$s.

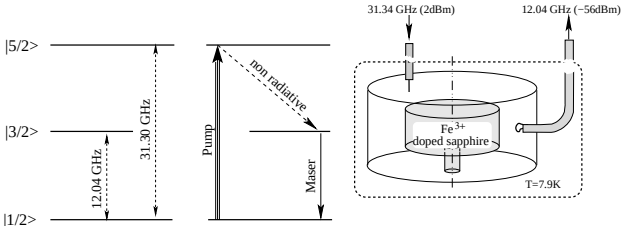

Figure 1: Principle of the whispering gallery mode maser oscillator.

The theory of the paramagnetic resonance [7] introduces two characteristic times to describe the dynamics of the spin system: T_1 and T_2 the spin-lattice and the spin-to-spin relaxation times respectively. Moreover the maser power depends on N the effective ions concentration. The aim of this paper is to present experiments made on our resonator to determine these three parameters. Moreover, the sensitivity of the maser frequency to an applied dc magnetic field has been measured.

II. MAGNETIC SUSCEPTIBILITY MEASUREMENT

In a pure sapphire resonator (i.e. in impurity free region), the frequency of the WG mode depends only on the geometry and on permittivity of the material. The Fe^{3+} paramagnetic impurities induce a magnetic susceptibility in the resonator which yields to shift the resonant frequencies of the different WGH modes around the ESR resonance at 12.04 GHz.

*Electronic address: karim.benmessai@femto-st.fr

If a strong signal at 12.04 GHz is applied to the resonator, the power absorbed by the magnetic resonance is no longer proportional to the incident power, but rather saturates. This led to a frequency shift of the surrounding WG modes back to the one they should have had in the abscence of impurities. This is explained by the fact that the magnetic susceptibility, which is proportional to the difference in population of the two lower levels, tends to zero.

The real part of the ac magnetic susceptibility is given by :

$$\chi' = \frac{4\pi^2 T_2^2 \chi_0 \nu_0 \Delta\nu}{1 + 4\pi^2 T_2^2 \Delta\nu^2} \quad (1)$$

where T_2 is the spin-spin decoherence time, χ_0 the dc-susceptibility, and $\Delta\nu$ the detuning parameter of the analysed WG mode with respect to the ESR-line (ν_0) and assuming that the energy is totally confined inside the sapphire (magnetic filling factor $\eta \sim 1$).

The measurement set-up is then represented in figure 3.

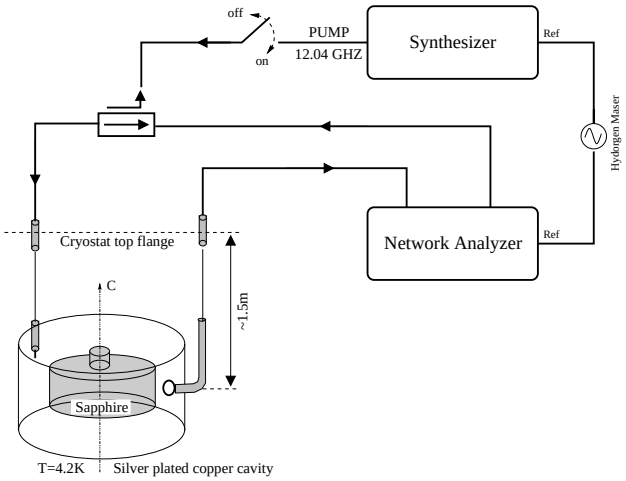

Figure 2: Set-up for electron paramagnetic resonance experiment.

A pump signal corresponding to the $WGH_{17,0,0}$ mode is sent to the resonator with the help of an external microwave synthesizer. The power -of about 3dBm- is high enough to saturate the transition. The detuned frequencies of each mode around $WGH_{17,0,0}$ are recorded via a network analyser. The real part of the magnetic susceptibility can be then evaluated and subsequently plotted as a function of the measured detuned parameter, as shown in figure 3.

An adapted fit to this curve related on eq. (1) give the dc susceptibility $\chi_0 \approx 10^{-9} \pm 0.1 \times 10^{-9}$ and the spin-spin relaxation time $T_2 \approx 2.2 \times 10^{-9}\text{s} \pm 0.8 \times 10^{-9}\text{s}$.

These values are of about one order of magnitude from other measurements[8]. As a matter of fact, the width of the ESR-line is known to be approximately equal to 27 MHz[9]. The equivalent Q-factor Q_{ESR} is then ≈ 450,

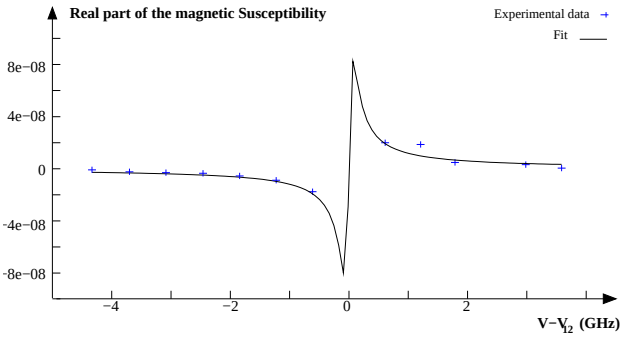

Figure 3: $\chi' = -2\frac{\Delta\nu}{\nu}$

therefore :

$$Q_{ESR} = \pi \nu_0 T_2 \quad (2)$$

Eq. (2) give $T_2 \approx 10^{-8}$, which is consistent with other measurements. A possible explanation of this discrepancy is the inaccuracy of the data fit due to the lack of data points near the sharp variation region of χ'.

A more physical one is also given there.

At thermal equilibrium, dc-susceptibility χ_0 can be given by :

$$\chi_0 = \frac{(g\beta)^2 \mu_0}{4 k_B T} N \quad (3)$$

with g the Landé factor ~ 2, β Bohr's magneton $= 9.27 \times 10^{-24}\text{Am}^2$, k_B the Boltzmann constant, and N the iron ions concentration. One can then evaluate the iron ions concentration to be $5.3 \times 10^{20}\text{ions m}^{-3}$. We have already pointed out that such a small concentration ($\approx$ 12 ppb) is enough to obtain a maser operation. This result is also consistent with our previous estimation based on the measured maser power[5]. However this value is far less than the Fe^{3+} ions concentrations obtained by spectroscopic methods in HEMEX sapphire samples [10] of about 2 ppm. This inconsistency may be explained by assuming the 12.04 GHz absorbtion line shape is inhomogeneously broadened[11] which led to a spin-spin relaxation time $T_2^\star << T_2$. Most of the spins have different precessional frequencies than in a homogeneous broadening situation. Their resonant structure is also known as *spin-packet.*

III. SPIN LATTICE RELAXATION TIMES

It has been shown (in the early 60s) [12, 13] that the determination of the spin-lattice relaxation time T_1 is more adapted using a time domain technique. The principle of this experiment was inspired from [13]. and is schematized in figure 4.

We build an oscillator loop around the cryogenic sapphire resonator. A cavity filter placed in this loop permits to get oscillation on the $WGH_{18,0,0}$ mode at 12.654 GHz. This mode was chosen because its frequency shift

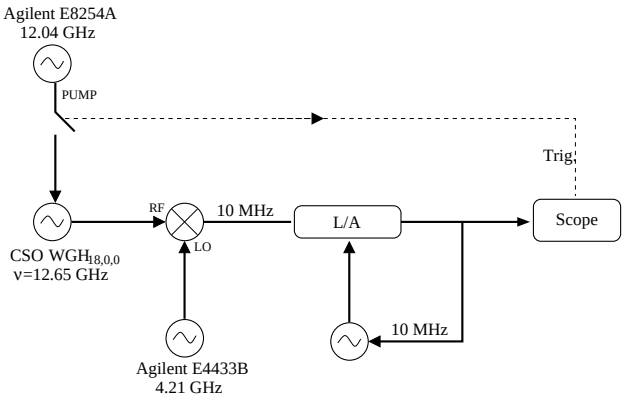

Figure 4: Principle of spin-lattice relaxation time measurement.

observed in the previous section is large: 120Hz. A microwave coupler is used to inject (in the loop at the resonator input) the signal coming from a synthesizer tuned to the ESR at 12.04 GHz. A power of -6dBm is sufficient to saturate the ESR. The oscillator output is sent to a specially designed system to analyze the fast change in the oscillator frequency when the pump is switched. The frequency of the analysed signal is firstly down-converted to low frequencies (10 MHz) by mixing it with an external microwave synthesizer. A 10 MHz VCO phase locked on this signal. The low frequency error signal is then an image of the VCO frequency and follows the frequency of the CSO. When the pump is switched on, the frequency change is recorded on an oscilloscope trigged to the microwave synthesizer pump via a quadratic detector.

We volontary increased the resonator coupling in order to get a loaded Q-factor of $30 \cdot 10^6$. Under these conditions, the intrinsic relaxation time of the resonator is 1 ms which is about ten times lower than the expected value of T_1. Figure 5 shows an example of the observed signal dur-

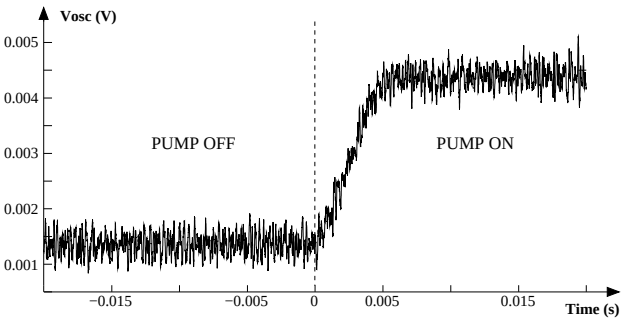

Figure 5: Oscilloscope trak example.

ing a 12.04 GHz pump-on/off cycle. As the voltage is directly proportionnal to the oscillator frequency, T_1 is determined by the time constant of this exponential function, that is $T_1 = 10$ ms.

We also conduct few measurements of T_1 by changing the resonator temperature. From 4.2 K to 7 K, T_1 decreases from 16.6ms to 11ms, as shown in figure 6.

This result is in a good agreement with the fact that the

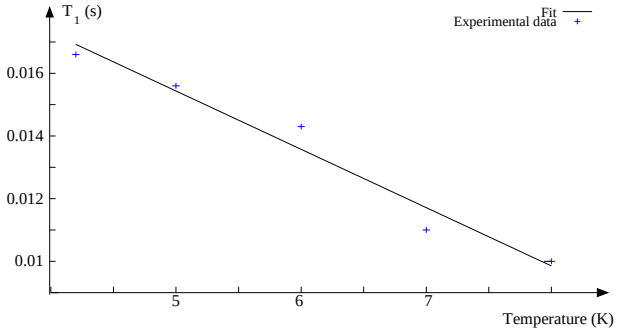

Figure 6: T_1 *vs* temperature.

spin-lattice relaxation time varies as T^{-1}.

IV. MASER SENSITIVITY TO AN EXTERNAL DC MAGNETIC FIELD

To build a useful frequency standard, sensitivity to environmental parameters should be known. One of them truly affects the inherent spin system: the magnetic field.

It is thus interesting to evaluate the maser's frequency sentivity to an applied dc magnetic field. The experimental set-up is drawn on figure 7. Specially wired Helmoltz coils were placed around the cryostat to generate a magnetic field along the sapphire lattice *c*-axis direction. The injected power is driven by a high-current stabilyzed source. In this configuration, we get 4 A gauss^{-1}. This

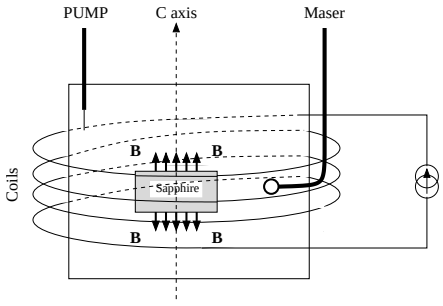

Figure 7: .

value has been previously measured at room temperature with a gauss-meter placed in the center of the coils inside the cryostat.

The dc magnetic field can be increased step by step while the whigmo is operating. Results are given in figure 8. For a *c*-axis (resp. -*c*-axis) oriented field, whigmo's frequency is shifted up (resp. down). Maser oscillation stops when the field reaches > 4 gauss. The ESR-line is then splitted and pulled away by Zeeman effect, and the $WG_{17,0,0}$ mode frequency is no longer located within the ESR's profile.

The measured sensitivity is of about 1.7 ± 0.1 Hz/gauss.

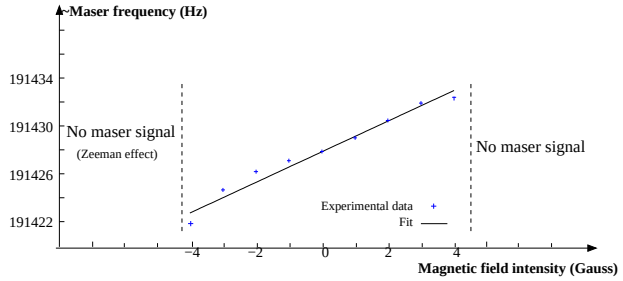

Figure 8: Whigmo's sensitivity to an external dc magnetic fi eld.

V. CONCLUSION

Experimental measurements of some paramagnetic properties of $Fe^{3+} : Al_2O_3$ ions have been presented. Our setups greatly differ from early measurements. Physical properties of our crystals need to be evaluated to understand more precisely the dynamics of the spin-system in a whigmo configuration. This paper presents some results such as $T_2 \sim 2 \times 10^{-9}$s, $\chi_0 \sim 10^{-9}$, and $N \sim 12$ ppb, which are not in good agreement with other publications but revealed the presence of an inhomogeneous broadening system. New measurements will be conducted soon for better understanding. We also have presented an original set-up to measure the spin-lattice relaxation time $T_1 \sim 10$ ms which is T^{-1} dependant. Finally, we have evaluated our whigmo's sensitivity of 1.7 Hz/gauss to an applied dc-magnetic field.

[1] A.Mann, G.Santarelli, S.Chang, A.N.Luiten, P.Laurent, C.Salomon, D.G.Blair, and A.Clairon, Proceedings of the IEEE International Frequency Control Symposium, Passadena, CA. pp. 13–17 (1998).
[2] P.Wolf, S.Bize, A. Clairon, A. N. Luiten, G. Santarelli, and M.E.Tobar, Physical Review Letters **90**, 060402 (2003).
[3] V.Candelier, P.Canzian, J.Lamboley, M.Brunet, and G.Santarelli, Proceedings of the Joint meeting 17th E.F.T.F and 2003 IEEE IFCS, Tampa, Fl pp. 575–582 (2003).
[4] A.N.Luiten, A.G.Mann, M.E.Costa, and D.G.Blair, IEEE Transactions on Instrumentation and Measurement **44**, 132 (1995).
[5] P.-Y. Bourgeois, M. Oxborrow, N. Bazin, Y. Kersal´e, M. E. Tobar, and V. Giordano, Proc. 19th European Frequency and Time Forum, Besançon, France (2005).
[6] P.-Y. Bourgeois, N. Bazin, Y. Kersal´e, V. Giordano, M. E. Tobar, and M. Oxborrow, Applied Physics Letters **87** (2005).
[7] A.E.Siegman, *Microwave Solod-state Masers* (1964).
[8] A.G.Mann, A.J.Giles, D.G.Blair, and M.J.Buckingham, J. Phys. D. Appl. Phys. **25**, 1105 (1991).
[9] H. F. Symmons and G. S. Bogle, Proc. Phys. Soc. **79**, 468 (1962).
[10] LCS six-month progress report LIGO-M0303366-00-M organization: Department of Physics, Southern University and AM College (2003).
[11] A. M. Portis, Phys. Rev. **91**, 1071 (1953).
[12] M. W. P. Strandberg, Phys. Rev. **110**, 65 (1958).
[13] J. C. F. Davis, M. W. P. Strandberg, and R. L. Kyhl, Phys. Rev. **111**, 1268 (1958).

Proceedings of the 20th EFTF, 2006

Progress in the Development of Cryogenic Sapphire Resonator Oscillator at NMIJ/AIST

K. Watabe[1], J. G. Hartnett[2], C. R. Locke[2], G. Santarelli[3], S. Yanagimachi[1], T. Ikegami[1], and S. Ohshima[1]
[1] National Metrology Institute of Japan(NMIJ), AIST, Tsukuba 305-8563, Japan.
[2] School of Physics, University of Western Australia, 35 Stirling Hwy, Crawley, WA, 6009 Australia.
[3] LNE-SYRTE, Observatoire de Paris, 61 avenue de l'Observatoire, 75014 Paris, France.
e-mail: k.watabe@aist.go.jp

In this paper, we describe the progress in the development of a cryogenic sapphire oscillator (CSO) at NMIJ, AIST. The oscillator was based on a high Q-factor cryogenic-sapphire-resonator cooled with liquid helium which operates on a Whispering Gallery mode. Two CSOs (CSO1 and CSO2) have been built to evaluate their stability at short averaging times. We measured a fractional frequency stability of 1.1×10^{-15} at averaging times of 1 s and a minimum frequency instability of 5.5×10^{-16} at averaging times of 20 s.

1. INTRODUCTION

Cryogenic sapphire oscillators (CSOs) are currently the most stable microwave frequency sources for averaging times from 1 to 100 s, exhibiting a fractional frequency instability of a part in 10^{15} to a few parts in 10^{16} [1], [2]. They are excellent local oscillators for a number of frequency standard applications, such as trapped ytterbium ion frequency standards [3], cold atomic fountain clocks [4] and trapped mercury ion frequency standards [5]. Other applications include fundamental tests of physics, such as tests of Lorentz invariance [6].

At NMIJ, AIST, a cesium atomic fountain frequency standard (NMIJ-F1) is operational [7]. For this standard, we are developing a microwave local oscillator using CSO under a collaboration with the University of Western Australia and LNE-SYRTE. Performance targets are a stability below 10^{-14} for averaging times of 1 s to 100 s, which is sufficient to operate an atomic clock at the quantum projection noise limit [4]. This excellent short term stability enables an evaluation of systematic frequency shifts and frequency comparisons between clocks at the 10^{-16} level over a few days [8].

In a previous paper, we reported that the stability of the CSO for averaging times shorter than 300 s could not be directly measured, it was masked by short-term fluctuations of the hydrogen maser reference [9]. In this paper, we report on the progress of the development of two CSOs (CSO1 and CSO2) at NMIJ, AIST to evaluate their stability at short averaging times.

II. CRYOGENIC SAPPHIRE RESONATOR

The sapphire crystals were manufactured from Crystal Systems "HEMEX" and supports a Whispering Gallery mode, $WGH_{15,0,0}$ at 10.8 GHz. The sapphire crystal for CSO1 (resonator 1) has a diameter of 50.0 mm and a height of 30.0 mm, with one 11.8 mm-diameter and 19.0 mm-long support spindle machined from a single piece of sapphire. The sapphire crystal for CSO2 (resonator 2) has the same diameter of 50.0 mm and height of 30.0 mm, with one 11.8 mm-diameter and 19.0 mm-long support spindle, and an additional 11.8 mm-diameter and 12.0 mm-long support spindle, machined from a single piece of sapphire. The 11.8 mm-diameter and 12.0 mm-long support spindle of the resonator 2 was used to handle the crystal easily without touching the main part after chemical cleaning to remove the surface contamination. Each resonator was placed in a silver-plated copper cavity and supported from the bottom in the cavity by the spindle and a clamp mechanism [10]. The inner diameter of the copper cavity was nominally 80 mm and 50 mm high. The sapphire-loaded cavity (SLC) was placed in a vacuum cylinder that was permanently evacuated, and sealed with Mylar gaskets. This inner cylinder was sealed inside a large stainless steel cylinder that is attached to a cryostat for cooling to liquid helium temperatures [11]. Each resonator has its own cryostat. The two cryostats are about 1.5-m apart. The CSO can operate continuously for periods of approximately three weeks with the cryostat.

The turning point temperature for the chosen mode of resonance ($WGH_{15,0,0}$) was measured at 6.1 K at 10.812300 GHz for the resonator 1 and at 7.0 K at 10.810148 GHz for that in the resonator 2. At these temperatures unloaded Q-factors of the resonator 1 and the resonator 2 exhibited 1.1×10^9 and 1.5×10^9, respectively. In both resonators, the mode frequency exhibits a maximum as function of temperature described by a fractional frequency curvature ($1/f\ d^2f/dT^2$) of $\sim -2 \times 10^{-9}\ K^{-2}$. The mode frequency also shows a dependence on the microwave power dissipated in the resonator due to the electromagnetic radiation pressure [12]. The magnitude of this dependence at operating injected power is $1/f\ df/dP \approx -7 \times 10^{-12}$/mW for the resonator 1 and $\approx -5 \times 10^{-11}$/mW for the

resonator 2, respectively. The temperature of both resonators is controlled within 1 mK at the turning point using a temperature controller with a calibrated carbon glass thermometer and a foil heater attached to the copper post just above the SLC, outside the inner vacuum can. Coupling to the resonator 1 was accomplished with a magnetic field loop probe from the side of the cavity at the primary input port and from the bottom at the output port with a straight antenna probe made from the inner conductor of the coaxial cable. Coupling to the resonator 2 was accomplished with a straight antenna probe from the bottom of the cavity at the primary input port and with a magnetic field loop probe from the side at the output port. The measured resonator couplings were set to $\beta_1 = 0.97$ on the primary reflection port and $\beta_2 = 0.26$ on the transmission port for the resonator 1, and $\beta_1 = 1.07$ and $\beta_2 = 0.15$ for the resonator 2.

III. LOOP OSCILLATOR

The CSOs employ a loop oscillator configuration, which is servo controlled by a Pound-type frequency stabilization scheme and a power control servo [13] as shown in Fig. 1. In transmission, the sapphire resonator is the primary frequency-determining element of the loop oscillator, while in reflection it also acts as the dispersive element in an active Pound-type frequency stabilization scheme to lock the oscillation frequency to the resonance of the sapphire resonator. The carrier signal incident on the sapphire resonator was phase modulated by a voltage-controlled phase shifter (VCPS1). The detector diode (D1) for the frequency stabilization has been placed near the resonator, outside the inner vacuum can in the vacuum region that is temperature controlled close to liquid helium temperatures, improving the noise floor of the frequency control servo because of the elimination of the 15 dB transmission line loss before D1. In both oscillators, microwave power dissipated in the sapphire resonator is typically 0.1 mW and is regulated by the power servo comprising the detector diode (D2) and voltage controlled attenuator (VCA). This servo compensates for amplifier power fluctuations, the variation of insertion loss of the error corrector (VCPS2) with the error voltage from the frequency stabilization servo and permittivity change induced by radiation pressure variation. D2 was also placed near the resonator in the cryogenic environment, outside the inner vacuum can. This eliminates both the long-term variation of incident power on the resonator due to the variation of transmission line attenuation with liquid helium bath level and the temperature dependence of the detector sensitivity. A 10 dB directional coupler and a 6 dB directional coupler in the cryogenic environment were used for the CSO1 and for the CSO2, respectively, to feed some of the incident signal power to a detector.

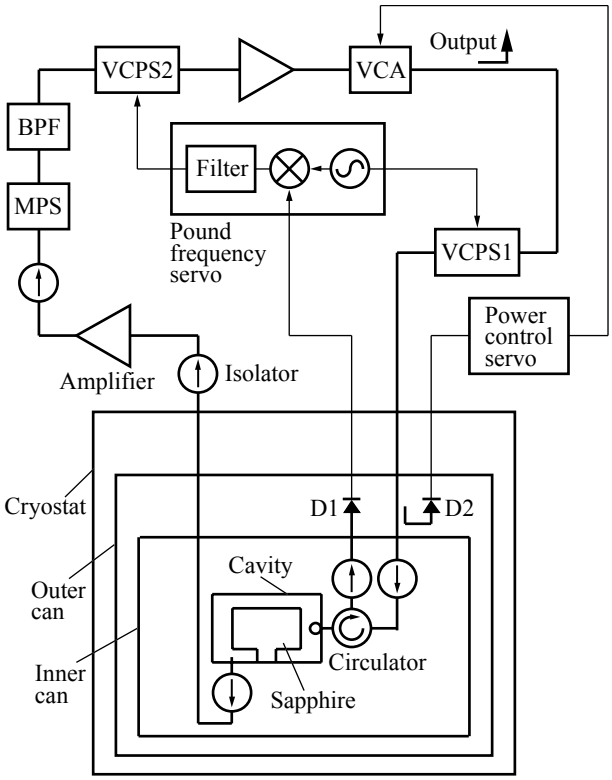

Fig. 1. Configuration of 10.8-GHz loop oscillator with Pound frequency control servo and power control servo. MPS is a mechanical phase shifter, BPS is a band-pass filter, VCPS is a voltage-controlled phase shifter, VCA is a voltage controlled attenuator, and D is a detector diode.

The resulting DC voltage signal is then subtracted from a stable reference, filtered and fed back into VCA to maintain constant power incident upon the sapphire resonator.

IV. OSCILLATOR FREQUENCY STABILITY

Figure 2 shows a schematic block diagram of the measurement system to evaluation the short-term frequency stability of two oscillators. The frequency difference of 2.152 MHz between two CSOs was mixed down to 1 kHz using a frequency synthesizer, designed in LNE-SYRTE, locked to the CSO1. Detailed descriptions for the synthesizer have been presented elsewhere [14]. A 1 GHz voltage-controlled oscillator (VCO) locked to the CSO1 was divided to 40 MHz using two prescalers of divide-by-5. The 40-MHz signal was used to phase lock to a direct digital synthesizer 2 (DDS2) to produce 2.151 MHz. The 1 kHz signal was counted using an Agilent 53132A frequency counter referenced to 10 MHz reference from a hydrogen maser.

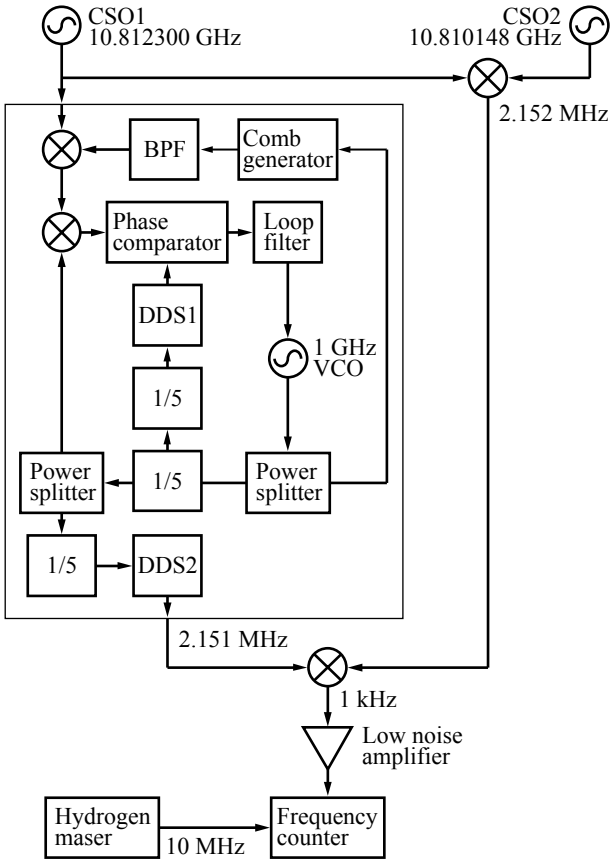

Fig. 2. Block diagram of the measurement system to evaluation the short-term frequency stability of two oscillators. VCO is a voltage-controlled oscillator, 1/5 is a prescaler of divide-by-5, DDS is a direct digital synthesizer, and BPS is a band-pass filter. The frequency difference of 2.152 MHz between CSO1 and CSO2 was mixed down to 1 kHz using a frequency synthesizer, designed in LNE-SYRTE, locked to the CSO1.

The Allan deviation calculated from the measured frequency data is shown in curve (i) of Fig. 3, along with the result compared CSO1 with a hydrogen maser. The frequency data was collected in three sets with gate times of 1 s for averaging times of 1 s and 2 s, those of 4 s for averaging times of 4 s and 8 s, and those of 10 s for averaging times longer than 10 s. A factor of square root of 2 has been removed to display the Allan deviation due to a single oscillator, assuming equal instability in each. We measured a fractional frequency stability of 1.1×10^{-15} at averaging times of 1 s and a minimum frequency instability of 5.5×10^{-16} at averaging times of 20 s. The fractional frequency drift is approximately 10^{-13}/day from the comparison with the hydrogen maser. It seems that the drift is caused by stress release in the sapphire resonator [15].

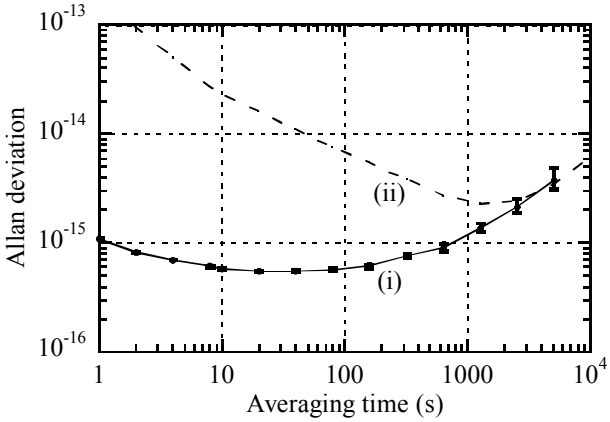

Fig. 3. Allan deviation of the beat frequencies. (i) represents results for single CSO and (ii) represents results of the comparison between CSO1 and a hydrogen maser.

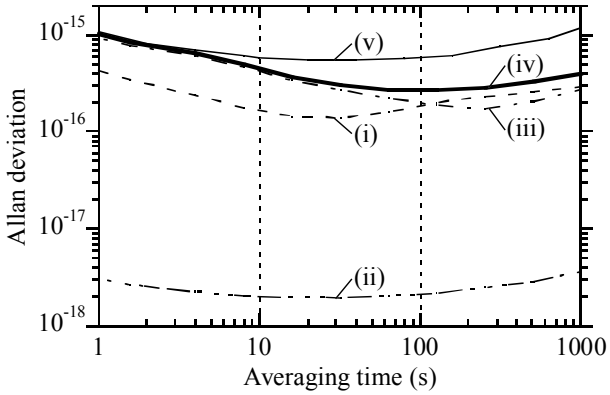

Fig. 4. Individual contribution to the frequency stability for the CSO1 of frequency control servo (i), power control servo (ii), spurious amplitude modulation (iii), and their sum (iv). (v) represents the observed frequency stability for single oscillator.

Figure 4 shows noise floors for the CSO1 of the frequency control servo, the power control servo, spurious amplitude modulation (AM) caused by the phase modulator, which are the individual contributions to the frequency stability, and their sum. The voltage noise was measured as was done in [10]. The short-term frequency stability is limited by noise in spurious AM. With an additional servo to suppress the spurious AM, this noise floor will be reduced and should result in an improved frequency stability.

V. CONCLUSION

The cryogenic sapphire oscillator at NMIJ, AIST has demonstrated an Allan deviation of 1.1×10^{-15} at

averaging times of 1 s and a minimum frequency instability of 5.5×10^{-16} at averaging times of 20 s. The short-term frequency stability is limited by noise in the spurious amplitude modulation. The CSO is expected to be installed at NMIJ-F1.

Acknowledgements

The authors wish to thank Dr. Clairon at LNE-SYRTE, and Prof. M. Tobar and A/Prof. E. Ivanov at the University of Western Australia for valuable advice and discussions.

REFERENCES

[1] S. Chang, A. G. Mann and A. N. Luiten: Electron. Lett. **36** (2000) 480.
[2] G. J. Dick and R. T. Wang: IEEE Trans. Ultrason. Ferroelectr. Freq. Control **47** (2000) 1098.
[3] P. T. H. Fisk, M. J. Sellars, M. A. Lawn and C. Coles: IEEE Trans. Ultrason. Ferroelectr. Freq. Control **44** (1997)344.
[4] G. Santarelli, P. H. Laurent, P. Lemonde, A. Clairon, A. G. Mann, S. Chang, A. N. Luiten and C. Salomon: Phys. Rev. Lett. **82** (1999) 4619.
[5] R. T. Wang and G. J. Dick: IEEE Trans. Instrum. Meas. **48** (1999) 528.
[6] P. Wolf S. Bize, A. Clairon, A. N. Luiten, G. Santarelli and M. E. Tobar: Phys. Rev. Lett. **90** (2003) 060402.
[7] S.Yanagimachi, K. Watabe, K. Hagimoto, T. Ikegami and S. Ohshima: submitted to Proc. 20th European Frequency and Time Forum, 2006.
[8] S. Bize, P. Laurent, M. Abgrall, H. Marion, I. Maksimovic, L. Cacciapuoti, J. Grunert, C. Vian, F. Pereira dos Santos, P. Rosenbusch, P. Lemonde, G. Santarelli, P. Wolf, A. Clairon, A. Luiten M. Tobar and C. Salomon: C. R. Physique **5** (2004) 829.
[9] K. Watabe, J. G. Hartnett, G. Santarelli, S Yanagimachi, T. Ikegami and S. Ohshima: Jpn. J. Appl. Phys. **44** (2005) 3283.
[10] C. R. Locke, S. Munro, M. E. Tobar, E. I. Ivanov and G. Santarelli: Proc. 2003 IEEE Int. Frequency Control Symp. & PDA Exhib. Jointly with 17th European Frequency and Time Forum, 2003, p. 350.
[11] J. G. Hartnett, J. D. Anstie, M. E. Tobar and E. N. Ivanov: Proc. 2003 IEEE International Frequency Control Symposium & PDA Exhibition Jointly with the 17th European Frequency and Time Forum, 2003, p. 376.
[12] S. Chang, A. G. Mann, A. N. Luiten and D. G. Blair: Phys. Rev. Lett. **79** (1997) 2141.
[13] A. N. Luiten, A. G. Mann, M. E. Costa and D. G. Blair: IEEE Trans. Instrum. Meas. **44** (1995) 132.
[14] D. Chambon, S. Bize, M. Lours, F. Narbonneau, H. Marion, A. Clairon, G. Santarelli, A. Luiten and M. Tobar: Rev. Sci. Instrum. **76** (2005) 094704.
[15] M. E. Tobar, E. N. Ivanov, C. R. Locke, P. L. Stanwix, J. G. Hartnett, A. N. Luiten, R. B. Warrington, P. T. H. Fisk, M. A. Lawn, M. J. Wouters, S. Bize, G. Santarelli, P. Wolf, A. Clairon and P. Guillemot: Proc. 2005 Joint IEEE International Frequency Control Symposium and Precise Time & Time Interval (PTTI) Systems & Applications Meeting, 2005, p. 350.

Proceedings of the 20th EFTF, 2006

Simulation of a parametric quartz crystal oscillator by the symbolic harmonic method

N. Ratier,* M. Bruniaux, S. Galliou, and R. Brendel
Institut FEMTO–ST, département LPMO & LCEP, CNRS UMR 6174
32 avenue de l'Observatoire, F-25044 Besançon, France

The Symbolic Harmonic Analysis (SHA) method is a frequency domain approach for computing the steady state of ultra stable quartz crystal oscillators. First, we present a general method to convert a set of differential equations into a system of non-linear algebraic equations that can be solved for the periodic steady state solution. Then, we apply this method to simulate the behavior of a parametric quartz crystal oscillator currently being developed at FEMTO–ST/LCEP. This oscillator uses a 10 MHz quartz resonator and a 20 MHz signal derived from the oscillator nonlinearities is used to pump a varactor-diode. The quartz resonator time constant induces too long simulation time with classical integration methods. So that the symbolic harmonic analysis offers a good alternative to quickly obtain the periodic steady state. Simulation results are compared with experimental data.

I. INTRODUCTION

The work described in this paper presents the latest development of a simulation method to determine in real time the steady–state solution of ultra–stable crystal oscillators.

Usually the method used to simulate this kind of circuit is the so–called "harmonic–balance" method [1]. Roughly, this numerical method amounts to compute the behavior of the linear part of the circuit in the frequency domain and the nonlinear part in the time domain. The name stems from an approach based on current balancing between the linear and nonlinear parts.

In our method, by using symbolic calculation, the system of nonlinear differential equations describing the oscillator circuit is replaced by a system of nonlinear equations of Fourier coefficients whose solution is an approximation of the steady–state response of the circuit. The harmonic analysis method imposes the steady–state conditions through a Fourier expansion of the unknown functions. This method in which the simulation time no longer depends on the transient is used to develop a real time simulation tool for ultra–stable oscillator circuits.

The main drawback of symbolic methods lies in the fact that they usually involve a very large number of terms. The first part of the paper proposes a solution based on "tree parsing" to solve this problem, while the second part applies the method to simulate a parametric oscillator.

*Electronic address: nicolas.ratier@lpmo.edu

II. PRINCIPLE OF THE SYMBOLIC HARMONIC ANALYSIS METHOD

$P(T_0)$ denotes the set of all periodic functions of bounded variation with period T_0. The system of differential equations under consideration is of the form (Eq. 1) where $u \in P(T_0)$ is the stimulus waveform, x is the unknowns waveform to be found and f is continuous and real.

$$f(x, x', u) = 0 \tag{1}$$

If the solution x exists, is real, and belongs to $P(T_0)$, it can be written as a Fourier series (Eq. 2) where $\omega_0 = 2\pi/T_0$.

$$x(t) = X_0 + \sum_{k=1}^{\infty} X_k \cos(k\omega_0 t) + \sum_{k=1}^{\infty} X_{-k} \sin(k\omega_0 t) \tag{2}$$

Since $x \in P(T_0)$ and $u \in P(T_0)$ imply $x' \in P(T_0)$ and $f(x, x', u) \in P(T_0)$, by substituting x, its derivative and u into f, the resulting equation can be written under a Fourier series form (Eq. 3).

$$f(x, x', u) = F_0 + \sum_{k=1}^{\infty} F_k \cos(k\omega_0 t) + \sum_{k=1}^{\infty} F_{-k} \sin(k\omega_0 t) \tag{3}$$

By using the orthogonality of sinusoidal functions, (Eq. 3) can be rewritten as a system of nonlinear equations (Eq. 4), one for each harmonic defined by the assumed solution. Then the nonlinear system (4) can be solved numerically to obtain the Fourier coefficients X_k of the unknowns.

$$F_k(X_k) = 0 \text{ for all } k \in Z \tag{4}$$

Nevertheless, even by truncating the Fourier series, a direct application by symbolic calculation of the method described above to build the nonlinear system leads to an exponential growth of the number of terms.

The method proposed to overcome this difficulty is to rewrite each differential equation of the system as a binary tree so that each node involves only one algebraic operation. Then the trees are progressively reduced in harmonic (i.e. Fourier series) form from the bottom to the top: at each node new coefficients expressed in function of the previous ones are generated. Eventually, it remains only a Fourier series with manageable coefficients.

The mapping of differential equations into binary trees is defined by the following abstract syntax: the `UNKNOWN` terminals are elements of the unknown vector $x(t)$ and the `FUNCTION` terminals are either constants or functions already in harmonic form, as the stimulus waveform $u(t)$ does.

```
type odeTree =
       SUM   of odeTree * odeTree
     | PROD  of odeTree * odeTree
     | POWER of odeTree * INTEGER
     | DIFF  of odeTree
     | EXP   of odeTree
     | COS   of odeTree
     | SIN   of odeTree
     | UNK   of UNKNOWN
     | FCT   of FUNCTION
```

Because only `EXP`, `COS` and `SIN` functions of Fourier series can be expanded into Fourier series, the grammar accepts only these transcendental functions. Any other transcendental function (log, tan, ...), inverse of a function, and composite function are rejected. To fit all ODE to the given grammar, one proceeds by introducing an additional unknown to the equation system, which transforms the initial differential equation system into an algebro–differential system. This handling is trivial as shown in the following example.

$$\cdots + \tan V_1 + \cdots + \arccos V_2 + \cdots = 0 \qquad (5)$$

becomes

$$\cdots + H_1 + \cdots + H_2 + \cdots = 0 \qquad (6)$$

$$H_1 \cos V_1 = \sin V_1 \qquad (7)$$

$$\cos H_2 = V_2 \qquad (8)$$

The latter equations are now recognized by the grammar. The same method can be directly applied to the inverse of a function and to the composite functions.

III. EVALUATION OF `UNK`, `FCT`, `SUM`, `PROD`, `DIFF`, `EXP`, `COS`, `SIN` NODES

Once the tree of the differential equation is built, each node of the tree can be progressively reduced (or evaluated). Assuming that $V_1(t)$ is an unknown function of the differential system and R_1 is a parameter, the reduction is performed as follow:

- `UNK(V1(t))` is replaced by its Fourier series limited to N terms, i.e. it returns:

```
  A00V1
+ A01V1 cos  wt + B01V1 sin  wt
+ A02V1 cos 2wt + B02V1 sin 2wt
+ A03V1 cos 3wt + B03V1 sin 3wt
```

- `FCT(R1)` is already under the right form, so it is replaced by itself.

- `SUM(S1,S2)` with

```
S1 = A00S1 + A01S1 cos wt
           + B01S1 sin wt + ...
S2 = A00S2 + A01S2 cos wt
           + B01S2 sin wt + ...
```

  is reduced by generating new coefficients

```
TT1 = A00S1 + A00S2
TT2 = A01S1 + A01S2
TT3 = B01S1 + B01S2
... = ...
```

  and returns:

```
TT1 + TT2 cos wt + TT3 sin wt + ...
```

- `PROD(S1,S2)`, `DIFF(S1)` are reduced in the same way as `SUM(S1,S2)`, but with a bit more complex generated coefficients.

- The "harmonization" of `EXP(S1)`, `COS(S1)` and `SIN(S1)` functions is explained in [2]. The solution of this problem is quite similar to the harmonization of ODE. A binary tree is constructed and new coefficients are generated as a function of the previous ones during the tree parsing. Each transcendental function has a different associated tree.

IV. EVALUATION OF POWERS (`POWER`)

Given x and n, where x is a Fourier series and n is a positive integer, we study the problem of computing symbolically `POWER(x,n)`, or x^n, efficiently. Here, "multiplication" means multiplication of series. Although we are concerned with multiplication of powers of x, the problem can be reduced to addition, since the exponents are additive. This leads to the following abstract formulation:

An addition chain for the integer number n is a sequence of integers

$$a_0 = 1, a_1, a_2, \ldots, a_r = n \qquad (9)$$

with the property that, for all $i = 1, 2, \ldots, r$:

$$a_i = a_j + a_k, \text{for some} k \leqslant j < i \qquad (10)$$

This means that each exponentiation in the chain can be evaluated by multiplying two of the previous exponentiation results. The optimal way to compute x^n by multiplication is given by the addition chain for n having the smallest length r. The smallest length r for which an addition chain for n exists is denoted by $l(n)$.

Despite numerous work in this area, the determination of a minimal–length addition chain generating the desired exponent is still an open problem is mathematics. The weaker problem to compute $l(n)$ is neither solved. However, a lower and a upper bounds of $l(n)$ are known.

$$\lceil \log_2 n \rceil \leqslant l(n) \leqslant \lfloor \log_2 n \rfloor + \nu(n) - 1 \qquad (11)$$

where $\lceil \log_2 n \rceil$ is the ceiling of x (smallest integer greater than or equal to x), $\lfloor \log_2 n \rfloor$ is the floor of x (greatest integer less than or equal to x) and $\nu(n)$ is the number of 1's in the binary representation of n.

Our SHA program use the following recursive algorithm to compute x^n for a Fourier series x and a positive integer n. This algorithm is known as the square–and–multiply algorithm [3]. The repeated application of this algorithm amounts to decompose the exponent into a sequence of squares and products. It requires only one temporary storage x (and of course the current partial result).

$$\text{Power}(x,n) = \begin{cases} x, & \text{if } n = 1 \\ \text{Power}(x^2, n/2), & \text{if } n \text{ is even} \\ x \times \text{Power}(x^2, (n-1)/2), & \text{if } n \text{ is odd} \end{cases} \qquad (12)$$

The square–and–multiply algorithm is used for two main reasons:

1. Although, it doesn't lead to an optimal addition chain, it is quite efficient. Compared to the ordinary method of multiplying x with itself $n-1$ times, this algorithm uses only $O(\log_2 n)$ multiplications. (The number of multiplications required to compute $x^n$by the square–and–multiply algorithm is exactly $\lfloor \log_2 n \rfloor + \nu(n) - 1$).

2. Unlike optimal addition chains, the addition chains computed by the square–and–multiply algorithm have always a binary tree structure. So the computation of x^n by this algorithm is naturally integrated into the SHA method as it is based on binary trees representation.

For example, table I shows the application of the square–and–multiply algorithm on x^9 and x^{10}. The second column follows the application of the algorithm giving the addition chains in reverse order, and the third column gives the algebraic equivalent.

The computation of x^9 and x^{10} are represented by the following binary trees (Fig. 1). It should be noted that each power of x has a different binary tree and two closed powers, for example x^n and x^{n+1}, don't have closed binary trees at all. The trees are reduced as explains in the previous section.

Power	Algorithm	Algebraic
x^9	$9, 8, 4, 2, 1$	$((x^2)^2)^2 x$
x^{10}	$10, 5, 4, 2, 1$	$((x^2)^2 x)^2$

TABLE I: Computation of x^9 and x^{10}

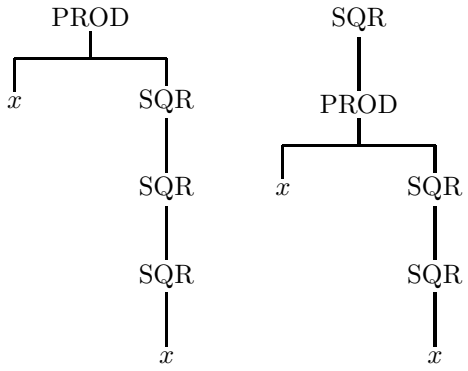

FIG. 1: Binary tree of x^9 and x^{10}

Table II illustrates the efficiency of the square–and–multiply algorithm to compute x^n. $l(n)$ is the minimal number of multiplications. For large n, the lower and upper bounds and computed by inequality (Eq. 11). $l^\star(n)$ is the number of multiplications required by the square–and–multiply algorithm. Results have to be compared to the ordinary method of powering which needs $n-1$ multiplications.

n	$l(n)$	$l^\star(n)$
10	4	4
100	8	8
1000	$10 \leqslant l(n) \leqslant 14$	14
10000	$14 \leqslant l(n) \leqslant 17$	17
100000	$17 \leqslant l(n) \leqslant 21$	21
1000000	$20 \leqslant l(n) \leqslant 25$	25
10000000	$24 \leqslant l(n) \leqslant 30$	30
100000000	$27 \leqslant l(n) \leqslant 37$	37
1000000000	$30 \leqslant l(n) \leqslant 41$	41

TABLE II: Efficiency of the square–and–multiply algorithm

V. APPLICATION: PARAMETRIC OSCILLATOR

The symbolic harmonic method is applied to analyze the forced–mode behavior of the parametric quartz oscillator (PXO) shown in Fig. 2. The principle of this oscillator developed at FEMTO–ST/LCEP is described in [4]. It uses a 10MHz quartz and a 20MHz pump U_{pmp} coming from the second harmonic at 20 MHz generated by a varactor-diode. For instance the parameters of the oscillator are $R_1 = 100\Omega$,

$$U_b + U_{\rm vd}(t) + R_2\frac{d}{dt}(C_{\rm vd}(t).U_{\rm vd}(t)) + L.\frac{d^2}{dt^2}(C_{\rm vd}(t).U_{\rm vd}(t)) = \quad (13)$$
$$-R_1\frac{d}{dt}(C_{\rm vd}(t).U_{\rm vd}(t)) - R_1C_q\frac{d}{dt}U_q(t) + V_p\sin(2\omega_q t)$$

$$U_q(t) + R_qC_q\frac{d}{dt}U_q(t) + L_qC_q\frac{d^2}{dt^2}U_q(t) = \quad (14)$$
$$-R_1\frac{d}{dt}(C_{\rm vd}(t).U_{\rm vd}(t)) - R_1C_q\frac{d}{dt}U_q(t) + V_p\sin(2\omega_q t)$$

$$C_{\rm vd}(t).H(t) = C_{0\,\rm vd} \quad (15)$$

$$1 + \frac{U_{\rm vd}(t)}{\phi_0} = H^2(t) \quad (16)$$

$R_2 = 300\Omega$, $U_b = -1V$, $U_{\rm pmp} = 4.5V$, and L is tuned at 10MHz with the varactor–diode capacitance value. The resonator is a 10MHz SC cut quartz crystal, exhibiting a unloaded quality factor of about 1 10^6.

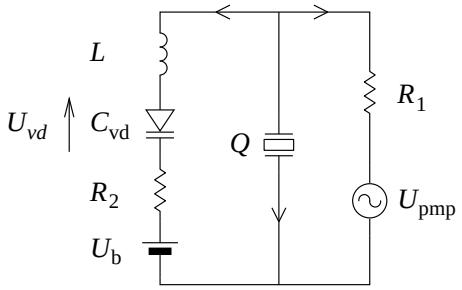

FIG. 2: Quartz crystal Parametric oscillator

The voltage–capacitance relationship of a varactor–diode is written [5] as Eq. (17), where $C_{\rm vd\,0}$ is the diode capacitance at $U_{\rm vd} = 0$ (typically a few tens of picofarad), ϕ_0 is the contact potential, and γ is the fractional change in capacitance ($\gamma = -1/2$ for abrupt junction, and $\gamma = -1/3$ for graded–junction varactors).

$$C_{\rm vd} = C_{0\,\rm vd}\left(1 + \frac{U_{\rm vd}}{\phi_0}\right)^{\gamma} \quad (17)$$

The circuit is described by the system of ordinary differential equations (Eq. 13) to (Eq. 16). The "harmonization" of Eq. 17 is done by introducing an additional unknown function $H(t)$. The equation of the varactor diode, for $\gamma = -1/2$ is then replaced by the two Eq. 15 and 16.

The unknowns of the system are the voltages across the varactor $U_{\rm cd}(t)$ and the quartz series capacitance $U_q(t)$, the capacitance $C_{\rm vd}(t)$ and the additional function $H(t)$. $H(t)$ doesn't have any physical meaning. The previous ODE system is then solved by SHA method by replacing all unknowns by Fourier series, building and reducing ODE trees. The resulting equations involving Fourier coefficients of the unknowns are then solved numerically. The varactor voltage $U_{\rm vd}$ versus time in plotted in Fig. 3.

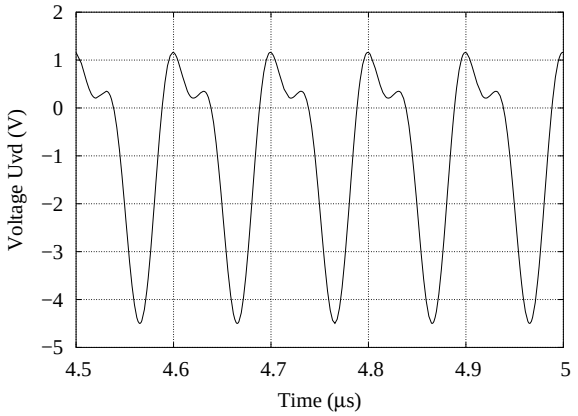

FIG. 3: SHA Simulation of the varactor–diode voltage $U_{\rm vd}$ versus time.

Fig. 4 shows experimental results performed in forced mode [6]. Theoretical results are in good agreement with experimental ones, although theoretical improvements still have to be done. The simulated curve plotted in Fig. 3 is computed in a few seconds. Numerical computation of the system (Eq. 13 to Eq. 16) done by usual techniques [6] need a few hours and give results not as good as the SHA method.

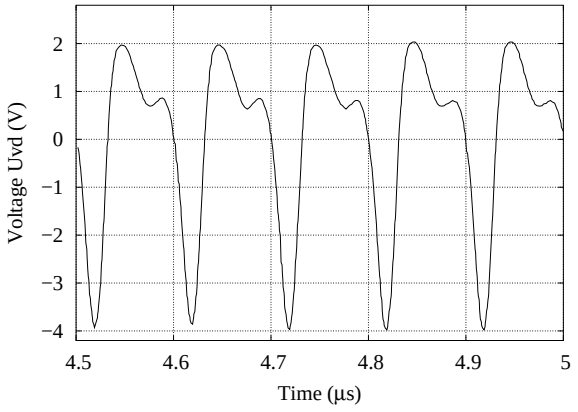

FIG. 4: Experimental varactor–diode voltage $U_{\rm vd}$ versus time.

VI. CONCLUSIONS

The principle of a symbolic–numeric method to analyze ultra–stable oscillators, presented in this paper and [2], allows one to replace a system of nonlinear differential equations by a system of nonlinear equations of Fourier coefficients, whose solution is an approximation of the steady–state solution. The method has been successfully applied to simulate a parametric oscillator.

A solution based on trees to manage the large number of coefficients inherent to symbolic computation has been proposed. At the opposite of all other harmonic methods, the linear and the nonlinear parts of the differential equation are processed in an uniform way in the Fourier domain.

Using symbolic computation technique is not common in the electronics circuit community, and in the time–frequency domain, whereas it proved its ability to solve quickly and efficiently the difficult problem of the simulation of quartz crystal oscillators. The gain in terms of computing time is in the order of decades for usual oscillator circuits.

The calculation times to solved the equations generated in the last step of the method is independent on the length of transients, because the symbolic harmonic method imposes the steady–state conditions by virtue of Fourier expansion of the unknowns.

No mention has been made about how to solve the system of nonlinear equations generated in the last step of the symbolic harmonic method. The resulting system is highly nonlinear and sparse. Efforts are currently made to develop specific and efficient numerical algorithms in this direction.

[1] K. S. Kundert, J. K. White, and A. Sangiovanni-Vincentelli, *Steady–State Methods for Simulating Analog and Microwave Circuits* (Kluwer Academic Publishers, 2003).

[2] N. Ratier, M. Bruniaux, S. Galliou, and R. Brendel, in *Proc. of the 19th European Frequency and Time Forum (EFTF)* (Besançon, France, March 2005), pp. 413–418.

[3] D. E. Knuth, *The art of computer programming, Vol II. Seminumerical algorithms* (Addison–Wesley, 1998), ISBN 0-201-89684-2.

[4] V. Komine, S. Galliou, and A. Makarov, IEEE Trans. Ultrason., Ferroelect., Freq. Contr. **50**, 1656 (2003).

[5] L. Blackwell and K. Kotzebue, *Semiconductor Diode Parametric Amplifiers* (Englewood Cliffs, N.J, Prentice–Hall, 1961).

[6] S. Galliou, R. Brendel, N. Ratier, M. Bruniaux, P. Abbe, and G. Cibiel, in *Proc. of the 19th European Frequency and Time Forum (EFTF)* (Besançon, France, March 2005), pp. 408–412.

Proceedings of the 20th EFTF, 2006

Experiments with a commercial multivibrator as a detector for high impedance patterns

J. A. PARTANEN[1], J. VOUTILAINEN[1,2], P. ESKELINEN[2]
[1] *Voyantic Ltd.*
Tekniikantie 21; FI-02150 Espoo; FINLAND
[2] *Helsinki University of Technology, Applied Electronics Laboratory, Finland*
Contact Email: juho.partanen@voyantic.com

Certain industrial detectors call for robust, low-cost varying oscillators in the MHz range. In our application, high impedance patterns in the frequency domain are detected by sensing a small capacitance change related to the pattern passing a detection plane. Various commercial building blocks are readily available e.g. in CMOS IC chip form. We have studied the applicability of some typical products such as TC74HC4060, however, in most cases the obtained dynamic range in frequency domain has been inadequate for our purposes.

A compact solution is the HEF4047B type multivibrator from the LOCMOS HE4000B family. A sensitive astable multivibrator circuit with a base frequency of 2.4 MHz has been constructed. By utilizing a simple counter, sensitivity in the range of 500 kHz/pF has been achieved. The response time far exceeds the requirements of this application. The sensor function is based on variable capacitance and therefore all stray sources must be carefully controlled. This has been accomplished through a dedicated printed circuit board layout. A buffer circuit is mandatory in the oscillator output not only to reduce the load pulling effects but also to provide convenient output levels.

1. INTRODUCTION

The adoption of radio frequency identification technology, later RFID, in item level tracking has been slow due to the relative high cost of RFID transponders. For the recent years this cost factor has been dominating the industry and has resulted in the emergence of certain printable RFID solutions. If the transponder could be assembled as a by-product during the existing processes of the packing industry, the cost could shrink down to fractions of a cent.

Capacitive coupling is a well understood phenomenon and it is used in a variety of applications. Meyer [1] reported an integrated capacitive position sensor already ten years ago. Some of the recent work includes pointing device that is based on capacitive coupling [2]. In the meantime, a similar technique has been widely used to sense the level of liquids, even in a restaurant application [3].

In this paper, a novel identification system is presented. The system is composed of conductive patterns on the surface of the package substrate and a handheld reading device that senses the patterns via capacitive coupling. The resulting system stores 96 bits in the area of 10*100 mm. This capacity suggests that the system can be used to produce an Electronic Product Code[1], later EPC [4].

[1] EPC is a trademark of EPCglobal

II. MATERIALS AND METHODS

The data is stored as a geometrical pattern as illustrated in Figure 1. The pattern is applied to the inner layer of a package making it undetectable from outside the package. Carbon ink, metals or certain polymer, polyaniline, is used to obtain electric conductivity for the pattern. Polyaniline has traditionally been used for electromagnetic interference shielding and microwave absorption [5] [6].

Figure 1: 96 bits stored in a geometrical pattern. The dimensions of the pattern are 10 mm (H) and 100 mm (W). This pattern is produced with carbon ink to obtain electrical conductivity.

To produce two bits per period, the pattern has four different heights: 1.25 mm, 2.5 mm, 5.0 mm and 10.0 mm. This choice of geometrical dimensions slightly emphasizes the difference between the two highest peaks making the pattern easier to interpret.

The resulting high impedance pattern is detected by sweeping the package with a reading device (Figure 2). As the pattern passes the detection planes, a resulting change in the capacitance is detected. The detection

circuit diagram is illustrated in Figure 3. The change in capacitance is transformed by a commercial multivibrator HEF4047B into a change of frequency as a function of time. This measurement data is further processed with a 16-bit counter of an ATMega88 microcontroller and transferred to a PC via USB interface. LabVIEW-software is then used to obtain the data stream that is stored in the pattern.

Figure 2: The reading device slides over the pattern that is hidden inside the box

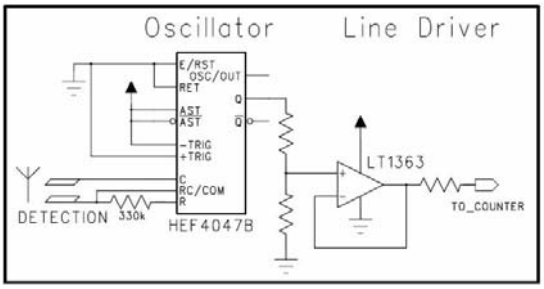

Figure 3: The diagram of the detection circuit. 'Detection' denotes the capacitive detection planes. A line driver in front of the counter is needed to reduce the load pulling effect. Bypass capacitors and other peripheral circuits are left out from the picture for clarity.

As we are sensing relatively small changes in capacitance in the range of 0.5...2.5pF, all stray sources must be carefully controlled. It is especially important to minimize the sources that change over time, such as the position of the operator's fingers as an example. This has been achieved through certain mechanical structures and careful circuit layout as illustrated in Figure 4. The length of all traces is minimized until the measurement signal has passed the line driver (LT1363). Ground planes are not allowed under the signal traces. The 330 kOhm resistor, that sets the base frequency to 2.4 MHz, is located directly under the pads of the detection plane.

The multivibrator circuit has a single supply of 10.0 V that is made with a switched-capacitor voltage converter. The measurement signal level is scaled down to 3.0 Vpp to suit the counter input of the microcontroller.

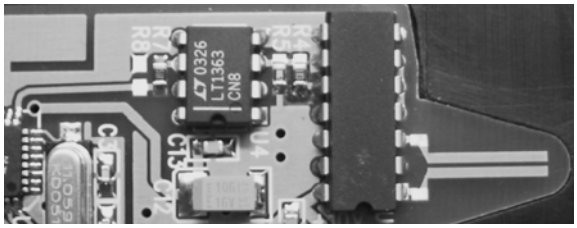

Figure 4: The lay-out of the analog electronics. The capacitive detection planes are connected to the multivibrator HEF4047B on the right and the buffer is in the center of the picture. The counter is in the far left corner of the picture. The length of the traces is minimized to control the sources of stray capacitance.

III. RESULTS

The obtained measurement signal from a single sweep is processed in three steps. The pattern is formed with carbon ink and the reading is performed through one layer of carton. The unprocessed 'rough' data is illustrated in Figure 5. The dynamic range of the data sequence is approximately 300 kHz.

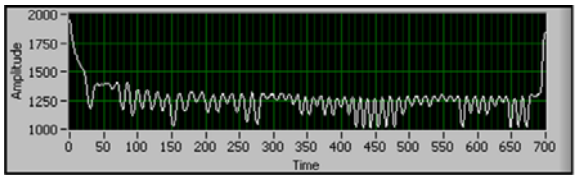

Figure 5: 'Rough' data that is transferred to a PC. The Y-axis represents the frequency (kHz) and X-axis the time (ms). The first clear peak downwards denotes the start signal. The data pattern results in a dynamic range of 300 kHz.

After some signal processing done in LabVIEW, the measurement signal that will be interpreted to data is illustrated in Figure 6.

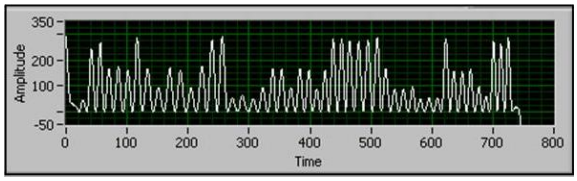

Figure 6: The change in frequency (kHz) as a function of time (ms).

To acquire the data, the decision levels have to be dynamically defined. Depending on the number of bits per period, there might be numerous decision levels. In this system, however, only four levels are needed (Figure 7).

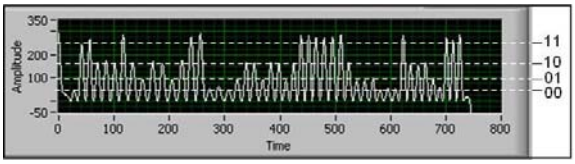

Figure 7: The data with the decision levels for 96-bit interpretation.

Figure 8: The original pattern without the start mark is repeated here for convenience.

The resulting sensitivity of the system is in the area of 500 kHz/pF.

IV. DISCUSSION

The correlation between the original pattern (Figure 8) and the measurement result (Figure 7) is almost perfect. The non-constant velocity of the sweep performed by the operator does cause some displacement of the peaks in comparison to the original pattern, but that does not result in any difficulties while interpreting the signal. However, if the velocity would temporarily drop to zero, it would obviously result in an error. As can also be noted, the wide patterns can be easily spotted as the high peaks in the signal. However, the lower peaks are more difficult to classify into three different categories, especially the two smallest ones could be hard to distinguish.

As the industrial applications ultimately call for the highest possible reading reliability, we will next discuss future improvement possibilities. The geometries should be adjusted so that the second and third levels would be slightly larger. A suitable scale might be 1.0 mm, 3.5mm, 6.0 mm and 10.0 mm. Furthermore, the current system does not support codes that have one or more peak levels totally missing. This, however, could be corrected by using certain coding methods.

The geometry of the detection planes is not optimized. It is probable that by slightly decreasing the distance of the planar detection planes from each other, the change of capacitance as the pattern passes over the plane would be increased. One should however make sure that the direct coupling between the planes will not develop to be the dominant capacitive component.

The sensitivity of the multivibrator could possibly be improved by tuning the value of the parallel resistor. We could also try to cancel the influence of the stray sources by organizing the capacitive detection in a different manner. Some ideas can be found from the work of Huang *et al.* [7]. The double differential operating principle [8] is another prominent option.

There are naturally plenty of alternatives for the oscillator circuit HEF4047B. Already we have tested the TC74HC4060 crystal oscillator but we found it not to be suitable for this purpose, because the sensitivity of the oscillation frequency was not high enough. Additionally we tried using a universal capacitive readout IC MS3110 from Irvine Sensors, but programming the circuit turned out to be unreliable, and the specifications did not hold up.

The fundamental problem in measuring the change of in capacitance is the limitation concerning the reading distance. If the surface of the box is rough or if the operator's hand trembles, the resulting error in the measurement signal cause the pattern to be falsely interpreted. The orientation of the reading device is also critical, and the issue has been taken into consideration during the mechanical design of the prototype. The upside of the limited reading range is that the detection process is well under control. For example, the disturbing effect of additional conductive planes, such as metallic blisters in typical pharmaceutical packages, is not a dominating problem in this system.

There are always ways to improve the instrumentation but as for now the sensitivity was graded high enough. The 96-bit capacity is compliant with the EPC tag data standards [4] and thus the proposed system is ready for piloting.

V. CONCLUSIONS

In this paper, a novel identification and brand protection system has been presented. The achieved sensitivity makes it possible to use inks that have relatively low conductivity, such as ones including polyaniline.

The system can be applied to RFID applications. It is especially suitable for brand protection purposes in the luxury product segment and for verifying the product authenticity in pharmaceutical application. The underlying benefit of the system is that it is very cost-efficient since the identification patterns can be applied to the packages during the existing processes of the packaging industry.

Acknowledgements

The authors would like to thank Tuomas Mustonen, M-real Corporation, for the freedom of operation that he allowed us and for the financial support as well. Additional contribution and fluent co-operation was received especially from Kirsti Ruutu, Panipol Ltd, and Kirsi Immonen, VTT Processes.

REFERENCES

[1] H. U. Meyer, *An Integrated Capacitive Position Sensor,* IEEE Trans. on Instrum. Meas, VOL. 45, NO.2, 1996

[2] E. C Tan, A. Wahab, K. M. Low, *Application of Capacitive Coupling to the Design of an Absolute-Coordinate Pointing Device*, IEEE Trans. on Instrum. Meas, VOL. 54, NO. 5, 2005

[3] P. H. Dietz, D. Leigh, W. S. Yerazunis, *Wireless Liquid Level Sensing for Restaurant Applications*, Mitsubishi El. Infor. Tech. Center, Cambridge, 2002

[4] *EPC Tag Data Standards Version 1.1 Rev.1.24*, EPCglobal, 2004

[5] C.Y. Lee *et al*, *Electromagnetic Interference Shielding Efficiency of Polyaniline Mixtures and Multilayer Films,* Synthetic Metals 102, 1999

[6] P. Chandrasekhar, K. Naishadham, *Broadband Microwave Absorption and Shielding Properties of Poly(aniline)*, Synthetic Metals 105, 1999

[7] S.M. Huang, R.G. Green, A. Plaskowski, M.S. Beck, *A High-Frequency Stray-Immune Capacitance Transducer Based on the Charge Transfer Principle*, IEEE Trans. on Instrum. Meas, VOL. 37, NO. 3, 1988

[8] D.M.G. Preethichandra, K. Shida, *A Simple Interface Circuit to Measure Very Small Capacitance Changes in Capacitive Sensors*, IEEE Trans. on Instrum. Meas, VOL. 50, NO. 6, 2001

Proceedings of the 20th EFTF, 2006

Low drive level sensitivity (DLS) of quartz crystal resonators

M. Addouche[1], R. Brendel[1], E. Rubiola[1], G. Cibiel[2]
[1] *FEMTO–ST – Laboratoire de Physique et Métrologie des Oscillateurs*
32*, avenue de l'Observatoire* – F25044 *Besançon cedex – France*
[2] *Centre National d'Études Spatiales*
18*, Avenue E. Belin* – F31055 *Toulouse Cedex – France*
Contact email address: brendel@lpmo.edu

Abstract: This work is a contribution to a better understanding of the DLS mechanism. The paper describes an experimental set-up allowing resonator's motional parameter measurements with variable drive level as low as – 100 dBm in a controlled temperature enclosure. As the drive level becomes very low, measurement becomes more and more noisy and difficult to exploit. Specific experimental procedures and data processing required to improve the signal-to-noise ratio are described. Resistance vs. drive level curve of several crystals exhibiting DLS reveal different behaviours that have been investigated. Phase noise measurement of resonators exhibiting DLS by using a high performance interferometric instrument developed in our lab are currently being performed at the idea of answering the question of the correlation between the two phenomena. Eventually, by using a submicron resolution scanning electron microscope, a number of surface defects have been observed on the surface of the resonators exhibiting DLS. The responsibility of these defects for the DLS is discussed.

1. INTRODUCTION

Drive Level Dependency (DLD) or Drive Level Sensitivity (DLS) of quartz resonators, i.e. the increase of the resonator's series resistance at low drive level is known for about fifty years [2, 3, 4, 12, 16, 20]. Very early, that phenomenon has been attributed to surface defects coming from microscopic scraps of various origin often associated with a sticky surface coating or surface scratches. A lot of work and experiments have been done and many models have been described to explain the DLS mechanism and to correlate the resistance increase with the surface defects [8, 9, 10, 11, 13, 14]. Attempts also have been made at relating the DLS with the noise of the resonator with contradictory conclusions [1, 6]. On the other hand, the need for resonators of higher and higher performance in the domain of telecommunication and/or space localization encourages to further investigate on this phenomenon. The reader can refer to [5] for a more complete bibliography on the DLS.

II. DESCRIPTION OF THE DLS

A large number of experiments carried on for decades have led to the following observations:

- Increase of the series resistance is always associated with a positive or negative frequency shift,
- The DLS "signature" strongly depends on temperature,
- The DLS behaviour can be modified or suppressed permanently or temporarily by overdriving the resonator, by polishing, etching or cleaning the crystal. Cleaning is often considered the most efficient [7, 13],
- The most disconcerting aspect of this phenomenon is its lack of reproducibility. Crystals seemingly identical may be drive sensitive or not, and DLS of crystals apparently cured may reappear after a long time of inactivity.

A lot of work and efforts have been put into understanding the origin of the phenomenon, and very early the attention has been focused on the surface imperfections as a possible cause of DLS. Among the most often reported defects one can cite:

- Particles of metal, quartz, or abrasive,
- Thin coat of resin or oil,
- Surface scratches,
- Flaking of quartz surface or metal electrode,
- Poorly adhesive electrodes or blisters,
- Surface stress.

Various experiments have proved the relationship of cause and effect between the surface pollution and DLS. For example, talc blown in the vicinity of an unsealed quartz resonator may induce DLS [4]. Another interesting and dramatic demonstration of the correlation between surface contamination and DLS has been reported a few years ago [6]: a 100 MHz 5th overtone AT-cut crystal resonator exhibiting no noticeable DLS has been opened and the surface has been sprinkled with alumina particles, after the resonator has been resealed, it presented an important DLS, and once the resonator has been reopened, cleaned

and resealed, it approximately recovered its original state (Fig. 1). It should be noted first that a single particle not bound to the surface, cannot induce the observed phenomenon.

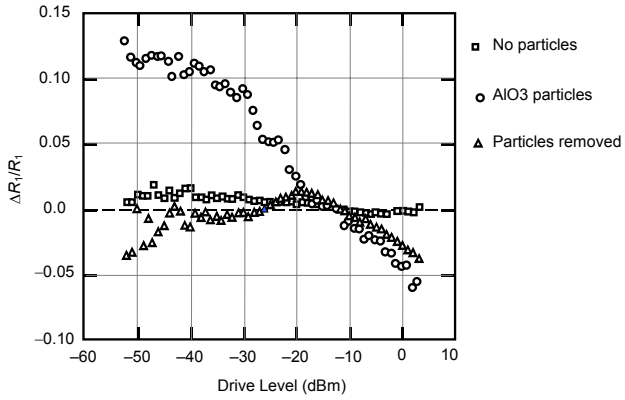

Figure 1: *Effect of a surface contamination* [6].

Similarly, a particle tightly bound to the surface acts as a loading mass and thus induces a negative frequency shift, which is often refuted by experiments. So, the observed phenomenon can be explained only if the particle is bound to the surface by an elastic force that can be due to a thin sticky coating of oil or resin, or any other attractive force such as Van der Waals, electrostatic, or capillarity forces for example. In this case, as the surface moves back and forth under the shear motion, the bounded particle acts as a small oscillating system that absorbs a part of the vibrating energy. Although this simple coupling system does explain that the resonant frequency can either decrease or increase, it doesn't account for the drive level sensitivity of the damping term that should be explained only if some non-linear mechanism is involved. Dworsky [8] has proposed a model assuming that the particles trapped in some surface imperfections experience inelastic collisions with scratch walls, thus inducing the required non-linear damping term.

III. EXPERIMENTAL SET-UP

Some preliminary experiments have been performed by using an Agilent 4395A Network-Spectrum-Impedance Analyser and the 43961A Impedance Kit [23]. The accuracy of the measurements has been improved by using a precision oven keeping the crystal at its turnover point as shown in Fig. 2. In addition, to comply with the standard motional parameter measurement technique, the experimental set-up has been modified as shown in Fig. 3 that implements the popular pi-network IEC–444 [15, 22]. A problem with our arrangement is that the network analyser is no longer able to extract the motional parameters, as it would do in normal conditions, and the measurements becomes more and more doubtful as the drive level decreases. So, the measurement relies only on amplitude and phase of the transfer function and on our own algorithms.

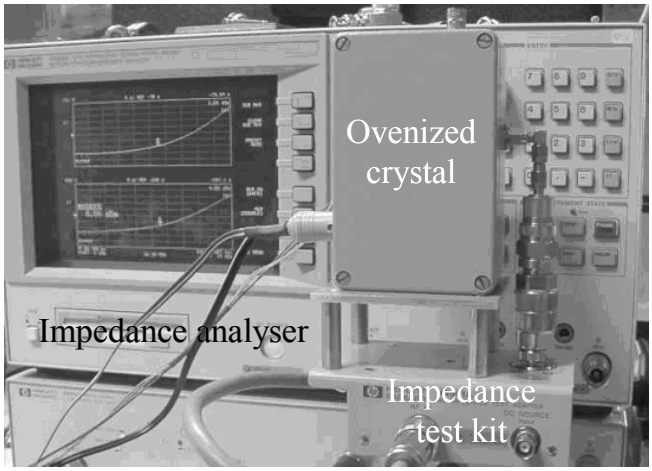

Figure 2: *Experimental set-up*.

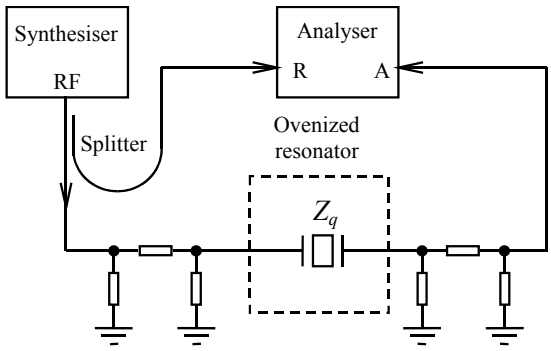

Figure 3: *Set-up using pi-network IEC–444*.

IV. DATA PROCESSING

Let first recall that in the Nyquist plane, the admittance of a resonator represented by its classical Butterworth - Van Dyke equivalent circuit shown in Fig. 4 follows approximately a circle whose diameter is the inverse of the series resistance R_q and the centre coordinates are $(\frac{1}{2R_q}, \omega_q C_p)$ where ω_q is the series resonant frequency and C_p the parallel capacitance (Fig. 5).

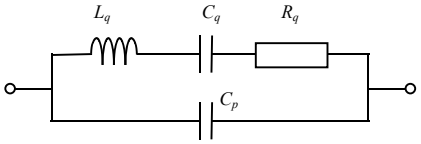

Figure 4: *Butterworth – Van Dyke equivalent circuit.*

The algorithm used to extract the motional parameters as well as their uncertainty from the experimental data is inspired by the method proposed by R. J. Williamson [19]. Given N measures of the real and imaginary parts (x_i, y_i) of the admittance, at frequencies f_i equally spaced

over a span Δf around the resonance, our problem is to calculate the centre coordinate (x_0, y_0) and the radius r_0 of the fitting circle (Fig. 6).

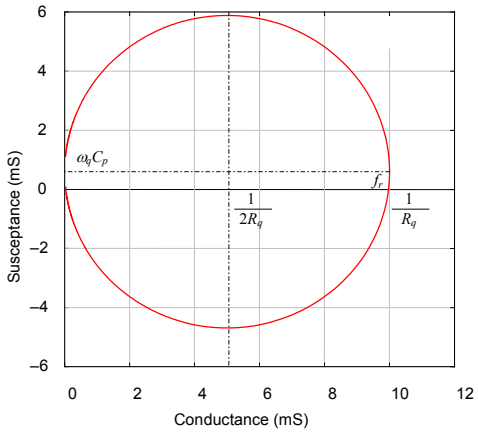

Figure 5: *Resonator admittance circle.*

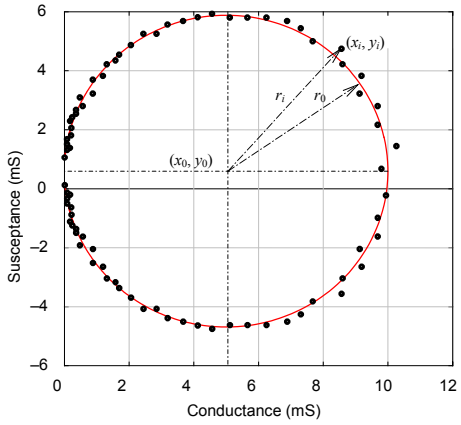

Figure 6: *Least squares fitting.*

Among several possible criteria to measure the closeness between the experimental data and the rebuilt circle, the best result has been obtained by using a norm defined as the difference between the squares of the experimental radius r_i and the expected radius r_0:

$$\varepsilon(x_i, y_i, x_0, y_0, r_0) = r_i^2 - r_0^2 = (x_i - x_0)^2 + (y_i - y_0)^2 - r_0^2$$

A cost function is then defined as the quadratic sum of the norms associated with each one of the N experimental data:

$$E(x_0, y_0, r_0) = \sum_{i=1}^{N} [\varepsilon(x_i, y_i, x_0, y_0, r_0)]^2$$

The unknown centre coordinates (x_0, y_0) and the radius r_0 of the expected circle are eventually calculated by a least square method that amounts to solve the following set of three partial derivative equations:

$$\begin{cases} \dfrac{\partial E(x_0, y_0, r_0)}{\partial x_0} = 0 \\ \dfrac{\partial E(x_0, y_0, r_0)}{\partial y_0} = 0 \\ \dfrac{\partial E(x_0, y_0, r_0)}{\partial r_0} = 0 \end{cases}$$

$$r_0 > 0$$

Usually, 401 data points equally spaced over a span of ± 250 Hz on either side of the resonant frequency have been used in the experiments presented in the next section. Fig. 7 shows the experimental data obtained with a –70 dBm drive level and the fitting circles calculated by the analyser internal algorithm and by the least squares method described above. An estimation of the uncertainty δ in the radius determination can be obtained by calculating the average difference between the experimental radii r_i^2 and the calculated radius r_0^2:

$$\delta = \frac{1}{N} \sum_{i=1}^{N} \frac{r_i^2 - r_0^2}{r_0^2} = \frac{E(x_0, y_0, r_0)}{N r_0^2}$$

In all experiments performed: $\delta < 1$ %.

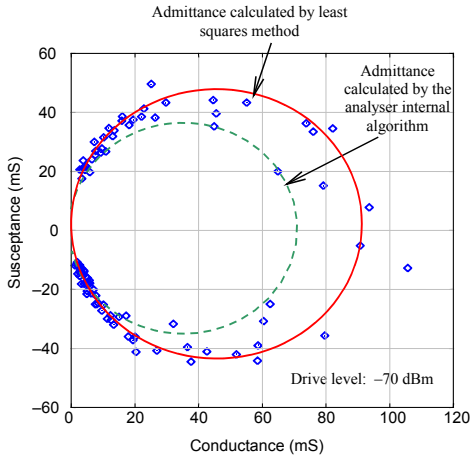

Figure 7: *Internal algorithm and least squares fitting.*

V. DLS MEASUREMENTS

We have measured a set of 11 resonators of frequency about 13 MHz AT-cut fundamental among which some pieces exhibited a strong DLS. The average series resistance of the group has been found to be about 10–20 Ω. This set has been mainly used to validate the correctness of data processing. Due to the resistance bridges of the pi-network, the drive level range was approximately –60 dBm to 0 dBm.

Fig. 8 shows a general picture of the series resistance vs. drive level of the group where it is obvious that parts #1, 3, 12, and 14 have a strong DLS, parts #5, 6, and 8 have a less marked defect, while parts #2, 4, 7, and 20 have no perceptible DLS.

To assess the reliability of the measurement procedure and data processing, five frequency sweeps are performed for each value of the drive level, Fig. 9 shows a pretty good reproducibility of the different sweeps.

As outlined in Sec. II and quoted in the literature [9, 10, 11], the resonator series resistance is not the only parameter affected by the DLS. From the admittance measurements, it is possible to obtain the resonant frequency f_r as the intersection of the admittance circle with the real axis (Fig. 5) and to plot this parameter vs. drive level as shown in Figs. 10 to 12. It can be observed in theses figures that the resistance change is always associated with an important frequency shift. Correlation between these two parameters can be evidenced by plotting the resistance change against the resonant frequency change.

For resonators having no DLS this representation would reduce to a single point since the two parameters do not depend on the drive level, for resonators having a marked DLS, the representation in the plane (*resistance* vs. *frequency*) forms more or less interlaced cycles that reveal a high degree of correlation as shown in Figs. 10 to 12.

After the first set of measurements, the resonators under test have been left fifteen days at rest and measured again. The curves obtained (in dotted line in Figs. 10 to 12) show that some parts seem cured, while other ones still have a DLS with a different location.

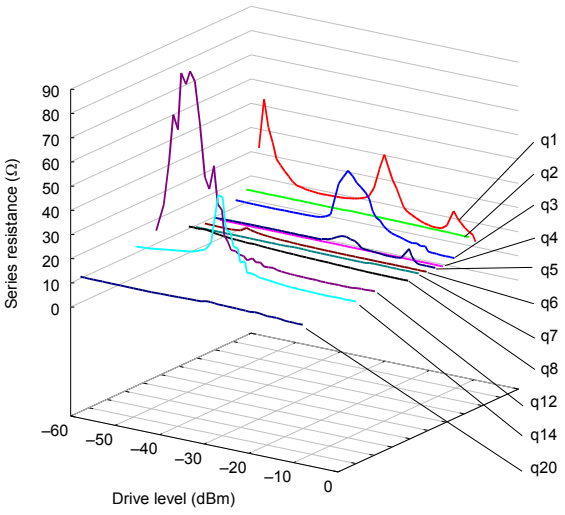

Figure 8: *Series resistance of a set of 11 resonators.*

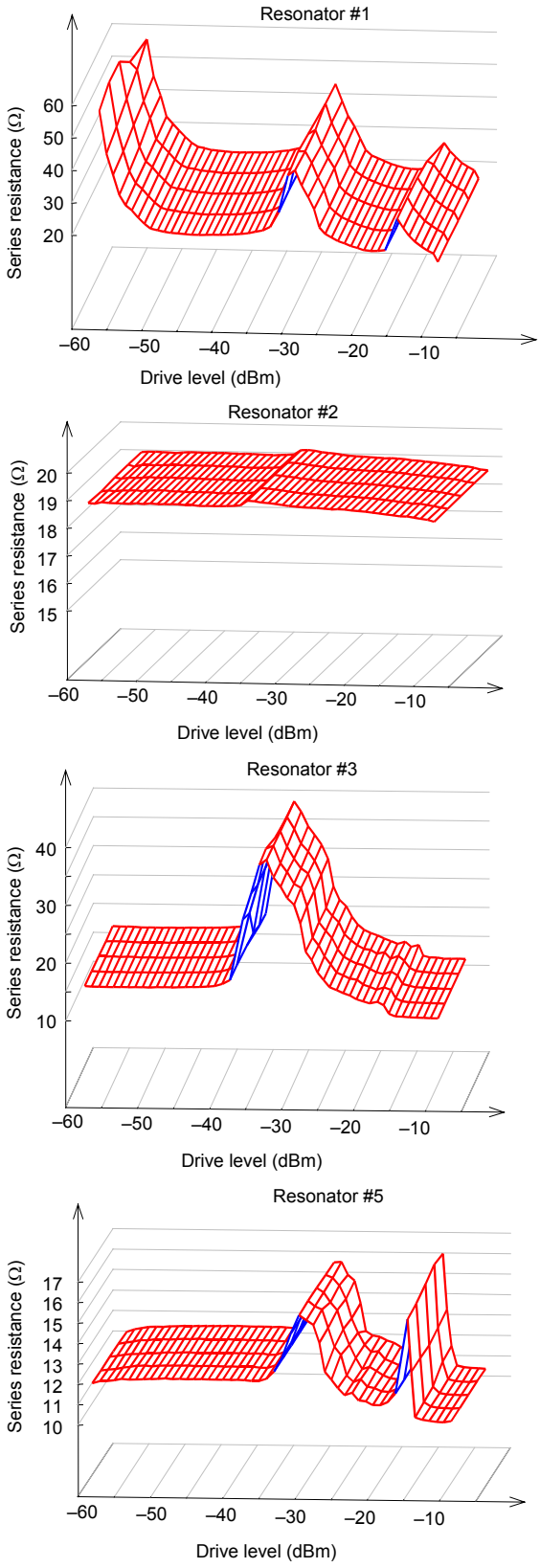

Figure 9: *Series resistance of some resonators.*

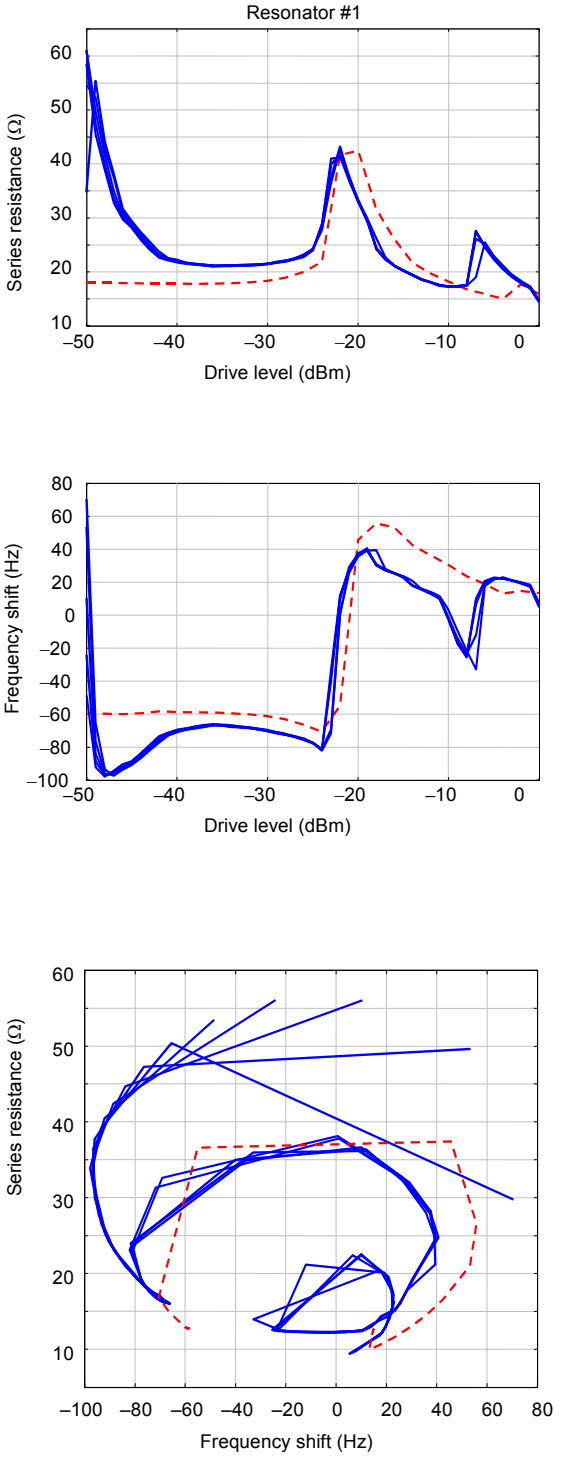

Figure 10: *Series resistance and resonant frequency of some resonators.*

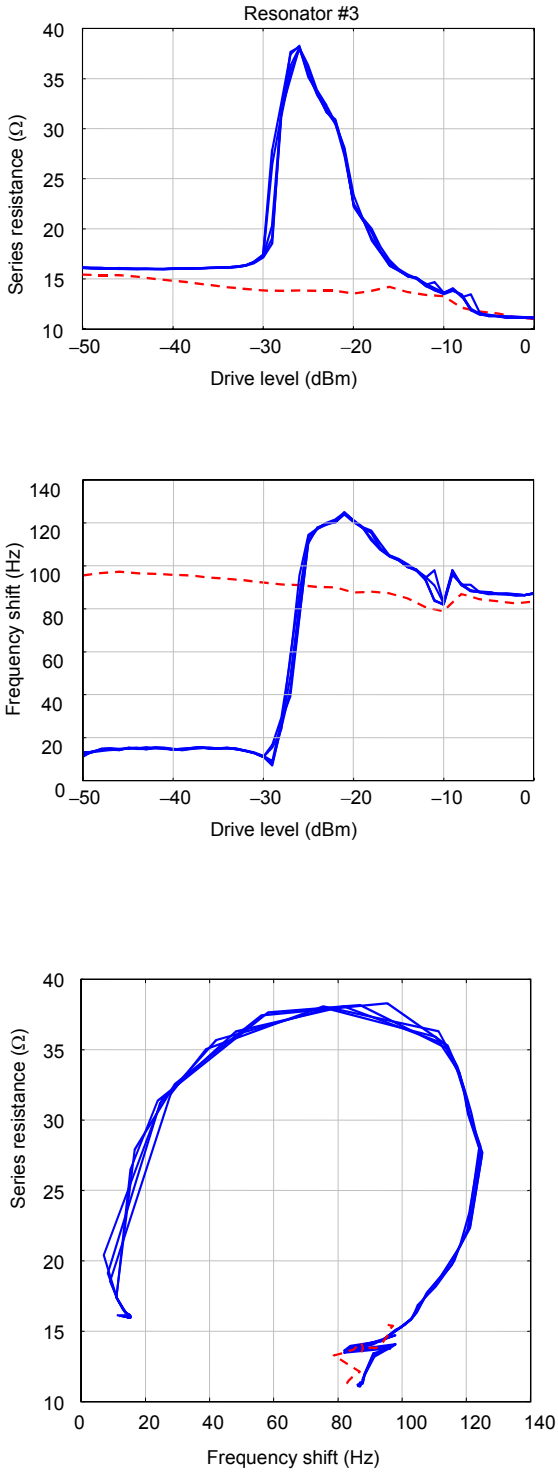

Figure 11: *Series resistance and resonant frequency of some resonators.*

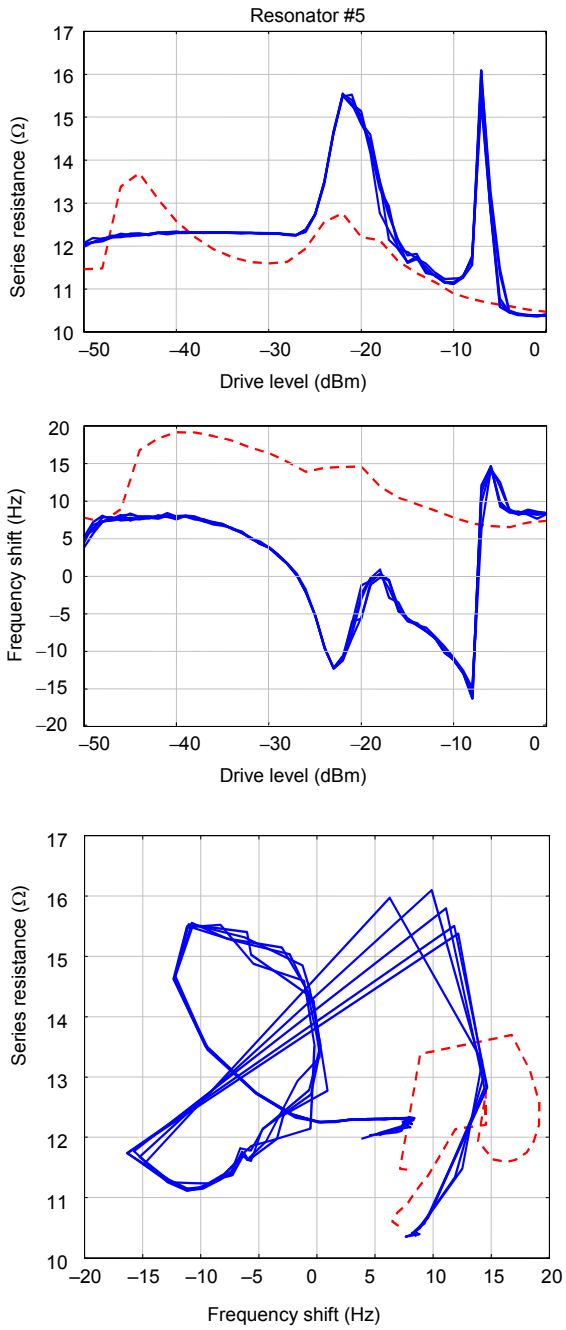

Figure 12: *Series resistance and resonant frequency of some resonators.*

VI. SURFACE SCANNING

Two of the 11 parts have been opened to examine their surface by using a scanning electron microscope. Fig. 13 is a picture of one of the taken down resonators. Numerous defects are observable in Figs. 14 and 15, in particular a blister in the electrode of the resonator #1 and two fragments, probably of quartz, on the surface of the resonator #2. In this latter case, the sharpness of the outlines indicates that the fragments have been trapped by the electrode plating during the fabrication process, in which case they cannot move anymore and cannot play a role in the DLS. Nevertheless, it is highly probable that other smaller particles, trapped in the numerous surface defects with a more or less degree of freedom, vibrate in their trap and thus take part in the DLS mechanism in absorbing a part of the acoustic energy.

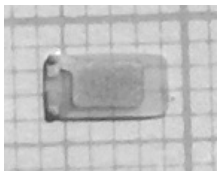

Figure 13: *Resonator* #1.

Figs. 14 and 15 show that the surface of resonators #1 and #2 are particularly irregular compared with the surface of a test resonator coming from another source (Fig. 16).

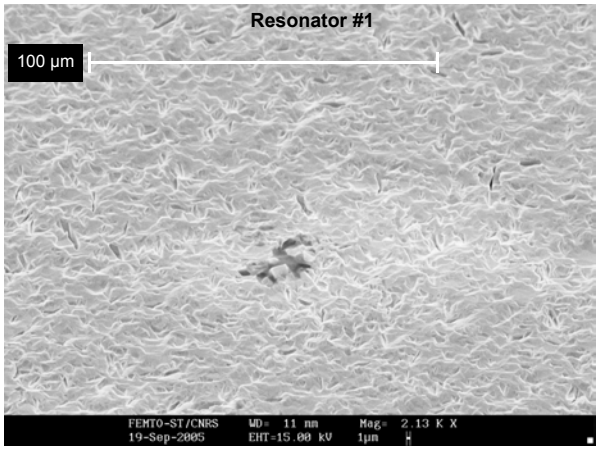

Figure 14: *Surface of resonator* #1.

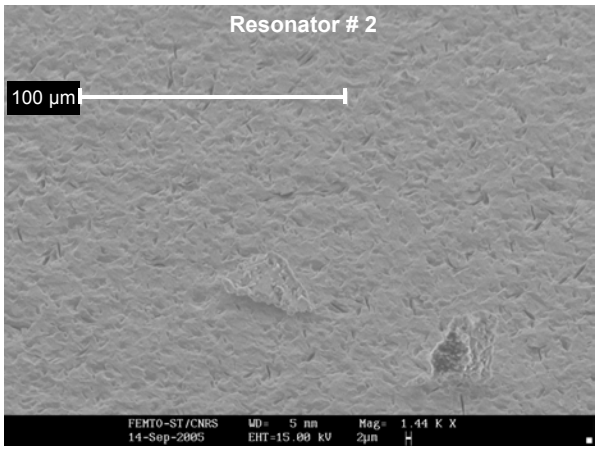

Figure 15: *Surface of resonator* #2.

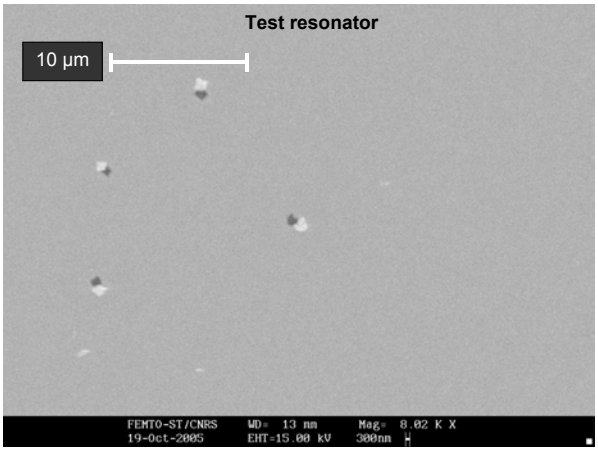

Figure 16: *Surface of a test resonator*.

VII. NOISE AND DLS

The main reason why these experiments are currently carried out is to check for a possible correlation between drive level sensitivity and noise of the resonators that should have the same origin. One of the possible mechanisms relating these two phenomena has been suggested in the past [21].

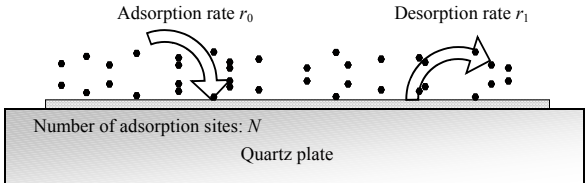

Figure 17*: Noise induced by a contaminant species* [21].

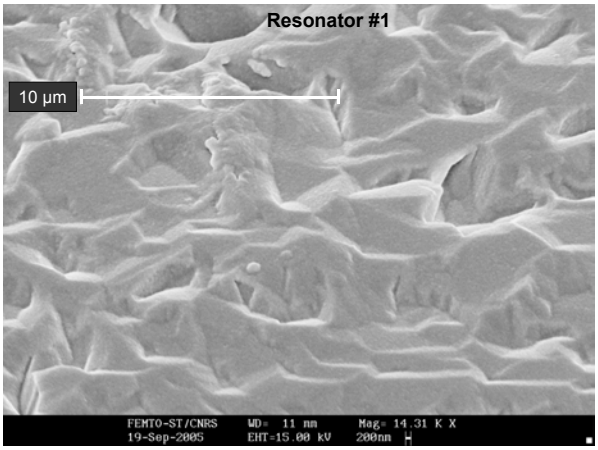

Figure 18: *Enlargement of Fig.* 14.

It assumed that some contaminant species are randomly trapped to and released from N possible surface sites at different rates, each trapped particle causing an average relative frequency shift $\Delta f/f$ (Fig. 17). This assumption can be considered plausible in looking at Fig. 18, which is an enlargement of Fig. 14, where a large number of surface defects, clearly visible in the picture are so many possible traps for contaminants.

Nevertheless, experimental verifications of the expected correlation between drive level sensitivity and resonator noise investigated so far have led to contradictory conclusions [1, 6] so that the question remains open.

A new series of experiments is going to be started to clarify this question based on the following assumptions:

– Small particles located on the surface of a resonator exhibiting DLS often induce a large frequency change.
– Submicron particles located on or near the surface of most resonators could bring about DLS not measurable at normal drive level but evidenced only at very low drive level and could also be partly responsible for the frequency noise of the resonator.
– Correlation between noise and DLS, if any, should be demonstrated by performing noise and DLS measurements in the same experimental conditions and, if possible, at the same time.

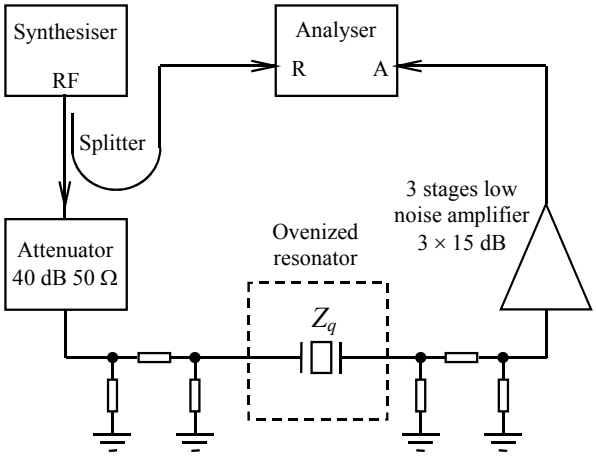

Figure 19: *Dedicated set-up for low level measurement*.

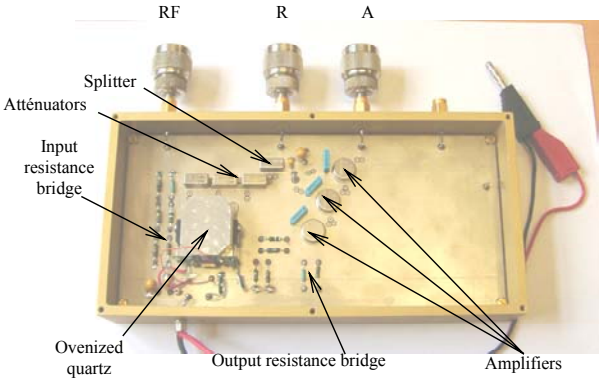

Figure 20: *Picture of the set-up*.

The high performance interferometric instrument currently developed in our lab to measure the intrinsic noise of resonators [17, 18] is being modified to allow simultaneous noise and DLS measurements. The

equipment used so far described in Sec. III, allows measurements from –50 dBm to +15 dBm. So as to lower the crystal drive level below the limits of the analyser, a dedicated arrangement has been designed as shown in Figs. 19 and 20.

A 40 dB wide band attenuator is inserted in between the synthesiser RF output and the pi-network input while the output signal, amplified by a three-stage low noise amplifier feeds the analyser measurement input. The analyser reference signal comes directly from the synthesiser.

The set-up allows measurement with crystal drive level as low as –100 dBm. It should be noted here that a careful attention has to be paid to the calibration procedure. In addition, as outlined in Sec. III, the measurement relies only on amplitude and phase of the transfer function and on our own algorithms.

VIII. CONCLUSION

SEM pictures of the surface of some resonators exhibiting DLS reveal a large number of particles and other defects. It is not proved that these defects are responsible for the DLS but there is a strong suspicion. The series resistance change in the DLS effect is always accompanied by an often important relative frequency change (several ppm). This experimental observation leads to the hypothesis that in any resonator, smaller particles loosely trapped near the surface by electrostatic forces or in structural cavities located under the electrodes could be, at least partly, responsible for the frequency noise of the resonator. Because of their small size, these nanoparticles could be activated and revealed by a much lower drive level as those used up to now. The imminent finalizing of a high performance interferometric instrument able to measure simultaneously very low level DLS and intrinsic noise of resonators should clarify the possible correlation between the two phenomena.

Acknowledgements

This work has been supported by CNES under contract: #04/CNES/1854/DCT094

REFERENCES

[1] P. Bates, Proc. 54th IEEE IFCS, 233 (2000)
[2] M. Bernstein, Proc. 21st AFCS, 244 (1967)
[3] V. E. Bottom, *Introduction to Quartz Crystal Unit Design* (Van Nostrand Reinhold Co., 1982)
[4] V. E. Bottom, Proc. 5th Crystal Conf., 245 (1983)
[5] R. Brendel, M. Addouche, P. Salzenstein, E. Rubiola, and Y. S. Shmaliy, Proc. 18th EFTF (2004)
[6] E. E. Carlson, T. E. Wickard, Proc. 55th IEEE IFCS, 338 (2001)
[7] R. C. Chittick, D. M. Hyland, Proc. 11th EFTF, 173 (1997)
[8] L. Dworsky, R. Kinsman, IEEE Trans. on UFFC, **41** (2), 261 (1994)
[9] G. L. Dybwad, J. Appl. Phys. **58** (7), 2789 (1985)
[10] E. P. EerNisse, Proc. 50th IEEE IFCS, 346 (1996)
[11] E. P. EerNisse, E. Benes, M. Schmid, Proc. 56th IEEE IFCS, 2 (2002)
[12] E. A. Gerber, Electronics, 161 (1954)
[13] J. E. Knowles, Proc. 29th AFCS, 230 (1975)
[14] L. Lindberg, G. Portnoff, Proc. 48th IEEE IFCS, 273 (1994)
[15] B. Neubig, Proc. 11th Quartz Dev. Conf., 60 (1989)
[16] S. Nonaka, T. Tuuki, K. Hara, Proc. 25th AFCS, 139 (1971)
[17] E. Rubiola, J. Groslambert, M. Brunet, V. Giordano, IEEE Trans. on UFFC, **47** (2), 361 (2000)
[18] E. Rubiola, V. Giordano, Rev. of Sc. Inst., **73** (6), 2445, (2002)
[19] R. J. Williamson, IEEE Trans. on UFFC, **34** (6), 681 (1987)
[20] J. S. Yerna, Proc. 38th AFCS, 499 (1984)
[21] Y. K. Yong, J. R. Vig, IEEE Trans. on UFFC, **36** (4) 452 (1989)
[22] *Basic Method for Measurement of Resonance Frequency and Equivalent Series Resistance of Quartz Crystal Units by Zero Phase Technique in a Pi_Network*, IEC Publication 444, (1973)
[23] *HP 4395A Network/Spectrum/Impedance Analyzer Operation Manual*, Hewlett Packard Part No. 04395-90000 (1997)

Proceedings of the 20th EFTF, 2006

Novel scanning probe method for visualization of standing acoustic waves in piezoresonators

G. Minchev,* T. Sukhikh, D. Dinchev and L. Trendafilov
Molecular Beam Epitaxy & Surface Analysis Laboratory, Institute of Solid State Physics, Bulgarian Academy of Sciences, 72 Tzarigradsko Chaussee blvd., 1784 Sofia, Bulgaria
**Electronic address:* MBE@issp.bas.bg

A scanning probe microscopy (SPM) for visualization of standing acoustic waves in piezoresonators based on registration at every pixel the wave inherent electric field (normal to surface) is developed. The physical background of the presented method is electric charge induction in a probe by wave electric field. As in any scanning probe microscopy, the probe is the key part and the resolution is the goal. For the case, the long-range nature of electric field rise the main hindrance. In the paper, a complete analysis of basic/fundamental requirements and interdependences of the method are presented together with analysis of probe functioning focused on effective aperture. An SPM system, builded in accordance with presented analysis, is described and images of standing waves of different modes are presented.

I. INTRODUCTION

Visualization of the acoustic wave patterns for the entire set of interacting vibration modes is an efficient instrument for analyzing, understanding and improving of piezoresonators.

Two modifications of the X-ray topography are mainly used for visualization of standing acoustic waves in single crystal piezoresonators: the large–focus X–ray topography (see, e.g., [1]), and synchrotron X–ray topography (see, e.g., [2]). Laser interferometry (see, e.g., [3]) and coherent radiation reflection [4] can also visualize acoustic wave patterns.

Both X–ray topography modifications have their intrinsic limitations: i) inherently they generate contrast through acoustic wave induced corrugation of atomic planes, a corrugation that breaks the Bragg relation for diffraction. Such a mechanism produces a highly nonlinear dependence between the deformation amplitude and the X-ray intensity change (i.e., no contrast at low amplitudes and fast saturation after certain amplitude); ii) crystal deformation is dynamic, therefore both methods average over time the momentary X-ray intensity, so a contrast is generated only for standing acoustic waves (although, the stroboscopic synchrotron topography could resolve wave fronts [5]); iii) any particular deformations and/or crystal imperfections also generate their own contrast, that adds to the useful picture; iv) large–focus X–ray topography is considerably time-consuming technique, synchrotron X–ray topography is expensive and difficult of access, and all X-ray methods are dangerous and relatively complicated.

The obvious desirable improvement is: an inexpensive scanning system that measures point by point the electric field inherent to the acoustic waves in piezoresonators, registers its amplitude and phase as acoustic wave amplitude and phase and then produces an image.

II. THE S P M SYSTEM

Every scanning probe system has three basic elements. The most important is the probe - it transforms the attribute of interest (in this case the acoustic wave inherent electric field) into some measurable quantity, and this transformation has to be done as locally as possible. The probe will be described in section III.

The second basic element, the scanner, moves the probe over the object (scans it). In our case dimensions of the objects (resonators) are determinated by acoustic waves length (some millimeters), so the requirements for the scanner are not very difficult to be engineered (figure 3).

The third basic element consists of a datalogger (collecting the raw data at every pixel), programs processing raw files and generating images (a false-colored maps representing the distribution of attribute of interest over the object) and programs processing images for obtaining some aggregate parameters. This third element is more or less the same for any SPM system, so we shall not enter in its detail description.

Visualization of standing acoustic waves (piezoelectric resonances) needs a specific fourth element. A resonance has existence only if feeded with energy, so a subsystem for excitation of standing

acoustic waves is obligatory. Designing our SPM system we face the fact that the requirements for the necessary excitation are very serious and complex and so the excitation subsystem has to be. Its creation becomes a distinct and sizable design task which results are presented in a separate paper [6].

On figure 1 the first generation SPM system is shown. Two second generation systems are already under development.

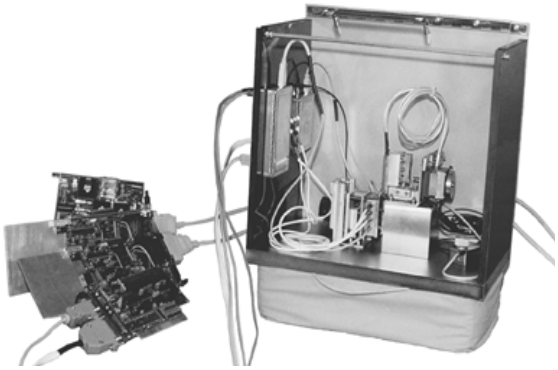

FIG. 1: **Prototype SPM system for visualization of standing acoustic waves in piezoresonators**. The system consists of intentionally heavy antidust housing over a massive base plate. The construction mass-center is engineered to be at a position (close to sonde tip) where the smallest amplitude of oscillations (if any) are generated by the mechanical scanner movements. The whole construction is placed over a damper cushion for vibration isolation and for suppressing possible self-generated oscillations.

To the left from the housing are the electronics PCB. At the left side-wall are bonded the probe electronics box (figure 3) and the excitation subsystem [6] (the foreseen metal box).

In the housing center is the changeable sample-holder block. The shown one is for resonators mounted on bases of industry standard metal cases/holders (all types - from 20x20 mm HC47 to the small TC39 watch crystals type). A manual translational movement and two-axis adjustment permit positioning the resonator surface exactly in the plane scanned by the sonde (section IV).

The SPM system scheme is presented on figure 2.

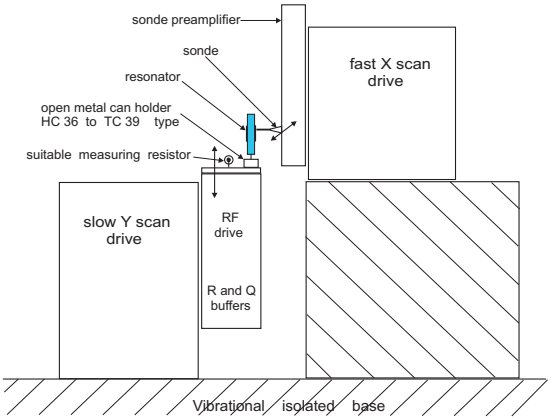

FIG. 2: **Structural scheme of shown on figure 1 system**. The probe assembly, in the center, is composed of sonde and the first stage of probe electronics (figure 3) and is affixed to the fast scanning stage (at horizontal direction of scanning corresponding to pixel rows in the images), the only potentional source of construction oscillations.

The sample-holder, shown below the probe assembly, contains the excitation and measuring buffers [6]. It holds the measuring resistor (figure 3 and reference [6]) and case/holder base with a resonator mounted in it. The resonator electrode facing the sonde tip is grounded and excitation voltage is applied to the opposite electrode, an electrode beyond the resonator's piezomaterial.

Sample-holder is affixed to the slow scan drive and is moved only upwards (a direction corresponding to pixel columns in the image) for the purpose of resonator assembly stability.

This SPM system is designed to be integrated with a personal computer. Electronics PCB are designed as PCI/ISA cards connected to the PC system bus and obtaining their supply from it.

System operation is simple: both scanner stages, under PC control, perform scanning of resonator surface by sonde tip and the datalogger accumulates measured electric field values from the sequential probe positions (pixels).

III. THE PROBE

The probe is the most important element of every scanning probe technique. For the case, it is composed of three components each with its own distinctive function.

Individual resonance excitation is provided by the subsystem described in [6], that ensures measurement conditions invariability and stability of corresponding standing acoustic wave.

The second element - sonde - is explained in section IV despite its fundamental self-consistency with probe electronics (figure 10).

Probe electronics is schematically presented on figure 3 and is similar to a section of the excitation subsystem described in [6].

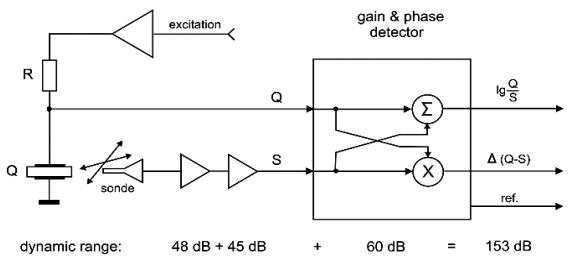

FIG. 3: **Probe electronics**. This probe is without selectivity and could process signals from LF up to 500 MHz. Its dynamic range is composed from dynamic capacity of all three

separate stages and is unnecessary large. First stage input noise does not exceed 1.1 nV $Hz^{1/2}$, what is close to the current state of the art for a non-cryo-cooled electronics. Overall sensitivity reaches $1.6 \cdot 10^{-17}$ coulombs (or 92 elementary charges) for the LSB, what is not sufficient in all cases, although such a value is rarely obtainable.

The logarithmic amplitude ratio and phase difference signals provided by gain & phase detector are fed to the datalogger and are registered with 0.7% resolution in amplitude ratio and 0.17 degree resolution in phase difference. Amplitude offset error is less than 1% and phase offset error is 0.1 degree and increases to about 1.0 degree around zero. For visualization purposes such resolution is quite satisfactory. Moreover, offset errors generate only image background and are not significant.

Excitation of the resonator (marked as **Q** on figure 3) is performed by the subsystem described in [6]. This is done by an alternating displacement current through the capacitor-like resonators structure. With continuous excitation frequency tuning the subsystem [6] keeps zero phase difference over the resistor **R** (i.e., resonators susceptance is kept zero, in other words, its impedance is kept active). The subsystem [6] not only keeps stable the excitation conditions, but performs precise measuring of all physically existing resonances (main, overtones, anharmonic, etc. for all inherent vibrational modes - thickness-shear, thickness-twist, etc.), and after selecting the resonance of interest locks on it. Then the SPM system visualizes the acoustic wave pattern associated with this selected resonance.

The probe electronics receives the resonator electrodes voltage on its **Q** input. The picked by the sonde signal **S**, after amplification in the first two stages, is compared with **Q** signal, so any changes in resonance (amplitude, frequency, etc.) or in excitation and measuring conditions will not disturb the obtained image.

IV. THE SONDE

The sonde is the key part of the probe. The physical background of the first step of its operation is electric charge induction from the electric field immediately over the resonator surface. Desiring to outline the normal to surface electric field component we acceded to design a coaxial in structure sonde which we expect to be the most insensitive to the tangential field.

Standing wave inherent electric field is alternating by nature, so it induces alternating electric charge in the central electrode what, in turn, generates alternating coaxial field in the sonde. This latter field propagates along the coaxial waveguide structure of the sonde to the matched impedance termination and the RF current produced there is detected in amplitude and phase by probe electronics. Detected signals are then fed to the datalogger where they are measured and registered.

The coaxial sonde tip in its close proximity to the resonator surface is presented on figure 4.

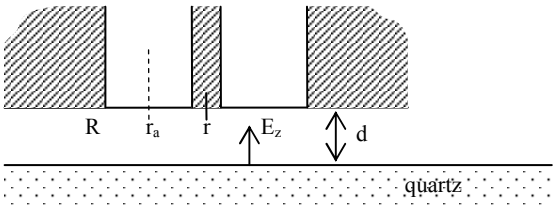

$$Q = \varepsilon\varepsilon_0 E_z \pi \left[Rr + \frac{\pi - 2}{4}(R - r)^2 \right]$$

FIG. 4: **Probe (sonde tip) working position over the resonator surface and expression for total charge Q induced in the central electrode**. Central coaxial electrode has radius **r**; coaxial shell radius is **R**; **ε** is the relative permittivity for both the sonde dielectric and the resonator piezomaterial; **d** is the tip to surface distance; and $\mathbf{E_z}$ is the normal component of acoustic wave electric field. The dashed line marks the sonde aperture radius $\mathbf{r_a}$.

The sonde aperture radius $\mathbf{r_a}$ is defined as the radius of the disk (of resonator surface) whose electric field has induced (is responsible for) half of the total induced in the central electrode charge.

The formula from figure 4 is deduced in compliance with significant assumptions: i) no manufacturing errors, or eccentricity of sonde construction exist and perfect accuracy is obtained; ii) electrode material is perfectly pure copper; iii) sonde dielectric has no inhomogeneities and is not with cylindrically layered structure; iv) resonator material and sonde dielectric permittivity have equal values; v) no deviation of sonde axis from surface plane normal is considered; vi) electric field is constant over the whole resonator surface.

In the following seven figures are presented the basic/fundamental requirements and interdependences of the method.

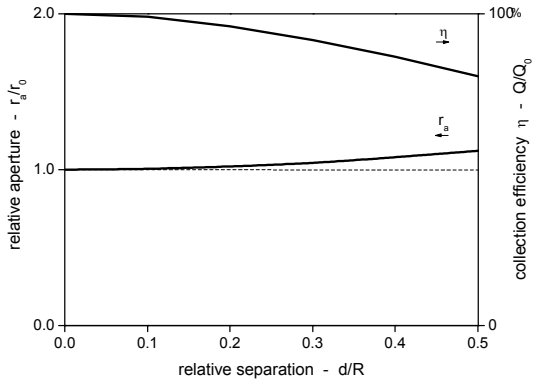

FIG. 5: **Change in sonde aperture and collected charge due to sonde tip to surface distance**. This figure shows the

advantageous difference between the presented method and others SPM techniques (scanning tunneling microscopy, atomic force microscopy, etc.) - it is not necessary to keep an extremely short distance between probe tip and the object. Charge collection efficiency - η is the ratio of collected by central electrode charge to the charge that could be induced in an infinite electrode by electric field originated only from a disk of radius **R** of resonator surface.

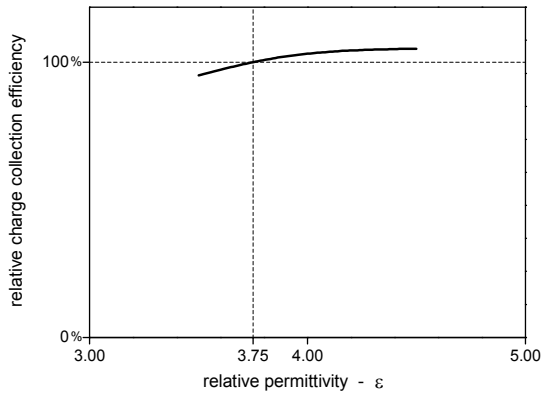

FIG. 6: **Influence of difference in relative permittivity between sonde dielectric and resonator material**. Sonde dielectric relative permittivity ε = 3.75. This small influence permits the designer to choose freely the sonde dielectric. Moreover, the SPM system will give similar (easy comparable) results for any piezomaterial and for any crystal orientation (if its permittivity changes with orientation).

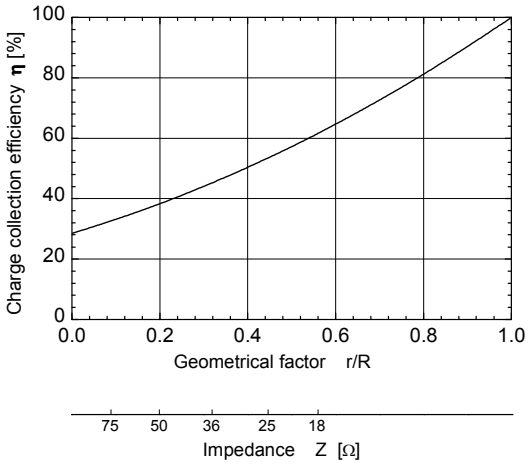

FIG. 7: **Dependence of sonde charge collection efficiency η on geometrical factor r/R, which also determines sonde impedance Z**. The marked impedance values are for sonde dielectric relative permittivity ε = 3.75. It is clearly seen that for a better resolution the designer must pay 2/3 of sonde charge collection capability.

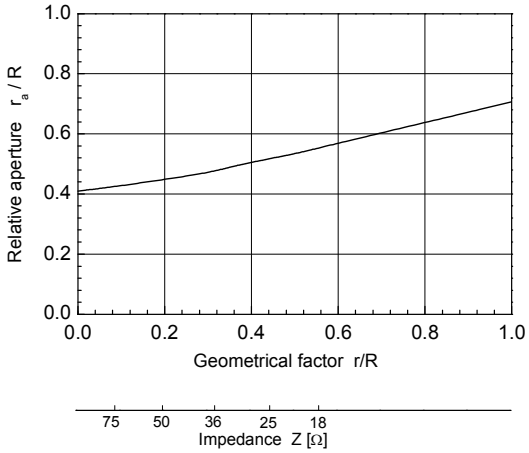

FIG. 8: **Aperture dependence on sonde geometrical factor**. Higher impedance values are preferable for higher resolution, but this is not very effective designer's approach.

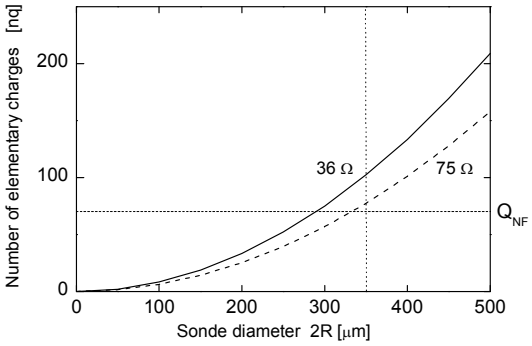

FIG. 9: **Dependence of minimal charge to be collected (in elementary charges - $1.60 \cdot 10^{-19}$ coulombs) on the sonde outer diameter**. Sonde impedance is the parameter. Q_{NF} is the apparent charge resulted from 1.1 nV $Hz^{1/2}$ input noise. It is assumed, that acoustic wave electric field under the sonde tip corresponds to 2.0 Vp-p voltage on resonator electrodes (if they were at the same place).

This figure presents the requirements to probe electronics sensitivity and the limiting role of input noise. It is not sufficient only to increase sensitivity (what is not very difficult) - it is necessary to decrease correspondingly the input noise (what is more difficult).

For the described first generation SPM system we have chosen 350 μm of sonde outer diameter and 36 Ω impedance.

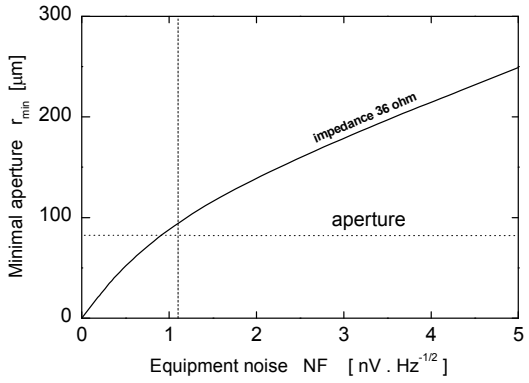

FIG. 10: **Dependence of achievable minimal aperture r_{min} on the equipment noise for 36 Ω impedance**. This figure makes clear that equipment noise, sonde impedance and achievable minimal aperture are not independent, but tightly related. This is the main fundamental limitation of the method and the designer main trade-off. For the described first generation SPM system we achieved 90 µm aperture.

Obviously, there are several approaches for resolution increasing, although acoustic waves of interest are waves without sharp slopes. Higher resolution may be important in the case of superposition of significantly different waves (as may be the case on figure 4).

One („system type“) approach is to use image processing programs for selfdeconvolution utilizing the aperture function of the sonde (what function is easily measurable and computable).

„Strengthening type“ approaches could be applied to the sonde (microstrip lines, „resonanced“ structures, microwave cavity sonde, etc.) or to the probe electronics. One obvious approach is to decrease input noise. Noise decreasing is the never-ending task for all electronic engineers - there are hundreds of approaches and a thousand of solutions. The prospect of an approach aimed at decreasing noise through narrowing the bandwidth is presented on figure 11.

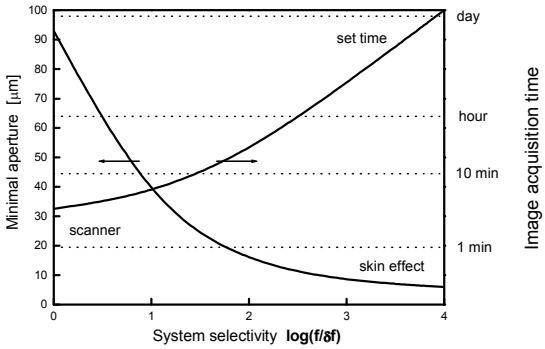

FIG. 11: **Minimal achievable aperture for selective probe electronics**. On the abscissa is plotted the logarithm ratio of pass bandwidth to the frequency of operation.

The left ordinate is for minimal aperture and it could be easily seen that skin effect fundamentally limits the coaxial construction sonde potential to about 20 µm (the curve is drawn for 20 MHz center frequency).

The right ordinate presents the standard image (512x512 pixels) acquisition time. Our human manner puts a 1 hour limit per image. The scanner has to mechanically move the probe over the whole object surface which can be done for at least a couple of minutes and this puts the bottom limit. Selective electronics need time to set to the corresponding voltage for every next pixel and this time adds to the time spent by the scanner to reach this next pixel. This leads to the observable increase of acquisition time, that effectively limits the system selectivity to a 0.5% pass bandwidth.

The general conclusion that can be drawn is that 25 µm is a practical limit for a selective system with about 1.0 nV Hz$^{1/2}$ input noise.

V. EXEMPLIFIED RESULTS

Experimentally obtained data yield maximum dividend when they can be directly compared to results from resonator computer modelling. „Line-scan“ mode generates single curves that facilitates obtaining quantitative valuation for the difference from the model predictions. The next three figures present the type of line-scan data results.

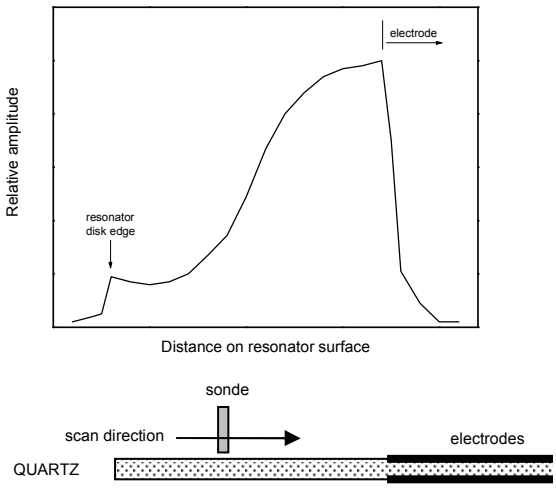

FIG. 12: **Scanning a radius of a disk resonator**. The resonator is AT-cut quartz oscillating on its main mode (12.875 MHz). The end of the quartz round slab and the beginning of the grounded resonator electrode are clearly manifested. Below the figure a schematic, but in real dimensions and strictly adjusted to the curve, for the resonator and sonde cross-section is depicted.

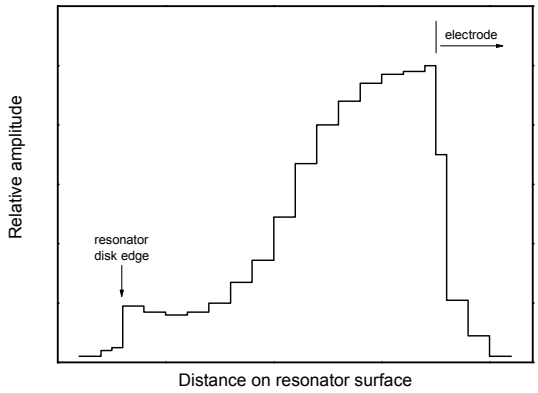

FIG. 13: **Alternate representation of figure 12 data**.

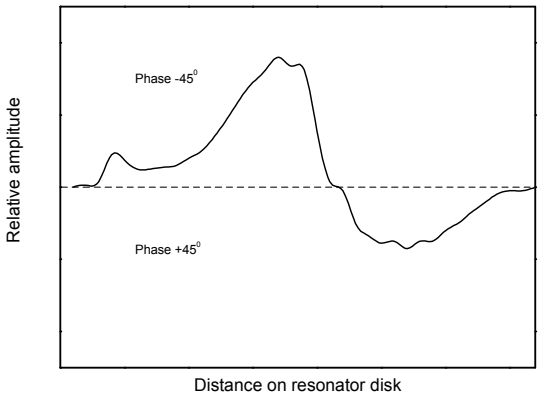

FIG. 14: **Scanning along upper side of a square slab resonator and outside (but close) to its square electrode**. Unknown crystal-cut, 2000 kHz quartz resonator. A fine structure is seen that resembles an overlapped second standing acoustic wave.

For easy transferring of our already customized on X-ray images visual perception for mode patterns a „conventional“ image type is presented on figure 15.

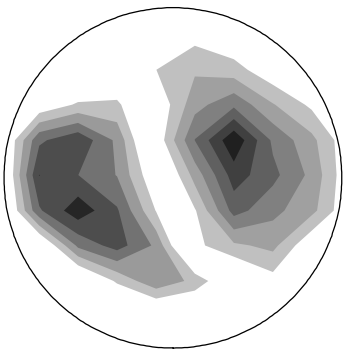

FIG. 15: **Image presented in a way as X-ray topogram looks like**.

An „artistic“ image type, intended to be perceived on the basis of scientist's intuitive feeling of nature, is presented on figure 16.

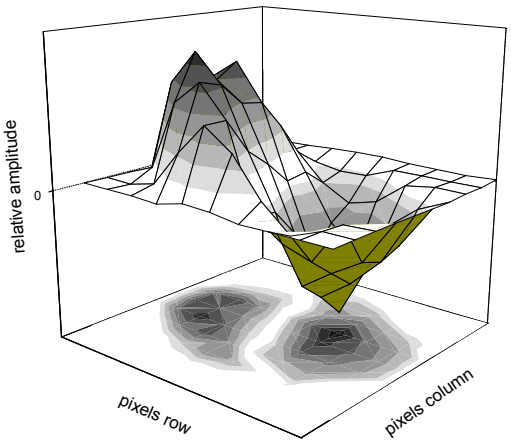

FIG. 16: **Three-dimensional, false-colored sculpture of a standing acoustic wave**. AT-cut 5000 kHz quartz resonator, 14 mm in diameter and 300 µm thick slab. Spurious resonance within 182 kHz from the main/fundamental resonance, having unusually high admittance (~70% of the main resonance admittance) what forces the crystal to run on this spurious response in a simple Colpitts oscillator scheme.

VI. CONCLUSION

It was developed a new technique [7] for visualization of standing acoustic waves both in single-crystal and in poly-crystal material piezoresonators. For the present, no obstacles are seen for visualizing propagating waves using synchronous amplitude measuring.

One advantage is that the acoustic wave amplitude is registered linearly, which will allow its easy comparing with computer models. Moreover, phase difference between the standing acoustic wave and resonator electrodes RF voltage is simultaneously registered. This phase information allows coexisting modes to be distinguished and complex structured standing waves to be better analyzed.

The presented technique visualizes acoustic waves only over the bare surface of the resonator, in contrast to X-ray topography for which the presence of electrodes is not an obstacle. However, for resonators with small area of electrodes or perforated electrodes, the images could be completed through amplitude interpolation below the electrodes.

The described technique and X-ray topography turn out to be complementary in a sense, since the X-ray methods visualize the sum of the acoustic wave amplitudes from the whole resonator volume, but the newly developed technique visualizes only near surface amplitude of the acoustic wave.

Acknowledgements

We would like to thank Mihail Hajitodorov for his help in the paper preparation.

This work was supported by „Science Buro“ Ltd. Bulgaria through building the described SPM system.

IV. REFERENCES

[1] A. Lindegaard-Andersen, B. Ribe, „Lang camera for large scale X-ray transmission topography”, J. Phys. E: Sci. Instrum. **9**, 659-661 (1976).

[2] G. Hildebrandt, „X-ray wave fields in perfect and nearly perfect crystals – theoretical background and recent applications”, J. Phys. E: Sci. Instrum. **15**, 1140-1155 (1982).

[3] A.B. Rinkevich, A.M. Burkhanov, D.V. Peroff, „Acoustic fields in a steel single and polycrystal”, in: XI Session of the Russian Acoustical Society, Moscow, 813-816 (2001).

[4] L. Wimmer, S. Hertl, J. Hemetsberger, E. Benes, „New method of measuring vibration amplitudes of quartz crystals”, Rev. Sci. Instrum. **55**, 605-609 (1984).

[5] D. Shilo, E. Zolotoyabko, „Visualization of short surface acoustic waves by stroboscopic X-ray topography: analysis of contrast”, J. Phys. D: Appl. Phys. **36**, A122-A127 (2003).

[6] G. Minchev, T. Sukhikh, „Piezoelectric resonances measuring system operating in a novel lock-on-resonance mode“, These Proceedings (20th EFTF, Braunschweig, Germany, 2006).

[7] Patent application 109390/21.12.2005.

Proceedings of the 20th EFTF, 2006

Piezoelectric resonances measuring system operating in a novel *lock-on-resonance* mode

G. Minchev and T. Sukhikh
Molecular Beam Epitaxy & Surface Analysis Laboratory, Institute of Solid State Physics, Bulgarian Academy of Sciences, 72 Tzarigradsko Chaussee blvd., 1784 Sofia, Bulgaria
Electronic address: MBE@issp.bas.bg

A complete system, USB 2.0 powered „virtual instrument", that excites and measures all physically existing resonances for all inherent vibrational modes in any type piezoelement is described. Measurements are performed after locking on the chosen resonance by a novel frequency neutral loop. Intrinsically detailed scanning by phase (in a deviation manner from resonance center) results in huge amount of precise data whose extensive processing determines the exact values of all resonance parameters.

I. INTRODUCTION

Measuring of resonance parameters is a common basic task in investigation, development and production of acoustoelectronic devices, and many different methods were developed for it. PI-network analyzers/measuring systems have become a standard tool and the measuring procedures were internationally standardized. Because of the predominant product types in acoustoelectronic industry, the established measuring methods are best for frequency stable resonances (i.e., for devices with stable frequency parameters).

This orthodox measuring approach faces difficulties in two fields. First in measuring piezoelements/sensors intrinsically unstable by frequency - i.e., temperature sensors (with sensitivity of ~1 kHz/K), piezoelements from unorthodox crystal cuts, elements made from piezomaterials in which thermocompensation is principally not achievable, etc. The second type of difficulties appear when precise and detail measurements of sharp, high quality resonances are necessary. Even very small mutual instability between measured resonance and measuring equipment leads to significant change in obtained raw numbers.

Stimulus for designing the described here system were the requirements for resonance excitation and evaluation for the novel scanning probe method [1] for visualization of standing acoustic waves in piezoresonators.

II. REQUIREMENTS

In order to overcome the mentioned in section I two types of difficulties and serve as excitation subsystem for standing wave visualization, a system has to be able to: i) scan the entire frequency range of interest and find all physically existing mechanical resonances (main, overtones, anharmonic, etc.) for all inherent vibrational modes (thickness-shear, thickness-twist, etc.); ii) choose/select any one of the located resonances regardless of their frequency instability, their admittance values (inherent loses), their close proximity to other (more easily excitable) resonances or for resonances with significant energy transfer to other resonances, etc.; iii) perform precise measurements with smaller than 1 ppm deviation steps from resonance center - both in frequency and amplitude/energy domains.

A system has to be: i) universal - could be usable with any type piezoelement, any piezomaterial, any electrodes structure, piezoelement shape, case, etc.; ii) easily integratable in larger systems - research, technological, production, etc.; iii) flexible - must perform all standardized (IEC 444-6) measurements and be easily user programmable for specific or novel measuring procedures.

An inexpensive system that fulfils all mentioned requirements to a satisfactory extent is shown at fig. 1.

FIG. 1: **The measuring system prototype SB-RMS61**. Preliminary parameters: 50 Ohm impedance for all inputs/ outputs; operating frequency range - 10 kHz to 180 MHz; specified performance frequency range - 100 kHz to 130 MHz with > 80 dBc SFDB @ 10 dBm; excitation frequency resolution - 0.1 Hz with 1 ppm stability; measured frequency resolution - 4 ppb; external frequency calibration to 0.1 ppm - yes; GPS descended 10 ppb stability - a future option;

amplitude resolution - 0.01 dB within 80 dB dynamic range; amplitude offset error - 0.1 dB; phase resolution - 0.01 degree; phase offset error - 0.1 degree, increases to 1 degree around zero; output phase noise - < -120 dB/Hz @ 1 kHz; amplitude measurement noise - 5 LSB @ 16 bit ADC; amplitude measurement time constant - 2 µs.; phase measurement noise - 3 LSB @ 16 bit ADC; phase measurement time constant - 10 µs.; instrument reconfiguration time constant - 6 ms.; dimensions - 120 x 60 x 18 mm; weight - 0.2 kg.

The system will include: full speed USB 2.0 connection to any PC; „virtual instrument" interface for Windows 98 or later; PC-installed Integrated program Development Environment (IDE) for transparent direct system-microcontroller programming.

III. SYSTEM OPERATION

A resonance has existence only if feeded with energy and this underlies the RMS61 design. The physical background of its operation is the balance between excitation energy-source and dissipation of energy in resonator loses (energy-sink).

The dominant portion of energy stored in a resonance is, generally speaking, mechanical energy, but the feeding energy-source is electrical energy (alternating electric field over piezoelectric material or alternating displacement current through capacitor structure of the resonator). Direct measurement of dissipated in the resonator energy is quite difficult. On the contrary, the displacement current is easily measurable (figure 2) and its contribution (adding or subtracting energy) clearly depends on its phase difference to the inherent electric field of the mechanical deformation (the acoustic wave).

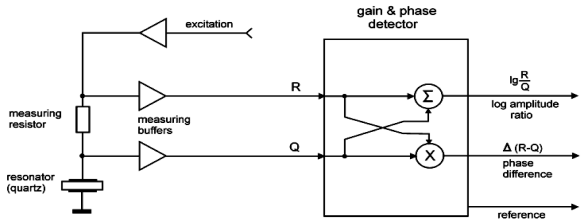

FIG.2: **Measuring setup**. Excitation RF voltage is precisely set to an appropriate amplitude (10 mVp-p to 2.0 Vp-p, typically 400 mVp-p). The changeable measuring resistor (noninductive) should have suitable value related to the admittance of the measured resonance.

The frequency of mechanical vibration (if existing) in the resonator is always equal to the excitation frequency. Vibration amplitude conforms to the stored in the resonance energy and is quite big for high Q-factor resonances.

At zero phase difference over the measuring resistor the current through it is the excitation displacement current and feeding energy is this current multiplied by the resonator electrodes voltage. The latter voltage is directly obtainable from the known excitation voltage and the measured amplitude ratio, that also determines the ratio of resonance admittance to the measuring resistor.

At frequencies slightly deviated from resonance frequency the energy accumulated in the resonance is much smaller, loses are also smaller and for restoring the source-sink energy balance a phase shift appears (over the measuring resistor) that effectively diminishes the energy feed from displacement current. In addition, a decrease of voltage over the measuring resistor (due to increase or resonator electrodes voltage with fixed excitation voltage) takes place, what decreases the displacement current itself.

IV. OPERATIONAL MODES

The RMS61 operates in three basic modes, each for a corresponding required task (Section II). Other modes could be easily developed by specific programming of the system-microcontroller through the USB port and PC-installed Integrated program Developing Environment (IDE). Figure 3 presents the system organization for scanning the range of interest by frequency and locating all existing in that range resonances.

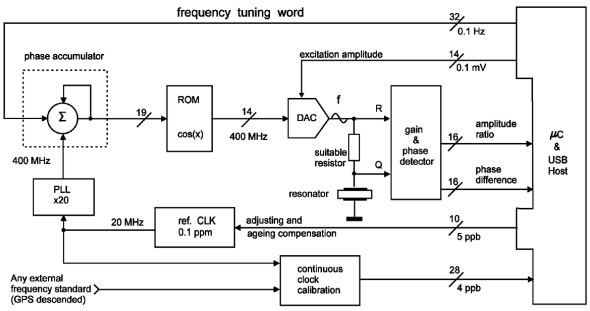

FIG. 3: **Setup for measuring the resonator response to the excitation frequency**. The setup could be functionally divided into three subsystems: i) precise gain & phase measuring; ii) phase lock loop, reference clock and clock calibration; iii) phase accumulator, read-only-memory containing look-in-table of cos(x) function and output DAC generating the excitation sinusoid (a kind of direct digital synthesizer [3]). Scanning is performed by the 32 bit „frequency tuning word" with minimal step of 0.1 Hz. Excitation voltage is set by 14 bit DAC with 0.1 mV resolution. The 20 MHz reference clock could be adjusted with 10 bit DAC, whose LSB increases the clock frequency by 5 ppb (0.1 Hz). This adjusting is based on an external frequency standard and is carried out by 28 bit independent subblock providing 4 ppb resolution. Amplitude ratio and phase difference are measured by 1µs., 16 bit ADC-system with resolution (figure 1 caption) limited by R and Q inputs noise summed with measuring resistor Johnson noise.

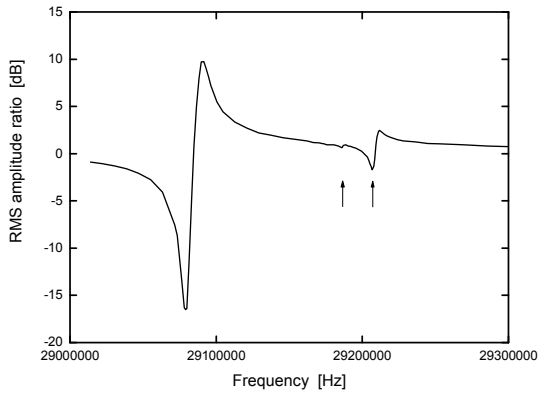

FIG. 4: **Example of „frequency scan" mode of RMS61 system**. Quartz blank cut at xyl/-31°.30', 5 mm resonator diameter, 82 µm quartz blank thickness, 2.9 mm electrodes diameter, 1 mm electrodes bars, electrode thickness 180 nm. Two spurious (anharmonic) modes could be distinguished along with the main mode (2140 Ohm comparing resistor, 1.0Vp-p excitation voltage).

As an example, on figure 4, the small region around main mode resonance for specific crystal-cut quartz temperature sensor is scanned. Observed resonances (the main one and two anharmonic) have fast changing center frequencies, that makes impossible their precise measuring or evaluation. It is the second basic operational mode that permits selecting and locking on each of them [2]. The system organization for that mode is presented on figure 5. It takes 6 ms. for system reconfiguration - figure 1 caption.

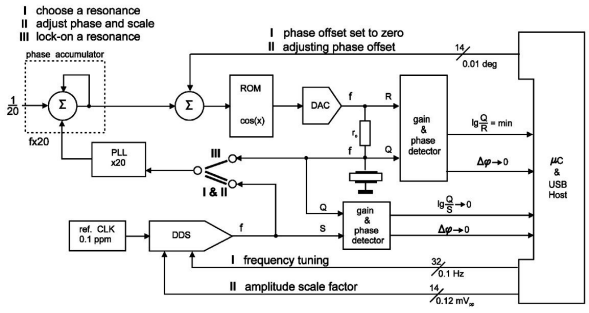

FIG. 5: **RMS61 configuration for the three steps procedure of resonance selection**. In this configuration there are two gain & phase detectors and two direct digital synthesizers (DDS). The three steps are marked I, II and III. The measuring resistor from figure 1 is marked as r_0 here.

The first step is for choice of resonance. The system-microcontroller scans the frequency range where the resonance of interest has been located during the previous observable mode. It carries out all this using the first DDS (depicted at the bottom of the figure 5 diagram) through its 32 bit frequency tuning word. The output signal of that first DDS is fed through a X20PLL to the upper (on figure 5) DDS-structure as clock signal. From this clock signal the DDS-structure produces a frequency twenty-fold lower (equal to the first DDS output frequency - i.e., a frequency equal to the system-microcontroller dictated frequency) and excites the resonator with it. A zero phase offset is added in the intermedial block (between phase accumulator and ROM lock-in table). Thus, the range is scanned transparently through the uninterfering second DDS-structure. Selecting the resonance occurs when the phase difference over the measuring resistor becomes zero (or close to zero) and amplitude ratio is at its minimal value (as seen from the upper gain & phase detector).

Then, as a second step, the system-microcontroller starts to adjust an additional phase offset injected into the DDS-structure (thus changing the excitation voltage phase) together with adjusting the amplitude of the first DDS output signal, until the outputs of the lower gain & phase detector become zeros - i.e., a condition when no phase difference exists between RF voltage on the resonator electrodes and first DDS output RF sinusoid together with equality of their amplitudes (zero in logarithmic output scale of gain & phase detector). This adjustment has to be performed, yet preserving the zero phase difference over the measuring resistor r_0. The latter needs a second adjusting loop and continuous frequency tuning for first DDS, but is not necessary for frequency stable resonances.

The third step is easy - the system-microcontroller simply switches the X20PLL input signal from DDS output to the completely equal signal from the resonator electrodes. This creates a frequency neutral loop - the signal from the resonator electrodes is fed to the X20PLL where it is multiplied 20 times, then divided 20 times in the phase accumulator and fed back to the resonator as excitation through the measuring resistor r_0. Any shift in center frequency of the resonance is forwarded through this loop and nothing changes. Thus, the system has „locked" on the selected resonance and begins to be continuously driven by that resonance.

Once the RMS61 is locked-on, a detailed and precise measuring becomes possible. Figure 6 presents the system configuration for making such measurements - i.e., the third basic operational mode. In fact, it is the configuration that appears after fulfilling all three steps from the previous mode.

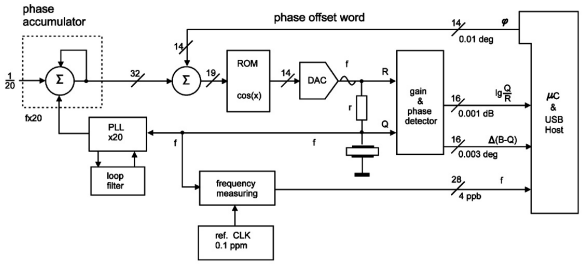

FIG. 6: **Configuration for measuring a resonance**. The dictated from system-microcontroller 14 bit phase offset word

is summed with the fourteen most significant bits of the 32 bit word from phase accumulator and produces, after truncation, a 19 bit index for the look-in-table in ROM. The table contains 14 bit values of cos(x) function that are sent to the output DAC. Amplitude ratio and phase difference are measured by 16 bit ADC-system and the current frequency is measured by a hardware block with 28 bit resolution and 0.1 ppm absolute accuracy.

Orthodox resonance measuring with scanning by frequency is always possible in mode 1. For frequency unstable resonances, measuring is carried in a slightly unusual way. The narrow range, just around resonance, is scanned by phase and not by frequency. A graphic explanation of this „phase scan“ is presented on fig. 7.

V. EXEMPLIFIED RESULTS

No matter how sharp is a resonance, a huge amount of precise data could be collected by phase scan. Extensive computer processing (fitting to measuring points some specific models of that resonance, or some „equivalent“ electrical circuits, or admittance locus curve, etc.) determines the exact values of all resonance parameters. Small physical effects/processes (small by energy engaged; small as „second order“ types; overlapped by stronger processes; etc.) could be distinguished thanks to the plentiness of precise data points. The lock-on mode provides examinational basis for designing novel resonance-based sensors with complex responses:

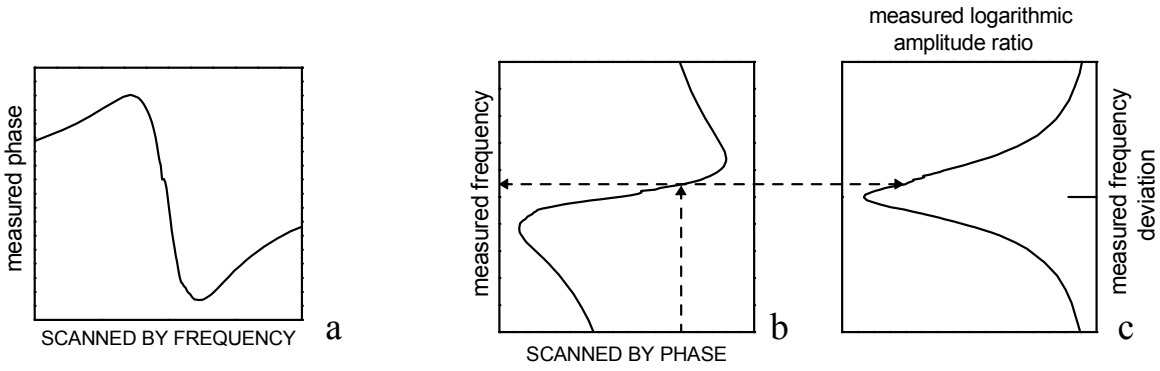

FIG. 7: **Phase scan of resonance vicinity**. The orthodox scanning by excitation frequency (7a) is the measuring method of the first operational mode. It maps the phase difference (over the measuring resistor) arousing to balance the energy source-sink (section III). A negative phase slope ($d\varphi/df < 0$) is always associated with a resonance and in this zone a „phase scan“ could be accomplished. First, a frequency neutral loop (feedbacking resonator frequency as digital synthesizer clock) should be established (figure 6). Adding a phase shift (by changing the „phase offset word“ from its nominal value) in this feedback loop forces a frequency change that creates a reciprocal phase shift at the measuring resistor, and thus restores the source-sink energy balance. By changing the phase within $d\varphi/df < 0$ zone (7b) a detail scan of resonance vicinity could be carried out („phase scan“). A change or a drift in center frequency of the resonance does not affect the current frequency deviation from center frequency, the current amplitude ratio or the measurement conditions.

The „negative phase slope“ zone is small by nature in the frequency domain, but is always associated with significant change in phase. Moreover, the sharper the resonance is, the shorter the zone and the smaller the scan step. This makes the „phase scan“ intrinsically detailed exactly in the resonance vicinity - a region where all resonance features and parameters strongly manifest themselves.

A measurement carried by phase scan (7c) returns two unchangeable relative results (a ratio and a deviation) and one absolute, but variable - the current frequency (the latter varies in conjunction with resonance center frequency, of course, if this center frequency varies at all).

sensors from unorthodox piezomaterials or with unorthodox piezocrystal cuts; multifunctional sensors that measure several physical quantities simultaneously; sensors sequentially operating at a number of resonances from different vibrational modes, etc.

The next figures (# 8, 9, 10 and 11) illustrate the data collected by RMS61.

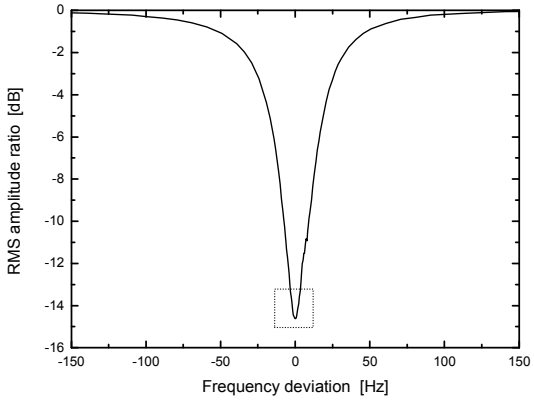

FIG. 8: **Frequency dependence of resonator electrodes RF voltage amplitude**. AT-cut quartz resonator; main resonance mode; resonance center frequency 1999707.3 Hz; comparing resistor 234.30 Ohm; exciting RF amplitude 400 mVp-p. **FWHM=15 ppm (29 Hz at -6 dB)**.

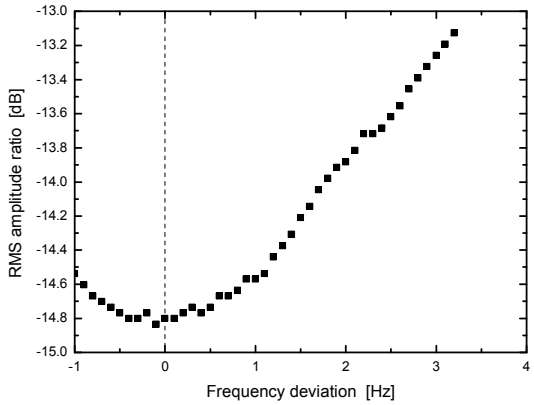

FIG. 9: **Magnified resonance center zone (marked on figure 8)**. The same resonator and measuring conditions as for fig. 8.

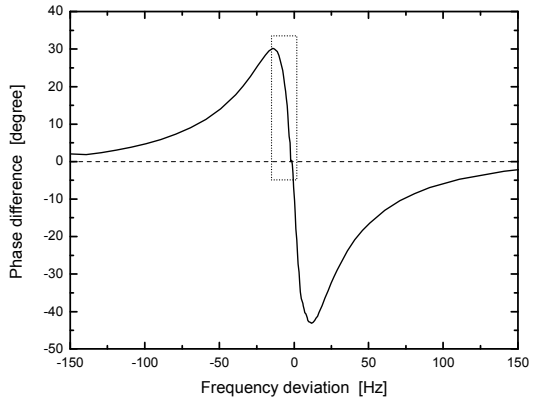

FIG. 10: **Phase shift between exciting RF voltage and resonator electrodes RF voltage**. The same resonator and measuring conditions as for figure 8. **Equipment created nominal phase offset (15.73 degree) already substracted**.

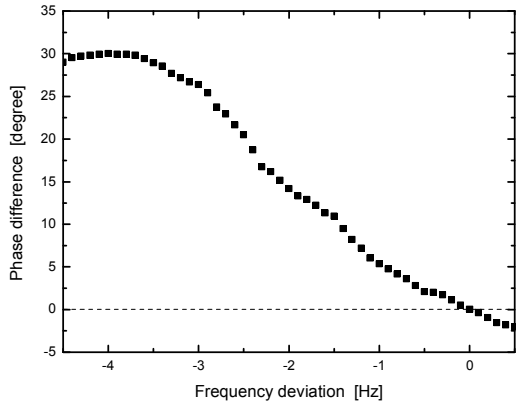

FIG. 11: **Magnified fast phase change zone (marked on figure 10)**. The same resonator and measuring conditions as for figure 8.

Acknowledgements

We would like to thank Eng. Panaiot Danchev for assembling RMS61 printed circuit board and Ludmil Trendafilov for drawing figures 2, 3, 5 and 6.

This work was supported by „Science Buro“ Ltd. Bulgaria through building the described measuring system prototype SB-RMS61.

VI. REFERENCES

[1] G. Minchev, T. Sukhikh, D. Dinchev, L. Trendafilov „Novel scanning probe method for visualization of standing acoustic waves in piezoresonators“ These Proceedings (20th EFTF, Braunschweig, Germany, 2006).

[2] Patent application 109486/24.03.06.

[3] Application note AN-237 „Choosing DACs for Direct Digital Synthesis“, Analog Devices, Inc.

Proceedings of the 20th EFTF, 2006

Fundamental Phase Jumps in Oscillators?

M. J. Underhill,*
Underhill Research and Toric Limited, Tandridge Lane, Lingfield. Surrey, RH7 6LL, UK
**Email*: mike@underhill.co.uk

Is there a fundamental and inevitable process that causes occasional phase jumps in any oscillator? Can such jumps be explained, for example as small randomly occurring frequency excursions? What is the occurrence rate of such jumps, and what is the maximum rate of phase change and frequency? Is there a dependency on, for example the energy density in the resonator? Is there any way in such a process could be controlled and minimised?

1. INTRODUCTION

In ensembles of clocks occasional phase jumps and frequency changes are observed. These may be caused by the means used for comparing the clocks. But if this is not the case then what is a possible cause? Is there a fundamental reason for frequency and phase jumps imposed by the laws of physics that can only be ameliorated but cannot be cured?

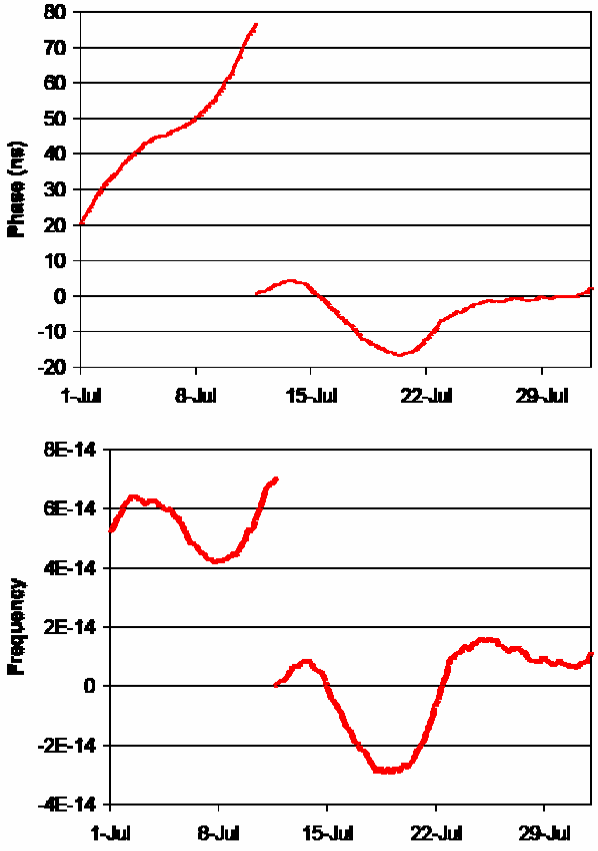

Figure 6 VRC long-term estimate of phase and frequency offsets with respect to the GPS time.

Fig. 1 Phase and Frequency Jumps in Clocks (from Forestieri and Prati [1])

Examples of frequency and phase jumps are shown in Fig. 1 [1]. These jumps are from all sources, for example including measuring apparatus and time transfer between the clocks which are not all in the same place. The question remains as to whether at least some of these jumps can be attributed to fundamental processes in the clocks themselves.

The Leeson oscillator model [2] shown in Fig. 1 predicts the fundamental and unavoidable phase noise spectrum of any otherwise 'perfect' oscillator. Can the model be expanded to predict a random occurrence of phase or frequency jumps?

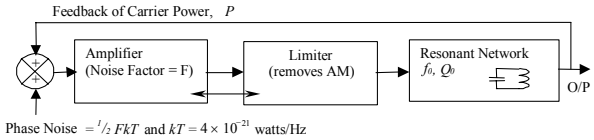

Fig. 1. Leeson Fundamental Model of Any Oscillator

Note that the limiter is an essential block in the Leeson oscillator model. It removes the amplitude part (half) of the input (equivalent) thermal noise FkT, and by limiting the output amplitude stops self-destruction of the oscillator. Below we consider whether the nature of the limiter (whether it has a 'hard' or soft' characteristic) affects the magnitude and occurrence of phase and frequency jumps?

II. OSCILLATOR SPECTRA

The Leeson Oscillator Spectrum

The Leeson oscillator model converts thermal noise to band-limited and amplitude limited phase noise. It predicts a phase noise spectrum that is 'flat' around the oscillator carrier frequency. The 3dB width of the spectrum is typically a few micro-Herz to a few milli-Herz. The Leeson model in effect states that an oscillator can always be considered as band-limited and amplitude-limited 'white' phase noise.

The 'flat' Leeson phase noise spectrum Sϕ(f) is shc in Fig 2. Its 'bandwidth' is directly proportional to magnitude of the phase noise spectrum. For exampl Sϕ(f) is -120dBc/√Hz at 1kHz sideband frequency oscillator spectrum bandwidth is two milli-H (2mHz).

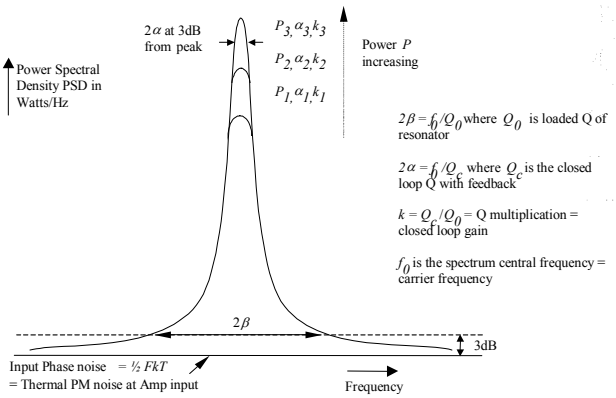

Fig. 2 Phase Noise Spectrum of Leeson Oscillator

The Leeson oscillator spectrum assumes that the resonator frequency is fixed and shows absolutely no variation in time. This is taken to be axiomatic in the analysis that follows.

The phase noise spectrum is as seen in a spectrum analyser with a bandwidth of a few microHerz. It obviously is not possible to observe this part of the spectrum directly except in the case of very low Q oscillators, which have a 'wide line-width'. However the shape of a high Q Leeson oscillator may be deduced after a noise demodulation process but only up to a point [3].

The flat portion of the spectrum implies an inescapable uncertainty in the oscillator frequency. The frequency could wander about anywhere in the closed loop bandwidth of the oscillator. But what are the expected time excursions of the frequency? Could the oscillator be 'trapped' at one frequency for a long time and then behave chaotically before being transferred to a 'trap' at a different frequency within the oscillator phase noise pass-band? Could there be a rapid frequency excursion that looked like a 'phase jump'.

Components of Gaussian Noise

Gaussian white noise can be analysed as a large number of independent discrete frequency components of equal power equally spaced in frequency over the bandwidth of interest. Such white noise has a random phase and a Rayleigh amplitude distribution as shown in Fig. 3.

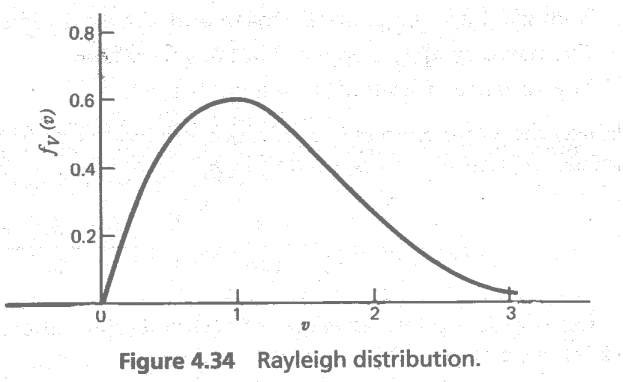

Fig. 3. Rayleigh Distribution (from Haykin [4])

But in a Leeson oscillator can the noise components truly independent? The output of an oscillator settles to be a constant amplitude signal, but it still has phase noise. This inevitably means that coupling is present between the noise components within the bandwidth of the oscillator. The coupling is caused by the amplitude limiting process in the oscillator whatever it is. What are the possible consequences of such coupling?

Can we consider that any one time one of these noise components can 'capture' the frequency of the oscillator?

Injection locking

Injection locking is control of the frequency and spectrum of an oscillator by a more stable external source having less phase noise [5]., [6]. See Fig. 4.

During the time that an oscillator frequency is stable we can regard the oscillator as being injection locked by its own fed back signal. This signal 'captures' the frequency of the oscillator.

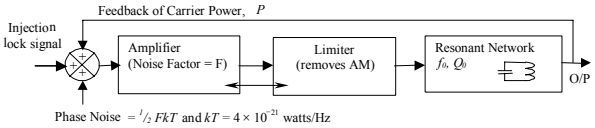

Fig. 4 Injection Locking of a Leeson Oscillator

An amplitude limiting process has to be present to avoid self-destruction of an oscillator. Limiting suppresses the sideband noise by 3dB relative to the carrier. In effect it removes the amplitude part of the noise sidebands. Fig. 5 illustrates this.

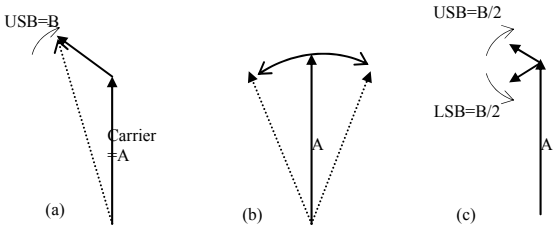

Fig. 5. Phasor Diagram of Limiter Action on 2 Signals A>B: (a) before limiting, (b) phasor trajectory after limiting,(c) sidebands formed by limiter USB=LSB=B/2.

Partial injection locking can be said to be chaotic. Then locking can occur at sub-harmonic of the difference between the injection and resonator frequencies. The resulting spectrum is shown in Fig. 6 for a 10MHz oscillator [6].

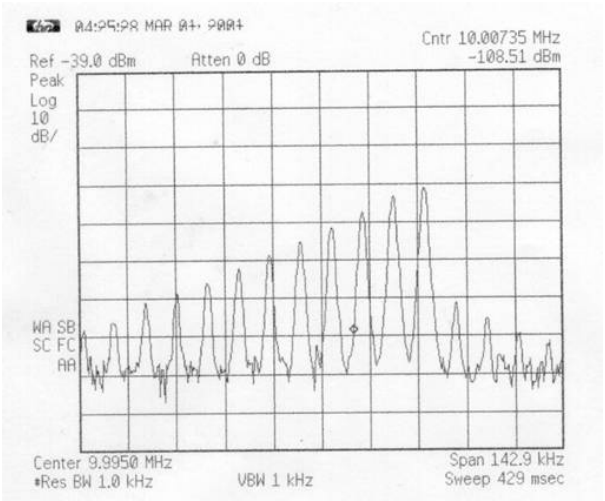

Fig. 6. Characteristic Spectrum of Partially Locked 10MHz Oscillator

The width of the straight line sloping segment of the envelope of the components is found to correspond to the open-loop bandwidth of the resonator.

Injection power	locking range	capture range
(dBm)	(kHz)	(kHz)
-10	282.25	153.08
-15	119.98	58.04
-20	75.908	46.538
-25	56.91	34.44

Fig. 7. Injection Locking of 2GHz Oscillator

The ratio of the locking range to the capture range depends on the excess loop gain available when the oscillator is starting up and the degree of non-linearity in the limiter.

An oscillator with a 'Hard Limiter' has a larger locking to capture ratio [6] and Figs, 7 and 8 contrast a 'hard' limiter with a 'soft' limiter. An injection locked oscillator with a 'hard' limiter tends to be more 'chaotic'.

Injection level	Locking range	Capture range
(dB)	(kHz)	(kHz)
-20	71.79	71.79
-25	41.19	41.19
-30	21.37	21.37
-35	8.78	8.78
-45	5.07	5.07
-50	2.79	2.79
-55	1.64	1.64

Fig. 8. Injection Locking of 10MHz Oscillator

III. FREQUENCY JUMPS

A frequency jump can be regarded as a cessation of oscillation at one frequency accompanied by an initiation of oscillation at a new frequency, presumed to be within the pass-band of the resonator.

But what is the trajectory of change from one frequency to another if we apply the constant waveform amplitude constraint that exists in the Leeson oscillator model?

We can however guess that the rate of change of frequency will be determined by the closed loop bandwidth 2α of the resonator. The time constant of this is $1/\alpha$ and this will typically amount to 100 to 100,000 seconds.

If the transfer from one possible oscillation frequency occurs at all it is extremely likely to be 'chaotic' but obviously with a very long time constant for the 'chaos'.

Chaotic Frequency Jumps

Chaos can occur if there are more than one resonant frequency modes and these are coupled together by a 'sufficient' non-linearity. The further requirement is that the total energy is kept constant (as it always is in an oscillator). Thus the conditions for chaos do appear to exist in any oscillator albeit constrained within a very small bandwidth.

With multi-resonator chaos the output frequency can be very stable for a long time and then suddenly change. When stable the system is said to be in a 'trap'. Fig. 7 shows chaotic 'traps'at the attractors in the phase plane of a chaotic system [7].

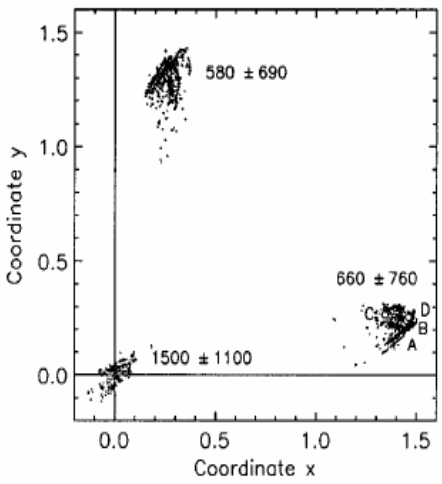

FIG. 7. Points of the chaotic attractor with distances smaller than $d=0.05$ from plane Π for noise amplitude $\sigma=0.03$ s^{-2}. A periodic orbit stable with very small noise only ($\sigma<10^{-6}$ s^{-2}) and period 2583.0 s is indicated by points $A-D$. The metrics chosen for Π and also for calculating distances is $g^i=(g^\varphi,g^\omega,g^{\nu_1},\ldots,g^{\nu_{12}})$ $=(1/2\pi,1/4,1,\ldots,1)$. The numbers indicate average recurrence times (in seconds) with standard deviations for the three regions around the three points chosen to define Π.

Fig. 9 Chaotic Traps at Attractor Points in Phase Plane (from Gassmann [7])

One can make a statistical assessment of how long any system will stay in one or more traps. But the moment of exit from a trap is only predictable for a short time before the system actually exits from the trap.

A large enough ensemble of clocks can detect the onset of chaos between a pair of modes or a frequency jump in any one oscillator. The probability of two clocks going chaotic at the same time must of course be taken into account.

But is there a way of enhancing the stability of a trap so that once in it the system stays in it? For example the time in the trap is in general a function of the naturally occurring noise level in the chaotic system. Can this be reduced sufficiently? Also could 'quantum' effects be used to avoid the chaos altogether?

Metastability.

Chaos is often characterised as an extreme sensitivity to initial conditions. In this respect 'metastability' is the same.

Metastability is normally regarded to be a property of digital flip-flop. There are two stable states in such a system. The 'metastable' point is where there is an equal probability that the system will move towards either of the two stable states ('flipped' or 'flopped'). The closer the initial conditions are to the metastable point the longer the metastable 'balance point' can last.

The initial error from the metastable point has a random value resulting from the sampling of random noise in the system, in this example at the input of the at the input of the flip-flop.

There is a direct relationship between the initial error *e,* the 'distance' *y* from the metastability point to the final state position and the time *t* taken to get there. In terms of $\sigma = 1/\alpha$ the time constant of the dominant 'pole' of the system the relationship is.

$$y = \varepsilon e^{\sigma t}$$

or

$$t = (1/\sigma)\, ln(y/\varepsilon)$$

The initial error ε in a flip-flop comes from the (Gaussian) thermal noise (FkTB) referred to the inputs of the flip-flop transistors, just as it is for the Leeson oscillator model.

An oscillator normally also starts up with an exponential increase in amplitude. Again this is similar to a flip-flop. So the starting up of an oscillation at a new frequency could be regarded as a recovery from a metastable state.

Experimental Confirmation of Metastability

Figure 10 shows the metastable state recovery time trajectories for two different types of flip-flops. At the top the flip-flop is the 'traditional' two transistor oscillator. At the bottom the flip-flop is made from standard off-the-shelf CMOS 'double-buffered' two input NAND gates. In both cases the flip-flops were triggered at a 5 kHz rate.

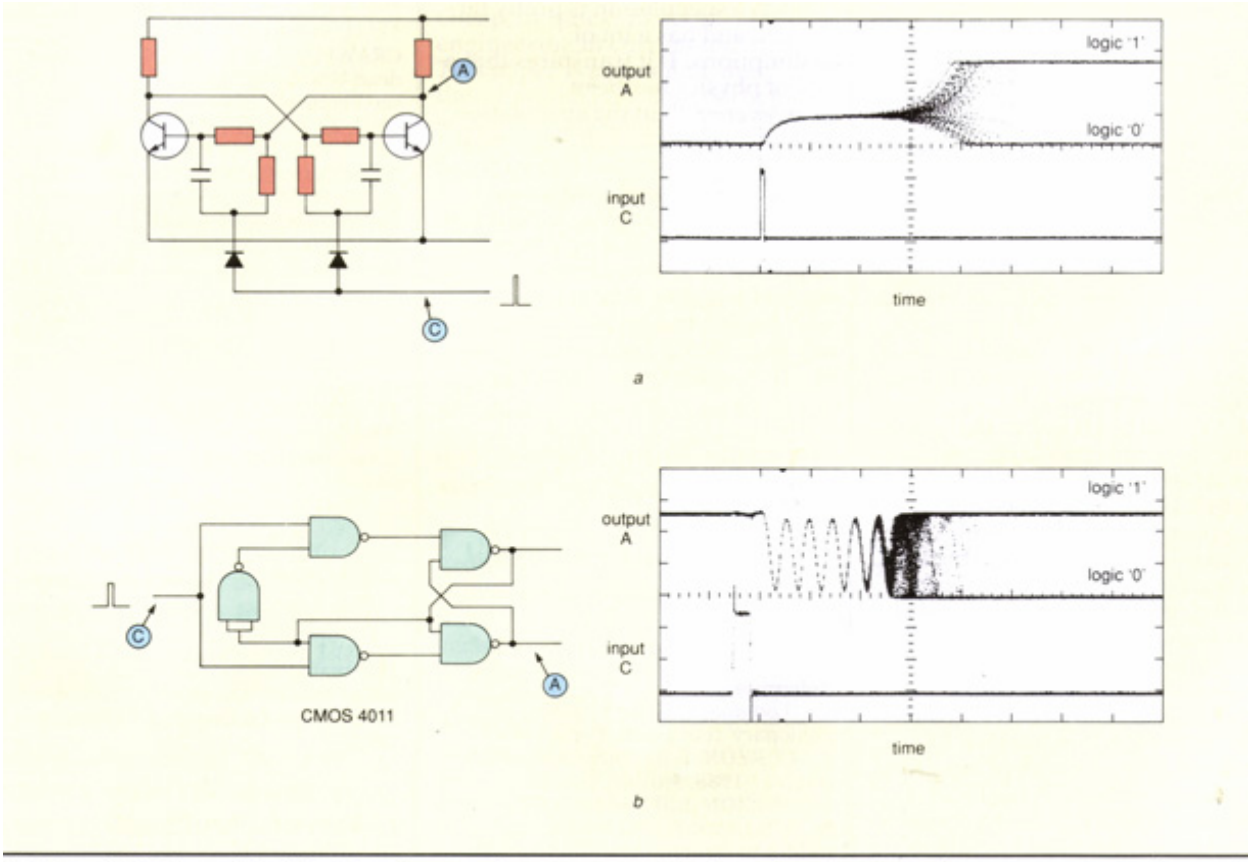

5 Metastability in any digital flip-plop takes several time constants to finally resolve: (*a*) circuit and successive time waveforms of basic flip-flop; (*b*) circuit and successive time waveforms of half D-type flip-flop

Fig. 10 Metastability Recovery Times Shown in Two Different Types of Flip-flop (from [8])

Not shown is a circuit that automatically adjusts the DC bias on the input signal so that the occurrence rate of the logic '0' and logic '1' states are approximately equal. This is achieved by taking negative feedback from the appropriate flip-flop output and filtering it with a long time constant to bias the input to the metastability point.

The existence, in the CMOS gate flip-flop, of several cycle of oscillation before recovery from the metastable state was a surprise. It is caused by the existence of 3 real poles for each of the two CMOS gates in the flip-flop. With positive feedback around the six equal open-loop poles we get a root locus as shown in Fig.11.

The consequence is potentially very serious for 'clock synchronisers'. For these, the occasional metastable state can never be avoided. Clock synchronisers should always be operated slowly enough for high probability of recovery by the time that the next clock pulse arrives.

The root locus of Fig. 11 was produced by the A2S2 simulator [9]. The oscillatory closed loop poles remain just on the imaginary axis poles (as in the Leeson model) until the real pole in the right hand plane has had time to build up exponentially to drive the output to either the '0' or'1' states. The Leeson feedback model can be seen to apply also in this case.

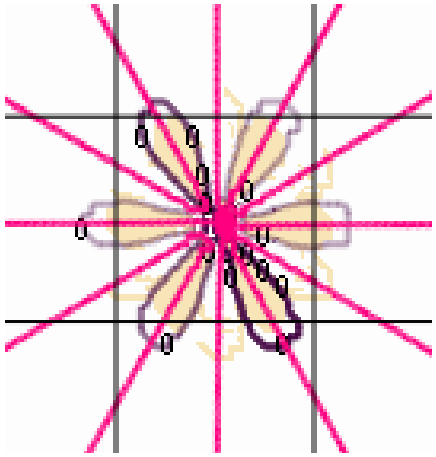

Fig. 11 Root Locus of Double Buffered Gate Flip-Flop having 6 poles total. The right-hand-plane starts at the vertical line to the right of the open loop pole cluster. The gain contours are for a gain just below the oscillatory gain, but sufficient for flip-flop action.

It confirms the general validity of the Leeson model and supports the assertion that it can be applied to any oscillatory system that has positive feedback.

In 1993 the as yet unpublished results shown in Fig 12 were obtained by M. J. Blewett and M. J. Underhill at the University of Surrey. Fig. 12 shows transistor flip-flop of Fig 10 being operated at 5 kHz rate corresponding to 432 million pulses a day for 4 days and 39 days respectively. The results show some possible signs of 'striations' at the longer recovery times. Striations would be expected if the bias voltage on the capacitors were quantised. However the observed distances between the striations correspond to a quantised charge on the capacitors that is many hundreds of time smaller than that caused by single electron charges. The tentative conclusion is that single electron charges do not exist in capacitors!

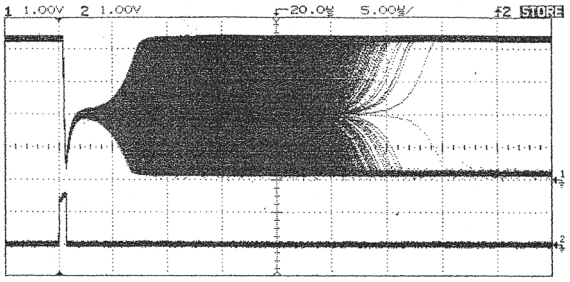

Fig. 2a Results after 96 hours (4 days)

1= Output
2= Set Pulse

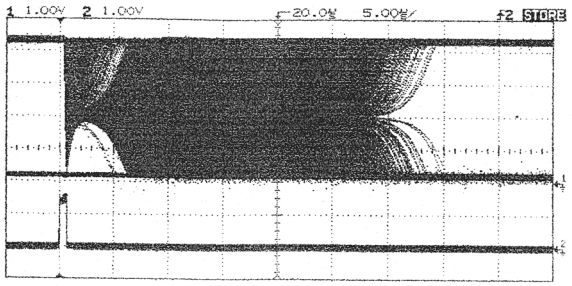

Fig. 2b Results after 39 days

1= Output
2= Set Pulse

Fig. 12 Flip-FlopMetastability Resolution Times for 5kHz clock rate

The conclusions from these experiments are:

1. The simple positive feedback model of an oscillator (Leeson's model) also can be used for metastability resolution in a flip-flop.
2. The recovery time from a metastable state can be more that twenty times the dominant system time constant.
3. This indicates recovery time from chaos in an oscillator could take up to twenty times the inverse of the oscillator closed loop half bandwidth.
4. There are no obvious quantum levels in the initial conditions that control metastability recovery time.
5. Thus quantum effects in an oscillator cannot be used to improve its stability within its Leeson bandwidth. or to control and reduce the occurrence of frequency jumps in an oscillator.
6. It is unlikely that charge in a capacitor is quantised into a whole number of electron charges.

FM Click Noise

In an FM receiver as In Fig. 13, having a limiting amplifier and IF filtering, impulse noise can become apparent when the input signal reduces towards the noise level [10] and [11].

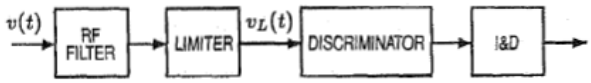

Fig. 1. System model for FSK receiver.

Fig. 13. FM Receiver (from Yavuz [11])

The FM 'clicks are caused by 2π radian phase jumps that can occur when the signal vector amplitude in Fig.15 is equal and opposite in phase to the instantaneous value of the noise component.

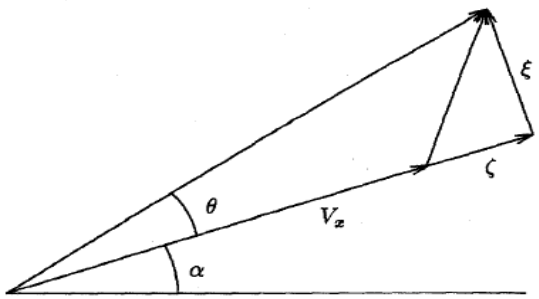

Fig. 2. Phasor representation of filtered modulated carrier and additive noise.

Fig. 14. Phasor Diagram for 2π radian Phase Jumps (from Yavuz [11])

The total phase excursion of a click is always taken to be 2π radians. One complete cycle of the clock is slipped in either a positive or a negative direction. The simple theory predicts equal probability of occurrence for positive or negative clicks. But a signal placed at one side of the bandwidth will increase the click rate

and produce more clicks of one sign than another. At the high side of the bandwidth more positive phase excursions are produced and vice versa for the lower side. This is shown in Fig. 15 [10].

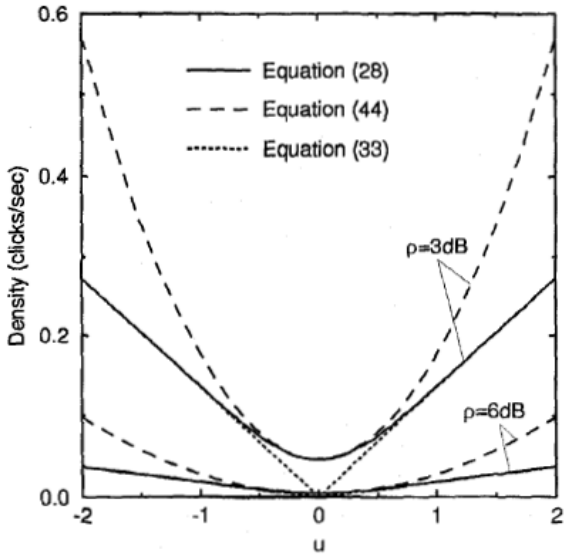

Fig. 3. Density of clicks vs. istantaneous frequency normalized to the effective filter bandwidth.

Fig. 15 Click rate versus Offset from Centre of Bandwidth [10]

FORESTIERI AND PRATI: FM CLICK STATISTICS IN THE PRESENCE OF PHASE NOISE

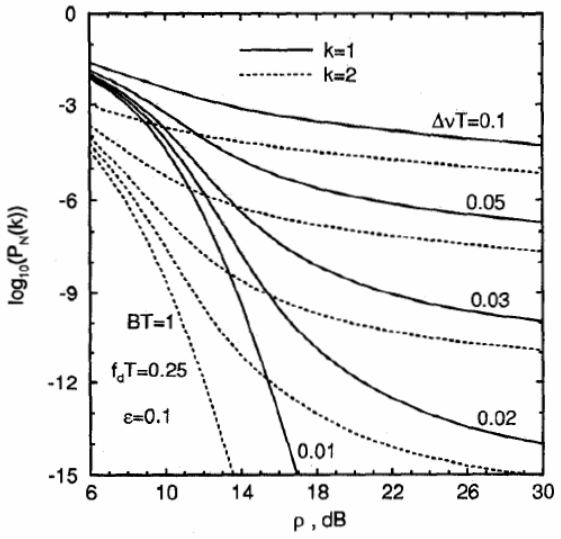

Fig. 4. Probability of clicks occurence vs. signal-to-noise ratio, for $k = 1, 2$, $BT = 1$, $f_dT = 0.25$, $\varepsilon = 0.1$ and various linewidths.

Fig. 16 FM Click Noise Occurrence as a Function of Signal to Noise Ratio and various Signal 'Linewidths' (as from [10])

The occurrence rate of these clicks is proportional to the (filter) bandwidth and decreases as the signal to noise ratio increases. [10], [11]. It also depends on the signal 'linewidth' as shown in Fig. 16.

Actual measurements have shown that the phase jumps are usually 'bi-modal' with two peaks and not the unimodal 'bell shaped curve usually assumed [11].

IV. PHASE JUMPS

Phase jumps in oscillators may be caused by the same mechanism that causes 'clicks' in FM demodulators. In a narrow bandwidth phase jumps occur slowly and can be regarded as a frequency excursion for a finite time. (By definition frequency is rate of change of phase.)

It is found that the clicks occur when the signal and noise components cancel to give a near zero resultant. The 'Rician' distributions of a signal in noise in Fig.17 For strong signals, with the higher values of α, the probability of cancellation to a low resultant amplitude is reduced. This implies a lowered click rate.

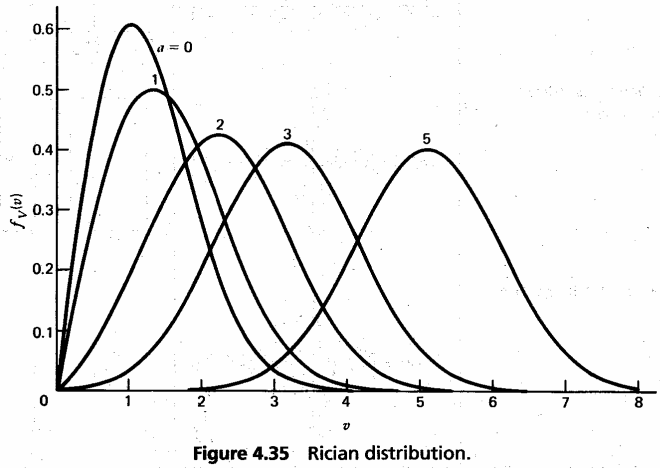

Figure 4.35 Rician distribution.

Fig. 17 Rician and Rayleigh (α=0) Noise Distributions (from Haykin [4])

Fig.18 shows the cancellation of two equal sinusoidal signals at different frequencies. The rate of change of phase of these is shown in Fig 19. The sign of the rate of change is shown alternating. The high positive and negative values correspond to large frequency excursion over a time or duration such that the total phase 'jumped' is always 2π radians. If one of the signals has significant phase noise the occurrence becomes randow but with equal positive and negative probabilities.

Note that the frequency excursions are well outside the bandwidth of a filter just containing the two signals.
Thus in a Leeson the frequency excursions are accompanied by a signal reduction that can stop the

oscillator at one frequency and let it build up at a new frequency within the oscillator closed loop bandwidth. In addition the possibility exists that the transfer from one frequency to another may be 'chaotic' for a substantial length of time beore full stability at the new frequency is achieved.

If the signal and noise are clipped and hard limited there is some expectation that the frequency changes may be more chaotic and less smooth.

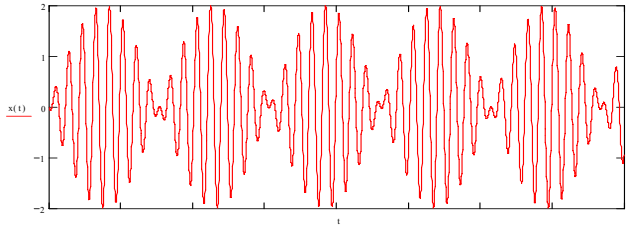

Fig. 18 Two Equal signals have Phase Jumps at the Amplitude Cancellation Points

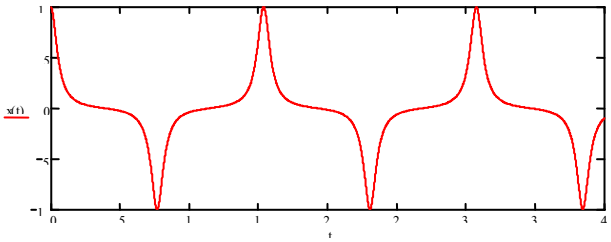

Fig. 19 Phase Excursions of Tweo Equal Signals

VI. CONCLUSIONS

1. Phase and frequency jumps could be a fundamental process in the Leeson oscillator model even if the resonator is perfectly stable.
2. It would appear that such error events cannot be 'cured' in the oscillator itself.
3. Reference to other stable sources of better stability as in a PLL with a stable reference could however detect and allow removal of such errors.
4. The question remains whether an ensemble of similar clocks all ultimately based on Leeson .oscillators can ever remove all such errors over an infinite time?
5. The click or phase jump occurrence, by analogy with the FM 'discriminator', is random but with a much longer average occurrence interval than the oscillator decay or build-up time.
6. "Metastability" occurs in partially triggered logic flip-flops. It can be "oscillatory" in its eventual resolution.
7. Metastability depends on a precise initial balance level that appears in practice to show no sign of (charge) quantisation.
8. Therefore do individual electrons exist in capacitors, or not?
9. Does this confirm the validity of the Leeson phase noise oscillator model?
10. Does it also provide a way to analyse phase jumps in oscillators?
11. Is there observable evidence for a phase jump process in any oscillator?
12. Is the process inevitable or can it be prevented?
13. What is the time profile of a phase excursion?
14. What are the consequences?

Acknowledgements

I would particularly like to thank. Mike Blewett, formerly of the University of Surrey, for obtaining the metastabily results used above.

REFERENCES

[1] F. Lehaye, P. Collins, P. Heroux, M. Daniels and J. Popelar, *Using the Canadian Active Control Systems (CACS) for real-time monitoring of GPS receiver external frequency standards,* ION-GPS 2001, (The Satellite Division of the Institute of Navigation 14th Technical Meeting), Salt Lake City, USA, September 11-14, 2001.

[2] D. B. Leeson, *A Simple model of feedback oscillator noise spectrum*, Proc IEEE, 54, No. 2, 1966, pp. 329-330.

[3] M. J. Underhill, *Demodulation of Noise Very Close To Carrier and Estimation of Total Jitter*, 19th EFTF, Besancon, France, 21-24 March 2005, pp. 400-404.

[4] S. Haykin, *Communication* Systems, John Wiley & Sons. 1994. ISBN 0-471-30584-7.

[5] M. J. Underhill, *Fundamental limitations of oscillator performance*, IEE Conf. Publ. 303, Frequency control and synthesis, 1989, pp 18-31.

[6] M. J. Underhill, N. Siripon, and N. Christophorou, *Determinationof the capture range and locking rangeof injection locked oscillators,* 15th EFTF, Neuchatel, Switzerland, March 2001, pp 232-236.

[7] Gassmann. *Noise-induced chaos order transitions,* Phys. Rev. E, **55**, 3, March 1997, pp. 2215-2221.

[8] M. J. Underhill, *The magic of marginal electronics*, IEE ECEJ December 1993, pp 359-367.

[9] M. J. Underhill, *The Noise and sppression transfer functions of the Anti-Jitter Circuit,* IEEE FCS and 17th EFTF, Tampa, Florida, USA, 20043, pp. 490-498.

[10] E. Forestieri and G. Prati, *FM click statistics in the presence of phase noise,* IEEE Trans. on Communications, Vol. 42, No. 2/3/4 February/March/ April, 1994 pp. 549-561.

[11] D. Yavuz, *FM click shapes,* IEEE Transactions on Communications, Vol. COM-19, No. 6 December, 1971, pp. 1271-1273.

Proceedings of the 20th EFTF, 2006

Chip Implementation of AJC Jitter Reduction Technology

Michael J Underhill* and James Brodrick†

*Underhill Research, Tandridge Lane, Lingfield. Surrey, RH7 6LL, UK
† Toric Limited, 63-71 Collier Street, London, N1 9BE
* Email: mike@underhill.co.uk
† Email: j.brodrick@toric .co.uk

The functions required for AJC jitter reduction technology have been assessed separately in a 3.5 micron 'proof-of-concept' (POC) CMOS chip. A simple AJC has been connected and shown to operate correctly and several improvements have been identified. In addition an experimental AJC has been simulated by a third party in 1.1 micron technology. Operation to over 1GHz was predicted and has been confirmed by the first results from a test chip.

1. INTRODUCTION

The Anti-Jitter Circuit (AJC), announced at EFTF 1996 has been progressively improved since then [1] to [12]. It is a feed-forward jitter cancellation device competing with the Phase-Lock Loop (PLL).

On an integrated circuit chip the performance of AJC technology can benefit from a number of advantages that are not available in discrete circuit AJC implementations. For example, current sources may be made with very low conductance and low noise. High conductance current sources may be made with very high output impedances and low 'Miller' capacitance. Low noise 'active' capacitors may be made on the chip. Low noise long time constant very high impedance low pass filter sections may be achieved using low capacitor values. Feedback gains may be tightly controlled if required. Presetting and 'Digital Feedback' Digital-to-Analogue Converters (DACs) are available with a low footprint. High source impedance charge pumps are available.

The performance benefits are: lower chip area, lower power consumption, higher maximum speed of operation, faster settling after a frequency jump (no loss of input pulses), lower suppression cut-off frequency, and lower internal AJC noise.

Toric Limited with Saul Research has produced a 0.35 micron CMOS test chip to assess these points. The chip is arranged so that each AJC block may be assessed separately. Also with switching and hardwiring it can implement a number of different AJC configurations. The recent results and conclusions from this chip are presented below.

In summary chip designs for operation above one GHz appear to be just feasible in 0.35 micron, promising pro-rata improvements with finer geometries.

II. SUMMARY OF AJC PRINCIPLES

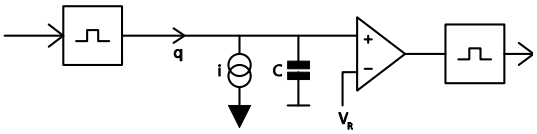

Fig. 1 The AJC Core

The core of an FFC consists of three blocks: a charge pump, an integrator, and a comparator.

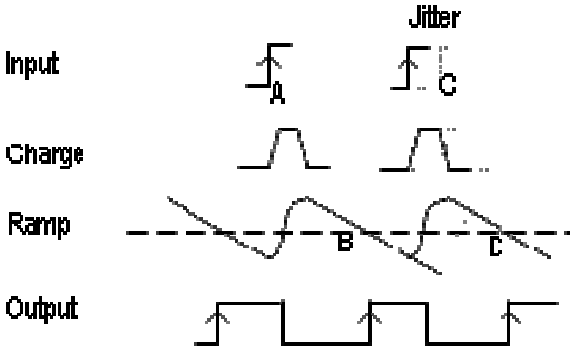

1. On each leading edge of the input clock waveform (A in Figure 2), the charge pump delivers a constant packet of charge *q* which causes a positive step in voltage equal to *q/C*.
2. The integrator consists of a capacitor *C*, connected to a constant-current sink.
3. The continuous current *i* drawn from the integrator capacitor balances the current from the charge pump over one cycle, ensuring that the net voltage drift is zero. The comparator switches when the integrator voltage crosses a reference DC level *VR* (B in Figure 2). This generates a rising edge, which becomes the new timing output of the AJC.
4. This edge can be used to trigger a monostable to produce a constant pulse width output.

5. When the input edge has jitter (C), the charge packet is delivered later in time. The time error is translated linearly into a DC offset of the ramp waveform.
6. A small delay in an input edge lowers the instantaneous value of the ramp waveform.
7. On the next cycle, the ramp waveform intersects VR sooner, and cancels the original time delay.
8. The output rising edge (D) occurs at the same instant, regardless of the amount of input jitter.
9. The jitter is largely cancelled.

III. POC CHIP DESIGN

Toric Limited with Saul Research has produced a 0.35 micron CMOS test chip to assess the AJC concept. Each (AJC) block in this 'Proof-of-Concept' (PoC) chip may be assessed separately. With switching and hardwiring a number of different AJC configurations can be implemented.

The Blocks in the chip are:

1. Two ring oscillator VCOs - to act as simple noise sources or in a PLL AJC combination
2. An input monostable based on gate delays.
3. An output (gate delay) pulse stretcher and with 'complementary' buffered outputs.
4. A fast main AJC comparator.
5. A pair of current (integrator discharge) sources
6. AJC (low-pass) filter components.
7. An optional 'Speed-up' time constant switching arrangement.
8. A 10 bit DAC current source to implement Digital Feedback (DF).
9. Two 'window' comparators to implement Digital Feedback (DF).
10. Two output buffers, direct and inverted, on the fast comparator output.

Fig. 3 shows a block diagram of the PoC chip with the pin accessible points identified.

The actual layout is shown in Fig. 4. Here it is obvious that it is the number of pads that is defining the chip size and not the are required for the AJC itself. The pads are 50 microns so the chip area is 650 by 650 microns or 0.4225 sq.mm.

The capacitors as expected take up the major part of the required area. The consequence is that the AJC has a very characteristic visual 'signature' on a chip.

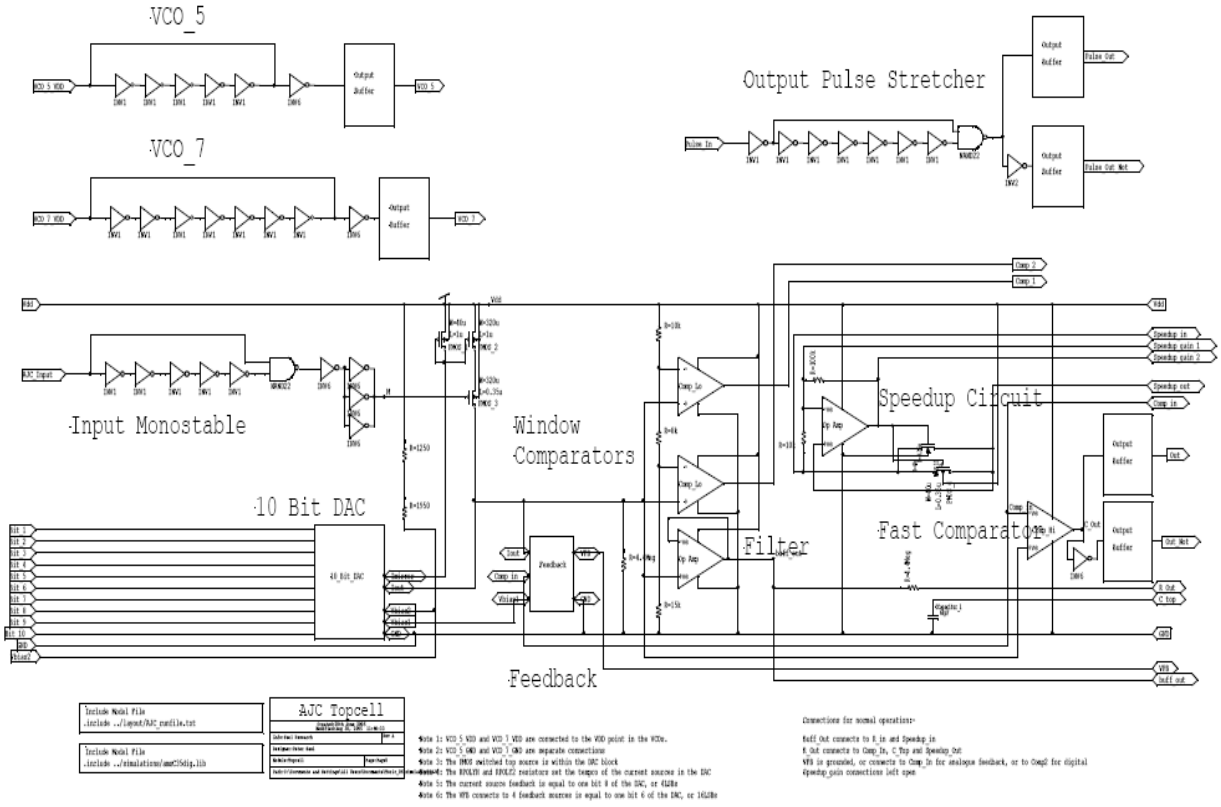

Fig3. The Toric AJC Proof of Concept (PoC) Chip By Saul Research (30 08 2005)

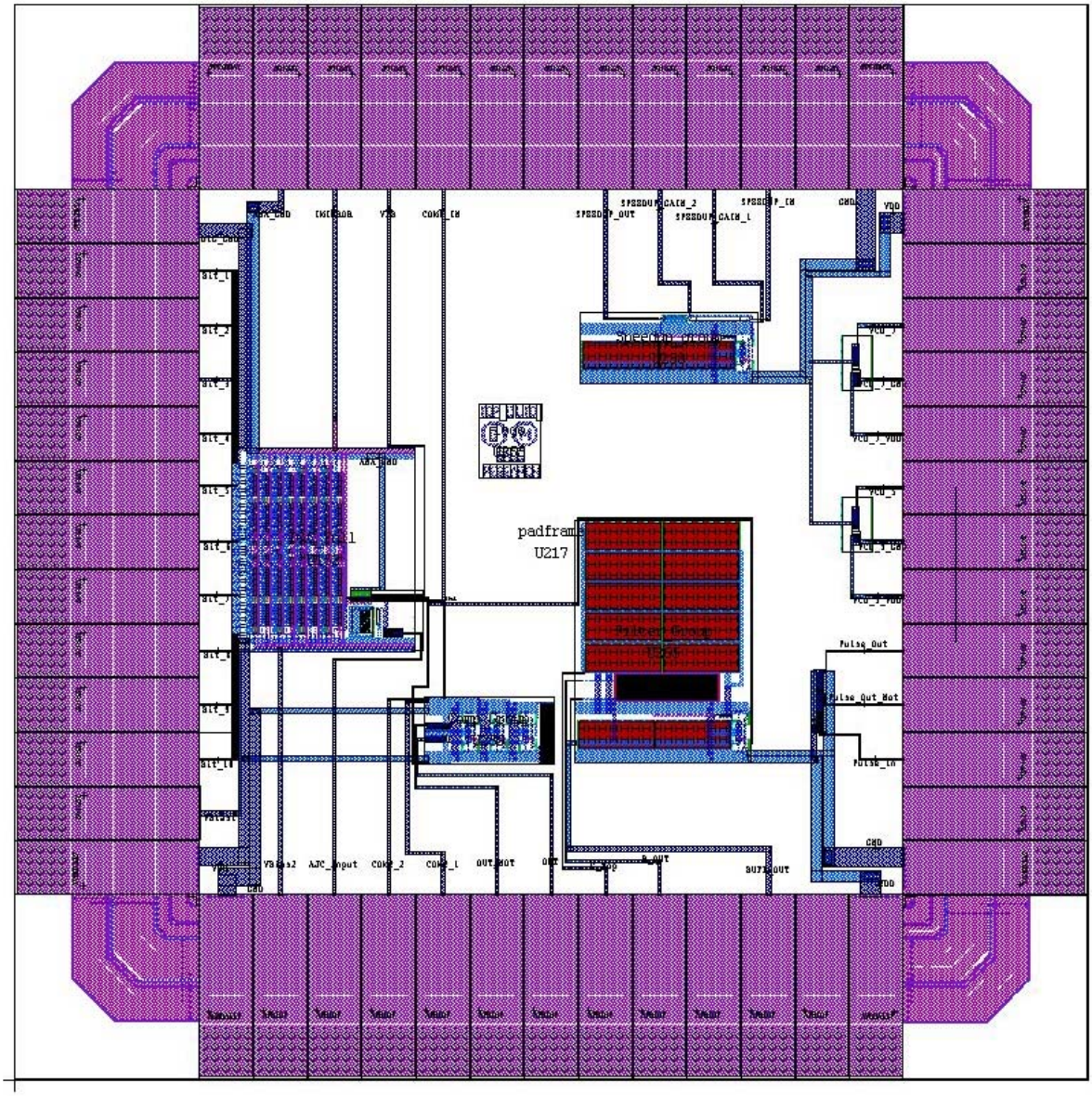

Fig. 4 Toric PoC Chip Layout

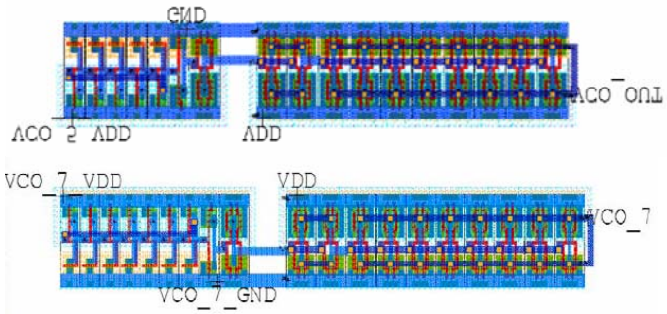

Fig 5. The Voltage Controlled Oscillators (above – 5 gates and below – 7 gates)

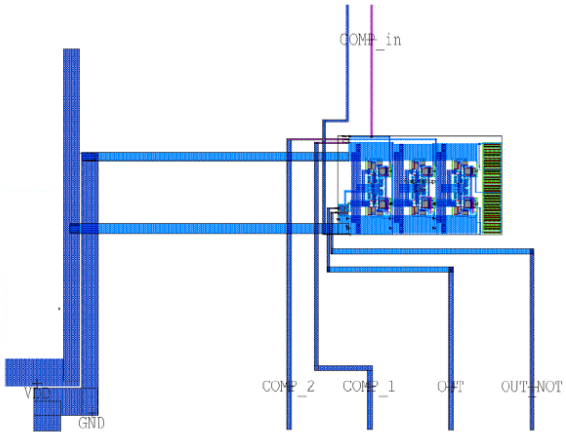

Fig6. The Comparator Group Including DF (Digital Feedback) Window Comparators

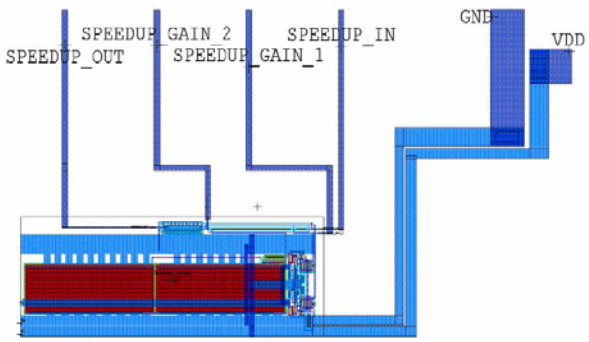

Fig 7. The Speed-up Circuit Layout

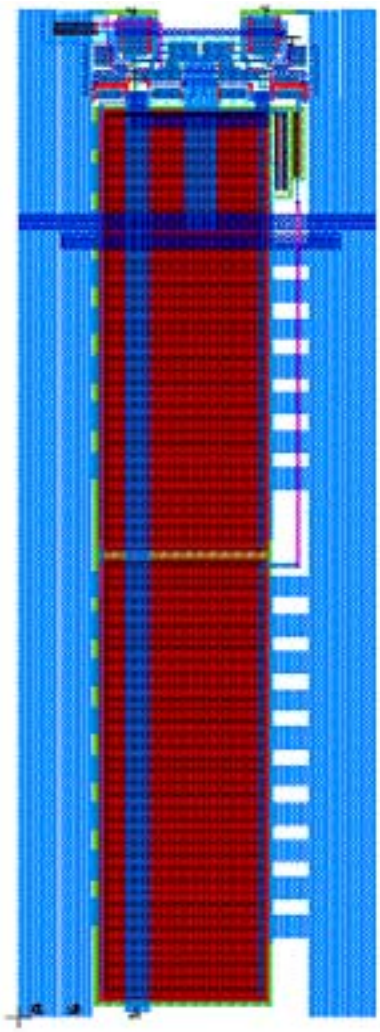

Fig 8. The Operational Amplifier Layout

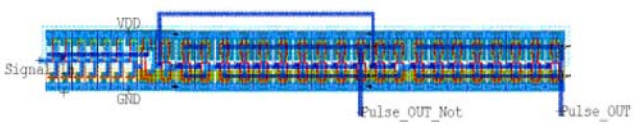

Fig 9. The Pulse Stretcher Layout

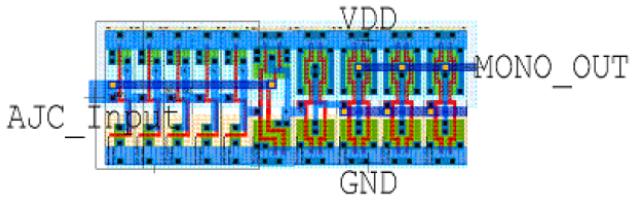

Fig 10. The Input Monostable Layout

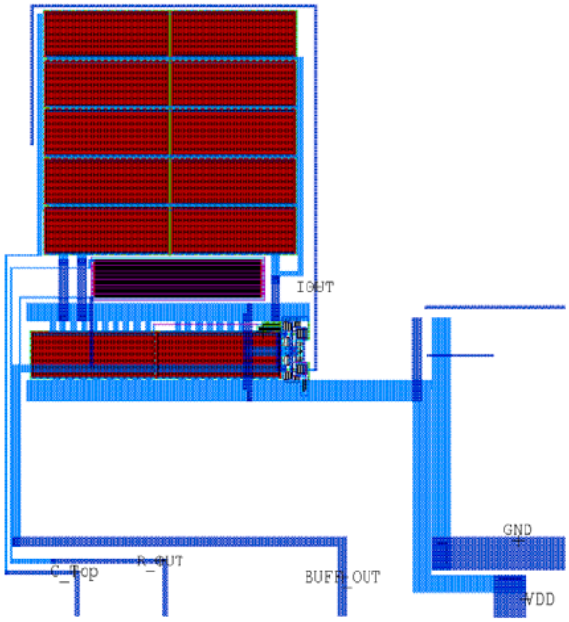

Fig. 11. The AJC Feedback Filter Layout

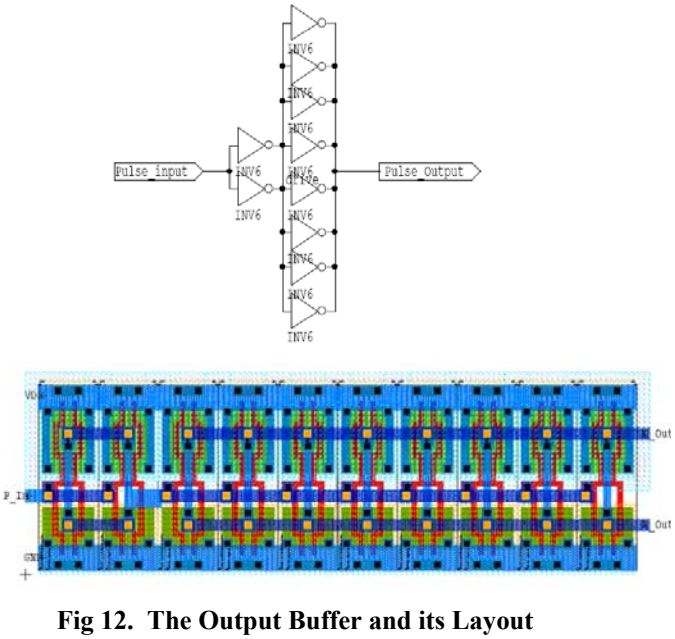

Fig 12. The Output Buffer and its Layout

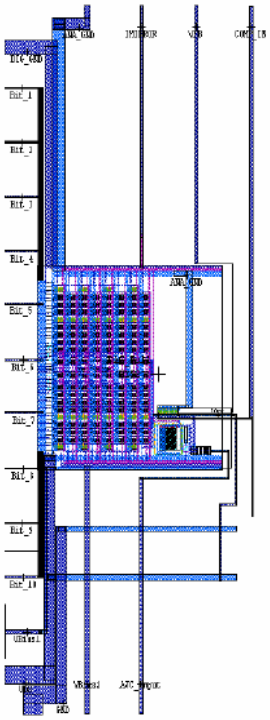

Fig 13. The DAC and Top Current Source

Figs 5 to 13 shown the various AJC blocks and these can easily be identified with the overall chip layout shown in Fig. 4. Fig.15 (Appendix) shows the type of lead frame used for the Toric PoC chip.

IV. MEASUREMENT OF AJC SUPPRESSION

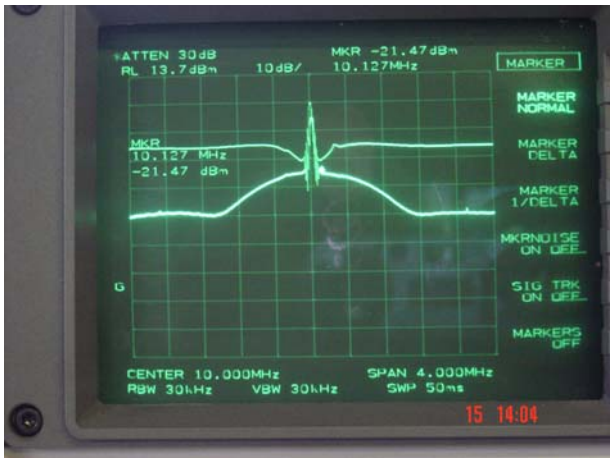

Fig 14. Measurement of AJC Suppression on an HP8552/3B Spectrum Analyser with Tracking Generator.

AJC suppression can be plotted against sideband frequency using the "Huddart method" [7]. The AJC is fed with a stable reference source. The tracking generator output of a Spectrum Analyser is added with the AJC output, with the tracking generator signal about 20dB down. The added signals are clipped and amplitude limited at the AJC input. The spectrum analyser plot of the AJC output is typically as shown by the lower trace in Fig. 14. In this example the stable reference source was at 10MHz. The lower plot shows AJC suppression against sideband frequency. In the past the reference 0dB level had to be obtained by a separate calibration process.

The upper curve is obtained by switching the output monostable to be triggered from 'noisy' edge of AJC comparator. (The comparator output signal can be 'inverted' in phase to achieve this.) The noise is increased by 6dB when the suppression is zero (approaching carrier).
The lower trace shows up to 18dB suppression on the normal AJC output, being the difference between the two curves.

V. RESULTS FROM POC AND CONCLUSIONS

1. The target of 1GHz AJC operation in 0.35µm CMOS has been achieved.
2. The ring oscillator VCOs operate up to 1.2GHz for 5 stages and 850MHz for 7 stages, both with 3:1 control ranges.
3. Operation at 3.3 to 4.7 volt rail voltage is possible.
4. The intrinsic phase noise is measured to be better than target of -120dBc/Hz.
5. In band noise is <105dBc/Hz.
6. The jitter suppression bandwidth at 1MHz did not meet the target of 20kHz, but reasons for this are have been established and can be addressed.
7. The footprint is less than 0.5 sq.mm which is well below the target of 0.72sq.mm.
8. Up to 24dB suppression can be achieved at lower frequencies decreasing to 6dB at the highest frequencies.
9. A conclusion is that the AJC is best suited to reduce cycle to cycle jitter for on chip reclocking.
10. A follow on 'Demonstrator Chip' incorporating DDS features is being planned.

REFERENCES

[1] M. J. Underhill and M. J. Blewett, *Spectral Improvement of Direct Digital Frequency Synthesisers and Other Frequency Sources,* Proc. 10th EFTF, Brighton, pp. 452-460, 5-7 March 1996.

[2] M.J. Underhill and M.J. Blewett, *Performance Assessment of a Delay Compensation Phase Noise*

and Time Jitter Reduction Method, Proc. 11th EFTF, Neuchatel, pp. 364-368, 4-6 March 1997.

[3] M.J. Underhill, S. Stavrou, M.J. Blewett and N. Downie, *The Anti Jitter Circuit for Low Spurious DDS Square Waves and Low Cost Fractional N Synthesis*, *Proc*. 12th EFTF, Warsaw, pp. 292-297, 10-12 March 1998.

[4] M.J. Underhill, *The Adiabatic Anti-Jitter Circuit*, Joint IFCS and 13th European Frequency and Time Forum, Besancon, pp. 611-614, 4-6 April 1999.

[5] M.J. Underhill, *The Adiabatic Anti-Jitter Circuit*, IEEE *Trans*. UFFC, Vol. 48, No. 3, pp. 666-674, May 2001.

[6] M.J.Underhill *Phase noise limits of the anti-jitter circuit and on-chip RC oscillators*, Proc. 14th EFTF, Torino, Italy, March 2000.

[7] M.J.Underhill, *The Noise and Suppression Transfer* Functions *of the Anti-Jitter Circuit*, Joint IFCS *and* 17th EFTF, Tampa, USA, 5-8 May 2003, pp. 490-498.

[8] M.J. Underhill, *Anti-Jitter Circuits, EF-AJC*, UK Patent *Application* #0416627.8, 26th July 2004.

[9] M.Underhill and P.Brown, *Estimation of Total Jitter and Jitter Probability Density Function from the Signal Spectrum*, Proc. 18th EFTF, Guildford ,UK, April 2004, pp. 502-508.

[10] M. J. Underhill and J. Brodick, The Performance of the Anti-Jitter Circuit with Enhanced Feedback ('EF-AJC'), Proc. 2004 IEEE FCS and Exposition, pp158-164. (2004 IEEE UFFC Joint 50th Anniversary Conference IFCS, Montreal, Canada, 23-27 August 2004).

[11] M. J. Underhill and J. Brodrick, *A Spice System Simulation Model for Phase-Lock Loops and Anti-Jitter Circuits,* 19th EFTF, Besancon, France, 21-24 March 2005, pp. 333-338.

[12] M. J. Underhill, *Demodulation of Noise Very Close To Carrier and Estimation of Total Jitter*, 19th EFTF, Besancon, France, 21-24 March 2005, pp. 400-404.

SSM P/N CQZ04405

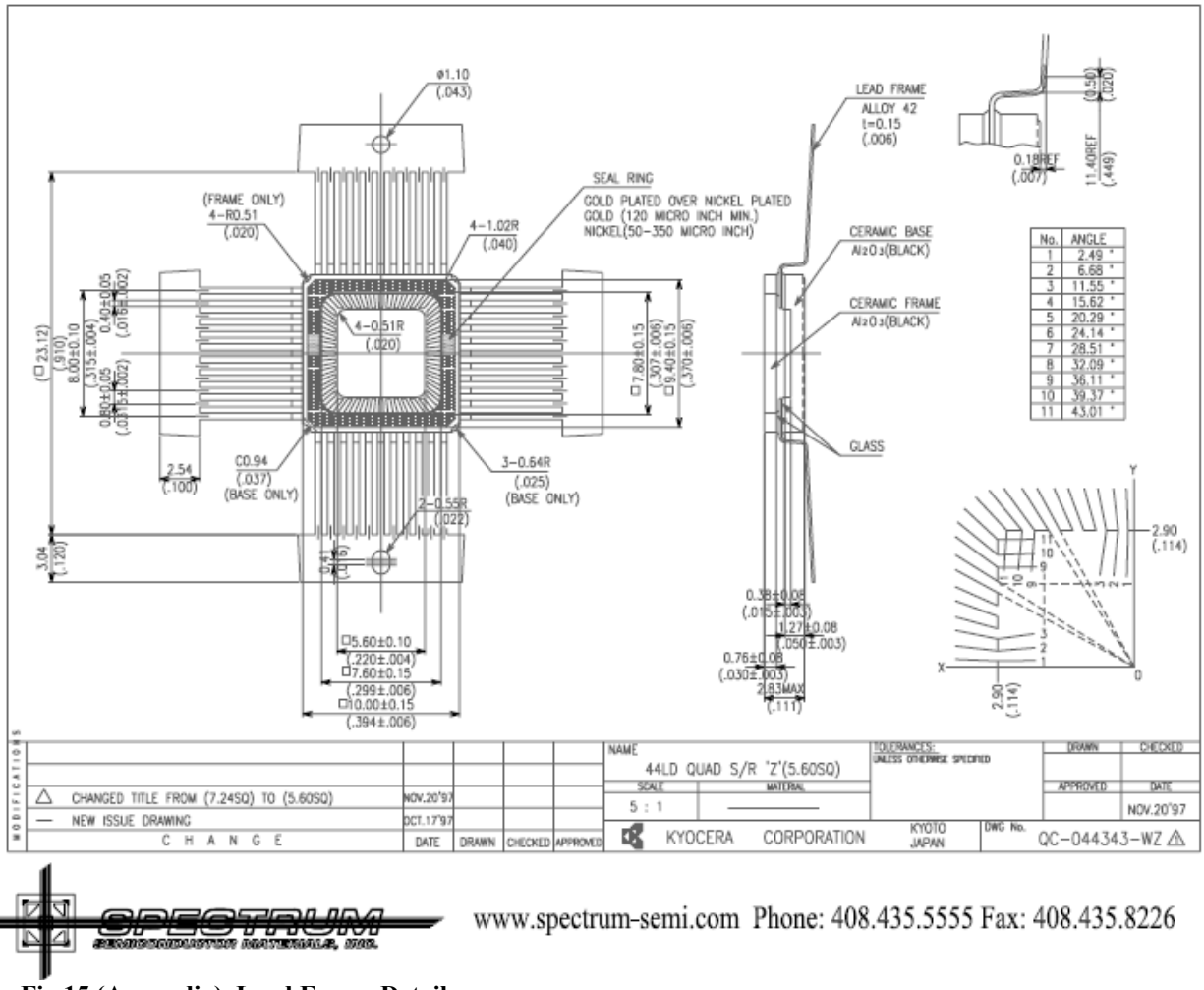

Fig 15 (Appendix) Lead Frame Details

Proceedings of the 20th EFTF, 2006

New frequency counting principle improves resolution

Staffan Johansson, staffan.johansson@pendulum.se
Pendululum Instruments AB, Box 20020, 16102 Bromma, Sweden

Abstract: Frequency counters have gone through several evolution stages in their design since their first appearance on the market:

Stage 1 until 70-ies	Conventional counting
Stage 2 1980-ies	Reciprocal counting (period measurement + inversion)
Stage 3 1990-ies	Interpolating Reciprocal Counting
Stage 4 2000-ies	Multiple Time Stamp Average Continuous Counting

This paper describes the theory and design of frequency counters, and analyses the improvements in the latest generation of frequency counters.

The newly introduced high-resolution CNT-90 Timer/Counter/Analyzer from Pendulum Instruments AB in Sweden is used as commercially available example of the latest design technology in this presentation.

The advantages of continuous time-stamping technique are discussed, for example regression analysis to reduce effects of measurement noise and to improve resolution to 12 digits for 1s of measuring time. Another example is the ability for seamless back-to-back measurements without missing any period, which is essential for theoretically correct calculation of Allan Deviation.

Keywords: Time-stamping, linear regression

1. Introduction

An ideal sine wave signal (carrier wave) $U(t) = A \cdot \sin(2\pi ft)$ has a constant frequency vs time behaviour, $f = f_0 = constant$. This means that the signal phase grows linearly with time:

$$\Phi(t) = 2\pi f_0 t + \Phi_0 \qquad [1.1]$$

The *mean* frequency of a continuous periodic signal over a certain *measurement time*, is illustrated in figure 1.

$$frequency\ (Hz) = \frac{number\ of\ complete\ cycles}{measurement\ time} \qquad [1.2]$$

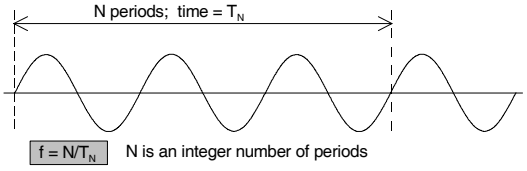

Figure 1. Definition of mean frequency

Even if the signal were assumed to be ideal, in the real world, it would be subject to noise processes and interference, which means that individual periods could vary. The concept of mean frequency involves integral numbers of counted signal cycles, at least one cycle. You cannot define a signals frequency by measuring a fraction of a cycle.

Real world signals do not have constant stable frequencies, not even clock oscillators as will be discussed in section 7. There could be modulated signals, frequency hopping signals, swept frequency signals, burst signals and much more. Then f is a function of time $f(t)$ and the phase function in [1.1] is expressed differently.

$$\Phi(t) = 2\pi f(t)t + \Phi_0 \qquad [1.3]$$

Please note that the concept of mean frequency may be useless for these types of signals. The average frequency over 80-channels WLAN using FHSS or the average of several burst cycles containing chirp radar frequency is not meaningful. Instead the challenge is to closely follow and represent the actual frequency over time $f(t)$ inside the burst or alternatively the statistical distribution of WLAN channels. This requires very fast and high-resolution measurements, found in very few frequency measurement devices today, one being the new CNT-90 Timer/Counter/Analyzer (Pendulum Instruments AB).

The rest of this paper will focus on frequency measurements on stable signals, where the concept of mean frequency is meaningful.

2. Conventional counters

Conventional counting was the first frequency counting method and these counters did not measure according to the definition of frequency above [1.2]. The conventional principle is to open an exact 1-second-gate and count the number of input cycle trigger events that occur during that second. The counting register contains the number of cycles counted during exactly one second, which is a sort of frequency (cycles/s). The precisely defined 1s gate-time is derived from a X-tal oscillator reference (usually a 10 MHz signal) with a good accuracy.

Gate time is *not* synchronized with the input signal. The uncertainty of the measurement is ±1 input cycle count, which means that the resolution is 1 Hz during a 1s gate time for *all* input signal frequencies. To allow measurements with a resolution other than 1 Hz, gate-times of a multiple (or a sub-multiple) of 1s are used. E.g. a gate time of 10 s will increase resolution tenfold and add one more digit to the read-out.

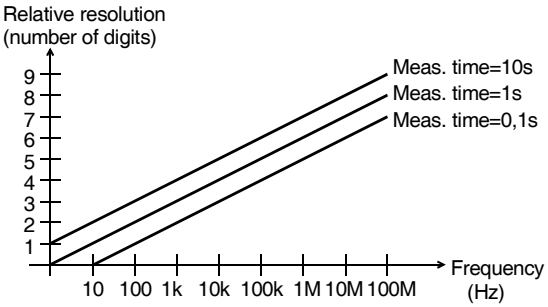

Figure 2. Resolution of a conventional counter is bad for low-medium frequencies and adequate for high frequencies only

3. Reciprocal counting

In the early 1980-ies, microcomputer based instruments started to use reciprocal counting. The input signal trigger, and not the internal oscillator, controls the gating of a multi-period average measurement. N input signal periods are counted during measurement time MT. They calculate mean cycle time $\overline{T} = MT/N$ and the *reciprocal* value; mean frequency $\bar{f} = 1/\overline{T}$.

Figure 3 shows the block diagram of a first generation reciprocal frequency counter. It contains two counting registers. One counts the number of input cycles and the other counts the clock pulses, to measure the time duration. Two synchronized main gates simultaneously control both counting registers.

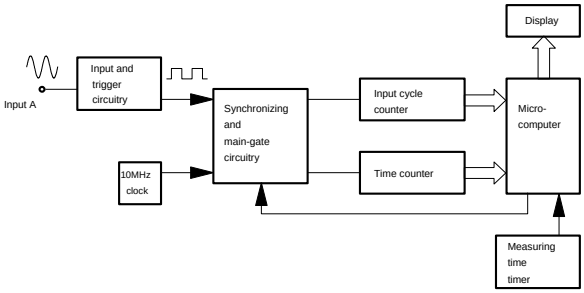

Figure 3. Block diagram for a reciprocal frequency counter

Unlike conventional frequency counters, the set measuring time is not an exactly defined gate time. The *desired* measuring time is set via the micro-computer, but the *actual* measuring time MT is synchronized to the input signal triggering. The measurement contains an exact number of input cycles. Thus the ±1 input cycle error is avoided. Truncation errors are now in the time count; i.e. ±1 clock pulse.

To obtain the mean frequency value, the following division is made:

$$frequency = \frac{Counted\ input\ \ cycles}{(Counted\ clock\ \ pulses) \times t_c} = \frac{N}{MT}$$

Where t_c is the time of one clock cycle

The relative resolution of the calculated result is: $resolution = \pm t_c / MT$ normally ± 100 ns$/MT$.

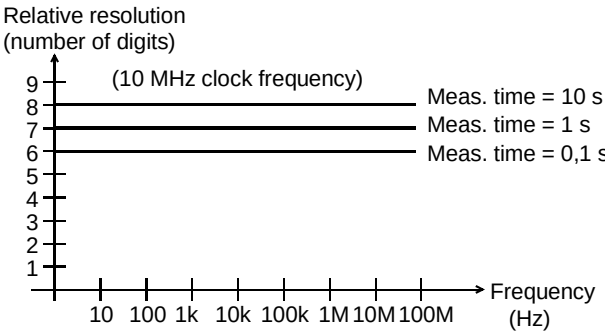

Figure 4. The relative resolution is independent of input frequency for a reciprocal frequency counter

To obtain a higher resolution, one could increase the clock frequency. E.g. a 100 MHz reference clock would give a relative resolution of ± 10 ns$/MT$, and thus one digit more in the displayed result, compared to a standard 10 MHz reference clock.

4. Interpolating reciprocal counting

The resolution of the 2:nd generation reciprocal counters is always $\frac{\pm 1 \ clock\ period}{Measurement\ time}$.

In the third generation of counters, resolution is improved by means of *analog interpolation* of the fractional clock pulse. Instead of just counting the clock pulse edges to determine the time between start and stop trigger, also the *fractional* clock pulse in the beginning and end of the measurement is captured.

Figure 5 shows the block diagram of an interpolating frequency counter, like the Pendulum CNT-85. Compared to the basic reciprocal counter (fig. 3) such a counter contain also two interpolators, one for the start trigger event and one for the stop event.

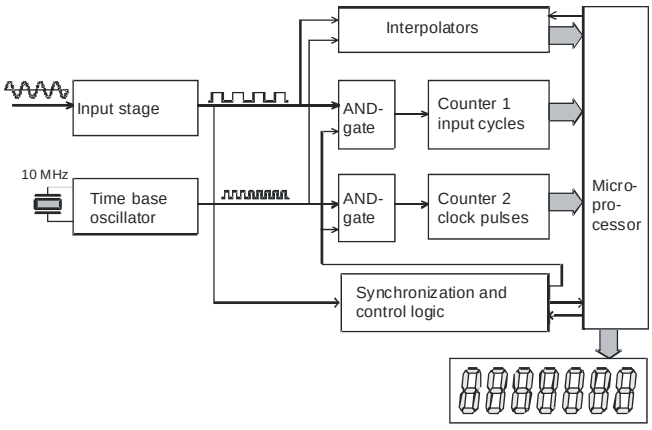

Figure 5. Block diagram for an interpolating reciprocal frequency counter

Figure 6 illustrates the interpolator's principle to capture the short fractional time between the start trigger and the following clock pulses, respectively the stop trigger and the following clock pulses.

The analog interpolator in figure 6 starts to charge the capacitor, with a constant current I, at the arrival of the trigger event and stops on the 2:nd following clock pulse. The capacitor is charged as $Q(t) = I \cdot t$. The voltage (U) over the capacitor is:

$$U(t) = Q(t)/C = (I/C) \cdot t \qquad [4.1]$$

The charge time (t) varies between 1 and 2 clock cycles, normally 100 to 200 ns. $U(t)$ also varies between U_0 (charge time is 1 clock cycle) and $2U_0$ (2 clock cycles). By selecting I and C ($U_0 = (I/C) \cdot t_c$), you can reach a convenient range (some Volts). The interpolator circuitry is duplicated for the stop trigger.

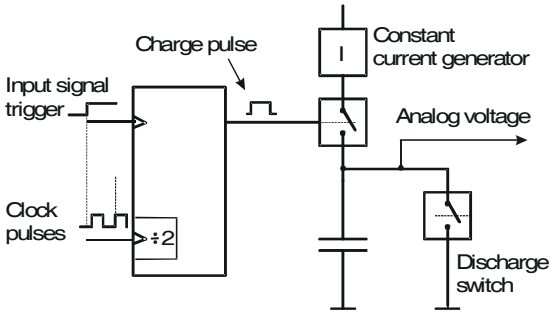

Figure 6. The basic principle of an analog interpolator is a time-to-voltage-conversion

The number of cycles counted N is as before an exact integer number, but the accuracy of the corresponding time (MT) is significantly improved. Instead of a resolution of ±1 clock cycle, as in classical reciprocal counting, the interpolated resolution is improved to less than a percent of a clock cycle. MT is calculated as $T_N + T_1 - T_2$, where T_N is the digitally counted time (number of clock cycles), T_1 is the interpolated fractional clock pulse between start trigger and following clock pulse and T_2 is the fractional clock pulse between stop trigger and following clock pulse.

The advent of interpolating reciprocal counters typically improved the time interval, or single period, resolution with 100 to 400 times, from 100 ns (single-shot) to 1 ns and below for a timer/counter with a 10 MHz time base oscillator. The Pendulum timer/counter model CNT-81 combines interpolation techniques with 10 times increased clock frequency (100 MHz vs. 10 MHz), and reaches 50 ps resolution as single period or time-interval resolution. This corresponds to a relative resolution in frequency measurements of $50\ \mathrm{ps}/MT$ (rms value), approx 1000 times improvement compared to typical 2:nd generation reciprocal counters ±100 ns/MT (limit value).

5. Continuous time stamping and statistical improvements

In reciprocal counters, with or without interpolation techniques, a frequency measurement has a defined start (= start trigger event), and a stop (= stop trigger event) plus a dead-time between measurements to read out and clear registers, do interpolation measurements and prepare for next measurement. *Continuous time stamping* changed that scenario.

In a *time-stamping counter*, the input trigger events, and the clock cycles, are continuously counted, without being reset. At regular intervals, pacing intervals, the momentary contents of the event count register and time count register is transferred to the memory. The read-out of register contents is always synchronized to the input trigger, so it is the trigger event that is time stamped. Each stored time stamp is also interpolated "on the fly" for improved resolution. The contents in the memory is thereafter post-processed.

A one-second frequency measurement in a fast processing counter could contain hundreds or thousands of paced time-stamped events, not just a start event plus a stop event. This makes it possible to use *linear regression using the least-squares line fitting* to further improve accuracy. See figure 7.

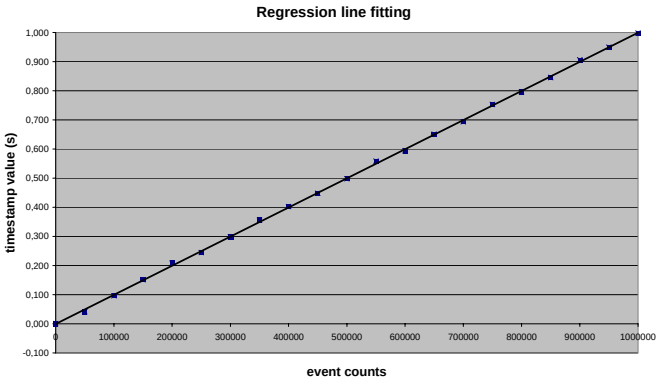

Figure 7. Time-stamping counters have a lot of intermediate time stamps of trigger events between the start and the stop of measurement

We have a series of data $\{x_k, y_k\}$, where x_k is the accumulated contents of the Event count register and y_k is the accumulated time at each sample point. The estimated frequency f^* is the inverse slope of the line that best fits this data set. Each x_k is an exact number, whereas each y_k has a basic uncertainty t_{RES}.

Our problem is to find the best estimate of the mean frequency over measurement time *MT*, by finding the straight line $y = a + b \cdot (x - x_0)$ using linear regression, where:

x = number of cycles counted (independent variable)
y = elapsed accumulated time (dependent variable)
a = time value for $x = x_0$ (first sample)

$b = f^{*-1} = T^*$, the slope of the regression line is the estimated mean period T^* or the inverse value of the estimated mean frequency f^{*-1}. From now on we will substitute the slope b with T^*.

From basic statistics we know that the regression line slope b (T^*) is calculated as:

$$T^* = \frac{n\sum x_k y_k - \sum x_k \sum y_k}{n\sum x_k^2 - \left(\sum x_k\right)^2} \qquad [5.1]$$

and that the variance of the slope b (or T^*) is

$$s^2(T^*) = \frac{s^2(y)}{\sum (x_i - \bar{x})^2} = \frac{s^2(y)}{s^2(x)\cdot(n-2)} \qquad [5.2]$$

$s(y)$ is the normal rms-resolution t_{RES} for a single time stamp, but what is $s(x)$? The independent variable X is assumed to have a linearly increasing distribution over the range x_0 to $x_0 + N$, with samples that are evenly spread over the full interval, that is

$$x_k = x_0 + \frac{kN}{n} \qquad [5.3]$$

For large values of n (number of samples), we can approximate the distribution with the continuous rectangular distribution with a density (probability) function of:

$$p(x) = \begin{cases} 0 & x < x_0,\ x > x_0 + N \\ 1/N & x_0 \le x \le x_0 + N \end{cases} \qquad [5.4]$$

For such a distribution we find

$$\mu = \int_{-\infty}^{+\infty} x p(x) dx = \frac{1}{N}\int_{x0}^{x0+N} x dx = x_0 + \frac{N}{2} \qquad [5.5]$$

$$\sigma^2 = \int_{-\infty}^{+\infty} (x-\mu)^2 p(x) dx = \frac{1}{N}\int_{x0}^{x0+N} (x - x_0 - \frac{N}{2})^2 dx = \frac{N^2}{12} \qquad [5.6]$$

Thus the standard deviation $s(x)$ for the discrete variable $X = \{x_k\}_0^n$ can be approximated to $s(x) \approx \sigma = \frac{N}{2\sqrt{3}}$ for large values of n

This approximation, plus the knowledge that $T^* = MT / N$ and $s(y) = t_{RES,}$ gives us the variance of the slope of the regression line from [5.2]:

$$s^2(T^*) = \frac{s^2(y)}{s^2(x)\cdot(n-2)} = \frac{1}{N^2}\cdot\frac{12s^2(y)}{n-2} = \frac{T^{*2}}{MT^2}\cdot\frac{12t_{RES}^2}{n-2} \qquad [5.7]$$

which finally leads us to the *relative* period or frequency uncertainty:

$$\frac{s(T^*)}{T^*} = \frac{s(f^*)}{f^*} = \frac{2\sqrt{3}\cdot t_{RES}}{MT\cdot\sqrt{n-2}} \qquad [5.8]$$

Using linear regression analysis (least square line fitting), gives a better estimate than just using the two end points for calculation and improves the relative resolution of the estimated frequency ($\Delta f/f^*$) from $\frac{\sqrt{2}\cdot t_{RES}}{MT}$ to $\frac{2\cdot\sqrt{3}\cdot t_{RES}}{MT\cdot\sqrt{n-2}}$, where:

t_{RES} = individual timestamp uncertainty

MT = Measuring Time

n = Number of event/timestamp value pairs used in the calculation.

The improvement in resolution between the two methods is thus:

$$\frac{2\cdot\sqrt{3}}{\sqrt{2}\cdot\sqrt{n-2}} = \frac{\sqrt{6}}{\sqrt{n-2}} \approx \frac{2.45}{\sqrt{n}}, \text{ for n>>2.} \qquad [5.9]$$

What if n is small, lets say $n = 6$? Then the approximation of a continuous rectangular distribution is no longer correct, and the standard deviation needs to be calculated based on discrete samples, which can be shown to give better resolution improvement than the approximation [5.9], for small values of n.

Example:

In the Pendulum model CNT-90, that uses the linear regression resolution improvement method, the random uncertainty is:

$$\frac{2\sqrt{3(t_{RES}^2 + (trigger\ error)^2)}}{MT\cdot\sqrt{n-2}} \times Frequency\ or\ Period \qquad [5.10]$$

t_{RES} = 70 ps and $n = \frac{800}{MT}$.

Trigger error is the effect of superimposed noise on the input signal, which can be neglected for ideal square wave signals. If we assume no contribution from trigger errors and a MT of 1s (n=800), we get a relative resolution of:

$$\frac{2\sqrt{3}\cdot 7\cdot 10^{-11}}{1\cdot\sqrt{798}} \approx 8.6\cdot 10^{-12}$$

The CNT-90 can also use traditional frequency calculation (using start/stop only), with the random uncertainty of:

$$\frac{\sqrt{2(t_{RES}^2 + (trigger\ error)^2)}}{MT} \times Frequency\ or\ Period \qquad [5.11]$$

which would give for MT = 1s, a relative uncertainty of $\sqrt{2}\cdot 70\text{ps}/1\text{s} \approx 1\cdot 10^{-10}$

The random uncertainty in this example is affected as predicted in [5.9] with the factor of $2.45/\sqrt{n-2} \approx 0.086$. Resolution is thus improved from 1E-10 (start-stop) to 8.6E-12 (regression).

The CNT-90 counter has an automatic mode, where the regression line fitting is executed at measuring times ≥200 ms and the number of samples used in the calculation are gradually reduced as measuring time increases $\left(n = \frac{800}{MT}\right)$. This gives the following resolution curve for CNT-90, see figure 8, where the dashed line is the traditional start-stop method. The resolution is improved for measurement times MT up to approx 100s and at 1s measuring time the improved resolution is typically 6E-12.

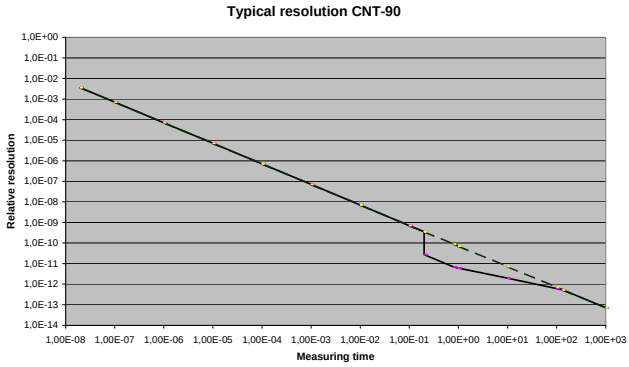

Figure 8. Resolution of the continuously time stamping counter CNT-90. Resolution improvement via linear regression occurs from measuring times from 200 ms up to 100s (auto mode)

6. Comparison of linear regression and traditional start-stop methods

One might believe that linear regression always is superior to traditional start-stop type of frequency measurements. But there are some limitations.

One obvious draw-back is that this post-processing of hundreds of sample data is time consuming, even if the raw data collection is fast. That means that the measuring speed of the frequency counter is reduced.

Linear regression is very useful, to reduce *random* noise in the measurement process, whether this noise is internally generated in the measuring device or externally added to the measurement signal. This method also assumes that the best fit is a *linear* approximation, that is a constant frequency during the measurement time *MT*, only subject to random noise, but without drift or intentional modulation.

A frequency source with a frequency drift, can be described as:

$$f(t) = f_0 + f_d(t) \qquad [6.1]$$

f_0 is the start frequency value

$f_d(t)$ is the frequency drift over time, with mean value ≠ 0 Hz

If $f_d(t)$ has a *linear* drift with time, then $f_d(t) \quad d \quad t$, where d is the frequency drift rate (Hz/s). A linear drift during the measurement would result in an accumulated phase $\phi(t)$ vs time relation that is expressed as:

$$\Phi(t) = 2\pi f_0 t + \pi d t^2 + \Phi_0 \qquad [6.2]$$

Figure 9 shows an example with an exaggerated frequency drift, according to [6.2]. This is obviously a 2:nd order function and should ideally be approximated with a 2:nd order polynomial and not a 1:st order straight line.

The main advantage of the linear regression method is to reduce the influence of noise from the measurement process and superimposed random noise on the test signal, and thus increase resolution.

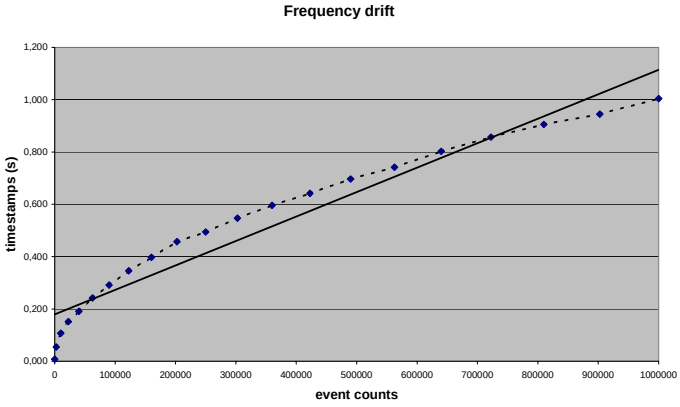

Figure 9. A regression line does not improve resolution if there is a frequency drift

Please note that the linear regression method only can improve the *frequency* resolution which contains several trigger events during the measurement. For single-shot *time interval* measurement it is the basic resolution of the traditional start-stop measurement t_{RES} that sets the limit.

Finally we can conclude that the *continuous timestamping* is the key to, and a prerequisite for, the regression analysis. This method is not possible in the 2:nd or 3:rd generation counters.

Continuous timestamping has another advantage, when it comes to characterizing the short-term stability of stable oscillator clocks. The dominating tool for this characterization is the calculation of *Allan Variance* (*AVAR*) and the *Allan Deviation* (*ADEV*), where $ADEV = \sqrt{AVAR}$.

The calculation is performed via a number of back-to-back (zero-dead-time) frequency measurements over a defined measurement time τ. For theoretically correct calculation of AVAR, to avoid dead-time between measurements, the continuous timestamping is also a prerequisite. Allan Deviation will be discussed in next section.

7. Allan Deviation and continuous time stamping

A stable clock oscillator has a frequency vs time characteristic that can be described as:

$$f(t) = f_N + f_{offs} + f_d(t) + f_r(t) \qquad [7.1]$$

f_N is the nominal frequency

f_{offs} is the initial frequency offset from nominal (calibration uncertainty)

$f_d(t)$ is the frequency drift over time (long term), with mean value ≠ 0 Hz

$f_r(t)$ is the random variation (short term stability), with mean value = 0 Hz

Typical clock oscillators, $f_d(t)$ have a non-linear drift over very long time periods (years), but for shorter periods (days, weeks) we can assume a linear drift with time, that is

$$f_d(t) \cong Df_N t \qquad [7.2]$$

where D is the fractional frequency drift rate and is assumed to be a constant.

All continuous periodic signals can be regarded as a sum of sine wave signals, so let us have a look at the relation between frequency, phase and time in a sine wave signal.

A continuous sine wave with constant amplitude *A*, can be expressed as $U(t) = A\sin\Phi(t)$, and its momentary or instantaneous frequency *f*(*t*) is expressed as:

$$f(t) = \frac{1}{2\pi} \cdot \frac{d\Phi(t)}{dt} \qquad [7.3]$$

Assuming that the frequency drift is linear with a constant drift rate, we can now combine [7.1], [7.2] and [7.3] to express the total phase of a sine wave signal in terms of the various frequency components. The term φ(*t*) is the *random* phase variation causing short-term frequency instability $f_r(t)$.

$$\Phi(t) = 2\pi(f_N + f_{offs})t + \pi Df_N t^2 + \varphi(t) + \Phi_0 \qquad [7.4]$$

The *fractional* random frequency deviation from the nominal value is commonly denoted *y*(*t*), where:

$$y(t) = \frac{f_r(t)}{f_N} \qquad [7.5]$$

The fractional random frequency deviation is:

$$y(t) = \frac{f_r(t)}{f_N} = \frac{1}{2\pi f_N}\frac{d\varphi(t)}{dt} \qquad [7.6]$$

And it is this random variable that is used to characterize the *short-term stability* of oscillators. Characterizing a stable oscillator includes measurement of all frequency components, nominal, offset, drift and short-term stability. However, measurement of frequency offset and drift can be made in a reasonably straightforward way, by applying a normal frequency measurement over sufficiently long measurement time. The random uncertainty of any frequency counter always improves with measurement time.

Measurement of short-term stability is more challenging, because you need to combine high-resolution measurements with short measurement times. The *Allan Deviation* or *Root Allan Variance* is the commonly accepted method for calculation of the short-term clock stability in the time domain. The common measure is Allan Deviation, which is expressed in Hz and not Hz^2 as is the case for AVAR.

$$ADEV = \sqrt{AVAR} = \sigma_y(\tau)$$

We have seen in [7.6] that the random phase variation $\varphi(t)$ causes the random frequency variation *y*(*t*). The random phase variation can in a similar way also be expressed as a *random time deviation*, which is useful for the analysis of Allan Deviation:

$$x(t) = \frac{\varphi(t)}{2\pi f_N} = \frac{T_N \cdot \varphi(t)}{2\pi} \qquad [7.7]$$

The random time variation *x*(*t*) at times $t = k \cdot T_N$ is a measure of the deviation between actual (noisy) signal relative to the ideal signal ($\bar{x}(t) = T_N \cdot \bar{\Phi}(t)/2\pi$) at the zero-crossings of the signal.

A true instantaneous frequency $f(t_0)$ or instantaneous fractional frequency $y(t_0)$ at time t_0 is not an observable quantity in practice, unlike e.g. the instantaneous phase $\phi(t_0)$. The measurement of frequency at start time t_k is always performed as an average value over a certain measurement time (τ) in all measurement equipment.

$$\bar{y}_k(\tau) = \frac{1}{\tau}\int_{t_k}^{t_k+\tau} y(t)dt \text{ or}$$

$$\bar{y}_k(\tau) = \frac{\varphi(t_k+\tau) - \varphi(t_k)}{2\pi f_N \tau} = \frac{x(t_k+\tau) - x(t_k)}{\tau} \qquad [7.8]$$

The Allan Variance is defined as:

$$AVAR = \sigma_y^2(\tau) = \frac{1}{2}\left\langle (\bar{y}_{k+1}(\tau) - \bar{y}_k(\tau))^2 \right\rangle \quad [7.9]$$

The Allan Variance AVAR is an estimate of the variations of a clock frequency over a given measurement time (τ) from one averaging period to the next. An Allan Deviation calculation should in theory be made over an infinite number of samples, each frequency sample being measured back-to-back to the previous, without any dead-time between samples. In practice there are no indefinite measurement periods, and the AVAR for a finite number of samples N can be expressed as:

$$AVAR = \sigma_y^2(\tau) \approx \frac{1}{2(n-1)} \sum_{k=0}^{k=n-1} (\bar{y}_{k+1}(\tau) - \bar{y}_k(\tau))^2 \quad [7.10]$$

Since short-term instability can be expressed arbitrarily as frequency, phase or time deviation [7.8], let us look at the AVAR expressed as random time deviation instead of random frequency deviation.

$$\sigma_y^2(\tau) \approx \frac{1}{2\tau^2(n-1)} \sum_{k=0}^{k=n-2} (x(t_k + 2\tau) - 2x(t_k + \tau) + x(t_k))^2 \quad [7.11]$$

This way of calculating Allan Variance is suitable for time stamping counters, with pacing period τ, because $x(t_k) = x(t_0 + k \cdot \tau)$ is simply the timestamp of the signal's zero-crossings, sampled every τ seconds, during the total measurement duration $n\tau$. A counting technique based on continuous time-stamping will also automatically lead to *zero-dead-time frequency measurements*, which is according to the underlying theory and definition. The CNT-90 Timer/Counter/Analyzer from Pendulum Instruments operates in this mode, enabling correct ADEV measurements and calculation.

Traditional counters, using start-stop frequency measurements over measurement time τ, will always cause a dead-time between measurements. No matter how short this dead-time is, it will be present with at least one cycle, due to the inherent counter design.

Figure 10. The CNT-90 Timer/Counter/Analyzer from Pendulum Instruments AB

References

[1] Enrico Rubiola, On the measurement of frequency and of its sample variance with high-resolution counters, arXiv physics/0411227 v2 31 Dec2004

[2] Stefano Bregni, Synchronization of Digital Telecommunications Networks, John Wiley and Sons Ltd 2002, 203-272

[3] Hewlett-Packard, Application Note 1289, The Science of Timekeeping, Hewlett-Packard 1997

[4] Pendulum Instruments AB, CNT-90 Timer/Counter/Analyzer User's manual, rev 2 2005

Author Biography

Staffan Johansson, born 1948, achieved his M.Sc. degree in Applied Physics at the Royal Institute of Technology (KTH) in Stockholm, Sweden in 1973. He has been active in the Test & Measurement business since 1981, when he joined the Philips development centre in Stockholm, for counters and pulse generators. Pendulum Instruments AB is a spin-off company from these Philips T&M activities (1998).

Staffan Johansson has made several international presentations and seminars in the field of counter technology, and is now responsible for Marketing, Strategic Product Management and New Product Definitions in the company.

Proceedings of the 20th EFTF, 2006

Phase noise inter-laboratory comparison preliminary results

P. Salzenstein[1], F. Lefebvre[2], R. Barillet[3], J. Čermak[4], W. Schaefer[5], G. Cibiel[6], G. Sauvage[7], O. Franquet[8], O. Llopis[9], F. Meyer[10], N. Franquet[1], X. Vacheret[1], A. Kuna[4], L. Šojdr[4], G. Hejc[5] and S. Gribaldo[9]

[1]*FEMTO-ST, CNRS, Associated to LNE, 32 av. Obs., F25044 Besançon Cedex, France*
Phone: +33(0)381853974 Fax: +33(0)381853998
[2] *OSCILLOQUARTZ, rue des Brévards 16, CH-2002 Neuchâtel 2, Switzerland*
[3] *Observatoire de Paris, CNRS, LNE-SYRTE, Bât B, 61 av. Obs., F75014 Paris, France*
[4] *Czech Academy of Science, Dpt of Standard Time & Frequency, Chaberska 57, 18251 Praha 8, Czech Republic*
[5] *TimeTech GmbH, Curiestrasse 2, D70563 Stuttgart, Germany*
[6] *CNES (Centre national d'Etudes Spatiales), 18 av. E. Belin, F31404 Toulouse Cedex France*
[7] *AEROFLEX, 5 Place du Général De Gaulle, F78990 Elancourt, France*
[8] *AR Electronique, rue du Bois de la Courbe, F25870 Châtillon-le-Duc, France*
[9] *LAAS CNRS, 7 av. du Colonel Roche, F31077 Toulouse France*
[10] *Observatoire de Besançon, CNRS, Associated to LNE, 41bis av. de l'Obs., BP1615, F25010 Besançon, France*

[1]*Electronic address:* patrice.salzenstein@femto-st.fr

ABSTRACT

Some phase noise benches used and developed by different research and commercial laboratories have to be tested. The problem is not to compare the performances of several oscillators, but to compare and to make an evaluation of the uncertainties, and of course, to compare the resolution and the reproducibility of the measurements, which are of interest for manufacturers. This comparison allows us to determine the ability to get various systems traceable together in order to increase the trust that one can have in phase noise measurements. Standards to be characterized during this comparison are 5 MHz, 100 MHz and microwave commercial oscillators. Obtained spectra can be affected by the
Environmental conditions: temperature, hygrometry, electromagnetic radiations, voltage supplies of oscillators under test and measurement instrumentation, but they also depend on starting conditions of the oscillators and due to their intrinsic nature, and to the time they have been stocked after being switched-off and to the benches themselves. The problem consists in evaluating the possible different contributions. These goals are ambitious, so it is preferable to investigate in priority the inter-laboratory reproducibility in using comparable benches or benches that use equivalent methods, but also measurements resulting from various methods, while we stay in the context of measurements performed in a laboratory. It began in October 2005 and will be finished in april 2006. Preliminary results are now available.

1. INTRODUCTION

An international comparison of phase noise was organized in 1993 and its results published in Germany during EFTF in 1994 [1]. More than ten years later, the new benches developed by different laboratories and commercial benches have to be tested. LNE (Laboratoire National de Métrologie et d'Essai, that now plays the role that BNM owns in the past) asked FEMTO-ST institute, as it is an LNE associate laboratory, (COFRAC accredited under number 2.13), to organize a comparison of phase noise with 5 MHz, 100 MHz and microwave oscillators. The problem is not to compare the performances of several oscillators, but to compare and to make an evaluation of the uncertainties, and the resolution and the reproducibility of the measurements. The aim of this comparison is not to lead a competition between different means of measurements but have the ability to get several systems traceable together in order to increase the trust that one can have for phase noise measurements. Oscillators to be characterized during this comparison are commercial oscillators. At 5 MHz, BVA oscillators are provided by Oscilloquartz company and FEMTO-ST. For 100 MHz oscillators, FEMTO-ST institute provides AR Electronique commercial oscillators. A commercial MITEQ Dielectric Resonator Oscillator (DRO) provided by LAAS-CNRS is to be used for 3.5 GHz microwave characterization. Ten laboratories from four different countries participate in this comparison.

II. GENERALITIES CONCERNING SPECTRAL MEASUREMENTS

Frequency stability can be characterized in the frequency domain by studying spectrum (FFT), or in time domain by means of a statistical processing of the frequency data (for example Allan variance). It allows characterization of the frequency stability versus integration time. Near the carrier, an oscillator presents flicker frequency noise, i.e. 1/f in the frequency fluctuation domain, which means $1/f^3$ for the phase noise density in the spectral domain. It corresponds to the so called "flicker floor" for Allan variance. Nevertheless this correspondence is not bijective : a $1/f^3$ phase noise gives an Allan variance floor, but the reverse proposal is not always true.

The main principle of the phase noise measurements consists in phase demodulating a signal by locking an oscillator, that is the Unit Under Test (UUT), on a reference signal, using a Phase Lock Loop (PLL).

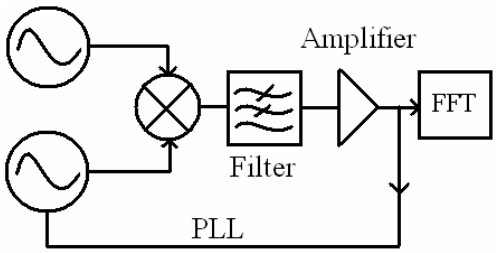

Figure 1: Usual principle for phase noise measurement of a couple of oscillators using a PLL

Especially in microwaves, the UUT is to be locked and not the reference that is already locked on a low frequency oscillator. The error signal of this locking is then proportional to the phase difference between the free running UUT and the reference. Outside the PLL bandwidth, it is proportional to the phase difference between the free running UUT and the reference. If the reference shows a very low noise, it is then proportional to the UUT phase noise. In the PLL bandwidth, it is proportional to frequency fluctuations. Results in the band pass of the locking cannot be used near the frequency cut-off of the PLL. The error bias is amplified and a FFT analyzer calculates the spectral density of phase noise fluctuations.

III. REPRODUCIBILITY OF THE MEASUREMENTS

Obtained spectra can be affected by the environmental conditions : temperature, hygrometry, electromagnetic radiations, …, but they also may depend on the time operation since switching the oscillators on, and to the time they have been stocked after being switched off and to the benches performances.

The problem consists in evaluating the possible impact of these different contributions on the measured phase noise. It is better to investigate in priority the inter-laboratory reproducibility using comparable benches or benches that use equivalent methods, but also measurements resulting from various methods, while we stay in the context of measurements performed in a metrological laboratory. As it is written in the introduction, the aim of this comparison is not to compare performances of oscillators, but to compare and evaluate uncertainties, resolution of the benches and reproducibility of the measurements. It is not a competition between measurement means but a way to have several systems traceable together in order to increase the trust that one can have for phase noise measurements done in laboratories.

IV. PROTOCOL OF MEASUREMENTS

Preliminary measurements:

Oscillators were to be measured at first by the reference laboratory at the beginning, then by each participant and at the end of this comparison one more time at the reference laboratory.

Reception of the standards:

When receiving the oscillators, each lab precised how the packing is and what information was important. Oscillators have been immediately switched on, and the measurement was made 48 hours later in the appropriate room. Frequency and power were preliminary verified. It must not be forgotten that the performances, specified by the manufacturers, are guaranteed at the end of one 90 days period without any interruption. However, it is not possible, within the framework of the circulation of the standards, to respect this time. Consequently we have decided to keep the oscillators "on" as long as possible before the measurements. In an empirical way, it must be envisaged latency doubles time of switch-off period. Moreover oscillators are sensitive to the shocks.

Measures:

Oscillators have been measured in terms of power spectral density of phase noise versus Fourier frequencies in the range 1 Hz - 100 kHz. However in the microwave domain, a DRO cannot be measured too close to the carrier due to free-running fluctuations that can be in the range of 1 rad^2/Hz. So the indicated range was only suitable for 5 MHz and 100 MHz. The DRO

has to be characterized from about 100 Hz. Measurements were given at 1 Hz, 10 Hz, 100 Hz, 1 kHz, 10 kHz, and 100 kHz within the 2 σ uncertainty. When it is possible, results given as a calibration certificate are appreciated, as several laboratories may be calibration centers, accredited or not.

The various laboratories have different kinds of phase noise measurement benches. They may have used these benches in order to compare them in the same laboratory.

Here are different commercial benches used in this comparison :

- Hewlett Packard bench
- Europtest bench
- Femtosecond bench
- Timing Solutions bench
- AR Electronique bench

Some laboratories which have a frequency stability bench have used it. It may be possible to deduce interesting information concerning phase noise.

In order to limit environmental effects in the different laboratories, it is interesting to know ambient conditions.

Such parameters are: room temperature, hygrometry rate, but also it is interesting to specify if oscillators or benches are in a special Faraday cage or something equivalent, and what voltage supplies are used, for example, batteries for the oscillators or sector for the instruments composing the bench.

It has been also precised if uncertainties are calculated from such parameters or given by an accreditation.

Sending the standards to the next laboratory:

The oscillators were packed and sent to the following laboratory, except if it was specified that there must be an inversion by the person in charge of the comparison.

Any information considered to be useful was transmitted to the person in charge of the comparison.

Transmission of the results:

The complete results were transmitted to the person in charge of the comparison, before the standards finished circulating between the participating laboratories.
The environmental conditions of the measurements were specified as explained above as well as the type of bench, the method used, the uncertainties…
The comparison is planned to be completed in April 2006. When it is finished, a report will be written with mention of the authors and their laboratories. However, in the graphs and in the presentation of the results, the different participating laboratories are codified by letters.

V. FIRST RESULTS

The obtained results concern at first phase noise measured values for each oscillator at 5 MHz, 100 MHz and 3.5 GHz. Comparison also gives interesting results concerning the benches.

Labs	10^0 Hz	10^1 Hz	10^2 Hz	10^3 Hz	10^4 Hz	10^5 Hz
LR1	-125.5 ±2	-145 ±2	-151.5 ±2	-156 ±2	-154 ±2	-156 ±2
LR2	-125±2	-136 ±2	-140 ±2	-154 ±2	-154 ±2	-155 ±2
A	-126±2	-145 ±2	-151.5 ±2	-155 ±2	-155 ±2	-155.5 ±2
B	-113 ±5	-135 ±5	-143 ±5	-149 ±5	-155 ±5	-157.5 ±5
C*	-126	-145.5	-151.5	-155	-155.5	-156.5
D*	-125.5	-145.5	-152	-156	-155.5	-156.5
E		-144 ±2	-154 ±2	-158 ±2	-158 ±2	-159 ±2
F*	-126			-155	-155	-155
G	-126 ±2	-144.5 ±2	-151.5 ±2	-155.5 ±2	-155.5 ±2	-156 ±2
H	-126.08 ±3	-145.30 ±3	-152.08 ±3	-155.57 ±3	-155.50 ±3	-157.59 ±3
I	-122.5 ±3	-142 ±3	-149 ±3	-154 ±3		
LR						

Table 1: SSB phase noise (dBc/Hz) versus Fourier Frequency at 5 MHz for each laboratory codified by a letter. Uncertainties given at 2σ

Table 1 presents results without any correction at 5 MHz for the two oscillators of the comparison. Notice that in the tables, sign * mentioned here indicates that uncertainties have not yet been established.

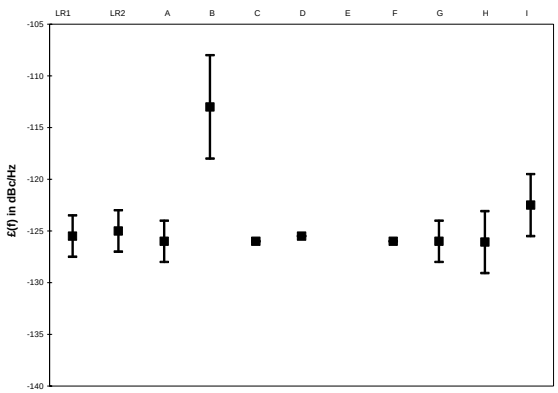

Figure 2: SSB phase noise at 1Hz from the 5MHz carrier. Uncertainties given at 2σ

The results are presented also in figures 2 and 3. The first one focuses on SSB phase noise at 1Hz from the 5MHz carrier. One participant had a problem, which is

to be investigated. Three other laboratories did not send yet their uncertainties, which are indicated without error bars in the figure. The noise floor seems to be similar for most of the participants in spite of an offset not already explained for one participant. Laboratories are codified by a letter, which is used to indicate the corresponding data point in the figures.

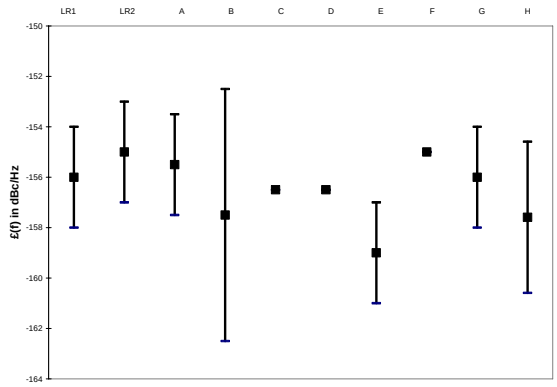

Figure 3: SSB phase noise at 100 kHz from the 5MHz carrier. Uncertainties given at 2σ

At 100 MHz, the results expressed in dBc/Hz are presented abroad also without any correction and comments.
The measurements seem to be consistent. But close to the 100 MHz carrier, a problem of stability in the phase lock loop probably made the measurement inaccurate, especially at 1 Hz. Discrepancies appears for some participants and would be investigated in order to be understood. For a 100 MHz quartz oscillator, it is more common to present the specification at 100 Hz from the carrier: results are presented in figure 4 expressed in SSB phase noise (dBc/Hz).

Labs	10^0 Hz	10^1 Hz	10^2 Hz	10^3 Hz	10^4 Hz	10^5 Hz
LR1	-64 ±2	-96 ±2	-131 ±2	-153 ±2	-161 ±2	-162 ±2
LR2	-58 ±2	-98 ±2	-129 ±2	-155 ±2	-162 ±2	-162 ±2
A	-64 ±2	-95.5 ±2	-129.5 ±2	-153.5 ±2	-160 ±2	-160 ±2
B	-65 ±3	-100 ±3	-133.5 ±3	-152 ±3	-160 ±3	-161 ±3
C*	-70	-102	-134	-155	-163	-163
D*	-73	-100	-131	-156.5	-162	-162.5
E			-135 ±2	-151 ±2	-158 ±2	-159 ±2
F*	-68		-128		-163	-163
G	-67 ±2	-97 ±2	-129.5 ±2	-153.5 ±2	-160.5 ±2	-160.5 ±2
H	-76.3 ±3	-96 ±3	-130.5 ±3	-154.8 ±3	-161.6 ±3	-161.7 ±3
I*	-86	-100	-129	-150	-158	
LR						

Table 2: SSB phase noise versus Fourier Frequency at 100 MHz for each laboratory codified by a letter. Uncertainties given at 2σ

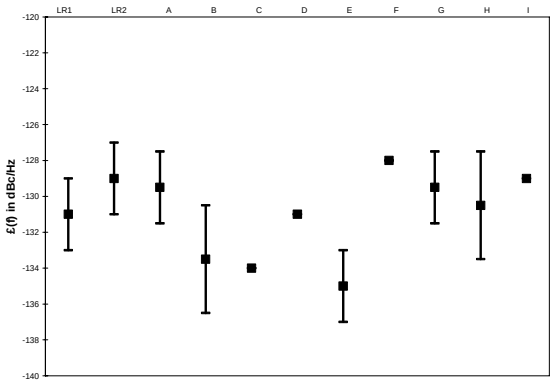

Figure 4: SSB phase noise (dBc/Hz) at 100Hz from the 100MHz carrier. Uncertainties given at 2σ

For one participant, the noise floor was not measured far from the carrier.
The uncertainty could not be evaluated yet by four participants, which are indicated without error bars in the figure. The noise floor far from the carrier is presented in figure 5.

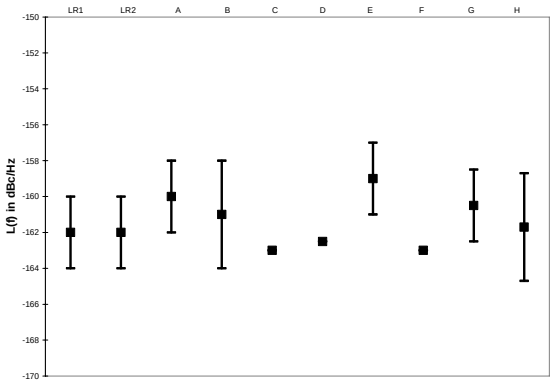

Figure 5: SSB phase noise at 100 kHz from the 100 MHz carrier. Uncertainties given at 2σ

Though the measurements are much closer, the differences should be explained by a very precise analysis of different parameters and in considering the way each participant led its measurement campaign.
We consider that, when the difference exceeds 2 dB, one must investigate the possible origins of the discrepancy.

VI. DISCUSSION

Environmental conditions are precised in table 3. In this table are reported several parameters like temperature or hygrometry rate, and it is indicated whether the oscillators under test were powered by batteries or from the mains. It is written also if the measurements were

realized in a Faraday cage to protect them from electromagnetic radiations.

	Temperature (°C)	Hygrometry (%)	Batteries	Faraday cage
LR 1	21.5 ±2.5	?	NO	NO
LR 2	25 ±2	36 ±5	NO	NO
A	23	44	YES	YES
B	22.5 ±1.5	?	NO	NO
C	23.5 ±2.5	42.5 ±12.5	YES	NO
D	20.5 ±2	?	YES	NO
E	23 ±3	?	YES	YES
F	room temperature	?	NO	NO
G	21 ±1	?		
H	23 ±1	16 ±5	YES	YES
I	22±1	?	NO	NO
LR				

Table 3: Measurement environmental conditions

Measurement conditions are not precised yet concerning the starting conditions. As oscillators are switched off during transport, it can have an impact on stability and on the phase noise at 1 Hz. Some data have not yet been collected at that step of the comparison. The oscillators are still under measurement in the last laboratory, waiting for their final measurements in the reference laboratory of this comparison campaign, in order to "close the loop" and begin the next step that is the very precise analysis of the results.

One can notice that reproducibility of phase noise measurements seems not to be affected by similar conditions concerning laboratory temperature.

Hygrometry has to be better known before any conclusion.

Contribution of batteries is a fact that does not clearly appears when we examine tables and figures. Anyway, on the curves issued from each laboratory, we observed that 100 Hz and its harmonics are reduced by the use of batteries. The 50 Hz spurious lines generally originate from ambient radiation of the mains or from inappropriate cables in the measurement system.

Faraday cage helps to define a better resolution for phase noise measurements, by significantly reducing the level of spurious signals.

The combination of optimum environmental conditions is helpful for such high performance phase noise measurements, and also for reproducibility.

VII. CONCLUSION

The aim of this phase noise comparison was to evaluate reproducibility of the measurements given by different kinds of benches used in metrological laboratories.

Most of the results confirm that the phase noise measurement uncertainties generally are about ±2 dB. A few discrepancies have been observed : it will be useful to understand their origin in order to avoid this kind of problem in future measurements.

Acknowledgements

We would like to thank LNE (Laboratoire National de Métrologie et d'Essai) and CNRS (Centre National de la Recherche Scientifique) for their financial support on this project.

REFERENCE

[1] F. L. Walls, R. Barillet, R. Besson, J. Groslambert, P. Schumcher, J. Rufenacht and K. Hilty, "International Comparison of phase noise", 8th EFTF, Technical University Munich, Weihenstephan, Germany, march 1994, pp. 439-456 (1994)

Proceedings of the 20th EFTF, 2006

Thermal effects on frequency fluctuations in quartz crystal oscillators

* F. Sthal, P. Abbe, P. Salzenstein and S. Galliou
FEMTO-ST, UMR CNRS 6174
ENSMM, 26 Chemin de l'Epitaphe, 25030 BESANCON CEDEX, FRANCE
**Electronic address:* fsthal@ens2m.fr

This paper deals with the correlation between the thermal behavior of the oven and phase fluctuations of the oven-controlled oscillator. Experiments to measure the thermal stability of the oven control are presented. A conventional oscillator equipped with a LD-cut quartz resonator is first used in the B-mode in order to measure the temperature fluctuations of its oven. The same resonator is then used in its C-mode to record the phase fluctuations of the oscillator. Obviously, the quartz resonator is previously characterized in terms of temperature dependence. Frequency-temperature curves are given for B and C modes in order to obtain the thermal sensitivity of the resonator. In a first step, thermal fluctuations of the oven are obtained through the measurement of the B-mode oscillator frequency in the time domain, by means of Allan standard deviation. Then, it can be translated into C-mode frequency fluctuations using the thermal sensitivity of the resonator C-mode.
At least, power spectral density of phase fluctuations of such an oven-controlled oscillator is related to temperature sensitivity and discussed.

1. INTRODUCTION

High performance crystal oscillators like oven controlled crystal oscillators (OCXO) employ temperature control circuitry to hold the crystal and critical circuitry at a precise, constant temperature used in ovenized oscillator [1-2]. Ultra-stable oscillators (USO) that we are working on have been designed with LD-cut quartz crystal resonators [3]. The latter are third overtone 10 MHz BVA resonators [4].
The aim of the paper is to report their analyses in terms of room temperature sensitivity. Temperature effects on oscillator frequency stability are measured by means of the power spectral density (PSD) or the Allan standard deviation.
Oscillator design and oven control are quite simple. Nevertheless, double ovens are used. The inner oven finely controls the resonator temperature whereas the outer one is working for just roughly limiting room disturbances onto electronics. Effects of each temperature regulator are examined.
It is well known that the resonator is the most temperature sensitive element transducing temperature fluctuations into frequency fluctuations. In a second level, the sensitivity of other electronic components such as capacitors or varactor diode associated to the resonator cannot be neglected. Otherwise, considering the medium-term measurement time (from 1 s up to 10 000 s), frequency drift can also mask thermal effects and must be taken into account.

II. BASIC REVIEW

II.1. SC-cut and LD-cut quartz resonators

The amplitude-frequency effect of the LD-cut resonator is about 10^{-11} μW^{-1} [4] which is hundred times lower than the SC-cut. The main drawback of the LD-cut compared with the SC-cut is its thermal sensitivity. Their classical third order polynomial approximations are shown in Fig. 1.

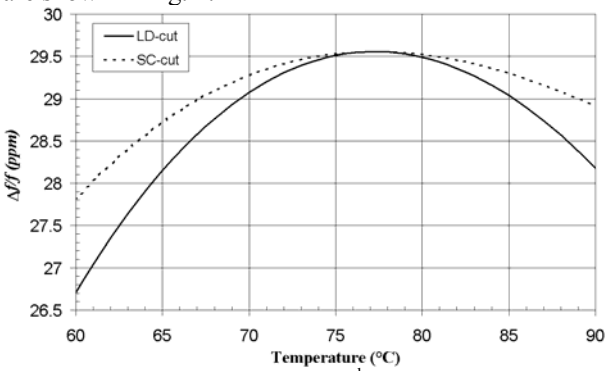

Fig. 1: Thermal behaviors of 3rd overtone 10 MHz C-mode LD and SC-cuts.

Note that for USO applications, the temperature turnover point of the C-mode is usually close to 80 °C. LD and SC-cut are doubly rotated cut. As a consequence, they exhibit a resonant thermometric mode (B-mode) in addition to the metrological mode (C-mode). In our case of a 10 MHz, the LD-cut has a B-mode frequency close to f_B = 10.7 MHz. Its frequency-temperature behavior has been measured (Fig. 2).

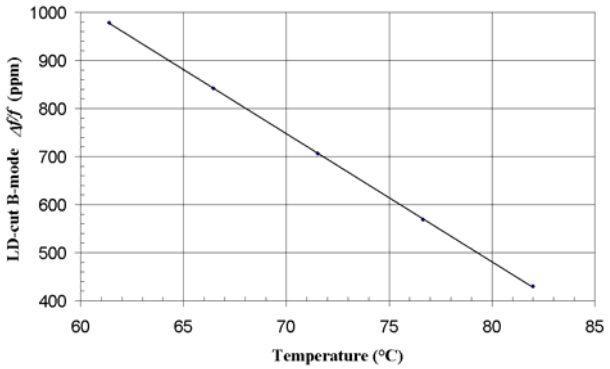

Fig. 2: Thermal behavior of LD-cut 3rd overtone 10.7 MHz B-mode.

Results give a linear relationship with a slope equal to $a_B \approx -280\ \mathrm{Hz \cdot K^{-1}}$.

II.2 Quartz crystal oscillator characterization

Oscillator stability is usually given in the frequency domain by means of PSD of relative frequency $(S_y(f))$ or phase fluctuations $(S_\phi(f))$. In the time domain, the Allan standard deviation $\sigma_y(\tau)$ can be obtained by experiments or computed from the PSD as follow [5]:

$$\sigma_y^2(\tau) = \frac{2}{(\pi \nu_0 \tau)^2} \int_0^\infty S_\phi(f) [\sin(\pi f \tau)]^4 df \qquad (1)$$

With $S_\phi = \left(\frac{\nu_0}{f}\right)^2 \cdot S_y(f)$

ν_0 = carrier frequency
f = fourier frequency

Conventional slopes of $S_\phi(f)$ and their corresponding slopes for $\sigma_y(\tau)$ are given in Table 1. In some cases, integration boundaries for calculation of (1) have to be limited to lower value f_L and upper value f_H.

Table 1: Corresponding slopes of $S_\phi(f)$ and $\sigma_y(\tau)$.

$S_\phi(f)$	$\sigma_y(\tau)$	Boundaries
-6	+1	$f_L \neq 0, f_H \neq \infty$
-5	+1	$f_L \neq 0, f_H \neq \infty$
-4	+1/2	
-3	0	
-2	-1/2	
-1	≈ -1	$f_H \neq \infty$
0	-1	

II.3 Temperature effect on oscillators

Room temperature changes can be attenuated by two ways. High frequency fluctuations are easily reduced by the filtering effect of the enclosure. Nevertheless, a thermal regulator should be added in order to suppress low frequency components.
For low Fourier frequencies, oscillators PSDs of phase fluctuations often give a f^{-4} slope. Generally, experience shows that this result is attributed to a thermal regulator behavior.

III. MEASUREMENT METHOD

Fig.3 shows the oscillator packaging. It is a very simple prototype version of a double ovenized oscillator.

Fig. 3: Oscillator packaging.

Experiments presented below are limited to room temperature fluctuations, that is to say in laboratory environment. Temperature influence is studied on 10 MHz LD-cut ovenized oscillators. These USO are double ovenized and provide a short term stability of a few 10^{-13} [3]. Their electronic circuitry can be easily switched from C-mode to B-mode. The B-mode of quartz crystal resonators is then used as a temperature sensor. The measurement process of each oscillator is as follow:

- First Step: reference measurements
  Records of Allan standard deviation and PSD of phase fluctuations of ovenized oscillators working in C-mode.
- Second Step: thermal measurements
  Oscillator under test is switched in B-mode and measured against a reference. Records of Allan standard deviation in B-mode with:
  - both ovens switched on
  - inner oven switched on, outer oven switched off
  - both ovens switched off
- Third Step: thermal qualification of resonators
  - records of frequency-temperature in B-mode
  - records of frequency-temperature in C-mode

Reverse operations allow to come back in C-mode and check the initial performances.

IV. RESULTS AND COMMENTS

Fig. 4 shows a typical phase fluctuations PSD of one LD-cut ovenized oscillator vibrating in C-mode. f^{-3} and f^{-1} classical slopes can be easily identified. Close to the carrier, the phase noise is going up according to f^{-6} slope. This behavior could be due to thermal effects, but also to frequency drift.

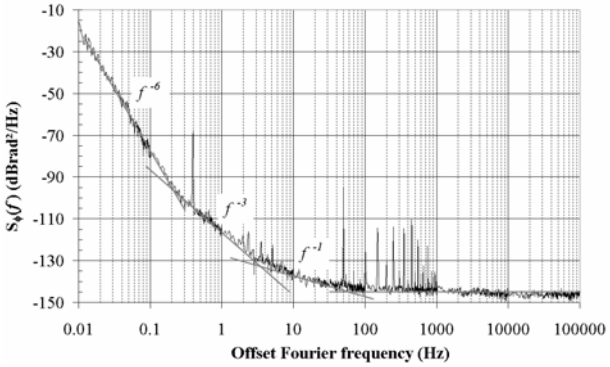

Fig. 4: PSD of phase fluctuations of a 10 MHz LD-cut doubly ovenized oscillator.

Corresponding measurements in the time domain are given in Fig. 5. Metrological C-mode standard deviation (lower curves) can be understood as the noise floor of oscillator electronics used in B-mode as well as in C-mode. For $\tau < 1$ s, the main slope is about τ^{-1} and for $\tau > 1$ s, it goes up in $\tau^{+\alpha}$ with $½ \le \alpha \le 1$. The latter behavior could be associated to PSD slopes from f^{-4} to f^{-6}.

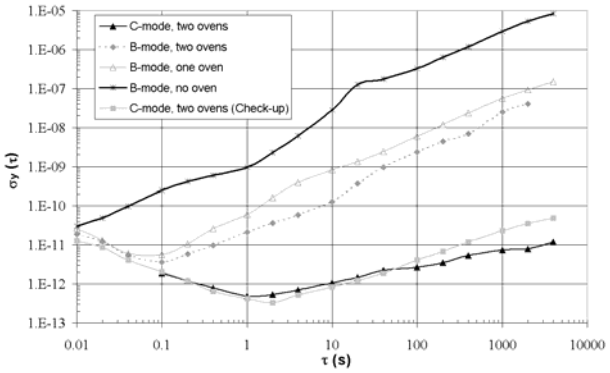

Fig. 5: Standard deviation in various thermal situations.

According to the described process, the tested oscillator is then switched in B-mode. When both ovens are still working on, the recorded standard deviation can be divided in two parts. In short term ($\tau < 0.1$ s), the B-mode standard deviation is equal to the C-mode one. Assuming that the B-mode is a good mean to separate thermal effects from other noise origins, this behavior can be due just to the noise of the electronics circuitry.
In medium and long term ($\tau > 0.1$ s), τ^{+1} slope could be mainly due to thermal effects, thus:

$$\sigma_{yB\ 2ov}(\tau) = K_{2ov} \cdot \tau^{+1} \qquad (\tau > 0.1\ s)$$

When the outer oven is switched off, performances are divided by about 3:

$$\sigma_{yB\ 1ov}(\tau) = K_{1ov} \cdot \tau^{+1} \qquad (\tau > 0.1\ s)$$

With $K_{1ov} \approx K_{2ov}/3$ $(\tau > 0.1\ s)$

In the case of two ovens switched off, the standard deviation coefficient (upper curve) is hundred times greater than K_{2ov}. Then, the thermal gain of the device can be evaluated to about 100. Residual thermal fluctuations of the resonator can be expressed as:

$$\Delta T = \frac{\Delta f_B}{|a_B|} \Rightarrow \Delta T = \frac{\Delta f_B}{f_B} \times \frac{f_B}{|a_B|}$$

As seen in Fig.5: $K_{2ov} = \left.\frac{\Delta f_B}{f_B}\right|_{\tau=1s} \approx 2.1 \cdot 10^{-11}$

Thus, the thermal stability of the resonator oven ΔT is given at 1 s by:

$$\Delta T(1\,s) = 2.1 \cdot 10^{-11} \times \left(\frac{10{,}7 \cdot 10^6}{280}\right) = 8 \cdot 10^{-7}\ K$$

Fig. 6 reminds the behavior of the quartz crystal resonator inserted in the inner oven. The ideal working point is the temperature of the turnover point T_{to}. Unfortunately, this point can never be exactly reached. Actually, an offset δT is observed between T_{to} and the operating point of the oven T_{op}:

$$\delta T = |T_{op} - T_{to}|$$

Then, the stability of the oscillator frequency depends on both quantities δT and ΔT when the resonator is working in C-mode according to its frequency-temperature behavior.

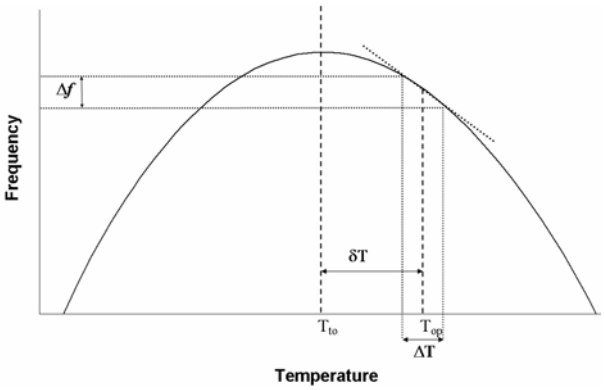

Fig. 6: Temperature effects on resonator frequency.

The classical 3rd order frequency-temperature equation of a resonator is usually referred to $T_0 = 25°C$, as:

$$f(T) = f_0(1 + \alpha(T - T_0) + \beta(T - T_0)^2 + \gamma(T - T_0)^3)$$

To quantify the thermal effects of the oven control, the coefficients α, β and γ of the LD-cut resonator (see Table 2) are used to obtain the slope a_C at T_{op}.

$$a_C = [2\beta + 6\gamma(T_{to} - T_0)] \cdot \delta T + 3\gamma \cdot \delta T^2$$

Table 2: Frequency Temperature Coefficient of 10 MHz third overtone LD-cut, quartz crystal resonator.

α	$1.23 \cdot 10^{-6}$
β	$-14{,}6 \cdot 10^{-9}$
γ	$36.1 \cdot 10^{-12}$

It is a fact that the typical tuning of the operating point is around δT = 0.1°C. In that case, according to Fig. 6, the frequency – temperature slope is about:

$$a_C \approx -1.8 \cdot 10^{-9}\ K^{-1}$$

with T_{to} = 77.25°C

As a consequence, the resulting frequency change of the C-mode frequency can be expressed as:

$$\frac{\Delta f}{f} = a_c \times \Delta T$$

$$\frac{\Delta f}{f} = 1.8 \cdot 10^{-9} \times 8 \cdot 10^{-7} = 1.44 \cdot 10^{-15}$$

This result obtained with τ = 1 s can be easily extended to other values of τ and different temperature offsets δT as shown in Fig. 7.

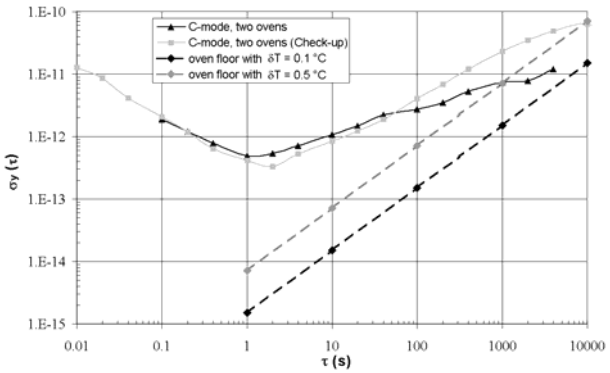

Fig. 7: Standard deviation measurements of oscillators compared with the floor of their ovens.

It is visible in Fig. 7 that the equivalent frequency stability of oscillator ovens is widely below the measured stability for τ < 1000 s. Thus, such ovens are not a limitation in terms of noise induced in the resonator in short terms. Then, in the PSD spectrum, the observed behaviors whose slopes are steeper than f^{-3} cannot be due to thermal effects on the resonator alone. Nevertheless, other electronics components are also temperature sensitive. Especially capacitors and the varactor diode associated to the resonator are not really taken into account in this measurement method.

Moreover, concerning frequency fluctuations, statistical fluctuations like external thermal ones, can be superimposed on deterministic changes.

So, a frequency drift can also be an extra-origin of the f^{-6} slope in the resulting ovenized-oscillator PSD, in addition to something like room temperature changes.

Indeed, measurements of the Picinbono standard deviation keep away from the Allan standard deviation showing that a frequency drift exists. In fact, the frequency drift of these analyzed resonators does not exceed $1 \cdot 10^{-10}$/day. Such a drift would lead to a very lower PSD than the measured one, not sufficient to explain the resulting PSD for low Fourier frequencies.

V. CONCLUSION

We were expecting to detect the origin of f^{-4} to f^{-6} slopes of the PSD, unfortunately the examined causes (thermal influence on the resonator + frequency drift) are not credible. The only relevant cause that we can assume remains the thermal influence of the electronics. Additional experiments have to be performed in that way.

REFERENCES

[1] Norton, J.R. and Besson, R.J., Proc. of the 47th Ann. Symp. on Freq. Cont., 1989, pp. 47-50.

[2] Ballato, A. and Vig, J. R., *Proc. 32nd Ann. Symp. on Freq. Cont.*, pp. 180-188, 1978.

[3] N. Gufflet, F. Sthal, J. J. Boy, R. Bourquin, M. Mourey, IEEE Trans. on Ultrason., Ferroelec. and Freq. Cont., vol. 48, no. 6, Nov., pp. 1681-1685, (2001).

[4] S. Galliou, F. Sthal, J.J. Boy, R. Bourquin, M. Mourey, Proc. IEEE Int. Ultrason., Ferroelec., and Freq. Cont. 50th Anniversary Joint Conf., Montreal, Canada, 24-27 August, pp. 475-477, (2004).

[5] J. Rutman, *Proc. of IEEE.* vol. 66, no. 9, Nov., pp. 1048-1074, (1978).

Proceedings of the 20th EFTF, 2006

Influence of Resonator Factors on Phase-Noise of OCXOs

I. Abramzon, A. Gubarev, O. Rotova, V. Tapkov
"Magic Crystal Ltd." K.Marx Av. 18, bld. 29, 644046 PO box 2313, Omsk, Russia
e-mail: mxl@omsknet.ru, website: www.magicxtal.com

The paper is devoted to study of physical causes of phase-noise of crystal oscillators associated with the crystal technology. It was found that this source contributes into the phase-noise though instability of the quartz - electrodes transition (QET) modulating the crystal parameters. A model linking the oscillator frequency fluctuations with instability of QET, equivalent parameters of the crystal, and some regimes of the sustaining circuitry was proposed and confirmed experimentally. Basing on this approach some ways of phase-noise reduction were proposed and discussed in the paper.

I. INTRODUCTION

Reduction of phase-noise of OCXOs has become nowadays one of the most important problem and subject of permanent efforts of researchers in the field. For a long time main noise sources of the phase-noise were associated with the sustaining circuitry while the crystal was considered as a noiseless filter element included in the oscillator feedback [1]. Although based on such approach Leeson's model proved its correctness for many practical cases a lot of experimental data don't obey predicted 30 dBc/decade slope in the crystal bandwidth exhibiting in reality up to 40 dBc/decade rate. Such discrepancy stimulated a search for alternative noise sources associated with physical properties of the crystal.

As possible mechanism causing degradation of phase-noise of an OCXO influence of temperature fluctuations of the oven construction on the crystal frequency via the thermodynamic effects was studied in many works. There was concluded that effect of thermodynamic factors on the phase-noise becomes substantial only at rather slow - below 0.1 Hz – fluctuations of the oven temperature and can be neglected at above 1 Hz frequency [2].

Another approach considering fluctuations of the crystal's equivalent parameters as main noise source was described in [3]. Proposed by the authors model provided adequate description of an oscillator phase-noise pattern basing on noise factor of motional resistance and capacity of the crystal. However physical causes of the fluctuations of the crystal parameters were not taken into account that didn't allow elaboration of any methods of phase-noise reduction.

Meantime many researchers noticed distinct correlation of the oscillator phase-noise properties with state of the transition between crystal surface and the film electrodes depending on quality of the surface and the film deposition process [4]. The idea of quartz-electrode transition (QET) as substantial factor of the oscillator phase-noise was confirmed by testing "electrodes-less" designs exhibiting utmost figures of the phase-noise and short-term stability [5].

A goal of the present work was experimental study and modeling of OCXO phase-noise factor associated with QET instability and basing on this ground elaboration of practical methods of phase-noise reduction.

II. EXPERIMENTAL STUDY OF RESONATORS PHASE-NOISE

To prove the crystal is a substantial source of an oscillator phase-noise providing additional rate to predicted 30 dBc/decade slope of the phase-noise pattern, we tested a number of 10 MHz SC-cut OCXOs comparing slope of their phase-noise patterns with the phase-noise level at 1 Hz offset. The results are depicted in fig.1.

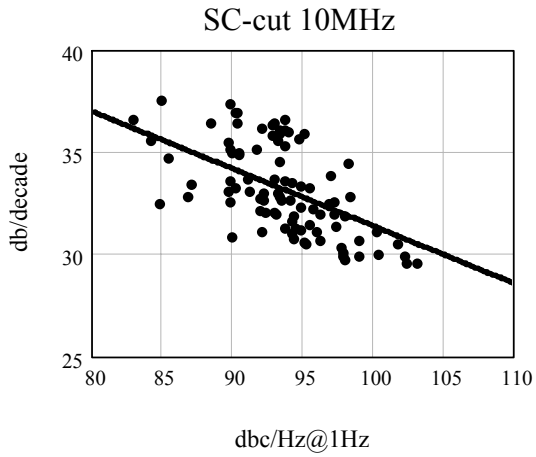

Fig. 1. The slope of OCXOs phase-noise patterns versus the phase-noise level measured at 1 Hz offset

As it follows from the data the rate of the slope falls with decrease of the phase-noise level approaching the "theoretical" 30 dBc/decade at about –105 dBc. Obviously higher than –105 dBc level of the OCXO noise should be related to the crystals intrinsic noise factors.

Indirect evidence of predominating role in the noise of factors associated with the crystals surface was derived by study of two batches of OCXOs using AT-cut 3d overtone crystals operating at 5 MHz and packaged in TO-8 holders. The OCXOs were divided into two groups differing in mounting structure of the crystals. While one group consisted of the crystals with two-point fixture of the blank another group contained crystals with four-point fixture. The difference in the blanks fixtures resulted in difference of the crystals Q-factor value measured about 1.5 million for two-point fixture and about 1.2 million for four-point fixture. Phase noise test results of the OCXOs are depicted in fig.2.

As it follows from the statistical data best figures for both groups reach about - 108 dBc at 1 Hz offset that roughly corresponds to best results achieved in similar oscillator design with 10 MHz 3d overtone SC-cut crystals in spite of essentially worse thermodynamic properties and drive level dependence (DLD) of the AT-cut resonators.

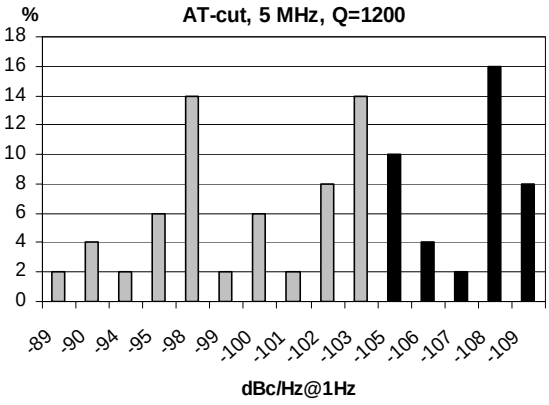

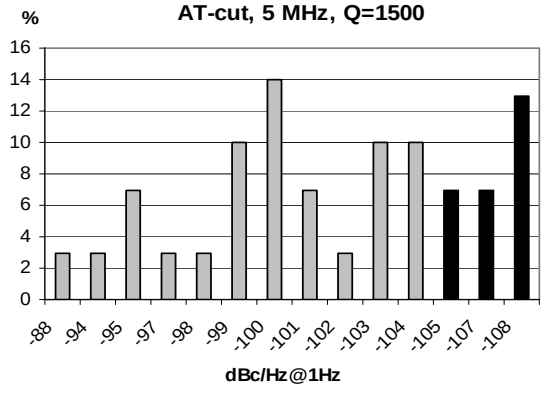

Fig. 2. Phase-noise test data of 5 MHz 3d OT AT-cut crystals

Another deduction drawn from the experimental data is some advantage of OCXOs using "low" Q-factor crystals over ones with "high" Q-factor units. While the first batch includes about 40% of units with better than –105 dBc phase-noise, the seconds have only 27% of the "low-noise" units. Such results can not be understood by Lesson's theory, but will be explained latter by the crystals intrinsic noise.

As was stated in many works the most substantial noise source associated with the crystal technology originates from instability of the quartz-electrodes transition (QET). Assuming that roughness of the crystal surface should be influential factor of QET instability we studied phase-noise of two groups of 10 MHz SC-cut crystals with different finish of their surfaces. While one group contained the units with perfectly polished surfaces another group consisted of crystals with 1μ finish surfaces. All the units passed through same fabrication process including microscope inspection of electrode deposition quality. Phase-noise of crystals was measured in special low-noise test design containing the oven to sustaining the crystals temperature within 0.2˚C about the turn-over point. Typical phase-noise patterns obtained with best units of each group are depicted in fig. 3.

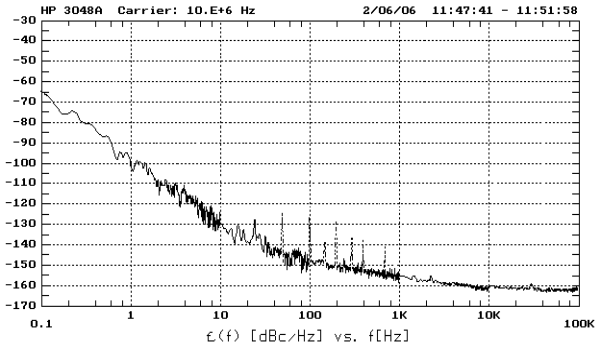

a)

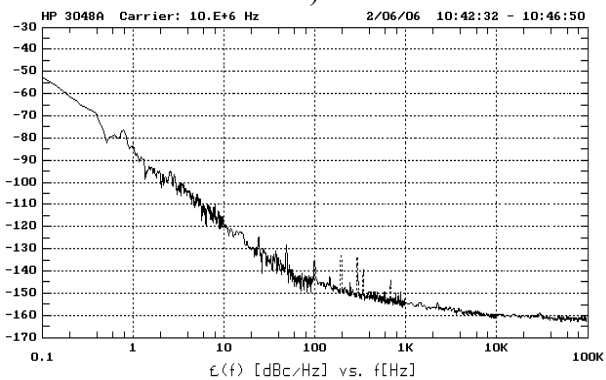

b)

Fig. 3. Comparative phase-noise tests of SC-cut crystals with different surface quality: a) typical phase-noise pattern for best units with polished surfaces;
b) typical phase-noise pattern for best units with 1μ finish surfaces.

As it follows from the data phase-noise figures for the best units with polished and 1 um finished surfaces differ for about 15 dBc at 1 Hz and 10 dBc at 10 Hz offset. Moreover the polished crystals provide within 0.1-10 Hz offset about 30 dBc/decade slope while the 1μ finished ones exhibited about 35 dBc/decade that implies existence of additional noise source inherent with the crystal surface.

III. MODELING THE INFLUENCE OF QUARTZ-ELECTRODES TRANSITION ON AN OSCILLATOR PHASE-NOISE

Carried out experimental study revealed predominating role of QET on the resonator noise properties. Obviously defects of the crystal surface, contaminations, and micro-particles under the electrode film and failures of the deposition process should lead to deterioration of adhesion properties of the electrode film. That results into additional dissipation of the oscillation energy and incomplete compensation of the surface charges impacting on the crystal's motional resistance and capacitance. Obviously under variation of temperature, mechanical stresses or vibrations of the crystal surface the state of QET may change that, in turn, should lead to fluctuations of the crystal parameters and the oscillator frequency.

Described physical model can be represented by equivalent network of the crystal depicted in fig. 4, where δR_q determines fluctuating part of losses in QET, C_{qe} is capacitance of QET, δC_{qe} is fluctuating part of C_{qe}.

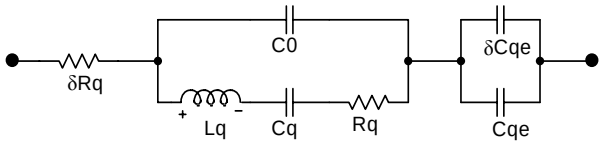

Fig. 4. Equivalent network of a crystal with QET fluctuations.

To define fluctuation of the crystal equivalent parameters caused by instability of QET state Q-factor of the crystal can be expressed as ratio of its kinetic energy W and sum of energies dissipating in quartz structure (E_q), in the quartz-electrodes transition (E_{qe}) and in the crystals periphery (E_p):

$$Q = W/(E_q + E_{qe} + E_p), \quad (1)$$

Differentiating (1) by E_{qe} and performing simple transformation a variation of Q-factor versus variation of E_{qe} can be expressed as:

$$\frac{\delta Q}{Q} = -\delta E_{qe} \cdot \frac{Q}{W}, \quad (2)$$

The energy lost in the film electrodes can be written as portion η of kinetic energy stored in the vibrating film (We):

$$\frac{\delta Q}{Q} = \delta(\eta \cdot W_e) \cdot \frac{Q}{W} = \delta\eta \cdot Q \cdot \frac{M_e}{M_q} = \frac{\gamma}{\Omega^k} \cdot Q \cdot \frac{M_e}{M_q}, \quad (3)$$

where $\delta\ \eta = \gamma/\Omega^k$ – fluctuation of energy lost in the film electrodes depending on value and density of defects in QET and obeying the flicker law; M_e and M_q – masses of the film electrodes and the quartz plate in the active area of the crystal.

As $\delta Q/Q = \delta R_q/R_q$ expression for (3) is also valid for simulation of the motional resistance variations.

For estimation of fluctuations of QET capacity we assumed that relative value of the fluctuation $\delta C_{qe}/C_{qe}$ should be in direct proportion with relative fluctuations of energy dissipating in the electrodes and then can be expressed as:

$$\frac{\delta C_{qe}}{C_{qe}} = \frac{\gamma}{\Omega^k} \cdot \psi, \quad (4)$$

where Ψ is some function linking relative variation of dissipating in the film energy with fluctuation of QET capacitance.

Substituting (4) into well-known expression for deviation of a crystal frequency caused by series connected capacitance (C_{qe} in our case) and taking into account that value of C_{qe} much exceeds the crystal shunt capacitance we comes to expression for crystal frequency fluctuation versus QET capacitance variations:

$$\frac{\delta F}{F} = \frac{\delta C_{qe}}{C_{qe}} \cdot \frac{C_q}{2C_{qe}} = \frac{\gamma}{\Omega^k} \cdot \psi \cdot \frac{C_q}{2C_{qe}}, \quad (5)$$

While variation of QET capacitance C_{qe} impacts on the oscillator frequency directly, variations of motional resistance and Q-factor produce frequency fluctuations via FM and AM of the drive current. The latter induces the frequency fluctuations through non-linearity of the varactor (in case of its usage) and DLD of the crystal.

Expressing the oscillator frequency fluctuations caused by modulation of the oscillation phase, varactor capacitance and DLD of the crystal via functions Φ_φ, Φ_v and Φ_{DLD} complete expression for the frequency fluctuations caused by QET instability can be written as:

$$\frac{\delta F}{F} = \Phi_\varphi\left(\frac{\delta Q}{Q}\right) + \Phi_v\left(\frac{\delta Q}{Q}\right) + \Phi_{DLD}\left(\frac{\delta Q}{Q}\right) + \frac{\gamma}{\Omega^k} \cdot \psi \cdot \frac{C_q}{2C_{qe}}, \quad (6)$$

Equations (3) and (6) in fact represent considered above physical model in terms of functional relationships. Although accurate definition of functions Φ_φ, Φ_v, Φ_{DLD} and Ψ is a difficult task and a subject of future researches the model links fluctuations of the oscillator frequency with equivalent

parameters of the crystal as well as with some regimes of the sustaining circuitry. Analysis of the model performed below allows better understanding observed phase-noise behavior of oscillators as well as leads to some methods of phase-noise reduction.

IV. ANALYSIS OF THE MODEL AND METHODS OF PHASE-NOISE REDUCTION

As it follows from considered model instability of QET defined by factor γ is main efficient of all expression for the crystal parameters variations. Then all improvements of polishing, cleaning, and film deposition processes providing reduction of this noise factor should result in decrease of the crystal noise.

Uncommon conclusion coming from the model is direct dependence of fluctuations of the crystal parameters on Q-factor at constant value of noise factor γ. This theoretical deduction was confirmed by experiments including one described above where better phase noise of OCXOs was reached with "lower" Q-factor AT-cut crystals. The phenomena can be understood from the fact that improvement of Q-factor of two-point fixture units was reached without reduction of energy losses in QET that even increased fluctuating portion of dissipated energy in the crystals.

Important conclusion drawn from the model is dependence of QET contribution into the crystal noise on the electrodes mass/crystal mass ratio. Hence minimization of the electrode mass and use of high overtone crystals should bring advantageous in phase-noise properties. Another argument in favor of the high-overtone crystals following from the model is essentially lower value of their capacitance resulting in reduction of the frequency fluctuations due to QET variations. To prove this conclusion we tested a group of 10 MHz 5th overtone SC-cut crystals fabricated with careful control of the polishing and deposition process. Typical phase-noise pattern for best measured units are depicted in fig. 5.

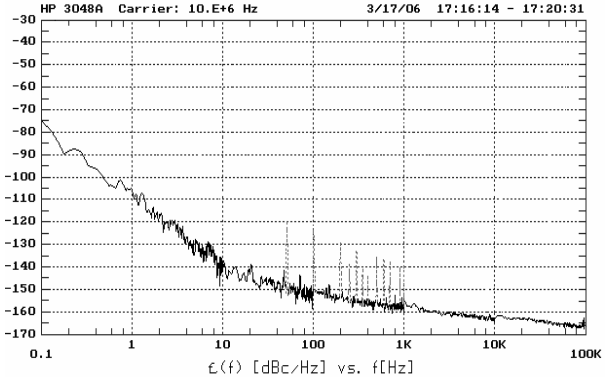

Fig. 5. Best phase-noise figures obtained with 5th overtone 10 MHz SC-cut crystals

As it follows from obtained results the 5th overtone crystals exhibit about –110 dBc at 1Hz and - 140 dBc at 10 Hz offset. These figures are about 6 dBc better than those obtained with best 3d overtone SC-cut crystals (fig. 3) that proves advantageous of the high-overtone crystals for low-noise applications.

CONCLUSION

1. Influence of quarts-electrode transition of the crystals was experimentally proved to be predominating factor of the oscillator near-the carrier phase-noise causing essentials (to 20 dBc) spread of the phase-noise figures due to imperfections of the crystal technology.

2. The model linking the oscillator frequency fluctuations with QET instability, the crystal parameters as well as with some sustaining circuitry regimes has been proposed and discussed in the paper.

3. Some ways of the phase-noise reduction following from the proposed model such as usage of high overtone crystals, low-mass electrodes, and others been suggested and confirmed experimentally.

REFERENCE

[1] D. B. Leeson, "A simple model of feedback oscillator Noise spectrum", Proc. IEEE, vol. 54, pp 329-330, Feb. 1966.

[2] I. Abramzon, V. Tapkov, S. Baranushkin, "Optimization of Drive-Level in High Stability Low-Noise OCXOs" - Proc. IEEE IFCS, 2004, pp.742-747.

[3] Y. Shmaliy, "The noise conversion method for oscillatory systems" - Proc. IEEE IFCS, 2004, pp. 706-709, 2004.

[4]J.Lamboley, V.Candelier, F.Courtade, M.Brunet,F.Deyzak, "Ultra-stable 5 MHz Xtal resonator with very long G-sensitivity and noise" - Proc. 18th European frequency and time forum, 2004.

[5] G.Ynushevsky, I.Abramzon, "High frequency resonators excited in the gap for low-noise oscillators" - Issues of Radioelectronics, 1988, vol. 12, pp. 83-87.

Proceedings of the 20th EFTF, 2006

Investigation of the distributed cavity phase shift in an atomic fountain

F. Chapelet [1,*], S. Bize[1], P. Wolf[1,2], G. Santarelli[1], P. Rosenbusch[1], M.E. Tobar[3], Ph. Laurent[1], C. Salomon[4], and A. Clairon[1]

[1] *LNE-SYRTE, Observatoire de Paris, 61 avenue de l'Observatoire, 75014 Paris, France*
[2] *Bureau International des Poids et Mesures, Pavillon de Breteuil, 92312 Sèvres cedex, France*
[3] *The University of Western Australia, School of Physics, 35 Stirling Highway, Crawley, Australia*
[4] *Laboratoire Kastler Brossel, Ecole Normale Supérieure, 24 rue Lhomond, 75231 Paris cedex 05, France*
**Electronic address:* Frederic.Chapelet@obspm.fr

We report on measurements to characterize phase gradients inside the Cs microwave cavity in the SYRTE double fountain FO2. The clock frequency is measured as a function of the tilt of launch velocity with respect to gravity, as a function of the microwave power and when feeding the Ramsey cavity from either sides or symmetrically using the two microwave feedthroughs. These measurements are made with typical uncertainty below 3×10^{-16} per point. They show clear non-vanishing results which can be compared to recent theoretical models of the phase distribution.

I. INTRODUCTION

LNE-SYRTE is developing three atomic fountains (FO1, FO2 and FOM) [1,2]. One of these fountains (FO2) routinely achieves fractional frequency instability of $1.6\times10^{-14}\ \tau^{-1/2}$ (where τ is the measurement time in seconds), thanks to the use of a cryogenic sapphire oscillator as an ultra-stable local frequency reference [3,4]. Presently this clock realizes the SI second and contributes to the elaboration of TAI with an accuracy of 6.5×10^{-16}. These fountain clocks are also used to test fundamental physical laws such as the stability of natural constants [5]. Recently we also performed a stringent test of Lorentz Invariance with the FO2 fountain [6,7].

Among several systematic effects, the distributed cavity phase shift is one of the significant limitations of atomic fountains. This effect arises when the moving cold atom cloud interacts with the imperfectly stationary microwave field inside the Ramsey cavity. It has been considered in several publications [8-12]. Usually under optimized clock operation the distributed cavity phase shift is expected to be quite small (less than few parts in 10^{16}) and there is no simple way to change or magnify it alone to obtain unambiguous measurements. Consequently most of the current evaluations of the distributed cavity phase shift are based on theoretical models of the phase distribution suffering from a lack of comparison with experiments.

In the present work, by appropriately exploring non-optimized clock conditions (fountain tilt, asymmetric feed of the cavity, elevated microwave power), we are inducing and measuring clear non-vanishing effects that we can relate to the phase distribution alone. As we will see, these measurements can be compared to theoretical predictions in order to assess the underlying model of the phase distribution.

In a first part we present the experimental setup of our fountain. Then we describe the experiment that we have performed to investigate the distributed cavity phase shift. In a third part we present the theoretical model that has been compared via a numerical simulation to our measurements. Finally we discuss the comparison between the experiment and the model.

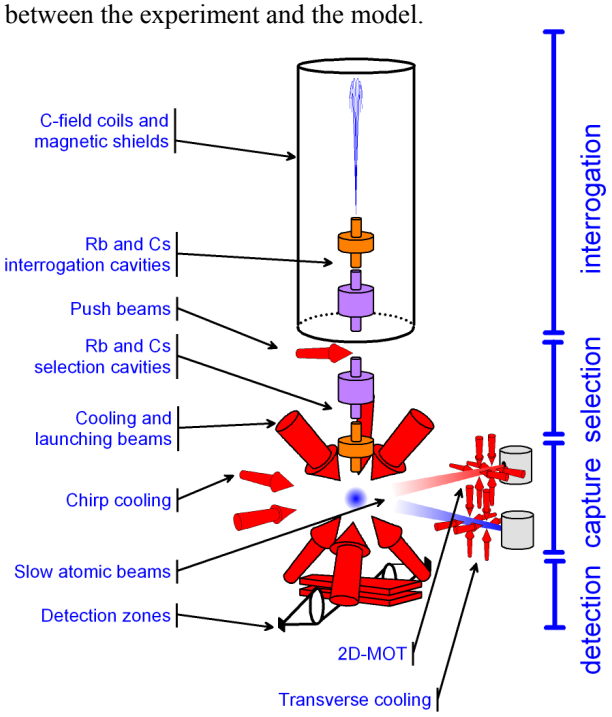

Fig. 1 – Sketch of the FO2 fountain. The fountain can run with either cesium or rubidium atoms. For the study of the distributed cavity phase shift the FO2 fountain was operated with cesium.

II. FO2 EXPERIMENTAL SETUP

The FO2 fountain [1-3] operates with an optical molasses. Six laser beams are aligned along the axes of a three-dimensional coordinate system, where the (111) direction is vertical. The optical molasses is loaded from a decelerated atomic beam. An additional transverse cooling reduces the beam divergence and increases the loading rate to 10^9 atoms in 100 ms. In the present experiment a loading time of 220 ms was used.
Atoms are launched upward with a velocity of 4.334 m.s^{-1} (apogee 0.957 m), cooled to ~1 µK and pass through a state selection microwave cavity. The F=3 m_F=0 state is selected by adiabatic population transfer. 52 cm above the capture zone, a cylindrical copper resonator is used to probe the hyperfine transition using the Ramsey interrogation scheme. This cavity has a quality factor Q=6600. Thanks to two opposite microwave feedthroughs, the cavity can be fed either symmetrically or asymmetrically. Resonant light is used to detect the populations of the F=3 and the F=4 states from which the transition probability is calculated.

The microwave signal probing the atomic transition is synthesized from a cryogenic sapphire oscillator (CSO) weakly phase-locked to a hydrogen maser [4]. The CSO has an excellent frequency stability (~10^{-15}) up to 800s, whereas the long-term stability is given by the maser. The 11.932 GHz output signal from the CSO is converted in order to synthesize 11.98 GHz and 100 MHz signals, both phase coherent with the maser. FO2 uses the 11.98 GHz signal to generate 9.192 GHz by a frequency chain which achieves a frequency stability of 3×10^{-15} at 1 second [4]. In order to tune the interrogation signal to the atomic transition, a ~7.3 MHz signal from a computer-controlled high-resolution digital synthesizer is added within the frequency chain. The detected atomic transition probability determines the frequency corrections applied via the synthesizer. These corrections are the basis for evaluating frequency stability and measuring frequency shifts.

III. EXPERIMENT

The Ramsey cavity of the FO2 fountain can be fed from two opposite feedthroughs located on the cavity midsection. An "asymmetric" feed configuration consists in feeding the cavity from only one side, the other feedthrough being loaded on 50 Ω by a microwave isolator. The "symmetric" feed configuration consists in feeding the cavity from both sides. This implies to equalize the microwave power of each feedthrough and the phase between them at the center of the cavity using the atoms as a probe. This is typically done to better than 1% in amplitude and 80 mrad in phase.

In asymmetric feed configuration it is expected that an energy flow is created from one coupling to the other. This energy flow and the related phase distribution can be modulated by switching between asymmetric and symmetric feed configurations.
The experiment is tailored to measure the distributed cavity phase shift difference between symmetric and asymmetric feed configurations as a function of the fountain tilt. The optical table on which the fountain lies is set on three feet the height of which can be adjusted manually. With this setup we are able to tilt the entire fountain and hence the launch direction (z-axis) with respect to gravity. As a result, we shift the center of the atomic cloud between the first and the second Ramsey interactions in order to explore the phase distribution in the cavity.
In this experiment we tilt the fountain around the two axes in the horizontal plane (Oxy): one parallel (x-axis) to the feeding direction and the other one perpendicular (y-axis). We measure the tilt using spirit levels with a resolution of ~0.025 mrad. In order to eliminate long term fluctuations, we perform differential measurements by cycling between three feed configurations each lasting 50 fountain cycles: symmetric feed, asymmetric feed from one side and asymmetric feed from the other side. For each tilt the sequence is repeated for 1 to 2 days to reach a statistical resolution below 3×10^{-16}.

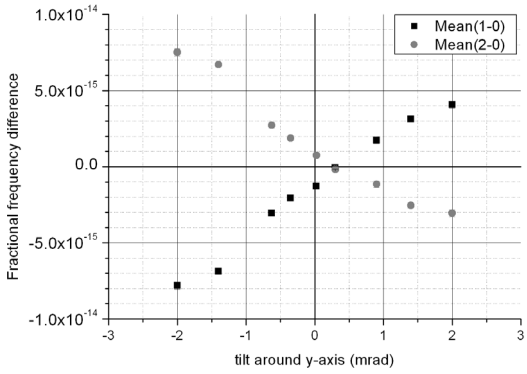

Fig. 2 – Fractional frequency difference between asymmetric (1 and 2) and symmetric (0) feed configurations for π/2 Ramsey pulses as a function of the fountain tilt parallel to the feed direction (tilt around the y-axis). ■ = asymmetric feed from side 1 ; ● = asymmetric feed from the opposite side.

In Fig. 2 measurements for π/2 Ramsey pulses are shown. It is the average fractional frequency difference between an asymmetric and the symmetric feed configurations as a function of the fountain tilt around the y-axis. With our typical resolution we see a clear linear dependence of the shift with the tilt parallel to the coupling irises. The sensitivity is about 4×10^{-15}/mrad. The sign is consistent with the simplest energy flow picture.

The maximal tilt (2 mrad) that we explored is determined by the truncation of the atomic cloud. For a tilt of 2 mrad almost half the atoms are lost.
We observe a good symmetry between the two asymmetric feed configurations. The shift cancellation appears for a tilt of 300 µrad which indicates a good ab initio alignment of the numerous mechanical and optical parts in the fountain.

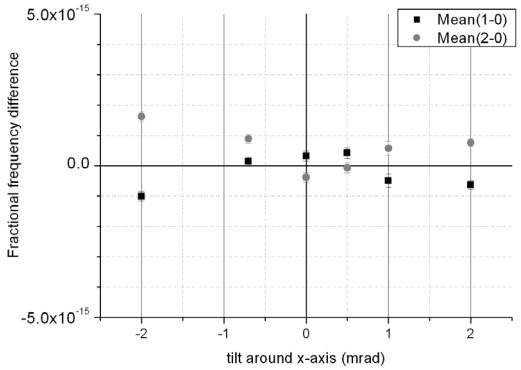

Fig. 3 – Fractional frequency difference between asymmetric (1 and 2) and symmetric (0) feed configurations for π/2 Ramsey pulses as a function of the fountain tilt perpendicular to the feeding direction (tilt around the *x*-axis). ■ = asymmetric feed from side 1 ; ● = asymmetric feed from the opposite side.

In Fig. 3 measurements for a tilt around the other axis are presented. As expected in the simplest energy flow picture the measured shifts are much smaller.

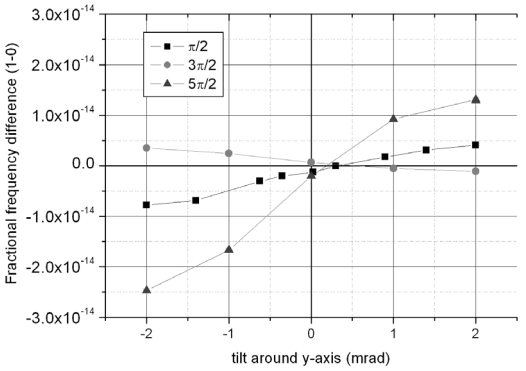

Fig. 4 – Fractional frequency difference between the asymmetric feed (from side 1) and the symmetric feed configurations for π/2, 3π/2 and 5π/2 Ramsey pulses as a function of the fountain tilt parallel to the feeding direction.

In Fig. 4 similar measurements for several microwave powers (π/2, 3π/2 and 5π/2 Ramsey pulses) are shown. Since the results have opposite sign for the two feed directions, only the measurements for one of the two asymmetric configurations are shown. Measurements in the other tilt direction are much smaller as for the π/2 case (see Fig. 3). Fig. 4 shows a dramatic change of the sensitivity to the fountain tilt which cannot be explained by the simple energy flow picture. Most notably the measurements at 3π/2 have a smaller slope than π/2 measurements with opposite sign. Note that a similar behavior was observed in early measurements with the FOM fountain [10] despite a substantially different aspect ratio of the Ramsey cavity.

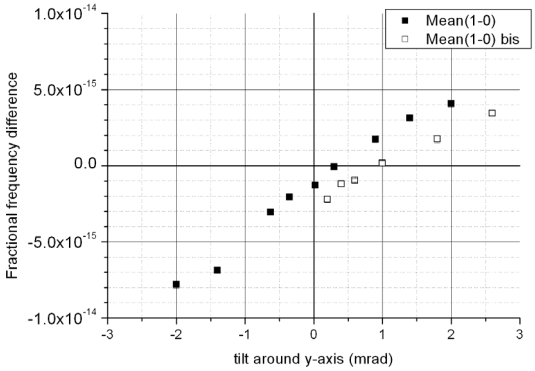

Fig. 5 – Fractional frequency difference between asymmetric (1) and symmetric (0) feed configurations for π/2 Ramsey pulses. ■ = asymmetric feed from side 1 ; □ = asymmetric feed from side 1, the power of the laser-cooling beams for the optical molasses being unbalanced at the 10-20% level.

Additionally, as shown in Fig. 5, we have measured a strong dependence of the shift with the laser power coupled into the laser-cooling beams. A power imbalance of the laser-cooling beams causes a shift of the atomic cloud center and/or a change of the launch direction. As illustrated in Fig. 5, a power imbalance at the 10-20% level induces an effective change in the launch direction of ~500 µrad.

Under optimized clock operation, the tilt is set to 300 µrad in order to cancel the feed dependent term based on measurements of Fig. 2 and the cavity is fed symmetrically. Estimating that the launch direction is kept stable within ± 100 µrad, the feed dependent shift remains smaller than 4×10^{-16}. Consequently we expect that the symmetric feed configuration cancels this term to 10^{-17} even for relatively large imperfections of the amplitude and phase adjustment.

IV. SIMULATION

Li and Gibble [11] have proposed an analytic calculation of phase variations in a TE_{011} cylindrical cavity with lossy copper walls and infinitely small feedthroughs. In this approach the phase distribution is decomposed in the following form:

$$\Phi(\vec{r}) = \sum_{m=0}^{\infty} \sum_{p=1+\delta_{m,0}}^{\infty} H_{m,p}(r, z, \phi)$$

$$H_{m,p}(r, z, \phi) = \delta\ \gamma_p \times \left(1 + \frac{2\,k_1^{\,2} R}{\gamma_1^{\,2} D}\right) \times \frac{1-(-1)^p}{2\left(1+\delta_{m,0}\right)} \times \frac{J_0(\gamma_1 R)}{J'_m(\gamma_p R)} \frac{J_m(\gamma_p r)}{J_0(\gamma_1 r)} \frac{\cos(k_p z)}{\cos(k_1 z)} \cos(m\phi) \qquad (1)$$

where δ is the skin depth, $k_p = p\pi / D$, $\gamma_p = \sqrt{\omega^2/c^2 - k_p^{\,2}}$, R and D are respectively the radius and the length of the cavity, $J_m(x)$ are Bessel functions and $J'_m(x)$ their derivatives. The Ramsey cavity of the FO2 fountain has a radius of 2.50 cm and a length of 2.68 cm. Its center is placed 51.85 cm above the center of the optical molasses.

In an attempt to compare our measurements to this model, we have performed a numerical simulation to compute the behavior of the main terms in Eq. (1). The numerical Monte Carlo (MC) computation is based on randomly drawing atomic trajectories in accordance with the experimentally measured space and velocity distributions. For each trajectory the evolution of the internal atomic state is calculated in a two-level atom model using the Runge-Kutta method with adaptative time step. The truncation of the atomic cloud by the cavity is taken into account both on the way up and on the way down. For each trajectory the transition probability is computed on both sides of the atomic resonance. The difference between the two transition probabilities is used as an error signal to run a numerical servo-loop identical to the one used in the fountain routine. In this simulation the microwave field amplitude is modeled as a perfect cylindrical TE_{011} mode. The phase is successively made equal to each of the $H_{m,p}$ terms in Eq. (1). The frequency shift is computed for several tilts with respect to gravity and for $\pi/2$, $3\pi/2$, $5\pi/2$ and $7\pi/2$ Ramsey pulses. Also the calculation has been made for an atomic cloud off-centered by 2 mm in the horizontal plane in the feeding direction. Since our experimental procedure based on measuring the frequency difference between symmetric and asymmetric feed configurations isolates odd terms (m=1, 3, 5…), only these terms are discussed here.

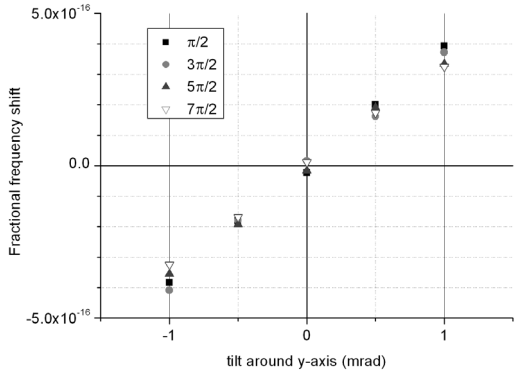

Fig. 6 – Fractional frequency shift induced by the $H_{m=1,p=1}$ term as a function of the tilt in the feed direction for several Ramsey pulse amplitudes and for a centered atomic cloud.

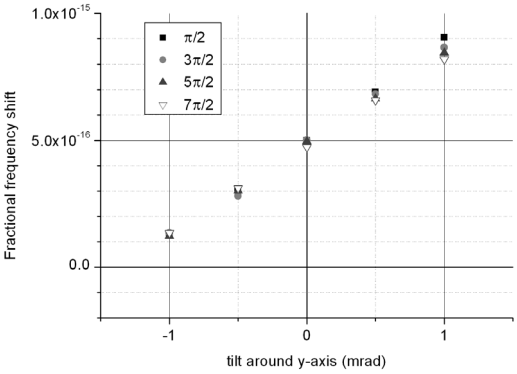

Fig. 7 – Fractional frequency shift induced by the $H_{m=1,p=1}$ term for an atomic cloud off-centered by Δx = -2mm.

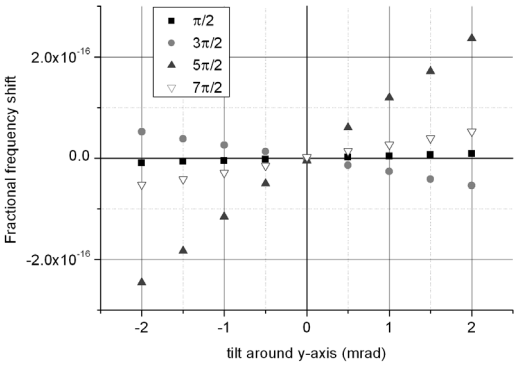

Fig. 8 – Fractional frequency shift induced by the $H_{m=1,p=3}$ term as a function of the tilt in the feed direction for several Ramsey pulse amplitudes and for a centered atomic cloud.

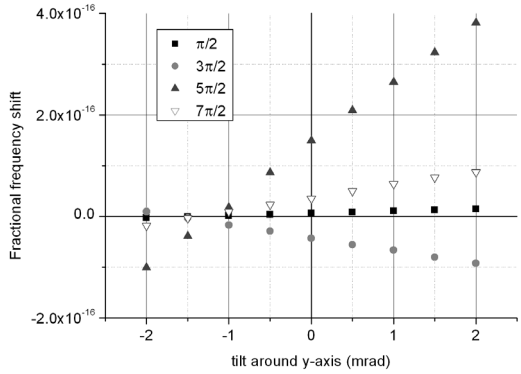

Fig. 9 – Fractional frequency shift induced by the $H_{m=1,p=3}$ term for an atomic cloud off-centered by Δx = -2mm.

Fig. 6-9 show the result of the numerical computation for $H_{m=1,p=1}$ and $H_{m=1,p=3}$ for a centered atomic cloud and a cloud off-centered by Δx = -2mm. As we can see, the lowest order term $H_{m=1,p=1}$ is mostly insensitive to change in microwave amplitude. Conversely the $H_{m=1,p=3}$ term exhibits magnitude and sign variations very similar to those observed in our measurements.

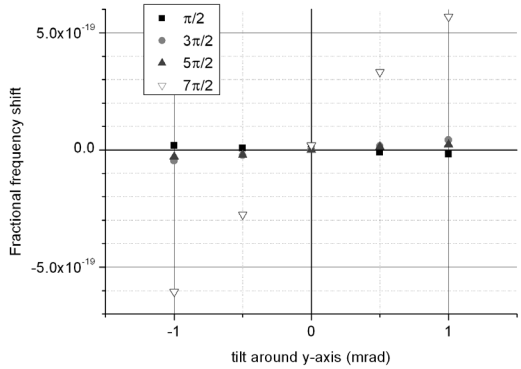

Fig. 10 – Fractional frequency shift induced by the $H_{m=1,p=5}$ term as a function of the tilt in the feed direction for several Ramsey pulse amplitudes and for a centered atomic cloud.

Fig. 10 shows the $H_{m=1,p=5}$ term. There is a sign change between π/2 and 3π/2, while 3π/2 and 5π/2 data have the same sign. The calculation for m>1 terms shows no clear variation with tilt. Additionally, as pointed out in [11], the influence of these terms is expected to be exponentially small.
Note also that we have verified that the numerical simulation produces no significant shift for a tilt in the other direction as observed in our measurements.

V. SIMULATION VS MEASUREMENTS COMPARISON

The above analysis suggests the possibility that our measurements could be described using only the two or three lowest order terms. To test this, we have performed a fit of our measurements assuming that the odd component of the phase distribution is simply a linear superposition of $H_{m=1,p=1}$ and $H_{m=1,p=3}$. We find $\Phi(r,z,\phi) = 4.7 \times H_{m=1,p=1} + 120 \times H_{m=1,p=3}$. The comparison between the measured slopes and the best fit results is given in Table 1. We can see that the agreement between the fit and the measurements is quite good, given the simplicity of the model.

Ramsey pulses	Measured sensitivity (Hz/rad)	Simulated sensitivity (Hz/rad)	Ratio
$\pi/2$	0.029	0.022	0.74
$3\pi/2$	-0.013	-0.012	0.95
$5\pi/2$	0.12	0.14	1.2

Table 1 – Comparison between the measured sensitivities to fountain tilt for different Ramsey pulse amplitudes and the sensitivities deduced from the best fit based on [11] and on the MC simulation ($\Phi(r,z,\phi) = 4.7 \times H_{m=1,p=1} + 120 \times H_{m=1,p=3}$).

We have also tested the fit using $H_{m=1,p=1}$, $H_{m=1,p=3}$ and $H_{m=1,p=5}$ and we find similar weights within 20% for the two leading terms.
From these results we can deduce a value for the phase gradient along the coupling axis at the center of the cavity. We find a gradient of ~93 µrad/mm with a contribution of ~79 µrad/mm for $H_{m=1,p=1}$ and ~14 µrad/mm for $H_{m=1,p=3}$. For comparison the order of magnitude for this gradient is given by $2\pi/R \times \pi/(2Q)$= ~60 µrad/mm.

The weights that we found for the two first odd terms differ very significantly from those predicted by the model of [11] reproduced in Eq. (1). Indeed our notations are such that agreement with [11] corresponds to weights equal to unity. In our view this illustrates the fact that the model of [11] is not fully adapted to describe our cavity. We believe that the main explanation for the mismatch is coming from the fact that the model assumes infinitely small feedthroughs and therefore a quality factor equal to the theoretical limit (Q=27500 in our geometry). Contrary to these assumptions our cavity has 5 mm diameter coupling irises leading to an overcoupled cavity with a quality factor of 6600. Interestingly the weight of the $H_{m=1,p=1}$ term is quite close to the ratio between the two quality factors ($27500/6600 \approx 4.2$). Compared to Eq. (1) the measured weight of the $H_{m=1,p=3}$ term is $120/4.7 \approx 25$ times larger. We think that one possible explanation for this mismatch is the fact that our 5 mm diameter iris

diffracts much less in high order $H_{m,p}$ terms than the infinitely small coupling, which therefore increases the weights of low order terms.

VI. DISCUSSION

As a follow-up to this work, it is necessary to confirm the above assumptions concerning the mismatch between our analysis and [11]. In particular a new derivation accounting for the finite size of the coupling irises should explain the weight of the $H_{m=1,p=3}$ term. As a second step we hope that the same derivation will allow us to estimate the weights of the lowest order even terms which are predominant under optimized clock operation (symmetric feed). Also the effect of the perturbation introduced by the cut-off waveguides [11] has to be considered even though we expect it to be small. Completing this program should eventually lead to estimating the uncertainty of the distributed cavity phase shift based on an experimentally proven model.

Acknowledgements

We thank the LNE-SYRTE electronics workshop staff and D. Chambon for valuable work on the microwave synthesis related electronics.

REFERENCES

[1] S. Bize *et al.*, C. R. Physique **5**, 829 (2004)

[2] S. Bize *et al.*, J. Phys. B: At. Mol. Opt. Phys. **38**, S449 (2005)

[3] C. Vian *et al.*, IEEE Trans. Instrum. Meas. **54**, 833 (2005)

[4] D. Chambon *et al.*, Rev. Sci. Instrum. **76**, 094704 (2006)

[5] H. Marion *et al.*, Phys. Rev. Lett. **90**, 150801 (2003)

[6] P. Wolf *et al.*, "Using a Cs fountain to test Lorentz Invariance", see these proceedings

[7] P. Wolf *et al.*, Phys. Rev. Lett. **96**, 060801 (2006)

[8] A. Khursheed *et al.*, IEEE Trans. Ultrason. Ferroelect. Freq. Contr. **43**, 201 (1996)

[9] R. Schröder *et al.*, IEEE Trans. Ultrason. Ferroelect. Freq. Contr. **49**, 383 (2002)

[10] M. Abgrall, "Evaluation des performances de la fontaine atomique PHARAO, Participation à l'étude de l'horloge spatiale PHARAO", Ph.D. dissertation, Université de Paris VI, France (2003)

[11] R. Li and K. Gibble, Metrologia **41**, 376 (2004)

[12] S. R. Jefferts *et al.*, IEEE Trans. Ultrason. Ferroelect. Freq. Contr. **52**, 2314 (2005)

Proceedings of the 20th EFTF, 2006

Phase Transient Measurement at the Micro radian level for Atomic Fountain Clocks.

G. Santarelli[1]*, G. Governatori[1], M. Lours[1], D. Chambon[1], F. Chapelet[1], S. Bize[1], M E. Tobar[2], Th. Potier[3] and A. Clairon[1].

[1] *LNE-SYRTE, Observatoire de Paris, 61, Av de l'Observatoire, 75014 Paris, France*
[2] *University of Western Australia, School of Physics, Stirling Hwy., Crawley, Australia.*
[3] *Thales Airborne Systems, 2, Av. Gay-Lussac, 78851 Elancourt, France.*
**Electronic address:* giorgio.santarelli@obspm.fr

This paper focuses on two effects due to the microwave interrogation signal imperfection. The first one deal with cycle synchronous phase transients due to the sequential operation of the atomic fountain. For the search of such a phase variations deeply buried in the synthesizer phase noise we have developed a triggered transient phase analyzer able to process the microwave signal in order to extract the phase in a synchronous fashion. With this device we check *"in vivo"* the FO2 interrogation signal with a resolution approaching 1microradian. Using this device we investigate a new generation of microwave switches able to reduce drastically the microwave leakage without inducing any phase transient on the microwave signal and we measure the microwave leakages on the FO2 atomic fountain at the 10^{-16}.

I. INTRODUCTION

Atomic fountain frequency standards are becoming the most widely used high accuracy atomic clock [1]. About six fountains currently participate at the definition of the SI second at a level of 10^{-15} or better [2-7] and at least fifteen more standards are under development [8]. Beside classical metrological and timekeeping tasks, accurate and stable atomic fountains clocks can perform fundamental physics tests like special relativity tests [9, 10] and of fundamental constant variations tests [11-15].

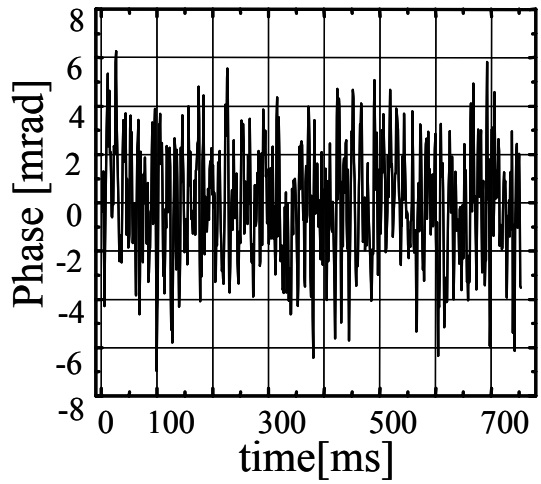

Figure 1. Temporal behavior of the phase of the interrogation oscillator during the fountain cycle

More than ten years after the first operation of an atomic fountain as a frequency standard [16] the projected goal of 10^{-16} accuracy has no yet been achieved. When approaching this level of accuracy all the systematic effects need to be evaluated at a level better than 10^{-16}.

The frequency synthesizer problematic has been already addressed for atomic fountains and different designs have been implemented [17-19]. In this paper we focus on two effects due to the microwave interrogation signal imperfections.

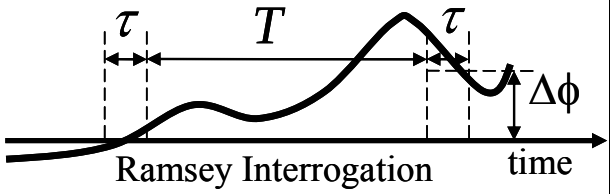

Figure 2. Phase transient during the Ramsey interrogation

The first effect is due to the sequential operation of an atomic fountain. Lets us suppose a phase perturbation hidden in the interrogation signal (see figure 1), synchronous with the interrogation cycle with an average value of $\Delta\phi$ [rad] between the two Ramsey interactions, the resonance central frequency will then be shifted by $\Delta\nu=\Delta\phi/(2\,\pi\,T)$ [Hz], where T is the Ramsey time (0.5 s typically) (see figure 2). For example a tiny 10 μrad average phase difference leads to an unacceptable fractional frequency offset of 3×10^{-16}.

The phase transient could be due to digital signal switching and RF power commutation on the acousto optic modulators (a few watts), affecting for example one of the phase locked loops inside the synthesizer via electromagnetic compatibility (EMC). The digital control command of the offset synthesizer [1] which provides frequency tunability and modulation to the output of the fountain microwave synthesizer can also lead to phase perturbations completely synchronous with the fountain interrogation cycle

The search for such a phase variations which are deeply buried in the noise is a quite difficult task. For such a purpose we have developed a triggered transient phase analyzer which is able to process the microwave signal in order to extract the phase with one to five milliseconds time resolution in a synchronous fashion. In the next chapter we will describe the measurement set-up and the related algorithms.

II. TRIGGERED PHASE TRANSIENT ANALYZER.

II.1 Hardware set-up.

In order to process the interrogation oscillator signal we first down convert from the microwave domain to acoustic frequency where it is possible to use an inexpensive and computer interfaced Analog–to-Digital sampling board. The schematic of the microwave demodulator is depicted in figure 3. This device has two inputs, one for the reference synthesizer one for the device under test (DUT). The reference input signal saturates the LO port of an I/Q microwave mixer and the DUT feeds the RF port, both signals are band pass filtered and the microwave isolators provides a good impedance matching at the measurement frequency (9.2 GHz). The mixer outputs are low pass filtered with microwave filters and amplified with AC coupled low noise audio amplifiers with a bandwidth of 10 kHz. The two input synthesizer have a frequency offset of 4.3 kHz. This beatnote signal is amplified to match the A/D converter input range (±5 V). The demodulator set-up provides the sampling clock at 250 kHz phase coherent with the microwave signals.

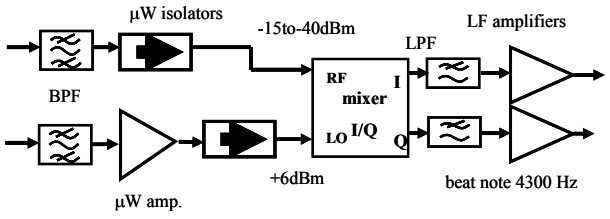

Figure 3. Microwave demodulator set-up

Both beat-notes contains the same amount of information, thus we use only one output of the demodulator (the two signals I&Q are used in the case of phase noise measurement on DC signals). The beatnote signal is acquired at 250 kS/s rate with 16 bit resolution (National Instrument NI-6143 PCI). The data acquisition board is embedded in a high performance computer. An asynchronous digital trigger signal is provided to the board by a Direct Digital Synthesizer (DDS).

II.2 DSP Algorithm description.

The data flow from the A/D board is handled by DSP software developed in a CVI environment. On the trigger edge the card start to digitize and the input sequence is stored in a vector. The data acquisition length can vary from 0.4 s to 2 s according to the fountain cycle. After the end of the data acquisition period, the sampled sequence is decimated and filtered down to a rate of 25 kS/s. This task is accomplished by a computing efficient two stages multirate polyphase Finite Impulse Response filters (FIR). This operation increases the effective dynamic range to 18 bits. The decimated sequence is then processed, with two different algorithms.

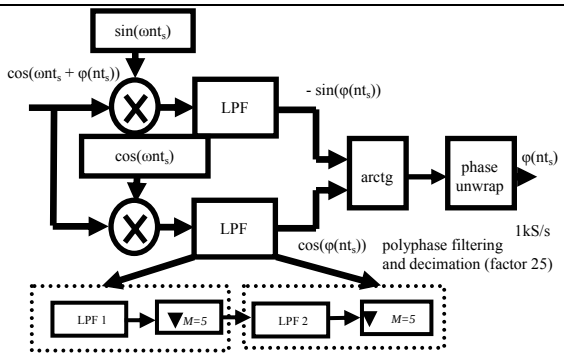

Figure 4. Block diagram of the I&Q digital demodulation algorithm

The first approach is the digital implementation of the well know analog I/Q demodulator. The data vector is multiplied with two sequences of sampled sine and cosine functions. The two outputs are then low pass filtered and decimated down to 1 kS/s (see figure 4). The phase is obtained by calculating arctangent function of the ratio followed by a phase unwrap operation. The equivalent bandwidth is 400 Hz. To check the consistence and the accuracy of the results, we implement a second approach to the phase calculation. The algorithm is based on a robust linear fit (Single Value Decomposition SVD) where the signal model is the sum of a sinus and a cosine function with know frequency and unknown amplitude. It is worth recalling that this is a linear fit. The 25 kS/s stored sequence is divided in 5 ms data packets. For each group the fit routine returns a value of the phase.
The DSP software includes a data rejection feature applied to both algorithms. At each cycle we compute the standard deviation of the phase samples and this value is compare to an operator settled limit. In case of overflow the complete data vector is discarded.

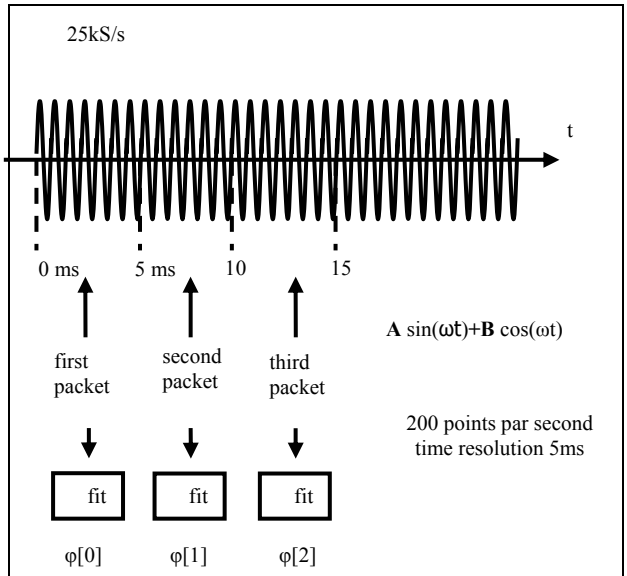

Figure 5. Fit algorithm description.

To reach the required phase resolution the DSP software averages the phase vectors and stores periodically the result. The resulting phase noise on the sampled phase decreases as the square root on the integration time. The consistence of the algorithms and the accuracy of the phase determination have been checked in many different ways. For example we slightly detune the DUT synthesizer output by a tiny 10μHz and we observe after few hours averages a linear phase ramp of 20π μradians over one second.

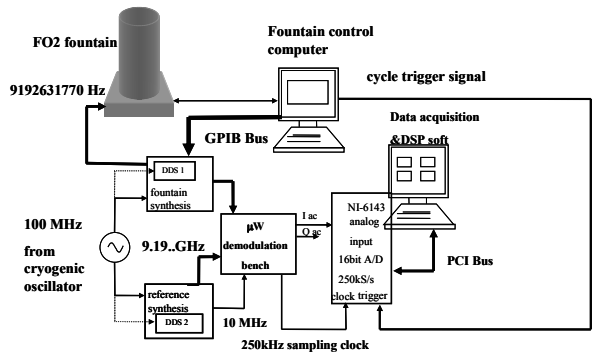

Figure 6. Phase transient measurement set-up on the FO2 fountain

The Triggered Phase Transient Analyzer (TPTA) resolution has been tested over a wide range of conditions (signal level, different microwave synthesizer) and the average phase routinely reach sub μrad resolution. The averaging time depends on the phase noise of the synthesizer (typically between a few hours to a few days integration time) for a sample length of about on second.

III. PHASE TRANSIENT EVALUATION ON THE FO2 FOUNTAIN.

With the TPTA we implement an "In vivo" phase transient evaluation of the FO2 fountain interrogation oscillator. Figure 5 shows the measurement set-up. The TPTA is connected to the fountain synthesizer and to an unperturbed reference synthesizer. The fountain clock operates in normal conditions and the control computer drives frequency and amplitude of the fountain synthesizer.

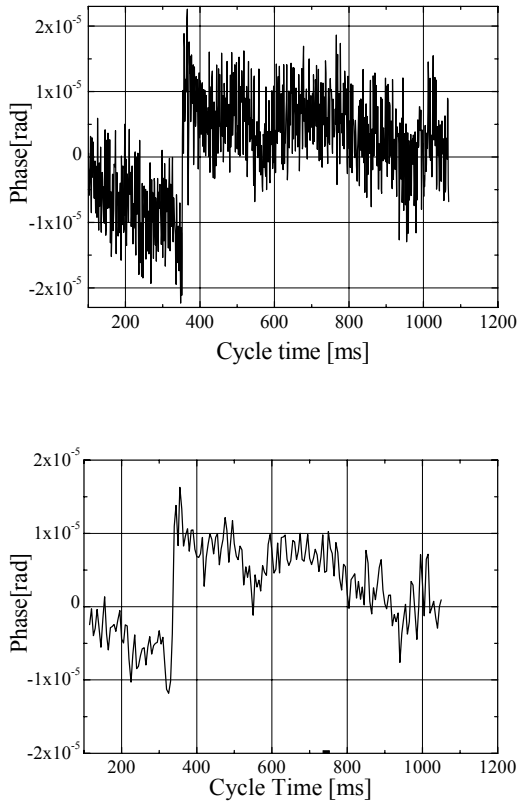

Figure 7. "In vivo" phase transient measurement on FO2 (upper plot is obtained with the digital I/Q algorithm and the lower graph with the SVD fit method).

The acquisition is triggered by the fountain cycle. Both synthesizers are driven by a 100 MHz derived from the cryogenic sapphire oscillator [19] with isolated paths. Figure 6 shows the measured phase transient on the fountain experiment. We can observe a well resolved phase jump of about 15 micro radians with both algorithms.
The phase jump occurs before the beginning of the Ramsey interaction.

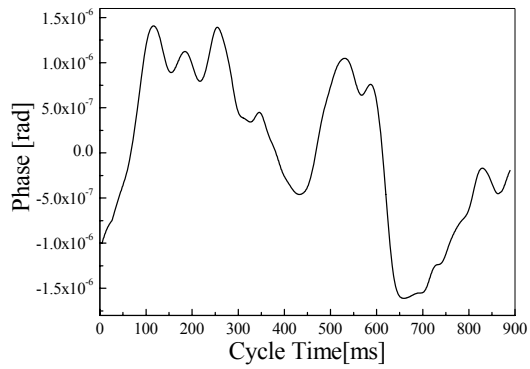

Figure 8. Residual phase transient in the FO2 fountain

After few measurements we discover that the phase jump is due to the power commutation on the acusto optic modulators (AOM). A better electrical configuration cancels out this effect. We also investigate phase gradient due to the modulation of the offset DDS synthesizer used in the local oscillator. We did not observe any effect at the micro radiant level which is compatible with an accuracy target of 10^{-16}. Figure 8 shows a typical phase plot with a resolution close to one μrad.

IV. THE MICROWAVE LEAKAGE SHIFT SUPPRESSION IN A FOUNTAIN CLOCK.

The microwave leakage is one of the most difficult technical effects to evaluate in a fountain accuracy budget. This effect has been studied for the first time in the case of thermal beams [20].

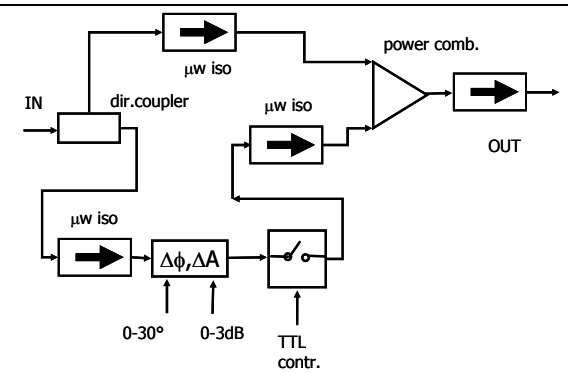

Figure 8. Schematic of the microwave Mach-Zehnder switch

More recently this effect has been addressed in the case of atomic fountain [21, 22] and despite the effort to model this shift it is difficult to use the power dependence when the fountain is operated to higher microwave powers (3π/2, 5π/2, 7π/2….) to evaluate the effect.

IV.1 Transient less microwave switch.

The sequential operation of the fountain allows switch-off the microwave field outside the interrogation cavity. This solution although appealing has a major drawback: a microwave switch shows strong phase transient with time constant of the order of a few hundreds milliseconds.

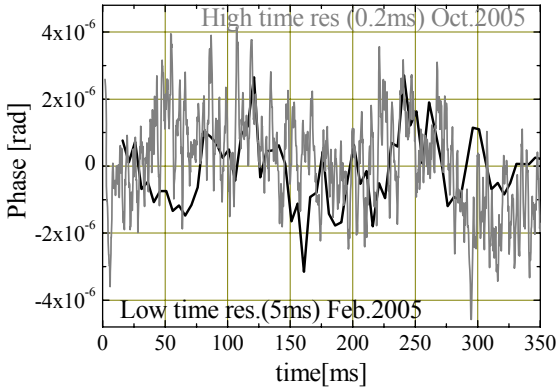

Figure 9. Phase transient analysis of the Mach-Zehnder switch (black line low time resolution n with SVD fit method, grey line high resolution digital I/Q algorithm).

A few years ago we develop a new kind of transient less microwave switch. The concept is rather simple; we realize a microwave Mach-Zehnder interferometer which contains in one of the arm a PIN diode microwave switch. If the interferometer is tuned to a dark fringe configuration, when the switch is on the interferometer output goes to low by a destructive interference.

In this way the microwave signal which interacts with the atoms is always unperturbed. Figure 7 shows the practical realization of this “smart switch”, the isolation and the impedance matching is improved using microwave isolators. The interferometer is coarse tuned in phase and amplitude by cable length adjustment and fixed attenuators; a combined voltage controlled phase shifter-attenuator (30° and 3dB range) is used to fine tune the destructive interference. A microwave high attenuation (80 dB) PIN diode switch is used in one arm. An extinction ratio of 60-75 dB can be easily obtained over short period of time.

A stable long term operation of 45-50 dB is ensured by careful mechanical layout and tight temperature control (<0.1°C). The switching time is dominated by the PIN diode switch and is well below 100 ns. The insertion

losses are quite high (~17 dB). Despite the relatively low attenuation, this switch is suitable to investigate the microwave leakage especially the one inside the fountain physical package. Using the TPTA we investigate the output phase of the Mach-Zehnder switch after switching. Figure 8 shows the result of two measurements with different time resolution and separated by more than six months. At the measurement resolution (2-3μrad) there is no clear signature of phase transient. The measurements have been repeated with different power levels and timings to validate the previous measurements. This experimental verification confirms the expected transient less properties of the switch.

IV.2 A leakage free interrogation oscillator.

In the previous measurements the RF input signal of the TPTA is switched and the result seems not to be affected by parasitic phase transients. This suggests that under some conditions is possible to switch the RF input of a microwave mixer without generating phase transients. To verify this conjecture we vary the driving level and the brand of the mixer, all the measurements are free of transient within the measurement resolution of a few micro radians

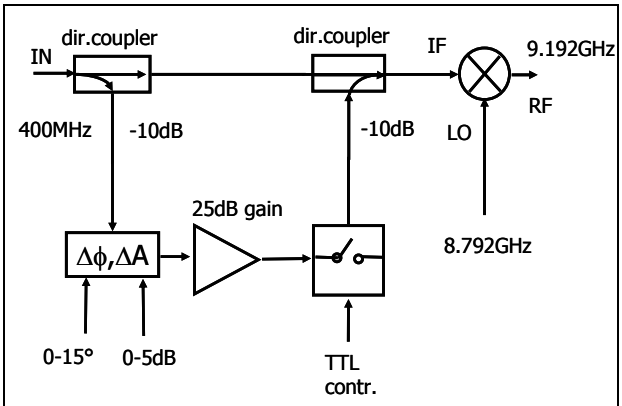

Figure 10. Schematic of the RF Mach-Zehnder switch with the related synthesizer.

. Let us consider the following synthesis scheme where the IF port of a mixer is driven by a signal at 400 MHz and the LO port with 8.792… GHz, at the RF output the Cs hyperfine frequency is obtained. In this way we can realize a leakage free synthesizer by switching the RF signal driving the IF port. Unfortunately after extensive tests with a few different technologies of RF switches (Bipolar, AsGa, PIN diodes, relay, MEMS….) we still observe large phase transient ranging from 20 μrad to 200 μrad with time constants in the hundreds of ms. Figure 11 Show the typical behavior of a switch.

IV.3 Transient less RF switch.

With the previous experience on the microwave Mach-Zehnder switch, we develop an RF dark fringe interferometer with the same approach.

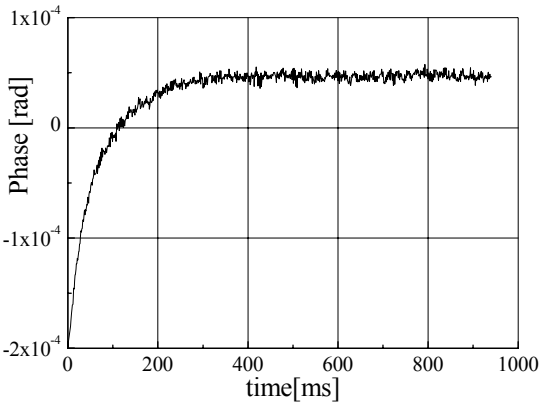

Figure 11. Typical phase transient behavior of an RF switch.

Figure 10 shows the scheme of the RF Mach-Zehnder switch and the related frequency synthesis configuration. This device has a few major advantages over his microwave counterpart: the phase and amplitude adjustments are much easier at RF frequencies; it is possible to obtain a stable 60 dB extinction ratio without temperature control. Using an inexpensive RF amplifier it is possible to have an insertion loss below 2 dB. Also, with the low cost of the device it is possible to cascade two of units to obtain a merely 120 dB extinction depth. Figure 11 shows the output phase after switching of the combination of the RF interferometer and the mixer model used in the atomic fountain FO2 in two different configurations. As expected it is impossible to detect phase transients within the measurement noise. We extensively investigate different mixer models and driving levels for IF and LO ports. The transient free behavior holds over a very large range of driving levels (LO -10 dBm to +6 dBm, RF -40 dBm to -10 dBm) provided that the LO level is 10-15 dB larger than IF.

V. INVESTIGATION OF THE MICROWAVE LEAKAGE ON THE FO2 FOUNTAIN.

Using the previously described combination of switched interrogation oscillator, we investigate the microwave leakage in the atomic fountain FO2.
In a differential configuration we alternatively drive every 50 cycles the atomic transition with the continuous and the switched interrogation oscillator microwave signal. The microwave signal extinction is

done when the atom cloud is in the cavity cut-off waveguides.
Figure 13 shows the relative frequency difference between the two configurations as a function of the microwave interrogation power level. Thanks to the non-dephasing switch and to the differential method, the effect of microwave leakage is well-isolated from other microwave amplitude dependent effects (distributed cavity phase shift, effect of spurious microwave lines, cold collision shift). Figure 13 shows a frequency shift due to leakage of $2x10^{-16}$ in normal clock operation ($\pi/2$ Ramsey pulses). For increase microwave amplitude, measurements of figure 13 are consistent with a shift proportional to the field amplitude with an oscillating sign which indeed is one possible signature of a leakage field in atomic fountains. Given this well understood behavior, it is probably feasible to use these measurements to correct this shift with an uncertainty slightly below 10^{-16}. Discussing this possibility goes beyond the scope of this paper. Alternately, the thoroughly tested non-dephasing switch can be used on a permanent basis under clock operation in order to fully eliminate the microwave leakage issue.

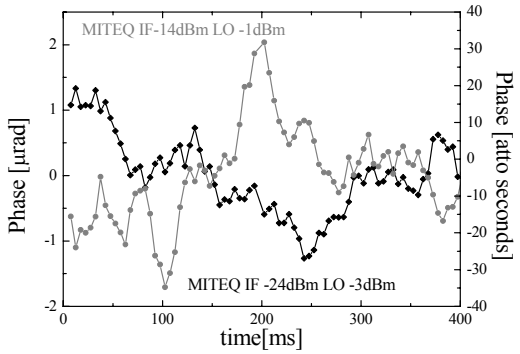

Figure 12. Measured phase transient of the combination of the RF Mach-Zehnder switch and a microwave mixer for the fountain operation conditions.

VI. CONCLUSIONS AND FUTURE DEVELOPMENTS.

We have developed a Triggered Phase Transient Analyzer with micro radian resolution to investigate the phase of the atomic fountain microwave interrogation oscillator. With this instrument we check "In vivo" the FO2 interrogation signal phase. The measurements are compatible with an accuracy target of $1x10^{-16}$.
Successively we address the microwave leakage issue.
To study this effect we first develop a transient less microwave switch based in an original Mach-Zehnder interferometer design. Using the TPTA we verify the absence of phase transient with a resolution approaching 10^{-6} radians. This test also reveals that a microwave mixer can operate as a non dephasing switch under certain conditions. This concept has triggered the development of a leakage free microwave synthesizer where the interrogating signal is generated only during atom interrogation. This device has been extensively measured to verify the absence of phase transient after the microwave switching at the micro radian level.

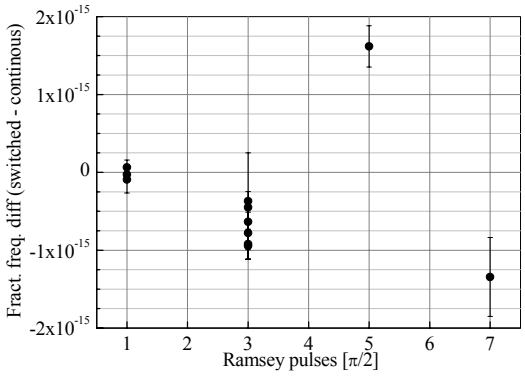

Figure 13. Relative frequency difference between the two configurations where the microwave field is continuous applied to the cavity or switched on only during the atoms are in the cavity in function of the interrogation power level.

Using this new synthesizer we investigate the microwave leakage on the atomic fountain FO2. The measurement shows a frequency shift due to leakage of $2x10^{-16}$ in normal clock operation ($\pi/2$ Ramsey pulses), well below the stated accuracy for the clock.
In the next future we plan to realize and test two more systems to be implemented on all LNE-SYRTE fountains and further investigate these devices with a resolution below 1 micro radian.

Acknowledgements

We want to thanks L. Volodimer for the valuable work for the RF electronic sub systems.

REFERENCES

[1] R. Wynands and S. Weyers, Metrologia, **42**, 64–79, (2005).
[2] S Weyers, U Hübner, R Schröder, C. Tamm and A Bauch, Metrologia, **38**, 343-35, (2001).
[3] F. Levi Levi, L. Lorini, D. Calonico, A. Godone, *IEEE Trans on Instrum. Meas.*, **52**, 267, (2003).

[4] K. Szymaniec *et al.*, Metrologia, **42**, 49–57, (2005).
[5] C. Vian et al., *IEEE on Trans Instrum. Meas*., **54**, 833-836, (2005).
[6] S. Bize *et al.*, Jour. of Phys. B: At. Mol. Opt. Phys., **3**8, 449-468, (2005).
[7] T. Heavner *et al.*, Metrologia, **42**, 411-422, (2005).
[8] The fountains clocks are at present developed at NMIJ and NICT (Japan), NIM an NTS XIAN (PRC), KRISS (South Korea), Taiwan, Mexico, UNSP (Brasil), VINIFRII (CSI), METAS (Swiss), NRC (Canada), USNO (USA).
[9] A. Bauch and S. Weyers, *Phys. Rev. D*, **65**, 081101(R), (2002).
[10] P. Wolf *et al., Phys. Rev. Lett,* (2006).
[11] M.Niering *et al.*, *Phys. Rev. Lett*., **84**,5496, (2000).
[12] S. Bize *et al.*, *Phys. Rev. Lett*., **90**, 150802, (2003).
[13] H. Marion *et al*, *Phys. Rev. Lett*., **90**, 150801, (2003).
[14] M. Fischer *et al.*, *Phys. Rev. Lett*., **92**, 230802, (2004).
[15] E. Peik *et al.*, *Phys. Rev. Lett*., **93**, 170801, (2004).
[16] A. Clairon, *et al., IEEE Trans IM*., **44**, 128-131, (1995).
[17] G. D. Rovera, G. Santarelli, and A. Clairon, *IEEE Trans on Ultra. Ferro. Elec Freq. Contr.*, **43**, (1996).
[18] A.S. Gupta, D. Popovic, F.L. Walls, *IEEE Trans on Ultra. Ferro. Elec Freq. Contr*, **47**, 475–479, (2000).
[19] Chambon *et al.* Rev. Sci. Instrum., 094704, **76**, (2005).
[20] B. Boussert, G. Theobald, P. Cerez, E. de Clercq, *IEEE Trans on Ultra. Ferro. Elec Freq. Cont,* **45**, 728, (1998).
[21] S. Jefferts *et al*, Proceedings of the 19 EFTF Besançon, 58-63, (2005).
[22] S. Weyers *et al*, Proceedings of the 20 EFTF Braunsweig, (2006).

Effects of microwave leakage in caesium clocks: theoretical and experimental results

Proceedings of the 20th EFTF, 2006

S. Weyers,* R. Schröder, and R. Wynands
Physikalisch-Technische Bundesanstalt, Bundesallee 100, 38116 Braunschweig, Germany

We investigated the effects of microwave leakage fields in an atomic fountain clock. In a series of experiments a test microwave signal was beamed into the vacuum system with controlled amplitude, phase, and timing. The observed frequency shifts can be explained by a theoretical model based on an iterative solution of the Bloch equations up to second order. This model applies to both caesium fountain clocks and conventional thermal beam clocks and provides new and essential insights into the problem of microwave leakage fields.

I. INTRODUCTION

In primary caesium atomic clocks caesium atoms are exposed to phase coherent microwave fields in two well-defined cavity regions (Ramsey configuration) in order to effect transitions between the two hyperfine ground state levels. Unless proper design measures were taken, additional microwave fields can escape from the microwave components of a clock (microwave synthesis setup, cables and the cavity regions) and leak into the vacuum regions outside the cavity. There the presence of such additional microwave fields results in extra rotations of the atoms' magnetic moment and thus can lead to a frequency shift that depends on amplitude and phase of those leakage fields.

Such frequency shifts were already observed in the thermal beam clock CSX at PTB and corrective steps were taken [1]. Later on, several experiments were performed in thermal-beam clocks, by increasing the microwave power inside the Ramsey cavities and looking for corresponding frequency shifts [2–4]. Using a microwave signal that was intentionally beamed into the vacuum system, several groups found an increase of the frequency shift in thermal beam clocks with the amplitude of the microwave test signal [5–7].

For special, idealized cases theoretical considerations were made. For instance, Boussert *et al.* [8] found a rather complicated power dependence for a running-wave leakage field between the two Ramsey zones in a thermal-beam clock, with the first-order term proportional to microwave amplitude and a second-order term proportional to microwave power. Other work [9] found a linear dependence on the amplitude of an additional standing-wave microwave field between the two Ramsey zones in a thermal-beam clock and a more complicated, phase-dependent shift when the Ramsey pulse area (Rabi frequency integrated over time) is changed synchronously with the leakage amplitude.

In atomic fountain clocks it has become a standard approach to check for the presence of microwave leakage fields by running the fountain clock with pulse areas of odd multiples of $\pi/2$. Such modes of operation cannot be realized in thermal beam clocks due to the broad range of velocities present in these clocks, which results in a destructive interference of the resonance features for different velocities. Jefferts *et al.* have treated the leakage problem in fountain clocks theoretically by solving the Schrödinger equation in a first-order approximation [10, 11]. They point out that frequency shifts are generally proportional to the microwave leakage amplitude.

Recently, frequency shifts observed in a primary caesium fountain standard were ascribed to additional microwave fields outside the Ramsey cavity [12, 13]. However, the quadratic dependence of the frequency shift on the microwave leakage field amplitude assumed in [12, 13] is in contradiction to the results of the earlier works.

We have chosen to study experimentally the shift of the output frequency of PTB's fountain clock CSF1 [14, 15] as a function of amplitude and phase of a test "leakage" field that we beam into the apparatus. This test field was time controlled by a PIN modulator, so that we were able to study the effect of leakage fields either after the Ramsey interactions or between the Ramsey interactions, and here for the two cases of a strongly asymmetric or a rather symmetric time structure of the leakage field with respect to the apogee of the ballistic flight of the atoms.

The experimental findings can be explained by our theoretical approach, which consists in the iterative solution of the Bloch equations up to the second order, distinguishing between the cases of leakage fields present between the Ramsey interactions and after the Ramsey interactions. Naturally, our first-order solutions come out identical to that given in Ref. [11]. For leakage fields present between the two Ramsey interactions, the first-order term vanishes in the cases of the optimum power condition, i.e., in the cases of pulse areas which are precisely odd multiples of $\pi/2$. In these cases the leading frequency shift contribution is by the second-order term, which exhibits a quadratic frequency shift dependence on the leakage field amplitude. A corresponding term for beam clocks was already calculated by Boussert *et al.* [8].

We could demonstrate in our fountain clock that in practice this quadratic frequency shift dependence

*Electronic address: stefan.weyers@ptb.de

will be undiscernible. It requires an unrealistically precise and stable adjustment of the optimum power condition and a strongly asymmetric leakage field for the ascending and descending atoms. Nevertheless, we could measure this quadratic frequency shift, but only by running the experiments under very special conditions not found in normal fountain operation.

However, we discovered another important effect for the case of leakage fields acting between the Ramsey interactions. The usual expectation is that all terms (first and higher order) vanish if the leakage field experienced by the atoms is symmetric with respect to the first and the second half of the free-evolution period between the Ramsey interactions. We could demonstrate that this is only true as long as the amplitudes of the microwave field in the Ramsey cavity seen by the atoms during the first and the second cavity passage, respectively, are equal.

As explained below, this is usually not the case in a real-world fountain clock. As a consequence, even in the "symmetric" leakage case a frequency shift results. Furthermore, this potentially large first-order frequency shift can depend quadratically on the leakage field amplitude.

II. THEORY

In our fountain clock CSF1 the state selection cavity is located immediately below the cut-off tube of the Ramsey cavity. Therefore leakage fields cannot interact with the atoms during the time interval between the state selection and the first Ramsey passage. We will therefore concentrate in the following on the cases of leakage fields either between or after the Ramsey cavity passages. By the way, leakage fields before the first Ramsey passage can be treated in an analog manner as leakage fields after the Ramsey cavity passages [8, 11].

We have solved the Bloch equations iteratively in the presence of time-dependent leakage fields with small amplitudes. We consider in the rotating-wave approximation an oscillating magnetic leakage field $\vec{B}(t) = \vec{B}_0 \cos(\omega t - \phi)$, where ϕ is the phase relative to the Ramsey cavity field. The generalized Rabi vector $\vec{\Omega}_{\text{eff}}(t)$ contains the in-phase (relative to the Ramsey cavity field) and quadrature components of the Rabi frequency of the microwave field $\vec{B}(t)$ present during the respective stage of the interaction. They are given by the real part $\Omega_r(t)$ and the imaginary part $\Omega_i(t)$ of $\vec{\Omega}_{\text{eff}}(t)$. For a two-level system the Bloch vector $\vec{b}(t)$ precesses around $\vec{\Omega}_{\text{eff}}(t) = (\Omega_r(t), -\Omega_i(t), -\delta)$, where $\delta = \omega - \omega_0$ is the detuning of the angular frequency ω of the electromagnetic field from the atomic transition frequency ω_0. The Bloch equations are correspondingly given by

$$\dot{\vec{b}}(t) = \vec{\Omega}_{\text{eff}}(t) \times \vec{b}(t). \qquad (1)$$

For the following discussions, without leakage fields $\vec{\Omega}_{\text{eff}}$ can be considered as time independent during the interactions with the Ramsey cavity field (each of duration τ), the free-evolution period between the two Ramsey interactions (duration T) and the free-evolution period between the second Ramsey interaction and the detection (duration T_d). In the first case it is given by

$$\vec{\Omega}_{\text{eff}} = (\Omega_R, 0, -\delta) \approx (\Omega_R, 0, 0), \qquad (2)$$

where $\Omega_R \gg \delta$ is the Rabi frequency corresponding to the interaction in the Ramsey cavity and where at first we do not distinguish between possible different Rabi frequencies for the ascending and for the descending atoms. For the free-evolution periods $\vec{\Omega}_{\text{eff}}$ is given by

$$\vec{\Omega}_{\text{eff}} = (0, 0, -\delta). \qquad (3)$$

The precession angle α of the Bloch vector is thus obtained from $\alpha = |\vec{\Omega}_{\text{eff}}|\, t_i$ with the respective interaction time t_i equal either to τ, T, or T_d.

Before the first Ramsey interaction the caesium atoms are prepared by a state selection process [16] in a hyperfine substate $|F = 3, m_F = 0\rangle$, here represented by the Bloch vector $\vec{b} = (0, 0, -1)$. Using Eq. (1) and Eq. (2), one finds that after the first Ramsey interaction the atom is in a coherent superposition of the states $|F = 3, m_F = 0\rangle$ and $|F = 4, m_F = 0\rangle$, the latter represented by the Bloch vector $\vec{b} = (0, 0, +1)$. This is because in normal operation the power in the Ramsey cavity is adjusted such that the precession angle due to a single cavity passage is given by $\alpha = \pi/2$ ($\pi/2$-pulse). However, for monokinetic atoms experiencing all the same microwave amplitude any odd multiple $\pi/2$-pulses work, as well. The probability of finding the atom in the states $|F = 3, m_F = 0\rangle$ or $|F = 4, m_F = 0\rangle$ is given by the simple relations $P(|F = 3, m_F = 0\rangle) = 1/2(1 - b_z)$ and $P(|F = 4, m_F = 0\rangle) = 1/2(1 + b_z)$, respectively, where b_z is the z-component of the Bloch vector $\vec{b}(t)$.

During clock operation usually the central Ramsey fringe is alternately probed at its full-width-at-half-maximum (FWHM) points [16], which corresponds to alternately detuning the Ramsey cavity field by $\pm\delta_{\text{FWHM}} = \pm\pi/(2T)$. That means that during the free-evolution period the Bloch vector evolves again according to Eq. (1), but now in combination with Eq. (3) and $\delta = \pm\delta_{\text{FWHM}}$ for the two sides of the central fringe. After the second Ramsey interaction, analogous to the first one, and another subsequent free evolution, the probabilities of finding the atoms in either state are detected. Therefore the detection process corresponds to a measurement of the final z-component of the Bloch vector $b_z(\pm\delta)$ for either detuning. The servo loop of the clock ensures that the final $\Delta b_z = b_z(+\delta) - b_z(-\delta)$ is kept at zero by adjusting the frequency of the probing microwave field.

Any process provoking $\Delta b_z \neq 0$ under open-loop conditions results in a frequency shift proportional to Δb_z when the loop is closed. In fact, from the open-loop Δb_z the resulting frequency shift in the closed-loop operation can be directly calculated by using the slope of the central Ramsey fringe. For a typical fringe width of 1 Hz, one can calculate the relative frequency shift as $\Delta\nu/\nu_0 \approx 2 \cdot 10^{-11} \Delta b_z$, with the caesium hyperfine transition frequency $\nu_0 = 9\,192\,631\,770$ Hz.

In order to take into account the effects of leakage fields present during the free-evolution periods between or after the Ramsey interactions, we used for a first-order solution the unperturbed solutions from above together with the generalized Rabi vector $\vec{\Omega}_{\rm eff}(t) = (\Omega_r^L(t), -\Omega_i^L(t), 0)$, now defined by in-phase and quadrature components $\Omega_r^L(t)$ and $\Omega_i^L(t)$ corresponding to the leakage field, as input for the Bloch equations (Eq. (1)). For our calculations we have assumed small leakage field amplitudes, i.e. $\Omega_r^L(t), \Omega_i^L(t) \ll \delta$. In a second step, the first-order solutions obtained in this way can be used as $\vec{b}(t)$ in Eq. (1) to obtain second-order solutions.

As a result we obtain for leakage fields between the Ramsey interactions, including first and second-order terms:

$$
\begin{aligned}
\Delta b_z \;=\; & \sin(2\,\Omega_R\,\tau)\cos\frac{\delta T}{2}\int_0^T \Omega_i^L(t)\;\sin\delta(t-\frac{T}{2})\;dt \\
+\; & 2\,\cos^2(\Omega_R\,\tau)\int_0^T\left[\Omega_i^L(t)\int_0^t\Omega_r^L(t')\;\sin\delta(t-t')\;dt' - \Omega_r^L(t)\int_0^t\Omega_i^L(t')\;\sin\delta(t-t')\;dt'\right]dt \qquad (4)\\
+\; & 2\,\sin^2(\Omega_R\,\tau)\int_0^T\left[\Omega_i^L(t)\;\sin\delta(T-t)\int_0^t\Omega_r^L(t')\;\cos\delta t'\;dt' - \Omega_r^L(t)\;\cos\delta(T-t)\int_0^t\Omega_i^L(t')\;\sin\delta t'\;dt'\right]dt,
\end{aligned}
$$

where the first term, representing the first-order solution, is in agreement with the solution found in Ref. [11]. This term vanishes due to the $\sin(2\,\Omega_R\,\tau)$ factor at optimum Ramsey pulse area settings $\Omega_R\,\tau = (2N+1)\,\pi/2$ with $N = 0, 1, 2, \ldots$, whereas maximum frequency shifts are obtained at Ramsey pulse areas $\Omega_R\,\tau = (2N+1)\,\pi/4$ with alternating sign for increasing N. The first-order term depends only on the quadrature component $\Omega_i^L(t)$ corresponding to the leakage field. This means that any resulting frequency shift is proportional to the leakage field amplitude. It can also easily be seen that as the sine function within the integral of the first-order term is an odd function with respect to $t = T/2$, for an even quadrature component $\Omega_i^L(t)$ the first-order term vanishes.

At optimum Ramsey pulse area settings $\Omega_R\,\tau = (2N+1)\,\pi/2$ with $N = 0, 1, 2, \ldots$ the only remaining term is the third term, obtained from the second-order solution. As it contains only products of the in-phase component $\Omega_r^L(t)$ and the quadrature component $\Omega_i^L(t)$, the frequency shift becomes proportional to the square of the amplitude of the leakage field. Furthermore, it does not change sign with increasing N. But it is important to note that for real clocks it is impossible to adjust the microwave power in the Ramsey cavity to much better than about 1%. Due to this fact, under normal circumstances the first-order term is dominating, unless the leakage field amplitude becomes rather large.

If leakage fields are present during one of the free-evolution periods, their most realistic and general characterization is that of a field which is variable in amplitude and phase along the atomic trajectories, depending in detail on the particular properties of the respective vacuum chamber. We will restrict the following discussions to the simple case of standing waves, consisting of two counterpropagating plane waves with equal amplitudes and polarizations. We have chosen this case because we have evidence of a strong standing wave character of our experimental test field inside CSF1. Our calculated results for traveling waves are qualitatively similar to those for standing waves and related details will be presented elsewhere [17]. For the polarization of the standing wave fields we assume in the following without loss of generality that the magnetic field vector $\vec{B}(t)$ of the leakage fields is always parallel to the constant magnetic field direction along the atomic trajectories.

For a standing wave field the in-phase and quadrature components of the generalized Rabi vector $\vec{\Omega}_{\rm eff}(t)$ seen by the atoms along their path $x(t)$ are given by

$$
\begin{aligned}
\Omega_r^L(t) \;&=\; \Omega^L(t)\cos\phi = \Omega_0^L\cos(kx(t)+\eta)\cos\phi \\
\Omega_i^L(t) \;&=\; \Omega^L(t)\sin\phi = \Omega_0^L\cos(kx(t)+\eta)\sin\phi, \qquad (5)
\end{aligned}
$$

where $k = 2\pi/\lambda$ is the wavenumber for wavelength λ, and η describes the spatial position of the standing wave field envelope with respect to the Ramsey cavity. We note that in the case of a standing wave the atoms experience a leakage field with a time varying amplitude $\Omega^L(t) = \Omega_0^L\cos(kx(t)+\eta)$ but a constant phase ϕ.

By inserting Eqs. (5) into Eq. (4) it can be seen immediately that for $\phi = N\,\pi$ with $N = 0, 1, 2, \ldots$ there is no frequency shift as in this case $\Omega_i^L(t) = 0$. From numerical integration of Eq. (4) we obtain the final Δb_z for a standing wave leakage field present between the two Ramsey interactions. Let us consider the case of an exposure of the atoms to the leakage field starting immediately after the first Ramsey cavity interaction. It is instructive to replace the upper limit T of the integrals of Eq. (4) by a variable t_l, which indicates the time when the exposure of the atoms to the leakage field stops. The resulting $\Delta b_z(t_l)$ is plotted in Fig. 1 for the case of a standing wave leakage field in an atomic fountain.

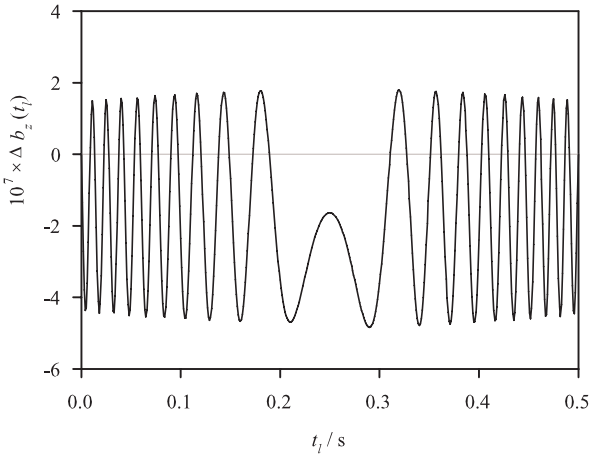

FIG. 1: Final Δb_z as a function of the time t_l (see text). $t_l = 0$ corresponds to the begin of the leakage field interaction just at the end of the first cavity passage and $t_l = 0.5$ s to the end of the leakage field interaction just at the begin of the second cavity passage. The initial velocity of the atoms is $v(t_l = 0) = 2.5$ m/s and the acceleration of gravity is assumed to be $g = 10$ m/s^2, so that $T = 0.5$ s and $\delta = \pi$ (operation at FWHM points). Other parameters have been arbitrarily chosen and do not have any particular significance: $\lambda = 0.0326$ m, $\eta = -\pi/6$, $\phi = \pi/4$, and $\Omega_0^L = 0.01$ rad/s. Depicted is the resulting curve for a realistic situation, where the optimum power is missed by 1%: $\Omega_R\,\tau = 0.99\,\pi/2$.

For $t_l = 0.5$ s we obtain $\Delta b_z = 0$, which is due to the fact that for the calculation of the graph in Fig. 1 we used the properties of the ballistic flight path of atoms in a fountain: in the ideal case the atoms are exposed to the same leakage field during their ascent and their descent. This happens in a symmetric way with respect to the apogee at time $T/2$. On the other hand, from the graph the resulting $\Delta b_z(t_l)$ can be read off when the leakage stops at any other time $0 \le t_l \le 0.5$ s. In this case the leakage field is of course no longer symmetric and consequently in general $\Delta b_z(t_l) \neq 0$ is obtained. But from the zero-crossings of $\Delta b_z(t_l)$ for certain values of t_l we recognize that the asymmetry of a standing wave leakage field is a necessary but not a sufficient condition for frequency shifts to appear.

This result is different from what is obtained if a leakage field with constant amplitude and phase is assumed like in Ref. [11]: in this case we calculate that $|\Delta b_z(t_l)|$ increases monotonically for $0 \le t_l \le 0.25$ s and decreases in a corresponding way for $0.25\,\text{s} \le t_l \le 0.5$ s. Moreover, due to the integration of a constant leakage field (Eq. (4)) the maximum value of $|\Delta b_z|$ reached at the apogee is generally much larger compared to the maximum $|\Delta b_z|$ for any t_l in the case of a standing wave or a traveling wave [17]. If we use in the calculation a constant field with parameters analogous to the situation of Fig. 1 ($\Omega_0^L = 0.01$ rad/s, $\phi = \pi/4$), the maximum $|\Delta b_z|$ is about a factor of 40 larger than the maximum $|\Delta b_z|$ obtained from Fig. 1. This means that in general the frequency shift is overestimated if it is calculated based on an un-physical "constant" leakage field, instead of a realistic standing or traveling wave leakage field.

Now we would like to point out another important effect, which at least for fountain clocks may usually be the dominating source of a frequency shift due to leakage fields present between the Ramsey interactions. This effect results from the fact that in general atoms traverse the Ramsey cavity at different distances from the vertical cavity symmetry axis during their first and second Ramsey passages, so that the atoms are exposed to different microwave amplitudes on their way up and on their way down. This is because in typical Ramsey cavities for fountain clocks the microwave amplitude across the cavity apertures varies by several percent. Depicting the Rabi frequencies for the first and the second cavity passage by $\Omega_R(\uparrow)$ and $\Omega_R(\downarrow)$, respectively, we obtain as a result that the angles $\alpha_1 = \Omega_R(\uparrow)\,\tau$ and $\alpha_2 = \Omega_R(\downarrow)\,\tau$ for the ascending and descending atoms can be slightly different. Instead of using Eq. (4) we find for the final Δb_z:

$$\Delta b_z \;=\; 2\left[\sin(\alpha_1+\alpha_2)\cos\frac{\delta T}{2}\int_0^T \Omega_i^{L,o}(t)\;\sin\delta(t-\frac{T}{2})\;dt \;+\; \sin(\alpha_1-\alpha_2)\sin\frac{\delta T}{2}\int_0^T \Omega_i^{L,e}(t)\;\cos\delta(t-\frac{T}{2})\;dt\right]$$

$$+\ \text{second-order terms}, \qquad (6)$$

where for the first-order term we have split the quadrature component due to the leakage field $\Omega_i^L(t)$ into an odd function of t (with respect to $t = T/2$) $\Omega_i^{L,o}(t)$, and into an even function of t (with respect to $t = T/2$) $\Omega_i^{L,e}(t)$. The second-order terms are identical to those of Eq. (4), with the exception that the factor $\cos^2(\Omega_R\,\tau)$ has to be replaced by $\cos(\Omega_R(\uparrow)\,\tau)\cos(\Omega_R(\downarrow)\,\tau) = \cos\alpha_1\cos\alpha_2$ and the factor $\sin^2(\Omega_R\,\tau)$ has to be replaced analogously.

The first term of Eq. (6) describes the effect of an asymmetric leakage field as discussed before, including now $\alpha_1 \neq \alpha_2$. It can still be made negligible by adjusting the microwave power such that $\alpha_1+\alpha_2 = (2N+1)\,\pi$ with $N = 0, 1, 2, \ldots$. The second term survives even at optimum power. It describes the frequency shifting effect of the condition $\alpha_1 \neq \alpha_2$ in the presence of a symmetric leakage field between the Ramsey interactions. In contrast to the behavior of this first-order term the second-order terms still vanish for perfectly symmetric leakage fields, even when $\alpha_1 \neq \alpha_2$.

In Fig. 2 the original result of Fig. 1 obtained from Eq. (4) for a standing wave leakage field (Eq. (5)) is compared to the result obtained from Eq. (6), where we have included the effect of $\alpha_1 \neq \alpha_2$. It becomes obvious that in the latter case the frequency shift does not vanish, even when the leakage field is symmetric ($t_l = 0.5$ s). Furthermore, even a very small difference between α_1 and α_2 of 0.5% results in much larger frequency shifts compared to the case $\alpha_1 = \alpha_2$ with asymmetric leakage field ($t_l < 0.5$ s).

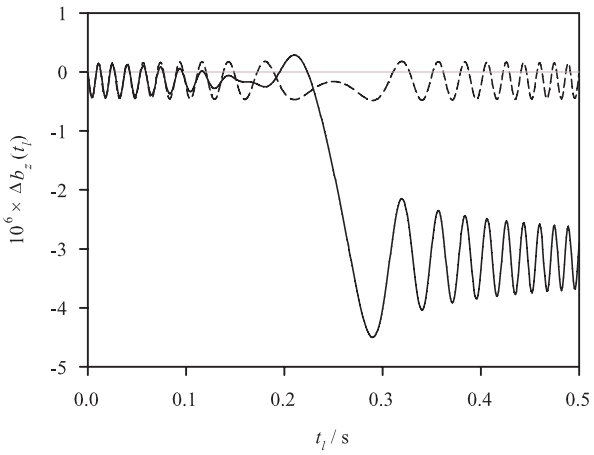

FIG. 2: Final Δb_z as a function of the time t_l. Broken line: Same curve as depicted in Fig. 1 ($\alpha_1 = \alpha_2 = 0.99\,\pi/2$). Full line: Δb_z calculated for $\alpha_1 = 0.99\,\pi/2$ and $\alpha_2 = 0.985\,\pi/2$), but otherwise identical parameters.

When the frequency shift is dominated by the effect due to $\alpha_1 \neq \alpha_2$, the resulting Δb_z for odd multiple $\pi/2$-pulse operation can be written in the explicit form:

$$\begin{aligned}\Delta b_z &= 2\,\sin((2N+1)(\tilde\alpha_1-\tilde\alpha_2))\sin\frac{\delta T}{2}\\ &\quad\times\int_0^T \Omega_i^{L,e}(t)\,\cos\delta(t-\frac{T}{2})\,dt\\ &\approx 2\,(2N+1)(\tilde\alpha_1-\tilde\alpha_2)\sin\frac{\delta T}{2}\\ &\quad\times\int_0^T \Omega_i^{L,e}(t)\,\cos\delta(t-\frac{T}{2})\,dt.\end{aligned} \tag{7}$$

with $N = 0, 1, 2, \ldots$ and $\tilde\alpha_1 \approx \tilde\alpha_2 \approx \pi/2$. This equation gives the remarkable result that by using odd multiple $\pi/2$-pulse operation modes we obtain a quadratic dependence on the microwave amplitude setting due to the product $(2N+1)\,\Omega_i^{L,e}(t)$, as long as the leakage field amplitude is proportional to the microwave field amplitude in the Ramsey cavity.

Finally, we also give here the calculated first-order solution for arbitrary types of leakage fields and Ramsey pulse area settings close to the optimum ($\alpha_1 \approx \alpha_2 \approx (2N+1)\,\pi/2$ with $N = 0, 1, 2, \ldots$), if leakage fields are present after the second Ramsey interaction ($t = 0$) until the atoms reach the detection region ($t = t_d$):

$$\Delta b_z = 2\,\sin\alpha_1\sin\delta T\int_0^{t_d}\Omega_i^L(t)\,\cos\delta t\,dt, \tag{8}$$

where we have omitted terms which due to Ramsey pulse area settings close to the optimum only give small contributions compared to the contributions from Eq. (8). Frequency shifts are proportional to the amplitude of the leakage field and alternate in sign for increasing N.

From Eq. (8) we obtain the same result as Levi *et al.* obtained for the special case of a leakage field of short duration after the second Ramsey interaction with amplitude and phase constant in time [11].

III. EXPERIMENTAL SETUP

The PTB caesium fountain CSF1 is described in detail elsewhere [14, 15]. For the experimental microwave leakage investigations we beam a test microwave field either through one of the optical access ports near the detection region or through the upper window for the vertical laser beams (Fig. 3). The electrical part of the experimental setup is relatively simple. The microwave signal produced by the 9-GHz synthesis chain for the Ramsey cavity is split into two paths. One of them supplies the interrogation microwave field for the Ramsey cavity in the usual way. The other path, which provides the test microwave field, consists of an X-band waveguide containing an adjustable attenuator, a variable phase shifter and a

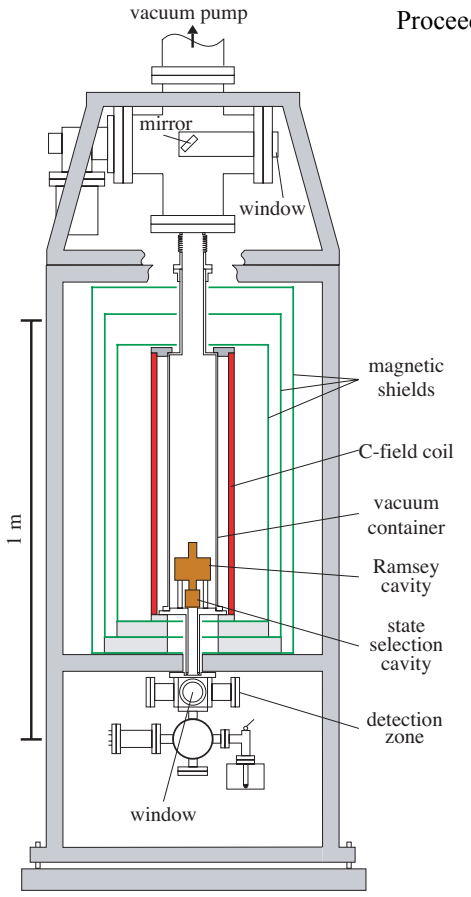

FIG. 3: Geometry of the vacuum subsystem of PTB's CSF1 caesium fountain clock. The horn antenna for the application of a test microwave field was positioned as close as possible to one of the two windows marked in the sketch.

PIN modulator, used as rf switch (extinction 117 dB). The X-band waveguide leads to a cable-coupled microwave horn, which is firmly positioned as close as possible to an unused window at the vacuum cross containing the detection zone, or at the top where one of the vertical laser beams enters the vacuum system (Fig. 3). This setup allows us to set the amplitude and phase of the test microwave field independently of the pulse area in the Ramsey cavity and to switch the test field on and off at well-defined times during the fountain operating cycle, i.e., when the atom cloud is at a specific position along its trajectory.

We note that any values of the phase of our test microwave field given in this publication refer to the reading of the dial of the phase shifter. There is a fixed, but unknown propagation delay between this device and the interior of the fountain. In particular, it would be an improbable coincidence if our "phase 0°" coincided with the "in-phase" situation described in Section II.

In the standard mode of operation of CSF1 the 9-GHz synthesis chain is locked to the center of the Ramsey fringe by controlling the frequency of a 5-MHz quartz oscillator. Its relative frequency is compared to the average relative frequency $y(\mathrm{H})$ of two hydrogen masers using a phase comparator. Depending on the size of the frequency shift an averaging time of 1-5 minutes is chosen in order to clearly resolve the shift within the frequency noise of the fountain at such short integration times. In the plots shown below a difference frequency of zero corresponds to the fountain output frequency in the absence of the test microwave field, while the statistical uncertainty is of the order of the data symbol size.

IV. EXPERIMENTAL RESULTS

In the fountain CSF1 atoms are launched with an initial velocity of 4.04 m/s. They pass through the Ramsey cavity after 130 ms for the first time and after 695 ms for the second time. The upper detection region is reached 795 ms after the launch. In the experiments described in the following, for a fixed amplitude setting the phase of the simulated leakage field was varied over a full cycle. It was checked in an auxiliary experiment that changing the setting of the phase shifter does not cause any noticeable amplitude change of the microwave signal passing through.

In fountain clocks leakage fields present between the first and the second Ramsey passage would be expected to exibit a highly symmetric time structure with respect to $t = T/2$. In our fountain such a leakage field was simulated by beaming a test field through the upper port starting when the atoms pass through the Ramsey cavity for the first time, and stopping when they pass through the Ramsey cavity for the second time. In Fig. 4 the resulting frequency shift is shown for a fixed test field power and for different Ramsey pulse areas.

In each case one observes an oscillating phase dependence that can very well be fitted by a sine function. These experimental results are explained by Eq. (7). From this equation we see that only the symmetric part of the test leakage field, described by $\Omega_i^{L,e}(t)$, contributes, so that the phase dependence is given by $\sin\phi$ (see Eq. (5)). Furthermore, in Fig. 4 one sees that for a fixed phase the frequency shift increases linearly with the pulse area, as expected from Eq. (7). Additional measurements of the frequency shift for a fixed phase and a fixed Ramsey pulse area (not depicted here) revealed that the frequency shifts for leakage fields between the Ramsey interactions are proportional to the leakage field amplitude over several orders of magnitude [17]. The combination of these experimental findings confirms a quadratic dependence of the frequency shift as predicted by Eq. (7), in the case that the leakage field amplitude is proportional to the amplitude in the Ramsey cavity. This is probably the explanation of the observed quadratic frequency shift dependence reported in Refs. [12, 13].

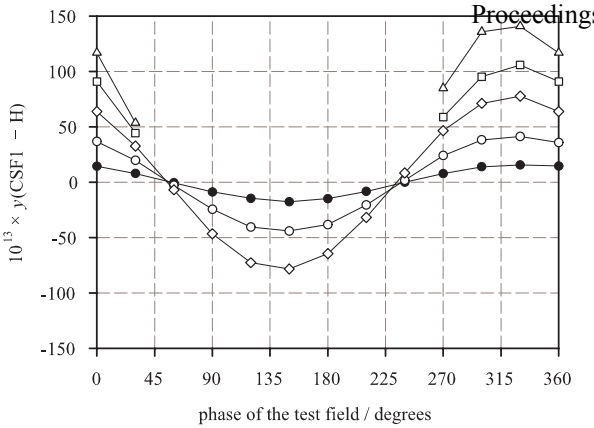

FIG. 4: Phase dependence of the relative frequency shift $y(\mathrm{CSF1} - \mathrm{H})$ due to a microwave test field of fixed amplitude, which is beamed into the apparatus from the upper port during the free-evolution period between the first and the second Ramsey cavity passage of the atoms (full circles: $1\,\pi/2$-pulse, open circles: $3\,\pi/2$-pulse, open diamonds: $5\,\pi/2$-pulse, open squares: $7\,\pi/2$-pulse, open triangles: $9\,\pi/2$-pulse). The solid lines connect the data points to guide the eye.

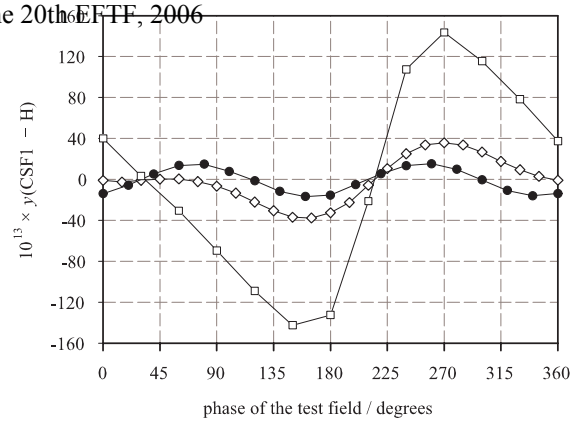

FIG. 5: Phase dependence of the relative frequency shift $y(\mathrm{CSF1} - \mathrm{H})$ due to pulsed microwave radiation, which is beamed into the apparatus from the upper port 220 ms after the launch of the atoms on their way up for a duration of 5 ms (full circles: optimized Ramsey pulse area ($\Omega_R \tau \approx \pi/2$), open diamonds: optimized Ramsey pulse area + 0.8 dB, open squares: optimized Ramsey pulse area + 3.5 dB). The solid lines connect the data points to guide the eye.

We should note here that the reason why the approximate solution Eq. (7) is sufficient to describe the measured frequency shifts of Fig. 4 is that other contributions from the more complete solution, Eq. (6), are negligible: the first term of Eq. (6) is small due to the factor $\sin(\alpha_1 + \alpha_2) \approx \sin(2N+1)\,\pi$ ($N = 0, 1, 2, \ldots$) and the second-order terms of Eq. (6) are small as they depend quadratically on the leakage field amplitude and the test leakage field is highly symmetric (second- and higher-order terms vanish for perfectly symmetric leakage fields).

In order to make visible the contributions by the second-order terms we induced a test leakage field exhibiting a highly asymmetric time structure with respect to $t = T/2$ by beaming a 5 ms test field into CSF1 through the upper port at a time 220 ms after the launch of the atoms. In Fig. 5 the resulting frequency shift is shown for a fixed test field power but varying Ramsey pulse area.

Due to the rather asymmetric character of the applied test field in this case, we recognize that now the second-order terms of Eq. (6) contribute to the frequency shift and may even become dominant when the test field amplitude is large enough. This is most clearly the case in the optimized Ramsey pulse area situation (full circles), where the contribution of the first term of Eq. (6) even vanishes due to the factor $\sin(\alpha_1 + \alpha_2) \approx \sin\pi$. In this situation contributions to the frequency shift mainly come from the product of the in-phase and quadrature components, $\Omega_r^L(t)$ and $\Omega_i^L(t)$, so that the resulting frequency shift depends on $\sin\phi\cos\phi \propto \sin(2\phi)$. The other curves of Fig. 5 show that away from the optimized Ramsey pulse area situation the first term of Eq. (6) becomes increasingly important and finally dominates, so that the resulting frequency shift depends mainly on $\sin\phi$ (open squares). Qualitatively similar results were calculated by Dorenwendt and Bauch [9].

Finally, in Fig. 6 the frequency shifts are plotted for experiments where a test field was applied between the second Ramsey interaction and the detection, 744 ms after the launch and for a duration of 5 ms.

The observed frequency shifts exhibit a sinusoidal dependence on the phase with alternating sign for an increasing odd number $2N + 1$ ($N = 0, 1, 2, \ldots$) of $\pi/2$-pulse areas as predicted by Eq. (8). The reason for the increased amplitude of the curves for $7\pi/2$- and $9\pi/2$-pulses is currently not clear.

Also in this case we performed measurements of the leakage amplitude dependence for a fixed phase and a fixed Ramsey pulse area (not depicted here), which revealed frequency shifts proportional to the test field amplitude as predicted by Eq. (8) [17].

V. CONCLUSION

By solving iteratively the Bloch equations we obtained general expressions for the frequency shifts in caesium clocks due to the presence of microwave leakage fields between or after the Ramsey interactions. An important finding, overlooked in the past, is the strong sensitivity of the clock frequency to leakage fields when the effective pulse areas for the first and second Ramsey pulse are not precisely equal. This may even be the dominating source of leakage-induced frequency shifts. It was also pointed out that it is nec-

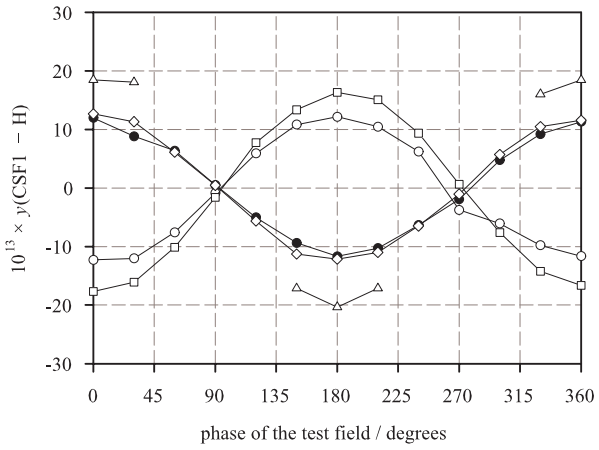

FIG. 6: Phase dependence of the relative frequency shift $y(\mathrm{CSF1} - \mathrm{H})$ due to a microwave test field of fixed amplitude, which is beamed into the apparatus from the lower port during 5 ms after the second Ramsey cavity passage and before the detection of the atoms (full circles: $1\,\pi/2$-pulse, open circles: $3\,\pi/2$-pulse, open diamonds: $5\,\pi/2$-pulse, open squares: $7\,\pi/2$-pulse, open triangles: $9\,\pi/2$-pulse). The solid lines connect the data points to guide the eye.

essary to take into account realistic leakage fields like standing wave fields or traveling wave fields in order to describe the effects due to leakage fields qualitatively and quantitatively correctly. Finally, conclusions from these theoretical findings are in full agreement with our experimental results.

All this has an important consequence for the operation of a primary frequency standard like CSF1. In case one finds significant frequency shifts due to microwave leakage upon variation of the Ramsey pulse area it is unrealistic to expect that a proper correction could be applied because this would require a model with enough sophistication to take account of the specific characteristics of the leakage fields along the trajectory of the atom cloud. Based on the results presented here one therefore has no choice but to work to remove any pulse-area dependence in the first place or to include the observed frequency variation into the uncertainty budget.

Acknowledgments

We would like to thank A. Bauch for a careful reading of the manuscript.

[1] T. Heindorff, A. Bauch, and R. Schröder, PTB-Mitteilungen **94**, 318–326 (1984)
[2] S.-I. Ohshima, Y. Nakadan, T. Ikegami, and Y. Koga, IEEE Trans. Instrum. Meas. **38**, 1100–1103 (1989)
[3] P. Petit, V. Giordano, P. Cérez, B. Boussert, C. Audoin, and N. Dimarcq, *Proceedings of the 8th European Frequency and Time Forum, Munich (DE)*, 517–522 (1994)
[4] G. D. Rovera, E. de Clercq, and A. Clairon, IEEE Trans. Ultrason. Ferroelectrics Freq. Control **41**, 245–249 (1994)
[5] W. D. Lee, J. P. Lowe, J. H. Shirley, and R. E. Drullinger, *Proceedings of the 8th European Frequency and Time Forum, Munich (DE)*, 513–516 (1994)
[6] J. H. Shirley, W. D. Lee, and R. E. Drullinger, Metrologia **38**, 427–458 (2001), Erratum **39**, 123–123 (2002)
[7] C. H. Oh, K. Hagimoto, S.-I. Ohshima, and Y. Nakadan, Bulletin of NRLM **44**, 7–10 (1995)
[8] B. Boussert, G. Théobald, P. Cérez, and E. de Clercq, IEEE Trans. Ultrason. Ferroelectrics Freq. Control **45**, 728–738 (1998)
[9] K. Dorenwendt and A. Bauch, *Proceedings of the Joint European Frequency and Time Forum and IEEE Frequency Control Symposium, Besançon (FR)*, 57–61 (1999)
[10] S. R. Jefferts, J. H. Shirley, N. Ashby, T. P. Heavner, E. A. Donley, F. Levi, *Proceedings of the IEEE International Frequency Control Symposium, Vancouver (CA)*, 105–110 (2005)
[11] F. Levi, J. H. Shirley, and S. R. Jefferts, *Microwave leakage induced frequency shifts in the primary frequency standards NIST-F1 and IEN-CSF1*, preprint
[12] K. Szymaniec, W. Chalupczak, P. B. Whibberley, S. N. Lea, and D. Henderson, *Proceedings of the 18th European Frequency and Time Forum, Surrey (GB)*, (2004)
[13] K. Szymaniec, W. Chalupczak, P. B. Whibberley, S. N. Lea, and D. Henderson, Metrologia **42**, 49–57 (2005)
[14] S. Weyers, U. Hübner, B. Fischer, R. Schröder, Chr. Tamm, and A. Bauch, Metrologia **38**, 343–352 (2001)
[15] S. Weyers, A. Bauch, R. Schröder, and Chr. Tamm, *Proc. 6th Symposium on Frequency Standards and Metrology (World Scientific)*, 64–71 (2002)
[16] R. Wynands and S. Weyers, Metrologia **42**, S64–S79 (2005)
[17] S. Weyers, R. Schröder, and R. Wynands, *in preparation*

Proceedings of the 20th EFTF, 2006

Power Dependence of the Shift Caused by Spurious Spectral Components in Atomic Fountain.

F. Levi[12*], J.H. Shirley[2], T.P Heavner[2], Dai-Hyuk Yu[23] and S.R. Jefferts[2]
[1] *INRiM – Str Delle Cacce 91- 10135 Torino Italy*
[2] *NIST-Time and Frequency Division - 325 Broadway Boulder, CO 80305 USA*
[3] *KRISS, 1 Doryong, Yuseong, Daejon 305-340 Korea*
**Electronic address: levi@inrim.it*

In this paper we analyze the behavior of the frequency shift caused by a spurious spectral component in the microwave spectrum against variation of the excitation microwave field.
The theory of the shift caused by the presence of spurs in the microwave spectrum was investigated in depth over many years, however for historical reasons the behavior was never analyzed when microwave power is varied far above optimum. The theoretical predictions are significantly different form the thermal beam case.
Furthermore the pulsed operation of a Fountain, with generally a well defined cycle time, set some new constraints on the size of carrier sidebands even when they are symmetric.

I. INTRODUCTION

For the past several decades, primary frequency standards were based on thermal atomic cesium beams. The thermal velocity distribution of these beam standards in general did not allow operation at high microwave power. High microwave power however became widely used in laser cooled devices to leverage the observation of various frequency shifts related to microwave excitation imperfections. In a typical Cs fountain primary frequency standard a sample of cold atoms passes through the Ramsey cavity at a speed of ~3 m/s with a spread in the average velocity due to the thermal distribution of only ~1 cm/s.
Experiments where the Rabi frequency of the atoms in the microwave field is varied to many times the optimum (with pulse areas ranging from $\pi/2$, $3\pi/2$, $5\pi/2$, ... $N\pi/2$ with $N \leq 13$), are commonly used to test for a variety of microwave induced anomalies and frequency shifts. Specifically, frequency shifts related to microwave spectrum, microwave leakage and distributed cavity phase are generally investigated by the use of this method [1-5]. This technique may offer leverage in the detection and calibration of the above mentioned shifts. However, as has been demonstrated for both the case of microwave leakage and distributed cavity phase shifts [6, 7], the behavior of the frequency shift at high power can be quite different from that obtained with an extrapolation performed around the optimum power and the presence of functions periodic in the Rabi frequency, tend to dominate the physical behavior of the shift. Therefore these tests must be carried out with a great deal of care and rigorous attention to the theoretical predictions.

II. THEORETICAL RESULTS

The effect of spurious components in the spectrum of the microwave excitation has been analyzed by many authors [8-10]. A complete theory of the shifts caused by single-sideband spurs in Cs beam primary frequency standards can be found in [11] and is the basis for the analysis reported here. From a theoretical point of view the analysis of the shift in frequency standards based on thermal beams or on laser cooled fountains is indistinguishable, with the exception that in fountain frequency standards integration over the velocity distribution is not strictly necessary. Also, the ratio of the Rabi to Ramsey lengths (l/L) is replaced by the ratio of the respective transit times (τ/T_R) for the varying velocity of the atoms during their ballistic flight in a Fountain cycle. The analytical derivation of the shift carried out in [11] is quite complete and obtained with only the approximations that each excitation has constant amplitude and that the spur power is much smaller than optimum power or the carrier power. We recall here for the reader's convenience the main result obtained for mono-velocity atoms in [11]:

$$\delta\omega = \frac{\tau}{T_R}\frac{b_1^{\,2}}{b_0}\left(y + z_1\cos(\Delta T_R) + z_2\sin(\Delta T_R)\right) \qquad (1)$$

where $\delta\omega$ is the frequency shift, τ is the interaction time inside the microwave cavity (Rabi time), T_R is the free flight time (Ramsey time), b_1 and b_0 are the Rabi frequencies of the spur and the carrier respectively, Δ is the detuning of the spur frequency from the carrier, and y, z_1 and z_2 are periodic functions of the excitation Rabi frequency and are given by the following formulae:

$$y = \frac{1}{b_0\tau\sin(b_0\tau)}\left\{\frac{b_0}{\Delta}\cos(b_0\tau)+\frac{1}{1-(\Delta/b_0)^2}\left(\frac{\Delta}{b_0}-\frac{b_0}{\Delta}\cos(b_0\tau)\cos(\Delta\tau)-\sin(b_0\tau)\sin(\Delta\tau)\right)\right\}$$

$$z_1 = \frac{\cos(b_0\tau)}{b_0\tau\sin(b_0\tau)}\frac{1}{1-(\Delta/b_0)^2}\left\{(\cos(b_0\tau)-1)\sin(\Delta\tau) + \frac{b_0}{\Delta}(1-\cos(\Delta\tau))\sin(b_0\tau))\right\} \quad (2)$$

$$z_2 = \frac{\cos(b_0\tau)}{b_0\tau\sin(b_0\tau)}\frac{1}{1-(\Delta/b_0)^2}\left\{(\cos(b_0\tau)+1)(1-\cos(\Delta\tau)) - \frac{b_0}{\Delta}\sin(\Delta\tau)\sin(b_0\tau))\right\}$$

It is evident from (2) that at those Rabi frequencies where $b_0\tau$ equals $N\pi$ the shift, given by Eq. (1), diverges. This has no particular physical meaning since at those points no microwave excitation occurs (the transition probability is zero). Further, even with the very narrow velocity distribution in a fountain, the Rabi frequency is not exactly the same for all the atoms.
However the shift behavior is dominated by those divergences and also in this case the precise setting of the excitation power is extremely important to minimize the frequency shift.
Even if it is clear from (1) that the shift is proportional to the spur power (when no other parameter varies with the spur amplitude), this statement is essentially of no practical utility, since as we will show, in almost all practical cases the theory predicts a completely different behavior for variation of the excitation power.
In the following sections of the paper, the analysis of the frequency shift induced by spurs will be divided in two parts, first a spur within the Rabi pedestal $\Delta \le b\tau$ and second a spur outside the Rabi pedestal $\Delta >> b\tau$.
In the following figures and theoretical evaluations and plots a Rabi time of 10 ms and a Ramsey time of .5 s is assumed if not stated differently in the text.

III. SPUR WITHIN THE RABI PEDESTAL

Within the Rabi pedestal the frequency shift associated with a spur of a given amplitude is a fast varying function of the frequency detuning from the carrier (figure 1). If the excitation power is properly set, this function is smooth, and the shift variation is "proportional" to $1/\tau$, while if the Rabi frequency of the carrier is not exactly set, a fast oscillation, whose frequency is equal to $1/T_R$ appears.

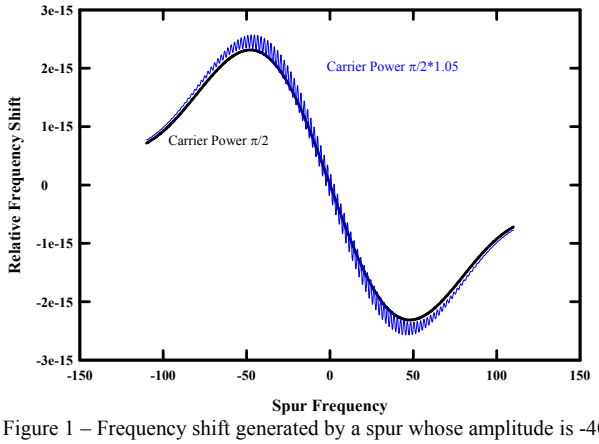

Figure 1 – Frequency shift generated by a spur whose amplitude is -40 dBc, for exact excitation power (π/2 pulse) and for 1.05 ×π/2 pulse.

At higher excitation power the functional behavior changes completely as can be seen in figure 2. For example, when the excitation power corresponds to exactly a 5π/2 pulse, we find the behavior shown in figure 2. If the spur power is kept constant, the modulus of the shift decreases with respect to the π/2 case. On the other hand, if the ratio between the spur and carrier power is kept constant, the shift can be either larger or smaller in modulus depending on the spur frequency. A π/2-5π/2 test (for example) to enhance the shifting effect of a generic spurious component can therefore be meaningless unless it is carefully coordinated with the appropriate theory.

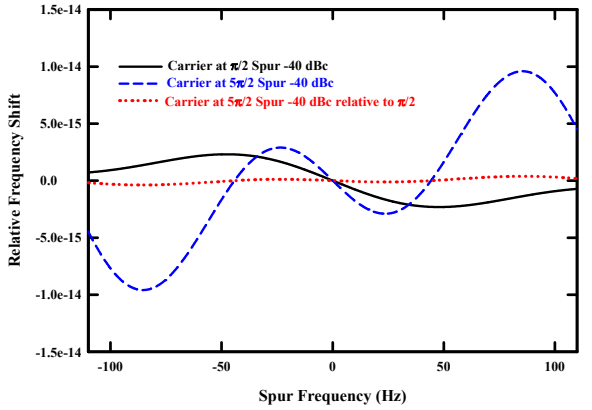

Figure 2 – Shift caused by a spur for excitation power corresponding to π/2 and 5π/2 pulses

In Fig. 3, we show the prediction and experimental data for the case of a single-sideband spur which is kept at -20 dBc while the frequency of the spur is varied. The data in red triangles are for the case of optimum Rabi frequency so that the pulse area is π/2

while the data in blue circles are from measurements where the Rabi frequency was such that the pulse area is 3π/2. All of the experimental data shown here were obtained with a Ramsey time of 0.565s and an effective Rabi time of 5.59 ms. The theoretical curves for these conditions, as predicted by Eq. 1, compare reasonably well with the experimental data. We believe the discrepancies between the prediction and data are mostly due to the pulsed operation of the fountain in the case of the π/2 data while these effects along with small mis-adjustments of the Rabi frequency are probably both apparent in the 3π/2data. The shape of the excitation profile inherent in the theory is different from the experimental excitation profile which is most evident at spur detuning larger than half the Rabi width (~15 Hz).

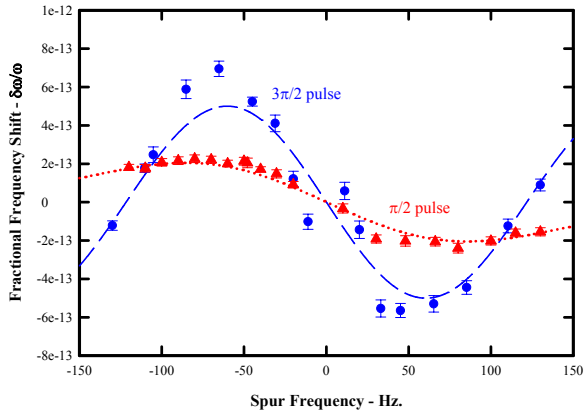

Figure 3 – Experimental results obtained for a spur of amplitude -20dBc for excitation power corresponding to π/2 and 3π/2 pulses.

We now analyze the frequency shift with excitation power in the neighborhood of optimum excitations, i.e., where the transition probability approaches unity. We find that the value of the frequency shift depends strongly on both how closely optimum microwave power is obtained and on the details of the spur frequency relative to the Rabi and Ramsey times. In Fig. 4, the value of the frequency shift caused by a spur 50 Hz from the carrier as well as one at 49 Hz, with a power -40 dBc is shown for the cases of optimum power, optimum power ±1% and optimum power ±2 % for the lowest occurrences of unity transition probability. It is difficult to set the excitation power at optimum better than a fraction of a percent in practice, both because the atom trajectory through the microwave cavity as well as variations in its velocity affect the optimum microwave power. It is evident from the striking differences between these two curves that the behavior of the frequency shift is quite rich. The value of the frequency shift at high microwave excitation amplitudes is dominated by whether the microwave field is slightly above or below optimum amplitude in the case of a 50 Hz spur while a very small change in the spur frequency causes the frequency shift to be essentially unaffected by small variations in the microwave field amplitude. The measured frequency shift at a given multiple of π/2 may therefore be determined mostly by the fact that the microwave power is different from optimum power and or by the details of the spur frequency with respect to the Rabi time. Small changes in launch velocity can therefore change the frequency shift associated with a spur in a relatively large fashion. Given the apparent large sensitivity to these effects it seems quite difficult in practice to use high power microwave tests alone to look for frequency shifts caused by spurs in the microwave spectrum.

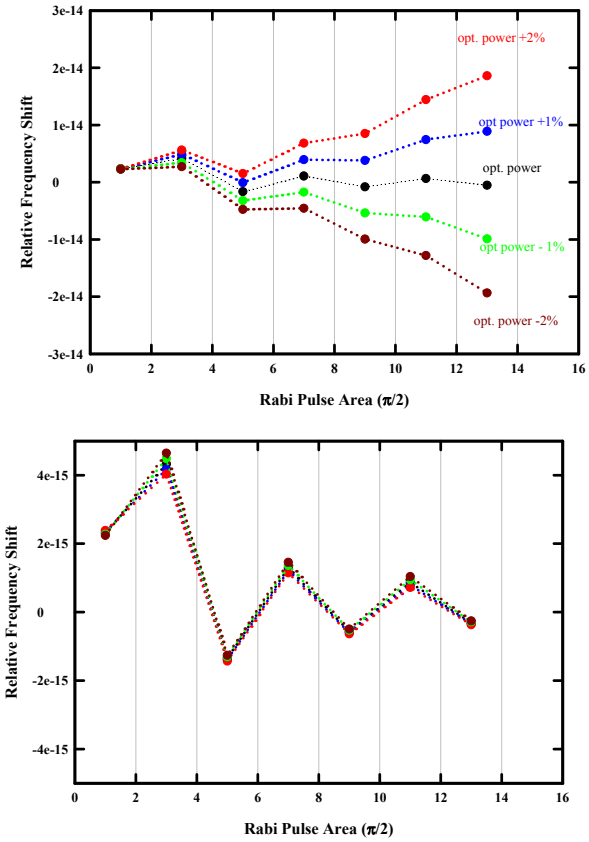

Figure 4 - Frequency shift calculated for a spur at 50 Hz and 49 Hz, for excitation powers not precisely set.

IV. SPUR OUTSIDE THE RABI PEDESTAL

A different behavior can be observed when the spur lays well outside the Rabi pedestal. For spur frequencies up to few hundred Hz, small oscillations are still present, however the behavior of the shift becomes quickly monotonic for spur frequencies well outside the Rabi pedestal; the shift decreases with respect to the spur frequency as 1/Δ (figure 5). In figure 5 the frequency of a spur, whose amplitude is -40dBc, is varied from 200 Hz to 10 kHz.

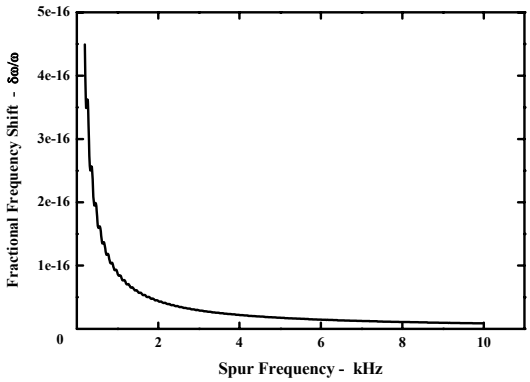

Figure 5 – Frequency shift calculated for a spur outside the Rabi pedestal

Analyzing the behavior of the spur with respect to the excitation power, when the spur frequency is well outside the Rabi envelope, the behavior of the shift changes dramatically because the y term in (1) becomes dominant as the Ramsey structure diminishes. The period of the singularities doubles with respect to the previous case, occurring at $b_0\tau=2N\pi$, and the behavior shown in Fig. 4 changes to a strong oscillation in the frequency shift pattern. "Bi-stable" linear behavior with microwave amplitude (and not power) can be observed, as shown in figure 6.

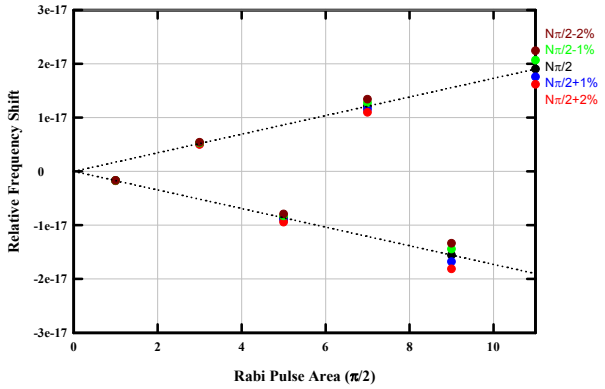

Figure 6 – Frequency shift calculated for a spur at 50 kHz for excitation powers not precisely set.

If the Rabi frequency of the carrier is changed without changing the spur amplitude, (this can be the case of an experiment where the carrier power is changed through the RF channel of a Mixer, while the Spur is originated in the LO channel), the magnitude of the shift decreases with increasing excitation power (figure 7).

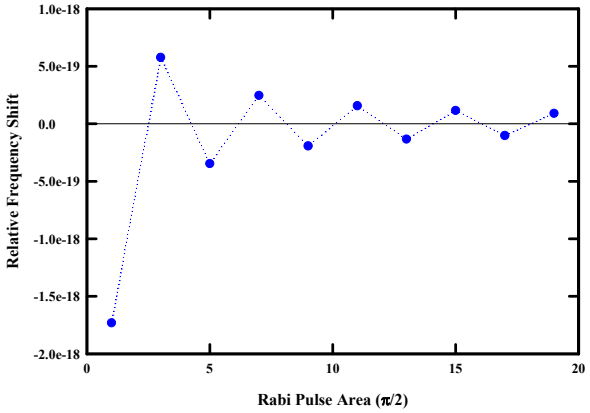

Figure 7 - Frequency shift calculated for a spur at 50 kHz whose amplitude is fixed while the carrier is varied.

V. PULSED OPERATION

Because most fountain frequency standards operate in the pulsed regime, it is worthwhile to examine the consequences of pulsed operation. If we consider the time-domain picture of the microwave field as seen by the atoms it is generically similar to that shown in Fig. 8. The microwave field is zero until the atom enters the Ramsey cavity. It turns on smoothly to a maximum and then turns off smoothly back to zero over a time τ (the Rabi time). The microwave field is then zero for a time T_R (the Ramsey time) at which point the microwave field again turns up smoothly to a maximum and then back to zero. This pattern is then repeated for each cycle of operation.

Suppose an unwanted pure frequency modulation at frequency ω_1 is present on the carrier. The extraneous phase introduced by this modulation can be written as:

$$\beta\cos(\omega_1 t) \qquad (3)$$

where β is the modulation index ($\beta=\Delta f/f_1$ where Δf is the frequency deviation produced by the frequency modulation). We assume that the atoms are centered in the cavity on the way up at t_1 and again on the way down at $t_2=T_R+t_1+\tau$, where t=0 is taken as the launch time. The change in phase between the two interactions due to the modulation is then given by:

$$\delta\varphi=\beta\left[\cos\omega_1 t_2-\cos\omega_1 t_1\right]= \\ -2\beta\sin\omega_1\left(t_1+\tfrac{1}{2}T_R+\tfrac{1}{2}\tau\right)\sin\omega_1\left(\tfrac{1}{2}T_R+\tfrac{1}{2}\tau\right) \qquad (4)$$

Associated with this phase difference would be a frequency shift of order $\delta\varphi/T_R$. N fountain cycles later

the phase difference would be the same, with t_1 augmented by NT_{cycle}

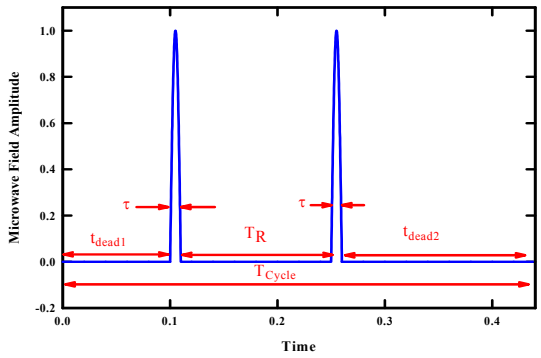

Fig. 8 - Amplitude modulation of the microwave power, as seen by the atoms, during a fountain cycle.

As long as $\omega_1 T_{cycle}$ is not an integer times π (or an integer times a rational fraction of π), this phase difference and any accompanying shift will average to zero after many fountain cycles. But if, for example, the modulation frequency is 50 Hz and the cycle time is exactly 1.020 s (51 cycles at 50 Hz), the same phase difference will occur during each fountain cycle and the associated shift will persist.

From a frequency point of view the microwave spectrum effectively has all the harmonic components that are multiples of $1/T_{cycle}$. If one of these spectral components is coincident with a component of the frequency modulated spectrum, it will produce an asymmetric sideband. Hence balanced sidebands present in the synthesizer can cause frequency shifts, because the pulsed operation of the fountain automatically generates amplitude sidebands that may interfere.

VI. CONCLUSIONS

Given the extremely complex behavior of the frequency shifts caused by the presence of spurious components in the microwave excitation spectrum, we conclude that high-power microwave tests are not well suited for the detection of anomalies due to the presence of spurious component in the microwave spectrum. And these test when applied should be carefully analyzed by comparison with appropriate theory. In general, no leverage can be expected with experiments carried out at higher excitation power. The amplitude and sign of the shift can vary widely, depending on the spur frequency, the Rabi-pedestal width, the Ramsey time and whether the microwave power is slightly above or below optimum. It is therefore very difficult to correct for shifts related to spectral components. This difficulty is compounded by the pulsed operation and possible synchronicity between the spur frequency and the fountain cycle time. Therefore, to guarantee a given level of accuracy in a fountain frequency standard, we must estimate the maximum ratio of acceptable spur to carrier in the spectrum, and ensure that this ratio has been met with independent measurements. For example, assume that a fountain is operated with T_R = 0.5 s and τ = 0.01 s and must be accurate at fractional level of 1×10^{-16} level. A spur within the Rabi pedestal must be reduced to almost -60 dBc. For a spur far off resonance the constraints are more relaxed since larger detuning allow higher spur powers. For example, a spur 50 kHz from the carrier can be -20 dBc and still allow an accuracy of 1×10^{-16}.

REFERENCES

[1] S.R. Jefferts, et al., Metrologia **39** pp. 321-336 (2002).
[2] S. Weyers, U. Hübner, R. Schröder, Chr. Tamm, and A. Bauch, Metrologia **38** pp 343-352. (2001).
[3] F. Levi, L. Lorini, D Calonico, A. Godone, IEEE trans UFFC. **51** 10 p 1216 (2004).
[4] K. Szymaniec, W. Chalupczak, P.B. Whibberley, S.N. Lea, D. Henderson, 42 pp. 49-57. (2005) .
[5] C.Vian, et al., IEEE Trans I.M., **54**(2) pp.833 (2005)
[6] F. Levi, J.H. Shirley, S.R. Jefferts, to appear on IEEE Trans UFFC.
[7] S.R. Jefferts, J.H. Shirley, N. Ashby, E.A. Burt, G.J.Dick IEEE Trans UFFC **52**(12) pp 2314-2321 (2005).
[8] N.F. Ramsey, Phys. Rev **100** 4 p 1191 (1955)
[9] J.H. Shirley, J. Appl. Phys. **34** 4 (part1) p 783 (1963)
[10] C. Cohen-Tannoudji, Metrologia **13** pp 161-166 (1977).
[11] C. Audoin, M. Jardino, L.S. Cutler, R.F. Lacey, IEEE Trans on Instr. and Meas. IM27 **4** p 325 (1978)
[12] W.D. Lee, J.H. Shirley, F.L. Walls, R.E. Drullinger, Proc. 1995 IEEE Intl. Freq. Cont. Symp. pp. 113-118 (1995).

Proceedings of the 20th EFTF, 2006

Towards a high-stability Rb fountain frequency standard

Yu. B. Ovchinnikov,* W. Chalupczak, K. Szymaniec, and G. Marra
National Physical Laboratory, Hampton Road, Teddington, Middlesex, TW11 0LW, UK

The design of the NPL's intense rubidium fountain frequency standard, which is using an optical molasses loadable from a continuous magneto-optical source of cold atoms, is described. The prospect and advantages of quasi-continuous regime of operation of the fountain are discussed.

I. INTRODUCTION

The primary purpose of the project is to build a Rb fountain frequency standard, the stability of which will exceed the stability of Cs fountains. The cold collision frequency shift of Rb^{87} atoms is by a factor of 50 to 100 smaller than that of Cs atoms [1, 2]. The relative fluctuations of the measured Rb clock transition frequency, caused by the shot-to-shot fluctuations in collisional shift (due to variations in atomic density), are expected to be below 10^{-16}. To use in full the advantage of a small collision cross section of Rb^{87}, all other major sources of frequency fluctuations have to be suppressed. The NPL's cryogenic sapphire oscillator [3] with relative frequency stability about 5×10^{-15} for averaging times between 1 and 10 seconds will be used as a local oscillator. The short term stability will be limited by the quantum projection noise at the level of $\sigma_y(\tau) = 5 \times 10^{-15} \times \tau^{-1/2}$. This corresponds to the number of detected atoms $N_{at} = 10^8$ provided by more than 10^9 atoms accumulated in an optical molasses from a continuous magneto-optical source of cold atoms [4]. The cavity pulling frequency shift [5] will be suppressed by precise tuning of the resonance of the cavity to the atomic resonance via precise temperature control of the fountain's C-field chamber. At a later stage of the experiment, the cavity pulling and collision frequency shifts can be reduced by operating the fountain in a quasi-continuous (QC) regime.

Another purpose of the project is to measure the frequency of the Rb hyperfine transition by comparing it to the frequency of the NPL's Cs primary frequency standard [6]. So far only one group has reported precise measurements of the Rb hyperfine frequency [7, 8].

II. DESIGN OF THE FOUNTAIN

The design of the fountain is shown in Fig. 1. An optical molasses chamber is designed to have the same angle $\alpha = 54.7°$ of all the molasses beams with respect to the vertical direction ($\langle 1,1,1\rangle$-configuration). The molasses is loaded from the magneto-optical low velocity intense source (LVIS), which provides a continuous flux of cold atoms about 8×10^9 at/s, at total laser power of 60 mW [4].

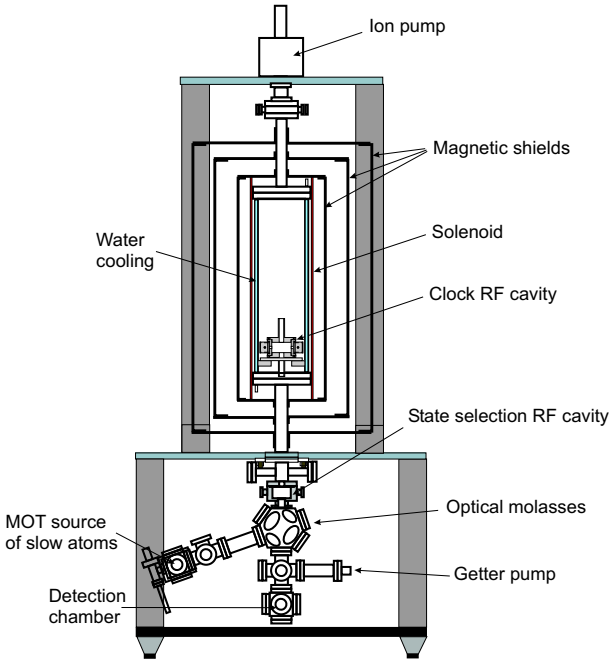

FIG. 1: Design of the vacuum part of the Rb fountain.

The loading from the LVIS serves several purposes. First, it allows rapid accumulation of a large atom number in the molasses without spoiling the main volume of the vacuum chamber with thermal Rb vapour. Second, the magneto-optical source cools down and extracts only the Rb^{87} isotope, while the Rb^{85} isotope stays unaffected by the cooling light and is not extracted from the LVIS chamber. The typical loading curves of the main magneto-optical trap (or an optical molasses) loaded from the LVIS source are shown in Fig. 2. One notes that the loading rate of the optical molasses is very close to that of the MOT and makes it possible to accumulate 10^9 atoms in a $\sim$ 100 ms loading period.

To control and stabilize the temperature of the clock microwave cavity, which is located inside the aluminium C-field tube, the latter is supplied with a water jacket. The temperature of the water is controlled with a thermoelectric chillier. Five type-T thermocouples are located on the body of the C-field chamber and another one is on the clock cavity. Two layers of thermal isolation, one at the outer surface of the

*Electronic address: yuri.ovchinnikov@npl.co.uk

C-field tube and another around the inner magnetic shield, are used.

The cylindrical TE_{011} state selection microwave cavity with a quality factor of $Q = 1100$ is made of stainless steel and is excited with a loop antenna. The clock cavity is also a cylindrical TE_{011} cavity, but made of copper and has a quality factor of $Q = 19500$. It is excited with two rectangular microwave transformers, which are coupled to the cavity through two side holes. The atomic flux transits the cavity through apertures of diameter d=1.6 cm in the top and bottom caps of the cavity.

The vacuum chamber is pumped by a small ion pump (20 l/s) at the top of the fountain and a getter pump, which is located between the molasses and the detection chambers.

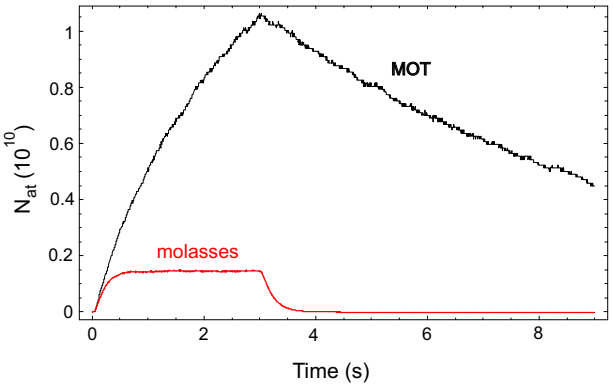

FIG. 2: Temporal dependence of the number of atoms in the main MOT (or molasses) loaded from the LVIS source during 3 seconds.

III. QUASI-CONTINUOUS FOUNTAIN

The usual way of operating an atomic fountain is to launch a ball-like cloud of cold atoms vertically upwards once per frequency measurement cycle. The juggling fountain [9], launches several atomic clouds in sequence during the parabolic flight period from the trap region and back. This is supposed to increase the fountain's stability by decreasing the dead time between subsequent frequency measurements and to reduce the density dependent frequency shifts. In that respect a continuous fountain [10] is the best solution. The main problem of the juggling and continuous fountains is that the resonant cooling light, scattered by atoms in the trap region of the fountain, might strongly interact with atoms in the interrogation zone of the fountain. In [10] the attenuation of the resonant light is achieved with a rotating velocity-selective shutter. Another proposal [11] takes advantage of successive launching of multiple balls of atoms of different velocities so that they reach the detection at the same time.

An alternative approach, which does not rely on invacuum shutters, is a QC-regime of operation of the atomic fountain. The idea is to produce a continuous flux of cold atoms generated by a special magneto-optical source and to interrupt it by switching off all the resonant cooling light when the atoms enter the interrogation region. Therefore, the resonant light is excluded from being inside the vacuum chamber of the fountain during the interrogation of the frequency of the clock transition.

The realization of that general idea in our Rb fountain is now described. First, a continuous beam of cold atoms with average velocity $\sim 10\,\mathrm{m/s}$ is generated with a LVIS source (Fig. 3a). After 100 ms of operation the cooling light of the LVIS is switched off and the flux of cold atoms is interrupted. Second, the cold atoms enter the bright moving molasses, which is further cooling these atoms and accelerating them upwards to a velocity of 4.5 m/s. Third, the transverse spread of the vertical slow atomic beam is reduced by cooling the atoms inside a far-detuned two-dimensional molasses. The state selection process can be added at this stage. After the atoms have passed the two stages of cooling and vertical acceleration, all light is switched off. As a result a cloud of cold atoms (Fig. 3b) with vertical length of about 40 cm and diameter 1.5 cm, which is moving upwards with average velocity about 4 m/s, is produced.

For a monochromatic atomic beam lasting for a duration Δt, which is launched upwards with initial velocity v_0, its vertical size is determined by the formula

$$\Delta s = (v_0 - gt)\Delta t + g\Delta t^2/2, \qquad (1)$$

where the time t is measured from the moment of launch of the first atoms and g is the gravity acceleration. This formula is valid for $t < v_0/g$, when all the atoms are moving in one direction, and shows a compression of the vertical size of the atomic cloud under its deceleration in the field of gravity. For example, at time $t = 0.145\,\mathrm{s}$ an atomic beam of duration $\Delta t = 0.11\,\mathrm{s}$ has a vertical length of $\Delta s = 0.4\,\mathrm{m}$. At the apogee of the atomic trajectory, where half of the atoms is already falling down, the vertical size of the atomic cloud reaches its minimum $\Delta s = g(\Delta t/2)^2/2 = 1.5\,\mathrm{cm}$.

The main advantages of the QC-operation of the fountain frequency standard are as follows. First, the cavity pulling frequency shift, which is proportional to the number of atoms inside the microwave clock cavity is expected to be suppressed by an order of magnitude. This expectation follows from the fact that for the same total number of atoms $\sim 10^9$ the vertical size of the atomic cloud is ten times larger than the height of the microwave cavity $h = 3.6\,\mathrm{cm}$; this means that only one tenth of the whole atomic cloud is present inside the cavity at each moment in time. Second, the large volume of the atomic cloud essentially reduces the density of atoms and the corre-

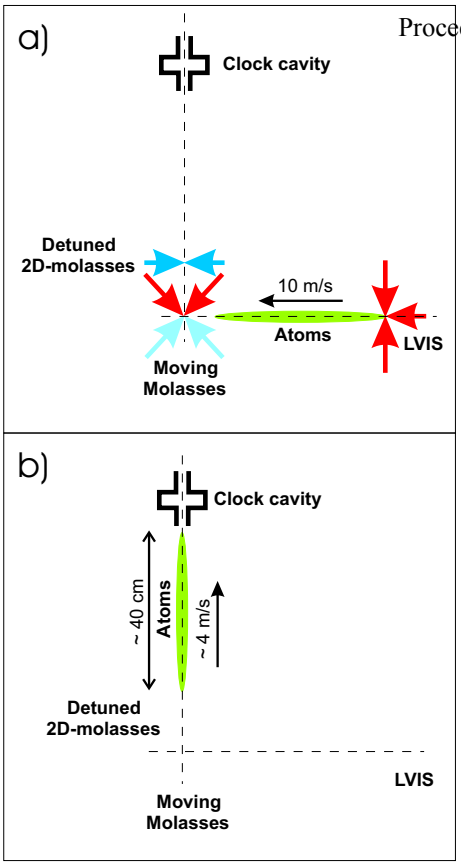

FIG. 3: The principle of the quasi-continuous fountain.

sponding collision shift of the frequency. However, the collisions of atoms in the QC-fountain are expected to be slightly different from those in the usual fountains. At the apogee region of the QC-fountain during 100 ms the atoms will collide with each other with relative velocities from 0 to 0.5 m/s. For that velocity range not only the s-wave collisions but also higher order partial wave collisions become important. To our knowledge the cross sections of the p-wave and d-wave collisions for the clock transition of Rb^{87} have not been measured so far. On the other hand theoretical calculations [12] and measurements [13] predict that the higher order partial wave cross sections of Rb atoms in fully stretched hyperfine magnetic ground substates do not essentially exceed the s-wave collision cross section. In reality the minimal vertical size of the compressed atomic cloud at the apogee of the fountain will be determined by the width of the vertical velocity distribution of atoms, which is expected to be of the order $\Delta v \sim 10\,\mathrm{cm/s}$, because the vertical cooling of atoms is produced by the bright optical molasses only (see Fig. 3). The corresponding length of the atomic cloud at the apogee is expected to be $\Delta s \sim 10\,\mathrm{cm}$.

An additional benefit of the QC-fountain is that the atoms are passing both molasses regions in sequence and therefore at each moment in time only a small part (1/40) is present at the cooling region. It allows deep cooling of a large number of atoms without being limited by re-absorption of scattered photons. Another practical advantage of the QC-fountain is that it uses only the laser beams of fixed frequency. It saves laser power and makes the fountains optical system simpler and more reliable.

In a future design of the QC-fountain, the space between the source of cold atoms and the clock cavity could be increased to several meters, which will increase the length and the total number of atoms in the QC atomic beam without essential increase of the fountain's cycle time.

Such a QC-regime of operation of an atomic standard based on laser cooling of atoms might be also interesting for slow-beam standards, which are designed to be used in space.

Acknowledgments

Many thanks to Dale Henderson for his contribution at the initial stage of the project, to Mark Oxborrow for his input into realization of the NPL's cryogenic sapphire oscillator, to David Head for his help on temperature measurements and to Alastair Sinclair for the comments to the paper.

[1] C. Fertig, K. Gibble, Phys. Rev. Lett. **85**, 1622 (2000)
[2] Y. Sortais, S. Bize, C. Nicolas, A. Clairon, C. Salomon, C. Williams, Phys. Rev. Lett. **85**, 3117 (2000)
[3] G. Marra, M. Oxborrow, D. Henderson (to be published).
[4] Yu. B. Ovchinnikov, Opt. Comm. **249**, 473 (2005)
[5] S. Bize, Y. Sortais, M. S. Santos, C. Mandache, A. Clairon, C. Salomon,
[6] K. Szymaniec, W. Chalupczak, P. B. Whibberley, S. N. Lea, D. Henderson, Metrologia **45**, 49 (2005)
[7] S. Bize, Y. Sortais, M. S. Santos, C. Mandache, A. Clairon, C. Salomon, Europhys. Lett. **45**, 558 (1999)
[8] H. Marion et al, Phys. Rev. Lett. **90**, 150801 (2003)
[9] R. Legere, K. Gibble, Phys. Rev. Lett. **81**, 5780 (1998)
[10] G. Dudle, A. Joyet, P. Berthoud, G. Mileti, P. Thomann, IEEE Trans. Instr. Meas. **50**, 510 (2001)
[11] F. Levi, A. Godone, L. Lorini, S. R. Jefferts, T. P. Heavner, C. Calosso, *Proc. of 6th Symp. Frequency Standards and Metrology* World Scientific, New Jersey, 2001
[12] P. Westphal, A. Koch, A. Horn, J. Schmand, H. J. Andrä, Phys. Rev. A **56**, 2784 (1997)
[13] Ch. Buggle, J. Leonard, W. von Klitzing, J.T.M. Walraven, Phys. Rev. Lett. **93**, 173202 (2004)

Proceedings of the 20th EFTF, 2006

Using a Cs Fountain to Test Lorentz Invariance

P. Wolf[1,2],* F. Chapelet[1], S. Bize[1], and A. Clairon[1]
[1] *LNE-SYRTE, Observatoire de Paris, 61 Av. de l'Observatoire, 75014 Paris, France*
[2] *Bureau International des Poids et Mesures, Pavillon de Breteuil, 92312 Sèvres Cedex, France*

We report on a new experiment that tests for a violation of Lorentz invariance (LI), by searching for a dependence of atomic transition frequencies on the orientation of the spin of the involved states (Hughes-Drever type experiment). The atomic frequencies are measured using a laser cooled ^{133}Cs atomic fountain clock, operating on a particular combination of Zeeman substates. We analyze the results within the framework of the Lorentz violating standard model extension (SME), where our experiment is sensitive to a largely unexplored region of the SME parameter space, corresponding to first measurements of four proton parameters and improvements by 11 and 13 orders of magnitude on the determination of four others. In spite of the attained uncertainties, and of having extended the search into a new region of the SME, we still find no indication of LI violation.

Lorentz Invariance (LI) is the fundamental postulate of Einstein's 1905 theory of relativity, and therefore at the heart of all accepted theories of physics. It characterizes the invariance of the laws of physics in inertial frames under changes of velocity or orientation. This central role, and indications from unification theories [1–3] hinting toward a possible LI violation, have motivated tremendous experimental efforts to test LI.

A comprehensive theoretical framework to describe violations of LI in all fields of present day physics has been developed over the last decade [4]: the Lorentz violating Standard Model Extension (SME), motivated initially by possible Lorentz violating phenomenological effects of string theory [1]. In its minimal form the SME characterizes Lorentz violation by 19 parameters in the photon sector and 44 parameters per particle [5, 6] in the matter sector, of which 40 are accessible to terrestrial experiments at first order in $v_\oplus/c$ [6] ($v_\oplus$ is the orbital velocity of the Earth and $c = 299792458$ m/s). Existing bounds for the proton (p^+), neutron (n) and electron (e^-) come from clock comparison and magnetometer experiments using different atomic species (see [5] and references therein, [7–10]), from resonator experiments [11–13], and from Ives-Stilwell experiments [14, 15]. They are summarized in tab. I, together with the results reported in this work.

Based on the SME analysis of numerous atomic transitions in [5, 6], we have chosen to measure a particular combination of transitions in the ^{133}Cs atom. This provides good sensitivity to the quadrupolar SME energy shift of the proton (as defined in [5]) in the spin 7/2 Cs nucleus, whilst being largely insensitive to magnetic perturbations (first order Zeeman effect). The corresponding region of the SME parameter space has been largely unexplored previously, with first limits on some parameters set only very recently [14] by a re-analysis of the Doppler spectroscopy experiment (Ives-Stilwell experiment) of [15]. Given the large improvements (11 and 13 orders of magnitude on four parameters) we obtain with respect to those results, and the qualitatively new region explored (first measurements of four parameters), our experiment had comparatively high probability for the detection of a Lorentz violating signal. However, our results clearly exclude that possibility.

TABLE I: Orders of magnitude of present limits (in GeV) on Lorentz violating parameters in the minimal SME matter sector and corresponding references. Indices J, K run over X, Y, Z with $J \neq K$. Limits from the present work are in bold type, with previous limits, when available, in brackets.

Parameter	p^+	n	e^-	Ref.
$\tilde{b}_X$, $\tilde{b}_Y$	10^{-27}	10^{-31}	10^{-29}	[7], [8], [9]
$\tilde{b}_Z$	-	-	10^{-28}	[9]
$\tilde{b}_T$, $\tilde{g}_T$, $\tilde{H}_{JT}$, $\tilde{d}_\pm$	-	10^{-27}	-	[10]
$\tilde{d}_Q$, $\tilde{d}_{XY}$, $\tilde{d}_{YZ}$	-	10^{-27}	-	[10]
$\tilde{d}_X$, $\tilde{d}_Y$	10^{-25}	10^{-29}	10^{-22}	[5], [10], [5]
$\tilde{d}_{XZ}$, $\tilde{d}_Z$	-	-	-	
$\tilde{g}_{DX}$, $\tilde{g}_{DY}$	10^{-25}	10^{-29}	10^{-22}	[5], [10], [5]
$\tilde{g}_{DZ}$, $\tilde{g}_{JK}$	-	-	-	
$\tilde{g}_c$	-	10^{-27}	-	[10]
$\tilde{g}_-$, $\tilde{g}_Q$, $\tilde{g}_{TJ}$	-	-	-	
$\tilde{c}_Q$	$\mathbf{10^{-22(-11)}}$	-	10^{-9}	[14, 15]
$\tilde{c}_X$, $\tilde{c}_Y$	$\mathbf{10^{-25}}$	10^{-25}	10^{-19}	[5], [11–13]
$\tilde{c}_Z$, $\tilde{c}_-$	$\mathbf{10^{-25}}$	10^{-27}	10^{-19}	[5], [11–13]
$\tilde{c}_{TJ}$	$\mathbf{10^{-21(-8)}}$	-	10^{-6}	[14, 15]

We use one of the laser cooled fountain clocks operated at the Paris observatory, the ^{133}Cs and ^{87}Rb double fountain FO2 (see [16] for a detailed description). We run it in Cs mode on the $|F = 3\rangle \leftrightarrow |F = 4\rangle$ hyperfine transition of the $6S_{1/2}$ ground state. Both hyperfine states are split into Zeeman substates $m_F = [-3, 3]$ and $m_F = [-4, 4]$ respectively. The clock transition used in routine operation is $|F = 3, m_F = 0\rangle \leftrightarrow |F = 4, m_F = 0\rangle$ at 9.2 GHz, which is magnetic field independent to first order. The first order magnetic field dependent Zeeman transitions ($|3, i\rangle \leftrightarrow |4, i\rangle$ with $i = \pm1, \pm2, \pm3$) are used regularly for measurement and characterization

*Electronic address: pwolf@bipm.org

of the magnetic field, necessary to correct the second order Zeeman effect of the clock transition.

A detailed description of the minimal SME as applied to the perturbation of atomic energy levels and transition frequencies can be found in [5, 6]. Based on the Schmidt nuclear model [17] one can derive the frequency shift of a Cs $|3, m_F\rangle \leftrightarrow |4, m_F\rangle$ transition in the SME

$$\delta\nu = \frac{m_F}{14h}\sum_{w=p,e}\left(\beta_w \tilde{b}_3^w - \delta_w \tilde{d}_3^w + \kappa_w \tilde{g}_d^w\right) - \frac{m_F^2}{14h}\left(\gamma_p \tilde{c}_q^p\right) + m_F K_Z^{(1)} B + \left(1 - \frac{m_F^2}{16}\right) K_Z^{(2)} B^2 \quad (1)$$

for the quantization magnetic field in the negative z direction (vertically downward) in the lab frame. The first two terms in (1) are Lorentz violating SME frequency shifts, the last two describe the first and second order Zeeman frequency shift (we neglect B^3 and higher order terms). The tilde quantities are linear combinations of the SME matter sector parameters of tab. I in the lab frame, with p,e standing for the proton and electron respectively. The quantities $\beta_w, \delta_w, \kappa_w, \gamma_w, \lambda_w$ depend on the nuclear and electronic structure, they are given in tab. II of [6], h is Planck's constant, B is the magnetic field seen by the atom, $K_Z^{(1)} = 7.0084$ Hz nT^{-1} is the first order Zeeman coefficient, $K_Z^{(2)} = 427.45 \times 10^8$ Hz T^{-2} is the second order coefficient [18]. The tilde quantities in (1) are time varying due to the motion of the lab frame (and hence the quantization field) in a cosmological frame, inducing modulations of the frequency shift at sidereal and semi-sidereal frequencies, which can be searched for.

From (1) we note that the $m_F = 0$ clock transition is insensitive to Lorentz violation or the first order Zeeman shift, while the Zeeman transitions ($m_F \neq 0$) are sensitive to both. Hence, a direct measurement of a Zeeman transition with respect to the clock transition allows a LI test. However, such an experiment would be severely limited by the strong dependence of the Zeeman transition frequency on B, and its diurnal and semi-diurnal variations. To avoid such a limitation, we "simultaneously" (see below) measure the $m_F = 3$, $m_F = -3$ and $m_F = 0$ transitions and form the combined observable $\nu_c \equiv \nu_{+3} + \nu_{-3} - 2\nu_0$. From (1)

$$\nu_c = \frac{1}{7h} K_p \tilde{c}_q^p - \frac{9}{8} K_Z^{(2)} B^2 \quad (2)$$

where we have used $\gamma_p = -K_p/9$ from [6] ($K_p \sim 10^{-2}$ in the Schmidt nuclear model). This observable is insensitive to the first order Zeeman shift, and should be zero up to the second order Zeeman correction and a possible Lorentz violating shift in the first term of (2).

The lab frame parameter $\tilde{c}_q^p$ can be related to the conventional sun-centered frame parameters of the SME (the parameters of tab. I) by a time dependent boost and rotation (see [6] for details). This leads to a general expression for the observable ν_c of the form

$$\nu_c = A + C_{\omega_\oplus}\cos(\omega_\oplus T_\oplus) + S_{\omega_\oplus}\sin(\omega_\oplus T_\oplus) + C_{2\omega_\oplus}\cos(2\omega_\oplus T_\oplus) + S_{2\omega_\oplus}\sin(2\omega_\oplus T_\oplus), \quad (3)$$

where $\omega_\oplus$ is the frequency of rotation of the Earth, $T_\oplus$ is time since 30 March 2005 11h 19min 25s UTC (consistent with the definitions in [19]), and with A, $C_{\omega_\oplus}$, $S_{\omega_\oplus}$, $C_{2\omega_\oplus}$ and $S_{2\omega_\oplus}$ given in tab. II as functions of the sun frame SME parameters. A least squares fit of (3) to our data provides the measured values given in tab. II, and the corresponding determination of the SME parameters.

The FO2 setup is sketched in fig. 1. Cs atoms effusing from an oven are slowed using a chirped counter propagating laser beam and captured in a lin $\perp$ lin optical molasses. Atoms are cooled by six laser beams supplied by pre adjusted optical fiber couplers precisely attached to the vacuum tank. Compared to typical FO2 clock operation [16], the number of atoms loaded in the optical molasses has been reduced to $\sim 2 \times 10^7$ atoms captured in 30 ms. This reduces the collisional frequency shift of ν_c to below 0.1 mHz, and even less ($< 1\mu$Hz) for its variation at $\omega_\oplus$ and $2\omega_\oplus$.

Atoms are launched upwards at 3.94 m.s^{-1} by using a moving optical molasses and cooled to ~ 1 μK in the moving frame by adiabatically decreasing the laser intensity and increasing the laser detuning. Atoms are then selected by means of a microwave excitation in the selection cavity performed in a bias magnetic field of ~ 20 μT, and of a push laser beam. Any of the $|3, m_F\rangle$ states can be prepared with a high degree of purity (few 10^{-3}) by tuning the selection microwave frequency. 52 cm above the capture zone, a cylindri-

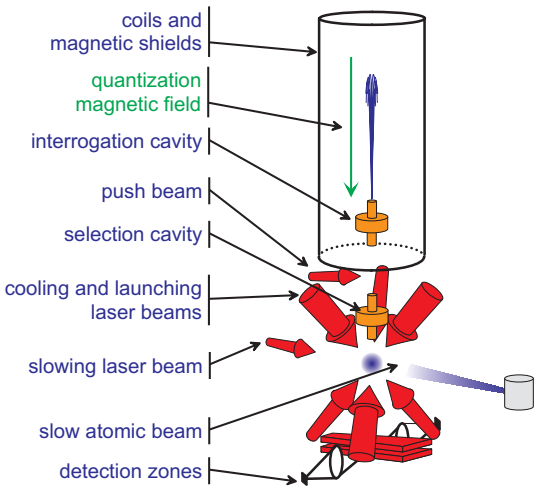

FIG. 1: Schematic view of an atomic fountain.

TABLE II: Coefficients of (3) to first order in $\beta \equiv v_\oplus/c$, where $\Omega_\oplus$ is the angular frequency of the Earth's orbital motion, T is time since the March equinox, $\chi = 41.2°$ is the colatitude of our lab, and $\eta = 23.3°$ is the inclination of the Earth's orbit. The measured values (in mHz) are shown together with the statistical (first bracket) and systematic (second bracket) uncertainties.

A	$\frac{K_p}{28h}(1+3\cos(2\chi))\,(\tilde{c}_Q + \beta\,(\sin(\Omega_\oplus T)\tilde{c}_{TX} + \cos(\Omega_\oplus T)\,(2\sin\eta\ \tilde{c}_{TZ} - \cos\eta\ \tilde{c}_{TY}))) - \frac{9}{8}K_Z^{(2)}B^2$	-5.3(0.04)(25)
$C_{\omega_\oplus}$	$-\frac{3K_p}{14h}\sin(2\chi)\,(\tilde{c}_Y + \beta\,(\sin(\Omega_\oplus T)\tilde{c}_{TZ} - \cos(\Omega_\oplus T)\sin\eta\ \tilde{c}_{TX}))$	0.1(0.06)(0.03)
$S_{\omega_\oplus}$	$-\frac{3K_p}{14h}\sin(2\chi)\,(\tilde{c}_X - \beta\,\cos(\Omega_\oplus T)\,(\sin\eta\ \tilde{c}_{TY} + \cos\eta\ \tilde{c}_{TZ}))$	-0.03(0.06)(0.03)
$C_{2\omega_\oplus}$	$-\frac{3K_p}{14h}\sin^2\chi\,(\tilde{c}_- + \beta\,(\sin(\Omega_\oplus T)\tilde{c}_{TX} + \cos(\Omega_\oplus T)\cos\eta\ \tilde{c}_{TY}))$	0.04(0.06)(0.03)
$S_{2\omega_\oplus}$	$-\frac{3K_p}{14h}\sin^2\chi\,(\tilde{c}_Z + \beta\,(\sin(\Omega_\oplus T)\tilde{c}_{TY} - \cos(\Omega_\oplus T)\cos\eta\ \tilde{c}_{TX}))$	0.03(0.06)(0.03)

cal copper cavity (TE_{011} mode) is used to probe the $|3, m_F\rangle \leftrightarrow |4, m_F\rangle$ hyperfine transition at 9.2 GHz. The Ramsey interrogation method is performed by letting the atomic cloud interact with the microwave field a first time on the way up and a second time on the way down. After the interrogation, the populations $N_{F=4}$ and $N_{F=3}$ of the two hyperfine levels are measured by laser induced fluorescence, leading to a determination of the transition probability. From the transition probability, measured on both sides of the central Ramsey fringe, we compute an error signal to lock the microwave interrogation frequency to the atomic transition using a digital servo loop. The frequency corrections are applied to a high resolution DDS synthesizer in the microwave generator and used to measure the atomic transition frequency with respect to the local reference.

The homogeneity and the stability of the magnetic field in the interrogation region is a crucial point for the experiment. A magnetic field of 203 nT is produced by a main solenoid (length 815 mm, diameter 220 mm) and a set of 4 compensation coils, surrounded by 5 cylindrical magnetic shields. Furthermore, magnetic field fluctuations are actively stabilized by acting on 4 additional hexagonal coils. The magnetic field in the interrogation region is probed using the $|3, 1\rangle \leftrightarrow |4, 1\rangle$ atomic transition. Measurements of the transition frequency as a function of the launch height show a peak to peak spatial dependence of 230 pT over a range of 320 mm above the interrogation cavity with a variation of ≤ 0.1 pT/mm around the apogee of the atomic trajectories. Measurements of the same transition as a function of time at the launch height of 791 mm show a magnetic field instability near 2 pT/$\sqrt{\tau}$. The long term behavior exhibits residual variations of the magnetic field (~ 0.7 pT at τ =10000 s) induced by temperature fluctuations.

The experimental sequence is tailored to circumvent the limitation that the long term magnetic field fluctuations could cause. First $|3, -3\rangle$ atoms are selected and the $|3, -3\rangle \leftrightarrow |4, -3\rangle$ transition is probed at half maximum on the red side of the resonance (0.528 Hz below the resonance center). The next fountain cycle, $|3, +3\rangle$ atoms are selected and the $|3, +3\rangle \leftrightarrow |4, +3\rangle$ transition is also probed at half maximum on the red side of the resonance. The third and fourth fountain cycles, the same two transitions are probed on the blue side of the resonances (0.528 Hz above the resonance centers). This 4180 ms long sequence is repeated so as to implement two interleaved digital servo loops finding the line centers of both the $|3, -3\rangle \leftrightarrow |4, -3\rangle$ and the $|3, +3\rangle \leftrightarrow |4, +3\rangle$ transitions. Every 400 fountain cycles, the above sequence is interrupted and the regular clock transition $|3, 0\rangle \leftrightarrow |4, 0\rangle$ is measured for 10 s allowing for an absolute calibration of the local frequency reference with a suitable statistical uncertainty. Using this sequence, magnetic field fluctuations over timescales ≥ 4 s are rejected in the combined observable ν_c and the stability is dominated by the short term ($\tau < 4$ s) magnetic field fluctuations.

We have taken two data sets implementing the experimental sequence described above (21 days in April 2005 and 14 days in September 2005). The complete raw data (no post-treatment) is shown in fig. 2, each point representing a $\sim$ 432 s measurement sequence of $\nu_{+3} + \nu_{-3} - 2\nu_0$ as described above. Fig. 2 also shows the frequency stability of a 10 day continuous stretch of data in the April set. We note the essentially white noise behavior of the data, indicating that the experimental sequence successfully rejects all long term variations of the magnetic field or of other perturbing effects. A least squares fit of the model (3) to the complete data provides the 5 coefficients and statistical uncertainties given in tab. II.

We note a statistically significant offset of the data from zero ($-5.3(0.04)$ mHz). This is partly due to the second order Zeeman shift (second term in (2)) which amounts to -2.0 mHz. The remaining -3.3 mHz are either due to a systematic effect or indicate a genuine Lorentz violating signal.

The dominant systematic effect in our experiment is a residual first order Zeeman shift. This arises when the $m_F = +3$ and -3 atoms have slightly different trajectories in the presence of a magnetic field gradient. The result is a difference in first order Zeeman shift and hence incomplete cancelation in the combined observable ν_c. The presence of this effect in our experiment is confirmed by the measured times of flight (TOF), which show a systematic difference of $\sim$ 158 μs between the centers of the $m_F = \pm 3$

TABLE III: Results for SME Lorentz violating parameters $\tilde{c}$ for the proton, in GeV and with $J = X, Y, Z$.

$\tilde{c}_Q$	$= -0.3(2.2)$	$\times 10^{-22}$
$\tilde{c}_-$	$= -1.8(2.8)$	$\times 10^{-25}$
$\tilde{c}_J$	$= (0.6(1.2), \quad -1.9(1.2), \quad -1.4(2.8))$	$\times 10^{-25}$
$\tilde{c}_{TJ}$	$= (-2.7(3.0), \quad -0.2(3.0), \quad -0.4(2.0))$	$\times 10^{-21}$

atomic clouds, which corresponds to a vertical separation of ≤ 623 μm at apogee. Using this in a Monte Carlo (MC) simulation with the measured vertical and horizontal (~ 6 pT/mm) magnetic field gradients we obtain a total offset in ν_c of $\sim$ 25 mHz, assuming that the horizontal separation between the $m_F = \pm 3$ atoms is identical to the measured vertical one. We consider this to be an upper limit (the horizontal separation is likely to be less than the vertical one due to the absence of gravity), and take it as the systematic uncertainty on the determined offset (A in tab. II). To obtain the corresponding systematic uncertainty on the sidereal and semi-sidereal modulations of ν_c we have fitted the model (3) to the $m_F = \pm 3$ TOF difference. We find no significant amplitudes, so we take the uncertainties of the least squares fit as the maximum value of the modulations, leading to the systematic uncertainties on the amplitudes in tab. II.

Finally we use the five measurements and the relations in tab. II to determine the values of the eight SME parameters. In doing so, we assume that there is no correlation between the three $\tilde{c}_{TJ}$ parameters and the other five parameters, and determine them independently. The results are given in tab. III.

In conclusion, we have carried out a test of Lorentz invariance in the matter sector of the minimal SME using Zeeman transitions in a cold ^{133}Cs atomic fountain clock. From our data and extensive analysis of systematic effects we see no indication of a violation of LI at the present level of experimental uncertainty. Using a particular combination of the different atomic transitions we have set first limits on four proton SME parameters and improved previous limits [14] on four others by 11 and 13 orders of magnitude.

Continuing the experiment regularly over a year or more will allow statistical decorrelation of the three $\tilde{c}_{TJ}$ parameters from the other five, due to their modulation at the annual frequency ($\Omega_\oplus T$ terms in tab. II). Further improvements, and new measurements, could come from the unique capability of our fountain clock to run on ^{87}Rb and ^{133}Cs simultaneously. The different sensitivity of the two atomic species to Lorentz violation (see [6]) and magnetic fields, should allow a measurement of all SME parameters in (1) in spite of the presence of the first order Zeeman effect. Ultimately, space clocks, like the planned ACES mission [20] will provide the possibility of carrying out similar experiments but with faster (90 min orbital period) modulation of the putative Lorentz violating signal, and correspondingly faster data integration.

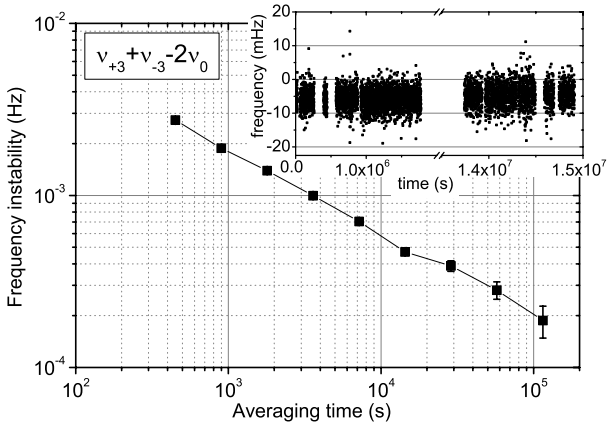

FIG. 2: Frequency stability (Allan deviation) of a $\sim$ 10 day continuous stretch of measurements of ν_c. The inset shows the raw data as a function of time since 30 March 2005 17h 39min 18s UTC.

[1] Kostelecký V.A., Samuel S., Phys.Rev.**D39**, 683, (1989).
[2] Damour T., gr-qc/9711060 (1997).
[3] Gambini R., Pullin J., Phys. Rev. **D59**, 124021, (1999).
[4] Colladay D., Kostelecký V.A., Phys.Rev.**D55**, 6760, (1997); Colladay D., Kostelecký V.A., Phys.Rev.**D58**, 116002, (1998); Kostelecký V.A., Phys.Rev.**D69**, 105009, (2004).
[5] Kostelecký V.A., Lane C.D., Phys.Rev.**D60**, 116010, (1999).
[6] Bluhm R., et al., Phys. Rev. **D68**, 125008, (2003).
[7] Berglund C.J., et al., Phys. Rev. Lett. **75**, 1879, (1995); Phillips D.F. et al., Phys. Rev. **D63**, 111101(R), (2001); Humphrey M.A., arXiv:physics/0103068; Phys. Rev. **A62**, 063405, (2000).
[8] Bear D. et al., Phys. Rev. Lett. **85**, 5038, (2000).
[9] Hou L.-S., Ni W.-T., Li Y.-C.M., Phys. Rev. Lett. **90**, 201101, (2003); Bluhm R. and Kostelecky V.A., Phys. Rev. Lett. **84**, 1381, (2000).
[10] Cané F. et al., Phys. Rev. Lett. **93**, 230801, (2004).
[11] Müller H., Phys. Rev. **D71**, 045004, (2005).
[12] Wolf P., et al., Phys. Rev. **D70**, 051902(R), (2004).
[13] Müller H. et al., Phys. Rev. Lett. **91**, 2, 020401, (2003).
[14] Lane C.D., Phys. Rev. **D72**, 016005, (2005).
[15] Saathoff G., et al., Phys. Rev. Lett. **91**, 19, 190403, (2003).
[16] Bize S., et al., J. Phys. **B38**, S449, (2005).
[17] As discussed in [5] the Schmidt nuclear model only allows an approximate calculation of the SME frequency shift, with more complex models generally leading to dependences on additional SME parameters. Nonetheless, the model is sufficient to derive the leading order terms and has been used for the analysis of most experiments providing the bounds in Tab. I.
[18] Vanier J., Audoin C., *The Qunatum Physics of Atomic Frequency Standards*, Adam Hilger, (1989).
[19] Kostelecky A.V. and Mewes M., Phys. Rev. **D66**, 056005, (2002).
[20] Salomon C., et al., C.R. Acad. Sci. Paris **2**, 1313, (2001).

Proceedings of the 20th EFTF, 2006

Initial Evaluation of the USNO Rubidium Fountain

S. Peil,* S. Crane, T. Swanson and C. R. Ekstrom
Clock Development Division, U.S. Naval Observatory
Washington, D.C. 20392
**Electronic address:* peil@atom.usno.navy.mil

We discuss the first rubidium atomic fountain at the U. S. Naval Observatory, NRF1, which has been built as a prototype for future devices to be included in the USNO timescale. The system has demonstrated a short-term Allan deviation of $1.35\times10^{-13}/\tau^{1/2}$ when measured against a hydrogen maser. We have directly compared NRF1's performance to that of our cesium fountain, NCF, demonstrating integration as $1/\tau^{1/2}$ below 1×10^{-15}, and performance that is consistent with 7×10^{-16} at 11 hours.

1. INTRODUCTION

The USNO Master Clock relies on a large ensemble of commercial cesium-beam clocks and active hydrogen masers. The timescale utilizes the superior short-term performance of the hydrogen masers and is steered in the long term to the cesium clocks. Future improvements to the Master Clock will be based on introducing advanced clock technology for more rapid and robust characterization of maser frequency drift. A program to build six rubidium atomic fountains for this purpose is underway.

II. FOUNTAIN DESIGN

Continuous, long-term operation in a stable environment requires a robust, compact fountain design. The entire system, described in detail elsewhere [1], will be contained in three 'equipment racks', one of which is the physics package. The other two racks contain computer control, electronics, and a miniature rack-mounted optical table [2].

A cut-away of the physics package of NRF1 is shown in Fig. 1(a). The physics package is enclosed in a set of three magnetic shields which provide a low magnetic-field environment for molasses cooling. Thus, all vacuum and optical components are required to be nonmagnetic.

Atoms are loaded into either a MOT with a modest magnetic-field gradient (2 G/cm along the axial direction) or a σ^+-σ^- optical molasses. All of the characterization presented here uses MOT loading. Launching, cooling and state-selecting provide a sample of $\sim10^7$ atoms at 1.5 μK. We run the fountain as a frequency reference by interrogating the central, ~1 Hz wide Ramsey fringe via phase modulation of the 6.8 GHz microwave interrogation field.

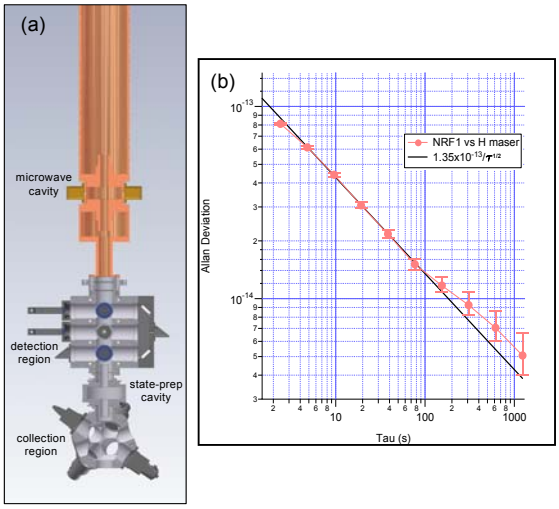

Figure 1 (a) Cross-sectional view of the vacuum chamber and optical couplers of NRF1. All of these components are made from nonmagnetic materials. (b) Short-term performance when measured against a hydrogen maser is as good as $1.35\times10^{-13}/\tau^{1/2}$. Deviation from white-frequency noise ($1/\tau^{1/2}$ behavior) due to maser frequency fluctuations occurs here at several hundred seconds.

III. CHARACTERIZATION

For typical fountain operation, the microwave interrogation drive is generated from the 5 MHz output of a BVA quartz crystal that is phase-locked to a hydrogen maser with a time constant of ~3 seconds. In this configuration, we can see a short-term Allan deviation of $1.35\times10^{-13}/\tau^{1/2}$ (Fig. 1(b)). After several hours of integration, the fountain-versus-maser performance becomes limited by maser frequency

fluctuations, which usually introduce a deviation from $1/\tau^{1/2}$ behavior at Allan deviations of several parts in 10^{15}.

In order to obtain a better medium-term characterization of NRF1 than we have achieved with a maser, we measure against our cesium fountain, NCF [3]. The method we use to compare the two devices is illustrated in Fig. 2. We generate the microwave drive for each fountain from the same quartz crystal, which we leave unlocked from any reference maser, removing an unnecessary component. The crystal also serves as the reference oscillator for a pair of adjustable frequency synthesizers. Each synthesizer is adjusted by one of the fountains and outputs the crystal frequency steered to that fountain. This 'open-loop' steering is carried out with a time constant of ~3.5 seconds and does not change the output of the quartz oscillator itself. The phases of the synthesizer outputs are differenced, and the resultant frequency fluctuations versus integration time can be determined. The interrogation cycles of the fountains are not synchronized [4].

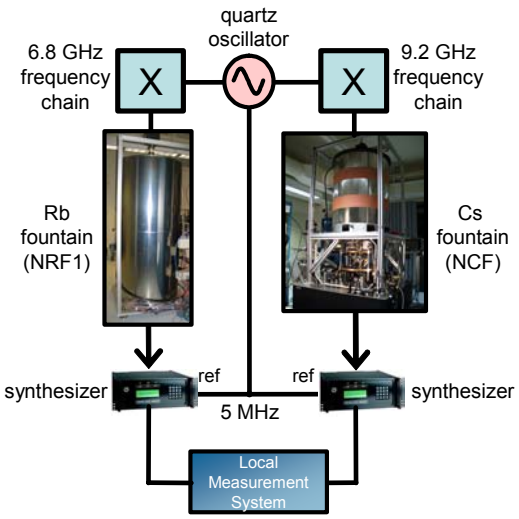

Figure 2 Illustration of the measurement of the relative stability of NRF1 and NCF. For short-term characterization, the crystal can be phase-locked to a maser and either fountain's performance can be measured. For higher-precision characterization, we measure the crystal's frequency with each of the two atomic fountains. Comparing these two measurements results in a fountain-to-fountain stability comparison.

This technique was employed for a 3 day run. Each atomic fountain's measurement of the crystal's frequency is shown in Fig. 3(a). The noise on the traces indicates a worse short-term performance of NCF compared to NRF1. The plot of Allan deviation versus integration time for the comparison between the fountains is shown in Fig. 4. The comparison shows a relative stability of $3\times10^{-13}/\tau^{1/2}$ and white-frequency noise behavior for integration times up to 11 hours. The relative stability at each point is equal to the quadrature sum of the individual fountain stabilities at that integration time – additional measurement noise does not contribute at this level of precision.

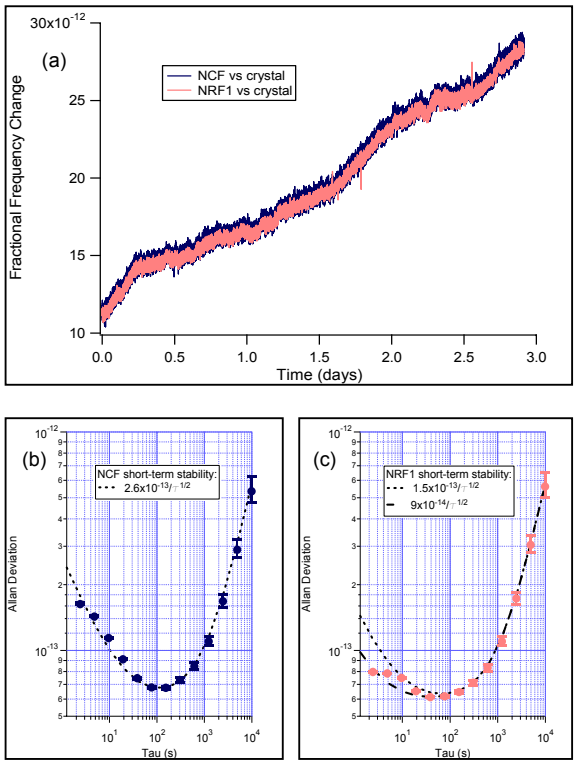

Figure 3 (a) Measurement of the crystal frequency versus time with each fountain. The Allan deviation of this frequency measurement for (b) NCF and (c) NRF1 shows frequency fluctuations from the crystal and from the fountain, enabling a determination of each fountain's short-term performance.

We can use the crystal frequency measurements of Fig. 3(a) to estimate the performance of each individual fountain – in particular, NRF1. The Allan deviation of each fountain-crystal comparison, shown in Fig. 3(b) & 3(c), exhibits frequency fluctuations comprised of contributions from fountain white-frequency noise ($\tau^{-1/2}$ dependence), crystal frequency flicker (τ^{0} dependence), crystal frequency random walk ($\tau^{1/2}$ dependence), and crystal frequency drift (τ^{1} dependence). Fitting the data with the constraint that the crystal noise terms are the same in each measurement gives each fountain's short-term performance. For NCF, this is $2.6(1)\times10^{-13}/\tau^{1/2}$, where the error bar represents combined systematic and statistical uncertainties. This is consistent with independent stability measurements made with a hydrogen maser.

Together with the relative fountain stability of $3\times10^{-13}/\tau^{1/2}$, this shows that the fountain comparison instability is dominated by the performance of NCF. Consequently, we expect the dependence on τ observed for the relative stability to be representative of the τ-dependence of NCF. We can then infer the stability of NCF for all $\tau \leq 11$ hours from $\sigma_{NCF}(\tau)=2.6(1)\times10^{-13}/\tau^{1/2}$. Finally, we can use the fact that the measured relative stability equals the quadrature sum of the individual fountain stabilities to extract the performance of NRF1 at each τ, shown as the filled, circular data points on Fig. 4. The uncertainties shown are derived from propagating the uncertainties on the comparison data and the uncertainty on the slope of the $1/\tau^{1/2}$ curve for NCF's performance. The estimated performance of NRF1 is consistent with white-frequency noise behavior over ½ day, reaching a stability of 7×10^{-16}.

The estimated NRF1 data fit well to a $1.5\times10^{-13}/\tau^{1/2}$ short-term stability. This value is consistent with what we see when measuring against a maser, but a bit high for what we see against a free-running crystal - Fig. 3(c) shows high and low estimates of NRF1's short-term performance during the fountain comparison run. This discrepancy is partly from taking the most conservative estimates for arriving at an implied performance for NRF1.

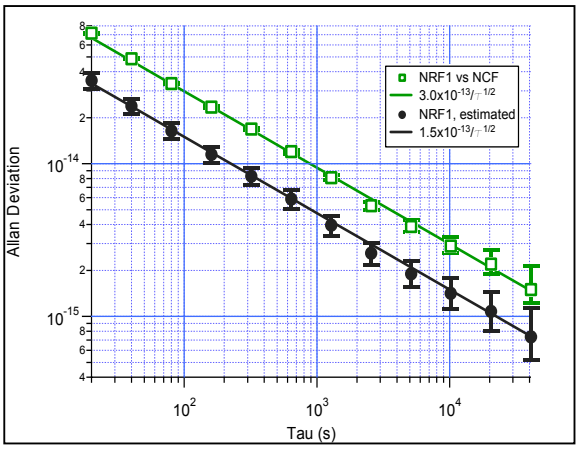

Figure 4 The hollow, square data points show the Allan deviation of the relative frequency fluctuations of NRF1 and NCF for integration times up to 11 hours. The filled, circular data points are the estimated Allan deviation of NRF1 from the comparison data and the expected behavior of NCF. The lines are fits to the data.

We would like to be able to measure lower values of the Allan deviation for NRF1, and ultimately reach a noise floor in the fountain comparison. This should be achievable with modest improvements to NCF; by improving the short-term stability, we will compare more efficiently, and by improving the robustness, we will enable comparisons of longer duration.

IV. CONCLUSIONS

We have presented short- and medium-term characterization of NRF1, and have demonstrated a maser-independent comparison of two atomic fountains. This technique has allowed us to demonstrate white-frequency noise limited performance of NRF1 to an Allan deviation below 1×10^{-15}.

REFERENCES

[1] S. Peil, S. Crane, T. Swanson, and C. R. Ekstrom, "Design and Preliminary Characterization of the USNO Rubidium Fountain," Proceedings of the IEEE International Frequency Control Symposium, 2005, pp. 304-307.

[2] S. Crane, S. Peil, and C. R. Ekstrom, "Miniaturized Atomic Fountain Optical Table," Proceedings of the IEEE International Frequency Control Symposium, 2005, pp. 301-303.

[3] C. R. Ekstrom, E. A. Burt, and T. B. Swanson, "Characterization of the USNO Cesium Fountain," Proceedings of the IEEE Frequency Control Symposium, 2001, pp. 53-56.

[4] S. Bize *et al*. "Interrogation Oscillator Noise Rejection in the Comparison of Atomic Fountains," IEEE Transactions on Ultrasonics, Ferroelectrics, and Frequency Control, Vol. 47, No. 5, September 2000, pp. 1253-1255.

Proceedings of the 20th EFTF, 2006

A new proposal for the measurement of blackbody radiation shift in a Cesium fountain (the Politecnico di Torino method)

G.A. Costanzo,* M. Berutto, M. Caldera, and A. De Marchi
Politecnico di Torino - Corso Duca degli Abruzzi 24 - 10129 - Torino - Italy

The AC Stark frequency shift induced by blackbody radiation (BBR) is presently a limiting factor toward the accuracy evaluation of Cs fountain frequency standards [1] [2]. In fact, at laboratory temperature, the AC Stark relative frequency shift is of the order of 10^{-14} and therefore the blackbody coefficient must be evaluated to the percent level if an accuracy below 10^{-15} is desired. The BIPM recommended coefficient is $-1.69(4) \cdot 10^{-14}$ for Cs atoms while recent BBR shift measurements performed at IEN (now INRIM) [3] [4] yield a value which differs by 18% from the accepted value. The Politecnico di Torino is now developing a new method for the measurement for the BBR shift, with the aim of resolving the discrepancy on the coefficient. In this paper the Politecnico di Torino method is analyzed with a full description of the new apparatus. The method is based on rapidly varying thermal cycles.

I. INTRODUCTION

In recent years, Cs frequency standards based on the fountain scheme reached a fractional 10^{-15} accuracy budget, mainly limited by few systematic effects; among them the "Blackbody radiation shift" (BBRS) provides the greatest uncertainty contribution. The physics of this systematic effect is due to the displacement of energy levels caused by AC Stark shift induced by black body radiation field. In order to evaluate the BBRS the commonly used equation is

$$\frac{\Delta\nu}{\nu} = \beta \cdot \left(\frac{T}{300}\right)^4 \left[1 + \epsilon \left(\frac{T}{300}\right)^2\right] \qquad (1)$$

where T is the absolute temperature experienced by the atoms during their parabolic flight.

The accepted values coefficients β and ϵ for Cs are $-1.69(4)\ 10^{-14}$ and $1.4 \cdot 10^{-2}$ respectively. This effect introduces a systematic relative shift of some 10^{-14} which must be evaluated at the percent level if the accuracy target is in the low 10^{-16}. Moreover the interest on this shift is increased because of results reported in [3], showing a value for β which would introduce a relative correction of $3 \cdot 10^{-15}$ if used.

A few years ago the Politecnico di Torino completed the realization of a fountain standard in collaboration with the national metrological institute INRIM and the NIST (USA). A full description of the whole apparatus can be found in [5][6]. In this paper we describe the Politecnico method for BBRS evaluation.

II. THE PROPOSED METHOD

Two methods have been proposed in the past for the evaluation of BBRS, both based on the measurement of the standard's output frequency in two different working conditions. In one method [4] what is changed between the two working conditions is the temperature of the vacuum chamber, where the Cs atoms undergo their ballistic flight. The blackbody temperature variations thus induce a systematic shift on the resonance frequency of the Cs atoms. This is therefore a direct measurement of the BBRS. Measurements are averaged in the long term in order to minimize the uncertainty by pushing the averaging time to the stability limits of the system. The approach is differential, but is slow, and is in any case limited by the long term stability of the standard and/or the frequency reference, which must then be either a Hydrogen Maser or another Cesium fountain. In the other method [7] an indirect measurement is performed: a static electrical field is applied to the flying atoms and the DC Stark coefficient is evaluated from the frequency shift of the standard. This coefficient is used, on the basis of a physical model, to evaluate the AC Stark shift, which is the BBRS.

The Politecnico method is based on fast temperature cycling of the drift tube in a Cs fountain. Two advantages are obtained in this way:

1. better reproducibility can be guaranteed between the two phases of the experiment for all shifts other than the targeted one, reducing the need for accuracy evaluations

2. the high pass filter introduced by the fast differential scheme is useful to filter out slow instabilities, reducing in this way the stability required of the external frequency reference.

A time periodicity of about 100s is planned, with a swing of 40K peak to peak. The only criticality of the method is the necessity to stabilize the temperature of the microwave cavity to a high degree because of the considerably high temperature swings imposed to the drift tube. In fact, cavity temperature variations during the atoms-microwave interactions can introduce a dynamic end-to-end Ramsey cavity phase shift. The latter must be limited to 10^{-16} if percent level ac-

*Electronic address: giovanni.costanzo@polito.it

curacy on β is the target. This implies a maximum temperature gradient of 10μK/s for the cavity.

III. EXPERIMENT

A. Description of the apparatus

In order to perform fast temperature cycling of the copper drift tube, a water circuit was realized with the aim to cool and heat the cylindrical vacuum tank inside which atoms perform the parabolic flight. In fact, cooling and heating are accomplished by means of a 30cm long water flux jacket, coaxial to the drift tube, which is centered about the apogee of the atoms parabolic flight. The thermal cycles are induced by flowing alternatively hot and cold water around the drift chamber. Temperature excursions of 40K peak-to-peak can be obtained. The temperature value is offset to 313K, where the cavity is tuned to the atomic transition. A mechanical pump ensures a 4l/min continuous flux of water, alternatively coming from a heated reservoir and the aqueduct. With this geometry, atoms can experience a cyclical temperature swing along their apogee, where they spend most of their drift time.

Because of the heat conductance between the Ramsey cavity and the drift tube, 0.5K peak to peak fluctuations are induced to the cavity during the temperature swing: this value is too high because it can induce detrimental dynamic end-to-end cavity phase shift reducing β measurement accuracy. A first passive solution was found by means of three copper buffer stages inserted in the 10cm drift tube section between the top of the cavity and the bottom of the flux jacket. The residual temperature variations are further reduced by active control of the resonance frequency of the cavity. As a matter of fact end-to-end phase shift can be monitored by direct measurements of the cavity resonance frequency. The latter is varying not only because of temperature variations (typical sensitivity coefficient is -160kHz/K) but also because of weight changes above the cavity as a consequence of water density variations during the thermal cycles (measured value is $+1$kHz/kg). This problem is overcome by measuring the resonance frequency instead of the temperature.

A classical phase detection scheme is then used to measure frequency variations of the cavity. The error signal is fed back to amagnetic heaters, directly wound around the cavity. An electronic circuit generates a symmetric PWM waveform, in order to avoid detrimental static magnetic field components. When the control loop is open and thermal cycles of $\Delta T = 40\mathrm{K_{pp}}$ are applied at the apogee, temperature fluctuations of the order of $120\mathrm{mK_{pp}}$ are measured on the cavity. In closed loop conditions, equivalent temperature fluctuations of $300\mu\mathrm{K_{pp}}$ are inferred from cavity frequency measurements. This residual temperature fluctuations can limit the accuracy on β, if the induced end-to-end cavity phase shift is not corrected for.

B. Thermal model for BBRS measurements

For the evaluation of the BBRS coefficient to 1%, an uncertainty of 1K is needed for the equivalent temperature along the drift tube. It follows that a thermal map reproducing the temperature is necessary with a time dependent analysis during the Cs atoms Ramsey time. Even if the Politecnico proposed method seems to be attractively easy, the thermal map must be evaluated in a complex system based on forced water with heat transfer due to different physical time dependent processes (radiative, conductive and convective). All these must be taken into account if the 1% accuracy goal must be fulfilled. Because of the heat transfer complexity, temperature measurements in specific points may not be sufficient and must be supported by calculations based on finite element. The latter seems to be an efficient and precise tool for modeling complex systems, but requires accurate analysis of the physical processes and subsequently model validation by means of direct temperature measurements.

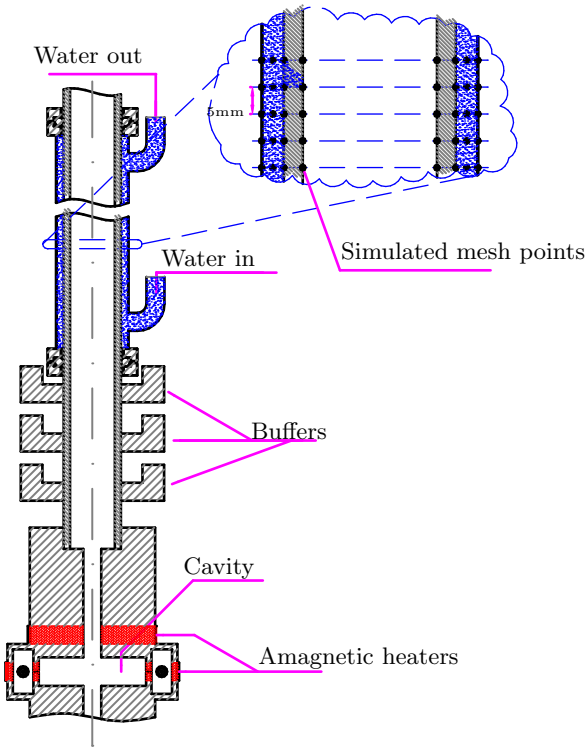

FIG. 1: Fountain apparatus for blackbody radiation frequency shift measurements.

A computation tool was implemented using Finite Differences Method in which both the spatial and transient behavior is studied along the cylindrical volume of the vacuum copper tube and the water coaxial

jacket. The method discretises the equations of thermal exchange for computational solution through the Taylor series expansion of functions of several independent variables describing the fluid motion and the heat transfer. Thermal and fluid dynamic behavior is modeled by control-volume formulation: the calculation domain is divided into a number of non overlapping volumes generating the mesh points for integration of heat exchange differential equations.

A cylindrical coordinate system is used, neglecting azimuthal variations for reduction of mathematical complexity. This solution seems to be adequate because of the huge conductivity of the copper tube. Fluid motion was then studied, because heat transfer in convective processes strongly depends on fluid dynamics. Because of the turbolent flow regime (Reynolds number > 2000), when heat exchange coefficient must be evaluated, the most widely applicable expression for Nusselt term Nu is the so called Sieder-Tate equation

$$Nu = 0.027 \cdot Re^{0.8} Pr^{\frac{1}{3}} \left(\frac{\mu_m}{\mu_p} \right)^{0.14} \qquad (2)$$

where the term $\frac{\mu_m}{\mu_p}$ takes into account the effect of the fluid viscosity μ_p, evaluated at the wall temperature, and the fluid viscosity μ_m evaluated at the adiabatic mean temperature. The convective coefficient α can then be calculated as $\alpha = \frac{Nu \cdot \lambda}{D_{eq}}$ where λ is the thermal conductivity and D_{eq} is a term depending on the mechanical geometry. The radiation heat exchange is obtained using Gebhart analysis method. Figure 1 shows an outline of the fountain mechanical part and the node division necessary to evaluate heat exchange.

C. Results

In order to confirm the theoretical model used for computer simulations, several thermocouples were placed in specific points. The space-time model elaborated numerically was then validated by means of temperature measurements along the drift tube. The calculation tool allows determinations of temperature values along the inner surface of the drift tube. Fig.2 shows thermal cycles applied to the fountain: close to the apogee the measured temperatures agree with the simulations within $0.4\mathrm{K_{rms}}$ as shown in the lower curve. This discrepancy arises mostly during transient when valves switch between hot and cold water.

IV. CONCLUSION

A novel method for BBRS evaluation was reported, aiming for uncertainty reduction on β coefficient. Fast thermal cycles applied to the drift tube of the Cs fountain apparatus at the Politecnico di Torino seems an easy tool for further investigation on frequency shift due to AC Stark effect. A numerical model was also developed in order to obtain the temperature map above the Ramsey microwave cavity.

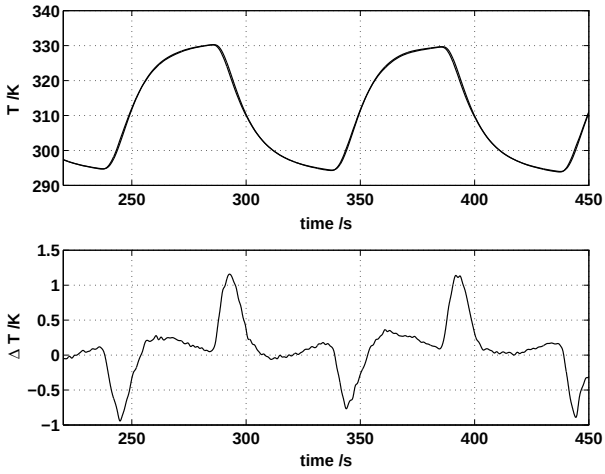

FIG. 2: Upper curve: computed temperature variation on the drift tube close to the apogee. Lower curve: temperature differences between simulations and measurements.

[1] C. Vian *et al.*, IEEE Trans. I&M **54**, 2, 2005.
[2] T.P. Heavner *et al.*, Metrologia **42**, 2005.
[3] S. Micalizio *et al.* Phys. Rev. A, **69**, 2004.
[4] F. Levi *et al.* Phys. Rev. A, **70**, 2004.
[5] G.A. Costanzo *et al.*, Proc.15^{th} EFTF, 2001.
[6] G.A Costanzo *et al.*, 6^{th} Symposium on Frequency Standards and Metrology, pub. 2002.
[7] E. Simon *et al.*, Phys. Rev. A, **57**, 1998.

Current status of PTB's new caesium fountain clock CSF2

Proceedings of the 20th EFTF, 2006

R. Wynands,* D. Griebsch, R. Schröder, and S. Weyers
Physikalisch-Technische Bundesanstalt, Bundesallee 100, 38116 Braunschweig, Germany

We give an overview of the caesium fountain clock CSF2 which is currently being put into operation at the Physikalisch-Technische Bundesanstalt in Braunschweig, Germany.

I. INTRODUCTION

CSF1, the first fountain clock at Physikalisch-Technische Bundesanstalt (PTB), has successfully been operating since 1999. It contributed many times to TAI and served as the reference for a number of optical frequency measurements.

Uncertainty evaluations and the optimization of operational parameters of CSF1 have always been hampered by the fact that only hydrogen masers have been available as a frequency reference, which unfortunately show a relatively large day-to-day frequency variation. This is one of the main reasons why it was decided to construct a second fountain clock, called CSF2. This fountain clock is now being put together and is expected to become fully operational sometime in 2006.

II. SETUP OF CSF2

CSF1 has been described in detail previously [1, 2]. The main difference between CSF2 and CSF1 is in the geometry of the laser beams in the trapping zone. In CSF1 we are using the so-called (100) geometry [3], in CSF2 the (111) geometry (Fig. 1). This allows us to use much larger beam diameters (22 mm at the $1/e^2$ points) so that we can start with an optical molasses as a first loading stage (instead of the MOT we have traditionally been using in CSF1) without too much a reduction in the number of atoms loaded compared to CSF1.

Several more changes with respect to CSF1 have been implemented in CSF2; here is a partial list:

- The trapping beams are arranged in the (111) configuration.
- Larger trapping beam diameters are used (22 mm at the $1/e^2$ points).
- The output couplers for the optical fibers transporting the laser light from the optical table are mounted directly on the vacuum window flanges.
- Atom loading starts with an optical molasses rather than a MOT.

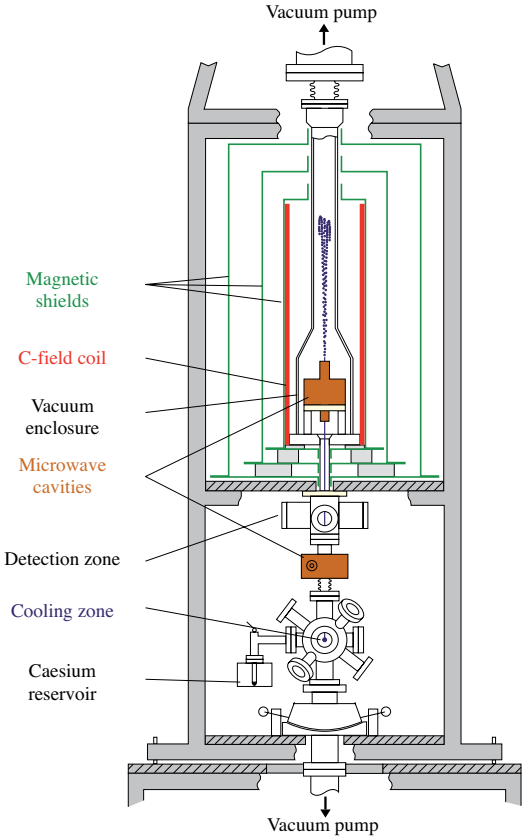

FIG. 1: Sketch of the geometry of CSF2

- There is an additional ion getter pump below the trapping region, to improve the background pressure in the trapping zone.
- The trapping zone is mounted on a spherical pivot mount in order to adjust the launch direction.
- The detection zone is situated above the state selection cavity.
- After inducing the transition $|F = 4, m = 0\rangle \rightarrow |F = 3, m = 0\rangle$ in the state selection cavity, the atoms not in the $|F = 3, m = 0\rangle$ state will be "blown away" by the detection laser beams.
- The geometry of the magnetic shields has been improved, in particular the mechanical joints between the two parts of each layer.

*Electronic address: robert.wynands@ptb.de

- The vacuum enclosure is made from copper instead of titanium, in order to reduce thermal gradients even further, and at the same time the vacuum pressure due to the better properties of copper as a material for vacuum enclosures.
- The vacuum enclosure tapers down towards the top of the fountain in order to reduce the internal surface area and therefore the outgassing, i.e., to improve the background pressure near apogee.
- The optical setup has been redesigned. For instance, a master laser injects two slave lasers, in order to provide enough power for efficient molasses operation and to saturate the cycling transition in the detection zone [4]. The master laser is locked to the caesium transition in such a way that no modulation is present on the useful output beam.

III. HOMOGENEITY OF THE C-FIELD

After a rough optimization of the most important parameters we have measured the homogeneity of the C-field in the standard way. A series of Ramsey fringe patterns on the $|F = 3, m = -1\rangle \rightarrow |F = 4, m = -1\rangle$ transition was recorded for gradually increasing toss height. From the position of the central Ramsey fringe one obtains the average field $\langle|B|\rangle$ seen by the atoms for that particular toss height. With a weighted differentiation procedure one can extract the actual, unweighted magnetic flux density $|B|$ at each position along the trajectory (Fig.2).

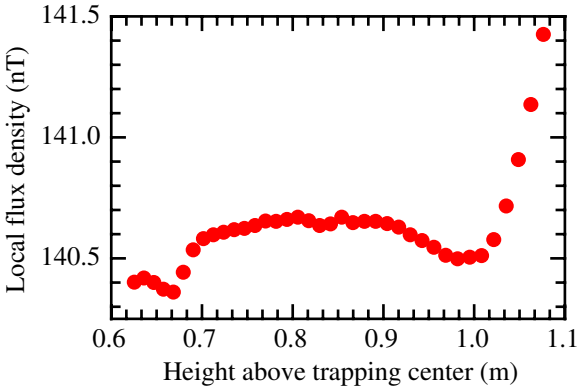

FIG. 2: Magnetic flux density inside CSF2 as a function of height above the center of the trapping zone

This field is remarkably homogeneous. When taking the weighted variance σ_B^2 of the magnetic flux density as a function of position along the trajectory, where each point is weighted by the duration of the time interval that the atom spends at this height, one arrives at a relative uncertainty of only 4×10^{-22} for the second order Zeeman correction [5] when the fountain is operated with a maximum toss height of 1.05 m. This uncertainty does not include, of course, the temporal instability of the C-field itself.

IV. FIRST RAMSEY FRINGES

We have measured the ratio $N = N_4/(N_3 + N_4)$ as a function of microwave frequency in the Ramsey cavity (Fig. 3). Here N_3 and N_4 are the integrated areas under the time-of-flight curves detected for atoms arriving in the $|F = 3\rangle$ and $|F = 4\rangle$ state, respectively. N_3 and N_4 therefore are a measure of the number of atoms arriving in the respective states. Consequently, the ratio N is equivalent to the transition probability for a given microwave frequency.

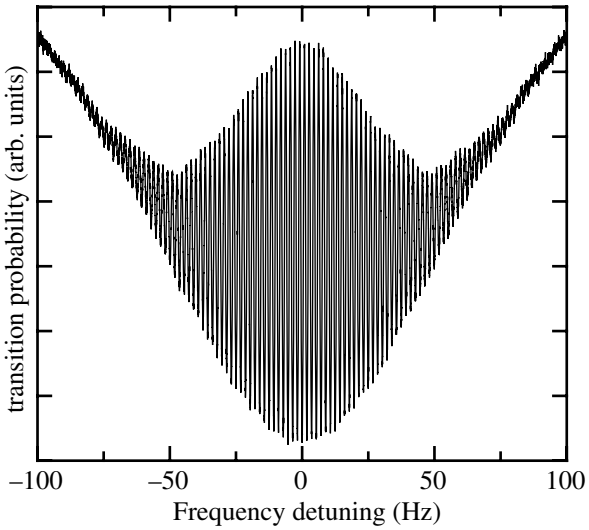

FIG. 3: A full Ramsey fringe pattern measured with CSF2 (each experimental point is the average of three tosses)

The contrast of the Ramsey pattern is 13.5%, which is about the maximum expected in the present case, where the state selection cavity and laser "blow-away" are not yet used. Figure 4 shows the central Ramsey fringes for a toss height of 1.04 m, resulting in a fringe width of 0.87 Hz.

V. THE FIRST RUN AS A CLOCK

To get an indication of the performance of CSF2 in the present, unoptimized state (and still without state selection) CSF2 was run as a clock in autonomous mode. The 9-GHz interrogation signal was symmetrically square-wave frequency modulated to the high- and low-frequency sides of the central Ramsey fringe. From the difference between the signal on the two sides of the fringe a correction signal is derived that is

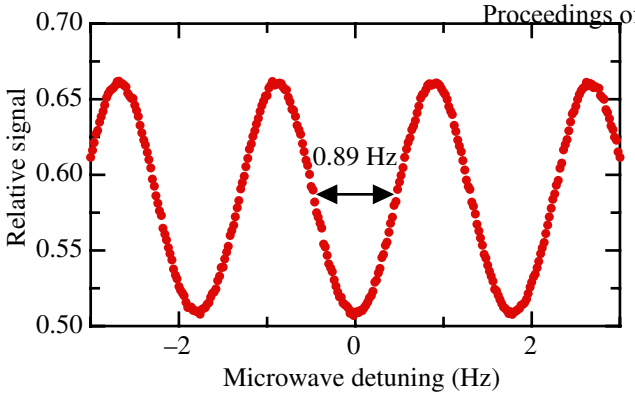

FIG. 4: Central Ramsey fringes on the clock transition in CSF2 (each experimental point is the average of three tosses)

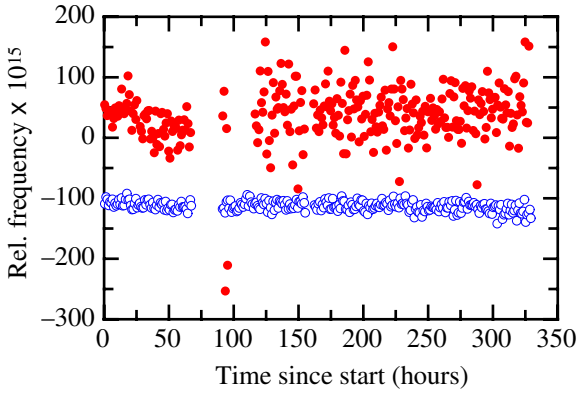

FIG. 5: The very first run of CSF2 (still without making use of the state selection cavity): one-hour frequency averages with respect to CSF1 (red solid dots). For comparison the frequency difference of hydrogen maser H5 and CSF1 was measured simultaneously (open blue circles). The gaps in the data series correspond to laser drop-outs.

fed to the 5-MHz quartz oscillator on which the 9-GHz signal is based. In a multi-channel phase comparator the frequency of this quartz oscillator is monitored with respect to the corresponding 5-MHz signals from CSF1 and from hydrogen maser H5 (Fig. 5).

Note that the data presented here constitutes the raw output data, with no frequency corrections applied. Since most corrections are expected to be small, the observed frequency difference is consistent with the difference in the magnitude of the C-field (100 nT in CSF1 vs. 140 nT in CSF2).

When as a first approximation the gaps in the data are ignored one can determine the Allan deviations plotted in Figure 6. In the plots the error bars correspond to the theoretical result for pure white frequency noise [6].

From the figure one can see that the noise nicely

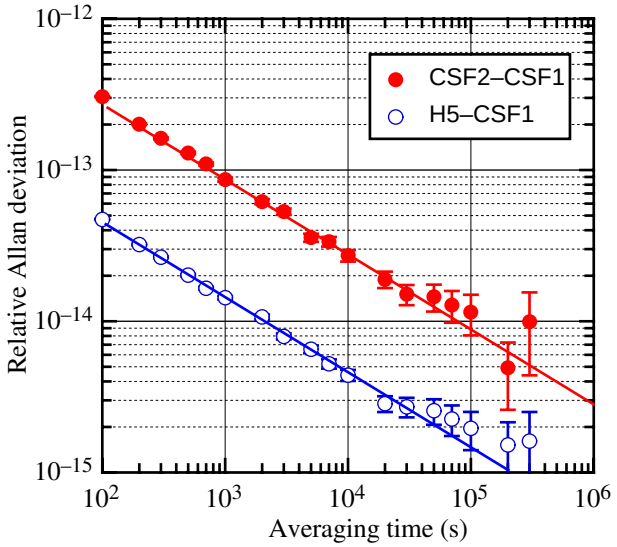

FIG. 6: Allan standard deviation of the data taken during the first two weeks of running CSF2 as a clock (see Fig. 5). Clearly, more work needs to be done on the short-term stability.

averages down according to the white-frequency-noise law (proportional to $\tau^{-1/2}$, solid lines in Fig. 6). For the frequency difference between H5 and CSF1 a plateau is reached for times of a day or more. This is attributed to the long-term instability of the maser.

Clearly, more work needs to be done on CSF2 to improve the short-term stability. For instance the data in Figure 5 was taken over the two weeks before the conference. Even after that rather long time the instability barely reaches 3×10^{-15}.

[1] S. Weyers, U. Hübner, R. Schröder, Chr. Tamm, A. Bauch, Metrologia **38**, 343–352 (2001).
[2] S. Weyers, A. Bauch, R. Schröder, Chr. Tamm, Proc. 6th Symposium on Frequency Standards and Metrology (World Scientific) vol. 5, Fife (GB), pp. 64–71 (2001).
[3] R. Wynands, S. Weyers, Metrologia **42**, S64–S79 (2005).
[4] S. Weyers, A. Bauch, D. Griebsch, R. Schröder, R. Wynands, Proceedings of the 19th European Frequency and Time Forum, Besançon, 205–207 (2005).
[5] S. Weyers, A. Bauch, U. Hübner, R. Schröder, Chr. Tamm, IEEE Trans. Ultrason. Ferroelectrics Freq. Control **47**, 432–437 (2000).
[6] P. Lesage, C. Audoin, IEEE Trans. Instrum. Meas. **22**, 157–161 (1973).

Proceedings of the 20th EFTF, 2006

The Progress of Cesium Fountain Clock at NIM

Lin Pingwei, Li Mingshou, Li Tianchu, Wang Ping, Chen Weiliang, Liu Nianfeng, Lin Yige

National Institute of Metrology (NIM), No.18, Bei San Huan Dong Lu, Beijing 100013, China
E-mail: linpw@nim.ac.cn

Abstract: NIM4 cesium fountain clock has been operating stably and sub-continually for more than 2 years. We in this paper present the improvements of NIM4 clock in 2004-2005 and most recent evaluation for its systematic frequency deviations during 7-8,2005 resulted an uncertainty of 5E-15. We also report the construction of NIM5 movable cesium fountain clock at NIM.

1. INTRODUCTION

The NIM4 laser cooling cesium fountain clock has been operating stably and sub-continually since August 2003. Following BNM/SYRTE fountain clock F01's configuration [1], NIM4 captures about 2E8 atoms in a horizontal-vertical (0,0,1) magneto-optical trap (MOT). MOT light is delivered through three PM fibers. The horizontal MOT light is delivered through a singe PM fiber to physical part and split by free-space optics to four beams for MOT and OM. After the atoms are captured in 1.4s in MOT, the anti-Helmholtz magnetic field is turned off, the atoms are further cooled and launched up to 56cm (16cm above the Ramsey microwave cavity). When atoms move up, they interact with microwave in the state selected microwave cavity and change from $|F=4, m_F=0\rangle$ state to $|F=3, m_F=0\rangle$ state, then a vertical down laser pulse pushes off all F=4 atoms.The left atoms interact twice with 9.192GHz microwave in their upward and downward movements and are detected by detectors. The distance of two detectors is about 9cm and the fluorescence collecting efficiency is about 8% . The Ramsey central fringe FWHM width is about 1.35Hz. The microwave is generated by a synthesizer, which is slow-locked to H-maser H1. The PC servo locked the 9.192GHz microwave frequency to the central frequency of Ramsey fringe by square wave frequency modulation.
We evaluated the systematic frequency shifts of NIM4 from August to December, 2003 for the first time. The combined uncertainty was 9E-15. [2] [3]

II. THE IMPROVEMENTS OF NIM4 CLOCK

We have made several improvements on laser-optical, electronic, and physical parts of NIM4 in 2004 and 2005. These improvements have greatly improved the performances of NIM4, especially its operation reliability, and uncertainty.

Optimizations of the optics and AOMs obtain each 6 mW for horizontal lights and 8 mW for each vertical for MOT and OM. Improvements of the mechanical shutters and their time sequences have improved the operation reliability of the whole clock.
The stabilizing electronics was optimized to ensure the master and re-pump lasers to operate for months without locking break.
A new H-maser of MHM2010 is available from 2005 to replace VCH 1003A as frequency reference of NIM4. H2 has better stability, reduces the uncertainties and shortens the time required for NIM4 frequency shifts evaluation.
All of these have improved the operation reliability of NIM4 clock to realize an operation ratio (effective period of operation over whole operation period time) of more than 95%.
The output laser power from optical fiber often decreases greatly in several days, this increases the work of NIM4 maintenance. We have manufactured a step motor control system to control the angle of the mirror before optical fiber. Experiment result shows this step motor control system can greatly improve the stability of output laser power from optical fiber. We will apply such system to NIM4 in the near future.
Figure 1 shows a Ramsey pattern of NIM4 in 2005, which is significantly better than observed previously.

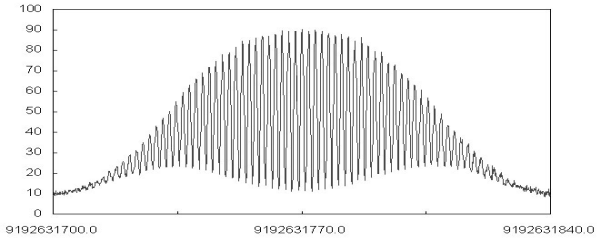

Figure 1, NIM4 Ramsey pattern with FWHM of ~1.4Hz

Confined by the design of NIM4 for the first time and as early as in 1997, the bottom hole of old magnetic shield of NIM4 is too big. This led to poor uniform of magnetic field in the region near the microwave cavity. The experiment shows there existed Majorana frequency shift and the Majorana shift was one of main source of the uncertainty at that time. In 2005 we put three μ-metal covers in the fountain tube corresponding to the three bottom end-rings of the existed μ-metal magnetic shield system outside the fountain tube to improve the efficiency of magnetic shielding. We measure the magnetic filed with magnetic meter before we put the fountain tube on. The measurement result shows that the uniform of magnetic field was improved remarkably.

As we had improved our laser optical system, we could get enough falling cesium atoms when we launched the cesium atoms higher. We re-positioned the microwave cavities 9 cm higher than before to move the interaction area of atoms with microwave to the more smooth C-field region in the middle part of the fountain tube.

We evaluated the main frequency shifts of NIM4 clock in August, 2005. The result in table 1 shows the combined evaluation uncertainty reached 5E-15 [4]. The Majorana frequency shift, previous existed in NIM4 clock, is eliminated to a negligible extent, the corresponding uncertainty evaluation limited by the H2 day stability 2E-15.

Table 1, An error budget of NIM4 evaluation in August, 2005

	Physical Effect	Bias Value (E-15)	Uncertainty (E-15)
1	Second order Zeeman	81.8	1.35
	H(L)≠H(l)	0.5	0.5
2	Cold atom collision	-23.7	3.2
3	Microwave power	18.8	1.6
4	Blackbody	-16	0.5
5	Gravitation	3.8	0.1
6	Majorana	0.0	2.0
7	Light shift	0.0	0.1
8	Cavity pulling:	0.0	0.1
9	Cavity phase distribution	0.0	0.1
	Combined:	65.2	4.4

Limited by the transfer link available at NIM, we compare the NIM4 with GPS time by GPS common view using the H-maser H2 as medium frequency reference. In Figure 2 the triangle curve is H2-NIM4 and circle is H2-GPS, solid line are least square fits. During 135 days NIM4 provided 94 day data. The two breaks in Figure2 were caused by laboratory temperature control system failures. The two least square fits indicate a ~2E-14 difference which is within the combined uncertainty of NIM4, NIM's GPS common view transfer and GPS.

Figure 2, H2-NIM4 and H2–GPS comparison: horizontal axis represents the time (day) and vertical frequency difference.

III. THE CONSTRUCTION OF NIM5 CESIUM FOUNTAIN CLOCK

We now is building our second fountain clock, the NIM5 movable laser cooling cesium fountain frequency standard, based on the experiences and lessons of NIM4 clock and consulting the new developments of fountain clocks. The NIM5 clock is consisted by a laser-optical bench, a physical package and two electronics-control cabinets. Be differ from NIM4 clock three 111 direction laser beams are used for cooling and trapping atoms in NIM5 clock. The new designed detection region is placed above MOT. The collection efficiency of the fluorescence emitted by the cesium atoms crossing the laser beam in their flight is about 6%.

The interaction region is composed of two microwave cavities and a fountain tube, realized in OFHC copper. The two cavities are vertically aligned and spaced by 8.3 cm. The first one is used as the backup of state selection cavity if the state selection cavity outside magnetic shield is not good enough. The second cavity is Ramsey cavity used for the clock interaction. Different from the cavity of NIM4 clock, this cavity have two symmetry microwave input waveguides. The Q factor of microwave cavity is about 10000. The microwave leakage from microwave cavity was carefully detected. We found putting Aluminum film on the contact plane of cylinder and waveguide of microwave cavity was very useful to prevent microwave leakage.

Outside the fountain tube in the interaction region there is the heater for vacuum baking and temperature control , the C-field map coils, the C-field solenoid and four coaxial layers of magnetic shields. In order to achieve much better magnetic field uniformity in the

region of microwave cavity, we also carefully designed magnetic covers. The hole diameter of bottom magnetic covers is 3.7 cm. Besides the earth magnetic field compensating coils, we carefully design the current compensating coils near the magnetic covers. The magnetic field fluctuation is less than 2 nT in the area where the distance is greater than 12 cm from the inner magnetic cover.

The optical system is composed of four laser diodes: a master, a re-pump and two slaves. The master laser frequency is shifted about 124 MHz by double passing AOM, then is locked on 4-4' and 4-5' cross line of ^{133}Cs by digital square wave frequency modulation. The master laser has no frequency modulation and is amplified by two slave lasers of 150mW each. The slave lasers produce the up laser beam and down laser beam respectively. Each slave laser beam single passes AOM first, then is injected in PM fiber.

The new AOM drivers have been designed and manufactured. The time sequence control system have been improved greatly by using a single chip computer in control board. The new time sequence control system can generate more pulses in one time sequence cycle, so it can control or trigger more complicated events, such as switch on and off laser beam many times in one time sequence cycle. Our old time sequence control system used in NIM4 clock can generate only one pulse in every time sequence cycle. The digital servo control system is similar to the system of NIM4 clock. The microwave synthesizer interface board, AD/DA converter board and GPIB board inside a PC are in charge of the various control functions. The whole electronic hardware system has been constructed. The whole software are being renewed and improved.

Though the three main parts (laser optical part, physics part and electronic part) have been almost finished, the three parts have not yet experimented together. The new clock is expected to be finished in 2007.

REFERENCES

[1] A. Clairon, P.Laurent, G.Santarelli et al, IEEE Trans.IM44, 128 (1995)

[2] T. Li, M. Li, P. Lin and B. Huang, ACTA. Metrologica Sinica, V25, N3, 193 (2004)

[3] T. Li, M. Li, P. Lin and B. Huang et al, UFFC2004(Montreal), 431 (2004)

[4] M. Li, T. Li, P. Lin and P. Wang et al, Proc. of 2005 Time & Frequency Symp.(Xian), 6 (2005)

Proceedings of the 20th EFTF, 2006

Low velocity, high flux, continuous source of cesium atoms

N. Castagna,* J. Guéna, M.D. Plimmer, and P. Thomann
Observatoire Cantonal, rue de l'Observatoire 58, CH 2000 Neuchâtel, Switzerland

We present a 2D magneto-optical trap (MOT) that uses an innovative simple optical configuration. Instead of mirrors and quarter-wave plates we use metal-coated retro-reflecting prisms so as to recycle the optical power of the cooling laser beam. We have characterised this source for three different configurations: with and without transverse magnetic field gradient, as well as with a pusher beam to produce a $2D^+$-MOT. The longitudinal velocity is about 25 $m{\cdot}s^{-1}$, with a transverse velocity spread ≤ 1 $m{\cdot}s^{-1}$, while the typical atomic flux density can be as much as $1.3{\times}10^{14}$ $at{\cdot}s^{-1}{\cdot}m^{-2}$ for a cesium vapour pressure of $\sim 4{\times}10^{-8}$ mbar in the source. We use this low velocity atomic beam, instead of thermal vapour, to load a 3D moving optical molasses that launches a continuous cold cesium fountain. We achieve a gain of a factor ~ 20 in the fountain's atomic flux.

I. INTRODUCTION

Slow atomic beam sources are useful tools for many applications in atomic physics: atom interferometers [1–3], fundamental symmetry tests [4, 5], atomic clocks [6, 7], degenerate matter [8] and atomic and molecular spectroscopy [9]. The work described here is closely linked to the development of a primary time standard using a continuous atomic fountain [10]. Such fountains have the advantage of a lower atomic density for a given signal-to-noise ratio than their pulsed counterparts, which helps reduce density related frequency shifts [6]. In addition, by using them, one can eliminate the intermodulation (*a.k.a.* Dick) effect stemming from local oscillator noise [11]. To take full advantage of the continuous fountain approach however, we wish to have a higher useful flux than that produced by the first continuous fountain FOCS-1. One way is to launch more atoms from the moving optical molasses source, which can be achieved by loading it from a slow atomic beam rather than by capture from the low-velocity tail of a thermal vapour. Low-velocity sources of atoms can be generated by a number of different configurations [12–24]. Several of them ([12], [15], [19], [20], [21]) require a laser beam to be superimposed with the atomic beam. Zeeman slowing of a continuous atomic beam [14] needs high magnetic fields, while chirp slowing [18] generates only bunches of atoms. Here we present a far simpler solution, namely a 2D magneto-optical trap of cesium atoms producing a continuous low velocity beam ($v \simeq$ 25 $m{\cdot}s^{-1}$). While 2D-MOT's have already been used elsewhere [3, 19, 22–24], the devices in question are usually somewhat expensive, requiring many large anti-reflection (AR) coated polarising optics. Furthermore, the laser power is divided at each stage so several hundred milliwatts are often necessary. In our version, we employ gold-coated prisms in place of mirrors and quarter-wave plates, and the optical power is recycled. This leads to a considerable saving both in complexity and financial cost without loss of performance with regard to the useful flux extracted from the source.

In these proceedings, we present the set-up and design (Sec. II). Then (Sec. III) we describe the characterisation of the slow atomic beam (longitudinal and transverse velocity distribution, spatial profile) and the optimisation of various parameters (laser power and polarisation, magnetic field gradient ∇B, laser detuning). We compare the results obtained i) with a magnetic field gradient (2D-MOT), ii) with no gradient, *i.e.* the so-called 2D optical molasses (2D-OM), and iii) with a pusher laser beam along the atomic beam ($2D^+$-MOT). In Sec. IV we analyse the capture of the slow atomic beam in a 3D static optical molasses, and the subsequent upward flux in the vertical launch fountain configuration (moving molasses). We compare the results with thermal vapour loading of the 3D optical molasses. This study is important for our evaluation of the potential improvement in stability achievable for an atomic fountain clock [10] incorporating such a slow beam device, hereafter called a pre-source.

II. EXPERIMENTAL SET-UP

An overview of the set-up is given in Fig. 1. The 2D-MOT pre-source provides a slow atomic beam directed towards a 3D-moving optical molasses region where it is simultaneously captured, cooled and launched vertically in a continuous atomic fountain. The cell axis is tilted at 45 ° with respect to the vertical in the xz plane.

A. Pre-source

A scheme of the pre-source is represented in Fig. 2. The glass cell (internal dimensions 30 mm × 30 mm × 150 mm) is connected to a UHV chamber via a titanium adaptor flange of internal diameter 16 mm that expands to 40 mm towards the vacuum chamber. The former diameter constitutes the tighest constric-

*Electronic address: Natascia.Castagna@ne.ch

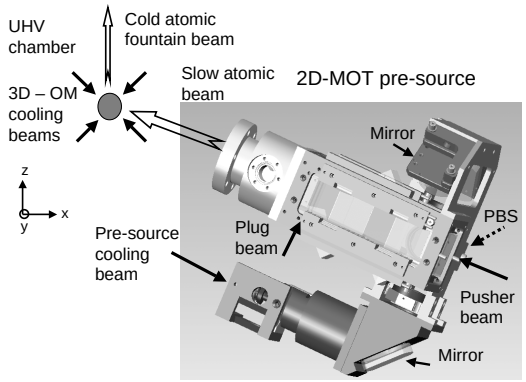

FIG. 1: Pre-source in an overview of the experimental set-up. The cooling beam is split into two parts by a polarising beam splitter (PBS). Each then propagates along the glass cell as described in Sec. II A.

tion between the pre-source and the 3D-OM region (Fig. 1), located in the centre of the UHV chamber some 500 mm away. Cesium vapour is injected directly into the cell. Using an adjustable bellows we can alter the tilt of the cell axis. The required ∇B is generated by four identical rectangular coils, fixed to a chassis that surrounds the cell. The magnetic field map has a quadrupole distribution in the transverse plane with a zero field line lying along the cell axis.

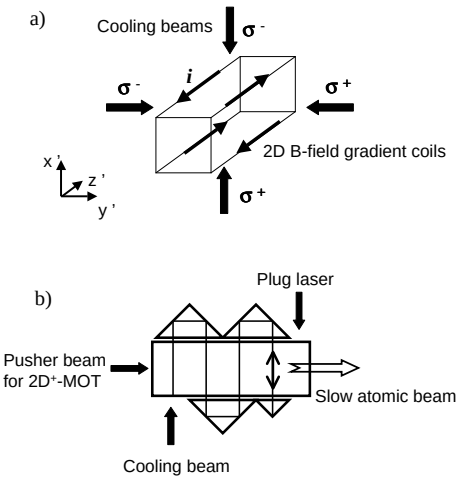

FIG. 2: Scheme of the pre-source: a) The four perpendicular cooling beams and the coils that generate the transverse magnetic field gradient. b) Beam geometry (for clarity only one of the two cooling directions is shown), see Sec. II A for details.

We use a cooling laser beam diameter of 30 mm to provide a large capture volume, and a total power up to 200 mW, divided by a polarising beam splitter cube (PBS) to supply the 2D cooling directions with equal power, as shown in Fig. 1. Two quarter-wave plates at the entrance of the glass cell provide the required circular polarisation. The light source is a home-made Extended Cavity Diode Laser (ECDL) centred on 852 nm (cesium D2 line) and injected into a Master Oscillator Power Amplifier (MOPA); its frequency is red detuned from the transition $6S_{1/2}, F = 4 \rightarrow 6P_{3/2}, F' = 5$ by typically 1.5Γ, where $\Gamma = 2\pi \times 5.22$ MHz [25] is the natural width. A repumper laser beam (ECDL, 1.5 mW), overlapped with the cooling beam and locked to the $6S_{1/2}, F = 3 \rightarrow 6P_{3/2}, F' = 4$ component, recovers the atoms pumped into $F = 3$. The two beams cover the volume of the cuvette by total internal reflection from a series of gold-coated right-angle optical prisms, see Fig. 2b, providing the required opposite circular polarisation for the successive passages. A film of index matching fluid (glycerine) between the cuvette and the prisms reduces reflection losses at the air-glass interfaces to a negligible level while an AR coating limits losses at the internal faces of the cuvette.

The optical set-up of the pre-source is completed by another couple of laser beams, both shown in Fig. 2: a plug and a pusher, both tuned to the $F = 4 \rightarrow F' = 5$ hyperfine component of the D2 line. The plug beam (power 3 mW) serves to measure the longitudinal velocity distribution by a time of flight technique (see Sec. III D). The pusher beam (power up to 2 mW, diameter 20 mm) is used to generate a $2D^+$-MOT configuration.

B. Optical molasses and detection

The collimated atomic beam produced by the pre-source reaches the centre of the UHV chamber 500 mm downstream where we perform diagnostics using another ECDL beam that crosses the atomic beam transversely along the y direction in Fig. 1. This probe laser, scanned over the $F = 4 \rightarrow F' = 5$ transition, has a power up to 2 mW and a beam waist radius of 2.8 mm. We select an output diameter of 5 mm using a diaphragm. A weak repumper laser beam (0.2 mW) stabilised on the $F = 3 \rightarrow F' = 4$ transition is overlapped with the probe laser so as to recycle atoms that leak into the $F = 3$ level. Two photodetectors, one opposite the probe laser and the second in the same plane but oriented along the x direction, allow us to detect simultaneously the transmission and fluorescence signals.

In this region we can switch on a 3D optical molasses (3D-OM) to capture the atomic beam. This arrangement is formed by six counterpropagating beams, red detuned by 12 MHz from the $F = 4 \rightarrow F' = 5$ transition and circularly polarised (each pair of counterpropagating beams has opposite $\sigma^+ - \sigma^-$ polarisation). The horizontal retro-reflected beam (x-axis) is overlapped with a weak repumper beam (power 0.1 mW). We can modify the central frequency of the upward and downward pairs of beams independently using different Acoustic-Optical Modulators (AOMs)

to make either a static or a continuous moving optical molasses [13]. The beams originate from a common laser (henceforth the 3D-molasses laser), an ECDL offset-locked by 160 MHz above the $F = 4 \rightarrow F' = 4$ transition and amplified by injection into a MOPA. The output of the MOPA passes through an AOM centered on 80 MHz to produce the desired cooling frequency. The power per beam is 7 mW and the waist radius 13 mm.

III. MAIN CHARACTERISTICS OF THE ATOMIC BEAM AND INFLUENCE OF PARAMETERS

A. Impact of cooling laser beam parameters

We have investigated the impact of various parameters on the detected atomic flux density. To do this we monitored the fluorescence emitted from the atomic beam following its excitation by a transverse probe laser, 500 mm downstream. For calibration, see Sec. III F.

Fig. 3 shows the effect of cooling laser power. For the maximum value available ($\sim$ 200 mW), the signal still increases though less steeply. This implies greater flux yields if we had more laser power at our disposal.

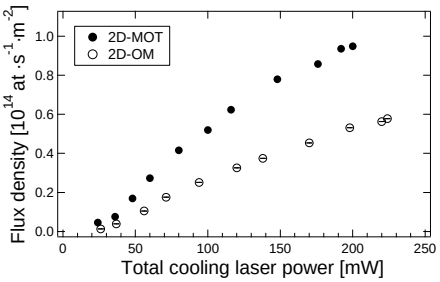

FIG. 3: Atomic flux density versus total cooling laser power measured 500 mm from the exit of the pre-source. The data points were obtained observing the fluorescence induced by the probe laser beam transverse to the atomic beam with a weak repumper overlapped. Cooling beam detuning from the $F = 4 \rightarrow F' = 5$ transition -8 MHz for both 2D-MOT and 2D-OM configurations. ∇B=2.6 G/cm for the MOT.

As for cooling laser detuning from $F = 4 \rightarrow F' = 5$, we find an optimum value around -1.5Γ for the 2D-MOT and somewhat higher for the 2D-OM (-2Γ). In the latter configuration we saw no dependence upon laser polarisation, consistent with the fact that Doppler cooling dominates over sub-Doppler cooling mechanisms.

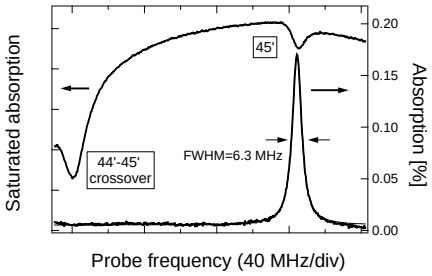

FIG. 4: Absorption spectrum of a probe laser beam transverse to the atomic beam 500 mm downstream. Probe saturation parameter of 0.2. The width of the resonance helps characterise the transverse velocity spread. Upper trace: saturated absorption signal providing frequency calibration.

B. Transverse velocity

To infer the transverse velocity spread of the collimated atomic beam, we observed the transmission of a weak probe laser beam oriented perpendicularly to the atomic beam. The $F = 4 \rightarrow F' = 5$ resonance curve observed has a FWHM of at most 6.3 MHz (see Fig. 4). Some of this broadening is attributable to slight irreproducibility of the frequency scan ramp. By fitting this curve with a Voigt profile (convolution between a gaussian velocity distribution and a lorentzian distribution with the 5.2 MHz natural width), we obtain a conservative upper limit of the full velocity spread of about 1 m$\cdot$s^{-1}. For a longitudinal velocity of 25 m$\cdot$s^{-1} (see Sec. III D) this corresponds to a full beam divergence $\leq$ 40 mrad. No significant difference was observed between the three pre-source configurations tested.

C. Atomic beam profile

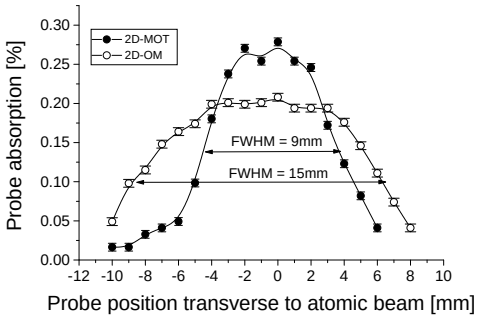

FIG. 5: Atomic beam profiles measured by probe absorption at a distance of 500 mm from the exit of the pre-source. Filled circles: standard 2D-MOT configuration; open circles: configuration with no magnetic field gradient (2D-OM); the solid lines are guidelines. Probe beam tuned to the $F = 4 \rightarrow F' = 5$ transition, diameter reduced to 2 mm.

To measure the transverse beam density profile, we translated the whole detection system (probe laser and transmission photodetector) perpendicularly to the axis of the atomic beam, with the probe transverse to the atomic beam. The width (FWHM) of the spatial distribution is found to be 9 mm for ∇B $\simeq$1.3 G/cm (value optimising the atomic flux) and 15 mm for ∇B= 0 (Fig. 5). For a point source these would correspond to maximum full beam divergences of 18 and 30 mrad respectively, compatible with the limit deduced from Doppler spectroscopy (see Sec. III B). The narrower profile obtained in the MOT configuration was expected since the Doppler cooling process operates in a tighter spatial confinement than in the OM. We conclude that the source is highly directional, a useful feature for efficient loading of a 3D-optical molasses.

D. Longitudinal velocity

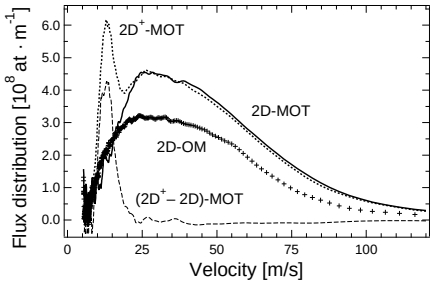

FIG. 6: Flux distribution as a function of the longitudinal velocity v for the three configurations of the pre-source extracted from TOF measurement. Crosses: 2D-OM, solid line: 2D-MOT, dots: $2D^+$-MOT and dashed line: difference between the $2D^+$- and 2D-MOT's. Cooling laser detuning -10 MHz, ∇B $\simeq$ 1.3 G/cm for the MOT's.

For TOF measurements, we use a plug laser modulated at 7 Hz by a mechanical chopper wheel and record the fluorescence induced by the cw transverse probe beam tuned to the $F = 4 \rightarrow F' = 5$ transition with the repumper overlapped, at a distance L=500 mm downstream. The fluorescence signal is proportional to the instantaneous atomic density *n(L,t)* from which the longitudinal velocity distribution of atomic flux density

$$\varphi(v)\ dv = v \cdot\ n(L,t)\ dt \qquad (1)$$

can be reconstructed using $v = L/t$. $\Phi = \int \varphi(v) dv$ is the total flux density. Fig. 6 shows the results for the different pre-source configurations. No marked difference is observed between the 2D-OM and 2D-MOT: peak velocity around 25 m·s^{-1} and full velocity spread about 50 m·s^{-1}, slightly larger for the OM case and the total flux $\simeq$ 30% smaller. However, for the $2D^+$-MOT configuration, on top of the distribution found in the 2D-MOT case, a narrow peak (FWHM 5 m·s^{-1}) appears centred at the low velocity of 13 m·s^{-1}. This structure increases the total flux, though by no more than 30%. Incidentally, we find the same gain in total flux for a configuration $2D^+$-OM with respect to the simple 2D-OM.
We have well confirmed these results by Doppler shifted absorption spectroscopy, using a probe beam aligned at $\pm 45\,^\circ$ to the atomic beam.

E. Magnetic field gradient

The optimal magnetic field gradient in our device lies in the range 1.0−1.5 G/cm, *i.e.* more than an order of magnitude lower than that used in [3, 23]. A low magnetic field gradient is desirable for many applications where stray fields are harmful (including our particular field of atomic clocks). What is more, the present source works almost as well with no gradient at all, which is even better from this point of view. This behaviour we attribute to the large diameter of the exit hole (16 mm) which allows cold atoms to contribute to the slow beam be they close to the axis or not.

F. Flux calibration

We have calibrated the atomic flux using probe absorption without repumper rather than fluorescence signals to be independent of light collection efficiency. We exploit the two $F = 4 \rightarrow F' = 4$ and $F = 4 \rightarrow F' = 5$ atomic resonances. Strictly we detect only atoms present in the $F = 4$ ground hyperfine level. On the former *open* (pumping) transition, absorption is limited by the hyperfine pumping time with an *absolute* value independent of probe beam intensity and size. The power subtracted from the beam yields directly the atomic flux. This method is the most reliable but gives small signals. For this reason, we also use the $F = 4 \rightarrow F' = 5$ transition as a transfer standard since it provides better S/N. On this *closed* (cycling) transition, the absorption is limited by the transit time and the *relative* absorption gives access to the atomic density. We have also exploited it to cross-check the $44'$ calibration. Many signals presented in this work were derived from fluorescence detection and calibrated by simultaneous recording of absorption signals.

IV. CAPTURING THE ATOMIC BEAM IN THE STATIC 3D OPTICAL MOLASSES AND LAUNCH CONFIGURATION

Our purpose for building the pre-source described above is to improve the useful atomic flux in a continuous cesium fountain clock [10]. This clock is cur-

rently fed by loading a 3D-OM from a thermal cesium vapour. Here we present the gain obtainable by loading a 3D-OM by the slow atomic beam provided by the pre-source. Fig. 7 shows the experimental arrangement.

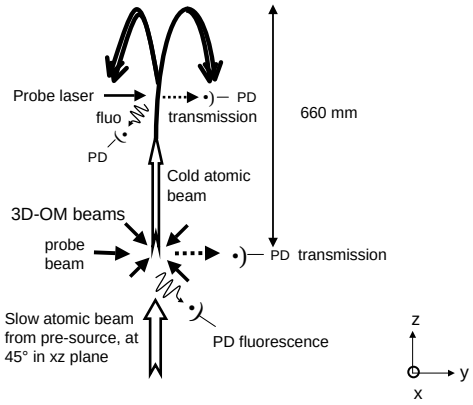

FIG. 7: Schematic of the launch configuration for the fountain. The 3D optical molasses is formed by six counter-propagating laser beams (the horizontal retro-reflected beam along x is not shown) with opposite circular polarisation capture the cesium atoms travelling through the intersection region. Measurements presented in Sec. IV A are obtained with a static 3D-OM, while for those in Sec. IV B the optical molasses is in a moving configuration. Two photodetectors (PD) allow simultaneous monitoring of the fluorescence and transmission signals induced by the probe beam.

A. Results in the static 3D optical molasses configuration

Diagnostics were performed using probe absorption. The 3D-molasses beams were turned on detuned by -12 MHz from $F = 4 \rightarrow F' = 5$, value found to optimise capture efficiency. The parameters of the pre-source were also adjusted to optimise the absorption signal (cooling laser detuning $\delta \simeq$-11 MHz and $\nabla B \simeq 0.8$ G/cm, slightly different than without capture). When we changed from the 2D- to the 2D$^+$-MOT configuration, most remarkably, the absorption signal was increased by a factor of $\simeq 1.8$ while without capture the gain was only 30% (see Fig. 6). A similar behaviour was observed for a 2D- versus 2D$^+$-OM comparison. These effects we ascribe to increased 3D-OM capture efficiency for slow atoms (peak around 13 m/s in Fig. 6).

To compare the 3D-OM loading by a thermal cesium vapour or by the slow atomic beam, we use a second reservoir and isolate the pre-source from the UHV chamber. Typical results are shown in Fig. 8. For loading from a vapour $\sim 10^{-8}$ mbar we observed a Doppler broadened absorption of the order of 10−15% along 250 mm of vapour column (internal diameter of the chamber) with small sub-Doppler peaks centered

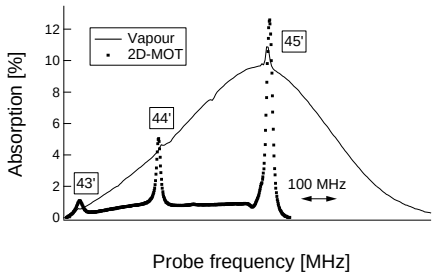

FIG. 8: Absorption spectra of the probe laser scanned across the D2 line in the 3D-optical molasses region. Loading by cesium vapour (solid line) or from the 2D-MOT slow atomic beam (dotted line). Probe laser beam (diameter 5 mm and total power 0.15 mW) overlapped by a weak repumper beam for vapour loading.

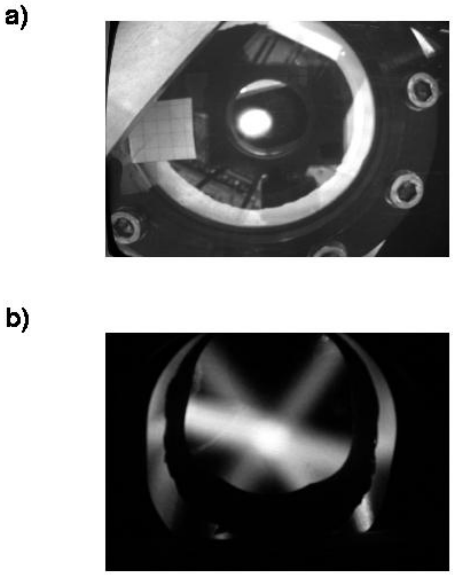

FIG. 9: Pictures showing the fluorescent light emitted in the 3D static optical molasses. a) Loading by the slow atomic beam: bright central spot of ∼15 mm diameter. Note the absence of fluorescence from the six molasses beams. b) Loading by a Cs vapour: the fluorescence induced by thermal vapour along the 3D-molasses laser beam axes, absent in a), is conspicuous.

on the $F = 4 \rightarrow F' = 4$ and $F = 4 \rightarrow F' = 5$ atomic resonances due to slow atoms captured in the 3D-OM. These have to be compared with the peaks associated with slow beam loading: the capture efficiency is ~ 8 times higher in the latter case. The striking difference between the two loading techniques is highlighted by the images recorded by a CCD camera (Fig. 9): fluorescent light along the 3D-molasses laser beam axes in Fig. 9b, indicating diffuse vapour is absent in Fig. 9a. This confirms the confinement of the atoms in the region of interest and *quasi*-absence (4×10^{-10} mbar) of thermal background atoms for slow beam loading the 3D-OM despite the large pre-source exit hole and the absence of getters.

TABLE I: Summary of methods for loading a continuous cold atom fountain. Atomic flux density Φ and transverse diameter ø of fountain beam at a distance of 470 mm above the 3D-OM source, with a vertical launch velocity of 3.6 m·s^{-1}. Comparison for pre-source (2D- and 2D$^+$-MOT) at Cs vapour pressure 1.2×10^{-7} mbar and for vapour loading at 0.8×10^{-8} mbar.

	Vapour	2D-MOT	2D$^+$-MOT
Φ (10^{13} at·s^{-1}·m^{-2})	0.4	4.5	8.5
ø (mm)	16.4 (0.3)	15.0 (0.1)	-

B. Launch configuration and impact of pre-source vapour pressure

The slow atoms captured by the 3D-OM were launched vertically using a *moving* optical molasses (upward and downward beams detuned to provide a launch velocity of 3.6 m·s^{-1}). The fountain beam was detected 470 mm above the 3D-OM using both fluorescence and absorption induced by the probe laser beam for different loading techniques of the source.

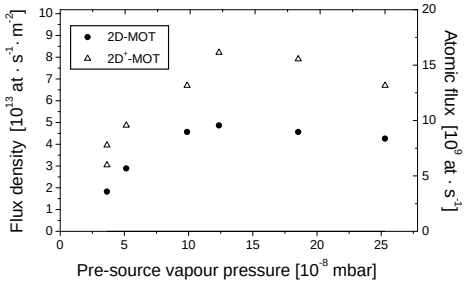

FIG. 10: Atomic flux launched vertically from a 3D moving molasses as a function of the cesium vapour pressure inside the pre-source used to load it, for both the 2D-MOT and the $2D^+$-MOT configurations. Detection by induced fluorescence with probe beam tuned to the $F = 4 \rightarrow F' = 5$ transition.

Fig. 10 shows the fountain atomic flux as a function of the cesium pressure inside the pre-source. We find a maximum value $\Phi = 8.5\times10^{13}$ at · s^{-1}· m^{-2} for the rather high value of 1.2×10^{-7} mbar (absorption of 17% in the pre-source for a 3 cm transverse path). For even higher pressure, the detected flux falls due to the greater collision rate and increased imbalance of the cooling laser beams due to higher absorption in the pre-source.

Finally, Fig. 11 shows the main result of this work, namely that *2D-MOT-slow-beam loading gives 10 times more flux than vapour capture; the 2D$^+$-MOT almost doubles this.* The transverse cold beam profiles also recorded for the 2D-MOT- and vapour-loading of the 3D-OM were quite similar. Tab. I summarises these results.

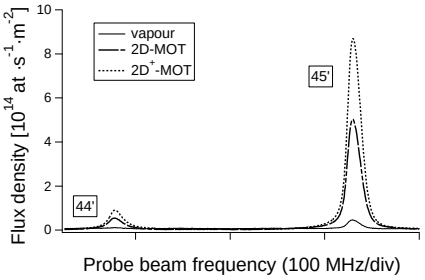

FIG. 11: Fluorescence spectrum calibrated in flux density detected 470 mm above the 3D-OM source in a launch configuration upwards. Comparison between the two different techniques to load the source: from cesium vapour (full line) or from the slow atomic beam produced by the pre-source in either the 2D-MOT (dashed line) or the 2D$^+$-MOT (dotted line) configuration. Vapour pressure $\simeq 1.2\times10^{-7}$ mbar in the pre-source and $\simeq 10^{-8}$ mbar in the UHV chamber.

V. CONCLUSIONS

We have developed and characterised a two-dimensional source of slow Cs atoms for the loading of a continuous atomic beam fountain. A comparison of the characteristics for the 2D-MOT, 2D-OM and 2D$^+$-MOT configurations is summarised in Tab. II. The innovative set-up with *i*) low cost optics, *ii*) absence of differential pumping and *iii*) an exit hole with no diaphragm, is shown not to limit the performance of our device. The slow atomic beam provided by the pre-source has been captured in a UHV chamber by a 3D-OM 500 mm downstream and then launched in a vertical flight. Loading the molasses using the 2D-MOT provides a gain in the detected flux by a factor of $\simeq 10$ compared with thermal cesium vapour capture, the method used heretofore to feed our atomic clock fountain. An added advantage is the *quasi*-absence of thermal background atoms. The introduction of a pusher beam in the pre-source (2D$^+$-MOT) increases the fountain flux by a further factor of $\simeq 1.8$, as a result of a more favorable longitudinal velocity distribution. This suggests we might boost the fountain flux even more by shortening the length of the pre-source cell, as demonstrated in [23]. At the optimum vapour pressure in the pre-source of 1.2×10^{-7} mbar and for a 2D$^+$-MOT configuration we achieved a highest flux density of 8.5×10^{13} at · s^{-1}· m^{-2}. Our results imply a potential gain of $\sqrt{20}$ in stability of an *atomic shot noise limited* fountain clock, though the signal-to-noise remains to be investigated. A more detailed account of this work will be published elsewhere [26].

Acknowledgments

This work was financed by the Swiss Federal Office of Metrology and Accreditation (METAS) and

TABLE II: Comparison of the characteristics of the slow atomic beam for the 2D-MOT, 2D-OM and 2D$^+$-MOT configurations. Φ is the maximum atomic flux density, v_L the peak longitudinal velocity and Δv_T the transverse velocity spread. The total flux is calculated using the transverse beam size measured at 500 mm from the exit (see fig. 5) and assuming it to be the same for the 2D- and the 2D$^+$-MOT configurations. Note that Cs vapour pressure in the pre-source is $\sim 4\times10^{-8}$ mbar, namely one third of the optimum value for fountain flux measurements, see Tab. I and Fig. 10.

	2D-MOT	2D-OM	2D$^+$-MOT
Φ (10^{14} at·s^{-1}·m^{-2})	1.0	0.7	1.3
v_L (m·s^{-1})	27	25	20*
Δv_T (m·s^{-1})	≤ 1	≤ 1	≤ 1
Total flux (10^{10} at·s^{-1})	1	1	1.3

* This value is found by averaging the two peaks that characterise the longitudinal velocity distribution for the 2D$^+$-MOT configuration (Fig. 6).

the Swiss National Science Foundation. The authors are grateful for helpful discussions with F. Fuso and Y.B. Ovchinnikov. The Observatoire Cantonal thanks the CNRS for making possible the stay of J.G. in Neuchâtel.

[1] P.R. Berman, *Atom Interferometry* (Academic Press, San Diego, 1997).
[2] J. Stuhler, M. Fattori, T. Petelski and G.M. Tino, J. Opt. B: Quantum Semiclass. Opt. **5**, S75-S81 (2003).
[3] S. Chelkowski, Diplomarbeit, Institut of Quantum Physics, University of Hannover (2002). Unpublished.
[4] S. Sanguinetti, J. Guéna, M. Lintz, Ph. Jacquier, A. Wasan and M.-A. Bouchiat, Eur. Phys. J. D **25**, 3-13 (2003).
[5] V. Natarajan, Eur. Phys. J. D **32**, 33-38 (2005).
[6] R. Wynands and S. Weyers, Metrologia **42**, S64-S79 (2005).
[7] J. Vanier, Appl. Phys. B **81**, 421-442 (2005).
[8] H.J. Metcalf and P. van der Straten, *Laser Cooling and Trapping* (Springer-Verlag, New York, 1999).
[9] A. Grabowski, R. Heidemann, R. Löw, J. Stuhler and T. Pfau, arXiv:quant-ph/0508082 v1 (2005).
[10] G. Dudle, A. Joyet, N. Castagna, G. Mileti, P. Thomann, C. Mandache and T. Acsente, in *Proceedings of the 16th EFTF, St. Petersburg, 12-14 March 2002* (St. Petersburg State University of Aerospace Instrumentation, Russia), E-014-E-016 (2002).
[11] A. Joyet, G. Mileti, P. Thomann and G. Dudle, IEEE Trans. Instr. Meas. **50**, 150-156 (2001).
[12] A. Composeo, A. Piombini, F. Cervelli, F. Tantussi, F. Fuso and E. Arimondo, Opt. Commun. **200**, 231-239 (2001).
[13] P. Berthoud, E. Fretel and P. Thomann, Phys. Rev. A **60**, R4241-R4244 (1999).
[14] M.A. Joffe, W. Ketterle, A. Martin and D.E. Pritchard, J. Opt. Soc. Am. B **10**, 2257-2262 (1993).
[15] J.M. Kohel, J. Ramirez-Serrano, R.J. Thompson, L. Maleki, J.L. Bliss and K.G. Libbrecht, J. Opt. Soc. Am. B **20**, 1161-1168 (2003).
[16] L. Cacciapuoti, A. Castrillo, M. de Angelis and G.M. Tino, Eur. Phys. J. D **15**, 245-249 (2001).
[17] H. Wang and W.F. Buell, J. Opt. Soc. Am. B **20**, 2025-2030 (2003).
[18] R.N. Watts and C.E. Wieman, Opt. Lett. **11**, 291-293 (1986).
[19] Y.B. Ovchinnikov, Opt. Commun. **249**, 473-481 (2005).
[20] Z.T. Lu, K.L. Corvin, M.J. Renn, M.H. Anderson, E.A. Cornell and C.E. Wieman, Phys. Rev Lett. **77**, 3331-3334 (1996).
[21] H. Chen and E. Riis, Appl. Phys. B **70**, 665-670 (2000).
[22] P. Cren, C.F. Roos, A. Aclan, J. Dalibard and D. Guéry-Odelin, Eur. Phys. J. D **20**, 107-116 (2002).
[23] J. Schoser, A. Batär, R. Löw, V. Schweikhard, A. Grabowski, Y.B. Ovchinnikov and T. Pfau, Phys. Rev. A **66**, 023410-1 - 023410-10 (2002).
[24] K. Dieckmann, R.J.C. Spreeuw, M. Weidemüller and J.T.M. Walraven, Phys. Rev. A **58**, 3891-3895 (1998).
[25] D.A. Steck, Los Alamos National Laboratory. Cesium D line data, http://steck.us/alkalidata.
[26] N. Castagna, J. Guéna, M.D. Plimmer and P. Thomann, Eur. Phys. J. AP, to appear.

Proceedings of the 20th EFTF, 2006

Microwave Interrogation System for VNIIFTRI Cesium Fountain

A. BOYKO, L. KOPYLOV, A. NOVOSELOV.
Institute for Metrology of Time and Space (IMVP FGUP "VNIIFTRI"),
Moscow Region, Mendeleevo, 141570 RUSSIA.
boyko@aspnet.ru

The input signal of the system is 5 MHz with a high long-term stability. 5 MHz quartz crystal oscillator of improved short-term stability (~$2\cdot10^{-13}$/1sec) is phase-locked to the input signal and controls, in turn, 1530 MHz oscillator. The 6-th harmonics of 1530 MHz signal forms 9.180 GHz interrogation signal. As essential point of developed system is that the H-maser of increased output power (~$1\cdot10^{-12}$ W) is used for further lowering of interrogation signal phase noise.

1. Introduction.

It is known, that the strict requirements are made for spectrum of probing microwave signal of cesium fountain standard. To solve this problem a special H-maser with increased power of the output signal was developed at VNIIFTRI. Double separation, selection of optimum spectral line Q-factor due to escape of atoms from a bulb, optimum connection of resonator with a load, and also a low-noise output signal amplifier were used to obtain the signal-to-noise ratio equal to 90 дБ in 1 Hz bandwidth. It must provide a potential possibility to reduce a random error in a signal frequency measurement of probing signal to $1\cdot10^{-13}$.

2. Principle of System Construction

The general principle for construction of probing signal system is the same as the principle for comparison system based on a classical cesium frequency standard, which has been used at VNIIFTRI from 1975 till now. After preliminary spectrum cleaning with the help of quartz phase-lock-loop oscillator (with a large time constant) the reference frequency of 5 MHz of a continuously operating H-maser with high long-time frequency stability included into H – maser clock ensemble for time-keeping is multiplied till 9180 MHz. The synthesizer frequency 12,631770 MHz is added to 9180 MHz. The synthesizer frequency measurement tuned to the spectrum line peak makes it possible to determine the real value of hydrogen clock frequency.

In our case besides of the spectrum cleaning at the frequency of 5 MHz an additional spectrum cleaning at a frequency of 1530 MHz is carried out. The synthesizer frequency is formed by auxiliary oscillator at a frequency of 100 MHz. Measuring the frequency of 100 MHz by a standard comparator makes it possible to determine a frequency of the H – maser included into time-keeping clock ensemble.

3. Frequency Multiplier from 5 MHz to 1530 MHz

The block-diagram of a multiplier is shown in Fig. 1.

As a quartz generator the quartz generator with a short-time stability of about 2×10^{-13} 1/s is used. The time constant of phase-lock-loop is about 100 s. The phase instability of the first four multipliers including a 20 MHz quartz filter does not increase the output signal phase instability because the phase auto-tuning of the quartz oscillator at the reference frequency is made by means of 80 MHz divided by 16.

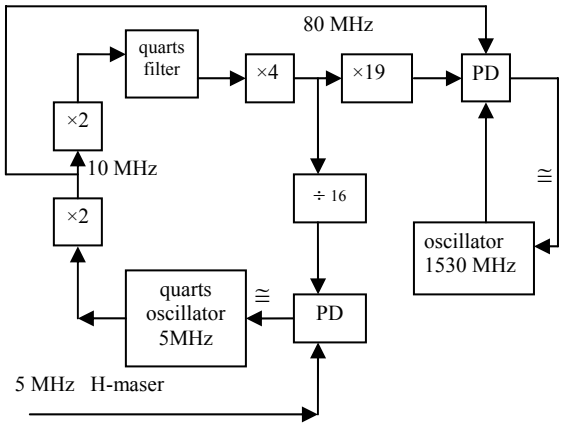

Fig.1

The multiplier to the frequency of 80 MHz and the phase-lock-loop quartz oscillator are located in a separate steel box with an additional acoustic lead

shield. The power of output signal 80 MHz at the load of 50 Ω is 13…15dBm.

A generator for frequency 1530 MH was designed and performed on the basis of a bulky cavity (wave TE_{011}) which is similar to that one used in hydrogen generator "Sphera". The resonator is made of fused quartz. Single-level temperature-controlling and vacuuming are used. There is a feedback system (amplifier M42115-1 and phase changer) inside the vacuum tank. The generator frequency can be changed by means of varicap within the limits of □5 кHz.

4. Filtration of Phase Noises with Hydrogen Maser

The block diagram of filtration is shown in Figure 2.

The hydrogen generator with a large time constant (1000 s) is tuned in accordance with the phase of multiplied signal in such a way that phase difference between a signal of 1530 MHz and H-maser is equal to 0. A variable component (in a frequency bandwidth from 0,01 Hz to 250Hz) is given to a phase changer of a signal of 1530 MHz. Thus, a signal phase of 1530 MHz in the mentioned frequency band repeats the H-maser signal phase. And slow drifts of H-maser frequency with the respect to reference signal frequency are traced by slow tuning of H-maser frequency.

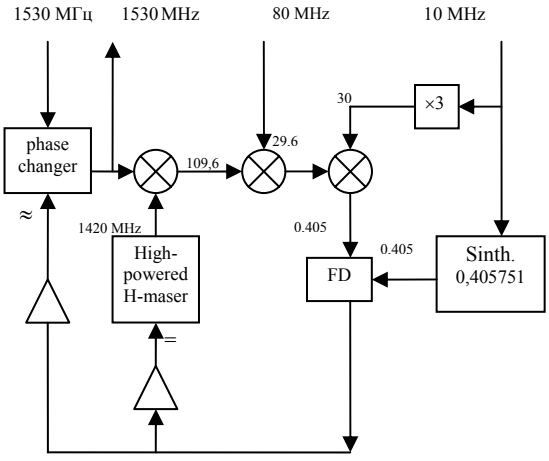

Fig.2

5. Frequency Multiplier up to 9,180MHz and Frequency Synthesizer

The block-diagram of final frequency multiplier is shown in Figure 3.

A signal with a frequency of 1530 MHz is amplified by the microwave amplifier ZR4-24004N and multiplied at a microwave diode up to the frequency of 9180 MHz (Fig.4). The synthesizer frequency of 12,6 MHz is added at the same diode. The output signal power of 9192,631 MHz is about 10^{-7} W.

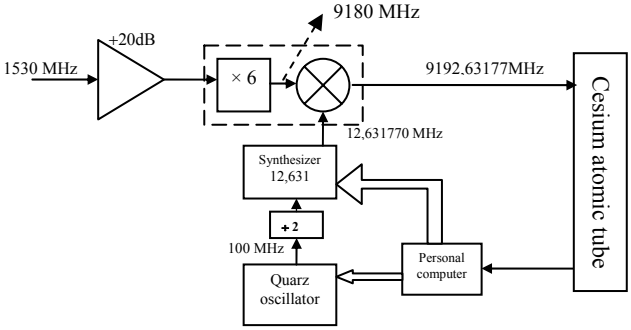

Fig.3

The synthesizer 12,63 MHz is performed on the basis of the chip AD7008 of the firm Analog Devices. This chip fulfils the direct digital signal synthesis of the defined frequency. The synthesis is made by 10-bit DAC with a refresh rate of 50 MHz. The chip gives possibility to specify the signal frequency with a step of about 12 mHz and the signal phase with a step of 1.5×10^{-3} rad.

The output chip signal is delivered to a low frequency filter which is a LC-filter consisting of two mid-shunt sections, then it is intensified by an amplifier with a programmable gain factor - chip AD8320 of Analog Devices. The chip makes it possible to specify a gain factor with a step of 0.5% of the maximum value.

The signal of 50 MHz is taken from a quartz oscillator of 100 MHz, which should be tuned to Cs spectral line.

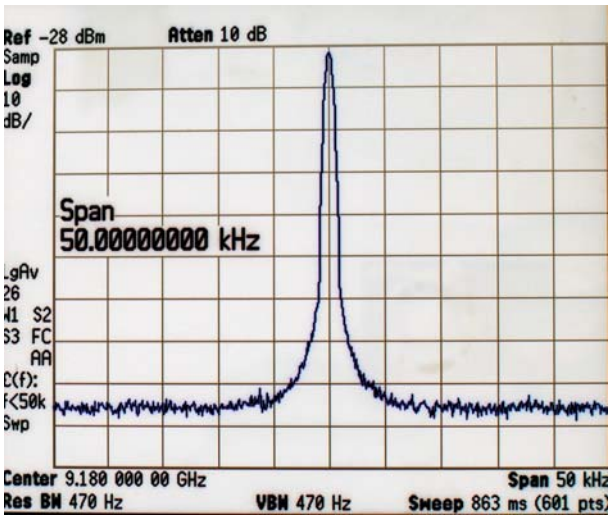

Fig.4. Spectrum of 9180 MHz (Span 50kHz, VBW 470Hz).

6. Conclusion

Thus, the interrogation system makes it possible to perform the tuning to the spectral line peak by means of a phase modulation of ± π/2 along with a direct measuring of H - maser reference frequency, to select the optimum power of a microwave signal and to measure a magnetic field in the drift region.

To suppress the phase noises of measured H-maser reference frequency three levels of spectrum cleaning are used: quartz oscillator with a high short-term stability, quartz filter at 20 MHz and special H-maser with high power of the output signal.

The operation ability of the interrogation system was tested on a Cesium fountain model. At present the activity on measuring a phase noise at the output frequency and on selecting the optimal time constants of phase auto-tuning system for quartz oscillator, H-maser, reference generator and phase changer is under the process.

Acknowledgements

The authors are grateful to Dr Yu. Domnin and Dr G. Yolkin for formulation of the problem and for discussion on the ways of its solution.

References

[1] Yu. Domnin, G. Yolkin, A. Novosyolov, V. Barychev, L. Kopylov, Yu. Malychev and V. Pal'chikov, 2002 VNIIFTRI ceium fountain *Can.J. Phys.* **80**, 1321-7

[2] A.Boyko, G.Yolkin, N.Gestkova, G.Kurnikov, V.Paramsin, Hydrogen Maser with Improved Short-term Frequency Stability// *Proc. 15-th EFTF '01 p.406. Neuchatel March 2001*

Proceedings of the 20th EFTF, 2006

Polarization-dependent optical pumping for the laser selection of Zeeman-states in cesium fountain

Yu. S. Domnin,* G. A. Elkin, A.V. Novoselov, L. N. Kopylov,
V. N. Baryshev, Yu. M. Malychev, and V. G. Pal'chikov
Institute of Metrology for Time and Space at National Research Institute for Physical–Technical and Radiotechnical Measurements, Mendeleevo, Moscow Region, 141579 Russia

This paper presents an experimental and theoretical analysis of a possible scheme to realize of optical pumping in the ground state ($F = 3$) of the cold ^{133}Cs atoms in atomic fountain. The efficiency of the population for the state sub-level $F = 3, M_F = 0$ build up is calculated for two limiting cases of the optical pumping : $F = 3 = F' = 2$ and $F = 3 = F' = 3$. This analysis takes into account the hyperfine structures of the energy levels for the ground $6^2S_{1/2}(F = 3)$ and excited states $6^2P_{3/2}(F' = 2)$, $6^2P_{3/2}(F' = 3)$ of cesium atoms.

I. INTRODUCTION

Recent progress in laser cooling, including temperatures as low a few microkelvin, and the demonstration of the ability to launch atom while maintaining these low temperatures, now allows the observation the Ramsey fringes for the "clock" transitions and to make the preliminary accuracy evaluation of a cesium fountain VNIIFTRI[1].

The main scope of this work is to discuss various aspects of an optical pumping for the laser selection of Zeeman-states in cesium in both theoretical and experimental nature. In particular, we consider the application of the optical pumping for increasing a number of Cs atoms in the ground state ($F = 3, M_F = 0$) before interaction with TE_{011} cavity of our cesium fountain (Fig.1).

Thus, the criteria for the most efficient pumping schemes are as follows:

- maximum population for the Zeeman state sub-level ($F = 3, M_F = 0$) , depending of the type of polarization and the orientation of the magnetic field as a quantization axis,
- optimal combination for the two pumping schemes: $F = 3 = F' = 2$ and $F = 3 = F' = 3$,
- independence on the initial population distribution for the Zeeman sub-levels of the Cs atom in the ground state $F = 3$.

II. EXPERIMENTAL SET UP

Figure 1 shows the scheme of the atomic cesium fountain developed at the VNIIFTRI. This apparatus has been desribed in detail in references[2, 3].

The vacuum part of the construction consists of five sections coupled with each other by flange sleeves with copper vacuum seals. The lower section, including two magnetic-ion pumps with a total pumping rate of $4L/s$, a mass spectrometer, a getter pump, and a vacuum valve, is made of a stainless steel. The other four sections (the detection region, the optical molasses region, the cavity region, and the free-flight or drift region) are made of titanium. The first results were obtained for the case when the detection region was located under the optical molasses region. The vacuum part of the device has eleven fused silica windows for injecting cooling and detecting laser beams as well as probe microwave radiation. The windows are soldered with lead to the inner surface of titanium cylinder rings, which in turn are welded to titanium vacuum flanges. The set up was annealed at 250°C

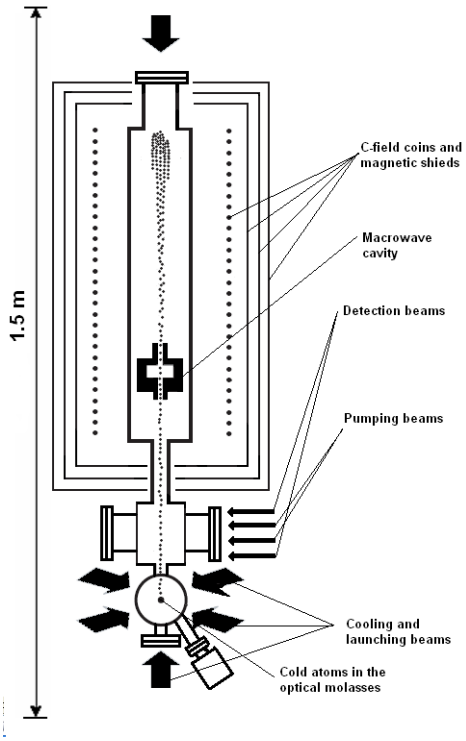

FIG. 1: Scheme of the atomic cesium fountain.

*Electronic address: y.domnin@imvp.ru

for 200H during vacuum pumping. The residual pressure 5×10^{-7} Pa was mainly determined by the partial pressure of molecular hydrogen.

A copper cylindrical microwave cavity is tuned to the TE_{011} mode. Coupling with an external signal is performed with the help of a symmetric waveguide joint through two diametrically opposite slits in the cavity walls. The Q-factor of the unloaded cavity is 20000, while that of the loaded cavity (for the chosen coupling strength) is 3000. to separate the states of atoms with different projections of the momentum of the quantization axis, we use the C-field representing a homogeneous magnetic field with the strength at which resonances at the transitions $\triangle F=\pm1, \triangle m=0 (F=3,4$ is the total momentum of a cesium atom in the ground state) are separated by a few kilohertz. This C-field was produced with the help of two bias windings, one of which formed a homogeneous axial magnetic field in the upper drift region of the set up, while another produced a magnetic field in the regions of the optical trap and optical detection. The detailed description for the other components of our fountain (laser system for cooling and detecting cesium atoms, a system for the frequency stabilization of the reference and pumping lasers, synthesis of the interrogation microwave signal, etc) are presented in[2, 3]. In contrast with previous versions of cesium fountain (see, for example, [4]) in our measurements we have used $F=3, M_F=0)$ ground state before entering to the microwave cavity[2, 3].

Figure 1 shows also the scheme of an optically pumped Zeeman sub-levels of the ground state $F=3$; the population inversion is achived by two pumping laser beams and the resonance phenomenon (Rabi or Ramsey fringes) is detected through fluorescence light induced by the detection lasers. A weak C-field removes the Zeeman degeneracy. In this work, we limit our attention to the evaluation of the population unbalance created in the optical pumping region. We will not consider here the Zeeman structures of the energy levels as a function of magnetic field.

The characteristics of the pumping laser beam are: intensity of 15 $\mu W/cm^2$ and spectral width of 0.5 MHz.

III. THEORY AND RESULTS OF OBSERVATIONS

From a general physical point of view a dynamics of an atom in a pumping laser field can be attributed to one or more basic types according to the ration between the contributions of the induced and spontaneous transitions[5, 6]. We take a semi-classical model in which the pumping laser field is written classically and the atomic system is treated through quantum-mechanics. In that case the density matrix formalism considers not only the populations, but also the coherence effects when an interaction couples two or more atomic levels[5].

In the case of the cold and slow atoms in fountain geometry (Fig.1), at large interaction time compared with the spontaneous decay times, spontaneous transitions and relaxation processes cannot play a noticeable role in atomic dynamics. In such a case, it's possible to use the simplified approach using the population rate equation:

$$P_i(m+1)=\sum_{k,j}P_k(m)\left|\mu_{kj}\right|^2\left|\mu_{ji}\right|^2 + P_i(m)\left(1-\sum_j\left|\mu_{ji}\right|^2\right), \quad (1)$$

where $P_i(m)$ is the population on the Zeeman sublevel i after m pumping cycles, $\left|\mu_{kj}\right|^2$ is the transition coefficients from state i to state j. We define the transition coefficients $\mu_{ij}\equiv a_{F_eM_e\rightarrow F_gM_g}$ by the relation

$$a_{F_eM_e\rightarrow F_gM_g}=(-1)^{1+I+J_e+F_e+F_g-M_e}(2F_e+1)^{1/2} \times(2F_g+1)^{1/2}\begin{Bmatrix}F_e & 1 & F_g\\ J_g & I & J_e\end{Bmatrix} \times\begin{pmatrix}F_e & 1 & F_g\\ -M_e & q & M_g\end{pmatrix}(2J_e+1)^{1/2}, \quad (2)$$

where $\begin{Bmatrix}j_1 & j_2 & j_3\\ m_1 & m_2 & m_3\end{Bmatrix}$ and $\begin{pmatrix}j_1 & j_2 & j_3\\ m_1 & m_2 & m_3\end{pmatrix}$ are 6-j and 3-j symbols and $q=0,\pm1$ denotes standard components of the electric dipole moment for the Zeeman sub-levels considered. These coefficients are related to the probability transition by:

$$A_{F_eM_e\rightarrow F_gM_g}=\left|a_{F_eM_e\rightarrow F_gM_g}\right|^2\frac{1}{\tau}, \quad (3)$$

where τ is 30 ns [7] in the case of the $6^2P_{3/2}$ level.

After applying the $F=3=F'=2$ pumping with horizontal polarization $(\sigma^++\sigma^-)/2$, more atoms were pumped to the Zeeman $M_F=0,\pm1$ sublevels while fewer atoms left in the $M_F=\pm2,\pm3$ sub-levels (Fif.2).

This picture demonstrated the relationship between the experimental observations for the central Rabi resonance (0-0) with and without optical pumping. A direct calculation using formulas presented above shows that the pumping efficiency is about 2 after several tens of pumping cycles.

If we look up at the formula for the transitions coefficients (2), we see that the transition between the Zeeman sub-levels $0\Leftrightarrow0$ is forbidden if we use π-type of polarized optical pumping $F=3=F'=3$. Consequently, this laser beam depopulated the all sub-levels with $M_F\neq0$. Thus, the atoms are finally accumulated only in the sub-level $(F=3, M_F=0)$. The Ramsey fringes for that case are presented in Fig.3.

The numerical calculations gives a pumping efficiency on the level 2.5. Combining these two types

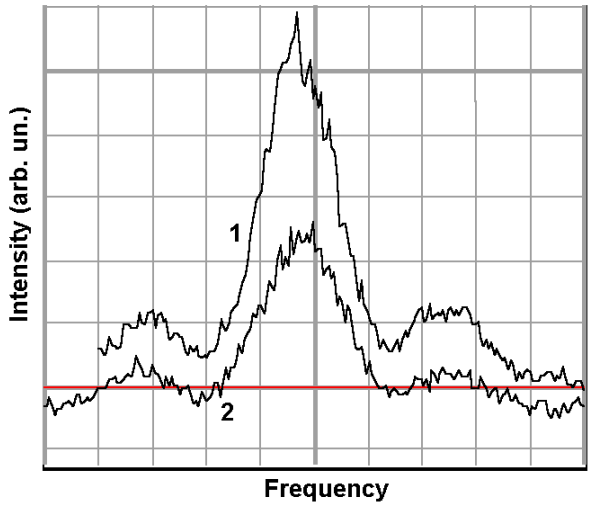

FIG. 2: The central Rabi resonance with (1) and without (2) optical pumping $F = 3 = F' = 2$. Velocity of the cold cesium atoms is about 3.3 m/s

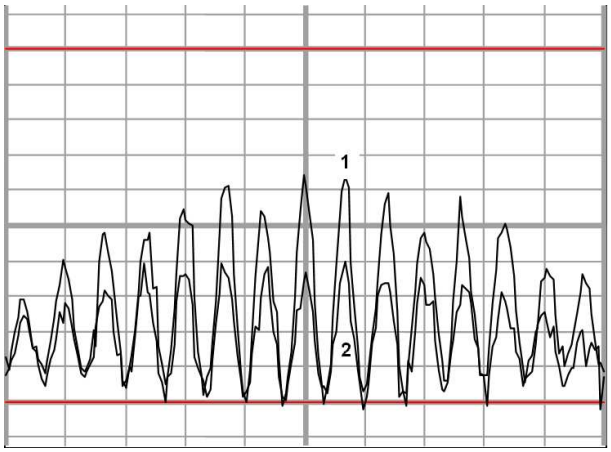

FIG. 3: Ramsey fringes with (1) and without (2) optical pumping $F = 3 = F' = 3$. Velocity of the cold cesium atoms is about 3.45 m/s

of the optical pumping, presented above, it is easy to show, that the final efficiency can increase up to the level 3.9.

IV. SUMMARY

The experimental and theoretical results of the present study enables us to make the following conclusions:

- the population for the Zeeman state sub-level $(F = 3, M_F = 0)$ depends strongly of the type of polarization and the orientation of the magnetic field as a quantization axis,
- the transfer of atoms into state $F = 3$ enable us to realize different ways of optical pumping and this may lead to several-fold increasing of the working cesium atoms compared to usual way of fountain operation ,
- the optical pumping, in principle, can be used for precise registering of the atoms in the state $F = 3$ and, hence, for calculation of spin-exchange frequency shift.

[1] Yu. Domnin, B. Gaigerov, N. Koshelyaevsky, S. Poushkin, F. Rusin, V. Tatarenkov, G. Yolkin, Metrolofia **42**, S55(2005).
[2] Yu. S. Domnin, G.A. Elkin, A.V. Novoselov, L.N. Kopylov, V.N. Baryshev, and V.G. Pal'chikov, Can. J. Phys.**80**, 1321(2002).
[3] Yu. S. Domnin, G. A. Elkin, A.V. Novoselov, L. N. Kopylov, V. N. Baryshev, Yu. M. Malychev, and V. G. Pal'chikov, Quantum Electronics,**34**, 1084(2004).
[4] S. Weyers, U. Hübner, R.Schröder, Chr. Tamm and A. Bauch, Metrologia, **38**, 343(2001).
[5] Karl Blum, "Density Matrix Theory and Applications" (Plenum Press, New York and London, 1981).
[6] S. Chang and V. Minogin, "Density-matrix approach to dynamics of multilevel atoms in laser fields", Physics reports, **365**, 65(2002).
[7] J. K. Link, J.Opt.Soc.Am. **56**, 1195 (1966).

Majorana Transitions in an Atomic Fountain Clock

Proceedings of the 20th EFTF, 2006

S. Weyers,* R. Schröder, and R. Wynands
Physikalisch-Technische Bundesanstalt, Bundesallee 100, 38116 Braunschweig, Germany

Recently, we observed quasi-periodic frequency oscillations in CSF1, the first caesium fountain clock at Physikalisch-Technische Bundesanstalt in Braunschweig, Germany. These oscillations could be traced back to Majorana transitions taking place between the second Ramsey interaction and the fluorescence detection. Such transitions mix the Zeeman sublevels in a coherent way and therefore lead to additional contributions in the interference pattern. Combined with the unavoidable $\Delta m = \pm 1$ transitions inside the Ramsey cavity, frequency errors can arise when the overall symmetry with respect to $\pm m$ is broken in the detection zone because of an m-dependent detection efficiency. A change in field configuration eliminated the Majorana transitions and with it the frequency oscillations.

I. INTRODUCTION

About a year ago we observed quasi-periodic frequency oscillations in CSF1, a caesium fountain clock at Physikalisch-Technische Bundesanstalt that went into operation in 1999 [1, 2]. This new effect had a characteristic signature (Fig. 1). When polarization oscillations were introduced for the laser light in the detection zone (with periods of hours) and when the state selection cavity was not used, the effect could be greatly enhanced—with frequency oscillation amplitudes of order 10^{-13}.

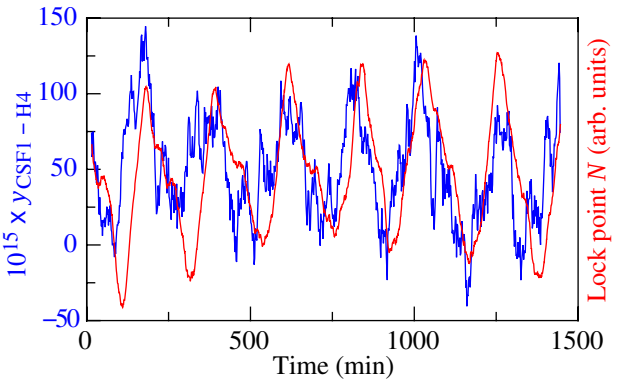

FIG. 1: Correlated oscillations of the output frequency of CSF1 relative to that of hydrogen maser H4 (noisy blue curve, left axis) and of the lock point $N = N_4/(N_3 + N_4)$ (smooth red curve, right axis)

An immediate suspicion was that this could have something to do with Majorana transitions somewhere along the path of the atom cloud. Majorana transitions can occur when the magnetic field seen by a particle possessing a magnetic moment changes its orientation rapidly compared to the Larmor precession frequency. Indeed, as explained below, it was found that at one point along the atomic trajectory such a relatively rapid field change was encountered by the atoms. In a multi-step process described in more detail in the following, this can lead to a frequency error in a fountain clock.

*Electronic address: stefan.weyers@ptb.de

II. EXPERIMENTAL EVIDENCE

The data in Figure 1 was taken without the state selection cavity in use and for an intentional small misalignment of the linear input polarizations with respect to the easy axis of the optical fibers bringing the laser light to the detection zone. This misalignment leads to polarization changes at the output of the fiber whenever the fiber temperature changes. As explained below, this polarization fluctuation with a period of hours modulates the frequency-shifting effect of Majorana transitions and thus makes the frequency shift easier to detect and characterize.

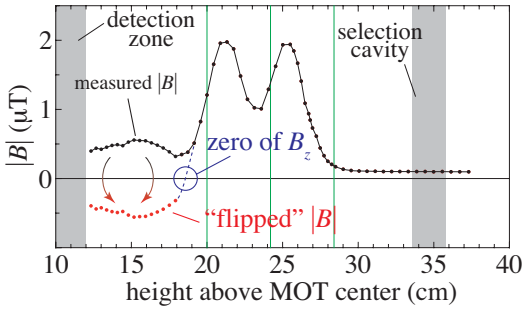

FIG. 2: Measured $|B|$ along the trajectory of the atoms in the original field configuration. The vertical green lines correspond to the positions of the bottom covers of the three magnetic shielding layers. The shaded areas indicate the spatial extent of the detection zone and the state selection cavity, respectively.

In order to determine whether Majorana transitions could occur for the given field structure inside CSF1, we have mapped the magnetic field structure in two ways. With a flux-gate sensor one can measure all three field components just outside the wall of the vacuum container in the area between the trapping

zone and the lower end of the magnetic shields. This gave rise to the suspicion that there might be a reversal of the vertical component B_z of the magnetic field inside the vacuum container.

In a second step we used the atoms themselves as a probe for the field inside the vacuum system. In CSF1 the state selection cavity does not have a cut-off tube at its lower end due to geometrical restrictions. Part of the field inside the cavity will therefore leak out into the rest of the apparatus. By coupling a sufficiently strong microwave pulse into the state selection cavity at a time when the atoms are at a height z_1 one can determine the magnetic field at z_1 by monitoring the resonance frequency of the field-sensitive transition $|F = 3, m = -1\rangle \rightarrow |F = 4, m = -1\rangle$. This is similar to the technique used, for example, on FO1 at LNE-SYRTE, where a small antenna was used to provide the microwave field pulse for a measurement of the field above the Ramsey cavity [4].

In this way we were able to measure the magnetic field all the way down to the detection zone (Fig. 2). A cursory glance at the figure does not arouse suspicion regarding the presence of a field zero. However, what is measured by following the resonance frequency of the $|3, -1\rangle \rightarrow |4, -1\rangle$ transition is the absolute value $|B|$ of the magnetic flux density, averaged over a spatial region corresponding to the size of the atom cloud (a few mm). In fact, as corroborated by qualitative calculations of the magnetic field using the RADIA code [5], there can be a zero of B_z hiding in the minimum indicated in the figure. In this region, the horizontal components B_x and B_y are very small due to symmetry, so that Majorana transitions can occur.

Such a zero crossing had been carefully avoided during setup of CSF1. Unavoidable compromises in the construction of the magnetic shields, however, led to a strong sensitivity of the field near the shield covers to mechanical stress in that area, so that over the course of time a field zero could develop along the atomic trajectory. Unfortunately, this did not show up in the usual "health checks" that we routinely perform on CSF1.

We have now corrected the field structure by adjusting the current in the coils for the compensation of the geostatic field so that no more Majorana transitions can happen there (Fig. 3). In addition, we have added new steps to the list of regular "health check" measures so that no harmful field change can remain undetected in the future.

As a result of the elimination of the Majorana transitions, there are no more correlated oscillations of lock point and output frequency (Fig. 4). By switching back and forth between the old and the new currents in the field coils we can reproducibly switch back and forth between the situations leading to Figures 1 and 4.

In the following we will give a semi-quantitative explanation of the frequency shifting effect of a Majorana transition after the second Ramsey interaction in a fountain clock.

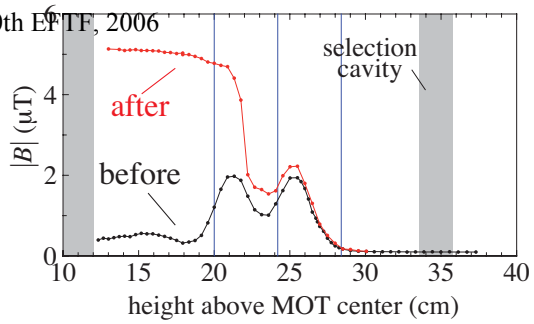

FIG. 3: Measured $|B|$ along the trajectory of the atoms. After adjustment of the coil currents a field zero no longer occurs.

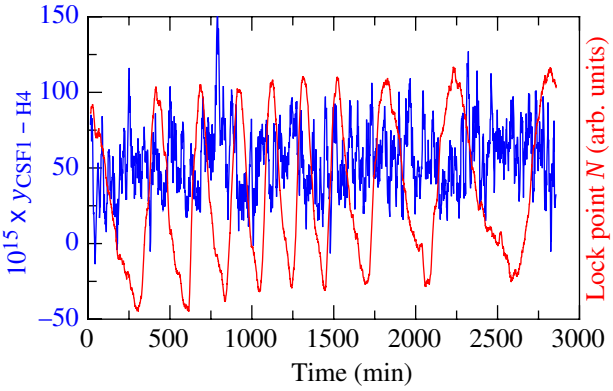

FIG. 4: After adjustment of the field configuration a variation of the lock point $N = N_4/(N_3 + N_4)$ (smooth red curve, right axis) no longer leads to correlated oscillations of the output frequency of CSF1 (noisy blue curve, left axis).

III. MAJORANA TRANSITIONS IN GENERAL

Majorana transitions can occur when the magnetic field seen by a particle possessing a magnetic moment changes its orientation rapidly compared to the Larmor precession frequency. The original treatment by Majorana [6] was rephrased and extended by Bloch and Rabi [7]. One of Majorana's results was that the dynamics of the spin orientation can be replaced by a sudden rotation in space by Euler angles determined by the magnitude of the magnetic moment and the field geometry only.

In the following we will present a brief synopsis of the theoretical description of Majorana transitions. Unlike in previous work [7, 8], where the "x-convention" for Euler angles was used (i.e., the second

rotation is around the intermediate x-axis), we will follow the "y-convention" in general use in quantum physics today. This basically changes some phases but in return allows us to use the standard rotation matrices.

We consider a "regular" zero-crossing, i.e., an odd-order zero crossing of one component of the magnetic field located in a small region of space. A typical example is the vicinity of the center of a spherical quadrupole field aligned along $\hat{e}_z$.

When the magnetic field, as experienced by an atom approaching with velocity $\vec{v} = v\hat{e}_z$, changes its orientation sufficiently slowly, the magnetic moment of the atom can follow this change adiabatically. Relative to a coordinate system that rotates with the local field direction the spin does not change its orientation. In the other extreme, when the field reversal appears instantaneous as seen by the atom, the spin keeps its orientation in a laboratory-fixed frame, i.e., a 180° Majorana flip has happened.

In the general case, the spin will afterwards point in some new direction characterized by Euler angles (ϕ, α, θ), where ϕ and θ are the rotation angles around $\hat{e}_z$ and $\hat{e}_{z'}$, the inital and the final z axes respectively, and α is the Majorana angle (rotation angle around the intermediate y-axis). By solving the time-dependent Schrödinger equation for a spin-1/2 particle experiencing a field corresponding to the vicinity of the center of a spherical quadrupole field, Majorana obtained for the angle α [6]:

$$\sin^2\frac{\alpha}{2} = \exp(-\frac{\pi}{2}\kappa) \qquad \text{with}$$
$$\kappa = \frac{g\mu_B B_y^2}{\hbar v |dB_z/dz|}. \qquad (1)$$

Here g is the gyromagnetic factor, which is $g = 1/4$ for the caesium state $|F = 4\rangle$, and μ_B is the Bohr magneton.

Another of Majorana's results is that the angle α does not depend on F or m [6]. He also gave a prescription for expressing the final state for a spin-F particle in terms of the result for the spin-1/2 case. In the process of making this connection between spin 1/2 and spin F [6, 7] one obtains quantities equivalent to what now are called the matrix elements of the rotation matrix for spin F [9].

For an atom initially in a pure state $\Psi_i = |F, m\rangle$ the final state Ψ_f after the Majorana transition is a coherent superposition given by an active rotation of Ψ_i:

$$\Psi_f = D^{(F)}(\phi, \alpha, \theta)\Psi_i = \sum_{m'} D^{(F)}_{m',m} |F, m'\rangle$$
$$= \sum_{m'} d^{(F)}_{m',m} \exp(-im\phi - im'\theta) |F, m'\rangle .$$

Here the $d^{(F)}_{m',m}$ are the matrix elements of the rotation operator $d^{(F)}$ for angular momentum $\hbar F$.

IV. MAJORANA TRANSITIONS IN A FOUNTAIN CLOCK

As in a fountain the atoms are quasi monokinetic (typically $\Delta v/v \approx 0.3\%$ when the atoms are launched) compared to the case of thermal beam clocks (typically $\Delta v/v \approx 10\%$ using magnetic state selection and even larger using optical pumping) we shall restrict the following discussion to a single velocity, in contrast to the treatment of Reference [8] for a thermal-beam clock. One important consequence of the small velocity spread in a fountain is that the frequency shifting effects are much less washed out compared to the situation in thermal beam clocks. In fact, in those clocks the most significant features were found for the case of a so-called double-zero, where the z-component of the magnetic field showed two zeroes within a short distance, so that the effects did not wash out [8].

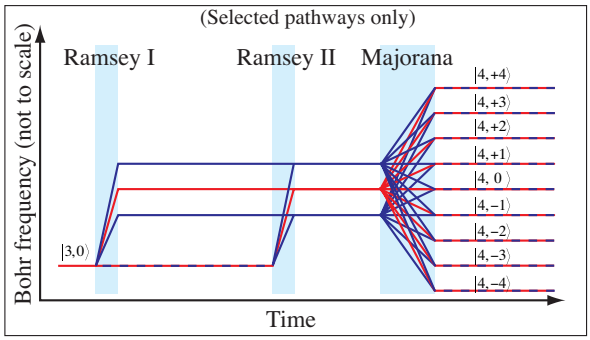

FIG. 5: Visualization of the effect of Majorana transitions, taking place after the second Ramsey interaction, on the final atomic state in a fountain clock with state selection (see text for explanation).

We will consider here the situation of a fountain clock with a state selection cavity (Fig. 5). Following the state selection process all atoms are in state $|F = 3, m = 0\rangle =: |3, 0\rangle$. This means that any coherences induced by Majorana transitions before the atoms reach the state selection cavity are quenched—no frequency bias is introduced. In the case of CSF1, both cavities are located already in the region of the very homogeneous C-field, so Majorana transitions cannot occur until after the atoms have fallen back through the state selection cavity.

In the course of the Ramsey interaction the atoms undergo transitions to $|4, 0\rangle$, induced by the oscillating magnetic field $\vec{B}_{\mu W}$ inside the Ramsey cavity. This field is nominally parallel to the direction of the C-field (i.e., in the vertical direction) so that selection rules in the ideal case would allow only the clock transition $|3, 0\rangle \rightarrow |4, 0\rangle$ to occur (π transition, $\Delta m = 0$).

However, in a real TE_{011} cavity the direction of $\vec{B}_{\mu W}$ is truly vertical only along the symmetry axis and on the central horizontal plane. At all other points there is some component in the horizontal di-

rection. This σ-polarized part of the oscillating magnetic field can induce σ-transitions ($\Delta m = \pm 1$), leading to a small admixture of the $|4, \pm 1\rangle$ states.

After the second Ramsey interaction the atomic state therefore is a superposition of three main components:

$$\begin{aligned} |\psi_R\rangle = \; & \beta_{+1} R_{+1} |4, 1\rangle \\ & + \beta_0 R_0 |4, 0\rangle \\ & + \beta_{-1} R_{-1} |4, -1\rangle . \end{aligned}$$

Here $|\beta_0| \gg |\beta_{\pm 1}|$ and from symmetry $|\beta_{+1}| = |\beta_{-1}|$. $|R_j|^2$ ($j = -1, 0, 1$) stands for a Ramsey fringe pattern centered on a microwave frequency $f_0 + (j/2) f_Z$, where f_0 is the resonance frequency of the "clock transition" $|3, 0\rangle \rightarrow |4, 0\rangle$ and f_Z is the resonance frequency of the field-sensitive $|3, 1\rangle \rightarrow |4, 1\rangle$ transition.

A Majorana transition taking place after the second Ramsey interaction leads to a quantum-mechanical rotation of the state. This means that in general each state $|4, m\rangle$ will be transformed into a coherent superposition of all states $|4, m'\rangle$, according to the elements $D^{(4)}_{m',m}$ of the quantum mechanical rotation matrix for spin 4 (Fig. 5):

$$\begin{aligned} |\psi_M\rangle = \; & \beta_{+1} R_{+1} \left[D_{+1,+1} |4, 1\rangle + D_{0,+1} |4, 0\rangle + D_{-1,+1} |4, -1\rangle + \text{analogous terms with all other } |4, m'\rangle \right] \\ & + \beta_0 R_0 \left[D_{+1,0} |4, 1\rangle + D_{0,0} |4, 0\rangle + D_{-1,0} |4, -1\rangle + \text{analogous terms with all other } |4, m'\rangle \right] \\ & + \beta_{-1} R_{-1} \left[D_{+1,-1} |4, 1\rangle + D_{0,-1} |4, 0\rangle + D_{-1,-1} |4, -1\rangle + \text{analogous terms with all other } |4, m'\rangle \right] . \end{aligned}$$

Here and in the following we have simplified the notation by writing $D_{m',m}$ instead of $D^{(4)}_{m',m}$. In the detection zone a projection of $|\psi_M\rangle$ onto the eigenstates $|4, m'\rangle$ is performed, resulting in a detected signal proportional to the rather complicated-looking expression

$$\begin{aligned} & \ldots + w_{+2} \left| \beta_{+1} R_{+1} D_{+2,+1} + \beta_0 R_0 D_{+2,0} + \beta_{-1} R_{-1} D_{+2,-1} \right|^2 && (2) \\ & + w_{+1} \left| \beta_{+1} R_{+1} D_{+1,+1} + \beta_0 R_0 D_{+1,0} + \beta_{-1} R_{-1} D_{+1,-1} \right|^2 && (3) \\ & + w_0 \left| \beta_{+1} R_{+1} D_{0,+1} + \beta_0 R_0 D_{0,0} + \beta_{-1} R_{-1} D_{0,-1} \right|^2 && (4) \\ & + w_{-1} \left| \beta_{+1} R_{+1} D_{-1,+1} + \beta_0 R_0 D_{-1,0} + \beta_{-1} R_{-1} D_{-1,-1} \right|^2 && (5) \\ & + w_{-2} \left| \beta_{+1} R_{+1} D_{-2,+1} + \beta_0 R_0 D_{-2,0} + \beta_{-1} R_{-1} D_{-2,-1} \right|^2 + \ldots . && (6) \end{aligned}$$

Here the $w_{m'}$ indicate a weighting factor proportional to the number of fluorescence photons that are captured from an atom reaching the detection zone in state $|F, m'\rangle$. Each of the terms $\beta_0 R_0 D_{m',0}$ by itself would give rise to an unshifted Ramsey fringe pattern.

In general, the overall "Ramsey" fringe pattern will have a more complicated shape. However, a frequency error will only result when this change in shape is asymmetric with respect to the undisturbed center frequency f_0. Here we find from the underlying symmetry of the rotation matrix and the transition probability amplitudes β_j that the asymmetries due to certain terms cancel each other.

For instance, the sum $\beta_{+1} R_{+1} D_{0,+1} + \beta_{-1} R_{-1} D_{0,-1}$ in term (4) is symmetric, so it does not contribute to a frequency error. The asymmetries contained in the corresponding sum $\beta_{+1} R_{+1} D_{+1,+1} + \beta_{-1} R_{-1} D_{+1,-1}$ in term (3) do not cancel each other, but closer inspection shows that they cancel the asymmetries of the sum $\beta_{+1} R_{+1} D_{-1,+1} + \beta_{-1} R_{-1} D_{-1,-1}$ in term (5) in the overall interference pattern. The same pattern holds for the asymmetries in terms (2) and (6), and so on.

This second type of cancellation, however, happens only if $w_{-m'} = w_{m'}$. This is in general not the case due to various optical pumping processes in the detection zone. Typically, the laser for detection of $|F = 4\rangle$ atoms is circularly polarized. An atom arriving, for example, in state $|4, -2\rangle$ needs more absorption-emission cycles that an atom initially in state $|4, +2\rangle$ to reach the strong cycling transition starting from $|4, +4\rangle$ and also has a higher probability of getting hyperfine-pumped into the $|F = 3\rangle$ ground state. Therefore it scatters less photons overall, and $w_{-2} < w_{+2}$.

The actual values of the $w_{m'}$ depend on the laser polarizations in the detection zone. This is why a slight misalignment of the laser polarization at the input end of the fiber can influence the occurrence and magnitude of Majorana-induced frequency shifts in such a dramatic way (Figures 1 and 4).

[1] S. Weyers, U. Hübner, R. Schröder, Chr. Tamm, A. Bauch, Metrologia **38**, 343–352 (2001).

[2] S. Weyers, A. Bauch, R. Schröder, Chr. Tamm, Proc.

6th Symposium on Frequency Standards and Metrology (World Scientific), Fife (GB), 64–71 (2001).

[3] R. Wynands, S. Weyers, Metrologia **42**, S64–S79 (2005).

[4] S. Zhang, *Déplacement de fréquence dû au rayonnement du corps noir dans une fontaine atomique à césium et amélioration des performances de l'horloge*, Ph.D. thesis, Université de Paris VI (2004).

[5] The RADIA code is an add-on to the commercial computer algebra system MATHEMATICA, allowing the calculation of magnetic fields and magnetizations in and around magnetic and non-magnetic bodies in the presence of fields produced by coils or magnetized bodies. RADIA can be downloaded for free from the website of the European Synchrotron Radiation Facility, http://www.esrf.fr/Accelerators/Groups/InsertionDevices/Software/Radia.

[6] E. Majorana, Nuovo Cim. N. S. **9**, 43–50 (1932).

[7] F. Bloch, I. I. Rabi, Rev. Mod. Phys. **17**, 237–244 (1945).

[8] A. Bauch, R. Schröder, Ann. Phys. **2**, 421–449 (1993).

[9] M. Chaichian, R. Hagedorn, *Symmetries in Quantum Mechanics*, Institute of Physics Publishing (Bristol 1998).

Proceedings of the 20th EFTF, 2006

Atom-based stabilization for laser-pumped atomic clocks

V. Gerginov[1],* V. Shah[2], S. Knappe[2], L. Hollberg[3], and J. Kitching[3]
[1] *Department of Physics, University of Notre Dame, Notre Dame, IN 46556*
[2] *Department of Physics, University of Colorado, Boulder, CO 80309 and*
[3] *Time and Frequency Division, National Institute of Standards and Technology, Boulder, CO 80305*

Progress towards simplification and improvement of the long-term stability of chip-scale atomic clocks is presented. The conventional technique of laser optical frequency and cell temperature control is compared with a novel technique which avoids the use of temperature sensors. The technique results in a simpler setup and improved long-term performance. Here, laser frequency, laser intensity, RF modulation index and vapor cell atomic density are stabilized using exclusively information from the atoms in the vapor cell. Different feedback schemes for laser intensity and frequency stabilization, as well as cell temperature control are experimentally compared. Their relevance to future design of chip-scale devices is discussed.

I. INTRODUCTION

Chip-scale atomic clocks (CSACs) with volumes of several cubic millimeters [1] and power consumption below 10 mW [2] have recently been introduced and are expected to provide precise timing in GPS receivers, network applications, and portable instrumentation systems. Integration of a chip-scale physics package with low-power local oscillator (LO) [3] of similar size and control electronics of cubic centimeter size seems possible [4].

Most CSACs are based on a coherent population trapping (CPT) scheme [5], using a vertical cavity surface emitting laser (VCSEL) to excite alkali atoms contained in a small buffer gas vapor cell [6]. The laser injection current is modulated by the LO, which produces sidebands in the optical spectrum of the laser. When the frequency difference between two components in the optical spectrum matches the frequency splitting of the atomic ground state, the optical field pumps part of the atoms into a state that absorbs less light. The decreased absorption is used to stabilize the LO frequency to the atomic transition.

The splitting of the atomic ground state can change due to the AC Stark effect. It is influenced by the optical field parameters such as optical frequency, total intensity, and intensity distribution among the spectral components of the light field. Another factor is the pressure of the buffer gas inside the cell, which depends on the cell temperature. A change in any of these parameters leads to a corresponding change in the LO frequency and to degradation of the clock performance.

The laser wavelength [7], intensity and modulation properties [8, 9] are very sensitive to temperature and injection current. When the laser optical frequency is stabilized by controlling the injection current, the laser intensity becomes coupled to its temperature through the injection current. Changes in the LO output power, RF coupling between the LO and the laser, or the laser modulation parameters (due to temperature, injection current or aging) all will lead to change in the optical field parameters which affect the clock frequency.

The cell temperature determines the buffer gas pressure, which affects the atomic ground state splitting through collisions. Through the use of a mixture of buffer gases, the sensitivity of the clock frequency to cell temperature can be reduced [10, 11]. This reduction is effective only in a limited temperature range because of the nonlinear behaviour of the clock frequency shifts with temperature for different gases.

The goal of the present work is to study the long-term frequency stability of CSAC devices and suggest design changes in both the physics package and control implementation that could lead to better performance under typical field-operated conditions. We describe a novel method, that uses the atomic absorption for stabilization of the optical field parameters and vapor cell temperature. In the conventional method the laser substrate temperature, laser optical frequency, LO output power and temperature of the cell exterior are stabilized. Here, the actual parameters that determine the clock frequency - laser intensity, optical frequency, intensity distribution among the spectral components, and the atomic absorption - are stabilized, which results in better long-term device performance and a simpler design. The new design makes the device largely insensitive to changes in the ambient temperature by eliminating temperature sensors and the thermal gradients associated with their usage.

II. EXPERIMENTAL SETUP

A. Conventional setup

The experiment is based on the physics package of a conventional chip-scale atomic clock design developed at NIST [12]. A VCSEL die [7], emitting in a single mode at 795 nm is used to excite the D_1 line ($5s\ ^2S_{1/2} \rightarrow 5p\ ^2P_{1/2}$) transition in ^{87}Rb. It is

*Electronic address: gerginov@nist.gov

mounted on a quartz substrate with a deposited thin-film heater. The laser substrate temperature is around 80^{o}C (stabilized to ∼1 mK using a thermistor and a temperature controller). The thermistor temperature coefficient is ∼ -4 %/K. The LO modulates the laser injection current at one half of the ground state splitting of the Rb atoms (6.835 GHz). The LO output power is chosen so that the first-order sidebands are maximized. The divergent and linearly polarized laser beam passes through a neutral density filter and a quarter-wave plate before entering the ^{87}Rb vapor cell of 1 mm^3 internal volume. The optical frequency of the laser carrier is tuned such that the first-order sidebands are in resonance with the two ground state components and it is locked to the maximum of the first-order sideband absorption.

The micromachined vapor cell is filled with isotopically enriched ^{87}Rb and a buffer gas mixture of argon and neon at total pressure of 16 kPa. The cell temperature is maintained in the vicinity of 85^{o}C with 1 mK precision using a thermistor equivalent to the one used for laser temperature control. The optical absorption of the first-order modulation sidebands in the laser optical spectrum is ∼20 %.

The LO frequency is stabilized to the $F = 1,\ m_F = 0 - F = 2,\ m_F = 0$ ground state hyperfine resonance. The CPT resonance has a linewidth of ∼7 kHz and an absorption contrast (defined as the CPT signal amplitude divided by the optical absorption of the first-order sidebands) of 3.3 %.

The conventional setup is shown in Figure 1 (a).

A fractional frequency instability plot is shown in Figure 1 (filled squares). The long-term stability is limited to $\sim 5 \times 10^{-11}$ at 200 s.

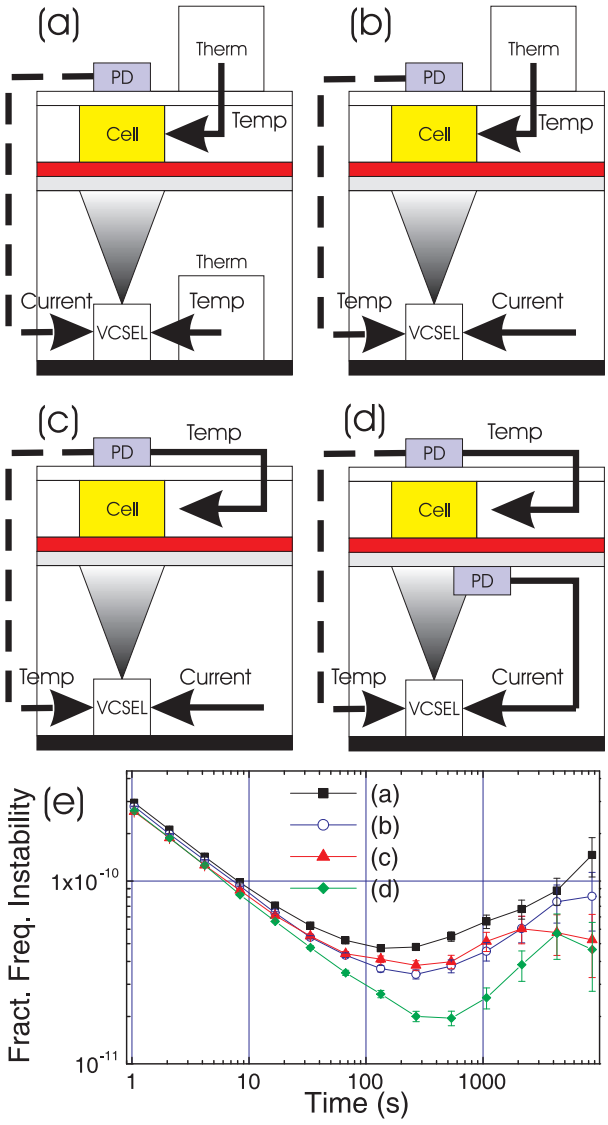

FIG. 1: Top - Experimental setup for CSAC parameter control. Solid lines represent DC signals and dashed lines represent phase detection signals. (a) Conventional setup, Section II A. (b) Laser frequency is controlled using temperature feedback, Section II B (c) Cell temperature is controlled using atomic absorption, II C (d) Laser intensity is controlled using a photodetector, II D. Bottom - fractional frequency instability plots corresponding to cases (a) through (d).

B. Laser temperature stabilization using atomic resonances

A problem in the conventional stabilization scheme (Figure 1 (a)) results from varying temperature gradients between the laser p-n junction and temperature sensor. These gradients change with the ambient temperature. This leads to variations in the laser temperature, and correspondingly, to changes in the laser injection current because of the optical frequency lock. Variations in the laser injection current lead to changes in the laser intensity, and instability of the clock frequency due to the AC Stark shift. A simple setup that stabilizes directly the laser p-n junction temperature is shown in Figure 1 (b). The setup is used to keep the laser frequency locked to the optical resonance by controlling the laser temperature. The laser is operated with a constant DC injection current with a superposed AC modulation at 17 kHz. The AC current modulation produces a corresponding laser frequency modulation which results in amplitude modulation after the frequency dependent optical absorption of the vapor cell. As the laser frequency changes (due to temperature changes or aging, for example) the demodulated photodetector signal can be fed back to the laser thin-film heater to adjust the laser temperature for constant frequency feedback. The bandwidth of the temperature control is limited to ∼30 Hz. The stability of the laser frequency is estimated to be ∼20 MHz, or 1 % of the linewidth of the absorption line, and is similar to that obtained with the conventional setup based on thermistor. A fractional frequency instability for the microwave clock transition is shown in Figure 1 (open

circles). It is clear that the reduced feedback bandwidth does not degrade the clock short-term stability and that this method of laser stabilization results in improved clock frequency stability ($\sim 3.5 \times 10^{-11}$ at 200 s).

C. Temperature stabilization of the vapor cell using optical absorption

A second problem with the conventional stabilization scheme (Figure 1 (a)) results from varying temperature gradients between the sensor measuring the cell temperature, and the cell interior. As a consequence, a change in the ambient temperature leads to varying temperature of the buffer gas. The Rb vapor density is a strong function of the temperature and so the optical absorption, and hence the light intensity transmitted through the cell, also depends on the cell temperature. Under typical operating conditions, we have change in the absorption of 1 %/K, similar to the change in the resistance of a typical thermistor. The DC signal of the photodetector placed behind the cell is a measure of the cell temperature and is used to stabilize it in the setup shown in Figure 1 (c). A fractional frequency instability plot is shown in Figure 1 (solid triangles).

D. All-optical laser frequency and intensity stabilization

The experimental setup for simultaneous laser intensity and frequency stabilization is shown in Figure 1 (d). The DC signal from the lower photodetector is used to stabilize the laser intensity using a current feedback. The laser beam transmitted through the cell is detected with a second photodetector. The DC signal from the upper photodetector is used to stabilize the cell temperature. The fractional frequency deviation is plotted in Figure 1 (solid diamonds). The stability of 2×10^{-11} at 200 s achieved with this system is improved by more than a factor of two over the frequency stability measured with the conventional setup of Figure 1 (a) using thermistors in a controlled laboratory environment, with changes in the ambient temperature of less than 2 K. At the same time, this technique simplifies the setup, since no thermistors are required, in contrast with previous work [13, 14].

The laser temperature is determined by the stability of the optical lock and the stability of the laser injection current. For 20 MHz optical frequency stability and 10^{-4} injection current stability, the laser temperature is stable to better than 2 mK. The cell temperature is determined by the stability of the voltage references used to control the DC signal on the two photodetectors ($\Delta V/V \sim 10^{-4}$), the optical absorption (20 %), and the dependence of the optical absorption on temperature (1 %/K). The stability of the cell temperature is on the order of 50 mK. These stabilities are expected to be largely independent of ambient temperature, since no temperature sensors are used in the setup shown in Figure 1 (d).

III. FIRST-ORDER SIDEBANDS AMPLITUDE STABILIZATION

In the experiments described above, a synthesizer with a very stable output power was used to modulate the VCSEL injection current. In portable CPT atomic clocks, the synthesizer is replaced with a compact low-power local oscillator (see, for example, [3]). Changes in the output power of the LO redistributes the optical power among the modulation sidebands. This, in turn, can change the clock frequency due to AC Stark shifts from the resonant and off-resonant sidebands. We find that the modulation index changes also with the laser temperature. The laser impedance is modified, and with it, the RF modulation index because of the different RF coupling. To illustrate this, the laser temperature was varied, and the RF power, applied to the VCSEL input in order to make the first-order optical sidebands intensity equal to 50% of the total laser intensity, was measured. The laser carrier was kept in resonance with $5s^2S_{1/2}$ $F_g = 1 \rightarrow F_e = 1, 2$ transition by a simultaneous change of the laser current. The results are shown in Figure 2.

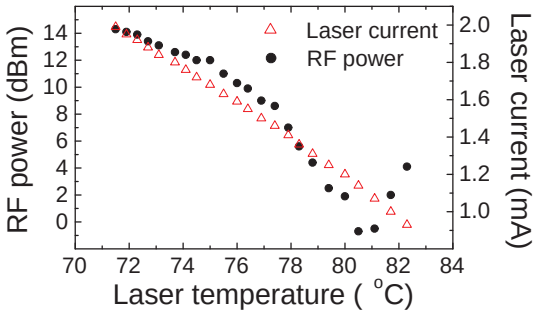

FIG. 2: RF power applied to the VCSEL input in order to make the first-order optical sidebands intensity equal to 50% of the total laser intensity, as a function of the laser temperature (circles). The laser injection current (triangles) was changed simultaneously with the laser temperature to keep the carrier in resonance with $5s^2S_{1/2}$ $F_g = 1 \rightarrow F_e = 1, 2$ transition.

It is clear that the RF power coupled to the laser has a strong nonlinear behaviour [8, 9], especially at injection currents close to the laser threshold (0.6 mA for the laser used here).

With the laser frequency and intensity stabilized as shown in Figure 1 (d), the remaining parameter that determines the AC Stark shift is the intensity distribution among the different spectral components. For laser frequency modulation, the fraction of output power contained in the first-order sidebands goes

through a maximum at a certain modulation index, and this can be used to maintain consistent modulation index. Since the first-order sidebands are resonant with the optical transitions, their power change will produce a change in the total atomic absorption.

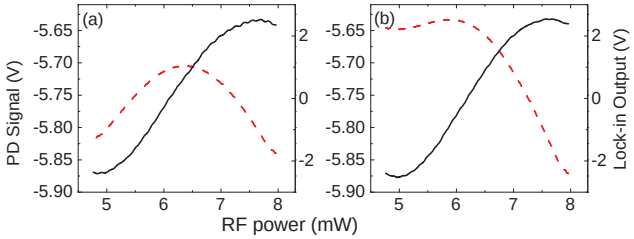

FIG. 3: Photodetector output (dashed) and error signal (solid) as a function of RF power coupled to the laser. Left plot - laser frequency locked using laser temperature. Right plot - laser frequency locked using injection current feedback. The RF power is linearly scanned for 1 s, resulting in RF power change of 40%. The AM modulation was 3% and lock-in amplifier time constant 100 ms.

Figure 3 shows the absorption change detected as a function of the LO output power. The difference between the photodetector signals is due to the way the laser frequency is locked. When thermistors are used, the RF power heats the p-n junction locally, the thermistor doesn't compensate this heating, and the laser power changes through the frequency lock. When the laser frequency is locked to the optical transition using temperature feedback, such local p-n junction heating is compensated by the laser heater, the intensity stays constant and the PD signal changes only because of the changes in the amplitude of the first-order sidebands. This clearly demonstrates the sensitivity of the technique described in Section II B to local temperature variations.

A method is described in Refs. [15–17], where the clock frequency is made insensitive to changes of laser intensity by choosing the RF modulation index such that the AC Stark shifts of each individual spectral component compensate each other. As shown [18], this works well in a narrow laser temperature region and does not provide active control of LO output power changes, RF coupling and laser diode aging.

When the amplitudes of the carrier and sidebands are fixed, and laser power and frequency are stabilized using the experimental setup from Figure 1 (d), the total AC Stark shift of the clock frequency is "frozen" because the optical frequency and intensity of each spectral component are constant. This approach is a powerful method to minimize clock frequency drifts due to changes in the light field of the laser. In contrast to the method suggested in References [15–17], it is immune to several systematic effects connected with the temperature control of the laser and effects from laser aging. Also, the CPT signal is optimized since it is produced by the two first-order sidebands which contain the maximum intensity available using laser frequency modulation.

IV. CONCLUSIONS

A new method is realized for laser frequency and power control without the use of temperature sensors. The clock physics package is simplified and allows for active stabilization of the laser power. Absorption cell temperature stabilization is based on optical attenuation measurements. This simplifies the experimental setup significantly and gives a direct measure of the vapor density inside the cell. All-optical implementation simultaneously stabilizes the laser power, frequency and RF modulation index - the parameters that determine the AC Stark shift of the clock frequency. Under fixed laser intensity and frequency, the clock frequency shows improved clock stability. Initial results of stabilizing the RF modulation index are obtained. This method provides the possibility for full control over the laser light field in a simple and compact way, and shows a great promise for chip-scale atomic devices, and could be implemented in other laser-based frequency standards.

Acknowledgments

This work was supported by the Microsystems Technology Office of the U.S. Defense Advanced Research Projects Agency (DARPA). This work is a contribution of NIST, an agency of the U.S. government, and is not subject to copyright.

V. REFERENCES

[1] S. Knappe, L. Liew, V. Shah, P. D. D. Schwindt, J. Moreland, L. Hollberg, and J. Kitching, Appl. Phys. Lett. **85**, 1460 (2004).

[2] R. Lutwak, J. Deng, W. Riley, M. Varghese, J. Leblanc, G. Tepolt, M. Mescher, D. K. Serkland, K. M. Geib, and G. M. Peake, in *Proc of the 36th Precise Time and Time Interval (PTTI) Systems and Applications Meeting* (Reston, Virginia, USA, 2004).

[3] A. S. Brannon, J. Breitbarth, and Z. Popovic, in *IEEE MTT-S 2005 International Microwave Symposium* (Long Beach, California, USA, 2005).

[4] G. Gerginov, S. Knappe, P. D. D. Schwindt, V. Shah, L. Liew, J. Moreland, H. G. Robinson, L. Hollberg, and J. Kitching, in *Proc. 2005 Joint Mtg. IEEE Intl.*

Freq. Cont. Symp. and PTTI Meeting (Vancouver, Canada, 2005).

[5] E. Arimondo, Prog. Opt. **XXXV**(35), 257–354 (1996).

[6] L. A. Liew, S. Knappe, J. Moreland, H. Robinson, L. Hollberg, and Kitching, J., Appl. Phys. Lett. **84**(14), 2694–2696 (2004).

[7] H. J. Unold, M. Grabherr, F. Eberhard, F. Mederer, R. Jäger, M. Riedl, and K. J. Ebeling, Electron. Lett. **35**, 1340–1341 (1999).

[8] S. Kobayashi, Y. Yamamoto, Y. Ito, and T. Kimura, IEEE J. Quantum Electron. **QE-18**(4), 582–595 (1982).

[9] P. N. Melentiev, M. V. Subbotin, and V. I. Balykin, Laser Physics **11**(8), 891–896 (2001).

[10] W. Happer, Rev. Mod. Phys. **44**(2), 169–249 (1972).

[11] J. Vanier and C. Audoin, *The Quantum Physics of Atomic Frequency Standards*, 1st ed. (Adam Hilger, Bristol, UK, 1989).

[12] J. Kitching, S. Knappe, M. Vukicevic, L. Hollberg, R. Wynands, and W. Weidmann, IEEE Trans. Instrum. Meas. **49**(6), 1313 – 1317 (2000).

[13] S. Yamaguchi and M. Suzuki, IEEE J. Quantum Electron. **19**(10), 1514–1519 (1983).

[14] D. E. Janssen and M. W. Levine, US Patent 6,222,424 (2001).

[15] J. Vanier, A. Godone, and F. Levi, in *Proc. Joint Meeting of Eur. Forum on Time and Frequency / Int. Freq. Control. Symp.*, pp. 96–99 (1999).

[16] M. Zhu and L. Cutler, in *Proc of the 32th Precise Time and Time Interval (PTTI) Systems and Applications Meeting*, pp. 311–324 (Reston, Virginia, USA, 2000).

[17] M. Zhu and S. Cutler, U.S. Patent 6,201,821 (2001).

[18] V. Gerginov, S. Knappe, P. D. D. Schwindt, V. Shah, and J. Kitching, J. Opt. Soc. Am. B **23**(4), 593–597 (2006).

Proceedings of the 20th EFTF, 2006

Realization of a Pulsed Optically Pumped Rubidium Frequency Standard

F. Levi,* S. Micalizio, A. Godone, C. Calosso, and Elio Bertacco
Istituto Nazionale di Ricerca Metrologica, INRIM, Strada delle Cacce 91, 10135, Torino, Italy
**Electronic address:* levi@inrim.it

In this paper we present the more recent developments of a vapor cell frequency standard based on a pulsed technique. The laboratory prototype we implemented has shown very interesting metrological features, such as negligible light-shift and strongly reduced cavity-pulling. Moreover, a frequency stability of $\sigma_y(\tau) = 1.2\times10\text{-}^{12}\ \tau^{-1/2}$ for measurement times up to $\tau \approx 100000$ s has been achieved.

I. INTRODUCTION

Light shift is recognized as one of the main physical effects limiting the frequency stability of optically pumped vapor-cell clocks. Changing the optical source from the lamp to the laser can in principle produce an improvement on the clock stability, since the optical pumping process is more efficient; but the high level of coupling between microwave and optical coherences induced by the laser results in a relevant noise conversion from the laser itself to the clock signal. A partial reduction of these problems can be achieved with the lambda configuration where the atoms are excited in a more symmetrical excitation scheme, but, in this way, the physical effects which impair the frequency stability may be compensated or reduced but not fully eliminated.
One of the more effective technique to reduce light shift is the pulsed scheme where the optical pumping phase is separated in time from the microwave excitation, in such a way the clock transition is observed in a nearly pure two level system. The coupling between optical and microwave coherences is avoided and a strong reduction of the light shift is achieved.
This idea was first considered by Alley [1] and applied to the field of frequency standards by Arditi and Carver [2]. We recently revisited this idea taking into account the technologies nowadays available, laser diodes and fast pulsed electronics, and taking also into account a deeper knowledge of the physics involved in this frequency standards [3]. In this paper we resume the interesting results obtained with a laboratory prototype of pulsed optically pumped (POP) frequency standard.

II. BASIC OPERATION

The basic operation of the POP frequency standard is well known [4]. We suppose to deal with a sample of ^{87}Rb atoms contained in a cell with a proper buffer gas. We refer to the three level system of Fig. 1: ω_0 is the angular frequency of the applied microwave field, ω_L is the angular frequency of the pumping laser, γ_1 and γ_2 are the relaxation rate of the ground state population and of the coherence respectively; Γ^* is the relaxation rate of the excited state population; Δ_0 is the laser detuning.

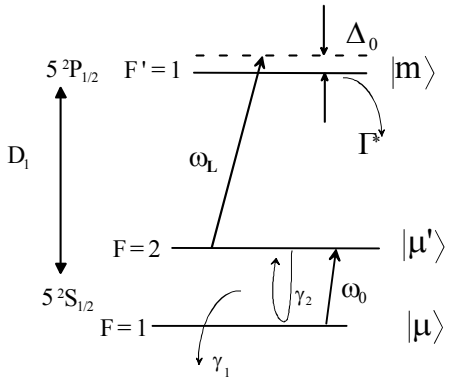

Fig. 1. Three level system considered in our analysis.

The timing pattern is shown in Fig. 2.
A strong laser pulse pumps almost all the atoms in one of the two ground state levels. Then the atoms are interrogated with two microwave pulses separated in time, and then a detection window is enabled so that the atoms that have made the clock transition are detected.

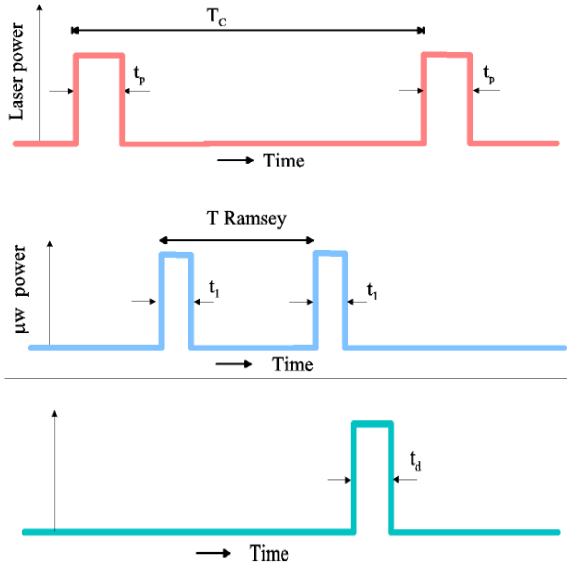

Fig.2. Timing pattern of the POP clock operation.

As for CPT standards, also in this case the detection could be in the optical domain or in the microwave domain. In the latter the so called "free-induction decay" signal is detected and the advantages of the microwave detection will be shown later on.

III. THEORETICAL CONSIDERATIONS

In normal operation, the POP clock timing sequence shown in Fig. 2 is periodic.
To separate the optical pumping from the microwave interrogation, the atoms should not have any memory of the previous cycle, or in mathematical terms the coherence at the beginning of the Ramsey interaction should be as small as possible, zero in the ideal case.
One possibility is obviously to wait a long time between one cycle and the following one so that the free-induction decay signal is completely extinguished. But due to the interaction with the buffer gas, the free-induction decay signal evolves in times that are as slow as a few ms. Therefore, to avoid long dead times in the POP clock operation, the laser pulse should assure not only a large population inversion in the ground state but also a strong reduction of the residual microwave coherence between a cycle and the next one.
Taking into account the optical length ζ of the atomic medium, it is easy to show [3] that the laser pumping rate Γ_p (which is proportional to the laser power) should satisfy the following relation:

$$\Gamma_p >> \zeta\gamma_1 + 1/t_p \qquad (1)$$

Under this conditions the optical pumping and the interrogation phases are really separated and there is no transfer of laser noise to the clock transition so there is no light shift.
In practice a residual light shift remains depending on how strong the inequality (1) is satisfied: in usual operating conditions, the residual resonant light shift (FM-FM conversion) has been evaluated of the order of 10^{-14} per MHz of laser detuning, while the off-resonant (AM-FM conversion) conversion turns out to be $\sim 10^{-13}$ per percent of laser power fluctuation.
Ramsey fringes can be calculated in the usual way, that is by using the product of interaction and free evolution matrices [4]. A very interesting property can be obtained when the microwave pulse area θ is $\pi/2$. The central fringe of the free induced decay shows an atomic quality factor that is twice that observed in the optical domain; in fact the coherence signal is proportional to $\sin^2(\Omega_\mu T)$, while the population inversion signal is proportional to $\cos(\Omega_\mu T)$ [5].
This is one reason why we decided to observe the clock transition through the microwave signal instead of the more common optical transmission signal. The other reason is that the microwave signal is observed without any background: the only background signal is due to the detection noise which is the ultimate physical limit while in the optical domain the useful signal is in general only a few percent of a much larger laser background signal.
Experimental Ramsey fringes will be shown in section V. During the Ramsey interaction the atoms are submitted to the cavity feedback, hence the cavity pulling is significant in the POP frequency standard. However, it is possible to demonstrate that there is a suitable value of θ which makes the cavity pulling negligible. From an experimental point of view, this means that adjusting properly the microwave power it is possible to find an operation point which minimizes the cavity pulling.
The theoretical results briefly summarized here are extensively discussed in [3].

IV. EXPERIMENTAL SET-UP

Figure 3 reports a scheme of the experimental set-up; it is composed of three parts: the optics, the physics package and the electronics.

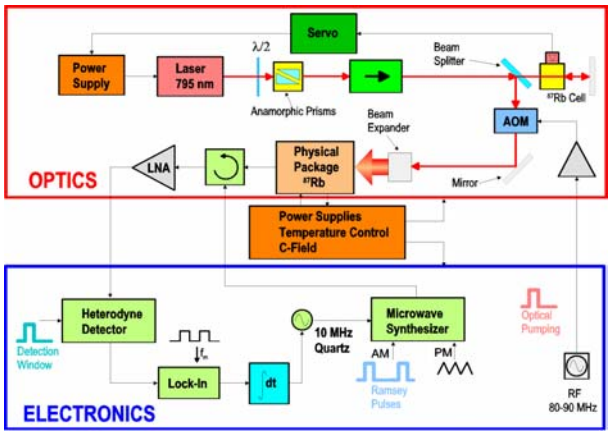

Fig. 3. POP clock experimental set-up.

The laser frequency is locked to the optical transition using an external cell containing ^{87}Rb only. The main part of the laser is sent to the physics package through an AOM that works as an optical switch. Once the atoms are pumped, the laser is off and the atoms are interrogated with two microwave Ramsey pulses. The microwave signal emitted by atoms is observed with an heterodyne detector. A lock in amplifier and an integrator provide the control signal to a 10 MHz quartz. A synthesizer is amplitude modulated to provide the Ramsey pulses. The interrogation signal is frequency modulated with a square wave signal whose frequency is of course one half the cycle frequency. The clock operation is similar to that of an atomic fountain but in the POP the cycle is 100 times faster, being of the order of 10 ms.

The physics package is composed of a quartz cell containing the Rb atoms and a thermally compensated buffer gas mixture. The cell has a length L = 18 mm and a radius R = 20 mm. The operating temperature of the cell is 60 °C, corresponding to an atomic density of $n \approx 3\times10^{11}$ cm^{-3}. For this cell we have: $\gamma_1 \approx \gamma_2 \approx 290$ s^{-1}, $\Gamma^* \approx 3\times10^9$ s^{-1} and the optical length of $\zeta \approx 3.5$.
The cell is placed in a thermally controlled microwave cavity. The cavity is made in Al and resonates at 6.8 GHz for the TE_{011} mode. Finally, a solenoid provides the quantization magnetic field.
More details on the experimental set-up are reported in [6].

V. EXPERIMENTAL RESULTS

Figure 4 shows a typical cavity output signal as detected by the spectrum analyzer.
To clarify the mechanism of the coherence destruction we used two different laser powers: 1 and 20 mW (figure 4).

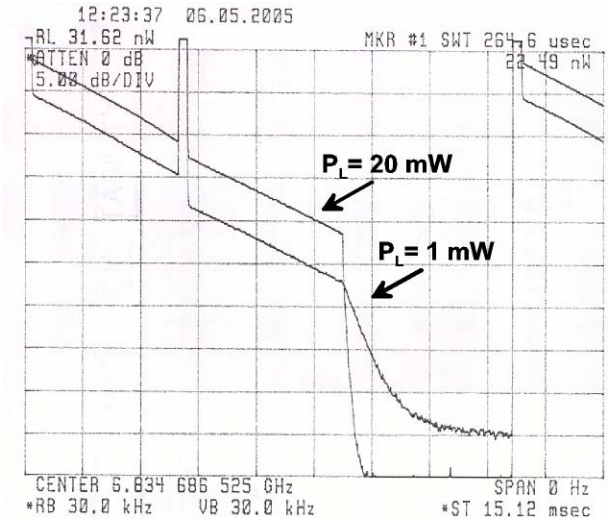

Fig. 4. Cavity output signal observed for two laser powers. P_L = 1 mW and 20 mW. The peak power is 9 and 23 nW (after LNA) respectively; the timing sequence is: t_1 = 220 μs; T = 4 ms; t_p = 4 ms; t_d = 3.8 ms; θ = π/2.

In the figure are clearly observable the two Ramsey pulses and the free induction decay signal observed at the spectrum analyzer (in the time domain).
This signal is proportional to the modulus squared of the coherence excited between the two grand state levels.
The signal obtained with 1 mW and 20 mW of laser are compared: while the microwave output power is quickly saturated (2.5 times increase in the output power over 20 times increase of the pumping light), the coherence destruction is not.
The role of the laser pulse during the pumping phase is evident. The microwave coherence is strongly reduced so that at the beginning of the new cycle the atoms do not have memory of the previous one. This is desirable for two reasons: reduction of the light shift and reduction of the dead time for the pumping process.
Ramsey fringes can be observed in the free induction decay signal by measuring the output power at the end of the second Ramsey pulse and then changing the microwave detuning, as observed in Fig. 5. The theoretical results mentioned before are clearly confirmed. The Ramsey fringe for θ = π/2 shows an atomic quality factor that is twice that of the fringe observed for a lower value of θ (~π/20).

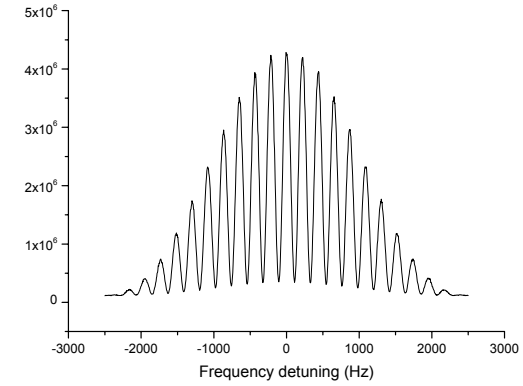

(a)

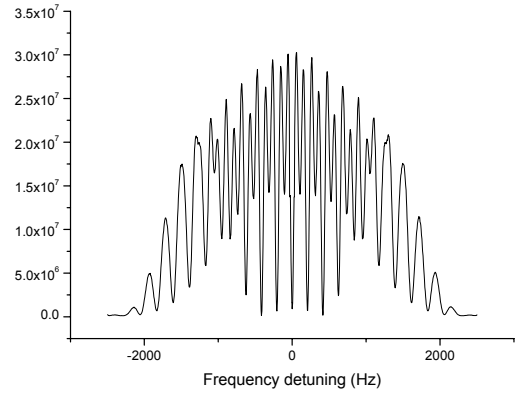

(b)

Fig. 5. Ramsey fringes detected in the microwave domain (free-induction decay signal); (a) θ ~π/20. , (b) θ = π/2.

We measured the POP clock frequency versus the microwave pulse area θ for three different values of the cavity detuning. According to the theory, there is a suitable value of θ so that the clock frequency does not depend on the cavity detuning and then there is an operation point where the cavity pulling effect is minimized.

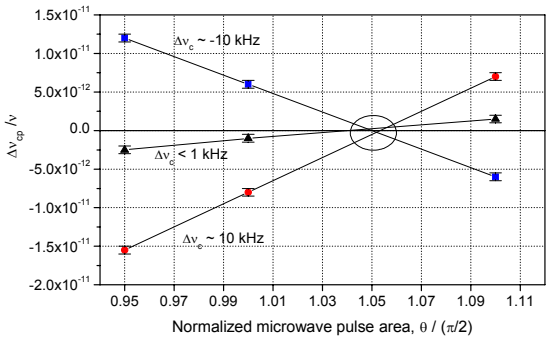

Fig. 6. Clock frequency versus θ for different values of the cavity detuning $\Delta\nu_C$.

In Fig. 7 we report the measured frequency stability of the POP frequency standard; the figure shows the overlapping Allan and the Thêo1 deviations.

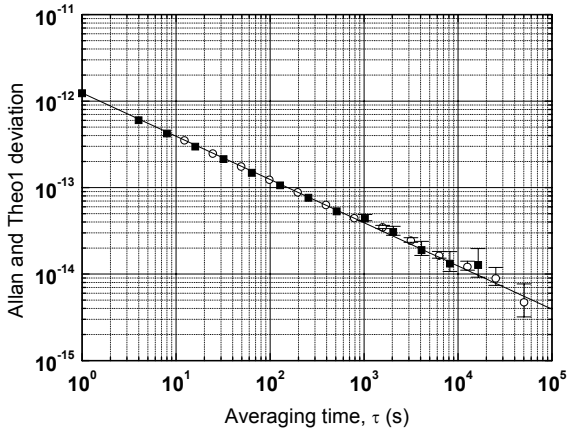

Fig. 7. Frequency stability; overlapping Allan deviation (black square), Theo deviation (open circle).

This result has been obtained with the following timing sequence: t_1 = 400 μs; T = 4.6 ms; t_p = 1 ms; t_d = 2 ms, and with a laser intensity of I_L=10 mW/cm^2. A frequency drift of 6×10^{-14} per day has been removed from the raw data.

VI. CONCLUSIONS

In this paper we reported the physical and metrological properties of a laboratory prototype of POP frequency standard. The experimental results are in good agreement with the theoretical prediction reported in [3]. In particular, the observation of the microwave emission allows to double the quality factor of the atomic transition with respect to the optical detection, and furthermore reduces the impact of the laser noise.
In suitable operating conditions, light shift and cavity pulling can be strongly reduced.

The short-medium term frequency stability has been measured and the result is among the best obtained in optically pumped vapor cell devices. An optimization of the system can possibly reach a relative stability of $\sigma_y(\tau)=7\times10^{-13}\,\tau^{-1/2}$; among possible improvements we indicate a quieter synthesis chain and an auto-tuned cavity to reduce the long term frequency drift.
Definitely, the results here reported show that a proper implementation of the POP clock is very attractive for several application where a stable, simple and reliable device is required, and for space applications.

VII. REFERENCES

[1] C. O. Alley, in Quantum electronics, edited by C. W. Townes, Columbia University Press, p.146, 1960, New York.
[2] M. Arditi and T. R. Carver, IEEE Trans. Instrum. Meas., vol. 13, p. 146, 1964.
[3] A. Godone, S. Micalizio, and F. Levi, Phys. Rev. A, vol. 70, p. 023409, 2004.
[4] M. Arditi, in Rendiconti della Scuola Internazionale di Fisica Enrico Fermi, LXVIII Corso, Metrology and Fundamental Constants, edited by Società Italiana di Fisica, (Bologna, Italy), pp.289-334, 1980.
[5] C. Audoin, in Rendiconti della Scuola Internazionale di Fisica Enrico Fermi, LXVIII Corso, Metrology and Fundamental Constants, edited by Società Italiana di Fisica, (Bologna, Italy), pp.223-259, 1980.
[6] A. Godone, S. Micalizio, C. E. Calosso, and F. Levi, IEEE Trans. Ultrason. Ferroelctr. Freq. Control **53**, 525 (2006).

Proceedings of the 20th EFTF, 2006

Estimation of the compact cold atom clock HORACE frequency stability

S. Trémine[1], F.X. Esnault[1], S. Guérandel[1], D. Holleville[1], J. Delporte[2] and N. Dimarcq[1] *
[1] *LNE-SYRTE – Observatoire de Paris 61, avenue de l'Observatoire – 75014 Paris – France*
[2] *CNES – 18 avenue Edouard Belin – 31055 Toulouse Cedex - France*
**Electronic address:* noel.dimarcq@obspm.fr

HORACE is a compact cold Cs atom clock where laser cooling, microwave interrogation and clock signal detection are all performed inside a spherical microwave cavity. We present the signals observed on the new clock prototype. The frequency stability is estimated from clock signal measurements.

I. INTRODUCTION

Atomic clocks are used in various applications which require different a trade-off between the frequency performance of the clock and its characteristics (volume, mass, electrical consumption). On one side, there are the ultrastable cold atom fountain which are laboratory devices (volume ≈ few m^3) offering outstanding performance (few 10^{-14} $\tau^{-1/2}$ stability level). On the other side, miniaturized chip scale clocks are suitable for a use in transportable systems such as GPS receivers. The chip scale clocks using the Coherent Population Trapping interrogation exhibit today stabilities better than 10^{-10} at 1 s for an overall volume of about 10 cm^3 [1]. In the intermediate region, one can find cesium beam clocks, rubidium cell clocks or passive hydrogen masers which have frequency stabilities in the range 8-50 10^{-13} for a volume of a few litres to a few tens of litres. These clocks are used in laboratories or in GNSS systems which require short term stabilities at 10^{-12} level. The HORACE concept should bring a breakthough since the objective is to reach a few 10^{-13} stability at 1 second with a compact device (physics package of about 1 litre). Moreover, the HORACE clock uses laser cooled atoms which are well suited for the improvement of the long term stability and the accuracy of the clock, as it has been already demonstrated in fountains. Moreover, cold atoms are also an advantage for an operation in microgravity.

The HORACE concept relies on the capability to laser cool the atoms directly inside the microwave cavity [2]. The use of "isotropic cooling" has demonstrated its capability to cool about 10^8 atoms at very low temperatures (few μK), even if the laser field distribution is randomised inside the cavity.
The HORACE operation is in time domain : the laser cooling, the microwave interrogation and the clock signal detection are performed inside a spherical microwave cavity, leading to reduced losses of cold atoms between two successive cycles.

Section II presents the optimised time sequence which should lead to the best clock performance. In Section III, we describe briefly the new clock prototype which has been built in SYRTE in order to improve the clock signal to noise ratio (S/N). In section IV, we show the preliminary results and we extrapolate the frequency stability which should be reached in nominal conditions.

II. OPTIMISATION OF CLOCK SEQUENCE

The HORACE clock sequence involves three durations :

- the cooling time T_{cool}
- the interrogation time T_i
- the detection time T_{det}

Thanks to the operation in "time domain", the dead times between the three major interactions (cooling, interrogation, detection) are negligible, in contrary to other cold atom clocks operating in "space domain". As a consequence, the cycle time T_{cycle} is simply given by $T_{cycle} = T_{cool} + T_i + T_{det}$.

The target frequency stability which can be reached in such a clock is determined by the quantum projection noise and is given by the following Allan deviation :

$$\sigma_{y,QPN}(\tau) = \frac{2}{\pi}\cdot\frac{1}{T_i}\cdot\frac{1}{S/N}\cdot\sqrt{\frac{T_{cycle}}{\tau}} \quad \text{(Eq. 1)}$$

where S/N is the signal to noise ratio over one clock cycle, and τ is the integration time.
Equation 1 shows that, in order to improve the clock stability, one has to increase the interrogation time T_i **and** decrease the cycle time T_{cycle}. Moreover, for a given interrogation time, the impact of aliasing effects (Dick effect) is decreased if the duty cycle $\eta = T_i/T_{cycle}$ is enhanced, i.e. if the cycle time is decreased.
The HORACE concept allows a better optimisation of the clock sequence for the following reasons :

- the cold atom losses between two successive clock cycles are reduced because the cold atoms do not exit the cavity

- the cycle rate (≈ 10 Hz) is rather large ; leads to a small T_{cycle} value in Eq. 1, thus improving the clock stability. Such a high cycle rate is well suited to relax the requirements on the local oscillator phase noise for reducing the impact of the Dick effect, as we will point out later.

The frequency stability given by Eq. 1 assumes a limitation by the quantum projection noise. Equation 2 gives a more realistic formula which takes into account instrumental contributions such as the Dick effect and additional noise sources perturbing the clock signal detection (AM and FM noises of detection laser, noisy fluorescence/absorption background due to thermal atoms, …).

$$\sigma_y(\tau) = (\sigma_y^2{}_{,QPN}(\tau) + \sigma_y^2{}_{,detection}(\tau) + \sigma_y^2{}_{,Dick}(\tau))^{1/2} \quad \text{(Eq.2)}$$

The contributions of the quantum projection noise and the detection noise depend on the number of detected cold atoms which is determined by T_{cool} , T_i and T_{det} : this number obviously increases if T_{cool} increases and T_i decreases. On the other hand, the contribution of Dick effect depends on the cycle rate $1/T_{cycle}$ and on the duty cycle η : it decreases if η increases towards 1.

In order to determine what is the best trade-off on T_{cool}, T_i and T_{det} which optimises the clock stability, an analysis was carried out previously [3]. This analysis relied on a Monte-Carlo simulation and it was taking into account realistic noise contributions (laser, local oscillator) deduced from real measurements. Table 1 summarizes the main conclusion of this optimisation, for an operation either on ground or in space.

	Operation on Earth	Operation in Space
Linewidth	12 Hz	3 Hz
Cycle duration	75 ms	220 ms
Detected atoms	$2.5\ 10^6$	$1.3\ 10^6$
Clock S/N	1200	750
Expected stability	$2\text{-}4\ 10^{-13}\ \tau^{-1/2}$	$1.\ 10^{-13}\ \tau^{-1/2}$

Table 1 - Clock features for an optimised operation

The previous experimental set-up was designed to study the isotropic cooling processes and was not adapted for the detection of a metrological signal. Thus, we have rebuilt a new clock prototype (physics package and optical bench) which should allow to reach the expected clock S/N. This new design is described in [4]. We remind in the next section the different detection possibilities.

III. IMPROVEMENT OF THE CLOCK PROTOTYPE

The new clock prototype offers the possibility to carry out three kinds of measurements (Figure 1).

The detection of the horizontal probe beam absorption gives some information on :

- the thermal atoms density in the storage bulb,
- the presence of cold atoms identified thanks to their narrow linear absorption lines,
- the cold atom cloud size by performing a time of flight (TOF) measurement corresponding to a null fall height (Figure 2). This measurement is important because it is not possible in this device to have any direct size measurement by imaging the fluorescence light onto a CCD camera. From the width Δt of the TOF signal, we can deduce a cloud size between 5 and 10 mm according the cooling sequence.

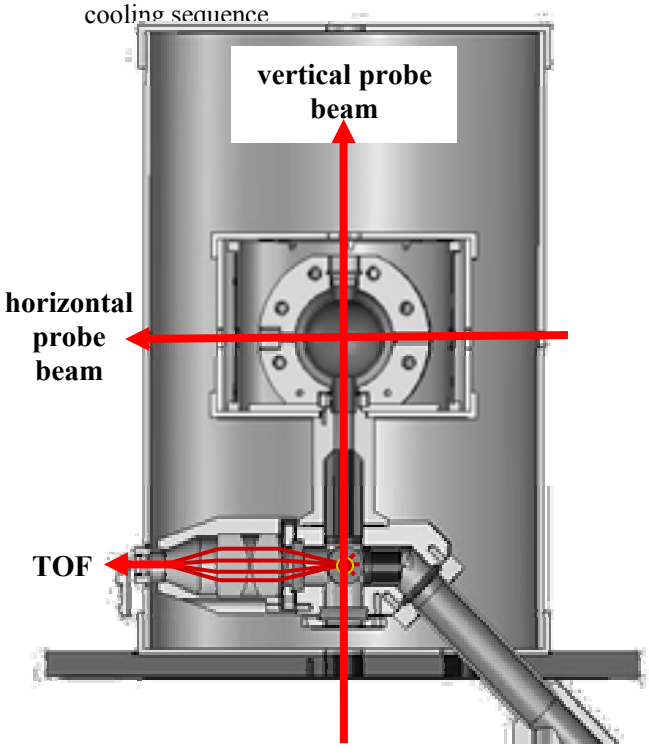

Figure 1 - Possible detections in the new clock prototype

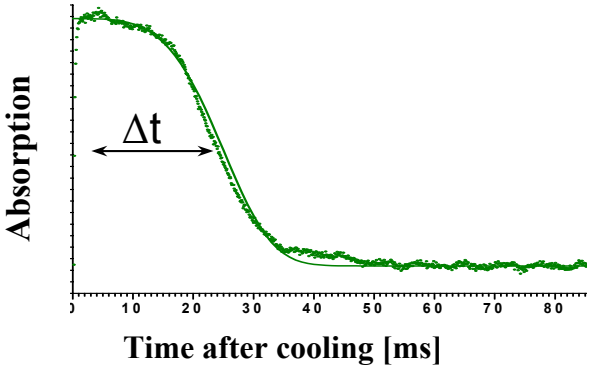

Figure 2 - Time of flight signal at altitude zero

The second detection is the well known time of flight (TOF) detection, below the cooling region, which allows the determination of the cold atom temperature (down to 2 µK with isotropic light). In the HORACE clock, this detection is used for diagnostics only since the cold atoms stay always inside the microwave cavity in nominal operation.

The third detection is the clock signal detection relying on the measurement of the vertical laser beam linear absorption (Figure 3). The clock signal will be deduced from the narrow peak amplitude which gives the number of atoms in $6S_{1/2}$, F=4 level.

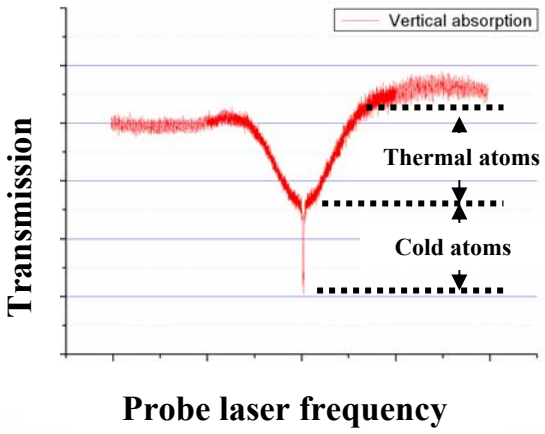

Figure 3 - Vertical probe beam linear absorption

IV. CLOCK SIGNAL MEASUREMENTS

In this section, we compare the clock signal detection possibilities, either the TOF fluorescence signal or the vertical beam absorption.

Clock signal detected by TOF below the cavity

The clock signal detected by TOF is shown on Figure 4 for two interrogation times :

(a) for T_i = 20 ms, the linewidth is about 25 Hz and the contrast is as high as 98 %
(b) for T_i = 50 ms, the linewidth is lowered to 10 Hz and the contrast is still acceptable (85 %).

For both cases, the S/N is about 200 without normalization. This value is equivalent to the ones usually measured in fountains in the same conditions. It demonstrates that isotropic cooling does not degrade the shot to shot atom number fluctuations, even if the cooling light intensity and polarization are less controlled. Thus, with normalization, one can expect to reach S/N higher than 1000.

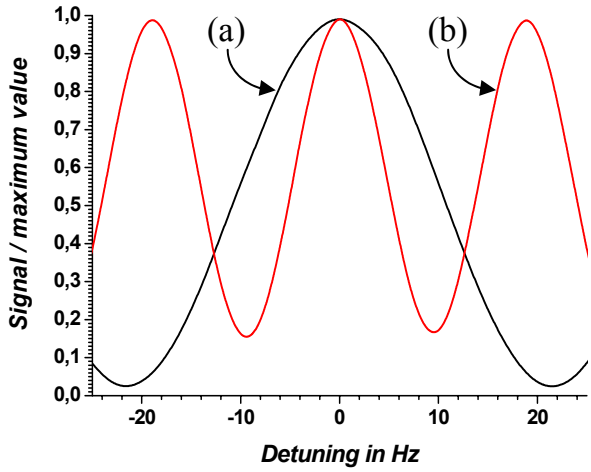

Figure 4 - Clock signal detected by TOF for two interrogation times : T_i = 20 ms (a) and T_i = 50 ms (b)

Clock signal detected by absorption

For the first time, we have detected the clock signal by measuring the absorption of cold atoms when they are still inside the cavity. Figure 5 shows the observed signal for two interrogation times :

(a) for T_i = 5 ms, the linewidth is about 100 Hz
(b) for T_i = 50 ms, the linewidth is about 10 Hz

It is important to point out that the observed clock signal is a few tens times narrower than the Cs beam clock ones, and "only" 10 times wider than the fountains.

However, the observed contrast is rather low (≈ 20 %) and the S/N is poor (≈ 40, without renormalization).

This degradation results from an uncontrolled instrumental perturbation which has not been identified yet. In principle, these values should reach the same as the ones obtained with the TOF.

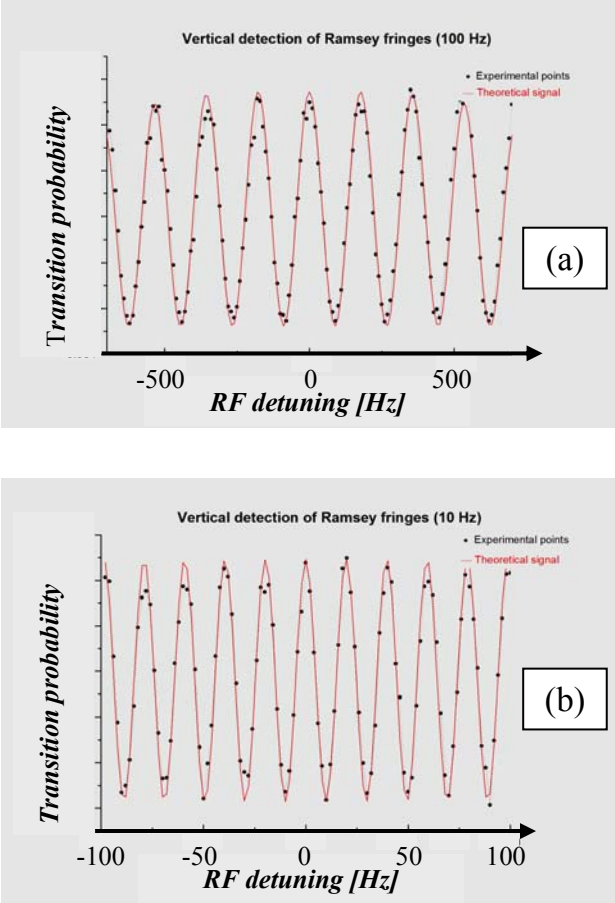

Figure 5 - Clock signal detected by absorption of cold atoms inside the cavity for two interrogation times : T_i = 5 ms (a) and T_i = 50 ms (b)

Table 2 summarizes the clock signal measurements and gives the corresponding frequency stability according to Eq. 1.

	Detection with TOF	Detection with absorption
Cycle time T_{cycle}	1000 s	75 ms
Linewidth	10 Hz	10 Hz
Clock S/N (over one cycle)	200	40
Frequency stability with the current S/N	$3.5\ 10^{-12}\ \tau^{-1/2}$	$4.8\ 10^{-12}\ \tau^{-1/2}$
Frequency stability with S/N = 200	$3.5\ 10^{-12}\ \tau^{-1/2}$	$9.7\ 10^{-13}\ \tau^{-1/2}$
Frequency stability with S/N = 1000	$7.\ 10^{-13}\ \tau^{-1/2}$	$2.\ 10^{-13}\ \tau^{-1/2}$

Table 2 – Synthesis of clock signal features. Estimation of the corresponding stability

If we use renormalisation techniques the clock S/N should be increased up to 1000, leading to an excellent level of stability of the clock.

V. CONCLUSION

A new HORACE clock prototype has been built in order to optimise the clock signal detection by the measurement of the linear absorption of cold atoms, directly inside the microwave cavity. The clock signal S/N currently measured is still low (≈ 40) but it is obviously limited by a spurious instrumental effect. Thus, there is room for frequency stability improvements and we hope that the low 10^{-13} level will be reached in a near future.

Acknowledgements

This work is supported by the French space agency CNES. F.X. Esnault is grateful to CNES and Thales Electron Devices (TED) for providing research studentship

REFERENCES

[1] S. Knappe,* V. Gerginov,† P. D. D. Schwindt, V. Shah,* H. G. Robinson, L. Hollberg, and J. Kitching ; Optics Letters, 30, p. 1361 (2005) ; Atomic vapor cells for chip-scale atomic clocks with improved long-term frequency stability

[2] E. Guillot, P.E. Pottie, N. Dimarcq ; Optics Letters 26, 1639 (2001) ; "3-D cooling of cesium atoms in a reflecting copper cavity"

[3] S. Trémine, S. Guérandel, D. Holleville, A. Clairon, J. Delporte and N. Dimarcq ; Proceedings of the 19th European Forum on Time and Frequency, Besançon, mars 2005 ; "Short term stability limitations in a compact cold atom clock"

[4] F.X. Esnault, S. Perrin, S. Trémine, S. Guérandel, D. Holleville, A. Gérard, N. Dimarcq, and A. Clairon ; Proceedings of the 20th European Forum on Time and Frequency, Braunschweig, mars 2006 ; "New design of the compact cold atoms clock HORACE"

Proceedings of the 20th EFTF, 2006

New design of the compact cold atoms clock HORACE

F.X. Esnault,* S. Perrin, S. Trémine, S. Guérandel, D. Holleville, A. Gérard, N. Dimarcq, and A. Clairon
LNE-SYRTE, 61 avenue de l'observatoire 75014 PARIS FRANCE

In the compact cold atoms clock HORACE caesium atoms are successively laser cooled, submitted to a Ramsey microwave interrogation scheme and then detected by linear absorption directly inside the microwave cavity. The whole physics package and optical bench have been entirely redesigned to optimize such an in-situ detection and to perform a normalization scheme. Main efforts have been concentrated on technical issues such as magnetic shielding, microwave cavity polishing and tuning, use of fast mechanical switches to realize the optical sequence.

I. INTRODUCTION

The aim of the HORACE project is to build a compact cold atoms clock for on-board systems. The HORACE clock takes benefit from cold, and therefore slow, atoms to realize all the interactions inside the microwave cavity. Using laser cooling techniques allows to reduce the volume of the clock to a few liters with an expected short term frequency stability in the range of $\sigma_y = 10^{-13}$ @ 1s under micro-gravity environment.
We will describe the new experimental set up including physics package, the new functionalities of the optical bench and the tuning process of the microwave cavity. Then a brief overview of the operation sequence will be presented.

II. THE EXPERIMENTAL SET UP

A. Physics package

The whole physics package has been entirely redesigned to perform a detection by linear absorption directly inside the microwave cavity.
The apparatus is made of laser-soldered titanium on top of which a quartz bulb of 33 mm diameter is stuck by means of a vacuum resistant glue(see Fig.1). The quartz bulb which contains the caesium vapor is surrounded by a spherical copper cavity which has two functions. The first one is to perform the cooling of the caesium atoms thanks to an isotropic cooling scheme [1]. The second one is to be a microwave resonator for the clock interrogation.

Caesium atoms are injected into the experiment with a capillary underneath the cavity (not represented on Fig.1). Caesium pressure is adjusted by controlling the temperature of the caesium reservoir so that the absorption of probe beams is typically 2 % . Graphite are used along vertical axis to prevent caesium vapor in the TOF area and to minimize thermal atoms column along the vertical beam. The vacuum (3.10^{-9} mBar) is maintained by a very compact 2 L/s ion pump.

At the bottom of the device, a time of flight detection region is dedicated to cold atoms diagnostics only, and is not used in the clock sequence.

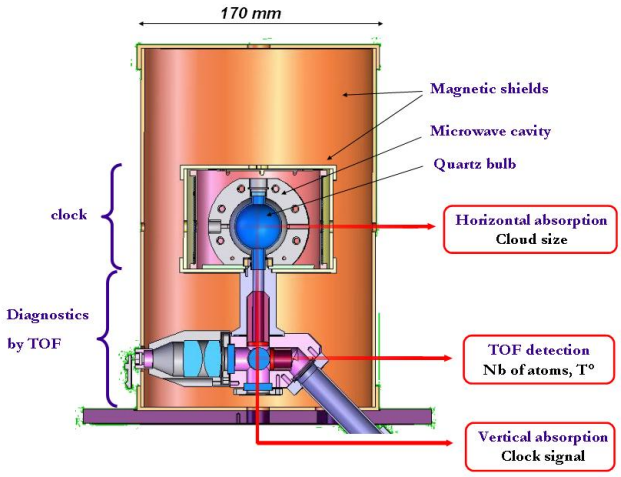

FIG. 1: Cross section of the whole physics package. The 3 detection beams are shown. Vertical beam is reflected with a mirror above magnetic shields (not represented)

Finally, two magnetic shields enclose the cavity region, realizing a longitudinal attenuation factor of about 5000 (see Fig.2).
Presently the volume of the physics package is about 5 liters, but without the diagnostic part, it finally could be reduced to 1 or 2 liters.

B. Detection beams

The HORACE clock uses 3 different detection beams all tuned to the $|F = 4\rangle \longrightarrow |F' = 5\rangle$ cycling transition (see Fig.1 and I). Singlemode and polarization maintaining fibers (SM/PM) provide a very clean gaussian intensity profile.

Firstly, an horizontal absorption beam crosses the cavity and is used to measure the cold atoms cloud size. Nevertheless due to the poor optical quality and

*Electronic address: francois-xavier.esnault@obspm.fr

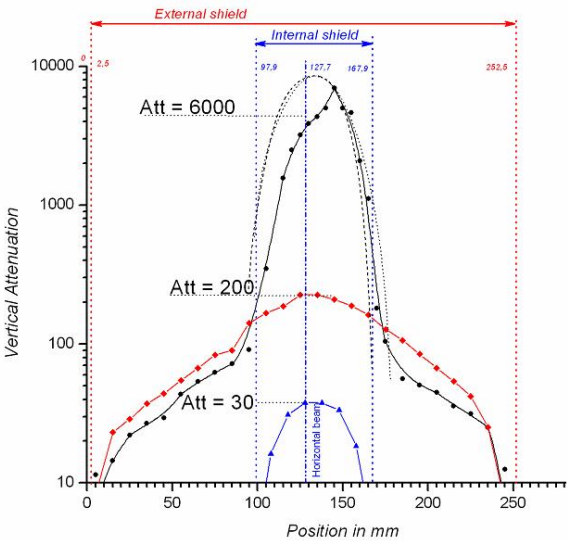

FIG. 2: Profile of the longitudinal magnetic attenuation. The distortion is due to asymmetrical magnetic shield covers. ▲ Internal shield only. ♦ External shield only. • Global attenuation. Dashed line is prediction from [5]

sphericity of the bulb along this direction it is not possible to use this beam for the clock operation.

Secondly, a simple time-of-flight detection is used to check and optimize the cooling parameters (number of cold atoms, temperature). The collection efficiency of the doublet (see Fig.1) is $\approx 3\%$.

Finally, a vertical absorption beam provides the clock signal. It takes benefit from the vertical holes required for caesium source and vacuum system. It crosses all the apparatus as shown on Fig.1 and is retro-reflected to prevent travelling waves which would heat cold atoms up.

The beam propagates 23 cm (and 60 cm due to retroreflection) from the collimator to the centre of the cavity, it has a waist of $w_o = 10$ mm and a diameter of 7 mm. Efforts have been made to reduce diffraction effects of the diaphragm by imaging it directly on the cold atoms cloud (centre of the cavity) for the direct and the retroreflected beams (see Fig.3 for the collimator design). This ensures that nearly identical intensity profiles are seen by the atoms in both directions. Fig.4 shows the difference between using the usual design (diaphragm on a collimated beam) and a design where the diaphragm is imaged on the atoms cloud.

	Horizontal	TOF	Vertical
Dim	$\phi = 2$ mm	1 mm x 12 mm	$\phi = 7$ mm
Power	10 μW	70 μW	60 μW
Config	travelling wave	lin $\perp$ lin	lin $\perp$ lin

TAB. I: HORACE detection beams

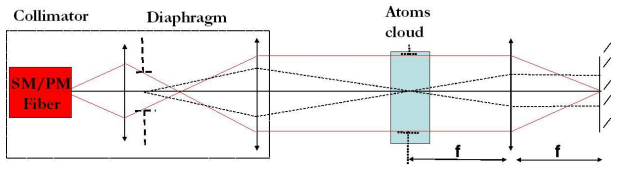

FIG. 3: Design of the vertical detection collimator. Dashed line shows how the diaphragm is imaged twice on the cold atoms cloud

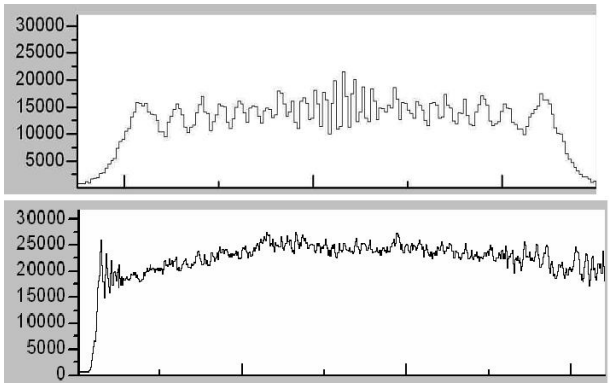

FIG. 4: Intensity profiles of vertical detection beam after 60 cm of propagation.
On top : The diaphragm creates important diffraction pattern on the collimated beam.
Bottom : Imaging the diaphragm nearly cancels diffraction effects.

C. Optical bench

The role of the optical bench is to generate and control the different laser beams used to cool, prepare and detect the atoms during a clock sequence.

To realize properly a normalization scheme a beam has been added. This beam, called depumper, is tuned to the $|F = 4\rangle \longrightarrow |F' = 4\rangle$ transition and provides optical pumping to the $|F = 3\rangle$ ground state.

The specific temporal operation of the HORACE clock requires to control very precisely the optical pulses. Moreover, as the atoms stay in the same place all along the clock sequence it is particularly critical to have a total extinction of the cooling light during the Ramsey interrogation. Any resonant photon (stray light from laser beams) destroys coherence between the clock states and consequently reduces signal to noise ratio. Unfortunately AOM can only provide an attenuation about -60 dB which is not sufficient. Furthermore, the optimum duration of detection pulses is about 1 ms which cannot be achieved with most of commercial shutters. Thus, to control the optical sequence we use fast mechanical scanners (Cambridge Technology ®) originally developed to deflect laser beams. Replacing the mirror by a very light razor blade and cutting the beam where it is focused (waist ≈ 50 μm) we are able to switch off the light in 80 ± 1 μs and to realize easily sub-ms optical pulses. One

should notice that those devices are completely tunable thanks to a CMOS analog driver, very compact ($L = 5$ cm, $\phi = 1$ cm) and quasi noiseless.

D. The microwave cavity

The microwave cavity of HORACE is the core of the experiment (see [2]). As all interactions take place inside it plays a double role. It's a reflecting cell for laser light and obviously a resonator for the microwave field.

FIG. 5: Spherical microwave cavity of HORACE. Internal diameter is $\approx$ 40 mm. Resonant with quartz bulb to the Cs transition.

1. *The optical cell*

The HORACE clock uses an isotropic cooling scheme. Laser beams are injected through a 1*6 standard multimode fiber coupler. This very robust kind of cooling scheme withstands up to 20 % power imbalances between fibers. The cavity is optically polished with a roughness of about $\lambda/10$. Using the high reflection coefficient of copper ($R = 96\%$) the isotropic light field is able to cool and trap 10^8 Cs atoms with a temperature as low as 2 μK.

2. *The microwave resonator*

The spherical cavity shown in Fig.5 is made of OFHC copper and has several holes. Two for the horizontal probe beam, six for multimode fibers (3D orthogonal config.), two for vertical probe beam and two slits for microwave evanescent coupling. It is resonant for a TE_{011} mode at 9.192 GHz shown in Fig.6. As the quartz bulb is inside the cavity , it shifts the resonance frequency. Unfortunately, making of quartz bulb is not reproducible (blown from a quartz tube) and each bulb is different from another so that the shifts induced are several hundreds of MHz. This implies that each cavity is to be tuned with a given bulb. The tuning of the cavity is realized in two steps. The coarse tuning is achieved by polishing the cavity until its resonance is about 1 MHz beyond Cs transition (ie : 9.193 GHz). The fine tuning is realized by adjusting the temperature of the cavity. As the copper expands with temperature, the resonance frequency decreases (-150 KHz/°C). The temperature of the cavity is then regulated with a commercial PID few degrees above room temperature (typ : 25°C). Finally,with the quartz bulb the quality factor is $Q \approx 3000$.

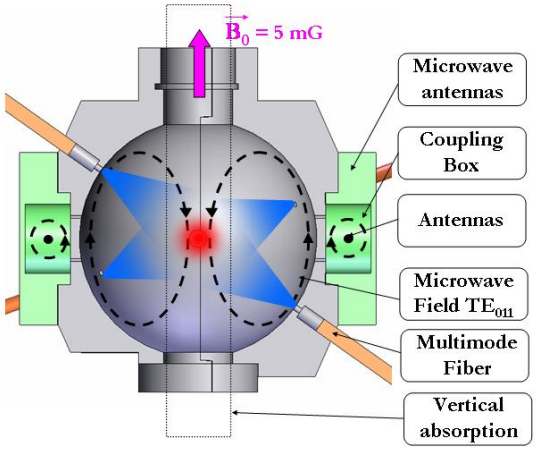

FIG. 6: Picture of the resonant microwave field and the evanescent coupling. Cooling light feeding and vertical absorption beam are also represented. Quartz bulb is not shown here.

III. OPERATION SEQUENCE AND SIGNAL PROCESSING

The clock sequence of HORACE is quite simple and represented on Fig.7 with typical parameters.

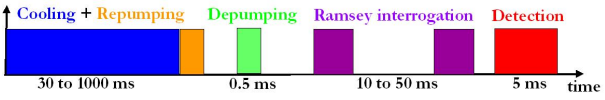

FIG. 7: Typical clock sequence. Long cooling time are used during diagnostics of cold atoms samples

The main difference from previous version of the experiment is the detection scheme. Clock signal is no longer derived from TOF signals but is obtained by measuring the absorption of cold atoms in each clock state. This type of detection allows to normalize the calculation of transition probability by measuring the population of the two clock states. It has been described in [2] and [3]. Thermal atoms which are present in the cavity contribute significantly to the absorption signal. So to extract the useful signal due to cold atoms only we have to substract the thermal background.

This is done with a short sequence of 3 pulses. First we detect the absorption of cold atoms and thermal

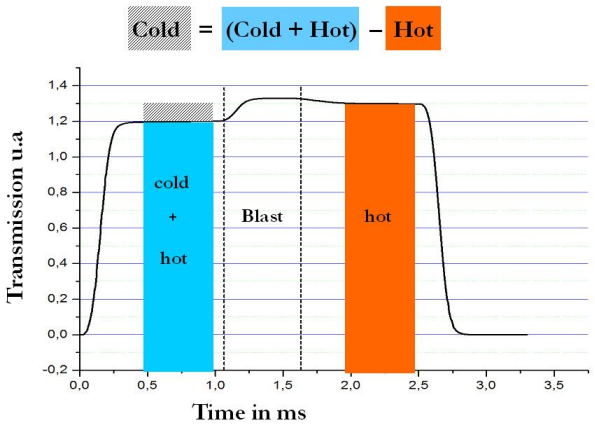

FIG. 8: Pulsed sequence of detection by absorption. This sequence shows the detection of a single population. The whole detection sequence has been detailed in [3].

background, then we blast the cold atoms using a blue shifted laser and then we detect the contribution of thermal background only (see Fig.8). The difference of the two absorption measurements (areas) gives the cold atoms signal and rejects environmental low-frequency noises such as laser intensity fluctuations.

IV. CONCLUSION

We have been able to perform both in situ detection and normalization sequence. We obtained very preliminary Ramsey fringes shown in [4]. Next step will be to optimize the detection sequence (4 optical pulses, 1 microwave π-pulse) to minimize losses of cold atoms.

Acknowledgments

We would like to thank D. Horville from GEPI / Observatoire de Paris for precious advices on ZEEMAX simulation (optical design software) during the collimator design. This work is supported by the French space agency CNES. F.X. Esnault is grateful to CNES and Thales Electron Devices (TED) for providing research studentship.

[1] S. Tremine, S. Guerandel, D. Holleville, N. Dimarcq, A. Clairon, *Development of a compact cold atom clock*, In Proc. of the FCS, Montreal, Canada (2004).
[2] S. Tremine, S. Guerandel, D. Holleville, N. Dimarcq, J. Delporte, A. Clairon, *Short term stability limitations in a compact cold atom clock*, In Proc. of the 19th EFTF, Besancon, France (2005).
[3] S. Tremine, S. Guerandel, D. Holleville, N. Dimarcq, J. Delporte, A. Clairon, *Limitations to the short term frequency stability in a compact cold atom clock*, In Proc. of the FCS , Vancouver, Canada (2005).
[4] N. Dimarcq, FX. Esnault, S. Perrin, S. Tremine, S. Guerandel, D. Holleville, J. Delporte, A. Clairon, *Estimate of the compact cold atom clock Horace frequency stability*, In Proc. of the 20th EFTF , Braunschweig, Germany (2006).
[5] TJ Sumner, JM Pendlebury and KF Smith *Conventional magnetic shielding*, J. Phys. D :Appl. Phys 1095-1101 (1987).

Proceedings of the 20th EFTF, 2006

Recent results on a pulsed CPT frequency standard

F. Dahes,* T.Zanon, S. Guerandel, E. de Clerc and N. Dimarcq
LNE-SYRTE – Observatoire de Paris 61, avenue de l'Observatoire – 75014 Paris – France
**Electronic address:* fariza.dahes@obspm.fr

We recall recent results using pulsed interrogation CPT scheme and report a theoretical study of the hyperfine coherence relaxation rate which is a limitation to clock stability as well as continuous excitation or pulsed regime method. The hyperfine coherence relaxation of caesium in a cylindrical cell filled with buffer gas is plotted versus following experimental parameters: the sealing pressure, cell dimensions and temperature. The coherence relaxation is minimized at 41rad/s for a sealing pressure of 11 Torr, with a cell radius of 2 cm and a length of 10 cm. Then the collisional pressure shift of caesium is studied to evaluate impact of the second buffer gas introduced in the cell on the CPT frequency resonance shift.

1. INTRODUCTION

We have developed a new interrogation technique using laser pulses inducing coherent population trapping (CPT).
Coherent Population Trapping (CPT) is a well known effect already used to produce narrow atomic resonances below 100 Hz in a three-level atomic system with buffer gas [1], [2]. The interrogation method usually involves continuous excitation of two ground states defining the Raman transition coupled to a common excited state by two coherent laser fields. Interference between amplitudes of transition in the two optical pumping channels cancels both fluorescence and absorption when the Raman resonance condition $\delta_R=0$ is fulfilled.
In this paper, important experimental details and results are recalled from previous work, in particular the pulsed interrogation CPT method. Then optimized experimental conditions are presented from calculation of hyperfine coherence relaxation rate due to different types of collisions in the atomic system with buffer gas.

II. EXPERIMENTAL SET UP

The experimental scheme is shown in Figure 1. Two coherent laser beams are emitted from two extended cavity laser diodes, with a frequency offset equal to 9.192 GHz (caesium clock transition frequency). The two laser sources are phase-locked. This method allows us: i) independent adjustment of frequency, intensity and polarization for each laser beam, and ii) getting two optical frequencies only, without other sidebands that generate distortion and frequency shifts on the CPT resonance. The master laser is frequency locked to the $6S_{1/2},F=4\leftrightarrow 6P_{1/2},F'=3$ D_1 line by saturated absorption in a vapour cell. The slave laser is phase locked to the master with a tunable frequency offset. Both beams are superposed on a polarizing beam splitter cube. One output provides the reference beat note at 9.2 GHz, and the other is sent to the atomic cell through an acousto-optical modulator. Previously, the cell at room temperature was filled with cesium vapour with 23 Torr N_2 buffer gas which was responsible for a collisionnal shift of the CPT resonance frequency.

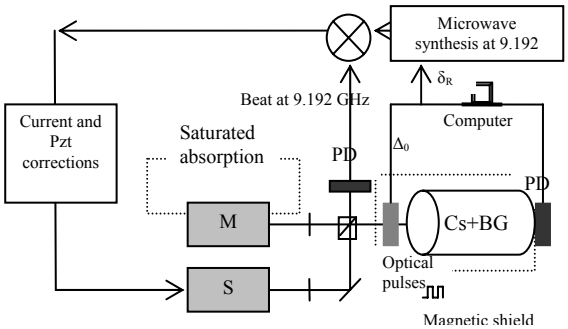

Figure1. Two phase-coherent laser beams (M and S) are emitted in lin-per-lin configuration through a beam splitter which one output is sent to a cell with caesium and buffer gases (BG) under a magnetic field, and which other one is sent to a detector that provides a microwave beat note.

Another relevant buffer gas is added to avoid such a frequency shift. A 20µT longitudinal static magnetic field is created by a surrounding solenoid and the whole physics package is magnetically shielded. With orthogonal linear polarizations, the laser beams parallel to the magnetic field make a double-lambda

configuration [3].

III. PULSED CPT INTERROGATION

To get clock signals with narrow line widths, two approaches are possible. On the one hand, continuous CPT interaction can be used at low laser intensity, since the width of this resonance is linearly dependent with the intensity, but eventually gives poor S/N. On the other hand, pulsed CPT interaction at high laser intensity has been demonstrated to give good S/N, inspired from earlier work [4], where line widths no longer depend on laser intensity but scale as 1/(2T). In our case, cesium atoms in the vapour cell are interrogated with a CPT pulse sequence [5]. The light pulse durations are controlled by an acousto-optical modulator. The time pulse sequence is achieved with an optical preparation pulse during τ followed by a free evolution time T in the dark. The intensity measurement is performed at a time τ_m after application of another light pulse.

By combining lin-per-lin polarizations with the pulsed CPT method, high contrast and narrow width signals were recorded as in Fig2.[5] We have to note that two regimes govern the measured transmitted intensity, and these regimes are determined by the choice of τ_m . For short τ_m, the transient atom-laser state is being pumped by spontaneous emission in the so-called dark state. In the transient regime, the oscillating Raman-Ramsey fringes are modulated by the Rabi envelope. For long τ_m, the atom-laser state evolves to the asymptotic situation where all the atoms are trapped in the dark state. In this stationary regime, the Lorentz signal width is determined by optical saturation.

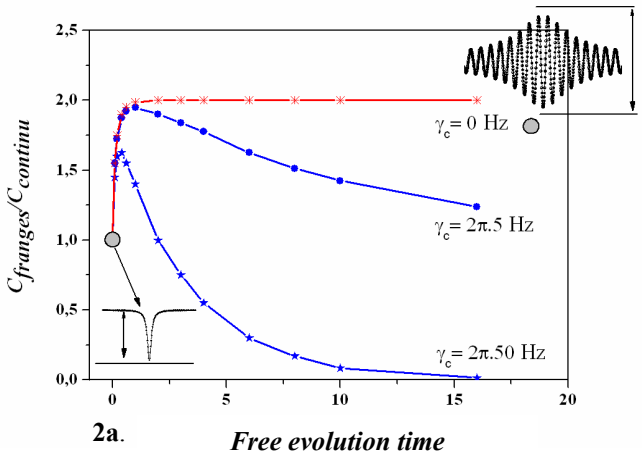

Figure 2.a. Gain on signal CPT contrast we obtain by CPT pulse method (in comparison to continuous excitation) for each γ_c value. The contrast decreases by increasing the detection pulse delay.

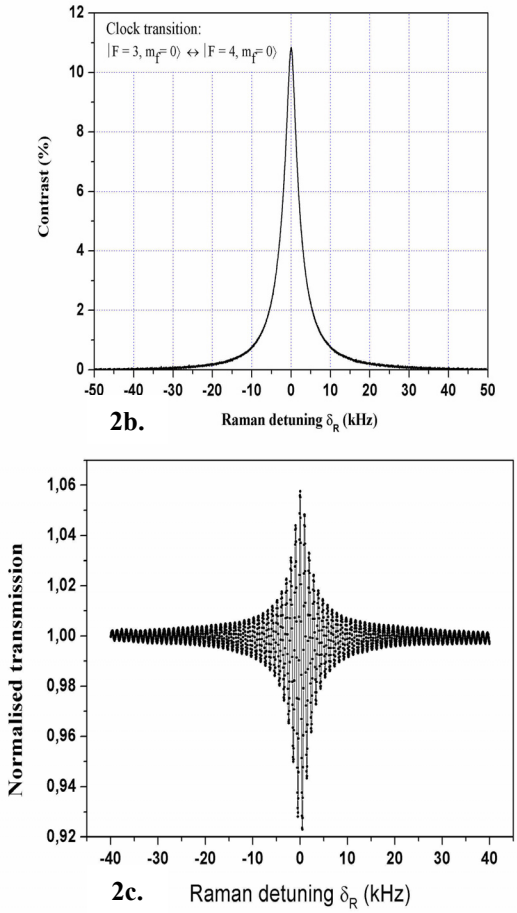

Figure 2.b. Continuous CPT absorption across resonance. The curve exhibits a Lorentz profile. **2.c.** Experimental saturated Raman-Ramsey fringes obtained with 5 ms preparation time and 5µs measurement time..

A time sequence optimization is given by measuring the central fringe contrast as a function of the three durations (τ, τ_m, T) separately in the sequence [6]. High contrast fringes (up to 14%) with small line widths (down to 60 Hz) were obtained. The pulse sequence was optimized for long preparation time (5ms), high laser intensities (a few µW/cm^2) and very short measurement time. The later the measurement the upper the hyperfine coherence relaxation and consequently the decreasing of the signal contrast.

IV. OPTIMIZATION OF PARAMETERS TO MINIMIZE THE HYPERFINE COHERENCE RELAXATION RATE

It is important to note that the hyperfine coherence relaxation rate play an important role in a CPT pulsed regime or a continuous excitation. In the first case this relaxation decreases the CPT signal contrast and in the second case it reduces the CPT signal Q-factor. In this paragraph we present a minimization of coherence relaxation by an optimization of

experimental parameters resulting from calculations.

Collision processes

Experiments with alkali-atoms in presence of buffer gases in the cell allow achieving a Lamb-Dicke regime. Interest of this confinement is to give the atoms a diffusion motion. The relaxation of the coherence ρ_{12} in the cell can be described by the following equation:

$$\frac{d}{dt}\rho_{12} = D\nabla^2\rho_{12} - K\rho_{12} \quad (1),$$

$D = D_0 \frac{P_0}{P}$ is the diffusion coefficient of the buffer gases and $K = L_0 \overline{v_r} \sigma \frac{P}{P_0}$ is the hyperfine coherence relaxation rate due to the buffer gas collisions with alkali atoms. L_0 is the Loschmidt coefficient, $\overline{v_r}$ is the relative velocity of the alkali and the buffer gas atoms, σ is the cross section collision between alkali and buffer gas atoms, P and P_0 are respectively the total and the reference pressure of the buffer gas.

A detailed solution of equation (1) and relevant data are found in ref [7]. By this way the atoms have a longer interaction time with beams. Without buffer gases, at room temperature, the hyperfine coherence would be lost essentially during collision processes with the cell walls. Three essential collision processes are in competition to relax hyperfine coherence. The total relaxation γ_{Total} is given by these three contributions:

$$\gamma_{Total} = \gamma_{SE} + \gamma_{Wall} + \gamma_{BG} \quad (2),$$

evaluated versus the operating temperature T, the sealing pressure P_s, the cell length L and the beam radius a (fig.5).

From expression for one buffer gas in literature [7] we derive relaxation rates for two gases:

Spin-exchange relaxation γ_{SE} :

$$\gamma_{SE} = \left(\frac{6I+1}{8I+4}\right)\sigma_{SE}\overline{v_{C_s-C_s}}\, d_{C_s} \quad (3)$$

I is the nuclear spin of Cs, d_{Cs} is the cesium density in the cell given by the perfect gas law with the saturated vapour pressure of cesium given by Taylor and Langmuir [9];

Wall-relaxation γ_{Wall}

$$\gamma_{Wall} = \left[\left(\frac{2.405}{a}\right)^2 + \left(\frac{\pi}{L}\right)^2\right] D \quad (4)$$

$D = \frac{D_{0N_2} D_{0Ar}(1+r)}{rD_{0N_2} + D_{0Ar}} \frac{P_0 T_s}{T_0^{3/2}} \frac{\sqrt{T}}{P_s}$ is the diffusion coefficient for a two-buffer-gas mixing (from Maxwell-Stefan equation), a and L are respectively the beam radius and the cylindrical cell length;

Buffer-gas relaxation γ_{BG}

$$\gamma_{BG} = L_0 \frac{\overline{v}_{Cs-N_2}\sigma_{N_2} + r\overline{v}_{Cs-Ar}\sigma_{Ar}}{1+r} \frac{P_s T}{P_0 T_s} \quad (5),$$

$\overline{v}_{Cs-N_2}$ and $\overline{v}_{Cs-Ar}$ are the mean relative velocity between cesium atoms and buffer gas atoms, T_s is the sealing temperature, P_0 and T_0 are reference pressure and temperature for which the diffusion constants D_{0N_2} and D_{0Ar} were measured, and r is the $\frac{P_{Ar}}{P_{N_2}}$ ratio determined by a specific condition we will discuss further.

We studied the experimental parameters that minimize the hyperfine coherence relaxation.

At room temperature a sealing pressure P_{smin} minimizes the coherence relaxation rate $\gamma_{totalmin}$ (Figure 3.a.) corresponding to the minimum on the total effects curve, and spin exchange rate has a fixed value. Care is required to control the sealing pressure of the cell because of difficulty to prevent impurities insertions into the cell.

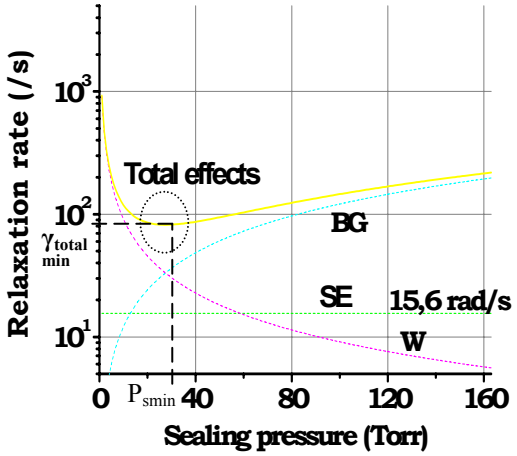

Figure 3.a. BG: buffer gas collisions ; SE : spin exchange collisions fixed at 15.6 rad/s at room temperature (295.15K) ; W : wall collisions. The encircled point corresponds to the optimum: Ps_{min}=27Torr; $\gamma_{totalmin}$=80rad/s.

For a cylindrical cell, we can note that elongated cells are more preferable than flat cells (Figures 3.b and 3.c). Indeed, collision rate with the wall is inversely proportional to the mean free path l of atoms:

$$l = \frac{2La}{L+a} \quad (6)$$

For a fixed value of a the mean free path l increases by elongating the cell. Moreover the bigger the cell radius the bigger the increasing of the mean free path. As a consequence collision rate is reduced by elongating cells.

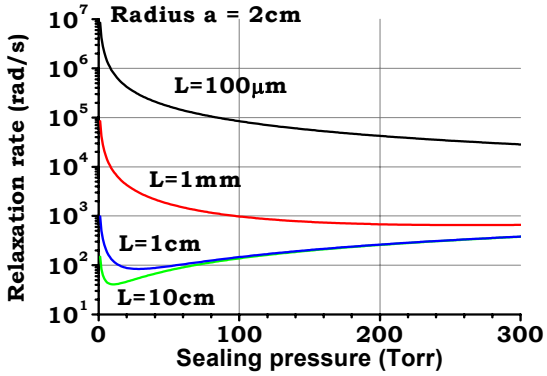

3. b.

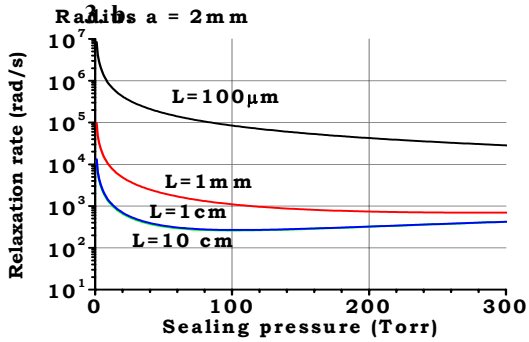

3. c.

Figure 3. b. and c. Total relaxation versus sealing pressure. The necessary sealing pressure to minimize γ_{total} is smaller for a cell radius much smaller than the cell length than for a cell radius of the order of the cell length. For a=2cm and L=10cm, the optimum is obtained for P_s=11Torr with $\gamma_{totalmin}$= 41rad/s. For a=2mm and L=10cm, the optimum is obtained for P_s=101Torr with $\gamma_{totalmin}$= 260rad/s.

Finally, by heating the cell even if buffer gas collisions tend to cross wall collisions (**Figure 3. d**.), spin exchange collisions dominate these contributions at a temperature before this crossing occurs. Thus, temperature is not a relevant parameter to minimize coherence relaxation.

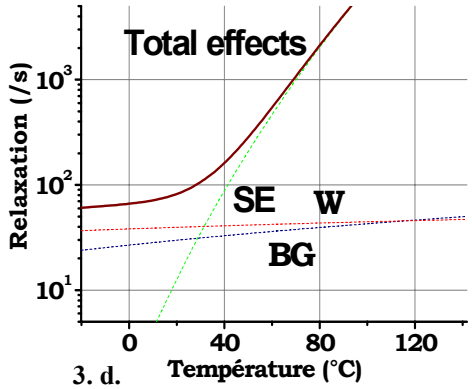

3. d.

Figure 1. d. By increasing temperature, total relaxation increases dramatically when spin exchange curve crosses buffer gas and wall relaxation curves.

Colisionnal shift

The N_2 buffer gas introduces a collisionnal shift of the CPT resonance frequency. Let us denote this shift by $\Delta\nu_{BG}$:

$$\Delta\nu_{BG} = P_{N_2}\left(\beta_{hf}^{N_2} + \delta_{hf}^{N_2}(T-T_0) + \gamma_{hf}^{N_2}(T-T_0)^2\right) \quad (7)$$

where $\beta_{hf}^{N_2}, \delta_{hf}^{N_2}, \gamma_{hf}^{N_2}$ are the collisionnal pressure shift coefficients of the alkali-atoms colliding with the N_2 buffer gas P_{N_2} is the nitrogen pressure in the cell and T_0 is the reference temperature for which collisionnal shift coefficients were measured [7], [8]. This equation exhibits two terms, linearly and quadratically depending on the temperature. It is possible to eliminate sensitivity to temperature by a relevant choice of a second buffer gas: the idea is to compensate the N_2 collisionnal shift by another buffer gas shift which pressure coefficient is of the opposite sign. If we denote the two buffer gas pressure ratio by r:

$$r = \frac{P_{Ar}}{P_{N_2}} \quad (8)$$

we can find a theoretical condition on this ratio r to eliminate the sensitivity in temperature by solving:

$$\frac{\partial}{\partial T}\Delta\nu_{BG} = 0 \quad (9)$$

r is then defined by the collisionnal pressure shift coefficients [8]:

$$r = \frac{2P_sT_s\gamma_{0s}^{N_2}(T_0-T)-P_0\delta^{N_2}T_0}{2P_sT_s\gamma_{0s}^{Ar}(T-T_0)+P_0\delta^{Ar}T_0} \quad (10)$$

The γ coefficients have been measured only for rubidium and that is the reason why in literature the quadratic temperature dependence is given up in the calculations for caesium and only the linear temperature dependence is eliminated by this relevant pressure ratio condition:

$$r = -\frac{\delta_{hf}^{N_2}}{\delta_{hf}^{Ar}} \quad (11)$$

where the δ pressure shift coefficients have been measured by different groups [7]. For rubidium it is possible to plot the collisionnal shift versus temperature with rubidium γ values and we assume a similarity with the case of rubidium atoms in the same conditions. Indeed, rubidium atoms have been more studied, and the quadratic pressure shift coefficients are known [7]. From the following expression for a two-buffer-gases mixing:

$$\Delta\nu_{BG} = \frac{P_s T_s}{T_0} \times$$
$$[\ (\beta_{0s}^{N_2} + r\beta_{0s}^{Ar}) + (\delta_{0s}^{N_2} + r\delta_{0s}^{Ar})(T - T_0) +$$
$$(\gamma_{0s}^{N_2} + r\gamma_{0s}^{Ar})(T - T_0)^2\ ] \quad (12)$$

the collisionnal shift of rubidium is plotted versus temperature in figure 6.

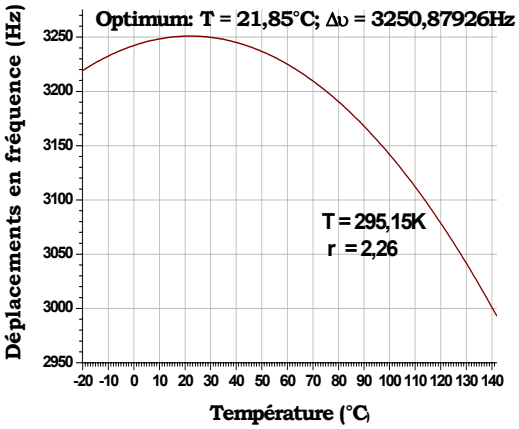

Figure 6. Theoretical curve of Rb collisional shift. The optimum corresponds to the relevant value of r for which one the collisionnal shift is constant at room temperature.

By solving the equation $\frac{\partial}{\partial T}\Delta\nu_{BG} = 0$, the idea is to fix the optimal temperature at room temperature and to find the pressure ratio *r* condition which minimizes the sensitivity of $\Delta\upsilon_{BG}$ to temperature. This pressure ratio needs complete data of pressure collisional shift coefficients. In the case of rubidium, the collisional shift versus temperature curve (Figure 6) shows the optimum corresponding to a collisional pressure shift independent on temperature. Such a situation is expected for cesium but a pressure ratio value is not predictable in this case because data are missing.

V. CONCLUSION

We have recalled double-lambda scheme and pulsed-CPT method efficiency in the clock stability by increasing CPT signal contrast and decreasing line width broadening. The optimized pulse sequence is obtained with a long preparation time (5ms) and a short measurement time.

Theoretical calculations were realized to optimize experimental parameters that minimize the hyperfine coherence relaxation in a cylindrical cell. Coherence relaxation is minimized (41 rad/s) for a sealing pressure of 11Torr, with a cell radius of 2cm and a length of 10cm.

Finally, a way to avoid sensitivity of collisional pressure shift to temperature is possible by a relevant choice of the *r* ratio between the two buffer gases pressure, and data existing only for rubidium it is possible to predict this ratio for this alkali. Extrapolation can be done if we assume similarity of caesium case to rubidium.

Acknowledgements

We would like to thank DGA for supporting this research.

REFERENCES

[1] S. Brandt, A. Nagel, R. Wynands, and D. Meschede, ″Buffer gas induced line width reduction of coherent dark resonances to below 50 Hz″, Phys. Rev. A, vol. 56, pp. R1063-R1066, (1997).

[2] M. Merimaa, T. Lindvall, I. Tittonen, and E. Ikonen, ″All-optical atomic clock based on coherent population trapping in $^{85}R_b$ ″, J. Opt. Soc. Amer., vol. B220, pp. 273-279, (2003).

[3] T. Zanon, S. Guérandel, E. de Clercq, D. Holleville, N. Dimarcq and A. Clairon ,Phys. Rev. Letters, 94, 193 002 (2005) ; "High contrast Raman-Ramsey fringes with CPT pulses in a Cs vapour cell"

[4] M.S. Shariar, P.R. Hemmer, D.P. Katz, A. Lee, M.G. Prentiss, ″ Dark state based three-element vector

[5] T. Zanon, S. Tremine, S. Guerandel, E. de Clercq, D. Holleville, N. Dimarcq, A. Clairon, ″Observation of Raman-Ramsey fringes with optical CPT pulses″, IEEE Trans. Instr. Meas., vol 54, N°2 p 776 (2005).

[6] T. Zanon, S. Guerandel, E. de Clercq, D. Holleville, N. Dimarcq, A. Clairon; "Time sequence optimization and optical detuning effects in a Raman-Ramsey frequency standard", in Proc. 19th European Frequency and Time Forum (2005).

[7] [153] J. Vanier; C. Audoin, The quantum physics of atomic frequency standards (Adam Hilger, Bristol, 1989).

[8] F. Strumia, N. Beverini, A. Moretti, G. Rovera, "Optimization of the buffer gas mixture for optically pumped Cs frequency standards," Freq. Contr. Symp. , 468 (1976).

[9] J. Taylor and I. Langmuir, Phys. Rev. 51, 753 (1937).

Proceedings of the 20th EFTF, 2006

Evaluation of the CPT pseudo-resonance scheme for all-optical ^{87}Rb frequency standard

*G. Kazakov[1], **E. Breschi[3], B. Matisov[1], I. Mazets[2], C. Schori[3], C. Affolderbach[3], J. Delporte[4], G. Mileti[3]
[1]St. Petersburg State Polytechnic University, Polytechnicheskaya 29, St. Petersburg 195251, Russia
[2]A.F. Ioffe Physico-Technical Institute, Polytechnicheskaya 26, St. Petersburg 194021, Russia
[3]Observatorie Cantonal Neuchâtel, rue de l'Observatoire 58, CH-2000, Neuchâtel, Switzerland
[4]Centre National D'Etudes Spatiales, avenue Belin 18, Toulouse 31401, France
**Electronic address:* kazjor@rambler.ru
***Electronic address:* evelina.breschi@ne.ch

We investigate a novel approach to all-optical frequency standards, based on a combination of the coherent population trapping effect and signal discrimination at the maximum of absorption of the probe radiation. The physics underlying this approach is dark resonance splitting caused by interaction of the nuclear magnetic moment with an external magnetic field. Theoretically it has been shown that this approach under ideal conditions can lead to an important enhancement of the clock stability. Here we present an experimental evaluation of the scheme in view its future application in the domain of vapor-cell atomic clocks. The present results point out that high-performances short-term stability can be obtained only with a high spectral quality light source. In contrast, for our compact and low-consumption setup, the shot-noise limited short-term stability calculated is about 10^{-12} $\tau^{-1/2}$, which is comparable to those presently measured for typical CPT-based atomic clocks.

I. INTRODUCTION

Some applications of atomic clocks, for instance in telecommunications, navigation and positioning, require stable and small frequency standards. For this reason, vapor-cell frequency standards have been largely studied. Most of commercially available standards are based on optical-microwave double resonance mechanism, but atomic clocks based on Coherent Population Trapping (CPT) are a promising alternative (see 0 and references therein). These two methods have been compared for Cs [2] and Rb [3] vapor cell. It as been demonstrated that each excitation scheme has its own advantages and disadvantages: the general situation sees the CPT excitation scheme more favorable for the application in miniaturized frequency standards, because of the absence of the microwave cavity. However, for high-performance compact clocks the better results have been reached with the double-resonance scheme [4], [5].

The main factor which limits the performance of the CPT-based atomic clock is the small amplitude of the CPT signal, which affects the short-term stability. The widely applied CPT interaction scheme using a two-frequency circularly polarized laser light field, has the disadvantage of putting most of the atoms into a "trap state" (or "pocket") that does not contribute to the clock signal. To avoid such pockets, different excitation schemes have been suggested [6]-[12]. In particular, Taichenachev and co-workers [11] showed that a high-contrast dark resonance can be obtained when co-propagating laser waves with parallel linear polarizations are resonant with the transitions between the ground state hyperfine sublevels and excited state F_e=1. In this case, however, the reference transition is between Zeeman sublevels with $|m_F|\neq 0$. In order to reduce the influence of external magnetic field fluctuations, it has been proposed [12] to use the maximum of absorption between two near degenerate CPT lines as a frequency reference. The splitting of the two CPT signals depends on the nuclear g-factor and the magnetic field strength. In this communication we report on our model and first experimental results on this pseudo-resonance scheme. The signal-to-noise ratio of the CPT pseudo-resonance has been studied to estimate the short-term stability reachable with this excitation scheme and the most important noise sources will be briefly discussed

II. EXCITATION SCHEME

Let us consider a ^{87}Rb gas cell excited by a two frequency laser field. We chose ^{87}Rb because its D_1 line satisfies the condition described in [11]. Moreover, the wavelength of the ^{87}Rb D_1 line is 795 nm and can be reached with commercial diode lasers. To achieve CPT, the two laser frequency components are tuned in resonance with the F_g=1 → F_e=1 and F_g=2 → F_e=1 transitions of the D_1 line. Both components are *linearly* polarized in the *same* plane, and a magnetic field parallel to the laser propagation vector is applied. In this case the working sublevels $|F_g = 1, m = 0\rangle$ and $|F_g = 2, m = 0\rangle$ belong to a "closed loop" interaction contour, see Fig.1 below. The strong dependence of the CPT resonance parameters on the

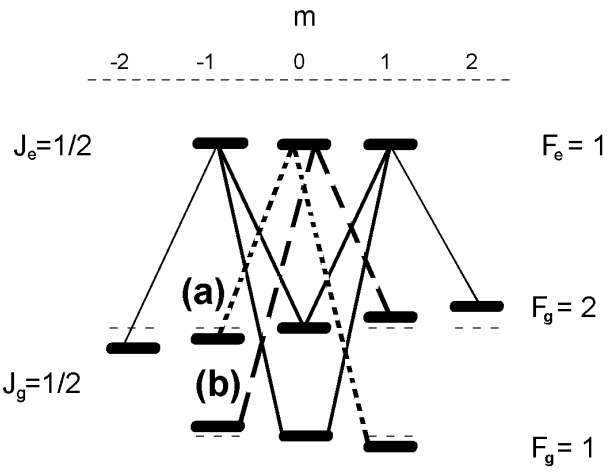

Fig. 1. Scheme of optically induced transitions in the ^{87}Rb atom, case of F_e=1. "Closed loop" involving the clock (0-0) transition is shown by thick solid lines. Additional Λ-schemes are shown by dotted and dashed lines.

total phase over such a closed contour [13] results to the absence of CPT on the working sublevel in this particular case.

However, there are two additional Λ-schemes, corresponding to quadrupole ($|\Delta m| = 2$) two-photon transitions and involving the pairs of Zeeman sublevels $\{|F_g = 1, m = 1\rangle, |F_g = 2, m = -1\rangle\}$ and $\{|F_g = 1, m = -1\rangle, |F_g = 2, m = 1\rangle\}$, labeled (a) and (b) on Fig.1, respectively. The splitting between these ground state Zeeman sublevels in the weak magnetic field B is [12]:

$$\omega_{a,b} = \omega_{hfs} \pm \varepsilon \frac{2 g_I \mu_B}{\hbar} B + \frac{3 g_J^2 \mu_B^2}{8 \omega_{hfs} \hbar^2} B^2,$$

where ω_{hfs} is the hyperfine splitting frequency the ground state HF components in the absence of the magnetic field, $\mu_B = e\hbar/(2m_e c)$ is the Bohr magneton, $\varepsilon = m_e / m_p$, m_e is the electron mass, m_p is the proton mass, g_J and g_I are the electronic and the nuclear Lande factor, respectively.

Note that one may erroneously treat these resonances as magnetically insensitive in the linear approximation if one does not take into account the magnetic moment of the nucleus, since the linear Zeeman shifts due to the electronic magnetic moment for each state in the pair $|F_g = 1, m = \pm 1\rangle$, $|F_g = 2, m = \mp 1\rangle$ are the same.

Therefore the magnetic field shifts the positions of the corresponding dark resonances which are close to the clock transition, due to the nuclear magnetic momentum. These shifts are symmetric (to the second order Zeeman effect) with respect to the position of the $|F_g = 1, m = 0\rangle \leftrightarrow |F_g = 2, m = 0\rangle$ clock transition.

Let us consider the line shape dependence on the magnitude B of magnetic field. If the magnetic field shift is small (in comparison with single resonance width) the two dark resonances are unresolved, see Fig.2, the dotted curve.

For intermediate values of B they are resolved partially, thus forming a minimum in the transmission spectrum between them, see Fig. 2, the solid curve. The position of the minimum coincides with the frequency of the $|F_g = 1, m = 0\rangle \leftrightarrow |F_g = 2, m = 0\rangle$ clock transition and can be implemented in a discriminator of an all-optical frequency standard. This structure formed between two maxima in the transmission spectrum, is referred to as a pseudo-resonance [12].

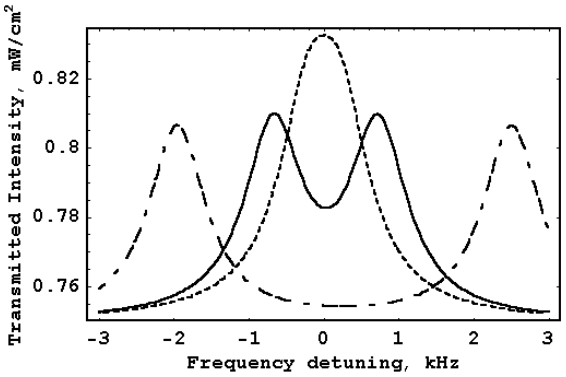

Fig. 2. Calculated transmission spectrum of the cell with the parameters specified in the text. Incident radiation intensity $U_0 = 1$ mW/cm^2 and a half of intensity is in the two resonant laser frequency components. The dotted curve corresponds to B = 0.05 G, the solid ones corresponds to B = 0.25 G and the dotted-dashed curve corresponds to B = 0.8 G.

Further increase of B makes the two dark resonances fully resolved. As a result the bottom of pseudo-resonance dip becomes flat, which is unsuitable for purpose of a frequency standard (see Fig. 2, the dotted-dashed curve).

III. EXPERIMENTAL SETUP

In our realization of the experimental setup, compactness and the simplicity have been privileged with respect to other aspects, motivated by the perspectives for application in atomic clocks. The multi-frequency laser spectrum is obtained by direct modulation of the injection current of a Vertical Cavity Surface Emitting Laser (VCSEL), emitting at the ^{87}Rb D_1 line (795 nm).

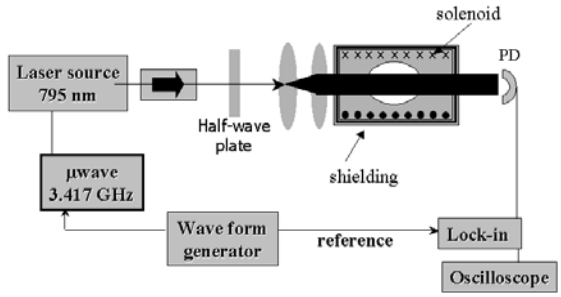

Fig. 3 Experimental Setup.

The VCSELs have been largely developed for their use in optical communications. Even if they have low power levels and broad spectra, VCSELs are more and more used in high precision spectroscopy. Remarkable results in the field of non-linear spectroscopy with VCSEL have already been achieved working on the hyperfine resonance of Cs atoms [14], [15]**.** The VCSEL used in our experiment has been characterized by means of a beat signal with an extended cavity diode laser. The total power emission on the ^{87}Rb D_1 line is about 0.3 mW and the line-width is (100 ± 20) MHz. The characteristic that makes VCSELs interesting for this kind of experiments is the very high current tuning coefficient (its value measured for our laser is -143 GHz/mA) which allows to reach phase-modulation index close to unity at high frequencies (3 to 4 GHz).
The block diagram of the experimental set-up is shown in Fig. 3. The VCSEL injection current was modulated at ν_M = 3.417 GHz via a commercial rf generator without further amplification. The generator was used as an analog sweeper. The ν_M was in turn modulated at $\nu_{Lock\text{-}in}$, whose signal has been used as reference for phase-sensitive lock-in detection. The polarization of the beam emitted from the VCSEL was linear. In order to enhance the interaction volume, a beam expander was placed in front of the cell, and the resulting diameter of the beam was about 0.4 cm. The cell (length and diameter of 1 cm), containing pure ^{87}Rb and 15 mbar of N_2, was placed inside a μ-metal cylinder, in order to reduce the influence of spurious magnetic fields. The longitudinal magnetic field was produced by a solenoid. The temperature of the cell was stabilized at 60°C. The light transmitted through the atomic sample was collected on a photo-diode whose output was sent to the lock-in amplifier and monitored by an oscilloscope. The optimal lock-in detection condition has been evaluated by studying the de-modulated CPT signal as a function of $\nu_{Lock\text{-}in}$.
A simple way to determine the VCSEL's phase-modulation index is to use the ^{87}Rb absorption lines as reference. An example is presented in Fig. 4. In the inset of the Fig. 4, the ^{87}Rb D_1 line absorption spectrum recorded by irradiating the atomic sample with single-mode laser light is shown, to be compared with the spectrum obtained with the modulated VCSEL.

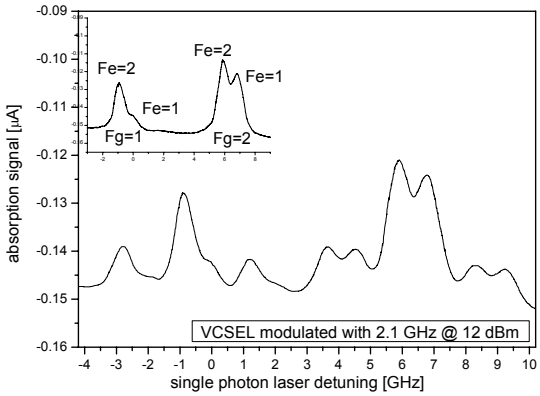

Fig. 4: The absorption spectrum of the VCSEL without rf modulation (inset) and at the frequency ν_M = 2 GHz with 12 dBm amplitude.

IV. EXPERIMENTAL STUDY OF THE SIGNAL-TO-NOISE RATIO.

The short-term frequency stability of an atomic frequency standard can be empirically estimated from the recorded signal and detection noise features. Therefore our evaluation of the CPT pseudo-resonance excitation scheme is based on an analysis and optimization of the signal-to-noise ratio.

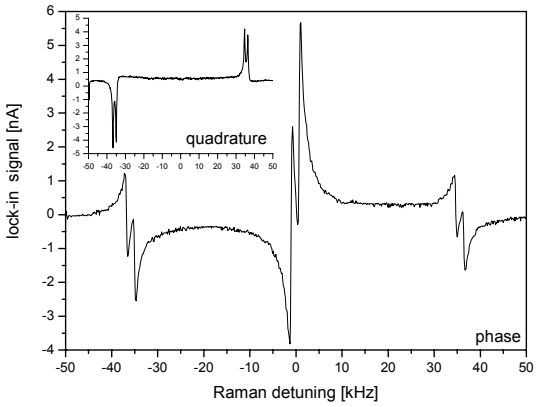

Fig. 5: The lock-in in-phase and quadrature signal for a CPT pseudo-resonance ($\nu_{Lock\text{-}in}$= 35 kHz).

We found experimentally that both the amplitude and the linewidth of the lock-in signal do not depend on $\nu_{Lock\text{-}in}$ (in the range from few hundred of Hz until few tens of kHz). It is, however, worth to notice that the interpretation of the lock-in signal is different depending on the $\nu_{Lock\text{-}in} / \Gamma$ ratio, where Γ is the line-width of the spectral feature of interest. In particular when $\nu_{Lock\text{-}in} / \Gamma > 1$, as in our case, the contributions to

the detected signal of different laser side-bands are well separated and both the in-phase and quadrature lock-in signal are needed to reconstruct the absorption signal [16]. An example of the experimental lock-in in-phase and quadrature signals are shown in Fig. 5. However, only the in-phase signal shows a dispersive shape and can be used as error signal for the clock reference. For simplicity, in the following we take into account only the in-phase signal of the lock-in amplifier.

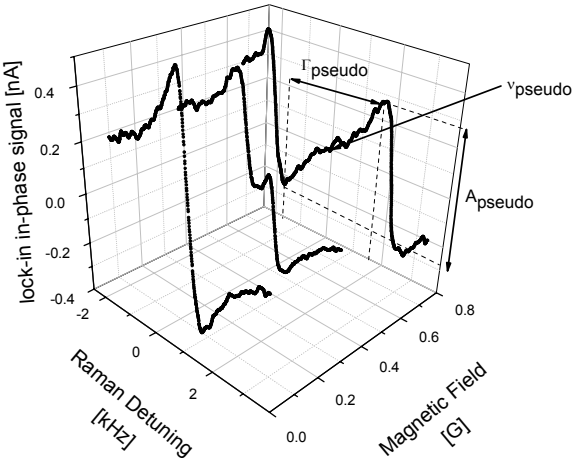

Fig. 6: Experimental dependence of the pseudo-resonance on the magnetic field, confirming the model prediction (Fig. 2). For $B < 0.1$ G the CPT signals are degenerate and no pseudo-resonance is observed.

In Fig. 6 the pseudo-resonance lock-in signal is shown for different strengths of the magnetic field B, 0.1 G < B < 0.7 G. The pseudo-resonance parameters of interest for an atomic clock are indicated and are: the amplitude A_{pseudo}, the line-width Γ_{pseudo}, and the central frequency ν_{pseudo}. Typical values are $A_{pseudo} \approx 100$ nA and $\Gamma_{pseudo} \approx 700$ Hz.

The noise on the detector has been measured to point out the main noise sources. In Fig. 7 the noise of the detector in the dark is compared with the noise at the maximum of absorption of the transition towards the excited level $F_e = 1$ for the VCSEL not modulated and modulated with $\nu_M = 3.417$ GHz at 13 dBm (which corresponds to a phase modulation index of about 1.8). The noise level has also been recorded for different values of laser detuning and no significant difference has been found. For the time being, the most important noise contribution is due to the modulation of the laser, and investigation is in progress in order to understand and reduce this effect.

From the analysis of the lock-in signal behavior and the detection noise measurements we found that optimized signal-to-noise ratio is obtained with $\nu_{Lock\text{-}in} > 5$ kHz where the detection noise is lower. In our CPT experiment, signal-to-noise ratios as high as 700 in 1 Hz bandwidth have been obtained.

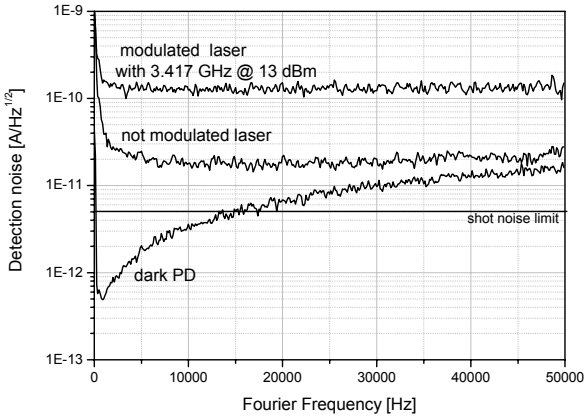

Fig. 7: Detection noise measured for the dark signal, and the interacting laser field tuned to the maximum of the transition toward F_e=1 for both the un-modulated and the modulated VCSEL.

As the largest possible amplitude of the pseudo-resonance is equal to the amplitude of the conventional CPT signal, this value of the signal-to-noise ratio is the same for both standard CPT or the optimized pseudo-resonance.

The short-term stability of an atomic reference in terms of Allan deviation can be predicted by the empirical expression [17]:

$$\sigma_{Allan} \approx \frac{0.2}{Q(S/N)} \tau^{-1/2}$$

where Q is the resonance quality factor and S/N is the signal-to-noise ratio. Table 1 lists the values of σ_{Allan} obtained in this way for both the experimental results and for the model taking into account the real experimental parameters or the optimal conditions.

	σ_{Allan}
Experiments	$3\times10^{-11}\tau^{-1/2}$
Theory (shot-noise limited, experimental conditions)	$10^{-12}\tau^{-1/2}$
Theory (shot-noise limited, optimal conditions)	$10^{-14}\tau^{-1/2}$

Table 1: Comparison between the σ_{Allan} estimated from the experiment and calculated both for the experimental parameters and for the optimal conditions (interacting laser intensity 0.4 mW/cm^2, laser linewidth 10 MHz, beam diameter 1 cm, 5 mbar Ne buffer gas).

The experimentally estimated short-term stability and its corresponding theoretical prediction are in satisfactory agreement if one considers that the present detection noise is 20 times higher than the shot-noise. This additional noise includes contributions from laser

intensity noise and FM-AM noise conversion in the vapor cell. However, the most important noise contribution here stems from the 3.4 GHz modulation applied to the VCSEL, as can be seen from Fig. 7. Furthermore, it is worth to notice that the calculated signal amplitude is slightly bigger than the measured one (see Fig. 8 below) which also contributes to the discrepancy in stability given in Table 1.

The predicted stability for the optimal model case differs considerably from both estimated values previously discussed for the experimental situation. This discrepancy is due to the fact that a certain number of parameters used in the experiment are far from their values for the ideal case. The comparison between the models allowed to identify the critical parameters for the optimization of this excitation scheme for frequency standard applications. In particular the main difference between the ideal case and the experiments is related to the characteristic of the light source: in the ideal case the light source is composed by two frequencies that interact separately with the two arms of the Λ-scheme. In the real case the VCSEL modulated contains, at least, the carrier, the first and the second-order side-band frequencies. Among them, only the first order side-bands are used for preparing the CPT pseudo-resonance signal while the other frequencies (especially the strong carrier which falls between the two HF transitions) merely add a bias signal on the detector. Thus these non-resonant side-bands contribute on one hand to a reduction of the signal contrast, on the other hand to an enhancement of detection noise. Moreover, the excitation of atoms by the carrier and the second order side-bands can also give rise to further CPT states with different phase, that represent a loss mechanism with respect to the reference signal. These contributions are not simple to quantify because it is not possible to isolate them from the experimental point of view and, presently, they are not taken into account into the model. Another relevant difference between the ideal case and the real one is the laser linewidth, which for the VCSEL used is 10 times broader than in the ideal situation. This difference in the laser linewidth value is very critical because the contribution of the transitions towards $F_e=2$ is not negligible for a broad laser linewidth even when the laser one-photon detuning corresponds to the maximum of transition towards $F_e=1$. Consequently, the CPT (and pseudo-resonance) amplitude is strongly reduced. Finally, the CPT contrast in our experiment is also low because the maximum power level of the VCSEL in our experiment is limited, presently 5 times smaller than on the ideal case.

V. PSEUDO-RESONANCE CONTRAST VERSUS LASER DETUNING

For a theoretical analysis of the pseudo-resonance amplitude dependence as a function of the laser detuning, we use the density matrix approach. We take into account the hyperfine (hf) and Zeeman structure of the ^{87}Rb D_1 line, as well as the exact values of the probabilities of the optically-induced one-photon transitions and relaxation of the optically excited states. Effects of the thermal motion of atoms (Doppler broadening) and the laser line width Γ_{laser} = 100 MHz also have been taken into account.

We present our calculations for the experimental parameters (dimension, temperature of the cell and so on) used in the experiments. For ^{87}Rb at 60° C the Doppler width of the D_1 line is about 450 MHz. The values of collisional quenching of the excited state [18] and of the pressure broadening of the Rb D_1 line at 15 mbar of N_2 (about 220 MHz [19]) were also used. For estimation of the relaxation rate Γ of coherences between the different ground state hyperfine- and Zeeman sublevels we use the methods described in [20], [21]. It results to $\Gamma \approx 90\ Hz$. The depolarization rate in ground state is assumed to be equal to Γ.

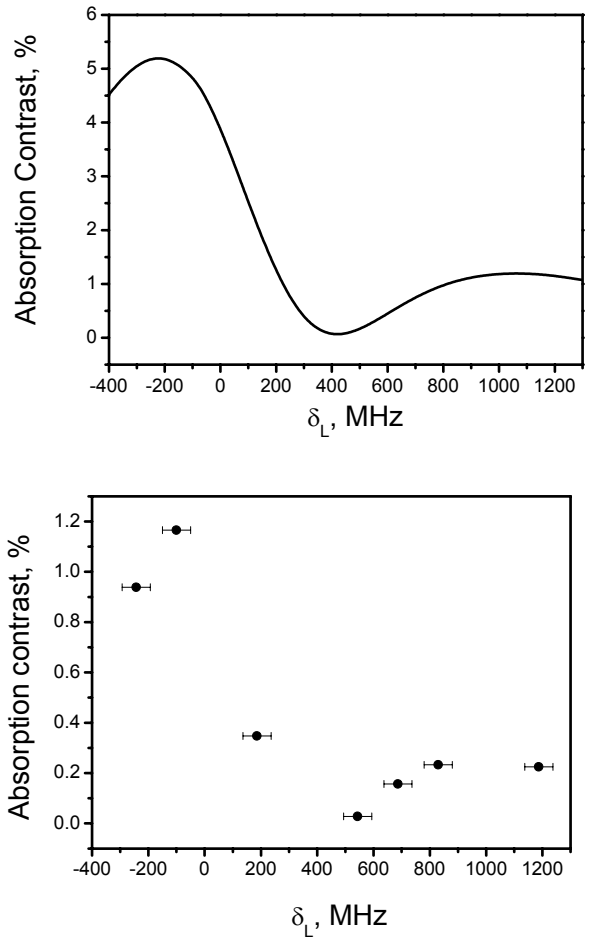

Fig. 8. Absorption contrast versus the laser detuning δ_L. The upper plot is the result of the numerical calculation while the lower plot shows the experimental results.

Since the splitting of the two hyperfine sublevels of the excited state is $\omega^*_{hfs} \approx 812$ MHz, we must also take into account the hyperfine sublevels of the excited states with $F_e = 2$. That causes the $|F_g = 1, m = \pm 1\rangle \leftrightarrow |F_e = 2, m = \pm 2\rangle$ and $|F_g = 2, m = \pm 1\rangle \leftrightarrow |F_e = 2, m = \pm 2\rangle$ transitions that partially destroy the CPT and reduces the dark resonance amplitude.

In this case both resonances (corresponding to the Λ-schemes shown on Fig. 1 (a) and (b)) are identical and their positions are symmetrical with regard to zero.

Let us consider the behavior of the dark resonance amplitude and its absorption contrast as a function of the laser detuning. Here, we define the Absorption contrast as the ratio between the amplitude of the CPT signal (or the pseudo-resonance signal) and the Doppler absorption under the same conditions. We provide numerical calculations for the case when the intensities of both the laser components are equal and the total laser field intensity in resonance sidebands is U = 0.15 mW/cm^2. The longitudinal magnetic field was B = 0.8 G. In this case the CPT linewidth was about 800 Hz and the shift induced by the magnetic field was 4.5 kHz then both resonances are resolved, and have the same amplitude, the dotted-dashed curve in Fig. 2. The calculated dependence of the absorption contrast for CPT resonance as a function of the laser detuning δ_L is shown in Fig.8, together with the experimental data.

One can see that the absorption contrast amplitude has two maxima. The maximum for $\delta_L \approx -100$ MHz corresponds the laser tuned in resonance with the $F_g = 1,2 \leftrightarrow F_e = 1$ transitions, and the maximum for $\delta_L \approx 900$ MHz corresponds the laser tuned in resonance with the $F_g = 1,2 \leftrightarrow F_e = 2$ transitions.

VI. CONCLUSIONS

We have studied theoretically and experimentally the properties of CPT pseudo-resonance. Our theoretically prediction for the pseudo-resonance parameters under optimal conditions makes this approach interesting in view of application in vapor-cell atomic clocks. For the time being, the experimental estimation for the short term stability is quite far from the best theoretical prediction. By comparing the experiments and the model, it has been shown that, presently, the main limiting factor to reach an high performance frequency standard based on this pseudo-resonance mechanism is due to the requirements in the spectral quality of the light source. After our analysis it seems that the pseudo-resonance mechanism can be interesting for high performance vapor-cell frequency standards at laboratory level, where the spectral quality of the light source can be improved by using a larger and more elaborated setup, for example two phase-locked laser and/or filtering of the optical spectrum. However, with respect to a simple and compact vapor-cell atomic clocks with low power consumption, as required in many applications, the currently available laser diodes do not show the required spectral characteristics (power, linewidth, etc.) and thus limit the obtainable short-term stability.

Acknowledgements

The authors are pleased to acknowledge the financial support of the INTAS-CNES (project No. 03-53-51-75), the Switzerland National Science Foundation (project No 200020-105624/1) and the Program Russian Leading Scientific Schools (grant 9879.2006.2).

Finally, we thank V. Yudin and S. A. Zibrov for the helpful discussion.

REFERENCES

[1] J. Vanier, Appl. Phys. B **81**, 421 (2005)

[2] R. Lutwak, D. Emmons *et al.*, 34th Annual Prec. Time and Time Int. Syst. App. Metting, 1 (2002).

[3] J. Vanier, M. Levine *et al.*, 6th Symposium on Frequency Standard and Metrology, 155 (YEAR)

[4] G. Mileti J. Deng F. L. Walls, IEEE J. Quantum Electron. **34**, 2 (1998)

[5] C. Affolderbach, F. Droz and G. Mileti, IEEE Trans. Inst. Meas. **55**, 2 (2006)

[6] A. V. Taichenachev, V. I. Yudin, V. L. Velichansky *et al*., JETP letters **80**, 236 (2004)

[7] S. V. Kargapoltsev, J. Kitching, L. Hollberg, *et al.,* Laser Phys. Lett. **1**, 495 (2004).

[8] G. Kazakov, I.Mazets, Yu. Rozhdestvensky, *et al.,* Eur. Phys. J. D **35**, 3, 445 (2005)

[9] A. B. Post, Y.-Y. Jau, N. N. Kuzma *et al*., Phys. Rev. A **72**, 033417 (2005)

[10] T. Zanon, S. Guerandel, E. de Clerq *et al*., Phys. Rev. Lett. **94**, 193002 (2005)

[11] A. V. Taichenachev, V. I. Yudin, V. L. Velichansky *et al*., Pis'ma v ZhETF **82**, 449 (2005)

[12] G. Kazakov, B. Matisov, I. Mazets, *et al*., Phys. Rev. A. **72**, 063408 (2005)

[13] D. V. Kosachev, B. G. Matisov, Yu. V. Rozhdestvensky, J. Phys. B **25,** 2473 (1992)

[14] R. Wynands and A. Nagel Appl. Phys. B **68**, 1 (1999)

[15] S. Knappe, V. Shah, P. D. D.Schwindt *et al*., Appl. Phys. Lett. **85,** 9, 1460 (2004)

[16] R.Wynands and A.Nagel, J. Opt. Soc. Am. B **16**, 10, 1617 (1999)

[17] J. Vanier, IEEE Trans. Instrum. Meas. **IM-30**, 4, 277 (1981)

[18] J. Vanier, C. Audoin, The quantum physics of atomic frequency standards (Hilger, Bristol, 1989)

[19] M. V. Romalis, E. Miron, and G. D. Cates, Phys. Rev. A **56**, 4569 (1997)
[20] M. Gornyi, D. Markman, B. Matisov, Radiotehnika i Elektronika **50**, 1780 (1985)
[21] E. Arimondo, Phys. Rev. A **54**, 2216 (1996)

Proceedings of the 20th EFTF, 2006

Double radio optical resonances in thermal ^{87}Rb vapor

G. Kazakov[1]*, B. Matisov[1], I. Mazets[2], Yu. Rozhdestvensky[3], J. Delporte[4], G. Mileti[5], and V. Zholnerov[6+]

[1]St-Petersburg State Polytechnic University, Polytechnicheskaya 29, St-Petersburg 195251, Russia
[2]A. F. loffe Physico-Technical Institute, Polytechnicheskaya 26, St-Petersburg 194021, Russia
[3]Institute for Laser Physics, Birzhevaya liniya 12, St-Petersburg 199034, Russia
[4]Centre National d'Etudes Spatiales, avenue Belin 18, Toulouse 31401, France
[5]Observatorie Cantonal de Neuchâtel, rue de l'Observatoire 58, CH-2000, Neuchâtel, Switzerland
[6]Russian Institute of Radionavigation and Time, Rastrelli square, 2, St-Petersburg 193124, Russia
*Electronic address: kazjor@rambler.ru +Electronic address: office@rirt.ru

In this paper we compare two different excitation schemes of rubidium gas-cell frequency standard. The first scheme is based on the one laser optical pumping and the second scheme is based on the "two-lasers" optical pumping firstly proposed by J. Deng for light shift compensation. We present stability estimations for both schemes supposing that the gas cell has 15 mb of N_2 and the laser line width is about 100 MHz. Our calculations do not show the expected significant improvement of the stability in the case of "two-lasers" scheme. This result is connected to the broadening of the absorption line. To avoid this broadening one needs to use a buffer gas pressure around 1 mb and a laser line width of 10 MHz or less.

1. INTRODUCTION

Quantum frequency standards are important for a variety of applications. There are two essential problems in this area: 1) the maximum value of stability, that can be, in principle, obtained and 2) the size of the standard, which should occupy a reasonable volume. E.g. atomic clocks, needed for space navigation and positioning, must have a stability of about 10^{-14} at ½ day and a volume about of 1-10 L. These parameters, in principle, can be obtained with frequency standards, which use an alkali atoms gas cell as reference element. In this case, there are two well-known known methods for obtaining such a stability. The first — the quantum frequency standard based on optical pumping by laser beam when the RF field is applied to transition between the two $m=0$ ground state sublevels (working sublevels) $|1\rangle = |F_g = 1, m = 0\rangle$ and $|2\rangle = |F_g = 2, m = 0\rangle$, (here F_g is the total angular momentum in ground state, and m — its projection). The second way uses the effect of coherent population trapping (CPT) [1,2,3]. For optimization of the CPT resonance parameters (width, amplitude, contrast) we recently proposed new excitation schemes using laser pumping [4], and a new pseudoresonance mechanism of all-optical frequency standard operation [5]. The comparison of these schemes with traditional ones involving the circularly-polarized laser beam shows a significant improvement of the dark-resonance parameters. In this work we analyze different excitation schemes for quantum frequency standard based on optical pumping.

Short-term frequency stability of a Rubidium Frequency Standard (RFS) is directly related to the signal-to-noise ratio (S/N) of the microwave-induced (6834 MHz) optical signal which is proportional to the fractional atomic population difference between the two working levels $|1\rangle$ and $|2\rangle$ of ^{87}Rb. In the present RFSs this fractional population difference is not maximized. S/N can be improved by concentrating *all* of the atoms in *one* of the two working levels. Potentially, this could lead to a significant improvement in the short-term stability of RFSs.

Traditionally one-laser pumping schemes are used (see Fig.1.). In these cases atoms are pumped off from one of the working sublevels and therefore the atomic population difference between the working levels is attained. However, in these cases there are always some "idle" states ("pockets"), which can trap atoms. Atoms are accumulated in these levels and do not contribute anymore to the signal formation on the working transition. It leads to a drastic decrease of the fractional atomic population difference between two working levels and, therefore, to a decrease of the stability.

To solve this problem, "two-lasers" pumping can be used [6]. In this case it is possible to develop such excitation schemes (see Fig. 2.) that are characterized by absence of "pockets" and, therefore, a significant improvement of the fractional atomic population difference between two working levels is expected.

II. EXCITATION SCHEMES

In this communication we compare two different excitation schemes: one-frequency pumping scheme shown on Fig.1 (e), and "two-laser" pumping scheme

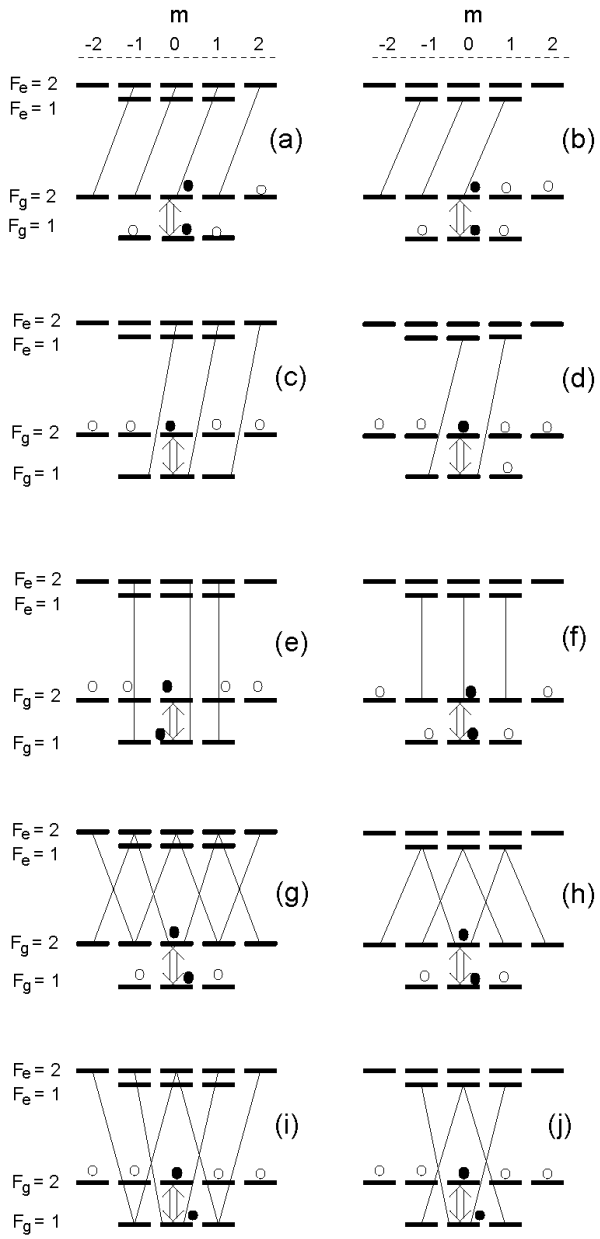

Fig.1. Different one-laser excitation schemes on ^{87}Rb D_1-line. Black circles show the working levels, white circles show "pockets". Optical induced transitions are shown by black lines and microwave transition is shown by arrow (negligible buffer gas broadening).

using π-polarized light shown on Fig. 2 (c). The second scheme is characterized by the absence of "pockets". Figure 3 shows an implementation of this scheme.

Let us suppose that ^{87}Rb atoms in a cell interact with the linearly-polarized "two-laser" field (the pumping field):

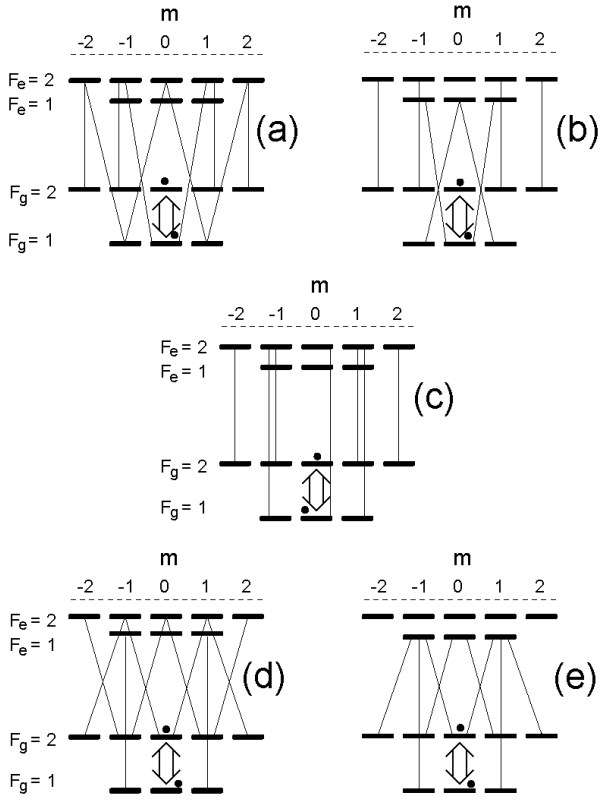

Fig.2. Different "two-laser" excitation schemes on ^{87}Rb D_1-line, characterized by the absence of trap states.

$$\vec{E}_{pump} = \frac{\vec{e}_z}{2}\left(E_1 \exp\left[i(k_1 x - \omega_1 t)\right] + E_2 \exp\left[i(k_2 x - \omega_2 t)\right]\right) + c.c. \qquad (1)$$

One of the components of this field (with frequency ω_2) is tuned on resonance with the $|F_g = 2\rangle \rightarrow |F_e = 2\rangle$ transition and the second (with frequency ω_1) component is tuned on resonance with the $|F_g = 1\rangle \rightarrow |F_e = 2\rangle$ transition, both of these transitions belonging to the D_1-line. In this case atoms are not pumped out from the working level $|2\rangle = |F_g = 2, m = 0\rangle$, since the corresponding Clebsch-Gordan coefficient and, hence, transition dipole matrix element is equal to zero. As a result, after a few optical pumping cycles (excitation followed by spontaneous relaxation of the optically excited state) atoms will be accumulated in the working level $|2\rangle$.

When we switch on a radiofrequency (microwave) field applied to transition $|1\rangle \rightarrow |2\rangle$, this field will move the

populations from level $|2\rangle$ to level $|1\rangle$, and therefore the laser field absorption will be increased. If we detune the frequency ω_{RF} of the radio field from the $|2\rangle \rightarrow |1\rangle$ transition frequency ω_{hfs}, the population of level $|1\rangle$ will be increased less, and laser field absorption will be decreased. So the laser field absorption has a maximum when $\omega_{RF} = \omega_{hfs}$, what we call the double radio optical resonance (DROR). Typical dependence of the photodetector signal as a function of the radio frequency detuning $\delta_{RF} = \omega_{RF} - \omega_{hfs}$ is shown on Fig. 4.

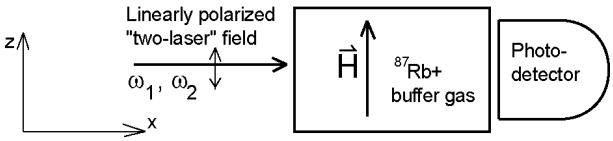

Fig.3. Spatial configuration realizing the scheme shown on Fig. 2 (c).

It should be noted that "two-laser" pumping schemes allow not only to collect all the atoms in one of the working sublevels, but also to avoid the hfs (hyperfine structure) light shift [6], i.e. the light shift connected with the change of hyperfine splitting constant in the laser field [7]. The light shift compensation is attained if the frequency difference $(\omega_1 - \omega_2)$ is equal to the hyperfine 0-0 transition frequency ω_{hfs}, and the intensities of two frequency components (or two lasers) satisfy the relation [6]:

$$U_1 / U_2 = 3/5, \qquad (2)$$

where U_1 and U_2 are the light intensities pumping the levels of $F_g = 1$ and $F_g = 2$ in the ground state respectively.

Note that the scheme shown on Fig. 2 (c) contains two Λ-schemes. One scheme involves the levels $|F_g = 1, m = -1\rangle$, $|F_e = 2, m = -1\rangle$ and $|F_g = 2, m = -1\rangle$, while the other scheme involves the levels $|F_g = 1, m = 1\rangle$, $|F_e = 2, m = 1\rangle$ and $|F_g = 2, m = 1\rangle$.

To avoid the unwanted CPT effect on these schemes the condition of CPT resonances should not be satisfied, i.e. this unwanted effect is absent for both these schemes if

$$\left| \omega_1 - \omega_2 - \omega_{hfs} \pm \frac{g_J \mu_B}{2\hbar} H \right| > W, \qquad (3)$$

where H is the static magnetic field, g_J is the electronic Lande factor, μ_B is the Bohr magneton, W is the DROR line width. Another possibility for avoiding these coherent effects consists in using a laser with non-correlated components, or two independent lasers.

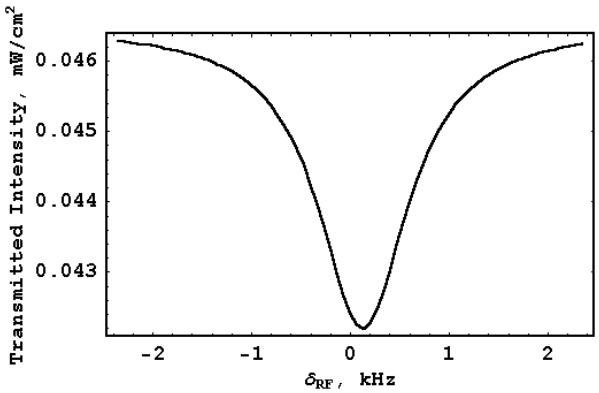

Fig. 4. Calculated transmission spectrum of the cell with the parameters specified in the text. Incident radiation intensity $U = U_1 + U_2 = 0.1$ mW/cm^2, $U_1 / U_2 = 3/5$, Rabi frequency of radio field $V_{RF} = 600\ s^{-1}$.

III. CALCULATIONS FOR THE GAS CELL WITH THE TYPICAL PARAMETERS

In this work we use the density matrix approach. We take into account the real hyperfine (hf) and Zeeman structure of the involved states as well as the exact values of the probabilities of the optically-induced one-photon transitions and relaxation of the optically excited states. Effects of the thermal motion of atoms (Doppler broadening) as well as the laser line width $\Gamma_{Laser} = 100$ MHz have also been taken into account.

We provide our calculations for the cylindrical gas cell with the following parameters: radius $R_c = 1$ cm, length $L_c = 2$ cm, temperature $T = 50°$ C, 15 mb of N_2 buffer-gas. The radius of laser beam in the gas cell is $R_b = 1$ cm.

For ^{87}Rb at 50° C the Doppler width of the D_1 line is about 450 MHz. The real values of collisional quenching of the excited state [8] and of the pressure broadening of Rb D_1 line (about 220 MHz [9]) were taken into account. For estimation of the relaxation rate Γ of coherences between the different ground state hyperfine- and Zeeman sublevels we use the methods described in [10,11]. It results to $\Gamma \approx 150\ s^{-1}$. The

depolarization rate in the ground state was supposed to be equal to Γ.

The detuning between the two hyperfine sublevels in the excited state is $\omega^*_{hfs} \approx 812$ MHz. We must take into account both hyperfine sublevels of the excited states with $F_e = 1$ and $F_e = 2$. It causes the light-induced transition $|F_g = 2, m = 0\rangle \leftrightarrow |F_e = 1, m = 0\rangle$. On one hand, this transition reduces the population on the level $|F_g = 2, m = 0\rangle$ and therefore reduces the amplitude of double radio optical resonance. On the other hand, it leads to the appearing of non-zero shift of DROR line for zero laser detuning. The dependence of this shift on the incident laser intensity and laser detuning is shown on Fig. 5.

One can see that for intensities of both laser components and $\delta_L \approx 170\,MHz$ (here the laser detuning $\delta_L = \omega_1 - \omega_{1,opt} = \omega_2 - \omega_{2,opt}$, where $\omega_{i,opt}$ is the frequency of the optical transition $|F_e = 2\rangle \rightarrow |F_g = i\rangle$) the shift disappears for any value of the total laser intensity.

In Fig. 6 we plot the population difference between the working sublevels $|1\rangle$ and $|2\rangle$. This result shows that the population difference for two-laser optical pumping and for one-laser optical pumping are approximately equal. The reason of it is the light-induced off-resonant transition $|F_g = 2, m = 0\rangle \leftrightarrow |F_e = 1, m = 0\rangle$ reducing the population difference.

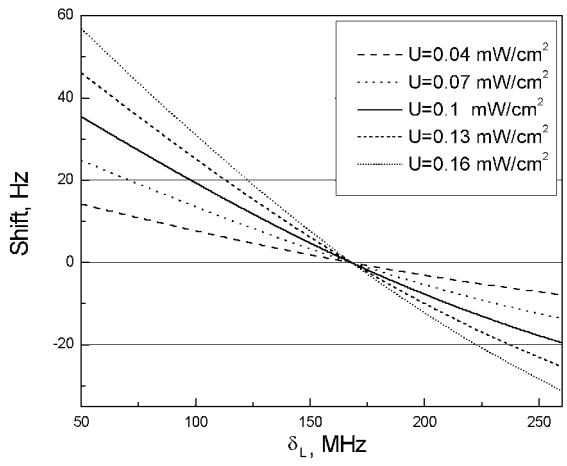

Fig. 5. Shift of the DROR line versus the laser detuning δ_L for different values of laser field intensity U. The relation of the laser field intensities is $U_1 / U_2 = 3/5$, $V_{RF} = 600$ s^{-1}.

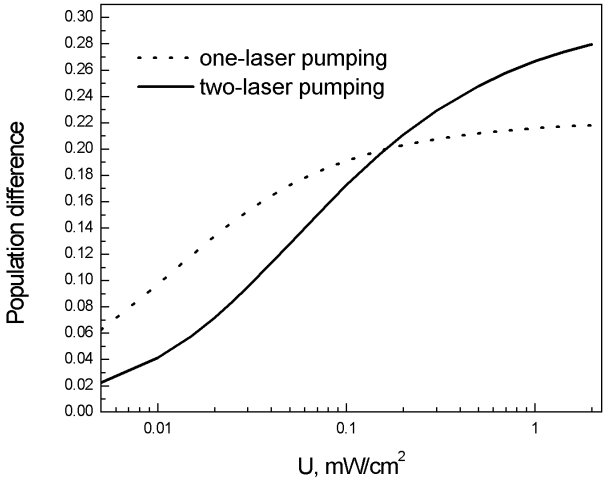

Fig. 6. Difference of population between the working sublevels $|1\rangle$ and $|2\rangle$ for the gas cell with "typical" parameters versus the total laser field intensity.

In Fig. 7 and Fig. 8 we plot the stability estimations [8] for the standard based on scheme 1(e) (Fig.7) and on the "two-laser" pumping scheme 2(c) (Fig.8) versus the total laser field intensity U for different Rabi frequencies V_{RF} of radio field. Integration time $\tau = 1$ s. Fig. 7 and Fig. 8 shows that the best stability for one-frequency as well as for "two-laser" pumping standard is about $6 \cdot 10^{-13}$ (Allan deviation for 1 s integration time).

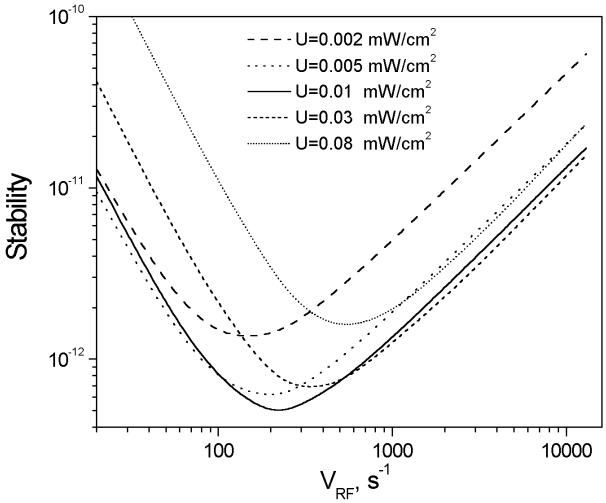

Fig. 7. Stability (Allan deviation for 1 s integration time) of the standard based on scheme Fig.1.(e) versus the total laser field intensity for different values of radio field Rabi frequency V_{RF}.

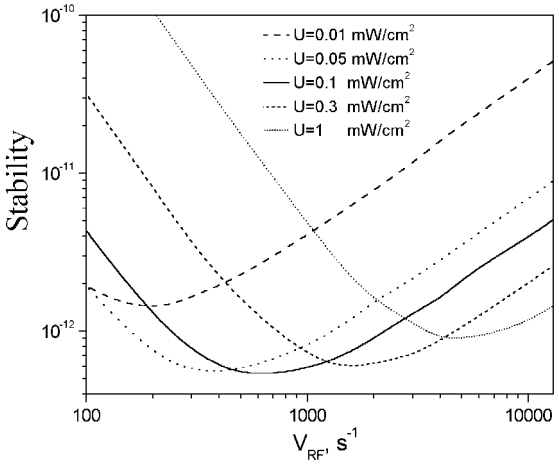

Fig. 8. Stability (Allan deviation for 1 s integration time) of the standard based on scheme Fig. 2(c) versus the total laser field intensity U for different values of radio field Rabi frequency V_{RF}. $U_1/U_2 = 3/5$.

IV. CALCULATIONS FOR THE GAS CELL WITH THE "IMPROVED" PARAMETERS

To improve the stability with two-laser pumping and to display its advantages one need to reduce the off-resonant transition $|F_g = 2,\ m = 0\rangle \leftrightarrow |F_e = 1,\ m = 0\rangle$. As it was shown on [12], the ratio of resonant transitions $W_{1,2}^{rez} \propto U_{1,2} \cdot G_2$, where $U_{1,2}$ is the intensity of the corresponding laser component,

$$G_2 = \sqrt{\frac{m}{2\pi T}} \int_{-\infty}^{+\infty} Y(\omega_1 + \Delta\omega) d\Delta\omega \int_{-\infty}^{+\infty} \exp\left(-\frac{m\upsilon_z^2}{2T}\right) \frac{\gamma'^2}{\gamma'^2 + (-k\upsilon_z + \Delta\omega)^2} d\upsilon_z,$$

whereas the ratio of the off-resonant transitions $W_{1,2}^{off-rez} \propto U_{1,2} \cdot G_1$, where

$$G_1 = \sqrt{\frac{m}{2\pi T}} \int_{-\infty}^{+\infty} Y(\omega_1 + \Delta\omega) d\Delta\omega \int_{-\infty}^{+\infty} \exp\left(-\frac{\upsilon_z^2}{\upsilon_T^2}\right) \frac{\gamma'^2}{\gamma'^2 + (\omega_{hfs}^* - k\upsilon_z + \Delta\omega)^2} d\upsilon_z$$

Here m is the mass of Rubidium atom, $k = \omega_1/c \approx \omega_2/c$, $Y(\omega)$ — normalized spectral distribution of the laser field intensity, υ_z is the z-projection of the atomic velocity, $\upsilon_T = 2T/m^2$, T — temperature (in the units of energy), γ' (about 210 MHz in our case) is half of the pressure-broadened transition width plus the laser line width [13], ω_{hfs}^* is the hyperfine splitting in excited state. In our case the ratio of $G_1/G_2 \approx 1/6$.

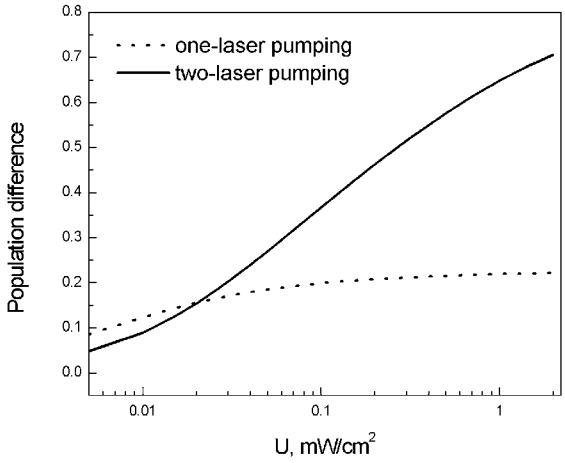

Fig. 9. Difference of population between the working sublevels $|1\rangle$ and $|2\rangle$ for the gas cell with the "improved" parameters versus the total laser field intensity.

One can see that to reduce the off-resonant transition $|F_g = 2,\ m = 0\rangle \leftrightarrow |F_e = 1,\ m = 0\rangle$ one needs reduce G_1/G_2, i.e. to reduce γ', due to reduction of the collision broadening and the laser line width.

To investigate the potential of this improvement we perform the calculations for a cylindrical gas cell with the following "improved" parameters: radius $R_c = 1.25$ cm, length $L_c = 1.25$ cm, temperature $T = 50°\,\mathrm{C}$, 3 mb of Ne buffer-gas. The radius of the laser beam in the gas cell is $R_b = 1.25$ cm. We suppose that the laser line width is equal to 10 MHz. In this case $G_1/G_2 \approx 1/80$, i. e. the off-resonant transitions are sufficiently suppressed.

In Fig. 9 we plot the population difference between the working sublevels $|1\rangle$ and $|2\rangle$ for this gas cell. One can see that in this case we can obtain the sufficient improvement of our DROR parameters using the two-laser pumping. Figs. 10 and 11 show the short-term stability estimations for the standard based on scheme 1(e) (Fig.10) and on the "two-laser" pumping scheme 2(c) (Fig.11) when we use the gas cell with the improved parameters. Fig. 10 and Fig.11 show that the best short-term stability for one-frequency pumping standard is about $3 \cdot 10^{-13}$ whereas for two-frequency laser pumping standard is about $6 \cdot 10^{-14}$.

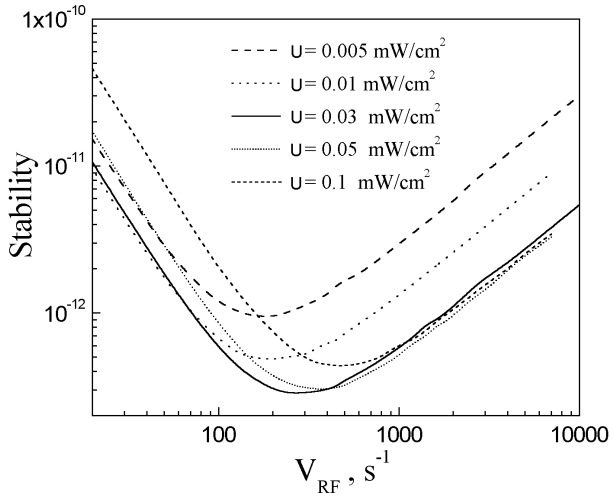

Fig. 10. Stability (Allan deviation for 1 s integration time) of the one-laser pumping standard versus the radio field Rabi frequency V_{RF} for different values of total laser field intensity U for the gas cell with "improved" parameters.

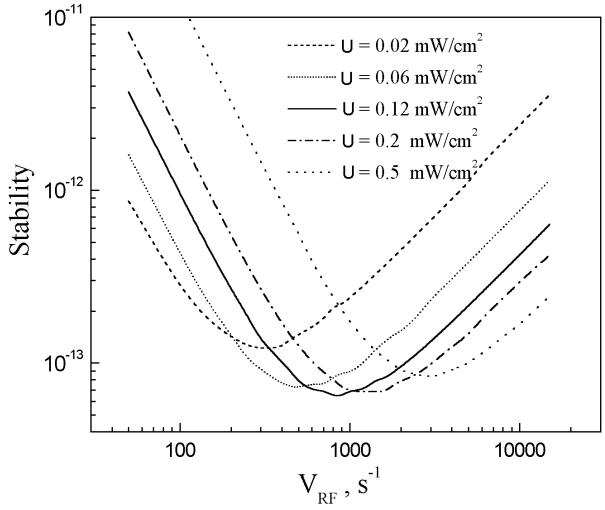

Fig. 11. Stability of the "two-laser" pumping standard versus the radio field Rabi frequency V_{RF} for different values of total laser field intensity U for the gas cell with "improved" parameters.

V. CONCLUSION

In this work we have compared the traditional one-laser optical pumping scheme with the "two-laser" pumping scheme proposed by Deng [6] for light shift compensation. We have first considered typical parameters of the gas cell and the laser. In this case our calculations show that the best stability for one-frequency as well as for "two-laser" pumping standard is approximately equal to $\sigma_y \sim 6 \cdot 10^{-13}$ (Allan deviation for 1 s integration time). Nevertheless the "two-laser" pumping standard seems to be preferable because it is free of the hyperfine light shift, i.e. the shift caused by changes in the laser frequency splitting.

The reason of the equality of the short-term stability calculated in the shot-noise limit is the bad collection of all the atoms in one of the working sublevels due to the large buffer-gas broadening and large laser line width. To reach the collection of all the atoms in one of the working level one needs to reduce the laser line width (to 10 MHz) and the buffer-gas pressure (to 3 mb or less). Note that the size of cell as well as the laser beam diameter should not be smaller than several cm to avoid the large wall relaxation in the ground state. Our calculations shows that for the gas cell with the improved parameters one can obtain a significant improvement of the short-term stability.

Acknowledgements

The authors thank J. Deng for fruitful discussions and for reading the manuscript. This research is supported by the INTAS-CNES, project 03-53-5175, by the Swiss National Sciences Foundation, project n. 200020-105624, and by the Program Russian Leading Scientific Schools (grant 9879.2006.2).

REFERENCES

[1] B. D. Agap'ev, M. B Gorny, B. G Matisov, et. al., Physics – Uspekhi, V. **36**, № 9, p.763 (1993)

[2] E. Arimondo, in *Progress in Optics*, Ed. E. Wolf, V. **35**, p. 257, (Amsterdam, 1996)

[3] J. Vanier, App. Phys. B **81**, 421 (2005)

[4] G. Kazakov, I.Mazets, Yu. Rozhdestvensky, *et. al.* Eur. Phys. Jour. D **35**, №3, 445 (2005)

[5] G. Kazakov, B. Matisov, I. Mazets, et. al., Phys. Rev. A. **72**, 063408 (2005)

[6] J. Deng, IEEE Trans. Ultrason. Ferroelectr. Frequency control, V. **48**, № 6, p. 1657 (2001)

[7] B. S. Mathur, H. Tang, W. Happer, Phys. Rev. **171,** №1, p. 11 (1968)

[8] J. Vanier, C. Audoin, The quantum physics of atomic frequency standards (Higler, Bristol, 1989)

[9] M. V. Romalis, E. Miron, and G. D. Cates, Phys. Rev. A 56, 4569 (1997)

[10] M. Gornyi, D. Markman, B. Matisov, Radiotehnika i Elektronika **50**, 1780 (in Russian, 1985)

[11] E. Arimondo, Phys. Rev. A **54**, 2216 (1996)

[12] V. S. Zholnerov., B. G. Matisov, I. N.Toptygin, J. of Techn. Physics (In Russian), 1980,V. 50, P. 1825

[13] Matisov B.G., Mazets I. E. Opt. Commun. **92**, 247 (1992)

Proceedings of the 20th EFTF, 2006

The Synthesized Rubidium Frequency Standard

A.S.Kleiman, A.I.Levenberg, S.I.Zub, V.S.Solovyov G.S.Sidorenko P.A.Kravchenko, T.A.Usenko
National Scientific Center "Institute of Metrology", Mironosytskaya Str. 42, Kharkov 61002 Ukraine
Electronic address: akleiman@metrology.kharkov.ua

The problems of synthesized rubidium frequency standard creation are considered in the article. Research results of this rubidium standard are represented

1. INTRODUCTION

The works to improve the characteristics of rubidium frequency and time standards are carried out in National Scientific Center "Institute of Metrology". The analysis of the main paths of improvement of accuracy characteristics of rubidium standards demonstrates, that it is necessary to reduce a line width of absorption and form fluctuation, and also to improve accuracy characteristic of electronics engineering.

II. THEORETICAL ANALYSIS

Theoretical and experimental reviewing of the factors, which have an influence on width and fluctuation of outline absorption line, demonstrates that it is defined quantum system behavior adequately with suggested model. The implementation of this system is offered as the synthesized quantum discriminator, which consists of number of interacting physical quantum systems, that results in increasing of reproduction accuracy of working transition frequency and decreasing of a line width.

Analysis of main paths of improvement of the precision characteristics of rubidium standard demonstrates that it is necessary to reduce fluctuations of the form of an absorption line, and also essentially improve an electronics engineering of the instrument.

The linewidth of quantum 0-0 transitions Rb87 in the absorption cell is defined by the contribution of a number of effects to Doppler effect and different collisions with walls of absorption cell and molecules of cushion gas. Filling the absorption cell by cushion gas reduces a lead-over linewidth.

The strong impacts lead to two types of interaction:

- magnetic dipole - dipole interaction between a moment of magnet of a valence electron Rb87 and moment of magnet of a core of atom of cushion gas;
- spin - orbit interaction, which is conditioned by interaction of a spin of a valence electron of alcali metal with a magnetic field, originating with distîrtion of orbital motion of electrons at collision, and depending from masses and speeds of clashing atoms.

The conducted calculations have shown, that the minimum contribution to a width of a line is given by mixtures of molecular gases of methane (CH_4) and azote (N_2) [7]. It is coupled that the free length of a molecule in 5,6 times is less, than for atom [8]. The designed dependence of the contribution both Doppler effect, and influencing of impacts with molecular gases demonstrates essential decrease of a linewidth for 50% azote - methanoic mixture.

Application of the absorption cell, filled optimum mixture (50 % azote - methane) lead to greater signal/noise ratio, as in such absorption cell because there is no an reradiation effect, and it lead to increasing the efficiency of optical pump and increase of a useful signal, and also smaller lead-over linewidth.

The results of long-time comparations of the the absorption cell with optimum mixture demonstrate, that the frequency change during the first five years makes $\sim 3 \cdot 10^{-10}$, and during the subsequent three years $\sim 1 \cdot 10^{-10}$.

In [6,7,9,10] theoretical and experimental reviewing of processes happening in one of the relevant units of the quantum discriminator (a filter cell) is conducted. There is rotined, that the problem of filtering is intimately coupled to long-time instability because of shift of an operating frequency producible by light of pump 0-0 transitions of atoms Rb87: each of components of light of pump (working and filtered), hitting in cell, effects on an operating level of atoms Rb87, shifting them in the different sides. Ar is used ss cushion gas in the filter sell. Application of methane (CH_4) as buffer molecular gas in the filter cell [11], by interaction with one the disconcerting cut (σ) spins of rubidium has minimum value in comparison with other gases.

III. EXPERIMENTAL RECEARCHES

The creation of the model of time and frequency standard have allowed to confirm experimentally theoretical conclusions: to get long-time frequency

instability per one day during observation time 271 day about $5{,}6 \cdot 10^{-13}$.

Accuracy characteristics of the designed rubidium standard are following:

-root-mean square two-sample frequency deviation (allan deviation) during
-100 s - $7 \cdot 10^{-13}$;
-1 day - $5{,}6 \cdot 10^{-13}$;
-5 day - $2{,}3 \cdot 10^{-13}$;
-average relative frequency change during one day - $3{,}7 \cdot 10^{-14}$.

The experimental researches to improve these characteristics are carried out.

REFERENCES

[1] Rubidium Frequency Standards, Jerusalem, AccuBeat ltd., 2000.

[2] «Радиоизмерения и электроника.КВАРЦ», Н.Новгород, ННИПИ «Кварц», 1993, № 1, с.30-31.

[3] The same, p. 32-33.

[4] Клейман А.С., Левенберг А.И., Сидоренко Г.С. и др.// Український метрологічний журнал.-1998.-Вип.4.-С.23-25.

[5] Бертен Ф. Основы квантовой электроники. -М.: Мир, 1971. -629 с.

[6] Arditi M. and Karver T.K. //Phys. Rev. –1961.-V.124.-P.800-809.

[7] А.с. 470028 СССР. Газовая ячейка пассивной квантовой меры частоты /А.С. Клейман, Б.Ю. Линкер, А.И. Самойлович, Н.С. Фертик //Открытия. Изобретения. -1975.

[8] Дэшман С. Научные основы вакуумной техники. -М.: Мир, 1964. -505 с.

[9] Клейман А.С., Левенберг А.И., Сидоренко Г.С. и др.// Український метрологічний журнал.-1 998.-Вип.2.- С.26-29.

[10] Клейман А.С., Линкер Б.Ю., Самойлович А.И., Фертик Н.С.//Исследования в области квантовой электроники: Тр. метрол. ин-тов СССР. Вып.163(223).-Л.:ВНИИМ им.Д.И.Менделеева, 1974.- С.46-50.

[11] А.с.1175327 СССР. Газовая ячейка-фильтр рубидиевого стандарта частоты/А.С.Клейман, Б.Ю.Линкер//Открытия. Изобретения.- 1982.- №14.

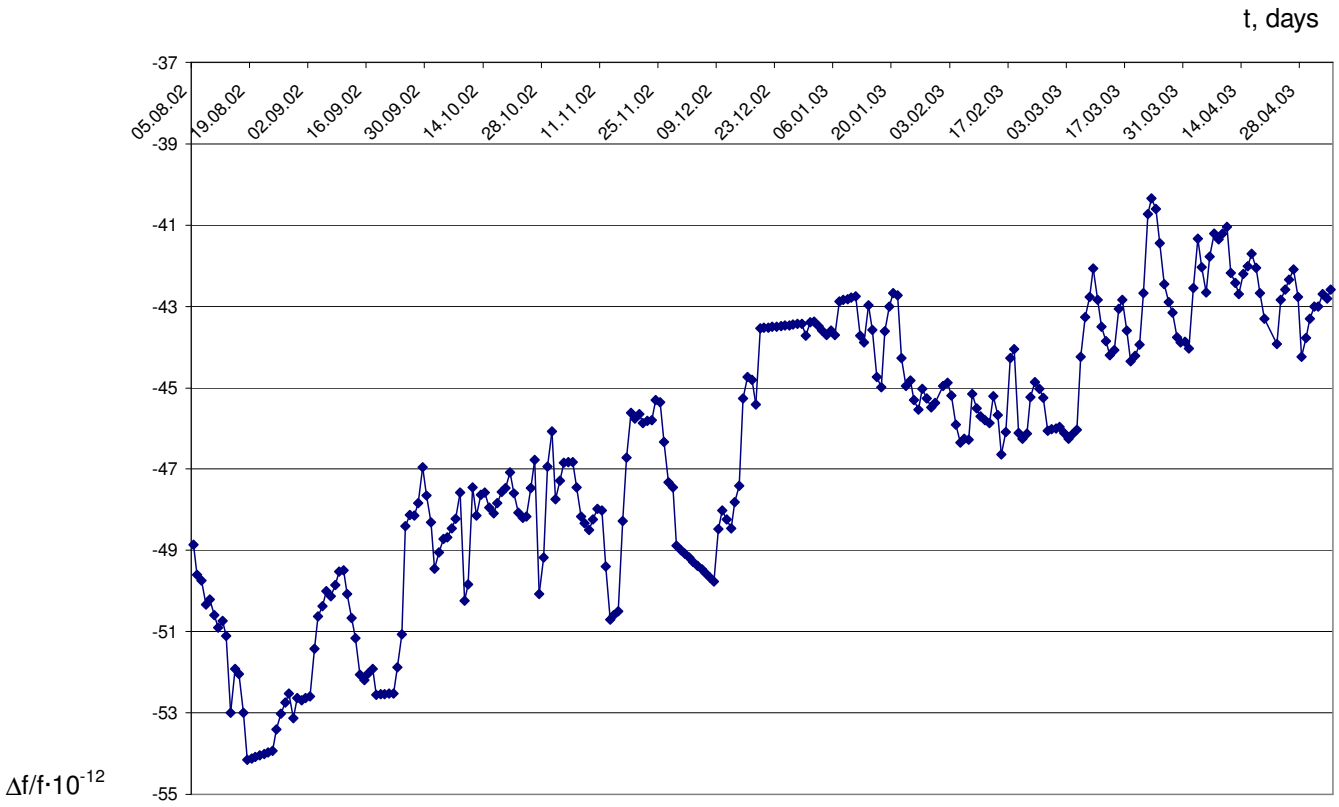

Figure 1

Proceedings of the 20th EFTF, 2006

Short and medium term frequency stability of a laser pumped rubidium gas-cell frequency standard for satellite navigation

A. Besedina[1], O. Berezovskaya[1], A. Gevorkyan[1], G. Mileti[2], V. Zholnerov[1]

[1]*The Russian Institute of Radionavigation and Time PJSC, 2 Rastrelli sq., St.-Petersburg, 191124, RUSSIA*
[2]*Observatoire Cantonal de Neuchâtel, Rue de l'Observatoire 58, CH-2000 Neuchâtel, Switzerland*
[1]*E-mail: office@rirt.ru*

1. INTRODUCTION

It is well known that the ultimate accuracy of positioning and timing services provided by the global navigation satellite systems (GNSS) is essentially defined by the parameters of the onboard clock used in these systems. The requirements on those clock are quite contradictory:

- provision for the best frequency stability;
- minimum dimensions and weight;
- minimum power consumption;
- lifetime of 10-12 years;
- tolerance for environmental conditions – temperature, magnetic field, space radiation, vibro and shock G-forces when launching a space vehicle, and so on.

The possible candidates for role of onboard atomic frequency standards (AFS) which could be produced industrially in appropriate volumes are:

- atomic beam AFS;
- gas-cell AFS with optical pumping;
- passive hydrogen maser.

Cesium and rubidium AFSs demonstrate high accuracy parameters in the course of many years' functioning aboard GLONASS and GPS satellites. The further improvement of these systems as well as the development of the European GALILEO generates, however, a need for improving the onboard AFSs. The rubidium frequency standards (RFS) is advantageously distinguished for its small size, low power consumption, long lifetime and high short-term and medium term frequency stability. The presence of a long-term frequency drift is adequately predicted and this drift can be compensated by introducing respective regular corrections transferred from the Earth to the navigation satellite.

One of the ways for improving RFS's accuracy parameters is to use laser pumping. As shown in several laboratories, the use of a laser diode instead of a discharge lamp has the potential to improve the short and the medium term frequency stability of optically-pumped Rubidium (vapor cell) frequency standards (RFS) [1]. We present here an on-going investigation held in RIRT in the frame of an INTAS-CNES collaboration aiming to develop a new RFS for satellite navigation capable of an instability below $1 \cdot 10^{-12}$ over 1 s and $1 \cdot 10^{-14}$ at 10'000 s.

2. EXPERIMENTAL INVESTIGATIONS

The goal of the first stage of experimental investigations was the comparison of parameters of signals of double radio-optical resonance (DROR) in two modes of atomic discriminator operation: with spectral lamp and with laser pumping.

In our study we used a breadboard of a commercial lamp-pumped RFS produced by the Russian Institute of Radionavigation and Time. Spectral lamp and isotopic filter were replaced with an external laser diode source.

The atomic discriminator (AD) is stabilized with two-stage temperature control which contains an absorption gas cell (sphere Ø13 mm) filled of Rb^{87} and Ar-Ne mixture with a total buffer gas pressure of 17.3 Torr (P_{Ar} = 5.8 Torr, P_{Ne} = 11.5 Torr). The cell is placed into the rectangular microwave cavity (H_{021}) being in the magnetic field H_0 = 0.08 G. The cell temperature was 65^0 C. The gas cell was irradiated by the optical beam from a "solitary" laser diode HL 7859 MG (D_2-line) having a line width < 10 MHz, and a power at the gas cell input of approximately 20 μW. The laser beam (Ø 2.5 mm) could be transmitted through an atomic Rubidium beam for obtaining frequency marks of hyperfine transitions when pumping from |2> or |1> levels' relative to the absorption line contour in the cell.

The DROR signal amplitude and noise at the output of the rubidium AD were measured as a function of the laser frequency, f_L (current, i_L). We observed that the laser frequency corresponding to the maximum SNR value does not coincide with the peak of the absorption line contour. It is below and coincides with a frequency corresponding to the minimum noise. According to our data the best stability is observed when tuning the laser frequency to the value corresponding to the point with the minimum noise.

The task at this stage was to study DROR signal and dependence of the conversion of laser-frequency modulation into intensity modulation (FM-AM) at the atomic absorption line in operating AD on used optical transition for pumping |F=2> or |F=1> the ground state levels, laser intensity and laser detuning from the peak of the

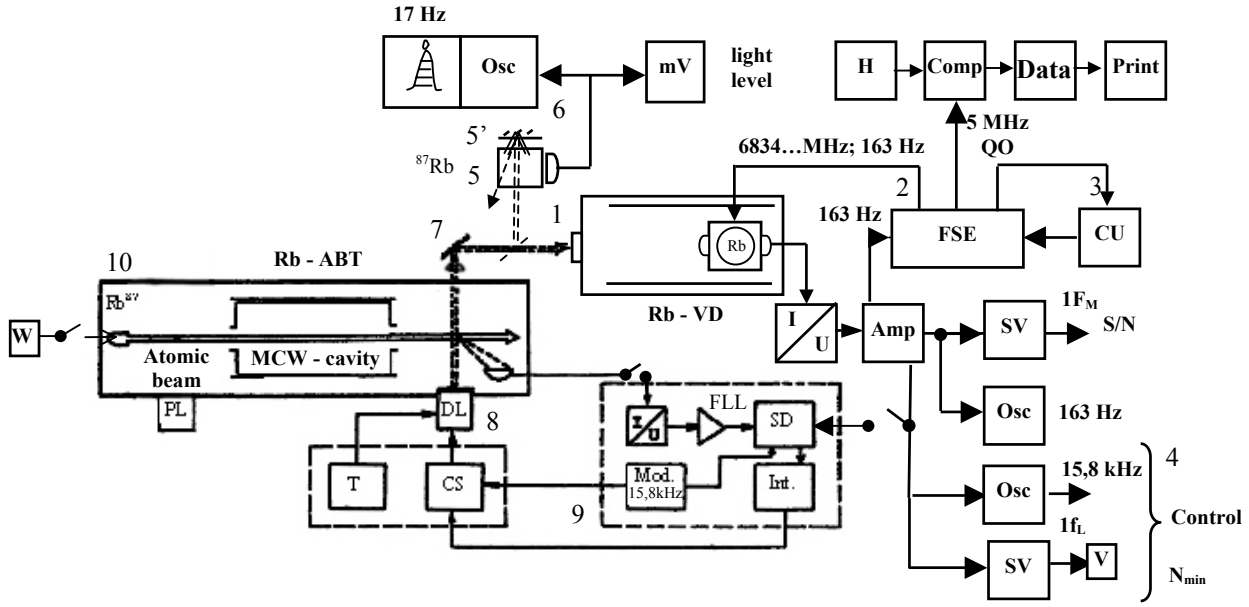

Fig. 1. Block diagram of a setup with the breadboard of a rubidium atomic frequency standard with a laser source: QO - quartz oscillator, Int – integrator, SD - synchronous detector, Mod – modulator, Amp – amplifier, SV - selective voltmeter, Osc – oscilloscope, CS - current source, T – thermoregulator, FLL - frequency-lock loop, DL - detection laser, ABT - atomic beam tube, VD - gas-cell discriminator, CU - control unit, H - Etalon (H – generator), Comp – comparator, Print – printer.

absorption line. Our purpose was to define with a possible accuracy a value of laser frequency detuning corresponding to the minimum of the conversion noise (maximum SNR value). The next step would consist in defining an acceptable method of laser frequency stabilization at the point of the minimum noise. Note that a simple idea to stabilize the LD using the atomic beam fluorescence was not suitable due to the non-coincidence of the minimum noise frequency with the frequency of non-indignant (2-2') transition in the atomic beam.

These investigations and the measurements of SNR and frequency stability were performed using an experimental setup which block diagram is given in Fig. 1.

The main setup's assemblies are as follows:

1 – physical package containing an gas cell within microwave cavity; 2 – electronic circuits of the frequency standard; 3 – control unit; 4 - units for measurements and control over the AD output signal (two-channel oscillograph; selective voltmeters for such frequencies as 163 Hz (F_m) and 15.8 kHz (f_m^L); 5 – additional gas cell containing Rb^{87} without buffer gas (T = 22^0 C); 6 – unit for recording a Doppler absorption line's contour; 7 – attenuator, opaque and semi-opaque mirrors for putting a laser emission to the main and additional gas cells; 8 – laser module (HL 7859 MG diode, micro-objective, micro-cooling); 9 – system for passive and active stabilization of the laser frequency; 10 – atomic beam tube for obtaining frequency marks of hyperfine transitions and their positions relative to Rb^{87} pure vapor absorption contour.

The determination of a laser's frequency detuning at which one can observe a disappearance of conversing the laser's frequency noise to the amplitude one, was performed using the method of additional known noise [1]. As a noise carrier which level can be changed and controlled a signal component at the AD output at the weak frequency modulation of the laser current, S ($1f_m^L$ =15.8 kHz), was used. S($1f_m^L$) = 0 point corresponds to laser's frequency detuning, $\Delta\nu_L^0$, at which the noise at the AD's output is minimum. This point does not coincide with that of maximum signal, but has a shift different for pumping cases from |2> and |1> levels. When observing a DROR signal, S($1F_m$ = 163 Hz), describing an absorption line contour in the operation cell when changing the laser frequency the oscillogram has shown not only a change in the amplitude noise, but also in the frequency noise which causes the amplitude one. The point of the AD's minimum noise accurately corresponded to the disappearance on the oscillograph traces of laser frequency modulation (f_m^L) and amplitude noise. The same pattern was observed at $2F_m$, when closing the AD's frequency lock loop. Using this technique, within limits of the current source's adjustment accuracy, a laser frequency was being set, i.e. a required detuning $\Delta\nu_L^0$, when measuring the AFS breadboard stability.

A value of $\Delta\nu_L^0$ was defined in relation with the peak of the absorption line in the additional cell 5 without buffer gas which was not broadened by collisions and optical pumping.

The examples of obtained dependencies for pumping variant from |1> level are presented in Figs. 2, 3. Here $S(1F_m = 163$ Hz) is a DROR signal describing an absorption line contour in the operation cell when changing the laser frequency.

The obtained values are: $\Delta\nu_L^0 \approx$ - 100 MHz for pumping from |2> level, $\Delta\nu_L^0 \approx 0$ in average for pumping from |1>. For these two variants the DROR signal is about equal.

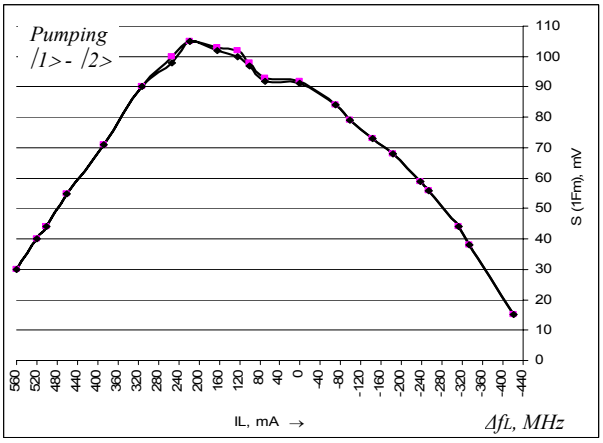

Fig. 2. Dependence of DROR signal on laser's frequency detuning from the peak of the absorption line.

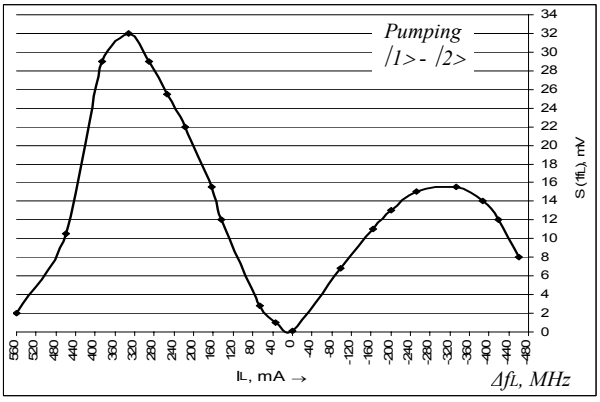

Fig. 3. Dependence AD's output signal at the laser's modulation frequency 15.8 kHz on LD detuning.

The RFS's SNR and short-term stability were measured using the HL 7859 MG laser with non-stabilized frequency – the laser was functioning in the free regime. At present, short-term stability measurement in RFS breadboard is: $\sigma_y(10\ s) = (2\text{-}4)\cdot10^{-12}$. The results of estimation such parameters as SNR and stability (Allan deviation) are: SNR = 6400, W = 520 Hz, figure of merit M = 12, $\sigma_y(\tau) = (2.4)\cdot10^{-12}\ \tau^{-1/2}$.

Fig. 4 presents a theoretical estimate for frequency stability of the RFS breadboard with laser pumping.

When theoretically estimating the instability, along with the data given above, one has used the experimental data on fluctuations of the constant magnetic field, gas cell temperature, laser emission intensity, microwave field phase as well as the data on the inherent instability of a crystal oscillator frequency. The spectral power density (SPD) of these fluctuations was adopted as follows:

$$S_i(\Omega) = \frac{A_i}{\Omega^2} + \frac{B_i}{\Omega} + C \qquad (1)$$

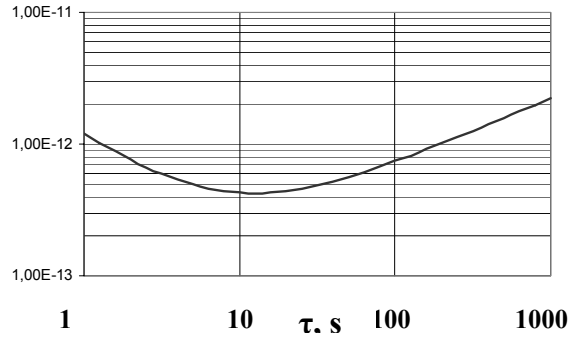

Fig. 4. Calculated frequency stability of breadboard of RFS with laser pumping.

For further analysis, Fig. 5 presents contributions of each of these destabilizing factors into the resulting RFS' frequency stability. The given data show that it is difficult to separate an effect of various fluctuations on short-, medium-, and long-term frequency stability. Nevertheless, one can separate the main instability sources specific for each time domain.

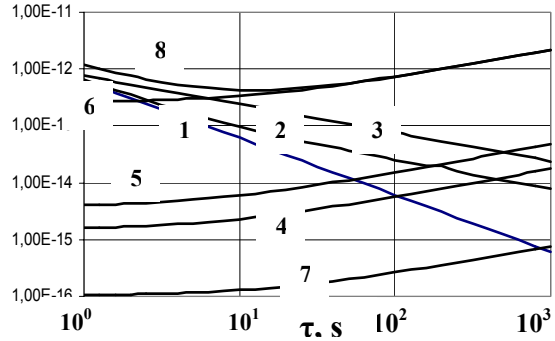

Fig. 5. The contributions of various fluctuations into resulting stability: 1 – crystal oscillator, 2 – phase fluctuations of microwave field, 3 – shot noise of AD, 4 – constant magnetic field, 5 – power of microwave field, 6 – gas cell temperature, 7 – laser power, 8 – resulting frequency stability.

3. SHORT-TERM FREQUENCY STABILITY

As is seen in Fig. 5, the main contribution to the short-term frequency stability is caused by inherent stability of crystal oscillator frequency and phase fluctuations of

the microwave field. The significant contribution to the short-term frequency instability can be caused by the stray transformation of the microwave phase fluctuations. This transformation is a consequence of the technique for obtaining an error signal based on the phase modulation of the microwave field with the subsequent synchronous detection [2-4]. This effect results in the appearance of the additional noise in the crystal oscillator's controlling voltage with a spectral density [2]:

$$S_{add}(\Omega) = 0{,}5^2 KS_D^2 \left[S_\delta(\Omega) + \right. \quad (2)$$
$$\left. + 0.25S_\delta(\Omega - 2\Omega_M) + 0.25S_\delta(\Omega + 2\Omega_M) \right],$$

where K – transfer ratio from the AD output to the controlling component of the crystal oscillator, $S_\delta(\Omega)$ – SPD of white frequency noise of the microwave field. The direct way to reduce the effect of stray fluctuations transformation on the passive ASF' frequency stability is to use a double rejecter crystal filter connected to the crystal oscillator's output and tuned to $\mathbf{\nu_0 \pm 2f_m}$ frequencies, where $\mathbf{\nu_0}$ – crystal oscillator's frequency and $\mathbf{f_m}$ – frequency of microwave field's phase modulation. This technique is, however, difficult for realization, since it requires using precise high-quality crystal resonators with temperature stabilization and low frequency drift. The more suitable technique for neutralization a stray fluctuations transformation is to use a square wave frequency modulation of the microwave field with quasi-stationary error signal's samples which start is shifted by duration of the transient process, $\boldsymbol{\theta}$, against the time of frequency switching. In this case, the error signal at the AD output is

$$A(t) = A(\delta + \Delta)\Pi[t, nT + \theta, (2n+1)T/2] + \quad (3)$$
$$+ A(\delta - \Delta)\Pi[t, (2n+1)T/2 + \theta, (n+1)T]$$

where $\Pi[t, \tau_1, \tau_2] = \delta_0(t - \tau_1) - \delta_0(t - \tau_2)$, T – modulation period, $\delta_0(t - \tau)$ - unit function:

$$\delta_0(t - \tau) = \begin{cases} 0 & t < \tau \\ 1 & t \geq \tau \end{cases}$$

While expanding A(t) to a series according to the degrees of small detuning, **δ,** near **δ = 0**, we obtain:

$$A(t) = \{A(\Delta) + \delta(t)S_+\}\Pi[t, nT+\theta, (2n+1T/2)] +$$
$$+ \{A(-\Delta) + \delta(t)S_-\}\Pi[t, (2n+1)T/2 + \theta, (n+1)T] \quad ,$$

where $S_+ = \left.\frac{\partial A(\delta + \Delta)}{\partial \delta}\right|_{\delta = 0}$, $S_- = \left.\frac{\partial A(\delta - \Delta)}{\partial \delta}\right|_{\delta = 0}$

For a symmetric line of the atomic resonance $\mathbf{S_+ = S_- = S_D}$, where $\mathbf{S_D}$ – slope of the amplitude-frequency characteristic of the AD, **A(Δ)=-A(-Δ).** After the synchronous detection of the variable signal part using a reference signal of the rectangular form, we obtain a following signal:

$$U_{out}(t) = k_a k_d S_D \delta(t) \Pi[t, nT + \theta, (2n+1)T/2] \quad (4)$$

where $\mathbf{k_a}$ and $\mathbf{k_d}$ – transfer ratios of the error signal amplifier and synchronous detector. As regards previous expressions, one implies the summation over **n.** While expanding (4) to the Fourier series, we have:

$$U_{out}(t) = k_a k_d S_D \delta(t) \{(1 - \vartheta) +$$
$$+ \frac{2}{\pi} \sum_{n=1}^{\infty} \frac{(-1)^{n+1} \sin n\pi\vartheta}{n} \cos 2n\Omega_M t \ \}$$

where $\vartheta = 2\theta / T$, $\Omega_M = 2\pi/T$ – angular modulation frequency.

Autocorrelation function and SPD of the synchronous detector output signal are equal to, respectively:

$$R_{det}(\tau) = k_c^2 R_\delta(\tau) \{(1 - \vartheta)^2 +$$
$$+ \frac{2}{\pi^2} \sum_{k=1}^{\infty} \frac{\sin^2 k\pi\vartheta}{k^2} \cos 2k\Omega_M t \} \quad (5)$$

$$S_{det}(\Omega) = k_c^2 \{(1 - \vartheta)^2 S_\delta(\Omega) + \quad (6)$$
$$+ \frac{1}{\pi^2} \sum_{k=1}^{\infty} \frac{\sin^2 k\pi\vartheta}{k^2} [S_\delta(\Omega + 2k\Omega_M) + S_\delta(\Omega - 2k\Omega_M)] \ \}$$

where $k_c = k_a k_d S_D$, $R_\delta(\tau)$ and $S_\delta(\Omega)$ - autocorrelation function and SPD of microwave field's frequency fluctuations. The SPD of the additional noise at the AD output generated by the stray transformation of crystal oscillator's frequency fluctuations is, in this case, equal to:

$$S_{ADadd}(\Omega) = \frac{2N^2 S_D^2 C_{QO}}{\pi^2} \sum_{k=1}^{\infty} \frac{\sin^2 k\pi\vartheta}{k^2} =$$
$$= N^2 S_D^2 C_{QO} \vartheta(1 - \vartheta) \quad (7)$$

Expression (7) shows that the lower ϑ value, the lower is the intensity of the additional noise. By reducing a modulation frequency, Ω_M, one can significantly reduce the effect of the stray transformation of microwave field's frequency fluctuations.

In such a way, the negative effect of the stray transformation of frequency fluctuations can totally be removed in practice, and the RFS' short-term stability will be defined by the crystal oscillator's inherent stability and level of phase fluctuations of a frequency synthesizer which transforms a crystal oscillator frequency into the atomic transition frequency. The achieved progress in the parameters of up-to-date crystal oscillators [6] and frequency synthesizers [2] enables one to support high short-term frequency stability.

4. BUFFER GAS MIX

The long-term frequency stability is defined by a presence of atomic transition frequency's shifts. The clock transition frequency corresponding to the stable point of frequency standard frequency-lock loop is equal to:

$$\omega_0 = \omega_H + \Delta\omega_{BG} + \delta_{els} \qquad (8)$$

where ω_H - hyperfine frequency value with the account for influence of the constant magnetic field within the gas cell area; $\Delta\omega_{BG}$ - frequency shift of the hyperfine transition due to the buffer gas effect; δ_{els} - effective light frequency shift of the clock atomic transition caused by influence of the pumping light intensity.

The frequency of the clock atomic transition depends on following external parameters: environmental temperature; microwave field power; strength of constant magnetic field; phase modulation index of microwave field and integral intensity of light emitted by the light source. Of the largest values can be differential parametric frequency shifts caused by changes of the pumping intensity and temperature of gas cell. The differential light shift can be defined by the following way:

$$D_J = \frac{J}{\nu_0}\frac{\partial(\Delta\nu_{els})}{\partial J} \qquad (9)$$

The temperature frequency shift of the clock atomic transition characterized by the temperature differential parametric frequency shift is a result of four components caused by a change of the effective light shift due to the change of the temperature of gas cell, as well as the change of the collisional frequency shift, $\Delta\nu_{BG}$, due to the cell temperature change. The effect of temperature on the frequency of the atomic gas cell frequency standard is realized in two ways. On one side, flicker fluctuations of operating temperatures gas cell result in long –term frequency fluctuations of the clock atomic transition. On the other side, changes in the external temperature due to the finite value of the isolation factor of the thermal-stabilization of the gas cell results in corresponding frequency shifts of the clock atomic transition. As far as changes in environmental temperature are, as a rule, slow, it is convenient, as mentioned above, in order to estimate a total temperature differential parametric frequency shift, to introduce coefficient of thermostating, k_{Tc} , being coefficient of transferring a temperature change to the object being thermostated (cell). Then a total temperature differential parametric frequency shift can be defined as follows:

$$D_T = \frac{\partial\Delta\nu_0}{\partial T_{ext}} = k_{Tc}\left[\frac{\partial\Delta\nu_{BG}}{\partial T_c} + \frac{\partial\Delta\nu_{els}}{\partial T_c}\right] \qquad (10)$$

where T_{ext} - external temperature.

The largest contribution is caused by D_T component related to the dependence of the frequency shift of the clock atomic transition due to collisions of rubidium atoms with buffer particles on the cell temperature. As experimental investigations has shown [7], a frequency shift of the clock atomic transition due to the buffer mix can be approximated as follows :

$$\Delta\nu_{BG} = \sum_i N_i k_B T_c(\gamma_i + \delta_i T_c) \qquad (11)$$

where N_i - volume concentration of the i-th buffer mix component, k_B - Boltzmann's constant, γ_i and δ_i - coefficients of the hyperfine frequency shift due to the i-th buffer gas [7], T_c -mix temperature. Experimental values of γ_i and δ_i coefficients for various buffer gases are given in Table 1.

Table 1
Experimental values of the coefficients of the hyperfine frequency shifts for various buffer gases

Buffer gas	γ, Hz/torr	δ, Hz/(torr ·°C)
N_2	848.2±2.0	- 1.0369±0.004
Ne	702.2±2.0	- 0.9988±0.004
Ar	- 7.439±0.03	- 0.16025±0.001
CH_4	- 760.0±2.0	0.8886±0.003
Kr	- 908.3±3.0	1.0652±0.004

Then a parametric temperature frequency shift due to the buffer mix is equal to

$$\frac{\partial\Delta\nu_{BG}}{\partial T_c} = N_M k_B \sum_i x_i(\gamma_i + 2\delta_i T_c) \qquad (12)$$

where N_M - volume concentration of the buffer mix, $x_i = N_i / N_M$ - fractional concentration of the i-th mix component.

Let us assume for a moment that remaining components of the total differential temperature frequency shift described by (11) are equal zero. Then, to provide a zero value of the collisional temperature frequency shift, (13), the equality should be satisfied:

$$\sum_i x_i(\gamma_i + 2\delta_i T_c) = 0 \qquad (13)$$

The specified value of the frequency shift, (11), and the zero value of the temperature frequency shift, (12), are realized in the cell manufacture using the calibration of cell against frequency. One of manufactured cells in-

stalled on the vacuum-pumping out setup [7] is placed to the dismountable atomic discriminator of the measurement frequency standard which frequency is compared to the frequency of reference standard. The gas cells are being filled with selected buffer gases until a frequency shift, (11), reaches the specified value, and a value of temperature frequency shift becomes zero with an accuracy of the measurement error. In the course of cell manufacture the technological errors of manufactured cells against frequency occur due to the warm-up of cells when thermally unsoldering those from the vacuum setup. This error is proportional to the frequency shift caused by the buffer mix, $\Delta\nu_{BG}$, and cell temperature increment when warming up, δT:

$$\delta\nu = \Delta\nu_{BG}\frac{\delta T}{T_c} \tag{14}$$

Therefore the mix parameters should be selected in a way that frequency shift, $\Delta\nu_{BG}$, and temperature coefficient would be of minimum value. The best mixes are such ones that provide at the same time the satisfaction of (13) condition and conditions when the total shift coefficient of the buffer mix, α_M, is equal zero :

$$\alpha_M = \sum_i x_i(\gamma_i + \delta_i T_c) = 0 \tag{15}$$

The simultaneous satisfaction of these conditions is possible when

$$\sum_i x_i\gamma_i = \sum_i x_i\delta_i = 0 \tag{16}$$

Unfortunately, no one of multi-component mixes composed of investigated gases satisfied this condition. Moreover, the numerical calculations show that the smallest value of the frequency shift, $\Delta\nu_{BG}$, corresponds to two-component mixes for which, taking into account an additional condition, $\sum_i x_i = 1$, we obtain:

$$\left.\begin{aligned} x_1 &= -\frac{\gamma_2 + 2\delta_2 T_c}{(\gamma_1-\gamma_2)+2T_c(\delta_1-\delta_2)} \\ x_2 &= \frac{\gamma_1 + 2\delta_1 T_c}{(\gamma_1-\gamma_2)+2T_c(\delta_1-\delta_2)} \end{aligned}\right\} \tag{17}$$

Table 2 gives parameters of such mixes for cell temperature of 328 K.

The N_2+CH_4 and N_2+Kr mixes have the smallest value of the shift coefficient, α_M. These mixes have also an additional advantage: the nitrogen presence in the cell provides the effective quenching of the resonance fluorescence, thus improving the optical pumping efficiency.

So, for a finite value of the efficiency of the temperature control of the gas cell oven, a temperature frequency stability of RFS is defined by technological capabilities of gas cell manufacture with a specified buffer gas mix. For example, in order to reach a value of $(1\text{-}5)\cdot10^{-14}$/ degree for the RFS temperature frequency coefficient with a static temperature control coefficient of the order 0.01, the temperature frequency coefficient caused by the buffer mix should be of order $(1\text{-}5)\cdot10^{-12}$/ degree, thus requiring to develop a sophisticated technology for the gas cell manufacture, especially in a case of small-size cells.

Table 2
Parameters of two-component mixes for cell temperature of 328 K

Mixture	X_1	X_2	α_M, Hz/torr
N_2+Ar	0.3835	0.6165	160.357
N_2+CH_4	0.5116	0.4884	31.189
N_2+Kr	0.5527	0.4473	31.204
Ne+Ar	0.6530	0.3470	228.615
Ne+CH_4	0.7601	0.2399	176.366
Ne+Kr	0.7889	0.2111	181.870

5. MULTI-PARAMETRIC OPTIMIZATION OF RAFS WITH LASER PUMPING

The objective for RFS multi-parametric optimization is an estimation of optimal standard's parameters providing the best frequency stability.

Numerical calculations show that a figure of merit dependence on temperature and length of gas cell T_c, L_c, pressure of buffer mix P_c, power and frequency detuning of laser emission J_{input}, ΔF_L, Rabi frequency R_{12} and frequency deviation of low frequency square wave modulation of microwave field Δ quantities is of extremal nature.

We can use a mean Allan variance as a criterion for complex optimization of RFS over the predefined measurement time interval:

$$\Xi = \frac{1}{\tau_2-\tau_1}\int_{\tau_1}^{\tau_2}\sigma(\tau, F, D_1, D_2, \ldots, \Omega_0)d\tau \tag{18}$$

In the same time the interval $[\tau_1, \tau_2]$ is usually quite broad, so, to level off weights of short-term and long term frequency stability, it is advisable to use log-log scale and define a generalized figure of merit of RFS as a criterion for complex optimization given by the following expression:

$$Z(\tau_1,\tau_2) = \frac{1}{\log(\tau_1/\tau_2)}\int_{\log\tau_1}^{\log\tau_2}\log[\sigma(\tau)]d(\log\tau) \tag{19}$$

This criterion is a surface under the $-\log[\sigma(\tau)]$ curve in function of $\log\tau$ over $[\tau_1,\tau_2]$ specified time interval. In order to perform calculations, the computer program OPTIM.CPP was developed written in C++ System. The program core is a kinetic equations system in the Vanier-Audoin's form for optical pumping. This system was complemented with the equation for optical emission transfer:

$$\frac{\partial I(\nu,z)}{\partial z}=-N_A I(\nu,z)\sum_{m,\mu}\frac{8a_{m\mu}\sqrt{\ln 2}\nu_{m\mu}\left|\left\langle\mu\left|\hat{\vec{d}}\vec{e}\right|m\right\rangle\right|^2\left[(g_1-1)\sigma_{\mu\mu}+\sigma_{11}\right]}{\varepsilon_0\hbar c\Delta\nu_{Dm\mu}\sqrt{\pi}}\int_0^\infty\frac{\exp(-y^2)dy}{(b_{m\mu}-y)^2+a_{m\mu}^2} \qquad (20)$$

where $a_{m\mu}, b_{m\mu}$ - parameters of Voigt contour of optical lines; $\nu_{m\mu}, \Delta\nu_{Dm\mu}$ - resonance frequency and Doppler broadening of optical lines; N_A - concentration of rubidium atoms; $\left\langle\mu\left|\hat{\vec{d}}\vec{e}\right|m\right\rangle$ - matrix element of electrical dipole moment; ε_0 - electrical constant; $\tilde{n}$ - light velocity; z - distance along the axis of the gas cell.

For numerical solving these integro-differential equations gas cell was being divided into 'n' layers of sufficiently small elongation along the light propagation direction. Within such a layer pumping rates, light shift and absorption coefficient can be considered constant quantities. For each layer such values were computed as local values of pumping rates $W_1^{(k)}$ and $W_2^{(k)}$, light shift $\delta_{lfs}^{(k)}$ and absorption coefficient, $k_a^{(k)}$, being a coefficient at $I(\nu,z)$ in the right part of (20). The population values required for calculation of absorption coefficient are solutions of kinetic equation system. The spectral distribution of light intensity at the k-th layer's output being an input value for the (k+1)-th layer is found from the solution of (20) for optically thin layer:

$$I^{(k+1)}(\nu,\delta,t)=I^{(k)}(\nu,\delta,t)\exp\left[-k_a^{(k)}(\nu,\delta,t)\Delta z\right] \qquad (21)$$

where Δz - thickness of the k-th layer. The integral light intensity on the photodetector is equal to

$$J(\delta,t)=S_c\int I_{out}(\nu,\delta,t)d\nu \qquad (22)$$

where $I_{out}(\nu,\delta,t)$ - spectral distribution of light intensity on the photodetector, S_c - surface square of the gas cell from which the light is collected to indicate an atomic resonance signal.

Let us define an atomic discriminator figure of merit in a following way:

$$F=\frac{S_{AD}}{e\left\{k_{PD}\left[\int_0^{T_M}J(\delta,t)dt\right]\right\}^{\frac{1}{2}}} \qquad (23)$$

where S_{AD} - slope of atomic discriminator gain-frequency curve, k_{PD} - photodetector efficiency, e - electron charge, T_M - period of low-frequency phase modulation of the microwave field. The denominator in the (23) is a spectral density of the photocurrent shot noise. Let us define the S_{AD} slope in a following way:

$$S_{AD}=\frac{d}{d\delta}\left|\frac{ek_{PD}}{T_M}\left[\int_{t_d}^{t_d+T_M}J(\delta,t)g_{SD}(t)dt\right]\right| \qquad (24)$$

where t_d - phase shift of the synchronous detector reference signal against the modulating signal phase corresponding to the maximum value of figure of merit; $g_{SD}(t)$ - reference signal of the synchronous detector with unit amplitude.

This program OPTIM.CPP comprises a subprogram for global optimization which performs search of a set of optimal values of RFS parameters providing a maximum value of the RFS generalized figure of merit through a technique of coordinate-by-coordinate lift. This technique involves a cyclic procedure for searching optimal value of each parameter using the "golden cut" method with remaining parameter values obtaining during the previous step. Within each cycle optimal values of the microwave excitation parameter and deviation of microwave field frequency are found and values of differential parametric frequency shifts of the clock atomic transition are also calculated.

The following dimensions of the gas cell were selected: length of 15 mm, diameter of 15 mm. The N_2 + Kr mix was selected as a buffer mix. The parameters of spectral densities as regards fluctuations of gas cell temperature, constant magnetic field, phase fluctuations of microwave field, power of the microwave field and parameters of crystal oscillator's inherent instability were selected based on capabilities of the up-to-date electronics.

Fig. 6 presents measurement results for a spectral density of laser emission power fluctuations for value of injection current 58.9 mA. The regression analysis of experimental data by analytical expression

$$S_{\Delta J/J}(\Omega) = \frac{A}{\Omega^2} + \frac{B}{\Omega} + C \qquad (25)$$

gives the following values of constants : A = $7.38 \cdot 10^{-7}$, B = $1.63 \cdot 10^{-7}$, C = $1.8 \cdot 10^{-9}$ for I_l = 52.9 mA.

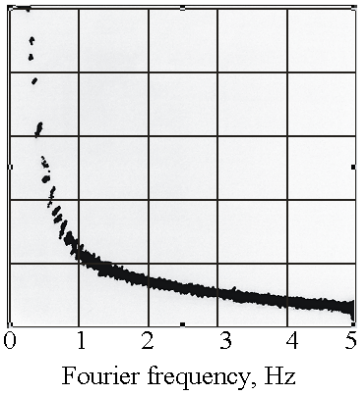

Fig. 6. SPD of low frequency fluctuations of laser light intensity for operation value of injection current

Depending on laser emission polarization and used atomic transitions, 15 variants for pumping schemes are possible for multi-parametric optimization of RFS. The schemes with "pockets" were excluded from consideration as ineffective ones. The optimization was performed in assumption about negligible value of FM-AM conversion.

Table 3 gives optimization results for these variants. One can see that the achievable stability level looks much the same for all schemes. The distinction is only observed in optimal values of atomic discriminator's parameters. Fig. 7 shows a stability curve when pumping by D_2 -line using |F=1>→ |F=1'> transition.

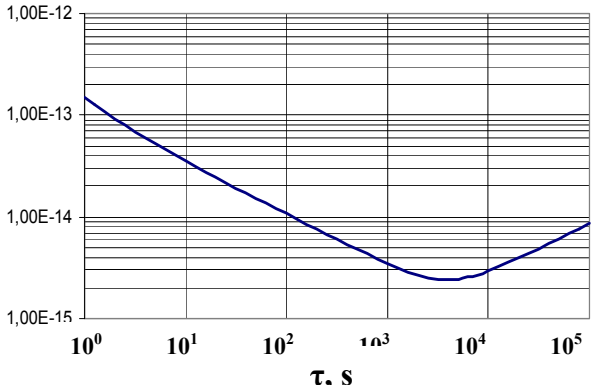

Fig. 7. Frequency stability RFS with laser pumping as result of multi-parametric optimization.

Table 3

The multi-parametric optimization results of the RFS depending on laser emission polarization and used atomic transitions for pumping

Variant	P_{N_2} / P_{Kr}	P_c, Torr	T_c, K	ΔF_L, MHz	P_L, W/m^2	ΔF_{mod}, Hz	Z
D1-line, σ, (1-2')	1.347	8.0	333.0	- 85.1	5.0	640.4	13.956
D2-line, σ, (1-2')	1.273	8.1	335.6	- 157.9	0.1	139.5	13.913
D2-line, σ, (2-3')	1.273	10.5	335.5	- 195.4	0.075	157.5	13.570
D1-line, π, (1-2')	1.3	13.2	342.5	- 82.7	5.0	1175.8	14.040
D2-line, π, (1-2')	1.3	19.2	343.0	- 139.7	0.4	326.9	13.958
D2-line, π, (2-3')	1.252	22.9	330.9	- 193.4	0.095	149.2	13.949
D1-line, linear, (1-1')	1.262	25.0	333.0	594.6	0.095	88.5	13.720
D1-line, linear, (1-1')	1.257	17.1	331.0	- 154.7	0.1	108.3	13.860
D1-line, linear, (2-1')	1.242	25.2	327.0	594.1	0.14	127.7	13.913
D1-line, linear, (2-2')	1.247	22.2	327.7	- 194.3	0.14	129.3	13.927
D2-line, linear, (1-1')	1.3	27.9	344.0	- 145.4	0.29	332.0	13.992
D2-line, linear, (1-2')	1.242	6.4	327.2	- 145.7	0.14	200.5	14.064
D2-line, linear, (2-1')	1.309	4.9	345.0	638.0	9.7	1469.4	14.090
D2-line, linear, (2-2')	1.237	8.8	325.0	100.0	0.25	190.4	14.08
D2-line, linear, (2-3')	2.262	10.6	332.7	- 180.9	0.18	192.0	14.008

6. CONCLUSION

In the case of a rubidium standard with laser pumping, a minimum value of the temperature-frequency coefficient should be provided for a gas cell to achieve high medium-term and long-term frequency stability. In this case, the best buffer mix is that of N_2 +Kr. The existing techniques for neutralization the stray transformation of microwave field phase fluctuations eliminate this effect totally in practice. All possible schemes for laser pumping demonstrate roughly the same capabilities as regards the realization of a high frequency stability of the order $1.5 \cdot 10^{-13}$ over 1 s and $1 \cdot 10^{-14}$ over 1 day.

REFERENCES

[1] G. Mileti, J. Deng, F. L. Walls, IEEE J. Quant. Electron., **34**, no 2 (1998) and references therein.

[2] V. Zholnerov, O. Kharchev, Proc. of the Joint Meeting 16th EFTF & 2002 IEEE Int. FCS, March 2002, St. Petersburg, Russia.

[3] G. I. Dick, J. D. Prestage, C. A. Greenhall, L. Maleki, Proc. 22nd Annual Precise Time and Time Interval Application and Planning Meet., Vienna, VA, 487 (1990).

C. Audoin, V. Candelier, N. Dimarcq, IEEE Trans. Instrum. Meas., **40**, no 2, 121 (1991).

[4] R. Barillet, V. Giordano, J. Viennet. C. Audoin, Proc. 6th EFTF, Noordwijk, Netherlands, 453 (1992).

[5] R. Barillet, D. Vernot, C. Audoin, Proc. 9th EFTF, Besançon, France, 147 (1995).

[6] Ja. Vorokhovsky, Piezotechnique (in Russian), no 9 (82),12 (2003)

[7] V. S. Zholnerov, Optics and Spectroscopy (in Russian), **43**, no 5, 956 (1977).

Acknowledgements

This research is supported by the INTAS-CNES project 03-53-517. The authors thank Jerome Delporte for his participation to the investigations and coordination activities.

Proceedings of the 20th EFTF, 2006

Preliminary results of investigation of the high-stable Rubidium atomic beam frequency standard with laser pumping/detection for space application

A. Besedina[1], A. Gevorkyan[1], G. Mileti[2], V. Zholnerov[1], and A. Bassevich[1]

[1] *"The Russian Institute of Radionavigation and Time" PJSC, 2 Rastrelli sq., St.-Petersburg 191124, RUSSIA, E-mail: office@rirt.ru*

[2] *Observatoire Cantonal de Neuchâtel, rue de l'Observatorie 58, CH-2000 Neuchâtel, Switzerland E-mail: gaetano.mileti@ne.ch*

We present our study on a ^{87}Rb atomic beam frequency standard with laser pumping and detection performed in the frame of an INTAS-CNES collaboration and in view of designing and realizing a spaceborne atomic clock with instability of $\sim 10^{-14}$ per day.

1. INTRODUCTION

In order to enhance the GPS system parameters and in the frame of GALILEO system deployment, several studies were undertaken on the design of spaceborne clocks with short-term instability $(2\text{-}4)\cdot 10^{-12}\cdot\tau^{-1/2}$ based on optical pumping and detection of cesium beam using single-frequency laser diodes with narrow radiation line [1-5]. The present piece of work represents a further investigation in RIRT in order to create a spaceborne frequency standard for GLONASS providing the instability of $\leq 1\cdot 10^{-14}$ per day [6-9].

The main distinctive feature of the developed breadboard is the choice of ^{87}Rb isotope as a working substance in which the optical pumping efficiency of working sub-levels can be nearly three times greater than in ^{133}Cs atom with significantly greater efficiency of optical detection [9]. In the atomic beam tube the most effective configuration of laser excitation is used: two-laser system with pumping on the 2-2'σ transition (with excluding the CPT effect) and detection on the cyclic transition 2-3'. The technology of performing the physical package and discriminator as a whole, optimization of pumping and detection processes in the Rb beam allowed to obtain the high figure of merit and short-term instability at the level of $\sim 1.4\cdot 10^{-12}\,\tau^{-1/2}$.

In the future we intend to improve the electronic system and investigate more carefully the noise sources in order to achieve better long-term stability.

II. OPTICALLY PUMPED RUBIDIUM ATOMIC BEAM DISCRIMINATOR

The atomic beam Rb discriminator (ABD) with laser excitation is based on a modified spaceborne Rubidium atomic beam tube (ABT), solitary laser diodes and original electronic control system. The setup with Rb atomic beam discriminator comprises:

a) a Rb atomic beam tube with a system for generating a microwave excitation signal, thermo-stabilized source of the intense atomic beam, three optical chambers and possibility to adjust a constant stable magnetic field within the pumping and detection chambers over a range of (0-2) G;

b) two laser sources which contain a single-frequency laser diode (LD), microobjective, microcooling, thermo-sensors;

c) two laser discriminators with their frequency lock loops (FLL): electronic systems for passive and active stabilization of the laser parameters and recording optical signals;

d) the equipment of the industrial spaceborne Rb traditional atomic beam tube standard in order to use the ABD in the frequency standard regime;

e) optical monochromator and video checking device.

The availability of optical bench with monochromator and video checking device allows to check the laser's spectrum and simplifies its adjustment to the single-frequency oscillation regime at the operating mode. The possibility to slowly scan the laser current enables one to observe a contour of each hyperfine line of the beam fluorescence and to check their resolution.

The Rb atomic beam discriminator specific feature is its realization in the simplest version - just as from view-point of design, so also as regards circuitry realization:

a) the ABT has a simple photon collection system with a single photodiode (PD), without lens system; it is, however, possible to use a version with two PD and signal adding;

b) standard industrial Si-PD are used (with selection of parameters);

c) single-frequency lasers with a narrow line (<10 MHz) are used, without system for line narrowing (optical feedback or electronic feedback);

d) LD frequency is directly tuned using fluorescence signals of the atomic beam, without additional devices with external cells of intra-Doppler absorption;

e) the structure of laser devices' breadboards allows to replace each component;

f) the electronic systems were adapted from those of an industrial traditional Rb beam frequency standard.

The block-diagram of the Rb atomic beam discriminator with laser excitation and the frequency standard is given in Fig.1.

2.1 Optically-Pumped Rubidium Atomic Beam Tube

The breadboard of the ABT with laser pumping and detection is based on industrial sample of ordinary Rb ABT used on first stage of GLONASS deployment.

Design aspects of the optically pumped rubidium ABT and its main components are as follows. It contains a multichannel source of intense atomic beam, a micro-wave coaxial–cylindrical quartz cavity (l_{res} = 16 cm) coated with copper based on oscillation type of TE_{01n}, 3 optical chambers with shielded solenoids producing a constant magnetic fields **B** for optimization of pumping and detection processes and built-in Si-photodiodes with a surface of ~ 0.8 cm^2 each for detecting the resonance fluorescence of the atomic beam. The detection chamber contains two photodiodes placed as close to the beam as possible – at a distance of 6.5 mm from the atomic beam axis - and located outside the vacuum system. The C-field is directed along the atomic beam and generated also by a solenoid. It allows more uniform magnetic field in the interrogation regions. The microwave cavity and its solenoid are shielded by the 3 – layer magnetic shield with a demagnetization system. The regions of cavity ends contain coils for compensation C-field inhomogeneities. The circular apertures of < 8 mm in the cavity ends define the interaction zones of the atomic beam. The loaded capacity of the cavity is ~ 700. The microwave power insertion with enhanced coupling is used, thus providing at Q_{cav} = 700 a small change in the microwave power within a cavity over a temperature range and a reduction of the frequency pulling effect. As a result, the ABT frequency-temperature coefficient is reduced. The ABT is adequately gettered, evacuated using one 0.5 l/s ion pump, and manufactured with titanium, windows - of leikosapphire. The blackening of internal atomic beam tube surfaces is performed (excluding optical windows and cavity). A total atomic flux in the detection zone is about $5 \cdot 10^{11}$ at/s. The ABT parameters are: length 44 cm, ∅80 mm; weight 6.5 kg; the typical oven temperature is T_{oven} = 145°C.

In the pumping and detection regions, laser beams are linearly polarized and intercept the atomic beam at right angles. The ABT currently uses D_2 line (780 nm): the (2-2'σ) pumping transition for the atomic preparation and the best (2-3') cycling transition for the detection.

2.2 Laser Devices

The laser devices are mounted directly on the envelope of the ABT. Several solitary LD ($\lambda \approx 780$ nm, D_2 line) with different spectral properties were tested for beam pumping and detection. The laser modules contain the LD, microobjective, microcooling, and thermosensors. The structure of modules breadboards allows to replace each component. The operation regime: continuous, single-frequency. The generation power for the main LD mode is 2÷3 mW. For the lasers from Hitachi and Mitsubishi manufacturers the line's width is < 10 MHz. For other lasers – up to 40 MHz. The laser beam cross section is 3÷5 mm, collimation ~ 10^{-2}.

2.3 Lasers' Electronic Frequency Control Systems

The study purposed for creating optimized laser systems for ^{87}Rb discriminators and low-noise systems for optical signal registration has been performed.

Electronic systems for stabilizing lasers' parameters and recording optical signals comprise the following parts.

1) Controlled current sources (0 ÷ 110 mA) with a current stability of $5 \cdot 10^{-6}$ for detection laser and $1 \cdot 10^{-5}$ for pumping laser. The circuit of the current source includes a system for protecting the LD from possible laser current surges, reverse voltage occurrence, interference and static charge influence, current excess against its operating value as well as possible use in the optical line scanning regime (at frequency of 17 Hz) and high-frequency sinusoidal modulation (f_{mod} = 15.8; 15.0 kHz) in the laser's frequency lock loop regime. The specific feature of the FLLs is the fact that, as reference signals, they use weak resonance optical signals (10…500 nA) from the ABT photoreceiver at frequencies up to 40 kHz without the loss of the signal level. As a result, a photoreceiver device (PRD) should have high sensitivity, low noise level and be interference-immune. One of the main parameters of a current source over control is a current fluctuation level at modulation frequency of 167 Hz which is equal to: 144 $nA/Hz^{1/2}$ for the pumping laser source and 19 $nA/Hz^{1/2}$ for the detection laser source. For operating currents of (30–75) mA, the instantaneous peak-to-peak

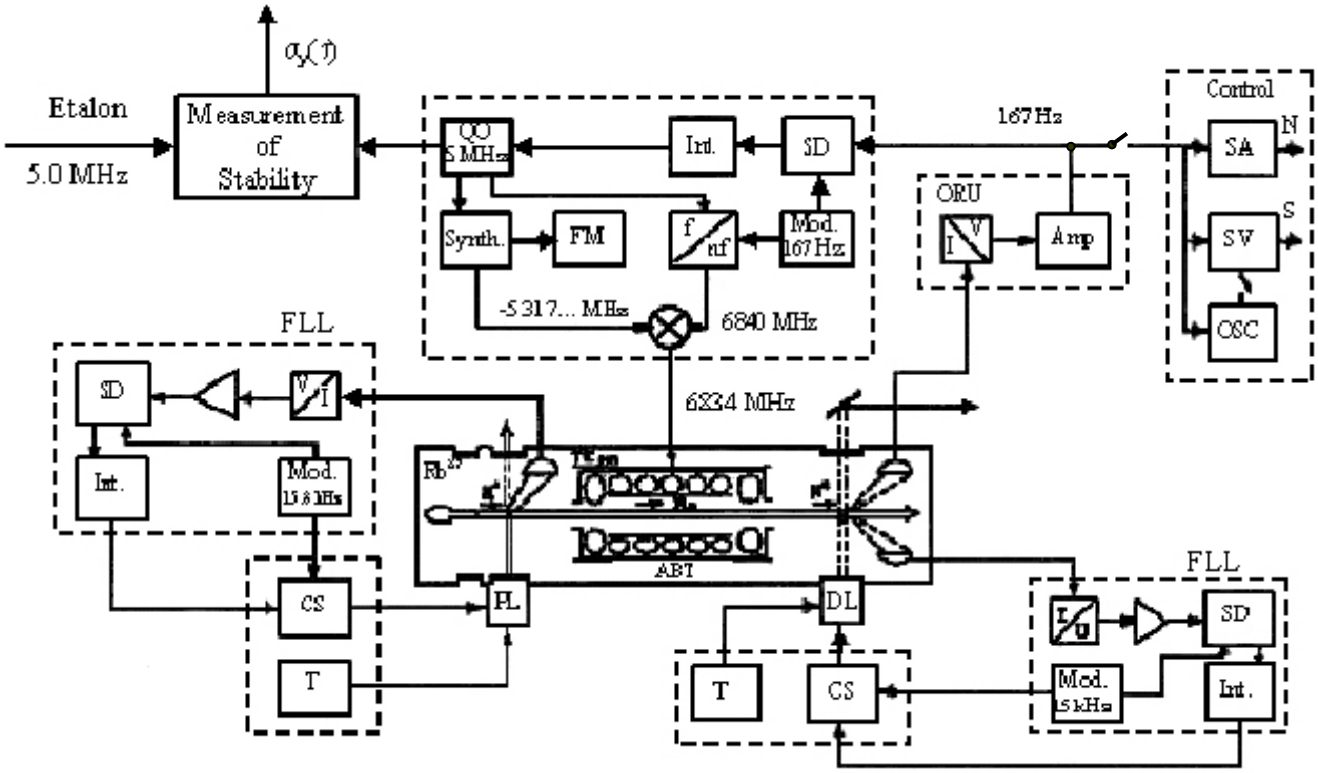

Fig. 1. Block diagram of a breadboard of the Rb atomic beam frequency standard with laser pumping. QO - quartz. oscillator, Synt – synthesator, FM – frequency meas., Int – integrator, SD - synchronous detector, Mod – modulator, Amp – amplifier, ORU - optical recording unit , SA - spectrum analyzer, SV- selective voltmeter, Osc – oscilloscope, CS - current source, T – thermoregulator, PL - pumping laser, DL – detection laser, ABT - atomic beam tube.

fluctuations of the laser frequency caused by current source fluctuations do not exceed 1 MHz/Hz$^{1/2}$; in this case, lasers' frequency stability is equal to approximately $2.6 \cdot 10^{-9}$/Hz$^{1/2}$ and $3.6 \cdot 10^{-10}$/Hz$^{1/2}$, respectively. The current drift is less than 5 μA/hour, the temperature drift is ~ 2 μA /°C.

2) Reversing systems of laser diode thermocontrol with an accuracy of specified temperature maintenance of ~ 0.02 °C/degree for one-stage regulation. The thermoregulator operates in the reversing regime against the environmental temperature (20±10)°C. The operating temperature range, ΔT, is (+10…+35)°C. The transient period for the operating temperature value is < 5 min.

The accuracy of setting a specified temperature value is ~ 0.001°C. For improving the stability of maintaining the operating temperature under conditions of changing environment temperature, the thermostat is developed with two-stage regulation comprising an additional internal copper envelope. The main parameters are as follows: stability of maintaining the temperature is $T_{envelope} = (5\text{-}9) \cdot 10^{-3}$ °C/degree for the internal copper envelope, $\Delta T_{laser} = (8\text{-}16) \cdot 10^{-4}$ °C/degree for the laser diode when a change of the environmental temperature $\Delta T_{environ} = 1 \div 6$°C. The current drift does not exceed 0.09 mA, the accuracy of setting the operating temperature in this device is better than 0.001°C.

3) Two laser's active FLL systems using atomic beam fluorescence lines with the laser current modulation and possibility to change a modulation index over a wide range.

4) Optical recording units with the photo-receiving device including I-V – converter. The unified PRDs are providing a constant sensitivity of the photo-receiver up to frequencies of $\geq 2f_m = 35$ kHz and placed in the pumping region (FLL of pumping laser) and in the detection region (FLL of detection laser; registration of the magnetic resonance signal, error signal). The signal-to-noise ratio (SNR) at $F_{mod} = 167$ Hz is measured using selective voltmeter ($F_{mod} = 167$ Hz, $\Delta f = 6.3$ Hz) and spectrum analyzer ($\Delta f = 3$ Hz).

5) Reference signals generator (167 Hz – a frequency of sinusoidal modulation of microwave signal; 15.8 kHz, 15.0 kHz – modulation frequencies for lasers' current $|F_s=2\rangle - |F'\rangle$ and $|F_s=1\rangle - |F'\rangle$ transitions' hyperfine components obtained when scanning the injection current of lasers within pumping and detection regions.

6) Scan generator for slow scanning a laser current (with a frequency of 17 Hz).

III. EXPERIMENTAL RESULTS

3.1 Fluorescence Spectrum of the optical transitions in the ^{87}Rb atomic beam and CPT effect

The investigations were performed using single-frequency lasers and LDs from Mitsubishi, Hitachi, Sharp and other Russian manufacturers of 780 nm wavelength (D_2 line). Fig.2 presents typical contours of fluorescence lines from $|F_s=2\rangle$ - $|F'\rangle$ and $|F_s=1\rangle$ - $|F'\rangle$ transitions' hyperfine components obtained when scanning the injection current of lasers within detection regions.

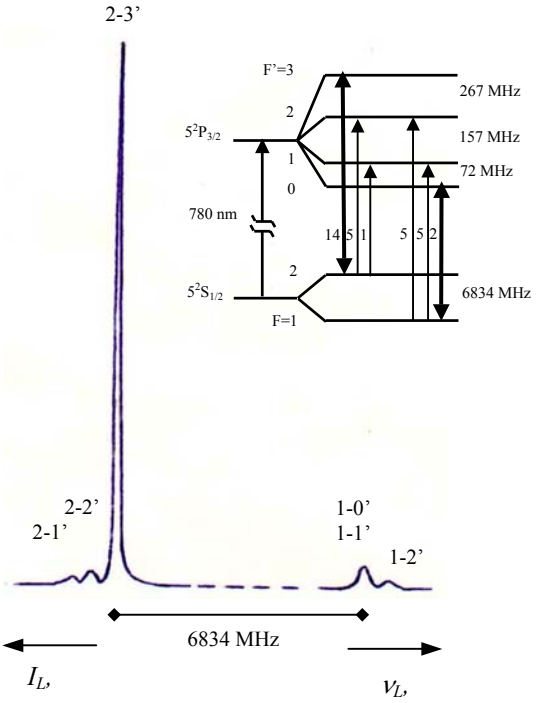

Fig. 2. Spectrum of the optical transitions in the ^{87}Rb atomic beam (detection region). Laser HL 7859 MG.
I_L = 58.3 mA, σ – polarization, B ≈ 0.
$S^{2-3'} \approx 0.5$ μA, $S^{2-2'} \approx 10$ nA

The investigation of ^{87}Rb beam pumping and detection efficiency on various hyperfine transitions has been performed as well as the influence of the laser intensity and the constant magnetic field strength in optical regions on these processes. The results of breadboard studies confirm the conclusion of our work [9]. When using a D_2 line, the most efficient scheme for this discriminator's breadboard is that of pumping at (2-2') transition with σ or (σ, π) – mixed polarization. In the last case (2-2', π) component equally pumps |2,0> and |1,0> sublevels without influence on the difference of populations. However, due to creation (σ, π) configuration the interaction time between atoms and light increases that leads to compensation of the decrease of **σ** - light component and simultaneously decrease the influence of coherent population trapping (CPT) effect.

Fig. 3 presents the spectra of $|F_s=1\rangle$ - $|F'\rangle$ hyperfine components obtained in cases of zero amplitude of additional magnetic field **B** within pumping region and with B ~ 0.8÷1.2 G. One can see the effect of CPT on the resolution of (1-1') and (1-0') hyperfine components during pumping from $|F_s=1\rangle$ level when using the light of **σ** – polarization.

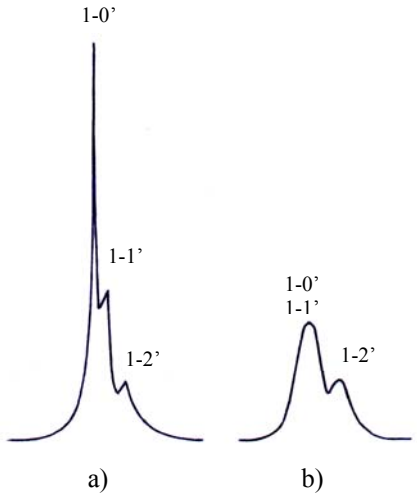

Fig. 3. Spectra of $|F_s=1\rangle$ - $|F'\rangle$ hyperfine components obtained within pumping region with additional field B > 0.8 G (a) and B = 0 (b). Laser ML 44114 R-01.
I_L = 65 mA, (σ, π) – polarization, $S^{1-0'} \approx 0.18$ μA

The strongest influence of this effect takes place with respect to (1-0') transition, and this is also confirmed by **B** field dependences within a pumping region (Fig.4).

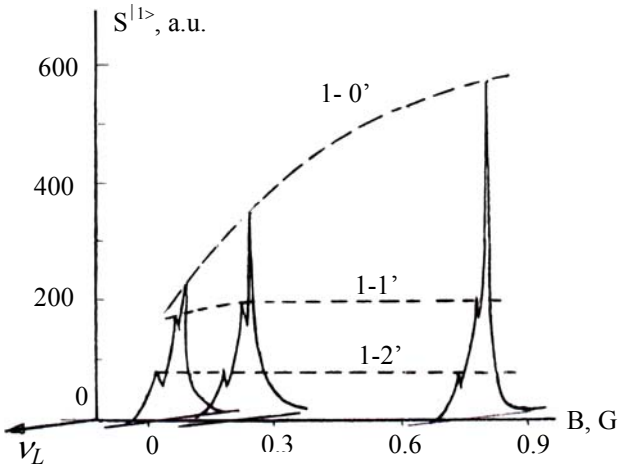

Fig. 4. Dependence of the $|F_s=1\rangle$ - $|F'\rangle$ hyperfine components as a function of the amplitude of the B field in the pumping region.

The influence of the CPT effect within a pumping region on the intensity of detection signal at the F_s= 2 – F'=3 transition and amplitude of the microwave signal at the detection region is shown in Fig. 5. $B_{opt} \geq 0.8$ G.

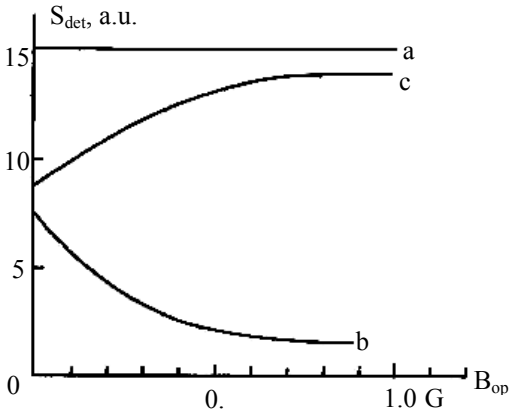

Fig. 5. Detection signal at the F_s= 2 – F'=3 transition vs the magnetic field strength $\mathbf{B}_{op}$ within a pumping region:
a – in the absence of pumping, I_{op}=0;
b – with optical pumping by wide-band laser, $I_{op} \neq 0$;
c – amplitude of the 1st harmonic of the "0-0" transition's signal at the F_{mod} of the microwave field.

The obtained pumping efficiency as regards $|F_s=2\rangle$ and $|F_s = 1\rangle$ levels achieves now (96÷99)% depending on the laser linewidth. The large value of a non-pumped atoms' signal with atomic shot noise at the detection zone defines mainly a noise level when detecting a magnetic resonance and SNR using the laser with a wide linewidth, $\Delta\nu_L > 30$ MHz . It is explained by the frequency fluctuations of the pumping laser. The contribution of the noise of the stray non-resonance irradiation is by 6 times lower. The inherent PRD noise in the recording channel at the F_{mod} = 167 Hz is a third-by-value limiting noise when measured a value of discriminator SNR and is by 1.6 times lower than the level of second noise. This noise decreases the discriminator SNR by ~ 20% and when improving a pumping efficiency and lowing the influence of non-resonance irradiation would be a main limiting factor.

3.2 Rb atomic beam discriminator with narrow-band lasers

Study of the laser line width effect on parameters of atomic beam and laser discriminators has shown that the problem of realization of a high-stable optically pumped Rb atomic beam frequency standard could be solved by using narrow-band laser diodes after optimization with respect to all parameters of discriminators.
Of all variants using various hyperfine transitions for pumping (2-2', 2-1'; 1-2', 1-1') and cycling detection (2-3'; 1-0') the best results were obtained in the following case: pumping on (2-2') transition within the additional magnetic field (B ~ 0.8 G) using ML 44114R-01 laser with (σ, π) - polarization relative to the **B** field; detection – on (2-3') transition with HL 7859 MG laser, (σ, π). The detection on (2-1') transition decreases the signal at the ABD output by ~ 100 times. The hyperfine structure of these transitions is shown in Fig.2 (insertion). Both lasers were stabilized by using the fluorescence signals of the atomic beam in pumping and detection zones. Note that with this method the detection laser's stabilization is only realized in the presence of the magnetic resonance signal and with the second photo-receiver device placed within a detection region. The lasers line width was measured to be below 10 MHz.

The preliminary results have shown that pumping with a narrow-band laser improved the spectral resolution of (2-2'), (2-3') components as well as (1-1') and (1-0'), decreased noise and increased SNR in the channel of pumping laser's frequency lock loop. With a selected pumping scheme, the difference in $|1\rangle$ and $|2\rangle$ levels' populations achieved 99 %. It reduced the total noise level in the detection zone. In this case when detecting a magnetic resonance the SNR was defined by the effective atomic shot noise as was expected according to [10]. In whole, it resulted in the stability improvement.

The saturation was achieved at the (2-3') transition within a detection region using a narrow-band laser. The largest atomic gain ($\beta \approx 190$ phot/at) was obtained when detecting with HL 7859 MG laser, (σ, π).

The measured width of Ramsey' resonance line with a modulation depth being close to the optimal value, depending on measurement conditions (laser's type, I_L), was of ~ (680-710) Hz. The shape of Ramsey's line is shown in Fig. 6.

The signal-to-noise ratio within 1 Hz band obtained at fluorescent cyclic detection of the Ramsey resonance with the linewidth of 680÷710 Hz achieves $(1\text{-}1.5)\cdot 10^4$.

3.3 Short-term instability of the Rb atomic beam frequency standard breadboard

When measuring the SNR and frequency instability of the AFS, the following parameters of atomic beam discriminator were checked and measured (Fig.1):

• LD operating point (laser current i_L, T) and environmental temperature, T_{room};

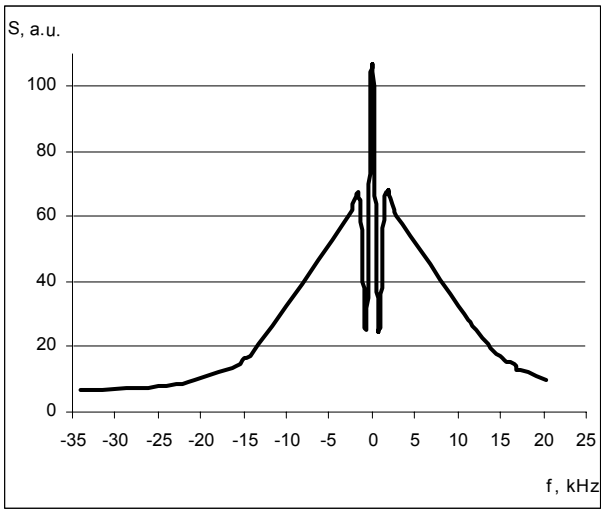

Fig. 6. Contour of Ramsey's line in the Rb ABT

• S_{mcw} ($1F_{mod}$ = 167 Hz) – ABD output signal amplitude at the modulation frequency of the microwave excitation signal;

• N – noise at the ABD output being measured at the F_m = 167 Hz within a band of the selective voltmeter Δf = 6.3 Hz when the microwave signal frequency is tuned to the resonance center and the modulation F_m is switched off; SNR = S_{mcw} / N_{1Hz}.

• $S_L(2f_{mod}$ = 31.6 kHz) – amplitude of the 2nd harmonic in the frequency lock loop of the pumping laser.

When recording the stability, the amplitude of the ABD output signal is also measured at the frequency 334 Hz. This signal is taken from the second PRD being in the frequency lock loop of the detection laser.

Preliminary results of the short-term instability measurements in ^{87}Rb atomic beam standard are given in Fig. 7.

IV. CONCLUSION

A breadboard of the ^{87}Rb atomic beam frequency standard with laser pumping and detection has been developed. The device is based on a modified ^{87}Rb atomic beam tube with using solitary laser diodes (without external grating) and the original electronic control systems.

The best results have been obtained using the D_2 line in the following configuration: laser pumping on 2-2', (σ, π) transition within the additional magnetic field (B > 0.8 G); and laser detection on (2-3') cycling transition. The most "atomic intensification" of about 190 photons/atom have been achieved. Preliminary measurements of the SNR in the ^{87}Rb atomic beam standard breadboard show the level of SNR (Δf = 1 Hz) ≈ (1.0-1.5)·10^4, W ≤ 710 Hz. The best results for short-term instability measurements in ^{87}Rb atomic beam standard are: $\sigma_y(\tau) \sim 1.4 \cdot 10^{-12}\, \tau^{-1/2}$, $10 < \tau < 10^4$ s (Allan Deviation).

The estimates based on measurements results obtained using the different of ABD parameters show that in the shot noise limiting we can achieve in this device such parameters as follows: SNR ≈ $1.5 \cdot 10^5$, feature of merit M ≈ 220 and $\sigma_y(\tau) \le 1.5 \cdot 10^{-13}\, \tau^{-1/2}$.

The obtained data and estimates could be improved with reduced the stray light flux and enhanced electronic devices.

The obtained results are promising and meet the requirements of spaceborne frequency standard concerning the metrological parameters.

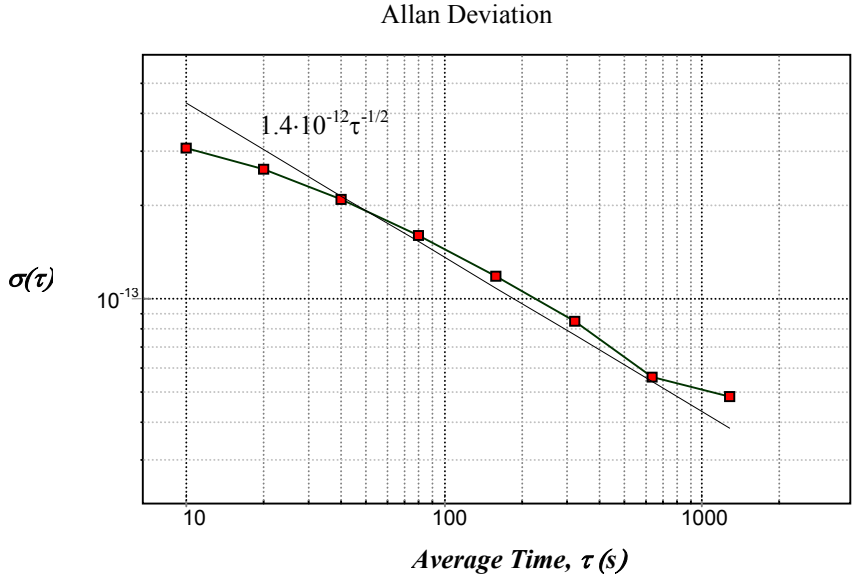

Average Time τ, sec	Sigma
10	$3.1 \cdot 10^{-13}$
20	$2.6 \cdot 10^{-13}$
40	$2.1 \cdot 10^{-13}$
80	$1.6 \cdot 10^{-13}$
160	$1.2 \cdot 10^{-13}$
320	$8.5 \cdot 10^{-14}$
640	$5.6 \cdot 10^{-14}$
1280	$4.8 \cdot 10^{-14}$

Fig. 7. Short-term instability of the ^{87}Rb atomic beam frequency standard. (Shown is according to a noise type close to a white-frequency noise)

These results confirm the conclusion of our work [9] relatively the advantages of using the ^{87}Rb isotope as a working substance as the alternative of ^{133}Cs atoms when developing a high-stable small-size atomic beam frequency standard with laser pumping.

Acknowledgements

We would like to acknowledge Dr. P. Berthoud (ON) and Dr. J. Delporte (CNES) for supporting this work and helpful discussions, Dr. Ch. Schori (ON) for measurement of the laser line-width and Prof. A. Chirkov (St.-Petersburg Technical University) for assistance in experimental data calculation.

REFERENCES

[1] C. Sallot, M. Baldy, D. Gin, and R. Petit, Proc. of the 2003 IEEE Int. FCS and PDA Exhibition Jointly with the 17th EFTF, 100 (2003)

[2] R. Lutwak, D. Emmons, R.M. Garvey, and P. Vlitas, 33rd Annual Precise Time and Time Interval (PTTI) Meeting, Long Beach, CA, USA (2001)

[3] R. Barillet, P. Cerez, G. Theobald, C. Sallot et al., Proc. of the Joint Meeting 16th EFTF & 2002 IEEE Int. FCS, St.- Petersburg , Russia, 148 (2002)

[4] S. Lecomte, M. Haldimann, R. Ruffieux, P.Thomann, and P. Berthoud, 20th EFTF, 2006, Braunschweig, Germany, in these proceedings

[5] V. Hermann, B. Leger, C. Vian, J.-F. Jarno, M. Gazard, 20th EFTF, 2006, Braunschweig, Germany, in these proceedings

[6] A. Besedina, V. Velichanskii, A. Zibrov, and V. Zholnerov, Sov. J. Quant. Electr., **18**, no 3, 367 (1991)

[7] A. Gevorkyan, A. Besedina, A. Bassevich, Proc. of the 1993 IEEE Int. Freq. Control Symp., 97 (1993)

[8] A. Besedina, A. Bassevich, A.Gevorkyan et al , 5th Russian. Symp. “Metrology of Time & Space”, VNIIFTRI, Moscow, Russia, 344 (1994)

[9] A. Besedina, A. Gevorkyan, V. Zholnerov, Proc. of the 19th EFTF, Besancon, France (2005)

[10] N. Dimarcq, V. Giordano, P. Cerez, G. Theobald, IEEE Trans. Instr. Meas. **42**, no 2, 115 (1993)

This work was supported by the INTAS-CNES Project no. 03-53-5175.

Proceedings of the 20th EFTF, 2006

Long Term Study of the H-Maser Clocks at the Royal Observatory of Belgium

F. Roosbeek* and P. Defraigne
Royal Observatory of Belgium
Avenue Circulaire, 3 – 1180 Brussels - Belgium
**Electronic address:* f.roosbeek@oma.be

Two hydrogen masers are in operation in the time lab of the Royal Observatory of Belgium. One is a CH1-75 operational since 1991 and the other one is a CH1-76 operational since the 1999. This second one is used to provide a frequency needed by the active HM CH1-75 for the cavity auto-tuning. The stability of the masers since their putting in operation is studied.

I. TIME LAB OF THE ROYAL OBSERVATORY OF BELGIUM

One of the missions of the Royal Observatory of Belgium (ROB) is to integrate Belgium into international space and time reference systems through "determination of Time", and precise positioning. The time scales where the ROB is involved are: UTC(ORB), local realization of UTC, TAI (basis of the legal time) and IGS Time scale IGST (IGS is the International GPS Service), which is provided in quasi-real time.

The time lab of the Royal Observatory of Belgium is presently equipped with 5 clocks: 3 HP5071A Cesium clocks with standard tubes (CES4, CES5 and CES6, see Picture 1) and 2 H-Maser clocks (1 active CH1-75 and one passive CH1-76, respectively MAS1 and MAS2, see Pictures 2 and 3). The UTC realization UTC(ORB) is obtained from the 5 Mhz frequency provided by the active H-Maser clock (CH1-75) of which the cavity auto-tuning is realized using the 5 Mhz frequency of the passive H-Maser (CH1-76). The maximum difference between UTC and UTC(ORB) is kept below 60 nanoseconds (ns).

As contribution to the TAI, the Royal Observatory of Belgium sends presently the data of 4 clocks (3 cesium clocks and the active Hydrogen Maser) to the BIPM. Furthermore, the ROB time laboratory contains GPS receivers which are used for both the time transfer (remote clock comparisons) and geodesy.

The monitoring of the clocks is realized by a comparison of their behavior with respect to UTC(ORB). The clocks are located in temperature stabilized basements, where the temperature is stable at the 0.1°C level.

The time lab has been installed in a new temperature stabilized room in April 2002. Figure 1 gives a diagram of the time lab.

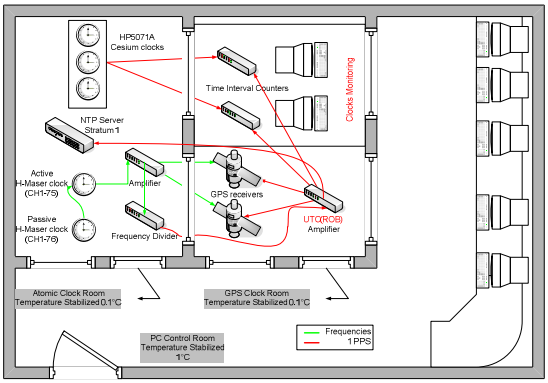

Figure 1. Diagram of the Time Lab.

II. EVENTS AND BREAKOUTS OF MASER CLOCKS SINCE NOVEMBER 2001

In the following tables, we give the special events and breakouts of our maser clocks since November 2001, which corresponds to the switch from CES5 to MAS1 for the realization of UTC(ORB).

Table 1 shows the manual frequency changes applied to MAS1 in order to be kept as close as possible to UTC.

Table 2 shows the periods when MAS2 was not functioning. During that time, MAS1 was working without cavity autotuning.

Table 3 shows the periods when MAS1 was not functioning. During that time, UTC(ORB) was realized by CES5.

Note that all these breakouts, listed in tables 2 and 3, are due to electronic problems in the clocks.

Finally, Table 4 shows special events that have occurred since November 2001 and that could influence the quality of MAS1.

TABLE I. MAS1 FREQUENCY CHANGES

Modified Julian Day	Frequency change (x 10-14 s/s)
52240	-1
52278	-2
52305	-2
52374	+3
52389	-3
52450	-4
52460	-5
52466	+1
52491	-4
52507	-4
52519	-18
52529	+19
52537	+5
52597	-1
52624	-2
52655	-2
52774	-1
52787	-2
52872	+1
52904	-1
53017	-2
53261	-1

TABLE II. MAS2 STOPPED

From	To
01 Dec 2001 (52244)	01 Mar 2002 (52334)
25 May 2002 (52419)	01 Sep 2002 (52518)
07 Nov 2003 (52950)	05 Mar 2004 (53069)

TABLE III. MAS1 STOPPED (ELECTRICAL PROBLEM INDUCING FREQUENCY CHANGE)

From	To
03 Jul 2003 (52823)	01 Aug 2003 (52852)

TABLE IV. SPECIAL EVENTS

From	To	Event
01 Apr 2002 (52365)	01 Sep 2002 (52518)	1 PPS out of order
16 Apr 2002 (52383)	19 Apr 2002 (52383)	New Time Lab
23 May 2002 (52417)	25 Jun 2002 (52450)	Microphase stepper activated
09 Sep 2003 (52891)	10 Sep 2003 (52892)	Air conditioning out of order
20 May 2005 (53510)	now	Decrease in the MAS1 generation power resulting in CAT system off

III. COMPARISONS

A. *UTC-UTC(ORB)*

The following graph (Figure 2) shows the differences between our reference clock (CES5 or MAS1) and UTC since July 1994.

We have intentionally removed data before July 1994, corresponding to the period when our reference clock was a rubidium one. We have used blue dots when the reference clock was CES5 and red dots when it was MAS1. The jump around MJD 51525 corresponds to a reset of UTC(ORB). Note also that due to a failure of MAS1 between MJD 52823 and MJD 52852, CES5 has been used as reference clock during that time.

The black curve is the sample set that we have chosen for studying the frequency stability when our reference clock was CES5. This corresponds to the period between mid-September 1997 and mid-December 1999 when no change was operated on the microphase stepper controlling CES5. The corresponding Modified Allan Deviation is given on Figure 3.

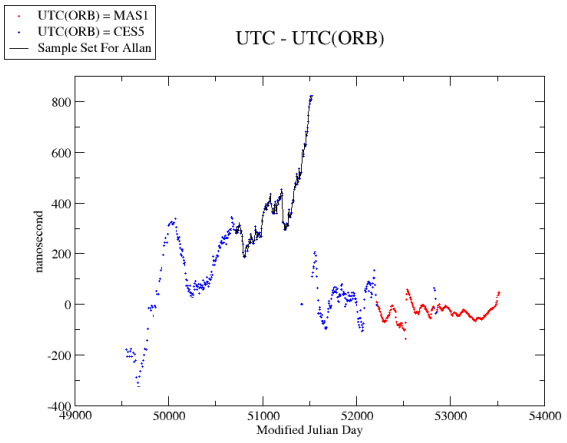

Figure 2. Differences between our reference clock (CES5 or MAS1) and UTC since July 1994.

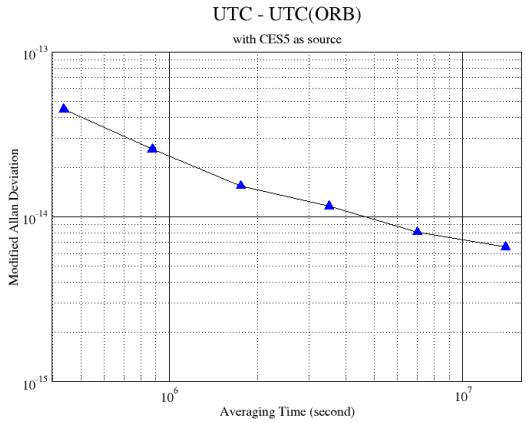

Figure 3. Modified Allan Deviation of Fig. 2

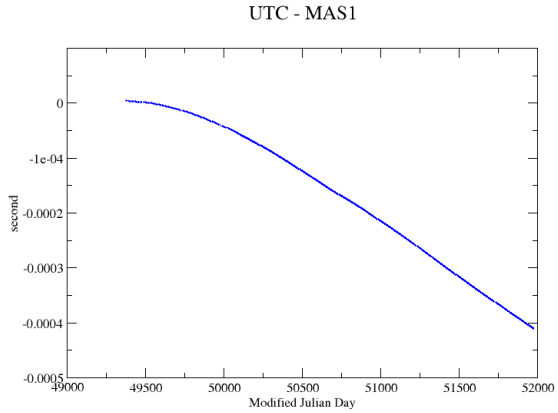

Figure 4. UTC - MAS1 when our reference clock was CES5 (between July 1994 and mid-March 2001).

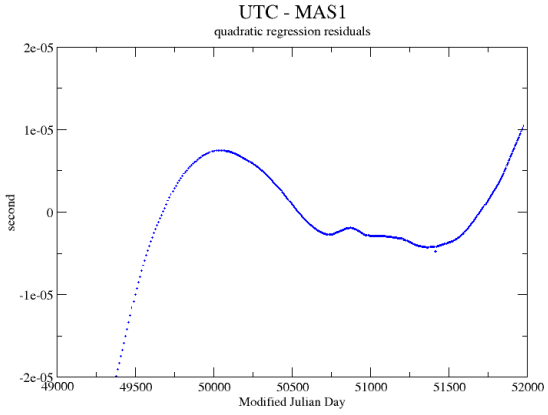

Figure 5. The same graph after removing a quadratic regression

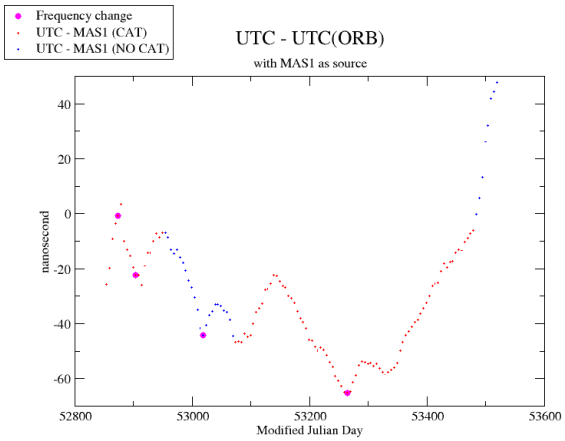

Figure 6. UTC-MAS1 since August 2003, when MAS1 was the reference clock for UTC(ORB).

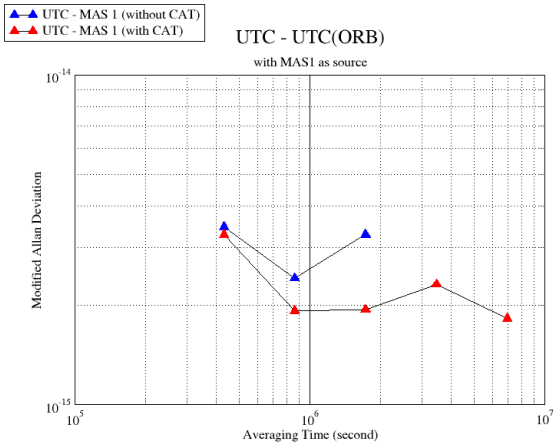

Figure 7. Modified Allan Deviation of Fig. 6

B. UTC-MAS1

These graphs have been obtained by differencing the values of UTC - UTC(ORB) given by the BIPM and the values UTC(ORB) - MAS1, available locally at the ROB.

The first graph (Figure 4) shows the values of UTC - MAS1 when our reference clock was CES5 (between July 1994 and mid-March 2001). No clock reset was applied to MAS1 during that time. The same graph after removing a quadratic regression is shown on Figure 5.

The second graph (Figure 6) shows the values of UTC-MAS1 since August 2003, when MAS1 was the reference clock for UTC(ORB). We have chosen this period in order to enlighten the effect of the cavity auto-tuning (CAT) done by our MAS2. The blue dots correspond to periods without CAT while the red dots correspond to periods with CAT. Note that, from MJD 53510, MAS1 gives larger variations due to a decrease in the Maser generation power. The corresponding

Modified Allan Deviation is given on Figure 7. Note that, because during that time MAS1 was the reference clock for UTC(ORB), some manual frequency changes have been applied in order to follow UTC. These changes have been removed before computing the Modified Allan Deviation.

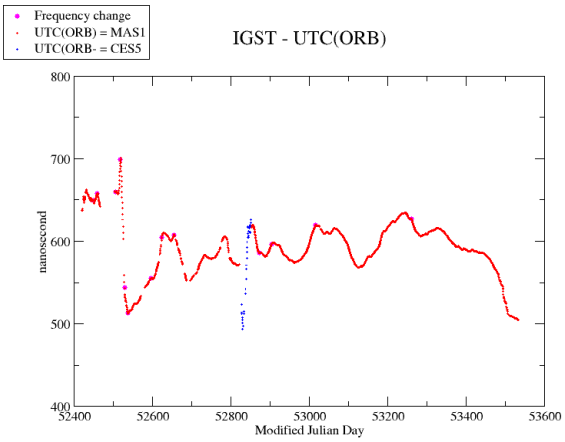

Figure 8. IGST - UTC(ORB) since June 2002.

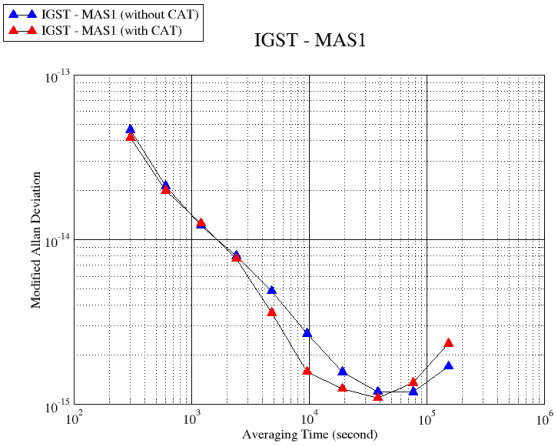

Figure 9. Modified Allan Deviation of Fig. 8

C. *IGST - UTC(ORB)*

Comparisons with UTC, with 1 point every 5 days give information about the long term stability of our maser clocks. For getting information about the short term stability, we make comparisons with the IGST time scale, for which the differences between IGST and UTC(ORB) are given every 30 seconds.

The Figure 8 shows the values IGST - UTC(ORB) since June 2002. During a breakout of MAS1, between MJD 32823 and MJD 52852, CES5 was used as UTC(ORB). This is shown in blue dots on the graph.

For studying the short term stability of MAS1, we have chosen two weeks on the graph: GPS week 1310 and GPS week 1250. the first one corresponds to a period with the CAT activated, while the second one doesn't have it. The corresponding Modified Allan Deviation are given on Figure 9.

Note that we choose the option to correct the time series for the day boundary jumps before computing the Allan deviations.

D. *MAS1 - MAS2*

We have also analyzed the short term stability of MAS2 by means of MAS1. We have compared the two maser clocks with a frequency and phase comparator A7 from QuartzClock during one month, starting from 25 July 2005. The sample step used in the measurements was 1 point every 30 seconds.

The resulting graph after removing a quadratic regression and the Modified Allan Deviation are given on Figure 10 and 11.

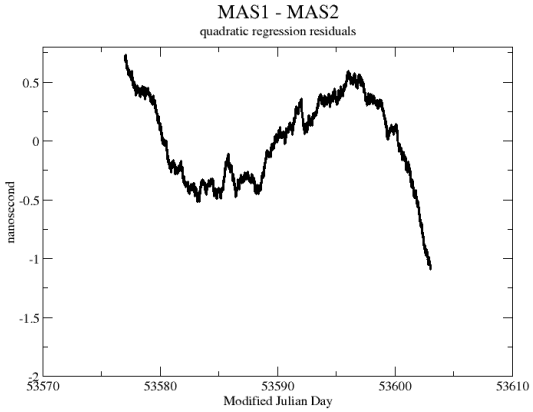

Figure 10. MAS1 – MAS2 after removing a quadratic regression

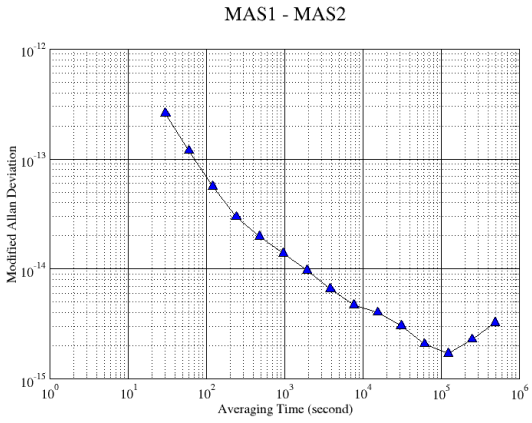

Figure 11. Modified Allan Deviation of Fig. 10

IV. CONCLUSION

MAS1 is used for the realization of UTC(ORB) since November 2001. During that time, it has been stopped only 1 month, in July 2003. Failures affecting MAS2 have also resulted in running MAS1 without cavity auto-tuning (CAT) at certain epochs (see table 2). Due to a decrease in the MAS1 generating power, it is also operating without CAT since 20 May 2005.

As we can see on Figure 9, the short term stability of MAS1 is not significantly modified when the CAT is running or not. On the contrary, on Figure 7, we see clearly the improvement of the CAT on the long term stability.

Finally, when we compare Figure 3 with Figure 7, we see that UTC(ORB) is more stable when it is realized by MAS1 with CAT than with CES5 with a standard tube (by a factor ~10 at 10 days averaging time and a factor ~3 at 100 days averaging time).

Proceedings of the 20th EFTF, 2006

On Secondary Representations of the Second

P. Gill* and F. Riehle**

** National Physical Laboratory, Hampton Road, Teddington, Middlesex, TW11 0LW, UK*
*** Physikalisch-Technische Bundesanstalt, Braunschweig, Germany*
**Electronic address:* patrick.gill@npl.co.uk

The emergence of microwave and optical frequency standards with accuracies close to those of caesium primary frequency standards has led to the concept of secondary representations of the second. The recently-formed Joint Working Group of the CCL / CCTF has now recommended as secondary representations to the CCTF / CIPM one microwave radiation in ^{87}Rb and three optical radiations in $^{199}Hg^{+}$, $^{88}Sr^{+}$ and $^{171}Yb^{+}$. This paper describes the rationale, evolution and development of criteria for acceptance of a radiation as a secondary representation, together with a review of the JWG assessment and recommendation of the four radiations already proposed.

I. INTRODUCTION

The year 2005 marked the 50th anniversary of the atomic clock, originally introduced by Louis Essen. Some twelve years after this introduction, the Conference Generale des Poids et Mesures (CGPM) adopted as a new definition of the SI unit of time, the second, in terms of the transition between hyperfine levels in the ground state of caesium. This definition has proved to be a durable one, with subsequent development of commercial caesium beam clocks for a wide variety of time and frequency applications such as satellite navigation. In addition the primary caesium frequency standards themselves have evolved considerably from Essen's original device. Contemporary primary standards now apply time-separated 9.2 GHz microwave Ramsey interrogation pulses to probe cold Cs atoms launched upwards in a 1-m fountain, and as they fall back under gravity. These cold atom fountain primary standards have demonstrated fractional uncertainties better than 1 part in 10^{15} over a day's averaging, with corresponding timing accuracy of ~ 100 picoseconds per day. There are to date, six Cs fountain primary standards operational at national metrology institutes (SYRTE, PTB, NIST, IEN, NPL and NMIJ) and which make a significant contribution to steering TAI. Additionally, with the emergence of high accuracy optical frequency standards based on cold atoms and cold trapped ions, the fountains currently provide the ultimate reference for highest accuracy femtosecond comb measurements of optical frequencies.

However, the international metrology community has long debated the potential of optical frequency standards to out-perform microwave standards in the long run. The reason for this is the much higher frequency of the optical standard, with a typical value approaching 10^{15} Hz, is some 10^{5} higher than the Cs frequency. With achievable linewidths in the 1 Hz range, whether dictated by interrogation time or natural decay time, this gives rise to significantly improved signal to noise, and hence reduced instability (σ) according to the equation:

$$\sigma(\tau) = \frac{1}{2\pi\nu\sqrt{NT_{\mathrm{int}}\tau}}$$

where ν is the clock transition frequency, N is the number of atoms or ions, T_{int} is the Ramsey interrogation time and τ the sampling time. With such improved stability in the optical relative to the microwave standards, this allows quicker and more rigorous assessment of the atomic optical clock's reproducibility with respect to environmental parameters such as electric and magnetic field variations, and hence potentially more accurate sub-division of the second.

II. IMPROVEMENTS IN OPTICAL FREQUENCY STANDARDS

The recent improvement in optical frequency standards can be contrasted against that for the primary microwave caesium clocks in figure 1. Over the past several years, optical standards based on cold atoms and cold trapped ions have benefited significantly from the advent of the self-referenced femtosecond comb [1, 2], with result that the rate of improvement for the optical standards is now such that comb measurement of optical frequencies will very soon be limited by the Cs microwave standard itself. It is anticipated that optical frequency uncertainties will likely demonstrate reproducibilities below that of caesium, raising the prospect of an optical redefinition of the second in the future.

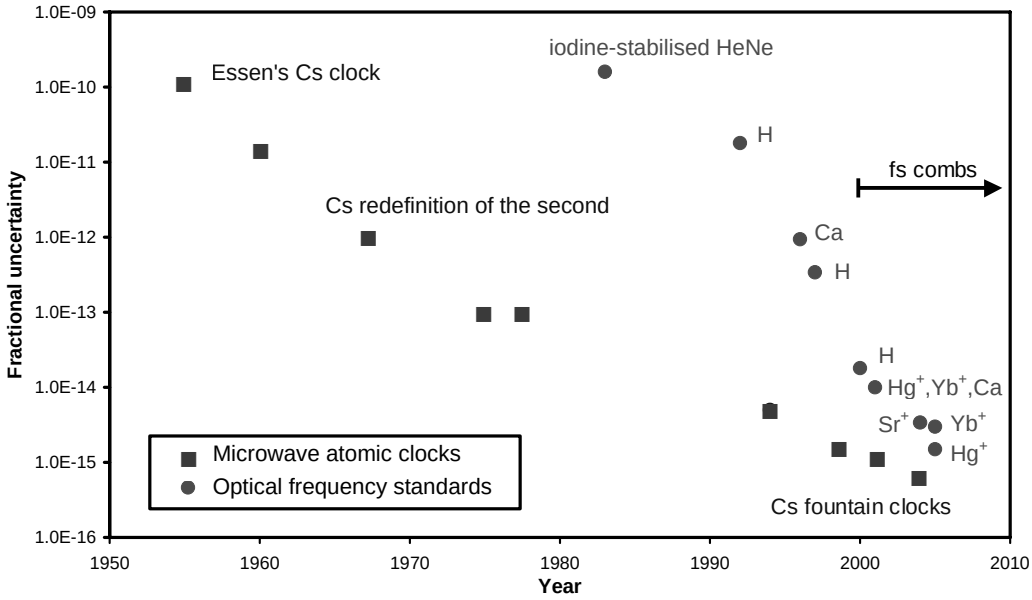

Figure 1: Improvements in atomic frequency standards

However, once the optical uncertainty becomes Cs-limited, the metrology community is faced with a position where optical standards are unable to demonstrate lower uncertainty until such time as a redefinition might occur, even though they may be shown to be more reproducible by eg comparing two optical systems directly. This projected difficulty led to an initial proposal from NIST to the 2001 CCTF to consider the establishment of secondary representations of the second [3], where such representations, whether optical or microwave, could be used to realise the second, provided that their accuracy was close to the Cs uncertainty. Obviously, their uncertainty could be no better than the Cs primary uncertainty. However, it was considered that the establishment of these representations would help with the detailed evaluation of reproducibility at the highest level, and significantly aid the process of comparing different standards in the preparation of a future redefinition.

III. SECONDARY REPRESENTATION CANDIDATES

The perceived range of alternatives as Secondary Representations included microwave standards such as Rb, $^{171}Yb^{+}$ and $^{199}Hg^{+}$ microwave transitions, and a variety of single cold trapped ion clock transitions in $^{88}Sr^{+}$, $^{199}Hg^{+}$, $^{171}Yb^{+}$, Ca^{+} and cold atom transitions in Sr, Yb, Ca and Hg. All these systems were potentially capable of demonstrating reproducibilities better than Cs, but of course, as Secondary Representations, would remain limited in uncertainty by Cs.

Against this background, a Joint Working group (JWG) of the CCL/CCTF was set up in Sept. 2003, reporting to the Presidents of the CCTF (Prof Leschiutta) and CCL (Dr Chung). The JWG comprised members from BNM-SYRTE, IEN, NMIJ, NIST, NPL, NRC, PTB and VNIIFTRI under the chairmanship of F Riehle and P Gill. The preliminary terms of reference of the JWG were to

- Ask for proposals from the NMIs for microwave and optical frequency standards to adopt as secondary representations.
- Meet to review the associated uncertainty budgets for these proposals.
- Evaluate the validity of the proposal and make recommendation to the CCTF for the addition of particular standards to the list of secondary representations.

IV. SECONDARY REPRESENTATION / MISE EN PRATIQUE RELATIONSHIP

The Mise en Pratique Working Group of the CCL (MePWG) already maintains a recommended radiation list for the realization of the SI metre and other frequency metrology applications [4]. There are some 22 radiations listed, including cold atom and trapped ion optical standards, gas-cell stabilized lasers and even discharge lamps, and the accuracies associated with this diverse list span several orders of magnitudes. This raised a number of issues, including:

- Relationship between SR and MeP lists?
- Common values and uncertainties?
- Whether / how to integrate the two lists?

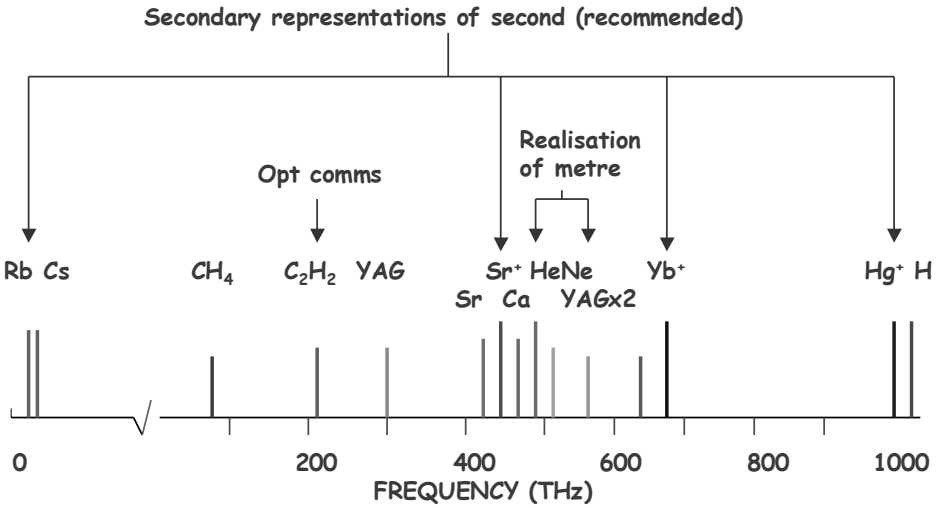

Figure 2: Example of a unified list of recommended radiations

As a result, the CIPM 2003 adopted a single list approach which should be periodically updated, where certain radiations could be

- approved by the CCTF as secondary representations of the second

and others

- accepted by the CCL as suitable for realization of the metre.

The consequences of this approach were that there would be no ambiguity in recommended frequency values, and that it strengthened the metre definition linking time and length measurement. However, it was recognized that the particular needs of the length and time communities were orthogonal in the sense that iodine-stabilised lasers, for example, were not well suited to time keeping requirements, and, conversely, microwave clocks were not at present so practical for length metrology.

V. CRITERIA FOR ADOPTION AS A SECONDARY REPRESENTATION

On the basis that a future CCTF will look to the list of secondary representations for a new definition of the second, the following criteria for adoption of a proposed radiation were derived:

1. "The SI value of the unperturbed frequency of a quantum transition suitable as a secondary representation of the second must have an uncertainty that is *evaluated* and *documented* so as to meet the requirements adopted for the primary frequency standard for use in TAI"
2. "This uncertainty should be no larger than about a factor of 10 of the primary standards *of that date* that serve as the best realizations of the second"

The implications of these criteria are such that only frequency standards with currently attributed accuracies of around 1 part in 10^{14} or better, should be considered. Thus it can be seen that these requirements are significantly more stringent than those relevant to incorporation into the MeP.

VI. RECOMENDED Rb MICROWAVE STANDARD

The 6.8 GHz cold Rb microwave fountain standard was reported to the JWG in 2004 by SYRTE, with a quoted uncertainty of 1.2 parts in 10^{15}, and subsequently confirmed in 2005 [5], with an uncertainty of 1.6×10^{-15}. As a result, the JWG recommended it as a secondary representation with a frequency value of

$$\nu(\mathrm{Rb}) = \mathbf{6\ 834\ 682\ 610.904\ 324\ Hz}$$

with a relative standard uncertainty of 3×10^{-15}. This was accepted by the CCTF and is awaiting ratification by the CIPM.

VII. PROPOSED OPTICAL RADIATION CANDIDATES

A number of possible optical frequency standard candidates were considered at the JWG meeting in September 2005. These are listed in Table 1. As can be seen from the Table, only three radiations were considered by the JWG to be appropriate for recommendation to the CCTF as secondary representations at this time. These were the $^2S_{1/2}$ F=0 - $^2D_{5/2}$ F=2 quadrupole transition in $^{199}Hg^+$ at 282 nm, the $^2S_{1/2}$ - $^2D_{5/2}$ quadrupole transition in $^{88}Sr^+$ at 674 nm and the $^2S_{1/2}$ F=0 - $^2D_{3/2}$ F=2 quadrupole transition in $^{171}Yb^+$ at 436 nm.

System	Studied at	Quoted uncertainty	MeP uncertainty	Conclusion
$^{199}Hg^+$	NIST	0.94 Hz	3 Hz (3 in 10^{15})	Recommended
$^{88}Sr^+$	NPL, NRC	1.5 Hz / 15 Hz Difference 0.6 Hz	3 Hz (7 in 10^{15})	Recommended
$^{171}Yb^+$	PTB	2 Hz	6 Hz (9 in 10^{15})	Recommended
^{40}Ca	PTB, NIST	3.4 Hz / 5.3 Hz Difference 8 Hz	8 Hz (1.6 in 10^{14})	Consider at next JWG meeting
^{87}Sr	Tokyo, JILA	15 Hz / 20 Hz Difference 85 Hz	85 Hz (1.7 in 10^{13})	Consider at next JWG meeting
$^{27}Al^+$	NIST	1.1 Hz	Not considered due to lack of published data	Presentation only

Table 1. Radiations considered at Sept 2005 JWG meeting

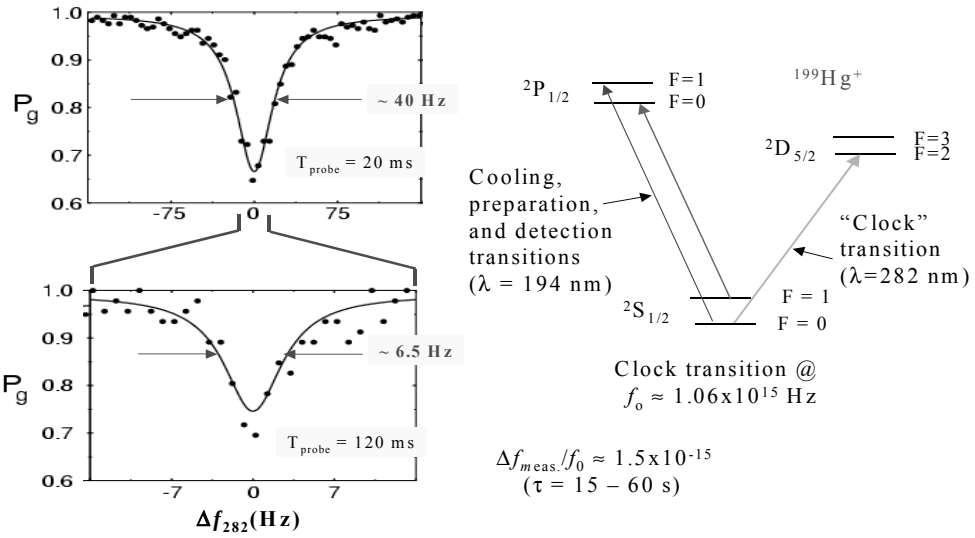

Figure 3: $^{199}Hg^+$ 282 nm quadrupole clock transition

VIII. $^{199}Hg^+$ 1.06 PHz CLOCK TRANSITION

The $^{199}Hg^+$ quadrupole transition at 282 nm (1.06 PHz) proposed by NIST has a lifetime of ~ 90 ms and corresponding natural linewidth of ~ 1.7 Hz. Figure 3 shows the partial energy level structure for the $^{199}Hg^+$ ion, together with the respective cooling and clock transitions. Also shown are the observed clock transition transform-limited linewidths for 20 ms and 120 ms interrogation pulses.

The most recent absolute frequency measurement of this $^{199}Hg^+$ 282 nm quadrupole transition [6] gives the value

1 064 71 609 899 144. 98 (0.94) Hz

which is in excellent agreement with the weighted mean of all measurements since 2001, which has the value

1 064 721 609 899 145.05 (0.74) Hz

The stability of the transition at the 10^{-16} level for ~ 100 second averaging times has been verified comparison with the 267 nm $^{27}Al^+$ clock transition by means of femtosecond comb comparison. Given the fact that this transition was only under study at NIST, the JWG accepted the MePWG recommendation that for its consideration as a secondary representation, the uncertainty should be increased to 3 Hz. As a result, the JWG recommended the $^{199}Hg^+$ 282 nm quadrupole clock transition to the CCTF as a secondary representation with a value

$$\nu(^{199}Hg^+) = \mathbf{1\ 064\ 721\ 609\ 899\ 145\ (3)\ Hz}$$

which applies to the unperturbed quadrupole transition

IX. $^{88}Sr^{+}$ 445 THz CLOCK TRANSITION

The $^{88}Sr^{+}$ quadrupole transition at 674 nm (445 THz) was proposed as a secondary representation by both NPL and NRC. It has a lifetime of ~ 0.4 s and corresponding natural linewidth of ~ 0.4 Hz. Figure 4 shows the partial energy level structure for the $^{88}Sr^{+}$ ion, together with the respective cooling, repumping and clock transitions.

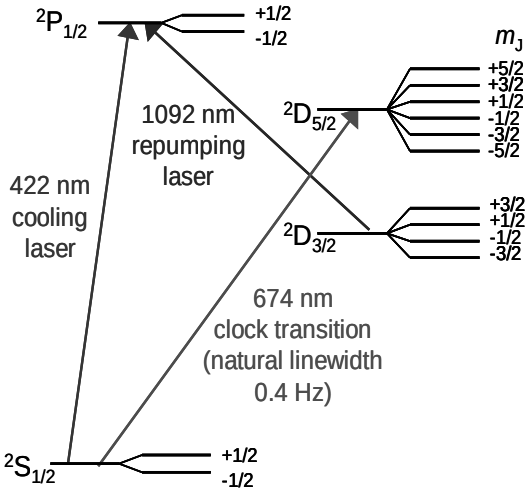

Figure 4: $^{88}Sr^{+}$ 674 nm quadrupole clock transition

The most recent absolute frequency measurement [7] at NPL gave the value

444 779 044 095 484.6 (1.5) Hz

in comparison with the measurement value from NRC [8]

444 779 095 484 (15) Hz.

There is excellent agreement between the measurements made on independent systems at the two laboratories, but recognising the order of magnitude difference in stated uncertainties between the laboratories, the JWG accepted the MePWG recommendation to increase the uncertainty by a factor of 2. As a result, the JWG recommended the $^{88}Sr^{+}$ 674 nm quadrupole clock transition to the CCTF as a secondary representation with a value

$\nu(^{88}Sr^{+})$ = **444 779 044 095 484.6 (3.0) Hz**

which applies to the unperturbed quadrupole transition and the centre of the Zeeman multiplet.

X. $^{171}Yb^{+}$ 688 THz CLOCK TRANSITION

The $^{171}Yb^{+}$ quadrupole transition at 436 nm (688 THz) was proposed as a secondary representation by PTB. It has a lifetime of ~ 40 ms and corresponding natural linewidth of ~ 3.1 Hz. Figure 5 shows the partial energy level structure for the $^{171}Yb^{+}$ ion, together with the respective cooling, re-pumping and clock transitions.

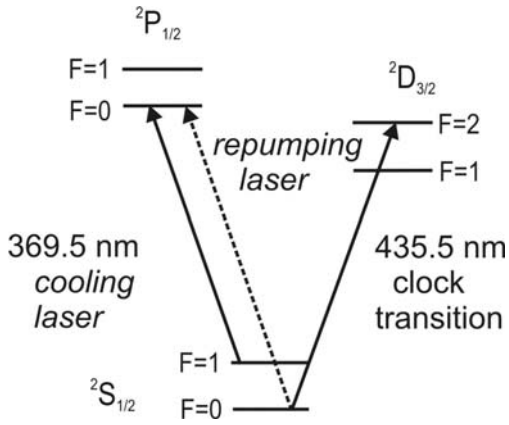

Figure 5: $^{171}Yb^{+}$ 436 nm quadrupole clock transition

The most recent absolute frequency measurement at PTB [9] gave the value

688 358 979 309 307.65 (2.14) Hz.

Combining this value with earlier frequency measurements yielded a mean frequency less than 0.3 Hz different from this value. Two-trap comparisons were carried out immediately prior to the measurement. The results of those comparisons [10] are consistent with a difference of 3.8 (6.1) $x10^{-16}$ between the two ytterbium standards. However, since the $^{171}Yb^{+}$ quadrupole standard was under investigation at PTB only, the MePWG considered it prudent to increase the uncertainty by a factor of ~ 3 to 6 Hz, and the JWG recommended the $^{171}Yb^{+}$ 436 nm quadrupole clock transition to the CCTF as a secondary representation of the second with a value

$\nu(^{171}Yb^{+})$ = **688 358 979 309 308 (6) Hz**

which applies to the unperturbed quadrupole transition.

XI. POSSIBLE CONTRIBUTION OF SECONDARY REPRESENTATIONS TO TAI

Currently, the CCTF working group on primary frequency standards is considering the standardisation of formats for the reporting of primary frequency measurements to BIPM. This comprises three components:

- Publication of experimental details and full uncertainty budget in peer-reviewed scientific journal.
- A report to BIPM detailing the results obtained in a particular reporting period.
- Results reported as frequency offsets from a clock contributing to TAI , and including uncertainty budget and references.

Data is then published in Circular-T within the section for primary frequency standards. With this protocol in mind, two possible levels of contribution of microwave or optical clock secondary representation data to TAI have been suggested by BIPM as:

1. A report to BIPM of secondary representation clock measurements against clocks already contributing to TAI (eg NPL's $^{88}Sr^{+}$ optical frequency standard against the NPL HM1 hydrogen maser). This data could then be itemised within circular-T as an offset from TAI, for information only.
2. Use of the secondary representation data reported by the NMIs to contribute to the steering of TAI in the same way as for primary frequency standards.

Thus, following CCTF and CIPM acceptance of a particular secondary representation, it is anticipated that the reporting only option itemized in 1 would apply for an initial period, with the introduction of 2 after a suitable period of reporting, as confidence in the reported representation data builds.

XII. EVOLUTION OF UNIFIED RECOMMENDED RADIATION LIST & CCL/CCTF WORKING GROUP

Mindful of the need for a unified recommended radiation list which caters for both requirements of CCTF secondary representations and CCL practical realizations, the 2005 JWG meeting has proposed a revised title for the unified list, and also a consolidation of working groups. This aims to ensure a future co-ordinated approach to the construction and updating of the recommended list, without duplication of effort and potential and potential contradictory decisions regarding frequency values and uncertainties. The name for the recommended radiation list proposed by the JWG to the CCTF is

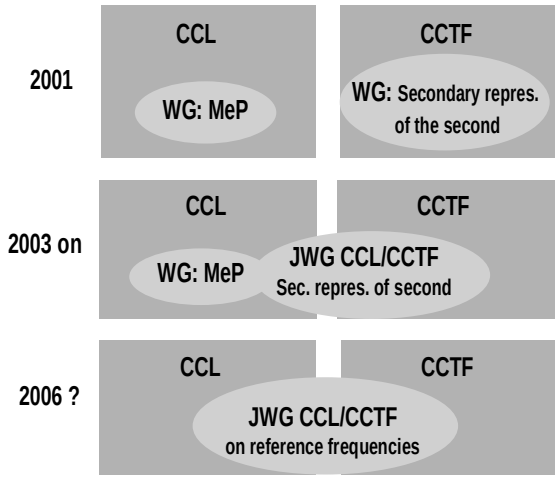

Figure 6: Evolution of respective CC working groups

"Recommended radiations, including practical realisations of the metre, and secondary representations of the second"

The proposed name for the consolidated working group is

Joint Working Group of the CCL/CCTF on Reference Frequencies

to replace the MePWG and JWG. The proposed Terms of Reference for the new WG are:

1. To recommend to the CCL, radiations for the practical realisation of the SI metre.
2. To recommend to the CCTF, radiations acceptable as secondary representations of the SI second.
3. To maintain a list of recommended frequency standard values and associated wavelength values for applications including the above.

.

XIII. NEXT STEPS AND SUMMARY

These proposals for a new combined list, combined WG and Terms of Reference were accepted by the September 2005 meeting of the CCL, and will be considered by the September 2006 meeting of the CCTF, in parallel with the JWG recommendations for the proposals of the three optical radiations as secondary representations. In addition, the existing JWG will next meet immediately prior to the CCTF 2006 meeting and consider further proposals and updated values for existing proposals. Decisions reached by the CCTF will then form the basis of recommendations to the CIPM 2006.

In the meantime, national measurement laboratories are encouraged to prepare fully documented proposals for secondary representations of the second for consideration by the CCTF, both in 2006 and by future

CCTF meetings. In addition, work is scheduled to start on the preparation of a Metrologia article itemising the full and updated recommended radiations list (rather than an electronic update) for publication after CIPM 2006.

With the approval of these JWG proposals, it is believed this will form an enduring basis for the incorporation of high accuracy optical and microwave clocks into the frequency standards infrastructure of the international metrology community, and establish their capability for the future. It is anticipated that this will provide significant support in the deliberations for a future possible redefinition of the SI second.

Acknowledgements

The Authors would like to acknowledge the significant contributions of all the members of the CCL/CCTF JWG in the consideration of the requirements of a secondary representation list and the development of strategies to achieve this.

REFERENCES

[1] T Udem, J Reichert, R Holzwarth and T W Hänsch, Phys. Rev. Lett. **82** 3568 (1999)
[2] J Ye, L S Ma and J L Hall, Phys. Rev. Lett. **87** 270801 (2001)
[3] Recommendation CCTF1, Report of the 16th Meeting of the CCTF (April 2004)}, p.38, BIPM http://www.bipm.org/utils/common/pdf/CCTF16.pdf
[4] T J Quinn, Metrologia **40** 103 (2003)
[5] Document CCL-CCTF/05-08 presented by LNE-SYRTE to the Joint Working Group at BIPM, August 2005, BIPM http://www.bipm.org/en/committees/cc/cctf/
[6] J C Bergquist, private communication
[7] H S Margolis, G P Barwood, G Huang, H A Klein, S N Lea, K Szymaniec, P Gill, Science **306** 1355 (2004)
[8] P Dube, A A Madej, J E Bernard, L Marmet, J-S Boulanger, and S Cundy, Phys. Rev. Lett, **95**, 033001 (2005).
[9] Document CCL-CCTF/05-09 presented by PTB to the Joint Working Group at BIPM, August 2005, BIPM, http://www.bipm.org/en/committees/cc/cctf/
[10] T Schneider, E Peik, and Chr Tamm, Phys. Rev. Lett. **94**, 230801 (2005).

Proceedings of the 20th EFTF, 2006

Blackbody radiation shift of the $^{27}Al^+$ $^1S_0 \rightarrow {}^3P_0$ transition*

T. Rosenband,† W. M. Itano, P. O. Schmidt,‡ D. B. Hume,
J. C. J. Koelemeij,§ J. C. Bergquist, and D. J. Wineland
National Institute of Standards and Technology, 325 Broadway, Boulder, CO 80305

The differential polarizability, due to near-infrared light at 1126 nm, of the $^{27}Al^+$ $^1S_0 \rightarrow {}^3P_0$ transition is measured to be $\Delta\alpha = 4\pi\epsilon_0 \times (1.6 \pm 0.5) \times 10^{-31}$ m^3, where $\Delta\alpha = \alpha_P - \alpha_S$ is the difference between the excited and ground state polarizabilities. This measurement is combined with experimental oscillator strengths to extrapolate the differential static polarizability of the clock transition as $\Delta\alpha(0) = 4\pi\epsilon_0 \times (1.5 \pm 0.5) \times 10^{-31}$ m^3. The resulting room temperature blackbody shift of $\Delta\nu/\nu = -8(3) \times 10^{-18}$ is the lowest known shift of all atomic transitions under consideration for optical frequency standards. A method is presented to estimate the differential static polarizability of an optical transition, from a differential light shift measurement.

The blackbody radiation shift [1] is a significant shift in all room temperature atomic frequency standards, as can be seen in Table I. It ranges from $|\Delta\nu/\nu| \approx 2 \times 10^{-14}$ for ^{133}Cs to $|\Delta\nu/\nu| \approx 8 \times 10^{-18}$ for $^{27}Al^+$, as reported here. In order to reach a systematic uncertainty of $|\Delta\nu/\nu| < 10^{-18}$, the transitions with a large room temperature blackbody shift may require a cryogenic operating environment, while $^{27}Al^+$ merely requires knowledge of the room temperature background with 5 K uncertainty.

We begin with a brief explanation of the blackbody shift, followed by an estimate of the shift in $^{27}Al^+$ based only on published oscillator strengths. The uncertainty in this estimate motivated us to measure the differential polarizability of the clock transition due to near-infrared light. This measurement allows a determination of the blackbody shift with reduced uncertainty.

TABLE I: Room temperature blackbody shifts and uncertainties of various species in use, or under consideration, as atomic frequency standards. Where no uncertainty is given, it is unknown. The $^{199}Hg^+$ optical transition is not listed, because this standard operates at 4.2 K, where the blackbody shift is reduced by 10^7 from the room temperature value.

species	transition	$\lvert\Delta\nu/\nu\rvert \times 10^{-18}$	reference
Al^+	$^1S_0 \rightarrow {}^3P_0$	8(3)	*this work*
In^+	$^1S_0 \rightarrow {}^3P_0$	< 70	[2]
Yb^+	$^2S_{1/2} \rightarrow {}^2D_{3/2}$	580(30)	[3]
Sr^+	$^2S_{1/2} \rightarrow {}^2D_{5/2}$	670(250)	[4]
Ca	$^1S_0 \rightarrow {}^3P_1$	2210(50)	[5]
Yb	$^1S_0 \rightarrow {}^3P_0$	2400(250)	[6]
Sr	$^1S_0 \rightarrow {}^3P_0$	5100(120)	[7]
Cs	F= 4 →F= 3	21210(260)	[8]

A. Blackbody shift

The blackbody shift results from off-resonant coupling of thermal blackbody radiation to the two states comprising the clock transition. The scalar polarizability α_a of an atomic state a driven by an electric field at frequency ω is

$$\alpha_a(\omega) = \frac{e^2}{m_e} \sum_i \frac{f_i}{\omega_i^2 - \omega^2}, \qquad (1)$$

with summation over all transitions connecting to state a with resonant frequency ω_i, and oscillator strength f_i. For monochromatic radiation $E_0 \cos\omega t$, this polarizability results in a dynamic Stark shift of $\Delta E_a = -\frac{1}{4} E_0^2 \alpha_a(\omega)$. The clock transition is subject to a blackbody radiation shift of

$$\Delta\nu = \frac{-1}{4\epsilon_0 \pi^3 c^3} \int_0^\infty \Delta\alpha(\omega) \frac{\omega^3}{e^{\hbar\omega/k_B T} - 1} d\omega, \qquad (2)$$

where we integrate over the power spectral density of the blackbody electric field, and $\Delta\alpha(\omega) = \alpha_P(\omega) - \alpha_S(\omega)$ is the difference between excited and ground state polarizabilities. Here, we first estimate the differential static polarizability $\Delta\alpha(0)$. This result is used to estimate the differential polarizability at blackbody frequencies $\Delta\alpha(\omega)$ for $\omega \approx 2\pi c/(10\ \mu\text{m})$.

B. The case of $^{27}Al^+$

The transitions from the $^1S_0$ and $^3P_0$ states that have been included in our estimate are listed in Table II. Oscillator strengths are taken from the *NIST Atomic Spectra Database* [9] where available, and from the *Opacity Project* [10] otherwise. From this we calculate for the $^3P_0$ state $\alpha_P(0) = 4\pi\epsilon_0 \times 3.65(73) \times 10^{-30}$ m^3. For the $^1S_0$ state $\alpha_S(0) = 4\pi\epsilon_0 \times 3.68(78) \times$

*Work supported by ONR and NIST
†Electronic address: trosen@nist.gov
‡Present address: Institut für Experimentalphysik, Universität Innsbruck, Austria; Supported by the Alexander von Humboldt Foundation
§Present address: Institut für Experimentalphysik, Heinrich-Heine-Universität Düsseldorf, Germany; Supported by the Netherlands Organisation for Scientific Research (NWO)

10^{-30} m^3. Thus, $\Delta\alpha(0) = 4\pi\epsilon_0 \times (-0.03 \pm 1.0) \times 10^{-30}$ m^3. The room temperature blackbody spectrum ($E_{rms} = 830$ V/m) is centered at 10 μm wavelength. This corresponds to a frequency ω in Eq. (1), which is 50 times lower than the lowest transition frequency ω_i. We may use the static polarizability without loss of accuracy, and find $\Delta\nu = -\frac{1}{2h}\Delta\alpha(0)E_{rms}^2 = (0.00 \pm 0.06)$ Hz, or fractionally $\Delta\nu/\nu = (0 \pm 6) \times 10^{-17}$, since $\nu \approx 1.1 \times 10^{15}$ Hz. In order to operate Al^+ as a frequency standard with fractional frequency uncertainty below 6×10^{-17}, the blackbody shift must be calibrated experimentally.

C. Near-infrared Stark shift measurement

Ideally, we would measure the shift of the clock transition due to a known intensity of 10 μm radiation, since the room temperature blackbody field is centered at this wavelength. However, the windows of our experimental apparatus are opaque to wavelengths longer than 3 μm. Instead, we measure the Stark shift due to near-infrared radiation, and use this measurement to estimate the blackbody shift.

The output of a fiber laser (600 mW with $\pm$200 mW fluctuations) at 1126 nm was focussed onto an Al^+ ion, and switched on and off at regular intervals. A stable ULE reference cavity was simultaneously locked to the $^1S_0 \rightarrow {}^3P_0$ transition, via an acousto-optic frequency shifter, and the frequency shift due to the Stark shifting beam was tracked and recorded. These measurements were repeated for various lateral (x,y) displacements of the Stark shifting beam, as shown in Figure 1, in order to estimate the beam waist ($w_0 = 100 \pm 10$ μm).

The resulting differential polarizability is $\Delta\alpha(2\pi c/(1126\text{ nm})) = 4\pi\epsilon_0 \times (1.6 \pm 0.5) \times 10^{-31}$ m^3, limited in accuracy by power fluctuations of the Stark shifting laser.

D. Extrapolation to zero frequency

The following relates this measurement to the differential polarizability at 0 Hz, by expanding Eq. (1) in small parameters. Two facts specific to Al^+ are used.

1. All strong transitions connecting to either clock state are in the deep UV ($\lambda < 186$ nm).

2. The strongest transitions contributing to the sum in Eq. (1) are near each other ($\lambda \approx 170$ nm).

Let $\delta_i \equiv (\omega/\omega_i)^2$. For the $^1S_0$ and $^3P_0$ states in Al^+, $\delta_i < 0.03$, when $\omega = 2\pi c/(1126\text{ nm})$. Expanding

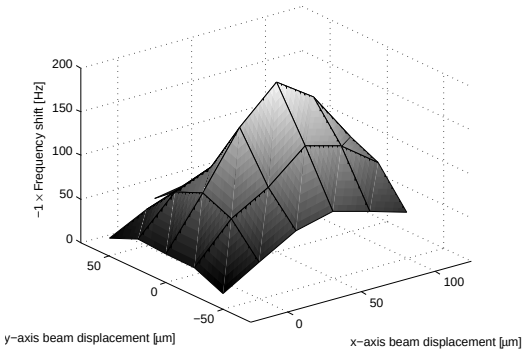

FIG. 1: Clock transition Stark shift vs. beam position. A Gaussian beam profile fit yields $w_0 = 100$ μm for the beam waist, with a peak shift of -190 Hz.

Eq. (1) in powers of δ_i yields

$$\alpha(\omega) = \alpha(0) + \frac{e^2}{m_e}\sum_i \frac{f_i}{\omega_i^2}(\delta_i + \delta_i^2 + ...). \qquad (3)$$

Thus, the differential polarizability between the $^1S_0$ and $^3P_0$ states is

$$\Delta\alpha(\omega) = \Delta\alpha(0) + \frac{e^2}{m_e}\sum_i \frac{f_i}{\omega_i^2}(\delta_i + \delta_i^2 + ...), \qquad (4)$$

where we sum over all transitions connecting to the $^1S_0$ and $^3P_0$ states. Positive oscillator strengths are used for the transitions connecting to $^3P_0$, and negative oscillator strengths are used for the $^1S_0$ transitions.

Now let $\delta_0 \equiv (\omega/\omega_0)^2$, where $\omega_0 = 2\pi c/(171\text{ nm})$, and let $\epsilon_i \equiv \delta_i - \delta_0$. This value of δ_0 is chosen because the strong transitions all lie near 171 nm. Then

$$\Delta\alpha(0) = \frac{\Delta\alpha(\omega) - \frac{e^2}{m_e}\sum_i \frac{f_i}{\omega_i^2}(\epsilon_i + \delta_i^2 + ...)}{1 + \delta_0}. \qquad (5)$$

All of the terms after the summation sign are small, as can be seen in Table II. For the strongest transitions ϵ_i is small, because all strong transitions are near 171 nm. For the weaker transitions f_i/ω_i^2 is small. To test the merits of this estimate, we propagate the uncertainties σ_{f_i} (see Table II) in the various f_i via Eq. (5), which results in an uncertainty in $\Delta\alpha(0)$ of

$$\sigma_{\Delta\alpha(0)} = \frac{e^2/m_e}{1+\delta_0}\sqrt{\sum_i \left[\frac{\sigma_{f_i}}{\omega_i^2}(\epsilon_i + \delta_i^2 + ...)\right]^2}. \quad (6)$$

Note that our choice of δ_0 minimizes the uncertainty $\sigma_{\Delta\alpha(0)}$. Numerically we find $\sigma_{\Delta\alpha(0)} = 4\pi\epsilon_0 \times 1.7 \times 10^{-33}$ m$^3 \approx 0.01 \times \Delta\alpha(2\pi c/(1126\text{ nm}))$. Thus, $\Delta\alpha(0)$ can be deduced from our measurement of $\Delta\alpha(\omega)$ at 1126 nm with an additional uncertainty of 1 %. Eq. (5) yields $\Delta\alpha(0) = 4\pi\epsilon_0 \times (1.5 \pm 0.5) \times 10^{-31}$ m^3.

E. Estimate of blackbody shift

Since the frequency of blackbody radiation (centered at 10 μm wavelength) is closer to 0 Hz than the frequency of the applied 1126 nm radiation, we expect to relate $\Delta\alpha(0)$ to $\Delta\alpha(2\pi c/(10\ \mu\text{m}))$ with even less uncertainty than our estimate of $\Delta\alpha(0)$ from $\Delta\alpha(2\pi c/(1126\text{ nm}))$. As before, we can propagate the errors σ_{f_i} through the result. The calculation follows from Section D and Eq. (2), and we simply write the room temperature result as

$$\Delta\nu = -\frac{\pi k_B^4 T^4}{60\epsilon_0\hbar^4 c^3}(\Delta\alpha(0) \times 1.00024), \quad (7)$$

or numerically, $\Delta\nu = -0.008(3)$ Hz.

F. Conclusion

We have measured the differential polarizability of the ^{27}Al$^+$ ^{1}S$_0 \rightarrow {}^3$P$_0$ clock transition at 1126 nm. We have also found expressions relating the differential polarizabilities at various drive frequencies, in which the effect of uncertainties in the oscillator strengths is minimized. In particular, $\Delta\alpha(0)$ is found from $\Delta\alpha(2\pi c/(1126\text{ nm}))$ with 1 % added fractional uncertainty, while allowing conservative uncertainties of 20 % or larger in the oscillator strengths. From $\Delta\alpha(0)$ we calculate the blackbody shift with negligible added uncertainty. The fractional room temperature blackbody shift $\Delta\nu/\nu = (-8 \pm 3) \times 10^{-18}$ is substantially lower for the ^{27}Al$^+$ ^{1}S$_0 \rightarrow {}^3$P$_0$ transition than for other atomic frequency standards currently under development (see Table I). The uncertainty in this value could be lowered substantially by improving the power stability of the 1126 nm Stark shifting laser.

[1] W. Itano, L. Lewis, and D. Wineland, Phys. Rev. A **25**, 1233 (1982).
[2] T. Becker, J. v. Zanthier, A. Y. Nevsky, C. Schwedes, M. N. Skvortsov, H. Walther, and E. Peik, Phys. Rev. A **63**, 051802 (2001).
[3] T. Schneider, E. Peik, and C. Tamm, Phys. Rev. Lett. **94**, 230801 (2005).
[4] A. A. Madej, J. E. Bernard, P. Dubé, and L. Marmet, Phys. Rev. A **70**, 012507 (2004).
[5] U. Sterr, C. Degenhardt, H. Stoehr, C. Lisdat, H. Schnatz, J. Helmcke, F. Riehle, G. Wilpers, C. Oates, and L. Hollberg, arXiv:physics/0411094 (v1 9 Nov 2004).
[6] S. G. Porsev and A. Derevianko, arXiv:physics/0602082 (v1 13 Feb 2006).
[7] A. D. Ludlow, M. M. Boyd, T. Zelevinsky, S. M. Foreman, S. Blatt, M. Notcutt, T. Ido, and J. Ye, Phys. Rev. Lett. **96**, 033003 (2006).
[8] T. P. Heavner, S. R. Jefferts, E. A. Donley, J. H. Shirley, and T. E. Parker, IEEE Trans. Inst. Meas. **54**, 842 (2005).
[9] NIST Atomic Spectra Database v. 3.03 (Standard Reference Database #78).
[10] TOPbase, the Opacity Project on-line atomic database, http://cdsweb.u-strasbg.fr/topbase.html.

TABLE II: Transition wavelengths (λ_i) and oscillator strengths (f_i) used to estimate $\Delta\alpha(0)$. Transitions are in descending order of f_i magnitude. Negative oscillator strengths are used for transitions connecting to the $3s^2\ {}^1S_0$ ground state. Fractional uncertainties $\sigma_{f_i}/|f_i|$ were taken from the NIST Atomic Spectra Database [9] where available, and doubled. Where no uncertainty is available, a fractional uncertainty of 1 is assumed. $\delta_i = (\omega/\omega_i)^2$ where $\omega = 2\pi c/(1126\text{ nm})$, $\omega_i = 2\pi c/\lambda_i$, and $\epsilon_i = \delta_i - (171/1126)^2$. The sixth column lists the summands of Eq. (5) truncated after δ_i^3.

f_i	$\sigma_{f_i}/\lvert f_i\rvert$	λ_i [nm]	δ_i	ϵ_i	$\frac{e^2}{m_e}\frac{f_i}{\omega_i^2}(\epsilon_i+\delta_i^2+\delta_i^3)$ $[4\pi\epsilon_0\times\text{m}^3\times10^{-33}]$	from	to	ref.
-1.830000	0.20	167.079	0.0220	-0.0010	2.005625	3s2 1S0	3s3p 1P1	[9]
0.903000	0.20	171.944	0.0233	0.0003	1.546615	3s3p 3P0	3s3d 3D1	[9]
0.612000	0.50	176.198	0.0245	0.0014	2.762716	3s3p 3P0	3p2 3P1	[9]
0.129000	0.20	185.593	0.0272	0.0041	1.541754	3s3p 3P0	3s4s 3S1	[9]
0.059000	1.00	118.919	0.0112	-0.0119	-0.701593	3s3p 3P0	3s4d 3D1	[9]
0.018000	1.00	104.789	0.0087	-0.0144	-0.202074	3s3p 3P0	3s5d 3D1	[9]
0.016556	1.00	120.919	0.0115	-0.0115	-0.196866	3s3p 3P0	3s5s 3S1	[10]
0.005922	1.00	105.460	0.0088	-0.0143	-0.066807	3s3p 3P0	3s6s 3S1	[10]
0.004078	1.00	98.598	0.0077	-0.0154	-0.043385	3s3p 3P0	3s6d 3D1	[10]
-0.003020	1.00	93.527	0.0069	-0.0162	0.030381	3s2 1S0	3s4p 1P1	[10]
0.002889	1.00	98.905	0.0077	-0.0153	-0.030830	3s3p 3P0	3s7s 3S1	[10]
0.001889	1.00	95.263	0.0072	-0.0159	-0.019393	3s3p 3P0	3s7d 3D1	[10]
0.001656	1.00	95.429	0.0072	-0.0159	-0.017030	3s3p 3P0	3s8s 3S1	[10]
-0.001100	1.00	71.470	0.0040	-0.0190	0.007625	3s2 1S0	3s7p 1P1	[10]
-0.001090	1.00	74.118	0.0043	-0.0187	0.007995	3s2 1S0	3s6p 1P1	[10]
-0.001050	1.00	69.949	0.0039	-0.0192	0.007035	3s2 1S0	3s8p 1P1	[10]
0.001050	1.00	93.341	0.0069	-0.0162	-0.010539	3s3p 3P0	3s9s 3S1	[10]
0.001019	1.00	93.241	0.0069	-0.0162	-0.010214	3s3p 3P0	3s8d 3D1	[10]
-0.000998	1.00	68.994	0.0038	-0.0193	0.006541	3s2 1S0	3s9p 1P1	[10]
-0.000948	1.00	68.353	0.0037	-0.0194	0.006120	3s2 1S0	3s10p 1P1	[10]
-0.000858	1.00	67.902	0.0036	-0.0194	0.005480	3s2 1S0	3s11p 1P1	[10]
0.000708	1.00	91.980	0.0067	-0.0164	-0.006985	3s3p 3P0	3s10s 3S1	[10]
0.000613	1.00	91.916	0.0067	-0.0164	-0.006048	3s3p 3P0	3s9d 3D1	[10]
-0.000567	1.00	79.448	0.0050	-0.0181	0.004612	3s2 1S0	3s5p 1P1	[10]
0.000501	1.00	91.041	0.0065	-0.0165	-0.004885	3s3p 3P0	3s11s 3S1	[10]
0.000398	1.00	90.997	0.0065	-0.0165	-0.003876	3s3p 3P0	3s10d 3D1	[10]
0.000124	1.00	70.040	0.0039	-0.0192	-0.000835	3s3p 3P0	3p5p 3P1	[10]
0.000116	1.00	65.800	0.0034	-0.0196	-0.000701	3s3p 3P0	3p6p 3P1	[10]
0.000083	1.00	63.690	0.0032	-0.0199	-0.000477	3s3p 3P0	3p7p 3P1	[10]
0.000059	1.00	62.480	0.0031	-0.0200	-0.000328	3s3p 3P0	3p8p 3P1	[10]
0.000043	1.00	61.710	0.0030	-0.0201	-0.000233	3s3p 3P0	3p9p 3P1	[10]
0.000032	1.00	61.190	0.0030	-0.0201	-0.000170	3s3p 3P0	3p10p 3P1	[10]
0.000001	1.00	80.860	0.0052	-0.0179	-0.000009	3s3p 3P0	3p4p 3P1	[10]
SUM					6.609223			
UNCERTAINTY					1.685575			

Proceedings of the 20th EFTF, 2006

$^{171}Yb^{+}$ single-ion optical frequency standard at 688 THz

Chr. Tamm*, B. Lipphardt, H. Schnatz, R. Wynands, S. Weyers, T. Schneider, E. Peik
Physikalisch-Technische Bundesanstalt, Bundesallee 100, 38116 Braunschweig, Germany
**Electronic address:* christian.tamm@ptb.de

Two $^{171}Yb^{+}$ single-ion optical frequency standards operating at 688 THz (436 nm) are compared in order to investigate systematic frequency shifts in the sub-Hertz range. In the absence of externally applied perturbations, a mean relative frequency difference of $3.8(6.1)\cdot10^{-16}$ is observed. This agreement is comparable to that of the most accurate comparisons between cesium fountain clocks. Using a femtosecond frequency comb generator based on a Er^{3+}-doped fiber laser, the frequency of the $^{171}Yb^{+}$ standard is measured with a relative systematic uncertainty of $3.1\cdot10^{-15}$ and a statistical uncertainty of $0.6\cdot10^{-15}$.

I. INTRODUCTION

A single laser-cooled ion in a radiofrequency trap is a nearly ideal reference for an optical frequency standard. For a number of atomic systems, one expects that systematic shifts of the atomic transition frequency can be reduced to the 10^{-18} range [1], which would improve by more than two orders of magnitude on the best available cesium fountain frequency standards. Optical frequency conversion techniques based on femtosecond comb generators permit the realization of practical single-ion frequency standards with output frequencies in the optical and microwave range.

Here we report recent investigations on the 688 THz $^{171}Yb^{+}$ frequency standard which is based on the $^{2}S_{1/2}(F=0) - {}^{2}D_{3/2}(F=2, m_F=0)$ electric-quadrupole transition at 436 nm [2]. This system and single-ion optical frequency standards based on $^{199}Hg^{+}$ and $^{88}Sr^{+}$ are presently under review at the BIPM as potential secondary representations of the SI second [3,4].

In order to overcome the accuracy and stability limitations associated with measurements relative to a microwave frequency reference, we compare two $^{171}Yb^{+}$ standards directly and observe their frequency difference with and without externally applied perturbations. The tensorial quadratic Stark shift and the quadrupole shift caused by static electric fields are investigated by determining the frequency difference for various orientations of the applied static magnetic field. In the absence of perturbations caused by external static electric fields, we find no evidence of magnetic field orientation dependent shifts larger than the statistical comparison uncertainty of $6\cdot10^{-16}$.

These observations enabled absolute measurements of the $^{171}Yb^{+}$ reference transition frequency with a systematic uncertainty contribution of the $^{171}Yb^{+}$ standard that is significantly smaller than in previous measurements [5,6]. In the recent measurements, long continuous averaging intervals of up to 36 h were realized with the use of a Er^{3+}-doped fiber laser comb generator [7], thus significantly reducing the statistical measurement uncertainty associated with the instability of the Cs fountain reference. The results of the new measurements are consistent with our previous results and yield the $^{171}Yb^{+}$ transition frequency with a statistical uncertainty of $0.6\cdot10^{-15}$ and a systematic uncertainty of $3.1\cdot10^{-15}$.

II. EXPERIMENTAL SYSTEM

The experiments use two radiofrequency (rf) Paul traps of identical design with ring electrode diameters of 1.4 mm. The ion is confined by an approximately cylindrically symmetric pseudopotential with an axial depth of 17 eV. In order to compensate any electric stray field at the location of the ion, compensation voltages are applied between the trap endcaps and to two additional electrodes. They are adjusted so that a laser cooled ion does not change its position by more than 2 μm when the trap potential is lowered to less than 0.25 eV. The remaining stray field induced displacement of the ion under normal operating conditions is then calculated to be less than 100 nm.

The ion is laser cooled to the Lamb-Dicke regime by a frequency doubled diode laser emitting at 371 nm. Metastable levels that are populated during laser cooling are depleted by diode laser radiation at 935 nm and at 639 nm. The reference transition which has a natural linewidth of 3.1 Hz, is probed by the frequency doubled radiation from a 871 nm diode laser. Its short-time frequency stability is derived from a temperature stabilized, seismically isolated high-finesse cavity. The $^{171}Yb^{+}$ reference transition can be resolved with a linewidth of 10 Hz [6]. A detailed description of the optical excitation scheme and of the spectroscopy of the reference transition is given in [8,9].

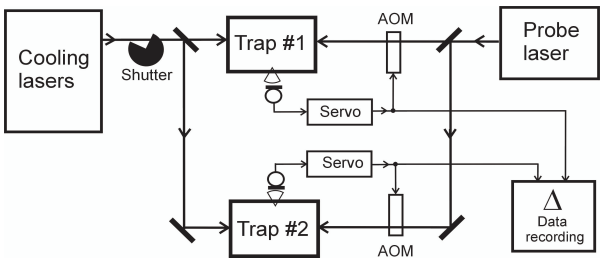

Fig. 1: Schematic of the experimental setup for comparison of two $^{171}Yb^{+}$ optical frequency standards. Two acusto-optical modulators (AOM) are used to independently shift the frequencies of the two probe beams interacting with the ions. A mechanical shutter blocks the cooling lasers while the probe beams interrogate the ions.

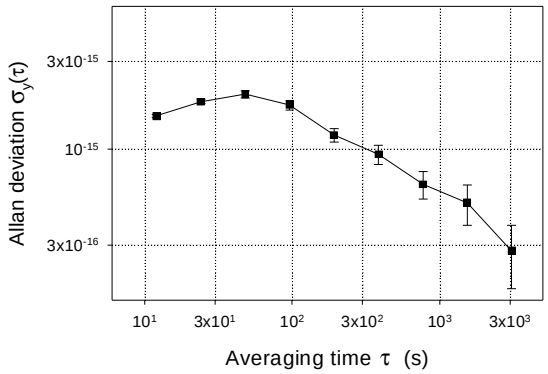

Fig. 2: Allan deviation of the relative frequency difference Δ/ν between two $^{171}Yb^{+}$ single-ion optical frequency standards at ν=688 THz.

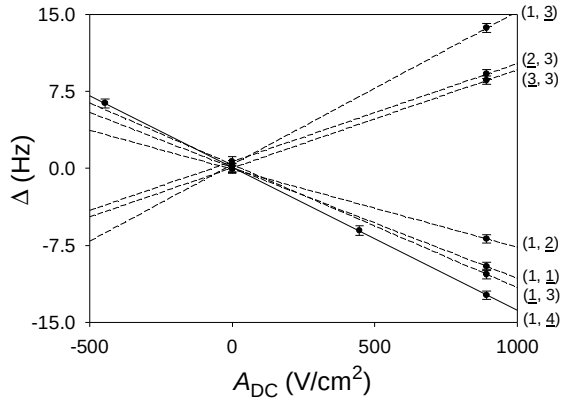

Fig. 3: Frequency difference Δ between the traps as a function of applied electric field gradient A_{DC} for various orientations of the magnetic field in trap 1 and trap 2. The numbers in brackets label the combinations of magnetic field orientations (trap 1, trap 2), and the underlines indicate in which trap the field gradient is applied. The orientations 1, 2, 3 are approximately orthogonal sets, while orientation 4 is perpendicular to the symmetry axis of the trap. The error bars denote the statistical uncertainty of the individual frequency comparisons and the lines are the results of linear regressions.

The setup of the comparison experiment between two $^{171}Yb^{+}$ traps is shown in Fig. 1. Two independent frequency shift and servo systems are employed to stabilize the probe beam frequencies to the line centers of the reference transitions in the two trapped ions. In order to minimize servo errors due to drift of the probe laser frequency, second-order servo algorithms are used [10]. For averaging times larger than the servo time constants (≈10 s), the optical frequencies probing the two ions can be regarded as independent and determined solely by the respective atomic transition frequencies. The servo frequency difference $\Delta = f(\mathrm{AOM2}) - f(\mathrm{AOM1})$ is recorded once per second.

The ions are interrogated every 90 ms by 30 ms pulses, so that the atomic resonance signals have essentially Fourier-limited linewidths of approximately 30 Hz. The resonant excitation probability is about 0.6. The relative instability of Δ measured by the Allan standard deviation under these conditions is shown in Fig. 2. The observed instability of Δ is dominated by the quantum projection noise in the interrogation of the two ions. The dynamic response of the servo systems leads to a maximum of the Allan deviation at $\tau \approx 50$ s. For longer averaging times $\tau > 100$ s, the Allan deviation decreases as $\tau^{-1/2}$. The observed stability of Δ is independent of the temporal overlap of the probe pulses applied to the two ions, and it is not the result of an exact matching of the time constants of the two servo systems. It thus appears that the stability of Δ is a meaningful measure for the stability of the individual standards. The experimental results are in good agreement with numerical simulations of the servo action which assume quantum projection noise as the only noise source [10].

III. QUADRUPOLE SHIFT

In most of the presently investigated single-ion optical frequency standards, a significant systematic uncertainty contribution can arise from the interaction of the atomic electric quadrupole moment with the gradient of the electric stray field. In order to eliminate the quadrupole shift, one can take advantage of the fact that it averages to zero over three mutually orthogonal directions of the magnetic quantization field [11,12]. Alternatively, the shift can be eliminated without changing the magnetic field orientation by averaging over the Zeeman and quadrupole shifts of all magnetic sublevels [13]. Both schemes also eliminate the tensor part of the quadratic Stark shift because it has the same dependence on magnetic field orientation and magnetic quantum number.

In order to investigate the quadrupole shift of the $^{171}Yb^{+}$ reference transition, a static field gradient A_{DC} is applied in one trap by superimposing a static (dc) voltage on the rf trap drive voltage of one trap. The resulting transition frequency shift is measured relative to the other trap

operating without dc voltage. Fig. 3 shows the frequency differences observed for various magnetic field orientations in both traps. The data shown are corrected for differences in the quadratic Zeeman shift, which was kept in the range of 0.1...0.5 Hz. The field orientations 1, 2, 3 are approximately orthogonal to each other with estimated uncertainties of 20° (trap 1) and 10° (trap 2). In order to determine the electric quadrupole moment $\theta(^2D_{3/2})$ of the upper level of the $^{171}Yb^+$ reference transition (for the $^2S_{1/2}$ ground state, $\theta=0$), the magnetic field orientation was adjusted to be perpendicular to the trap axis, so that the quadrupole shift assumes a local maximum. The corresponding measurement is labeled (1,4) in Fig. 3. From this, the quadrupole moment is determined as $\theta(^2D_{3/2}) = 9.32(48)\cdot10^{-40}$ Cm^2, in good agreement with the result $\theta(^2D_{3/2}) = 9.754\cdot10^{-40}$ Cm^2 obtained in recent atomic-structure calculations [14].

IV. QUADRATIC STARK SHIFT

The quadratic Stark shift of the $^{171}Yb^+$ reference transition has contributions from the scalar polarizability of the ground state, $\alpha_S(^2S_{1/2})$, and from the scalar and tensorial polarizabilities of the $^2D_{3/2}$ state, $\alpha_S(^2D_{3/2})$ and $\alpha_T(^2D_{3/2})$. In order to determine $\Delta\alpha_S = \alpha_S(^2S_{1/2}) - \alpha_S(^2D_{3/2})$ and $\alpha_T(^2D_{3/2})$, we determine Δ for the case that in one of the traps a variable offset is added to the compensation voltage applied between the trap endcap electrodes. In this case, the ion is displaced by a distance Δz from the trap center so that it is subject to the quadratic Stark shift caused by the rf trap field at the displaced position. The polarizabilities $\Delta\alpha_S$ and $\alpha_T(^2D_{3/2})$ can then be inferred from measurements with different orientations of the magnetic field.

The results of these measurements are shown in Fig. 4. The data shown are corrected for differences in the quadratic Zeeman shift. The data taken at $\Delta z \neq 0$ are also corrected for the calculated second-order Doppler shift which amounts to –0.35 Hz at $\Delta z = 1.1$ μm. At $\beta=90°$ no significant shift is observed, indicating an accidental cancellation of the scalar and tensorial shift contributions at this angle. From the experimental data, we obtain $\Delta\alpha_S = -6.9(1.4)\cdot10^{-40}$ Jm^{2}V^{-2} and $\alpha_T(^2D_{3/2}) = -13.6(2.2)\cdot10^{-40}$ Jm^{2}V^{-2}. The experimental results are close to the polarizabilities inferred from theoretical oscillator strengths that are scaled with experimental lifetime data. These calculations yield the polarizabilities $\Delta\alpha_S = -5.20(16)\cdot10^{-40}$ Jm^{2}V^{-2} and $\alpha_T(^2D_{3/2}) = -12.13(13)\cdot10^{-40}$ Jm^{2}V^{-2} [15].

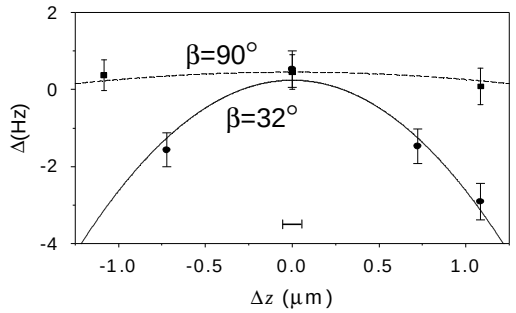

Fig. 4: Frequency difference Δ between the traps as a function of the displacement Δz of the ion in trap 2 from the saddle point of the rf trap potential. β denotes the angle between trap axis and magnetic field as inferred from the quadrupole shift measurements shown in Fig. 3. The lines are least-squares fits of parabolas centered at $\Delta z = 0$. The horizontal bar in the lower part of the Figure denotes the uncertainty range of the position $\Delta z = 0$ which remains after the compensation of the electric stray field.

V. AGREEMENT BETWEEN TRAPS

Figure 5 shows measurements of the frequency difference Δ for $A_{DC} = 0$ and $\Delta z = 0$ in both traps. The weighted mean difference of all eight measurements is $\langle\Delta\rangle = 0.26$ Hz and the average statistical uncertainty is 0.42 Hz. The contribution of the quadratic Zeeman shift to the systematic uncertainty of the measurements is smaller than 0.05 Hz. Using a stray field compensation procedure as described above, the uncertainty contribution from quadratic Stark shift and second-order Doppler shift is below 0.01 Hz [16]. The blackbody ac Stark shift expected from the measured polarizability $\Delta\alpha_S$ is –0.37(5) Hz at 300 K. Additional ac Stark shifts due to ambient heat sources and laser stray light are estimated to be smaller than 0.2 Hz. The uncertainty contribution resulting from servo errors is smaller than 0.1 Hz [10].

A χ^2 test indicates that within the statistical uncertainty of the data shown in Fig. 5, there is no evidence of frequency shifts that depend on the orientation of the magnetic quantization field [16]. This permits the conclusion that stray field induced quadrupole shifts were smaller than 0.5 Hz under the conditions of the measurement. For an uncertainty estimate on the observed mean frequency difference $\langle\Delta\rangle = 0.26$ Hz, it

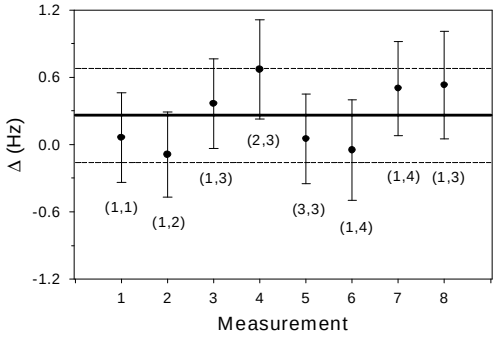

Fig. 5: Frequency difference in the absence of external perturbations, showing the measurements presented in Fig. 3 at $A_{DC} = 0$ (1-6) with two more data points added. The data were taken within two days and are displayed in temporal order. The solid line is the weighted average of the data and the dashed lines mark the average statistical uncertainty of the data points.

would appear justified to regard the scatter of the data as random. Nevertheless, as it is difficult to determine the contribution of systematic shifts to the scatter of the data points, we estimate the uncertainty of $\langle\Delta\rangle$ as the average statistical uncertainty of the data points.

The observed relative frequency difference between the two $^{171}Yb^+$ standards of $\langle\Delta\rangle/\nu = 3.8(6.1)\cdot10^{-16}$ is comparable to the best result found in a comparison of cesium fountain clocks [17], which are the most accurate clocks at present. This agreement represents an improvement by more than 2 orders of magnitude over previous comparisons between single-ion frequency standards [18].

VI. ABSOLUTE FREQUENCY MEASUREMENT

For the absolute frequency measurements, the second harmonic of the probe laser frequency is stabilized to the reference transition of a trapped $^{171}Yb^+$ ion. A part of the 871 nm probe laser output is passed through a 8 m fiber link to produce a beat signal with the frequency-doubled output of a Er^{3+}-doped fiber frequency comb generator [7]. The comb generator is referenced to the 100 MHz signal of a hydrogen maser that is continuously compared with the primary cesium fountain frequency standard CSF1 of PTB.

Four absolute frequency measurements with continuous averaging times of up to 36 h were conducted during 2005. The $^{171}Yb^+$ trap serving for the frequency measurements was operated without externally applied perturbations and with a constant orientation of the magnetic quantization field. A comparison between the two traps was carried out immediately before one absolute frequency measurement interval and yielded results consistent with the measurements shown in Fig. 5.

The results of the absolute frequency measurements are listed in Table 1. The obtained statistical measurement uncertainties u_{Ai} are dominated by the white frequency noise of the Cs fountain reference. The systematic uncertainty contribution of the Cs fountain $u_B(Cs)$ reflects the state of a new uncertainty evaluation of CSF1 at the time of the measurements. The systematic uncertainty of the $^{171}Yb^+$ standard, $u_B(Yb^+)$, is dominated by the contribution from the stray-field induced quadrupole shift. Here an uncertainty 1 Hz is assumed which is approximately a factor of two larger than the statistical uncertainty of the frequency comparison measurements shown in Fig. 5.

The new frequency measurements from 2005 are in excellent agreement with our earlier results [5,6]. The individual results contribute to the mean frequency ν with weights proportional to $(u_{Ai}^2 + u_B^2(Cs) + u_B^2(Yb^+))^{-1}$. Excluding the earlier measurements from the weighted average would shift the frequency value by 0.3 Hz only. The total 1σ uncertainty of the inferred value of ν of u = 2.2 Hz that is noted in Table 1 is calculated as $u = (u_A^2 + u_B^2(Cs) + u_B^2(Yb^+))^{1/2}$ where $u_A = (\Sigma_i(u_{Ai})^{-2})^{-1/2}$ = 0.4 Hz. The corresponding relative statistical and systematic uncertainties are $u_A\nu^{-1} \approx 0.6\cdot10^{-15}$ and $(u_B^2(Cs) + u_B^2(Yb^+))^{1/2}\nu^{-1} \approx 3.1\cdot10^{-15}$, respectively. It should be noted that the frequencies given in Table 1 refer to measurements performed at room temperature. Extrapolating to zero temperature the frequency value would have to be corrected for the blackbody shift, i.e., increased by 0.37(5) Hz.

Acknowledgement

This work was supported in part by DFG through SFB 407.

ν_i = 688 358 979 309 000 + x_i Hz; i: number of measurement

i	Starting Date	x_i (Hz)	u_{Ai} (Hz)	$u_B(Cs)$ (Hz)	$u_B(Yb^+)$ (Hz)
1	5.7.2005	307.84	3.43	1.82	1.05
2	6.7.2005	307.51	0.46	1.82	1.05
3	9.8.2005	307.49	1.01	1.82	1.05
4	10.8.2005	307.07	0.64	1.82	1.05

Weighted mean including earlier results (Ref. 5):

$\nu[^{171}Yb^+, {}^2S_{1/2}(F=0) - {}^2D_{3/2}(F=2)]$ **= 688 358 979 309 307.7(2.2) Hz**

Table 1: Summary of the results of the absolute frequency measurements of the $^{171}Yb^+$ standard performed in 2005. The transition frequencies ν_i are corrected for the quadratic Zeeman shift present during the measurements. The measurements were carried out with the ion trap operating at room temperature. The ν_i values are not corrected for the blackbody shift (see text). The 1σ statistical uncertainties of the measurements are denoted with u_{Ai}. The systematic uncertainty contributions (1σ) of the $^{171}Yb^+$ standard and of the cesium fountain reference are respectively denoted with $u_B(Cs)$ and $u_B(Yb^+)$. All uncertainty data are scaled to the frequency of the $^{171}Yb^+$ standard (688 THz).

REFERENCES

[1] See, e.g., P. Gill *et al*., Meas. Sci. Technol. **14**, 1174 (2003), and references therein
[2] T. Schneider, E. Peik, Chr. Tamm, Phys. Rev. Lett. **94**, 230801 (2005)
[3] www.bipm.org/utils/common/pdf/CCTF16.pdf
[4] P.Gill, F. Riehle, "On secondary representations of the second", see these proceedings
[5] J. Stenger, Chr. Tamm, N. Haverkamp, S. Weyers, H.R. Telle, Opt. Lett. **26**, 1589 (2001)
[6] E. Peik, B. Lipphardt, H. Schnatz, T. Schneider, Chr. Tamm, S.G. Karshenboim, Phys. Rev. Lett. **93**, 170801 (2004)
[7] F. Adler, K. Moutzouris, A. Leitenstorfer, H. Schnatz, B. Lipphardt, G. Grosche, F. Tauser, Optics Express **12**, 5872 (2004)
[8] Chr. Tamm, D. Engelke, V. Bühner, Phys. Rev. A **61**, 053405 (2000)
[9] Chr. Tamm, T. Schneider, E. Peik, in *Laser Spectroscopy XIV*, eds. P. Hannaford, A. Sidorov, H. Bachor, K. Baldwin (World Scientific, Singapore, 2004), and physics/0402120
[10] E. Peik, T. Schneider, Chr. Tamm, J. Phys.B: At. Mol. Opt. Phys. **39**, 145 (2006)
[11] W.M. Itano, J. Res. Natl. Inst. Stand.Technol. **105**, 829 (2000)
[12] W.H. Oskay, W.M. Itano, J.C. Bergquist, Phys. Rev. Lett. **94**, 163001 (2005)
[13] P. Dubé, A.A. Madej, J.E. Bernard, L. Marmet, J.-S. Boulanger, S. Cundy, Phys. Rev. Lett. **95**, 033001 (2005)
[14] W.M. Itano, Phys. Rev. A **73**, 022510 (2006)
[15] S.N. Lea, S.A. Webster, G.P. Barwood, "Polarisabilities and blackbody shifts in Sr^+ and Yb^+", see these proceedings
[16] T. Schneider, *Optical frequency standard with a single $^{171}Yb^+$ ion*, Ph.D. thesis (Univ. Hannover, 2005) and PTB-Bericht PTB-Opt-70 (Braunschweig, 2005)
[17] S. Bize et al., C.R. Physique **5**, 829 (2004)
[18] G.P. Barwood, K. Gao, P. Gill, G. Huang, H.A. Klein, IEEE Trans. IM-**50**, 543 (2001)

Proceedings of the 20th EFTF, 2006

An optical frequency standard based on the $^2S_{1/2}$—$^2F_{7/2}$ transition in $^{171}Yb^+$

S. A. Webster,* A. Stannard, K. Hosaka, and P. Gill
National Physical Laboratory, Hampton Road, Teddington, Middlesex, TW11 0LW, UK
**Electronic address:* stephen.webster@npl.co.uk

The $^2S_{1/2}$ (F = 0) – $^2F_{7/2}$ (F = 3, m_F = 0) transition at 467 nm in a single, trapped, laser cooled ion of $^{171}Yb^+$ has the potential to be an extremely accurate optical frequency reference. Systematic shifts have been evaluated and are currently dominated by the ac-Stark shift. However, this is not expected to be the case as probe laser linewidth is reduced. A heterodyne measurement of the probe laser shows it to have a width of 20 Hz on a 1 minute timescale. The atomic spectrum on the other hand, has been found to have a broadened width of 200 Hz. Using heterodyne detection of light reflected from the trap electrodes, Doppler shifting due to vibration of the trap is identified as the additional source of broadening.

I. INTRODUCTION

The term scheme for $^{171}Yb^+$ is shown in Figure 1. The $^2S_{1/2}$ (F = 0) – $^2F_{7/2}$ (F = 3, m_F = 0) transition at 467 nm is being developed as an optical frequency standard. The upper state is extremely long-lived with a lifetime on the order of years [1]. Subsequently, the natural linewidth of the absorption is ~ nHz, and as such will never limit the width that can be observed, which will instead be limited by the linewidth of the probe laser in the frame of the ion. The advantage of using the odd isotope is that it has an m_F=0 – m_F=0 transition which is free from the first-order Zeeman effect.

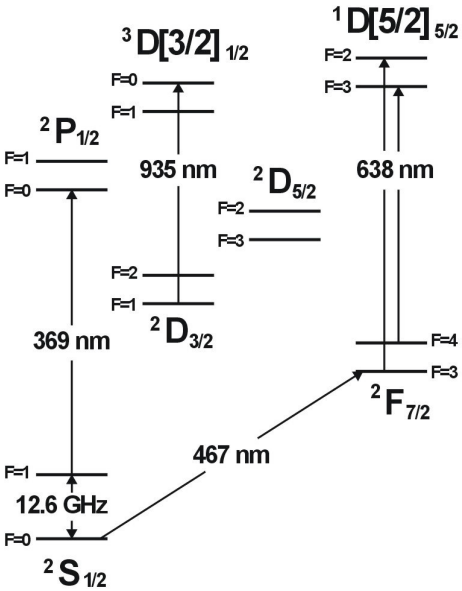

Figure 1. Term scheme for $^{171}Yb^+$.

II. SYSTEMATIC SHIFTS

It has been possible so far to measure two of the systematic shifts for this atomic system as shown in Figure 2.

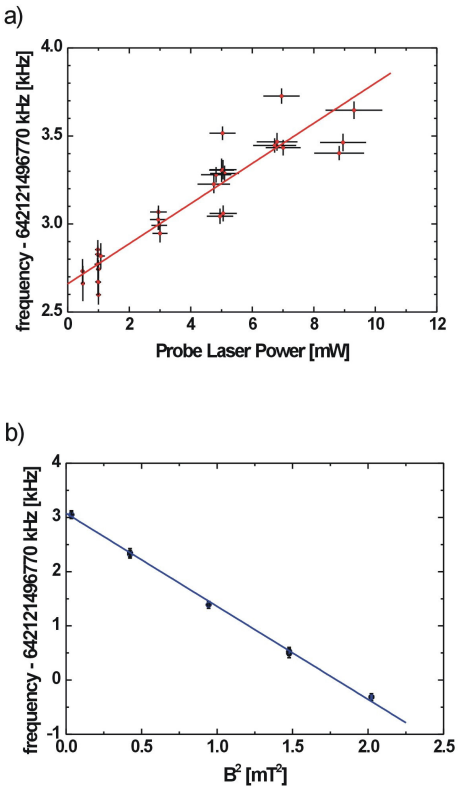

Figure 2a) AC-Stark and b) second-order Zeeman shifts of the $^2S_{1/2}$ (F = 0) – $^2F_{7/2}$ (F = 3, m_F = 0) transition. Straight line fits to the data give shifts of 0.11(1) kHz/mW and −1.72(3) mHz/(μT)^2 respectively [2]. This data was taken with an absorption width of 300 Hz, a spot size of 15 μm and interrogation time of 0.3 s. A power of 1mW gives a 50 % excitation probability.

The ac-Stark effect is due to the off-resonant interaction of probe light with strongly allowed transitions from the S- and F-states and is linearly dependent on intensity. The intensity required to drive the transition at a given rate is dependent on the spectral intensity at the transition frequency in the frame of ion. With an observed absorption width of 300 Hz, the intensity required is relatively high and the ac-Stark is the largest systematic shift. However, as this width is reduced, it will be possible to excite the transition with the same probability at a reduced total intensity. Further, it will also be possible longer to use longer interrogation times, again allowing for a reduction in intensity. One can therefore project, that, with an absorption width of 0.1 Hz, an interrogation time of 10 s and spot size of 1 mm, the shift will be ~1 mHz/mW. At this level it will no longer be the dominant systematic effect.

The second order Zeeman shift is currently significant due to the presence of a relatively large B-field of 200 µT, which is used to prevent population trapping on the cooling transition. Recently, an additional coil has been added that will allow the B-field to be switched to a low value during the probe pulse. Operating at a field of 1 µT, the resulting shift will be –2 mHz.

Other systematic effects that have been calculated, but which are not yet at a measureable level, are detailed in Table 1. The quadrupole shift has been evaluated assuming a common dc offset potential of 1V on upper and lower electrodes of the trap and a quadrupole moment of $-0.22ea_0^2$ calculated using the Cowan code [3]. The uncertainty in the shift may be further reduced by either averaging over three orthogonal states of the B-field [4], or by averaging over Zeeman components of the transition [5]. The Blackbody shift is evaluated using oscillator strengths calculated by Biemont et al. [6], and scaled using experimental data where available [7]. The uncertainty is dominated by the uncertainty in the calculated polarizabilities. Further reduction will be possible with a measurement of the dc-Stark shift [8].

Shift	Value / Hz
Quadrupole	0 (± 0.4)
Blackbody	-0.15 (± 0.08)
DC-Stark	-0.04 (± 0.04)
2^{nd}-order Doppler	0 (± 0.05)

Table 1. Other systematic shifts at their current level of evaluation.

III. PROBE LASER AND ATOMIC SPECTRA

The laser used to probe the octupole transition is a frequency-doubled Ti:Sapphire at 467 nm. Light at the fundamental wavelength (934 nm) is frequency-stabilised to a high-finesse Fabry-Pérot etalon using the standard frequency modulation technique [9]. Feedback is to an external double-passed AOM, and with this a servo bandwidth of 250 kHz is achieved, which is sufficient to suppress the residual noise from the laser to a level where it no longer dominates the frequency noise of the stabilised light. Rather, this is determined by the frequency stability of the cavity. This has a finesse approaching 200,000 (FWHM of the fringe is 8.41(1) kHz) and is construced from ultra-low expansivity glass. With a two-layer temperature control, the frequency drift is typically ~0.1 Hz/s, above a long-term isothermal drift of 50 mHz/s. The cavity is kept within a vacuum chamber which is situated on a passive vibration isolation platform within an acoustically isolating box.

Two nominally identically cavities were set-up with light independently stabilised to each one.

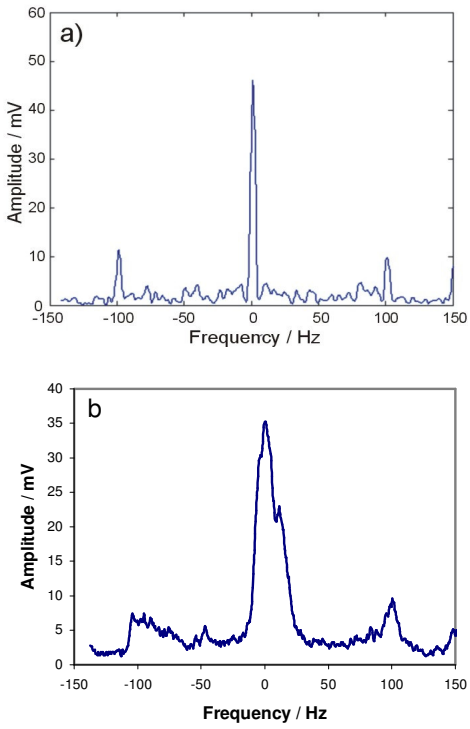

Figure 3. Heterodyne beat between light locked to two independent cavities, a) 1 s acquisition, linewidth (FWHM) = 4.7 Hz, b) average over 1 minute, linewidth (FWHM) = 18 Hz.

A heterodyne beat between the light stabiltised to each cavity is shown in Figure 3. The short-term linewidth is ≈ 5 Hz, however, on averaging for 1 minute this broadens out to ≈ 20 Hz. The atomic absorption spectrum measured over a similar timescale is shown in Figure 4. The observed width is ≈ 200 Hz, an order of magnitude greater than one would expect if it were due to the probe laser alone. Clearly, another broadening mechanism is present.

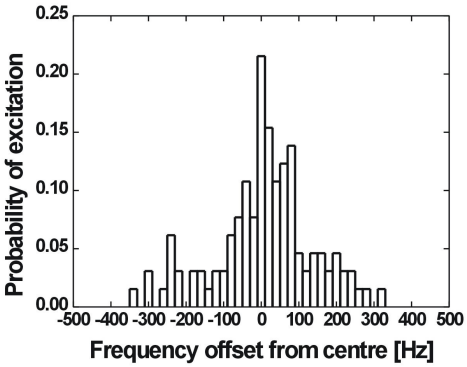

Figure 4. Absorption spectrum on $^2S_{1/2}$ (F=0)—$^2F_{7/2}$ (F=3, m_F=0) transition. FWHM = 180±10 Hz, 20 Hz resolution.

IV. TRAP VIBRATION

Following stabilisation, light is transmitted to the ion across a path of approximately 5 meters, including a 2 m section of optical fibre. Any relative movement between the frame of reference of the ion (defined by the trapping potential) and the cavity will introduce a Doppler shift. A heterodyne measurement, using light reflected back along the majority of the transmission path, showed the broadening on the carrier to be ≪ 1 Hz with some small (<10 % intensity) sidebands, at 10-100 Hz from the carrier. This could not therefore account for the observed broadening of the atomic transition.

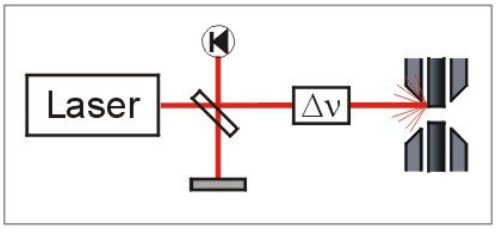

Figure 5. Schematic for heterodyne measurement of trap vibration. An AOM shifts the frequency of the light in the path to and from the trap. This is combined with a reference beam on a photodiode and the heterodyne beat detected.

An experiment was then done to determine the level of broadening introduced by the trap itself, as shown in Figure 5. Light was either reflected directly off the electrodes or off a mirror attached the vacuum chamber housing the trap. The measured heterodyne beat for both cases is shown in Figure 6.

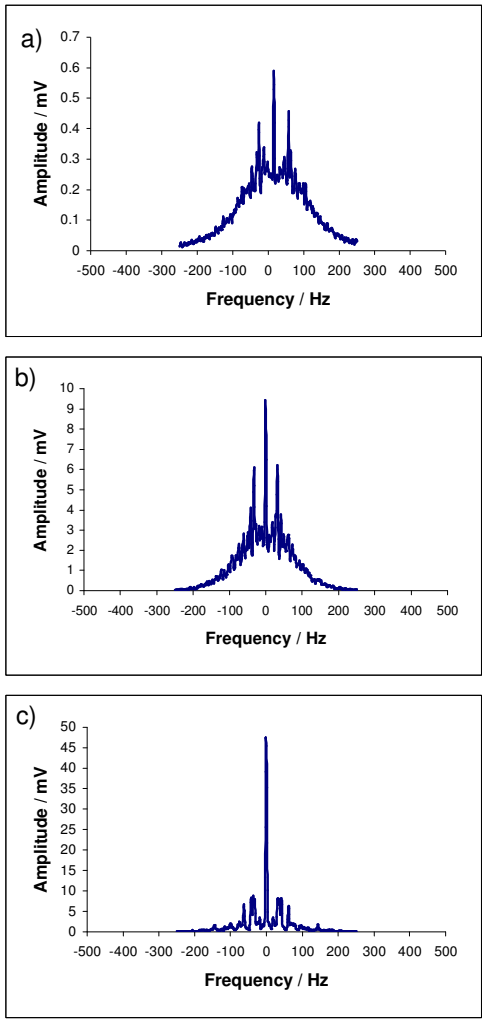

Figure 6. Heterodyne beat between reference beam and light reflected off a) trap electrodes, b) mirror attached to vacuum chamber and c) with the vacuum chamber supported from below.

A broad pedestal is observed having a width of around 200 Hz with a narrow carrier and sidebands at the UK mains frequency visible above it. This corresponds well to the atomic spectrum, and one can conclude that trap vibration is the source of broadening. The mounting of the vacuum chamber was improved with the addition of mechanical support from below, resulting in a much reduced width. It is now expected that a narrower width will be observed on the atomic transition.

Acknowledgements

This work is supported by the NMS Quantum Metrology Programme under contract No. FQM1/AO1.

REFERENCES

[1] M. Roberts, P. Taylor, G. P. Barwood, W. R. C. Rowley, and P. Gill, Phys. Rev. A. **62,** 020501(R) (2000).
[2] K. Hosaka, S. A. Webster, P. J. Blythe, A. Stannard, D. Beaton, H. S. Margolis, S. N. Lea, and P. Gill, IEEE Trans. Instrum. Meas. **54**, 759 (2005).
[3] R. D. Cowan, *The Theory of Atomic Structure and Spectra*, (University of California Press, Berkely, CA, 1983).
[4] W. M. Itano, J. Res. Natl. Inst. Stand. Technol. 105,829 (2000).
[5] P. Dube, A. A. Madej, J. E. Bernard, L. Marmet, J.-S. Boulanger, and S. Cundy, Phys. Rev. Lett, **95**, 033001 (2005).
[6] E. Biémont, J.-F. Dutrieux, I. Martin, and P. Quinet, J. Phys. B. **31**, 3321 (1998).
[7] S. N. Lea, S. A. Webster, and G. P. Barwood, in this proceedings.
[8] T. Schneider, E. Peik, and Chr. Tamm, Phys. Rev. Lett. **94**, 230801 (2005).
[9] R. W. P. Drever, J. L. Hall, F. V. Kowalski, J. Hough, G. M. Ford, A. J. Munley, and H. Ward, Appl. Phys. B. **31**, 97 (1983).

Proceedings of the 20th EFTF, 2006

Polarisabilities and blackbody shifts in Sr^+ and Yb^+

S. N. Lea,* S. A. Webster, and G. P. Barwood
National Physical Laboratory (NPL), Hampton Road, Teddington, Middlesex TW11 0LW, UK

The polarisabilities and blackbody Stark shifts of transitions in $^{88}Sr^+$ and $^{171}Yb^+$ which are used as optical frequency standards are calculated. Where data is available, oscillator strengths derived from experimental lifetime measurements are used in place of theoretical values.

I. INTRODUCTION

The accepted frequency values of atomic optical frequency standards follow the definition of the SI second in refering to an unperturbed atom at $T = 0$ K [1]. Most trapped ion standards operate near room temperature. A frequency correction has to be applied to account for the Stark shift due to interaction with blackbody radiation. With the demonstration of techniques for nulling the electric quadrupole shift [2–4], it is likely that the uncertainty in the blackbody Stark shift will soon be the dominant contribution to the error budget for a number of these standards. This uncertainty arises from uncertainties in (i) the temperature of the blackbody radiation experienced by the ion and (ii) the atomic polarisabilities.

This paper presents calculations of the polarisabilities and blackbody Stark shifts of three transitions used as the basis of optical frequency standards: the $5s\,^2S_{1/2} - 4d\,^2D_{5/2}$ electric quadrupole ($E2$) transition at 674 nm in $^{88}Sr^+$, used at NRC [2] and NPL [3]; the $4f^{14}\,6s\,^2S_{1/2} - 4f^{14}\,5d\,^2D_{3/2}$ $E2$ transition at 436 nm in $^{171}Yb^+$, used at PTB [5]; and the $4f^{14}\,6s\,^2S_{1/2} - 4f^{13}\,6s^2\,^2F_{7/2}$ electric octupole ($E3$) transition at 467 nm in $^{171}Yb^+$, also used at NPL [6].

Previous estimates of the blackbody Stark shifts of the transitions used at NPL make use of calculated oscillator strengths [3, 7]. Comparison of experimental values of the $^2S_{1/2}-{}^2P_{1/2,3/2}$ resonance transition lifetimes in Sr^+ and Yb^+ with lifetimes obtained from the calculated oscillator strengths reveals discrepancies of up to 15%. With the inclusion of this experimental data, better values of the polarisabilities can be obtained. For $^{171}Yb^+$, measurements of the quadratic Stark shift of the 436 nm $E2$ transition at PTB have provided experimental polarisability data which provides a further check on the calculations [5].

In this paper the polarisabilities are calculated for the static (dc) case which is appropriate to an estimation of the blackbody Stark shift. However, the calculation can be readily adapted to the dynamic case, required for evaluation of ac Stark shifts due to radiation at optical frequencies. A similar approach to calculation of the polarisabilities for a wider range of ions has been presented by Warrington [8].

*Electronic address: stephen.lea@npl.co.uk

II. FORMALISM

The scalar polarisability $\alpha_{sc}(\gamma, J)$ of a state $|\gamma, J\rangle$ gives rise to a scalar quadratic Stark shift in an external electric field E,

$$\Delta W_{sc} = -\tfrac{1}{2}\alpha_{sc}(\gamma, J)E^2, \quad (1)$$

and the tensor polarisability $\alpha_{ten}(\gamma, J)$ gives rise to a tensorial shift,

$$\Delta W_{ten} = -\tfrac{1}{4}K(J, M_J)(3\cos^2\theta - 1)\alpha_{ten}(\gamma, J)E^2, \quad (2)$$

where

$$K(J, M_J) = \frac{3M_J^2 - J(J+1)}{J(2J-1)} \quad (3)$$

and θ is the angle between the direction of the external E-field and the quantisation axis of the ion trap defined by an applied magnetic field.

Following the formalism of Angel and Sandars [9, 10], the polarisabilities can be calculated in second order perturbation theory by a summation over all allowed electric dipole ($E1$) transitions to states $|\gamma', J'\rangle$. For the static (dc) field case,

$$\alpha_{sc}^{dc}(\gamma, J) = \frac{e^2}{m_e}\sum_{\gamma' J'}\frac{f(\gamma J \to \gamma' J')}{\omega^2}$$

$$\alpha_{ten}^{dc}(\gamma, J) = (-1)^{2J}\frac{e^2}{m_e}\left[\frac{30J(2J-1)(2J+1)}{(2J+3)(J+1)}\right]^{\frac{1}{2}} \times \sum_{\gamma' J'}(-1)^{J'-J}\begin{Bmatrix} 1 & 1 & 2 \\ J & J & J' \end{Bmatrix}\frac{f(\gamma J \to \gamma' J')}{\omega^2}, \quad (4)$$

where $f(\gamma J \to \gamma' J')$ is the oscillator strength and ω the angular frequency of the transition. For $^{171}Yb^+$, the tensor polarisability of the hyperfine state $|\gamma, J, F\rangle$ is defined as

$$\alpha_{ten}(\gamma, J, F) = K'(I, J, F)\alpha_{ten}(\gamma, J). \quad (5)$$

The numerical factor $K'(I, J, F)$ is given by

$$K'(I, J, F) = (-1)^{I+J+F}\begin{Bmatrix} J & 2 & J \\ F & I & F \end{Bmatrix} \times \left[\frac{(2F+1)F(2F-1)(2J+3)(2J+1)(J+1)}{(2F+3)(F+1)J(2J-1)}\right]^{\frac{1}{2}}, \quad (6)$$

the term in curly braces being a Wigner 6-j symbol.

III. POLARISABILITIES OF $^{88}Sr^+$

The polarisabilities are calculated at three levels of complexity: including only the dominant transitions; adding transitions to higher-lying states; and adjusting the oscillator strengths in the light of experimental lifetime data.

1. *Using oscillator strengths tabulated by Brage et al.*

This calculation uses oscillator strengths tabulated by Brage *et al.* [11] for the transitions making the dominant contribution to the polarisabilities. The calculation of the ground state polarisability includes only the oscillator strengths of the $5s\,^2S_{1/2} - 5p\,^2P_{1/2,3/2}$ resonance lines, whilst for the $4d\,^2D_{5/2}$ state, the oscillator strengths of the transitions to $5p\,^2P_{3/2}$ and $4f\,^2F_{5/2,7/2}$ are included. Neglecting transitions to higher-lying states results in an underestimate of the scalar polarisabilities (all terms have the same sign) and an error in the tensor polarisability of the $4d\,^2D_{5/2}$ state (terms due to $J' = 5/2$ states have opposite sign to terms due to $J' = 3/2, 7/2$ states). The results are given in column 1 of table II.

2. *Adding higher-lying states*

Biémont *et al.* have performed pseudo-relativistic Hartree-Fock (HFR) calculations of the radiative lifetimes of higher-lying states in $^{88}Sr^+$ [12]. These calculated lifetimes can be used to provide oscillator strengths for transitions to the $5s\,^2S_{1/2}$ and $4d\,^2D_{5/2}$ states if the branching ratios are known. Even without this knowledge, reasonable approximations can be made. For the $5s\,^2S_{1/2}$ state, the approximation made is that the $(n > 5)p\,^2P_{1/2,3/2}$ states decay only to the ground state, neglecting transitions to higher S-states and to D-states. The latter approximation is justified since transitions with $\Delta L = +1$ are generally weaker than transitions with $\Delta L = -1$. For the $4d\,^2D_{5/2}$ state, transitions to $(n > 5)p\,^2P_{3/2}$ states and also to $(n > 4)f\,^2F_{5/2}$ states, which decay preferentially to $^2D_{3/2}$ states, are neglected. However, transitions to $(n > 4)f\,^2F_{7/2}$ states are included, neglecting their decays to higher $^2D_{5/2}$ states. Overall, this approximation will overestimate the scalar polarisabilities.

Including oscillator strengths derived from the lifetimes of states up to $n = 10$, the values given in column 2a of table II are obtained. These results hardly differ from the simple case. A grosser overestimation is to include the transitions to $(n > 4)f\,^2F_{5/2}$ states in the calculation for the $4d\,^2D_{5/2}$ state, yielding the values in column 2b. The results are a little different but hardly significantly so, indicating the robustness of the approximations made in method 1. The oscillator strengths of these higher-lying levels contribute only 0.8% to the $5s\,^2S_{1/2}$ state polarisability and 2.5% to the scalar polarisability of the $4d\,^2D_{5/2}$ state.

TABLE I: Comparison of calculated [12] and experimental [12, 13] lifetimes of levels contributing > 1% to the dc scalar polarisability of the $5s\,^2S_{1/2}$ and $4d\,^2D_{5/2}$ states in $^{88}Sr^+$. The fractional (percentage) contribution of each level to the dc scalar polarisability is also indicated.

Energy cm^{-1}	Level	% of α_{sc}^{dc} $^2S_{1/2}$	$^2D_{3/2}$	τ_{calc} ns	τ_{exp} ns
23715	$5p\,^2P_{1/2}$	33.49		7.71	7.43(5)
24517	$5p\,^2P_{3/2}$	65.61	80.72	6.96	6.65(5)
60992	$4f\,^2F_{5/2}$		0.68	3.17	3.09(6)
60992	$4f\,^2F_{7/2}$		14.10	3.23	2.97(5)
71066	$5f\,^2F_{7/2}$		2.24	5.33	
76553	$6f\,^2F_{7/2}$		1.00	8.53	
other levels		0.90	1.26		

3. *Using experimental lifetimes*

Biémont *et al.* [12] also quote experimental lifetimes for the $5p\,^2P_{1/2,3/2}$ and $4f\,^2F_{5/2,7/2}$ states, summarised in table I. The P-state lifetimes quoted are weighted means of 4 ($^2P_{1/2}$) and 5 ($^2P_{3/2}$) measurements, dominated by those of Pinnington *et al.* [13]. The F-state lifetimes are solely from the latter work. These can be used to scale the calculated oscillator strengths according to

$$f_{exp} = (\tau_{calc}/\tau_{exp}) f_{calc}, \qquad (7)$$

where it is assumed that the calculated branching ratios for the decay channels from the upper state of the transition are correct. Since the calculation of the oscillator strength for each decay channel depends on the overlap integral with the lower state of the transition, it is not clear that this is a good assumption. However, for the states in question the branching ratios for decay channels other than the transition of interest are small. For the $5p\,^2P_{1/2,3/2}$ states the calculated lifetimes given by Biémont *et al.* give oscillator strengths a few percent larger than those used in method 1, as expected given that the branching ratios to the D-states have been neglected. The oscillator strength used in method 1 has then been scaled by the ratio of Biémont's calculated lifetime to the weighted mean experimental lifetime. The oscillator strength is assigned an uncertainty corresponding to that of the lifetime. The affected oscillator strengths are for the $5s\,^2S_{1/2} - 5p\,^2P_{1/2,3/2}$ and $5d\,^2D_{5/2} - 5p\,^2P_{3/2}$ transitions. A similar modification to the F-state oscillator strengths affects the $5d\,^2D_{5/2}$ polarisabilities by a small amount. Here the lifetimes are calculated from the oscillator strengths quoted by Brage *et al.* (taking into account both decay channels for the $4f\,^2F_{5/2}$

TABLE II: Static (dc) polarisabilities of the states $5s\,^2S_{1/2}$ and $4d\,^2D_{5/2}$ states in $^{88}Sr^+$, in units of 10^{-39} J V^{-2}m^2, for the three calculations discussed in the text. The final line gives the polarisability of the $5s\,^2S_{1/2} - 4d\,^2D_{5/2}$ transition, used to calculate the blackbody Stark shift. The values used by Madej *et al.* [14], based on calculations similar to these performed by the NRC group and by Warrington, are also given.

	Calculation method				Ref. [14]
	1	2a	2b	3	
$\alpha_{sc}^{dc}(^2S_{1/2})$	1.387	1.401		1.461(8)	1.40(6)
$\alpha_{sc}^{dc}(^2D_{5/2})$	0.737	0.775	0.803	0.835(6)	0.8(2)
$\alpha_{ten}^{dc}(^2D_{5/2})$	−0.671	−0.684	−0.652	−0.723(9)	−0.7(2)
$\alpha_{sc}^{dc}(^2S_{1/2}) - \alpha_{sc}^{dc}(^2D_{5/2})$	0.650	0.626	0.598	0.626(10)	0.6(2)

state). This gives lifetimes somewhat larger than in Biémont's calculation so the ratio of this calculated lifetime and the experimental lifetime is used. The polarisabilities in column 3 of table II are calculated including the $(n > 5)p\,^2P_{1/2,3/2}$ states and the $(n > 4)f\,^2F_{7/2}$ states as above, the results agreeing well with the simple case.

In conclusion, the final line of table II gives the scalar polarisability of the $5s\,^2S_{1/2} - 4d\,^2D_{5/2}$ transition. The values range between 0.598 and 0.650 × 10^{-39} J V^{-2}m^2, with the value obtained using experimental lifetime data lying in the middle of this range. It therefore seems reasonable to take this range as representing a 95% (2σ) confidence range, enabling the uncertainty in the blackbody Stark shift at 297 K to be reduced from 0.08 Hz [3] to 8 mHz (relative uncertainty 2×10^{-17}).

IV. POLARISABILITIES OF $^{171}Yb^+$

The calculation presented here extends that of Webster *et al.* [7]. The atomic structure of YbII is considerably more complex than that of a true alkali-like ion such as SrII, because of the existence of levels arising from the excitation of an electron from the 4f shell in addition to levels arising from excitation of the valence 6s electron alone. The principal configurations which need to be taken into account to calculate the polarisabilities of the $4f^{14}\,6s\,^2S_{1/2}$ and $4f^{14}\,5d\,^2D_{3/2}$ states are $4f^{13}\,5d6s$ and $4f^{13}\,5d^2$. For the $4f^{13}\,6s^2\,^2F_{7/2}$ state, the principal configurations are $4f^{13}\,6s6p$ and $4f^{13}\,5d6p$. The $4f^{13}\,5d^2$ and $4f^{13}\,5d6p$ configurations are examples of doubly-excited configurations (f-shell hole plus two valence electrons), as is the $4f^{13}\,6s^2\,^2F_{7/2}$ state, which can, exceptionally, be described in *LS*-coupling, as the two valence 6s electrons form a closed shell. The energy levels have been calculated by Fawcett and Wilson [16] and classified in the *LSJLSJ*-coupling scheme, *e. g.* $4f^{13}\,5d6s\,^2F_{7/2}[^3D_{3/2}]_{3/2}$, where the first *LSJ* term represents the state of the f-shell hole, the second, bracketed, *LSJ* term represents the state of the pair of valence electrons and the final subscript represents the total angular momentum of the state.

Biémont *et al.* have calculated oscillator strengths and lifetimes for all the relevant transitions and energy levels [15]. Levels making a fractional contribution greater than 1% to the dc scalar polarisabilities are listed in tables III and IV, with their calculated and, if available, experimental lifetimes.

The calculation of the polarisabilities is summarised in table V. The values in the column headed 'Theory' are obtained using solely the theoretical oscillator strengths. The values in the column headed 'Lifetimes' are obtained by scaling the calculated oscillator strengths by the ratio of the calculated and experimental lifetimes, as for $^{88}Sr^+$. The assumption is made that the branching ratios calculated by Biémont *et al.* are accurate. The uncertainty ascribed to these modified values is obtained by propagating the uncertainties of the measured lifetimes and ascribing an uncertainty of 20% to the oscillator strengths to states for which there is no experimental lifetime data. There is good agreement between experimental and calculated lifetimes for the even parity states contributing to the polarisability of the $4f^{13}\,6s^2\,^2F_{7/2}$ state (table IV) but agreement is only at the 20% level for the odd parity states (table III). There is no experimental lifetime data available for two states which contribute at the 2% level to the polarisability of the $4f^{14}\,6s\,^2S_{1/2}$ state.

Also included in table V are values for the difference of the $^2S_{1/2}$ and $^2D_{3/2}$ scalar polarisabilities and the $^2D_{3/2}$ tensor polarisability derived from measurements made at PTB of the dc Stark shift of the 435 nm quadrupole transition [5]. One way to interpret these measurements is to note that 95.5% of the value of $\alpha_{sc}^{dc}(^2D_{3/2})$ is due to the oscillator strengths of the transitions to the $4f^{14}\,6p\,^2P$ states and thus one can be confident of the polarisability calculated using the experimental lifetime data, whereas 25% of the value of $\alpha_{sc}^{dc}(^2S_{1/2})$ is due to the oscillator strengths of transitions to states other than $4f^{14}\,6p\,^2P_{1/2,3/2}$. The value of $\alpha_{sc}^{dc}(^2D_{3/2})$ calculated

TABLE III: Fractional (percentage) contributions of levels contributing > 1% to the dc scalar polarisability of the $4f^{14}\,6s\,^2S_{1/2}$ and $4f^{14}\,5d\,^2D_{3/2}$ states in $^{171}Yb^+$, together with comparison of calculated lifetimes (from Biémont *et al.* [15]) with experimental lifetimes.

Energy cm^{-1}	Level designation (Fawcett & Wilson [16])	% of α_{sc}^{dc} $^2S_{1/2}$	$^2D_{3/2}$	τ_{calc} ns	τ_{exp} ns	
27062	$4f^{14}\,6p\,^2P_{1/2}$	28.43	86.75	8.60	8.07(9)	[17]
28758	$4f^{13}\,5d6s\,^2F_{7/2}[^3D_{3/2}]_{3/2}$	2.39		149.11		
30392	$4f^{14}\,6p\,^2P_{3/2}$	46.56	8.73	7.23	6.15(9)	[17]
32982	$4f^{13}\,5d6s\,^2F_{7/2}[^3D_{5/2}]_{3/2}$	1.02		157.40	196(20)	[18]
33654	$4f^{13}\,5d6s\,^2F_{7/2}[^3D_{3/2}]_{1/2}$	2.44	1.52	32.10	39(3)	[18]
34575	$4f^{13}\,5d6s\,^2F_{5/2}[^3D_{1/2}]_{3/2}$	7.90		29.39	28.6(4)	[19]
44941	$4f^{13}\,5d^2\,^2F_{7/2}[^3F_{3/2}]_{3/2}$	2.92		14.46	20.3(3)	[19]
45737	$4f^{13}\,5d6s\,^2F_{7/2}[^1D_{3/2}]_{3/2}$	1.79		27.70	30.9(6)	[20]
46903	$4f^{13}\,5d^2\,^2F_{7/2}[^3F_{3/2}]_{1/2}$	2.04		12.15		
47005	$4f^{13}\,5d6s\,^2F_{5/2}[^1D_{1/2}]_{3/2}$	2.50		19.02	19.7(5)	[20]
	other levels	2.01	3.00			

TABLE IV: Comparison of calculated and experimental lifetimes of levels contributing > 1% to the dc scalar polarisability of the $4f^{13}\,6s^2\,^2F_{7/2}$ state in $^{171}Yb^+$. Calculated lifetimes from Biémont *et al.* [15]. The fractional (percentage) contribution of each level to the dc scalar polarisability is also indicated.

Energy cm^{-1}	Level designation (Fawcett & Wilson [16])	% of α_{sc}^{dc} $^2F_{7/2}$	τ_{calc} ns	τ_{exp} ns	
48900	$4f^{13}\,6s6p\,^2F_{7/2}[^3P_1]_{7/2}$	1.48	31.80		
49301	$4f^{13}\,6s6p\,^2F_{7/2}[^3P_1]_{9/2}$	2.87	29.18		
49498	$4f^{13}\,6s6p\,^2F_{7/2}[^3P_1]_{5/2}$	2.07	28.82		
56376	$4f^{13}\,5d6p\,^2F_{7/2}[^1P_1]_{5/2}$	7.99	3.76	3.78(7)	[20]
57765	$4f^{13}\,6s6p\,^2F_{7/2}[^1P_1]_{9/2}$	24.86	2.80	2.87(11)	[20]
58824	$4f^{13}\,5d6p\,^2F_{7/2}[^3F_2]_{5/2}$	5.92	3.73	3.59(7)	[20]
59090	$4f^{13}\,6s6p\,^2F_{7/2}[^1P_1]_{7/2}$	22.18	2.40	2.31(10)	[20]
61215	$4f^{13}\,5d6p\,^2F_{7/2}[^3F_2]_{9/2}$	2.71	4.11		
63234	$4f^{13}\,5d6p\,^2F_{7/2}[^3D_1]_{5/2}$	3.11	2.67		
63727	$4f^{13}\,5d6p\,^2F_{7/2}[^3D_1]_{9/2}$	1.69	2.94		
64598	$4f^{13}\,5d6p\,^2F_{7/2}[^3D_1]_{7/2}$	1.32	3.06		
65200	$4f^{13}\,5d6p\,^2F_{7/2}[^1D_2]_{9/2}$	1.44	2.83		
	other levels	22.36			

TABLE V: Calculated static (dc) polarisabilities of the $4f^{14}\,6s\,^2S_{1/2}$, $4f^{14}\,5d\,^2D_{3/2}$ and $4f^{13}\,6s^2\,^2F_{7/2}$ states in $^{171}Yb^+$, in units of 10^{-39} $J\,V^{-2}m^2$. The values calculated by Warrington, quoted in [5], and measured at PTB [5] are also given.

Polarisability	Theory	Lifetimes	Warrington	Experiment
$\alpha_{sc}^{dc}(^2S_{1/2})$	0.880	0.963(10)		
$\alpha_{sc}^{dc}(^2D_{3/2})$	1.386	1.483(13)		
$\alpha_{ten}^{dc}(^2D_{3/2}, F=2)$	−1.147	−1.213(13)	−1.15	−1.36(22)
$\alpha_{sc}^{dc}(^2S_{1/2}) - \alpha_{sc}^{dc}(^2D_{3/2})$	−0.506	−0.520(16)	−0.44	−0.69(14)
$\alpha_{sc}^{dc}(^2F_{7/2})$	1.073	1.077(25)		
$\alpha_{ten}^{dc}(^2F_{7/2}, F=3)$	−0.020	−0.008(20)		
$\alpha_{sc}^{dc}(^2S_{1/2}) - \alpha_{sc}^{dc}(^2F_{7/2})$	−0.193	−0.114(27)		

TABLE VI: Blackbody Stark shifts at 297 K, in Hz, from the polarisabilities quoted in tables II and V. The value in italics for the $E3$ transition is obtained by combining the PTB measurement of the polarisability of the $E2$ transition with the calculated ('lifetimes') values of the $^2D_{3/2}$ and $^2F_{7/2}$ state polarisabilities (see text).

Ion	Transition	This work		Warrington	Experiment
		Theory	Lifetimes	Refs. [5, 14]	Ref. [5]
$^{88}Sr^+$	$5s\,^2S_{1/2} - 4d\,^2D_{5/2}$	0.313(8)	0.314(5)	0.3(1)	
$^{171}Yb^+$	$4f^{14}\,6s\,^2S_{1/2} - 4f^{14}\,5d\,^2D_{3/2}$	−0.254	−0.261(8)	−0.22	−0.35(7)
$^{171}Yb^+$	$4f^{14}\,6s\,^2S_{1/2} - 4f^{13}\,6s^2\,^2F_{7/2}$	−0.097	−0.057(14)		*−0.15(7)*

using the $4f^{14}\,6p\,^2P$ lifetimes can be used to extract an value of $\alpha_{sc}^{dc}(^2S_{1/2}) = 0.79(14) \times 10^{-39}$ J V^{-2}m^2 from the PTB measurement. Combined with the calculated value of $\alpha_{sc}^{dc}(^2F_{7/2})$, which can be considered robust as there is good agreement between the experimental and theoretical lifetimes (table IV), a value of $\alpha_{sc}^{dc}(^2S_{1/2}) - \alpha_{sc}^{dc}(^2F_{7/2}) = -0.29(14) \times 10^{-39}$ J V^{-2}m^2 is obtained for the polarisability of the $E3$ transition.

V. BLACKBODY STARK SHIFTS

The blackbody Stark shift is calculated in the static (dc) approximation. In this approximation, the blackbody Stark shift of a transition between a ground state g and an excited state e is

$$\Delta\nu_{BB}(g - e) = \frac{1}{2h}\left[\alpha_{sc}^{dc}(g) - \alpha_{sc}^{dc}(e)\right]\langle E^2\rangle, \qquad (8)$$

where $\langle E^2\rangle$ is the average (rms) value of the blackbody radiation field,

$$\langle E^2\rangle = \frac{4\sigma}{\epsilon_0 c}T^4 = 66.5\,\mathrm{V^2cm^{-2}} \text{ at } T = 297\,\mathrm{K}, \qquad (9)$$

σ being the Stefan-Boltzmann constant. The blackbody radiation is isotropic and hence the tensor component of the Stark shift averages to zero.

This dc approximation is valid so long as the fraction of the blackbody field which is resonant with any $E1$ transition to either of the states g or e is negligible. If this is not the case, there will be an ac contribution to the polarisabilities proportional to the spectral intensity of the radiation within the transition bandwidth. For $^{88}Sr^+$, the lowest frequency transition entering the calculation is the $4d\,^2D_{5/2} - 5p\,^2P_{3/2}$ transition at 1033 nm, which gives rise to 97% of the polarisability of the $4d\,^2D_{5/2}$ state. For the $E3$ transition in $^{171}Yb^+$, the lowest frequency transitions making a significant contribution to the polarisabilities are the the resonance lines at 369 nm and 329 nm but for the $E2$ transition there is a significant contribution to the polarisability of the $^2D_{3/2}$ state from transitions at 2.44 μm and 1.34 μm. Inspection of a tabulation of the integral from 0 to λT of the spectral distribution of the blackbody radiation [21] shows that, at $T = 297$ K, only 1.6×10^{-5} of the radiation is at wavelengths shorter than 2.7 μm, this fraction falling to less than 10^{-7} at 2.0 μm. The ac scalar polarisabilities differ from the dc scalar polarisabilities calculated below by no more than a few % for 2 μm radiation, *i. e.* an overall contribution at the parts-in-10^9 level. The fraction of the blackbody radiation resonant with the resonance lines is still lower, offsetting the rather large modification to the ac scalar polarisabilities at these frequencies. This issue has also been considered by Warrington [8].

Table VI summarises the blackbody Stark shifts at 297 K for three transitions under discussion, using the static polarisabilities quoted in tables II and V. As discussed in section III, for the 674 nm $E2$ transition in $^{88}Sr^+$, there is good agreement between various approaches to the calculation of the polarisabilities, enabling the uncertainty in the blackbody Stark shift at 297 K to be reduced from 0.08 Hz [3] to 8 mHz (relative uncertainty 2×10^{-17}).

The atomic structure of $^{171}Yb^+$ is very much more complicated than that of a true alkali-like ion such as $^{88}Sr^+$. Consequently, the theoretical calculation of oscillator strengths is more involved and many more transitions have to be taken into account in evaluating the state polarisabilities. In the light of the relatively poor agreement between values for the polarisability of the $^2S_{1/2}$ state in particular, greatest confidence has to be placed in the values of the blackbody Stark shifts derived from the PTB measurement: −0.35(7) Hz at 297 K for the $E2$ transition at 435 nm and −0.15(7) Hz at 297 K for the $E3$ transition at 467 nm. The latter figure is presented in italics in table VI. In both cases, the 0.07 Hz uncertainty corresponds to a fractional frequency uncertainty of 1×10^{-16}.

The uncertainty in the blackbody Stark shift due to an uncertainty in the ambient temperatue u_T is a factor of $4u_T/T$ smaller than the magnitude of the shift; this uncertainty can be comparable to the uncertainty in the magnitude of the shift. The coefficient for $^{88}Sr^+$ at 297 K is 4 mHz K^{-1} (1×10^{-17} K^{-1}); for $^{171}Yb^+$, the coefficients are −5 mHz K^{-1} (-7×10^{-18} K^{-1}) for the $E2$ transition and −2 mHz K^{-1} (-3×10^{-18} K^{-1}) for the $E3$ transition, using values derived from the PTB measurements. To achieve an uncertainty at the

1×10^{-17} level, the temperature of the blackbody radiation experienced by the ion must be known and stable at the 1 K level (around 297 K). This is potentially a challenging experimental requirement: apart from the uniformity and stability of the temperature of the vacuum system enclosing the ion trap, local heating effects due to the rf trapping field at the trap electrodes may result in a large uncertainty in the temperature and isotropy of the blackbody radiation field experienced by the ion.

It would clearly be highly desirable for the PTB measurements to be repeated and refined and for similar measurements to be made for the 467 nm electric octupole transition and, indeed, for $^{88}Sr^{+}$, providing experimental verification of these calculations. Equally, more work is required to establish the actual radiation temperature experienced by the trapped ion.

Acknowledgments

The authors would like to thank K. Szymaniec for assistance in the preparation of this paper and to acknowledge fruitful discussions with A. G. Sinclair (NPL) and correspondence with R. B. Warrington (NMI, Australia). This work is supported by the DTI National Measurement System Length and Quantum Metrology programmes.

[1] Proc. Verb. CIPM **65** (1998).
[2] P. Dubé, A. A. Madej, J. E. Bernard, L. Marmet, J.-S. Boulanger, and S. Cundy, Phys. Rev. Lett. **95**, 033001 (2005).
[3] H. S. Margolis, G. P. Barwood, G. Huang, H. A. Klein, S. N. Lea, K. Szymaniec, and P. Gill, Science **306**, 1355 (2004).
[4] W. H. Oskay, , W. M. Itano, and J. C. Bergquist, Phys. Rev. Lett. **94**, 163001 (2005).
[5] T. Schneider, E. Peik, and C. Tamm, Phys. Rev. Lett. **94**, 230801 (2005).
[6] K. Hosaka, S. A. Webster, P. J. Blythe, A. Stannard, D. Beaton, H. S. Margolis, S. N. Lea, and P. Gill, IEEE Trans. Instrum. and Meas. **54**, 759 (2005).
[7] S. A. Webster, P. J. Blythe, K. Hosaka, G. P. Barwood, and P. Gill, NPL Report CBTLM 31 (2003).
[8] R. B. Warrington, presentation at the Workshop on the Latest Developments in Atomic Frequency Standards, satellite meeting to the 2003 International Conference on Lasers and Spectroscopy (Sydney, 21 July 2003).
[9] J. R. P. Angel and P. G. H. Sandars, Proc. Roy. Soc. A **305**, 125 (1968).
[10] W. M. Itano, J. Res. Natl. Inst. Stand. Technol. **105**, 829 (2000).
[11] T. Brage, G. M. Wahlgren, S. G. Johansson, D. S. Leckrone, and C. R. Proffitt, Astrophys. J. **496**, 1051 (1998).
[12] E. Biémont, J. Lidberg, S. Mannervik, L.-O. Norlin, P. Royen, A. Schmitt, W. Shi, and X. Tordoir, Eur. Phys. J. D **11**, 355 (2000).
[13] E. H. Pinnington, R. W. Berends, and M. Lumsden, J. Phys. B **28**, 2095 (1995).
[14] A. A. Madej, J. E. Bernard, P. Dubé, L. Marmet, and R. S. Windeler, Phys. Rev. A **70**, 012507 (2004).
[15] E. Biémont, J.-F. Dutrieux, I. Martin, and P. Quinet, J. Phys. B **31**, 3321 (1998).
[16] B. C. Fawcett and M. Wilson, At. Data Nucl. Data Tables **47**, 241 (1991).
[17] E. H. Pinnington, G. Rieger, and J. A. Kernahan, Phys. Rev. A **56**, 2421 (1997).
[18] Z. S. Li, S. Svanbeg, P. Quinet, X. Tordoir, and E. Biémont, J. Phys. B **32**, 1731 (1999).
[19] R. W. Berends, E. H. Pinnington, B. Guo, and Q. Ji, J. Phys. B **26**, L701 (1993).
[20] E. H. Pinnington, R. W. Berends, and Q. Ji, Phys. Rev. A **50**, 2758 (1994).
[21] Kaye and Laby, *Tables of Physical and Chemical Constants* (Longmann, Harlow, 1995), 16th ed.

Proceedings of the 20th EFTF, 2006

Shift estimation of the $^{43}Ca^{+}$ S-D transition frequency

Masatoshi Kajita*, Ying Li, Kensuke Matsubara,
Kazuhiro Hayasaka, and Mizuhiko Hosokawa
National Institute of Information and Communications Technology
**Electronic address:*kajita@nict.go.jp

We are in procedure to develop the optical frequency standard using the $^{43}Ca^{+}$ S-D transition, whose frequency uncertainty is mainly determined by the quadratic Zeeman shift and the electric quadrupole shift. This paper gives a proposal to eliminate these both frequency shifts without changing the magnetic field direction.

1. INTRODUCTION

Optical frequency standards based on narrow line width transitions in trapped ions have been studied for accuracy and stability higher than microwave standards. Some prototypes using $^{199}Hg^{+}$ [1,2], $^{171}Yb^{+}$ [3,4], $^{115}In^{+}$ [5], and $^{88}Sr^{+}$ [6] ions have been developed and their uncertainties have been estimated. Each species has its own advantages, and the total performance is determined not only by the inherent properties but also experimental advantages. NICT Atomic Frequency Standard Group is on procedure to develop an optical frequency standard based on the $^{43}Ca^{+}$ ($^{2}S_{1/2}$ $F = 4$ $m = 0$) - ($^{2}D_{5/2}$ $F = 6$ $m = 0$) transition. Lifetime of the $^{2}D_{5/2}$ state is 1.2 s, that gives a very high line-Q value [7]. It has the advantage of the development, that is, laser cooling (397 nm), repumping (866 nm) and probing (729 nm) can be performed by using only fundamental waves of compact laser diode. Although the natural abundance of this odd isotope is low (0.14 %), a recent report demonstrated generation of pure single $^{43}Ca^{+}$ ion from natural sample by using resonant photo-ionization with two violet diode lasers [8].

The uncertainties of $^{199}Hg^{+}$ and $^{171}Yb^{+}$ clock transitions are determined mainly by the electric quadrupole shift. In principle, the electric quadrupole shift can be nulled by averaging the measurements of the clock transition frequencies giving the magnetic field in three mutually orthogonal orientations [2,3]. It is actually difficult to keep the magnetic field strength constant and to give accurately orthogonal directions.

The quadratic Zeeman effect is also significant for the $^{43}Ca^{+}$ clock transition [9,10]. Therefore, also the magnetic field strength must be monitored with high accuracy than for $^{199}Hg^{+}$ and $^{171}Yb^{+}$ clock tranistions, where the quadratic Zeeman shift is much smaller.

This paper gives a proposal to eliminate these both shifts of the $^{43}Ca^{+}$ clock transition using also the ($^{2}S_{1/2}$ $F = 4$ $m = \pm 4$) - ($^{2}D_{5/2}$ $F = 6$ $m = \pm 6$) transition frequencies. We don't need to change the magnetic field direction and the experimental apparatus is simplified.

II. QADRATIC ZEEMAN SHIFT

The quadratic Zeeman shift coefficient of the $^{43}Ca^{+}$ ($^{2}S_{1/2}$ $F = 4$ $m = 0$) - ($^{2}D_{5/2}$ $F = 6$ $m = 0$) transition, α, is theoretically obtained as -89.9 kHz/G^2 [9,10] using the hyperfine constants A = -3.8 MHz and B = -3.9 MHz [11]. However, the accuracy of the hyperfine constants are still not high enough. It is necessary to get the accurate value of α experimentally.

α is obtained measuring the clock transition frequencies ν_0 with different values of the magnetic field B keeping any other values constant. Measuring ν_0 with two different magnetic field strengths ($B(1)$ and $B(2)$), α is obtained by

$$\alpha = \frac{\nu_0(1) - \nu_0(2)}{B(1)^2 - B(2)^2} \qquad (1)$$

Table 1 shows the quadratic Zeeman shift coefficients of the clock transitions of $^{199}Hg^{+}$, $^{171}Yb^{+}$, and $^{87}Sr^{+}$ ions.

$^{199}Hg^{+}$ $^{2}S_{1/2}$ $F = 0 \rightarrow {}^{2}D_{5/2}$ $F = 2$	-0.19 kHz/G^2
$^{171}Yb^{+}$ $^{2}S_{1/2}$ $F = 0 \rightarrow {}^{2}D_{3/2}$ $F = 2$	+0.52 kHz/G^2
$^{87}Sr^{+}$ $^{2}S_{1/2}$ $F = 5 \rightarrow {}^{2}D_{5/2}$ $F = 7$	+64 kHz/G^2

Table 1: Quadratic Zeeman shift coefficients of clock transitions of $^{199}Hg^{+}$, $^{171}Yb^{+}$, and $^{87}Sr^{+}$ ions

The magnetic field can be accurately monitored by measuring the ($^{2}S_{1/2}$ $F = 4$ $m = \pm 4$) - ($^{2}D_{5/2}$ $F = 6$ $m = \pm 6$) transition frequencies ($\nu_{\pm 6}$) which have purely linear Zeeman shifts with definite coefficients $\pm 2\mu_B$ (μ_B: Bohr magneton). Using $\nu_{\pm 6}$, the magnetic field strength is obtained by

$$B = \frac{\nu_{+6} - \nu_{-6}}{4\mu_B} \qquad (2)$$

Measuring ν_0 and $\nu_{\pm 6}$ within the accuracy of 10 Hz with B = 0 – 1 G, α is obtained with the accuracy of 10^{-4}. This measurement is feasible considering that the linear

Zeeman shift of the $^{88}Sr^+$ $^2S_{1/2} \rightarrow {}^2D_{5/2}$ transition frequencies are eliminated and the clock transiiton frequency is determined with the accuracy of 3×10^{-15} [6].

After the accurate value of α is obtained, the quadratic Zeeman shift $\Delta\nu_Z$ is evaluated by

$$\Delta\nu_Z = \alpha B^2 = \alpha\left(\frac{\nu_{+6}-\nu_{-6}}{4\mu_B}\right)^2 \qquad (3)$$

Assuming B = 10 mG, the quadratic Zeeman shift is in the order of 9 Hz. Measuring $\nu_{\pm 6}$ within the accuracy of 10 Hz, the uncertainty of the quadratic Zeeman shift is in the order of 4 mHz (1×10^{-17}) . The influence of the magnetic fluctuation should be reduced using the magnetic shield, as NPL group did for the measurement with $^{88}Sr^+$ ion [6].

III. ELECTRIC QUADRUPOLE SHIFT

The electric quadrupole shift is significant for the S-D transitions of trapped ions, because of large electric field gradient at the trap center. The electric quadrupole shift is caused only for the D state. The electric quadrupole shift at the D state $\Delta\nu_Q$ is given by

$$\Delta\nu_Q = \beta Q_d\left(3\cos^2\theta - 1\right)$$

$$\beta = \frac{2e}{7}\left\langle nd\left|r^2\right|nd\right\rangle(2F+1)\begin{pmatrix} F,2,F \\ -m,0,m\end{pmatrix}\begin{Bmatrix} J,2,J \\ F,I,F\end{Bmatrix}\begin{pmatrix} J,2,J \\ -J,0,J\end{pmatrix}^{-1}$$

$$\propto 3m^2 - F(F+1) \qquad (4)$$

where θ is the angle between the electric field-gradient direction and the quantization axis of the ion, Q_d is the electric field gradient. Through computer calculation of the atomic wavefunctions, value of $<3d|r^2|3d>$ of $^{43}Ca^+$ ion was found to be 1.9×10^{-16} [12] and β is calculated to be 0.82 Hz mm^2/V for the $^{43}Ca^+$ clock transition[9,10].

Because the average of $\left(3\cos^2\theta - 1\right)$ is zero, the electric quadrupole shift is eliminated by measuring the clock transition frequencies for three mutually orthogonal orientations of magnetic field. However, it is actually difficult to get the accurate three mutually orthogonal directions [2,13]. When there is an angle error of δ, the electric quadrupole shift is reduced with a factor of (2/3)sin δ. It is also important to change the magnetic field direction keeping the magnetic field constant. When there is a change of the magnetic field δB , the change of the quadratic Zeeman shift is $2\alpha B(\delta B)$. To keep the quadratic Zeeman shift constant within the accuracy of 0.1 Hz with B = 10 mG, δB must be smaller than 0.05 mG for the $^{43}Ca^+$ clock transition. Therefore, it seems difficult to eliminate the electric quadrupole shift from the $^{43}Ca^+$ clock transition frequency with this method.

Note also that $3m^2 - F(F+1)$ becomes zero averaging all values of *m*. NPL group used also the method to eliminate the electric quadruple shift of $^{88}Sr^+$ $^2S_{1/2}$ – $^2D_{5/2}$ transitions measuring three pairs of transition frequencies

$^2S_{1/2}$ $m = \pm1/2$ → $^2D_{5/2}$ $m = \pm1/2, \pm3/2, \pm5/2$.

This method gives lower uncertainty of the electric quadrupole shift than the method shown above [6]. However, also this method is difficult to apply for the $^{43}Ca^+$ clock transition, because the degeneracy of the $^2D_{5/2}$ F = 6 state is higher than that of $^{88}Sr^+$ ion.

We propose a method to eliminate the electric quadrupole shift using ν_0 and $\nu_{\pm6}$. Using Eq. (4), the ratio of the electric quadrupoe shifts of these transitions is obtained to be

$$[\Delta\nu_0]_Q : [\Delta\nu_{+6}]_Q : [\Delta\nu_{-6}]_Q = 7 : -11 : -11 \qquad (5).$$

The difference of the electric quadrupole shifts of these transitions are obtained by

$$[\Delta\nu_0]_Q - [\Delta\nu_{\pm6}]_Q = \nu_0 - \frac{\nu_{+6}+\nu_{-6}}{2} - \alpha B^2 \qquad (6).$$

Using Eqs. (4) and (5), the electric quadrupole shift of the $^{43}Ca^+$ clock transition is given by

$$[\Delta\nu_0]_Q = \frac{7}{18}\left[\nu_0 - \frac{\nu_{+6}+\nu_{-6}}{2} - \alpha B^2\right] \qquad (7)$$

With this method, the electric quadrupole shift is eliminated just measuring three transition frequencies (with NPL method, six transitions). It is not necessary to change the magnetic field direction and the experimental apparatus is much simpler than previous methods.

The electric quadrupole shifts of clock transitions of $^{199}Hg^+$, $^{171}Yb^+$, and $^{88}Sr^+$ ions are in the order of several Hz [1-3, 6]. The uncertainty of the electric quadrupole shift is less than 10 mHz for $^{88}Sr^+$ clock transition, whose β is 1.4 Hz mm^2/V [13]. For the $^{43}Ca^+$ clock transition, β is smaller (0.82 Hz mm^2/V) than that for $^{88}Sr^+$ clock transition. Note also that $^{43}Ca^+$ ion is trapped at a smaller value of Q_d than $^{88}Sr^+$ ion at a factor of mass ratio (43/88). Therefore, the uncertainty of the electric quadrupole shift of the $^{43}Ca^+$ clock transition can be less than 10 mHz (2.5×10^{-17}).

IV. OTHER EFFECTS

The electric field leads to a quadratic Stark shift on the transition frequency. The scalar polarizabilities of Ca^+ ion in the $^2S_{1/2}$ and $^2D_{5/2}$ states are roughly obtained to be 0.011 nm^3 and 0.0035 nm^3, respectively. The quadratic Stark shift coefficient of the clock transition is near 6 mHz/(V/cm)^2. Assuming that the electric field at the trapping position is less than 0.1 V/cm, the quadratic

Stark shift caused by the trapping electric field is less than 0.2 mHz.

The averaged quadratic electric field-strength of the black-body radiation is given by 69.2 $(V/cm)^2[T(K)/300]^4$, where T is the temperature of the chamber. The shift caused by the black body radiation is in the order of 0.4 Hz (10^{-15}), assuming T = 300 K. The uncertainty of the black body radiation shift is reduced down to 10^{-17} stabilizing the chamber temperature within 1 K.

The quadratic Zeeman shift cause by the black-body radiation is less than 1 μHz, because the frequency of the black body radiation (peak at 3×10^{13} Hz) is much higher than the hyperfine splitting of the $^2D_{5/2}$ and $^2S_{1/2}$ states.

The second-order Doppler shift is less than 0.74 mHz, assuming that the secular motion energy is lower than 1 mK (the Doppler limit is 550 μK). The laser condition to minimize the cooling period is shown in Ref. [10].

The light shift caused by the clock laser with power density 1 $\mu W/mm^2$ is estimated to be less than 10 mHz [9].

V.CONCLUSION

The frequency shift of the $^{43}Ca^+$ ($^2S_{1/2}$ $F = 4$ $m = 0$) - ($^2D_{5/2}$ $F = 6$ $m = 0$) transition is mainly caused by the quadratic Zeeman shift and the electric quadrupole shift. These both effects can be eliminated measuring also the ($^2S_{1/2}$ $F = 4$ $m = \pm 4$) - ($^2D_{5/2}$ $F = 6$ $m = \pm 6$) transition frequencies without changing the magnetic field direction. After the quadratic Zeeman shift coefficient is measured, the shift of the ($^2S_{1/2}$ $F = 4$ $m = 0$) - ($^2D_{5/2}$ $F = 6$ $m = 0$) transition frequency caused by these two effects are given by

$$\begin{aligned}\Delta\nu_0 &= [\Delta\nu_0]_Z + [\Delta\nu_0]_Q \\ &= \frac{11}{18}\alpha B^2 + \frac{7}{18}\left[\nu_0 - \frac{\nu_{+6}+\nu_{-6}}{2}\right] \\ &= \frac{11}{18}\alpha\left[\frac{\nu_{+6}-\nu_{-6}}{4\mu_B}\right]^2 + \frac{7}{18}\left[\nu_0 - \frac{\nu_{+6}+\nu_{-6}}{2}\right]\end{aligned}$$

The experimental apparatus is simpler than those shown in Ref.[1,3,6]. Eliminating these both effects, the uncertainty of the intrinsic shifts are reduced lower than 10^{-16}. The frequency uncertainty is determined by the technical uncertainties: light shift caused by the cooling laser (intrinsically this laser should be turned off at the measurement), servo errors, maser reference frequency etc. [6]. The possible frequency uncertainty is actually estimated to be 10^{-15}.

We have constructed an ion trap apparatus and observed the quantum jump signal with a single $^{40}Ca^+$ ion. Frequencies of cooling and repumping lasers are stabilized simultaneously using a transfer cavity system [14]. The linewidth of clock laser was reduced down to 53 Hz [15].

REFERENCES

[1] R. J. Rafac *et al*., Phys. Rev. Lett. 85, 2462 (2000).
[2] W. M. Itano, J. Res. Natl. Inst. Stand. Technol. **105**, 829 (2000).
[3] C. Tamm *et al*., Phys. Rev. A **61**, 053405 (2000).
[4] S. A. Webster *et al*., Phys. Rev. A **65**, 052501 (2002).
[5] Th. Becker *et al*., Phys. Rev. A **63**, 051802 (R) (2001).
[6] H. S. Margolis et al., Science **306**, 1355 (2004).
[7] M. Knoop *et al*. ,Euro. Phys. J. D **29**, 163 (2004).
[8] D. M. Lucas *et al*, , Phys. Rev. A **69**, 012711 (2004).
[9] C. Champenois *et al*., Phys. Lett. A **331/5**, 298 (2004).
[10] M. Kajita *et al*., Phys. Rev. A **72**, 043404 (2005).
[11] W. Noertershaeuser *et al*., Euro. Phys. J. D **2**, 33 (1998).
[12] W. M. Itano, private communication
[13] G. P. Barwood *et al*., Phys. Rev. Lett. **93**, 133001 (2004).
[14] K. Matsubara *et al*., Jpn. J. Appl. Phys. Part 1 **44**, 229 (2005).
[15] Y. Li et al., Jpn. J. Appl. Phys. submitted

Proceedings of the 20th EFTF, 2006

Ultracold Molecular Hydrogen Ions in a Linear Radiofrequency Trap: Novel systems for Molecular Frequency Metrology

B. Roth, H. Daerr, J. Koelemeij, A. Nevsky, and S. Schiller
*Institut für Experimentalphysik, Heinrich–Heine–Universität Düsseldorf, 40225 Düsseldorf, Germany**

We have measured the ro-vibrational infrared transition $(v = 0, J = 2) \rightarrow (v = 4, J = 1)$ in ultracold HD^+ molecular ions embedded inside Be^+ Coulomb crystals, by 1+1 REMPI spectroscopy. The molecular ions, trapped in a linear radiofrequency trap, were cooled to temperatures of few tens of mK, via sympathetic cooling using laser-cooled Be^+ ions. For detection, we have used secular excitation of the HD^+ ions to monitor their loss rate. The transition frequency agrees with a theoretical prediction.

Diatomic molecular hydrogen ions are of fundamental importance in nature. They are three-particle systems, with only a single electron, and as such among the simplest molecules. This makes them accessible to ab-initio high-precision theoretical calculations, including higher order corrections, such as non-adiabatic, relativistic, and QED corrections [1, 2, 3, 4, 5, 6, 7, 8]. Precise measurements on these systems can therefore test quantum chemical calculations at their current state of accuracy or better and stimulate the development of more advanced theoretical models [9, 10]. Furthermore, these simple molecular systems have the potential to be used for measurements of electron to nuclear mass ratios and their time variation or for a test of the universality of the coupling of gravitation to matter [3, 11, 12].

In particular, comparison of frequencies of two vibrational transitions of HD^+ would allow setting limits on the time dependence of both the electron-to-proton (m_e/m_p) and the proton-to-deuteron mass ratio m_p/m_d. A comparison between transition frequencies in HD^+ and H_2^+ could be used to determine the individual contributions [3]. Apart from such measurements, high-precision spectroscopy on ultracold HD^+ ions could allow determining molecular physics effects such as (i) the dependence of the hyperfine coupling constants on the rotational quantum number [6, 13, 14], (ii) identification of the nuclear spin rotation interaction effect [15], (iii) measurement of the electric quadrupole interaction contribution [16], and (iv) identification of the effects of the anapole magnetic moment of the molecule [17, 18].

The molecular hydrogen cation has been subject of several experimental studies in the past. The main work has been on the hyperfine structure in several low-lying vibrational states, by Dehmelt and others [19, 20, 21], and on vibrational transitions between states close to the dissociation limit, by Carrington and coworkers [22]. To our knowledge, there has been only a single study of laser-induced transitions of low-lying vibrational levels, performed by Wing and coworkers thirty years ago [23]. These studies were performed on uncooled samples or ion beams.

The extension of such measurements to the ultracold temperature regime could increase the spectroscopic accuracy, possibly by several orders of magnitude, due to the reduction of first-order Doppler broadening and of systematic effects. Molecular hydrogen ion ensembles at $< 20\,\mathrm{mK}$ were recently produced by sympathetic cooling using laser-cooled atomic ions stored in a linear radiofrequency trap [24]. In this unique environment, the molecular ions are well-localized inside ordered structures, Coulomb crystals, where they can be stored on the time scale of several minutes, favorable for long interrogation times in spectroscopic measurements. Within the crystals, the particles are in an isolated, nearly collisionless regime (typical interparticle distances are in the range of several tens of micrometers), hence collisional or pressure broadening of the transition lines is insignificant.

We have demonstrated a novel technique for high-resolution laser spectroscopy on ultracold molecular hydrogen ions, HD^+, in traps. Using the method developed, we have performed a first measurement of the ro-vibrational transition $(v = 0, J = 2) \rightarrow (v = 4, J = 1)$ at 6991.1 cm^{-1} $(1.430\,\mu\mathrm{m})$. Here, v and J are the vibrational and rotational quantum numbers in the HD^+ electronic ground state. The method developed can be applied to a vast number of other molecular ion species.

We simultaneously store both Be^+ ions and molecular ions in a linear radiofrequency trap, enclosed in a UHV chamber kept below 10^{-10} mbar, driven at 14 MHz, with a peak-to-peak amplitude of 380 V. This leads to a radial Mathieu stability parameter $q_r \simeq 0.04$, [25], and a (single-particle) radial secular oscillation frequency of 280 kHz for the Be^+. For the deuterium hydride ions, HD^+, $q_r \simeq 0.12$ and the (single-particle) radial oscillation frequency is 840 kHz.

The Be^+ ions are laser-cooled to millikelvin temperatures using a 313 nm UV laser [26]. For strong cooling, the ions are nearly localized in ordered structures, denoted as Coulomb crystals [27]. Due to the long-range electrostatic interaction between atomic coolants and molecular ions, the latter are efficiently cooled to translational temperatures $< 20\,\mathrm{mK}$ and embedded around the axis of the Be^+ ion crystals, due to their smaller mass-to-charge ratio. Due to the weak coupling between external and internal degrees of freedom, the in-

ternal temperature of the HD^+ ions is expected to be at 300 K [28], in thermal equilibrium with the vacuum chamber. We use molecular dynamics (MD) simulations to deduce ion numbers, three-dimensional spatial distributions, and upper limits for the translational temperature of each species contained in the crystal. The simulations include full Coulomb interaction, light pressure forces, anisotropies of the effective trap potential, and species-dependent heating rates. We identify the trapped species by excitation of their mass-dependent motional (secular) frequencies. For individual ions in a radiofrequency trap, the motional frequencies are inversely proportional to their mass. A detailed description of our procedure can be found in [24, 29, 30, 31].

We perform 1+1 REMPI spectroscopy, using a tunable infrared (IR) diode laser with a maximum output power of 4 mW to excite the ro-vibrational overtone transition $(v = 0, J = 2) \rightarrow (v = 4, J = 1)$ at around 1430 nm. The diode laser has a jitter limited linewidth < 5 MHz. Its wavelength was calibrated using a water absorption cell. Subsequently, the excited HD^+ ions in the $v = 4$ vibrational level are state-selectively dissociated, [32], using a continuous wave 266 nm UV laser source: $HD^+(v = 4) + h\nu \rightarrow H + D^+$ or $H^+ + D$.

For detection, we observe the loss rate of ultracold HD^+ ions from the trap, while scanning the frequency of the IR excitation laser in a range of several 100 MHz around the (calculated) ro-vibrational transition frequency [1]. The above loss rate is determined by repeated excitation of the HD^+ secular motion in the trap, after turning on the excitation and dissociation lasers, and observation of the change induced in the Be^+ fluorescence, due to heating of the atomic coolants by the molecular ions.

The HD^+ decay rate was measured as a function of the frequency of the IR laser, by scanning the latter in discrete 15 MHz steps. Prior to each measurement, the frequency of the IR laser was calibrated, via absorption spectroscopy in a water vapor cell. The accuracy of the calibration is ± 30 MHz. We have fitted a Gaussian to the line, in order to determine the line center. We find good agreement of the value for the line center obtained with the calculated transition frequency 6991.1092 cm^{-1} from Ref. [1]. The width of the line was 0.0032 cm^{-1}, corresponding to 96 MHz.

Several effects contribute to the observed line widths, e.g., hyperfine splitting of the ro-vibrational transitions [14], residual Doppler broadening, saturation broadening, and Zeeman splitting by the 10 G bias magnetic field used for Be^+ cooling.

In summary, we have measured a ro-vibrational overtone transition, on ultracold trapped HD^+ molecular ions, cooled to approximately 20 mK via laser-cooled Be^+ ions. After excitation to the $v = 4$ vibrational level, using a tunable diode laser at 1.4 μm, the molecules were state-selectively disscociated via a 266 nm UV laser. We used secular excitation mass-spectroscopy to monitor the HD^+ loss rate from the trap, as a function of the frequency of the IR laser, calibrated using water absorption spectroscopy.

The method demonstrated represents a promising route towards the application of ultracold, trapped molecules for high-precision measurements of ro-vibrational transitions, possibly leading to an improvement of the spectroscopic accuracy by several orders of magnitude.

For Doppler-free spectroscopy and mimization of systematic effects, it appears feasible to use a single ultracold HD^+ molecular ion in the Lamb-Dicke regime, coupled to a single Be^+ atomic ion, which is used for both cooling the translational energy of the HD^+ and state-selective detection of the molecular state [33].

Acknowledgements We thank the Deutsche Forschungsgemeinschaft (DFG) and the EC network HPRN-CT-2002-00290 for support. We thank H. Wenz, T. Fritsch, and M. Okhapkin for helpful assistance and discussions.

* Electronic address: Bernhard.Roth@uni-duesseldorf.de

[1] G.G. Balint-Kurti et al., Phys. Rev. **A 41**, 4913 (1990).
[2] R.E. Moss Mol. Phys. **78**, 371 (1993).
[3] S. Schiller and V. Korobov, Phys. Rev. **A 71**, 032505 (2005).
[4] J. F. Babb et al. Current Topics in Physics, vol. 2, 531, World Scientific, Singapore (1998).
[5] V. I. Korobov, Phys. Rev. **A 70**, 012505 (2004).
[6] R. D. Ray and P. R. Certain, Phys. Rev. Lett. **38**, 824 (1977).
[7] C. A. Leach and R. E. Moss, Annual Review of Physical Chemistry **46**, 55 (1995).
[8] Z.-C. Yan, J.-Y. Zhang, and Y. Li, Phys. Rev. **A 67**, 062504 (2003).
[9] Z. Amitay et al., Science **281**, 75 (1998).
[10] A. D. J. Critchley, A. N. Hughes, and I. R. McNab, Phys. Rev. Lett. **86**, 1725 (2001).
[11] L. Hilico et al., Eur. Phys. J. D **12**, 449 (2000).
[12] U. Fröhlich. et al., Lect. Notes. Phys. **648**, 297 (2004).
[13] A. Carrington et al., Mol. Phys. **72**, 735 (1991).
[14] D. Bakalov, V. Korobov, priv. comm. (2005).
[15] J.F. Babb, Phys. Rev. Lett. **75**, 4377 (1995).
[16] J.F. Babb, arXiv:physics/9701007.
[17] I.B. Khriplovich and M.E. Pospelov, Z. Phys. D **17**, 81 (1990); R.R. Lewis, Phys. Rev. **A 49**, 3376 (1994).
[18] R. Alheit, Ph.D. dissertation, Univ. Mainz (1997).
[19] C. B. Richardson, K. B. Jefferts, and H. G. Dehmelt, Phys. Rev. **165**, 80 (1968).
[20] K. B. Jefferts, Phys. Rev. Lett. **23**, 1476 (1969).
[21] Z. W. Fu, E. A. Hessels, and S. R. Lundeen, Phys. Rev. **A 46**, 5313 (1992).
[22] A. Carrington, I. McNab, and C. Montgomerie, J. Phys. B: At. Mol. Opt. Phys. **22**, 3551 (1989).
[23] W. H. Wing et al., Phys. Rev. Lett. **36**, 1488 (1976).
[24] P. Blythe, B. Roth, U. Fröhlich, H. Wenz, and S. Schiller, Phys. Rev. Lett. **95**, 183002 (2005).
[25] D. J. Berkeland et al., J. Appl. Phys. **83**, 5025 (1998).

[26] H. Schnitzler et al., Applied Optics **41**, 7000 (2002).
[27] R. Blümel et al., Nature **334**, 309 (1988).
[28] A. Bertelsen, S. Jorgensen, and M. Drewsen, J. Phys. B: At. Mol. Opt. Phys. **39** 83 (2006).
[29] B. Roth, U. Fröhlich, and S. Schiller, Phys. Rev. Lett. **94**, 053001 (2005).
[30] B. Roth, P. Blythe, and S. Schiller, "Motional Resonance Coupling in Cold Multi-Species Coulomb Crystals", in prep. (2006).
[31] U. Fröhlich, B. Roth, and S. Schiller, Phys. Plasmas **12**, 073506 (2005).
[32] M. Tadjeddine and G. Parlant, Mol. Phys. **33**, 1797 (1977).
[33] P.O. Schmidt et al., Science 309, 749 (2005).

Proceedings of the 20th EFTF, 2006

Optical Lattice Clock with Ultracold Strontium Atoms

M. M. Boyd,* A. D. Ludlow, T. Zelevinsky, S. M. Foreman, S. Blatt, T. Ido, J. Ye
JILA, National Institute of Standards and Technology and the University of Colorado, and Department of Physics, University of Colorado, Boulder, CO 80309-0440, USA
**Electronic address:* boydmm@colorado.edu

We report recent progress on an optical atomic clock based on the ultranarrow $^1S_0$-$^3P_0$ transition in fermionic neutral strontium atoms confined in an optical lattice. A detailed systematic study of the clock transition frequency is presented along with the recent improvement in the measured line quality factor which is expected to lead to an accuracy of 10^{-15} or better in the near future.

1. INTRODUCTION

Ultranarrow optical resonances in alkaline-earth atoms, and atoms with similar level structure such as Yb and Hg, show great promise as optical frequency standards and optical atomic clocks. Atomic strontium is an exciting candidate as the level structure provides multiple narrow clock transitions as well as means for efficient laser cooling to μK temperatures. A variety of measurement techniques are currently being considered for the strontium clock transitions including free space spectroscopy of the narrow (7.4 kHz) $^1S_0$-$^3P_1$ transition in cold bosonic ^{88}Sr [1], optical lattice based spectroscopy of the sub-Hz hyperfine induced $^1S_0$-$^3P_0$ transition in fermionic ^{87}Sr [2,3,4], and spectroscopy of the strictly forbidden $^1S_0$-$^3P_0$ transition in ^{88}Sr using electromagnetically-induced-transparency (EIT) [5,6], or a DC magnetic field [7] to provide the necessary state mixing to observe the transition. In the case of the $^1S_0$-$^3P_0$ transitions in ^{87}Sr and ^{88}Sr, accuracies (stabilities) may eventually reach below the 10^{-17} (10^{-18}) level. Detailed systematic evaluations of the clock transition frequency of ^{87}Sr atoms confined in state-insensitive [8,9,10] optical traps are under way.

II. LASER COOLING AND TRAPPING OF NEUTRAL STRONTIUM

Reaching ultracold temperatures with large atom numbers (N) is essential for the development of optical atomic clocks. Lower temperatures permit reduced Doppler effects in free space and also allow atomic confinement in the Lamb-Dicke regime of a trapping potential, essentially eliminating Doppler effects on clock performance. Large atom numbers can improve stability of the clock by $\sqrt{N}$. The Sr level structure provides two useful cooling transitions which we exploit for preparing an ultracold ensemble. The strong 461 nm $^1S_0$-$^1P_1$ transition (~ 32 MHz) is used to create a Magneto-Optical Trap (MOT) which is loaded from a Zeeman slowed beam of strontium atoms. The mK $^1S_0$-$^1P_1$ MOT serves as an excellent pre-cooling stage for loading a second-stage MOT based on the narrow 689nm $^1S_0$-$^3P_1$ transition (~7.4 kHz). A complete description of our laser cooling apparatus and detailed studies of narrow-line cooling dynamics have been described elsewhere [11-15].

III. $^1S_0$-$^3P_0$ SPECTROSCOPY IN AN OPTICAL LATTICE

To fully exploit the sub-Hz linewidth of the clock transition, it is necessary to probe the atoms for long periods of time while keeping the atoms in a perturbation free environment. An atomic fountain geometry is conceivable for alkaline-earth atoms, however, the nature of optical transition makes the residual Doppler effect troublesome when aiming for accuracy at the 10^{-17} level and below, as has been seen in the case of free space measurements with Ca [16] and Sr [1]. An attractive alternative for increasing the interaction time utilizes an optical lattice operating at a 'magic' wavelength where the AC stark shifts of the $^1S_0$ and $^3P_0$ clock levels are equal [2], allowing accurate measurement of the clock transition. One major advantage of this scheme is that the atoms can be trapped in the Lamb-Dicke regime, in which spectroscopy can be done nearly free of any recoil or Doppler shifts, similar to the case of trapped ions [17]. Furthermore, a three dimensional lattice can be

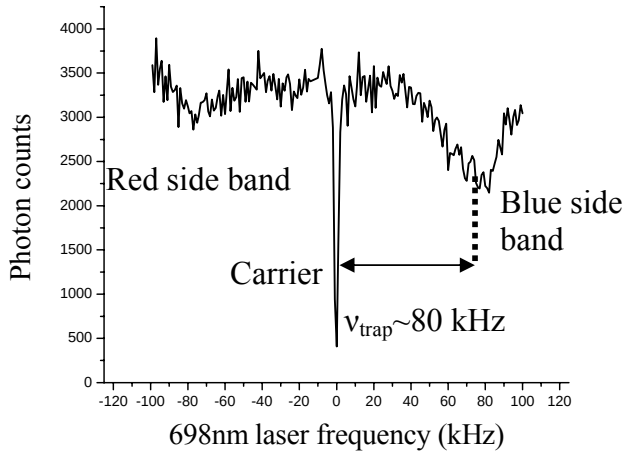

Figure 1. Direct observation of motional sidebands in the 1D optical lattice. The red (blue) sideband represents an absorption and spontaneous emission event in which $\Delta n = -1$ ($\Delta n = +1$) where n represents the nth harmonic oscillator level in the lattice potential. The center peak, or carrier, corresponds to the clock transition shown and is due to transitions with $\Delta n = 0$. In this case, the carrier transition is strongly saturated to allow observation of the sidebands. In this case the background counts are near 500.

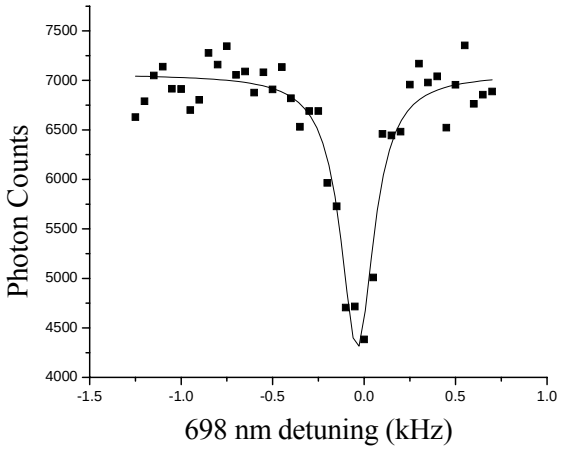

Figure 2. Spectroscopy of the narrow carrier transition. The black line is a lorentzian fit of the data points with a FHWM of 220(30) Hz.

employed to eliminate collisions between atoms, and hence eliminate collisional shifts. A frequency standard based on neutral atoms in an optical lattice combines some of the best features of single trapped ions and free space neutral atoms by allowing measurement of the clock transition in the Lamb-Dicke regime, while enhancing the signal to noise ratio by using many quantum absorbers. To implement the lattice clock with ^{87}Sr, we have constructed a one-dimensional optical lattice using ~500 mW from a Ti:Sapphire laser tuned near the magic wavelength of ~813.4 nm. During the narrow-line cooling stage, the one-dimensional optical lattice (oriented nearly parallel to gravity) is overlapped with the MOT, resulting in more than 10^4 ^{87}Sr atoms at ~4 μK temperatures available for spectroscopy. The axial trap frequency of the optical lattice is ~80 kHz, in comparison to the recoil frequency of ~ 5 kHz, corresponding to a Lamb-Dicke parameter of ~0.23 and thus the tight atomic confinement limit. In the axial direction, the trap frequency is significantly larger than both the transition linewidth and the atomic recoil frequency, hence the quantized motional states of the nearly harmonic potential can be easily resolved from the carrier transition, as shown in Fig. 1. Spectroscopy of the motional sidebands is a powerful tool for studying trap dynamics as it allows measurement of the atom temperature, trap frequencies, and the band structure of the trap due to the anharmonicity of the potential.

A typical measurement of the carrier, shown in Fig. 2, yields a linewidth of ~220 Hz, or a line Q of ~2×10^{12}. During spectroscopy the absolute frequency of the clock laser is measured using an octave spanning fs-comb [18, 19] referenced, via an optical fiber link [20], to a hydrogen maser calibrated by the NIST primary cesium standard. For the measurements reported in this work, the maser provided a reference in our lab with an instability of 3.7×10^{-13} at one second. The combination of the narrow Sr spectral width and the high stability reference frequency provided by the hydrogen maser, allowed rapid averaging for measurements of potential systematic errors for the lattice clock.

IV. SYSTEMATIC EVALUATION (2005)

To determine the $^1S_0$-$^3P_0$ transition frequency with high precision and accuracy, we performed a detailed investigation of systematic shifts. The sensitivity of the clock transition to the lattice wavelength and intensity near the magic wavelength was a primary concern for a high accuracy measurement. At our typical lattice

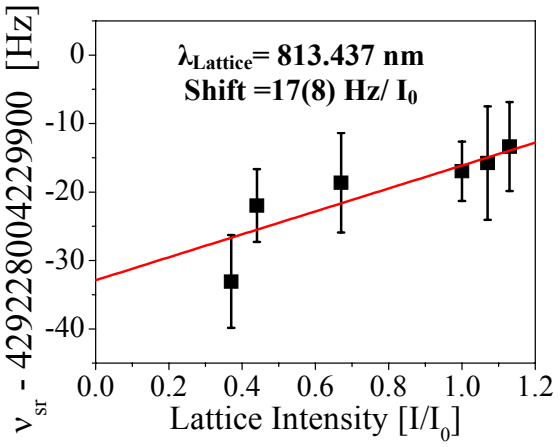

Figure 3. Measured transition frequency versus lattice intensity for an operating wavelength of 813.437 nm. I_0=10 kW/cm^2 is our typical operating intensity

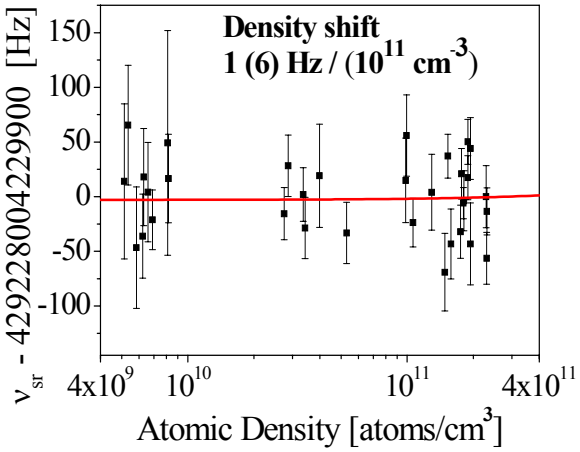

Figure 4. Measured transition frequency versus average atomic density in each lattice site.

operating wavelength of 813.437(2) nm, we measured the clock transition as a function of lattice intensity, as shown in Fig. 3, and found that at our operating intensity of I_0= 10 kW/cm^2, a correction of -17(8) Hz was necessary. We have also experimentally determined that, at a lattice intensity of I_0, the sensitivity of the clock transition to the lattice wavelength deviation from the magic wavelength is ~2 mHz/MHz. Therefore the lattice frequency only needs to be stabilized to the magic wavelength within 500 kHz to achieve clock accuracy below the 10^{-18} level. Using the measured Stark shift at 813.437 nm, and the measured sensitivity to lattice wavelength deviations, we find that the magic wavelength is 813.418(10) which is in good agreement with values reported in [2, 4].

The same nuclear-spin induced state mixing that enables the weak $^1S_0$-$^3P_0$ transition for spectroscopy also provides a differential g-factor [21] of ~100 x m_f Hz/G between the two clock states. Careful consideration must be taken concerning stray magnetic fields as they can result in broadening or shifting the measured frequency depending on the population distribution between the 10 magnetic sublevels in ^{87}Sr. For this reason we also measured the clock transition frequency as a function of magnetic field using three orthogonal sets of Helmholtz coils and were able to determine that any shifts were smaller than 12 Hz.

We also considered atomic collisions in the 1D lattice as a potential systematic error. We investigated the possibility of collision shifts by varying the number of atoms in the lattice by a factor of 50, as shown in Figure 4. We did not find any statistically significant shifts for our typical density of ~2x10^{11} cm^{-3}, within an uncertainty of 12 Hz. While a number of other effects were also considered and measured, the uncertainty associated with the lattice Stark shift, residual magnetic field, and density shift dominated over all others, giving a total systematic uncertainty of 19 Hz, corresponding to a fractional uncertainty of 4.5x10^{-14}. The excellent stability and reproducibility of our apparatus is evident from the statistical uncertainty of 2.8 Hz, corresponding to 6.5x10^{-15}, over the entire span (~ 3 months) of our measurement period. Our measurement record is shown in Fig. 5 yielding a value for the ^{87}Sr $^1S_0$-$^3P_0$ transition of 429,228,004,229,869 +/-19_{sys} +/-2.8_{stat} Hz [3]. Note that the number reported here disagrees at the three standard deviation level with that of [2] which was measured using a GPS uplink for the absolute frequency reference.

While the attainable accuracy and precision provided by the optical lattice technique are already impressive, the systematic uncertainties reported above are by no means a limit to the system. The 19 Hz uncertainty can be drastically reduced with a few straightforward improvements, which are currently being implemented in our lab. Operating the lattice precisely at the magic wavelength should eventually reduce that systematic shift and uncertainty well below the 10^{-17} level [4]. At this point the uncertainty associated with the atomic density is completely limited by averaging time and can be easily reduced with a reduction in atomic linewidth or the instability of our frequency reference. A higher

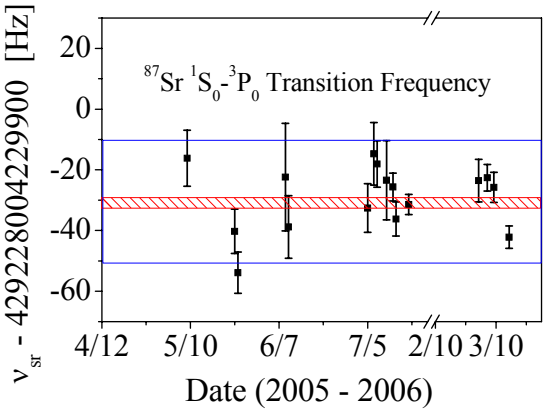

Figure 5. $^1S_0$-$^3P_0$ frequency measurement spanning a ten month period. The 2005 data (before the break) represents the span of measurements reported in [3]. The overall statistical uncertainty is show as the shaded bar. The systematic uncertainty is shown as the solid lines. The final four points are recent measurements with an improved line signal. The axis break represents a seven month separation between measurements.

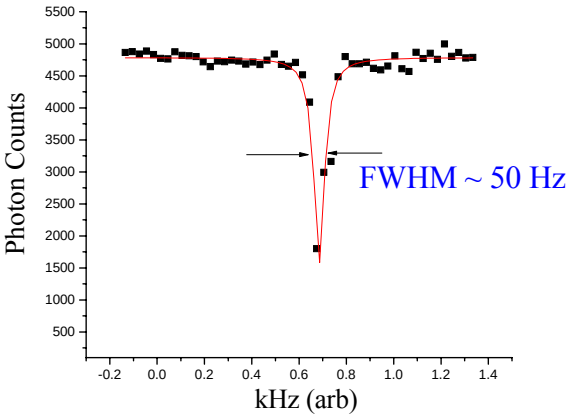

Figure 6. Improved transition measurement. The 50 Hz FWHM corresponds to a line Q of 2.9×10^{12}. The trace is taken without averaging or normalization. This signal contrast is ~70%. An estimate based on the S/N suggests a clock instability of a few parts in 10^{-15} should be possible at 1second.

atomic line quality factor would also improve the uncertainty in the residual magnetic field as the g-factor can set an upper limit on the linewidth for a given field.

V. RECENT IMPROVEMENTS

Recently we have made a number of improvements to our spectroscopic signal with the goal of reducing the major sources of error discussed above. Figure 6 shows a recent spectroscopic trace of the clock transition yielding a typically achieved linewidth and quality factor of 50 Hz and 2.9×10^{12} respectively. Atomic lines as narrow as 15 Hz (Q~3×10^{13}) have been observed and line quality factors above 10^{14} should be achievable with improvements to the probe laser.

The improved quality factor and signal to noise ratio shown in Fig. 6, along with a recent reduction in our microwave reference instability to ~2×10^{-13} at one second, should allow at least an order of magnitude increase in accuracy with our current setup.

As the first example on improvements in systematics, we have re-investigated the magnetic field dependence of the clock transition. We again applied magnetic fields along three orthogonal directions during spectroscopy and measured both the frequency and linewidth of the transition as a function of the field. Figure 7 shows how the frequency varied with the magnetic field along the polarization axis of the lattice and probe. A slope of -47(32) Hz/G was measured along the polarization axis while the other two axes yielded 10(19) and 14 (20) Hz/G respectively. The nonzero slope in Fig. 7 suggests that the population distribution in the hyperfine sublevels is slightly unbalanced, emphasizing the importance of characterizing this systematic shift. The linewidth data revealed the magnetic field zero (minimum linewidth field) with an uncertainty of less than 15 mG for each axis, yielding a total systematic uncertainty for the field related frequency shift of 0.5 Hz (1×10^{-15}). This is a reduction by a factor of 20 from our previous data in 2005. Reducing the other major contributors to the accuracy uncertainty below 10^{-15} should also be possible, but the evaluation will be eventually limited by the long averaging time required when using the Cs calibrated-maser as a reference. With this in mind we have recently locked the probe laser to the narrow Sr transition with the eventual goal of comparing the Sr clock to nearby optical clocks at NIST such as Hg^+, Al^+, Ca and Yb. It should be noted that the final four points in Fig. 5 were taken with our improved signal and agree well with the previous data, showing the long-term reproducibility of the system.

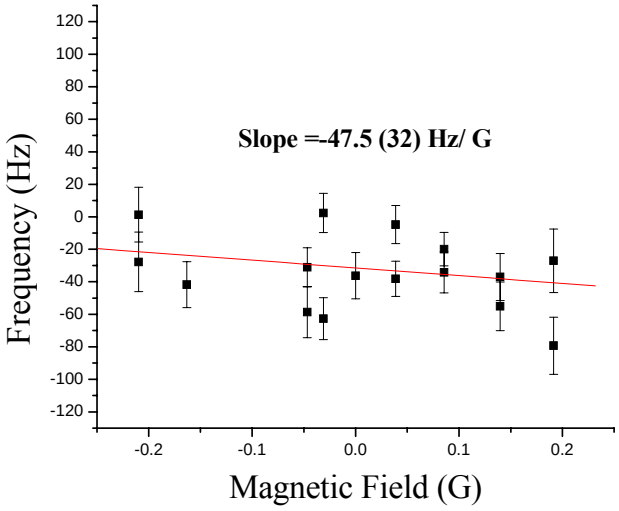

Figure 7. Transition frequency plotted against magnetic field. The non-zero slope is most likely due to a population imbalance in the magnetic sublevels.

VI. CONCLUSION

We have performed a high precision measurement of the ^{87}Sr $^1S_0$-$^3P_0$ clock transition in an optical lattice and report a frequency of 429,228,004,229,869 +/-19$_{sys}$ +/-2.8$_{stat}$ Hz. We found the magic wavelength of the lattice to be 813.418(10) nm and the sensitivity of the transition to lattice frequency fluctuations to be ~2mHz/MHz for a 10kW/cm^2 trapping potential. Transition linewidths of 50 Hz are routinely obtained and lines as narrow as 15 Hz have been observed. One of the main systematic errors from previous measurements which results from the stray magnetic field has now been reduced to 1 x 10^{-15}. We expect to improve the overall systematic uncertainty of the clock transition frequency to below 10^{-15} in the near future.

Acknowledgements

The authors wish to thank S. Diddams, T. Parker, L. Hollberg, and J. Bergquist for facilitating the maser transfer and M. Notcutt and J. Hall for help with the interrogation laser. We acknowledge funding from ONR, NSF, NASA, and NIST

REFERENCES

[1] T. Ido *et al.*, Phys. Rev. Lett. **94**, 153001 (2005).
[2] M. Takamoto *et al.*, Nature **435**, 321 (2005).
[3] A. Ludlow *et al.*, Phys. Rev. Lett. **96**, 033003 (2006).
[4] A. Brusch *et al.*, Phys. Rev. Lett. **96**, 103003 (2006)
[5] R. Santra *et al.*, Phys. Rev. Lett. **94**, 173002 (2005)
[6] T. Hong *et al.*, Phys. Rev. Lett. **94**, 050801 (2005)
[7] Z. Barber *et al.*, Phys. Rev. Lett. **96** *083002* (2006)
[8] J. Ye *et al.*, Phys. Rev. Lett. **83** *4987* (1999)
[9] T. Ido *et al.*, Phys. Rev. A **61**, 061403 (2000)
[10] H. Katori *et al.*, Phys. Rev. Lett. **91**, 173005 (2003)
[11] T. Loftus *et al.*, Phys Rev. *A* **70**, 063414 (2004)
[12] T. Loftus *et al.*, Phys Rev. Lett. **93**, 073003 (2004)
[13] H. Katori *et al.*, Phys. Rev. Lett. **82**, 1116 (1999)
[14] X. Xu *et al.*, Phys. Rev. Lett. **90**, 193002 (2003)
[15] T. Mukaiyama *et al.*, Phys. Rev. Lett. **90**, 113002 (2003)
[16] U. Sterr et al., C.R. Physique **5**, 845 (2004)
[17] R. J. Rafac et al., Phys. Rev. Lett. **85**, 2462 (2000)
[18] T. M. Fortier et al., Optics Letters **28**, 22 (2003)
[19] D. J. Jones et al., Science **288**, 635 (2000)
[20] J. Ye et al., J. Opt. Soc. Am. B.-Opt. Phys. **20**, 1459 (2003)
[21] E. Peik et al., Phys. Rev. A **49**, 402 (1994)

Proceedings of the 20th EFTF, 2006

Higher order effects in a Sr optical lattice clock

Anders Brusch, Rodolphe Le Targat, Xavier Baillard, Mathilde Fouché, and Pierre Lemonde*
LNE-SYRTE, Observatoire de Paris
61, Avenue de l'Observatoire, 75014, Paris, France

We report the observation of the higher order frequency shift due to the trapping field in a ^{87}Sr optical lattice clock. We show that at the magic wavelength of the lattice, where the first order term cancels, the higher order shift will not constitute a limitation to the fractional accuracy of the clock at a level of 10^{-18}. This result is achieved by operating the clock at very high trapping intensity up to 400 kW/cm^2 and by a specific study of the effect of the two two-photon transitions near the magic wavelength.

I. INTRODUCTION

Cold atoms confined in optical lattices have become tools of growing importance to several fields in physics such as quantum computing [1], matter wave manipulation [2], cavity QED [3, 4] or precision measurements [5–9]. Examples of their interesting features are long quantum coherence times, controllable collisions, controllable position of the atoms and Lamb-Dicke confinement. All the related experiments share the same need for a constantly improved control of the atom-lattice interaction. For instance, trapping a single atom in a high-Q cavity in the strong coupling regime has been achieved by adjusting the trap parameters to make it "state insensitive" [3]. In another experiment, the lifetime of the quantum coherences of atomic qubits is limited by the fluctuations of the differential light shift due to the lattice [10]. The energy shift of the atomic levels induced by the relatively strong lattice field is a topical problem and is the subject of this letter.

The challenge is easily understood in the case of atomic clocks which are more specifically studied here. In this domain, the recent proposal [11] and preliminary realizations [7–9] of optical lattice clocks open a promising route towards frequency standards with a fractional accuracy better than 10^{-17}. A large number of atoms are confined in the Lamb-Dicke regime which in principle allows both the high signal to noise ratio of optical clocks with neutral atoms [12] and the cancellation of motional effects of trapped ion devices [13–16]. For an optical lattice clock with Sr atoms, the typical requirement in terms of trapping depth is about $10\,E_r$ with E_r the recoil energy associated to the absorption of a lattice photon [17]. The corresponding frequency shift of both clock states amounts to 36 kHz at 800 nm, while a relative accuracy goal of 10^{-18} implies a control of the differential shift at the 0.5 mHz level, or 10^{-8} in fractional units.

The frequency of the clock transition in a lattice of depth U_0 is shifted with respect to the unperturbed frequency ν_0 according to

$$\nu = \nu_0 + \nu_1 \frac{U_0}{E_r} + \nu_2 \frac{U_0^2}{E_r^2} + O\left(\frac{U_0^3}{E_r^3}\right), \qquad (1)$$

with ν_1 and ν_2 proportional to the (dynamic) polarizability and hyperpolarizability difference between both states of the clock transition [11]. By principle of the optical lattice clock, ν_1 cancels when the trapping laser is tuned to the "magic wavelength" λ_m. Although this remains to be demonstrated experimentally, a control of this first order frequency shift to better than 1 mHz seems achievable [11].

The higher order term is a priori more problematic with no expected cancellation. A theoretical calculation of the effect is reported in Ref. [11] predicting a frequency shift of $-2\,\mu\text{Hz}/E_r^2$ for a linear polarization of the lattice. The calculation however was performed at the theoretical magic wavelength of 800 nm. The actual value [24], $\lambda_m = 813.428(1)$ nm (see [7, 9] and below), lies near two two-photon resonances which may considerably enhance the effect and impede the realization of an accurate clock. The first one couples $5s5p\,^3P_0$ to $5s7p\,^1P_1$ (Fig. 1) and is at a wavelength of 813.36 nm, or equivalently 30 GHz away from the magic wavelength. Although this $J = 0 \rightarrow J = 1$ two-photon transition is forbidden to leading order for two photons of identical frequencies [18], it is so close to the magic wavelength that it has to be a priori considered. The second one resonantly couples $5s5p\,^3P_0$ to $5s4f\,^3F_2$ at 818.57 nm and is fully allowed.

II. EXPERIMENTAL SETUP

We report here an experimental study of higher order effects in a ^{87}Sr optical lattice clock operating at a very high trapping depth up to $1400\,E_r$ and for a linear polarization of the lattice. This depth is about a factor of ten higher than in the other reported systems [7, 9] which enhances the sensitivity to higher-order frequency shifts by two orders of magnitude. The high trapping depth is reached thanks to an enhancement Fabry-Pérot cavity around the 1D vertical lattice. The circulating power reaches 16 W for a 650 mW input at 813 nm. The mode has a waist radius of 90 μm corresponding to a maximum $U_0 = 1400\,E_r$

*Electronic address: pierre.lemonde@obspm.fr

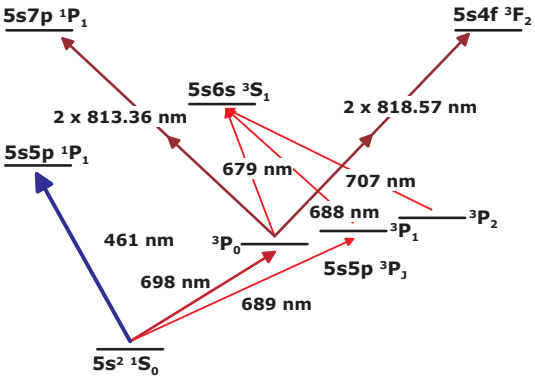

FIG. 1: Energy levels of Sr relevant to this paper. The clock transition at 698 nm couples the two lowest energy states of the atom.

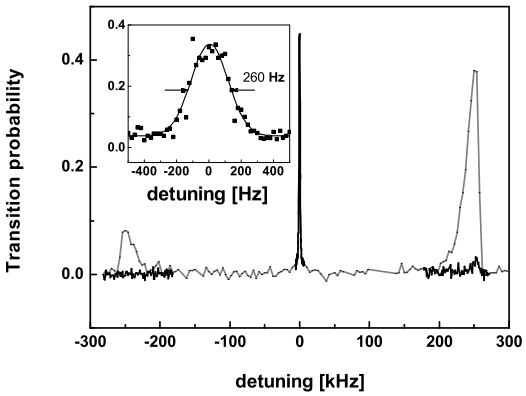

FIG. 2: Motional spectrum of the atoms in the optical lattice. Each point corresponds to a single measurement of 1 s total duration. Black curve: optimal operating conditions (probe pulse of 10 ms duration and 2 μW power). The inset is a zoom on the carrier. Grey curve: the first order longitudinal motional sidebands are enhanced by applying long probe pulses of 200 ms at the maximum available power at 698 nm (2 mW).

and an axial (resp. radial) oscillation frequency of 260 kHz (resp. 540 Hz). An intracavity dichroic mirror separates the lattice light from that which probes the clock transition. It induces negligible intracavity loss at 813 nm while ensuring that less than 10^{-3} of the incident power at 698 nm is reflected back to the atoms by the cavity mirror. The lattice polarization is interferometrically filtered by an intra-cavity quarter wave plate which lifts the degeneracy between the linear polarization states parallel to the eigen axis of the plate by half a free spectral range. The resulting polarization of the trapping light is linear to better than 10^{-3}. Its wavelength λ_L is controlled by means of a wave meter with an accuracy of 10^{-3} nm.

Atoms are loaded into the optical lattice from the magneto-optical trap (MOT) described in [19]. Throughout the loading cycle the lattice is overlapped with the MOT. Cold atoms at the center of the trap are selectively optically pumped to the metastable $^3P_{0,2}$ states by means of two "drain" lasers of waist radius 50 μm that are aligned to the lattice. They are tuned to the $^1S_0 - {}^3P_1$ and $^3P_1 - {}^3S_1$ transitions at 689 and 688 nm respectively (Fig. 1). Atoms in the metastable states remain trapped provided their energy is smaller than the 200 μK lattice depth. This leads to a continuous loading of the lattice at a rate of about 10^5 atoms/s. After half a second of loading time the MOT and drain lasers are switched off, and the atoms are repumped back to the ground state using two lasers tuned to the $^3P_{0,2} - {}^3S_1$ transitions at 679 and 707 nm. They are then cooled in the lattice to $\sim$ 10 μK in 50 ms with the narrow $^1S_0 - {}^3P_1$ intercombination line at 689 nm [20].

Following this preparation stage we probe the $^1S_0 - {}^3P_0$ clock transition at 698 nm. The frequency of the probe laser is referenced to an ultra-stable cavity as described in Ref. [21]. The probe beam is aligned parallel to the lattice and has a waist radius of 200 μm. Its polarization is linear and parallel to the lattice polarization. After the probe pulse, the transition probability to $^3P_0$ is measured in a few ms by laser induced fluorescence. A first detection pulse at 461 nm gives the number of atoms remaining in the ground state and ejects these atoms from the trap. Atoms in $^3P_0$ are then repumped to the ground state with the 679 nm and 707 nm lasers and detected similarly. This method allows a transition probability measurement which is insensitive to the atom number fluctuations. The resonance is shown in Fig. 2. The central feature (the carrier) is zoomed in the inset of the figure. Its linewidth is 260 Hz in optimal operating conditions: $\lambda_L = \lambda_m$, probe pulse of 10 ms duration and 2 μW power. The resonance plotted here was obtained at the maximum trapping depth and we observed no clear dependence of its width and contrast with U_0. The present limitation to the width of the resonance is probably of technical origin, since linewidths in the 10 Hz range have already been observed in optical lattice clocks [7, 8].

The carrier is surrounded by motional sidebands shifted by the oscillation frequency along the lattice direction. They are hardly visible in optimal operation but can be enhanced by applying long pulses of 200 ms duration at the maximum available power (2 mW) of the probe beam. The resulting spectrum is plotted in grey in Fig. 2. The 1:5 ratio between the red and blue sidebands show that 80% of the atoms populate the $|n_z = 0\rangle$ motional state along the lattice axis, corresponding to a temperature of 8 μK. The transverse temperature is 10 μK.

III. EXPERIMENTAL RESULTS

The effect of the trap on the clock transition is measured by locking the frequency of the probe laser to the carrier for various values of U_0 and λ_L. The trap depth U_0 is adjusted to its desired value between $200\,E_r$ and $1400\,E_r$ by a linear ramp of 1 ms duration between the cooling and probing phases. This slightly decreases the transverse temperature while the longitudinal motion is adiabatically cooled by following the ramp. To lock the probe laser frequency we alternatively probe both sides of the resonance and compute an error signal from the difference between two successive measurements of the transition probability. This also gives a measurement of the difference between the atomic transition and the reference cavity frequency which slowly fluctuates due to thermal effects. These fluctuations behave essentially as a sine wave of peak to peak amplitude 300 Hz and period 10 minutes. To derive the frequency shift due to the lattice, we reject the cavity frequency fluctuations by a factor 100 by a differential method [22]. We interleave measurements at 4 different lattice depths. We run the clock for 19 cycles before U_0 is changed to the next of the four interleaved values. The entire sequence is repeated typically 16 times. The cavity fluctuations are then modelled as a polynomial which is determined by a least square fit of the data [25]. The data are corrected for the modelled cavity frequency fluctuations and averaged. This yields 4 statistically independent measurements [26] of the clock transition frequency versus U_0 with a standard deviation of about 5 Hz. A typical set of such points is shown in Fig. 3(a).

We perform a quadratic least square fit of each set of four points which gives a measurement of the coefficients ν_1 and ν_2 of Eq.(1). The coefficient ν_2 is plotted in Fig. 3(c) and found compatible with zero for the whole range [813.3 nm, 813.5 nm] to within a few tens of μHz. A specially interesting wavelength region is around 813.36 nm where the $^3P_0 \rightarrow {}^1P_1$ two-photon transition is expected. The contribution of a two-photon transition to ν_2 varies as Δ^{-1}, with Δ the detuning of the lattice with respect to the resonance. We magnify this contribution by systematically spanning a frequency range of ± 5 GHz with a 1 GHz step around the expected value (Fig. 3(c)). The null results of all these measurements demonstrate that the higher order shift due to the $^3P_0 \rightarrow {}^1P_1$ transition is less than $1\,\mu\text{Hz}/E_r^2$ for $\lambda_L = \lambda_m$. Despite its proximity to the magic wavelength, this two-photon transition is forbidden enough to not be a problem.

This set of experiments around 813.4 nm can also be used to derive an accurate value of λ_m. Having shown that ν_2 is negligible for $\lambda_L \sim \lambda_m$, better estimates of ν_1 are obtained with linear fits of each set of four points. They are plotted in Fig. 3(b). We find $\lambda_m = 813.428(1)$ nm in agreement with previously published values [7, 9] as shown in the inset of Fig. 3(b). The improvement by one order of the accuracy of this measurement is a nice illustration of the amplification of the effects of the lattice offered by a deep trapping potential.

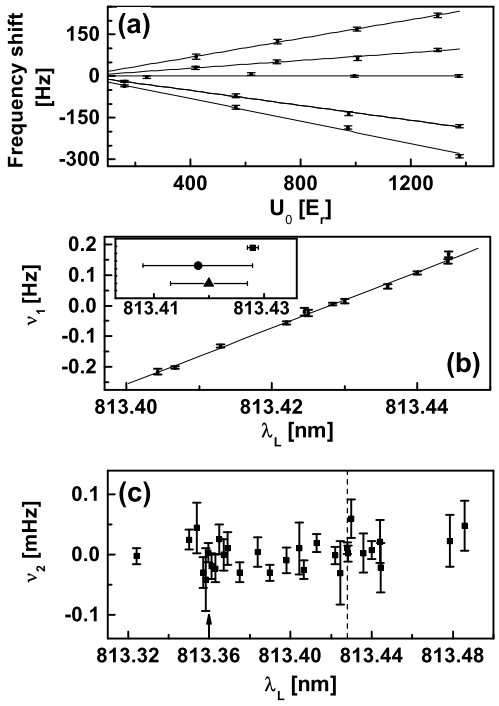

FIG. 3: (a): Typical experimental data used to derive the first and second order frequency shift coefficients plotted in (b) and (c). Shown here is the frequency shift of the clock transition vs lattice depth for 5 different lattice wavelengths: 813.406 nm (four lowest points in the graph), 813.413 nm, 813.428 nm, 813.436 nm and 813.444 nm (four highest points). Also shown is a linear fit of each of these five sets of data. (b): First order frequency shift vs λ_L scaled back to $U_0 = E_r$. Also plotted is a linear fit of these data ($\chi^2 = 1.1$). The inset shows measurements of λ_m. ■ : this work. ▲ : Ref. [7]. ● : Ref. [9]. (c): Higher order frequency shift vs λ_L scaled back to $U_0 = E_r$. All these points are compatible with zero. Their average is $-4(36) \times 10^{-7}$ Hz ($\chi^2 = 1.02$). The arrow on the λ_L axis corresponds to the $^3P_0 \rightarrow {}^1P_1$ transition at 813.360 nm. The vertical dotted line is at the magic wavelength 813.428 nm.

We also studied the effect of the other two photon transition in this wavelength region, the $^3P_0 \rightarrow {}^3F_2$ at 818.57 nm. When tuned 5 nm away from λ_m we expect, in addition to the effect of the two-photon coupling, a trivial quadratic dependence of the atomic frequency vs U_0 due to the imperfect cancellation of ν_1 and to the inhomogeneity of the laser intensity experienced by the atoms. We do observe a substantial broadening and asymmetry of the resonance due to this effect similar to what was reported in Ref. [23]. The associated trivial quadratic frequency shift amounts to $0.8\,\text{mHz}/E_r^2$ as measured several GHz away on both sides of the two photon transition.

When tuned closer to the resonance, we clearly ob-

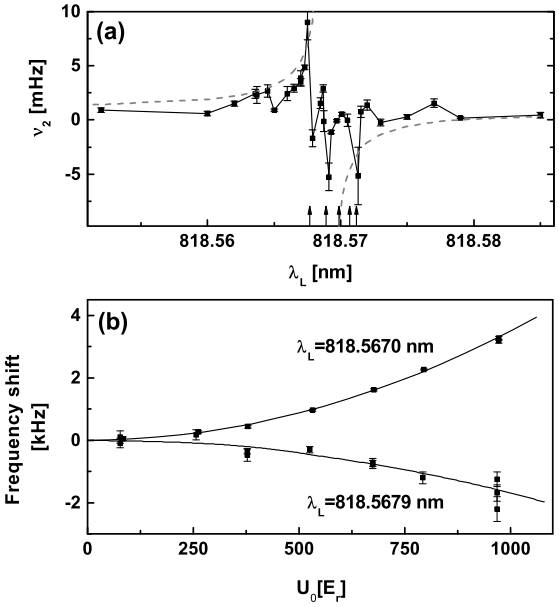

FIG. 4: (a): Higher order frequency shift around the $^3P_0 \rightarrow {}^3F_2$ transition at 818.570 nm scaled back to $U_0 = E_r$. The five vertical arrows on the wavelength axis correspond to the hyperfine sub-states of $5s4f\,{}^3F_2$ ($F = 13/2$ to $F = 5/2$ from left to right). (b): Atomic frequency shift vs trapping depth for two lattice wavelengths on both sides of the two-photon transition to sub-state $F = 13/2$. The linear light shift has been removed for clarity. The bold line is a fit of the data with a parabola.

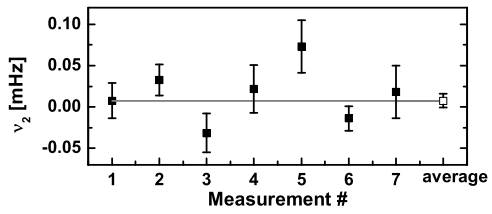

FIG. 5: Higher order frequency shift at the magic wavelength scaled back to $U_0 = E_r$. The value of the open square is the weighted average of the seven other points ($\chi^2 = 1.8$).

serve the non-trivial quadratic frequency shift due to the two-photon resonance itself. The effect is shown in Fig. 4. Quadratic frequency shifts of several kHz and changing sign depending on the side of the transition being probed are observed as shown in Fig. 4(b). This is a clear signature of the higher order effects due to the particular transition under investigation. When tuned exactly onto one of the five transitions corresponding to the hyperfine structure of $^3F_2$, the lattice laser induces severe loss (up to 90%) of atoms when the 698 nm probe laser is tuned to resonance. This effect, which we attribute to three-photon ionization from $^3P_0$, was used to determine the position of the five hyperfine sub-states shown by arrows in Fig. 4(a). The hyperfine structure of $^3F_2$ leads to a complex dependence of the quadratic frequency shift on the lattice wavelength around resonance. The contribution of the five substates can interfere with each other, which may be the cause of the oscillations of ν_2 seen in Fig. 4(a) on both sides of the hyperfine manifold. We can deduce from our measurements a conservative estimate of the contribution of the $^3P_0 - {}^3F_2$ resonance to the higher order effects at $\lambda_L = \lambda_m$. The grey dashed curved plotted in Fig. 4(a) scales as the inverse of the detuning of the lattice with respect to the center of gravity of the hyperfine structure of $^3F_2$ and envelopes experimental points. When extrapolated to the magic wavelength, it gives a contribution to ν_2 of 2 μHz, or equivalently a quadratic frequency shift of 0.2 mHz for a lattice depth of 10 E_r.

Finally we have performed an extensive series of measurements of the clock frequency as a function of the lattice depth at $\lambda_L = \lambda_m$. The values of ν_2 derived from these measurements are plotted in Fig. 5. Their weighted average gives $\nu_2(\lambda_m) = 7(6)\,\mu$Hz. For a lattice depth $U_0 = 10\,E_r$ the corresponding frequency shift is lower than 1 mHz (one sigma) or 2×10^{-18} in fractional units.

IV. CONCLUSION

These results demonstrate that the frequency shift due to the atomic hyperpolarizability constitutes no impediment to the accuracy of a Sr optical lattice clock down to the 10^{-18} level. In addition, the effective laser intensity seen by the atoms is certainly controllable at the percent level [27]. The performance of the system would then be immune to higher order frequency shifts over a broad lattice depth range, possibly up to $U_0 = 100\,E_r$. This would provide a powerful lever for the experimental evaluation at the 10^{-18} level of other effects associated for instance to the dynamics of the atoms in the lattice or to cold collisions. Collisions are expected negligible with polarized fermions, but they have to be considered if one uses bosonic isotopes [8], such as ^{88}Sr. By varying the trapping depth, one can adjust the tunnelling rate and then control the overlap of the wave functions of atoms confined in the lattice, allowing the study of cold collisions in a new regime.

Acknowledgments

SYRTE is Unité Associée au CNRS (UMR 8630) and a member of IFRAF (Institut Francilien de Recherche sur les Atomes Froids). This work is supported by CNES and DGA.

[1] J. J. Garcia-Ripoll, P. Zoller, and J. I. Cirac, J. Phys. B: At. Mol. Opt. Phys. **38**, S567 (2005).
[2] I. Bloch, Nature Physics **1**, 23 (2005).
[3] J. McKeever *et al.*, Phys. Rev. Lett. **90**, 133602 (2003).
[4] S. Nußmann *et al.*, Phys. Rev. Lett. **95**, 173602 (2005).
[5] I. Carusotto *et al.*, Phys. Rev. Lett. **95**, 093202 (2005).
[6] P. Cladé *et al.*, Phys. Rev. Lett. **96**, 033001 (2006).
[7] M. Takamoto, F.-L. Hong, R. Higashi, and H. Katori, Nature **435**, 321 (2005).
[8] Z. W. Barber *et al.*, arXiv:physics/0512084 (2005).
[9] A. D. Ludlow *et al.*, Phys. Rev. Lett. **96**, 033003 (2006).
[10] S. Kuhr *et al.*, Phys. Rev. A **72**, 023406 (2005).
[11] H. Katori, M. Takamoto, V. G. Pal'chikov, and V. D. Ovsiannikov, Phys. Rev. Lett. **91**, 173005 (2003).
[12] U. Sterr *et al.*, C. R. Physique **5**, 845 (2004).
[13] H. S. Margolis *et al.*, Science **306**, 1355 (2004).
[14] W. H. Oskay, W. M. Itano, and J. C. Bergquist, Phys. Rev. Lett. **94**, 163001 (2005).
[15] T. Schneider, E. Peik, and C. Tamm, Phys. Rev. Lett. **94**, 230801 (2005).
[16] P. Dubé *et al.*, Phys. Rev. Lett. **95**, 033001 (2005).
[17] P. Lemonde and P. Wolf, Phys. Rev. A **72**, 033409 (2005).
[18] G. Grynberg and B. Cagnac, Rep. Prog. Phys. **40**, 791 (1977).
[19] I. Courtillot *et al.*, Opt. Lett. **28**, 468 (2003).
[20] T. Mukaiyama *et al.*, Phys. Rev. Lett. **90**, 113002 (2003).
[21] A. Quessada *et al.*, J. Opt. B : Quantum Semiclassical Opt. **5**, S150 (2003).
[22] Y. Sortais *et al.*, Phys. Rev. Lett. **85**, 3117 (2000).
[23] M. Takamoto and H. Katori, Phys. Rev. Lett. **91**, 223001 (2003).
[24] All wavelengths throughout the paper are in vacuum.
[25] We use a tenth order polynomial fit of the data. For any polynomial order between 5 and 14, the results are unchanged to within a fraction of the error bars.
[26] except for a common offset which doesn't play any role in further data analysis.
[27] A control to within a few percents is already achieved in our setup as evidenced by the nice alignement of the measurements of ν_1 shown in Fig. 3(b).

Proceedings of the 20th EFTF, 2006

Spectroscopy of neutral ^{174}Yb in a one-dimensional optical lattice

C. W. Hoyt,* Z. W. Barber,† C. W. Oates, A. V. Taichenachev,‡ V. I. Yudin,‡ and L. Hollberg
National Institute of Standards and Technology
325 Broadway, Boulder, CO 80305, USA

We report spectroscopy of the ^{1}S$_0$ - ^{3}P$_0$ clock transition in neutral ^{174}Yb atoms confined to a one-dimensional optical lattice at the ac Stark shift-canceling wavelength of 759.35 nm. Spectroscopic linewidths as narrow as 4 Hz, full width at half-maximum, are shown with good contrast and signal-to-noise ratios. An upper limit on frequency instability is demonstrated to be 3×10^{-15} at one second by measuring with respect to another stable laser through a Ti:sapphire femtosecond laser frequency comb.

Precision spectroscopy has played a central role in the dramatic advances of time and frequency metrology in recent years. In particular, stable local oscillators have been referenced to optical transitions in single ions and ensembles of neutral atoms to achieve remarkable levels of frequency stability and accuracy. A relatively new implementation of this is the neutral-atom optical lattice clock [1, 2] – a system that is expected to combine the accuracy of single-ion standards with exceptionally high stability. Crucial to this scheme is an atom with a narrow-linewidth clock transition that is insensitive to external fields and lattice perturbations. Several groups have recognized ytterbium as an excellent candidate and are pursuing lattice-based clocks that will use its $^1S_0 \leftrightarrow {}^3P_0$ transition [3–6].

In 2005 this narrow (∼10 mHz natural linewidth) transition at 578.42 nm was observed in the odd isotopes of Yb [4, 5] and its frequency was measured with an uncertainty of 4.4 kHz [5]. In these experiments, a cold atomic cloud in a magneto-optical trap was probed with narrow-linewidth light. The resulting spectroscopic linewidths were Doppler-broadened to hundreds of kilohertz or a few megahertz as set by atomic temperatures. Narrower lines are needed for high-accuracy and -precision clocks. In addition to extended probe interaction times, the removal of Doppler broadening is a primary benefit of optical clocks based on tight (Lamb-Dicke) confinement to a lattice. Here we demonstrate narrow spectroscopic lineshapes – as narrow as 4 Hz – using ^{174}Yb confined to a one-dimensional (1D) optical lattice.

Until the work presented here, lattice clocks have been based on the use of odd isotopes in alkaline earth-like atoms (^{87}Sr [1, 2, 7], ^{171,173}Yb [3–5]). The hyperfine interaction in these isotopes that have non-zero nuclear spin leads to a narrow natural linewidth on the clock transition (∼10 mHz). This linewidth is attractive for optical clocks that promise high accuracy and stability, and the J=0↔J=0 clock transition is insensitive to lattice polarization. However, the hyperfine interaction leads to first-order sensitivity to magnetic fields (∼1-10 kHz/mT, or ∼0.1-1 Hz/mG), some residual lattice polarization sensitivity, and optical pumping issues [8, 9]. The use of even isotopes in alkaline earth-like atoms (zero nuclear spin) would remove or significantly reduce these issues [10–12]. However, the $^1S_0 \leftrightarrow {}^3P_0$ clock transition is normally completely forbidden in the even isotopes.

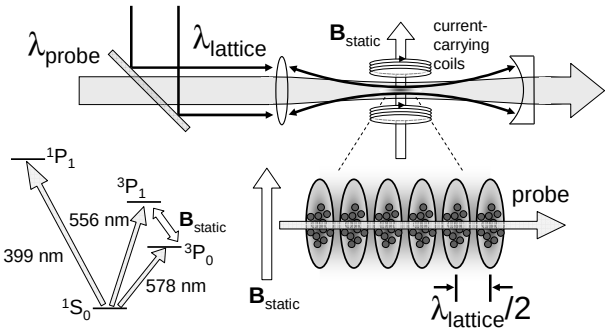

FIG. 1: Magnetic field-induced lattice spectroscopy. Approximately ten thousand ^{174}Yb atoms were cooled, trapped, and loaded into a lattice at the Stark-free wavelength of 759.35 nm. A pair of current-carrying coils generated a static magnetic field to mix a small portion of the $^3P_1$ state into the $^3P_0$ clock state split by a frequency Δ. A single 578.42 nm spectroscopic laser was aligned collinear to the lattice with a dichroic mirror. The tight confinement of the atoms in the probe direction provided for Doppler- and recoil-free excitation of the clock transition. Excitation was measured by ground-state fluorescence of the atoms on the 398.9 nm transition. The simplified energy level diagram is not to scale.

As illustrated in Fig. 1, a static magnetic field can be used to induce a non-zero transition probability on the clock transition in even isotopes [12]. The applied external magnetic field mixes a fraction of the nearby $^3P_1$ state into the upper clock state, $^3P_0$. The mixing fraction is the ratio of magnetic dipole interaction energy ($\hbar\Omega_B \equiv \langle {}^3P_1, m_J = 0 | \vec{\mu} \cdot \mathbf{B} | {}^3P_0 \rangle$) to the $^3P_0$–$^3P_1$ fine structure splitting, Δ. The induced Rabi frequency on the clock transition with a laser tuned to the $^1S_0 \leftrightarrow {}^3P_0$ optical splitting can be written $\Omega_B \Omega_L / \Delta$, where Ω_L is the laser field Rabi frequency

*Electronic address: hoycha@boulder.nist.gov
†also at Univ. of Colorado, Boulder, CO 80309, USA.
‡Institute of Laser Physics SB RAS, Novosibirsk 630090, Russia
Novosibirsk State University, Novosibirsk 630090, Russia

for the $^1S_0 \leftrightarrow {}^3P_1$ transition. This means that the induced Rabi frequency for the clock transition is proportional to $\sqrt{I}|B|$, where I is the laser intensity and $|B|$ is the magnetic field magnitude. The constant of proportionality in this relationship is similar for the alkaline earth-like atoms Yb, Sr, Ca and Mg (see Ref. [12]), suggesting that this method is widely applicable.

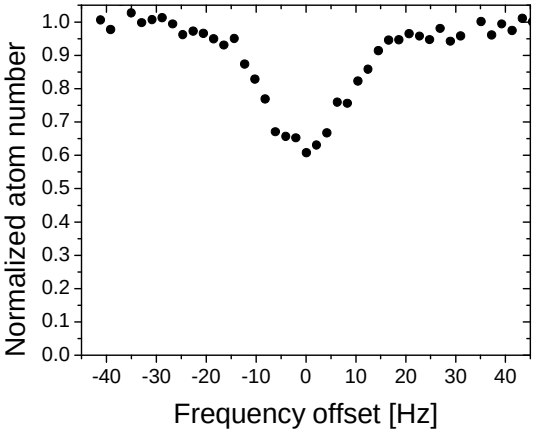

FIG. 2: Spectrum of magnetic field-induced $^1S_0 \leftrightarrow {}^3P_0$ resonance in lattice-confined ^{174}Yb atoms. The lattice laser was tuned close to the Stark-free wavelength of 759.35 nm. Each data point represents a 400 ms cycle of cooling, trapping, probing and detection (see text for details). A Gaussian fit to the line yields a full width at half-maximum of 20.3 Hz.

Figures 2 and 3 show lineshapes obtained using the magnetic field-induced spectroscopic technique with ^{174}Yb atoms confined to a 1D lattice. The experimental details are described comprehensively in Ref. [6]. For the data in Fig. 2, a single 400 ms measurement cycle begins with two sequential stages of magneto-optical traps (MOTs) on the $^1S_0 \leftrightarrow {}^1P_1$ (398.9 nm) and $^1S_0 \leftrightarrow {}^3P_1$ (556 nm) transitions. Approximately 10^4 atoms with a temperature of 40 μK were then loaded into the lattice ($1/e^2$ waist of $\sim$30 μm) that was generated by $\sim$1.1 W of light from an injection-locked Ti:sapphire laser [13]. A 64 ms pulse from a highly stable (sub-hertz linewidth [14]) dye laser at 578.42 nm was applied along the 1D lattice axis as shown in Fig. 1. The static magnetic field had a value of $|B| = 1.29$ mT – obtained by switching the current direction in one of the MOT coils – and the probe intensity was $I \approx 280\,\mathrm{mW/cm^2}$. The remaining ground state population was then measured with a 398.9 nm probe. The total scan time in Fig. 2 was $\sim$20 s. A Gaussian fit to the line yields a full width at half-maximum (FWHM) of 20.3 Hz. The depletion of 40 % was achieved with single pulse excitation.

The resonance lineshape in Fig. 3 was obtained under conditions similar to those for the data in Fig. 2. The vertical axis in Fig. 3 is not normalized to full atom depletion as is the case in Fig. 2. In Fig. 3 the excitation pulse duration was increased to 200 ms and

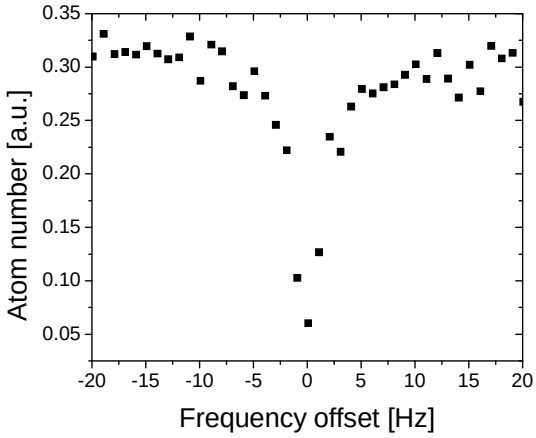

FIG. 3: Spectrum of magnetic field-induced $^1S_0 \leftrightarrow {}^3P_0$ resonance with the lattice laser tuned close to the Stark-free wavelength. Each data point represents a $\sim$540 ms experimental cycle. A Gaussian fit to the line yields a Fourier transform-limited FWHM of approximately 4 Hz. The vertical scale is not normalized to full atom depletion.

the cycle time was correspondingly increased. Additionally, the $1/e^2$ width of the probe beam in the vicinity of the atoms was increased from $\sim$40 μm to $\sim$120 μm with respect to the conditions in Fig. 2, although this change alone was shown to have no noticeable effect on linewidth. The power was adjusted for the increased beam width and pulse duration such that a π-pulse was achieved with the same magnetic field ($\sim$1.3 mT). A Gaussian fit to the line yields a transform-limited FWHM of approximately 4 Hz.

Estimates of potential frequency instability can be made from the lineshapes in Figs. 2 and 3. Using a signal-to-noise ratio of 10 for the former, the data support a one-second frequency instability of $\sim 3 \times 10^{-15}$. The narrowing of linewidth by a factor of five in Fig. 3 implies a potential one-second instability of 6×10^{-16}, or about $\sim$300 mHz at the clock frequency. With straightforward efforts this can be improved even further. The cycle-to-cycle noise that dominates the noise in Figs. 2 and 3 can be significantly decreased by use of a normalization scheme based on optical pumping from the metastable ^{3}P$_0$ clock state. Possible transitions include ^{3}P$_0 \leftrightarrow {}^3$S$_1$ (6s7s) and ^{3}P$_2 \leftrightarrow {}^3$S$_1$ (6s7s) by use of lasers at 770 nm and 649 nm, or ^{3}P$_0 \leftrightarrow {}^3$D$_1$ (6s6p) with a single laser at $\sim$1.39 μm. Together with a very stable local oscillator, a factor of five improvement in signal-to-noise ratio would support one-second instabilies for Yb below 100 mHz. This degree of precision would allow rapid (10 mHz in $\sim$100 s) exploration of systematic uncertainties for frequency measurements, delivering one of the key benefits that neutral-atom standards have promised.

The lattice-confined Yb system has already demonstrated high stability. Figure 4 shows a diagram of the technique used to lock the clock laser to the ^{174}Yb

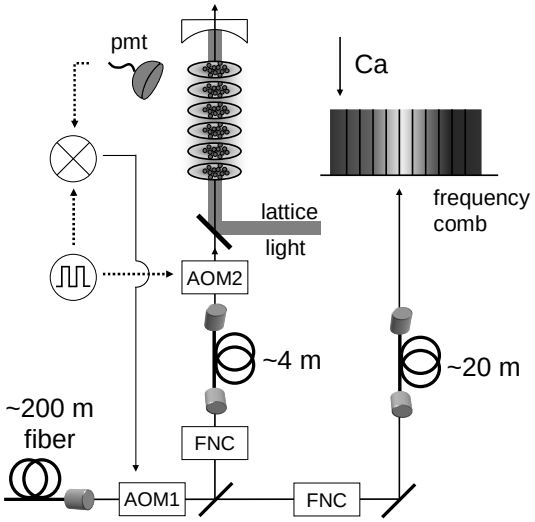

FIG. 4: Diagram of the technique used to lock the local oscillator at 578.42 nm to the clock resonance ($^1S_0 \leftrightarrow {}^3P_0$) of lattice-confined ^{174}Yb atoms. AOM2 is used as a switch that determines probe pulse duration, and is also frequency modulated across the spectroscopic line (see text for details). Also shown is the transfer of locked light to a femtosecond laser-based optical frequency comb. Fiber noise canceler (FNC); acousto-optic modulator (AOM); photomultiplier tube (pmt).

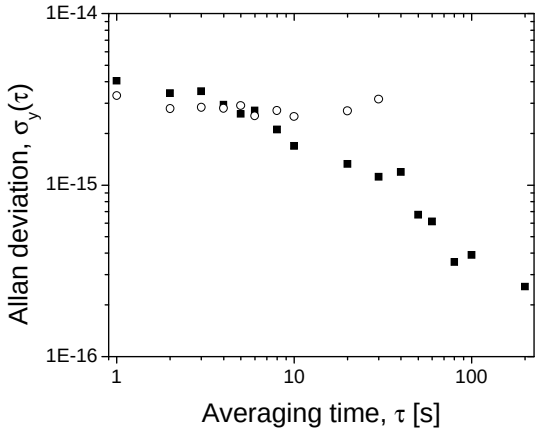

FIG. 5: Frequency instability of the lattice-based Yb optical standard using a lineshape with a 20 Hz width under the same conditions as those for the data in Fig. 2 (i.e., S/N $\sim$ 10, total measurement time $\sim$800 ms). A beat frequency with light at 657 nm is measured with a Ti:sapphire femtosecond-laser based frequency comb. The 657 nm light was locked to the clock transition in Ca (filled squares) and locked only to a stable cavity (open circles). A cycle period of 7 ms and spectroscopic linewidth of 1.15 kHz were used in locking the 657 nm light to the Ca atoms.

$^1S_0 \leftrightarrow {}^3P_0$ resonance. The stable light at 578.42 nm for spectroscopy was transferred from another laboratory through $\sim$200 m of fiber and passed through an acousto-optic modulator (AOM1) that was used for low-frequency corrections to the atomic resonance. Noise induced by transferral through the long fiber is canceled before the fiber in a standard manner by use of phase information from the output facet internal (back) reflection [15, 16]. After exiting the long fiber and passing through AOM1, part of the light was directed through another fiber noise canceler and through a short length of fiber to the experiment. The probe light then passed through another acousto-optic modulator (AOM2) near the experiment that was used as a switch to define the probe pulse duration. AOM2 was frequency modulated with a square wave: modulation depth was equal to half the spectroscopic linewidth, and the modulation period was twice the cycle time (*e.g.*, 2 $\times$ 400 ms for a 20 Hz linewidth). After AOM2 the probe light was combined with the lattice light by means of a dichroic mirror. The spectroscopic signal from a photomultiplier was demodulated by a microprocessor, and a correction signal – proportional to the signal difference between both sides of the lineshape – was sent to AOM1, as shown in Fig. 4.

Also shown in Fig. 4 is the method used to measure relative optical frequency stability. A fraction of the stabilized light at 578.42 nm was sent to a self-referenced optical frequency comb [17, 18]. The comb was locked to the Yb light, enabling the comb to coherently transfer the stability of the Yb laser to a comb component [19] near the frequency of the NIST neutral Ca frequency standard at 657 nm [20, 21]. We recorded the beat frequency between the 657 nm light and its nearest Yb-referenced comb component for a 1 s gate time. Figure 5 shows the results of the Ca-Yb comparison, where frequency instability is expressed as the Allan deviation. The open circles indicate measurements taken when the light at 657 nm was not locked to the Ca atoms, but only to its stable optical cavity. The one-second value of $\sim 3 \times 10^{-15}$ continues for gate times up to 30 s, consistent with long-term cavity drift. The filled squares show results obtained with the 657 nm light locked to the Ca atoms by use of a cycle time of 7 ms and spectroscopic linewidth of 1.15 kHz. With decreased cycle time and increased servo gain for the Ca system the one-second instability can be decreased to $\sim 3 \times 10^{-15}$.

The preliminary data in Fig. 5 suggest that the upper limit on the ten-second instability of the Yb frequency reference is $\sim$1-2 x 10^{-15}. As can be seen in the figure, the relative frequency imprecision between Ca and Yb reached the mid-10^{-16} level in less than 100 s of averaging. This means that with a 20 Hz linewidth and a signal-to-noise ratio of 10 – both of which can be significantly improved, as we have seen – systematic uncertainties can be evaluated for the Yb clock at the 100 mHz level in $\sim$100 s.

What are the dominant inaccuracies that need to be evaluated for an Yb optical lattice clock? For any

lattice clock the residual light shift due to the lattice laser must be suppressed. To first order in intensity, the slope of the differential light shift with respect to lattice laser frequency is $\sim 10^{-8}$ Hz/Hz in the vicinity of the ac Stark shift zero-crossing for the upper and lower clock states. A millihertz frequency shift, for example, would be caused by a lattice laser frequency shift of ~100 kHz away from the shift-canceling wavelength (λ_{sc}). Control of the lattice laser frequency to this level should be straightforward, but λ_{sc} would need to be measured to $\sim 10^{-4}$ pm for millihertz-level uncertainty. Our preliminary measurements yield λ_{sc}=759.3547 ± 0.0005 nm. While determining λ_{sc} to three more digits is nontrivial, the stability improvements indicated above should allow identification of λ_{sc} to sufficient precision. The odd isotopes have an additional requirement on the first-order light shift cancelation for millihertz uncertainty: because of the vector nature of the states, the lattice laser polarization must be controlled to 1 mrad or better [8, 9].

Suppression of the first-order light shift is sufficient only if higher-order terms in lattice intensity can be neglected. This is the case for the Sr lattice clock, where higher-order effects have been shown to contribute a fractional frequency uncertainty of 10^{-18} (<1 mHz) [7]. The second-order polarizability, or hyperpolarizability, generally depends strongly on polarization and proximity to two-photon resonances. For Yb, the ^{3}P$_0$ (6s6p)↔^{3}P$_0$ (6s8p) transition at 2 × 759.7098 nm is the nearest allowed two-photon transition. Since this is only ~200 GHz from λ_{sc}, it will be necessary to look carefully for nonlinear frequency shifts with lattice intensity. So far we have seen no nonlinearities at the hertz level for intensity variations in the ~30-85 kW/cm^2 range for lattice wavelengths ranging from 759.350 to 759.357 nm. If necessary, this resonance can be suppressed by ensuring a single circular lattice polarization at each atom, which can be achieved for multidimensional lattice geometries [22].

A lattice clock based on the odd isotopes (nonzero nuclear spin) must control the magnetic field at the atoms to 0.1-1 nT (1-10 μG) in order to reach millihertz uncertainty [2, 9]. As stated above, for Yb and Sr this is due to the hyperfine mixing between the upper clock state (^{3}P$_0$) and the nearby ^{3}P$_1$ (6s6p) state (i.e., g$_J$ nonzero for ^{3}P$_0$), which brings first-order field sensitivity [23]. Although at first it may seem problematic to build a frequency standard based on a relatively high bias magnetic field, the even-isotope (zero nuclear spin) scheme described above appears more amenable to minimizing B-field uncertainty. Specifically, the requirements for field control leading to millihertz uncertainty are relaxed by one to two orders of magnitude, and the even isotopes have no magnetic substructure. In the case of Yb, the field at the atoms can be calibrated through spectroscopy on the field-sensitive ^{1}S$_0$ (m=0) ↔ ^{3}P$_1$ (m=±1) transition at 556 nm. The Lande-g factor is known to be 1.49282 for this transition [24]. Resolution of kilohertz shifts on this transition corresponds to 0.1 μT (1 mG) field resolution, which could be done with lattice-based or even cold atomic cloud spectroscopy. For a bias field of ~1 mT (~10 G) as is used in even-isotope spectroscopy, the quadratic Zeeman shift on the clock transition is a few hertz. As shown in Fig. 5, we can readily observe frequency shifts at the 100 mHz level and lower. Together with 0.1 μT (1 mG) knowledge and control of the field – through fine control of low current in a second set of coils collocated with the MOT coils, for example – this should allow us to determine the second-order Zeeman shift coefficient to sufficient precision for millihertz confidence on the field-related clock frequency shift. The use of magnetic field shielding is not necessary in this process, which presumably could be necessary with the ~1-10 kHz/mT (~0.1-1 Hz/mG) sensitivity of an odd-isotope lattice clock.

Frequency shifts due to atom-atom interactions are expected to be negligible for three-dimensional lattice clocks with less-than-unity occupation [8, 25]. The fermionic odd isotopes can generally have the advantage of negligible collision shifts, but the ensemble must be nuclear spin-polarized into a single M$_F$ state. (Isotopes ^{87}Sr, ^{173}Yb, and ^{171}Yb have nuclear spin I=9/2, 5/2, and 1/2, respectively.) The magnitude of the density shift is unknown for bosonic ^{174}Yb and must be experimentally determined. The blackbody shift (BBS) for Yb has been calculated to be -1.25 ± 0.13 Hz at T = 300 K [26]. The fractional frequency error due to the uncertainty in this calculation is $\sim 3 \times 10^{-16}$. High precision experiments – using an off-resonant infrared laser, for example [27]– are ultimately needed to determine the frequency inaccuracy due to the BBS. The high stability shown here should allow us to evaluate systematic error in the Yb lattice clock to high precision. Focusing first on the higher-order lattice light shift and the density shift, we could be able to report a sub-hertz ($<10^{-15}$) absolute frequency measurement in the near future.

The authors thank Jim Bergquist for invaluable assistance with the clock laser and helpful discussions. They also appreciate support with the Ca frequency standard from Yann LeCoq. Tara Fortier, Jason Stalnaker, and Scott Diddams provided generous help with the frequency comb measurements. C. W. H. acknowledges financial support from the National Research Council.

[1] M. Takamoto, F. Hong, R. Higashi, and H. Katori, Nature **435**, 321 (2005).
[2] A. D. Ludlow, M. M. Boyd, T. Zelevinsky, S. M. Foreman, S. Blatt, M. Notcutt, T. Ido, and J. Ye, Phys. Rev. Lett. **96**, 033003 (2006).
[3] C. Y. Park and T. H. Yoon, Phys. Rev. A **68**, 055401 (2003).
[4] T. Hong, C. Cramer, E. Cook, W. Nagourney, and E. N. Fortson, Opt. Lett. **30**, 2644 (2005).
[5] C. W. Hoyt, Z. W. Barber, C. W. Oates, T. M. Fortier, S. A. Diddams and L. Hollberg, Phys. Rev. Lett. **95**, 083003 (2005).
[6] Z. W. Barber, C. W. Hoyt, C. W. Oates, A. V. Taichenachev, V. I. Yudin, and L. Hollberg, Phys. Rev. Lett. **96**, 083002 (2006).
[7] A. Brusch, R. Le Targat, X. Baillard, M. Fouché, and P. Lemonde, Phys. Rev. Lett. **96**, 103003 (2006).
[8] H. Katori, M. Takamoto, V. G. Pal'chikov, V. D. Ovsiannikov, Phys. Rev. Lett. **91**, 173005 (2003).
[9] S. G. Porsev, A. Derevianko, and E. N. Fortson, Phys. Rev. A **69**, 021403(R) (2004).
[10] R. Santra, E. Arimondo, T. Ido, C. H. Greene and J. Ye, Phys. Rev. Lett. **94**, 173002 (2005).
[11] T. Hong, C. Cramer, W. Nagourney, and E. N. Fortson, Phys. Rev. Lett. **94**, 050801 (2005).
[12] A. V. Taichenachev, V. I. Yudin, C. W. Oates, C. W. Hoyt, Z. W. Barber, and L. Hollberg, Phys. Rev. Lett. **96**, 083001 (2006).
[13] E. A. Cummings, M. S. Hicken, and S. D. Bergeson, App. Opt. **41**, 7583 (2002).
[14] B. C. Young, F. C. Cruz, W. M. Itano and J. C. Bergquist, Phys. Rev. Lett. **82**, 3799 (1999).
[15] J. C. Bergquist, W. M. Itano, and D. J. Wineland, Proc. 1992 Intl. School Phys., 359 (1992).
[16] L.-S. Ma, P. Junger, J. Ye, and J. L. Hall, Opt. Lett. **19** 1777 (1994).
[17] T. M. Ramond, S. A. Diddams, L. Hollberg, and A. Bartels, Opt. Lett. **27**, 1842 (2002).
[18] A. Bartels and H. Kurz, Opt. Lett. **27**, 1839 (2002).
[19] L.-S. Ma, Z. Bi, A. Bartels, L. Robertsson, M. Zucco, R. S. Windeler, G. Wilpers, C. W. Oates, L. Hollberg and S. A. Diddams, Science **303**, 1843 (2004).
[20] C. W. Oates, E. A. Curtis, and L. Hollberg, Opt. Lett. **25** 1603 (2000).
[21] U. Sterr, C. Degenhardt, H. Stoehr, Ch. Lisdat, H. Schnatz, J. Helmcke, F. Riehle, G. Wilpers, Ch. Oates, and L. Hollberg, Compt. Rend. Phys. **5**, 845 (2004).
[22] G. Grynberg, B. Lounis, P. Verkerk, J.-Y. Courtois, and C. Salomon, Phys. Rev. Lett. **70**, 2249 (1993).
[23] E. Peik, G. Hollemann, and H. Walther, Phys. Rev. A **49**, 407 (1994).
[24] W. C. Martin, R. Zalubas, and L. Hagan, *Atomic Energy Levels – The Rare-Earth Elements* (U.S. GPO, Washington, 1978).
[25] D. E. Chang, J. Ye, and M. D. Lukin, Phys. Rev. A **69**, 023810 (2004).
[26] S. G. Porsev and A. Derevianko, arXiv:physics/0602082 (v1 13 Feb. 2006).
[27] T. Rosenband, W. M. Itano, P. O. Schmidt, D. B. Hume, J. C. J. Koelemeij, J. C. Bergquist, and D. J. Wineland, in *Proceedings of the 20th European Frequency and Time Forum* (PTB, Braunschweig, 2006).

Proceedings of the 20th EFTF, 2006

Optical lattice-field-induced $^1S_0 - ^3P_0$ transitions in even isotopes of alkaline-earth atoms

Vitaly D. Ovsiannikov[1],* Vitaly G. Pal'chikov[2], Alexey V. Taichenachev[3], and Valeriy I. Yudin[3]
[1] *Physics Department, Voronezh State University, Universitetskaya pl. 1, 394006, Voronezh, Russia*
[2] *Institute of Metrology for Time and Space at National Research Institute for Physical–Technical and Radiotechnical Measurements, Mendeleevo, Moscow Region, 141579 Russia*
[3] *Institute of Laser Physics SB RAS, Lavrent'ev Avenue 13/3, Novosibirsk 630090, Russia Novosibirsk State University, Pirogova st. 2, Novosibirsk 630090, Russia*

The circular polarized laser beam of the "magic" wavelength used to produce an optical lattice for the time-frequency standard on neutral atoms may mix the $^3P_1$ state to the long-living metastable state $^3P_0$ thus providing significant enhancement of the strongly forbidden $^1S_0 - ^3P_0$ clock transition in even isotopes of alkaline-earth-like atoms. We present a detailed analysis of various factors influencing resolution and uncertainty for this kind of optical standard, including precise estimations of the "magic" wavelengths, transition matrix elements and field induced second- and fourth-order ac Stark shifts for the ground and metastable alkaline-earth-like atoms.

I. INTRODUCTION

Extremely narrow atomic line corresponding to a strictly forbidden $^1S_0 - ^3P_0$ transition between ground and metastable states of alkaline-earth-like atoms (such as Mg, Ca, Sr, Yb, Zn, Cd), currently considered as worthwhile candidates for an optical frequency standard, may be observed either on free odd isotopes [1, 2] or on even isotopes in external fields [3–6]. The mixing of the $^3P_1$ and $^3P_0$ states by the hyper-fine interaction in the odd isotopes and by the external field in the even isotopes is the basic effect which removes the general selection-rule restrictions on the $0-0$ radiation transition. Alternatively, a sharp resonance line of even alkaline-earth-like atoms that appears in three-photon transitions between the $^1S_0$ and $^3P_0$ states in a $J{=}0 \to 1 \to J{=}0$ three-level system is proposed recently as an optical frequency standard [3].

Intensive investigations of even alkaline-earth-like isotopes during the last year were stimulated by a possibility to design a new frequency standard based on an oscillator with the record high quality Q-factor. However, in all the methods based on interrogation of the strongly forbidden $^1S_0 - ^3P_0$ transition in the even isotopes embedded into an optical lattice, engineered so as to equalize the upper- and lower-level Stark shifts, some additional radiation [3, 4] or static [5, 6] fields were applied.

In this article we propose to use a circularly (elliptically) polarized wave of the "magic" wave length λ_{mag} (corresponding to the so-called "Stark-cancellation" regime, see e.g. [1, 7]) in addition to the optical lattice field in order to mix the $^3P_1$ state to the $^3P_0$ state.

*Electronic address: ovd@phys.vsu.ru

II. THEORY AND NUMERICAL ESTIMATIONS

Since in even isotopes the nuclear momentum equals zero, both the initial and the final states of the frequency standard transition (the "clock" transition) have zero total momenta, without hyperfine structure splitting and without antisymmetric and tensor increments to the ac dipole polarizabilities and to the Stark effect. This makes the Stark shift of the upper and lower levels independent of polarization of external fields. Meanwhile the circular polarization of a laser wave allows for the second-order dipole-dipole mixing of the $^3P_1$ state to the metastable $^3P_0$ state, which is strictly forbidden for the linear polarization.

So, the role of the optical lattice field consists in trapping near the standing-wave antinodes millions of neutral atoms effectively free from collisions and Doppler effect (Lamb-Dicke regime) as well as from the light field perturbations [1], whereas the additional circularly polarized radiation will induce the strictly forbidden radiation transitions via mixing the $^3P_1$ state to the metastable $^3P_0$ state. The two waves may be completely independent, each properly adjusted to some particular conditions. So they may have different intensities, polarizations, wave vectors and even different wavelengths, subject, however, to the Stark-cancellation regime.

The origin of the laser radiation-induced mixing consists in the possibility of the second-order dipole transition between the $^3P_1$ state and the metastable $^3P_0$ state in ac field of a "magic" frequency $\omega = \omega_m = 2\pi c/\lambda_{mag}$ (c is the speed of light) with a non-zero degree of circular polarization. To this end, in addition to the the standing wave, the circularly polarized running wave component of the lattice field should exist with the electric field vector

$$\boldsymbol{F}_r(\mathbf{r},t) = F_r \mathrm{Re}\left\{\mathbf{e}\cdot\exp[i(\mathbf{k}\cdot\mathbf{r}-\omega t)]\right\}, \qquad (1)$$

where F_r is a real scalar amplitude, $\mathbf{e}$ is a complex

unit polarization vector, $\mathbf{k} = \mathbf{n}\omega/c$ is the wave vector with the unit vector $\mathbf{n}$. The contribution of the $^3P_1$-state wave function into the metastable $^3P_0$-state wave function is determined by the ratio of the field-induced $^3P_0$–$^3P_1$ transition amplitude (Rabi frequency) W_{10} to the fine-structure splitting Δ_{10}=$E_{^3P_1}$ – $E_{^3P_0}$. In the lowest non-vanishing (second) order in F, the amplitude [15]

$$W_{10} = -\frac{F_r^2}{4\sqrt{6}}\,\xi\,\alpha^a_{^3P}(\omega_m) \qquad (2)$$

is directly proportional to the circular polarization degree $\xi = i(\mathbf{n}\cdot[\mathbf{e}\times\mathbf{e}^*])$ and to the antisymmetric part $\alpha^a_{^3P}(\omega_m)$ of the^3P_J triplet state ac polarizability, which e.g. for the state with maximal total momentum $J = L + S = 2$ is (see [8, 10]):

$$\begin{aligned}\alpha_{^3PJM}(\omega) &= \alpha^s_{^3P}(\omega) + \frac{M}{2J}\xi\alpha^a_{^3P}(\omega) \\ &\quad -\frac{3M^2 - J(J+1)}{2J(2J-1)}\,\alpha^t_{^3P}(\omega), \qquad (3)\end{aligned}$$

here M is the magnetic quantum number. In the one-electron approximation $\alpha^a_{^3P}(\omega_m)$ may be written in terms of the second-order frequency-dependent radial matrix elements, as follows [9, 10]

$$\alpha^a_{^3P}(\omega) = \frac{1}{3}\left\langle {}^3P\left| r\left[g_2^{\omega} - g_2^{-\omega} - g_0^{\omega} + g_0^{-\omega}\right] r\right| {}^3P\right\rangle \qquad (4)$$

with the radial Green's functions $g_L^{\pm\omega}$ of energy $E_{^3P} \pm \omega$ in the subspace of triplet states with the angular momentum L. The superscripts (s) and (t) in (3) indicate the scalar and tensor parts of ac polarizability $\alpha_{^3PJM}(\omega)$.

Actually, the amplitude (2) may be compared to the amplitude of the hyperfine interaction, which mixes the states in the odd isotopes, or to the magnetic-field-induced amplitude when the atoms experience the action of a magnetic field, which may also be used for the $^3P_0$–$^3P_1$ state mixing [5, 6]. Numerical computations carried out in the single-electron approximation [9] with the use of the model potential for describing analytically the radial wave functions and Sturm-function basis for the Green's functions $g_L^{\pm\omega}$ [8], gave the numerical values of the ac antisymmetric polarizabilities presented in Table I for Mg, Ca, Sr, Yb, Zn and Cd atoms at the "magic" wavelength corresponding to equal second-order ac Stark shifts $\Delta E(^3P_0) = \Delta E(^1S_0) = E_L^{(2)}$ of the metastable and ground states (the lattice depth)

$$E_L^{(2)} = -\frac{1}{4}\alpha^s(\omega_m)F^2, \qquad (5)$$

where $\alpha^s(\omega_m) = \alpha_{^1S_0}(\omega_m) = \alpha_{^3P_0}(\omega_m)$ is the ac polarizability of the "clock" levels; F represents the lattice standing-wave amplitude or the running-wave (1) amplitude, both of the "magic" frequency ω_m.

TABLE I: Numerical values of the "magic" wave length λ_{mag}, $^3P_1$–$^3P_0$ splitting $\Delta_{10} = E_{^3P_1} - E_{^3P_0}$, antisymmetric polarizability $\alpha^a_{^3P}$, transition matrix element W_{10} and the lattice-field-induced second-order Stark shift (lattice depth) $E_L^{(2)}$ for the ground-state and metastable alkaline-earth-like atoms in the optical lattice of the magic wave length and intensity I_L=10 kW/cm^2.

Atom	λ_{mag}, nm	Δ_{10}, cm^{-1}	$\alpha^a_{^3P}(\omega_m)$, $a.u.$	W_{10}/ξ, kHz	$E_L^{(2)}$, kHz
Mg	432	20.06	538.5	−103	−49.3
Ca	680	52.16	−1054	202	−102
Sr	796	186.83	−1044	200	−116
Yb	754	703.57	−1084	208	−78.7
Zn	382	190.08	329.4	−63.1	−21.3
Cd	390	542.1	390.6	−74.8	−25.8

The Rabi frequency for the running-wave-induced transition (2) is directly proportional to the product of the wave intensity I_r=$cF_r^2/8\pi$ and to the antisymmetric polarizability $\alpha^a_{^3P}$, and may be presented in kHz, as follows

$$W_{10} = -0.01915\,\xi\alpha^a_{^3P}(\omega_m)I_r, \qquad (6)$$

where I_r is taken in kW/cm^2 and $\alpha^a_{^3P}$ in atomic units. The value of W_{10} determines the magnitude of the coefficient

$$a_1 = \frac{W_{10}}{\Delta_{10}} \qquad (7)$$

for the running-wave-induced contribution of the $^3P_1$ state to the wave function of an atom initially (when the field (1) is off) in the metastable $^3P_0$ state

$$\begin{aligned}\psi &= |^3P_0\rangle + a_1|^3P_1\rangle \\ &= |^3P_0^{(0)}\rangle + a_1\left(a|^3P_1^{(0)}\rangle + b|^1P_1^{(0)}\rangle\right), \qquad (8)\end{aligned}$$

where the superscript (0) indicates a pure LS-state. The mixing coefficients in (8) are calculated using the ratio of the lifetimes $\tau(^1P_1)$ and $\tau(^3P_1)$:

$$\frac{b^2}{a^2} = \frac{\tau(^1P_1)\lambda^3(^3P_1 - {}^1S_0)}{\tau(^3P_1)\lambda^3(^1P_1 - {}^1S_0)}. \qquad (9)$$

For I_r in kW/cm^2, Δ_{10} in cm^{-1} and $\alpha^a_{^3P}$ in atomic units the rate of the laser field-induced radiation transition $^3P_0 \to {}^1S_0$ may be written as

$$w_L = |a_1|^2 w_{ic} = 0.4080\cdot 10^{-18}\left(\frac{\xi\alpha^a_{^3P}(\omega_m)I_r}{\Delta_{10}}\right)^2 w_{ic}, \qquad (10)$$

where w_{ic} is the field-free $^3P_1 \to {}^1S_0$ intercombination transition rate, the data for which is presented in Table II (see e.g. [11, 12]).

As follows from the data of Tables I, II, at the intensity I_r=50 kW/cm^2, the absolute value of the magic-wave-induced amplitude (6) may amount to one MHz,

that is equivalent to the amplitude induced by a magnetic field of 1 G [5]. With account of the data for the spin-orbit splitting of the lowest (metastable) triplet state ^3P_J (see e.g. [13]) the admixture of the $^3P_1$ state in the $^3P_0$-state wave function at these conditions does not exceed 10^{-6}. Similar estimates indicate that the $^1P_1$ singlet state admixture in (8) at these conditions is yet 2 to 3 orders smaller. However, the $^3P_1$-state admixture may be sufficient to induce the radiation transition between the ground and metastable states and to amplify the $^3P_0$ level width by 5 to 7 orders of magnitude, up to μHz, making detectable the clock transition $^1S_0 \rightarrow ^3P_0$ with the use of a probe field of the "clock" frequency.

Together with the radiative decay rate (10), the important characteristic of the magic-wave-induced $^1S_0 - ^3P_0$ dipole transition, probed by the clock-frequency radiation, is the amplitude (Rabi frequency) of the clock tramsition:

$$\Omega = \langle\, ^3P_0^{(0)} | \hat{v}_p | \, ^1S_0^{(0)} \rangle = \beta I_r \sqrt{I_p}\, \left(i \left[\mathbf{e} \times \mathbf{e}^* \right] \cdot \mathbf{e}_p \right), \tag{11}$$

where $\hat{v}_p$ is the Hamiltonian of the dipole interaction between atom and probe field of intensity I_p and the unit polarization vector $\mathbf{e}_p$ which, evidently, should be parallel to the running-wave vector $\mathbf{k} \propto i[\mathbf{e} \times \mathbf{e}^*]$, thus implying that the running wave should propagate perpendicular to the probe beam. So, in the case of a 1D optical lattice the Doppler-free interrogation is possible when the probe beam propagates along the lattice and is polarized along the mixing beam wave vector.

The coefficient β may be presented in the units of $\mu Hz/(\sqrt{mW/cm^2} \cdot kW/cm^2)$, as follows:

$$\beta = 102.4 \frac{\alpha^a_{^3P}(\omega_m) \langle\, ^3P_0^{(0)} | r | \, ^1S_0^{(0)} \rangle}{\Delta_{10}}\, b, \tag{12}$$

with the antisymmetric polarizability and the radial matrix element in atomic units, the splitting Δ_{10} in cm^{-1}. The factor b determines the amplitude of singlet-triplet mixing of P states with the total momentum J=1 (see eq.(9)). According to the calculated numerical values of β presented in Table II, the Rabi frequency in Sr and Yb atoms (11) may achieve 0.4 mHz for the lattice field intensity I_L=10 kW/cm^2 and the probe field of I_p=1 mW/cm^2.

In the Stark-cancellation regime, when the second-order lattice-field-induced Stark shifts of the clock levels (5) are made equal to one another, the clock frequency may be distorted by the probe-field-induced quadratic ac Stark shift $E_p^{(2)}$ (linear in intensity I_p) and the fourth-order ac Stark shifts of the clock levels $E_L^{(4)}$ and $E_r^{(4)}$ (quadratic in intensities I_L and I_r, correspondingly), induced by the lattice field and the mixing wave also including the bilinear in the intensities I_L and I_r fourth-order correction $E_{Lr}^{(4)}$. This shift may be written as

$$\Delta\omega_c = \kappa_p^{(2)} I_p + \kappa_L^{(4)} I_L^2 + \kappa_r^{(4)} I_r^2 + \kappa_{Lr}^{(4)} I_L I_r, \tag{13}$$

TABLE II: Numerical values of the "clock" wave length λ_c, coefficients $\kappa_p^{(2)}$ and $\kappa^{(4)}$ of the second-order probe-field-induced and fourth-order lattice-field- and/or the mixing-wave-induced clock frequency Stark shift (13), the rate w_{ic} of spontaneous intercombination transition $^3P_1 \rightarrow ^1S_0$ and the coefficient β for the Rabi frequency (11). The number in parentheses determines the power of ten.

Atom	λ_c	$\kappa_p^{(2)}$	$\kappa_L^{(4)}$	w_{ic}	$\lvert\beta\rvert$
	nm	$\frac{mHz}{mW/cm^2}$	$\frac{\mu Hz}{(kW/cm^2)^2}$	s^{-1}	$\frac{\mu Hz}{kW/cm^2\sqrt{mW/cm^2}}$
Mg	458	4.27	176	2.78(2)	7.36
Ca	660	−4.50	260	2.94(3)	25.1
Sr	698	−44.2	137.1	4.70(4)	34.2
Yb	578	24.5	43.7	1.15(6)	39.6
Zn	309	0.816	6.96	4.0(4)	3.08
Cd	332	23.0	10.3	4.17(5)	4.72

where the constant $\kappa_p^{(2)}$ is determined by the difference of the upper- and lower-level polarizabilities at the clock-transition frequency ω_c. For $\kappa_p^{(2)}$ in the units of $mHz/(mW/cm^2)$ the relation is

$$\kappa_p^{(2)} = -0.0469 \left[\alpha_{^3P_0}(\omega_c) - \alpha_{^1S_0}(\omega_c) \right], \tag{14}$$

where polarizabilities $\alpha_{^3P_0}(\omega_c)$ and $\alpha_{^1S_0}(\omega_c)$ are in atomic units.

The coefficients $\kappa_L^{(4)}$ and $\kappa_r^{(4)}$ are determined by the difference of hyperpolarizabilities at the lattice-wave frequency ω_m (similar to polarizabilities, the hyperpolarizabilities for states with total momentum J=0 include only scalar parts),

$$\kappa_{L(r)}^{(4)} = -8.359 \cdot 10^{-8} \left[\gamma_{^3P_0}(\omega_m) - \gamma_{^1S_0}(\omega_m) \right], \tag{15}$$

where $\kappa^{(4)}$ is in the units of $\mu Hz/(kW/cm^2)^2$, with $\gamma_{^1S_0}(\omega_m)$ and $\gamma_{^3P_0}(\omega_m)$ in atomic units. We assume that both the lattice and the running waves have one and the same frequency. Nevertheless, the hyperpolarizabilities of the both states depend on polarization of the waves and may differ essentially for the linear and circular polarization [8, 10], thus resulting in difference between $\kappa_L^{(4)}$, $\kappa_r^{(4)}$ and $\kappa_{Lr}^{(4)}$. Moreover, the hyperpolarizability for the interference term $\kappa_{Lr}^{(4)}$ depends on the relative orientation of the mixing and probe beam polarization vectors $\mathbf{e}$ and $\mathbf{e}_p$. That is why, the fourth-order corrections from the both waves should be taken into account together with the mixed biquadratic (bilinear in the field intensities) correction $\kappa_{Lr}^{(4)} I_L I_r$, although the state-mixing running wave (1) may be essentially stronger than the standing wave of the optical lattice.

The numerical values of $\kappa_p^{(2)}$ and $\kappa^{(4)}$ (the latter - for the circular polarization of the laser beam) are presented in table II. In estimating hyperpolarizability for the Mg, Zn and Cd atoms we took into account only the "resonant" terms, determined by the antisymmetric and tensor polarizabilities [14]. The single-

channel model potential approach [8, 9] was used in all numerical calculations.

The values of susceptibilities $\kappa^{(2)}$ and $\kappa^{(4)}$ of Table II is a useful data to control the higher-order corrections appearing with the increase of the probe and running wave intensity. The method of the lattice-field-induced spectroscopy of strongly forbidden 0-0 transition presented in this paper seems rather worthwhile for the lattice-based optical atomic clock with the magic-wave control of the probed transition.

Acknowledgments

VDO acknowledges the support from the CRDF (USA) and MinES of Russia (BRHE program, award VZ-010), AVT and VIYu were supported by RFBR (grants 05-02-17086, 04-02-16488, 05-08-01389).

[1] M. Takamoto and H. Katori, Phys. Rev. Lett. **91**, 223001 (2003).
[2] C. W. Hoyt, Z. W. Barber, C. W. Oates, T. M. Fortier, S. A. Diddams, and L. Hollberg, Phys. Rev. Lett. **95**, 083003 (2005).
[3] T. Hong, C. Cramer, W. Nagourney, and E. N. Fortson, Phys. Rev. Lett. **94**, 050801 (2005).
[4] R. Santra, E. Arimondo, T. Ido, C. H. Greene, and J. Ye, Phys. Rev. Lett. **94**, 173002 (2005).
[5] A. V. Taichenachev, V. I. Yudin, C. W. Oates, C. W. Hoyt, Z. W. Barber, and L. Hollberg, Phys. Rev. Lett. **96**, 083001 (2006).
[6] Z. W. Barber, C. W. Hoyt, C. W. Oates, L. Hollberg, A. V. Taichenachev, and V. I. Yudin, Phys. Rev. Lett. **96**, 083002 (2006).
[7] H. Katori, M. Takamoto, V.G. Pal'chikov, and V.D. Ovsiannikov, Phys. Rev. Lett. **91**, 173005 (2003).
[8] N. L. Manakov, V. D. Ovsiannikov, and L. P. Rapoport, Phys. Rep. **141**, 319 (1986).
[9] V. D. Ovsiannikov, V. G. Pal'chikov, H. Katori, and M. Takamoto, Quantum Electronics **36**, 3 (2006).
[10] V.A. Davydkin, V.D. Ovsiannikov, and B.A. Zon, Laser Physics **3**, 449 (1993).
[11] S. G. Porsev, M. G. Kozlov, Y. G. Rakhlina and A. Derevianko, Phys. Rev. A **64**, 012508 (2001).
[12] I. M. Savukov and W. R. Johnson, Phys. Rev. A **65**, 042503 (2002).
[13] NIST Atomic Spectra Database Levels Data, http://Physics.nist.gov
[14] V. A. Davydkin and V. D. Ovsiannikov, J. Phys. B: At. Mol. Opt. Phys. **17**, L207 (1984).
[15] the atomic units are used in this paper

Proceedings of the 20th EFTF, 2006

Optical frequency standard with ultra-cold strontium atoms

N. Poli,* R. E. Drullinger, G. Ferrari, F. Sorrentino, and G. M. Tino
Dipartimento di Fisica and LENS, Università di Firenze
Via nello Carrara 1, 50019 Sesto Fiorentino, Italy
INFN, sezione di Firenze
Via Sansone 1, 50019 Sesto Fiorentino, Italy

M. Prevedelli
Dipartimento di Chimica Fisica, Università di Bologna
Via del Risorgimento 4, 40136 Bologna, Italy

We report on our progress toward the realization of an optical frequency standard referenced to strontium intercombination lines. While first frequency measurement of the weakly allowed $^1S_0$-$^3P_1$ transition was done with saturation spectroscopy on a thermal beam, we are preparing the experimental setup for high resolution spectroscopy on ultracold atoms of the doubly forbidden $^1S_0$-$^3P_0$ line. Our current setup allows the capture more than 10^7 atoms at 1 μK in 500 ms in two stages of magneto-optical trapping. We also demonstrated the dipole trapping of ultracold strontium isotopes for accurate spectroscopy and collisional measurements. A semiconductor laser source at 698 nm has already been locked to a pre-stabilization cavity obtaining a fast linewidth of less than 1 kHz. Second stage stabilization of the clock laser to ultra-high finesse cavity is in development. Recent measurement of elastic and inelastic cross-sections of the two most abundant ^{88}Sr and ^{86}Sr isotopes are also presented.

I. INTRODUCTION

Thanks to the ultra-narrow intercombination transitions, strontium has recently become the object of intense study in the field of optical frequency metrology [1]. These studies open the way to the realization of a new optical frequency standard with unprecedented stability and accuracy. Proposals based on different interrogation schemes for both fermionic (^{87}Sr) and bosonic (^{88}Sr, ^{86}Sr, ^{84}Sr) isotopes have been put forward (optical lattice clock [2], engineered atom clock [3, 4, 5, 6]) suggesting the possibility to reach the 10^{-17} level of overall accuracy. Indeed, thanks to the higher oscillator frequency, a clock in the optical domain could potentially reach a stability level of 10^{-18} at 1 s [2] which represents a factor of 10^4 improvement with respect to the best microwave standards [7]. A clock with such stability and accuracy could be used as a powerful test for relativistic theory, searching for deviations of fine structure constant and to define a new atomic time standard. The high stability optical clock signals would find direct application in deep space navigation, remote sensing, secure telecommunications and ultra-precise geodesy.

The level scheme allows the possibility to efficiently cool strontium with standard Doppler cooling techniques to temperature well below 1 μK in hundreds of milliseconds using two steps of trapping and cooling in magneto-optical trap, working first on the dipole allowed $^1S_0$-$^1P_1$ at 461 nm and, subsequently, on the $^1S_0$-$^3P_1$ transition at 689 nm. The fast cooling process toward μK temperatures enables short cycle times, relaxing the demands on frequency stability of the clock laser source used for interrogating the transition [8].

The possibility to cool strontium atoms with visible light, easy reachable with semiconductor source, is in turn interesting from the point of view of realizing compact and portable source of cold atoms to be used in future application both on earth and in space.

Moreover, bosonic ^{88}Sr isotopes have already been trapped in pure optical dipole traps at high phase-space densities of $\rho = 0.1$ [9, 10]. While further increase of ρ with standard evaporative cooling technique is limited by the very low elastic cross section at low temperatures of ^{88}Sr atoms, different cooling techniques, based on sympathetic cooling with isotopic mixtures can be applied [10].

Finally, due to both the special strontium level structure and its cold collision properties, ultra-cold ^{88}Sr has been demonstrated to be particularly suited for applications in the field of quantum sensor. Long lived Bloch oscillation of ^{88}Sr atoms in a vertical standing wave trap has been reported, enabling high sensitive measurement of gravity forces [11].

The structure of the article is the following. Section 2 describes the previous absolute frequency measurements of intercombination lines $^1S_0$-$^3P_1$ of strontium. In section 3, 4 and 5 we present the work in progress for preforming spectroscopy on the doubly forbidden $^1S_0$-$^3P_0$ transition for bosonic isotopes. Section 6 describes the apparatus for cooling and trapping strontium atoms, while section 7 and 8 describes the latest results obtained with cold atoms trapped in optical dipole traps, mainly concerning cold collision physics and Bloch oscillations of ^{88}Sr atoms in 1D vertical standing wave trap.

*Electronic address: poli@lens.unifi.it

II. FREQUENCY MEASUREMENT OF THE $^1S_0$-$^3P_1$ TRANSITION

Our first setup was used for the absolute frequency measurement of the $^1S_0$-$^3P_1$ intercombination line of ^{88}Sr and ^{86}Sr isotopes at 689 nm ($\Gamma/2\pi$ = 7.6 kHz). For the absolute frequency measurement we used a fs-optical-comb-generator; details of the experimental apparatus can also be found in [12]. Part of the light coming from a pre-stabilized 689 nm source (extended cavity diode laser - ECDL - tightly locked to Fabry-Perot cavity with finesse of about 10^4) is coupled into a polarization maintaining fiber and delivered to a strontium thermal atomic beam, while a second light beam is sent towards the comb with a 20 meter long fiber. From the frequency noise measured with a second independent cavity we can infer a linewidth of 20 Hz for the 689 nm source [13].

With standard saturation spectroscopy techniques we obtained a sub-Doppler signal used for long term stabilization of the length of the cavity. The values measured for the two most abundant isotopes are 434 829 121 311 (10) kHz for ^{88}Sr and 434 828 957 494 (10) kHz for ^{86}Sr. The latter value has been derived by difference from the measurement of the ^{88}Sr-^{86}Sr isotopic shift (163 817.4 (0.2) kHz). In the absolute frequency measurement, one of the main limitation was found to be the instability of our GPS referenced quartz oscillator used as frequency reference for the comb [12, 14]. These values are consistent with other determinations with spectroscopy on cold atoms both at SYRTE [15] and at JILA-NIST laboratories [16].

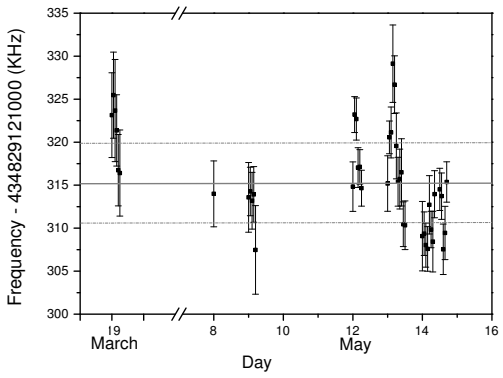

FIG. 1: Frequency measurement of the intercombination line $^1S_0$-$^3P_1$ for the bosonic ^{88}Sr atoms. The data points are the mean values of a set of measurement over 200-300 s, while the error bars are the standard deviation over each set. The final corrected value for ^{88}Sr is 434 829 121 311 (10) kHz

While the ultimate performance of an optical clock working on the $^1S_0$-$^3P_1$ transition for the most abundant ^{88}Sr isotope is limited by the linewidth of the transition (stability 10^{-14} at 1 s, accuracy 10^{-15}[17]), a clock working on the doubly forbidden $^1S_0$-$^3P_0$ transition could overcome the limitations both in stability and accuracy.

III. SPECTROSCOPY ON THE DOUBLY FORBIDDEN $^1S_0$-$^3P_0$ TRANSITION FOR ^{88}SR

The most interesting transition in strontium for the realization of an optical frequency standard is the doubly forbidden line $^1S_0$-$^3P_0$ at 698 nm. Within the framework of the optical lattice clock [2], spectroscopy on this line could produce a frequency reference in the optical regime with unprecedented level of accuracy and stability. In the fermionic (^{87}Sr) isotope the hyperfine mixing due to a non-zero nuclear spin ($I = 9/2$) gives a finite lifetime for the $^3P_0$ state allowing the possibility to observe the transition with direct spectroscopy schemes. Spectroscopy of ^{87}Sr trapped in 1D optical lattices at the magic wavelength, has already been performed in other labs [2, 18, 19].

The case of the bosonic isotopes is different: the nuclear spin is zero and the transition is forbidden at all the orders; in this case different techniques have to be used. Recently many spectroscopic schemes have been proposed to "engineer" the clock transition by mixing the metastable $^3P_0$ level with other short living upper levels, by the use of other coupling light field [3, 4], by trapping the atoms in optical lattice done with elliptical polarization [6], or by using a static magnetic field [5]. While the former schemes are experimentally more complex, the most promising seems to be the one that uses a static magnetic field to mix the $^3P_0$ and $^3P_1$ levels.

Following the treatment in ref. [5] it is possible to calculate the induced transition rate V_{12} for the $^1S_0$-$^3P_0$ transition with a fixed applied $\mathbf{B}$ field and a fixed light intensity I resonant with the $^1S_0$-$^3P_0$ transition. The transition rate is given by the equation $V_{12} = \alpha\sqrt{I}|\mathbf{B}|$, (where $\alpha^{\mathrm{Sr}} = 99\,\mathrm{Hz/T}\sqrt{\mathrm{mW/cm^2}}$ [5]) while the fraction of the state $^3P_1$ mixed to the $^3P_0$ is given by the ratio of the Rabi frequency $\omega_{\mathbf{B}}$ and the fine structure energy splitting Δ_{32} between the two states $^3P_0$ and $^3P_1$ ($\Delta_{32}{}^{\mathrm{Sr}}/2\pi$=5.6 THz).

Within this framework it is possible to calculate the quadratic Zeeman correction for the $^1S_0$-$^3P_0$ transition $\Delta_{\mathbf{B}} = \beta|\mathbf{B}|^2$, and the AC Stark shift is $\Delta_L = kI$ where the two coupling constant for strontium have been calculated to be β^{Sr}=-23.3 MHz/T^2, k^{Sr} =-18 mHz/(mW/cm^2) [5].

If one considers a magnetic field of $|\mathbf{B}|$ = 10 gauss ($\pm$ 1 mgauss) and an intensity of the interrogating light of I = 10 mW/cm^2($\pm$1%), the fraction of the state $^3P_1$ mixed is $\omega_{\mathbf{B}}/\Delta_{32} = 2\times10^{-6}$, giving a transition Rabi frequency of $V_{12} \sim 0.3$ Hz.

Due to this very small contribution of state $^3P_1$ to the mixture, the sensitivity to lattice light polarization

is reduced to about 500 mHz/rad. The correction for quadratic Zeeman effect for the $^1S_0$-$^3P_0$ transition is $\Delta_B = -23.3\,\text{Hz}(\pm 5\,\text{mHz})$, and the AC Stark shift is $\Delta_L = -180(2)\,\text{mHz}$.

It seems reasonable that using this scheme, spectroscopy on the $^1S_0$-$^3P_1$ transition could be performed with an overall accuracy of some parts in 10^{-17}.

The $^1S_0$-$^3P_0$ transition in ^{88}Sr has not been observed yet, but its frequency can be calculated from the value reported in [15] with an accuracy of about 100 kHz. In order to find the first time the transition it is possible to increase the transition probability by increasing both the intensity of the interrogating light and the intensity of the static magnetic field. In our experimental system, the maximum intensity of the interrogating light is about $I_{\max} \sim 1\,\text{W/cm}^2$ where the maximum magnetic field at the center of the trap is of the order of $\mathbf{B}_{\max} \sim 100\,\text{gauss}$. The maximum transition frequency rate is then $V_{12}{}^{\max} = 30\,\text{Hz}$.

While this transition has never been observed for bosonic isotope of strontium, this spectroscopy scheme has already been applied to observe the $^1S_0$-$^3P_0$ transition in bosonic ^{174}Yb atoms [20].

The experimental setup for magnetic-field induced spectroscopy is reported in details in ref. [20]. The spectroscopy is done with atoms trapped in 1D optical lattice at magic wavelength. The red interrogating light is superimposed to the trapping light with a dichroic mirror and focused with an achromatic lens.

IV. ULTRA-STABLE LASER SOURCE AT 698 NM

For performing spectroscopy on the doubly forbidden $^1S_0$-$^3P_0$ line of strontium we are preparing a 698 nm ultra-stable source based on a semiconductor ECDL stabilized in two steps with two cavities of increasing finesse [21]. The source is pre-stabilized with standard Pound-Drever-Hall lock scheme to the same medium finesse cavity used for the stabilization of the 689 nm laser resonant with the $^1S_0$-$^3P_1$ transition. In order to reduce the RF pick-up between the two servo electronics, we used different RF frequency to drive the two electro-optic modulators working at the two different wavelength. With this stage of stabilization the fast linewidth of the laser has been reduced to about 700 Hz. While there is room to reduce the high frequency noise of the laser by optimizing the servo electronics, already long term stability at sub-kHz level is achieved by locking to this resonant cavity, whose length is stabilized to the $^1S_0$-$^3P_1$ transition [12]. Part of the light is then delivered to the high finesse cavity for second stage stabilization. The new high finesse cavity is realized with a specially cut 10 cm ULE spacer for symmetric horizontal suspension [22, 23, 24]. The ULE spacer (Corning 7972) has a turning point for temperature expansion coefficient near room temperature (20°C-25°C), with a residual sensitivity of less than $10^{-9}/°\text{C}$. Two SiO_2 mirrors are optically contacted to both ends of the spacer. The mirrors have a transmission coefficient of 3 ppm (loss due to scattering and absorption < 1 ppm), giving a finesse of about 5×10^5, while the use of silica mirrors, could reduce the mechanical fluctuation induced by thermal noise as pointed out in recent works [25, 26].

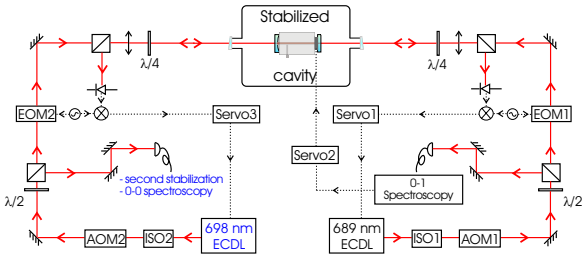

FIG. 2: *Experimental setup for clock laser at 698 nm. The ECDL laser is pre-stabilized on the same cavity used for the stabilization of the light at 689 nm, resonant with the $^1S_0$-$^3P_1$ transition of strontium. Second step of stabilization is done with a frequency lock to a fringe of high-finesse cavity. ECDL extended cavity diode laser, AOM acusto-optical modulator, EOM electro-optical modulator, ISO optical isolator.*

With a temperature stabilization of the cavity of the order of 10 mK and seismic noise acceleration of the order of $1\,\mu g_{rms}$, we expect a sub-Hz long term stability of the cavity length.

V. TRAPPING LASER AT 813 NM

The laser source we are preparing for optical dipole trapping at magic wavelength is a single mode tunable infrared source at 813 nm based on a master ECDL plus a tapered amplifier laser. The maximum optical power is 650 mW. The 1D standing wave trap is then obtained by focusing the light to the atom region and retro-reflecting back the light. With a waist of 30 μm we calculate a maximum trap depth of U_0=30 μK, with a scattering rate $\Gamma_s = 0.6\,\text{s}^{-1}$.

With similar trap geometry done at slightly different wavelength we have observed an atom transfer efficiency from the MOT of the order of 10% [27]. It is then possible with our experimental setup to trap more than 10^6 ^{88}Sr atoms in less than 1 s with lifetimes of the order of 5 s.

VI. TRAPPING AND COOLING STRONTIUM

Strontium atoms are first trapped from a slowed and collimated atomic beam in a magneto optical trap operated on the dipole allowed $^1S_0$-$^1P_1$ transition at 461 nm. Further details on the experimental setup can be found in [27].

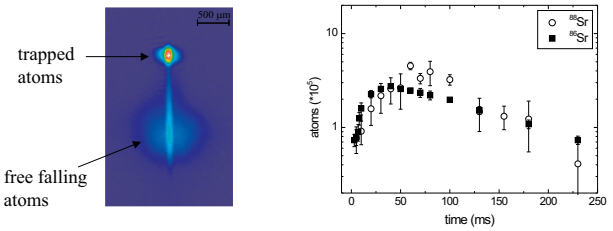

FIG. 3: Crossed-beams FORT loading. The inset shows an in-situ image of trapped atoms. The graph shows the measured FORT population as a function of the time overlap between FORT and red MOT.

The beam is originated by evaporating strontium in an oven at typical temperature of 500°C. The loading in the blue MOT is further improved with the use of a green repumping laser at 497 nm resonant with the $^3P_2$-$^3D_2$ transition. Typically we trap more than 2×10^8 ^{88}Sr atoms in 200 ms at a temperature of 2 mK. The cooling then proceeds with a second stage Doppler cooling working on the intercombination $^1S_0$-$^3P_1$ line. For this, the red light produced with slave laser optically injected with light coming from frequency stabilized master source at 689 nm, is superimposed with the blue light used for the first trapping. Typically more than 10^7 ^{88}Sr atoms at 1 μK are prepared for subsequent transfer into pure optical dipole trap.

With a small change in our setup we prepare an isotopic mixture of bosonic ^{88}Sr and ^{86}Sr isotopes. We start accumulating ^{88}Sr and ^{86}Sr in the $^3P_2$ magnetic trappable state [28], then, the blue laser is turned off and the repumper is flashed on for a few ms. This puts the atoms back in their singlet ground state where we proceed with the second-stage cooling, recapturing them into a red double MOT operated with two slave lasers tuned to the different isotopes. During the last 50 ms of MOT operation the dipole trap laser is superimposed to the MOT allowing the transfer of the mixture in the dipole trap. The number of atoms finally trapped in the dipole trap depends mainly on the time sequence in the first collection in the magnetic trap. At maximum we have obtained more than 10^6 ^{88}Sr atoms and 3×10^5 ^{86}Sr atoms.

VII. COLLISIONAL MEASUREMENT ON ^{88}SR^{86}SR

Optical dipole traps are the best environment for the study of collisional dynamics of ultracold atoms. This study, being of fundamental importance for understanding the possibility to reach quantum degeneracy with standard evaporative technique, is also crucial for understanding the dynamics at low temperatures for ultra-sensitive spectroscopy.

TABLE I: Sr collisional cross-section

elastic cross-section	
σ_{88-88}	$3(1) \times 10^{-13}$ cm^2
σ_{86-86}	$1.3(0.5) \times 10^{-10}$ cm^2
σ_{88-86}	$4(1) \times 10^{-12}$ cm^2
inelastic parameter	
K_{88}	$< 10^{-27}$ cm^{6}s^{-1}
K_{86}	$1.0(0.5) \times 10^{-24}$ cm^{6}s^{-1}

More specifically, we evaluated the elastic cross-sections σ_{i-j} $(i, j = 86, 88)$ for both intra and inter-species collisions, and the three-body recombination coefficients K_i $(i = 86, 88)$ in the FORT. The elastic cross-sections were deduced by driving the system out of thermal equilibrium and measuring the thermalization rate together with the sample density. For the inelastic collisions, we measured instead the density dependence of the trap loss rate. The results [10] are summarized in table I.

Our results show significant differences in the collisional properties of the two isotopes. Both the elastic cross-section and the three-body collision coefficient were found to be several orders of magnitude larger in ^{86}Sr than in ^{88}Sr and consistent with recent independent measurements of the scattering length [29, 30], while the inter-species cross-section σ_{86-88} is much larger than the intra-species cross-section σ_{88-88}. The results obtained indicate that forced evaporation toward BEC would be difficult for both ^{88}Sr and ^{86}Sr isotopes. The large interspecies elastic cross section instead could be used in order to perform an optical sympathetic cooling scheme of a large cloud of an isotope with a small cloud of the other isotope. With this technique a reduction of a factor of two of the temperature of a cloud of ^{88}Sr atoms has been obtained applying optical cooling to the other species (^{86}Sr) [10].

VIII. CONCLUSION

We presented our progress toward the realization of an optical frequency standard based on strontium intercombination transition. High resolution spectroscopy on the doubly-forbidden $^1S_0$-$^3P_0$ transition can be performed also in the more abundant even isotope at the level of 10^{-17}, and we are preparing the experimental setup consisting of clock laser and trapping laser at magic wavelength.

Interesting collision properties of bosonic strontium atoms at low temperatures have been exploited allowing the possibility to apply different cooling techniques. More recently, trapped ^{88}Sr atoms in a vertical 1D lattices has been demonstrated to be a highly sensitive sensor of gravity forces, well suited for application in measurements at short distances.

Funding has provided by ASI, INFM, INFN, and

Cassa di Risparmio di Firenze.

[1] H. Katori, M. Takamoto, V. G. Pal'chikov, and V. D. Ovsiannikov, Phys. Rev. Lett. **91**, 173005 (2003)
[2] M. Takamoto, F.-L. Hong, R. Higashi and H. Katori, Nature **435**, 03541 (2005)
[3] T. Hong, C. Gramer, W. Nagourney, and E. N. Fortson, Phys. Rev. Lett. **94**, 050801 (2005)
[4] R. Santra, E. Arimondo, T. Ido, C. H. Greene, and J. Ye, Phys. Rev. Lett. **94**, 173002 (2005)
[5] A. V. Taichenachev and V. I. Yudin, C. W. Oates, C. W Hoyt, Z. W. Barber, and L. Hollberg, Phys. Rev. Lett. **96**, 083001 (2006)
[6] V. D. Ovsiannikov, V. G. Pal'chikov, A. V. Taichenachev, V. I. Yudin, 20$^{\text{th}}$ EFTF Conference, Braunschweig (2006)
[7] H. Marion, F. Pereira Dos Santos, M. Abgrall, S. Zhang, Y. Sortais, S. Bize, I. Maksimovic, D. Calonico, J. Grünert, C. Mandache, P. Lemonde, G. Santarelli, Ph. Laurent, and A. Clairon, C. Salomon, Phys. Rev. Lett. **90**, 150801 (2003)
[8] A. Quessada, R. P. Kovacich, I. Courtillot, A. Clairon, G. Santarelli and P. Lemonde, J. Opt. B: **5**, 150 (2003)
[9] T. Ido, Y. Isoya, and H. Katori, Phys. Rev. A 61, 061403 (2000)
[10] G. Ferrari, R. E. Drullinger, N. Poli, F. Sorrentino, and G. M. Tino, Phys. Rev. A **73**, 023408 (2006)
[11] G. Ferrari *et al.*, to be published
[12] G. Ferrari, P. Cancio, R. Drullinger, G. Giusfredi, N. Poli, M. Prevedelli, C. Toninelli, and G.M. Tino, Phys. Rev. Lett. **91**, 243002 (2003)
[13] N. Poli, G. Ferrari, M. Prevedelli, F. Sorrentino, R.E. Drullinger, G.M. Tino, Spectrochimica Acta A **63**, 981986 (2006)
[14] R. W. Fox, S. A. Diddams, A. Bartels, and, L. Hollberg, Appl. Opt. **44**, 113, (2005)
[15] I. Courtillot, A. Quessada-Vial, A. Brusch, D. Kolker, G. D. Rovera and P. Lemonde, Eur. Phys. J. D 33, 161-171 (2005)
[16] T. Ido, T. H. Loftus, M. M. Boyd, A. D. Ludlow, K. W. Holman, and J. Ye, Phys. Rev. Lett. **94**, 153001 (2005)
[17] Values are calculated assuming a quantum projection noise limited measurement done with 10^6 free falling atoms at 400 nK with a cycle time of 350 ms.
[18] A. D. Ludlow, M. M. Boyd, T. Zelevinsky, S. M. Foreman, S. Blatt, M. Notcutt, T. Ido, and J. Ye, Phys. Rev. Lett. **96**, 033003 (2006)
[19] A. Brusch, R. Le Targat, X. Baillard, M. Fouché, P. Lemonde, 20$^{\text{th}}$ EFTF Conference, Braunschweig (2006).
[20] Z. W. Barber, C. W Hoyt, C. W. Oates, and L. Hollberg, A. V. Taichenachev and V. I. Yudin, Phys. Rev. Lett. **96**, 083002 (2006)
[21] B.C. Young, F.C. Cruz, W.M. Itano, J.C. Bergquist, Phys. Rev. Lett. **82**, 3799 (1999)
[22] T. Rosenband, private comm.
[23] M. Notcutt, *et al.*, Opt. Lett. **30**, 1815 (2005)
[24] T. Nazarova, U. Sterr and F. Riehle, 20$^{\text{th}}$ EFTF Confererence, Braunschweig (2006).
[25] M. Notcutt, L.-S. Ma, A. D. Ludlow, S. M. Foreman, J. Ye, and J. L. Hall, Phys. Rev. A **73**, 031804(R) (2006)
[26] K. Numata, A. Kemery, and J. Camp, Phys. Rev. Lett. **93**, 250602 (2004)
[27] N. Poli, R. E. Drullinger, G. Ferrari, J. Léonard, F. Sorrentino, and G. M. Tino, Phys. Rev. A **71**, 061403(R) (2005)
[28] S. B. Nagel, C. E. Simien, S. Laha, P. Gupta, V. S. Ashoka, and T. C. Killian, Phys. Rev. A 67, 011401 (2003)
[29] M. Yasuda, T. Kishimoto, M. Takamoto, and H. Katori, Phys. Rev. A **73**, 011403 (2006)
[30] P. G. Mickelson, Y. N. Martinez, A. D. Saenz, S. B. Nagel, Y. C. Chen, T. C. Killian, P. Pellegrini, and R. Côté Phys. Rev. Lett. **95**, 223002 (2005)

Proceedings of the 20th EFTF, 2006

Quantum interference spectroscopy in the vacuum ultraviolet

K.S.E. Eikema,* R.Th. Zinkstok, S. Witte, W. Hogervorst, and W. Ubachs
Atomic, Molecular and Laser Physics Group, Laser Center Vrije Universiteit, De Boelelaan 1081, 1081 HV Amsterdam, the Netherlands

With two experiments on respectively krypton at 2×212 nm and xenon at 125 nm we have demonstrated the method of quantum interference spectroscopy in the deep- and vacuum-ultraviolet. Multiple pulses from a frequency comb laser are amplified and frequency converted and used in a Ramsey-like direct excitation scheme. In the Kr experiment we achieved a 150 kHz accuracy for isotope shift values and a 3.5 MHz accuracy for the absolute transition frequency. With the Xe experiment we demonstrated that the same method can be used in combination with frequency upconversion in a gas without significant distortion of the phase coherence, therefore allowing sub-MHz resolution spectroscopy at VUV and XUV wavelengths.

I. INTRODUCTION

Frequency comb devices based on mode-locked lasers at infrared wavelengths have led to dramatic progress in fields such as ultra-high precision frequency metrology [1, 2], optical clocks [3, 4], and ultrafast laser science [5]. In precision spectroscopy, frequency comb lasers are widely used as a phase-coherent link between the radio-frequency and optical frequency domains. The optical cycles of a stabilized narrow-band continuous wave (cw) laser used for the actual spectroscopy can be phase-locked and counted directly with respect to an absolute frequency standard such as an atomic clock [6, 7]. The resultant frequency measurements approach a precision of 1 part in 10^{15} in certain cases, which can be used e.g. in the search for a possible drift in the fundamental constants [1, 8]. However, many atomic transitions (in e.g. helium and hydrogen-like ions) that are of interest for testing fundamental theories such as quantum-electrodynamics, require excitation with vacuum ultraviolet (VUV) or even extreme ultraviolet (XUV) radiation. Suitable narrow-bandwidth cw sources hardly exist at such short wavelengths [9], while frequency combs operate in the infrared.

New measurement schemes based on excitation of atomic transitions with phase-locked pulse sequences [10–14] may provide a solution. A cw laser is not required anymore, while frequency upconversion through harmonic generation is facilitated by the high peak intensity of the ultrashort pulses. However, upconversion is a potential source for concern, as the interaction of the required gaseous nonlinear medium with such high intensity laser pulses can degrade the pulse-to-pulse phase stability: the harmonic generation process itself [15] as well as competing ionization effects [16] will adversely affect the phase coherence. Still, such upconversion has recently been demonstrated with un-amplified frequency comb lasers, using a gas jet inside an external enhancement cavity [17, 18]. Radiation down to a wavelength of 60 nm at 112 MHz repetition rate [17] was generated, albeit at relatively low power per pulse, and phase coherence was confirmed only at 266 nm through comparison with the third harmonic generated in crystals. Other experiments in the XUV spectral range have qualitatively shown a certain degree of temporal [19, 20] and spatial coherence [21], by upconverting two replicas of a single amplified pulse and recording the resulting interference patterns on a CCD camera. Similarly, frequency domain studies of the phase coherence have also been reported, using pulse pairs created with an interferometer [22, 23] or a birefringent crystal [24]. However, in all these experiments the pulse delay could only be varied on a ∼100 fs timescale, while the phase difference between the pulses could not be measured. As a result, the spectral resolution was limited in all cases to the THz range, which is still far below the requirements of precision spectroscopy.

We have demonstrated that frequency comb spectroscopy can be extended to the VUV with sub-MHz accuracy by amplification and subsequent frequency conversion of trains and pairs of comb laser pulses. We have performed two experiments, respectively on krypton at 2×212 nm and on xenon at 125 nm. In the first experiment we demonstrated the potential of quantum interference spectroscopy in the deep-UV by measuring the absolute transition frequency and the isotope shifts of a transition in Kr. In the second experiment we showed that when comb pulses are upconverted trough harmonic generation in a gas their coherence is not noticeably distorted, by detecting very narrow quantum interference fringes upon excitation of Xe atoms. Furthermore we found that changing the relevant parameters for harmonic generation did not introduce significant phase shifts.

The method employed is related to Ramsey's principle of separated oscillatory fields [25], which probes the phase evolution of an atom in spatially separated interaction zones. This technique is widely used in the RF domain for atomic fountain clocks [26]. By extension, in the optical domain excitation can be performed by pulses separated in time, rather than in space, to maintain phase coherence between the

*Electronic address: kjeld@nat.vu.nl

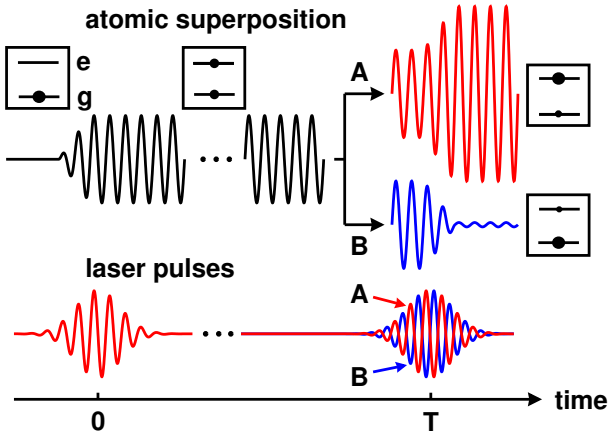

FIG. 1: The principle of quantum interference metrology, time domain picture.

excitation contributions. Several experiments have been performed to investigate Ramsey-type quantum-interference fringes in the optical domain [10, 11, 27–29] and phase-stable amplification of single pulses [30]. Actual quantitative spectroscopy with phase-coherent light pulses has been limited to a few relative frequency measurements on fine and hyperfine structure of atoms [11, 29, 31]; absolute frequency measurements have been frustrated by an unknown phase difference between the pulses or by limited resolution.

II. QUANTUM INTERFERENCE SPECTROSCOPY

In quantum-interference spectroscopy (Fig. 1), an atom is excited by a train of N phase-locked laser pulses, all separated by a time T. The first pulse creates a coherent superposition of the ground and excited state, with an initial phase difference between the states determined by the laser pulse. After the initial excitation, the superposition will evolve freely with a phase velocity $\omega_0 = (E_e - E_g)/\hbar$, where $E_e - E_g$ is the energy difference between the states. After a time T, the next pulse with a controlled phase illuminates the atom, interfering with the atomic superposition. Depending on the phase and the time delay T, the total $|g\rangle \rightarrow |e\rangle$ excitation probability can be either enhanced (case A) or suppressed (case B). The resulting excited state population after the pulse train can be written as:

$$|b_N|^2 = \left| \sum_{n=1}^{N} a_n e^{i(n-1)(\omega_0 T + \varphi)} \right|^2 , \qquad (1)$$

where φ is the phase difference between subsequent laser pulses, and a_n is the excitation amplitude for the n^{th} pulse. Thus $|b_N|^2$ is a periodic function of both the pulse delay T and the phase difference φ. The resonance frequency ω_0 is encoded not just in the amplitude a_n, as with conventional spectroscopy, but also in the phase of the oscillating population signal. At the maxima of the periodic signal, the second laser pulse arrives in phase with the atomic superposition. If the time delay and the pulse-to-pulse phase shift are known, the exact transition frequency can be derived from the position of these maxima. This method can also be considered in the frequency domain (see Fig. 2): a single pulse has a continous frequency spectrum, but an infinite pulse train has a spectrum that consists of sharp modes, spaced by $f_{\text{rep}} = 1/T$. Therefore, scanning T is equivalent with scanning f_{rep}, and the maxima in the oscillating population signal occur when the comb modes are in resonance with the transition. If the time delay and the pulse-to-pulse phase shift are known, the exact transition frequency can be derived from the position of these maxima. Because the transition frequency can now be obtained from the phase of the signal, the measurement is largely insensitive to the laser pulse spectral shape, which only influences the general signal amplitude. Therefore spectral distortions of the laser pulses, due to amplification or harmonic generation, have little influence on the measurement, provided the distortion is identical from pulse to pulse. In contrast, traditional single pulse spectroscopy is strongly affected by chirp [32, 33]. However, the periodicity of the signal with respect to T leads to an inherent ambiguity in the determination of the transition frequency. This ambiguity can be resolved if a previous measurement with an accuracy much better than the repetition frequency exists; otherwise the measurement can be repeated with different repetition rates, as we have done in the Kr experiment discussed below.

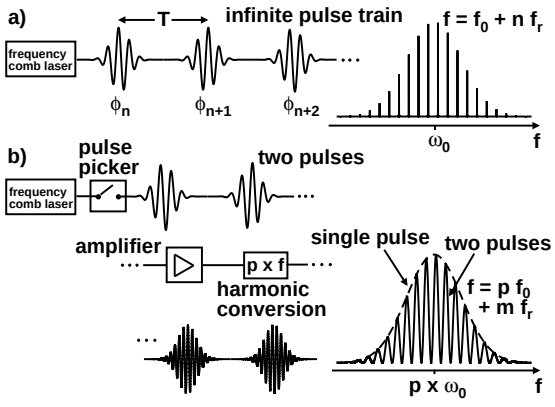

FIG. 2: The principle of quantum interference metrology, frequency domain picture. a) The case for an infinite pulsetrain; b) In our experiments, limited pulse trains or pairs are selected from the laser output, yielding a spectrum with relatively wide fringes.

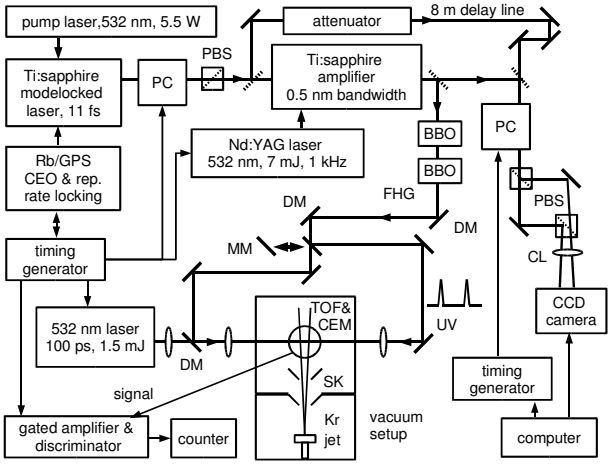

FIG. 3: Schematic of the experimental setup. Details in the text.

III. QUANTUM INTERFERENCE METROLOGY ON KRYPTON

A. Laser system

Fig. 3 shows the setup used for the experiments. The frequency comb is based on a mode-locked Ti:Sapphire oscillator that emits 7 nJ pulses with a FWHM-bandwidth of about 90 nm, centered at 800 nm, and with an adjustable repetition rate between 60.9 and 79 MHz. For frequency accuracy, both the repetition rate and the phase of the pulses are locked to a Global Positioning System-disciplined Rb atomic clock [34–37]. An electro-optic modulator (EOM) is used to select two or three consecutive pulses from the mode-locked pulse train. These pulses are amplified in a six-pass Ti:Sapphire amplifier to an energy of about 15 μJ/pulse. We employ a non-saturating amplifier, as standard amplifiers that operate in saturated mode (to reduce output power fluctuations) can amplify only one pulse. In this experiment, the number of pulses that can be amplified is limited to three by the EOM, which has to be switched off before any backreflections from the amplifier can reach the oscillator. For the xenon experiment described below, this restriction has been removed. Spectral filtering is applied in the amplifier to limit the bandwidth of the amplified pulses to <0.5 nm. This filtering reduces the complexity of the signal, as only a single transition will be excited (see below).

B. Amplifier-induced phase shifts

The amplification process gives rise to a small phase shift (∼100-200 mrad) between the pulses, which we can measure with a 1σ accuracy of 25 mrad ($< 1/250$ of an optical cycle). These measurements are performed by placing the amplifier in one arm of a Mach-Zehnder interferometer and recording spatial interferograms on a CCD camera (see Fig. 4). An electro-optic modulator (EOM) and polarizing optics were used to project the interference patterns for two consecutive pulses simultaneously and vertically displaced from one another on the CCD camera; a snapshot is shown in the upper right corner of Fig. 4. The relative positions on the CCD (up or down) were alternated by switching the EOM, in order to cancel out any misalignment effects. The thin lines in Fig. 4 show the measured phases of these interferograms. The relative phase shift to the comb laser was then determined by looking at the phase difference in both projection situations, which is a square wave (the thick line in the figure), due to the projection switching. Its peak-to-peak amplitude is twice the magnitude of the pulse-to-pulse phase shift introduced by the amplifier.

C. Atomic beam setup

To demonstrate high frequency quantum-interference metrology in the deep-UV we selected the $4p^6 \rightarrow 4p^5 5p[1/2]_0$ two-photon transition in krypton at a frequency of $\omega_0/2\pi = 2821$ THz. The required wavelength of 212.55 nm for the two-photon krypton resonance was obtained by fourth-harmonic generation of the amplifier output at 850.2 nm through sequential frequency doubling in two BBO crystals. The resultant 212.55 nm pulses (1.6 μJ) were focused in a highly collimated atomic beam of

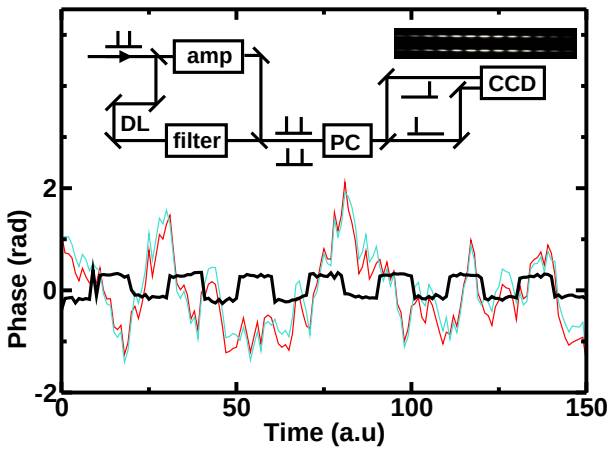

FIG. 4: Amplifier phase shift measurements and a schematic of the setup used. DL: delay line, amp: Ti:Sapphire amplifier, filter: attenuation and 0.5 nm spectral filtering to match the spectrum and divergence of the aplifier output, EOM: electro-optic modulator, CCD. A camera snapshot of the measured interference fringes is shown in the top right. The thin lines in the graph are the phases retrieved from these two interferograms, and the thick line represents the difference of the two.

krypton. The excited state population was probed by a delayed 532 nm ionization pulse (1.5 mJ, 100 ps) from a Nd:YAG laser-amplifier system, after which ions are detected in a time-of-flight tube capable of clearly resolving the various Kr isotopes. The whole experiment is repeated at 1 kHz. As both the ground and excited state of the transition are J=0 states, the atoms can be considered as two-level systems. In general, multiple magnetic sublevels can be present, which may complicate the signal if stray magnetic fields are not properly shielded.

The isotope shift and the absolute transition measurements described below can be influenced by a possible systematic Doppler shift as a result of non-perpendicular excitation. Therefore all measurements were performed from two opposite sides, with the average taken to determine the Doppler-free signal. The Doppler shift can in principle be reduced on a two-photon transition by measuring with colliding pulses from opposite sides. This arrangement also enhances the signal, as was seen experimentally. However, contrary to cw spectroscopy, Doppler-free signal (photons absorbed from opposite sides) and Doppler-shifted signal (two photons from one side) cannot be distinguished properly in the case of excitation with two ultrashort pulses, because the large bandwidth always contains a resonant frequency. This situation might lead to a calibration error when there is an imbalance in signal strength from opposite sides.

The total Doppler shift can only be determined modulo the repetition rate. The difference in Doppler shift for the isotopes, which is on the order of a few hundred kHz, therefore provides a valuable initial estimate of about 25 MHz for this shift. From the measurement of the absolute positions, one can then determine the Doppler shift for each of the counter-propagating beams, which in this case was 29 MHz.

D. Experimental results

The data depend on the number of phase-locked pulses used to excite the transition (Fig. 5A). The pulse delay T was scanned on an attosecond timescale by changing the comb laser repetition frequency, which is near 75 MHz. With a single pulse the excitation probability is constant. With two pulses a clear cosine oscillation is observed, with a contrast reaching 93%. Three pulse excitation gives the pulse-like structure predicted by eq. 1 ($N = 3$), as well as an expected narrowing by 3/2 compared to two pulse excitation. The solid lines are fits using eq. 1, including an additional amplitude scaling factor to account for signal strength variations between the traces. In the three-pulse case, we took into account that the amplitude contribution of the pulses is not exactly equal, due to spontaneous emission of the 5p state (lifetime is 23 ns) and differences in energy between the three pulses (energy ratio pulse 1 : pulse 2 : pulse 3 = 1.0 : 0.91 : 0.6; in all measurements with two pulses, the pulse energies have been kept equal to within about 5%). The dependence on the pulse-to-pulse (carrier-envelope) phase shift φ_{CE} (Fig. 5B) is in complete agreement with expectations: the interference signal moves by one fringe when φ_{CE} is scanned through a complete cycle.

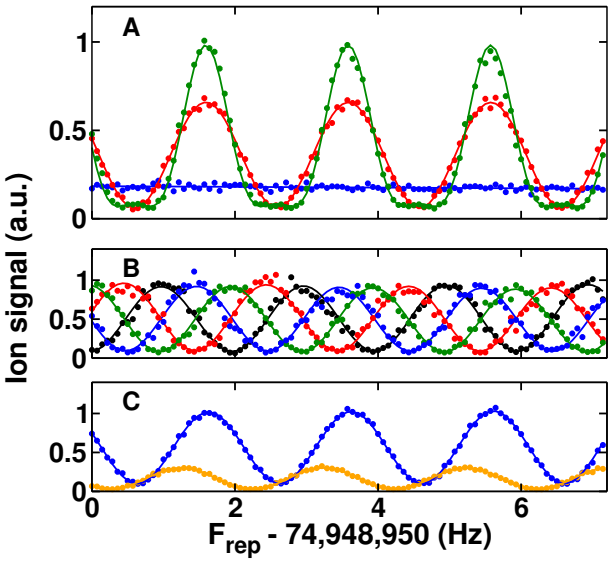

FIG. 5: Demonstration of quantum-interference metrology. A: ^{84}Kr signal as a function of the repetition rate of the comb laser for one, two, and three pulses 13.3 ns apart. The solid lines are fits to the theory (see text). B: Measurement of the quantum-interference signal for various phase differences between two excitation pulses, with the pulse-to-pulse phase shift as seen by the atom set to $0, \pi/2, \pi$ and $3\pi/2$, respectively. C: Measurement of the isotope shift between ^{84}Kr and ^{86}Kr (lower amplitude trace). The isotope shift can be determined modulo 75 MHz from the phase shift between these two simultaneously recorded scans.

Isotope shifts can be measured straightforwardly. The broad spectrum of the pulses places a frequency ruler on all isotopes simultaneously, so spectra of ^{80}Kr through ^{86}Kr could be acquired at the same time (Fig. 5C). The measurements of Kaufman [38] were used for identification of the proper comb line for each isotope. The resulting shifts (^{84}Kr − ^{X}Kr), based on at least 6 measurements per isotope, are: 302.02 (28) MHz (^{80}Kr), 152.41 (15) MHz (^{82}Kr), 98.54 (17) MHz (^{83}Kr), and −135.99 (17) MHz (^{86}Kr). The values are in good agreement with those reported by Kaufman [38], while the stated uncertainties (1σ) are between 20 and 40 times smaller than the 6 MHz uncertainty there.

In the measurement of the absolute transition frequency, an additional issue is the determination of the mode that corresponds to the true position of the resonance. The most accurate measurement to date [40] has an uncertainty of 45 MHz, which is not sufficient to assign the mode with confidence. Therefore measurements were repeated at repetition rates near

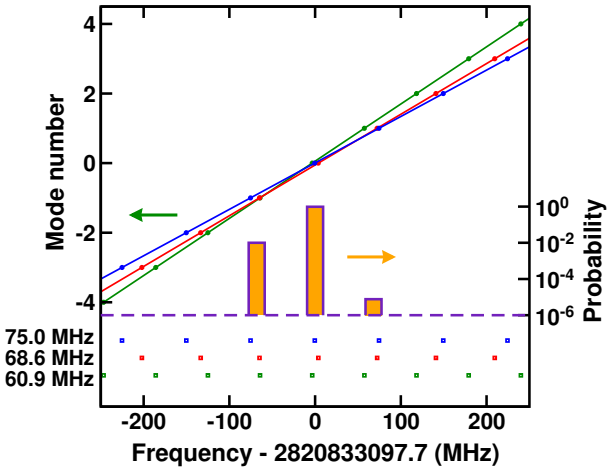

FIG. 6: Absolute calibration of the $4p^6 \rightarrow 4p^5 5p[1/2]_0$ transition in krypton. The bars (logarithmic scale) show the normalized statistical probability per mode for each measured mode position, revealing the location of the most probable coincidence.

60.9 MHz, 68.6 MHz and 75.0 MHz to find the point at which the measurements coincide. We performed 4 to 9 measurements at each repetition rate, and the results are shown in Fig 6. There are two systematic effects that dominate the determination of the resonance frequency: the phase shifts induced by the amplifier (100-200 mrad in the infrared, see section III B), and the residual Doppler shift (2 MHz) due to possible misalignment of the counter-propagating beams. Other effects include light-shifts (0.47 ± 0.44 MHz), static field effects ($\ll$ 100 kHz), the second order Doppler shift ($\sim$1 kHz), and a recoil shift (209 kHz). The phase shift due to the pulse-picker electro-optic modulator is negligible (<5 mrad) when it is aligned such that it acts as a pure polarization rotator, which we verified experimentally. The phase shift due to frequency doubling is negligible as well, being estimated on the order of a mrad in the UV, based on the model of [39]. After correction of the data for these effects, there were 3 sets of possible positions for the 5p resonance transition (Fig. 6). The measurements have one clear coincidence (with an estimated probability of 98%, based on a statistical uncertainty of 2.5 MHz for each data point) near the literature value. Combining the three sets leads to an absolute frequency of 2,820,833,097.7 MHz with a 1σ uncertainty of 3.5 MHz (statistical and systematic errors combined), which is an order of magnitude smaller than the previous determination using single nanosecond laser pulses [40].

IV. QUANTUM INTERFERENCE SPECTROSCOPY ON XENON

A. Experimental setup

In order to demonstrate the potential of quantum interference spectroscopy at even shorter wavelengths, in the vacuum ultraviolet and beyond, we have performed a second experiment in which we employed harmonic generation in a gas. This time, the $5p^6\ {}^1S_0 \rightarrow 5p^5\ ({}^2P_{3/2})\ 5d[1/2]_1$ transition at 2.398×10^{15} Hz (125 nm) in xenon was excited. To this end, we altered some parts of the setup described in the previous section. A second EOM was added so either one pulse, two pulses separated by an integer number of oscillator roundtrip times, or a pulse train consisting of up to six pulses could be selected from the frequency comb output. The Ti:Sapphire amplifier was tuned to 750 nm and an extra pass through the crystal was added, yielding about 25 μJ per pulse while clipping the spectrum to a width of 0.7 nm. The amplified pulses were frequency doubled in a BBO crystal, and the resulting 10μJ pulses at 375 nm were focused into a gas cell filled with either oxygen or acetylene, to generate the third harmonic at 125 nm (see Fig. 7). Since phase-matching is not possible at this wavelength due to a positive phase-mismatch in most gases, we focused the UV pulses through a 0.1 mm pinhole, and employed differential pumping to create a sudden pressure drop across the pinhole. This provides the asymmetry necessary for third harmonic generation (THG), producing about 50 fJ per pulse at 125 nm. After the pinhole, the VUV radiation was collimated using a MgF_2 lens and perpendicularly intersected a beam of xenon atoms. The VUV intensity was monitored using a channel electron multiplier (Dr. Sjuts Optotechnik GmbH) behind a VUV filter. A second differentially pumped gas cell in front of the MgF_2 lens ensured a steady gas flow away from the lens, to prevent contamination of its surface. The atomic beam setup and the ioniza-

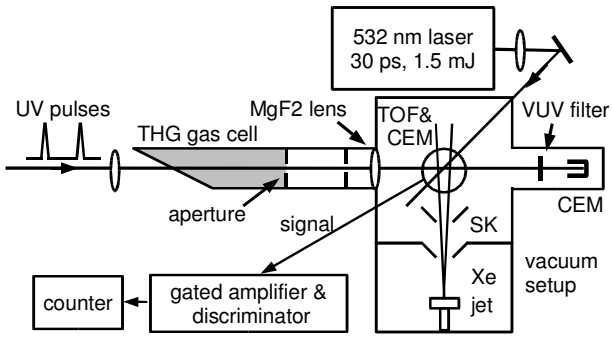

FIG. 7: The setup used for VUV quantum interference spectroscopy on xenon. CEM, channel electrom multiplier, TOF, time-of-flight mass spectrometer. THG, third harmonic generation.

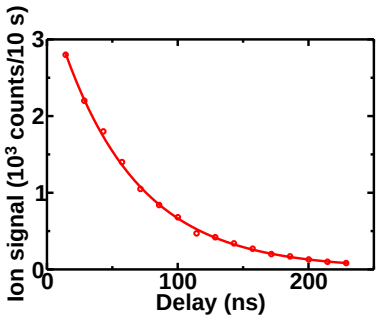

FIG. 8: The single pulse signal shows the lifetime decay curve of the $5p^5$ ($^2P_{3/2}$) $5d[1/2]_1$ level in Xe

tion/detection scheme needed only slight changes to accomodate the Xe atoms. We measured the lifetime of the $5p^5$ ($^2P_{3/2}$) $5d[1/2]_1$ state very precisely using a single VUV excitation pulse and scanning the time delay of the ionization pulse. Fitting the obtained exponential decay curve (see Fig 8) yields a value of 58.9 (1.3) ns, which compares well with theoretical estimates [41].

B. Excitation with pulse trains

Again, quantum interference in the excitation process is seen when two VUV pulses are used and the time delay between them is scanned: the results are shown in the first panel of Fig 9a. To increase the frequency resolution, more pulses are added, this time up to six pulses. The fringes retain the 74.8 MHz period, and narrow down as expected. However, the amplifier introduces slightly different phase shifts within the pulse train (varying by a few hundred mrad). As a result, the excitation contributions of later pulses cause small shifts of the fringe position and an asymmetry in the fringe shape (see Fig 9(a)), which hampers an accurate determination of the transition frequency. To obtain maximum contrast, the intensity of the VUV pulses should be matched to the surviving amplitude in the excited state, which would require an independent control over the intensity of the individual VUV pulses. In the present situation the later pulses contribute less to the final excitation amplitude, which slows down the narrowing of the interference fringes: ideally, the six-pulse train for example should yield about 11.5 MHz wide fringes, while the measured width is 16.9 MHz. Furthermore, intensity variations in the pulse train are a cause for concern as the phase of harmonics generated in a gas might be influenced by processes such as ionization and dissociation that create a time dependent refractive index [24]. Pulse intensity jitter can then lead to differences in the degree of ionization of the harmonic gas, possibly causing detrimental phase fluctuations that do not occur when crystals are used (see the Kr experiment described above). Although the presence of high-contrast interference fringes in Fig. 9 demonstrates that such phase fluctuations are not very large for the THG process in a gas these effects are difficult to measure quantitatively in longer pulse trains.

C. Excitation with pulse pairs

A simple solution that enables the determination of such unknown phase shifts without loss of resolution is to use pulse pairs instead of longer pulse trains. The advantage of using two pulses is that phase shifts between only two pulses caused by the amplifier system can be measured with high accuracy (see section III B), and that phase shifts in the THG process will be visible as a simple shift of the quantum interference pattern. Note that the frequency resolution of a pulse pair spaced by e.g. 67 ns is similar to what can be obtained with a pulse train of six pulses spaced by 13.4 ns. This is demonstrated in Fig 9(b), where a series of pulse pair measurements with delays ranging from 13.4 to 67 ns is shown. The narrowest resonance that is observed has a full width at half maximum (FWHM) of 7.5 MHz, which is a 13-fold improvement compared to any other measurement performed so far at such short wavelengths using nanosecond pulsed lasers [42] or cw lasers [9]. The frequency resolution demonstrated in this measurement is 3×10^{-9}, constituting an improvement of about 6 orders of magnitude compared to previous experiments using Michelson interferometers and ultrashort pulses [22, 23]. The decrease in fringe contrast with increasing T as seen in Fig. 9(b) can be explained with a model that includes the measured pulse intensity ratios, the lifetime of the upper state, and the Doppler width, the latter being the dominant factor. By investigating transitions to longer-lived states, and reduction of the Doppler width through e.g. cooling techniques and confinement in an ion trap, much narrower fringes can in principle be measured with high contrast using this method. But even from a relatively low-contrast interferogram as shown in the bottom panel of Fig. 9(b) the fringe position can be extracted reliably, since the rapid sine wave oscillation allows to fit many periods simultaneously.

The control over the measurement resolution by changing the pulse delay can be used to overcome the ambiguity in the determination of the right mode when absolute frequencies are to be measured. An initial measurement with sufficiently short time delay T allows identification of the mode by comparison with existing low-resolution data. Here we demonstrate (Fig. 9b) that the measurement accuracy can be improved by increasing T to zoom in on the transition, while keeping track of the previously determined excitation mode. This is illustrated by the dotted line in Fig. 9(b). Apart from the normal systematic effects in laser spectroscopy (e.g. Doppler shift and AC Stark shift), the amplifier phase shift error (6×25 mrad) to-

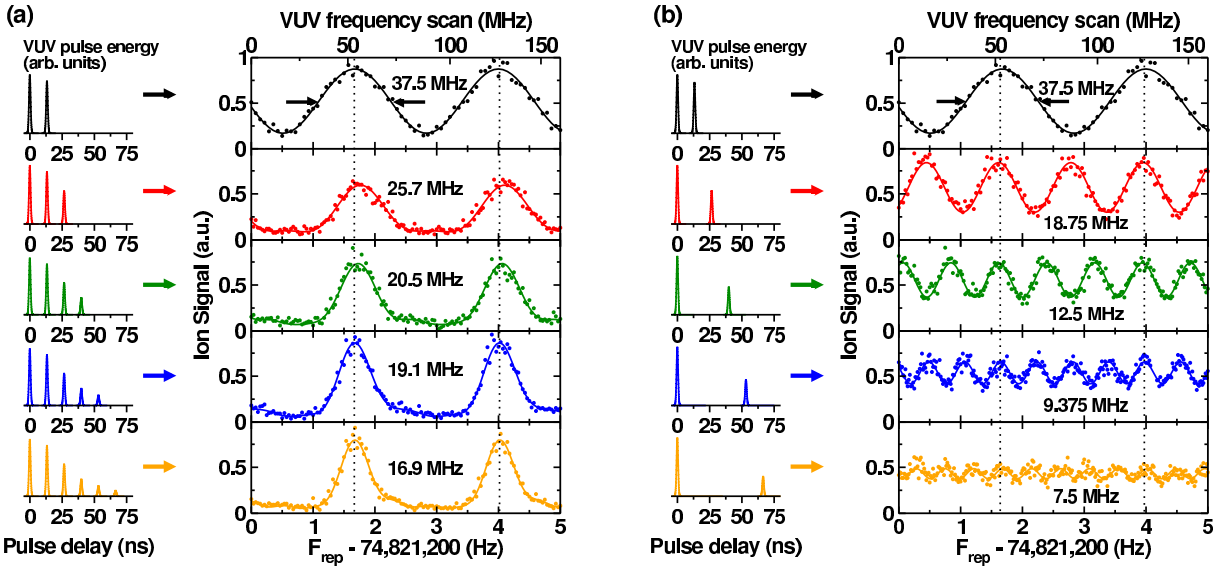

FIG. 9: Quantum interference signals at 125 nm in ^{132}Xe. (a) Measured signals using a VUV pulse train of increasing length. (b) Measured signals using two VUV pulses with increasing delays. Relative pulse intensities and time delays are shown on the left of the graphs, and the width of the resonances (FWHM) is denoted in each panel. The solid lines represent fits to model interference pattern functions, allowing for an intensity difference between the excitation pulses, as well as a varying pulse-to-pulse phase shift $\Delta\varphi$ in graph (a) due to the amplifier (see text). The upper panel is identical in both graphs, as all data was acquired during the same measurement run.

gether with the statistical fit uncertainty amount to an error in the VUV of about 1 MHz for $T = 13.4$ ns. As the pulse delay increases, the influence of the amplifier phase shifts is progressively reduced inversely proportional to T. For example, at $T = 67$ ns the uncertainty due to phase shifts and the fitting procedure has improved to 270 kHz (1×10^{-10} accuracy). The absolute transition frequency has not been calibrated here, as no spectroscopic data with sufficient accuracy for mode identification exists at present for the studied xenon transition, in contrast to the experiment Kr experiment. As this transition in itself is of no fundamental spectroscopic importance, no further efforts were undertaken to perform an initial calibration by traditional means.

However, if absolute frequency measurements are to be performed the possibility of a systematic phase shift caused by the THG process needs to be investigated precisely. We have done this by systematically varying the parameters relevant to THG, in particular the gas pressure and laser intensity. The xenon atoms are now used as high-resolution VUV phase detectors, by recording two-pulse interferograms with 13.365 ns time delay at various gas pressures and laser intensities. Fig. 10 shows the retrieved phases when using oxygen (O_2) for THG. Linear fits to both curves yield slopes of -0.12 (0.29) mrad/mbar (corresponding to -1.5 (3.4) kHz/mbar at the VUV frequency) and -8.7 (5.8) mrad/μJ (-104 (70) kHz/μJ), respectively (1σ error bars). Hence, no real phase shifts are observed within 1/30th of a VUV cycle, even though the VUV intensity changes by an order of magnitude and shows signs of saturation. We repeated these mea-

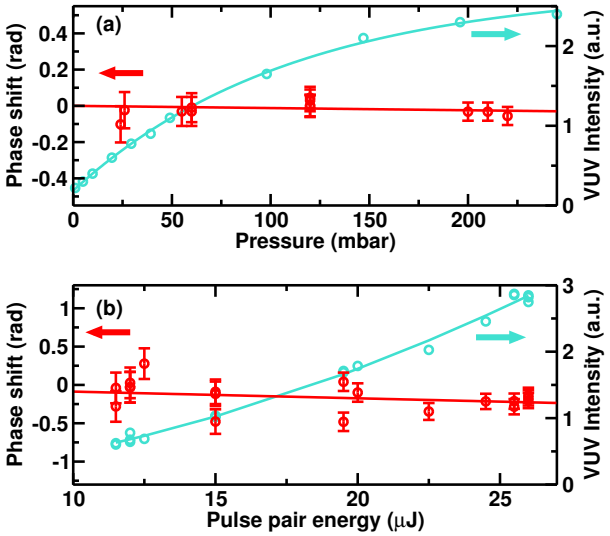

FIG. 10: Dependence of the relative phase between the VUV pulses on the THG process in O_2. Measurements of the phase shift of the quantum interference signals in xenon (as shown in Fig. 9), using two VUV pulses (a) as a function of the O_2 pressure in the gas cell. (b) as a function of incident laser pulse energy (sum of the two pulses). The phase shift is set to zero at zero intensity and pressure. The light blue curves indicate the generated VUV intensity.

surements using acetylene as the nonlinear medium, which already saturates at a pressure below 1 mbar, but displays a maximum THG efficiency at 10 mbar, comparable to O_2 at about 200 mbar. Also with acetylene, no phase shift is observed within the measurement resolution. This ensures that when a sufficiently long time delay between the pulses is used, a sub-MHz resolution can indeed be achieved.

V. CONCLUSION

With the experiments described here, we have demonstrated the use of quantum interference spectroscopy in the deep-UV and VUV. It is shown that absolute frequency measurements with a MHz accuracy and relative frequency measurements with a $\sim$ 100kHz accuracy can be performed at such short wavelengthts. Furthermore, we have demonstrated that frequency combs can be transferred to the VUV by harmonic up-conversion in a gas while distortion of the phase coherence between subsequent comb pulses is well within 1/30th of a VUV cycle. Therefore we conclude that quantum interference is a powerful tool for high-resolution spectroscopy at VUV and shorter wavelengths, possibly even down to the soft-X-ray regime when a more powerful amplifier is used. In addition, separate pump pulses could be used to increase the time delay between the VUV pulses, potentially improving the resolution to the kHz level. In the near future, we plan to perform measurements on the $1s^2 \rightarrow 1s2s$ two-photon transition at 2×120 nm in helium with a target accuracy of $\sim$500 kHz, which would lead to two orders of magnitude improvement in the determination of the ground state Lamb shift [9]. Applying the technique of quantum interference spectroscopy to trapped ions may lead to the emergence of a new generation of ultra-precise clocks, operating in the XUV domain.

Acknowledgments

This project is financially supported by the Foundation for Fundamental Research on Matter (FOM), the Netherlands Organization for Scientific Research (NWO), and the EU Integrated Initiative FP6 program.

[1] M. Fischer *et al.*, Phys. Rev. Lett. **92**, 230802-1 (2004).
[2] H.S. Margolis *et al.*, Science **306**, 1355 (2004).
[3] M. Takamoto, F.-L. Hong, R. Higashi, and H. Katori, Nature **435**, 321 (2005).
[4] S.A. Diddams *et al.*, Science **293**, 825 (2001).
[5] M. Hentschel *et al.*, Nature **414**, 509 (2001).
[6] M. Niering *et al.*, Phys. Rev. Lett. **84**, 5496 (2000).
[7] Th. Udem *et al.*, Phys. Rev. Lett. **86**, 4996 (2001).
[8] J. P. Uzan, Rev. Mod. Phys. **75**, 403 (2003).
[9] K.S.E. Eikema, J. Walz, and T.W. Hänsch, Phys. Rev. Lett. **86**, 5679 (2001).
[10] R. Teets, J. N. Eckstein, T. W. Hänsch, Phys. Rev. Lett. **38**, 760 (1977).
[11] M. Bellini, A. Bartoli, T. W. Hänsch, Opt. Lett. **22**, 540 (1997).—
[12] S. Witte, R.Th. Zinkstok, W. Ubachs, W. Hogervorst, and K.S.E. Eikema, Science **307**, 400 (2005).
[13] A. Marian, M.C. Stowe, J.R. Lawall, D. Felinto, J. Ye, Science **306**, 2063 (2004).
[14] A. Marian, M.C. Stowe, D. Felinto, and J. Ye, Phys. Rev. Lett. **95**, 023001 (2005).
[15] H.J. Shin *et al.*, Phys. Rev. A **63**, 053407 (2001).
[16] P.B. Corkum, Phys. Rev. Lett **71**, 1994 (1993).
[17] C. Gohle *et al.*, Nature **436**, 234 (2005).
[18] R.J. Jones, K.D. Moll, M.J. Thorpe, and J. Ye, Phys. Rev. Lett. **94**, 193201 (2005).
[19] C. Lyngå *et al.*, Phys. Rev. A **60**, 4823 (1999).
[20] M. Bellini *et al.*, Phys. Rev. Lett. **81**, 297 (1998).
[21] R. Zerne *et al.*, Phys. Rev. Lett. **79**, 1006 (1997).
[22] M. Kovačev *et al.*, Phys. Rev. Lett. **95**, 223903 (2005).
[23] S. Cavalieri, R. Eramo, M. Materazzi, C. Corsi, M. Bellini, Phys. Rev. Lett. **89**, 133002 (2002).
[24] P. Salières *et al.*, Phys. Rev. Lett. **83**, 5483 (1999).
[25] N. F. Ramsey, Phys. Rev. **76**, 996 (1949).
[26] A. Clairon, C. Salomon, S. Guellati, W. D. Phillips, Europhys. Lett. **16**, 165 (1991).
[27] M. M. Salour, C. Cohen-Tannoudji, Phys. Rev. Lett. **38**, 757 (1977).
[28] M. M. Salour, Rev. Mod. Phys. **50**, 667 (1978).
[29] M.J. Snadden, A.S. Bell, E. Riis, A.I. Ferguson, Opt. Comm. **125**, 70 (1996).
[30] A. Baltuška *et al.*, Nature **421**, 611 (2003).
[31] J. N. Eckstein, A. I. Ferguson, T. W. Hänsch, Phys. Rev. Lett. **40**, 847 (1978).
[32] K. S. E. Eikema, W. Ubachs, W. Vassen, W. Hogervorst, Phys. Rev. A **55**, 1866 (1997).
[33] S. D. Bergeson *et al.*, Phys. Rev. Lett. **80**, 3475 (1998).
[34] D. J. Jones *et al.*, Science **288**, 635 (2000).
[35] R. Holzwarth *et al.*, Phys. Rev. Lett. **85**, 2264 (2000).
[36] A. Apolonski *et al.*, Phys. Rev. Lett. **85**, 740 (2000).
[37] S. Witte, R. Th. Zinkstok, W. Hogervorst, K. S. E. Eikema, Appl. Phys. B **78**, 5 (2004).
[38] V. Kaufman, J. Res. Natl. Inst. Stand. Technol. **98**, 717 (1993).
[39] R. DeSalvo *et al.*, Opt. Lett. **17**, 28 (1992).
[40] F. Brandi, W. Hogervorst, W. Ubachs, *J. Phys. B* **35**, 1071 (2002).
[41] A.V. Loginov, and P.F. Gruzdev, Opt. Spectrosc. **41**, 104 (1976).
[42] Th.A. Paul, and F. Merkt, J. Phys. B: At. Mol. Opt. Phys. **38**, 4145 (2005).

Proceedings of the 20th EFTF, 2006

A Compact High Stability Optical Clock Based on Laser-Cooled Ca

C. W. Oates,* Y. Le Coq, G. Wilpers †, and L. Hollberg
National Institute of Standards and Technology 325 Broadway Boulder, CO 80305 USA

We report new measurements and modifications for a simple, compact, Ca atomic clock at 657 nm. External measurements were made against an independent Yb lattice optical clock via a fs-laser frequency comb. These results lead to upper limits for the Ca clock instability that are competitive on short time scales with the best existing atomic standards.

I. INTRODUCTION

This is an exciting time in the field of optical atomic clocks. Not only have the optical clocks been demonstrating higher stability than their microwave counterparts [1], but they are beginning to show excellent reproducibility as well [2]. Very accurate clocks will find important applications in precision metrology as well as enabling a possible redefinition of the second. However, widespread applications (space navigation, communications, etc.) may benefit more from the precise timing that results from high stability rather than extreme accuracy. It is perhaps timely to consider how such applications might access the timing revolution that is promised by the optical sources.

The problem of transferring the high stability of the optical clocks to the more tractable microwave domain has already been addressed by the fs-laser frequency comb [3]. But the challenge of getting the stable light (or microwaves) to the end users still remains. This challenge is particularly daunting since most optical atomic clock apparatus are fairly complicated, sometimes covering multiple optical tables. One approach is to keep the clocks at a few sites and then to disseminate the stable time through optical fibers. This possibility is under investigation, but will require significantly more infrastructure than currently exists to disseminate high stability clocks with high fidelity [4]. An alternative approach, considered here, is to make a compact optical clock that can be transported to the location where it is needed.

The idea of transportable optical clocks based on atoms in beams or molecules in vapor cells has been investigated previously [5, 6]. Here we describe a system based on laser-cooled atoms that could achieve the goal of transportability while still achieving extremely low instability (approaching 10^{-15} at 1 s). This system uses the clock transition at 657 nm in neutral calcium, which has been studied by various groups for over 25 years now. Previous demonstrations in our lab and at PTB used two stages of laser cooling to reduce the atom temperature to 10 microkelvin in order to achieve an absolute frequency uncertainty of 10^{-14} or below [7, 8]. In this paper we describe a simpler version of this clock that can still achieve high stability (albeit with higher systematic uncertainty) but with an apparatus whose size could be reduced to the transportable level. In contrast to state-of-the-art lattice-based [9] or trapped-ion clocks [2], which have measurement cycle times of 100's or 1000's of ms, our system has a cycle time of 3.5 ms, which reduces problems associated with cavity noise and simplifies the apparatus. Internal measurements on an earlier version of a compact Ca clock led to an estimated fraction frequency instability of 4 x 10^{-15} at one second [10]. Here we present independent measurements of the performance of a recent version of this clock, which show an upper limit for the fractional frequency instability of 3 x 10^{-15} at one second, averaging down to the mid 10^{-16} range at 200 s.

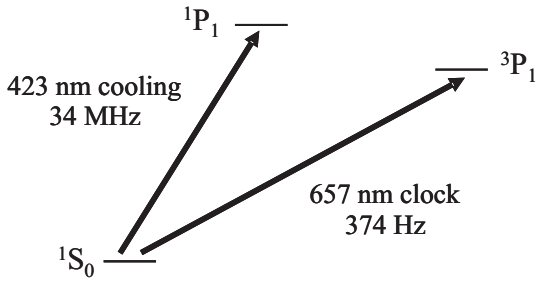

FIG. 1: Partial energy level scheme for neutral ^{40}Ca, showing transitions relevant to the Ca optical frequency standard.

II. EXPERIMENTAL APPARATUS

The experimental setup has been described in detail in earlier publications [10, 11], but here we summarize the apparatus and describe recent modifications. The $^1S_0$ (m=0)→ $^3P_1$ (m=0) intercombination line at 657 nm (see Figure 1) is well-suited for a frequency standard due to its narrow linewidth (374 Hz), convenient wavelength, and inherent insensitivity to external perturbations. In order to reduce first-order Doppler uncertainties, we use laser cooling to reduce the temperature of the atomic sample to 2 mK before performing the clock spectroscopy. The atoms are then excited with a diode laser whose frequency is pre-stabilized by locking it tightly to a narrow fringe of an environmentally isolated Fabry-Perot cavity. The

†present address National Physical Laboratory, Teddington, Middlesex, TW11 0LW, United Kingdom
*Electronic address: oates@boulder.nist.gov

resulting spectroscopic signals from the clock transition are then used to fix the frequency of the clock laser on the center of the atomic transition.

Since it is necessary to extinguish the laser cooling light before performing the spectroscopy (to minimize light-induced shifts of the clock frequency), we employ a sequential measurement cycle. The cycle commences with a loading period (3 ms duration) during which we fill a magneto-optic trap based on the strong cooling transition at 423 nm with atoms from a thermal calcium beam. The resulting atomic sample contains roughly 5 x 10^6 atoms and has a (near Doppler-limited) temperature of 2 mK. The cooling light is generated by doubling the frequency of the light from a semiconductor laser system at 846 nm to produce 40 mW of light at 423 nm.

The atoms are then released to expand ballistically and excited by a four-pulse Bordé-Ramsey sequence [12]. With this method the atoms are first illuminated by a pair of pulses (separated in time by a duration, T) from one direction, and then are immediately illuminated by a second pair from the opposite direction. This pulse sequence leads to a sinusoidal excitation probability with a period of 1/(2T). This spectroscopic technique enables high resolution while maintaining a high signal-to-noise ratio. The degree of excitation induced by probe pulse sequence is read out by a single near-resonant pulse at 423 nm, which measures (with a high signal-to-noise ratio) fluorescence from the depleted ground state.

The red probe laser power (12 mW) is about one third that used in ref. [10] due to the demise of a high power optical amplifier at 657 nm. We partially offset this loss by using a beam with a $(1/e)^2$ diameter of only 3.3 mm. We also have added a Zeeman slower to our apparatus, which increases the loading rate of atoms into our trap by a factor of five. Since we no longer chop a linear (or quadrupole) magnetic field in this present version, we have been able to reduce power supply line noise that was written on to our atom number via the magnetic field. Another modification to the setup described in [10] is the addition of 657 nm velocity probes in all three dimensions. These probes enable us to minimize atomic cloud drift velocities thereby rendering the setup less sensitive to drifts in laser beam alignment. Reduction of the cloud drift velocity should enable the clock to be more stable on long time scales.

III. POTENTIAL ADVANTAGES OF A SHORT CLOCK CYCLE

The Bordé-Ramsey sequence described in the previous section takes about 0.5 ms, yielding a total measurement time of 3.5 ms. While our short measurement time means that the achieved line Q is lower than that of some other cold atom clocks, there are several potential advantages to the short cycle. First, because the vast majority of the atoms do not have time to leave the trap volume during the spectroscopy, they can be recaptured by the next trap cycle. This recycling of the atoms leads to a large number of atoms with a short loading time. The large number of atoms yields a high signal-to-noise ratio for the spectroscopic signals.

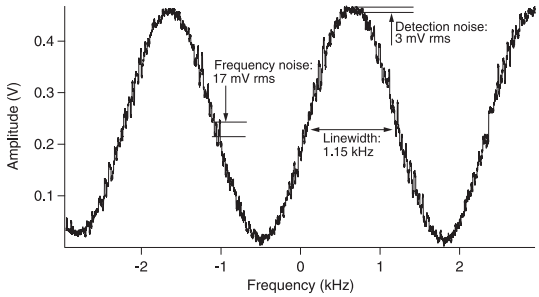

FIG. 2: The central fringes of the Bordé-Ramsey signal taken with a resolution of 1.15 kHz. The signal is the result of a single 2 s scan (no averaging) with a measurement time of 3.5 ms per point.

A second advantage of the short measurement cycle is that we can potentially have reduced frequency noise. The fairly large servo bandwidth (> 150 Hz) for correcting reference cavity fluctuations greatly relaxes the performance requirements for the optical cavities - we can operate the clock in the presence of residual seismic noise below 5 Hz (and large thermally driven cavity drifts) without significant concern. Minimizing the duration of the loading cycle also reduces the optical Dick effect [13], which aliases noise from higher Fourier frequencies into the spectroscopic signal. Finally, thermal noise levels for optical reference cavities [14], which may limit the achievable noise floor for lasers locked to such cavities, are predicted to be lower at higher Fourier frequencies (for the calcium clock, the relevant frequencies are around 1 kHz). Perhaps it will be possible to reduce deleterious effects of fundamental thermal noise in optical cavities by locking rapidly to atoms.

A third advantage of the short cycle is that the atom trap fluctuations are much smaller on the millisecond scale than they are on the second scale. For a modulation frequency of 160 Hz, we find that we can run the clock without needing to normalize against shot-to-shot trap number fluctuations. This simplifies the apparatus and reduces the amplitude noise.

IV. MEASUREMENTS OF THE CLOCK STABILITY

Shown in Figure 2 is the spectroscopic signal taken at our usual working resolution of 1.15 kHz. From this signal we estimate an amplitude noise level limit to the frequency instability of 1 x 10^{-15} at 1 s for the Allan Deviation, with a frequency noise level 5-

6 times higher. Since the majority of the frequency noise is measured to be around 50-60 Hz, we should expect some suppression of this noise due to our high bandwidth. For an external evaluation of the Ca clock performance, we sent light from the Ca-stabilized laser to a fs-laser comb that was locked to a Yb lattice-based clock [15], which also has high stability. The noise introduced by the fibers transporting the light from the standards to the combs was measured and actively cancelled. In Figure 3 we show the measured fractional frequency instability for the beat between the Ca light and the nearest comb tooth for averaging times from 1 to 400 s.

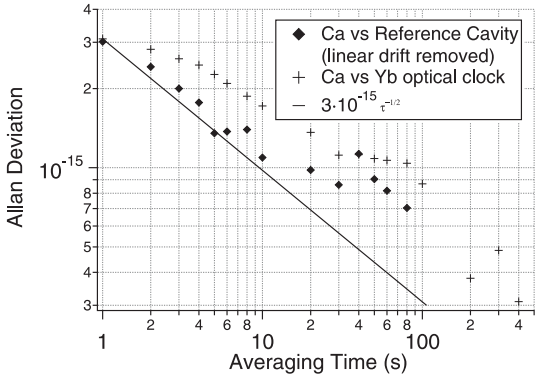

FIG. 3: Allan Deviation of the beatnote between the Ca and Yb optical clocks (crosses). Also shown (diamonds) is the Allan Deviation for the beatnote between the Ca clock and Yb clock laser locked to its reference cavity (with the linear drift removed). For reference we have included a solid line showing an Allan Deviation of 3 x $10^{-15}\tau^{-1/2}$.

Since the Yb clock servo system has an attack time of several seconds, the instability at 1 s is probably that of the Ca system. On longer times the measured fluctuations are probably that of the Yb clock, as is implied by the difference between the measurements for the Yb laser when it is locked to the atoms or just to its reference cavity. The reference cavity for the Yb clock is the same as that used for the Hg^+ optical clock and has demonstrated a 1 s instability below the levels measured here [16]. Based on this data, we estimate that the Ca clock has an instability at or below 3 x $10^{-15}\tau^{-1/2}$ (the solid line in the figure) out to 100 s. Clearly, more measurements (with longer averaging times) are needed to verify these results as well as to determine the time scale on which the long-term drifts of the Ca clock begin to be significant.

V. FUTURE PLANS

In the near term we plan to continue simplifying and reducing the size of the apparatus. Since the clock is based on just two semiconductor laser systems, it could be contained in a fairly small volume. Additionally, a more compact arrangement of the optical system could substantially reduce its present 3-4 square meter footprint. With the implementation of more powerful probe lasers, we can improve the contrast of the fringes and perhaps reach a one second instability of 1 x 10^{-15}, a value we think we can hold for times of several 1000 seconds or longer. It will also be interesting to make some absolute frequency measurements to see how reproducible the frequency of this standard could be - a level of 10^{-14} seems feasible.

Acknowledgments

We thank Chad Hoyt and Zeb Barber for providing the Yb lattice clock light and Tara Fortier, Jason Stahlnaker, and Scott Diddams for their help with the fs-laser comb measurements. We also thank Jim Bergquist for his help with the Yb laser and sharing his experimental expertise. Finally, we thank Davi Ortega and Flavio Cruz for helpful discussions and experimental assistance.

[1] S. A. Diddams, T. Udem, J. C. Bergquist, E. A. Curtis, R. E. Drullinger, L. Hollberg, W. M. Itano, W. D. Lee, C. W. Oates, K. R. Vogel, et al., Science **293**, 825 (2001).
[2] W. H. Oskay, W. M. Itano, and J. C. Bergquist, Phys. Rev. Lett. **94**, 163001 (2005).
[3] T. M. Ramond, S. A. Diddams, L. Hollberg, and A. Bartels, Opt. Lett. **27**, 1842 (2002).
[4] K. W. Holman, D. D. Hudson, J. Ye, and D. J. Jones, Opt. Lett. **30**, 1225 (2005).
[5] P. Kersten, F. Mensing, U. Sterr, and F. Riehle, Appl. Phys. B **68**, 27 (1999).
[6] J. Ye, L. S. Ma, and J. L. Hall, Phys. Rev. Lett. **87**, 270801 (2001).
[7] U. Sterr, C. Degenhardt, H. Stoehr, C. Lisdat, H. Schnatz, J. Helmcke, F. Riehle, G. Wilpers, C. W. Oates, and L. Hollberg, Compt. Rend. Phys. **5**, 845 (2004).
[8] C. Degenhardt, H. Stoehr, C. Lisdat, G. Wilpers, H. Schnatz, B. Lipphardt, T. Nazarova, P. E. Pottie, U. Sterr, J. Helmcke, et al., Phys. Rev. A **72**, 062111 (2005).
[9] M. Takamoto, F.-L. Hong, R. Higashi, and H. Katori, Nature **435**, 321 (2005).
[10] C. W. Oates, E. A. Curtis, and L. Hollberg, Opt. Lett. **25**, 1603 (2000).
[11] C. W. Oates, F. Bondu, R. W. Fox, and L. Hollberg, Eur. Phys. J. D **7**, 449 (1999).
[12] C. J. Bordé, C. Salomon, S. Avrillier, A. Van Lerberghe, C. Bréant, D. Bassi, and G. Scoles, Phys. Rev. A **30**, 1836 (1984).
[13] A. Quessada, R. Kovacich, I. Courtillot, A. Clairon,

G. Santarelli, and P. Lemonde, J. Opt. B: Quantum Semiclass. Opt. **5**, S150 (2003).
[14] K. Numata, A. Kemery, and J. Camp, Phys. Rev. Lett. **93**, 250602 (2004).
[15] Z. W. Barber, C. W. Hoyt, C. W. Oates, L. Hollberg, A. V. Taichenachev, and V. I. Yudin, Phys. Rev. Lett. **96**, 083002 (2006).
[16] B. C. Young, F. C. Cruz, W. M. Itano, and J. C. Bergquist, Phys. Rev. Lett. **82**, 3799 (1999).

Proceedings of the 20th EFTF, 2006

A widely tuneable and narrow linewidth diode laser for coherent spectroscopy

A. Wicht* and N. Strauß, I. Ernsting, S. Chepurov, S. Schiller
Institut für Experimentalphysik, Heinrich-Heine Universität Düsseldorf, Universitätsstr. 1, D-40225 Düsseldorf, Germany

P. Huke, R.-H. Rinkleff, K. Danzmann
Institut für Gravitationsphysik, Universität Hannover, Callinstr. 38, D-30167 Hannover, Germany

We report on the development of a diode laser system which is optimized for precision spectroscopy. It is based on a combination of diode lasers with optical feedback from a grating and diode lasers with optical feedback from a resonant cavity. So far we have achieved overall tuneabilities on the order of 50 nm, continuous tuneabilities in excess of 40 GHz, and short term linewidth below 66 kHz measured over 2.9 s in a 15 MHz scan. In comparison to grating stabilized diode lasers these lasers should feature reduced frequency noise at high Fourier-frequencies which should significantly ease phase-locking to a frequency comb. These lasers will be used for precision spectroscopy and coherent manipulation of ultra-cold HD^+ molecules.

I. INTRODUCTION

Diode lasers are an important tool in (precision) spectroscopy for a number of reasons. Diode lasers are compact, relatively cheap, and even single mode diode lasers provide modest output powers typically in the 10 mW to 100 mW range. Furthermore, they are available for many different wavelength, from the deep-blue to the near IR, and they are well tuneable coarsely as well as continuously. Finally their frequency or phase can easily be modulated all the way from dc up to RF-frequencies. The most common type of single mode diode laser used for spectroscopy is based on the extended cavity design, which stabilizes the laser frequency by means of optical feedback from a grating (Littman or Littrow design)[1].

One of the shortcomings of grating stabilized diode lasers is their modest passive frequency stability, especially the frequency noise at high Fourier-frequencies, which necessitates a fast frequency control when narrow linewidth is required. Although the laser diode current can be modulated at frequencies as high as many GHz, frequency control with a servo bandwidth beyond a couple of 100 kHz is hard to achieve. This is mainly due to the physical processes inside the laser diode chip, which convert a laser diode current modulation into a frequency modulation [2]: at modulation frequencies typically below a few 100 kHz the current modulation mainly modulates the temperature. Beyond that typical frequency, carrier density modulation is the dominant source for frequency modulation. At the cross-over frequency between these regimes the current-to-frequency modulation transfer function features huge phase shifts which are hard to compensate electronically. In order to circumvent the need to employ very fast external or laser-internal frequency or phase shifters (see, for example [3]) it is therefore desirable to investigate new diode laser concepts for precision spectroscopy which intrinsically provide a narrow linewidth, and for which the frequency noise at high Fourier-frequencies is significantly smaller than for grating stabilized diode lasers.

Diode lasers based on optical feedback from a resonant cavity have been described by Dahmani and co-workers [4] and by Li and Telle [5] first in 1987 and have been used specifically in applications for which diode lasers had to be phase-locked to each other, e.g for experiments on atomic coherence [6]. These lasers provide significantly smaller linewidth than grating stabilized diode lasers and specifically feature reduced frequency noise at high Fourier-frequencies. Phase -locking of these lasers does not require very fast frequency control-loops and there is no need to use pre-scalers and digital phase detectors to allow for a residual closed-loop peak phase error of 1 rad or more. However, the excellent passive frequency stability comes at the price of some shortcomings: (i) the overall tuneability is typically limited to a few nm due to the lag of an element which provides coarse frequency tuning, (ii) the continuous tuneability is limited to a few 100 MHz, and (iii) the operation of a diode laser with resonant optical feedback is by far not as reliable as the operation of a grating stabilized diode laser.

There have been attempts to combine the concept of the grating stabilized diode laser with the concept of resonant optical feedback. Patrick and Wieman [7] first described a grating diode laser which employed additional optical feedback from a resonant SHG-cavity through the 0-th diffraction order of the grating. Later, this concept was also studied by Hayasaka [8] and Toyoda [9]. The main shortcoming in this setup is that there are two channels which compete in providing optical feedback to the laser diode. Whereas the grating only provides feedback around one specific wavelength, and thus ensures coarse wavelength selection, the cavity feeds back light at many frequencies within the gain bandwidth of the diode laser. The

*Electronic address: andreas.wicht@uni-duesseldorf.de

competition between the feedback channels is hard to control, and the effect of the competition strongly depends on the relative strength of the feedback channels.

Following an optical layout originally analyzed by Belenov and co-workers [10] within a different context we combined the grating stabilization and the stabilization through feedback from a resonant cavity in an only slightly but nevertheless crucially different way: optical feedback from a resonant cavity is provided through the 1-st diffraction order of the grating. Now, the two feedback channels act in series rather than in parallel, and optical feedback is only provided if the "resonance condition" is met by both, the cavity and the grating feedback, at the same time. This way the excellent passive frequency stability of diode lasers with resonant optical feedback is maintained, and it is combined with good coarse and continuous frequency tuneability as well as with the reliability of grating diode lasers. Our setup can be thought of to be a Littman configuration, in which the retro-reflecting mirror is replaced by folded resonant cavity, see Fig.1. It turns out that the key-point in this setup is to find an appropriate cavity geometry which preserves the spectral selectivity of the grating [11]. As an illustrative example, one can think of replacing the retro-mirror in a Littman setup by a curved mirror with a focal length which equals the distance of the mirror from the grating. This would perfectly cancel the spectral selectivity of the grating and would make stable operation of the laser as difficult as the operation of diode lasers with resonant optical feedback. The cavity geometry obviously has to be designed in a way which avoids this type of "geometrical cancellation" of the spectral selectivity of the grating. Our analysis [11] suggests that a folded confocal cavity geometry should be best suited for this "grating enhanced external cavity diode laser" (GEECDL). Ewald and co-workers [13] preferred a planar cavity, which we found to be inferior to a confocal cavity mainly due to the well known problems related to the alignment and stability of cavities which are located at the boundary of the stability regime.

In this paper we present the status of our activities aiming at the development of lasers based on the GEECDL concept. We briefly describe our setup and present results regarding linewidth measurements, frequency stability, and tuneability. The main goal of this project is to provide narrow linewidth diode lasers which can easily be phase-locked to a frequency comb. A set of these lasers operating between 1400 nm and 1500 nm will be used for precision spectroscopy of ultra-cold HD^+ molecular ions. By phase-locking two of these diode lasers to a frequency comb, we will be able to generate a bi-chromatic optical field which features an ultra-stable frequency difference in the few THz range between the two spectral components. This bi-chromatic field will be used to generate and investigate quantum coherence between individual molecular rotational states of the vibrational ground state of HD^+. To analyze the frequency stability and frequency modulation capability of our diode lasers we have developed a purely analog frequency-phase detector, which - in contrast to commonly used digital frequency-phase detectors - also provides a true frequency-lock between two lasers if the corresponding RF-beat note signal is available. It can also be used as a pre-lock for the phase stabilization servo-loop. We give a description of this frequency-phase detector in Sec.III.

II. GEECDL LASER SYSTEM

Fig.1 describes the GEECDL setup schematically. The 1400 nm laser system is based on a *Sacher Lasertechnik SAL-1380-10* single mode laser diode which is AR coated with a residual reflectivity of 1.3×10^{-4}. After collimation by an aspheric lens (*Thorlabs C390TM-C*, NA=0.65, f=2.76 mm) the laser beam hits a custom made volume holographic transmission phase grating (*Wasatch Photonics*, 980 l/mm) which provides a maximum diffraction efficiency in excess of 95% at the Bragg angle. By detuning the grating from the Bragg angle, the diffraction efficiency can be reduced significantly, e.g. to $\approx$ 50% at a detuning of 8 deg. The first diffraction order of the grating is then coupled to the external cavity, which has a folded confocal geometry of length L=75 mm. The input coupler is planar and has a transmission of 8.2% for s-polarization which is the polarization state of the laser field. The curved mirrors provide a reflectivity of 99.7%. At a diode current of 90 mA an optical power of about 5 mW is available at the output of the laser (before the isolator).

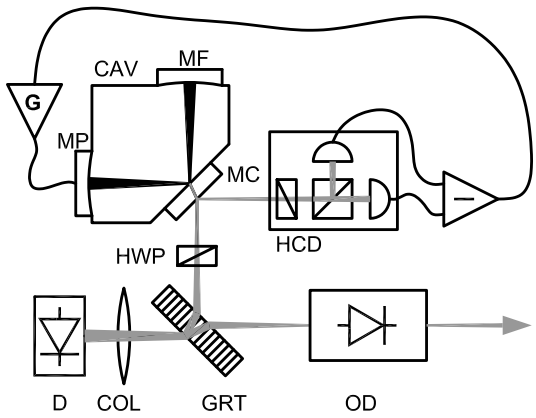

FIG. 1: Schematic setup. *D*: laser diode, *COL*: collimator, *GRT*: grating, *OD*: optical diode, *CAV*: external cavity, *HCD*: balanced polarization sensitive detector for Hänsch-Couillaud stabilization, *HWP*: half wave plate *G*: corresponding loop filter, *MF, MP*: curved HR-mirrors, R=75 mm, *MC*: planar coupling mirror, T=8.2%

The optical layout can be considered a coupled cav-

ity: the first cavity (*laser cavity*) is formed by the end mirror MF and the rear facette of the diode laser chip, whereas the second (*external cavity*, CAV) is defined by the end mirrors MP and MF. As is well known from diode lasers with resonant optical feedback, the diode laser chip basically locks to a resonance frequency of the external cavity as long as the detuning between the two cavities is not too large. To ensure this, we apply a polarization sensitive stabilization scheme first described by Hänsch and Couillaud [14]. In contrast to the original scheme we do not use a birefringent crystal inside the cavity but make use of the polarization dependence of the input coupler's reflectivity: for p-polarization the finesse of the external cavity is significantly smaller than for s-polarization. Therefore, the polarization of the reflected light changes as the laser frequency is scanned across the cavity resonance. The corresponding error signal is feed back to the position of the mirror MP which is actuated by means of a PZT. This ensures that the slow drift between the *external cavity* and the *laser cavity* is eliminated and stable operation can be guaranteed for extended periods. Finally, the frequency of the laser system is tuned by controlling the position of mirror MF which is also actuated by a PZT.

With the Hänsch-Couillaud lock activated we have been able to continuously tune the frequency of the 1400 nm laser system by 20 GHz, which was limited by the dynamic range of the PZTs. With a similar system at 850 nm [12] a continuous tuning range in excess of 45 GHz was achieved, again limited by the dynamic range of the PZTs. These tuning ranges are significantly larger than the largest tuning ranges achieved with diode lasers with resonant optical feedback. Further, due to the coarse frequency pre-selection by the grating, our laser system can be coarse-tuned to cover about the same wavelength range as would be reachable with a grating diode laser setup: the 850 nm laser was tuneable by 36 nm, whereas the 1400 nm laser can cover at least 1370 nm-1420 nm (all at constant diode temperature). Again these excellent overall tuning characteristics are unmet by diode lasers with resonant optical feedback.

We are currently setting up a second GEECDL operating at 1400 nm. With this laser we will be able to determine the short term linewidth and frequency noise spectrum of our diode laser system in a beat note experiment with the first laser. Recently we have been able to estimate the short term linewidth of a GEECDL for the 850 nm system by taking a beating note spectrum between the 850 nm GEECDL and a regular diode laser with resonant optical feedback, which should provide about the same short term linewidth. In order to reduce jitter at low frequencies the GEECDL was frequency-locked to the second laser with a servo bandwidth of about 400 Hz, for which the mirror MF was used as the actuator. The corresponding spectrum is shown in Fig.2 and reveals a FWHM-linewidth of 66 kHz measured with a spectrum analyzer sweep time of 2.9 s and a span of 15 MHz. Phase-locking of this laser will require control at higher Fourier-frequencies which will be provided by actuating the laser diode current. The 1400 nm GEECDL provides 0.6 MHz/mA conversion at dc. This conversion factor is smaller than the corresponding factor for regular grating diode lasers by orders of magnitude, so that the stability-requirement for the current controller is by far less stringent than for regular grating diode lasers. Nevertheless, it is large enough to provide sufficient dynamic range at large Fourier-frequencies for phase-locking of the GEECDL.

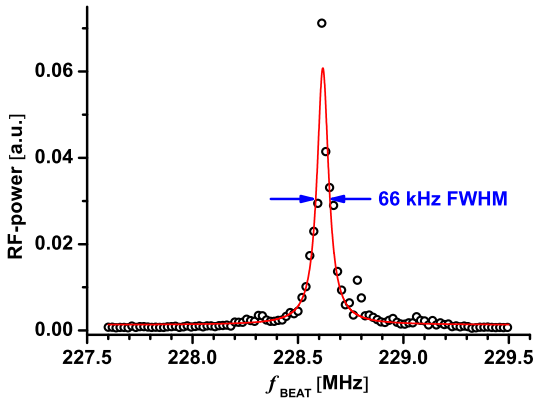

FIG. 2: Beat note spectrum between the GEECDL and a regular diode laser with resonant optical feedback, both operating at 852 nm. For the measurement the GEECDL was frequency-locked to the second laser with a servo bandwidth of about 400 Hz. The spectrum was taken with a resolution bandwidth of 3 kHz in a sweep time of 2.9 s for a span of 15 MHz. The linewidth (FWHM) resulting from a lorentzian fit is 66 kHz.

To test the frequency stability of the free-running GEECDL we have performed a beat note measurement between the 1400 nm GEECDL and a frequency comb (*MenloSystems FC8004*), which was stabilized to a maser (*VREMYA-CH VCH-1005*) and served as an absolute frequency reference. The beat note spectrum was taken with a *Thorlabs D400FC* InGaAs photodetector and the peak of the spectrum was recorded with an *Agilent 4440A* spectrum analyzer at a rate of 10 Hz (with a RBW of 91 kHz and a sweep time below 10 ms). The resulting frequency trace is shown in Fig.3. Trace (*a*) denotes the free-running GEECDL and reveals a drift of 4 MHz/min derived from 5.5 min of data. The rms-frequency jitter is on the order of 0.5 MHz. We next frequency-locked the GEECDL to the frequency comb by means of the frequency-phase detector which will be described in the next section. The servo-loop is a simple integrator and provides a bandwidth of a few 100 Hz in order to eliminate drift and jitter at low acoustic Fourier-frequencies. This eliminates the drift (now at 16 kHz/min derived from 7 min of data), see trace (*c*). The rms-frequency jitter is at the level of 0.4 MHz. For comparison we

show the corresponding measurement for an *Agilent 8164A* diode laser, module *81480A*, which features internal frequency stabilization. Its drift corresponds to 200 kHz/min measured over 8 min, and the rms-jitter is about 2 MHz. The result for the GEECDL shows a passive frequency stability which is significantly better than the typical passive stability of grating diode lasers. A PZT-based servo bandwidth of a few hundred Hz is enough to reduce the jitter to well below 1 MHz, so that current control at high Fourier-frequencies provides enough dynamic range to phase-lock the diode laser. Further, we conclude that the frequency-detector part of our frequency-phase detector provides the possibility to implement a pre-lock which should significantly ease phase-locking of the GEECDL.

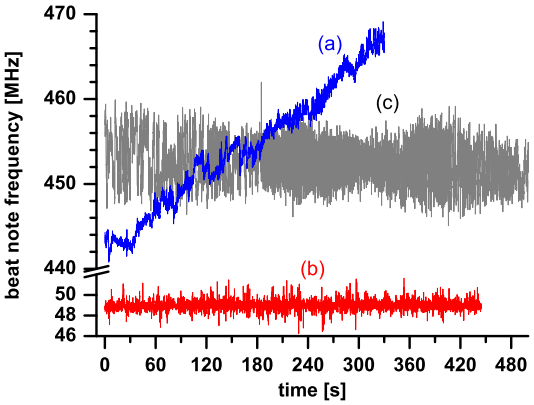

FIG. 3: Beat note spectrum between the 1400 nm GEECDL and a fs-frequency comb. The peak of the beat note spectrum was recorded at a rate of 10 Hz (spectrum analyzer RBW 91 kHz). Trace (a) shows the free running GEECDL, (b) shows the GEECDL when frequency-locked to the frequency comb (servo bandwidth corresponds to a few hundred Hz), (c) shows an *Agilent 8164A*, module *81480A*, diode laser with internal stabilization for comparison.

III. FREQUENCY-PHASE DETECTOR

Experiments on molecular coherence between individual ro-vibronic states will require simultaneous phase-locking of multiple GEECDLs to the frequency comb. In order to make optical phase-locked loops (PLLs) robust, typically digital phase detectors with some kind of pre-scalers or combinations of digital and analog phase detectors are used [15]. Purely digital phase detectors are typically slower than analog detectors (basically balanced mixers) and also tend to be more noisy. More importantly, digital frequency-phase detectors do not support true frequency detector operation, because they rail for non-zero frequency difference and thus only deliver binary information about whether the beat note frequency is larger or smaller than the reference frequency. These detectors therefore do not provide an error signal which is proportional to the frequency difference between the beat note and the local oscillator. However, this is desirable e.g. if (i) frequency noise spectra or (ii) frequency modulation transfer functions of lasers have to be measured. Further, (iii) a combination of a true analog frequency detector and an analog phase detector should significantly ease phase-locking of lasers and provide robust locking, because the frequency part of the detector "takes over control" as soon as the phase-lock fails. Since analog phase detectors cannot provide the dynamic range for phase detection which is typical for digital phase detectors, it is clear that the analog frequency-phase detector will only work in "phase-detection mode" (i.e. provide true phase tracking) if the residual peak phase error is smaller than 1 rad.

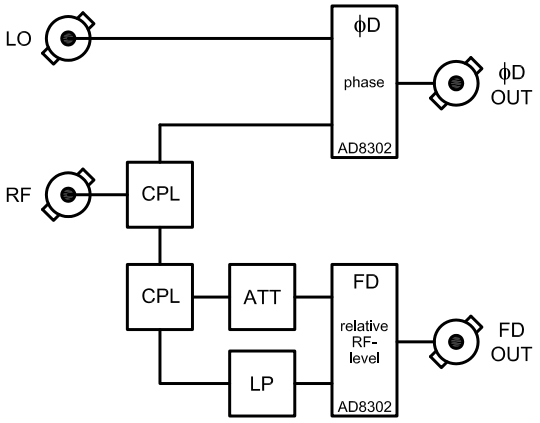

FIG. 4: Schematic setup of the purely analog frequency-phase detector. *LO*: local oscillator input; *RF*: RF-(beat note) input; *CPL*: directional coupler; *ATT*: attenuator; *LP*: low pass, e.g. *Minicircuits SCLF*-series; *FD OUT*: frequency detector output; *ϕD OUT*: phase detector output

We have developed a purely analog frequency-phase detector which can be operated at a user-defined carrier frequency between 20 MHz and 1 GHz, and provides a nominal phase and frequency modulation detection bandwidth of 30 MHz. It is based on the *AD8302* RF-gain and phase detector, which features two functions. The first is a phase detector of multiplier type which delivers the phase shift between the two RF-inputs. The signal is linearized for phase shifts of $0 \ldots \pi$. The second function is a relative RF-power meter, which provides information about the relative RF-power level of the two RF-inputs. The RF-power meter function together with a steep RF-low pass provides a simple, flexible, and reliable frequency detector as shown in Fig.4.

The beat note signal (*RF*) is split by a directional coupler *CPL*. One of its outputs is directed to the phase detection unit ϕD, which also receives the local oscillator signal *LO*. The other output is split again by

a directional coupler. One of the corresponding outputs is appropriately attenuated and passed on to the frequency detector unit *FD*. The second output of the coupler is filtered by a steep low pass filter *LP* and then also passed on to the frequency detector unit. The latter basically determines the transfer function of the filter, or equivalently, if the transfer function is known, provides RF-amplitude independent information about the frequency of the RF-signal.

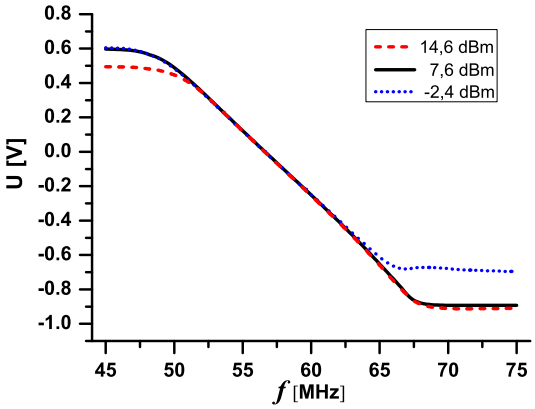

FIG. 5: Frequency-to-voltage conversion provided by the frequency detector unit. Characteristics are shown for the nominal RF-power level of +7.6 dBm, as well as for +14.6 dBm (+7 dB) and -2.4 dBm (-10 dB). Data was taken by applying an RF-signal generated by a μ-wave synthesizer. At the linear part of the trace the slope is 76.9 mV/MHz

The frequency detector operation is characterized in Fig.5. An RF-signal generated with a μ-wave synthesizer is applied to the RF-input of the frequency-phase detector. As can be seen, the detector provides a linear frequency-to-voltage conversion between 50 MHz and 67 MHz and rails for RF-frequencies outside this window. The low pass used for the data shown here (*Minicircuits SCLF-44*) maintains the information about whether the detector is railing at too low or too high frequencies between 20 MHz and 350 MHz. We have alternatively used a *Minicircuits SCLF-190* low pass, which provided a working point of 320 MHz and delivered "frequency-too-low" or "frequency-to-high" information between 20 MHz and 1 GHz. Near the working point, i.e. typically at the center of the linear detection range, the output signal is basically independent of the RF-power level, which is shown in Fig.5 by comparison of the traces for the three RF-power levels, that differ by as much as 17 dB.

To analyze the power noise-to-frequency noise cross talk in more detail we set the μ-wave synthesizer to a fixed frequency of 60 MHz, which is about the center frequency of the frequency detector's linear range. We vary the RF-power level and record how the output of the frequency detector changes. From the detector slope (see Fig.5) we can infer an apparent frequency shift, which is shown in Fig.6. For a typical application we can assume that the RF-beat note power will be stable to better than ±6 dB. Within this RF-power range the in-lock beat note frequency will change at most by 50 kHz, so the frequency drift and jitter caused by RF-power fluctuations will well below 100 kHz.

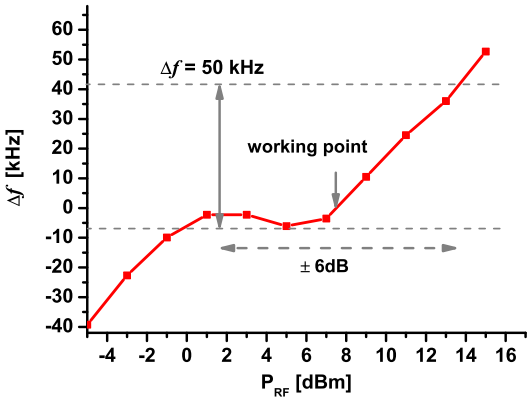

FIG. 6: RF-power level-to-frequency cross talk of the frequency detector unit. The graph shows the apparent frequency shift, caused by a modification of the RF-power level. RF-frequency: 60 MHz. For a typical application, RF-beat notes will be power stable to better than ± 6dB, which corresponds to an apparent frequency shift of 50 kHz peak-peak.

The frequency detector unit makes use of the steep slope of a low pass filter. Any drift of the filter's transfer function will therefore result in a drift of the in-lock beat note frequency. In order to quantify this effect we record the frequency detector output signal for a 60 MHz RF-signal at the input during 1 h of warm up. The overall drift is 2.1 mV corresponding to 27 kHz, whereas half of the drift occurs during the first 5 min after power on. Hence, thermal drifts of the frequency detector are well below 100 kHz. We conclude that the frequency detector provides an absolute frequency stability on the order of 100 kHz if the leading systematic effects, namely thermal drift and RF-power -to-frequency cross talk are considered. This stability is significantly better than what is required for a frequency pre-stabilization as part of a PLL, or for supporting automatic lock acquisition for a PLL. It is even stable enough for many spectroscopic applications where a frequency stability just below 1 MHz is sufficient, e.g. for offset-locking of lasers used for optical cooling.

Please note that the frequency detector performance relies on an excellent signal-to-noise ratio of the RF-beat note signal. Broadband RF-noise will show up as a strong offset to the total RF-power level at both inputs of the AD8302 frequency detector. This offset is partially cancelled because the AD8302 measures the relative power between the two inputs. Besides generating an offset, significant RF-noise power will also shift the negative (i.e. high frequency) rail

towards positive voltage, i.e. towards smaller frequencies. The frequency-to-voltage conversion characteristic will resemble that trace in Fig.5, which corresponds to an RF-level of -2.4 dBm. The larger the broadband RF-power noise the narrower the linear part of the characteristic will be. The frequency detector is therefore best suited for frequency-locks between two sufficiently powerful lasers. However, its performance will be reduced if used to lock a laser, for example, to a single comb line of a frequency comb which typically provides an optical power between 10 nW and 100 nW only. We are currently investigating the dependence of the frequency detector performance on the beat note signal-to-noise ratio. Despite this foreseeable problem we have been able to frequency-lock the 1400 nm GEECDL to the frequency comb by means of the frequency detector unit, see Fig.3. In this experiment, the signal-to-noise ratio of the RF-beat note was typically 30 dB at a resolution bandwidth of 91 kHz, and the RF-noise bandwidth was about 60 MHz. Hence, on the 60 MHz noise bandwidth the signal-to-noise ratio corresponded to a few dB only.

IV. CONCLUSION

We presented the development of a diode laser system for precision spectroscopy, more specifically for coherent spectroscopy of ultra-cold HD^+ molecular ions in the 1400 nm. . . 1500 nm wavelength range. The novel diode laser concept is based on a combination of the scheme using feedback from a grating and the scheme using feedback from an external cavity. This Grating Enhanced External Cavity Diode Laser (GEECDL) provides the narrow linewidth of diode lasers with resonant optical feedback, but at the same time guarantees the good overall (>50 nm) and continuous (>20 GHz) tuneability as well as the reliable operation of grating diode lasers. After elimination of frequency noise below a few hundred Hz we find an upper limit for the laser linewidth of 66 kHz measured over 2.9 s for a 15 MHz span. We have successfully implemented the polarization sensitive Hänsch-Couillaud locking scheme to lock the coupled cavities to each other. The novelty here is that we do not make use of any birefringent elements inside the external cavity but solely rely on the polarization dependence of the mirror reflectivities. We are currently implementing a second laser system, which will provide 10-fold increased output power, and which will allow a true determination of the laser linewidth through a beat note measurement against the first laser system.

We further presented a novel analog frequency-phase detector concept. In contrast to digital phase detector concepts it provides true frequency-detector operation, i.e. an output signal which is proportional to the frequency difference between an RF-beat note and an RF-reference signal. The frequency detector unit can be used to characterize frequency noise of lasers as well as their frequency-modulation transfer functions, and it can serve as a frequency pre-lock for an optical PLL. It provides an absolute frequency stability on the order of 100 kHz at an operational RF-frequency of 60 MHz. We are currently investigating the dynamic performance of the frequency and phase detector units, as well as the dependence of the performance on the beat note's signal-to-noise ratio. Following the design goals we expect a phase and frequency modulation detection bandwidth of about 30 MHz.

Acknowledgments

We thank Frank Lewen, I. Physikalisches Institut der Universität zu Köln, for helpful discussions regarding the electronic implementation of the frequency-phase detector. This work is supported by the Deutsche Forschungsgemeinschaft.

[1] M. W. Fleming, A. Mooradian, IEEE J. Quantum Electron. **17**, 44 (1981); C. E. Wieman, L.Hollberg, Rev. Sci. Instrum. **62**, 1 (1991).
[2] H. R. Telle, Spectroch. Acta Rev. **15**, 301. (1993).
[3] A. Wolf, B. Bodermann, H. R. Telle, Optics Lett. **25**, 1098 (2000).
[4] B. Dahmani, L. Hollberg, R. Drullinger, Opt. Lett. **12**, 876 (1987); R. Fox, C. Gates, L. Hollberg: In *Cavity-enhanced spectroscopy*, ed. by R. van Zee, J. Looney, (Academic Press, Amsterdam 2002) pp. 1-46.
[5] H. Li, H. R. Telle, IEEE J. Quantum Electron. **QE-25**, 257 (1989).
[6] S. Brandt, A. Nagel, R. Wynands, D. Meschede, Phys. Rev. A **56**, R1063 (1997); L. Spani Molella, R.-H. Rinkleff, K. Danzmann, Phys. Rev. A 72, 041802(R) (2005).
[7] H. Patrick, C. E. Wieman, Rev. Sci. Instrum. 62, 2593 (1991).
[8] K. Hayasaka, Opt. Commun. **206**, 401 (2002).
[9] K. Toyoda, Y. Kubota, T. Okano, S. Urabe, Appl. Phys. B **82**, 25 (2006).
[10] É. Belenov, V. L. Velichanskiĭ, A. S. Zibrov, V. V. Nikitin, V. A. Sautenkov, A. V. Uskov, Sov. J. Quantum Electron. **13**, 792, (1983).
[11] A. Wicht, M. Rudolf, P. Huke, R.-H. Rinkleff, K. Danzmann, Appl. Phys. B **78**, 137 (2004).
[12] A. Wicht, P. Huke, R.-H. Rinkleff, K. Danzmann, Physica Scripta **T118**, 82 (2005).
[13] G. Ewald, K.-M. Knaak, S. Götte, K. D. A. Wendt, H.-J. Kluge, Appl. Phys. B **80**, 483 (2005).
[14] T. W. Hänsch, B. Couillaud, Opt. Commun. **35**, 441 (1980).
[15] L. Cacciapuoti, M. de Angelis, M. Fattori, G. Lamporesi, T. Petelski, M. Prevedelli, J. Stuhler, G. M. Tino, Rev. Sci. Instrum. **76**, 053111 (2005), and references therein.

Proceedings of the 20th EFTF, 2006

Atomic and molecular spectroscopy with a continuous-wave, doubly-resonant, monolithic optical parametric oscillator

T.Ikegami,* H.Inaba, and S.Ohshima
Time Standards Section, Time and Frequency Division,
National Metrology Institute of Japan, AIST,
AIST Tsukuba Central, Tsukuba-Shi, Ibarki-Ken 305-8563, Japan
**Electronic address:* t.ikegami@aist.go.jp

Doppler-broadened atomic and molecular spectra were observed with a 1-octave tunable, continuous-wave, doubly resonant, monolithic optical parametric oscillator (OPO) using 5%-MgO-doped $LiNbO_3$ as a nonlinear crystal. By tuning the frequency of a pump laser, longitudinal mode selection over 20 successive modes, corresponding to a 60 GHz span, was possible. Continuous frequency tuning was achieved using an external waveguide-type electrooptic phase modulator (EOM). We could observe the Cs-D_1 (894 nm), Cs-D_2 (852 nm), Rb-D_1 (795 nm), acetylene R9 (1520 nm) and P9 (1530 nm) transitions with the single monolithic OPO.

1. INTRODUCTION

An optical parametric oscillator (OPO) is a highly coherent and widely tunable source of optical radiation. Contrary to pulsed OPOs, the continous-wave (cw) OPO has not been recognized as a practical light source because of the instability of operation and the difficulty of frequency tuning [1,2]. These problems have recently been overcome, owing to the development of highly efficient and high-quality nonlinear optical crystals such as periodically poled lithium niobate, and narrow-spectral-linewidth, highly stable solid state light sources [3-17].

A monolithic cw OPO, in which an optical coating is directly applied to the polished surfaces of a crystal, is an attractive device due to its simple structure and high mechanical stability [18-22]. Because there is no extra surface leading to a parasitic resonance, its mode selection and tuning characteristics are very simple compared with common OPOs which use separate mirrors. However, the continous frequency tuning of the monolithic OPO over a wide range is difficult because it is not easy to change its cavity length (=crystal length).

In this paper, we demonstrate the usefulness of the monolithic cw OPO as a spectroscopic light source by observing Doppler-broadened atomic and molecular transitions, using an EOM as an external, continuous frequency tuning device. We believe that this is the first result of atomic and molecular spectroscopy using a monolithic cw OPO.

II. EXPERIMENTAL SETUP

The experimental setup is shown in Fig.1. A frequency-doubled Nd:YAG laser was used as a pump source for the OPO. The nonlinear optical crystal, 5% MgO-doped LiNbO3, was cut along the y axis of the crystal refractive index ellipsoid for use with birefringent phase matching. Its size was 2.3 mm x 2.5 mm x 22 mm. The two 2.3 mm x 2.5 mm faces of the crystal were polished spherically with a radius of curvature of 25 mm, forming a standing-wave monolithic cavity. The input face had an antireflection coating at 532 nm (R < 20 %) and high-reflection coating (R > 98.5 %) from 750 nm to 1700 nm. The output face was designed to have a high reflectivity at 532 nm (R > 85 %) and a transmission of 0.5 % ± 0.5 % from 750 nm to 1700 nm. As a result, the crystal was in a double-path pump configuration.

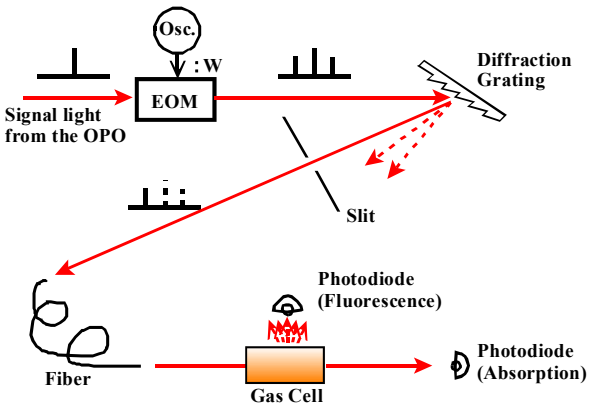

Figure.1 Experimental setup. Osc: microwave oscillator, EOM:waveguide-type electrooptic phase modulator, Gas cell: Rb, Cs vapor cells, or acetylene gas cell. Diffraction grating and slit are optional.

The signal and idler beams were separated with a prism. The separated signal light or idler light was introduced to a waveguide-type electrooptic phase-modulator

(EOM), whose modulation bandwidth is 20 GHz. The bandwidth of the microwave amplifier driving the EOM was from 6 GHz to 18 GHz. The phase-modulated light was introduced to a vapor or gas cell and one of the optical sidebands was used to observe an absorption signal or a fluorescence signal from the cells. Vapor cells were used for the observation of Rb and Cs transitions and the gas pressure was a saturated vapor pressure at room temperature. A gas cell with a length of 50 mm and a pressure of 50 Torr at room temperature was used for the observation of acetylene ($^{12}C_2H_2$) transitions.

III. RESULTS

The detailed operational characteristics of the OPO are described in [23] and we briefly describe its oscillating characteristics. The OPO was tunable over 1 octave from 777 nm to 1687 nm by changing the crystal temperature from 108 ºC to 235 ºC. When the OPO was pumped at a pump power of 100 mW, the typical signal and idler power were 5 mW to 10 mW, respectively. We operated the OPO at a pump power smaller than 150 mW. The OPO operated in a single longitudinal mode pair of signal and idler stably under free running condition without any active control of the cavity length, owing to the thermal self-locking mechanism [24].

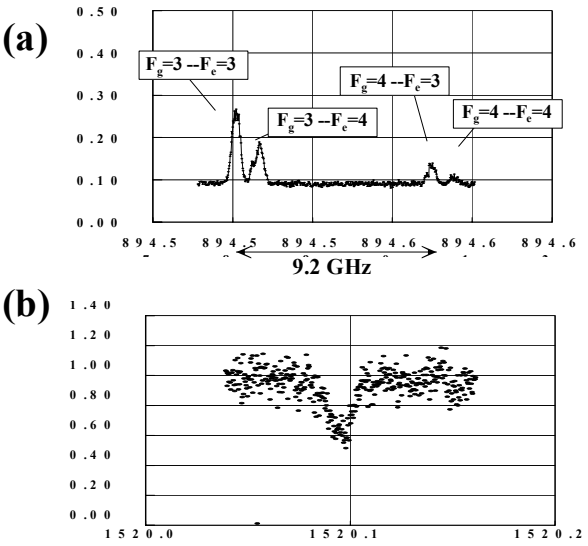

Figure.2 Observed Doppler broadened spectra for (a) Cs-D_1 line (894 nm), (b) actylene R9 line (1520 nm).

The tuning to a desired atomic or molecular transition frequency is performed as follows. (1) First, oscillating wavelength (signal light or idler light depending on the required wavelength) was tuned coarsely within the ±0.1 nm of the target wavelength by tuning crystal temperature. (2) Next, pump laser frequency was tuned continuously to tune oscillating wavelength within 1 FSR of the target wavelength. (3) Once the oscillating wavelength becomes within 1 FSR of the target wavelength, the light was modulated with the EOM and the upper or lower sideband frequency was swept through the atomic or molecular transition wavelength. The carrier or the unused sideband was not removed because it was far from the transition and did not influence the results, although it lead to a DC bias of the transmitted power. Because the optical power was decreased by 1/10 due to the insertion loss of the EOM, and the power was distributed almost equally to the carrier, the lower sideband, and the upper sideband, the available power for the spectroscopy became approximately 1/30 of the input power to the EOM and was typically 200 μW.

Figure 2 shows the observed signals. For observation of the transition whose wavelength is smaller than 1 μm (Cs), the signal light was used, and for transitions longer than 1 μm (acetylene), the idler light was used. For Rb and Cs, fluorescence was observed. For acetylene, the absorption signal was observed because fluorescence cannot be observed. By scanning the microwave frequency to the EOM, we were able to observe the Doppler-broadened profiles of the atomic and molecular transions with the single monolithic cw-OPO. Similarly, we could observe the profiles for Rb-D_1 line (795 nm), Cs-D_2 line (852 nm) and Acetylene P9 line (1530 nm), too.

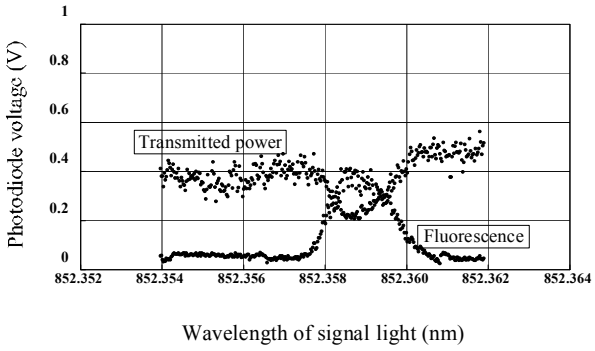

Figure.3 Doppler-broadened fluorescence and absorption spectra for Cs-D_2 (852 nm) line, F=4 → F'=3,4,5 components, observed with single sideband from EOM.

Finally, we tried to remove the carrier and the unused sideband for the higher contrast observation of the absorption signal. For this purpose, the phase-modulated light was applied to a diffraction grating (2160 lines/mm). After the 1st order diffracted light propagated by a distance of 5 m or so, the carrier, the lower sideband and the upper sideband become spatially separated. The single sideband necessary for the

experiment was extracted and an unnecessary carrier and another sideband were removed by a spatial filter. The extracted sideband was applied to the vapor cell. We observed fluorescence and the absorption signal from F=4 → F'=3,4,5 components of Cs-D_2 transition simultaneously, which is shown in Fig.3. From the depth of the absorption, we can confirm that the unnecessary carrier or unused sideband are filtered out effectively.

IV. CONCLUSIONS

We observed the Doppler broadened atomic and molecular profiles from Rb-D_1, Cs-D_1, D_2 and acetylene R9 and P9 transitions with a single, cw monolithic OPO using an EOM as an external frequency tuning element. We also succeeded in the observation of saturated absorption from the Cs-D_1 transition at 894 nm with the same cw OPO, phase-locked to an optical comb, which will be published in [25, 26]. Thus, the monolithic cw OPO was demonstrated to be a useful spectroscopic light source, which has a phase-locking capability for extraction and amplification of a single comb from the densely spaced modes of a mode-locked laser. It will be an important tool for the development of optical frequency standards because they sometimes require curious wavelengths, which are not available with conventional lasers. Also, we came one step closer to realizing an continuous-wave optical frequency synthesizer, which can generate arbitrary-wavelength light with a precisely fixed frequency and power.

Acknowledgements

We thank Dr. K.Waseda at the National Astronomical Observatory, Japan and Dr. M.Ohashi at the Institute for Cosmic Ray Research, Japan, belonging to the Japanese gravitational group for ultrawideband coatings. We appreciate Dr. A.Onae in NMIJ, Japan for calibrating our wavelength meter and Dr. F.L.Hong in NMIJ for loaning the microwave synthesizer.

REFERENCES

[1] R.G.Smith et al., Appl. Phys. Lett. **12**, 308 (1968) .
[2] R.G.Smith, IEEE J. Quantum Electron. QE-**9**; 530 (1973).
[3] J.Opt.Soc.Am.B **10**,No.9 (1993), the special issue on OPO and OPA.
[4] S.T.Yang et al., Opt. Lett. **18**, 971 (1993).
[5] W.R.Bosenberg et al., Opt. Lett. **21**, 713 (1996).
[6] P.E.Powers et al., Opt. Lett. **23**, 159 (1998).
[7] R.G.Batchko et al., Opt. Lett. **23**, 168.
[8] M.E.Klein, et al., Opt. Lett. **25**, 490 (2000).
[9] M.Ebrahimzadeh et al., J. Opt. Soc. Am. B **16**, 1499 (1999).
[10] R.Al-Tahtamouni et al., Appl. Phys. B **66**, 733 (1998).
[11] A.Garashi et al., Opt. Lett. **23**, 1739 (1998).
[12] A.J.Henderson et al., Opt. Lett. **25**, 1264 (2000).
[13] A.Douillet and J.-J.Zondy, Opt. Lett. **23**, 1259 (1998).
[14] D.Lee and N.C.Wong, J. Opt. Soc. Am. B **10**, 1659 (1993).
[15] M.Tsunekane et al., Appl. Opt. **37**, 6459 (1998).
[16] U.Stroessner et al., Opt. Lett. **24**, 1602 (1999).
[17] T.Ikegami et al., Jpn. J. Appl. Phys. **35**, 2690 (1996).
[18] C.D.Nabors et al., Opt. Lett. **14**, 1134 (1989).
[19] D.C.Gerstenberger and R.W.Wallace, J. Opt. Soc. Am. B **10**, 1681 (1993).
[20] D.K.Serkland et al., Opt. Lett. **19**, 1046 (1994).
[21] G.Breitenbach et al., J. Opt. Soc. Am. B **12**, 2095 (1995).
[22] R.C.Eckardt et al., J. Opt. Soc. Am. B **8**, 646 (1991).
[23] T.Ikegami, S.Slyusarev, and S.Ohshima, Opt.Commun. **184**, 13 (2000).
[24] P.L.Hansen and P.Buchhave, Opt. Lett. **22**, 1074 (1997).
[25] H.Inaba et al., IEEE J. Quantum Electron. **40**, 929 (2004).
[26] H.Inaba et al., submitted to Appl.Optics.

Proceedings of the 20th EFTF, 2006

NOISE REJECTION DEVICE FOR LASER STABILIZATION

G. Tetchewo, C. Laissoub, O. Lopez, and F. du Burck*
Laboratoire de Physique des Lasers, 99 av. J.-B. Clément, 93430 Villetaneuse, France
**Electronic address:* duburck@galilee.univ-paris13.fr

The improvement of the short term stabilization scheme of an Ar^+ laser for the realization of an optical frequency standard at 501.7 nm is described. The laser frequency is locked to a Fabry-Perot resonator mode for the very short term stabilisation and to a hyperfine transition detected in iodine for frequency correction in the range 1-100 Hz. A device for the amplitude noise rejection is developed to increase the signal to noise ratio of the detected signal. The new stabilization system leads to frequency stability at the 10^{-13} level for 1 s integration.

1. INTRODUCTION

We develop an optical frequency standard at 501.7 nm based on an Ar^+ laser locked to hyperfine transitions of iodine. The accuracy of a frequency standard is limited by the width of the transition used as frequency reference. The natural linewidth of hyperfine components in iodine decreases near 500 nm, the dissociation limit of the molecule. In particular, we measured HWHM ≈ 30 kHz for the hyperfine components of R(26)62-0 transition at 501.7 nm [1].

In our set-up, the spectral purity of the laser is first enhanced by prestabilization on a Fabry-Perot resonator mode. For long term stabilization on the iodine hyperfine transition frequency, the narrow line is detected in a low pressure iodine cell. It is 4 m long. The pressure, controlled by thermostabilization of a cold finger, is in the range 0.07-0.7 Pa (0.5-5 mTorr). The cell is pumped during the experiment in order to minimize the effect of buffer gases and impurities. The frequency band of the servo loop for the long term stabilization of the laser is smaller than 1 Hz because of the poor signal to noise ratio (SNR) of the detected signal. With this set-up, the absolute frequency of a hyperfine component of R(26)62-0 transition was measured for the first time [1]. The stability was found to be $\sim 10^{-12}$ for 1 s integration time. We have observed that in the range 1-100 Hz the stability was limited by mechanical vibrations of the Fabry-Perot cavity used for the laser prestabilization.

We describe here a technique to overcome this effect by an additional servo loop working up to about 1 kHz. Before locking the prestabilized laser frequency on the narrow hyperfine transition detected in the low pressure iodine cell, it is locked on the same transition detected in another cell at a higher pressure. The SNR of the detected signal must be sufficiently large to allow the correction of the frequency noise up to 1 kHz. With this aim, we have developed a system for the rejection of the probe beam intensity noise in a 1 kHz wide frequency band centred at the detection frequency (625 kHz). A noise rejection larger than 30 dB is reached and we show that the width of the rejected band is sufficient for the detection of the frequency noise above 100 Hz.

The paper is organized as follows. In Sect. II, we present the set-up for laser prestabilization. In Sect. IIII, we describe the noise rejection device and we give its performances. In Sect. IV, we show that the noise rejection device offers the possibility to increase the detection of frequency noise. Sect. V is a brief conclusion.

II. THE LASER PRESTABILIZATION SET-UP

Fig. 1 shows the laser prestabilization set-up. The line of the single mode Ar^+ laser is locked to a Fabry-Perot resonator mode by a Pound-Drever-Hall technique. A hyperfine component of the R(26)62-0 iodine transition at 501.7 nm is detected with saturation spectroscopy technique in a 50 cm long sealed cell. The iodine pressure in the cell, of about 4 Pa (30 mTorr), is controlled by thermostabilization of the cold finger.

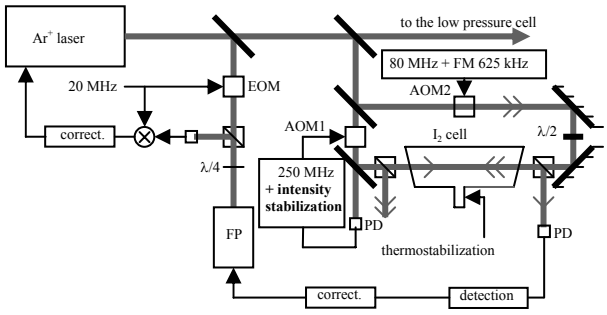

Fig 1: Ar^+ laser stabilisation scheme (FP: Fabry-Perot resonator; correct.: controller; PD: photodiode; AOM: acousto-optic modulator; EOM: electro-optic modulator).

Probe and saturating beam frequencies are shifted by 250 MHz and 80 MHz respectively by the acousto-optic modulators AOM1 and AOM2. The error signal is

obtained by modulation transfer technique: the saturating beam is frequency modulated at 625 kHz by AOM2 and the first harmonic of the saturated absorption signal is detected on the probe beam. It constitutes the error signal for the laser frequency stabilization up to 100 Hz. The correction signal is applied to a piezoceramic transducer that controls the length of the Fabry-Perot resonator. AOM1 is used for the rejection of the probe beam intensity noise around 625 kHz. The set-up for long term stabilization of the laser on the narrow line detected in the low pressure cell does not appear in Fig. 1.

III. THE NOISE REJECTION DEVICE

The principle of rejection of a beam intensity noise was previously described in [2]. It is based on an electronic controller derived from the adaptive noise cancelling techniques. The disturbance corrupting a primary signal is estimated by an adaptive filter from a correlated auxiliary signal (reference input). The estimate is then subtracted from the primary signal [3]. In case of the rejection of a single frequency, the reference signal is a sinusoid and the estimate results from the in-phase and quadrature analysis of the error signal. Fig. 2 shows the principle of the beam intensity noise rejection at 625 kHz. The cancelling signal drives the RF input power of an acousto-optic modulator which controls the beam intensity. The first order output beam is split into the probe beam and the correction beam. The intensity of this latter is monitored by a photodiode to generate the error signal.

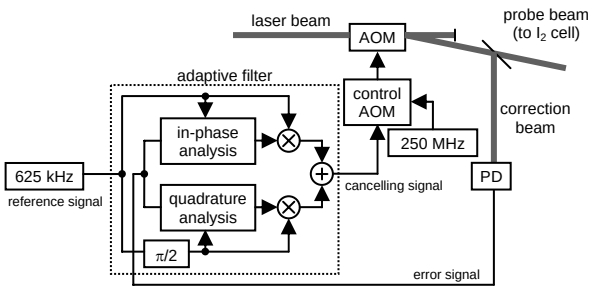

Fig 2: Principle of intensity noise rejection device (PD: photodiode; AOM: acousto-optic modulator)

The adaptive filter is developed in numeric solution that presents a better accuracy for IQ modulation/demodulation and better offset characteristics than analogical solution. It is implemented in a Memec Spartan-3 LC development board based on a Xilinx Spartan-3 FPGA and a daughter card with analogue input/output. A 20 MHz oscillator pilots the sample rate of the input/output 12 bit analogue converter, the FPGA internal clock and the 625 kHz signal used for the detection of the iodine transition. The processing rate is 2.5 MHz, 4 times the frequency modulation. This is its smallest possible value. A decimation by 8 of the input signal and interpolation by 8 of the output signal are introduced. To process independently both channels in-phase and quadrature (accumulator and variable gain stage), an I/Q demodulation at 625 kHz is first operated. Afterwards, channels are modulated at 625 kHz, one in phase the other in quadrature, and phase shifted before being added. The delay in the loop due to the processing time in the controller can make the loop unstable. The phase shift is introduced to avoid this effect [4]. The rejection bandwidth is adjusted by the loop gain.

Fig. 3 shows the intensity noise spectral density of the correction beam around 625 kHz with or without the correction. It is measured by a spectrum analyzer connected at the output of the in-loop photodiode (error signal). With the correction, a large rejection in a narrow band centered at 625 kHz is observed. The precise value of noise rejection at 625 kHz is measured with a zero span (Fig. 4). A rejection of 41 dB is found.

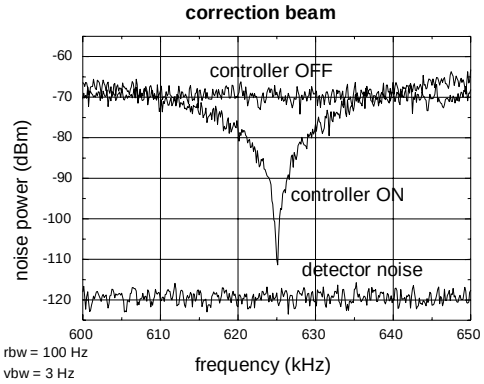

Fig 3: Noise spectral density of the correction beam near 625 kHz.

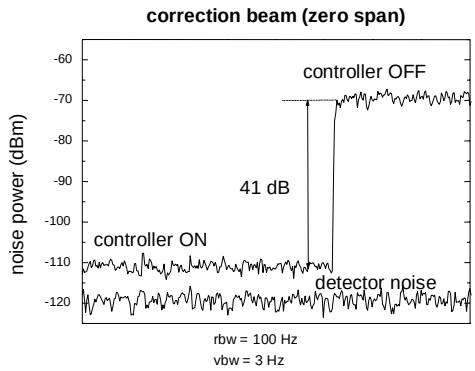

Fig 4: Noise rejection at 625 kHz (correction beam).

The intensity noise spectral density of the probe beam near 625 kHz is shows in Fig. 5. It is obtained at the output of the photodiode which measures the probe beam intensity at the output of the I_2 cell. As for the correction beam, a large noise rejection is seen around 625 kHz. The measurement with a zero span gives 32 dB (Fig. 6).

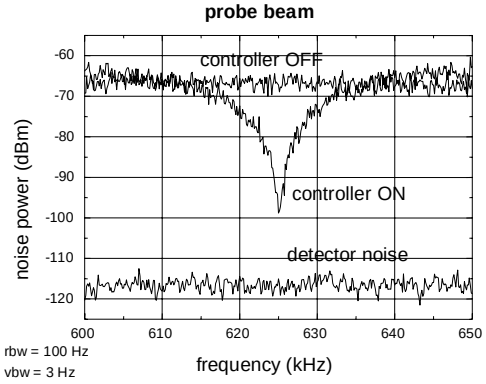

Fig 5: Noise spectral density of the probe beam near 625 kHz.

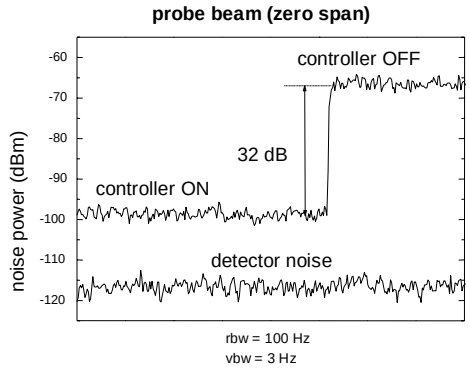

Fig 6: Noise rejection at 625 kHz (probe beam).

IV. FREQUENCY NOISE DETECTION IN THE RANGE 1-100 HZ

To evaluate the possibilities offered by the noise rejection device in term of laser stabilization in the range 1-100 Hz, the spectral densities of signals detected in the cell at 625 kHz in various cases are shown in Fig. 7. The vertical scale for spectral density expressed in Hz^2/Hz is deduced from the slope of the detected line corresponding to the hyperfine transition. In all cases, the laser is prestabilized on a mode of the Fabry-Perot resonator.

In a first step, we have recorded the noise spectral density with and without intensity noise rejection when no saturated absorption signal is detected (the pump beam is suppressed). Without noise rejection (controller OFF), an equivalent noise spectral density larger than 10^6 Hz^2/Hz is observed. With noise rejection (controller ON), the noise spectral density is decreased by 30 dB, which gives 3000 Hz^2/Hz, in a frequency band larger than 100 Hz.

In a second step, the noise spectral density is recorded when the laser is locked to the iodine hyperfine transition detected in the cell. The frequency band of this servo loop is small enough to have the laser only prestabilized on the Fabry-Perot resonator mode for frequencies above 1 Hz. Without intensity noise rejection, the spectral density of the error signal is the same as that measured with the unlocked laser. In this case, the components due to frequency noise are much smaller than the probe beam intensity noise and no frequency correction is possible. With noise rejection, the frequency noise components appear clearly above the amplitude noise level (3000 Hz^2/Hz) in a frequency range larger than 100 Hz. The frequency correction is now possible in this range.

It is interesting to evaluate the expected laser stability assuming a white noise with a spectral density 3000 Hz^2/Hz. In this case, the linewidth of the laser would be ~10 kHz (FWHM) and the relative Allan deviation would be at the 10^{-13} level for 1 s integration time. Experimentally, the stability is obtained from the direct measurement of the absolute frequency of the laser by comparison to a mode of a femtosecond laser, the optical spectrum of which is enlarged by a photonic crystal fibre. The repetition rate of the femtosecond laser is locked to a local oscillator driven by a reference signal with a high level of stability and accuracy received from BNM-SYRTE (Observatoire de Paris) through a 43 km long optical fibre [1]. The stability of the Ar^+ laser with the prestabilization system described here is found to be $2x10^{-13}$ @ 1 s, which corresponds to the expected value. The previous system had stability at the 10^{-12} level [1].

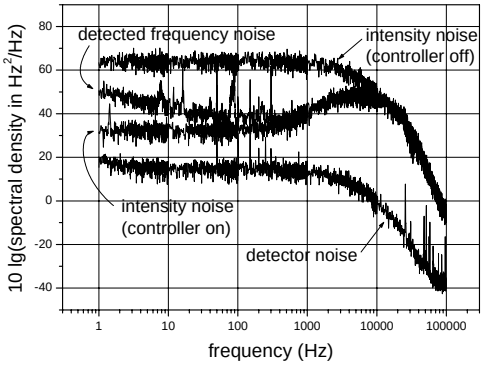

Fig 7: Noise spectral density of the error signal of the laser stabilisation on iodine.

V. CONCLUSION

We have described the improvement of the short term stabilization of an Ar^+ laser for the realization of an optical frequency standard at 501.7 nm. To overcome the limitations due mechanical vibrations of the Fabry-Perot resonator used for the enhancement of the laser spectral purity, an additional feedback loop for the frequency correction in the range 1-100 Hz. is introduced. It is based on detection of an iodine hyperfine transition in a cell at a pressure of 4 Pa. We have shown that this scheme gives the opportunity to detect the laser frequency noise up to 100 Hz. The short term stability obtained with the new scheme is found to be at the 10^{-13} level.

REFERENCES

[1] F. Du Burck, C. Daussy, A. Amy Klein, A. N. Goncharov, O. Lopez, C. Chardonnet, J.-P. Wallerand, IEEE Trans. Instrum. Meas., **54**, 754 (2005)

[2] F. Du Burck, O. Lopez, Electron. Lett., **38**, 1447 (2002)

[3] B. Widrow, J. R. Glover, JR., J. M. McCool, J. Kaunitz, C. S. Williams, R. H. Hearn, J. R. Zeidler, E. Dong, JR., R. C. Goodlin. Proc. IEEE, **63**, 1692 (1975)

[4] F. Du Burck, G. Tetchewo, Electron. Lett., **41**, 1365 (2005)

Proceedings of the 20th EFTF, 2006

Phase-sensitive detection of the atomic resonances by using an acousto-optical modulator in a Raman-Nath diffraction mode.

V. Baryshev, Yu. Domnin, and L.Kopylov.
Institute for Metrology of Time and Space (IMVP FGUP "VNIIFTRI"), Moscow Area, Mendeleevo, 141570 RUSSIA.

e-mail: barychev@aspnet.ru

A new method for frequency stabilization of an external cavity diode laser without the use of direct injection current modulation is presented. A Pound-Drever FM sideband technique with AOM operating in a single pass Raman-Nath diffraction mode as an external phase modulator and atomic resonance as the frequency reference are used to produce an error signal for frequency locking of the laser diode to the resonances within caesium D_2 spectral line.

1. INTRODUCTION

Reduction of semiconductor laser frequency noise is essential in a variety of fields, including metrology, precision optical measurements. The free running linewidth of an external cavity diode laser (ECDL) is of the order of a few megahertz and is limited by the mechanical and acoustic vibrations of the external cavity. Such frequency fluctuations can be removed by electronical feedback to the laser diode (LD) injection current. At present, a conventional Pound-Drever FM sideband technique [1,2] with electro-optical modulator (EOM) as an external phase modulator is used to provide the error signals for extremely high speed servo-loops for frequency stabilization of a variety of the lasers, including diode lasers. It has been found [3] that acousto-optical modulator (AOM) operating in a Raman-Nath diffraction mode can be used as an external phase modulator in Pound-Drever FM sideband technique converting the single mode diode laser input into a pure frequency-modulated (FM) spatially separated optical spectrum. When driven sinusoidally and for normal incidence, AOM can be used to generate frequency sidebands symmetrically spatially located around cw optical beam. Sinusoidal modulation at acoustic wave frequency Ω generates frequency sidebands at multiples of Ω about the central optical frequency ω. The electric field of the optical beam after passing through AOM can be described by well known formula as [4]:

$$E = E_0 e^{i[\omega t + m\sin(\Omega t)]} =$$

$$= E_0 \left\{ \sum_{k=0}^{\infty} J_k(m)\, e^{ik\Omega t} + \sum_{k=1}^{\infty} (-1)^k J_k(m)\, e^{-ik\Omega t} \right\} e^{i\omega t}$$

This is the spectrum of a phase-modulated electric field and it is given by Bessel functions. The amplitude of the k^{th} sideband at $\omega+k\Omega$ is proportional to $J_k(m)$, where J_k is the Bessel function of the order k and m is the peak phase modulation. The diffraction angle ϑ_k for k^{th} sideband with frequency $\omega + k\Omega$ is defined by $\sin\vartheta_k = k\lambda/\Lambda$, where λ and Λ are light and acoustic wavelengths respectively.

In this report a new method for frequency stabilization of an external cavity diode laser without the use of direct injection current modulation is described. A Pound-Drever FM sideband technique with AOM operating in a single pass Raman-Nath diffraction mode as an external phase modulator and atomic resonance as the frequency reference are used to produce an error signal for frequency locking of the diode laser to the resonances within caesium D_2 spectral line.

II. EXPERIMENTAL SET-UP AND RESULTS

The experimental set-up is shown in Fig.1. Grating stabilized SDL-5422 (USA) and IDL150S-850 ("Polyus", Russia) laser diodes in a Littrow configuration provided tunable single-frequency input radiation at 851nm.

The modulator was ISOMET 1205-C2 AOM (which is specified as acousto-optical deflector with 80 MHz center frequency and with sweep bandwidth of 40 MHz) driven by approximately 100 mW of rf power at frequencies (in the 30 – 40 MHz range) large compared to the 5 MHz of natural linewidth of the optical transitions.

For such modulation parameters and for some certain adjustment of input light beam, the AOM output

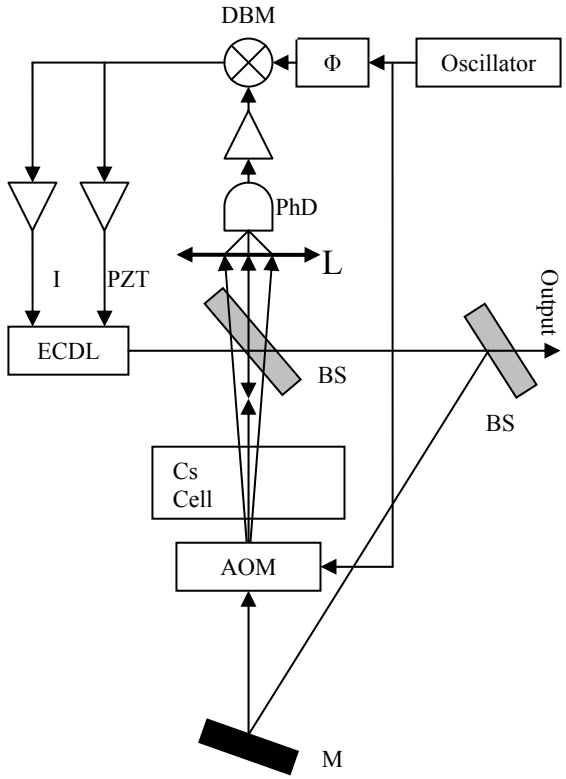

Fig.1. Experimental set-up. ECDL – external cavity diode laser; PZT – piezoelectric transducer; Φ – phase adjuster; BS – beam splitter; M – mirror; AOM – acousto-optical modulator; L – lens; PhD – photo-detector; I – injection current; DBM – double-balanced mixer.

consisted only of three beams corresponding to the carrier light and to the nearest sidebands of the ±1-st diffraction order with the measured diffraction angle $\vartheta_{\pm 1} \cong 0.5^{o}$. The AOM single pass output presenting pure frequency modulated and spatially separated optical spectrum was used as a probe beam for saturated absorption spectroscopy in a caesium vapour cell at room temperature and was focused on a p-i-n photodetector which had a bandwidth of 40 MHz. The ratio of powers of each ±1-st diffraction order sidebands to the carrier power in front of the input window of the Cs cell was equal to $P_{\pm 1} / P_0 = 65\ \mu W / 1.75\ mW \cong 0.04$. The rf beat was detected by heterodyne detection using double-balanced mixer (Mini-Circuits SRA-1), which produced dc signal served as an error signal for fast electronical feedback circuit. Fig.2 and Fig.3 show dispersion like shaped error signals with zero background level obtained when the laser frequency is scanned across Doppler profile of caesium D_2 absorption line and coincides with optical transition frequencies $6S_{1/2}$, F = 4 – $6P_{3/2}$, F' = 3,4,5, where F и F' are the total angular momenta of the atom in ground and excited states. The only experimental parameter varied during recording of these figures. That was the modulation frequency, which had values of 30.1 and 34.3 MHz.

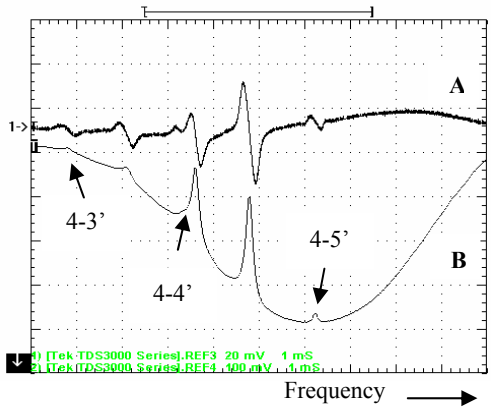

Fig.2. Curve A: Error signal. Curve B: Saturated absorption signal simultaneously recorded in a different cell and given for reference. Modulation frequency – 30.1 MHz.

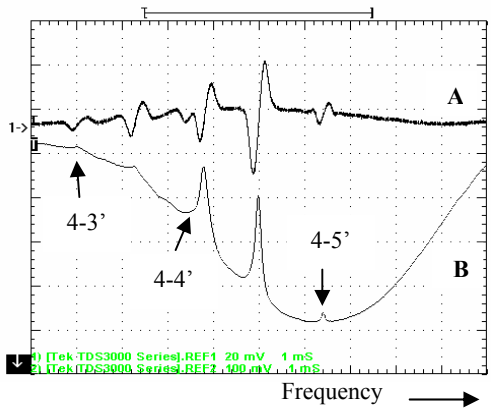

Fig.3. Curve A: Error signal. Curve B: Saturated absorption signal simultaneously recorded in a different cell and given for reference. Modulation frequency – 34.3 MHz.

For fixed modulation frequency, the similar change of the error signal shape and slope sign is obtained by adjustment of the phase relation between mixer input signals. This adjustment is readily accomplished by varying the length of the cable connecting the mixer and RF oscillator. A second, low-frequency servo-loop was used to compensate for slow drifts caused by thermal and mechanical perturbations. The amplified and integrated output of the mixer is fed to piezo-electric transducer (PZT), which controls the grating position.

It should be noted that FM sideband spectroscopy with AOM serving as an external phase modulator demonstrates the similar response to the noise sources, degrading the sensitivity of the method, as it has been described in detail in [2]. One of such detrimental effects is the presence of residual AM noise arising from the fact that the available optical phase modulators do not produce the pure FM spectrum. Small imbalance in the amplitudes of the sidebands or a relative shift in phase can prevent the beat signal from vanishing exactly. This residual AM can be detected by the photodiode and introduces a nonzero baseline whose level can fluctuate with the laser power fluctuations. This noise can be minimized by careful aligning the input and output polarizations of the modulator to balance the sidebands and by adjusting the relative phase of the local oscillator and signal to minimize the offset due to residual AM. In our case we do not care about the input and output polarizations of the light passing AOM at all. The balance of the sidebands is accomplished simply by the rotation of AOM in the horizontal plane.

After some reassembling of optical set-up (mainly due to the changes of the cables) we have found the same response of the system at modulation frequencies of 23.8 and 26.8 MHz, in frequency region where efficiency of AOM to operate in both Bragg and Raman-Nath diffraction modes even weaker than that descriebed before. Fig. 4,5 show the error signals with the same slope sign reversal as we observed for modulation frequencies of 30.1 and 34.3 MHz.

Surprisingly and as another proof of high sensitivity of the method, we have obtained the error signals at frequencies (around 10 MHz) where acousto-optical modulators used not to be used in a Bragg difraction mode. In this case the 1-st Raman – Nath diffraction order sidebands are nearly vanished. However, they are still strong enough to induce FM spectroscopy at such low modulation frequencies (Fig. 6,7).

Thus, changing only the modulation frequency value (in 10 MHz - 40 MHz region) we could readily distinguish two modes of the FM spectroscopy method, when the modulation frequency was so high that only one of the sidebands interacts strongly with the absorbing medium [2] or when two sidebands were located within sub-Doppler resonances width [1].

As we need to shield the detection units from detrimental electromagnetic radiation scattered, for instance, by the relatively strong amplifier driving AOM, it seems advantageous to use lower modulation frequencies.

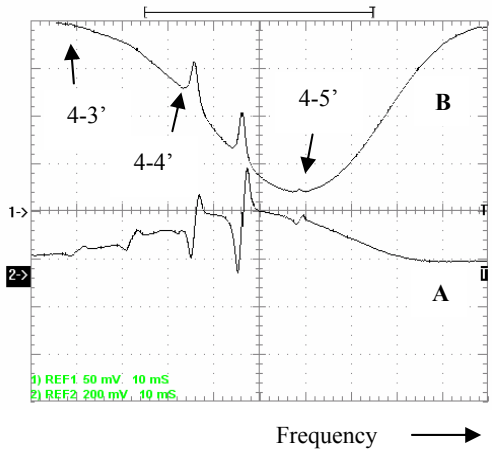

Fig. 4. Curve A: Error signal. Curve B: Saturated absorption signal simultaneously recorded in a different cell and given for reference. Modulation frequency – 23.8 MHz.

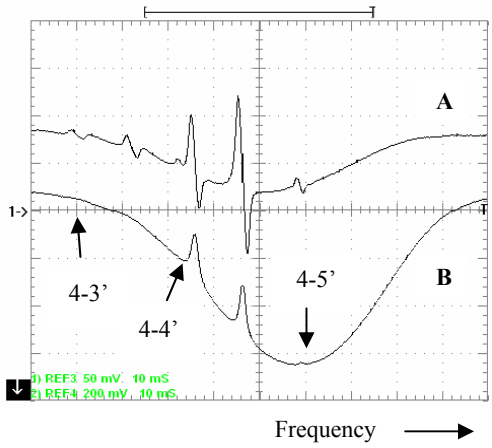

Fig. 5. Curve A: Error signal. Curve B: Saturated absorption signal simultaneously recorded in a different cell and given for reference. Modulation frequency – 26.8 MHz.

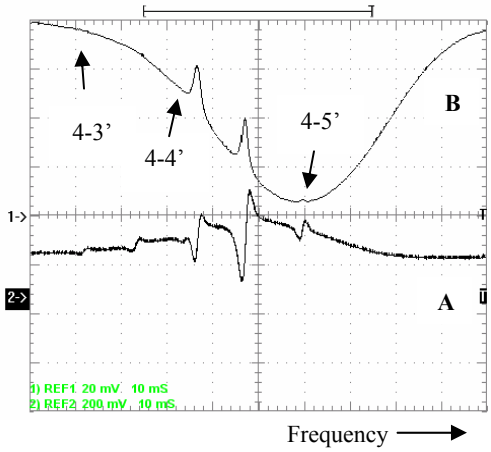

Fig. 6. Curve A: Error signal. Curve B: Saturated absorption signal simultaneously recorded in a different cell and given for reference. Modulation frequency – 12.2 MHz.

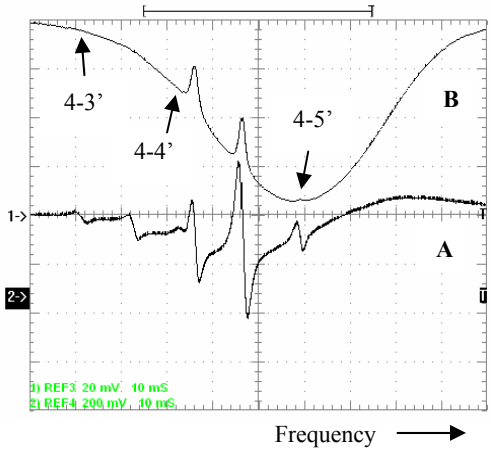

Fig. 7. Curve A: Error signal. Curve B: Saturated absorption signal simultaneously recorded in a different cell and given for reference. Modulation frequency – 11.2 MHz.

III. CONCLUSIONS

Phase-sensitive and fast detection of the atomic resonances has been carried out by means of FM sideband spectroscopy with AOM operating in a single pass Raman-Nath mode as an external phase modulator. Acceptable level of the obtained in a wide modulation frequency range mixer output signals allowed to use them as the error signals for a high speed servo-loop. With the use of Pound-Drever FM sideband technique and negative electronical feedback, wide-bandwidth frequency noise suppression and stable frequency locking of the external cavity diode lasers to the sub-Doppler resonances within D_2 absorption line of Cs atom are achievable.

REFERENCES

[1] R.Drever, J.Hall, F.Kovalski, J.Hough, G.Ford, A.Munley, and H.Ward, Appl. Phys. B, **31**, 97 (1983).
[2] G.Bjorklund, M.Levenson, W.Lenth, and C.Ortiz, Appl. Phys. B, **32,** 145 (1983).
[3] V. Barychev, Proceedings of SPIE, **5480**, 20 (2004).
[4] Dieulesaint et D.Royer, Ondes Elastiques Dans Les Solides, Masson et C^{ie}, 1974, (russian edition: Uprugie Volny v Tverdyh Telah, M:Nauka, 1982).

Proceedings of the 20th EFTF, 2006

Vibration-insensitive mounting of a reference cavity for an optical clock

T. Nazarova, F. Riehle, and U. Sterr *
Physikalisch-Technische Bundesanstalt, Bundesallee 100, 38116 Braunschweig, Germany
**Electronic address: Uwe.Sterr@ptb.de*

We report on a novel vibration-insensitive mounting design of the reference cavity used for stabilization of the clock laser in an optical frequency standard. The cavity is supported in the horizontal symmetry plane on four supporting points while the optical axis is oriented horizontally. The positions of the points have been optimized by finite element analysis. This has resulted in a measured sensitivity to acceleration of 1.5 kHz/(m/s^2) in the vertical and 14 kHz/(m/s^2) in the horizontal direction. This is a reduction of two orders of magnitude in the vertical and one order of magnitude in the horizontal direction compared to the support from below.

I. INTRODUCTION

Highly stable and spectrally narrow lasers [1],[2],[3] are necessary as local oscillators in optical frequency standards [4],[5],[6] where they deliver the short-term stability between interrogations of the atomic transition. They also find applications in high-resolution spectroscopy [7], tests of fundamental physics [8], and interferometric measurements [9].
In the case of atomic clocks where a narrow atomic transition is interrogated discontinuously, the Dick effect leads to degradation of the frequency stability through the aliasing of high frequency laser noise [10],[11]. Thus to exploit the ultimate stability of a frequency standard given by the quantum projection noise [12] the spectral density of the laser's frequency noise in the low frequency range must be reduced.
A stable optical oscillator is realised by locking a laser to a narrow resonance of a high finesse cavity [13]. In the low frequency range (below 100 Hz) the stability of the laser is limited by fluctuations of the optical length of the reference cavity caused by acoustic and seismic vibrations which lead to quasi-static deformations of the cavity. Thus for achieving a laser linewidth in the range of a few Hertz, demanding vibration isolation systems are employed. For further improvement it is necessary to design the cavity in a such way that it shows a low sensitivity to accelerations.

II. Ca-FREQUENCY STANDARD

At PTB, we operate an optical frequency standard based on the optical intercombination transition $^1S_0 - {}^3P_1$ at 456 THz (λ = 657 nm) in ^{40}Ca atoms [4]. Ca atoms are cooled to a temperature of about 2 mK in the first cooling stage on the strong $^1S_0 - {}^1P_1$ (423 nm) transition (Fig. 1). In 10 ms about 10^7 atoms are trapped.

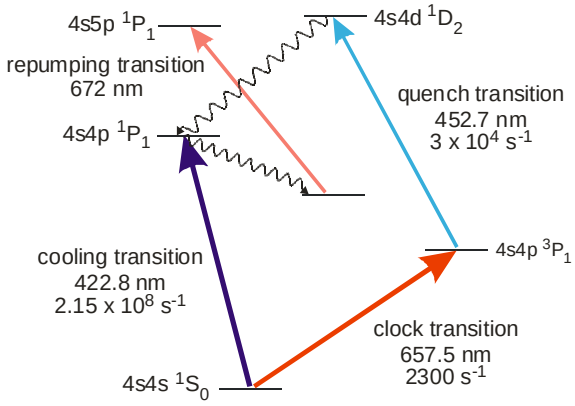

Fig. 1: Partial energy level scheme for ^{40}Ca with transition wavelengths and Einstein A coefficients

A second cooling stage is performed by using the clock transition. The absorption rate and the cooling force are increased by a quench laser at 453 nm that deexcites atoms from $^3P_1$ state to the ground state via the $^1D_2$ state. With this method $3 \cdot 10^6$ atoms are cooled down to 12 µK, corresponding to an rms velocity of 10 cm/s.

III. PROBING THE CLOCK TRANSITION

To interrogate the optical intercombination transition a frequency-dependent 4-pulse Ramsey-Bordé interferometer in the time domain is used [14]. The temperature of the ensemble is low enough to allow the necessary $\pi/2$-pulse to address the entire velocity distribution of the atomic ensemble. A high efficient electron-shelving method is used to measure both outputs of the atom interferometer.
The interrogation laser for the calcium 657 nm intercombination line is an extended cavity diode laser in Littman configuration which is locked to a high finesse (F=79000) reference cavity by a Pound-Drever-

Hall technique [13]. The laser setup is described in detail elsewhere [3]. The reference cavity is a non-tunable Fabry-Perot resonator made from ultra-low expansion glass (ULE). It has a diameter of 8 cm and a length of l = 10 cm.
With this setup a laser linewidth of 1 Hz has been demonstrated [3]. The measured spectral density of the frequency fluctuations is shown in Fig. 2. The rise of the frequency fluctuations in the range below 100 Hz is due to acoustic and seismic vibrations.

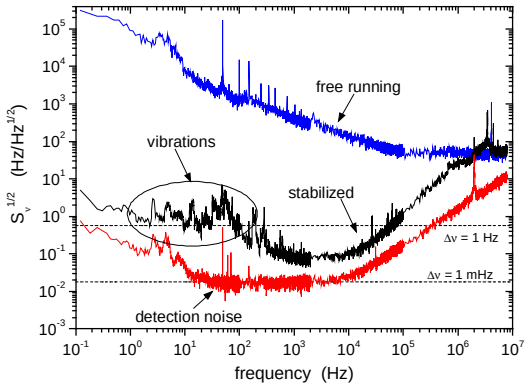

Fig. 2: Spectral density of the frequency fluctuations of the clock laser measured with an independent system

When the laser is stabilized to the calcium clock transition a stability of $\sigma_y(1\text{s}) = 2\cdot10^{-14}$ was reached recently [4] which was mainly limited by the Dick effect. The fundamental limit given by the quantum projection noise (QPN) amounts in our case for $N = 3\cdot10^6$ atoms and cycle time of $T_c = 25\,\text{ms}$ to $\sigma_y(1\text{s}) = 5\cdot10^{-16}$. To reach the QPN the frequency stability in the low frequency range limited by acoustic vibrations must be improved.

IV. ASYMMETRICAL MOUNTING

In our previous setup the cavity was supported from below at the points at the distances $0.21\cdot l$ from both ends by four small cylindrical elastomer pieces (Viton) under an angle of 35° with respect to the vertical direction.
Vibrations couple through the mounting to the cavity and cause forces which lead to deformations of the cavity and change its length.
For the case of this asymmetrical mounting configuration we used the finite element method (FEM) to calculate the deformations of the cavity resulting from vertical accelerations. The results are shown in Fig. 3.

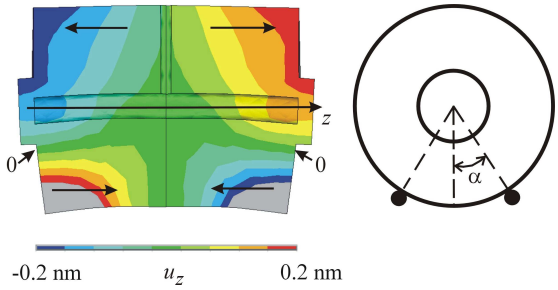

Fig. 3: Calculated displacement u_z of a cavity supported from below under a vertical acceleration of a_y = 10 m/s^2. The deformation is magnified by a factor of 10^7.

The change of the distance between the mirrors amounts in this case to $3.7\cdot10^{-10}$ m leading to a calculated sensitivity to vertical accelerations k_y = 170 kHz/(m/s^2).
To measure the acceleration sensitivity the platform where the cavity is situated was manually excited and the acceleration of the platform and the beat frequency with an independent laser were recorded simultaneously (Fig. 4).

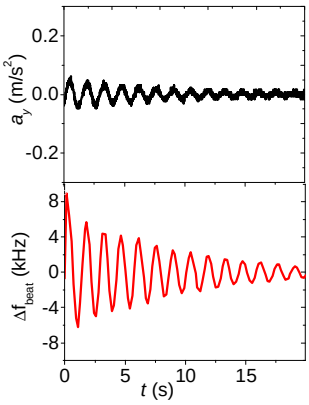

Fig. 4: Measurement of the acceleration sensitivity for the vertical direction for the asymmetrical mounting. Upper graph: acceleration a_y of the resonator platform, lower graph: beat frequency Δf_{beat} with an independent laser.

The measured acceleration sensitivity for the vertical direction amounts to k_y = 120 kHz/(m/s^2).
We use a simple model to illustrate the principles of the mounting. As example a cuboid-shaped spacer of dimensions d_x, d_y, d_z is considered where the cavity is held in a plane. Therefore no cavity bending occurs which otherwise would appear when the cavity is held in discrete points. The acceleration induced length change (shown in Fig. 5) for the vertical direction y can be calculated as:

$$\Delta d_y = \frac{F d_y}{E A} = \frac{\rho d_y^2}{E} a_y \qquad (1)$$

where F denotes the acceleration force, ρ the density, E Young's modulus, A the area perpendicular to the acceleration a_y.
For the axial direction z one obtains:

$$\Delta d_z = \nu \frac{\rho d_z d_y}{E} a_y \qquad (2)$$

with ν Poisson's ratio.

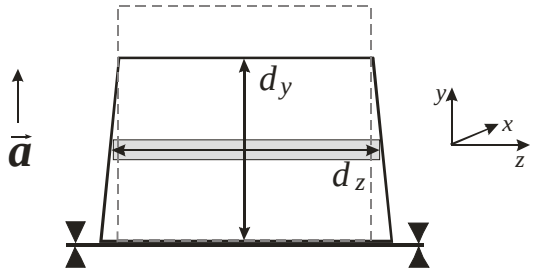

Fig. 5: Acceleration induced deformations of a cuboid-shaped spacer

Approximating our cavity by a cuboid of dimensions $d_x = d_y = 0.08$ m, $d_z = 0.1$ m we can estimate the acceleration sensitivity in the vertical direction using eq. (2) to k_y = 200 kHz/(m/s^2).

V. PRINCIPLES OF THE SYMMETRICAL MOUNTING

The idea of reducing the acceleration sensitivity by supporting a cavity in its symmetry plane has been discussed since several years [15],[16]. In this case one half of the cavity is compressed due to the acceleration while the other half expands. This leads via Poisson's ratio to the expansion of the first half and compression of the second half in the direction of the optical axis (see Fig. 6 right). On the optical axis both effects are compensated which results in a reduced sensitivity to accelerations.
This idea was recently applied for a cavity with a vertical optical axis [17]. With this configuration a sensitivity of the eigenfrequency on accelerations of 10 kHz/(m/s^2) was achieved.

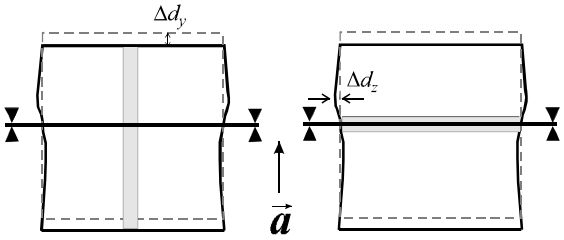

Fig. 6: Different designs of symmetrical mountings: vertical (left) and horizontal (right) orientation of the optical axis.

Fig. 6 shows the both cases of the symmetrical mounting. A symmetrical mounting of the reference cavity with a horizontal optical axis has the following advantages compared with a mounting with a vertical axis. For suspended cavities with a vertical optical axis, the two relative length changes $\Delta d_y / d_y$ which must be compensated depend linearly on the cavity length (eq.1). For cavities with horizontal axis the relative length change $\Delta d_z / d_z$ is reduced by the Poisson's ratio (eq.2) which is ν = 0.17 for ULE and does not depend on the cavity length. This allows one to use longer cavities for reducing the thermal noise without compromising the vibrations sensitivity.

VI. NOVEL DESIGN

Our novel cavity mounting [16] that we have realized is shown in Fig. 7. The cavity is supported in its horizontal symmetry plane on four support points.

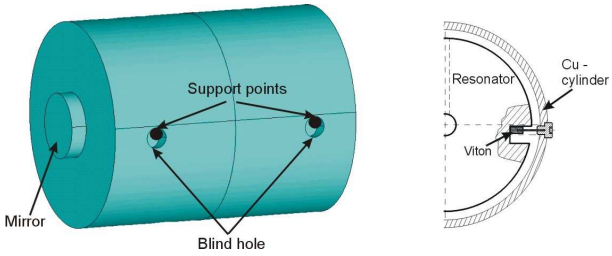

Fig. 7: Vibration-insensitive mounting of a reference cavity with a horizontal optical axis.

Since the cavity is held in discrete points a bending of the cavity occurs in addition to the change of the distance between the mirrors. This leads to a mirror tilt about the geometrical axis which can result in an additional length change if the optical axis is not exactly centered in the middle of the mirrors. Thus analytical considerations are not sufficient to determine the position of the support points. Therefore we performed finite element analysis to find the best positions where both the length change between the mirrors and the mirror tilt are minimal under vertical acceleration.
Fig. 8 shows the calculated displacement u_z along the z-direction for the optimal position of the support points. In this configuration the minimum of the length change is on the optical axis. In our particular case the optimal position of the support points amounts to $y = 0.9$ mm along the vertical axis and $z = 35$ mm along the horizontal axis measured from the center of the cylinder.

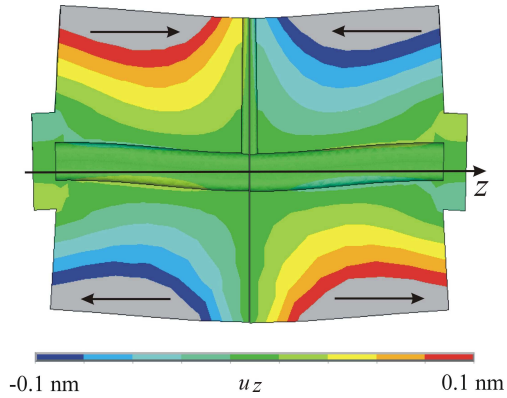

Fig. 8: Calculated displacement u_z of a cavity supported symmetrically in the horizontal plane under an vertical acceleration of a_y=10 m/s^2. The deformation is magnified by a factor of 10^7.

The technical implementation of the cavity suspension is shown in Fig. 7 (on the right-hand side). Four blind holes with a diameter of 8 mm and a depth of 10 mm are milled in the cavity at the positions determined by the simulation. Since the support plane is over-determined by four points an elastic support on Viton cylinders put on spring wires is used. The Viton cylinders of 3 mm diameter and 7 mm length also damp oscillations of the mounting.

VII. IMPROVED ACCELERATION SENSITIVITY

We measured the acceleration sensitivity of the symmetrical mounting in three directions. The result for the vertical direction is shown in Fig. 9. For the symmetrical mounting the acceleration sensitivity for the vertical direction amounts to $k_y = 1.5$ kHz/(m/s^2). This is an improvement of two orders of magnitude compared with the asymmetrical mounting. The acceleration sensitivities for the horizontal directions are $k_z = 14.5$ kHz/(m/s^2) for the direction along the optical axis and $k_x = 11$ kHz/(m/s^2) for the perpendicular direction and thus one order of magnitude higher than for the vertical direction. While for the vertical forces each force acts symmetrically on the cavity and the distribution between the four points is not essential the situation for the horizontal forces is quite different. There each force acts asymmetrically and only if the forces are distributed equally between the supports the net length change is compensated.
The observed sensitivity in the horizontal direction corresponds to an asymmetry of the forces of 6 %. As in the laboratory horizontal vibrations can be isolated easier than the vertical ones the higher acceleration sensitivity in this direction is not limiting the overall performance.

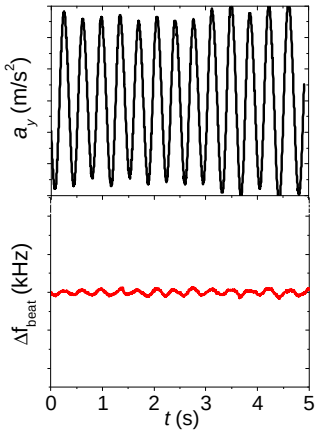

Fig. 9: Measurement of the sensitivity to the vertical acceleration for the symmetrical mounting. Upper graph: acceleration a_y of the resonator platform, lower graph: beat frequency Δf_{beat} with an independent laser.

VIII. STABILITY OF Ca-FREQUENCY STANDARD

With the reduced acceleration sensitivity and improved passive vibration isolation system we expect that we will be able to reduce the spectral density of the frequency fluctuations in the low frequency range to $\sqrt{S_\nu} = 0.08\,\mathrm{Hz}/\sqrt{\mathrm{Hz}}$ (Fig. 10). White frequency noise of this level corresponds to a laser linewidth of 30 mHz. However for low frequencies thermal noise must be taken into account. This noise arises from thermal excited vibration modes of a rigid reference cavity and fundamentally limits the frequency stability [18] which becomes important for longer interrogation times which are used in single ion standards or in optical lattices.

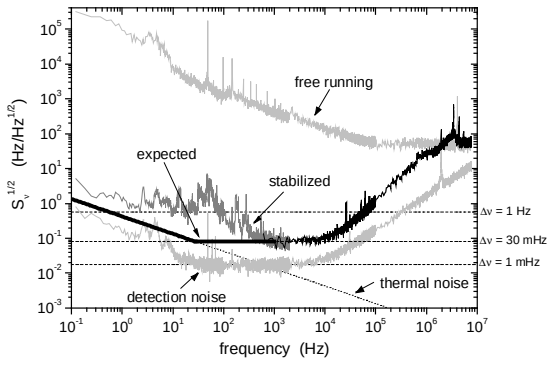

Fig. 10: Expected spectral density of the frequency fluctuations of the clock laser with the new vibration insensitive mounting including the thermal noise of the cavity.

We calculated the contribution of the Dick effect to the frequency stability in Ca atomic clock for the expected frequency noise as shown in Fig. 10. This noise is given by the thermal noise for frequencies up to approximately 30 Hz. It corresponds to a white frequency noise in the range form 30 Hz to 20 kHz and shows a rise for frequencies higher than 20 kHz caused by insufficient gain of the servo loop.
The Dick effect limits the frequency stability to [11]:

$$\sigma_y{}^2(\tau) = \frac{1}{\tau}\sum_{k=1}^{\infty} S_y(kf_c)\left|\frac{g_k}{g_0}\right|^2 \qquad (3)$$

where g_y und g_k are the 0th and kth Fourier coefficients of the sensitivity function g, and f_c denotes the cycle frequency. The sensitivity function $g(t)$ describes the change in the signal, e.g. the change in the excitation probability at the operation point of the frequency standard due to a small δ-like frequency fluctuation of the interrogation laser at time t.
Eq. (3) indicates that one way to reduce the Dick effect is to increase the cycle frequency resulting in a smaller number of low frequency contributions.

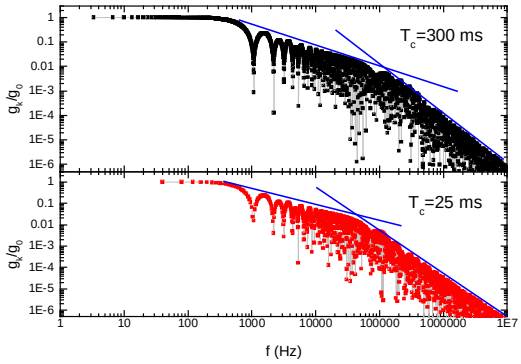

Fig. 11: Normalized Fourier coefficients g_k/g_0 of the sensitivity function: (top) for long cycle time (300 ms) and short interrogation pulse (1.5 µs) as used in a previous measurement, (bottom) for short cycle time (25 ms) and long pulse (5 µs) as intended for use in the future.

We calculated the normalized coefficients g_k/g_0 of the sensitivity function of 4-pulses Ramsey-Bordé atom interferometer for long cycle times (T_c = 300 ms) and short pulses (T_p = 1.5 µs) as used in the previous measurement (Fig. 11, top) as well as for shorter cycle times (T_c = 25 ms) and longer pulses (T_p = 5 µs) as we want to use in next measurements.
The first point of the coefficients of the sensitivity function is at the cycle frequency f_c. Three different regimes in the course of the coefficients of the sensitivity function can be distinguished. The coefficients remain constant for frequencies up to the inverse duration of the interrogation sequence (typically up to 10^3 Hz). Then they decrease like $1/f$ due to the rectangular shape of the sensitivity function [11]. Above a frequency corresponding to the inverse width of the interrogation pulses the coefficients decrease like $1/f^2$.
According to eq.(3) the frequency stability due to the Dick effect is the sum of the spectral density of the frequency fluctuations S_y weighted by the normalized coefficients of the sensitivity function g at multiples of the cycle frequency f_c.

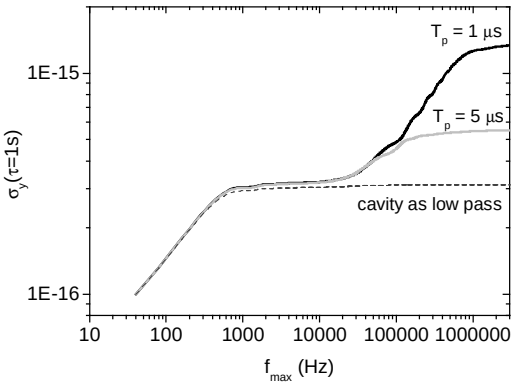

Fig. 12: Partial sum of the contributions to the Dick effect to the Allan standard deviation calculated with the expected frequency noise up to a frequency f_{max}.

To visualize the different contributions to the frequency stability the partial sum of eq.(3) is performed up to a frequency f_{max}. It is shown in Fig. 12 for different pulse durations T_p. The steep rise in the range up to 1 kHz is given by summing up the frequency noise weighted by the Fourier coefficients of the sensitivity function which remain constant in this range. Then the partial sum in the range where the coefficients decrease remains constant. The final rise is due to the increase of the frequency noise at higher frequencies. Above frequencies determined by the inverse pulse width it again remains constant.
For short pulses high frequency fluctuations (f > 20 kHz) provide the main contribution to the instability. Thus the stability can be improved by using longer interrogation pulses. In this case the sensitivity function starts to fall already at smaller frequencies and the high frequency fluctuations add less to the instability. On the other hand the Fourier width of the pulses must be large enough to address the whole velocity distribution of the atoms. Thus for ballistic atoms the pulse width is limited. We find that for a temperature of 10 µK pulse widths of up to 5 µs are possible without reducing the signal.

IX. CONCLUSION

We have demonstrated a considerable reduction of the acceleration sensitivity of an optical reference cavity by

supporting the cavity in its symmetry plane. We have measured an acceleration sensitivity of 1.5 kHz/(m/s^2) in the vertical and 14 kHz/(m/s^2) in the horizontal direction. With the reduced sensitivity and improved vibration-isolation system vibrations will contribute with 30 mHz to the laser linewidth at optical frequency of 456 THz and will not be the most dominant contributions anymore.
With the new experimental parameters (T_c = 25 ms, T_p = 5 µs and reduced S_y) we will be able to reduce the contribution of Dick effect to $\sigma_y(1\text{s}) = 5 \cdot 10^{-16}$ in one second making it possible to operate the frequency standard at the quantum projection noise.

Acknowledgements

We thank the Deutsche Forschungsgemeinschaft for supporting this work under SFB 407.

REFERENCES

[1] B. C. Young, F. C. Cruz, W. M. Itano, and J. C. Bergquist, *Visible lasers with subhertz linewidths*, Phys. Rev. Lett. **82**, 3799-3802 (1999)

[2] S. A. Webster, M. Oxborrow, and P. Gill, *Subhertz-linewidth Nd:YAG laser*, Opt. Lett. **29**, 1497-1499 (2004)

[3] H. Stoehr, F. Mensing, J. Helmcke, and U. Sterr, *Diode laser with 1 Hz linewidth*, Opt. Lett. **31**, 736-738 (2006)

[4] C. Degenhardt, H. Stoehr, Ch. Lisdat, G. Wilpers, H. Schnatz, B. Lipphardt, T. Nazarova, P.-E. Pottie, U. Sterr, J. Helmcke, and F. Riehle, *Calcium optical frequency standard with ultracold atoms: Approaching 10^{-15} relative uncertainty*, Phys. Rev. A **72**, 062111-1-17 (2005)

[5] H. S. Margolis, G. P. Barwood, G. Huang, H. A. Klein, S. N. Lea, K. Szymaniec, and P. Gill, *Hertz-Level measurement of the optical clock frequency in a single $^{88}Sr^+$ ion*, Science, **306**, 1355-1358 (2004)

[6] M. Takamoto, F.-L. Hong, R. Higashi, and H. Katori, *An optical lattice clock*, Nature **435**, 321-324 (2005)

[7] W. H. Oskay, W. M. Itano, and J. C. Bergquist, *Measurement of the $^{199}Hg^+$ $5d^96s^2$ $^2D_{5/2}$ electric quadrupole moment and a constraint on the quadrupole shift*, Phys. Rev. Lett. **94**, 163001-1-4 (2005)

[8] E. Peik, B. Lipphardt, H. Schnatz, T. Schneider, Chr. Tamm, and S. G. Karshenboim, *Limit on the present temporal variation of the fine structure constant*, Phys. Rev. Lett. **93**, 170801-1-4 (2004)

[9] O. Jennrich (Ed.) *Proceedings of the 5th International LISA Symposium*, ESTEC, Noordwijk, The Netherlands, 12-15 July 2004 Special issue of Class. Quantum. Grav. **22**, number 10

[10] G.J. Dick, *Local oscillator induced instabilities in trapped ion frequency standards*, in Proceedings of 19th Annu. Precise Time and Time Interval Conf., Redendo Beach, 133-147 (1987)

[11] A. Quessada, R. Kovacich. I. Courtillot, A. Clairon G. Santarelli, and P. Lemonde, *The Dick effect for an optical frequency standard*, J. Opt. B **5**, S150-S154 2003)

[12] W. M. Itano, J. C. Bergquist, J. J. Bollinger, J. M. Gilligan, D. J. Heinzen, F. L. Moore, M. G. Raizen, and D. J. Wineland, *Quantum projection noise: Population fluctuations in two-level systems*, Phys. Rev. A. **47**, 3554-3570 (1993)

[13] R. W. P. Drever, J. L. Hall, F. V. Kowalski, J. Hough, G. M. Ford, A. J. Munley, and H. Ward, *Laser phase and frequency stabilization using an optical resonator*, Appl. Phys. B **31**, 97-105 (1983)

[14] C. J. Bordé, *Atomic interferometry with internal state labelling*, Phys. Lett. A **140**, 10-12 (1989)

[15] M. Notcutt, C.T. Taylor, A.G. Mann, R. Gummer, and D.G. Blair, *Cryogenic system for a sapphire Fabry-Perot optical frequency standard*, Cryogenics **36**, 13-16 (1996)

[16] This has been suggested by Till Rosenband e.g. at the CAUAC meeting in Porquerolles in April 2004

[17] M. Notcutt, L.-S. Ma, J. Ye, and J. L. Hall, *Simple and compact 1 Hz laser system via an improved mounting configuration of a reference cavity*, Opt. Lett. **30**, 1815-1817 (2005)

[18] K. Numata, A. Kemery, and J. Camp, *Thermal-noise limit in the frequency stabilization of lasers with rigid cavities*, Phys. Rev. Lett. **93** 250602-1-4 (2004)

Proceedings of the 20th EFTF, 2006

Beyond One-Second Laser Coherence via Active Optical Atomic Clock

Wei Zhuang, Jingbiao Chen*
Key Laboratory for Quantum Information and Measurements, Ministry of Education,
School of Electronics Engineering & Computer Science,
Peking University, Beijing,100871, P. R. China

In this report we present the possibility to realize laser coherence time beyond one second via the principle of active optical atomic clock, which is a laser with cavity mode linewidth is much wider than the linewidth of medium gain profile. By optimizing the parameters of active optical atomic clock based on laser cooled atomic beam, the calculation shows one can reach ten-second coherence time of laser light. More longer coherence time is still possible along this new way.

I. INTRODUCTION

Recently, femtosecond laser physics has been extented to attosecond laser physics [1]. However, for the long time counterpart of ultrashort laser physics, the longest coherence time of laser light has been around one second almost for twenty years [2, 3]. The coherence time of ultra-stable cavity-stablized lasers [2–4] is finally limited to one second by the inevitable thermal Brownian motion noise [5], and unfortunately cryogenic cavity system will be interrupted by liquid nitrogen refilling in every few hours [6].

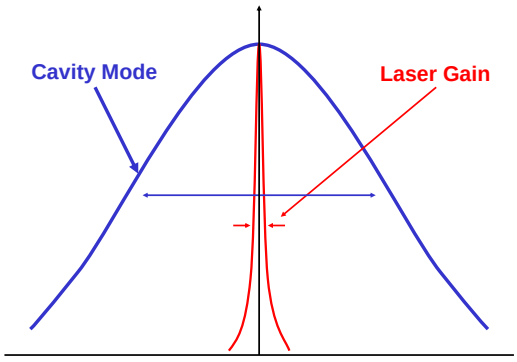

FIG. 1: In an active optical atomic clock, the linewidth of laser gain medium is much narrower than the cavity mode linewidth.

To develope the long-time coherence laser physics, say thousand-second coherence laser physics, is essential to the next generation of high-accuracy optical clocks and high-precision laser spectroscopy. For example, it is impossible to resolve atomic transition line with linewidth less than 0.1 Hz [7] at present for optical clock reference because the available longest coherence-time of a laser is one-second [2, 3]. However, the principle of active optical atomic clock [8, 9] provides the possibility to push the one-second laser coherence to thousand-second laser coherence. In this report, we will describe a detailed experimental scheme to realize laser coherence time beyond one-second to reach ten-second coherence laser light. More longer coherence time is still possible along this new way [9].

*Electronic address: jbchen@pku.edu.cn

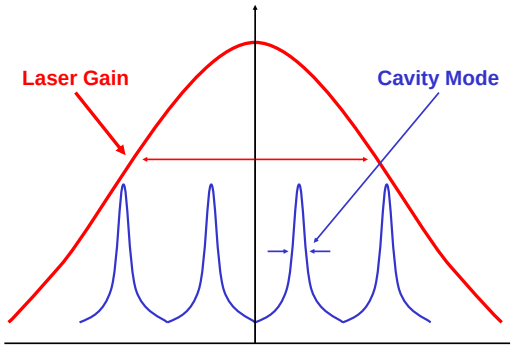

FIG. 2: The linewidth of laser gain medium is much wider than the cavity mode linewidth in a conventional laser.

II. A LASER BASED ON LASER COOLED SLOW MAGNESIUM-BEAM

Generally speaking, an active optical atomic clock is a special laser, in which the linewidth of laser cavity mode is much wider than the laser gain linewidth [8–10] as shown in Fig.1. As a comparison, in a conventional laser, the linewidth of laser cavity mode is much narrower than the laser gain linewidth as shown in Fig.2. And the laser gain medium can be any non-perturbed atoms, molecular, or ions with narrow linewidth transition as that are recommended for optical clock reference transitions [7].

The first advantage of an active optical clock is its very narrow linewidth of output laser [8, 9]. The second advantage is, like its microwave counterpart, the active Hydrogen clock [11], the output frequency of an active optical atomic clock does not follow the cavity-length variation noise tightly, but in the form of dramatically reduced cavity-pulling shift [11–13] when

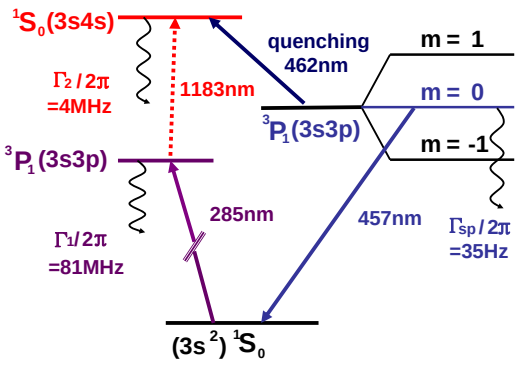

FIG. 3: Energy level diagram of Magnesium

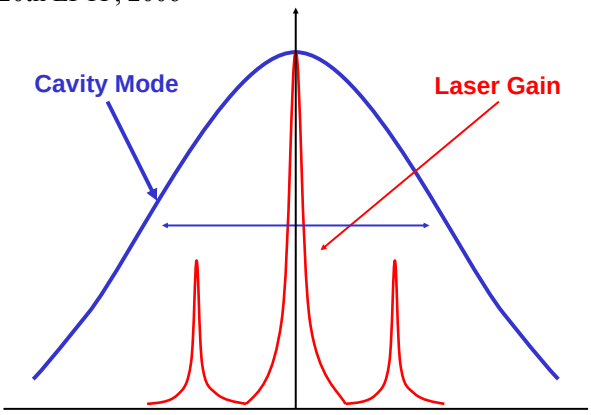

FIG. 4: Sideband of atomic level within 2D Tunnel lamb-Dick regime

the laser cavity mode is much wider than the laser gain linewidth [8, 9]. And this optical clock configuration can be realized with any narrow linewidth transition of Alkaline-earth species, which currently are the candidates of clock transitions of passive optical clock [7].

By optimizing the parameters of active optical atomic clock [8, 9] with laser cooled Magnesium-beam, one can reach ten-second coherence time of laser light. As shown in Fig.3, the lasing transition is the 457nm line of $3s3p\ ^3P_1(m=0)$ to $3s^2\ ^1S_0$ with the spontaneous decay rate of $\Gamma_{sp}/2\pi$= 35 Hz. Assuming the Mg atomic beam is laser cooled to a velocity of 10 m/s, the transit time is $t_{transit} = \sqrt{\pi}W_0/v$=143$\mu$s with a cavity mode waist of W_0=0.8mm, thus the transit-time broadening is $\Gamma_{transit}$=4.3kHz. When the cavity length is 2cm, the atom-cavity coupling constant is $g/2\pi$ = 68Hz. Suppose the atoms can be cooled in the transverse direction to a temperature of the recoil temperature level of 10μK (v_{recoil}=6cm/s) with the quenched narrow-line cooling [14], the residual Doppler broadening will still be about 130 kHz, which is much broader than the transit-time broadening $\Gamma_{transit}$=4.3kHz, thus we propose to use optical tunnels consists of 2D standing wave at magic wavelength [15, 16]. Therefore the first-order Doppler broadening effect will be eliminated. The second-order Doppler broadening can be neglected here. In this case the transit-time broadening $\Gamma_{transit}$=4.3 kHz can be thought as the gain linewidth of laser medium since it is the dominant term among various spectral broadening mechanisms. Once atoms are moving within the Lamb-Dick regime along the 2D magic optical tunnels, the natural linewidth of the excited state, 35 Hz for Mg $3s3p\ ^3P_1(m=0)$, will be the laser gain linewidth [9]. When the linewidth of laser cavity mode is 430 kHz, the ratio of the linewidth of laser cavity mode to gain profile linewidth is about 100. It should be noted that the sidebands of motion levels of magic optical tunnel will produce multi-mode competition in laser caused by the multi-mode gain profile as shown in Fig.4, this effect will be discussed in more detail elsewhere.

Put all these parameters into the theory of active optical clock [8] at laser pumping parameter is around 2, one get the laser emission coefficient of each atom is 25 s^{-1}, the needed atomic flux is 2×10^8 atoms/s, the average intracavity photon number is 600, the output laser power is 60pW, the linewidth is output laser is 17 mHz, which corresponding to a coherence time of about 10 second. There are two main technique challenges, one is to build a special magic optical tunnels for 1D laser cooled atomic beam. The second one is to stabilize the drift of the laser cavity mode as small as 1.7 Hz during this 10 second coherence time with super-cavity system [2–4]. Otherwise one have to increase the ratio of the linewidth of laser cavity mode to gain profile linewidth to a more larger value, in this way to decrease the effect from the cavity length noise. But the cost is one needs much higher atomic flux at low velocity. The light shift due to pumping laser should be decreased and stabilized. As discussed in [9], once the light shift due to pumping laser can be decreased to a very small value, using the optical lattice trapped atoms as laser gain medium directly will be much better since there is no spectral broadening.

The experimental layout of this scheme is shown in Fig.5. After effused from the oven, the Magnesium atomic beam is cooled by Zeeman slowing laser beam with gradient magnet. Applying quenched narrow-line cooling [14], the beam is reflected and collimated. Then, through the adiabatic pumping process [17], Mg atoms are injected into the cavity in the excited state, and laser is released from the cavity by stimulated emission process. It is worth noting that laser cooled atoms is necessary for high-accuracy optical clock even working at active mode. But as a long-time-coherence laser, an active optical clock with thermal beam can also provides a very narrow linewidth if one has an atomic flux strong enough.

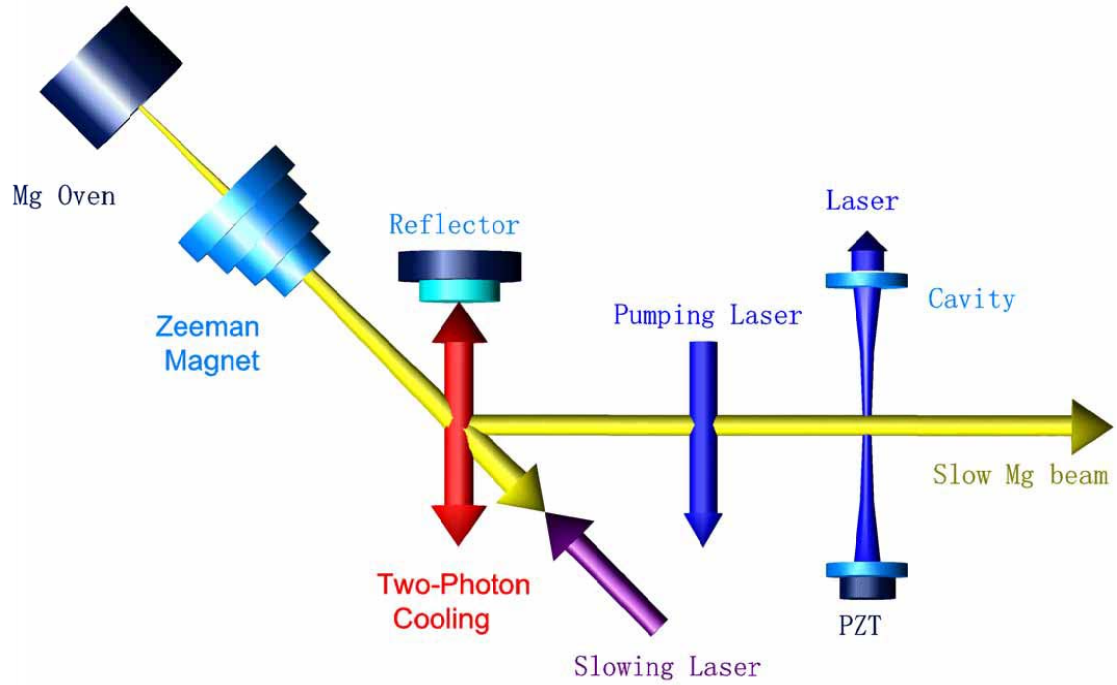

FIG. 5: Sketch of the Active Optical Atomic Clock setup. After effused from the oven, the atomic beam is cooled by Zeeman slowing laser beam with gradient magnet. Applying quenched narrow-line cooling, the beam is collimated. Then, through the adiabatic pumping process [17], and laser is released from the cavity.

III. SUMMARY

We have presented the possibility to push the coherence-time of laser field to as long as ten-second by applying the principle and technique of active optical clock. It provides a novel way for long-time-coherence laser source, which is a prerequisite for precision laser spectroscopy and optical clock with linewidth narrower than one hertz.

Acknowledgments: We would like to thank Yiqiu Wang, Donghai Yang, Xuzhong Chen, Xiaoji Zhou, Hong Guo, and Kaikai Huang for discussions. Funding is provided by NSFC, and MOST (Grant No. 2005CB3724500).

[1] E. Goulielmakis, et al., Science, **305**, 1267 (2004).
[2] D. Hils and J. L. Hall, "Ultra-stable cavity-stablized lasers with subhertz linewidth" in *Frequency Standards and Metrology*, Editor: A. DeMarchi, Springer-Verlag Berlin, Heidelberg 1989.
[3] B. C. Young et al., Phys. Rev. Lett. **82**, 3799 (1999).
[4] D. Hils, J. E.Faller, and J. L. Hall, Rev. Sci. Instrum. **57**, 2532 (1986).
[5] K. Numata, A. Kemery, and J. Camp, Phys. Rev. Lett. **93**, 250602 (2004).
[6] H. Müller, S. Herrmann, C. Braxmaier, Phys. Rev. Lett. **91**, 020401 (2003)
[7] P. Gill, Metrologia **42**, S125(2005).
[8] Jingbiao Chen, arXiv:physics/0512096.
[9] Jingbiao Chen, and Xuzong chen, Proc. of IEEE 2005 Freq. Contr. Symp., 608 (2005).
[10] S. J. M. Kuppens et al., Phys. Rev. Lett.,**73**, 3815 (1994).
[11] H. M. Goldenberg et al., Phys. Rev. Lett., **5**, 361 (1960).
[12] Yiqiu Wang et al., *The Principle of Quantum Frequency Standard*, (Science Press, Beijing, 1986, in Chinese).
[13] J. Vanier and C. Audoin, *The Quantum Physics of Atomic Frequency Standards*, (Adam Hilger, Bristol and Philadelphia, 1988).
[14] E. A. Curtis, C. W. Oates, and L. Hollberg, Phys. Rev. A,**64**, 031403(R) (2001).
[15] H. Katori *et al.*, Phys. Rev. Lett. **91**, 173005 (2003).
[16] M. Takamoto, F. -L. Hong, R. Higashi, and H. Katori, Nature 435,321,(2005).
[17] J. P. C. Kroon *et al.*, Phys. Rev.A **31**, 3724 (1985).

Proceedings of the 20th EFTF, 2006

SMALL COMPACT CALCIUM-BEAM OPTICAL FREQUENCY STANDARD IN PEKING UNIVERSITY AND ITS NEW SCHEME

Kaikai Huang, Donghai Yang, Jingbiao Chen*
Key Laboratory for Quantum Information and Measurements, Ministry of Education,
School of Electronics Engineering & Computer Science,
Peking University, Beijing,100871, P. R. China

In this report, we will first present the most recent experimental progress of small compact Ca-beam optical frequency standard at 657nm wavelength at Peking university. Second, we will discuss our new scheme, which combining pre-pumping, shelving detection, and sharp-angle velocity selection detection. Comparing previous schemes, we expect the short-term stability can be improved at least by a factor of 30, and an expected factor of 10 for uncertainty in our new scheme since Doppler effect can be calibricated with higher accuracy.

I. INTRODUCTION

The reported best performance of Ca-beam optical frequency standard at 657nm wavelength showed the relative frequency uncertainty is 1.3×10^{-12} , and one-second sampling stability is 5×10^{-13} [1–4], which is very close to that of commercial 5071 Cs microwave clock(From HP to Agilent, now Symmetricom company). While many research groups are pursuing the expected high-performance optical clock based on lattice trapped atoms [5–10], we have a goal to make small compact Ca optical clocks with potential performance much better than small Cs microwave clock based on an improved experimental scheme. In this report, we will first present the most recent experimental progress of small compact Ca-beam optical frequency standard at 657nm wavelength at Peking university. Second, we will discuss our new scheme, which combining 657nm pre-pumping [11], 423nm recycling-transition shelving detection [11], and sharp-angle velocity selection detection [12, 13]. Comparing previous schemes [1–4, 12, 14], we expect the short-term stability can be improved at least by a factor of 30, and a factor of 10 for uncertainty in our new scheme since Doppler effect can be calibrated with much higher accuracy.

II. CURRENT STATUS OF THE CA-BEAM OPTICAL FREQUENCY IN PEKING UNIVERSITY

A Calcium thermal beam tube, as shown in Fig.1 has been tested works well at temperature of 700^oC.

We have locked a commercial 657 nm laser diode (Toptica LD-658-0030-1) in an ECDL(external cavity diode laser) Littrow configuration to a high finesse Fabry-Perot cavity by Pound-Drever-Hall method [15], and the laser linewidth is narrowed from 800 kHz to about 6 kHz. The Fabry-Perot cavity is a planar-concave type composed of two high reflectivity mirrors (New port Super Mirror 10CM00SR.30T and 10CV00SR.30T) glued to a 10-cm Zerodur spacer as shown in Fig.2. The manufacture-quoted reflectivity is higher than 99.94% and the central part is polished to less than one angstrom rms microroughness for both of these two mirrors. The nominal finesse of this cavity is about 5000.

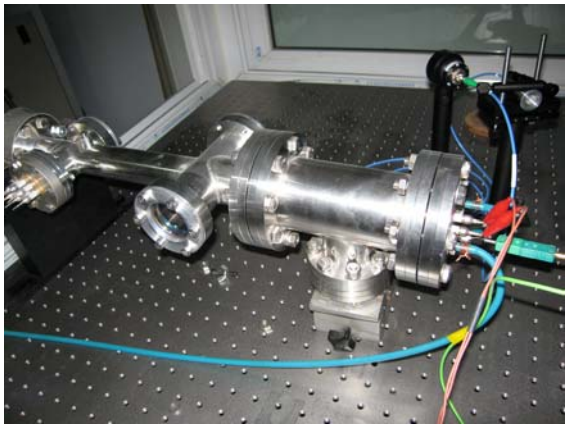

FIG. 1: A small Calcium-beam tube.

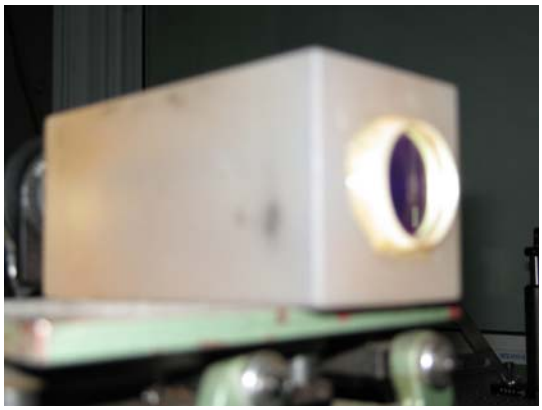

FIG. 2: The Fabry-Perot cavity with Super-mirrors.

About 0.2 mW laser light injects into the cavity via an electro-optic modulator(EOM) which is phase

*Electronic address: jbchen@pku.edu.cn

modulated at 21.4 MHz. The reflected laser light from the cavity is detected by a wideband Avalanche Photodiode(APD). This detected error signal is fed to the laser cathode through a fast feedback circuit, and fed to the PZT of ECDL grating though an integrator.

The Fourier transform of the locked error signal recorded by a 100 MHz bandwidth oscilloscope (Tektronix DS3210B) is shown in Fig.3. The low frequency noise is strongly suppressed.

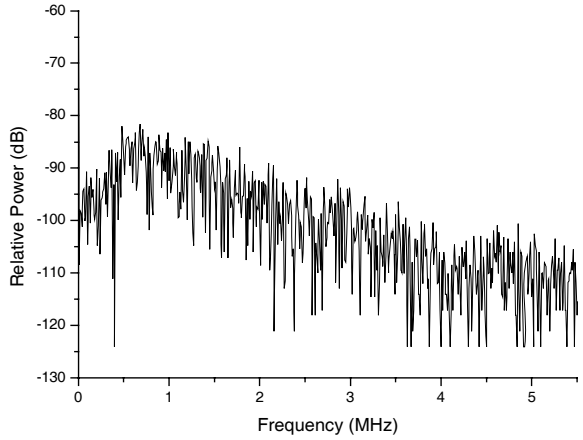

FIG. 3: The Fourier transform spectrum of the locked error signal when the laser is tightly locked to the cavity with both current and PZT feedback.

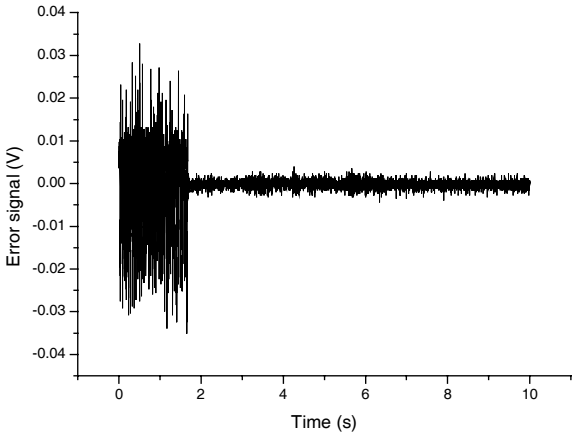

FIG. 4: The detected error signal when laser is roughly locked to the cavity only by PZT feedback at the left side, and the right side is the error signal with both current and PZT feedback locking.

In Fig.4, the detected error signal when laser is roughly locked to the cavity only by PZT feedback is at the left side, and the right side is the error signal with both current and PZT feedback locking. The slope of the error signal at center is calibrated to be 6 kHz/mV. The estimated laser linewidth is about 6 kHz with the typical rms value of the error signal at 1mv when both current and grating PZT servo loops are locked.

With the above described small Calcium thermal beam tube and 6 kHz linewidth 657nm diode laser, we are expect to observe an optical Ramsey spectrum of Ca-beam within several months.

III. NEW SCHEME FOR SMALL CA-BEAM OPTICAL CLOCK

The electron shelving detection [16, 17] has been used in the measurement of quantum jumping [17], and in ion frequency standard, and recently the optical clock with neutral atoms [4]. Strictly speaking, to the best of our knowledge, it has never been effectively used in the optical clock with the thermal atomic beam. We have just proposed to apply this shelving detection in Ca-beam optical clock [11]. We explain this scheme simply in the following.

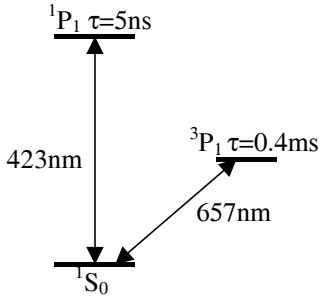

FIG. 5: Energy levels related to Ca-beam optical clock.

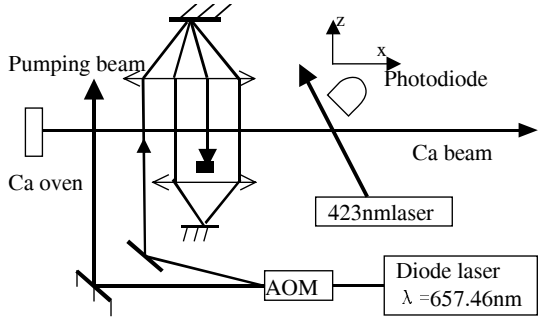

FIG. 6: New thermal Ca-beam optical clock scheme.

As the energy levels of Ca related to Ca-beam optical clock shown in Fig.5, in a conventional thermal Ca-beam optical clock [1–4, 12, 14], after Ramsey interrogation, the signal is detected by the weak fluorescence decay from the 0.4 ms long life state $^3P_1$, thus

the detection efficiency of excited state atoms is lower than 1%. In our proposal [11], the detection efficiency of interrogated atoms can be as high as 100% once the 423 nm shelving detection is used. We conclude it is possible to improve the stability by a factor of 30 at least comparing with previous work [1–4, 18] since we can reach the projection quantum noise limit.

This new scheme is implemented as shown in Fig.6. In this scheme, we also consider to use the sharp-angle velocity selection detection [12, 13]. With the accurately selected velocity group atoms, the major systematic shift error in atomic-beam optical clock [1–4], the Doppler shift can be evaluated in a much higher accuracy. Hopefully we expect the accuracy of the Ca-beam optical clock will be improved by a factor of 10 with the help of much better stability and the velocity selection detection.

It is worth mention that we will also try to build an optical clock with quantum emitter [19]. As shown in Fig.6, the atoms will be pumped into the excited state $^3P_1$ first before the Ramsey interrogation. Or say the optical clock is working under the mechanism of stimulated emission process not the conventional absorption process.

Acknowledgments

We would like to thank Yiqiu Wang, Xuzhong Chen, Xiaoji Zhou, Hong Guo for discussions. Funding is provided by NSFC, and MOST (Grant No. 2005CB3724500).

[1] P. Kersten, F. Mensing, U. Sterr, F. Riehle, Appl. Phys. B 68, 27 (1999).
[2] C. W. Oates, M. Stephens, and L. Hollberg, Proc. of IEEE Int. Freq. Contr. Symp., 219,1997.
[3] N. Ito, J. Ishikawa, and A. Morinaga, Opt. Commun. **109**, 414 (1994).
[4] F. Riehle, *Frequency Standard: Basics and Applications*, (Wiley-VCH Verlag GmbH & Co. KGaA, Germany, 2004).
[5] M. Takamoto, F. -L. Hong, R. Higashi, and H. Katori, Nature **435**,321,(2005).
[6] R. Santra *et al.*, Phys. Rev. Lett. **94**, 173002 (2005).
[7] T. Hong *et al.*, Phys. Rev. Lett. **94**, 050801 (2005).
[8] A. V. Taichenachev *et al.*, Phys. Rev. Lett. **96**, 083001 (2006).
[9] Z. W. Barber *et al.*, Phys. Rev. Lett. **96**, 083002 (2006).
[10] A. Brusch *et al.*, Phys. Rev. Lett. **96**, 103003 (2006).
[11] Kaikai Huang et al., "Application of 423nm shelving detection in thermal Ca-beam frequency standard ", unpublished.
[12] A. Morinaga and N. Ito, CPEM'88 DIGEST, 227 (1988).
[13] Jingbiao Chen et al. , Proc. of IEEE Int. Freq. Contr. Symp., 97,2001.
[14] J. Kowalski, F. Träger, M. Vollmer, and G. zu Putlitz, Z. Phys. A 320, 353 (1985).
[15] R. W. P. Drever *et al.*, Appl. Phys. B, **31** 97 (1983).
[16] H. G. Dehmelt, Bull. Am. Phys. Soc. **20**, 60 (1975).
[17] W. Nagourney, J. Sandberg, and H. Demelt, Phys. Rev. Lett. **56**, 2797 (1986).
[18] J. J. Snyder, J. Helmcke, and D. Zevgolis, Appl. Phys. B 32, 25 (1983).
[19] J. Chen, "Optical clocks based on quantum emitters", Abstract accepted by 2006 IEEE International Frequency Control Symposium.

Proceedings of the 20th EFTF, 2006

Development of the active space hydrogen maser for the ACES space experiment of ESA

P. Berthoud, D. Goujon, D. Gritti, A. Jornod, C. Weber, M. Dürrenberger, H. Schweda, and M. Roulet
B. Thieme*, and G. Baister*
Observatoire de Neuchâtel, Rue de l'Observatoire 58, CH-2000 Neuchâtel, Switzerland
**Contraves Space AG, Schaffhauserstrasse 580, CH-8052 Zürich, Switzerland*
Contact person: patrick.berthoud@ne.ch

In the frame of the scientific mission Atomic Clock Ensemble in Space (ACES), Observatoire de Neuchâtel (ON), Switzerland, is developing the Space Hydrogen Maser (SHM) in collaboration with Contraves Space AG (CSAG), Switzerland. The Physics Package of the Engineering Model is assembled and performs as specified: for nominal operational parameters, the long-term frequency stability is 1×10^{-15} @ 10'000s, thanks to the Automatic Cavity Tuning (ACT). The ACT concept based on a pulsed interrogation scheme of the cavity has been developed and demonstrated with a laboratory demonstrator at ON. The space compatible electronics package is being assembled by CSAG and preliminary functional tests are satisfactory.

I INTRODUCTION

The two frequency standards that will be part of the Atomic Clock Ensemble in Space (ACES) payload to be flown on the International Space Station (ISS) are firstly a cold Cesium clock (PHARAO) required for its outstanding long-term frequency stability ($\tau \geq 3000$ s) and accuracy [1], and secondly an active Space Hydrogen Maser (SHM) mandatory for its ultimate frequency stability performance in the mid-term range ($3\text{ s} \leq \tau \leq 3000$ s) [2]. With a double servo loop configuration (short-term and long-term), ACES output signal will take advantage of the best frequency stability for each integration time (PHARAO frequency locked to SHM for the short and mid-term, and SHM frequency steered to PHARAO for the long-term). The ultimate frequency stability of SHM is essential for ground users, because of the limited time availability of the clock signal (typically 400 s) due to the ISS fast rotation.

As prime contractor, Observatoire de Neuchâtel (ON) is concentrating on the development and manufacturing of the SHM Physics Package (PP), having Contraves Space AG (CSAG) as subcontractor for the development and the manufacturing of the space-qualified Electronics Package (EP). The main objective of the current phase (2006) is to perform an end-to-end performance demonstration with representative hardware, to be used as a stepping stone for pursuing the development of the SHM and aiming at the delivery of the SHM Engineering Model (EM) in 2007, and finally the SHM Proto Flight Model (PFM) in 2008. This development will lead to the lightest ever built active hydrogen maser.

In these proceedings, we first recapitulate the SHM instrument architecture, emphasizing some specific design issues (chap. II). Then we focus on the latest developments of the SHM PP at the Engineering Model level (chap. III), and on the SHM EP at the Elegant Breadboard (EBB) level (chap. IV). Finally, we summarize and present the next steps of the SHM development towards the Proto Flight Model (PFM) (chap. V).

II SHM INSTRUMENT OVERVIEW

The SHM is divided into two principal functional packages, the Physics Package, which provides the actual atomic oscillator, and the Electronics Package, which provides the atomic signal processing circuits, parameter control functions, telemetry and telecommand (Fig. 1). Both packages will be fixed on the ACES structural baseplate, which provides the mechanical and thermal interface with the spacecraft. The SHM external connections (telecommands/telemetries, input power and output frequency) are interfaced respectively on the control unit, the power supply unit and the RF unit.

The keys to miniaturization of a space hydrogen maser (design goal: 35 kg) with respect to a traditional ground hydrogen maser, which typically weighs 100 kg, is first the use of a smaller microwave cavity which also allows to reduce the size of the magnetic shields. In order to keep high values for the loaded cavity quality factor (35'000) and for the RF filling factor to let the maser self-oscillate, the RF cavity is loaded with a sapphire single crystal (hydrogen storage bulb). The second key to miniaturization is the removal of the external vacuum enclosure which provides the so called "thermal vacuum". This vacuum, which is mandatory to thermally isolate the microwave cavity, will be provided instead and directly by the "space vacuum", given that the SHM is operating in the space environment.

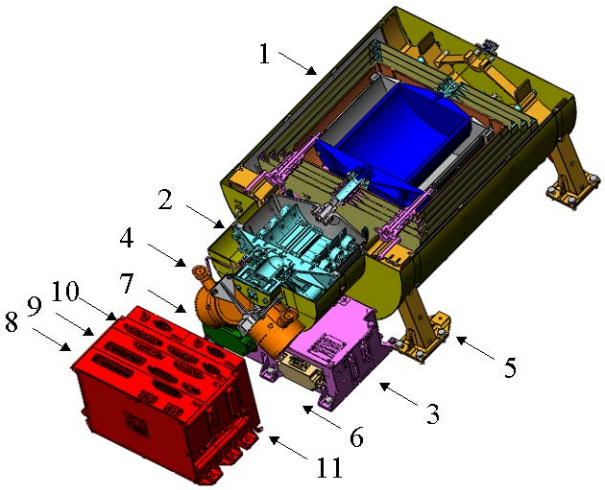

Fig. 1: Cut view of the SHM instrument:
1: Microwave cavity and shields assembly; 2: H-vacuum assembly; 3: H-distribution assembly; 4: Ions pumps; 5: External fixation structure; 6: H-dissociation power amplifier; 7: Low noise RF amplifier; 8: RF unit; 9: Control unit; 10: Power supply unit; 11: HV unit.

The PP is composed of several sub-assemblies for proper atomic hydrogen preparation and clock frequency investigation. In the H-distribution assembly molecular hydrogen gas (3 bar) is supplied from a solid-state metal hydride storage container and delivered through a nickel flow control valve into a low-pressure gas bulb (0.1 mbar typical), where a plasma discharge (10W max) dissociates the molecules into atoms (H-vacuum assembly). By differential pumping, hydrogen atoms leave the dissociator bulb through a single-hole collimator (0.5 mm∅ x 1 mm) and enter a vacuum chamber where they form a collimated beam. The atomic hydrogen beam flux stabilization is achieved by regulating the molecular hydrogen low pressure in the dissociation bulb. The hydrogen pressure is measured with a specially developed Pirani sensor and the molecular flow is constantly adjusted by changing the heating current of the nickel flow control valve. In order to create the necessary population inversion mandatory for detecting the atomic oscillations, the atoms pass through the high magnetic field gradient (1.8 T/mm) of a quadrupole state selector. Undesired atoms are deflected off the beam axis while remaining atoms enter downstream a storage bulb (1.7 liter). This bulb is lined with an appropriate Teflon coating, which allows many collisions of the atoms with the wall without perturbation of their atomic state. The bulb is situated at the center and integral part of a cylindrical titanium microwave cavity resonant at 1.42 GHz (TE_{011} mode). It consists of a single sapphire crystal cylinder, which is vacuum-tightly bonded to the end faces of the cavity and whose crystallographic axis is aligned with the cavity revolution axis. As such it provides an almost loss-free dielectric loading, leading to a significantly reduced cavity size. A weak static magnetic field (360 μOe) is applied parallel to the cavity axis by a solenoid to separate the magnetic Zeeman sublevels. To decrease the influence of a changing external magnetic field (e.g. Earth field) on the clock transition frequency, the cavity is surrounded by four concentric magnetic shields and a fifth external magnetic shield providing the necessary shielding factor (10^5). An additional active magnetic compensation system is also implemented. The microwave cavity is operated around 48°C and temperature stabilized (1 mK) by a three-stage temperature control system to reduce the influence of thermal expansion on the cavity frequency. The remaining frequency variations of the cavity are compensated by an active control, the Automatic Cavity Tuning (ACT), through a varactor diode inserted in the microwave cavity. Finally, the internal vacuum where the hydrogen beam propagates is maintained by an array of non-evaporable hydrogen getters. Two additional ion pumps (2 l/s) are mounted to absorb other background gases.

The functional block diagram of the EP with its various connections to the PP and the instrument interfaces to the spacecraft is detailed in Fig. 2. The EP is composed of an RF unit (RFU) in charge of frequency locking the local quartz oscillator on the hydrogen clock transition frequency as well as frequency locking the microwave cavity using the ACT, of providing the proper microwave frequency to the hydrogen dissociation power amplifier, and finally of delivering a stable 100 MHz signal to the ACES payload. The Control Unit (CU) and the Power Supply Unit (PSU) provide and/or control the necessary powers for an optimal operation of SHM (cavity heaters and thermostats, hydrogen pressure measurement and active control, external magnetic measurement and internal compensation, C-field, neck coil, demagnetization and Zeeman frequency measurement). The CU also controls the high voltage supply unit (HVSU) for proper operation of the two small ion pumps. Finally, the CU interfaces to the ACES payload in terms of telecommands and telemetries.

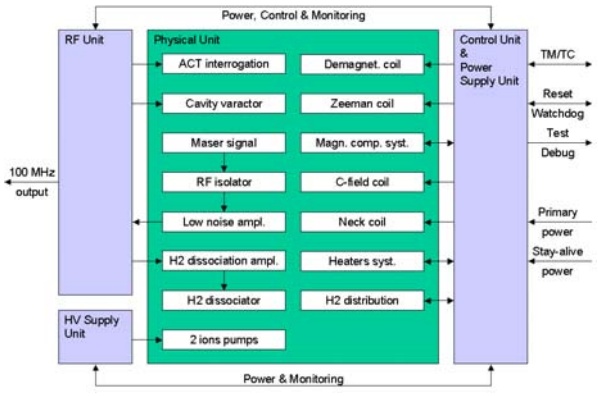

Fig. 2: The functional block diagram the SHM Electronics Package.

III PROGRESSES ON THE PP

The SHM EM Physics Package has been fully assembled (Fig. 3), with the exceptions of the vacuum pumping devices (ion pumps and getters), as well as the hydrogen distribution assembly (presently ground equipment are installed, but the EM H-distribution assembly is under validation process). The PP has been baked out and properly started (cavity thermalization and hydrogen plasma dissociation). Two limiting factors have been readily identified and properly corrected: excessive magnetic inhomogeneities due to thermo-electric currents between the microwave cavity and the fixation structure have been solved by appropriate electrical isolations; a too low atomic quality factor has been improved by replacing a deficient hydrogen dissociation bulb.

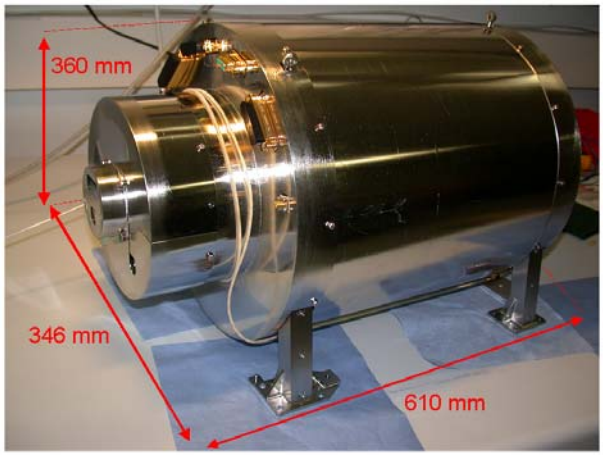

Fig. 3: The SHM EM Physics Package assembled, but with ground ion pumps and hydrogen distribution assembly.

After these tuning adjustments, the functional tests of the PP under vacuum have shown compliant performances:

- the maser output signal at 1.42 GHz is -104 dBm (specs: ≥ -105 dBm);
- the atomic line quality factor is 1.5×10^9 (specs: ≥ 1.5×10^9);
- the required static magnetic C-field is nominal (360 μOe);
- the magnetic shielding factor is 200'000 (specs: ≥ 100'000);
  note: if this provision is confirmed on the PFM, the requirement on the active magnetic compensation will be reduced;
- the loaded cavity quality factor is 35'000 (specs: ≥ 35'000);
- the cavity temperature stability is < 1 mK (specs: ≤ 1 mK) using standard laboratory electronics.

By operating the SHM PP with these nominal functional parameters and with the ON EP demonstrator (RFU, ACT, CU and PSU), its output frequency has been compared to a reference hydrogen maser. Fig. 4 shows two sets of measurement data compared to the SHM specifications: the crosses have been obtained without actively controlling the cavity frequency (ACT off), while the dots have been recorded with the ACT on (will be discussed below). For integration times $\tau < 100$ s both curves are in specifications, but obviously the ACT becomes mandatory for longer integration times. Note that the SHM specifications have been corrected on the Fig. 4 in order to take into account the influence of the reference maser noise and of the measuring system noise.

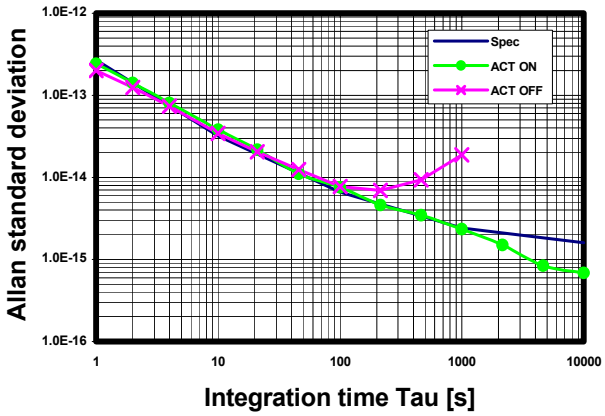

Fig. 4: Allan standard deviation of the SHM PP with the ON EP demonstrator vs. a reference hydrogen maser. The ACT function is either operating (dots) or not (crosses). Note that the specifications have been corrected in order to take into account the influence of the reference maser noise and of the measuring system noise.

IV PROGRESSES ON THE EP

The long-term frequency stability of SHM (1.5×10^{-15} @10'000s) is dramatically dominated by the cavity frequency pulling (2×10^{-5}), which calls for a cavity frequency stability at the level of 0.1 Hz at the hydrogen clock transition frequency (1.42 GHz). Although regulating the cavity temperature at the mK level, the residual cavity frequency variation is about ±50 Hz, which is unacceptable to meet the long-term frequency stability.

ON has developed an Automatic Cavity Tuning based on a pulsed interrogation scheme (Fig. 5). Two side frequencies, which are generated digitally, are alternatively sent into the microwave cavity (F_1 and F_2), ±15 kHz apart from the cavity center frequency F_{cav}. The duty cycle of F_1 and F_2 can be finely adjusted for

optimizing the long-term performance of the ACT. Note that the cavity center frequency is adjusted to the atomic spin-exchange tuning point for minimizing the hydrogen flux-related frequency dependence. F_{cav} is blue-detuned with respect to the hydrogen clock transition frequency F_0. Finally, the output signals are amplitude-compared and the error signal (ppm level) is fed-back to the microwave cavity varactor diode for controlling the cavity resonance frequency.

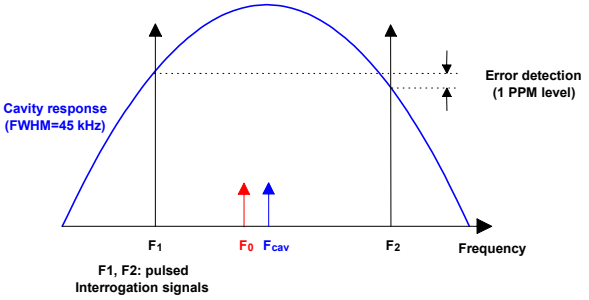

Fig. 5: Cavity response to the ACT interrogation signals: F_{cav} is the cavity center frequency adjusted to the spin-exchange tuning point, but blue-detuned with respect to the hydrogen clock transition frequency F_0; F_1 and F_2 are the two side frequencies injected in the cavity for the ACT.

The ACT demonstrator developed by ON has been implemented onto the SHM PP. Fig. 4 shows the significant improvement of the SHM Allan standard deviation for integration times $\tau > 100$ s when the ACT is switched on (dots), which is compliant with the SHM long-term frequency stability specifications.
With this ACT proof-of-concept at the laboratory demonstrator level, this technology has been transferred from ON to CSAG for the development of the complete SHM Electronics Package. Presently, CSAG is upgrading its EP to the EBB level, with the following design improvements:

- upgrading of the RFU analog module to combine the first stages of the frequency down-conversion chain (1420 MHz down to 5 MHz) for the main OCXO and the ACT lock loops,
- upgrading of the RFU digital module to combine the direct digital synthesis for the maser output frequency adjustment, for the ACT interrogation signals generation and for the ACT digital processing of the cavity response,
- upgrading of the design and the layout of the RFU boards for a phase noise reduction, and a phase temperature sensitivity reduction,
- splitting of the electronics boxes for improving the thermal power dissipation.

The preliminary frequency stability of the SHM PP (EM) and the SHM EP (EBB) is reported on Fig. 6. For this measurement, only the maser receiver electronics was operating, while the ACT was off. The Allan standard deviation for both the ON laboratory demonstrator (crosses) and the CSAG space electronics (dots) shows similar and in specification performances for integration times $\tau < 100$ s. The degraded frequency stability around $\tau = 50$ s is ascribed to perturbations from the thermal vacuum chamber on the SHM PP. This fact has been proven by stopping temporarily this thermal environment regulation, which eliminated this perturbation. Finally, an excessive phase noise of the space electronics has been recorded, which is currently under investigation and improvement.

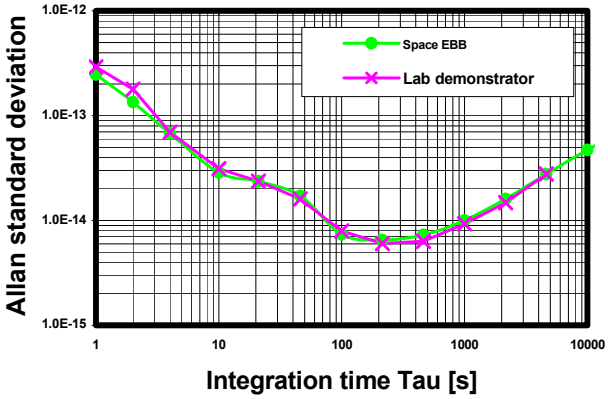

Fig. 6: Allan standard deviation of the SHM PP with both the ON laboratory demonstrator (crosses) and the CSAG space electronics (dots) vs. a reference hydrogen maser. Only the maser receiver is operating (ACT is off).

V CONCLUSIONS AND OUTLOOK

We have reported in these proceedings on the development of the Space Hydrogen Maser (SHM) for the scientific mission of Atomic Clock Ensemble in Space (ACES). The Engineering Model of the SHM Physics Package has been fully assembled, with exceptions of the two ions pumps, the hydrogen getters and the hydrogen distribution assembly (non critical sub-assemblies for the performance demonstration). By using ground electronics, we have experimentally demonstrated the specified performance of the SHM PP ($< 1\text{x}10^{-15}$ @ 10'000 s). The functionality and the performance of the last missing key electronics function (Automatic Cavity Tuning) have also been demonstrated at the laboratory demonstrator level, which secures the complete SHM development. Improvements on the space electronics have led to preliminary and satisfactory functionalities and performances of the SHM RF and control units.

The forthcoming major milestones are the SHM end-to-end performance demonstration in 2006, the delivery of the validated SHM Engineering Model in 2007, and finally the space-qualified SHM Proto Flight Model in 2008.

VI ACKNOWLEDGEMENTS

The ON and CSAG project team would like to thank the Canton of Neuchâtel, the Swiss Space Office and the European Space Agency for their financial support to the development of the "Space Hydrogen Maser for ACES" through the Swiss Prodex program and other ESA programs.

VII REFERENCES

[1] Ph. Laurent et al., *Experimental measurements on the engineering model of the space clock PHARAO,* 20th European Time and Frequency Forum, 2006, Braunschweig, Germany, in these proceedings.

[2] A. Jornod, D. Goujon, D. Gritti and L.-G. Bernier, *The 35kg space active hydrogen maser (SHM-35) for ACES*. in Proc. of the 2003 IEEE Frequency Control Symposium & PDA Exhibition jointly with the 17th European Time and Frequency Forum, 2003, Tampa, FL, USA.

Proceedings of the 20th EFTF, 2006

The ACES ground user network

N. Dimarcq[1 *], E. Cortiade[2], D. Massonnet[2], S. Zouiten[2]
[1] *LNE-SYRTE – Observatoire de Paris - 61, avenue de l'Observatoire – 75014 Paris – France*
[2] *CNES – 18 avenue Edouard Belin – 31055 Toulouse Cedex - France*
**Electronic address:* noel.dimarcq@obspm.fr

We present the ACES ground segment concept and describe the roles of the ACES science team, the ground users and the control center.

I. INTRODUCTION

The ACES mission (Atomic Clock Ensemble in Space) is an ESA project which aims at installing on board the International Space Station ISS two ultrastable clocks (a cold atom clock PHARAO and an hydrogen maser SHM) and comparing them to ground based clocks. The ensemble of space clock will have a frequency stability and a frequency accuracy at the level of $\Delta f/f = 10^{-16}$. Among all scientific objectives, one can point out the improvement of fundamental physics tests precision (special and general relativity), the worldwide comparison of atomic clocks contributing to atomic time scales, …

PHARAO frequency will be compared to SHM in space and to ground based clock frequencies using a microwave link MWL [1]. This T/F transfer technique is expected to have a time instability lower than 0.3 ps (over one 300 seconds ISS pass) and 10 ps over 1 day integration time (Figure 1). This is at least one order of magnitude better than the time transfer techniques currently used (GPS,TWSTFT).

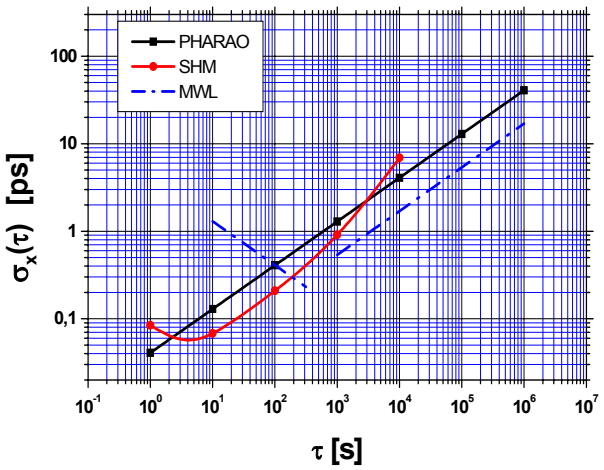

Figure 1 - Time deviation of PHARAO, SHM and the microwave link MWL.

With ACES, it will be possible to perform comparisons between ground clocks either in common view or in non-common-view with a resolution at the ps level. This will allow to compare ground clocks with a frequency stability of 10^{-17} at 1 day.

II. ORGANISATION OF THE ACES GROUND SEGMENT

The ACES ground segment includes different contributors (Figure 2) :

- the ACES science core team
- the ground users
- the mission and control center

The ACES Science Core Team, which is composed of PI laboratories with the support of instrument developers, optimizes the space clocks (PHARAO, SHM) operation. For this purpose, the team receives data from the ACES platform and from the type A ground users. After data analysis, the team sends data commands to the ACES control center for telecommands to the ISS.

The Users "type A" are worldwide laboratories equipped with a ground MWL terminal and one or several ultra-stable clocks. They can compare their local clock to PHARAO/SHM. User A ground clocks can be compared by common or non common views. Users A may operate either during the whole ACES flight or only during a fraction of the ACES flight. For these short experiments, it will be possible to use a mobile MWL terminal. This mobile terminal will be also necessary for calibration purposes.

The Users "type B" are the other users without MWL terminal. They will have access to specific ACES data for analysis.

The ACES Mission and control Center has many functions of interest for the ground users :

- it organizes the MWL comparison sessions (ground clock status, available MWL channels, ISS status/visibility/elevation, …) under the ACES science team responsibility,

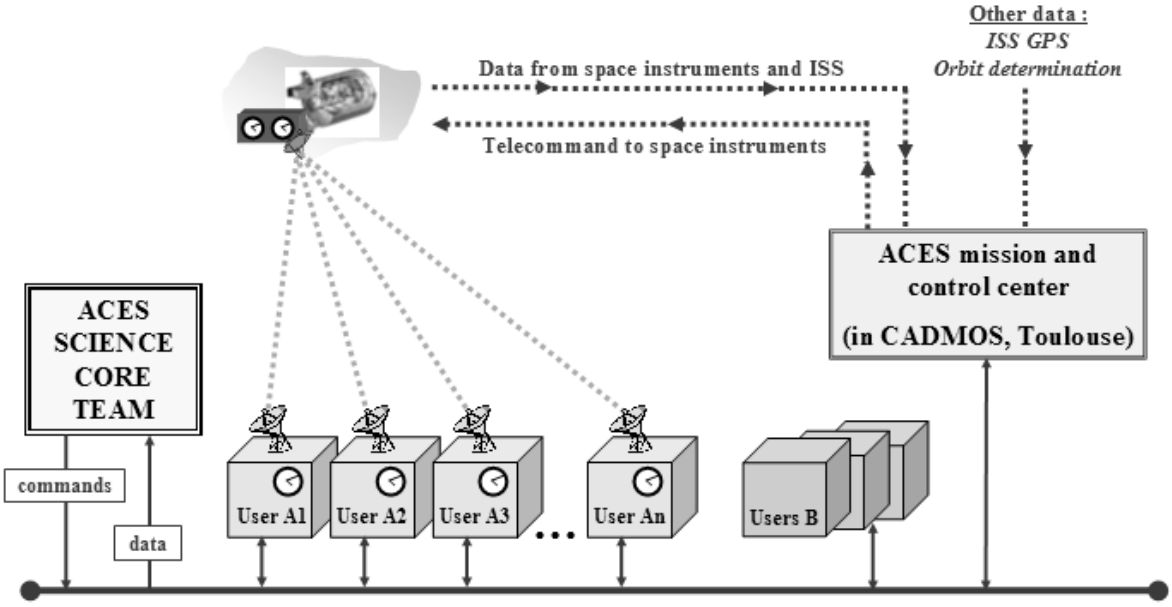

Figure 2 - ACES ground segment organisation

- it collects, stores, and pre-processes data issued from payload, ground users « type A », other data (ISS orbit, microvibrations, …)
- it organizes the data in a database using a single time scale (UTC) and builds specific products provided to ground users
- it sends to the ACES Science Core Team the data required for the optimisation of space instrument operation and transmits to the ACES payload the telecommands to set space instrument parameters
- it sends to ground users « type A » all the data needed for space-ground comparisons : comparison schedule, ISS orbit (predictive, near real time, precise), space clock status, …
- it sends to ground users « type B » specific data and products for analysis

The ACES control center will be also the MWL master station, and it will house the reference instruments for ground tests of telecommands, validation of software patches and trouble shooting activity.

II. GROUND USERS WITH A MWL TERMINAL

At least 5 "type A" ground users are required to fulfil the science objectives : large variety of ground clocks in microwave and optical domain for the search of constant drifts, worldwide distribution for the Lorentz invariance test. However, the expected number of laboratories equipped with MWL terminals is between 10 and 20, depending on the cost of each MWL terminal.

"Type A" ACES ground users will be equipped with (Figure 3) :

- ultrastable atomic clocks
- a MWL terminal
- probably GPS, GALILEO or TWSTFT (Two-way T/F transfer) receivers in order to cross correlate ground clocks comparisons performed with ACES and with these techniques.

The processing of raw data acquired by the MWL terminal will be done by the control center and the computer controlling the MWL terminal. The objective is to have a "plug and play" MWL station which computes all the necessary corrections and provides the final comparison result to the user. The combination of all the data will be easier if each ground user is synchronised to an international time scale (UTC, TAI)

During the mission, each "type A" ground user will exchange data with the mission and control center.

Data received by ground users with MWL stations (from the control center) :

- before a comparison : ISS orbit data for MWL antenna tracking and Doppler pre-setting
- during the comparison : the results of the phase comparisons both in ground and space

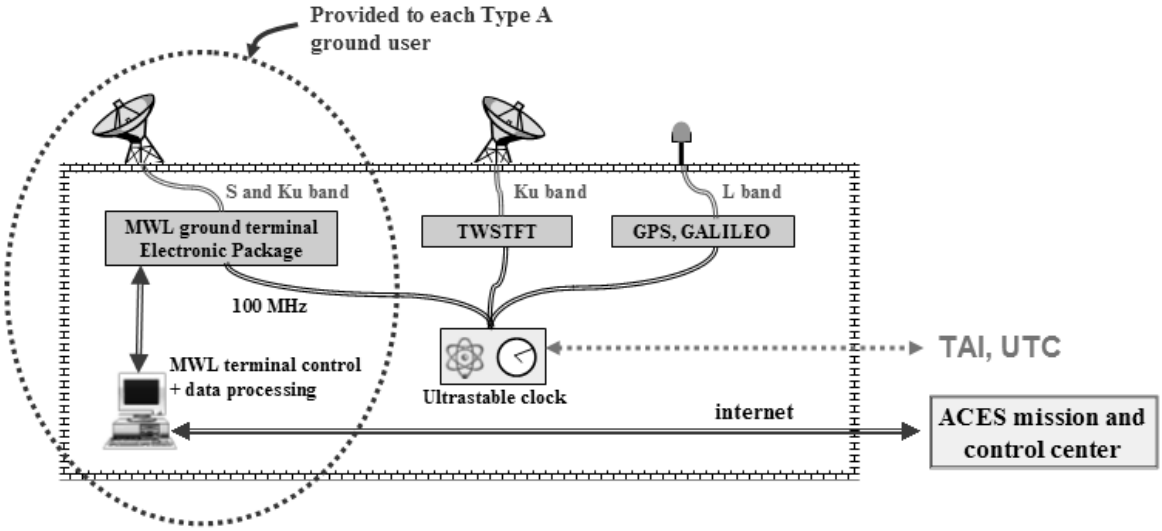

Figure 3 - ACES ground user equipment

MWL terminals (transmitted in real time by MWL down link)

- just after the comparison : ISS orbit data to correct relativistic effects at 10^{-15}
- a few hours after the comparison : the status of space instruments, the confirmation of the data measured on board, the ISS orbit data to correct relativistic effects at 10^{-16}, …

The correction of relativistic effects requires the knowledge of ISS orbit with a very low uncertainty. The corresponding Allan deviations are shown on Figure 4 for the altitude and on Figure 5 for the velocity. In order to properly correct the effects at 10^{-16}, we require a resolution of 25 cm on the altitude and 0.3 mm.s^{-1} on the velocity, for an integration time of 10 days.

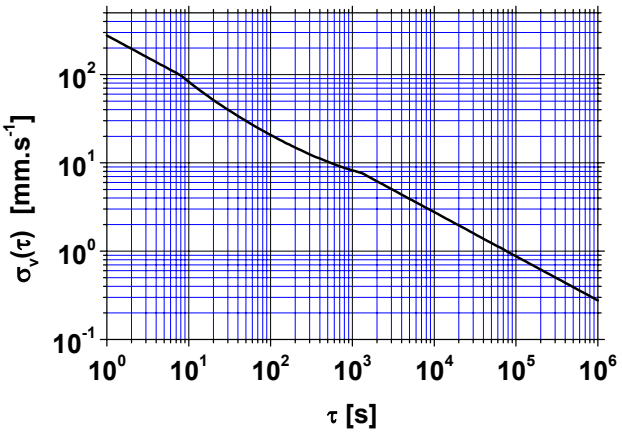

Figure 4 - Required Allan deviation of the uncertainty on ACES payload altitude

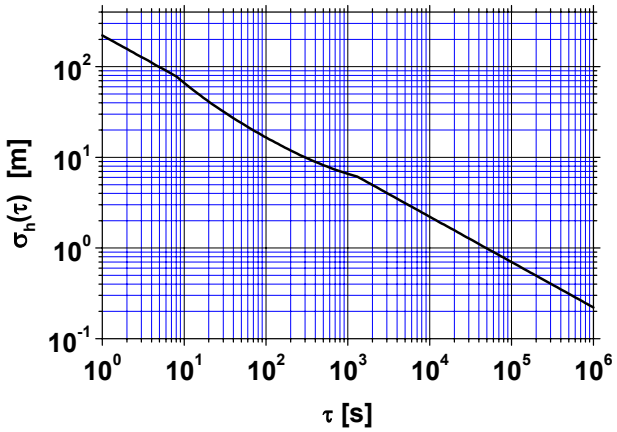

Figure 5 - Required Allan deviation of the uncertainty on ACES payload velocity

Data provided by "Type A" ground users (to the ground center) :

- the status of their clock (stability, accuracy, gravitation potential, position of the ground MWL antenna, …)
- specific data (meteorological, …)
- MWL ground terminal data : phase comparison data, signal amplitudes, temperatures, ...
- results of comparisons with other techniques (GPS, TWSTFT, GALILEO, optical fibers)

REFERENCES

[1] W. Schäfer, S. Feltham, I. Aguilar, A. Seidel, M.P. Hess, J. Kehrer, G. Hejc, S. Föckensperger, H.-V. Heyer, Proceedings of the 20th European Forum on Time and Frequency, Braunschweig, mars 2006 ; "Clock comparisons in the ACES project"

Proceedings of the 20th EFTF, 2006

PHARAO Microwave Source : a short term frequency stability of 7.10^{-14} at 1 second.

M. CHAUBET[1], D. CHEBANCE[1], M. ABGRALL[7], G. CIBIEL[1], Ch. DELAROCHE[1], Ch. SIRMAIN[1], Ph. GUILLEMOT[1], J.F.VEGA[1], G. SANTARELLI[2], A.CLAIRON[2], Ph. LAURENT[2], Y. MAKSIMOVIC[2], S. BIZE[2], Ch. SALOMON[3], M. E. TOBAR[4], Th. POTIER[5], Y. COSSARD[5], P. CANZIAN[6], V. CANDELIER[6]

[1] CNES, French Space Agency Toulouse, France
[2] LNE-SYRTE, Paris, France
[3] ENS-LKB, Paris, France
[4] UWA, Perth, Australia
[5] THALES Airbornes Systems, Elancourt, France
[6] CMAC, Argenteuil, France
[7] Alten SO, Toulouse France
Corresponding Author: michel.chaubet@cnes.fr

1. INTRODUCTION

CNES is funding the development and realization of the PHARAO space clock program [1,2], since 2001. The first step is to build an Engineering Model of the cold cesium atoms space clock and to evaluate its performances. The Microwave Source (SH) is one of the four main PHARAO subsystems (the others are the Cesium Tube, the Laser Source, the onboard Computer and its Flight Software). CNES is procuring the different subsystems [3,4] from several subcontractors. PHARAO EM will be integrated and tested in Toulouse CNES Space Center. A second clock, the Flight Model, will follow the same logic and will be mounted on the ESA ACES payload, planned to be installed onboard the International Space Station (ISS) on the Columbus Module. The SH main functions [5] are to provide 2 ultrastable signals at 9.192631770 GHz to drive the microwave cavities (preparation and interrogation) inside the Cesium Tube, and also to provide a metrological 100 MHz signal for the comparison with SHM Maser via the Frequency Comparator and Distributor Package (FCDP). The development of the SH was contracted to THALES Airbornes Systems (TAS) : 3 models have been delivered, the Mechanical Structural Thermal Model, The Engineering Qualification Model and the Flight Model. The SH is the only subsystem in straight interface with the ACES payloads beside the digital buses which currently connects the payload computers of each ACES instrument. Moreover the SH is at the hearth of the PHARAO clock accuracy, and very special care has been devoted to the requirements, the design/realization and the tests/measurements of the SH in stand alone configuration or connected to an atomic fountain in full operation condition.

2. REQUIREMENTS & DESIGN GUIDELINES

The projected accuracy of the PHARAO Clock is 10^{-16} with an expected frequency stability of $10^{-13}\tau^{-1/2}$. In order to reach this ambitious target the Microwave Source (SH) needs to be carefully designed.
The clock operation requires 2 microwave outputs with large power range (60dB) and fine frequency tuning. Here we shortly recall the main requirements and the related main challenges :

- Phase noise < -60 dBrad^2@1Hz at 9.192 GHz
- Electromagnetic leakage level relative to the output signal : -70 dBc
- Phase stability below 2.5 ps in the thermal environment (3°C peak-to-peak over 90 min) 100 MHz to 9.2 GHz synthesis
- Spurious levels below -70 dBc (1<f<100 Hz) at 9.2 GHz
- Harmonic and spurious levels at the 100MHz output below -70 dBc
- Output frequency resolution 10^{-15}
- Phase drift during the atom interrogation <10 µrad .

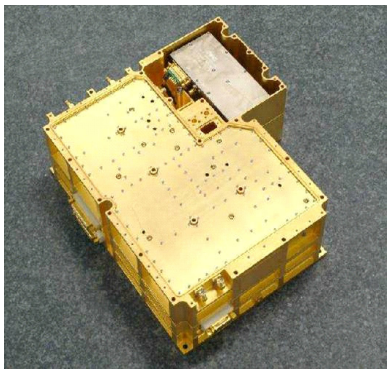

Figure 1 : SH Flight Model (top cover removed).

3 OUTPUT SIGNALS FEATURES

To fulfil the metrological objectives of the ACES mission, the interface signal at 100 MHz has been strictly defined. All the timing errors need to be kept below 10^{-16}. Hence the VSWR of the input/output is bounded on 1.5 10^{-3} peak-to-peak over 1 day for the expected temperature variations in the ACES space environment. The signal level is set to 0 dBm to optimize the harmonic content while having a good SNR. The harmonics (200 and 300 MHz) are specified to be -70 dBc in order to reduce the errors in the phase comparators inside the ACES FCDP. Special care is devoted to the reverse isolation (better than 80 dB for the FCDP) to further reduce timing error in the system.
The 2 microwave outputs at 9.2 GHz are also very critical. The clock accuracy depends on the characteristics of these signals. For instance the output amplitude control needs to be strictly monotonic over 60 dB range and very linear over a smaller 10 dB fine tuning range with an integral deviation from the ideal behaviour below 0.1 dB and a resolution of 0.02 dB. The outputs are tuneable in the range of +/- 100 kHz around 9.192631770 GHz.

4 SYNTHESIZER SCHEMATIC

The clock frequency stability is given by the close to the carrier (<10 Hz) phase noise of the interrogation signal. For this reason, the synthesizer design, described in Figure 2, starts from a very low phase noise 5 MHz quartz oscillator USO (CMAC). To overcome all the problems related to the tuning of this oscillator, a sophisticated synthesis scheme which includes a 48 bits Direct Digital Synthesizer (DDS1), produces a low noise tuneable 100 MHz signal. It is worth noting that the signal is generated by phase locking a low noise 100 MHz quartz oscillator, which acts as a clean-up.

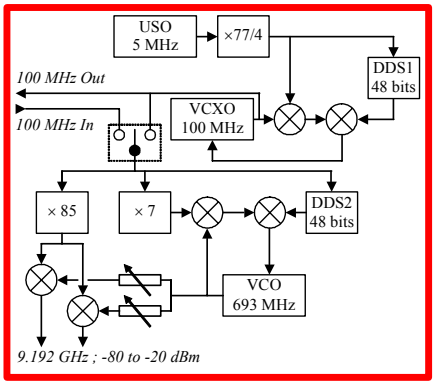

Figure 2 : schematics of the PHARAO SH synthesizer.

From the 100 MHz we derive the metrological output to the ACES and by successive multiplications a microwave signal at 8.5 GHz.

The last step to synthesize the Cesium hyperfine signal is accomplished by mixing a fine amplitude and phase tuneable 693 MHz signal coherent with the 100 MHz pivot signal. A second 48 bits DDS2 allows the modulation and the fine tuning of the output microwave signals.
An auxiliary 100 MHz input provides the possibility to switch off the internal SH 100 MHz synthesis and to use an external 100 MHz signal to drive the 100 MHz to 9.2 GHz synthesis.

5. SPACE RELATED SH/USO CHARACTERISTICS

In addition to the metrological requirements, the SH has been design to withstand space environment. The allocated volume is 8.3 l (dimensions 270 x 300 x 100 mm^3), the mass is 7 kg and the power consumption 24.5 W. The operating and storage temperature are respectively 10 to 33.5°C and -50 to +75°C. The SH mechanical structure has been qualify for acceleration levels such as 11.5 grms that will be seen during the launch of PHARAO/ACES by the space shuttle. The SH is compliant with EMC/EMI required by the autocompatibity with PHARAO/ACES and the other ISS payloads. The SH radiated susceptibility to magnetic field is below 145 dBpT between 1 Hz and 50 Hz which is compatible with 160 dBpT at PHARAO outer surface. The effect of microvibration onboard the ISS is mainly a degradation of the USO phase noise. The ISS microvibration PSD may vary from 10^{-9} g^2/Hz (0.3 Hz) to 10^{-7} g^2/Hz (60 Hz). The first version of the USO that equipped the SH had a sensitivity of 2.10^{-9}/g, a bit too high for our application. For SH FM, a new USO has been developed by CMAC (figure 3) with an acceleration sensitivity of 1.810^{-10}/g, to overcome the influence of the microvibration environment.

Figure 3 : PHARAO Ultra stable oscillator.

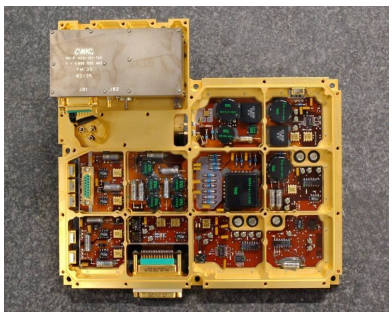

Figure 4 : view of the SH bottom section (DC-DC converter and the USO).

6. TESTS WITH AN ATOMIC FOUNTAIN

The SH EQM has been extensively tested on the FO2 atomic fountain at LNE-SYRTE during the summer 2004 : the schematics is presented in Figure 5, below. The FO2 frequency stability using the SH as interrogation oscillator is $7.10^{-14}\tau^{-1/2}$ (Figure 6). It is the best stability ever achieved with a quartz oscillator.

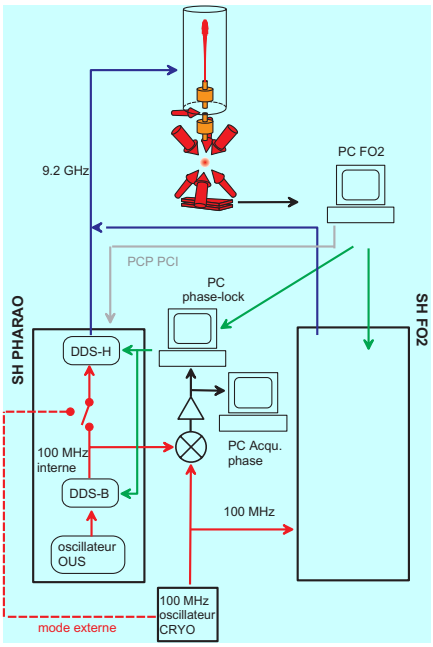

Figure 5 : differential frequency comparisons between SYRTE synthesizers and the SH EQM with FO2 fountain.

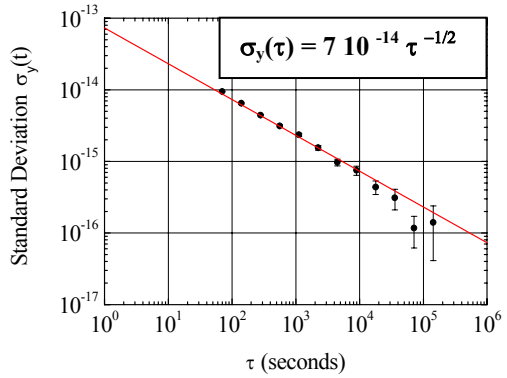

Figure 6 : fractional frequency stability of the FO2 atomic fountain using the SHP EQM.

Using a set of high performance frequency synthesizers developed at the LNE-SYRTE in conjunction with a cryogenic sapphire oscillator (CSO), the SH has been tested in a differential configuration driving the atomic fountain. A frequency offset of $\sim 6\times10^{-16}$ has been measured between the two operation modes. This frequency shift is due to a phase jump of ~10 µrad on the 100 MHz output synchronous with the digital signal which drives the atomic preparation stage (40 ms). This jump is integrated by the external phase lock loop (response time ~1s) and produce a phase drift during the interrogation.

7. TESTS IN TOULOUSE

After their characterization by TAS and their delivery to CNES, the performances of both the SH EQM and FM have been verified in Toulouse by comparison to a CSO and an H Maser, thanks to the Time & Frequency service facilities [6].

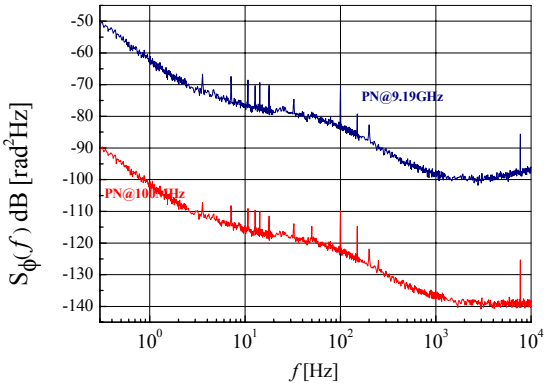

Figure 7 : SH FM Phase noise measured against a CSO in CNES Toulouse.

Complementary tests have been performed to investigate in details the phase perturbations due to the numerical commands. Only the ones synchronous to the PHARAO clock cycle could be problematic. The 9.2 GHz frequency commands produce dispersive shaped perturbations that average to zero within 0.5 µrad @ 100 MHz. The preparation switch actuation produces a phase jump. For the SH EQM, it is on the order of 10 µrad @ 100 MHz and it may vary within ~10% in relation with the environment. The effect on the FM, 10 times lower, is on the edge to be acceptable for the goal of PHARAO accuracy at 10^{-16}.
To completely cancel out this phase perturbation, a simple procedure is applied to the phase lock performed by the ACES FCDP. It consists in holding the error signal during the preparation command (Blanking).

8. CONCLUSIONS & PROSPECTS

The PHARAO microwave source development is close to be completed. The tests performed on both the EQM and the FM demonstrated high performances, in terms of phase noise, spectral purity and electromagnetic leakage, compatible with the cold atoms clock accuracy objectives, within the constrains of the space mission. A short term stability of $7.10^{-14}\tau^{-1/2}$ has been obtained when operating the SH EQM with an atomic fountain.

Extensive tests showed that the delivered interrogation signal is free of phase transient during nominal cycling operation, except because of the preparation pulse command. This defect is 10 times smaller on the FM. Furthermore, any effect of the command will cancel out, thanks to a blanking procedure applied in the ACES FCDP phase lock loop.

The next step is the tests of the ACES loop at CNES Toulouse using SH EQM, FCDP EM and a CSO. Later, the SH will be integrated in PHARAO, and new measurements of its performances will be performed to validate the autocompatibility with the other subsystems, and after, at ACES level. Presently, the SH FM is upgraded with a USO having a lower acceleration sensitivity, to reduce the effect of the microvibrations onboard the ISS.

REFERENCES

[1] I. Maksimovic et al., 'Current status of the Space Clock PHARAO', EFTF 2004.

[2] C. Sirmain et al.,'The PHARAO project', 'Atomic Clock Ensemble in Space Workshop ESA', 10/11 october 2005.

[3] G. Santarelli et al., 'The space clock PHARAO : sub-systems performance characterization', FCS-PTTI Vanvouver, 2005.

[4] Ph. Laurent et al., 'PHARAO hardware highlight and performance measurements for scientific interest', 'Atomic Clock Ensemble in Space Workshop ESA', 10/11 october 2005.

[5] M. Chaubet, D. Chebance, G. Cibiel,G. Santarelli, A. Clairon, M. Abgrall, T. Potier, Y. Cossard, P. Canzian, V. Candelier, CMAC, 'PHARAO Microwave Source Poster', 'Atomic Clock Ensemble in Space Workshop ESA', 10/11 october 2005.

[6] Ph. Guillemot, J.F. Dutrey, J.F. VEGA, M. Chaubet, C. Sirmain, G. Santarelli, D. Chambon, Ph. Laurent, C. Locke, E. Ivanov, M. Rousselet, Th. Potier,'The PHARAO time and frequency performance verification system', Proceedings of IEEE International Ultrasonics, Ferroelectrics, and Frequency Control 50th Anniversary Joint Conference, 24/27 August 2004, Canada.

Proceedings of the 20th EFTF, 2006

Timing Infrastructure for Galileo System

R. Hlaváč[1], M. Lösch[1], F. Luongo[1] and J. Hahn[2]
[1]*Galileo Industries GmbH, Lise-Meitner-Strasse 2, Gebäude 10.0, 85521 Ottobrunn, Munich, Germany*
[2]*European Space Agency, ESTEC, Keplerlaan 1, P.O Box 299, 2200 AG Noordwijk ZH, Netherlands*
roman.hlavac@galileo-industries.net

Following a successful launch of EGNOS (European Geostationary Navigation Overlay System) services in 2005, Europe is now well under its way towards implementation of its own global satellite navigation system called Galileo. Its full operation capability is expected from 2010 onwards. Galileo is a third addition to GNSS (Global Navigation Satellite System), however it is the only system under a civilian control as opposed to its military controlled counterparts GPS and GLONASS.

This paper is aiming to outline the Galileo System timing architecture and infrastructure. A description of the different time related actors and their corresponding roles within and outside the Galileo core infrastructure will be given. The main contributors in this context are the Precision Timing Facility (PTF) being part of the Galileo Ground Mission Segment (GMS), the Time Service Provider (TSP) and the GPS system for the provision of GGTO (the latter two both external to the Galileo core infrastructure.

The purpose of the Galileo timing infrastructure is to:

- generate a stable time scale (GST) to fulfil the navigation needs
- provide UTC parameters for broadcast
- determine GPS to Galileo time offset (GGTO) in order to improve interoperability of the two systems.

The core function of the PTF is to generate a stable time scale (GST) including a physical realization for the metrological purposes and for providing timing reference signals to all elements within the Galileo system. The main task of the TSP is to provide the GST to UTC mod 1 sec steering corrections, and the offset between GST (Galileo System Time) and UTC as required for the provision of the UTC time dissemination service.

I. INTRODUCTION

Galileo system represents a third addition to the GNSS world. The state of the art system backed up with the cutting edge technology aims to provide exceptional timing and navigational performance hand in hand with the level of integrity [1] which can not be provided by the other currently existing navigation systems. The services offered by Galileo ranging from Open Service, Safety of Live service, Commercial and SAR (Search and Rescue) services to Public Regulated Services covering all the needs of modern societies they could have on navigation system. The Galileo Global Component and its infrastructure were designed to mitigate the issues related to the provision of the above services and to meet their required performance.

The Galileo Global Component consists of the Ground Mission Segment (GMS), Ground Control Segment (GCS) and Space Segment (SSgt). The high level overview of the system is given in Figure 1.

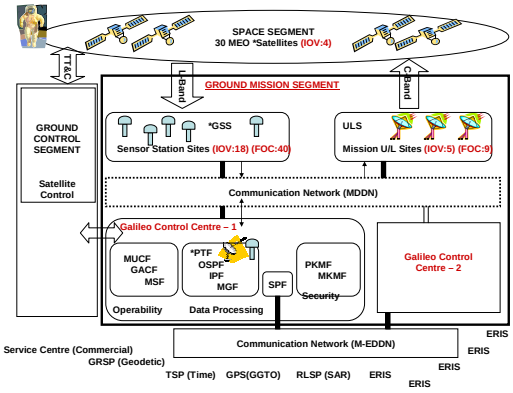

Figure 1: Overview of Galileo System

The timing infrastructure, which is the backbone of the Galileo system, is spread across the Galileo Segments, however it is the GMS above all, which plays the major role. The Galileo timing infrastructure is also supported by the TSP, the entity external to Galileo Global Component. Please refer to Figure 1 where the elements critical for the Galileo timing infrastructure are highlighted with an asterisk.

Thus the Galileo timing infrastructure consists of two PTF's allocated one of each per Control Centre, a number of globally distributed GSS's and the 30 satellites. The following table summarizes the number and type of clocks being deployed within the Galileo timing infrastructure.

		Type and number of clocks per element in FOC				
	No. of elements	Cs	A-HM	RAFS	SRAFS	P-HM
PTF	2	4	2			
GSS	40			2		
Spacecraft	30				2	2

Table 1: Clocks within the timing infrastructure.

Each element is backing up the most important functionalities of Galileo timing infrastructure which are:

- autonomous generation of a stable timescale for the purposes of
  - the internal synchronisation of the elements with Galileo system (PTF)
  - the navigation needs (PTF, GSS &OSPF)
- provision of the UTC dissemination timing services (PTF+TSP)
- GGTO determination for the Galileo interoperability with the GPS (PTF+GPS)

The performance of the Galileo timing infrastructure from the Open Service (OS) user point of view is driven by system level timing and frequency accuracy requirements these can be translated as follows:

- Timing accuracy sets the upper limit of the UTC prediction by the user equipped with a standard timing/ calibration laboratory receiver conforming to the Galileo receiver functional and performance specifications, operating under the normal OS environment for fixed users and receiving the OS signals on E5a and L1 or E5b and L1 to be less than 30 ns for 95% of any 24 hours, without any other aids, providing the TSP interface is operational.
- Frequency accuracy sets the upper limit of the frequency determination uncertainty (retrospective) expressed as a normalised frequency offset relative to UTC in terms of Allan standard deviation in any 24 hours to be better than 3x10e-13 (2σ), without any other aids, providing the TSP interface is operational

Besides the navigation accuracy is also tightly linked with the timing infrastructure and its performance.

Taking into the consideration the system level specification for the offset between the GST and UTC mod 1 sec (to be less than 50 ns for 95% of time,) the user shall be able to retrieve from the Galileo SIS the time information which is within 50ns from the UTC with the overall uncertainty of maximum of 30 ns (95% of time) at user level.

II. GALILEO SYSTEM TIME

Galileo System Time (GST) is the system reference timescale for Galileo. As such, GST will serve as a basis

for characterisation and prediction of satellite clocks which will be executed at OSPF in the frame of the ODTS processing. OSPF will access GST through Galileo Signal in Space (SIS) measurements collected by a Galileo time receiver operated at the GSS (Galileo Sensor Station) collocated with the PTF. The GST is based on the PTF clock ensemble. The ensemble will consist of at least 4 Caesiums (Cs) and 2 Active Hydrogen Masers (A-HM). One maser will provide GST(MC) (GST Master Clock), while the other maser and one caesium will be working in a hot-redundant mode as a backup, see Figure 2 refer also to a section III .

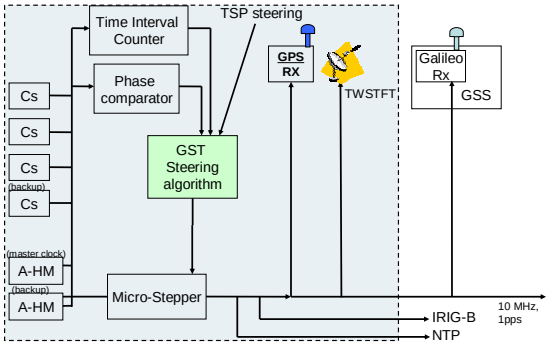

Figure 2: Overview of PTF physical architecture

The GST is in its autonomous mode generated by steering the output of the Master Clock to the ensemble of caesium clocks. Each clock of the ensemble is "weighted" against the MC, the results of such weighting process are fed into the GST algorithm. The GST algorithm then generates a composite clock which as indicated above is based on the weighted average of the Cs clocks ensemble. The capability of the inclusion of the GSS clocks (Rubidium Atomic Frequency Standard) together with the spacecraft clocks (Space qualified RAFS and Passive Hydrogen Masers), thus adding more than 70 clocks into the composite is already being built into the system, allowing an enhancement of the clock ensemble for future phases of Galileo beyond the clocks installed in the local PTF.

The GST autonomy requirement dictates that GST shall not accumulate more than 28 nanoseconds uncertainty over 10 days with 95% confidence, should be the GST to UTC mod 1 sec steering correction as provided by TSP not available. The above process is also described as „navigational" timekeeping of the GST. The „metrological" timekeeping of GST is under the TSP responsibility, which is further detailed in section IV and V respectively. The task of the TSP is to supply to PTF the GST to UTC mod 1 sec steering corrections to keep the GST with in the specified offset (50ns for 95% of time) and uncertainty (28 ns for 95% of time).

Following versions of the GST are defined within the GMS:

- GST(MC)
- GST(GSS)
- GST(OSPF)
- GST(USER)

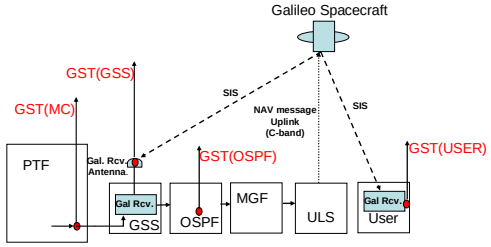

Figure 3: Different realisations of the GST.

By the definition the GST(MC) is defined at a fixed and clearly identified physical point of the electrical path at PTF output of the timing signal used as reference by the GSS Galileo receiver. Note that the GST(MC) at the Master PTF is the reference point where the TSP has to reference his steering products to.

The GST(MC) is characterized by its frequency stability expressed in terms of Alan deviation which shall meet the stability requirements given in the following table:

τ (s)	ADEV
1	3 E-13
10	4 E-14
100	7 E-15
1000	4 E-15
10000	2 E-15

Table 2: GST(MC) Short Term Frequency Stability

In addition to specification given in the Table 2, the stability of GST(MC) in terms of Allan standard deviation shall be lower than 4.3x10e-15 in any 24 hours, including the contribution due to corrections for the steering towards UTC mod 1sec. GST(MC) contribution to the UTC dissemination uncertainty includes the intrinsic characteristics of the MC itself, the contribution due to the UTC mod 1sec steering and due to hardware biases within the PTF.

The GST(GSS) is defined at the antenna phase centre of the Galileo receiver located at the GSS collocated with the PTF. Thus GST(GSS) contribution to the UTC dissemination uncertainty includes also the GSS hardware biases, however without considering the measurement noise of the GSS receiver.

The GST(OSPF) is the representation of the GST as seen by the OSPF through the processing of Galileo SIS measurements collected by the Galileo receiver at the GSS collocated with the PTF, thus the receiver noise is also included. During the PTF normal operation the GST(OSPF) should not differ from the GST(GSS), however any additional contributions to the UTC dissemination due to the switching will apply.

GST(USER) is the realisation of the GST as obtained by the Galileo user through the reception of the Galileo SIS. The realisation of the GST is essentially based on the GST(OSPF), however additional uncertainty contributions apply due to the user equipment biases, uncompensated SIS propagation effects and uncertainties of the satellite orbit and clock parameters in the Galileo navigation message. At the end the OS user should be able to obtain the UTC information with a maximum uncertainty of 30ns for 95% of time.

III. PRECISION TIMING FACILITY

The PTF represents the core of Galileo timing infrastructure and it is inevitably one of the most important elements inside the GMS. The PTF's main task is to provide the GST "navigational" timekeeping, hence to generate the GST and distribute its physical realisation within the Galileo Core System via NTP, IRIG-B and locally also via 10MHz RF and 1pps interface. PTF infrastructure, see Figure 4, is to a certain extend similar to the infrastructure of a primary timing laboratory. Thus inside the PTF there will be atomic clocks, basis for the Galileo timescale generating the Galileo System Time (GST), the time and frequency distribution systems, processing, measurement, steering and time transfer facilities all connected to each other. The communication and distribution of the data and reference signals within the PTF will be catered for with the LAN, RF and 1pps interfaces, see also Figure 2.

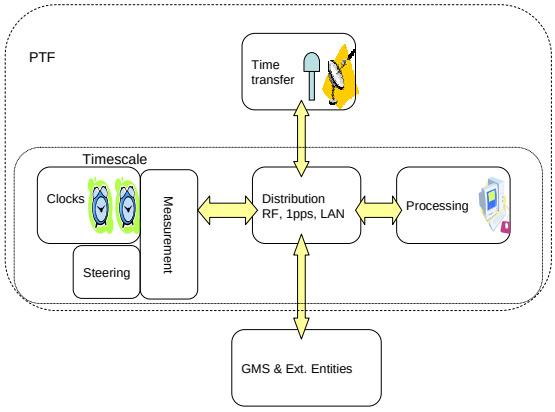

Figure 4: The Structure of the PTF

The atomic clock ensemble at each PTF will consist of at least 4 high performance Caesium (Cs) clocks and 2 Active Hydrogen Masers (A-HM). Refer to Table 3 and Table 4 respectively for the PTF clock specifications.

Noise	Experimental Allan Variance
White phase 1 HzBW	$\sigma_y^2(\tau) = (2.0 \times 10^{-13} \times \tau^{-1})^2$
White frequency	$\sigma_y^2(\tau) = (4 \times 10^{-14} \times \tau^{-1/2})^2$
Flicker frequency	$\sigma_y^2(\tau) = (2 \times 10^{-15} \times \tau^{0})^2$
Random walk of frequency	$\sigma_y^2(\tau) = [(2 \times 10^{-15})^2/\text{day}] \times \tau$

Table 3: AHM frequency standard stability

Noise	Experimental Allan Variance
White frequency	$\sigma_y^2(\tau) = (8.5 \times 10^{-12} \times \tau^{-1/2})^2$
Flicker frequency	$\sigma_y^2(\tau) = (2 \times 10^{-14} \times \tau^{0})^2$

Table 4: Caesium frequency standard stability

Time transfer facility will include Ku-band VSAT (Very Small Aperture Terminal), TWSTFT modem to allow for the state of the art time transfer using the TWSTFT method [2], [3] (Two Way Satellite Time and Frequency Transfer). As a backup there will be also a multi-channel dual frequency GPS timing receiver to accommodate for the GPS-Common View time transfer [4], [5], [6]. The IOV (In Orbit Validation-current phase of the Project) deployment of the GPS-CV is necessary due to a limited number of Galileo satellites (4 only) being available during the IOV, thus deteriorating the performance of the Galileo-CV. Concerning Galileo Common View, the PTF time transfer facility will rely on a GSS equipped with Galileo receiver which will be collocated and its infrastructure connected with the PTF,

thus it is assumed that the PTF can reuse the receiver for the time transfer purposes if required. The GSS collocated with the PTF will not be equipped with the RAFS as opposed to remaining GSS, instead the GSS receiver will be fed with the GST(MC) reference signals from the PTF, refer to Figure 2. This receiver will be used by OSPF to have GST available and to provide navigation SIS observables for the navigation processing.

The time transfer facility will be deployed for the purposes of GST synchronisation with the TSP, GPS and also for inter PTF synchronisation. As mentioned above there will be two PTFs to provide the continuous availability of the GST. The PTF's will be simultaneously operated working in a Master Slave concept. Should the Master PTF fail, it will be immediately replaced with the Slave PTF, which from that point onwards will act as the Master. The process of the PTF switching is controlled by the OSPF as part of its ODTS (Orbit Determination and Time Synchronisation) duties. In order to keep the impact of switching to the Galileo navigation and UTC dissemination services negligible, the OSPF will apply during the transition period a steering law to compensate for the time and frequency offset between the PTFs. The PTF's will be connected to each other by the means of TWSTFT link, refer to Figure 5, which will be periodically calibrated in order to know the difference between the GST(MC) realisations with the uncertainty less than 2 ns (1σ). The Galileo and GPS CV synchronisation links will be used as a backup.

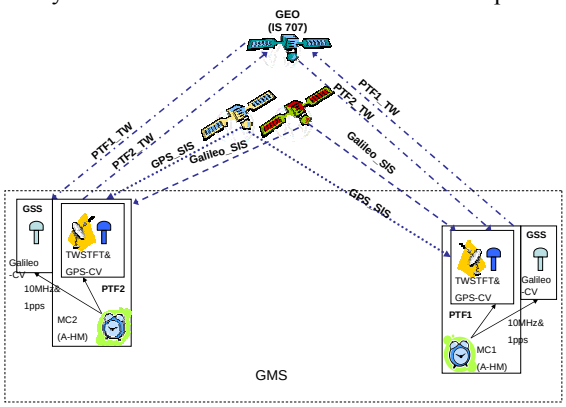

Figure 5: The high level overview of PTF synchronisation interfaces.

IV. TIME SERVICE PROVIDER

The TSP is the entity external to Galileo Global Component core, as mentioned above the TSP is charged with the task of the "metrological" timekeeping of the GST. The TSP fulfils its task by generating the frequency steering corrections for the alignment of the GST(MC) to UTC mod 1 sec in terms of normalised frequency steering correction and time of application. In addition the TSP is also responsible for the provision of the following products:

- GST-UTC mod 1sec time offset, phase and frequency offset prediction and their uncertainties
- Leap seconds: entire number of seconds to recover UTC time scale information, starting from the provided GST-UTC mod 1 sec offset
- Detected PTF data anomalies (clock and time transfer)
- TWSTFT and CV schedules
- Results of monitoring the Galileo signal in space regarding the validation of GST and UTC dissemination performance

The TSP however can not deliver all these products on its own, mainly because the TSP is in fact considered a processing and management facility and as such it will not include any timing and time transfer infrastructure. Therefore the TSP relies on the external support from the timing community, such as the BIPM time section and UTC(k) laboratories as well as on the delivery of the timing data from the PTF. Limited number of UTC(k) laboratories (also referred to as TSP/UTC(k)) selected and contractually bounded with the TSP are considered to play an active role in the GST to UTC mod 1sec steering. Involvement of the other than TSP/UTC(k) laboratories will be most likely limited to the provision of their timescale data to TSP.

As indicated above the PTF needs to deliver to TSP products as follows:

- PTF internal clock comparison data for all the PTF clocks including physical clock hardware steers.
- TWSTFT and CV measurements taken at the PTF
- Time and magnitude of GST(MC) steering correction actually applied at both PTFs
- Bulletins containing information on the GST quality: information on the quality of GST physical realisation necessary to the TSP for its timing processing capabilities. It mainly consists of reports on short, medium/long term stability of the GST physical realisation in the time range under observation.

In order to generate and exchange all of the products outlined above it will be necessary to establish a number

of interfaces between the PTF and TSP, these are identified in Figure 6.

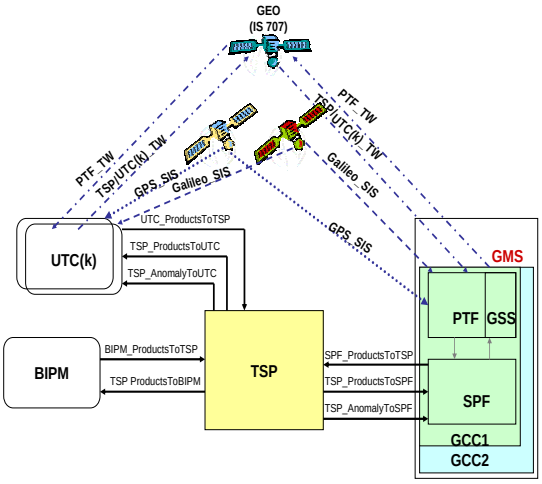

Figure 6: Interfaces between the TSP and PTF.

The quality of the TSP steering products is driven with the following performance requirements:

- The Time Service Provider shall ensure a GST(MC) frequency accuracy (expressed in terms of normalised GST (MC) frequency offset relative to UTC mod 1 sec frequency) better than 5.4x10e-14 (95% confidence level) in any period of 24 hours, excluding the normalised GST(MC) –UTC mod 1 sec frequency offset contribution due to GMS. Note that The GMS contribution to the GST frequency accuracy (in terms of normalized GST-UTC mod 1 sec frequency offset) shall not exceed 3.6x10e-14 (95% confidence level) averaged over 24 hours, excluding the contributions due to PTF-TSP synchronisation link uncertainty external to GMS
- The contribution to GST(MC) stability due to the GST(MC)-to-UTC mod 1 sec steering corrections as computed by the TSP shall not exceed 3x10e-15 in terms of Allan deviation over 24 h.
- The offset between GST and UTC mod 1 sec shall be less than 50 ns for 95% of time
- The offset between GST(MC) and UTC mod 1 sec shall be determined by the TSP with a maximum uncertainty of 26 ns to 95% confidence level assuming the estimation of UTC mod 1 sec six weeks in advance, excluding the GST(MC) –UTC mod 1 sec offset uncertainty contributions due to GMS. Note that the GMS contribution to the uncertainty of the GST- UTC mod 1 sec by the GMS shall not exceed 9 ns (95% confidence level), excluding PTF-TSP synchronisation link uncertainty contributions external to GMS.

V. GST Steering Principle

The process of the considered GST to UTC mod 1 sec steering is depicted in Figure 7. During the normal operation, when the TSP corrections are available, the steering correction of the master clock is generated by the GST algorithm which combines the steering contribution derived from the paper composite clock based on PTF caesium clock ensemble and TSP contributions. In case, that the TSP steering corrections are missing, the output of the MC is steered towards the output of the composite clock. In this case the caesium clock ensemble needs to perform to such extent so that the GST autonomy requirement to not to accumulate the uncertainty of more than 28 ns over 10 days is met.

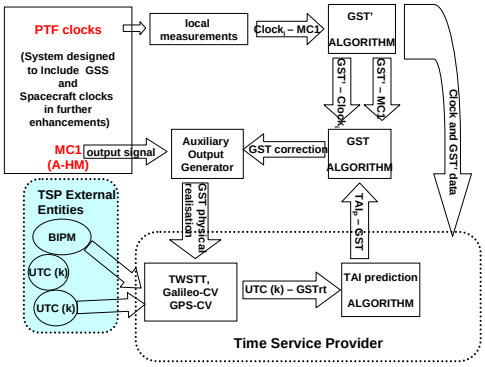

Figure 7: GST to UTC mod 1 sec steering

TSP generates GST to UTC mod 1 sec steering corrections based on its UTC mod 1 sec prediction algorithm. The prediction algorithm is fed with the data representing the differences between the timescales of TSP/UTC(k) labs and the GST timescales (realised at PTFs) as obtained by the means of the TWSTFT and GPS/Galileo-CV time transfer links connecting the TSP/UTC(k) labs with PTF. The TSP will gather this comparison data from the PTFs and TSP/UTC(k). Note the Galileo-CV is not envisaged to be used in the IOV (In Orbit Validation) phase, as it will not be possible to meet the required performance with only 4 Galileo satellites available, however it will be fully implemented for the FOC (Full Operational Capability) phase, when the Galileo-CV is expected to replace the GPS-CV.

In addition the TSP will use the Circular-T bulletin to obtain further GST-UTC(k) data and perhaps also other BIPM products. Note the Circular-T bulletin contains the information on the offset between the timescales of the primary timing laboratories (UTC(k)) and UTC timescale. The bulletin is issued every six weeks and contains the data span of four weeks. For the delivery of other products, see section IV, TSP uses also the information on the quality of the GST (long/short term stability), and GST clock ensemble measurements.

VI. GALILEO GPS TIME OFSET (GGTO)

The GGTO determination and its further distribution is provided by Galileo Global Component in order to enhance interoperability of the Galileo system with the GPS. The GGTO is understood as the offset between the GST and GPS Time as visible to users (i.e. as obtained from the Galileo and GPS signal in space). From the user point of view the offset between GPS and Galileo system time can be calculated by the means of combined receiver, however one additional range will have to be "sacrificed" to solve for the system time difference between Galileo and GPS. While the signals from at least four satellites are required to solve the positioning solution within one of the two navigation systems (Galileo or GPS), at least a fifth signal is required to fix the position in three dimensions if working in an environment using satellites of both constellations at the same time.

However, this might be an issue when navigating in areas of reduced visibility of the satellite constellations, as e.g. in urban canyons, where the reception of signals only from a limited number of satellites is available. The difference between the GPS and Galileo timescale will result into ranging error prohibiting user from fixing its true position with the required accuracy. Whilst with the inclusion of GGTO in the navigation message transmitted by the Galileo and GPS satellites, the user can use all the satellites in view in order to determine its position without having to sacrifice the 5th range in order to solve for the time difference between the systems. Note that the current GPS design implementation does not consider the European Galileo constellation and the GGTO will not be transmitted by the current GPS satellites. It is foreseen that future evolutions of GPS will consider the dissemination of GGTO in the GPS SIS.

From Galileo system point of view the function of determination and dissemination of GGTO is allocated to GMS. Inside the GMS it is the PTF element, which is charged with the task of GGTO determination. On the GPS side the USNO (U.S. Naval Observatory) is considered to act as GPS agent and as such it will operate in coordination with the PTF the GGTO-related interfaces between Galileo and GPS.

The detailed process of GGTO determination will not be further discussed in this paper. For further information please refer to reference document [7], [8]. However for the sake of completeness, the GGTO Galileo system level related requirements are given below.

Following performance constraints apply:

- The GGTO, once computed shall be valid 1 day.
- The accuracy of GGTO (modulo 1 sec) shall be less than 5 ns (2σ) over any 24 hours
- The stability of GGTO, expressed as an Alan deviation shall be better than 2x10e-14 over any period of 24 hours.

Following implementation constraints apply:

- Galileo and GPS shall establish an interface for TWSTFT, so that the difference between GST(MC) and GPS time scale is known with the total uncertainty lower than 2 ns (1 sigma).

VII. CONCLUSIONS

With the addition of Galileo System to the GNSS the users worldwide will be able to freely use and rely on the state of the art navigation system.

The Galileo system will provide to it's users various services, which rely on a highly accurate and stable timing reference. In order to achieve this objective, a timing infrastructure with shared responsibilities is considered to be implemented. The various players are the Galileo Global Component with the PTF element, the TSP and the GPS system.
Within the scope of the timing infrastructure following functions will be provided either by core elements or by cooperating with the external elements.

- PTF:
  - Navigation Time keeping
  - Installation of clocks
  - Physical realisation of GST
  - Synchronisation of the GMS and GCS elements
  - GGTO determination
- TSP
  - Metrological Timekeeping
  - Interacting with e.g. BIPM (e.g. leap seconds)
  - Providing steering corrections to PTF clocks, enabling PTF to meet it's performance objectives
- GPS

- Contribute to elaboration of GGTO
- Dissemination of GGTO in future evolutions of GPS

The Galileo Global Component will operate two PTFs working in parallel. These will be equipped with the best COTS time and frequency hardware available in order to generate autonomously the stable timescales and to allow for the implementation of the cutting edge time transfer techniques such as TWSTFT and CV. Furthermore Galileo spacecrafts will be flying PHM, the best clocks being ever flown, thus providing the unprecedented ranging signals parameters and performance. The design of the PTFs is considered to be expandable in order to include in the future other clocks in addition to the clocks installed locally at each PTF. Such extension of the PTFs clocks ensemble will allow for even more resilient timescales to be generated.

With the support of the TSP Galileo System Time will be kept within the close agreement with the UTC and by providing the UTC corrections Galileo users will be able through the reception of the Galileo SIS to reconstruct with the high accuracy the UTC information. The Galileo System will even further enhance the Galileo GPS interoperability by including the GGTO into its navigation messages.

Disclaimer

The opinions discussed in this paper are those of the authors and do not necessarily represent those of Galileo Industries GmbH and ESA .

Acknowledgements

The author would like to express his gratitude to co-authors for their contributions and also to colleagues from the GaIn system engineering team for their comments and support.

REFERENCES

[1] F. Luongo, The Galileo Integrity Concept, ION GPS/GNSS 2004, Long Beach, California, 21-24 September 2004
[2] D. Hanson, Fundamentals of Two-Way Time Transfer by Satellite, 43rd. Annual Frequency Control Symposium, 1989
[3] Recommendation ITU-R TF.1153-2, The Operational Use of the Two-Way Satellite Time and Frequency Transfer Employing PN Codes
[4] T. Parker, D. Matsakis, Time and Frequency Dissemination: Advances in GPS Transfer Techniques, GPS World, November 2004
[5] D. Allan, M. Weiss, Accurate Time and Frequency Transfer During Common-View of a GPS Satellite, 34th. Annual Frequency Control Symposium, May 1980
[6] M. Lombardi, L. Nelson, A. Novick, V. Zhang, Time and Frequency Measurements Using the Global Positioning System, Cal Lab: The International Journal of Metrology, July-September 2001
[7] J. Hahn, E. Powers, Implementation of the GPS to Galileo Time Offset (GGTO), proc. Joint IEEE International Frequency Control Symposium and Precise Time &Time Interval (PTTI) Systems &Applications Meeting, pp. 33-37, Vancouver, BC ,Canada, 29-31 August 2005
[8] F. Luongo, Galileo-GPS Interoperability and Compatibility: A Synergic Viewpoint, ION GPS/GNSS 2003, Portland, Oregon, 9-12 September, 2003

Proceedings of the 20th EFTF, 2006

ESA's Frequency and Timing Systems for Deep Space Operations and Radio Science Investigations

W. Schäfer[1], J. DeVicente[2]
[1] *TimeTech GmbH, Stuttgart, Germany, Wolfgang.Schaefer@timetech.de*
[2] *European Space Agency (ESA), Darmstadt, Germany, Javier.DeVicente@esa.int*

Following the successful operation of the first Deep Space Antenna (DSA1) in New Norcia, Australia [1] and the recent inauguration of the 2nd Station (DSA2) in Cebreros, Spain [2], the European Space Agency (ESA) is currently expanding its Deep Space tracking capabilities, the next facility to be constructed in Kourou, French Guyana.

Deep space operations and research impose demanding phase stability on ground station equipment, high frequency stability of the reference system and excellent phase noise of the distributed reference signal. The combination of these aspects is certainly unique for Frequency and Timing systems. An outline of ESA's past and future design- and development activities in support of advanced F&T systems is given, which demonstrates ESA's commitment to continuously improve its support of Deep Space Missions.

The paper describes the 2nd generation Hydrogen-Maser based Frequency and Timing System in Cebreros, which has been optimized for a high stability and low phase noise 100 MHz distribution system. The architectural design and its operational aspects are presented. The actual performance is given in terms of

- Allan Deviation (< 1E-15 between 1000 and 10000 seconds),
- Phase Noise (–102 dBc at 1 Hz offset for 100 MHz)
- Long-Term Stability (1.2e-15/day).

The paper puts the present performance of ESA's stations in perspective with future mission requirements, which traditionally arise from state-of-the-art Radio Science research. The evolution path to meet future mission demands, which might arise from ambitious projects like BepiColombo [3], is presented.

I. INTRODUCTION

Deep Space missions impose stringent requirements on the performance of radio links, both for system operation and in support of Radio Science investigations. Routine operations require high availability combined with fully automatic operation, while Radio Science is performed during dedicated parts of the mission by extracting additional information from the received signal. This rather unique combination of performance- and operational aspects call for excellent short- and medium-term frequency stability in addition to state-of-the art phase-noise performance on the Frequency & Time sources within the ground segment. Active Hydrogen Masers are the main references, as they are today's most suitable frequency sources to meet the target specifications.

This paper describes the architecture and performance of the Frequency and Timing (F&T) Systems for ESA's new Deep Space Facilities. The first ESA station has become operational in March 2003. It is located in New Norcia [1], near Perth, Western Australia. The second station is located at Cebreros, north of Madrid, Spain, which is operational since September 2005. Kourou, French Guayana, will become a backup station by end of 2006. A further installation is presently under consideration to achieve a full 24-hour coverage.

II. DEEP SPACE APPLICATIONS

ESA's stations are designed to support multiple tasks while using radio links. Although the primary objective is support of deep-space missions, satellites in near-earth orbits can be operated as well. There are two major application areas

1. Support of spacecraft operations
2. Conduction of Radio Science using RF links

Spacecraft operations include en-route tracking using one-way and two-way Doppler data and round trip signal delay measurements [4]. Main emphasis is on frequency stability to support Doppler data during observation periods of up to 8 hours. Orbit maneuvers, including insertion into planetary orbits, comet encounters etc., require accurate time for the precise knowledge of the satellite's position.

Radio Science Investigations add requirements on short-term stability for $0.1s \leq \tau \leq 45min$ for occultation experiments. Bi-static radar techniques and observations of back-scatter from rough surfaces call for best phase noise at offsets of 0.1Hz to 50 Hz from the carrier. The detection of gravity waves and general planetary research requires optimum frequency stability for time periods ranging from seconds up to 20 min. [5]

These few samples already demonstrate the challenge in the design of deep space stations and its F&T system.

Figure 1: Deep Space Antenna at Cebreros

The stations at New Norcia and Cebreros are equipped with a 35m diameter antenna. They use low loss beam wave-guide feed systems to ensure a low system noise temperature. All major RF elements are placed at ground level in the Antenna Equipment Room (AER) within the antenna support structure. This includes cryo-cooled LNAs, up- and down-converters, high power RF amplifiers and the F&T generation and distribution system itself. The Kourou station, acting mainly as backup station, has a 15m dish antenna only.

III. F&T SYSTEM ARCHITECTURE

The Frequency and Timing systems are designed around EFOS-C type masers, manufactured by the Observatory of Neuchâtel, Switzerland. This is an enhanced version compared to previous models using improved thermal stabilisation of the electronics and relying on low phase-noise 5 MHz USOs of selected performance. The BVA-type USOs, model 8607, are manufactured by Oscilloquartz, Neuchâtel, Switzerland. The masers are located in a dedicated maser room inside the Antenna Equipment Room, well separated electrically and environmentally from the remaining station elements, and running from their dedicated un-interruptible power supplies.

The electronics rack implements two redundant signal generation chains, with outputs of 5, 10 and 100 MHz, IRIG-1B and a proprietary 5 MHz IRIG code, 1pps pulses and an optical cross-site link to distant installations. The system has built-in performance monitoring by phase-frequency comparators used to compare the two masers and to monitor high-performance output signals. Two GPS receivers (Motorola UT-Oncore) are used for long-term frequency monitoring and time comparison to UTC. An internal time-scale is maintained to supply the estimate of UTC to the station elements via IRIG and NTP.

The system operates unattended. It is under remote control by the European Space Operations Centre, ESOC, Darmstadt, Germany. The monitoring system relies on redundant Linux-based controllers, which maintain history logs for all relevant measurement data and a set of event logs. Telemetry data is retrieved regularly from each maser, together with environmental data (temperature, humidity and magnetic field) and phase/frequency measurements to assess the short- and long-term behavior of the masers.

System monitoring includes input and output level of each signal. The systems signal chains may be re-configured under operator control. The only automatic reconfiguration changes the reference maser once in case of failure of the primary maser.

The redundancy concept is based on input signal selection between redundant signal sources for each distribution element and cross-strapping between redundant chains. This scheme has been adopted in favor of output signal switching to minimize the amount of switches. Each signal user is supplied with two redundant reference signals.

IV. F&T SYSTEM DESIGN

The first station at New Norcia is based on a 5 MHz distribution system [6], whereas the 2nd station at Cebreros relies on a 100 MHz distribution system, with 5 MHz signals being still available for secondary and lower performance users. Enhancements include

- Improved 100 MHz signals from masers
- Multi-channel 100 MHz Phase Comparator
- Lower thermal sensitivity (1.5ps/K)

- Phase noise at 100 MHz: -130 dBc, 100 Hz offset
- Dual 100 MHz Clean-up Oscillators
- Digital control loops in clean-up units
- Maser selection without phase discontinuity
- Coherent signal combination to reduce noise
- Improved thermal stabilisation of masers

The block diagramme of the overall F&T system is contained in Annex 1-1. Major signal specifications are listed in Table 1 below, which apply to the outputs at the system's interface panel.

Item	unit	100 MHz	5 MHz
Phase noise @ 1 Hz	dBc/Hz	- 102	-126
Phase noise @ 100 Hz	dBc/Hz	- 131	-145
Harmonics	dBc	≤ 40	≤ 53
Spurious	dBc	≤ 90	≤ 105
Isolation (I/O)	DB	80	80
Return Loss (I/O)	DB	40	35
Level	dBm	11.5	13

Table 1: Signal specifications

Table 2 shows the approximate gain in frequency stability by use of the 100 MHz outputs instead of the 5 MHz outputs of the same maser. The table shows average ADEV results from two units operated under laboratory conditions, valid for a single maser.

ADEV @ t [s]	5 MHz	100 MHz	Gain [%]
1	1.3E-13	**1.0E-13**	~ 20
10	2.0E-14	**1.8E-14**	~ 9
100	4.4E-15	**2.8E-15**	~ 30
1000	1.5E-15	**1.0E-15**	~ 30

Table 2: ADEV improvement by using 100 MHz

A six-channel phase comparator is used for the clean-up oscillators, to monitor the relative frequency stability of the masers and to measure the phase at the output of the 100 MHz distribution amplifier. Its residual Allan Deviation is shown in Table 3.

Recorded phase data between the two masers may be analysed a-posteriori to identify the possible cause or nature of delay variations observed on the satellite signal links and to enhance the confidence into the primary maser acting as frequency reference to the station.

ADEV @ t [s]	100 MHz
1	1.8E-14
10	2.3E-15
100	3.3E-16
1000	8.5E-17
10000	2.7E-17
40000	1.6E-17

Table 3: Residual ADEV of 100 MHz phase comparator

Delay variation vs. temperature has been characterized by means of the phase comparator. Together with precise temperature readings, they are used for digital compensation of the system's temperature coefficient, resulting in approximately 1.5ps/K between reference maser and user outputs at 100 MHz.

Significant emphasis has been laid on the phase noise of the 100 MHz signal between 1 Hz and 100 Hz offset from carrier. Two clean-up oscillators are locked to the reference maser by a digital PLL (see Annex 1-2).

The 100 MHz outputs of both units are kept in phase. They are subsequently combined to form a single reference to the distribution chains. After combination, the 100 MHz phase-noise improves. There is even a slight reduction on ADEV at 1 s. Ideally, the phase noise improvement would be 3 dB assuming two similar clean-units. The actual gain (see Table 4 below) is smaller because of minor differences between the units.

Offset from carrier [Hz]	Single CLEAN	Combined CLEANs	Gain [dB]
1	-101.7	-102.7	1
10	-117.2	-118.7	1.5
100	-130.0	-131.8	1.8
1000	-154.5	-155.7	1.2

Table 4: Phase-noise [dBc], improvement at 100 MHz

The series connection of maser source and clean-up units causes a slight deterioration of the resulting ADEV, in particular for t around the loop time constant. The measured degradation is shown in Table 5 below, together with the final system performance, when the masers are operated inside the heater-cooler boxes.

ADEV @ t [s]	Maser Degradation	Final System Performance
1	9 %	1.0E-13 *)
10	9 %	2.0E-14
100	4 %	3.1E-15
1000	4 %	8.6E-16 **)
10000	~ 0	5.9E-16 **)

*) includes improvement due to combination of two clean units
**) Masers are operated in heater-cooler boxes

Table 5: Maser ADEV degradation due to clean-up units

The digital phase comparator and the digitally controlled phase-lock loop of the clean-up oscillators provide an elegant means to select the reference maser by selection of the respective phase comparator channel. Any switchover is smoothed relying on the short-term stability of the USOs inside the clean-up units. Changing the reference maser results in a typical phase-transition of approx. 1ps within 10s at the 100 MHz outputs, see Figure 2.

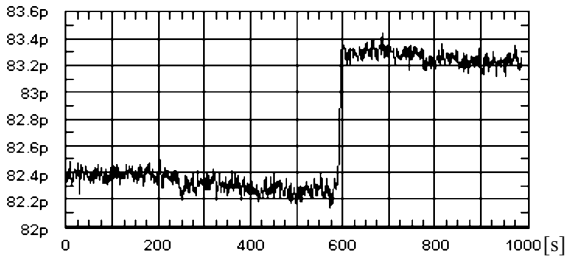

Figure 2: Phase transition after maser re-selection [ps]

Each maser is operated inside its own heater-cooler box, to keep the inside temperature unaffected from the thermal variations due to the air conditioning system, to slow down any external temperature variation and to shield a maser during maintenance activities on the other unit. The thermal gain of a heater-cooler box is 20, see Table 6.

Location	Temperature [°C]	Stability [K]	Thermal gain
Maser Room	20.5 °C	1	-
Maser Unit	26.3 °C	0.05	20
Maser Electronics	47 °C	0.01	100

Table 6: Maser temperature and temperature stabilities

V. NEXT STATION: KOUROU

For the next facility at Kourou, French Guyana, the masers have been accepted already. Being a backup station, a 5 MHz distribution system has been selected. A major challenge for the Kourou installation is the distance between the masers and the antenna site of approx. 200 m. Even high quality cables would exhibit prohibitively large temperature coefficients. Although there are excellent optical link designs [7], their use had been ruled out because of their mostly experimental nature. Based on extensive tests, the Andrew cable type FSJ4, UMTS grade, not thermally compensated, was selected together with an active delay compensation. The thermally compensated variant of the same cable type ironically showed slightly worse result for the relevant temperature range.

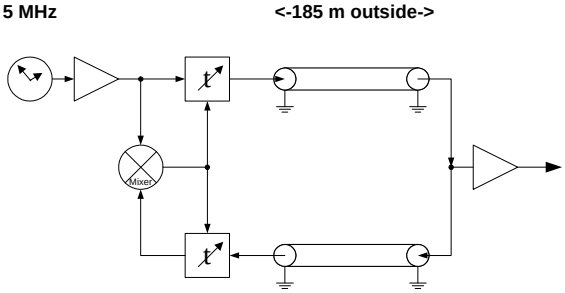

Figure 3: 5 MHz delay compensation for Kourou station

The delay compensation uses a bi-directional link with symmetric paths and compensation elements. The electronic phase shifters have no discernible impact on the system's phase noise and on its short-term TDEV.

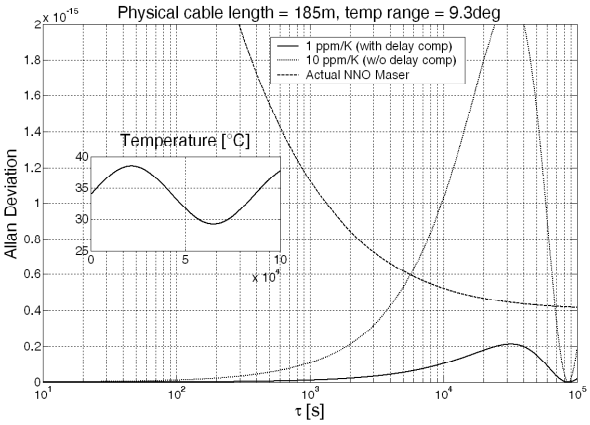

Figure 4: 5 MHz delay compensation for Kourou

Predicted performance based on thermal tests is shown in Figure 4 for a 185m cable run subject to daily temperature variations of 9.5K. For comparison, the actual maser stability from New Norcia is included in the same figure. The thermally induced cable delay variation causes an increase of 12% of the maser's ADEV for τ around 30.000s. It is believed, that the final system will be even better after fine-tuning of the residual asymmetries of the system and by careful selection of matching cable pairs.

VI. MASER LONG-TERM STABILITY

Long-term performance data lasting about 1.5 years exist for the two masers at New Norcia. The relative frequency stability between the two masers is measured by a phase-frequency at 5 MHz. Best stability is around 30.000s (see Table 7), which coincides well with the useful tracking time of approx. 8 h for a single satellite.

ADEV @ t	5 MHz New Norcia
10 s	1.4E-14
100 s	2.8E-15
1000 s	8.5E-15
10000 s	5.0E-16
30000 s	3.5E-16
1 d	4.3E-16
3 d	5.7E-15

Table 7: Frequency stability, New Norcia, single unit

The long-term stability and ageing is determined by comparison to GPS. The results are shown in Table 8.

	Maser I	Maser II
Data set	620d	180d
Ageing	2.6E-16/d	1.3E-15/d

Table 8: Aging measured vs. GPS, New Norcia

The Hadamard Deviation presented in Table 9 shows the excellent predictability of the maser's frequency.

HDEV @ t	5 MHz
14 d	1E-15
54 d	2E-15 ± 0.5E-15

Table 9: Hadamard deviation, New Norcia, two units

VII. MISSION SUPPORT

Up to now several deep-space missions have been supported, including

- Ulysses
- Rosetta
- Mars Express
- Venus Express (orbit insertion: April 11th, 2006)

The network is ready for further missions, like

- Herschel Planck
- LISA Pathfinder
- Gaia
- BepiColombo

among others, all scheduled for launch in the next decade.

VIII. SUMMARY

The European Space Agency ESA is pursuing major technological developments in the following key areas related to Ground Frequency and Time Generation:

- Optical clocks: first studies awarded
- Sapphire Clock research: under consideration
- Optical fibre distribution: studies ongoing [7]
- Improved electrical distribution systems: ongoing

To support future needs and requirements for

- Precise spacecraft tracking, incl. formation flying
- Radio Science
- Fundamental Physics missions
- Clocks on-board space-craft
- Time Keeping

A good overview about clocks on-board space-craft can be found in [8]. Up to now, two stations became operational, already actively tracking key deep space missions. The network is planned to be expanded to ensure full 24h coverage.

This ambitious long-term programme ensures continued research and development activities in the field of Frequency and Timing systems, which will further fuel the commercialization of key technologies. This enables more applications and commercial opportunities, for example in the field of global navigation systems. Finally, access to high performance and highly accurate Frequency- and Timing systems will be available for larger communities on a commercial basis.

Acknowledgements

This work is performed under ESA contract No. 17137/03/D/SW.

REFERENCES

[1] www.esa.int/esaCP/SEMACK2A6BD_index_0.html
[2] www.esa.int/esaCP/SEM7BO7X9DE_index_0.html
[3] L. Iess, G. Boscagli: *Radio Science Experiments for the Mission BepiColombo to Mercury*, TTC 2001
[4] C. L. Thornton et al, *Radiometric Tracking Techniques for Deep-Space Navigation,* DESCANSO
[5] S. W. Asmar and N. A. Renzetti, *The Deep Space Network as an Instrument for Radio Science Research*, JPL Publication 80-93, 1993
[6] W. Schäfer, J. A. Jornod, J. DeVicente, Proceedings, ATF 2004, pp 332 ff
[7] O. Lopez et al, in these proceedings
[8] C. Lämmerzahl et al, Ann. Phys. 11 (2002) 2, 95-150

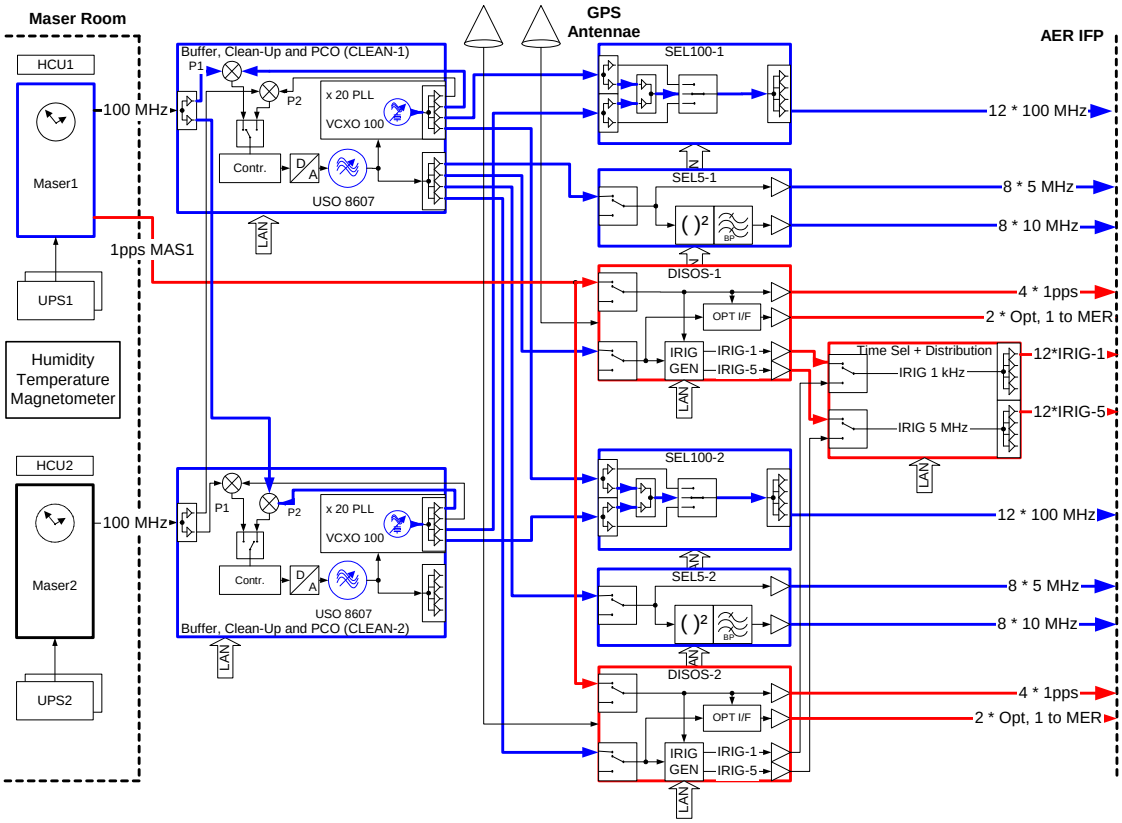

Annex 1-1: F&T architecture, 100 MHz distribution with clean-up units, Cebreros

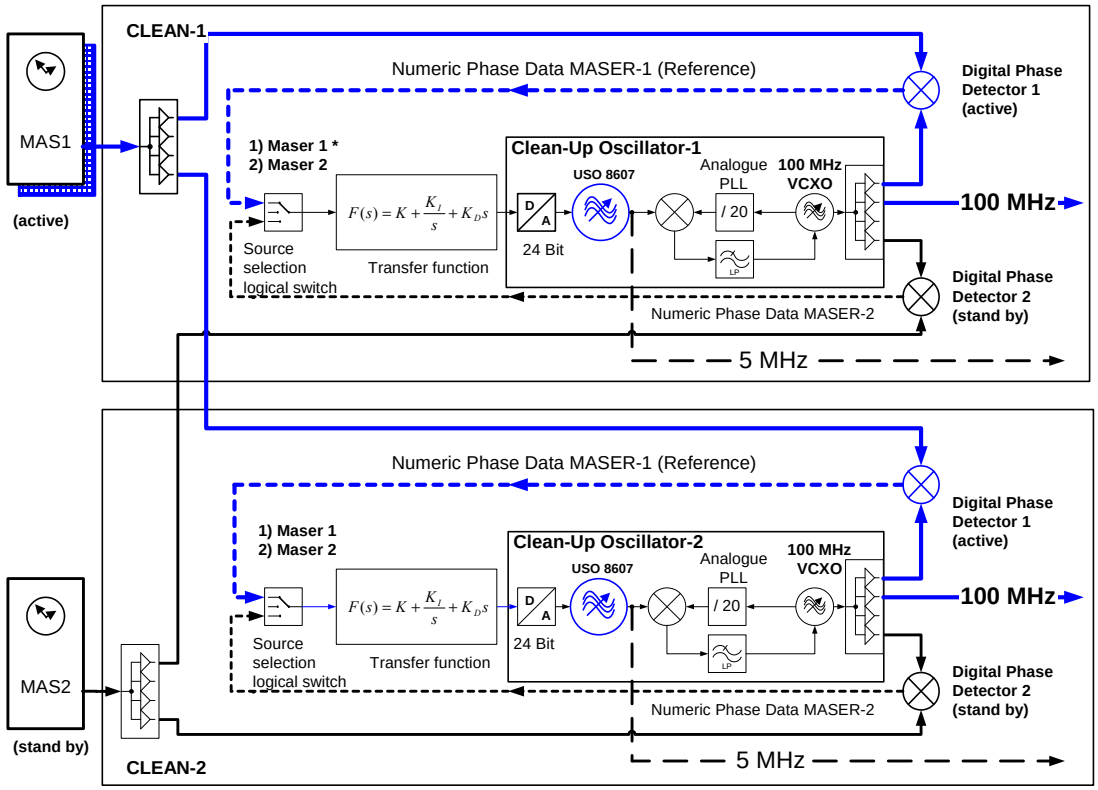

Annex 1-2: 100 MHz Clean-up unit design, digital PLL and cross-strapping scheme (Cebreros)

Proceedings of the 20th EFTF, 2006

Time and frequency requirements for geodetic space techniques

W. Schlüter
Bundesamt für Kartographie und Geodäsie, Fundamentalstation Wettzell
Sackenrieder Str. 25, D-93444 Kötzting
E-mail: wolfgang.schlueter@bkg.bund.de

Precise geodetic space techniques as Very Long Baseline Interferometry (VLBI), Laser Ranging to artificial Satellites or to the Moon (SLR/LLR) and the geodetic application of Global Navigation Satellite Systems as GPS, GLONASS and in the future GALILEO are based -in general- on measurements of time and time intervals. The epochs of the global observations are referenced to the timescale UTC. The offsets to UTC have to be known in the domain of some nanoseconds. The observations require absolute frequencies which are generated by precise frequency standards. To avoid scaling errors the frequencies offsets should be less than 10^{-12}. Moreover e.g. VLBI demands short term frequency stability which active H-Masers are capable to provide today.

Recently the International Association of Geodesy (IAG) released its Project "Global Geodetic Observing System (GGOS)", which will result in the realisation of a global reference frame with a relative precision of 10^{-9}, harmonizing the geometric and geophysical parameters to the same level of precision. The reference frame should be stable for decades. GGOS will become a backbone for research in the area of geosciences. It will demand continuous observations of geodetic parameters as station positions and monitoring of the Earth motions by the geodetic space techniques. The accuracy of the geodetic observation techniques will be improved, which consequently will demand appropriate clocks.

This paper will summarise the status of the geodetic space techniques, in particular the achieved accuracy and some plans to increase the accuracy in order to meet the requirements for GGOS. In particular it will focus on the demands for atomic frequency standards, applied in the geodetic observation techniques.

I. EVOLVEMENT OF GEODETIC SPACE TECHNIQUES PRECISION

Before geodetic space techniques were applied, intercontinental distances were calculated from latitude and longitude coordinates with reference to an ellipsoid, best fitted to the figure of the Earth. Latitude and Longitude were derived from astronomical observations. Considering the systematic errors, in particular due to personal influence of the observer, the intercontinental distances could be estimated with an accuracy of the order of only 100m. After the launch of balloon satellites in the 60ies, which could be observed with cameras, satellite triangulation technique was developed which allow the measurement of directions between far separated ground stations. A first global network was established and simultaneous observations with cameras were carried out, which provides the directions between the network points. In combination with a few distances, which were observed between a few network points, employing classical terrestrial geodetic techniques, coordinates were derived with an accuracy of ~10m. During the 60ies, developments in technology made enormous progress. Atomic clocks, time interval measuring devices and LASERs were invented. Employing a pulse laser, distance measuring systems to artificial satellites could be set up. Satellite Laser ranging systems of the 1st Generation achieved an accuracy of the order of 1m. The first Satellite Navigation System TRANSIT, based on Doppler technique reached comparable precision in the submeter domain during the 70ies. In the 80ies the technology continued to improve. Satellite Laser Ranging (SLR) achieved the centimeter domain. Very Long Baseline Interferometry (VLBI), an observation technique developed for Radioastronomy, was applied for the geodetic research. Intercontinental baselines could be measured with an accuracy of ~3 cm. The modern and precise techniques enable since the 80ies to observe plate motion. The evolvement of technology still improves and reached the level a few millimeters today. The most important developments, driving the progress

in geodetic observing technique, employ time and time intervals measurements. Satellite based navigation systems as GPS, GLONASS or in the future Galileo make use of atomic clocks orbiting the Earth.

Precise geodetic observation techniques are the basis for the research of plate motions, sea level rise, Earth tides, ocean and atmospheric loadings and Earth rotation etc..

Continuous observations are required for monitoring the variations in order to improve the models for predictions and to understand the geophysical phenomena.

Global reference frames are established in order to describe positions in space -e.g. for positioning of space crafts or satellites - and on Earth – e.g. for surface positions. The global reference frames fixed in space is realised by about 600 Quasars, for which positions are known by coordinates as declination and rectascension. The realisation is the International Celestial Reference Frame (ICRF), see Figure 1.

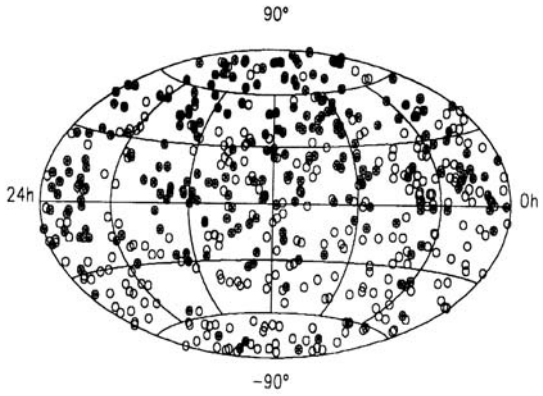

Figure 1, The International Celestial Reference Frame (ICRF), distribution of Quasars

The Earth fixed reference frame is materialized through geodetic observatories, for which the positions and the velocities are known at an epoch e.g. 2000.0. The realisation in know as International Terrestrial Reference Frame ITRF2000 (figure 4). The transformation between both global reference frames needs the knowledge of the Earth Rotation, which is described by the Earth Orientation Parameter (EOP), as direction of the rotation axis in both frames and the velocity of rotation (figure 5). ICRF and ITRF are fundamental for research in all geosciences and related disciplines. Due to the variations the global reference frames ICRF and ITRF as well as the EOP's need continuous maintenance.

The International Association of Geodesy established the project GGOS (Global Geodetic Observing System), which should realise a global reference frame with relative precision of 10^{-9}, consistent in the geometrical and physical parameters describing the GGOS and stable for decades [1].

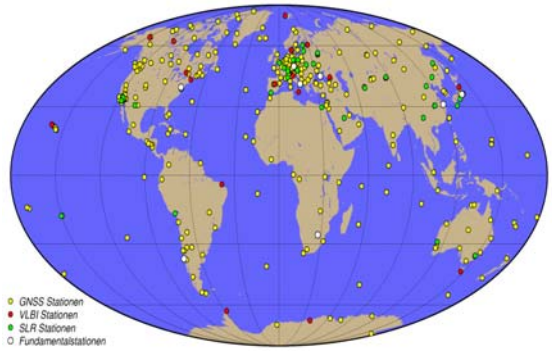

Figure 2, the distribution of the global sites realizing the ITRF

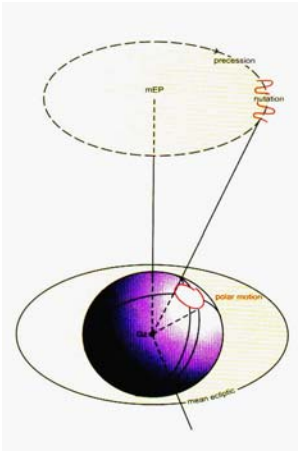

Figure 3, Earth Rotation, described as precision and nutation, polar motion and variations in the rotation (UT1- UTC)

II. GEODETIC SPACE TECHNIQUES

The space techniques, which support the maintenance of global reference frames are

- VLBI (Very Long Baseline Interferometry)
- SLR/LLR Satellite/Lunar Laser Ranging
- GNSS (GPS, GLONASS, future: Galileo)
- DORIS (Doppler Orbitography and Radio Positioning Integrated by Satellite)

The techniques are coordinated through international services of the International Association of Geodesy

(IAG) and of the International Astronomical Union (IAU) as

- International VLBI Service for Geodesy and Astrometry (IVS)
- International Laser Ranging Service (ILRS)
- International GNSS Service (IGS)
- International DORIS Service (IDS)

The services coordinate the observations, the data flow and the analysis and are finally responsible for the timely provision of proved results.

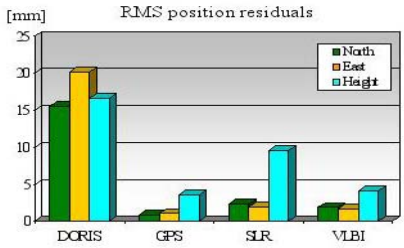

Figure 4, RMS position residuals from the space techniques (from D. Angermann, Deutsche Geodätische Forschungsinstitut, München)

The accuracies in the north-, east- and height components achieved by the four techniques are shown in figure 4.

III. PRINCIPAL OF VLBI

Very Long Baseline Interferometry (VLBI) is employed in Radioastronomy e.g. to investigate structures of radiosources and in Geodesy to measure the baseline lengths between radiotelescopes. The principle (figure 5) is based on the determination of the delay τ and the assumption, that the positions of Quasars are known (ICRF). Simultaneous observation signals emitted from quasars with a set of radiotelescopes (minimum two) and recording the signals including precise clock information, derived from a H-Maser, allow the determination of τ through a correlation process. Up to 400 quasars are observed during a 24h session. The recorded data were transferred to a corellator in general via courier or via Internet - if high speed Internet facilities are available. Corellators, employing the NASA recording technology MK5, are located in Washington-USA, Haystack-USA and Bonn-Germany. Out of the observables τ the following products can be derived:

- Baseline-vectors and positions in order to maintain ITRF
- Earth Orientation Parameter (EOP) for monitoring the Earth rotation
- Quasar positions in order to maintain the ICRF
- Tropospheric, ionospheric parameter
- Physical parameter (love numbers)
- Clock parameter (need to be considered in the analysis).

The accuracy is dependant on the

- Signal resolution (bandwidth, signal/noise), the recorded data stream is < 1Gbps
- Clock stability, H-Maser are used due to the high short term stability up to parts in 10^{-15}.

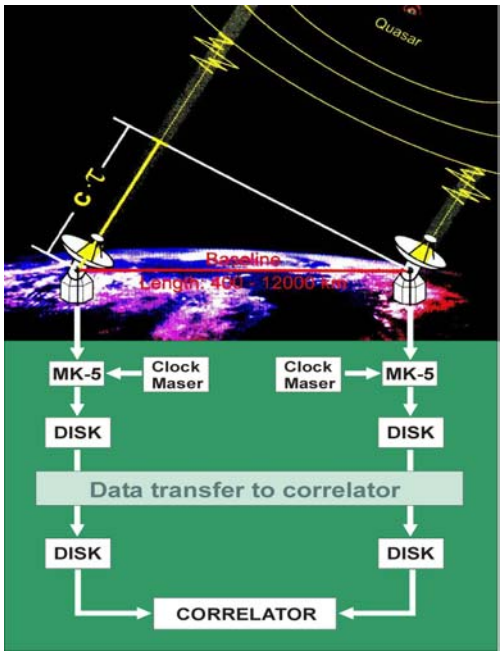

Figure 5, Scheme of the principal of VLBI

Figure 6 give an overview about the VLBI components coordinated within the International VLBI Service for Geodesy and Astrometry (IVS) [2]. Figure 7 shows the 20m Radiotelescope of the Fundamental Station Wettzell.

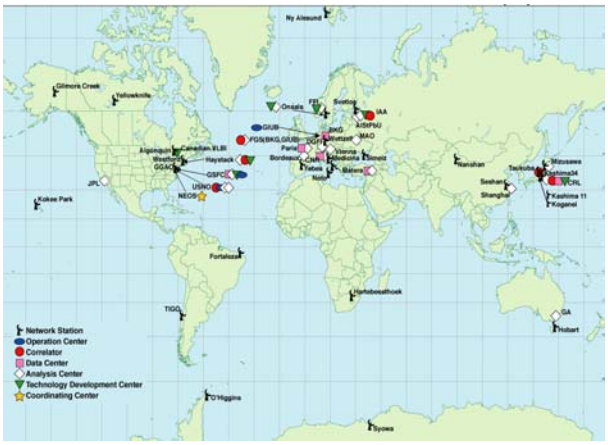

Figure 6, IVS, global distribution of IVS components

Figure 7, 20m Radiotelescope of the Fundamental Station Wettzell, Germany

The strengths of VLBI are:

- only VLBI realizes and maintains the ICRF,
- only VLBI allows the determination of a complete set of Earth Orientation Parameter and
- uniquely VLBI provides the Earth rotation parameter UT1-UTC, which is urgently needed for satellite orbit determination or space missions.

The IVS recently release the document VLBI 2010 [3], summarizing the visions for the future to evolve the next generation VLBI in order to meet future requirements. Components will be developed or improved, as digital recorders for data streams up to 2Gbps, e-VLBI, employing Internet data transmission to provide products in near real time and to perform continuous observations. Frequencies will be used in the domain of 1 to 16Ghz. Finally the delay τ should be observed better than 4ps. This leads to a request for improvement of the time frequency devices, which are currently used in VLBI.

IV. T&F REQUIREMENTS FOR VLBI

The requirements for the clock and frequency generator can be estimated from the basic equation in VLBI, with the extension to clock parameters (offset and frequency)

$$c\tau = 1/c\ \mathbf{(s\ b)} + c\Delta T + c\,(T\text{-}T_0)\,\Delta f/f + \ldots.$$

as

$$cd\tau = c\,d\Delta T + c(T\text{-}T_0)\,d\Delta f/f$$

where

c:	speed of light
τ:	time delay
s:	unit vector in direction to Quasar
b:	baseline vector
ΔT :	clock offset
$d\Delta T$:	error of the clock offset
$T\text{-}T_0$:	elapsed time
$\Delta f/f$:	relative frequency offset
$d\Delta f/f$:	error of the frequency offset

Under the assumption, that the influence should be less than 1mm ($cd\tau$ < 1mm), the results are:

$$d\Delta T = 1[mm]/c \sim 3\ ps \qquad (1)$$

$$d\Delta f/f = 1[mm]/(c(T\text{-}T_0)) \sim 3.3 * 10^{-12}/(T\text{-}T_0) \qquad (2)$$

The clock offset should be known to 3ps. As no time transfer allow this accuracy so far, the offset is estimated in the analysis. VLBI has the potential for time transfer at highest level, but calibration of the internal delays is still problematic.

The frequency offset provides a scale error. It should be known better than 10^{-12}, which is not a problem at all employing regular time transfer technique. The frequency offset can also be estimated by considering the offset in the analysis. Correlation of timing parameters with the height component and the troposphere parameter occur.

More problematic is the noise in the frequency (2) - see

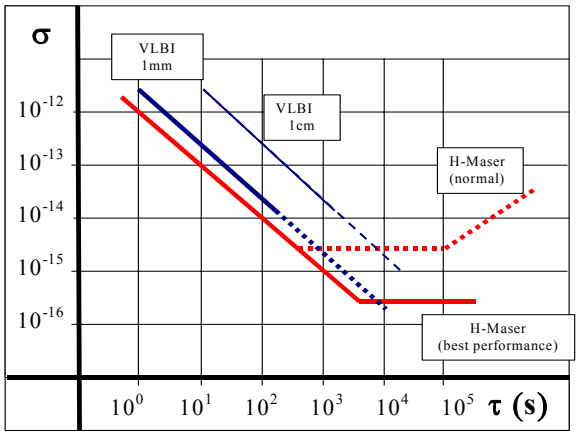

the sigma-τ plot in figure 8 (Allan Variance).

Figure 8, VLBI requirements versus H-Maser stability

The diagram shows generally the Allan Variances for a Maser as it is under normal conditions and as it could be for a best performing Maser. The two other curves show the requirements for VLBI calculated from equation (2)

under the assumption for cdτ not larger than 1cm (thin blue curve) or 1mm (thick blue curve).

During the single scans, within some minutes, the frequency stability is o.k.. After approximately 2 to 3 hours, however, the noise of the H-Maser does not meet the wish to have coherent timescale precise enough for more scans, which are observed during a period of longer than 3h. Usually this problem is solved by the estimation of clock parameters in the analysis. For VLBI 2010, the best H-maser should be requested, which today reaches stabilities in parts of 10^{-16}.

V. PRINCIPAL OF SLR/LLR

Satellite or Lunar Laser Ranging SLR resp. LLR is based on the determination of the propagation delay of a light pulse transmitted from an observatory to the target and back (figure 9). The targets, satellite or the moon, are equipped with corner cubes (figure 10), which allow to return the pulse back to the observatory. Short Laser pulses (pulse length: 30...100ps) are generated by Nd:YAG- (1064/532nm) or TiSaPP-Lasers (850/425nm). Precise tracking of the target requires an optical telescope (figure 11). Photomultipliers or avalanche diodes are employed for the detection of the returns at single photon level. Event timers measure the propagation delay a few picoseconds precise. The events are recorded with respect to UTC. Calibration internal and external is required for the determination or elimination of systematic biases.

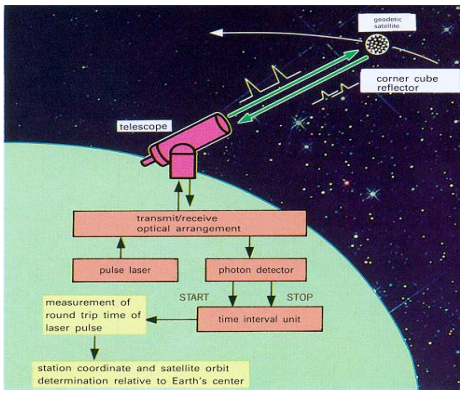

Figure 9, Scheme of SLR

Laser ranging products are

- precise satellite orbits
- station coordinates and velocities with respect to the Geo-center
- contributions to gravity field
- Polar motion
- Time transfer
- etc.

The Accuracy is dependant on

- Event timer resolution
- Pulse lengths,
- receiving pulse (single photon level)
- Calibration
- Statistics (normal points)
- etc.

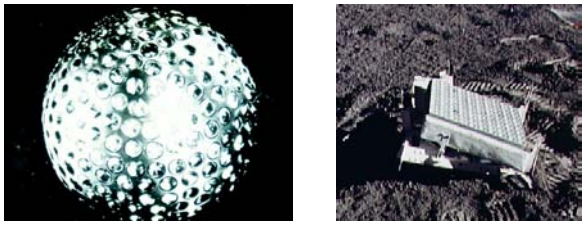

Figure 10, LAGEOS with corner cubes and reflector on the Moon from Apollo-missions

Figure 11, 75cm Telescope of the WLRS (Wettzell Laser Ranging System)

The mostly tracked satellites are

- LAGEOS1
- LAGEOS2
- Starlette
- Stella
- ETALON1
- ETALON2
- GPS35
- GPS 36
- 6 GLONASS
- ERS 2
- ENVISAT
- AJISAI

For Lunar tracking the NASA Apollo missions and Russian missions placed reflectors to the Moon. Figure 12 show the distribution of the SLR tracking sites.

Figure 12, Distribution of the SLR-tracking sites

Future developments focus on the increase of the Laser repetition rate. While today 10Hz repetition rate is applied in the future 1KHz will be realized for some stations. Employing two wavelengths (e.g. 850nm and 435nm) will give additional information to the troposphere and support to improve the knowledge about refraction. Laser transponders will be developed in order to employ the technique for very long distances to high orbiting satellites, to the moon or even for interplanetary missions.

VI. SLR/ LLR: T&F REQUIREMENTS

The requirements for SLR and LLR today are estimated considering the Assumption:

- ~1cm rms single shot
- ~ 3-4 mm rms normal points
- Satellite velocity ~ 7… 8 km/s

The event timer has to provide a read out of better than 20 ps rms in order to derive the elapsed time between the events of transmission and receive better than 30ps. For the determination of the epoch of the observations, the event timer has to be synchronized to the global timescale UTC better than 100ns. Such an accuracy could be easy achieved with the available time transfer techniques. During 100ns the Satellite motion is approximately 1mm and does not significantly influence the observation accuracy of 1cm.

As a frequency offset effect the distances measurement with a scale error ($\Delta s/s = \Delta f/f$), the frequency offset has to be eliminated with a resolution of

$\sim 1 \times 10^{-10}$ for satellites and

$\sim 1 \times 10^{-11}$ for the Moon

with a stability of

$\sim 1 \times 10^{-10}$ for satellites over τ 0.3 s and

$\sim 1 \times 10^{-11}$ for the Moon over $\tau = 3$s

The employment of 1kHz Laser and two color system, promises to reach the mm domain (< 1mm rms), it will allow to see the structure of the reflector, and the estimation of the spin of the satellite. The requirements in time and frequency will increase by one order in magnitude as

- Event timer resolution $< 2 \ldots 3$ ps
- Epoch with ref. to UTC ~ 10ns
- Frequency offsets $< 10^{-12}$
- Frequency stability $< 10^{-12}$ for $\tau \sim 0.3$ s

The use of Rubidium frequency generators and employing GPS time transfer technique will be sufficient for SLR and LLR.

VII. T&F SYSTEM OF FS WETTZELL

The requirements from the space techniques can be met with a timing system generating a time scale which is in real time available with a

- precision of ~ 10ns

and providing frequencies with an

- offset of $< 10^{-12}$ (absolute: compared to a normal frequency) and a
- stability of 10^{-15} for $\tau \sim 10^3$s

At the Fundamental Station Wettzell the hardware devices are

- 5 Cs-Standards HP5071
- 3 H-Maser (EFOS)
- GPS-receivers, 1 Channel (AO 6TR, K&K)
- GPS modified geodetic receivers (Ashtech Metronome, Septentrio)

Figure 13, H-Maser EFOS 18

The H-Maser (EFOS 18) , shown in figure 13 drives

- VLBI -clock and -frequency devices directly
- SLR/LL event timer via 1 frequency distributor
- GPS oscillators via 3 frequency distributors.

Figure 14, Cs-atomic clocks, HP5071

CS-Standard, an HP 5071 (figure 14) drives the master clock which generates the timescale UTC(IFAG).

The time comparison to connect UTC(IFAG) to the international timescale UTC is done with the modified geodetic GPS receiver, developed by Ashtech and Septentrio. The receivers are named in the IGS community as WTZA or WTZS.

Figure 15 shows the T&F devices for comparisons and for maintenance.

Figure 15, T&F devices for comparison of the clocks

REFERENCES

[1] Drewes, H, and C. Reigber, The IAG Project "Integrated Global Geodetic Observing System (IGGOS)" – Setup of the Initial Phase, IVS 2004 General Meeting Proceedings, p.186-190, Washington, 2004

[2] W. Schlüter, D. Behrend, E. Himwich, A.Nothnagel A. Niell, A. Whitney: IVS High Accurate Products for the Maintenance of the Global Reference Frames as Contribution to GGOS, Proceedings of the IAG General Meeting, Cairns, 2005

[3] A. Niell, A. Whitney, W. Petrachenko, W. Schlüter, N. Vandenberg, H. Hase, Y. Koyama, C. Ma, H. Schuh, G. Tuccari: VLBI2010: Current and Future Requirements for Geodetic VLBI Systems, IVS WG3 Report, Washington, 2005

Proceedings of the 20th EFTF, 2006

Clocks in space missions*

C. Lämmerzahl† and H. Dittus‡
ZARM, University of Bremen, Am Fallturm, 28359 Bremen, Germany

The status of present day physics which essentially is encoded in the Einstein Equivalence Principle is reviewed. This includes the Universality of Free Fall, the Universality of the Gravitational Redshift and the local validity of Lorentz invariance. This implies that gravity is a metric theory. This metric can be explored by positioning of freely falling objects or by clocks. The need of a theory of quantum gravity implies small deviations from this standard physics picture so that, e.g., different clocks are expected to behave differently in gravitational field. Furthermore, there are some observations which until now did not found a convincing explanation and may suggest that gravity should be modified at large distances. Clocks play an important role in space explorations of such modifications.

I. INTRODUCTION

Clocks play a fundamental role in the exploration of the laws of physics. At first, they provide the time parameter for the description of dynamical processes, and second, since clocks are by itself are governed by physical laws, they give information of the physical processes underlying the clocks. A particular connection exists between clocks and the theories of relativity, namely Special Relativity (SR) and General Relativity (GR). The reason is that these are theories describe properties of space and time and, thus, the measurements of time and distances. Since, furthermore, within SR and GR the measurement of distances can be replaced by the measurement of time, clocks are the absolute basic and fundamental tools in space–time theories.

Therefore it is not astonishing that most of the principles underlying SR and GR are related to a particular behavior of clocks. In particular, SR can solely based on the properties of clocks, and GR is based on SR, the behavior of clocks in gravitational fields and on the free fall properties. Therefore, but the free fall GR is based solely on the behavior of clocks.

One consequence of that is that clocks are also a basic tool for the search of deviations from SR and GR. From the fact that GR and quantum theory are not consistent and other reasons there are strong expectations that GR has to be modified. Such a modification are expected to lead to tiny deviations from SR and GR, in particular, to tiny violations of their underlying principles.

Here we first describe the status of present day physics and then go to the hitherto unsolved problems and observation and then describe use of clocks in exploring these issues. In doing so we emphasize the use of space missions for that purpose.

*We like to dedicate this article to H. Binnenbruck on occasion of his 65th birthday.

†Electronic address: laemmerzahl@zarm.uni-bremen.de
‡Electronic address: dittus@zarm.uni-bremen.de

II. PRESENT STATUS

The present scheme of physics is mainly encoded in the Einstein Equivalence Principle consisting of (i) the Universality of Free Fall (UFF), (ii) the Universality of the Gravitational Redshift (UGR), and (iii) the validity of Local Lorentz Invariance. These three principles imply that gravity can be geometrized and can be described by a space–time metric $g_{\mu\nu}$ [1], that is, within a Riemannian geometry. See Fig.1. For recent reviews on the experimental status of tests of gravity, see [2]. For technological applications, see [3].

A. Universality of Free Fall

UFF holds for neutral point–like particles only. The corresponding tests compare the accelerations a of these particles in the reference frame of the gravitating body. The characteristic quantity is the Eötvös factor $\eta = 2\frac{a_1+a_2}{a_1+a_2}$. In the frame of Newton's theory this can be expressed as $\eta = 2\frac{\mu_1+\mu_2}{\mu_1+\mu_2}$ with $\mu = m_{\rm g}/m_{\rm i}$, where $m_{\rm g}$ is the gravitational and $m_{\rm i}$ the inertial mass. The most precise tests yield a verification of the UFF at the order $5\cdot 10^{-13}$ [4]. Free fall tests led, due to the short time span of free fall, to slightly less accurate results [5]. UFF tests have also been carried through with quantum systems, namely neutrons [6] and atoms [7].

Charged or spinning particles couple to curvature and, thus, violate UFF. However, since this violation is extremely small, it makes sense to look for an anomalous coupling of spin and charge to the gravitational field [8]. For charged particles the UFF has been confirmed with a precision of approx. 10% [9] and for particles with spin with a precision of 10^{-8} [10]. UFF experiments with antimatter are in preparation [11] with an anticipated accuracy 10^{-3} on ground and possibly 10^{-5} in space.

Physical system	Method	Result: $\eta <$
neutral bulk matter	torsion balance	$5\cdot 10^{-13}$ [4]
polarized matter	weighting	10^{-8} [10]
charged particles	time–of–flight	10^{-1} [9]
Quantum system	atom interferometry	10^{-9} [7]
antimatter	not yet carried through	

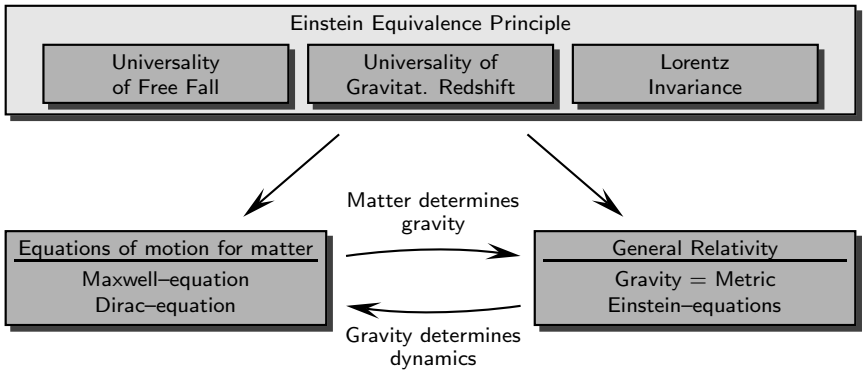

FIG. 1: The Einstein Equivalence Principle and its implications.

B. Universality of Gravitational Redshift

For a test of this principle the run of clocks based on different physical principles has to be compared during their common transport through a gravitational potential. Clocks that have been used are (i) light clocks (optical resonators), (ii) atomic clocks based on electronic hyperfine transitions characterized by $g(m_e/m_p)\alpha^2 f(\alpha)$, where g and f are some functions, and m_e and m_p are the electron and proton mass, respectively, and where α is the fine structure constant, (iii) atomic clocks based on electronic fine structure transitions, (iv) atomic clocks based on electronic principal transitions, (v) molecular clocks based on rotational transitions characterized by m_e/m_p, (vi) molecular clocks based on vibrational transition given by $\sqrt{m_e/m_p}$, (vii) gravitational clocks based on revolution of planets or binary systems, (viii) pulsar clocks based on the spin of stars, and (ix) clocks based on the decay time of elementary particles.

The possibility that the gravitational redshift of clocks may depend on the used clock is described by an additional clock–dependent parameter $\alpha_{\rm clock}$:

$$\nu(x_1) = \left(1 - (1+\alpha_{\rm clock})\frac{U(x_1) - U(x_0)}{c^2}\right)\nu(x_0)\,. \tag{1}$$

This absolute gravitational redshift has been best tested by the GP-A mission where a hydrogen maser in a rocket has been compared with a ground maser. With $U = GM/r$ the result was $|\alpha - 1| \le 7\cdot 10^{-5}$ [12]. The comparison of two collocated clocks gives

$$\frac{\nu_1(x_1)}{\nu_2(x_1)} \approx \left(1 - \Delta\alpha_{\rm clock2}\frac{U(x_1) - U(x_0)}{c^2}\right)\frac{\nu_1(x_0)}{\nu_2(x_0)}\,, \tag{2}$$

where $\Delta\alpha = \alpha_{\rm clock2} - \alpha_{\rm clock1}$. If this frequency ratio does not depend on the gravitational potential then the gravitational redshift is universal. It is preferable to have available a large difference in the gravitational potential. In the clock comparison experiments listed below the variation of U was induced by the motion of the Earth around the Sun what implies that the used clocks should have a very good long term stability.

Comparison	Result: $\lvert\Delta\alpha\rvert$
Cs – Resonator	$2\cdot 10^{-2}$ [13]
Mg – Cs (fine structure)	$7\cdot 10^{-4}$ [14]
Resonator – I_2 (electronic)	$4\cdot 10^{-2}$ [15]
Cs – H-Maser (hf)	$2.5\cdot 10^{-5}$ [16]
H – Anti-H	not yet carried through

C. Local Lorentz invariance

Lorentz invariance can be based on two postulates: (i) the speed of light c is constant, and (ii) the relativity principle. These two postulates have immediate consequences which all can be tested in experiments:

- c does depend neither on the velocity of the source or of the observer, on the direction of propagation, nor on the polarization or frequency of the light ray.

- The relativity principle implies that the limiting velocity of all particles is the speed of light and that *all* physics is the same in *all* inertial systems, that is, experimental results do neither depend on the orientation of the laboratory nor on the velocity of the laboratory.

Accordingly, we have the following classes of experiments:

a. Constancy of c The independence of the speed of light from the velocity of the source has been examined by (i) the observation by Brecher [17] who analyzed the time of arrival of X–rays emitted from distant a bright star orbiting a dark, heavy central star, and at CERN where the velocity of light emitted by pions moving with $v = 0.99975\,c$ has been measured. Within the model $c' = c + \kappa v$ one obtains $\kappa \le 10^{-10}$ and $\kappa \le 10^{-6}$, respectively.

b. Universality of c The equality of the maximum speed of electrons, photons in various velocity ranges, neutrinos and muons has been tested in laboratory experiments and astrophysical observations leading to a relative equality at the 10^{-6} level [18]. Furthermore, a birefringence in vacuum can be ruled out at 10^{-32} level [19].

c. Isotropy of c The relative difference of the speed of light in different directions is smaller than $\Delta_\vartheta c/c \leq 10^{-16}$ [20].

d. Independence of c from the velocity of the laboratory The difference of the speed of light in differently moving inertial systems is now smaller than $\Delta_v c/c \leq 10^{-16}$ [21].

e. Time dilation Also the time dilation factor has been confirmed with much better accuracy using ions in an storage ring moving with a velocity of $v = 0.064\,c$. With the time dilation factor γ in the parametrization $\gamma(v) = 1 + \left(\frac{1}{2} + \alpha\right)\frac{v^2}{c^2} + \ldots$ (for SR we have $\alpha = 0$) the most recent experiment gave $|\alpha| \leq 2.2. \cdot 10^{-7}$ [22]. Time dilatation has also be verified by the decay of moving elementary particles, see [23] for a recent version of these experiments where time dilation has been verified at the 10^{-3} level.

f. Isotropy in the matter sector Other aspects of violations of SR are anomalous inertial mass tensors [24] in quantum equations or orientation–dependent spin effects, and effects related to higher order derivatives in the Maxwell or Dirac equations. Anomalous mass tensors are looked for in the famous Hughes–Drever experiments [25] constraining these effects by an order of 10^{-30}. Also tests of anomalous couplings of the spin to some given cosmological vector or tensor fields destroys the Lorentz invariance gave no evidence, neither for the neutron [26], the proton [27], nor the electron [28, 29] which are all absent to the order of 10^{-31} GeV (for a recent review on the experimental search for anomalous spin couplings, see [30]). Spectroscopy of anti–hydrogen which may yield information about the validity of the *PCT* symmetry is in a planning status.

All the experiments testing the isotropy of c up to the isotropy in the matter sector can be interpreted as clock comparison tests, see Fig.2.

Since, as explained above, SR and GR are the physics of space and time and since the measurement of time and of positions is at the very foundation of metrology, one may regard SR and GR as being equivalent to fundamental metrology, see Fig.3 for the important implications of the validity of the Einstein Equivalence Principle for metrology. Furthermore, SR and GR are necessary for a lot of technical applications in daily life [3].

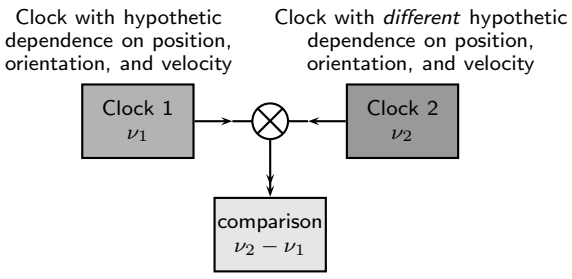

FIG. 2: Comparison of clocks of different nature and in different states of motion yield a complete test of Special Relativity and also test UGR.

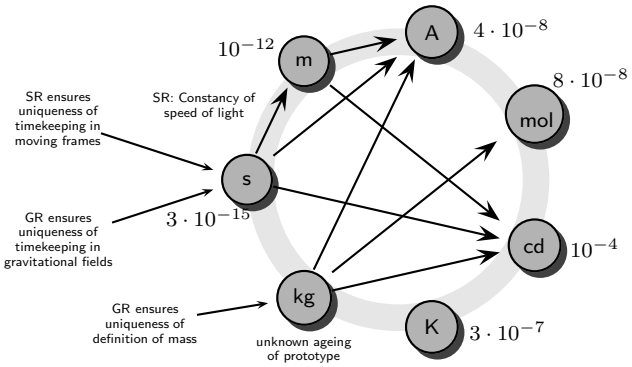

FIG. 3: Metrology and the Einstein Equivalence Principle.

III. PRESENT PHYSICS HAS TO BE MODIFIED

Though until now all these high precision tests are fully described within the present theoretical scheme given by the Einstein Equivalence Principle, there are difficulties with this scheme. One difficulty is that there are some observations which do not fit into that scheme (see below) and the other is that this scheme is not theoretically consistent. The inconsistency is due to the fact that all known quantization schemes are not applicable top GR and that time in GR has a different meaning than in quantum theory; while in GR time is a dynamical variable, in quantum theory it is an externally given parameter. The need for a quantized version of GR emerges from the fact that if matter is quantized also the interaction field has to be quantized. Furthermore, there is the expectation that with a quantization of the gravitational one might get rid of the problem of gravitational singularities, see e.g. [31].

Due to these reasons there *has to be* a new theory of gravity and of the quantum phenomena. Since the standard theories like GR, QED etc. are based on the Einstein Equivalence Principle, at least parts of this principle has to be violated in the new theory. Since most tests of this principle are based on clock experiments, clocks play an essential role in the search for a new quantum gravity theory.

IV. "PREDICTIONS" FROM QUANTUM GRAVITY

From string theory one can derive and motivate an effective Lagrangian for gravity with a long–ranged

dilaton–like scalar field [32]

$$L_{\rm eff} = \frac{1}{16\pi G}R(g) - \frac{1}{8\pi G}D_\mu\varphi D^\mu\varphi - \frac{1}{4e^2(\varphi)}F_{\mu\nu}F^{\mu\nu} - \sum_A \left(\bar\psi_A\gamma^\mu(D_\mu - iA_\mu)\psi_A + m_A(\varphi)\bar\psi_A\psi_A\right) \qquad (3)$$

where φ, $F_{\mu\nu}$ and ψ_A are the dilaton, the electromagnetic and fermion fields, respectively. This scalar field splits into a vacuum expectation value and small deviations from that: $\varphi = \varphi_0 + \delta\varphi$ where φ_0 is the vacuum expectation value given by cosmological evolution. As a consequence, the masses of the fermions $m_A(\varphi)$ and the charge $e(\varphi)$ now depend on the dilaton field. Also the energy levels will depend on the scalar field.

The strength of the coupling of the matter parameters to the scalar field is given by (i) $\alpha_A = (\partial \ln m_A(\varphi)/\partial\varphi)_{\varphi=\varphi_0}$ of coupling of dilaton to mass m_A, (ii) $\alpha_{\rm em} = (\partial e^2(\varphi)/\partial\varphi)_{\varphi=\varphi_0}$ of coupling of dilaton to electromagnetism, and (iii) $\alpha_{AA'} = (\partial E_{AA'}(\varphi)/\partial\varphi)_{\varphi=\varphi_0}$.

Since the masses depend on the scalar field, also the gravitational constant will depend on it. The gravitational attraction of a mass 2 exerted on a test mass 1 at distance r_{12} is given by $(m_i)_1 a_1 = (m_g)_1 G (m_g)_2/r_{12}^2$, where $(m_i)_1$ and $(m_g)_1$ are the inertial and gravitational mass of the test body. $(m_g)_2$ is the gravitational mass of the gravitating body and G the bare gravitational constant. Therefore

$$a_1 = G\frac{(m_g)_1}{(m_i)_1}\frac{(m_g)_2}{(m_i)_2}\frac{(m_i)_2}{r_{12}^2} = G_{12}\frac{(m_i)_2}{r_{12}^2}\,. \qquad (4)$$

Using $(m_g)_{1,2}/(m_i)_{1,2} = 1 + \alpha_{1,2}$ we obtain

$$G_{12} = G\frac{(m_g)_1}{(m_i)_1}\frac{(m_g)_2}{(m_i)_2} \approx G\,(1 + \alpha_1\alpha_2)\,. \qquad (5)$$

what is the effective gravitational constant which now depends on the material. This implies (i) a violation of UFF which may be as big as 10^{-13}, (ii) a violation of UGR, and (iii) modified PPN–parameters β and γ which influence the dynamics of particles and light rays [32, 33].

Another scalar–tensor theory with a very similar mathematical structure is an effective grand unified model with a time–dependent cosmon field χ where all mass scales and coupling constants depend on χ [34]. Here the ratio of the Planck mass to the GUT mass scale are a function of χ and, thus, time dependent. Furthermore, all particle parameters depend on χ which is related to quintessence which is the dynamical description of the dark energy in the universe. The prediction is a violation of UFF at the 10^{-14} and of UGR at the 10^{-18}–level.

A further scenario is given be a varying elementary charge e [35]. This again leads to a time– and space–variation of the fine structure constant which implies a violation of UGR and also of UFF.

Apart from these predictions, there are already some observations which seem not to fit into the present standard theories and, thus, have the potential to be first hints to a new theory replacing the present standard model:

V. UNEXPLAINED OBSERVATIONS IN GRAVITY

Though the above scheme seems to be in full accordance to all tests there are a few observations which still lack a convincing explanation. These observation are (i) dark matter, (ii) dark energy, (iii) the Pioneer anomaly, (iv) the flyby anomaly, (v) the increase of the Astronomical Unit, and (vi) the quadrupole and octupole anomaly.

g. Dark matter Dark matter has been introduced in order to "explain" the stronger gravitational field needed for the galactic rotation curves, the gravitational lensing of galaxies, and the formation of structures in our universe [36]. It also appears in the spectral decomposition of the cosmic microwave background radiation [37]. Dark matter is needed if one assumes Einsteins field equations to be valid. However, since there is no observational hint at particles which could make up this dark matter there are attempts to describe the same effects by a modification of the gravitational field equations or by a modification of the dynamics of particles.

h. Dark energy Recent observations of type Ia supernovae indicate that the expansion of the universe is accelerating and that 75% of the total energy density consist of a dark energy component with negative pressure [38]. Furthermore WMAP measurements of the cosmic microwave background [39], the galaxy power spectrum and the Lyman-alpha forest data lines [40] also indicate – when compared with standard cosmological models – the existence of Dark Energy that leads to the acceleration of the universe, rather than a modification of the basic laws of gravitation [41]. Recently it has been claimed that dark energy or, equivalently, the observed acceleration of the universe can be explained by inhomogeneous cosmological models, such as the spherically–symmetric Lemaitre–Tolman–Bondi model, see, e.g., [42].

i. The Pioneer anomaly The Pioneer anomaly is an unexplained acceleration $a_{\rm Pioneer} = (8.74 \pm 1.33)\cdot 10^{-10}$ m/s^2 of the two Pioneer 10 and 11 spacecraft which started with the last flyby at Saturn. This acceleration is constant and directed toward the Sun [43, 44].

No systematic error for this acceleration has been found. There were speculations that the accelerated expansion of our universe might be the reason for this acceleration. However, an analysis of the Doppler tracking, was well as of the modification of the gravitational field of the Sun and the planetary orbits all embedded in an expanding universe shows that the influence of the expansion is by orders of magnitude too small to be responsible for the observation. An-

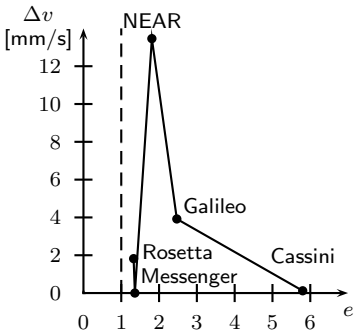

FIG. 4: The velocity increase Δv as function of the eccentricity e.

other speculation was that a quadratic drift of time $t \to t + \alpha_{\rm Pioneer} t^2$ for $\alpha \approx 2a_{\rm Pioneer}/c \approx 1.5 \cdot 10^{-17}$ s^{-1} of the clocks on Earth may in principle be possible for such an observation. However, this does not seem to be compatible with the the tracking and ranging data of other spacecraft [44] and with astrophysically defined clocks like pulsars and binary systems.

j. The flyby anomaly It has been observed at various occasions that satellites after an Earth swing–by acquire a significant unexplained velocity increase by a few mm/s. This unexpected and unexplained velocity increase is called the *flyby anomaly*. No anomaly has been observed for the direction.

The data can be put into diagrams where the velocity increase can be plotted as function of the eccentricity e, see Fig.4. Though from four data points it is much too early to draw any serious conclusion one may speculate the following: If the velocity increase really is due to an unknown gravitational interaction, then it makes sense that (i) the effect goes down with increasing eccentricity, and (ii) that it also should go down for an eccentricity approaching $e = 1$ because the transition to bound orbits, where no effect has been seen, certainly should show no discontinuity.

In addition, these available data suffer from low cadence (the anomaly often appears between two data points). Precise data at a much higher cadence of all the motion parameters of the spacecraft prior to, during and after the flyby would allow a qualitatively improved analysis.

The anomalous acceleration, estimated by the velocity increase during the time of flight near the Earth, is of the order 10^{-4} m/s^2. This is considerably larger than the above discussed Pioneer anomaly. The velocity increase has been observed in the two–way Doppler measurements as well as in the ranging measurements.

An analysis covered all possible influences on the spacecraft: (i) atmospheric mismodeling, (ii) ocean tides, (iii) if the spacecraft becomes charged, then it may experience an additional force due to the Earth's magnetic field, (iv) also the interaction of a hypothetical magnetic moment of the spacecraft with the Earth's magnetic field may give an additional force, (v) ion plasma drag, (vi) Earth albedo, and (vii) Solar wind. Even with very rough pessimistic assumptions none of these can be held responsible for the flyby anomaly [45].

In order to be able to pin down a specific interaction term it is necessary to make detailed studies of the nature of the velocity increase: In the near future there will be two Earth flybys (November 2007 and November 2009) and one Mars flyby (February 2007) by Rosetta [46]. We strongly suggest that one should use these opportunities in order to carry through a better observation of the Rosetta flybys. In particular, a continuous observation also should give hints to the particular direction of the local acceleration and also on the strength and, thus, to the position dependence of the anomalous force. Furthermore, since Mars possesses other conditions than the Earth (weaker atmosphere, almost no magnetic field, other gravitational field, lower thermal radiation, etc.) the effect, if it will be observed, will turn out to be universal.

k. The increase of the Astronomical Unit From the analysis of radiometric measurements of distances between the Earth and the major planets including observations from Martian orbiters and landers from 1961 to 2003 a secular increase of the Astronomical Unit of approximately 10 m/cy has been reported [47] (see also [48] and the discussion therein).

This increase cannot be explained by a time–dependent gravitational constant G because the $\dot{G}/G$ needed is larger than the restrictions obtained from LLR. Also a hypothetical time–dependent change in the velocity of light cannot be responsible for this effect [45]. It also can be shown that the influence of cosmic expansion by many orders of magnitude too small, see [49, 50]. An increase of ranged distances might also be due to a drift of the time scale of the form $t \to t + \alpha t^2$ for $\alpha > 0$. From Kepler's third law one obtains $\alpha \approx 3 \cdot 10^{-20}$ s^{-1} what is astonishing close to the clock drift needed for a clock drift simulation of the Pioneer anomaly.

l. The quadrupole and octupole anomaly Recently an anomalous behavior of the low–l contributions to the cosmic microwave background has been reported. It has been shown that (i) there exists an alignment between the quadrupole and octupole with $> 99.87\%$ C.L. [51], and (ii) that the quadrupole and octupole are aligned to Solar system ecliptic to $> 99\%$ C.L. [52]. No correlation with the galactic plane has been found. The reason for this is totally unclear.

VI. SCHEME OF EXPLORATION

Art first one has to state that the observations concerning dark matter and dark energy are beyond any doubt. The issues which are of concern here are the Pioneer anomaly, the flyby anomaly and the increase of the Astronomical Unit. These effects may have some

relation to the behavior of clocks and may be explored by clocks. However, at first one always has to take into account that the above effects are the result of some systematic errors.

Below we propose a general scheme of how to treat these anomalous effects. Since gravity is related to the measurements of time and position, we introduce two different concepts, namely a space–time metric and paths. The metric describes the behavior of clocks, the path the motion of spacecraft.

m. Clocks In Special Relativity the proper time of clocks is given by $ds^2 = \eta_{\mu\nu}dx^\mu dx^\nu$ where $\eta_{\mu\nu} = \mathrm{diag}(+1,-1,-1,-1)$ is the Minkowski metric. Since Special Relativity should be the local limit of a theory of gravity, the general metric may be given the form (we choose $c = 1$)

$$g_{\mu\nu} = \begin{pmatrix} 1-2U & g_{0i} \\ g_{i0} & \delta_{ij}\,(1-V) \end{pmatrix}, \qquad (6)$$

where U, V, and $g_{0i} = g_{i0}$ are assumed to be small quantities. U may be identified with the Newtonian potential. We denote $ds^2 = g_{\mu\nu}dx^\mu dx^\nu$. By definition, the readout of moving clocks is given by

$$\begin{aligned} T &= \int_{\text{worldline of clock}} ds \\ &\approx \int \left(1 - U + \tfrac{1}{2}\dot{x}^2 - \tfrac{1}{2}V\dot{x}^2\right)dt + \int \boldsymbol{h}\cdot d\boldsymbol{x} \end{aligned} \qquad (7)$$

which is the proper time of the clock. A clock at rest will measure the gravitational redshift given by

$$\frac{\nu_1}{\nu_2} = \sqrt{\frac{g_{00}(x_1)}{g_{00}(x_2)}} \approx 1 + U(x_2) - U(x_1)\,. \qquad (8)$$

One may further generalize this to Finslerian metrics where the distances are not given by a quadratic form but, instead, by a form being just homogenous of degree 2. We will not do this here.

If, e.g., a Newtonian potential is responsible for the Pioneer anomaly, that is, if $a_{\text{Pioneer}} = \partial U/\partial r$, then this would result in an additional time shift of

$$\frac{\Delta T_{\text{Pioneer}}}{T} = \frac{a_{\text{Pioneer}}L}{c^2} \approx 10^{-13}\,, \qquad (9)$$

for $L \sim 90$ AU and where T is the time needed for traversing the distance L. That means, a clock is needed with a stability of 10^{-13} over a timescale of 20 y. This should be available with modern clocks. If the Pioneer anomaly is due to the V term instead, then the clock on board a Pioneer mission should show the standard time. – In the case that the other potential V are considered to be the reason for the Pioneer anomaly, then we have to take $a_{\text{Pioneer}} = \dot{x}^2\partial U/\partial r$ which then results in a velocity dependent clock readout.

Performing the same sort of analysis for the flyby anomaly, then a Newtonian cause for this would result in a time shift of

$$\frac{\Delta T_{\text{flyby}}}{T} = \frac{a_{\text{flyby}}L}{c^2} \approx 10^{-14}\,, \qquad (10)$$

where now L and T are now of the order 10000 km and 1 h, respectively.

n. Paths An arbitrary path fulfilling the UFF and the condition that posing an initial position and initial velocity uniquely determines the path is described by a second order differential equation

$$0 = v^\nu\partial_\mu v^\nu = \left\{ {\mu \atop \rho\sigma} \right\} v^\mu v^\sigma + \gamma^\mu(x,v) \qquad (11)$$

where $\left\{ {\mu \atop \rho\sigma} \right\} = \frac{1}{2}g^{\mu\nu}\left(\partial_\rho g_{\sigma\nu} + \partial_\sigma g_{\rho\nu} - \partial_\nu g_{\mu\nu}\right)$ is the Christoffel connection and $\gamma^\mu(x,v)$ some function of the position and the velocity. From this general equation of motion we can derive the 3–acceleration

$$\begin{aligned} \frac{d^2x^i}{dt^2} &= -\left(\left\{ {i \atop \mu\nu} \right\} - \left\{ {0 \atop \mu\nu} \right\}\frac{dx^i}{dt}\right)\frac{dx^\mu}{dt}\frac{dx^\nu}{dt} \\ &\quad + \frac{1}{\left(\frac{dt}{ds}\right)^2}\left(\gamma^i(v,x) - \frac{dx^i}{dt}\gamma^0(v,x)\right) \\ &\approx \underbrace{\partial_i U}_{\text{Newton}} + \underbrace{(\partial_i h_j - \partial_j h_i)\dot{x}^j}_{\text{Lense–Thirring}} + \dot{x}^2\partial_i V + \dot{x}^i\dot{V} \\ &\quad + \Upsilon^i + \Upsilon^i_j\dot{x}^j + \Upsilon^i_{jk}\dot{x}^j\dot{x}^k + \dots\,, \end{aligned} \qquad (12)$$

where we neglected all relativistic corrections since these play no role in the Pioneer and flyby anomalies. The term $\dot{x}^2\partial_i V$ is compatible with what we obtained for the time–keeping. Note also that the Universality of Free Fall is respected. However, it is no longer possible to make a transformation to a coordinate system so that gravity disappears at one point (Einstein's elevator is not possible). Physically this means that, e.g., the acceleration of a body toward the Earth can depend on the velocity of the body.

The first term in (12) is the ordinary Newtonian acceleration and the second term the action of the gravitomagnetic field on the orbit of a satellite which has been observed by LAGEOS with a 10% accuracy [53]. This field also acts on spinning objects like gyroscopes and should be confirmed by GP-B with an accuracy better than 1%.

The other terms are hypothetical terms beyond ordinary post–Newtonian approximation. The V term which can be motivated by a running coupling constant to be proportional to the distance, $V \sim r^2$ [54] can account for the Pioneer acceleration. The other terms, most of then are velocity dependent, have not yet been analyzed. Since the influence of an arbitrary force being responsible for the Pioneer anomaly is not compatible with the recent analysis of the motion of the outer planets [55] the modification of the equation of motion should include velocity–dependent terms.

The coefficients $\Upsilon^i_{jk\dots}$ depend on the position only and may vanish for vanishing gravitating mass. Therefore, the coefficients can contain M, r, and r^i only. Accordingly, these coefficients can be of the form

$$\Upsilon^i = A_{11}\frac{GM}{r^2}\frac{r^i}{r} \qquad (13)$$

$$\Upsilon^i_j = A_{21}\frac{GM}{r^2}\frac{r^i r^j}{r^2} + A_{22}\frac{GM}{r^2}\delta^i_j \qquad (14)$$

and similar expressions for $\Upsilon^i_{jkl\ldots}$, giving accelerations

$$\ddot{x}^i = A_{11}\frac{GM}{r^2}\frac{r^i}{r} \quad (15)$$

$$\ddot{x}^i = A_{21}\frac{GM}{r^2}\frac{r^i \boldsymbol{r}\cdot\dot{\boldsymbol{r}}}{cr^2} + A_{22}\frac{GM}{r^2}\frac{\dot{r}^i}{c} = (A_{21}+A_{22})\frac{GM}{r^2}\frac{r^i \boldsymbol{r}\cdot\dot{\boldsymbol{r}}}{cr^2} + A_{22}\frac{GM}{r^2}\frac{\dot{r}^i_\perp}{c} \quad (16)$$

and similar terms for higher order $\Upsilon^i_{jkl\ldots}$, where $r^i_\perp = r^i - r^i(\boldsymbol{r}\cdot\dot{\boldsymbol{r}})/r^2$ is the body's velocity orthogonal to the vector $\boldsymbol{r}$, and the A_{ij} are some numerical factors.

The first term associated with A_{11} is of Newtonian form and amounts to a redefinition of the gravitational constant. The A_{22} term describes an additional acceleration in direction of the velocity. The A_{21} term projects the component of the velocity which is parallel to the connecting vector and leads to an acceleration in direction of the connecting vector. This term vanishes at the perigee.

These A_{21}– and A_{22}–terms yield

$$\ddot{x}^i = \begin{cases} A_{22}\dfrac{GM}{r^2}\dfrac{\dot{r}^i}{c} & \text{for } r \approx r_{\text{perigee}} \\ (A_{21}+A_{22})\dfrac{GM}{r^2}\dfrac{\dot{r}^i}{c} & \text{for } r \text{ large} \end{cases} \quad (17)$$

Therefore, in principle it is possible to have an acceleration near the perigee (for $A_{22} > 0$) and a deceleration or vanishing acceleration for large distances (for $A_{21}+A_{22} < 0$ or $= 0$). Note that for a typical perigee and velocity at perigee the acceleration at perigee for $A_{22} = 1$ is about 10^{-4} m/s^2 what is just the value given for a typical Earth flyby. This model does not include the Pioneer deceleration. The higher order terms will be of more complicated but similar structure. A general discussion of the influence of a term of the form (16) on general features planetary and satellite orbits, e.g., the perihelion shift, is in progress.

In general, this equation of motion does not respect energy conservation: multiplication of (12) with the velocity yields

$$\frac{d}{dt}\left(\tfrac{1}{2}\dot{\boldsymbol{x}}^2 - U\right) = 2\dot{x}^2\dot{V} + \dot{\boldsymbol{x}}\cdot\boldsymbol{\Upsilon} + \Upsilon^i_j\dot{x}^j\dot{x}^i + \ldots \quad (18)$$

Therefore, the terms on the right hand side might be candidates for effects reducing or enlarging the kinetic energy of moving bodies and, thus, may play a role in the description of the flyby or the Pioneer anomaly.

It should be clear from the independence of the metric from the equation of motion for point particles, that it is necessary both to track position and velocity of the satellite and to have a clock on board in order to determine all components of the space–time metric.

VII. CONCLUSION

From our analysis above we conclude that there are at least four important issues which may be resolved using precise clocks:

- Clocks comparison between Earth bound clocks and stellar systems like pulsars, binary systems etc. This may be of particular importance for the analysis of the Pioneer anomaly and the increase of the AU.
- Exploration of the Pioneer anomaly with clocks (for these clocks with a stability of 10^{-13} in 20 y are needed).
- Exploration of the flyby anomaly with clocks (needs clocks with a stability of 10^{-14} in 1 h).
- Search for position– and time–dependence of fundamental constants (ACES, PARCS, RACE, SPACETIME, OPTIS).

In any case, any improvement of the accuracy and stability of clocks is mandatory for the exploration of new physical regimes. For that, space clocks are best suited.

Acknowledgments

Financial support of the German Aerospace Agency DLR and the German Research Foundation DFG is gratefully acknowledged.

[1] C. Will, *Theory and Experiment in Gravitational Physics (Revised Edition)* (Cambridge University Press, Cambridge, 1993).
[2] C. Will, Living Rev. Relativity (2001, ww.livingreviews.org/lrr-2001-4). G. Amelino-Camelia, C. Lämmerzahl, A. Macias, and H. Müller, in *Gravitation and Cosmology*, ed. A. Macias, C. Lämmerzahl, and D. Nunez (AIP Conference Proceedings 758, Melville, New York, 2005), p. 30. D. Mattingly, Living Reviews **8**, http://www.livingreviews.org/lrr (2005 (cited on April 4, 2006)). C. Lämmerzahl, in *Quantum Gravity*, ed. B. Fauser (Springer, Berlin, 2006), to appear.
[3] C. Lämmerzahl, Ann. Phys. (Leipzig) **15**, 5 (2006).
[4] S. Baeßler *et al*, Phys. Rev. Lett. **83**, 3585 (1999).
[5] T. Niebauer, M. McHugh, and J. Faller, Phys. Rev. Lett. **59**, 609 (1987). K. Kuroda and N. Mio, Phys. Rev. Lett. **62**, 1941 (1989). K. Kuroda and N. Mio,

Phys. Rev. **42**, 3903 (1990).
[6] L. Koester, Z. Physik **198**, 187 (1967). L. Koester, Phys. Rev. **D 14**, 907 (1976). S. Werner and H. Kaiser, in *Quantum Mechanics in Curved Space–Time*, ed. J. Audretsch and V. de Sabbata (Plenum Press, New York, 1990), NATO ASI Series B 230, p. 1.
[7] A. Peters, K. Chung, and S. Chu, Nature **400**, 849 (1999). A. Peters, K. Chung, and S. Chu, Metrologia **38**, 25 (2001).
[8] H. Dittus, C. Lämmerzahl, and H. Selig, Gen. Rel. Grav. **36**, 571 (2004).
[9] F. Witteborn and W. Fairbank, Phys. Rev. Lett. **19**, 1049 (1967).
[10] C.-H. Hsieh *et al*, Mod. Phys. Lett. **4**, 1597 (1989).
[11] J. Walz and T. Haensch, Gen. Rel. Grav. **36**, 561 (2004).
[12] R. Vessot and M. Levine, Gen. Rel. Grav. **10**, 181 (1979). R. Vessot et al., Phys. Rev. Lett. **45**, 2081 (1980).
[13] J. Turneaure and S. Stein, in *Near Zero*, ed. J. Fairbank *et al*, (Freeman, New York, 1988), p. 414.
[14] A. Godone, C. Novero, and P. Tavella, Phys. Rev. **D 51**, 319 (1995).
[15] C. Braxmaier *et al*, Phys. Rev. Lett. **88**, 010401 (2002).
[16] A. Bauch and S. Weyers, Phys. Rev. **D 65**, 081101(R) (2002).
[17] K. Brecher, Phys. Rev. Lett. **39**, 1051 (1977).
[18] B. Brown *et al*, Phys. Rev. **30**, 763 (1973). Z. Guiragossian *et al*, Phys. Rev. Lett. **34**, 335 (1975). J. Alspector *et al*, et al., ibid. **36**, 837 (1976). G. Kalbfleisch *et al*, ibid. **43**, 1361 (1979). L. Stodolsky, Phys. Lett. **B 201**, 353 (1988). M. Longo, Phys. Rev. Lett. **60**, 173 (1988).
[19] A. Kostelecky and M. Mewes, Phys. Rev. **D 66**, 056005 (2002).
[20] P. Antonini *et al*, Phys. Rev. **A 71**, 050101 (2005). P. Stanwix *et al*, Phys. Rev. Lett. **95**, 040404 (2005). S. Herrmann and A. Peters, in *Special Relativity: Will It Survive the Next 100 Years?*, ed. J. Ehlers and C. Lämmerzahl (Springer, Berlin, 2005), to appear.
[21] P. Wolf *et al*, Phys. Rev. **D 70**, 051902 (2004).
[22] S. Saathoff *et al*, Phys. Rev. Lett. **91**, 190403 (2003).
[23] J. Bailey *et al*, et al., Nature **268**, 301 (1977).
[24] M. Haugan, Ann. Phys. **118**, 156 (1979).
[25] J. Prestage *et al*, Phys. Rev. Lett. **54**, 2387 (1985). S. Lamoreaux *et al*, Phys. Rev. Lett. **57**, 3125 (1986). T. Chupp *et al*, Phys. Rev. Lett. **63**, 1541 (1989).
[26] D. Bear *et al*, Phys. Rev. Lett. **85**, 5038 (2000). Phys. Rev. Lett. **89**, 209902(E) (2002).
[27] M. Humphrey *et al*, Phys. Rev. **A 68**, 063807 (2003).
[28] L.-S. Hou *et al*, Phys. Rev. Lett. **90**, 201101 (2003).
[29] B. Heckel, in *CPT and Lorentz Symmetry III*, ed. V. Kostelecky (Word Scientific, Singapore, 2004), p. 133.
[30] R. Walsworth, in *Special Relativity*, ed. J. Ehlers and C. Lämmerzahl (Springer–Verlag, Berlin, 2006), vol. LNP, in press.
[31] C. Kiefer, *Quantum Gravity* (Oxford University Press, Oxford, 2004).
[32] T. Damour, F. Piazza, and G. Veneziano, Phys. Rev. Lett. **89**, 081601 (2002). Phys. Rev. **D 66**, 046007 (2002).
[33] T. Damour, *Gravity, equivalence principle and clocks*, Proceedings of the Workshop on the Scientific Applications of Clocks in Space (JPL, Pasadena, November 7-8, 1996). T. Damour, in *Gravitational Waves and Experimental Gravity*, ed. J. Trân Tanh Vân *et al* (World Publishers, Hanoi, 2000), p. 357.
[34] C. Wetterich, Phys. Lett. **B 561**, 10 (2003). Astropart. Phys. **10**, 2 (2003).
[35] J. Bekenstein, Phys. Rev. **D 25**, 1727 (1992). H. Sandvik, J. Barrow, and J. Magueijo, Phys. Rev. Lett. **88**, 031302 (2002).
[36] T. Sumner, Living Rev. Relativity **5**, http://www.livingreviews.org/lrr (2002).
[37] W. Hu, Astrophys. J. **557**, L79 (2001).
[38] A. Riess, A. Filippenko, and P. Challis et al., Astron. J. **116**, 1009 (1998). S. Perlmutter *et al*, Astroph. J. **517**, 565 (1999).
[39] C. Bennet et al, Astrophys. J. Suppl. Ser. **148**, 1 (2003). N. Spergel et al, Astrophys. J. Suppl. Ser. **148**, 175 (2003).
[40] C. van de Bruck J. Overduin and W. Priester, Naturwiss. **88**, 229 (2001). M. Tegmark et al, Phys. Rev. **D 69**, 103501 (2004).
[41] P. Peebles and B. Ratra, Rev. Mod. Phys. **75**, 559 (2003).
[42] M. Celerier, Astron. Astroph. **353**, 63 (2000). R. Vanderveld, E. Flanagan, and I. Wasserman, *Mimicking dark energy with lemaitre-tolman-bondi models: Weak central singularities and critical points*, astro-ph/0602476. P. Apostolopoulos *et al*, *Cosmological acceleration and gravitational collapse*, astro-ph/0603234.
[43] J. Anderson *et al*, Phys. Rev. Lett. **81**, 2858 (1998).
[44] J. Anderson *et al*, Phys. Rev. **D 65**, 082004 (2002).
[45] C. Lämmerzahl, O. Preuss, and H. Dittus, *Is the physics within the Solar system really understood?*, gr-qc/0604052.
[46] T. Morley, *Private communication*, .
[47] G. Krasinsky and V. Brumberg, Celest. Mech. & Dyn. Astron. **90**, 267 (2004).
[48] E. Standish, in *Transits of Venus: New Views of the Solar System and Galaxy, Proceedings IAU Colloquium No. 196*, ed. D. Kurtz (Cambridge University Press, Cambridge, 2005), p. 163.
[49] C. Lämmerzahl and H. Dittus, *Doppler tracking in the expanding universe* (2005), preprint, ZARM, University of Bremen.
[50] T. Carrera and D. Giulini, *On the influence of the global cosmological expansion on the local dynamics in the solar system*, gr-qc/0602098.
[51] A. de Oliveira-Costa *et al*, Phys. Rev. **D 71**, 043004 (2005).
[52] D. Schwarz *et al*, Phys. Rev. Lett. **93**, 221301 (2004).
[53] I. Ciufolini, Gen. Rel. Grav. **36**, 2257 (2004).
[54] M.-T. Jaekel and S. Reynaud, Mod. Phys. Lett. **A 20**, to appear (2005).
[55] L. Iorio, *What do the orbital motions of the outer planets of the solar system tell us about the Pioneer anomaly?*, gr-qc/0601055.

Proceedings of the 20th EFTF, 2006

The On-Board Galileo Clocks: Rubidium Standard and Passive Hydrogen Maser - Current Status and Performance-

Fabien Droz, Pierre Mosset, Gerald Barmaverain, Pascal Rochat, Qinghua Wang
Temex Neuchatel Time / Switzerland

Marco Belloni, Liano Mattioni *Galileo Avionica / Italy*

Ulrich Schmidt, Timothy Pike *EADS Astrium / Germany*

Francesco Emma, Pierre Waller
European Space Agency (ESTEC) / Netherlands

Galileo program is approved by the European Commission and the European Space Agency (ESA). The activities related to GSTBV2 experimental satellite provide the first results and the implementation of the In Orbit Validation (IOV) phase are in progress. Atomic clocks represent critical equipment for the satellite navigation system and clocks development has been continuously supported by ESA. The Rubidium Atomic Frequency Standard (RAFS) and the Passive Hydrogen Maser (PHM) are at present the baseline clock technologies for the Galileo navigation payload. This article gives a general overview on the RAFS and the PHM developments and evolution up to now. It also provides updated information on the performance measurement results on ground and the preliminary information available related to the In Orbit behavior.

I. INTRODUCTION

GALILEO is a joint initiative of the European Commission and the European Space Agency (ESA) for a state-of-the-art global navigation satellite system, providing a highly accurate, guaranteed global positioning service under civilian control. It will probably be inter-operable with GPS and GLONASS, the two other Global Navigation Satellite Systems (GNSS) available today.

The fully deployed Galileo system consists of 30 satellites (27 operational and 3 active spares), stationed on three circular Medium Earth Orbits (MEO) at an altitude of 23 222 km with an inclination of 56º to the equator.

Atomic clocks represent critical equipment for the satellite navigation system. The Rubidium Atomic Frequency Standard (RAFS) and Passive Hydrogen Maser (PHM) are at present the baseline clock technologies for the Galileo navigation payload. According to the present baseline, every satellite will embark two RAFSs and two PHMs. The adoption of a "dual technology" for the on-board clocks is dictated by the need to insure a sufficient degree of reliability (technology diversity) and to comply with the Galileo lifetime requirement (12 years). Both developments are based on early studies performed at the Observatory of Neuchatel (ON) from end of 1980s and Temex Neuchâtel Time (TNT) since 1995. These studies have been continuously supported by Switzerland within ESA technological programs especially since the set-up of the European GNSS2 program.

The activities related to Galileo System Test Bed (GSTB-V2) experimental satellite as well as the implementation of the In Orbit Validation phase are in progress. Two experimental satellites will be launched by the end of 2005 or beginning of 2006, to secure the Galileo frequency fillings, to test some of the critical technologies, such as the atomic clocks, to make experimentation on Galileo signals and to characterise the MEO environment. There will be one PHM and two RAFS on board the satellite supplied by Galileo Industries and two RAFS on the satellite supplied by Surrey Satellite Technologies Ltd.

This article gives a general overview on the space RAFS and the PHM developments and evolution up to now, lifetime expectation and qualification status.

II. DEVELOPMENT ACTIVITIES OF ON-BOARD CLOCKS

A. Development & Qualification Activities of Rubidium Atomic Frequency Standard

The RAFS development milestones are chronologically listed as below:

1) The first development activity kicked off at TNT in 1997, and completed in 2000 with one Engineering Model (EM) RAFS1 produced [1].

2) The updated RAFS1 development started in June 2000 and completed at the beginning of 2002. The industrial consortium is led by TNT with Astrium Germany as the subcontractor for the electronics package. In this phase, the achieved activities include:

- Improved clock stability with inclusion of thermally regulated base plate. Fig. 1 is the picture of the updated RAFS1.
- Review of electronics package layout and components in view of flight production.
- Manufacturing of 5 Engineering Qualification Models (EQM) for lifetime qualification. Fig. 2 shows 5 EQMs without external cover and 5 vacuum chambers for life test with 'Picotime' measurement systems.
- Manufacturing of 1 Qualification Model (QM).

Besides the vibration and EMC/EMI qualification tests, two radiation tests were carried out at CNES in Toulouse: one test with Galileo orbit simulation, i.e. 4 cycles of 3rad per day during one week, and the other with total dose simulation over the mission duration, i.e. 30 krad continuous radiation @ 400 rad/h during 3 days. No frequency radiation sensitivity was observed during the former test. For the latter test no electronic failure or performance degradation was observed, but it showed the need for wider compensation of the drift of the crystal oscillator. The modification has been implemented on subsequent models. The stability achieved $<2.5*10^{-14}$/day in 'best temperature conditions' under vacuum of the RAFS1 model is shown in Fig. 3.

3) A third development and qualifications step was initiated at the end of 2001 and completed at the beginning of 2003 with the delivery of an EM, which is the baseline unit for the development of the flight models for GSTB-V2. Two main objectives were achieved [2]:

Figure 1. Picture of the updated RAFS1 once closed including the thermally regulated base plate

Figure 2. Five EQMs without external cover and vacuum chambers for life test with 'Picotime' measurement systems

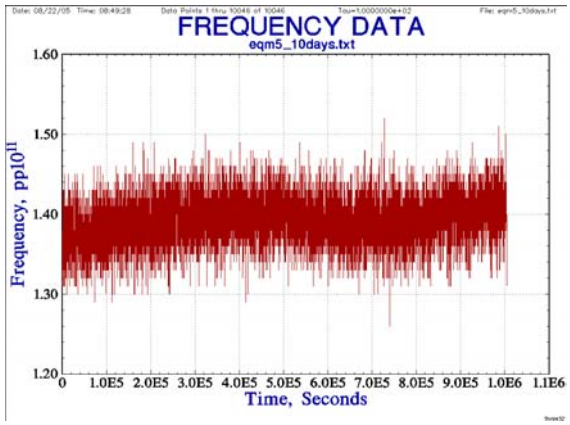

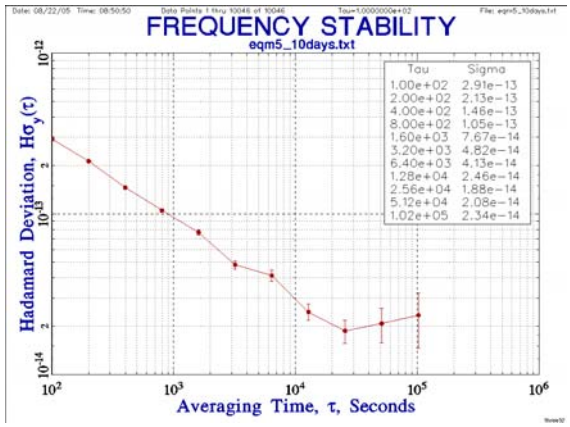

Figure 3. RAFS1 EQM frequency data and frequency stability

- Further optimisation of the physics package to reduce temperature sensitivity resulting better short/mid term stability with a temperature & vacuum environment similar to satellite platform environement (with +- 1°C temperature changes).
- Inclusion of a DC/DC converter and the satellite TT&C interface compatible with ESA's new requirements. Fig. 4 shows the performances achieved in term of frequency & time stabilities. Within this configuration RAFS2 shows capabilities to perform time stability close to 1 ns over 1 day.

Fig. 5 shows the internal construction consisting in RAFS core unit equipped with the thermally regulated baseplate & DC-DC converter.

Figure 4. RAFS2 core model frequency and time stabilities

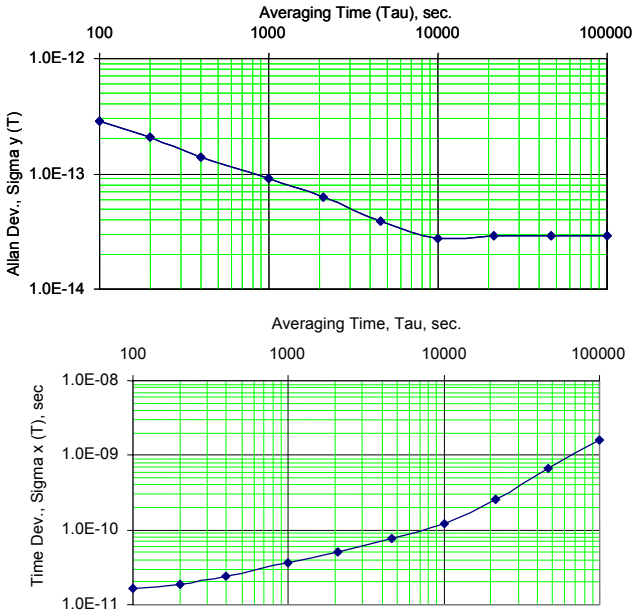

Figure 5. RAFS2 internal construction

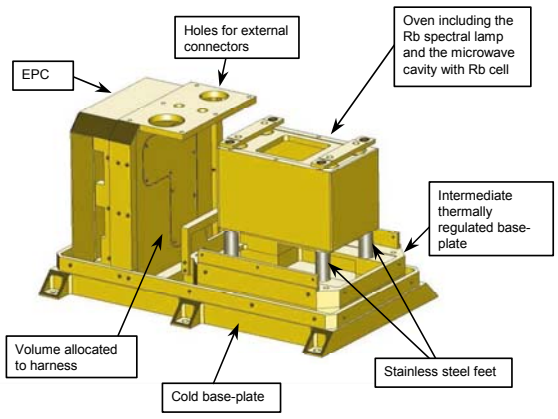

4) In the frame of GSTB-V2, one EQM, one Proto-Flight Model (PFM) and five Flight Model (FM) units have been delivered. The PFM and FM1 are integrated in GIOVE-B and ready for launch. The FM4 and FM5 are integrated in GIOVE-A and in orbit since 28th December 2005. In additon, the FM2 and FM3 are available as FM spare units. Table I lists the achieved RAFS performance for GSTB-V2. Fig. 6 shows the measured frequency stability of GSTB-V2 PFM and FM1 to FM5.

5) Further investigations to improve the flicker floor and temperature sensitivity are under way . Beside the 'zero' temperature coefficient provided by the light shift and gaz pressure shift into the cell , the lamp has also been optimized and demonstrates 'zero' temperature coefficient. Nevertheless, still temperature coefficients of $5*10^{-14}$/°C have been observed. By improving the RF atomic interrogation signal stabilisation circuitry , RAFS has demonstrated stabilities in a range fo $7*10^{-15}$ for half of day (Fig. 7) or more observation time. Power shift coefficient has been measured arround $1*10^{-10}$/dB change in power. Therefore, few ppm / °C of atomic interrogation signal is required to reach stabilities within the 10^{-15} range. A carreful worst case analysis of possibles temperature drifts of parameters associated to the automatic gain control has been performed and demonstates the feasibility and possible repeatability of a RAFS having short term stability over one day lower than $1*10^{-14}$.

TABLE I. RAFS FOR GSTB-V2 PERFORMANCE ACHIEVED

Parameter	Measurement
Frequency stability	< $4*10^{-14}$ @ 10'000 sec
Flicker floor	< $3*10^{-14}$ (drift removed)
Thermal sensitivity	< $5*10^{-14}$ /°C
Magnetic sensitivity	< $1*10^{-13}$ / Gauss
Mass and volume	3.3 kg and 2.4 liter

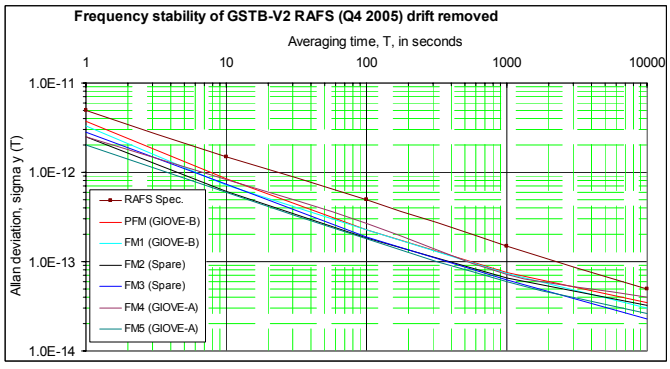

Figure 6. GSTB-V2 RAFS2 frequency stability

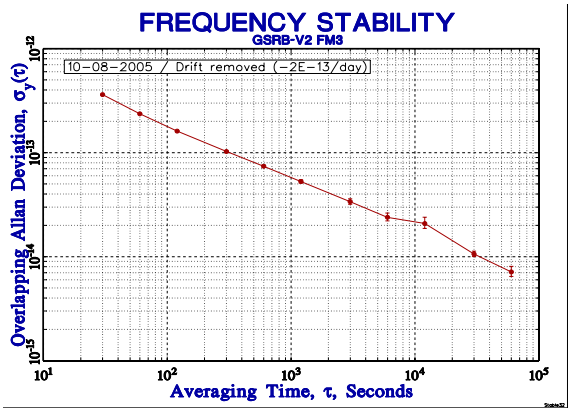

Figure 7. RAFS3 frequency stability

B. *Development & Qualification Activities of Passive Hydrogen Maser*

The space hydrogen maser will be the master clock on the Galileo navigation payload. The first maser development activity tailored to navigation applications was kicked off in 1998. It was initiated by the development of an active maser at ON However, at the Galileo definition phase, it became clear that the accommodation of the active maser on the satellite was too penalizing in term of mass and volume, and the excellent frequency stability performances of the active maser were not required. In 2000 it was re-orientated towards the development of a PHM based on the industrial design and ON heritage on active maser studies.

The development of the EM (Fig. 8) [3] was completed at the beginning of 2003, under the lead of ON with Galileo Avionica (GA) subcontractor for the electronics package and TNT supporting the activity in view of the future PHM industrialisation. The instrument has been under continuous test since June 2003 for assessment of long term performance and early identification of reliability and lifetime problems. This EM model (Fig. 9) shows the frequency and time stability at first stage. By comparison, about 5 years of design optimisation and intensive testing has been necessary to reach such level of performances with the RAFS.

The industrialization activity aimed at PHM design consolidation for future flight production was started in January 2003 [4]. The industrial consortium is led by GA designing the electronics package with TNT responsible for the manufacturing of the physical package and the ON supporting the transfer of technology. The overall structure of the instrument was reviewed to increase compactness and to ease the Assembly, Integration and Test (AIT) processes on the satellite by the inclusion of an external vacuum envelope. Main efforts in the industrialization frame focused on the definition of repeatable and reliable manufacturing processes and fixtures, particularly for the physical package:

Figure 8. Picture of PHM EM. ON&GA

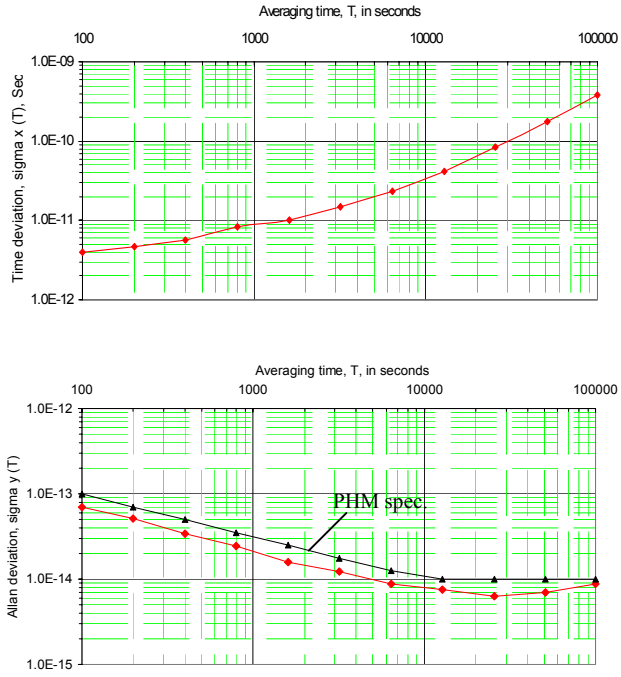

Figure 9. PHM EM frequency and time stabilities

- Teflonization of the quartz storage Bulb
- Hydrogen beam assembly
- Getters assembly
- Tuning of the microwave cavity
- H2 purifier assembly
- Magnetic shield assembly
- State selector assembly
- Hydrogen supply and dissociator

Fig. 10 shows the atomic response of the PHM physics package, measured with 15Hz span exhibiting atomic signal gain of 3.8dB and atomic line width of 2 Hz.

The new design of the physics package has been also focussed on parts count reduction. Less than one half individual parts has been used in the new design compared to the EM model.

For the electronics package and the whole instrument:

- Reduction of PHM volume and footprint
- Improvement of TM/TC interface
- Ground operability at ambient pressure
- Redesign of hydrogen dissociator
- Improvement of thermal and pressure controls
- Redesign of PHM and Purifier supply

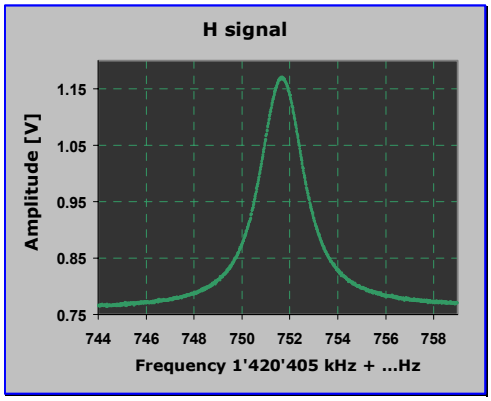

Figure 10. PHM atomic signal measured in FM1

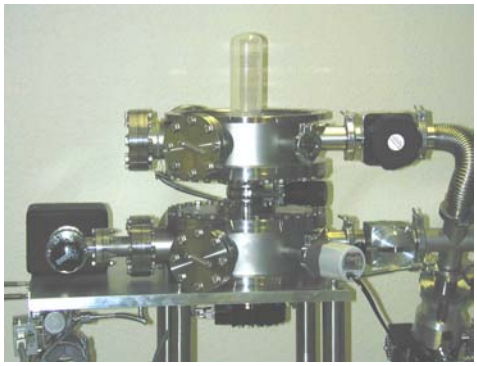

Figure 11. Technological models with/without cover

Two technological models (Fig. 11), a Structural Model and an EQM were built for these objectives and to qualify the new upgraded design. In addition, four EQMs for life demonstration are being manufactured and will be submitted to prolonged testing. In the frame of GSTB-V2, which is presently being tested at P/L level (GIOVE-B), one PFM (Fig. 12) has completed the proto-qualification testing and has been delivered. One spare FM has been delivered by Q1 2006. Table II shows the achieved performance of PHM/PFM for GSTBV2. Significant improvement has been achieved by a better silver coating process and surface polishing of the magnetron cavity (Fig 13). Fig. 14 is showing the performances improvements of the physics package of FM1 model before its integration, obtained by the quality factor improvement.

Figure 12. Picture of PHM PFM

TABLE II. PHM FOR GSTB-V2 PERFORMANCE ACHIEVED

Parameter	Measurement
Frequency stability	$< 1*10^{-14}$ @ 10'000 sec
Flicker floor	$< 7*10^{-15}$
Thermal sensitivity	$< 3*10^{-14}$ /°C
Magnetic sensitivity	$< 4*10^{-14}$ / Gauss
Mass and volume	18 kg and 28 liter

Figure 13. PHM magnetron cavity

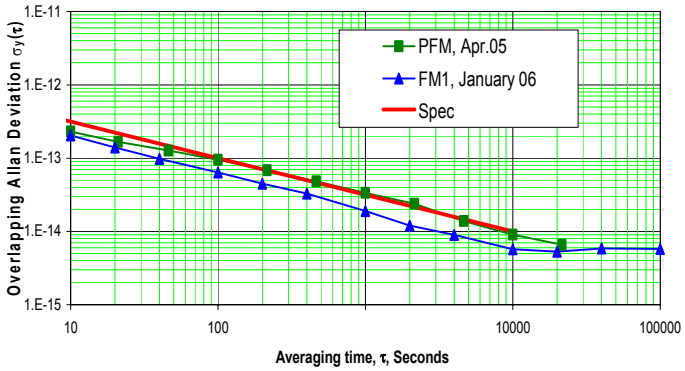

Figure 14. PHM performance improvement

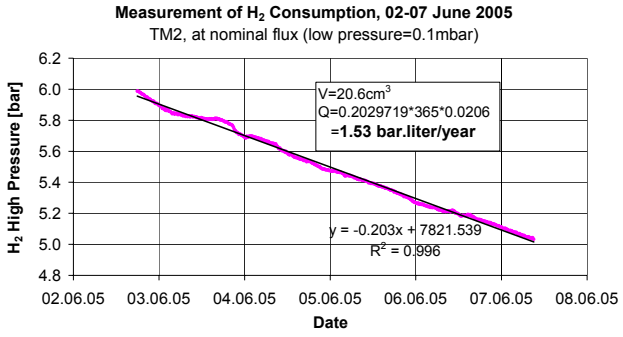

Figure 15. H2 consumption test

PHM Lifetime

The PHM is being sized to guarantee 12 years of orbit life plus 1 year of ground storage, as well as the complete AIT program. The operational life is mainly limited by capacities of the hydrogen container (for H_2 supply), bulk getters (for H_2 sorption), ion pump (for pumping ungetterable background gases) and the total dose of ionising radiation. The lifetime is assessed by analysis and tests of subassemblies.

Fig. 15 shows the H_2 consumption test made in June 2005, which indicates the consumption of 1.53 bar*l/year at nominal flux, by measuring the pressure decay in the known volume of the high pressure pipeline. Taking account of the margin from the real consumption and the retrievable H_2 amount in the fixed pressure of the metal hydride, the H_2 container with the capacity of 30 bar*l is sufficient for the operational life time.

A novel custom built getter pump is developed for the PHM. The getter material provides high sorption capability and mechanical stability. The H_2 sorption test on the getter cartridge was performed in Sep 2003. Fig. 16 shows several cycles of the H_2 filling and pumping during the test. It has demonstrated that the getter pump is capable of sorbing the required amount of H_2 of 20 bar*l without embrittlement and the base pressure after the sorption was in the low 10^{-7} mbar range with only the getter cartridge pumping.

For the ion pump, the operating life at $5*10^{-6}$mbar is specified 8000 hours, corresponding to 400'000 hours (45 years) at the nominal high vacuum of 10^{-7} mbar. Moreover, accelerated lifetime tests of the pump in a gas composition as close to the PHM situation as possible will be performed to assure the pump life.

The total dose of ionising radiation over the mission lifetime on board of the Galileo Spacecraft was analysed on the PHM physics package and electronics package, respectively by the approach of 'sector'. The radiation test will be performed.

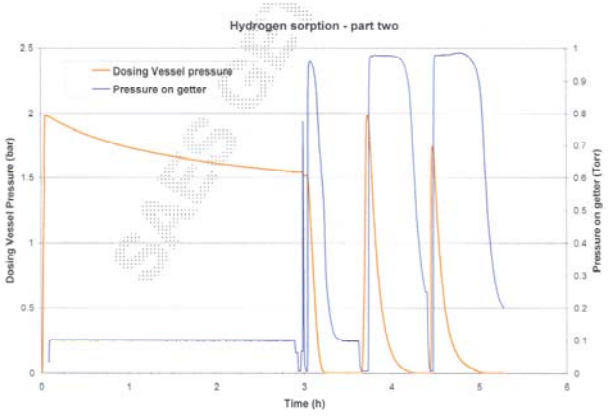

Figure 16. H_2 sorption test

In order to gain more field data on the reliability and lifetime of PP subassemblies four EQMs will be produced dedicated to the lifetime. The objective of the lifetime test is to monitor, during the scheduled two years, the critical parameters drift or degradation in order to predict the lifetime of the instrument and identify possible correction areas.

III. CONCLUSIONS

Table III summarizes the Galileo clocks status up to now. Both clocks are subjected to electrical (functional, thermal vacuum, EMC, etc.), as well as, mechanical tests (shock and vibrations). Eight flight models were produced for GSTB-V2, which provide the first flight opportunity for Galileo clocks qualification. GIOVE-A with two RAFS on-board is in orbit since 28th December 2005. Both RAFS are fully operational with expected very good frequency stability. With more than 10 years of efforts, two clock technologies for Galileo are qualified. Those clocks use reliable and mature technologies leaving room from further improvements in term of mass & performances.

TABLE III. GALILEO CLOCKS STATUS

Steps	RAFS	PHM
BB	Completed in 1995	BB activity and EM design started in 2000
EM	Completed in 2000	Completed in Q1/2003 (under life test since June 2003)
EQM	5 models built and under lifetime tests since 2002	4 models available in 2006 for lifetime tests
QM	1 model (RAFS1) fully qualified Rad. test Q1/2003	1 model
EQM for GSTB-V2	1 model delivered in August 2004	1 model completed in February 2005
FM for GSTB-V2	6 models delivered, 2 for GIOVE-A, 2 for GIOVE-B.	2 models delivered, 1 for GIOVE-B 1 Spare FM.

REFERENCES

[1] A. Jeanmaire, P. Rochat, F. Emma, "Rubidium atomic clock for Galileo," 31st Precise Time and Time Interval (PTTI) Meeting, 07-09 December, 1999, California (USA), pp. 627-636.

[2] F. Droz, P. Rochat, G. Barmaverain, M. Brunet, J. Delporte, J. Dutrey, F. Emma, T. Pike, and U. Schmidt, "On-Board Galileo RAFS, current status and Performances," 2003 IEEE International Frequency Control Symposium Jointly with the 17th European Frequency and Time Forum, 05-08 May, 2003, Tampa (USA), pp. 105-108.

[3] P. Berthoud, I. Pavlenko, Q. Wang, and H. Schweda, "The engineering model of the space passive hydrogen maser for the European global navigation satellite system GalileoSat," 2003 IEEE International Frequency Control Symposium Jointly with the 17th European Frequency and Time Forum, 05-08 May, 2003, Tampa (USA), pp. 90-94.

[4] L. Mattioni, M. Belloni, P. Berthoud, I. Pavlenko, H. Schweda, Q. Wang, P. Rochat, F. Droz, P. Mosset, and H. Ruedin, "The development of a passive hydrogen maser clock for Galileo navigation system," 34th Precise Time and Time Interval (PTTI) Meeting, 03-05 December, 2002, Reston (USA), pp. 161-170.

Proceedings of the 20th EFTF, 2006

Development of a single-frequency optically-pumped cesium beam resonator for space applications

S. Lecomte*, M. Haldimann, R. Ruffieux, P. Thomann, and P. Berthoud
Observatoire de Neuchâtel
Rue de l'Observatoire 58
CH-2000 Neuchâtel, Switzerland
**Electronic address:* steve.lecomte@ne.ch

Observatoire de Neuchâtel (ON) is developing a compact optically-pumped cesium beam frequency standard in the frame of an ESA-ARTES 5 project. The simplest optical scheme, which is based on a single optical frequency for both preparation and detection processes of atoms, has been chosen to fulfill reliability constraints of space applications. With our laboratory demonstrator, we have measured a frequency stability of $\sigma_y=2.74\text{x}10^{-12}\ \tau^{-1/2}$, which is compliant with the Galileo requirement. Present performance limitations are discussed and further improvements are proposed in order to reach our ultimate frequency stability goal of $\sigma_y=1\text{x}10^{-12}\ \tau^{-1/2}$.

I INTRODUCTION

Several space applications like navigation systems, telecommunications, long-term missions, and scientific missions require atomic clocks. The system capability is mainly defined by the atomic clock performance. Although atomic clock technology is well mastered for ground systems, they have to be adapted to the space environment in order to exhibit similar performances with rugged packaging and high system reliability as well as with strong reductions of mass, volume and power consumption.

The two atomic clocks foreseen to take place onboard the first generation of Galileo satellites are respectively the Passive Hydrogen Maser (PHM) and the Rubidium Atomic Frequency Standard (RAFS). While the RAFS is a very compact clock (2.4 litres, 3.4 kg), the PHM is bigger (26 litres, 18 kg) [1], but exhibits a 5-fold improvement of the long-term frequency stability σ_y ($< 10^{-14}$ for $\tau > 10^4$ s). These two frequency standards being operated in vapour cell conditions, the influence of the environment is dramatic (frequency temperature coefficient). To overcome the long-term frequency instability of these standards, the atomic-beam frequency standard is an elegant alternative presently in wide use for GPS and GLONASS. Compared to a magnetically-deflected atomic-beam device, a laser-pumped device has a better short-term stability, owing to the fact that it makes use of the full atomic velocity distribution and of the 2-fold increase of the useful atoms due to optical pumping, and can compete with the PHM in terms of frequency stability. Moreover, due to its inherently simple design, its manufacturing and its reliability can be strongly improved with respect to the PHM.

Observatoire de Neuchâtel (ON) is presently developing such an Optically-pumped Space Cesium Atomic Resonator (OSCAR) in the frame of an ESA-ARTES 5 project. Our goal is to demonstrate a frequency stability of $\sigma_y \leq 1\text{x}10^{-12}\ \tau^{-1/2}$ with a compact atomic resonator and only one optical frequency. This choice is motivated by space application prerequisites and has already been discussed [2]. The best measured frequency stability with a 1-frequency scheme is $\sigma_y=4\text{x}10^{-12}\ \tau^{-1/2}$ with a compact laboratory atomic resonator and a single laser diode (852 nm, 25-MHz linewidth) [3]. By also using a compact atomic resonator, but a more complex optical setup (2-frequency scheme: one laboratory extended-cavity diode laser and one acousto-optic modulator), the frequency stability was improved to $\sigma_y=1.4\text{x}10^{-12}\ \tau^{-1/2}$ using either a Cs beam [4,5] or a Rb beam [6].

In these proceedings, we report on developments of our compact atomic resonator. First we describe the experimental setup (§II), then we present the experimental results and discuss the current limitations to the frequency stability performances (§III). Finally we present solutions to improve the atomic resonator frequency stability in the conclusion (§IV).

II EXPERIMETAL SETUP

The architecture of the frequency standard is shown in Fig. 1: the Physics Package (PP) is composed of the Atomic Resonator (AR), while the Opto-Electronics Package (OEP) contains the Optics and Laser modules (OL), the Optics and Laser Control module (OLC) and the Atomic Resonator Control module (ARC).

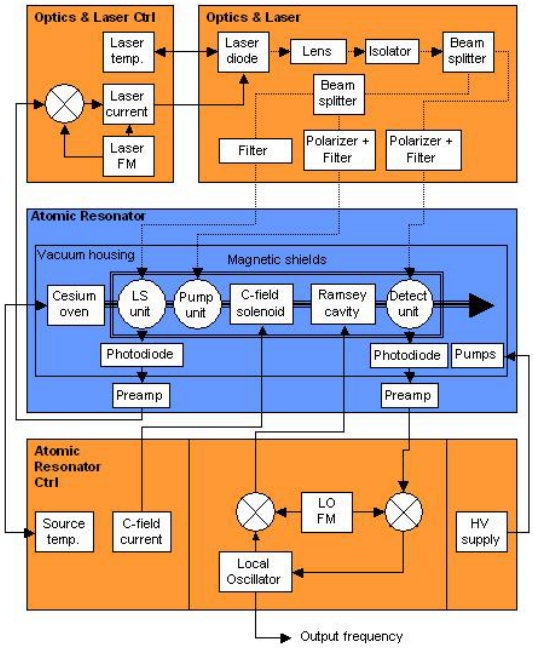

Fig. 1 : Block diagram of the Optically-pumped Space Cesium Atomic Resonator (OSCAR). The blue module in the middle is the Physics Package and the orange side modules are parts of the Opto-Electronics Package.

The AR is fairly standard for an optically-pumped atomic beam resonator. This atomic beam is produced by an oven containing 2g of Cesium, fitted with a multi-channel collimator. It crosses a first laser beam in the Laser Stabilization Unit (LSU), which takes advantage of the fluorescence signal to stabilize the laser frequency. Then, the atomic beam propagates through a second zone to achieve the required ground state population inversion (Pumping Unit, PU). Subsequently, the atomic beam crosses a short Ramsey cavity (12 cm), where the microwave resonance takes place. Finally, the atomic beam crosses the third laser beam (generated by the same laser) in the Detection Unit (DU), in which the final atomic state is optically probed. In both the LSU and in the DU, the atomic beam fluorescence light is first collected by a specially-machined optical module, then converted into photo-currents by a Si photodiode (100 mm^2) placed under vacuum, and finally converted into a photo-voltage by a low noise pre-amplifier outside of the vacuum enclosure. The three optical units and the microwave cavity are surrounded by a solenoid coil which produces a uniform magnetic C-field (52 mG). The AR is maintained under ultra high vacuum by Cesium getters (graphite) and by a commercial ion pump.

The OL has been assembled to operate the atomic resonator with the 1-frequency scheme. Note however that it could be easily adapted for the 2-frequency scheme, by simply adding an acousto-optic modulator to frequency shift the laser detection beam.

The optical beam propagates in free space. The single 852-nm laser source is a Distributed Feed-Back diode (DFB), with an output power > 15 mW and a spectral linewidth < 2 MHz. The diverging laser beam is first collimated, then isolated (40 dB), and finally split into three beams. Neutral density filters and polarisers properly prepare their respective power and polarisation before entering the AR by windows.

The ARC is composed of the necessary power supplies and driving electronics for the Cs oven temperature regulation, for the C-field solenoid current provision and for the ion pump high voltage supply. The microwave frequency chain (local oscillator, frequency multiplier and phase modulator) is a commercial device. The frequency locking of the quartz oscillator and of the laser diode are performed digitally in a single Digital Signal Processor (DSP). In addition, the C-field amplitude and the RF interrogation power servo-loops are implemented sequentially with the quartz frequency servo loop. Their different relevant parameters such as modulation amplitudes, gains, duty cycle and filter topologies can be adapted very conveniently with a digital electronics. Moreover it offers additional capabilities such as automatic atomic line searching, which however has not yet been implemented.

The OLC uses the Cesium beam inside the AR as the frequency discriminator (LSU photo-detector). The laser frequency is modulated by its injection current at 10 kHz and locked on the pumping transition line Cs D2:44' by synchronous detection. This hyperfine transition has been chosen for its highest population inversion ratio (15.5%), and for its high fluorescence yield (2.4 ph/at) [7]. Because of the residual cesium vapor in the LSU, the frequency of the fluorescence peak, which is on the side of a broad Doppler background, has a frequency offset with respect to the same hyperfine transition peak in DU (no residual Cs vapor, so no Doppler background). This offset is electronically corrected in order to minimize the clock signal noise.

III EXPERIMENTAL RESULTS

Before investigating optically the atomic beam, we have calibrated its overall flux with an ionization detector located downstream of the atomic resonator. Its detection solid angle is 6.6×10^{-5} sr (open surface of 5 mm^2 at a distance of 275 mm from the oven). The flux has been measured for oven temperatures from 90 °C to 130 °C by steps of 10 K. The measured ion current (proportional to the atomic flux) has been compared to the calculated Cs vapor density (Fig. 2). Both increase monotonously with the oven temperature up to about 100 °C. For higher temperature, the atomic flux starts to saturate with respect to the Cs vapor density, which indicates the transition from molecular flow to viscous flow in the collimator). The useful atomic flux for the

atomic resonator (atoms in the $m_F = 0$ hyperfine state) is 4.2×10^9 at/s at the oven temperature of 130°C.

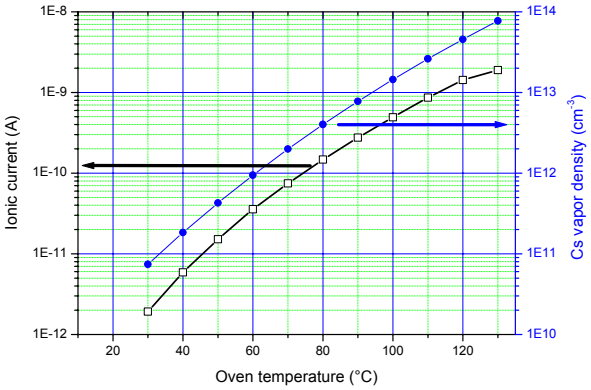

Fig. 2: Measured Cs beam ionic current and calculated Cs vapor density vs. oven temperature.

The two fluorescence light collection optics with 100-mm^2 silicon photodiodes collect about 24% of the fluorescence photons. Ideally the collection efficiency should be 42%. This is justified by the fact that the quantum selection rules of the Cs D2:44' transition emits 2.4 photons on average until the atom has changed its quantum state and becomes optically transparent to the laser light. This implies that there is optimum collection efficiency at $2.4^{-1} = 42\%$: lower detection efficiency will reduce the available Ramsey signal whereas higher detection efficiency will introduce additional partition noise. This collection efficiency is presently limited by the optical surface quality, and by the low reflectivity of aluminum at 852 nm.

The laser beams in the PU and the DU are depolarized by using a birefringent optical element [8]. A polarization gradient along the atomic beam increases the efficiency of the optical pumping in the PU without requiring a strong static magnetic field [9], or a 1D optical molasses [10].

The optical power in both the PU and DU was optimized for maximum SNR in order to increase the frequency stability of the standard. In the PU, the atoms are pumped with 1 mW of optical power whereas we apply 150 µW in the DU. In the LSU, the SNR for laser stabilization is maximum with 35 µW of optical power.

In Fig. 3, the central Ramsey fringe recorded at an oven temperature of 130°C is plotted. A weak and uniform C-field of 52 mG in applied over all optical units (LSU, PU, and DU) and over the microwave Ramsey cavity (Fig. 1). The RF power is adjusted for maximizing the clock signal. The AR has the following performances: the atomic linewidth is 940 Hz, yielding an atomic quality factor of 10^7, the Ramsey central fringe peak-to-valley photo-current is 727 pA, the background photo-current is 1.1 nA, and the noise current density at resonance is of 49 fA/Hz$^{1/2}$ yielding a clock SNR of 14'800 Hz$^{1/2}$.

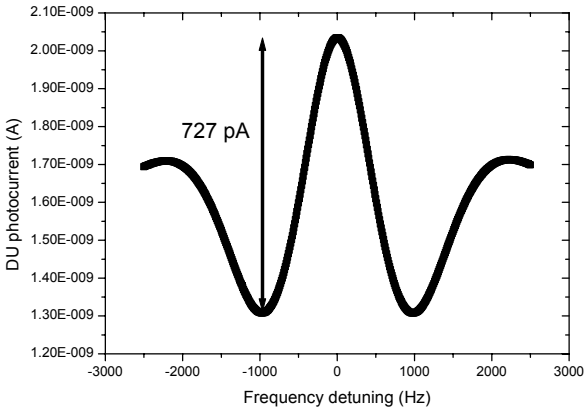

Fig. 3: Ramsey central fringe recorded with an oven temperature of 130°C.

By operating the atomic resonator with these optimal parameters, and frequency locking the quartz local oscillator with the digital electronics, we have measured its frequency stability with respect to an active hydrogen maser (Fig. 4). The Allan deviation extrapolated down to 1s gives at short term frequency stability of $\sigma_y = 2.74 \times 10^{-12}\ \tau^{-1/2}$. To the best of our knowledge, this frequency stability of is the best ever measured with a compact optically-pumped atomic beam frequency standard operated with a single optical frequency scheme (single laser diode, but no acousto-optic modulator). For short integration time constants (up to 10s), the improved short-term frequency stability with respect to the atomic resonator performance extrapolation, is due to a better quartz frequency stability but a short time constant of the quartz frequency lock loop. For long integration time constants (from 2000s), environmental magnetic and thermal perturbation degrade the clock frequency stability. For this laboratory demonstration, we remind that only a single magnetic shield is assembled. Moreover, neither C-field nor RF power servo loops are operating.

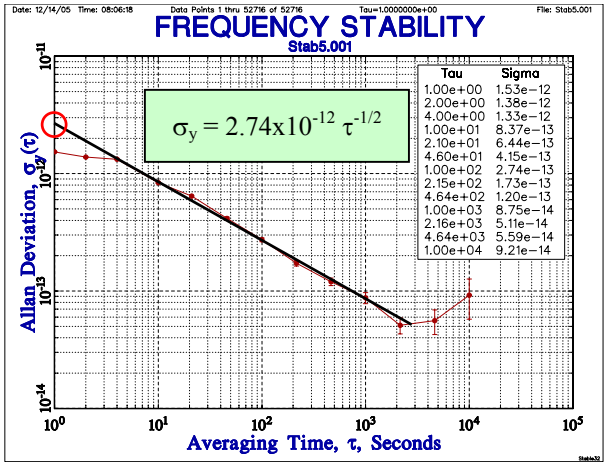

Fig. 4: Measured frequency stability of OSCAR operated with a single wavelength (852nm).

Although the stability of the clock is better than the requirement for the Galileo satellite navigation system ($\sigma_y \leq 3x10^{-12}\ \tau^{-1/2}$), the ultimate frequency stability goal of $\sigma_y \leq 1x10^{-12}\ \tau^{-1/2}$ has not been yet reached. In fact, the clock noise is not atomic shot-noise limited. In the following we will analyze the various noise contributions to the total clock noise and discuss the improvements to be performed in order to increase the clock SNR and reach the atomic shot-noise limit.

In Fig. 5, we plot the different noise current densities as a function of the Ramsey peak-valley photocurrent. The corresponding oven temperatures are given for information.

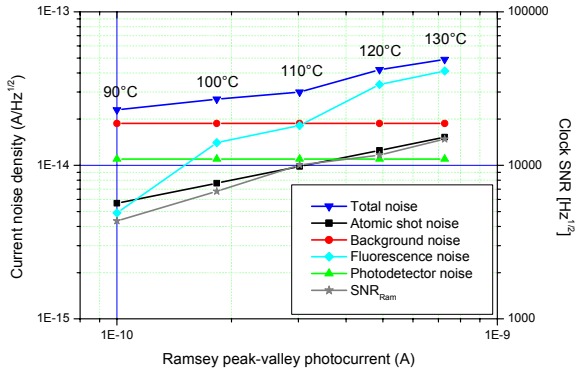

Fig. 5: Noise budget and overall SNR of OSCAR.

We have identified four noise contributions in the clock signal noise budget:

1. *Photodetector noise*: it is measured in the dark and is independent of the Ramsey photocurrent; for nominal operating atomic flux, this contribution is negligible in the overall noise budget.
2. *Stray light noise*: it is measured with the nominal optical power but off-resonance, is proportional to the square root of the DC stray light level (shot noise), but is independent of the Ramsey photocurrent; this technical noise contribution is mainly due to strong light scattering by the optical windows mounted on the vacuum enclosure.
3. *Atomic shot-noise*: it is calculated as the square root of the atomic signal; presently this noise contribution is largely dominating the technical noise.
4. *Fluorescence noise*: it is computed from the total noise minus the other contributions in RMS values. This noise contribution appears to be proportional to the Ramsey signal and is related to the residual frequency noise of the laser converted into amplitude the atomic beam frequency discriminator.

At high atomic flux where the atomic resonator will finally operate, the major noise contribution is the fluorescence noise (Fig. 5). In order to reduce it, the residual frequency noise of the laser has to be minimized in closed loop operation. Presently, our laser stabilization electronics has a very narrow servo-loop bandwidth (<100 Hz), limited by the ADC/DAC stage of our digital electronics. By increasing it by a factor 100, the amount of proportional noise should be reduced to an acceptable value.

The second major noise contribution arises from the stray light level and its associated shot-noise. While the light traps placed under vacuum are sufficiently absorbent, the large amount of stray light is induced by the laser scattering on the optical windows of the vacuum enclosure. New windows of better optical quality with efficient anti-reflection (AR) coating will be mounted and should strongly reduce the amount of stray light. By effectively reducing these two major noise contributions, the total noise of the clock should be close to the atomic shot-noise contribution.

IV CONCLUSIONS AND OUTLOOK

We have reported in these proceedings on the experimental setup of an optically-pumped cesium beam frequency standard. Its concept relies on the simplest optical scheme, in which we use only one optical frequency (one laser, no AOM). By depolarizing the laser beams for the optical pumping processes (preparation and detection), we can use a single, uniform and weak magnetic C-field for the optical units without trapping atoms in dark states. A fully digital electronics based on a DSP processor has been specially developed for frequency locking both the laser and the quartz local oscillator. This digital electronics also allows to sequentially lock the magnetic C-field and the RF injection power in the Ramsey cavity.

We have demonstrated what is, to the best of our knowledge, the best ever-measured frequency stability of $\sigma_y = 2.74x10^{-12}\ \tau^{-1/2}$ with a compact optically-pumped atomic beam frequency standard operated with a single optical frequency scheme. Although the demonstrated frequency stability is sufficient for Galileo, the clock SNR is not yet limited by the atomic shot-noise. The noise budget has identified the two major noise sources: the "fluorescence noise" and the "stray light noise". While the former could be reduced by increasing the laser frequency servo loop bandwidth, the later will call for top quality optical windows. The marginal fluorescence light collection efficiency will be increased by implementing new and optimize optical collectors. Finally, the presence of a significant Cs vapor pressure close to the oven will be addressed by using more efficient Cs getters. All these improvements are under way in order to reach on OSCAR our ultimate frequency stability goal of $\sigma_y \leq 1x10^{-12}\ \tau^{-1/2}$.

V ACKNOWLEDGEMENTS

The ON team would like to thank ESA for supporting the development of this "Ultra Stable Atomic Beam Clock for Telecom Space Applications and Long-Term Space Missions" (ESA contract 18040/04/NL/DS).

VI REFERENCES

[1] F. Droz et al., *The On-board Galileo Clocks: Rubidium Standard and Passive Hydrogen Maser -Current Status and Performance-*, 20th European Time and Frequency Forum, 2006, Braunschweig, Germany, in these proceedings.

[2] P. Berthoud et al., *A feasibility study of an optically-pumped cesium beam resonator for space applications*, 19th European Time and Frequency Forum, 2005, Besançon, France.

[3] P. Petit et al., *Performance of a 2 dm^3 optically pumped cesium beam tube: a progress report*, 8th European Time and Frequency Forum (EFTF), 1994, Munich, Germany.

[4] R. Lutwak et al., *Optically-pumped cesium beam frequency standard for GPS-III*, 33rd Annual Precise Time and Time Interval (PTTI) Meeting, 2001, Long Beach, CA, USA.

[5] S. Guérandel et al., *Compact cesium beam frequency standard: improvements of the frequency stability towards the 10-12 t-1/2 level*, 16th European Time and Frequency Forum, 2002, St-Petersburg, Russia.

[6] A. Besedina et al., *Preliminary results of investigation of the high-stable Rudidium atomic beam frequency standard with laser pumping/detection for space,* 20th European Time and Frequency Forum, 2006, Braunschweig, Germany, in these proceedings.

[7] N. Dimarcq et al., *Comparison of pumping a cesium beam tube with D_1 and D_2 lines,* J. Appl. Phys., **69** (3), p. 1158-1162 (1991).

[8] P. Berthoud and P. Thomann, patent pending.

[9] V. Giordano et al., *New design for a high performance optically pumped cesium beam tube*, IEEE Transactions on Ultrasonics, Ferroelectrics, and Frequency Control, **38** (4), p. 350-357 (1991).

[10] J. H. Shirley and R. E. Drullinger, *Zeeman coherences and dark states in optically pumped cesium frequency standards*, IEEE Prec. Electromagn. Meas., 1994, Boulder, CO, USA.

Proceedings of the 20th EFTF, 2006

INDUSTRIAL DEVELOPMENT OF AN OPTICALLY PUMPED Cs BEAM FREQUENCY STANDARD FOR HIGH PERFORMANCE APPLICATIONS

Virgile HERMANN*, Benoit LEGER, Céline VIAN, Jean-François JARNO and Maryse GAZARD
Thales Electron Devices - 2, rue Latécoère F-78141 Vélizy - FRANCE
*virgile.hermann@thales-electrondevices.com

Since 2003, Thales Electron Devices (Thales ED) develops frequency standards activities with the objective to set-up an industrial and reliable European source of Cs beam tubes and Cs clocks for space, metrology, military and telecom applications.

In the framework of these activities Thales ED realizes an industrial prototype based on the technology developed by Tekelec and transferred to Thales ED end of 2003. Thales ED's objective is to demonstrate the frequency performances required for ground applications with technical solutions compatible of the industrial means. The main critical item in a industrial Cs frequency standard is the atomic resonator. Several compact laboratory breadboards demonstrated frequency unstability down to $1.4 \times 10^{-12}\ \tau^{-1/2}$ with the two laser frequencies optical configuration, and $4 \times 10^{-12}\ \tau^{-1/2}$ with the single laser frequency setup. [1]

The atomic resonator developed by Thales ED gives a quality factor in magnitude of 14×10^{6} and a measured signal to noise ratio in a 1Hz bandwidth higher than 12000 leading to a theoretical stability lower than $4 \times 10^{-12}\ \tau^{-1/2}$. This demonstrator, realized with industrial processes, includes a 2 liter vacuum chamber and uses the single frequency laser optical configuration. Contrary to other industrial developments [2][3], we chose this simplest optical architecture in view of space developments. An optimization study allowed us to identify significant potential improvements on sub-systems of the Cs tube. This lead us to be confident in the achievement of the frequency stability required for satellites navigation systems such as Galileo ($3 \times 10^{-12}\ \tau^{-1/2}$) with a sufficient margin to guarantee the industrialization of the clock.

I. INTRODUCTION

More and more application domains require new atomic clocks allowing to reach greater frequency specifications. However, although the European scientific activity in the time-frequency domain is very productive, the European industrial production of atomic clocks remains limited compared to the American production.

It is in this framework that a few years ago Thales Electron Devices identified Cs beam atomic clocks as a diversification activity because of several synergies with its core activity. First of all, technological synergies: Between electron tubes and atomic clock resonator, the ultra-high vacuum techniques or the hyperfrequency domain are two important common competencies. It is also about market synergies: as electron tube amplifiers, atomic clocks are highly technological and strategic products, made in small series.
Our short term objective is to use all our expertise from microwave tubes and devices to develop and manufacture Cs atomic resonators and Cs atomic clocks with the purpose to set up a reliable European industrial source of Cs frequency standards.

The initial contribution of Thales ED in the time-frequency domain was on PHARAO with the realization of the microwave interrogation cavity. This cavity, with very high microwave specifications, was the occasion for Thales to develop new processes of brazing. The flight model of the PHARAO's cavity was tested last year at SYRTE (Observatoire de Paris) on the Cs fountain FO1. The results were impressive especially the cavity phase shift which was measured under the specification of 100 µrad with an important margin.

In fact, the time-frequency activity began at Thales ED with a license agreement signed with TEKELEC for the transfer of their past activities on optically pumped Cs clocks. The optical pumping technology was chosen by Thales for those new developments mainly for the short and middle term stability potential. The laser optical pumping represents an innovative solution to improve

the clock performances, today limited with the existing technology based on the magnetic deflexion. The optical pumping technology is compatible with the frequency stability and the life time specifications required for satellite navigation.

Several studies on optical pumping have been realized by SYRTE since the beginning of the 80s. Thales ED benefits from this know-how with the transfer to Thales facilities of the lab atomic clock prototype Cs4. This demonstrator was developed in the beginning of the 90s and was used until 2002. Cs4 has been the experimental device of many SYRTE publications on compact optically pumped Cs beam clocks.

Building on those different competency acquisitions, we began this industrial development activity on Cs atomic frequency standards.

II. DESCRIPTION OF THE THALES BREADBORD DEVELOPMENT

Following the acquisition of the Tekelec know-how, our main objective was to validate the industrial files by using our industrial processes. But, the performance demonstration has not been done already, so we decided first to build a new atomic resonator breadboard to insure the frequency stability demonstration.

Our development project is called Thales Optically Pumped Cs (TOP-Cs) and it is constructed in 4 phases. The first one involves the critical analysis of the Tekelec industrial files.
The second phase is the development of a new atomic resonator followed by its validation using a lab optical bench and a lab electronic.
Once the tube breadboard has been evaluated, the third phase is the validation of the other industrial sub-systems of the clock like the industrial optical bench and the industrial electronic setup.
Currently, we are concluding the second phase with the final evaluations of the tube breadboard and in parallel we are beginning the third phase.
After those three first development phases, we will perform the industrialization of the clock.

During the first phase of the project, to insure the stability performance demonstration, we decided to develop a dismountable vacuum chamber to make iterations possible. But of course we took into account all the industrial constraints to be as close as possible of the future industrial prototype.
As it's shown on Figure 1, the TOP-Cs tube breadboard has the same vacuum volume, and the same optical and electrical interfaces as the mechanical prototype.

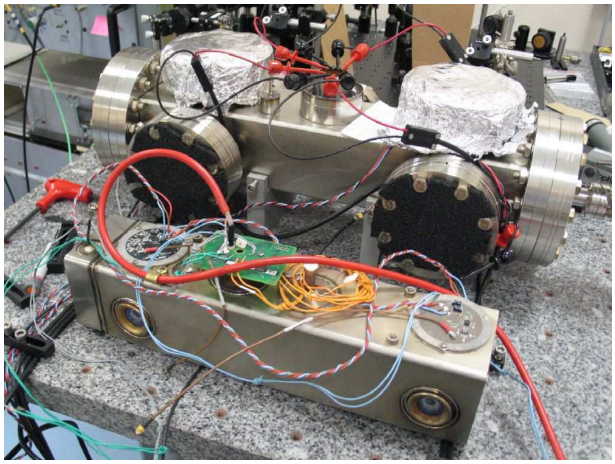

Figure 1. The TOP-Cs tube breadbord (background) vs the industrial mechanical prototype (foreground).

It is also important to mention that we built the TOP-Cs breadboard with industrial processes. For example, this tube is adapted for high temperature baking over 300°C.

The scientific choices for the heart of the clock resonator come from SYRTE technology. The configurations of the main sub-systems are the following:
- The microwave cavity is a "dark fringe" configuration of 17.5 cm length where the tube signal is minimal at resonance. The corresponding expected bandwidth is in the order of 650 Hz leading to a quality factor of 14×10^6.
- The magnetic field configuration is developed with three magnetic regions to minimize dark state effects [4]. Two magnetic shields are inside the vacuum chamber.
- Both optical regions (pumping and detection) use an external photodiode. The frequency locking of the laser diode is made on the fluorescent signal of the pumping region.
- The Cs oven has a common structure with multi-channel collimator.
- The optical configuration is on the single-frequency setup. Contrary to other industrial developments [2][3], we chose this optical architecture for its simplicity with respect to its potential performances.

III. FIRST RESULTS

The first step of the breadboard validation was to measure the optimal signal to noise ratio (SNR). For those measurements, the breadboard has been tested with a lab electronic and a lab optical bench on the single frequency configuration using a DBR laser diode at 852 nm. All results have been obtained with the D2:3-3' atomic transition in pumping and detection regions.

Figure 2 presents the inversed Ramsey fringe of the resonator. The resonance bandwidth is in the order of 650 Hz, the fringe amplitude is 58 mV for a background level of 60 mV. These two values lead to a contrast ratio in magnitude of 1. This good contrast can also be observed on the measured microwave spectrum of the tube (Figure 3).

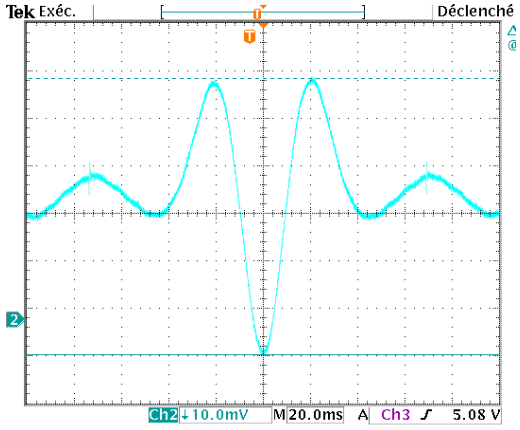

Figure 2. TOP-Cs measured Ramsey fringe with a minimal signal at resonance (dark fringe).

The Ramsey fringe was obtained with a useful atomic flux in the detection region of $3x10^{9}$ at/s leading to a theoretical Cs consumption in magnitude of 0.1 g/year.

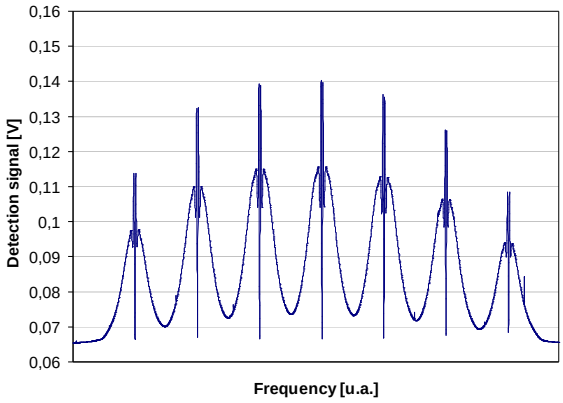

Figure 3. Measured microwave spectrum of the atomic resonator.

The noise density at the frequency modulation depth, measured in a 1 Hz bandwidth is 4.8 µV.Hz$^{-1/2}$. It leads to a signal to noise ratio higher than 12000 Hz$^{-1/2}$ with a very good reproducibility. The expected theoretical frequency stability for this value of SNR is lower than $4x10^{-12}$ at 1 s.

The second step of the breadboard evaluation is of course the frequency stability measurement. However, our experimental setup is limited to the short term stability because of our frequency reference. For the moment, we are only using a high performance quartz oscillator as frequency reference. This quartz is good enough to measure a frequency stability in order of 10^{-12} until a few 10^{2} s. So this frequency reference is sufficient to measure the frequency stability at 1 s and to identify the characteristic slope in $\tau^{-1/2}$, signature of the atomic resonator. Figure 4 presents a first stability measurement, with the theoretical stability objective of $4x10^{-12}\,\tau^{-1/2}$ in green.

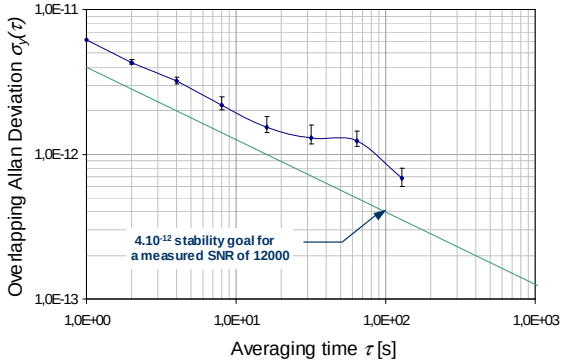

Figure 4. Frequency stability measurement limited to the short term stability by the used frequency reference

At this time, we measure a short term stability of $6.1x10^{-12}$ at 1 s. This measurement is limited by electronic issues that we recently identified. In the upcoming weeks, we will optimize the electronic setup to cancel this limiting factor on the frequency stability measurement. The final objective of the breadboard validation phase is to measure a frequency stability with respect to our signal to noise ratio measurements.

IV. PERSPECTIVES

Besides the electronic issue which limits the stability measurement, the signal to noise ratio SNR of the resonator is limited today by three different noise factors. The photodetector noise (3.2 µV.Hz$^{-1/2}$) and the stray light noise (3.8 µV.Hz$^{-1/2}$) are in the same magnitude as the total measured noise. The stray light could be reduced with very high quality processes on the optical windows with the purpose of reducing the laser beam scattering, the main source of stray light.
However, the principal gain could come from the detection noise itself. Today the collection efficiency of the detection region is not sufficient enough to detect all the atoms of the beam and reach the atomic shot noise. This collection efficiency has been evaluated in order of 25% by using two different numerical simulation softwares. As the average number of emitted photons

per atoms is 4, it will be interesting to develop a new optical region to increase the collection efficiency. With an optical simulation study, we identified several possibilities to optimize the design of our optical regions to reach the atomic shot noise.

V. TOWARDS A SPACE PROJECT

One of the applications for an optically pumped Cs clock is satellite navigation systems. This is why, Thales ED submitted, in association with a French-Swiss consortium, a proposal to the European Space Agency (ESA) for the development of a Galileo space Cs clock.

The consortium is composed by two important European laboratories and two space industries : Observatoire de Neuchâtel (ON) in Switzerland, SYRTE (Observatoire de Paris) in France, Contraves Space in Switzerland and Thales Electron Devices in France. This consortium, led by Thales ED, has a very important background in atomic clock activities and in space projects. For example, ON was involved in many space clock developments such as the Rb clock for RadioAstron, the Space Passive Hydrogen Maser (SPHM) for Galileo or the Space active Hydrogen Maser (SHM) for ACES.
Since 1981, SYRTE has been involved in many optically pumped Cs activities, including a pre-industrial development of compact Cs beam clocks during the 90's.
As it is presented in this paper, the industrial partners have also competencies in the time frequency domain. But Thales ED and Contraves Space have especially an important know-how in space developments and space products.

Our first step objective is to share our different competencies inherited from French and Swiss Cs activities, to define the best clock architecture. The Thales ED's results on Cs developments, as well as the recent results obtained by ON from the OSCAR project [5] make us very confident on the achievement of the frequency stability required for GALILEO ($3x10^{-12}\tau^{-1/2}$) with sufficient margin to guarantee the industrialization of the clock.

ACKNOWLEDGEMENTS

The authors would like to thank SYRTE for their helpful contribution in the evaluation of the TOP-Cs breadboard.
The Thales activity on optically pumped Cs frequency standards was supported by internal funding.

REFERENCES

[1] S. Guérandel, and al. "*Operation of has compact cesium beam frequency standard: how to improve the stability towards $10^{-12}\tau^{-1/2}$ level*." IEEE International Frequency Control Symposium. 2002
[2] R. Lutwak, and al. "*Standard for GPS-III Optucally-pumped cesium beam frequency*." 33rd Annual Precise Time and Time Interval (PTTI) meeting. 2001
[3] C. Sallot, and al. "*$3\times10^{-12}\tau^{-1/2}$ on industrial prototype standard optically pumped cesium beam frequency*." Frequency Control Symposium & 17th European Time and Frequency Forum (EFTF). 2003
[4] G. Théobald, and al. "Ground state Zeeman coherence effects in an optically pumped cesium beam." Optics Comm., 5, June 1989, p.256.
[5] S. Lecomte, and al. "*Development of a single-frequency optically-pumped cesium beam resonator for space applications*." 20th European Frequency and Time Forum (EFTF). 2006

Proceedings of the 20th EFTF, 2006

Using a redundant time link system in TAI computation

G. Petit* and Z. Jiang
Bureau International des Poids et Mesures, 92312 Sèvres, France
**Electronic address:* gpetit@bipm.org

The network of time links for the computation of TAI has always be chosen such as to allow a unique solution, i.e. not using any redundancy. In the present situation, many links can be computed with two or more techniques (mostly Two Way time transfer -TW- and Global Positioning System -GPS-) and the TW network itself is highly redundant. Therefore it makes sense to use all the available information and to compute TAI links using the available redundant network. In the paper, we examine a practical formalism to be used in this aim and we present results of test computations using real TAI data.

1. INTRODUCTION

The network of TAI time links has always been non-redundant and the measurements used are considered independent. This choice was adapted to the situation that prevailed until the end of the 1990s when a single time transfer technique was used, GPS with Common-view computation, in which correlations are also difficult to estimate. Now two main techniques are used for TAI time links (GPS and TW), several types of measurements exist for each technique (e.g. single frequency or dual frequency code, or dual frequency code and phase for GPS), and, at least in the case of the TW network that encompasses Europe and North America, a nearly complete set of redundant measurements is available. In addition, other systems are already available, or may soon become available, such as GLONASS, GPS augmentation systems and GALILEO. We have therefore to envision a better use of all the data available for the computation of TAI time links.

In a preceding paper [1] we studied the general formalism used to solve the time scale system with redundant time links. However we considered an ideal situation where all techniques used are perfectly calibrated and where no systematic effects exist between techniques. In the real world, we have to account for the fact that these systematics exist and we here propose a method to account for these. In section II we present the practical implementation of the formalism of the redundant time link system. In section III, we present some tests carried out with the whole TAI network of links. Finally we discuss the results in section IV.

II. FORMALISM OF THE REDUNDANT TIME LINK SYSTEM

The basic equation of a time link measurement (index k) between laboratories i and j participating to TAI is

$$UTC_i(t) - UTC_j(t) + b_k(t) = x_k(t) + v_k(t)$$

Where t is a date of computation of TAI (MJD ending with 4 and 9 at 0h UTC), $b_k(t)$ is a bias value associated to this particular link at time t, $x_k(t)$ is the measured link value, and $v_k(t)$ is the residual error of the measurement. Having N laboratories and M time link measurements, we consider here the redundant case where $M > N-1$. The uncertainty $u_k(t)$ associated with measurement k represents the statistical uncertainty of the link, represented as the u_A values for the TAI links in [2].

Using M measured links, we want to determine at time t (N-1) independent link values and M bias parameters, which form together the parameter vector Y of dimension (M+N-1), along with its covariance matrix S_Y. As such a system is clearly underdetermined, we introduce as additional measurements two series of constraints on the bias parameters:

a) Continuity constraints of the form

$$b_k(t) - b_k(t-\delta t) = vco_k(t) \pm sco_k(t)$$

where $vco_k(t)$ is the expected variation of the value of the bias parameter between time t and the preceding time $t-\delta t$ (in the context of TAI, δt can be taken as the interval between TAI standard dates, i.e. 5 days). Usually, the value $vco_k(t)$ is zero and the uncertainty $sco_k(t)$ associated to this constraint is chosen in consideration of the expected instability of each link. However it can also be used to either give precedence to a given type of link (by setting sco to a small value) or alternately to effectively remove the measurement from the ensemble (by setting sco to a large value) e.g. in case of an unexpected step of a given link.

b) Calibration constraints of the form

$$b_k(t) = ca_k \pm sca_k$$

where ca_k represents the a priori value of the technique biases obtained by calibration and sca_k is the uncertainty of the calibration.

The number of continuity constraints is M while the number of calibration constraints may be between 0 and M. However we can consider for simplicity M calibration constraints, assuming that any non-existent calibration is introduced with a very large uncertainty. The time link system, augmented by the constraints, may be written as

$$C\,Y = L + V$$

where C is the (3*M,M+N-1) design matrix, Y is the (M+N-1,1) vector of parameters, L is the (3*M,1) vector of measurements and V is the vector of residuals. C, Y and L may be more explicitly represented as in Figure 1, where $co_k = b_k(t-\delta t) + vco_k(t)$.

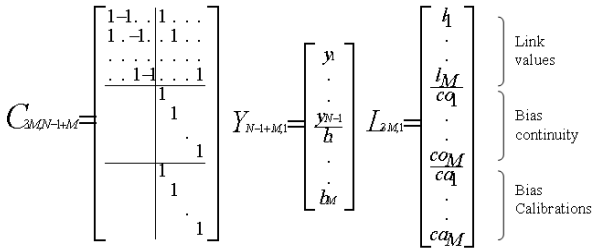

Figure 1: The redundant time link system, augmented for continuity constraints and calibration constraints.

If the covariance matrix of L is noted S_L, the system is solved as

$$Y = (C^T S_L^{-1} C)^{-1} C^T S_L^{-1} L$$

and the covariance matrix S_Y is obtained as

$$S_Y = (C^T S_L^{-1} C)^{-1}.$$

III. TESTS WITH THE REAL TAI NETWORK

We have carried out some tests of the formalism above using the network of TAI links over four months, from October 2005 to January 2006. As seen on Figure 2, the network of TAI links consists of some 55 "official" links (solid lines) and a number of back-up links (dashed lines). Not shown on Figure 2 are additional TW links, e.g. the extra links between all stations participating to the Europe-USA TW network. The techniques used are designated TW for TW in the Ku band, X band for TW in the X band, GPS P3 for dual frequency P-code, GPS MC for single frequency multi-channel C/A code, GPS SC for single frequency single channel C/A code.

All these links are regularly computed every month, the official links being used for the TAI computation and the back-up links being used for checking. Most of the link comparisons can be found on the web site [3]. We directly used the link results from the TAI computations of the four months to carry out these tests.

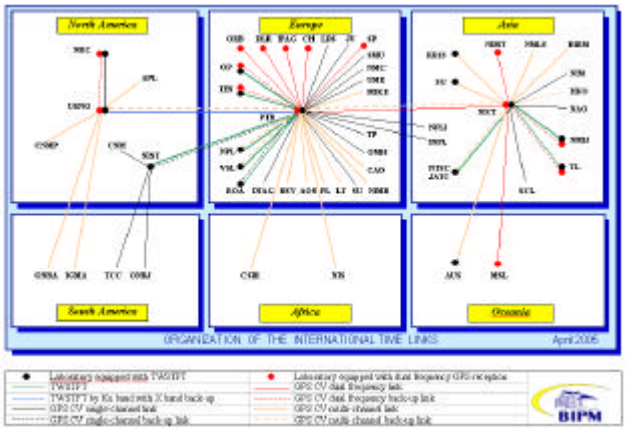

Figure 2: The network of TAI links in April 2005.

For each TAI standard date (MJD ending with 4 or 9) from MJD 53644 to MJD 53764, we compute a redundant solution (noted RED in the following) using the formalism in section 2, with the choices below:
Uncertainties $u_k(t) = u_A$ values taken from [2].
Uncertainties $sco_k = u_k/v2$
Uncertainties $sca_k = u_B$ values taken from [2] for official links, additional links unconstrained.
Biases values for additional links were initialized at MJD 53639 to a priori values derived from the previous TAI computation.

The RED solutions were then derived and compared to the standard TAI solutions. For each link which has some redundancy we compare 1. the link values, 2. the link standard uncertainties, 3. the biases for the different techniques.

For the link values, we find that the TAI and RED solutions differ typically by less than their standard uncertainty, after removing a bias. It is expected that significant biases may exist between the TAI and RED solutions e.g. because the additional TW links (which are not used in TAI) have generally not been calibrated. For the link USNO-PTB, shown in Figure 3, the two solutions differ by 0.41 ns RMS, after accounting for a mean bias, while the standard uncertainty of the link is 0.50 ns for TAI and 0.35 ns for RED (see Table 1). However a mean bias of around 1.5 ns exists between the two solutions. Therefore, in practice, some a priori calibration should be performed before actually using such redundant links for TAI, if such a redundant computation was actually performed.

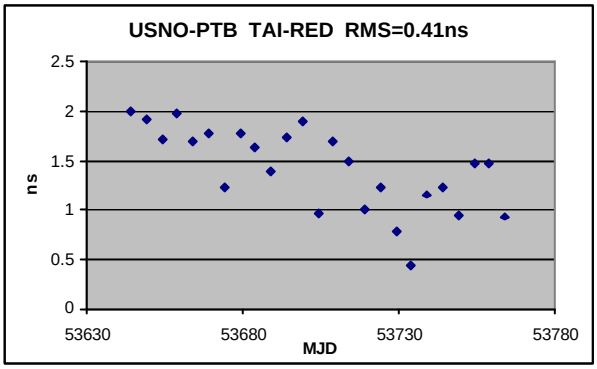

Figure 3: Difference between the TAI and RED solutions for the link USNO-PTB from October 2005 to January 2006.

For the link standard uncertainties we find that, as expected, they are reduced in the RED solutions with respect to the TAI one (see Table 1). Note that the RED standard uncertainties are all the more decreased when the sco_k values are chosen small. It is possible that the values chosen for this test ($sco_k = u_k/v2$) may be somewhat conservative.

Link with PTB	USNO	NIST	NPL	OP	IT	ROA	CH	NICT
Standard TAI	0.50	0.50	1.5/0.5	0.50	0.50	0.70	0.70	1.50
Redundant (typ.)	0.35	0.40	0.31	0.32	0.48	0.61	0.50	1.45/0.6

Table 1: Standard uncertainties in the TAI solution and the corresponding typical values in the RED solution for some of the links with redundancy. Note that the link NICT-PTB has two values for the RED solution, the value 0.6 ns corresponds to one month when TW data was available in addition to GPS-P3 and GPS-MC.

Note also that the standard uncertainty in the RED solution generally do not decrease for a given link if the redundant technique has an uncertainty $u_k(t)$ typically much larger than that of the standard TAI technique. This is because each additional technique needs an additional bias parameter, which affects the number of degrees of freedom and the covariance matrix of the system. This is e.g. the case if the redundant technique is GPS Common View with a single channel receiver (GPS SC) for which the u_A values are of order several ns [2]. Therefore it is advised, when computing a redundant solution, to use only techniques with comparable uncertainties. In our RED solution, no additional GPS SC link was used.

For the biases between different techniques we find that the stability of the series of biases do represent the stability of each technique. However the series have to be checked for trends and steps which may indicate problems in the corresponding link and technique. As an example we show (Figure 4) a link where one of the techniques (GPS P3) experiences an unexpected systematic variation in the second half of the interval.

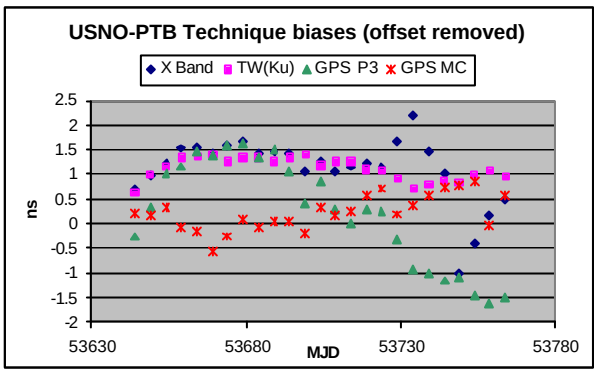

Figure 4: Technique biases in the RED solutions for the link USNO-PTB from October 2005 to January 2006, after removing a mean bias value for the GPS P3 technique.

IV. CONCLUSIONS AND PROSPECTS

The TAI link network is now highly redundant, but this capacity is not used. Using redundancy is expected to improve both the uncertainty and the reliability of the results. It has also been shown [4] that the present non-redundant network of TW links may limit the achievable stability of the TAI links.

We have tested a formalism to introduce the available redundant measurements, accounting for the known systematics between techniques. If the correlations between the different measurements used are known, they can be readily introduced in this formalism. Thus it is particularly adapted to using a TAI network composed of all available and calibrated TW links plus the All-in-view links to GPS time for all laboratories.

It is to be noted that using a redundant network is all the more important when several techniques of similar quality are available. This is now the case if one considers that 31% of TAI laboratories, providing 80% of the total clock weight and all primary standards, are equipped with TW and with GPS dual frequency receivers providing code and carrier phase measurements [5]. These techniques use completely independent equipments and provide results of comparable quality [5,6]. The future availability of multi-systems GNSS receivers providing measurements on GPS, Galileo and GLONASS satellites, will further enhance the need of using all available information in a redundant solution.

Acknowledgements

We thank the laboratories contributing to TAI that provide for TAI computation the data used in this study.

REFERENCES

[1] G. Petit, Z. Jiang, Redundancy and correlation in TAI time links, Proc. FCS/PTTI, 2005.
[2] BIPM, Circular T, monthly publication, section 6
[3] ftp://tai.bipm.org/TimeLink/LkC/)
[4] Z. Jiang, G. Petit, Redundancy in the TAI TWSTFT time transfer network, these proceedings, 2006.
[5] Z. Jiang, R. Dach, G. Petit, T. Schildknecht, U. Hugentobler, Comparison and combination of TAI time links with continuous GPS carrier phase results, these proceedings, 2006.
[6] G. Petit, Z. Jiang, Stability of geodetic GPS time links and their comparison to two way time transfer, Proc. 36th PTTI, pp.31-39, 2004.

Proceedings of the 20th EFTF, 2006

COMPARISON AND COMBINATION OF TAI TIME LINKS WITH CONTINUOUS GPS CARRIER PHASE RESULTS

Z. Jiang[1], R. Dach[2], G. Petit[1],
T. Schildknecht[2], U. Hugentobler[2]

1 Bureau International des Poids et Mesures
2 Astronomical Institute of University of Bern
zjiang@bipm.org

The time transfer techniques used to generate TAI are currently the TWSTFT (TW), GPS C/A, and GPS P3. About 19% of all TAI laboratories possess P3, 12% possess TW backed up with P3, i.e., in total only 31% of the TAI laboratories transfer 100% of the primary frequency standards (PFS) including all the Cs fountains and 80% of the total weighted clocks for TAI. GPS carrier phase (CP) data are co-products of P3 receivers and they are never used in TAI. An effective strategy to improve TAI is to strengthen these TW+P3 links by using the already available CP information.

We first review the classical TAI time transfer techniques and solutions of different analysis strategies of the CP data, namely the IGS [1], the AIUB [2], and the NRCan PPP [3]. To evaluate all the different time transfer techniques, we carried out an extensive comparison between the above techniques, over different periods from hours to 4 months and over different distances on inner- resp. inter-continental baselines between laboratories in Asia, Australia, Europe, and America. We conclude that the CP only solution without using the pseudorange data at all supplies high short term time stability. Comparison over 4 months between all the GPS code supported CP solutions agree perfectly with each other within 0.5 ns and their agreements with TW are of the order of 1 ns or below. However neither TW nor GPS has as a single technique a dominant advantage w.r.t. the others: the TW would be affected by a diurnal disturbance, the CP only by a drift and the P-code solutions by strong noise.

The solutions of IGS, AIUB, and PPP are the direct combinations of GPS only Code+CP observations. In fact, the GPS CP-only information can be combined with any absolute time scale [4]. We briefly discussed the concept of the post combination of CP with TW, GPS P3 and C/A code. We studied the methods to combine different techniques which allow maintaining the advantages of a link while reducing its disadvantages. The Vondrak-Cepek method is applied [5]. We prove that the combination of TW and CP greatly reduces the diurnal disturbance in TW Ku band as well as the drift effect in CP only solutions such that the short and long stabilities are both improved. With a careful configuration of the weights and filters, it is possible to combine more than three types of links, like TW, P3, and CP. This allows us to improve both the uB and uA uncertainties in the TAI time transfer. With the help of the high precision TW and CP solutions, we evaluated also the GPS common view (CV) and all in view (AV) time transfer techniques [6]. The latter is considered to replace the common view in the TAI computation.

I. INTRODUCTION

I-1 A strategy to improve the TAI

The general goal of this study is to improve the TAI time transfer stability. Till now, TW (TWSTFT, Two Way Satellite Time and Frequency Transfer), GPS C/A and GPS P3 are used to generate TAI (cf. Fig. I-1). However, the TAI international time transfer network is highly redundant [4]. About 26% of the TAI time laboratories are equipped with both TW and GPS receivers providing dual frequency code data for GPS P3 and carrier phase measurements (CP). 12% of them use TW as their official transfer links (cf. Fig. I-1 and Tab. I-1). In total 31% of the laboratories possess GPS CP receivers though the CP information has never been used for TAI. On the other hand, these laboratories contribute about 80% of the total weighted clocks and they host all the PFS (Primary Frequency Standards) including all the Cs fountains for the TAI computation. Improving these links implies a direct gain in the TAI. An effective and potentially the simplest strategy is to fully use the already available CP information.

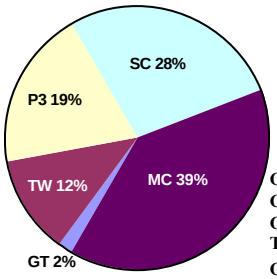

GPS SC: 1-frequency, single-channel C/A code
GPS MC: 1-frequency, multi-channel C/A code
GPS P3: 2-frequency, multi-channel P codes
TW: Two Way Time Transfer
GT: GPS Time and internal link

Fig. I-1: Time transfer techniques used in TAI

Tab. I-1 Equipment at the 8 laboratories owning PFS fountains or contributing to TAI with heavy clock weight

LAB	TAI link	Back up 1	Back up 2	Back up 3
IEN	TW	P3/CP	MC	SC
NIST	TW	P3/CP	SC	SC
NICT	P3/CP	TW	MC	SC
NMIJ	P3/CP	TW	MC	SC
NPL	TW	P3/CP	MC	SC
OP	TW	P3/CP	MC	SC
PTB	TW	P3/CP	MC	SC
USNO	TW	TW-X band	P3/CP	MC

I-2 Application of the CP information in TAI

The GPS CP measurements are two orders of magnitude more precise than the GPS code data and much less sensitive to multi-path effects, one of the dominant errors in usual GPS time transfer based on the code measurements (GPS C/A and GPS P3). A main characteristic of the CP method is the one-to-one correlation between the phase ambiguity and the clock parameters. For time transfer the code data may be used to solve this problem [7]. If the combined code and phase data processing is performed in the form of daily independent solutions, the continuous ambiguities are artificially interrupted at midnight which may produce the so called day-boundary discontinuities of up to one nanosecond. Such solutions are not used in the TAI generation due to the unwanted discontinuities although they are routinely produced by the International GNSS Service (hereafter IGS solution) for a large number of stations including several timing laboratories [1].

New approaches allow producing continuous GPS CP solutions for the time transfer.

Recent developments in the Bernese GPS Software package [10] carried out at the Astronomical Institute of the University of Bern (AIUB) enable the reconnection of the phase ambiguities from two days at midnight to generate continuous GPS carrier phase solutions [2]. These continuous solutions can use either the code plus the carrier phase observations (hereafter Code+CP solution), or the carrier phase data only (hereafter CP or CP-only solution) as long as they are continuously available. As the IGS solution, both solutions are the result of a global consistent network adjustment.

In Precise Point Positioning (PPP) [3], phase and code measurements from a dual frequency geodetic-type time transfer receiver, together with the IGS precise orbits and clock solutions for the GPS satellites, are used to continuously determine the offset between the local clock and the IGS time reference. Similar as the CCTF-CGGTTS standard data set, the PPP solution is a single point solution. Any time link between participating stations can then be computed by forming the simple differences. We use the GPSPPP software [3], developed by NRCan. Among other features, the software allows nearly infinite continuous processing of a time solution by ensuring the continuity of phase ambiguities at day boundaries.

The Combined-Smoothing-Solution (hereafter combined solution) is a single baseline solution. Two or more links measured by different techniques are combined. One of the links supplies the absolute time scale, for example TW, and the other, for example the CP, supplies the derivatives of the link, that is, the variations of the clock differences in time.

Using the derivatives of the CP solutions for the combination has the advantage that the undetermined (CP only) or less accurately determined (Code+CP, resp. PPP) time difference, possible discontinuities in the CP solutions caused by interrupts in the continuous tracking of the phase measurements, as well as potential inter-technique biases are cancelled. The drift in the CP only solution as it will be described in Section II-2.1 can also be mitigated in this way. With this a posteriori combination any two different techniques can be combined, such as TW and GPS CP. By an optimal configuration of the weights and filters of the smoothing function, it is possible to combine also three or more types of links, like TW, P3, and CP. The inter-techniques' biases and the calibration errors as well as the measurement errors are averaged out. This approach allows us to improve both the type A and type B uncertainties (uA, uB) in the TAI time transfer.

We compare the new solutions with each other and with the classical TAI time transfer techniques. Special attention is paid to the estimation of the long-term stability (days to months averaging time), which is essential for TAI computation. Among the TAI techniques, we also examine the GPS AV (all in view [6]) method which is considered to replace the CV (common view) in the TAI computation.

I-3 Data

All available linking techniques are studied: TW, GPS P3, MC, SC (CV/AV), CP only, Code+CP, PPP. Data were analysed over different periods: short period of hours to 10 days and long period of 4 months (Oct. 2005 to Jan. 2006) and over different distances: inner- resp. inter-continental links between Asia, Australia, Europe, and America.

Data analysed stem from 13 laboratories which possess both the TW and GPS P3/CP receivers: AUS, CH, IEN(IT), KRIS, NICT, NIST, NPL, OP, PTB, ROA, SP, TL, and USNO. More than 300 links were computed and 500 pairs of links were compared and analysed.

Since Oct. 2005, a new TW schedule of 12-24 points per day is used and new inter-continental links between Europe, America, Asia, and Australia are measured. This gives on one hand an independent control to estimate the stability of the GPS CP solutions and on the other hand enables us to study the potential disturbances in the TW links and to improve the TW with the help of the CP information. In addition to Ku band links, there are also X band TW data between USNO and PTB available. The X band link is more stable than the Ku band data due to its higher density, better continuity and lower diurnal disturbance [8].

Discontinuities in the CP-solution caused by the loss of continuous tracking of the carrier phase to the satellites or by other receiver tracking problems are repaired by using a linear regression of the clock rate.

II. COMPARISONS OF DIFFERENT TIME TRANSFER TECHNIQUES

The goal of this comparison is to study the advantages and disadvantages of the each technique. The method used is to analyse the Time Deviations (TDev) and to make the inter-technique comparisons over different periods and distances. Currently the values in the Circular T are given up to a tenth of a nanosecond. Our analysis stops at the order of 0.05 ns. The main goal of this paper is to improve the uncertainty type A: uA. Hence the mean value of a comparison is often removed in the following discussions and figures.

II-1 Short term comparisons

We study the link stability over an averaging time of less than or about one week.

II-1.1 Diurnal disturbances in TW links

Thanks to the density that changed from 4 to 12 resp. 24 points per day since Oct 2006 a diurnal signal in some of the TW links was detected. The upper plots in Fig. II-1 and II-2a show typical TW links between NICT-PTB and USNO-PTB as they are used for the monthly TAI computation (here TAI 0512 resp. Dec. 2005 as an example). As in all similar plots, the numbers give the values for the points marked by the triangles.

We clearly see that for the entire time interval the TW link NICT-PTB (Fig. II-1) shows significant diurnal signals of 2 to 3 ns peak to peak. The lower plot of Fig. II-1 is a zoom of 8 days. The TDev (Time Deviations) in the lower right plot confirms the diurnal signal in the TW series of this baseline. In the TDev plots, h stands for hour, d for day, ddd for 3 days and wk for week.

In the USNO-PTB link (Fig. II-2a), similar signals of 1 to 2.5 ns peak to peak are found, but only for a period of 9 days (MJD 53724 to 53733). However these diurnal variations are not found in the TW X band link nor in the GPS CP links for the same periods. Comparing the related TDev of different techniques in Fig. II-2a and 2b, we know that these diurnal variations are not caused by the clocks but originate from the TW Ku band time transfer.

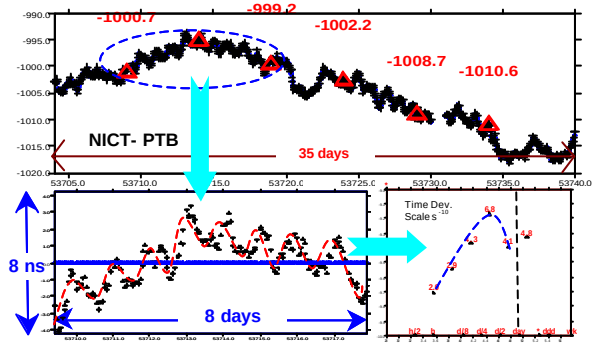

Fig. II-1 TW link NICT-PTB for TAI0512

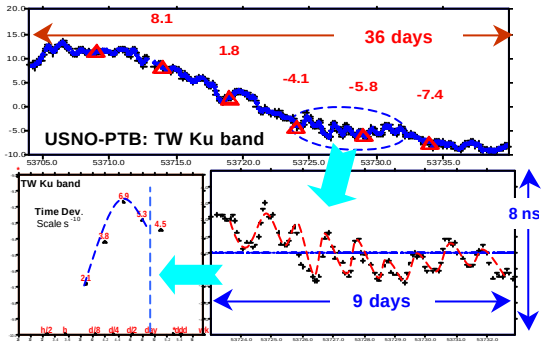

Fig. II-2a TW Ku link USNO-PTB for TAI0512

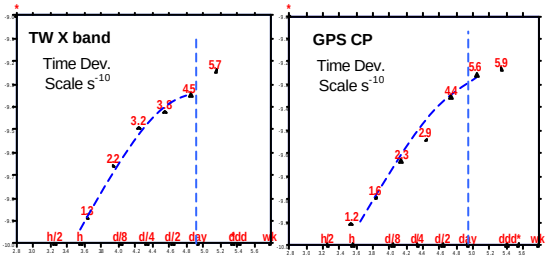

Fig. II-2b TDev of TW X band and GPS CP links of USNO-PTB for TAI 0512

Also other baselines are affected by the diurnal variations. Fig. II-3 shows comparison of the TW and GPS CP links of NIST-NPL. The diurnal variations exist only in the TW Ku link but not in the CP link. Fig. II-4 shows the TDev of three baselines linked with OP: OP-USNO, OP-NIST, and OP-PTB for the same period of 53744 to 53754. Again there are diurnal signals in the TW Ku band links. By now, we can conclude that the TW links measured using different satellites and ground equipment over different areas seem to be disturbed from time to time by a diurnal disturbance. The reason is unknown at present. The amplitudes of this disturbance may reach a magnitude of 1 up to 3 ns.

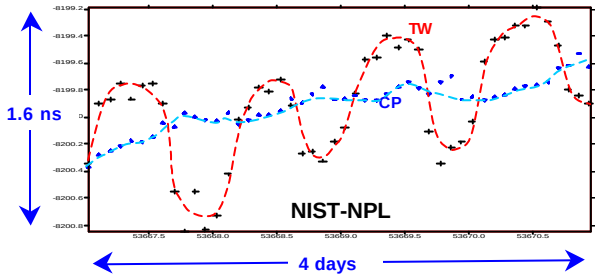

Fig. II-3 Link comparison of TW Ku band and GPS CP for MJD 53660 to 53671

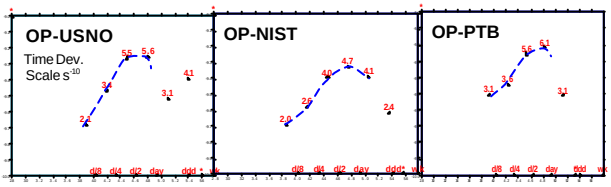

Fig. II-4 TDev of TW Ku links (MJD 53744-53754)

II-1.2 Day-boundary discontinuities in the IGS daily solutions

We compare three time transfer solutions based on a combined processing of GPS code and phase measurements: IGS, AIUB (Code+CP), and PPP. The upper plot in Fig. II-5 shows the typical day-boundary discontinuities in the IGS solution. For the period of 11 days there are 11 pieces with 10 discontinuities at the day-boundaries which are as large as 1 ns (or in a few cases even bigger). TAI is computed and published for midnight of the standard MJDs and the values are given up to a tenth of a nanosecond. These day-boundary discontinuities thus cannot be accepted for TAI time transfer. The lower plot in Fig. II-5 shows the continuously generated PPP solution for the same period. The PPP solution is in general very close to the AIUB Code+CP solution within 0.1 to 0.4 ns. Both results stem from a continuous analysis of the CP data. They agree with the corresponding TW link within 1 ns.

The baseline NPL-NIST is a trans-Atlantic link between two H-masers. It should be pointed out that the magnitude of these day-boundary discontinuities is not related to the length of the baseline but to the noise behaviour of the code data. The day-boundary discontinuities of the individual stations are regularly monitored within the IGS [11].

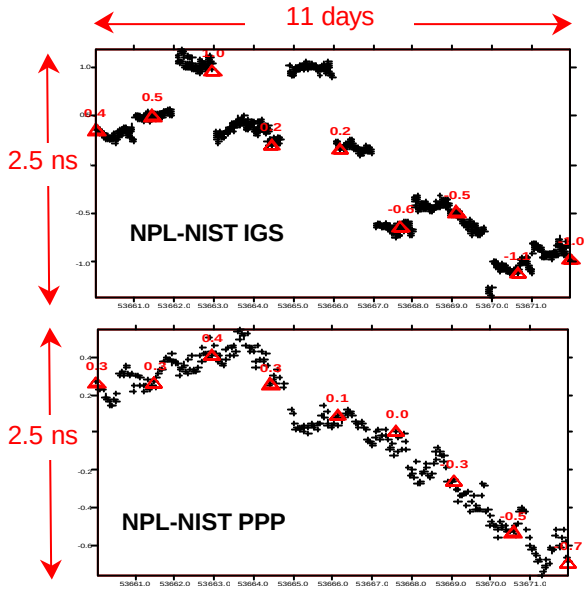

Fig. II-5 Links of NPL-NIST (MJD 53660-53672) top – IGS solution; bottom – PPP solution

II-1.3 Noise characteristics and short term TDev of different techniques

Fig. II-6 displays the time differences between USNO and PTB obtained with different techniques for the interval of MJD 53723-53733. The results for the individual techniques are shifted by 8 ns for plotting. The scatter indicates the short term noise level of each time transfer method. The TDev(2h) computed from the 11 day interval is added to the labels in the plot. The PPP and AIUB Code+CP solutions are very close to each other and therefore shown together.

From the figure, the short term stabilities over two hours for the GPS P3 and MC are 0.5 and 0.8 ns respectively. That of the TW, the GPS CP only and Code+CP/PPP solutions are all about 0.2 ns. The CP information may mainly contribute to reduce the noise in the GPS code data. The TW Ku band link seems to be affected by the diurnal disturbance during the interval displayed in the Figure. USNO-PTB is a trans-Atlantic baseline. The clock at USNO is a H-maser and that at PTB is a Cs standard. The TDev of the inner-continental baselines is in general better.

II-2 Long term comparisons

Long term means in this context a period of days to months which is essential for TAI stability. A time transfer technique might be affected by a bias which can be detected by comparing with other completely independent techniques. Long-term inter-technique comparisons of GPS and TW may help to investigate the influence of common biases on the results of the

GPS based techniques due to, for example, the IGS corrections of the orbit, clock, atmosphere models etc. Extensive comparisons were made between more than 500 pairs of the inner resp. inter-continental baselines. We show here only some examples.

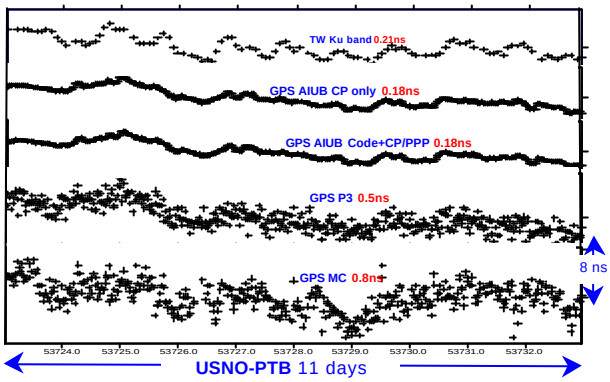

Fig. II-6 Comparison of the time differences between USNO and PTB obtained with different techniques. The TDev(2h) computed from the data is added to the labels

II-2.1 Long term comparison of TW vs. GPS CP contributed solutions

The upper plots in Fig. II-7 and II-8 are two different link results and lower plots are the differences of the two links. Fig. II-7 compiles the time transfer results from TW and the AIUB Code+CP solution for the link NIST-OP, which is a trans-Atlantic baseline between two H-masers. Tab. II-1 provides the statistical results of the comparisons. Most TAI baselines are shorter and their inter-technique discrepancies are usually smaller. In Tab. II-1, all the P-codes contributed CP solutions of IGS, Code+CP (AIUB) and PPP agree with each other within 0.3~0.4 ns (St.D.). Their agreements with the TW Ku link are within 0.7~0.8 ns, noting that the TW Ku link may be disturbed by the diurnal variations. It is interesting to note that the time transfer based only on the SC (single channel GPS C/A code) links agree within a St.D. of 0.9~1.1 ns with the other 'high precision' techniques, like TW or CP.

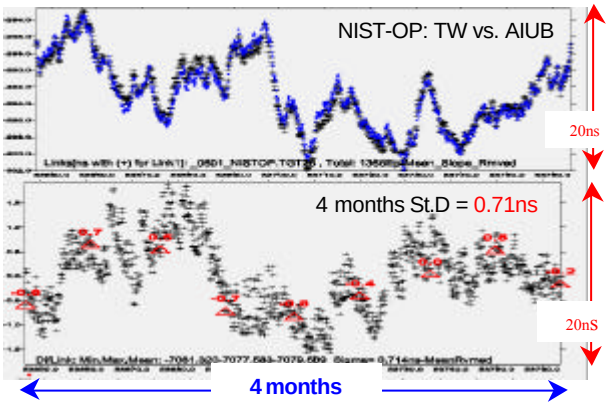

Fig. II-7 Long term comparison over four months of TW and AIUB Code+CP solution for NIST-OP

The CP only solution is affected by a quasi-linear drift. Fig. II-8 is an extreme example of the drift with a frequency shift of about $2*10^{-15}$. Comparisons for other baselines show that similar drifts exist in almost all baselines although they may have a smaller magnitude or are not always so quasi-linear. For example, the drift of USNO-PTB was very small during Oct.-Nov. 2005 but became stronger for the following two months. For this moment, we cannot explain the reason of this drift. However it is important to point out that this drift does not affect solutions that use the code measurements together with the phase data in a combined analysis (IGS, Code+CP, and PPP, see Tab. II-1).

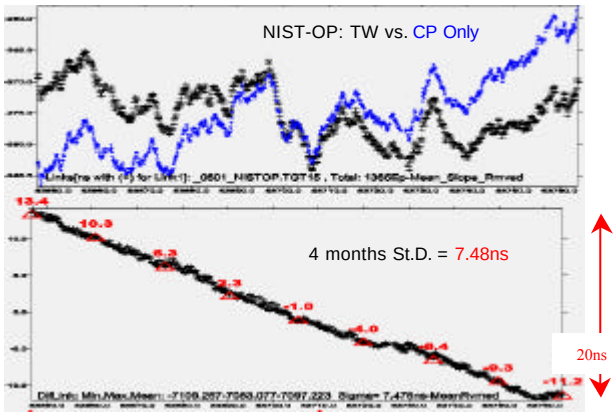

Fig. II-8 Long term comparison over four months of TW and AIUB CP only solution for NIST-OP

Tab. II-1 Inter-technique comparison NIST-OP
(Standard deviation of the differences over four months)

Link comparison	St.D./ns
TW-(Code+CP)	0.71
TW - IGS	0.77
TW - PPP	0.79

Link comparison	St.D./ns
SC-(Code+CP)	0.95
SC - IGS	1.08
SC - PPP	1.01
SC - TW	1.10

Link comparison	St.D./ns
(Code+CP) - PPP	0.29
(Code+CP) - IGS	0.39
IGS - PPP	0.25

II-2.2 Comparison of long term stability of different techniques

Fig. II-9 shows TDev of the 6 techniques for the baseline USNO-PTB over an averaging time of four months. The TW Ku band link is disturbed by diurnal variations. The short term stability of GPS P3 and the GPS multi channel C/A code are limited by the noise of the GPS code data. The TW X band data provide good short term stability. Nevertheless, the GPS CP

contributed solutions have even a slightly better short term stability. For the averaging time of 1~3 days, the solutions using only GPS code data P3 and MC have worse stability than the others. MC shows the largest instability. For an averaging time longer than 3 day, all the techniques have almost the same TDev.

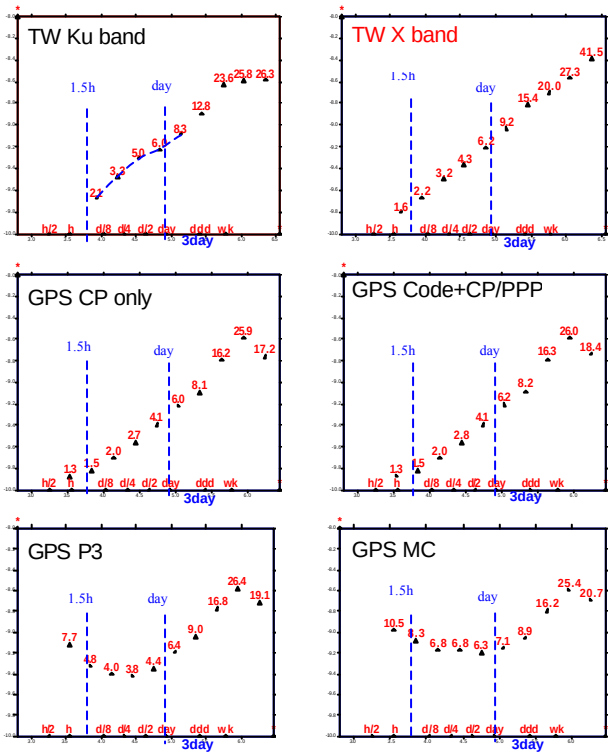

Fig. II-9 Long term comparison over four months of TDev between 6 different techniques for USNO-PTB

Tab. II-2 Comparison of the results obtained from different techniques with respect to the TW X band for the baseline USNO-PTB
(Standard deviation of the differences over four months)

X band compared to	St.D./ns
TW Ku	0.90
AIUB Code+CP	0.80
PPP	0.68
IGS	0.70
AIUB CP only	1.25

As shown in Fig. II-9 and as concluded in [8], for at least the period of Oct. 2005 – Feb. 2006, the TW X band is more accurate than TW Ku band and can be used as a good reference for the comparisons. Tab. II-2 gives the comparison of the TW X band link with respect to the others. The standard deviation of the differences between TW X and Ku bands is 0.90 ns. This is more than that between the TW X band and the three independent GPS solutions: 0.68~0.80 ns. Probably the diurnal disturbance in Ku band increases its error budget. The standard deviation for the differences between the TW X band and the CP only solution is 1.25 ns, for Oct.-Nov. 2005 it is 0.53 ns while for Dec. 2005 – Jan. 2006 it rises to 1.49 ns, dominated obviously by the drift in the CP-only solution.

III. COMBINATION OF DIFFERENT TIME TRANSFER TECHNIQUES

The TAI network is highly redundant. This redundancy can be adjusted at the global network level as discussed in [4] and [9] or at the baseline level as follows. As shown above, none of the single techniques has an absolute advantage vs. the others: TW is affected by the diurnal disturbances; CP only solutions by the drift and missing access to a time scale; the IGS, AIUB Code+CP and PPP solutions, e.g., by multipath effects of the code data.

It is preferable to combine the different techniques in order to keep the advantages and overcome the disadvantages of each of them. The baseline combination is easier than the network adjustment. If we consider a series of time transfer observation $L(T)$ as a function of time, the derivative at a time epoch i can be defined by $[L(T_{i+1})-L(T_i)]/(T_{i+1}-T_i)$. The principal idea of the baseline combination is to use a redundant link measurement as the derivatives to smooth the link function measured by another technique. Obviously the CP only solution is the best candidate for the derivatives due to its high short term stability while its ambiguities, discontinuities and drifts are cancelled or greatly reduced. In such a way the CP information can be combined with one or several 'absolute' links. The latter(s) supply the 'absolute' time scale. By an optimal configuration of the weights and filters, we can greatly improve the uncertainty uA thanks to the high short term accuracy of CP and the uncertainty uB thanks to the combination of different 'absolute' techniques, such as the TW and GPS P3. We do not give here all the details in the methodology that will be discussed in another paper.

There exist numerous smoothing techniques using the measured derivatives. We decided to use the Vondrak-Cepek combined smoothing method [5] because it is adapted for the application in timing metrology.

As Fig. II-2a has shown the USNO-PTB TW Ku link was seriously disturbed by the diurnal variations during the period of MJD 53723-53733. In Fig. III-1a the combined TW Ku and CP result for the same period is plotted. The curve and its TDev in Fig. III-1b confirm the diurnal disturbances in TW Ku band have disappeared thanks to the contribution of the GPS CP information. To prove that the combined result approaches really the true value, we use the independent and more accurate TW X-band link as an objective reference. Fig. III-2 contains the comparison of the combined TW Ku band and the CP only results with the independent TW X band measurements. It confirms that

the drift of the CP only solution as well as the diurnal variations in the TW Ku band results are smoothed out.

Tab. III-1 gives the comparison of TW X band with different combined results for a period of 4 months for the baseline USNO-PTB. The standard deviation of the differences between the TW X band and TW Ku band of 0.90 ns is reduced to 0.64 ns due to the combination with the CP only solution. In analogy, the combination of GPS C/A MC resp. GPS P3 with the CP only solution reduces the standard deviation of the differences with the TW X band results from 1.66 to 1.15 ns and from 0.98 to 0.71 ns respectively. The latter is at the same level as the comparison of the results from the rigorous combined GPS code and CP analysis w.r.t. the TW X band measurements listed in Tab. II-2. The CP information helps to reduce the error budgets by mitigating the influences on the resulting time series of diurnal disturbances in the case of TW Ku band; of the effects of the troposphere and multi-path in the case of P3; of the noise, the ionosphere and troposphere delays as well as the effects of multi-path in the case of C/A MC. On average, a gain of 20 to 30 % is obtained due to the combination of the results from the individual time transfer techniques with the CP only information.

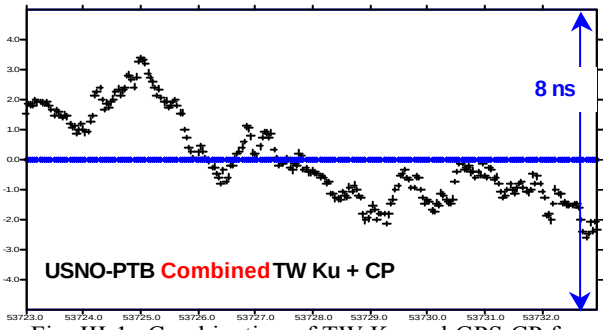

Fig. III-1a Combination of TW Ku and GPS CP for USNO-PTB MJD 53723-53733

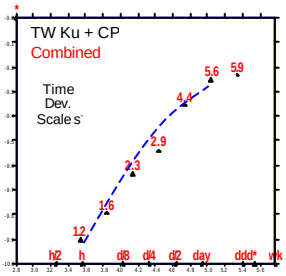

Fig. III-1b TDev of Fig. III-1a

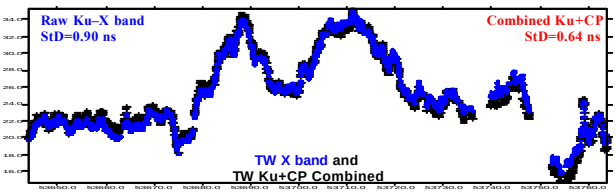

Fig. III-2 Comparison of TW X band and the combined Ku+CP for USNO-PTB over four months

Tab. III-1 TW X band compared to the combined links
(Standard deviation of the differences over four months)

X band Compared to	St.D./ns	Main error sources
Raw TW Ku band	0.90	diurnal variation
Combined KU+CP	0.64	
Raw P3 CV	0.98	tropo, multi-path
Combined P3+CP	0.71	
Raw C/A MC CV	1.66	iono, tropo, multi-path
Combined MC+CP	1.15	

IV. GPS ALL IN VIEW AND COMMON VIEW

GPS AV (all in view) is considered to replace the GPS CV (common view) in the near future for the TAI generation. As shown in Fig. IV-1, for the baseline USNO-OP between two H-masers the TDev issued by GPS P3 AV is obviously lower than that by GPS P3 CV for averaging times less than one day.

Tab. IV-1 presents the standard deviation of the differences over four months of the GPS P3 AV and GPS P3 CV compared to related TW and PPP solutions. The baselines in Tab. IV-1 are listed according to their lengths. The NICT-PTB is the longest baseline in the TAI world-wide network about ten thousand kilometres. The AV results are closer to TW and PPP solutions than the CV results. The averaged gain is from 4% to 30% according roughly to the distance. In most cases, the AV is more advantageous than the CV, especially for the very long baselines. The exceptions are often caused by gaps due to missing data.

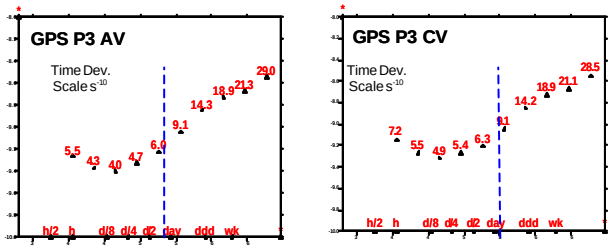

Fig. IV-1 TDev of GPS P3 AV and P3 CV for USNO-OP over four months

Tab. IV-1 Comparison over four months of GPS P3 AV and CV vs. TW and PPP solutions
(Standard deviation of the differences in ns)

Baseline	Length /km	TW -AV	TW -CV	PPP -AV	PPP -CV	Gain
OP-PTB	696	0.77	0.80	0.67	0.71	~4%
SP-USNO	7004	1.23	1.38	0.85	1.05	~15%
USNO-PTB	7032	0.88	0.95	0.64	0.82	~14%
NICT-PTB	10640	1.30	1.67	0.69	1.48	~30%

V. CONCLUSION

The combined solutions derived from the code and the continuous carrier phase observations using the Bernese GPS Software (AIUB) or the GPSPPP program provided by NRCan have high short term stability. The long term agreement with TW measurements based on the standard deviation of the differences is in the order of 0.8 ns. Carrier phase solutions that are processed in daily independent batches (e.g. the IGS solution) are disturbed by day boundary discontinuities with a magnitude of up to 1 ns. Furthermore, earlier conclusions [6] on the advantages of GPS AV w.r.t. GPS CV – especially for long and very long baselines - are confirmed by this study. The long term agreements between all the above listed solutions are within or at about 1 ns.

The comparison study has pointed out a few items that need further investigations. First some of the TW links are disturbed by diurnal variations of 1 ~ 3 ns peak to peak in maximum. Furthermore, the GPS CP only solution is affected by a drift with a magnitude of usually several nanoseconds (up to 20 ns for some stations) over four months.

To benefit from the advantages of each technique the combination of the individual results seems to be preferable. The Vondrak-Cepek combined smoothing method for the TW measurements and the GPS CP only solution was carried out. It can considerably reduce the diurnal disturbance in the TW Ku band links and absorb the drift in the GPS CP solution. The results of the a posteriori combination of GPS P3 with CP only are comparable with the combined continuous analysis of the code and carrier phase data (PPP and Code+CP solution of AIUB). Because the same data are used this agreement confirms the adequate data processing and the correct setup of the combination filter.

The rigorous combination of TW, GPS code, and carrier phase information for the generation of TAI can considerably improve the uncertainties of both uA and uB. The advantage of this approach is that the TAI laboratories need no further hardware investments because the GPS P3 receivers also provide the carrier phase data that is currently not used for the TAI generation. This is supported by the fact that 80% of total weighted clocks and 100% of primary frequency standards are contributed by only 31% of the total TAI laboratories. All of them are equipped with both TW and GPS P3/CP receivers.

Acknowledgements

We would like to thank for the data made available by the TAI laboratories: AUS, CH, INRIM (IEN), KRIS, NICT, NIST, NPL, OP, PTB, ROA, SP, TL, and USNO.

REFERENCES

[1] J. Ray and K. Senior: Geodetic Techniques for Time and Frequency Comparisons Using GPS Phase and Code Measurements, Metrologica, vol. 42, pp. 215-232, 2005.

[2] R. Dach, L.G. Bernier, G. Dudle, T. Schildknecht, and U. Hugentobler: Geodetic Frequency Transfer - recent developments in the AIUB-METAS collaboration, IN Proc. 19th EFTF 2005.

[3] J. Kouba, P. Héroux: Precise Point Positioning using IGS orbits and clock products, GPS Solutions, 4, p.31, 2001.

[4] Z. Jiang and G. Petit: Redundancy in TAI TW network, IN Proc. EFTF 2006.

[5] J. Vondrak and A. Cepek: Combined smoothing method and its use in combining Earth orientation parameters measured by space techniques, IN. Astronomy and Astrophysics, Sept. 2000.

[6] Z. Jiang and G. Petit: Time transfer with GPS satellite all in view, Proc. Asia-Pacific Workshop on Time and Frequency, IN ATF 2004.

[7] T. Schildknecht, G. Beutler, W. Gurtner, and M. Rothacher: Towards sub-nanosecond GPS time transfer using geodetic processing techniques, IN Proc. 4th EFTF 1990.

[8] Z. Jiang: One Year Comparison of USNO-PTB TW Ku and X band Time Links, TM142 of BIPM, Jan. 2006

[9] G. Petit and Z. Jiang: Using a redundant time link system in TAI computation, IN Proc. EFTF 2006.

[10] U. Hugentobler, R. Dach, and P. Fridez, eds.: The Bernese GPS Software Version 5.0, (in preparation) University of Bern: Astronomical Institute, February 2006.

[11] https://goby.nrl.navy.mil/IGStime/daybdy/

Proceedings of the 20th EFTF, 2006

On Optimizing the Configuration of Time-Transfer Links Used to Generate TAI

D. Matsakis[1*], F. Arias[2 3], A. Bauch[4], J. Davis[5], T. Gotoh[6], M. Hosokawa[6], and D. Piester[4]

[1] U.S. Naval Observatory (USNO), 3450 Massachusetts Ave, NW, Washington, DC, 20392, USA,
[2] International Bureau of Weights and Measures (BIPM), Sèvres, France
[3] Associate Astronomer to Observatoire de Paris, SYRTE
[4] Physikalisch-Technische Bundesanstalt (PTB), Braunschweig, Germany
[5] National Physical Laboratory (NPL), Teddington, England
[6] National Institute of Information and Communications Technology (NICT), Koganei, Japan
**Electronic Address*: Matsakis.Demetrios@usno.navy.mil

Recent work on the uncertainties of [*UTC-UTC*(*k*)] has made it possible to quantify the effects of different configurations of the time-transfer links used to generate International Atomic Time (TAI). The optimal topology depends upon the magnitude and character of the time-transfer noise of the relevant systems, the correlations between the time-transfer links, the required degree of robustness, the operational practices and equipment at pivot and crossover sites, and the operational complexity of generating TAI on a routine basis. The authors are members of a study group of the Consultative Committee for Time and Frequency (CCTF) Working Group on TAI that is studying these issues, and this paper will present considerations relevant to the problem.

I. INTRODUCTION

Time transfer for the generation of International Atomic Time (TAI) is achieved by a variety of techniques, including single-channel and multi-channel GPS Common View (CV), dual-frequency P-Code GPS data from geodetic receivers (P3), Ku-band Two Way Satellite Time and Frequency Transfer (TWSTFT), and X-band TWSTFT [1]. In order to improve TAI-generation, the BIPM Time Section has asked the CCTF to study certain proposals. One involved replacing CV time transfer by GPS All-in-View (AV) [2-4] time transfer. The difference is minimal on short links. Long-distance links would benefit through the greater number of observations and the more equal distribution of satellite observation angles, at the price of sensitivity to the corrected time of the satellites.

This paper is presented by a study group of the Working Group on TAI to analyze possible means of combining the set of available time-transfer links to reduce the uncertainties in and increase the robustness of the creation of TAI. The existing theory is described, the utility of using redundant links is discussed, and the importance of monitoring hardware at crossover sites is developed.

II. THEORY OF TIME TRANSFER UNCERTAINTIES

The theory described in this section has recently been developed for numerical computation of the uncertainty of the difference [*UTC-UTC*(*k*)] between Coordinated Universal Time (UTC) and its realization by any laboratory k, UTC(k) [5-7].

UTC is generated by adding leap seconds to TAI. TAI is generated by steering the Free Atomic Timescale (Echelle Atomique Libre, EAL) to a weighted average of the frequencies of primary frequency standards so that the TAI second will realize the SI second. EAL is created by averaging clock data from participating laboratories, whose times are differenced via the several time-transfer links. TAI and EAL are currently created using the minimum necessary number of time transfer links between laboratories. One significant element in the uncertainty analysis is the distinction between link-based uncertainties and site-based uncertainties (Figure 1). Site-based uncertainties depend only on the site and contribute equally to all links involving the site. Link-based uncertainties are a property of the pair of sites that make up the link. They cannot be estimated from separately-computed uncertainties of each site. The total uncertainty of any link is assumed to be the quadratic sum of the link-based

uncertainty and the two laboratories' site-based uncertainties.

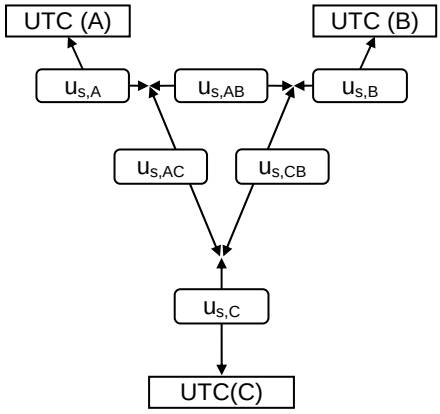

Figure 1. Site-based uncertainties ($U_{s,X}$) and link-based uncertainties ($U_{s,XY}$).

In a network dominated by site-based noise, it makes no difference which links are used to create the non-redundant set. In the example shown in Figure 1, the time transfer between any two sites or clocks A and B is written A-B. Time transfer between A and B achieved by links with C would be written as (A-C) + (C-B). If all uncertainties associated with C are site-based, then A-B is independent of C. Also, the closure of the three signed pair-differences between any three systems, (A-C)+(C-B)+(B-A), is zero. Hence, averaging redundant links would have no effect and TAI would be independent of the topology of any network dominated by site-based noise.

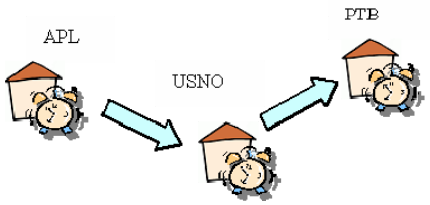

Figure 2. Example in which the USNO is a crossover site if the APL-USNO link is via GPS and the USNO-PTB link is via TWSTFT.

In contrast, link-based noise contributes to the uncertainties between all pairs of laboratories that include the link in the chain of timing links between them. If link-based noise was not negligible compared to site-based noise, the numerical computation of EAL would be topology-dependent. The weight of the primary standards used to measure the frequency difference between TAI and the SI second would also be topology-dependent. Numerical computations show that a system dominated by an equal amount of site-based noise in all links has 50% smaller uncertainties than one dominated by an equal amount of noise per link, but which is link-based [7]. The effects of link-based noise would be reduced by averaging redundant links, and this is investigated below.

The uncertainties of GPS observations are largely site-based because antenna, receiver, and signal-path delays depend only on the satellite in view, the laboratory receiver system, and their geometric relationship. In CV, however, link-based uncertainties are generated through link-dependent sampling in time and observation direction. In unfiltered AV link-based noise is nonexistent because the time and satellite direction samplings do not depend on the link. Link- based noise can exist in filtered AV, if the BIPM applies Vondrak smoothing after generating AV differences between two sites. This can be observed through nonzero closures [8].

The uncertainties of TWSTFT are largely site-based and typically attributed to uncalibrated long-term delay variations in the full signal path. However, some link-dependent effects come into play. Systematic effects are due to the slightly different frequencies used in some links, the slightly different spread-spectrum codes in the links, the link-dependent character of the calibrations, and multiplicative bandpass effects. The latter is due to the overall instrumental delay being the average of the delays at each frequency, weighted by the product of the amplitudes of the two system bandpasses. Link-dependent noise is also introduced from equipment and timescale instabilities between observations.

Of particular interest for TAI-generation are “crossover sites”, which are pivot sites that involve links using different techniques or different equipment. Because the uncertainties in TWSTFT and GPS are completely uncorrelated, at crossover sites even a system dominated by site-based uncertainties acts as if the uncertainties were link-based. In a hybrid situation in which a TWSTFT link is calibrated by GPS, the crossover properties would apply only to the uncertainties that do not involve the calibration.

The topologies used by the BIPM involve a minimum number of pivots, all of which are currently crossover sites. Numerical simulations using the tools developed for references [5-7] have confirmed that such topologies can minimize the overall effect of link-based noise. For example, assume that all TWSTFT observations have link-based uncertainties of 400 ps. In this case the USNO-PTB TWSTFT link could be replaced by a USNO-NPL TWSTFT link, which would act in conjunction with the NPL-PTB TWSTFT link already in use. But this would add the NPL-PTB link's 400 ps uncertainty to every link between the USNO and the European, Asian, Australian, and American laboratories linked to the USNO via NPL. This includes almost every other laboratory, and would raise the uncertainty of [*UTC-UTC*(*USNO*)] due to statistical (type A) errors by 25%, and those of other laboratories by 5-10%.

III. THE CROSSOVER SITES

Although interesting studies of the benefits of averaging different modes of time transfer data are underway [9], in practice the BIPM has followed a strategy of shifting from GPS links to more precise and accurate TWSTFT links. Should the BIPM switch to the AV methodology, link-based noise will virtually disappear from all GPS links. At the crossover sites, however, all site-based GPS and TWSTFT uncertainties, noise, and uncalibrated delay variations will act as if link-based. For this reason the ideal crossover site would have at least two TWSTFT and GPS systems so that instrumental effects can be identified and removed. Traceability to a site maser would be needed so as to have the ability to relate observations made at different times should it be necessary. The environmental effect on observations should be minimized through environmentally insensitive components, with minimal exposure to exterior or even room temperature variations. Multipath due to reflections from exterior structures and to reflections within cables should be minimized. All key components should be monitored electronically and through human oversight. An automated warning system will allow rapid correction of problems, while a postprocessed analysis will ensure data quality.

The current configuration of time links used for TAI (Figure 3) includes four crossover sites: NICT, NIST, PTB, and USNO, with most of the links going to PTB or NICT. To optimize the precision and accuracy of the configuration, it is best to minimize the number of crossover sites, because each one contributes link-based errors that affect all time transfer between laboratories on one side of the site and those on the other side. If one were to measure the overall sensitivity to biases at crossover sites by the product of the weighted number of clocks on each side and the sensitivity of their UTC-measurement to a bias at the crossover site, then one can show that it is almost always better to have fewer crossover sites. It is better to have multiple GPS receivers at any crossover site, if an average bias can be determined by zero baseline CV between the GPS receivers.

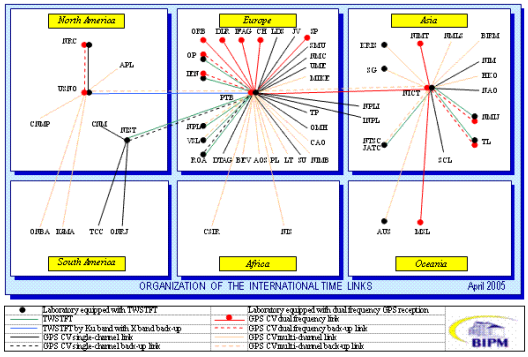

Figure 3. Links used in April, 2005 by the BIPM to generate EAL, and with it TAI and UTC.

In the case of GPS time-transfer via AV the concept of averaging collocated receivers at crossover sites can be extended to a global average over all or most sites that have operational TWSTFT and GPS systems. This averaging can be realized in the form of a least-squares fit to determine one bias parameter per crossover site, with an overall average bias constrained to be zero. The solution to that fit yields extra link calibrations for input into the BIPM's software package used to generate EAL and therefore TAI. Alternately, this fit can be used to monitor the delay variations at the crossover site. A simulation assuming TWSTFT data have 300 ps of link-based noise and that GPS has 100 ps of link-based noise plus 1.0 ns of site-based noise at five TWSTFT and GPS-enabled sites indicated that any bias variation at the crossover site can be identified to within

80 ps. The magnitude of the fitted bias is decreased by the contribution of the crossover site's simulated bias change to the average bias.

IV. USE OF REDUNDANT TWSTFT LINKS

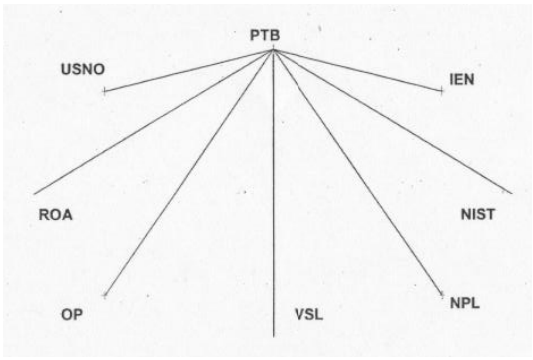

Figure 4. Non-redundant configuration of TWSTFT links in which PTB is the pivot.

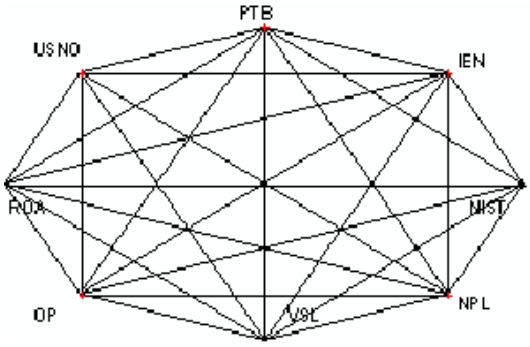

Figure 5. Complete set of European and American TWSTFT links available from sites contributing to previous figure.

It may be possible to improve TWSTFT time transfer through use of redundant links [10-11]. In order to study this, a trial least-squares fit was made using TWSTFT data, taken every 2 hours, from European and North American labs (Figures 4 and 5). The first step was to create a software calibration of all links not involving the reference laboratory, so that they would be consistent with the links between each laboratory and a reference laboratory. Once the calibrations were made consistent, the fits used as reference laboratory either the PTB (the current pivot used by the BIPM, whose time reference is the primary clock CS2 [12] or NPL whose time reference is a maser. These fits determined the time of each laboratory's master clock relative to the reference laboratory, weighting all links equally. No significant statistical reduction in the scatter of the master clock differences was noted between observations, even in the 2-hour intervals. The RMS difference between the actual link between each lab and the PTB differed from the fitted master clock difference between 100 and 400 ps. From this we conclude that no significant precision improvements can be expected from the simplest method of averaging redundant TWSTFT links. The robustness of the system would be improved through averaging, but only if the data inspection and integrity checking procedures were improved commensurately with the increased complexity. Figure 6 shows histograms of the difference between using the direct link to determine [*UTC*(*PTB*)-*UTC*(*k*)] and using the fit, for all October, 2005 data. Figure 7 shows the closure about all possible triplets of North American and European labs in 2005. The results are consistent with an overall link-based uncertainty of 300-400 ps for TWSTFT.

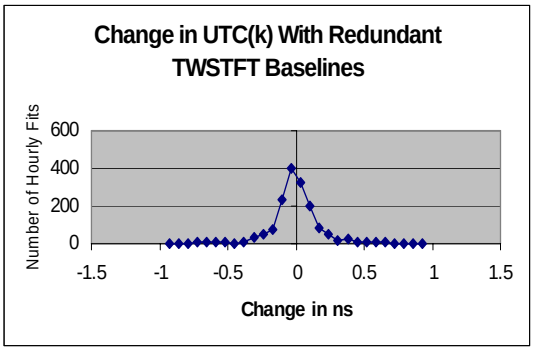

Figure 6. Histogram of differences in UTC(k) generated by including redundant links to TAI-generation. [*UTC*(*k*)-*UTC*(*PTB*) was computed for each hour using redundant links, and differenced with direct measurements.

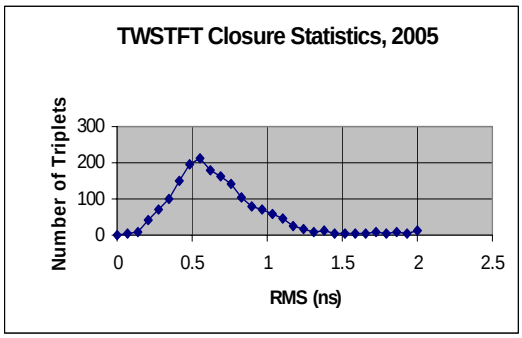

Figure 7. Histogram of hourly closures of available over all triplets of N. American and European labs. RMS was computed from algebraic sum of timing differences for each triplet, and is thus a measure of the link-based noise over the three links.

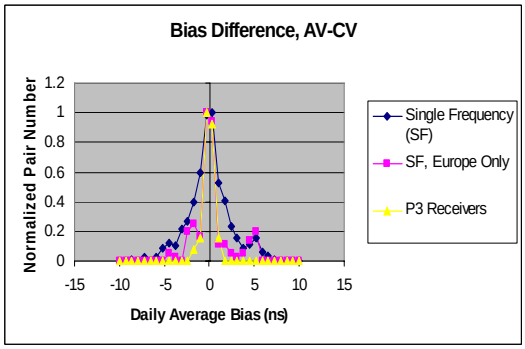

Figure 8. Histogram of daily bias between CV and AV techniques, over all laboratory pairs. differences reflect link-based effects with CV that are not present in AV.

V. USE OF REDUNDANT GPS LINKS

Because unfiltered AV has no link-based noise, no improvement could be expected from averaging redundant AV links. In order to study possible benefits from averaging redundant CV differences, ionosphere and orbit-corrected GPS time transfer data made publicly available by the BIPM were analyzed for the year 2005. Figures 8 and 9 show the biases and RMS differences between AV and CV for all pairs of laboratories. Figures 10 and 11 show analogous histograms of the CV closures among all triplets of laboratories.

Figures 12 and 13 show the average and RMS differences between daily averages of all GPS data taken towards one hemisphere at the site (east or north) and those data taken towards the opposite hemisphere (west or south). Also shown are the differences between all data taken above 30 degrees elevation and between 10 and 30 degrees elevation. These differences cause link-based effects in CV that are not present in AV. Note that northern observations tend to be low-elevation at higher latitudes.

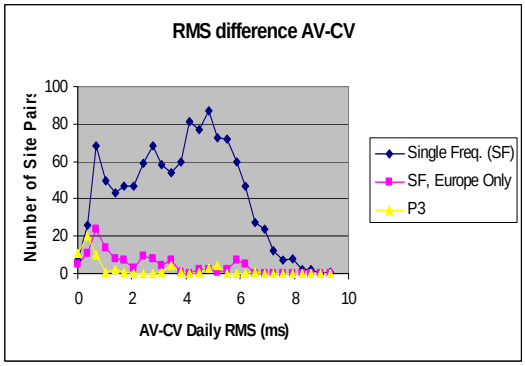

Figure 9. Histogram of RMS of daily difference between AV and CV techniques, over all laboratory pairs.

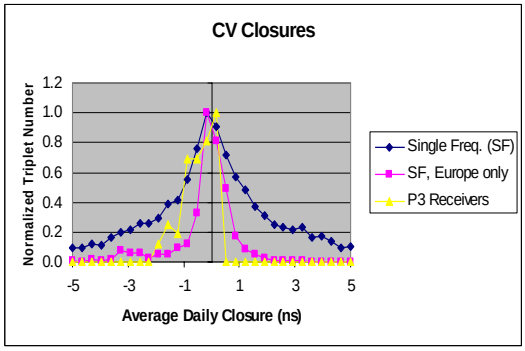

Figure 10. Histogram of bias of closure of daily CV reductions over all lab triplets. Plots are normalized for display.

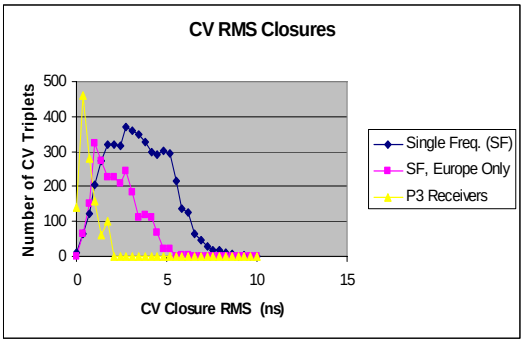

Figure 11. Histogram of RMS of closures of daily CV reductions over all lab triplets. For display, the number of European SF triplets is multiplied by 5, and of P3 triplets by 20.

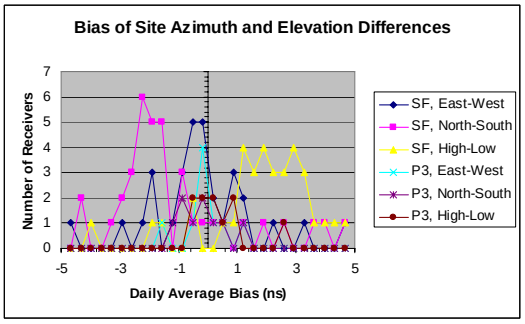

Figure 12. Histogram of difference between daily averages of all GPS observations at different elevations or opposing cardinal directions, for all labs.

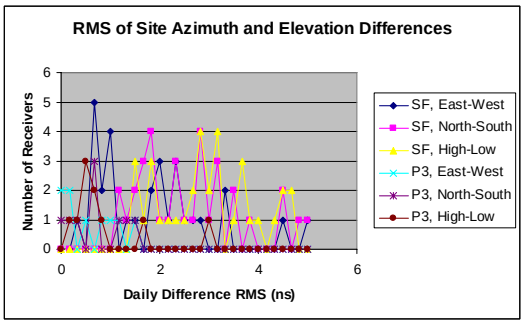

Figure 13. Histogram of RMS of daily difference between averages of all GPS observations at different elevations or opposing cardinal directions, for all sites.

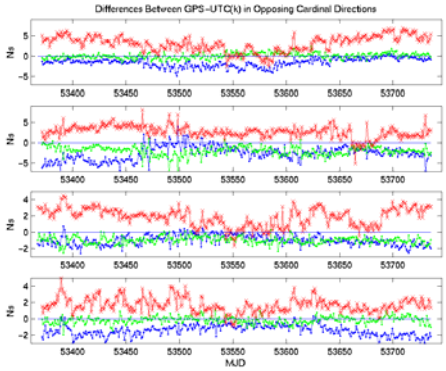

Figure 14. Differences between ionosphere and orbit-corrected single-frequency GPS observations at different elevations or in opposing cardinal directions, from the four crossover sites. Sites from top down are NICT, NIST, PTB, and USNO. North-south differences are shown by a blue dot, east-west differences by a green +, and hi-low elevation differences by a red x. Seasonal effects are apparent. Plots are not to same vertical scale.

Figure 15. Hemispheric differences of orbit-corrected P3 data from three crossover sites. Sites from top down are NICT, PTB, and USNO, and otherwise as in previous figure.

Since the crossover sites are of particular concern, their hemisphere differences are plotted next. Seasonal effects are apparent, as is the higher quality of the P3 data.

For completeness, we also show how the receiver instrumental delay at the L1 frequency has varied between two receivers at each of the 3 crossover sites contributing to the P3 program.

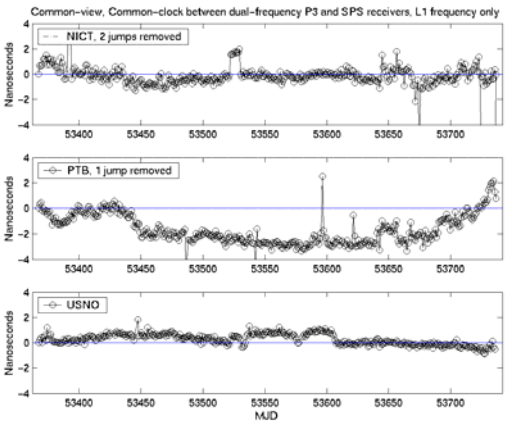

Figure 16. Differential delay variations between the single-frequency and the P3 receivers at 3 crossover sites. Data are common clock and show the variation at the L1 frequency only.

Figures 9-16 show a consistent pattern that CV results in calibration biases and daily scatters at the level of a few ns in single frequency receivers. Inter-European CV data are of higher quality because CV link-based noise increases in long baselines. In general, P3 data show less bias and RMS scatter than the single frequency (SF) receivers; this is likely due to better multipath rejection. However, the geodetic receivers used in the P3 experiment can show sudden calibration jumps at the ns level [13].

Should the BIPM continue using CV, redundant GPS links could be averaged and still conform to the current practices giving 100% weight to all TWSTFT links. A fit would determine the bias between TWSTFT and GPS systems at the crossover sites. It would use TWSTFT link data and all redundant links from those laboratories that do not do TWSTFT, under the constraint that the average bias parameter is zero.

Whether GPS time transfer is achieved by AV or CV, fits that average GPS with TWSTFT are possible. Such averages would also help detect outliers and identify calibration variations.

VI. CONCLUSIONS

The time-transfer links used to generate TAI could be improved through careful monitoring of the TWSTFT and GPS equipment at crossover sites, and analytically determining the bias between them. Use of redundant TWSTFT links may not improve precision, and use of redundant AV links would make minimal difference to precision or robustness. Combining different techniques could lead to still more improvements, but this has not been investigated.

REFERENCES

[1] F. Arias "The metrology of time", Phil. Trans. R. Soc. A, **363**, pp 2289-2305, (2005)

[2] Z. Jiang and G. Petit, "Time Transfer with GPS setellite All-in-View", Proc. ATF 2004, p 236, (2004)

[3] T. Gotoh, "Improvement of GPS Time Link in Asia wih All in View", Proc. 2005 Joint IEEE International Frequency Control Symposium and PTTI Systems and Applications Meeting, pp.707-711, (2005)

[4] M. Weiss, G. Petit and Z. Jiang, "A comparison of GPS Common-View time transfer to All-in-View", Proc. 2005 Joint IEEE International Frequency Control Symposium and PTTI Systems and Applications Meeting, pp. 324-328, (2005)

[5] W. Lewandowski, D. Matsakis, G. Panfilo, and P. Tavella, "The evaluation of uncertainties in [*UTC – UTC(k)*]", Metrologia (accepted for publication in May 2006).

[6] W. Lewandowski, D. Matsakis, G. Panfilo, and P. Tavella, "Refining the uncertainties in [*UTC–UTC(k)*]", Proceedings of the International Frequency Control Symposium/Precise Time and Time Interval Applications System and Planning Meeting (2005)

[7] W. Lewandowski, D. Matsakis, G. Panfilo, and P. Tavella, "Analysis of correlations, and link and equipment noise in the uncertainties of [*UTC–UTC*(*k*)]", subm. to IEEE Transactions on Ultrasonics, Ferroelectronics, and Frequency Control (2006)

[8] Z. Jiang and G. Petit, BIPM Technical Memo **132**, (2004)

[9] J.A. Davis, P.W. Stacey, P.M. Harris, and G. M. Cox, "Combining Time Transfer Measurements Using a Kalman Filter", Proceedings of the 34th Annual Precise Time and Time Interval Applications Systems and Planning Meeting, pp. 53-68 (2003)

[10] Z. Jiang, "Redundancy in the TAI Two Way Time Transfer Network", these proceedings (2006)

[11] G. Petit, "Using a Redundant Time Link System in TAI Computation", these proceedings (2006)

[12] A. Bauch, "The PTB primary clocks CS1 and CS2", Metrologia **42**, pp. S43 – S54 (2005)

[13] R. Dach, T. Schildknecht, U Hugentobler, LG. Bernier, and G. Dudle, "Continuous Geodetic Time Transfer Analysis Methods", IEEE Trans. Ultrason. Feroelectr. Freq Contr., in press (2006)

Proceedings of the 20th EFTF, 2006

Calibration of dual frequency GPS receivers for TAI

G. Petit,[1]* P. Defraigne,[2] B. Warrington,[3] and P. Uhrich[4]
[1] *Bureau International des Poids et Mesures, 92312 Sèvres, France*
[2] *Royal Observatory of Belgium, Avenue Circulaire, 3, B-1180 Brussels Belgium*
[3] *National Measurement Institute, Bradfield Road, Lindfield NSW 2070, Australia*
[4] *LNE-SYRTE, UMR 8630, Observatoire de Paris, 61 avenue de l'Observatoire, 75014 Paris, France.*
**Electronic address:* gpetit@bipm.org

Dual-frequency P-code GPS receivers have been used for time comparisons for several years. They are now standard equipment with units in operation in some 25 time laboratories contributing to TAI. Calibration of these receivers is necessary to ensure the accuracy and long-term stability of time links used in the computation of TAI. A few years ago, only one model of dual-frequency receiver was commercially available and the calibration effort was focused on this receiver. Presently, several different models of receivers are available and used in time laboratories. The paper presents inter-comparison methods and calibration procedures for these three types of receivers, along with some results of differential calibrations. The list of such receivers is due to expand as new models are being introduced.

Disclaimer: Some commercial equipment are identified in this paper in order to describe the experimental procedure adequately. It does not imply recommendation or endorsement by the authors or their institutions.

1. INTRODUCTION

Dual-frequency P-code GPS receivers have been used in geodesy for many years. After their adaptation to the needs of time transfer [1], they have been used for time comparisons in the computation of TAI for several years [2]. They are now standard equipment with several tens of units in operation in nearly half the time laboratories contributing to TAI. Calibration of these equipment is necessary to ensure the accuracy and long-term stability of time links used in the computation of TAI. A few years ago, only one model of dual-frequency receiver (Ashtech Z12T) was commercially available and the calibration effort was focused on this receiver [3,4]. Nearly all units of this type, in operation in TAI laboratories, have been differentially calibrated with respect to one unit from the BIPM travelling to each laboratory. Presently, several different models of receivers are available and used in time laboratories. The paper presents inter-comparison methods and calibration procedures that allow three types of receivers (Ashtech Z12T, Septentrio PolaRx2, Topcon Euro80) to be meaningfully intercompared.

In section II we present the general procedure use to differentially calibrate dual frequency receivers. In section III, we present three such receivers presently used in time laboratories and some results on their calibration are shown in section IV. Finally we discuss the results in section V.

II. CALIBRATION OF DUAL FREQUENCY GEODETIC-TYPE GPS RECEIVERS

Geodetic GPS receivers used for time transfer are characterized by two features: 1. The internal clock of the receiver is driven by an external frequency provided by the laboratory; 2. the receiver accepts an 1PPS input that allows to unambiguously define an "internal reference" from the internal clock. The precise definition of the internal reference may depend on each model of receiver.

Calibration of GPS receivers is usually performed by differential measurements with respect to a travelling receiver, where the two receivers are referenced to the same clock. The usual set-up of each system is that given is Figure 1. We define standard notations to represent the various delays that enter in the procedure of calibration.

X_{Si} is the antenna delay at frequency i.
X_{Ri} is the receiver internal delay at frequency i. The delay is measured from the internal reference, as defined for each type of receiver.
X_C is the delay of the antenna cable.

X_O is the delay from the 1PPS-input to the internal reference.
X_P is the delay from the laboratory reference to the 1PPS-input.

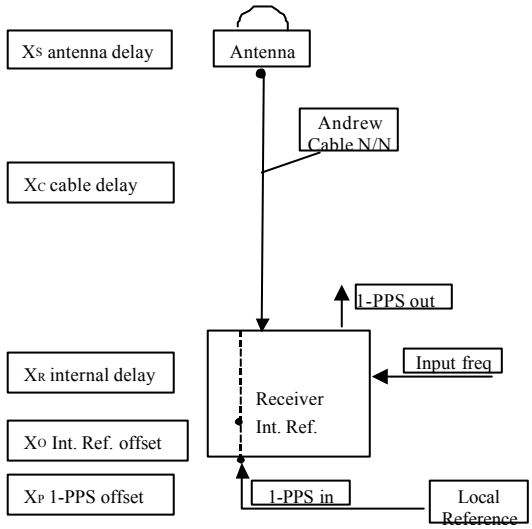

Figure 1: Standard set-up of a receiver showing the definition of the different quantities that enter in the calibration.

Using the above notations, the procedure to carry out the differential calibration of a geodetic-type dual frequency receiver consists of two steps

a) Determine all measurable delays, i.e. the antenna cable X_C and the sum $X_O + X_P$, which relates the internal reference of the receiver to the laboratory reference: The procedure for obtaining X_O depends on each type of receiver and is further described in the next section.
b) Operate the two systems side by side, with independent set-ups, and using the same laboratory clock as a reference ('short-baseline' configuration). The difference in the measured pseudo-ranges at frequency i yields, after taking into account the geometric term due to the different positions of the two antennas, the difference in $X_{Ri} + X_{Si} + X_C - X_O - X_P$ between the two receivers. Thus the values of $X_{Ri} + X_{Si}$ for the receiver under calibration are determined with respect to the travelling receiver.

With less than one day of data, the difference in the pseudo range measurements may easily be performed with a 1σ statistical uncertainty from the measurement noise well below 100 ps. The dominant uncertainty on this quantity is likely to be the sensitivity of the equipment to the temperature and the multi-paths which effect will be different for the two receivers. Overall it is expected that the values $X_{Ri} + X_{Si}$ may be determined with a 1σ uncertainty of order 2 ns at each of the two frequencies, and that the inter-frequency bias may be determined with a 1σ uncertainty of order 1 ns.

III. THREE EXISTING SYSTEMS

III.1. The Ashtech Z12-T

The Ashtech Z12-T receiver performs pseudo-range and carrier phase measurements which are referred to an "internal reference" derived from an externally provided 20 MHz signal. The externally provided 1-PPS signal allows the receiver to unambiguously choose one particular cycle of the 20 MHz to form the internal reference, therefore providing repeatability of this reference in case of any interruption of the tracking or operation of the receiver. According to the Ashtech documentation, we define the internal clock as the input 20 MHz inverted and delayed by 15.8 ns. For some versions of the receiver equipped with a 20 MHz output, the internal clock should coincide with this signal, advanced by 2.4 ns. The internal reference is then defined as the first positive zero crossing of the internal clock following the 1-PPS in signal [3].

The delay X_O between the 1-PPS signal entering the receiver and the internal reference is to be measured with a digital oscilloscope, where the 1-PPS signal triggers the data acquisition. By direct measurement on the oscilloscope display, it is possible to determine the relative phase of the two signals with an uncertainty of a few hundred ps. It is reminded that, for proper operation of the receiver, X_O may not be arbitrary fixed but a small range of values is excluded [4].

As of 2005, the Ashtech Z12-T is no more commercially available.

III.2. The Septentrio PolaRx2

The Septentrio PolaRx2 receiver provides dual-frequency tracking of the GPS signal and simultaneous tracking of up to 6 Space-Based Augmentation System (SBAS) satellites. The receiver accepts a 10 MHz external frequency and an associated 1 pps input. As for the Ashtech Z12T, the receiver internal time scale is synchronized on the 1 pps signal, providing repeatability of this reference in case of any interruption of the tracking or operation of the receiver. The internal clock is 30 MHz frequency, obtained from the input 10 MHz frequency, through a multiplication by 6 followed by a division by two. The receiver synchronizes its

measurement latching with the first low-to-high transition it detects on the 1PPS input connector. The delay between a low-to-high transition on the 1PPS input connector and the latching of the measurements in the receiver is between 221.7 and 255ns (±2ns). The exact delay depends on the phase relationship between the 10-MHz frequency reference and the 1PPS input signal. This delay is constant, and is insensitive to powering off and on the receiver. In order to measure the delay between the 1PPS input pulse and the measurement latching, it is possible to synchronize the 1PPS output signal from the receiver with the measurement latching epoch. The constant offset between the 1pps output and the measurement latching is indicated in Septentrio PolaRx2's documentation: "measurement latching" = "Output 1PPS" plus 8.7 ns (for firmware version 2.3 and higher).

Thus, by measuring the delay from the 1PPS input to the 1PPS output, we have access to the internal reference that we have defined.

III.3. The Euro-80

The Topcon Euro-80 receiver refers pseudo-range and carrier phase measurements to an internal reference oscillator. The receiver provides raw GPS data, including pseudo-ranges and ephemerides, that are used to generate GPS time-transfer data referred to the 1PPS-in, following the standard CGGTTS protocol for common-view data processing. Time-transfer systems developed at the National Measurement Institute in Australia (NMIA) and based on this receiver are in use in a number of laboratories in Asia.

The Euro-160 receiver, in the same OEM family, also accepts an external 10 MHz reference, and an external 1 pps 'event marker' input identifies a particular cycle of the 10 MHz reference as for the Z12-T. Data from this receiver can therefore be processed independently into two standard formats: CGGTTS for time transfer, and RINEX for geodesy. A number of stations in the IGS geodetic network use the Euro-160 as the local receiver, for example including the SYDN node at NMIA in Sydney.

The Euro-80 and Euro-160 receivers are no longer manufactured, but new OEM receivers in the same family are available from Javad Navigation Systems (a five-year agreement between Topcon and Javad expired in September 2005).

IV. SOME CALIBRATION RESULTS

We present some results of differential calibrations for the receivers. For the PolaRx2, the calibration campaign has not yet stared and we only report on the procedure that will be used in coming calibration exercises.

IV.1. Repeated calibrations of Z12-T systems.

The BIPM started regular calibration campaigns for Z12-T receivers in 2001-2002 and some receivers have been calibrated several times. This would allow to estimate the long term (years) stability that can be expected from these receivers, however in many cases the set-up of the receiver is not kept unchanged during several years so that results cannot be meaningfully inter-compared. In Table 1, results of repeated calibrations are shown for three receivers. Two of them (BP0M at the BIPM and PTBB at the PTB) have been kept in a stable set-up and the results indicate consistency at a level of 1 to 1.5 ns peak to peak. The third one displays larger variations (a few ns) which are correlated to set-up changes between 2001 (no antenna splitter), 2002 (one antenna splitter used) and 2004 (two antenna splitters used).

Receiver	Date	Ref.	P1 result	P2 result
BP0M	05/2004	BIPC	Ref - 0.3 ns	Ref + 2.0 ns
BP0M	02/2005	BIPC	Ref - 0.8 ns	Ref + 2.8 ns
BP0M	03/2005	BIPC	Ref - 1.2 ns	Ref + 2.3 ns
BP0M	02/2006	BIPC	Ref - 2.0 ns	Ref + 2.2 ns
PTBB	07/2002	BIPC	Ref - 1.5 ns	Ref - 3.4 ns
PTBB	06/2003	BIPC	Ref - 0.6 ns	Ref - 2.6 ns
PTBB	08/2004	BIPC	Ref - 1.6 ns	Ref - 2.9 ns
OPMT	03/2001	BIPC	Ref + 4.9 ns	Ref + 0.2 ns
OPMT	02/2002	BIPC	Ref + 6.0 ns	Ref + 1.3 ns
OPMT	06/2004	BIPC	Ref + 8.8 ns	Ref + 4.5 ns

Table 1: Results of some repeated calibrations of Z12-T receivers. Note that, for OPMT, the set-up has changed between the measurements (see text).

IV.2 Calibration procedure for the Septentrio PolaRx2.

For this receiver, the delay X_o from the 1PPS input to the "measurement latching" depends on the phase relation between the 10MHz-in and the 1PPS-in, and should be between 221.7 and 255.0 ns (+/- 2ns), as indicated in the receiver manual. We have measured X_o for various values of the phase relation covering the whole range of one 10MHz cycle (Figure 2). For all values of the phase that have been tested, the results are consistent with the stated interval.

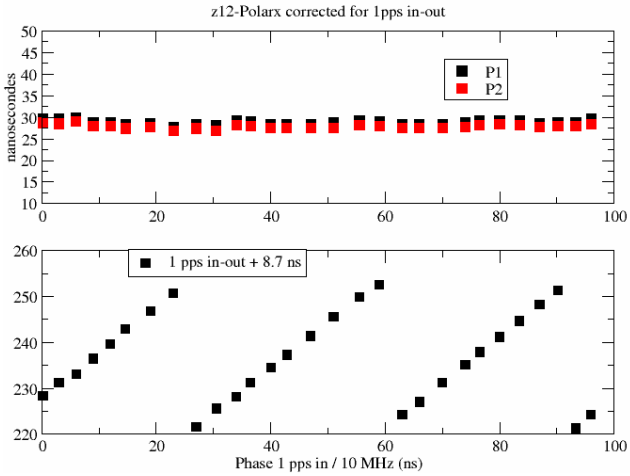

Figure 2: Values of the quantity X_{O} in ns for various values of the relative phase of the input frequency vs. the 1PPS-in (bottom plot). Properly accounting for the measured reference delays, the internal delay of the PolaRx may be obtained vs the Z12-T in all cases (top plot).

In the differential calibration of a complete system "Study" with respect to a reference system "Ref", we have

$$(X_{Ri} + X_{Si} + X_C - X_O - X_P)(\text{Study}) - (X_{Ri} + X_{Si} + X_C - X_O - X_P)(\text{Ref}) = D\text{Pi}$$

where DPi is the average difference of the pseudo-ranges at frequency Li, corrected by taking into account the different positions of the antenna phase centers. Thus, when the reference receiver is in a constant set-up, DPi + X_O(Study) should be constant.

We have tested this for the PolaRx2 receiver, using various values of the phase relation between the 10MHz-in and the 1PPS-in, by comparing the PolaRx2 to an Ashtech Z12T kept in a stable set-up. The results are shown in Figure 2 for the P1 and P2 measurement. The values obtained for DPi + X_O(Study) are indeed constant; the standard deviation of the points measured is 0.5 ns.

We therefore propose the following calibration procedure for the Septentrio PolaRx2 (noted Study); it differs from that of the Z12T only in the determination of X_O.

If the reference receiver is a Z12-T, the values X_O(Ref) and X_P(Ref) are determined according to the usual calibration guidelines.

a) Synchronize the 1PPS output signal from the PolaRx2 receiver with the measurement latching epoch using the command:

"SetPPSParameters 1 0 local"

(or equivalently "spp 1 0 3")

b) Measure the delay between 1PPS-in and 1PPS-out. Then add 8.7 ns to obtain X_0(Study)

c) Measure the delay between local reference and 1PPS-in: X_P(Ref) and X_P(Study).

d) Measure the delay between 1PPS-in and internal reference of the reference receiver: X_O(Ref).

e) Also measure the antenna cable delay X_C(Study).

Obtain a few days of differential pseudo-range measurements and average to obtain DPi.

Then

$$(X_{Ri} + X_{Si})(\text{Study}) = D\text{Pi} + (X_{Ri} + X_{Si} + X_C - X_O - X_P)(\text{Ref}) - (X_C - X_O - X_P)(\text{Study})$$

IV.3. Comparison of different calibrations of Euro-80 systems.

Several different calibration measurements are available for a network of Euro-80 receivers:

a) C/A calibration trips organized by the BIPM, and also by the Asia-Pacific Metrology Program (APMP).

b) Calibration of P1-P2 for a receiver at NMIA obtained using synthetic data from a Global Simulation Systems STR 4760 GPS simulator at the Australian Defence Science and Technology Organisation (DSTO) in Salisbury near Adelaide. The 1σ statistical uncertainty in this value is estimated to be 0.3 ns, and the uncertainty associated with the L1/L2 bias of the simulator is specified to be less than 0.17 ns.

c) Calibration of C/A and P1-P2 delays for Euro-80 systems now in operation at APMP institutes, by transfer from an NMIA receiver calibrated by (a) and (b).

d) During a Z12-T calibration trip in 2005, it was possible to compare the travelling receiver from the BIPM to several Euro-80 units in the Asia-Pacific region. Note that the results presented here compare the P1 measurements from the Z12-T to the C/A measurements from the Euro-80, which are not directly comparable due to different biases in the satellites and in the receiver.

The agreement between these complementary calibration results appears encouraging (see Table 2). In particular, there appears to be good agreement between the two independent methods of determining P1-P2 for the NMIA receiver, with reference to the BIPM Z12-T and to the DSTO simulator. The history of C/A calibration values extends over a number of years, and like the Z12-T suggests good consistency of this internal delay at the level of 2–3 nanoseconds in the best cases.

Note that it is also possible to compare the BIPM Z12-T to the Euro-160 which forms the IGS SYDN node, using data already recorded for both receivers at NMIA,

but this analysis has not yet been completed. Note also that there has not yet been any comprehensive study of the P1-C/A offset for these receivers, as noted above (d).

Receiver	Date	Ref.	C/A result	P1 - C/A	P2-P1 (Z12-sim)
NMIA/DF1	09/2005	BIPC		- 3.8 ns	- 1.6 ns
NMIA/DF1	09/2002	BIPH	37.5 ns		
NMIA/DF1	2005	APMP	42.5 ns		
TL	05/2005	BIPC		-1.5 ns	-1.6 ns
TL	09/2002	BIPH	45.1 ns		
TL	01/2005	APMP	47 ns		
KRISS	08/2005	BIPC		-3.2 ns	-2.1 ns
KRISS	08/2003	BIPK	36.5 ns		
NICT	06/2004	BIPC		0.3 ns	-1.4 ns
NICT	11/2003	BIPK	42.4 ns		

Table 2 Results of different calibrations of Euro-80 receivers. Values in red are nominal values to be presently used in the receivers.

V. CONCLUSIONS

Dual-frequency GPS time receivers are now common-place in the TAI network and are regularly used for TAI links. At least 3 different systems are currently in regular operation, with a few more coming. Calibration of Z12-T systems has been operational for some years and has shown consistency at the level of less than 2 ns peak to peak over several years in the best cases. Calibration of new systems will start soon, that will allow to compute mixed links using dual frequency (P3) code (or code + phase) measurements for TAI links. Other systems using both C/A and P3 codes are operationally used. Inter-comparison with Z12-T shows good consistency of the independent calibrations.

Acknowledgements

We thank the laboratories contributing to TAI that participated to calibration exercises mentioned in this study. BW thanks Peter Fisk for his work developing the Euro-80 time-transfer system and DSTO for use of the simulator.

REFERENCES

[1] T. Schildknecht and G. Dudle, “Time and Frequency Transfer: high precision using GPS phase measurements”, *GPS World*, Feb. 2000, pp. 48-52.
[2] P. Defraigne and G. Petit, "Use of geodetic receivers for TAI", *Metrologia* **40**, 184, 2003.
[3] G. Petit, Z. Jiang, J. White, R. Beard, E. Powers, “Absolute calibration of an Ashtech Z12-T GPS receiver”, *GPS Solutions* 4-4, pp. 41-46, 2001.
[4] G. Petit, Z. Jiang, P. Moussay, “Progresses in the calibration of geodetic type GPS receivers”, Proc. EFTF, 2002.

Proceedings of the 20th EFTF, 2006

Calibration of Six European TWSTFT Earth Stations Using a Portable Station

D. Piester[1,*], J. Achkar[2], J. Becker[1], B. Blanzano[3], K. Jaldehag[4], G. de Jong[5], O. Koudelka[3], L. Lorini[6], H. Ressler[3], M. Rost[1], I. Sesia[6,7], and P. Whibberley[8]

[1]*Physikalisch-Technische Bundesanstalt (PTB), Braunschweig, Germany*
[2]*LNE-SYRTE, Observatoire de Paris (OP), Paris, France*
[3]*Joanneum Research GmbH and Technical University Graz (TUG), Graz, Austria*
[4]*Swedish National Testing and Research Institute (SP), Borås, Sweden*
[5]*NMi Van Swinden Laboratorium B. V. (VSL), Delft, Netherlands*
[6]*Istituto Nazionale di Ricerca Metrologica (INRIM), Turin, Italy*
[7]*Politechnico di Torino, Turin, Italy*
[8]*National Physical Laboratory (NPL), Teddington, UK*
**Electronic address:dirk.piester@ptb.de*

Two-way satellite time and frequency transfer (TWSTFT) has become an important component in the international network for comparing time scales. To employ the full potential of the technique a calibration of the internal delay of each ground station is necessary. Only a few calibration campaigns have previously been carried out in the European network of TWSTFT links. We report on the first recalibration of TWSTFT links during a campaign involving six European time institutes. The campaign was performed using a portable ground station assembled and operated by TUG/Joanneum Research, Graz, that visited the sites of INRIM, NPL, OP, PTB, SP, and VSL, travelling a total distance over 7000 km during a three-week period in October/November 2005. Differential delays of earth stations were determined in the common clock mode relative to the portable station. Combined uncertainties ranging from 0.9 ns to 1.3 ns for all calibrated links were achieved in this campaign.

Keywords: calibration, TAI, two-way satellite time and frequency transfer, TWSTFT, uncertainty budget

I. INTRODUCTION

During the last decade time transfer via geostationary satellites has been developed into a widely used method for remote clock comparisons [1,2]. The two-way technique provides a method of cancelling out unknown delay variations on the signal path. While two-way satellite time and frequency transfer (TWSTFT) has been in operational use it has been shown that remote clocks can be compared at the 10^{-15} level (using a dense measurement schedule) [3] and time scales can be compared with nanosecond accuracy [4]. The latter requires a measurement of the internal delays of the earth stations. This can be done by means of a portable station (PS) which is operated in consecutive experiments side-by-side with the participating earth stations in a common clock set-up. Worldwide only three institutes perform TWSTFT calibration campaigns. These include the United States Naval Observatory (USNO) [5] and the National Institute for Information and Communications Technology (NICT) in Tokyo [6], covering North America and Asia respectively. In Europe, TWSTFT calibrations have been conducted by Joanneum Research, a spin-off of the Technical University of Graz in Austria (TUG). Including the exercise reported here four calibration campaigns have been carried out since 1997 in Europe. The calibration campaigns and the visited institutes are listed in Table 1. The institutes participating in one or more campaigns were the Deutsche Telekom AG (DTAG), the Italian Istituto Nationale di Ricerca Metrologica (INRIM, formerly Istituto Elettrotechnico Nazionale – IEN), the National Physical Laboratory (NPL) of the UK, the French National Metrology Institute for Time and Frequency LNE-SYRTE Observatoire de Paris (OP), the German Physikalisch-Technische Bundesanstalt (PTB), the Swedish National Testing and Research Institute (SP), and the National Metrology Institute Van Swinden Laboratorium B. V. (VSL) in the Netherlands.

In each campaign the measurements at the first site were repeated after visiting all other participating institutes to verify the stability of the portable station during the trip.

Since in every one of the first three campaigns no link was calibrated twice, the 2005 campaign was the first repetition of a TWSTFT link calibration by means of the same technique. Furthermore, the calibration of six earth stations and thus 15 individual links in a single campaign is a record.

After a brief description of the calibration technique (references for a detailed study are given in the text below) and the course of the trip, the results of the single common clock experiments are presented. Thereafter, we discuss the uncertainty budget evaluation including a short analysis of a possible uncertainty impact of PRN code changes which are necessary for the technique used in this work. Finally, we compare the new results with previous calibrations.

II. CALIBRATION TECHNIQUE

The internal delays in TWSTFT earth stations can be observed and measured by suitable equipment and procedures. Because a local absolute calibration of a complete TWSTFT ground station set-up – providing knowledge of the overall internal delay - has not yet been demonstrated, different approaches to measuring the internal delays of ground stations relative to a dedicated standard are in use at present. Three different methods are employed to calibrate TWSTFT links which are part of the worldwide network established for the production of "Temps Atomique International" (TAI) and supervised by the BIPM. One is the use of independent and calibrated time transfer equipment such as GPS receivers. The others make use of a portable TWSTFT station (PS), either as an independent time transfer technique (similar to GPS) (IND) or as a reference to determine the relative delays of the earth stations to be calibrated with respect to the PS (REL). However, only the use of portable TWSTFT equipment has up to now allowed time transfer with nanosecond accuracy. Details of the measurement techniques are described elsewhere: for IND see [4] and for REL see e.g. [9].

Here we give only a rough sketch of the REL method applied in the current campaign. As depicted in Fig. 1, the PS is operated at two different sites *k* and *l*. At each site both stations, the PS and the station to be calibrated,

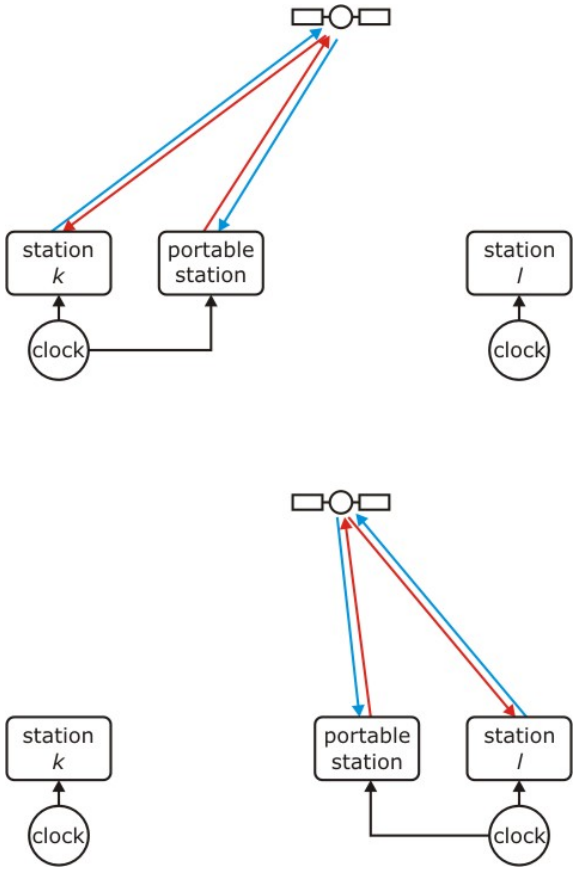

Fig. 1: Schematic of the set-up of the portable station sequentially operated at two different sites *k* (top) and *l* (bottom) to determine the common clock difference (CCD) at each site.

are connected to the same clock. The result of a TWSTFT experiment between the collocated stations (exchanging pseudo-random noise (PRN) signals via a geostationary communication satellite, as described e.g. in Ref. [1]) is the difference of the internal delays of both stations operated in the common clock mode, which is named the common clock difference CCD. After determination of the CCD at at least two sites *k* and *l*, a calibration constant CALR(*k*,*l*) for a time comparison between *k* and *l* can be computed using

Table 1: History of European TWSTFT calibration trips using the portable station of TUG

No.	Year	Participating Institutes	Reference	
#1	1997	TUG-DTAG-PTB-TUG	Kirchner et al.	[7]
#2	2003	IEN-PTB-IEN	Cordara et al.	[8]
#3	2004	PTB-VSL-OP-NPL-PTB	Piester et al.	[9]
#4	2005	PTB-SP-VSL-NPL-OP-INRIM-PTB	this work	

$$\begin{aligned} \mathrm{CALR}(k,l) = {} & \mathrm{CCD}(l,\mathrm{PS}) - \mathrm{CCD}(k,\mathrm{PS}) \\ & + \mathrm{TCD}(l) - \mathrm{TCD}(k) \end{aligned} , \qquad (1)$$

where TCD(i) is the Earth rotation correction (Sagnac effect) for the one-way signal path from the satellite to station i, calculated as described in [10]. Having completed this exercise, the difference between the time scales UTC(k) and UTC(l) can be later determined by routine TWSTFT operations according to

$$\begin{aligned} \mathrm{UTC}(k) - \mathrm{UTC}(l) = {} & \tfrac{1}{2}\left[\mathrm{TW}(k) + \mathrm{ESDVAR}(k)\right] \\ & - \tfrac{1}{2}\left[\mathrm{TW}(l) + \mathrm{ESDVAR}(l)\right] \\ & + \mathrm{REFDLY}(k) \\ & - \mathrm{REFDLY}(l) \\ & + \mathrm{CALR}(k,l) \end{aligned} , \qquad (2)$$

where TW(k) is the result of time-of-arrival measurements at station k of signals transmitted by l and vice versa. ESDVAR(i) is the monitored differential earth station delay variation due to changes in the cabling, etc. This value is set to zero at the moment when a new calibration value is applied. REFDLY(i) represents the relation between the modem time reference and the clock representing UTC(i).

III. THE 2005 CALIBRATION TRIP

The CCDs between six European earth stations and the PS were determined during the campaign described in the following. The campaign started on 19th October 2005 at Graz with measurements on 21st October (MJD 53664) at PTB in Braunschweig, followed by measurements at SP in Borås (24th-25th October, MJD 53667-8), VSL in Delft (28th-29th October, MJD 53671-2), NPL in Teddington (31st October-1st November, MJD 53674-5), OP in Paris (3rd-4th November, MJD 53677-8), INRIM in Torino (6th-7th November, MJD 53680-1), and again at PTB (10th November, MJD 53684). The PS was transported in a van and accompanied by one engineer. However, installation at the laboratories required the support of the local staff. In Figure 2 the route of the van is depicted. A total distance of more than 7000 km required additional overnight stops (open symbols in Figure 2) and days off rest. The campaign was thus completed on 12th November in Graz after 25 days of travelling.

The set-up of the portable station [11] was generally the same as used for previous calibration campaigns. For the set-up and modifications see Ref. [7] and [8,9], respectively. As an example, in Fig. 3 the PS at SP is shown. In the foreground of Fig. 3 a) the outdoor equipment is installed on the roof top of SP just beside

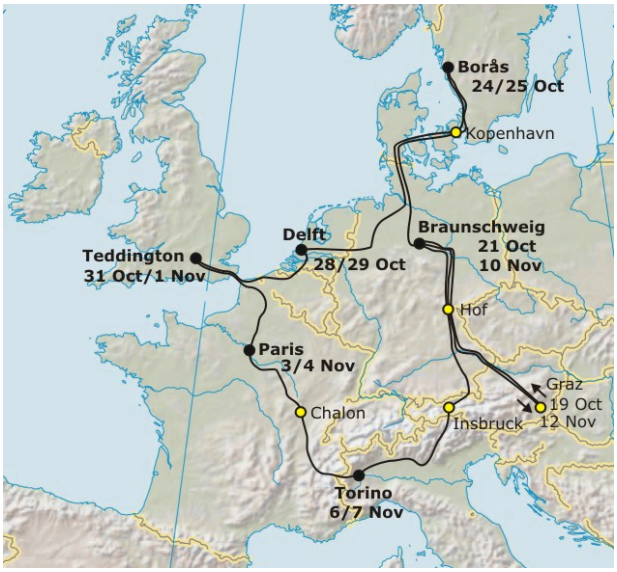

Fig. 2: Route of the calibration trip. Calibration locations and dates are indicated by bold letters, overnight stops by open symbols.

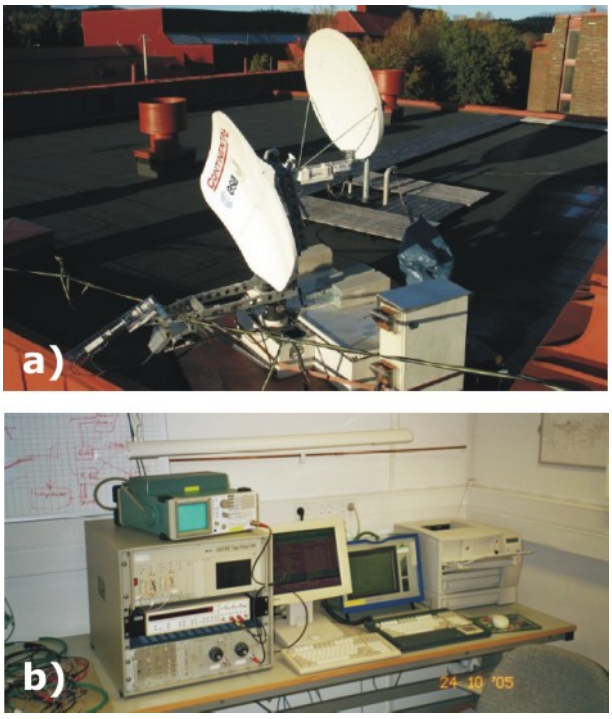

Fig. 3: The TUG portable station collocated at the SP TWSTFT earth station. Photograph a) shows the outdoor set-up and b) shows the indoor set-up.

the outdoor parts of the TWSTFT station to be calibrated. The indoor set-up is shown in Fig 3 b).

To determine the CCD(i) at each site, pseudo-random noise (PRN) phase-modulated spread-spectrum signals

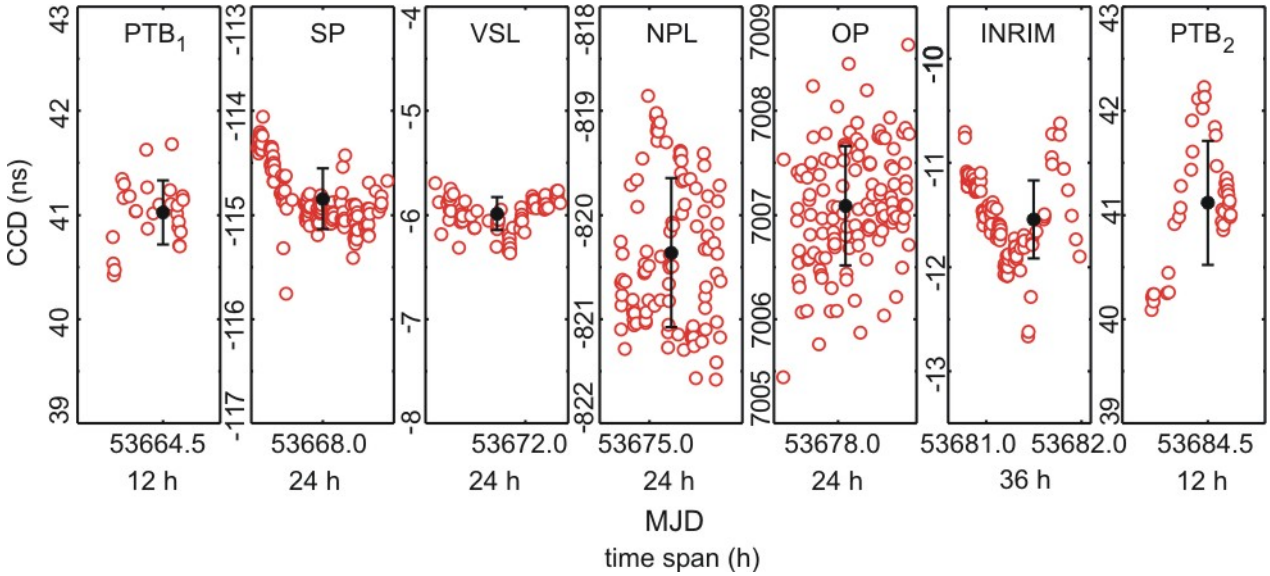

Figure 4: Single CCD measurements (open dots), mean values (solid dots) and standard deviations (bars) of the single CCDs between the PS and the local station.

were exchanged via the Intelsat geostationary satellite IS 707 at 307°E with up- and downlink frequencies of 14013.2 MHz and 12518.2 MHz, respectively. Each station transmitted a predetermined characteristic PRN signal at 2.5 MChip (one of the MITREX compatible codes 0 to 7 [12]), and locked its receiver to the PRN-coded signal of the collocated stations following a predetermined schedule which was added to the routine TWSTFT schedule. A standard session in this schedule consists of 120 time difference values (one measurement each second). The midpoint of a quadratic fit function is calculated at each station *i* and exchanged among the stations, as proposed in the ITU-R recommendations [10]. While every station to be calibrated has its own designated transmission code, the PS switched between several codes following a predetermined schedule. For example, at INRIM the PS transmitted with four different codes, with the MITREX code numbers 0, 2, 3, and 5.

In total 15 TWSTFT links between European time laboratories were calibrated, representing 5 links used by the BIPM in the production of TAI.

IV. RESULTS

Determination of the CCD was done in the same way as in all previous calibration campaigns listed in Table 1. A detailed description is given in Ref. [9]. In the following, only the TAI links are discussed in the text but the results regarding all links are summarised in Tables 2 and 3 to enable future retrospective evaluations of all links. In Fig. 4 the results are depicted. Open dots represent single CCD measurements; the mean values and standard deviations around the mean are depicted as full dots with error bars. The standard deviation is a useful measure of the data scatter if they are randomly distributed. However, some measurement series (INRIM, PTB_2 and to some extent SP, VSL) show significant drifts. These drifts are not visible in the internal REFDLY measurements of the PS and do not occur at every site and must therefore be attributed to instabilities in the local 1pps distribution or frequency distribution system or the local TWSTFT station being calibrated. For example, the course of the CCD values measured at INRIM correlates with the environment temperature. However, the origin of the drifts as well as the difference in the data scatter is not well understood at present and should be investigated in future calibration exercises.

Table 2: Results of the common clock differences (CCD) and standard deviations (SD) together with the station-associated Sagnac “downlink” correction (TCD).

station	CCD (ns)	SD (ns)	TCD (ns)
IEN01	279.528	0.304	134.441
IEN02	-11.543	0.375	134.441
NPL01	-820.363	0.716	108.152
OP01	7007.088	0.573	118.128
PTB01	41.071	0.495	119.383
SP01	-114.844	0.294	106.383
VSL01	-5.988	0.158	113.149

The calibration results shown in Fig. 2 are summarized in Table 2. Note that INRIM calibrated two stations: IEN01 and IEN02. If the link to INRIM is discussed in the following, only the station IEN02 is referred to. The highest standard deviation (SD) of the CCD(i) is 0.7 ns; the average SD is 0.416 ns.

The resulting calibration constants CALR(k,l) appearing in Eq. 2 are listed in Table 3. For completeness all link combinations and the associated uncertainty budgets are given. The overall uncertainty U for one link is the geometric sum of the single uncertainty contributions listed in the table. $u_{A,i}$ is the standard deviation of the single CCD(i) from its mean. Ideally the determination of the two CCD(i) for one link calibration should be performed simultaneously. In practice this is not possible. An estimate of the stability of the stations involved can be derived from the two measurements at PTB, the initial and the closure. The mean values of both measurements show excellent agreement, 41.025 ns and 41.116 ns respectively. However there is a significant drift in CCD values, especially during the closure measurements, and thus the standard deviation of the second data set is much bigger than the difference between both mean values. We account for this by applying the "combined" SD of the initial and the closure measurement $u_{B,1}$ = 0.671 ns. The PS has to be related to the local UTC(i) which requires a measurement of the UTC(i) reference with the PS's time interval counter (TIC) for REFDLY(i) determination. We take this into account by applying $u_{B,2}$ = 0.5 ns according to the TIC specifications. $u_{B,3}$ reflects all other systematic errors, e.g. the stability of the connection to the local UTC (0.1 ns), possible influence of code changes, Tx and Rx power, C/N_0 (overall 0.2 ns). PTB used a portable caesium clock to connect the PS to UTC(PTB). Thus an additional 0.3 ns uncertainty is assumed for links where PTB is involved. The total estimated 1-σ uncertainty ranges from 0.9 ns to 1.3 ns.

As mentioned, the TWSTFT calibration in the REL mode requires the use of additional PRN codes compared with the routine link operation between the ground stations. In principle, a time transfer measurement should be independent of the PRN code used. However, delay changes of up to 0.5 ns coinciding with code changes were reported [13]. We tested whether a significant delay change occurred if the PRN codes in use were changed. The test measurements were part of the predetermined schedule which was repeated every two hours. Thus, the code sequence was repeated

Table 3: Calibration constants and uncertainty budget (1-σ) of all links between two stations k and l. CALR and U values are applied in the data files according to Ref. [10], rounded to one decimal place.

Link k-l	CALR(k,l) (ns)	$u_{A,k}$ (ns)	$u_{A,l}$ (ns)	$u_{B,1}$ (ns)	$u_{B,2}$ (ns)	$u_{B,3}$ (ns)	U (ns)
IEN01 – NPL01	-1126.180	0.304	0.716	0.671	0.5	0.22	1.163
IEN01 – OP01	6711.247	0.304	0.573	0.671	0.5	0.22	1.081
IEN01 – PTB01	-253.515	0.304	0.495	0.671	0.5	0.37	1.084
IEN01 – SP01	-422.430	0.304	0.294	0.671	0.5	0.22	0.963
IEN01 – VSL01	-306.808	0.304	0.158	0.671	0.5	0.22	0.931
IEN02 – NPL01	-835.109	0.375	0.716	0.671	0.5	0.22	1.184
IEN02 – OP01	7002.318	0.375	0.573	0.671	0.5	0.22	1.103
IEN02 – PTB01	37.556	0.375	0.495	0.671	0.5	0.37	1.106
IEN02 – SP01	-131.359	0.375	0.294	0.671	0.5	0.22	0.988
IEN02 – VSL01	-15.737	0.375	0.158	0.671	0.5	0.22	0.956
NPL01 – OP01	7837.427	0.716	0.573	0.671	0.5	0.22	1.261
NPL01 – PTB01	872.665	0.716	0.495	0.671	0.5	0.37	1.263
NPL01 – SP01	703.750	0.716	0.294	0.671	0.5	0.22	1.161
NPL01 – VSL01	819.372	0.716	0.158	0.671	0.5	0.22	1.134
OP01 – PTB01	-6964.762	0.573	0.495	0.671	0.5	0.37	1.188
OP01 – SP01	-7133.677	0.573	0.294	0.671	0.5	0.22	1.079
OP01 – VSL01	-7018.055	0.573	0.158	0.671	0.5	0.22	1.050
PTB01 – SP01	-168.915	0.495	0.294	0.671	0.5	0.37	1.081
PTB01 – VSL01	-53.294	0.495	0.158	0.671	0.5	0.37	1.052
SP01 – VSL01	115.622	0.294	0.158	0.671	0.5	0.22	0.927

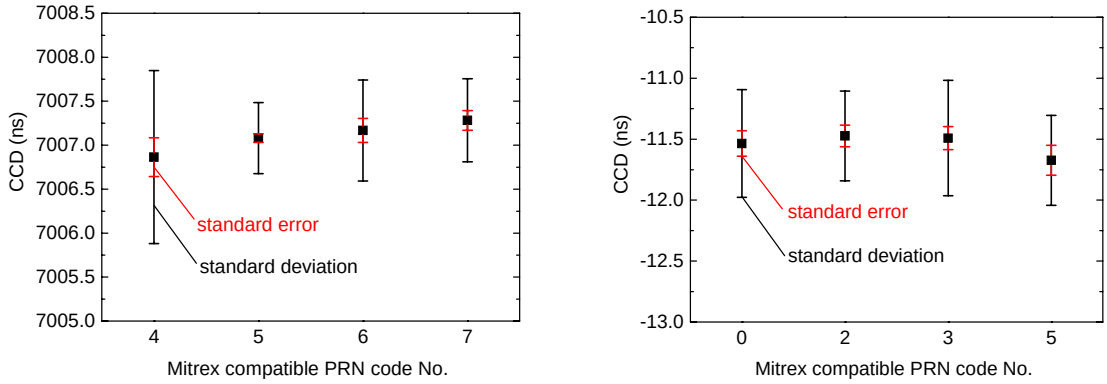

Figure 5: Two examples of using different codes at the Tx channel of the PS. The left (right) graph CCD measurements at OP (INRIM) arranged according to the codes used by the PS.

several times when the PS was operated for around one day at some sites. In Figure 5 two examples of the CCDs sorted by the associated PS codes are shown. For example, when the PS was operated at OP, MITREX codes 4, 5, 6, and 7 were used (see left graph) while at INRIM (right graph) the codes 0, 2, 3, and 5 were employed. No significant dependency of the CCD(*i*) on the code used is observed. If we take the deviation of the mean, the so-called standard error (SE), instead of the SD, it can be seen that the 1-σ error bars of code 4 and 7 (left graph) do not overlap. However, SE reflects the uncertainty of the mean only if the single measurements are normally distributed.

V. HISTORY OF EUROPEAN TWSTFT TAI-LINKS

Except for the links to SP, whose TWSTFT equipment was recently installed and thus had not been calibrated, all other links had been calibrated before by means of TWSTFT. However, various events may have degraded the calibration uncertainties achieved previously, e.g. the change of the satellite used affected all links, and major setup changes happened at VSL. Comparison of the present CALR values (column 2 in Table 3) with previous ones requires some caution. The uncertainty of the CALR(*i*) values had to be adjusted after satellite or even transponder frequency changes and the uncertainty was increased as a result (see e.g. Ref. [4]). The earth station delay variations ESDVAR(*i*) (see Ref. [10]) changed due to equipment modifications which may have introduced additional uncertainty.

In Fig. 6 the long term records of the differential corrections of the European TAI links UTC(*i*) – UTC(PTB) are depicted. The links to INRIM, NPL, and OP were initially calibrated using Circular T (i.e. relying on GPS measurements and calibration), and were calibrated with the TWSTFT technique in 2003 (INRIM) and 2004 (NPL, OP). For each link the left coloured bar (± 5 ns) reflects the uncertainty of the GPS calibration. In the case of VSL the uncertainty of a clock transportation from PTB to VSL is shown which was never applied in the TWSTFT evaluation (see Ref. [9,14] for details). The differential corrections of the 2003 and 2004 campaigns are labelled with the "serial" number as given in Table 1. Each time a new calibration is applied the time transfer uncertainty is estimated at the nanosecond level. This uncertainty is increased whenever an occurrence renders continuous TWSTFT operations impossible. Increased error bars and labels indicate the date and what had happened (e.g. IS706 – IS903 for a satellite change and IEN01-IEN02 for a station change).

The actual calibration values deviate only slightly from previous values in the case of the links IEN01 – PTB01 (-0.76 ns), NPL01-PTB01 (-0.62 ns), and OP01-PTB01 (-1.53 ns). The mean of these changes, -0.97 ns, indicates a potential instability of the PTB01 earth station. The differential correction of the links IEN02-PTB01 (+2.5 ns) and VSL01-PTB01 (+12.1 ns) are unexpectedly large. However, the change from IEN01 to IEN02 was necessary due to a failure of hardware components of IEN01 and thus happened without sufficient time to determine the CALR for IEN02. In the case of VSL the setup was disassembled and rebuilt due to the move of the whole time laboratory to a different building over a distance of about 3 km. Both experiences prove that it is highly desirable to recalibrate a TWSTFT earth station after major setup changes to keep the uncertainty at the 1 ns level. The link SP01-PTB01 (+7.9 ns) had not been calibrated before but a comparison with Circular T (i.e. with GPS CV time transfer) shows very good agreement, within the estimated uncertainty of the GPS calibration

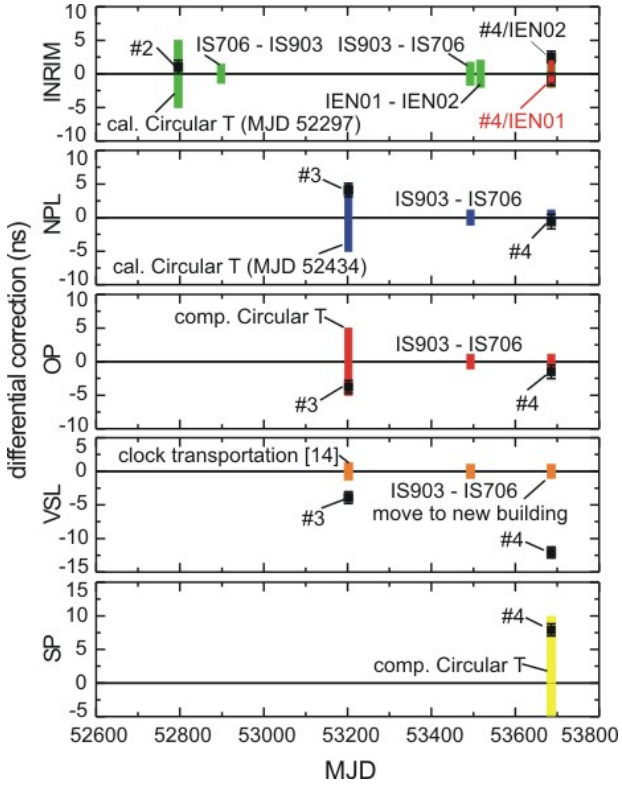

Figure 6: Differential corrections applied to the European TWSTFT links UTC(*i*) – UTC(PTB) contributing to TAI from MJD 52600 (Nov 2002) to MJD 53800 (Mar 2006). The error bars reflect the estimated uncertainty of the calibration; the coloured bars represent the estimated uncertainty of the link at the day of calibration including uncertainties due to possible bridging procedures.

($u_B = \pm 10$ ns) [15]. Note that the calibration was performed back in 1997 using a single channel single frequency GPS receiver.

VI. CONCLUSION

The differential delays of six European TWSTFT earth stations were determined by using a portable TWSTFT station. The whole campaign spanned over 7000 km and was conducted by one engineer during 24 days of travelling. Calibration constants with estimated uncertainties down to 0.9 ns were achieved. In this first recalibration of TWSTFT calibrated time links an average reproducibility of 0.97 ns is consistent with the estimated uncertainties of the links and of the calibration values.

ACKNOWLEDGEMENTS

The enormous efforts of Bernd Blanzano during the transport and operation of the portable station during the whole of the campaign are gratefully acknowledged by the other authors. Free satellite transponder time was generously provided by INTELSAT on IS 707. We thank Andreas Bauch for a critical reading of the manuscript.

REFERENCES

[1] D. Kirchner: Two-Way Time Transfer Via Communication Satellites; *Proc. of the IEEE*, vol. 79 (7), pp. 983-989, 1991.

[2] D. Kirchner: Two-Way Satellite Time and Frequency Transfer (TWSTFT): Principle, Implementation, and Current Performance; *Rev. of Radio Science*, Oxford University Press, pp. 27-44, 1999.

[3] A. Bauch, J. Achkar, S. Bize, D. Calonico, R. Dach, R. Hlavać, L. Lorini, T. Parker, G. Petit, D. Piester, K. Szymaniec, P. Uhrich: Comparison between frequency standards in Europe and the US at the 10^{-15} uncertainty level; Metrologia, Vol. 43, No. 1, pp. 109-120, 2006.

[4] D. Piester, A. Bauch, J. Becker, T. Polewka, A. McKinley, D. Matsakis: "Time Transfer between USNO and PTB: Operation and Calibration Results"; *Proc. of the 35th PTTI*, San Diego, December 2003, pp. 93-101, 2004.

[5] L. Breakiron, A. L. Smith, B. C. Fonville, E. Powers, D. N. Matsakis: The Accuracy of Two-Way Satellite Time Transfer Calibrations; *to be published in Proc. of the 36th PTTI*, Washington, DC, December 2004.

[6] M. Fujieda, personal communication, 2006.

[7] D. Kirchner, H. Ressler, P. Hetzel, A. Söring: The calibration of three European TWSTFT stations using a portable station and comparison of TWSTFT and GPS common-view measurements; *Proc. of the 27th PTTI*, Reston, December 1998, pp. 365-376, 1999.

[8] F. Cordara, L. Lorini, V. Pettiti, P. Tavella, D. Piester, J. Becker, T. Polewka, G. de Jong, O. Koudelka, H. Ressler, B. Blanzano, C. Karel: Calibration of the IEN-PTB TWSTFT Link with a Portable Reference Station; *Proc. of the 18th EFTF 2004*, Guildford, April 5-7, paper 137, 2005.

[9] D. Piester, R. Hlavac, J. Achkar, G. de Jong, B. Blanzano, H. Ressler, J. Becker, P. Merck, O. Koudelka: Calibration of four European TWSTFT Earth Stations with a Portable Station through Intelsat 903; *Proc. 19th European Frequency and Time Forum - EFTF 2005*, Besancon, France, 21-24 Mar 2005, pp. 354-359, 2006.

[10] Recommendation ITU-R TF.1153-2. The operational use of two-way satellite time and frequency transfer employing PN time codes; Geneva, last update 2003.

[11] O. Koudelka, H. Ressler, B. Blanzano: Two-Way-Satellite-Time-Transfer Calibration Campaign, *Report: IAS.2005.AF.009-01*, Joanneum Research, Graz, 2005.
[12] P. Hartl, N. Gieschen, K.-M. Müssner, W. Schäfer, C.-M. Wende: "High Accuracy Global Time Transfer Via Geosynchronous Telecommunication Satellites with Mitrex", Z. Flugwiss. Weltraumforsch. Vol. 7, No. 5, pp. 33-342, 1983.
[13] F. Ascarrunz, S. Jefferts, T. Parker: Earth Station Errors in Two-Way Time and Frequency Transfer; IEEE Trans. Inst. Meas., Vol. 46, No. 2, pp. 205-208, 1997.
[14] D. Piester, P. Hetzel, A. Bauch: Recent Time and Frequency Activities at PTB, Proc. Of the 34th PTTI, Reston, Virginia, USA, Dec 2002, pp. 365-376, 2003.
[15] Circular T 214, BIPM, November 2005, see http://www.bipm.fr/en/scientific/tai/time_ftp.html.

Proceedings of the 20th EFTF, 2006

Redundancy in the TAI TWSTFT Time Transfer Network

Z. Jiang and G. Petit
Bureau International des Poids et Mesures (BIPM)
zjiang@bipm.org

TWSTF (TW) is a precise time transfer technique and has being used to generate the TAI since 1999. From the beginning with only 3 measured points per week over a few baselines to now 12-24 points per day and measured as a worldwide network, the TW observable becomes highly redundant. However single baseline is still the only geometry in TAI time transfer practice. As shown in Fig. I-1, among the 35 measured links carried out by 9 European-American TW laboratories, only the 8 links directly with PTB (double lines) are used for the TAI computation. The rest 27 links are in fact wasted. Generally, for a network of N points, there are N(N-1)/2 measured links. The actual European-American TW network is consisted of 12 TW laboratories. This situation that TW links are measured as a network but still used as single baselines is becoming more and more critical with the recent increase of the number of the TW laboratories, especially in Asia-Pacific areas. This is only the geometry redundancy. The TAI network is redundant also in multi-techniques.

Unlike GPS, the TW links are independently measured. Theoretically, the sum of the three link vectors of a triangle should be zero. This is called a triangle closure condition. The triangle closures are the true errors that provide a good measure of the measurement errors and meanwhile a reasonable constrain to adjust the TW observations.

Based on the triangle closure analysis, the authors propose a global network least square adjustment to fully use the redundant information. The traditional TW baseline transfer is then becoming a network time transfer. When the adjustment is performed epoch independently without any constraint between the measurement epochs, the comparison between the Allan and Time Deviations of before and after the adjustment can be used to judge the ameliorations. They show a considerable improvement in the time transfer stability. This adjustment model allows introducing other observations, parameters and constrains so as to adjust altogether the total redundancies of the TAI network. Although TW links take only 12% of the total TAI links, they transfer more than 60% of the total weighted clocks and most of the primary frequency standards contributing to TAI. Improving the stability of the TW links implies a direct improvement in the uncertainties of TAI and UTC.

I. Introduction

Nowadays, the TW time transfer is one of the most precise techniques thanks to its symmetric measuring procedure. The uA (uncertainty type A) of the TW link is declared to be about 0.5 ns. This implies that the uncertainty of a three link closure in a triangle geometry, that is, the sum of the three link vectors of the triangle, should be about $\sim\sqrt{3}$ *0.5 ns or 0.9 ns. However the link closure analysis shows that the closures may be up to 2 or even more. The baseline dependent uncertainties due to probably the local and global environment variations would be responsible. Recently reported diurnal disturbances in TW links may be up to 1 or 2 ns peak to peak [5]. These errors would cover the advantages of the TW links. Are we at the limit of this technique? On the other side, the discrepancy that the TW are measured as a network but used as single baselines tells us a lot of TW measures are wasted. As show the Fig. I-1 and Tab. I-1, among the 66 measured links in the 12 European TW labs, only 11 official links are used for the TAI. The 55 measured redundant links do not contribute anything to TAI.

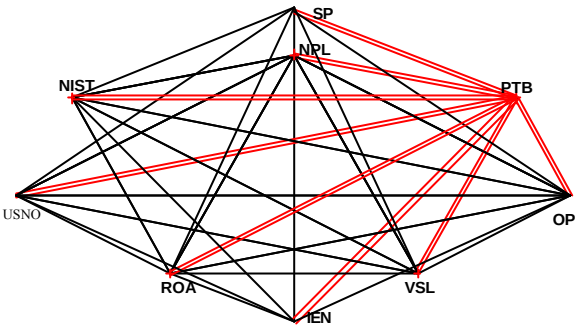

FIG. I-1: Status of the measured European-American TW network in Aug. 2005 and the actual TAI pivoted single baseline time transfer geometry (double lines)

Lab. Number	Total Links	TAI Links	Redundant Links
3	3	2	1
7	21	6	15
8	28	7	21
12	66	11	55
20	190	19	171

TAB. I-1 TAI and redundant links in a TW network

We propose a least square network adjustment to fully use the potential of the total measured links. The adjustment gives also the estimation of the baseline dependent measurement error information: the link corrections on every measuring epoch and their variances.

Like in geometry, the sum of tree measured internal angles minus 180° is the *true* error. A closure of the 3 link vectors in a triangle is also the *true* measurement error because the three clocks involved are removed (Fig. I-2, eq. 1-1, 1-2). The adjustment proposed is based on the closure analysis. We do not need complex hypothesis to complete its mathematical model. After the adjustment the network becomes structurally more homogeneous and more robust than the traditional single baseline time transfer with all the closures being zero. This "network approach" contributes also to better understanding the non-zero closures due to measuring and calibration errors.

Modified Allan and Time Deviations are useful tools to examine the instability of transfer techniques. Because the least square adjustment is, theoretically and practically, completely independent of the Allan stability theory, the two deviations are the objective index to verify the improvement in the adjusted time links. By the least square theorem, we can predict that most part of the improvement is in the white phase segment.

The adjustment of a network can be of free or fixed or quasi-stable. The latter may be used for the calibration of the TW equipment. If in a network, there are well calibrated links, we may relatively calibrate the others with the uncertainty of the TW using the closure conditions in the whole network.

I-1 Redundancies in the TAI TW network

The redundant observable is the back up observable that is measured but not used. TAI network is highly redundant, not only in geometry but also in density and multi-techniques.

LAB	TAI link	back up 1	back up 2	back up 3
NIST	TW	P3	SC	SC
IEN	TW	P3	MC	SC
USNO	TW	TW-Xband	P3	MC
NPL	TW	P3 (CP)	MC	SC
NICT	P3	TW	MC	SC
OP	TW	P3	MC	SC
PTB	TW	P3	MC	SC

TAB. I-2 Examples of the redundancy of multi-techniques in the TW laboratories

Geometric redundancy: As shown in Fig. I-1 and Tab. I-1, TW is measured as network but used as single baseline. Geometrically, if there are N laboratories, the Number of total links $=N(N-1)/2$ and the Number of independent triangle closures $= N(N-1)/2-(N-1)=(N^2-3N+2)/2$. In Fig. I-1, N=9, there are 8 TAI links against totally 36 measured links and 36-8=26 redundant links. This situation is becoming more critique as new TW laboratories are coming, especially in Asia-Pacific areas.

Density redundancy: Since Oct. 2005, density of the TW measurement is augmented from 4 to 12 points/day. In Asia-Pacific areas, there are 24 measured points/day since Nov. 2005. For TAI computation, only 2 points are used per 5 days while 60-120 points are measured per 5 days.

Multi-technique redundancy: All the TW laboratories are backed up at least one GPS techniques: GPS C/A code or/and P3-carrier phase receivers. As shown in Tab. I-2.

I-2 Closure and the baseline dependent errors

Each triangle is consisted of three link vectors. The sum of the three vectors is a closure *'C'* which is in most cases non-zero (Fig. I-2, I-3 and Tab. I-3):

$$C = \mathrm{Link}_1+\mathrm{Link}_2-\mathrm{Link}_3 = [\mathrm{UTC(B)-UTC(A)} + V_1] - [\mathrm{UTC(B)-UTC(C)} + V_2] - [\mathrm{UTC(C)-UTC(A)} + V_3] \quad (1\text{-}1)$$

Here, V_1, V_2 and V_3 are the estimations of the baseline dependent measurement errors in Link_1, Link_2 and Link_3. Removing parentheses, we have the fundamental relation between the closure and the baseline dependent errors:

$$C = V_1 + V_2 + V_3 \quad (1\text{-}2)$$

The purpose of the adjustment is to determine the values V_1, V_2 and V_3: called usually in the least square adjustment the adjusted corrections and the estimation of their adjusted mean square errors or variations.

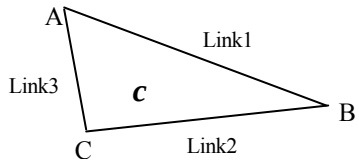

Fig. I-2 Closure of a triangle ? (A,B,C)

The closure values and their variations may be up to several ns, much bigger than the given uncertainty of the TW techniques. The raison of the non-zero closures or the baseline dependent errors is complex. In general, it may be due to: the hardware of the Satellite-TW equipment; direct or indirect effect of the temperature variations; the errors in the data treatment (interpolation etc.); uncertainties of the measurements, calibrations… We have shown the diurnal disturbances in TW would be of an order of 1 ~ 2 ns peak to peak [5].

If we do not use the CALR and ESDVAR values in the ITU TW data file, the calibration uncertainties should not appear in the closures. And if the CALR and ESDVAR values are not exact, we should also have the non-zero closures:

$$(CALR_1 + ESDVAR_1) + (CALR_2 + ESDVAR_2) - (CALR_3 + ESDVAR_3) = C \text{ (Calibration)} \qquad (1\text{-}3)$$

As we know, the CALR and ESDVAR values are constant (with uncertainty uB) which should not mixed with the TW link measurement uncertainties (uA). Therefore, the least square adjustment would be carried out in two steps with and without the CALR and ESDVAR values. In this paper, we discuss mainly the linking measurement errors uA. In the following discussion, by default, the CALR and ESDVAR are not taken into account.

```
 PicoSec|No.|
   -1250|  1| +
   -1000|  4| ++++
    -750|  3| +++
    -500|  9| +++++++++
    -250| 13| +++++++++++++
       0|  9| +++++++++
     250| 14| ++++++++++++++
     500| 17| ++++++++++++++++++
     750| 10| ++++++++++
    1000|  4| ++++
    1250|  3| +++
    1500|  0|
    1750|  1| +
```

FIG. I-3 Histogram of the closures of the triangle ? PTB-VSL-OP with mean=0.16 and rms=0.60ns

Triangle	53404	53409	53414	53419	53424	53429
PTB IEN NIST	1.0	-0.3	0.6	0.4	-0.2	0.0
PTB NIST NPL	1.0	0.4	0.1	-0.1	0.8	0.2
PTB NPL VSL	1.3	0.8	0.5	1.3	0.2	1.0
PTB VSL OP	-0.7	-0.1	0.4	0.3	0.7	3.1
PTB OP ROA	-0.1	-0.1	0.1	-0.1	-0.3	0.4
PTB ROA USNO	-1.3	-2.0	-1.5	-0.9	-0.7	-1.4
IEN NIST NPL	1.9	-0.4	-0.5	-0.3	-0.8	2.4
IEN NPL VSL	4.7	5.6	6.5	5.4	6.2	3.8
IEN VSL OP	0.0	-0.7	-0.6	0.6	-0.8	1.6
IEN OP ROA	-3.7	-3.6	-3.8	-3.8	-3.9	-2.6
IEN ROA USNO	-0.9	-0.4	1.5	2.6	2.4	0.8
IEN USNO PTB	-0.8	-1.8	-2.9	-3.6	-2.6	-2.7
NIST NPL VSL	2.8	-0.4	-1.0	-0.8	-0.1	1.2
NIST VSL OP	-2.6	-0.7	0.0	0.6	0.6	1.6
NIST OP ROA	0.1	0.2	0.0	0.1	-0.6	0.7
NPL VSL OP	0.1	0.3	0.3	1.0	0.2	0.6
NPL OP ROA	0.1	-0.1	0.2	0.3	0.3	0.5
NPL ROA USNO	-1.2	-0.9	-0.1	1.0	-0.7	2.5
NPL USNO PTB	0.2	-0.7	-0.9	-1.7	0.1	-0.5
VSL OP ROA	-0.6	-0.8	-0.1	-0.4	-0.1	-2.2
VSL ROA USNO	-2.4	-1.0	-0.1	0.6	0.6	5.4
VSL USNO PTB	0.9	-0.4	-0.8	-0.9	-0.8	-1.1
OP ROA USNO	-0.7	-1.0	0.3	0.0	-0.2	0.0
OP USNO PTB	-0.7	-1.1	-1.7	-1.0	-0.8	-1.0

TAB. I-3 Triangle closures on standard MJD of TAI0502 (Feb. 2005)

I-3 General considerations of the adjustment

What we will obtain by the least square adjustment? Briefly: Detect the non random errors; Determine the linking measurement errors so as to improve the time link stability; Estimate the uncertainty of time links, etc.

II. Mathematical Model

Adjustment with the Closure condition

In metrology practice, it is rare to know the true uncertainties. Usually, we estimate the uncertainties based on some assumes or statistical methods. However the link triangle closure C is a true error. Although the baseline dependant errors V_1, V_2 and V_3 are determined with the least square laws but the sum of them is known as true value (eq. I-2). We call this the *'closure condition'*. It gives an idea control for the adjustment and a hint of how to adjust the linking errors. The estimated V_1, V_2 and V_3 and their variances Var_1, Var_2 and Var_3 give us good information in the time transfer results: $Link_1$, $Link_2$ and $Link_3$. The adjustment is based on the true errors analysis thanks to the redundant measurements which form the closure conditions and the whole network.

The mathematical model applied is the 'indirect' or 'parameter' least square adjustment. It is a common method and widely used in the metrology data processing. Without proving in details, we give here only a quick recall of the equations. For details, one can refer to [1]. In following formula all terms except for s_0^2 are represented with the matrix forms.

The function model and random model of the indirect adjustment are:

$$\hat{L} = B\hat{X} + d \qquad (2\text{-}1)$$

$$D = s_0^2 Q = s_0^2 P^{-1} \qquad (2\text{-}2)$$

here $\hat{L}$, B, $\hat{X}$ and d are the adjusted observations, the coefficients, the adjusted unknown vectors and the constant terms. D and P are the variances and weights. $Q = P^{-1}$ is the carrier containing all the uncertainty information. s_0^2 is the unit weight variance.

The observation (correction) equation is:

$$V = B\hat{x} - l \qquad (2\text{-}3)$$

$$l = L - L^0 = L - (BX^0 + d) \qquad (2\text{-}4)$$

or

$$l = L - F(X^0) \qquad (2\text{-}5)$$

with V the correction vectors (V_1, V_2 … V_N); L and L^0 the observations and their approximation values; $\hat{x}$ the unknown vector corrections $\hat{X} = X^0 + \hat{x}$, X^0 the approximation of the unknowns X and $F(X^0) = (BX^0 + d)$. Here the physical meaning of the adjusted values $\hat{X}$ is not important. They are only the

intermediate values by which we determine the link measurement corrections: V_1, V_2 and V_3. However the physical meaning of the differences of the elements in $\hat{X}$ is clear: they are the adjusted link values as given in equations (1-1) and (1-2). Take the example of Fig. I-2: X_A-X_B = Link_{AB} + V_{AB}. Link_{AB} is the measured raw link and V_{AB} is the adjusted correction or the estimated measurement error of Link_{AB}. In this sense, the X_A and X_B can be considered as the pseudo-clock values of lab A and B. It is important to understand that it is not the clock values but the link values that are to be adjusted.

The normal equation reads:

$$B^T PB\,\hat{x} - B^T Pl = 0 \qquad (2\text{-}6)$$

The solution of the adjusted unknown corrections under the least square condition $V^T PV = \min$ exists and unique:

$$\hat{x} = (B^T PB)^{-1} B^T Pl = N_{BB}^{-1} W \qquad (2\text{-}7)$$

with $N_{BB}^{-1} = (B^T PB)^{-1}$ and $W = B^T Pl$.

The adjusted observations and unknowns:

$$\hat{L} = L + V \qquad (2\text{-}8)$$

$$\hat{X} = X^0 + \hat{x} \qquad (2\text{-}9)$$

The U.W.M.S.E (unit weight mean square error.):

$$\hat{s}_0 = \sqrt{\frac{V^T PV}{r}} = \sqrt{\frac{V^T PV}{n-t}} \qquad (2\text{-}10)$$

Here n is the total observation number, t the non-redundant observation number and $r=n-t$ is the redundant number.

The variance-covariance of the adjusted unknowns:

$$D_{\hat{X}\hat{X}} = s_0^2 Q_{\hat{X}\hat{X}} = \hat{s}_0^2 N_{BB}^{-1} \qquad (2\text{-}11)$$

The adjusted links are the functions of the determined unknowns. The adjusted corrections V are the differences of the measured raw links and the adjusted links. From the equation (2-3), the corrections V are the functions of the adjusted unknowns $\hat{x}$. We can determine the variance of the adjusted links by the uncertainty propagation law. We give here only the general form. The weight function and the variance are:

$$dj = F^T \hat{x} \qquad (2\text{-}12)$$

$$D_{j\hat{j}} = F^T Q_{\hat{X}\hat{X}} F = F^T N_{BB}^{-1} F \qquad (2\text{-}13)$$

Finally, we define the weight P. In the TW time transfer, the measurements can be considered independent. For example, the links between NPL-PTB and USNO-PTB. The measurements are carried out on different timing tags. The signals sent out from the pivot lab PTB to NPL and to USNO are not the same and are not on same epochs. No common signals are shared. Therefore even if exist there the correlations between the TW links, they should be weak and can be ignored if there are no strong station based noise.

The weight of the link_i is defined by:

$$P_i = \frac{s_0^2}{M_i^2} \qquad (2\text{-}14)$$

here M_i is the a priori measurement uncertainty that can be defined in different ways: (1) Equal weight: for example: $M_i = s_0$ = constant, so P = 1; (2) Use the uA given in the section 6 of Circular T; (3) Use the closure information: $M_i = \sqrt{\frac{\sum (Closure)^2}{N}}$. We know that the weight is a relative concept and is proportional to the s_0. The closure uncertainties will be adjusted according to their weights. The adjusted corrections are independent on the value of s_0. However, from equation (2-14), the term s_0 makes an important role for the uncertainty estimation. In practice, we can do some iteration and compare the a priori s_0 and the a posteriori $\hat{s}_0$.

III. Numerical Test

We used the data TW Network of TAI0502 (Feb. 2005) to test the adjustment model (cf. Fig. I-1). IEN is not included in the adjustment due to its huge closures (Tab. I-3). The method and the software developed allow making the adjustment of multi-techniques with various constrains but we here tested only the simplest case: a free network adjustment with an arbitory point/clock PTB fixed (fixing another point will not change the result).

The adjusted results

The main results of the adjustment are the adjusted links (that is the sum of the measured raw link and adjusted correction V) and their uncertainty estimations, variance or m.s.u (Mean Square Uncertainty). Note that, the closures of the adjusted links should be zero. The quality of the adjusted links will be given by the analysis of the Modified Allan and Time Deviations.

III-1. The adjusted links, link corrections and the mean square uncertainties m.s.u. ~ variance

There are totally 1456 independent links in the network to be adjusted. A link here is a measurement between two labs on an individual MJD epoch: MJD_i. Each links gets a correction V_i and related $m.s.u._i$. Fig. III-1 and III-2 are the histograms of these two values. Fig. III-1 shows the V ~ Normal distribution with 90% of them between +/- 1 ns. But indeed, 10% of the corrections are bigger than +/- 1 ns. This shows an important role of the network adjustment is to be able to detect the gross errors thanks to the redundant measurements forming the network.

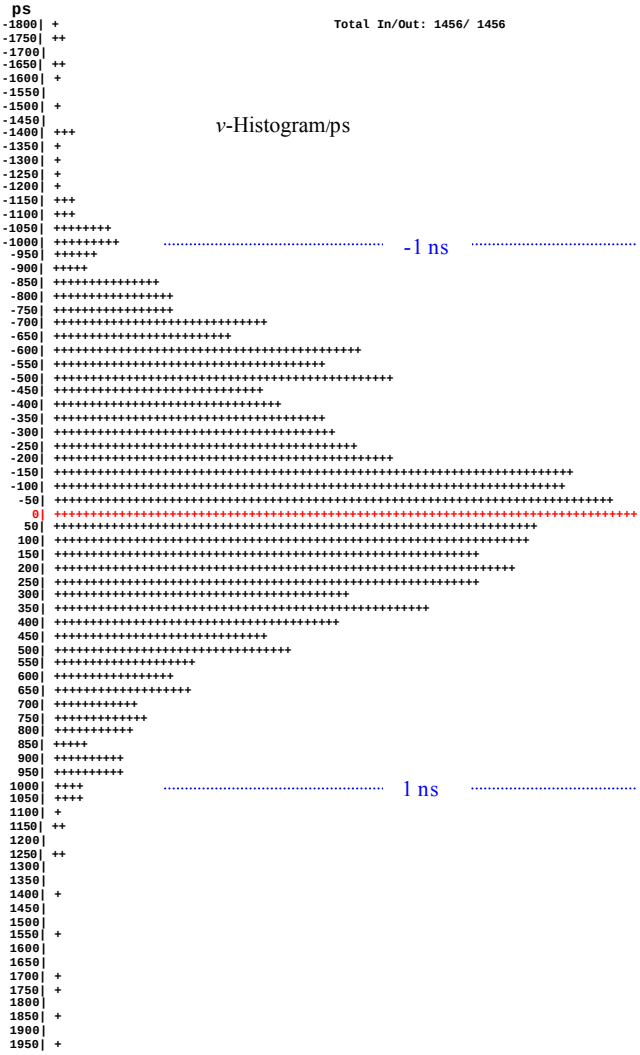

FIG. III-1 Histograms of the adjusted link corrections (V/ps)

The V-histogram in Fig. III-1 gives the distribution of all the adjusted link corrections: V. Fig. III-3 shows particularly the V-histograms of the two high precision baselines: NPL-USNO and NPL-NIST.

The a posteriori $\hat{s}_0$ is 0.823 ns vs. the a priori s_0 1 ns. The m.s.u. of the adjusted link are between 0.1 ~ 0.8 ns and 90% of them are 0.1 ~ 0.5. This can be considered as an approach of the uA. In 10% of cases, we have the estimated uA > 0.5 ns.

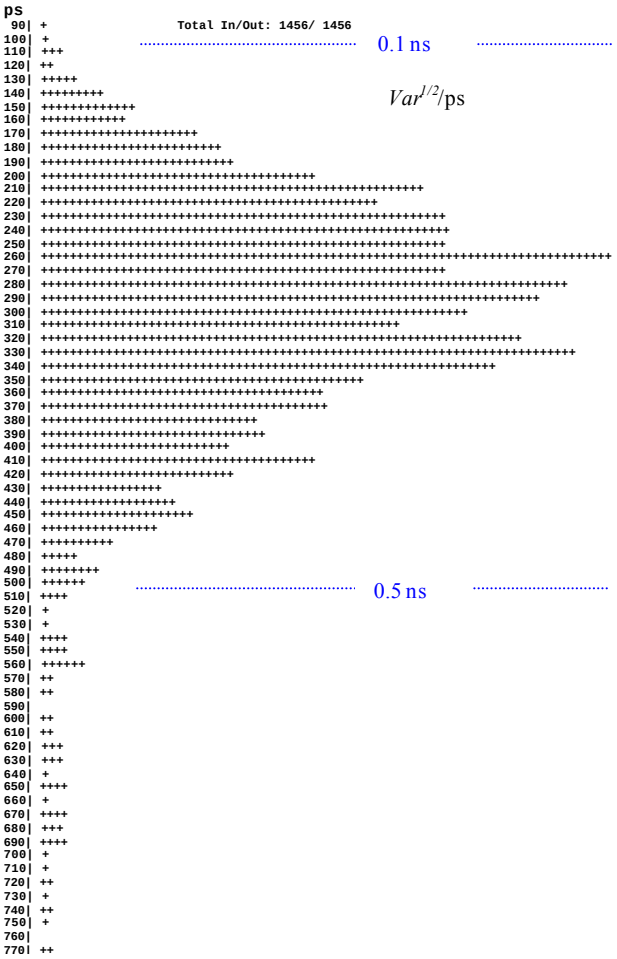

FIG. III-2 The Mean Square Uncertainties m.s.u. ~ Variance$^{1/2}$ of the adjusted link corrections

III-2. Improvement in time stability given by Mod. Allan and Time Deviations

The adjustment, as triangle closures, is made on each individual measurement epoch MJDi. On average, there are 4 measured epochs/day adjusted in the test example. The average interval is about 6 hours.

Theoretically, we can predict that: if the adjustment can really improve the stability, the improvement will be expected mainly on the short term of t_0 ~ 6 hours and then slightly decrease with the averaging time increasing and disappear in the end of several days or about.

As we know, the Modified Allan Deviation and Time Deviation are very important indexes of the time-frequency transfer stabilities. By the development of the mathematical

model of the least square adjustment, none of hypothesises concerning the time depending serious processing have been used. It is a pure measurement error adjustment and every measuring epoch is independent. Therefore, the Allan and Time Deviations measures if there will real improvement of the adjustment.

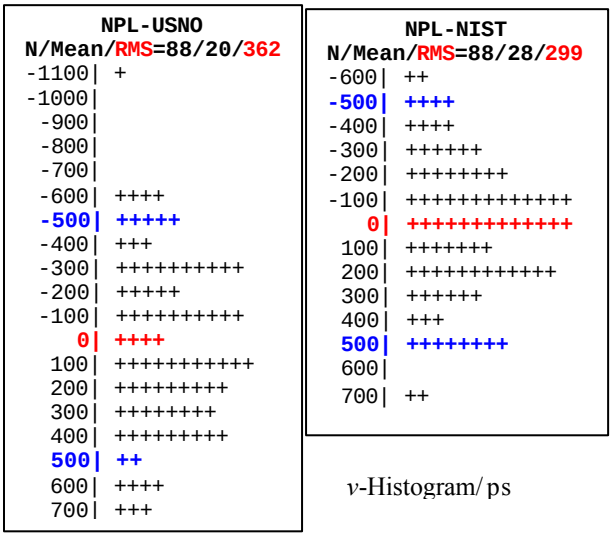

FIG. III-3 Histogram of the adjusted corrections

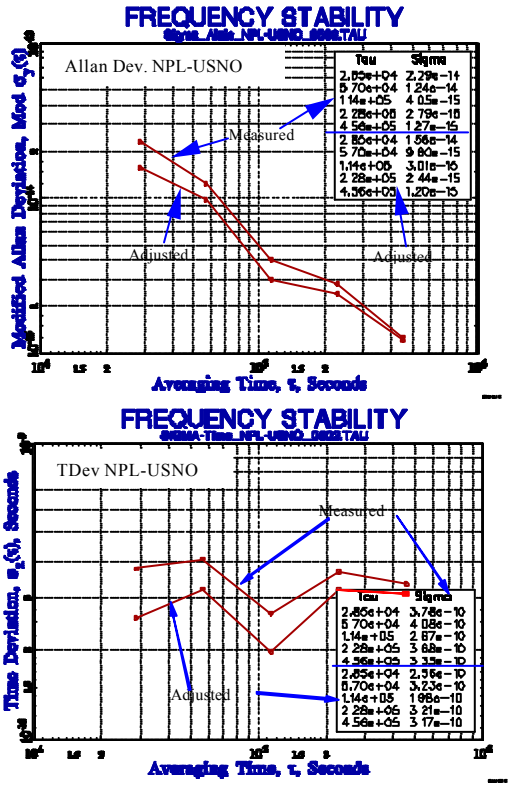

FIG. III-4a Comparisons of the Allan (up) and TDev (down) before and after the adjustment of NPL-USNO

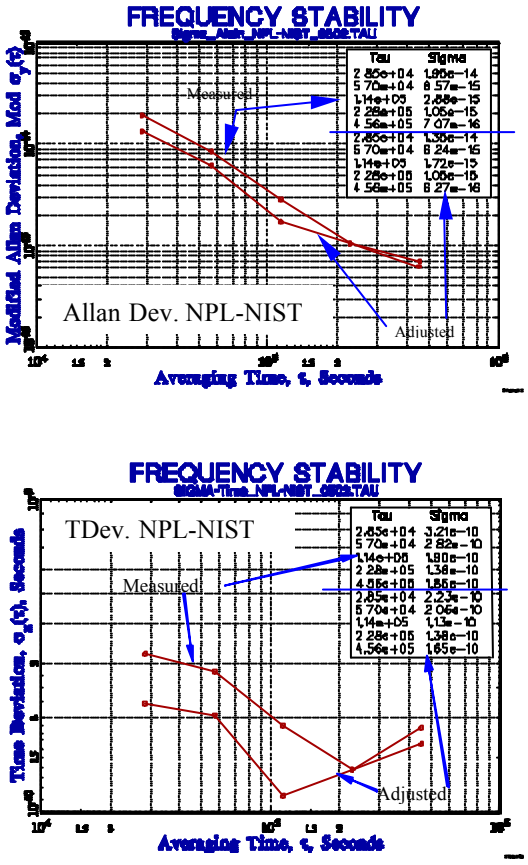

FIG. III-4b Comparisons of the Allan (up) and TDev (down) before and after the adjustment of NPL-NIST

Fig. III-3 is the statistics of the corrections V_i for the links NPL-USNO and NPL-NIST. Both are maser-maser baselines. Fig. III-4a and 4b are the comparisons between the Mod. Allan and Time Devotions computed before and after the adjustment. The comparisons are made between the measured raw links and the adjusted links. We can see a net improvement in these deviations. We have no room to list the results of all the baseline statistics of the network. Most baselines especially the short terms of the long distance baselines have a gain of 5 ~ 30%.

We point out that compared with the long baselines, the gains of short baselines are less important but this does not mean that the adjustment for short distances is useless. Because the short baselines supply the redundant measurements to form the closure conditions for the adjustment, they indirectly contribute to the long baselines through the network geometry. Without the short baselines, there would not the adjustment of the redundancy.

The least square adjustment is no doubt helpful to have improved the instability of the TW time transfer by using the already available redundant data in the TW network.

IV. Combination of the Multi-technique redundancies with the network adjustment model

So far, the adjustment is carried out on each independent measuring epoch without any constrains between. In fact as shown in Fig. IV-1, we can make constrains between the adjacent measuring epochs by applying a second independent observation, such as the carrier phase information. Assuming the time transfer link is a function of time, on the measuring epochs i and i+1, its values are $L(T_i)$ and $L(T_{i+1})$. The constraint condition can be described simply as:

$$L_1(T_{i+1}) - L_1(T_i) = L_2(T_{i+1}) - L_2(T_i) \qquad (4\text{-}1)$$

Here L_1 and L_2 are two independent linking techniques for the same baseline on the same time. As we know that one of the difficulties to combine different links is the inter-technique biases caused by the calibration errors or the long term instability or the ambiguities in time scale etc. In general we have:

$$L_1(T_i) = L_2(T_i) + B_i \qquad (4\text{-}2)$$

Here B_i is the total biases at epoch i between the two techniques: L_1 and L_2. By differential of the above equation w.r.t. time, we have:

$$dL_1(T_i) = dL_2(T_i) \qquad (4\text{-}3)$$

Equation (4-3) is the differential representation of the constraint defined in equation (4-1).

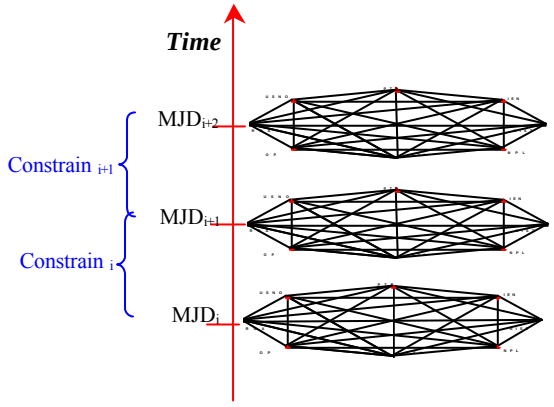

FIG. IV-1 Constraints between the MJD epochs

The advantage of the constraintt (4-1 or 4-3) is the biases B_i disappear when forming the differentials of the measurements between two measuring epochs and we do not require the long term stability in a tiny time difference between the two techniques. In this way the carrier phase information can be used.

The carrier phase information is characterized by its advantage of very good short term precision better than the codes and its disadvantages of poor long term instability due to the problems of cycle determination, discontinuities and frequency drifts [5]. For these reasons, carrier phases are not used for time transfer and not suitable for long term frequency transfer.

Setting L_1 = TW and L_2 = CP (carrier phase) in equation (4-1 or 4-3), we can have a general relation:

$$\int_{Mjd\,1}^{Mjd\,2} L_1(TW)\,dt = \int_{Mjd\,1}^{Mjd\,2} L_2(CP)\,dt$$

Introducing this constraint into the network adjustment model allows us to take the advantages of the CP information and reduce the effects of its disadvantages. Here, the absolute time scale is supplied by TW code information. Till now, the TW carrier phase data are not available. However the GPS carrier phase information is measurable by GPS receivers. Because the TW and GPS are two completely independent techniques, the combination of TW and GSP through the constraint condition should greatly improve the short and long term stabilities and make the combined solution more robust.

Finally it should be pointed out that the global adjustment model can be used directly to combine all kinds of redundant time links with the observation equation (2-1) without changing any procedures of the adjustment. For example, the latest developments [2], [3] supply the continuous combined GPS P code and CP solutions, known as the AIUB and PPP solutions. It is proven that their short and long term stabilities are comparable with TW. Their long term agreements with TW are within or about 1 ns [5]. This implies that the biases between TW and the AIUB or PPP solutions are negligible. We can therefore use directly the TW and GPS solutions to establish the observation equations and adjust them as a whole. However, unlike TW, GPS links are not independent. In an independent triangle, there are only two independent links.

V. Conclusion

TW network is highly redundant in geometry, in density and in multi-technique measures. However, Single baseline time transfer is still the only way in TAI practice. For N TAI laboratories, only N-1 single baselines are used. The European-American TW is actually measured as a network comprised of 12 TW laboratories. It supplies 66 measured links of which 55 redundant links, that is, 83% of the total measurements are not used in TAI. We propose a method to ameliorate the traditional single baseline transfer with a network time transfer through a global least square adjustment. The global network adjustment is theoretically serious, fully profits the total redundancy of a network, allows combining different techniques and gives variance-

covariance information for the uncertainty estimation. Obvious improvement in stability and in solution is expected without new more measurements required.

TW is at present one of the most precise time transfer techniques. However the closure analysis shows it is limited by the baseline dependant uncertainties. One of them is probably the diurnal disturbances. The closures of three time links are the true measurement errors because the three clocks involved are removed in the closing geometry. The closure analysis and network adjustment show: TW baseline dependent measurement errors may be up to 2 ns in maximum. The adjustment is based on the closure analysis. We do not need any complex hypothesis to complete its mathematical model. After the adjustment the network becomes structurally more homogeneous. The network time transfer is more robust than the traditional single baseline time transfer.

A test adjustment was carried out using the TAI0502 TW network. Numerical experiences show about 90% of the measurement corrections (error estimated) is less than 0.5 ns but till some 10% between 0.5 ~ 2 ns. The 90% of uA is estimated less than 0.5 ns with about 10% between 0.5 ~ 0.8 ns. These results agree with the closure analysis.

Mod. Allan and Time Deviations are the common tools to examine the time transfer quality. Because the least square adjustment is completely independent of the Allan stability theory, these two deviations are the objective index to verify the improvement in the adjusted time links. The Allan stability analysis shows that the proposed adjustment improves the stability with a gain up to 30% for long baseline. It gives also the uncertainty estimation on every measuring epoch. The gains come from the contribution of the redundant measurements.

Because the major resources in the uncertainty budget of the UTC-UTC(k) are from the link uncertainty and the TW laboratories transfer more than 60% of the TAI clocks, any gain in the TW time transfer will bring a direct amelioration of the quality of TAI.

GPS CP (carry phase) only information and the combined P-code and CP solutions can be used as constraints or/and independent observation in the TW network adjustment. The fact that the TW and GPS are completely independent techniques guarantees their combination being able to improve the short and long term stabilities and increase the robust capability. We are facing an epoch of multi-technique-network time transfer.

We developed the related mathematical model and an automatic procedure which has been installed in TAI computation software Tsoft.

Acknowledgement

The authors would thank all the TW laboratories for their data contributions to TAI and Dr. Demetrios Matsakis of USNO for the helpful discussions exchanged.

Reference

[1] Wuhan University of Surveying and Mapping: Theory of Errors and Foundation of the Surveying Adjustment, Publish House of the Wuhan University, 2003

[2] R. Dach, L.G. Bernier, G. Dudle, T. Schildknecht, and U. Hugentobler, Geodetic Frequency Transfer - recent developments in the AIUB-METAS collaboration, IN Proc. 19th EFTF 2005.

[3] J. Kouba, P. Héroux, Precise Point Positioning using IGS orbits and clock products, GPS Solutions, 4, p.31, 2001.

[4] Petit G. and Z. Jiang: Using a redundant time link system in TAI computation, IN this Proc. EFTF 2006

[5] Jiang Z., R. Dach, G. Petit, T. Schildknecht, U. Hugentobler: Comparison and combination of the TAI time links with continuous GPS carrier phase results, IN this Proc. EFTF 2006

Proceedings of the 20th EFTF, 2006

Comparing high accuracy frequency standards via TAI

P. Wolf,* G. Petit
BIPM, Pavillon de Breteuil, 92312 Sèvres, France

E. Peik, C. Tamm, H. Schnatz, B. Lipphardt, S. Weyers, R. Wynands
PTB, Bundesallee 100, 38116 Braunschweig, Germany

J-Y. Richard, S. Bize, F. Chapelet, F. Pereira dos Santos, A. Clairon
LNE-SYRTE, Observatoire de Paris, 61 av. de l'Observatoire, 75014 Paris, France

**Electronic address:* pwolf@bipm.org

Over the last few years the number of high accuracy (uncertainties in the low 10^{-15} or less) primary frequency standards contributing to TAI has increased significantly from only two over the period 2000 - 2002 to seven over the period 2002 - 2005. As a consequence the number of individual measurements of TAI frequency by such standards over the period 1999 to 2005 is > 60 and increasing rapidly. Additionally, several other atomic transition frequencies (Rb, Yb^+, Hg^+, Sr^+,...) have been repeatedly measured over the same period with comparable accuracies. The resulting overall set of data is now sufficiently large to be able to obtain meaningful statistics for the complete data set and, in some cases, for the contributions from individual standards. We show the ensemble of the data available to the BIPM at the time of the conference together with the results of some basic statistical analysis. In particular, we investigate the impact of these standards on the overall uncertainty of the realisation of the SI second via TAI, and the performance of some individual standards. Our results indicate that while there is good self coherence of most studied standards (especially for recent data) there seems to be significant disagreement between individual standards. We briefly discuss some potential sources of that disagreement (time transfer noise, uncertainties of the standards, instability of the reference timescale, etc…). We hope that, in the long term, this ongoing study will allow a better characterisation of the ensemble of standards and their impact on TAI.

I. INTRODUCTION

Over the last decade of the 20th century and the first few years of the 21st, the uncertainty of atomic clocks has decreased by about two orders of magnitude, passing from the low 10^{-14} to the low 10^{-16} [1,2,3], in relative frequency. This rapid evolution is essentially due to the technological applications of laser cooling and trapping of atoms and ions, and the resulting construction of fountain clocks using freely falling laser cooled atoms, and of trapped ion and neutral atom clocks.

In particular, numerous fountain clocks based on the hyperfine transition frequency of the Cs atom (Primary Frequency Standards, PFS) have been built and operated over the last decade or so, some of them now reaching uncertainties in the low 10^{-16}. Such clocks directly realize the present definition of the SI second, and as such are used to calibrate the International Atomic Time (TAI), whose scale unit is defined as equal to the SI second on the rotating geoid.

Atomic transitions other than the hyperfine Cs line are increasingly being investigated in order to overcome some basic limitations of the Cs clocks. These are mainly the hyperfine Rb transition measured in Rb fountain clocks and optical transitions in ions (Yb^+, Hg^+, Sr^+, Al^+,…) and neutral atoms (Sr, Yb, Ca,…). Such transitions can be related to the SI second via a conventional reference frequency expressed in SI seconds and based on the complete body of measurements available. Throughout this paper we refer to non-Cs transitions as Secondary Representations (SR) of the SI second.

Comparing such standards (PFS and/or SR) at the achieved levels of uncertainty is no easy task, even when the standards are in the same lab, but even less so when they are in distant locations. Several comparison campaigns have been carried out for fountain PFS, either on site [1], by transporting the only available transportable caesium fountain SYRTE-FOM to PTB and comparing it with PTB-CSF1, or by using remote time/frequency comparison methods [5,6,7]. Whilst accurate into the low 10^{-15} or slightly below these methods have the disadvantage that they require simultaneous operation of the different standards as well as of the used time/frequency comparison methods, which can pose a number of organisational and

technological difficulties. Mainly for that reason the number of such comparison campaigns has been very limited.

An alternative is the comparison of standards using a globally available continuous reference time scale like TAI. This allows each standard to be operated whenever convenient, but has the disadvantage of adding the instability of the reference time scale when comparing measurements by two standards taken at different epochs. Nonetheless, we show that the large number of available measurements (69 Cs fountain measurements in the period 2000-2005) allows meaningful statistics in the 10^{-16} uncertainty region when comparing individual measurements from the same standard and measurements from different standards.

In this paper we investigate the ensemble of measurements of TAI frequency by Cs fountain PFS reported to the BIPM over the period 2000-2005 and of a few measurements from SR (Rb hyperfine and Yb^+ optical transition). We study the impact of the advent of high accuracy fountain standards on the knowledge of the TAI scale unit, the self-coherence of individual standards (comparing individual measurements from the same standard), and the behaviour of individual standards with respect to all others (comparing different standards). We consider this paper as a first step of an ongoing study providing documentation and characterisation of PFS and SR over extended periods of time, which, we hope, will lead to improvements in the overall characterisation of the ensemble of standards and their impact on TAI.

II. DATA

The first step of TAI calculation is the comparison (at 5 day intervals) of approximately 250 commercial freely running atomic clocks that are located in timing labs distributed world-wide. From these raw measurements the BIPM constructs a freely running atomic time scale (Echelle Atomique Libre, EAL) using a stability algorithm designed for a compromise between overall reliability and medium term (~ 30 days) stability [8]. The frequency of EAL with respect to the SI second on the rotating geoid (the definition of TAI frequency) is obtained from measurements of the EAL frequency by the PFS (see below). TAI is then obtained from EAL by frequency steering following those measurements and limited in amplitude in order to not degrade the short and medium term stability. Hence the frequency difference between EAL and TAI is deterministic (reported in section 3 of circular T of the BIPM) and the uncertainty in the knowledge of the TAI scale unit is equal to the uncertainty of the determination of EAL frequency from the PFS measurements.

In practice, PFS are used to determine the frequency of EAL in the following way: The frequency of a local clock that participates to EAL (in general a H-maser) is measured over a given interval using the PFS, and the result is reported to the BIPM. The BIPM then calculates the frequency of EAL with respect to that PFS over the appropriate interval using the known frequency difference between the local clock and EAL. Concerning SR, the same method is used, with the difference that the conventional SR-Cs difference is taken into account in the initial measurement of the frequency of the local clock.

Fig. 1 shows all measurements of EAL frequency by PFS sent to the BIPM over the period 1999 – 2005, together with five measurements from the LNE-SYRTE Rb fountain and two measurements from the PTB Yb^+ optical frequency standard, which were reported for the purposes of this work. Each point in Fig. 1 corresponds to a measurement of average EAL frequency over different time intervals, ranging from 5 to 60 days, and plotted for the central date of the interval. For clarity Fig. 2 shows the same data but only for Cs fountain PFS and the two SR. The reference frequencies used for the two SR were

$$f_0(\mathrm{Rb}) = 6\,834\,682\,610.904\,324\ \mathrm{Hz} \qquad (1)$$
$$f_0(\mathrm{Yb}^+) = 688\,358\,979\,309\,308\ \mathrm{Hz}$$

where the Rb frequency is the one recommended by Recommendation CCTF 1 (2004) of the CCTF, and the Yb^+ frequency is the best estimate by PTB, based on all existing measurements.

Fig. 1 also shows the EAL-Tp frequency difference, where Tp is a BIPM estimate of the realization of the SI second for a given interval, using all PFS measurements 360 days before and after that interval. For Fig. 1 Tp was calculated for each interval over which a PFS or SR measurement was reported (sometimes overlapping) and plotted for the centre of that interval. Roughly speaking, Tp is a weighted average of all measurements one year before and after the considered interval, where the weights take into account the uncertainty of each measurement, and the distance of the measurement from the interval under consideration (via the instability of EAL). The details of the algorithm are described in [9]. It minimises the overall error in the estimation of EAL-SI for a given interval, taking into account the uncertainty of the EAL-PFS measurements and a model of EAL instability. The latter is specified in each monthly circular T (header of section 4) of the BIPM time section. It is estimated by comparing EAL to other atomic time scales and modelled using conservative noise estimates that fit the resulting Allan variances. Over the last few years the instability of EAL has been

modelled using the quadratic sum of three noise contributions:

$$s_y(t)^2 = (3\ 10^{-15}\ t^{-1/2})^2 + (0.5\ 10^{-15})^2 + (0.1\ 10^{-15}\ t^{1/2})^2 \quad (2)$$

with t in days.

Table 1 summarises the most recent measurement from each fountain PFS and from the two SR, including its duration, the dead time, and uncertainty contributions. The last two columns provide the uncertainty of the EAL-Tp frequency difference for the same interval when calculated using all PFS and when using all PFS except the one under consideration.

	days	dead %	u_A	u_B	$u_{l/lab}$	$u_{l/TAI}$*	u_{Tp}*	u_{Tp}* (-PFS)
IEN-CSF1	25	40	0.6	0.6	0.4	1.2	0.7	0.8
NIST-F1	40	57.5	0.34	0.31	0.30	0.75	0.6	0.8
NMIJ-F1	10	5.9	1.1	4.2	0.5	3.0	1.2	
NPL-CSF1	30	13.3	0.48	1.0	0.41	1.0	0.8	-
PTB-CSF1	15	0.9	1.0	0.9	< 0.1	2.0	1.1	1.3
SYRTE-FO2	25	20.5	0.071	0.58	0.14	1.2	0.7	0.8
SYRTE-FOM	30	27.5	0.3	1.1	0.7	1.0	0.8	-
PTB-Yb^+	10	79.6	0.39	1.53	0.82*	3.0	1.3	-
SYRTE-RbF	10	74.9	0.17	1.04	0.58	3.0	1.4	-

Tab. 1: Data from the most recent measurement of each standard. All values are in 10^{-15} except when indicated otherwise. An asterisk indicates values calculated by the BIPM.

Finally, Figure 3 shows the difference Tp-standard. The error bars include the uncertainties of the measurement, the uncertainties of the link between the standard and the reference clock in the lab (including contribution from dead time), the uncertainty from the link to TAI (essentially time transfer noise), and the uncertainty of Tp for the interval of the measurement. Note that there is, of course, significant correlation between Tp and the individual measurements, as each value of Tp is largely determined by the measurement of the PFS over the same interval. As a result, the spread of the points in Fig. 3 is certainly underestimated (Tp "follows" the individual PFS measurements) and the error bars are certainly overestimated (Tp uncertainty depends on the uncertainty of the PFS, so to some extent error sources are "doubled" when adding u_{Tp} to the uncertainty of the PFS).

III. UNCERTAINTY OF TAI

Every month the BIPM publishes in its Circular T (section 4) the frequency offset between the BIPM estimate of all PFS standards (equivalent to Tp for a monthly interval) and TAI, together with its uncertainty. The same offsets are recalculated once per year (see the BIPM time section annual report table 7), using all available PFS data at the time of calculation (including measurements taken after the initial publication in circular T).

In this section we estimate the impact of high accuracy PFS (Cs fountains, FO) on the knowledge of the TAI frequency. To do this we calculate Tp for monthly intervals from mid 1999 to the end of 2005, once using all PFS and once excluding all FO. Fig. 4 shows the uncertainty in the calculated value of TAI-Tp frequency (characterising our knowledge of TAI frequency) for both cases. Two features can be observed: First, a difference in uncertainty of the two calculations starting when the first FO measurements were reported and reaching about a factor 2 in recent years. Second, a step in the uncertainty of both calculations around MJD 51900 (Dec 2000 – Jan 2001). The latter corresponds to a change in the EAL stability model, implemented following a change in the EAL weighting procedure and a resulting improvement in EAL stability.

It is interesting that the advent of Cs fountains has lead to an improvement of the uncertainty in Tp by "only" about a factor 2, when the total uncertainty from such standards as reported to TAI (including time transfer uncertainty) is about a factor 5 to 10 smaller than that from Cs beam standards. This is due to a combination of two factors: the density of fountain measurements and the instability of EAL. For PFS measurements that are not exactly coincident with the monthly interval of Tp evaluation, the weight of that measurement is decreased due to the influence of EAL instability. This effect is less critical for Cs beam standards as the contribution of their intrinsic uncertainty remains dominant with respect to that of EAL instability, but not so for fountain PFS for which the contribution from EAL instability may become significant for intervals as short as one month or less. As a result, for a given month only the FO that are coincident with that month contribute significantly whereas, in the case where only Cs beam standards are used, earlier and later measurements also contribute significantly (leading to an overall improvement of, roughly, vN where N is the number of contributing standards).

IV. INDIVIDUAL STANDARDS

Four of the reported PFS fountain standards had submitted a sufficient number of measurements (≥ 10) to allow significant statistics of those measurements, and their comparison to the ensemble of the other PFS. These were IEN-CSF1, NIST-F1, PTB-CSF1, and SYRTE-FO2. For each of these PFS we have calculated Tp for the intervals of measurement of the PFS under study but excluding its own measurements from the Tp calculation. In that way, Tp reflects the best estimate of the SI second as realized by all other PFS ("the rest of the world") for the intervals of measurement of the PFS under study. The PFS measurements and Tp are then statistically completely independent and meaningful quantitative estimates can be drawn from the results.

Figure 5 shows the four resulting frequency differences Tp-PFS, with the error bars including the uncertainties from the PFS, the dead time and link inside the lab, the time transfer, and the Tp calculation. For each PFS we have calculated the weighted average of all points (WA), the uncertainty of that weighted average (u_{WA}), and the reduced χ^2 sum (χ) around WA defined as

$$c = \frac{1}{N-1}\sum_{i=1}^{N}\frac{(y_i - WA)^2}{u_i^2} \qquad (3)$$

where N is the total number of measurements, y_i are the individual Tp-PFS frequency differences, and u_i the associated 1s uncertainties. The value of χ reflects the statistical coherence of the data, $\chi = 1$ corresponding to a normally distributed data set, and $\chi > 1$ indicating a spread of the data that is too large, given the stated uncertainties. The results for WA, u_{WA} and χ are also shown on figure 5.

We note, that all four PFS display a reasonable spread of the data around their weighted average (values of χ ranging from 0.4 to 1.2), and even more so for recent data. However, none of the four PFS agree with the "rest of the world" on average, i.e. in all cases the value of WA is non-consistent with zero within its uncertainty, the discrepancies ranging from 1.8s to 4.6s.

The fact that we can average a number of PFS measurements in each case allows us to perform the comparisons between individual standards and the "rest of the world" with uncertainties (u_{WA}) in the mid 10^{-16}, in spite of the added time transfer noise and the instability of EAL. This is of the same order or better than the best direct on-site comparison reported in [1] or the long distance comparison campaigns [5,6,7].

V. SECONDARY REPRESENTATIONS

Five measurements of EAL frequency by the SYRTE Rb fountain and two measurements from the PTB Yb^+ optical frequency standard are also shown on Figs. 1 to 3. The raw measurements are the SR-clock (H maser in both cases) frequency differences, corrected using the reference frequencies given in (1). The measurements were extrapolated to intervals ranging from 5 to 60 days, taking into account the resulting uncertainty from dead time. Thus, the error bars in Fig. 3 include u_A, u_B of the standards, the uncertainty from dead time, from the link inside the lab, and from the link to TAI (time transfer). They do not include the uncertainties of the reference frequencies f_0.

We note that all measurements from SR agree with the ensemble of PFS within the uncertainties, i.e. they agree with zero on Fig. 3. This in itself is not surprising as the reference frequencies used are determined to a large extent by the same measurements when compared locally to the available Cs reference. Nonetheless, some preliminary conclusions can be drawn. The five Rb measurements all agree with Tp, indicating that there is good coherence between the individual measurements (no drift of the Rb-Cs frequency) as already reported in other publications [1], but also that there is good coherence between the local Cs references used (SYRTE-FO2 and SYRTE-FOM) and all other PFS. Of particular interest in this respect is the first Rb measurement (of duration 60 days) which confirms the good agreement between the local SYRTE Cs reference at the time and the "rest of the world" although the SYRTE Cs was not reported to the BIPM. A similar conclusion (albeit with larger uncertainty) can be drawn from the Yb^+ measurements which agree well with Tp. This indicates that PTB-CSF1, which was used as the reference to determine f_0, agreed well at that time with "the rest of the world", although it was not reported to the BIPM.

In the long run, reporting SR to the BIPM and using them for studies of the type presented here should allow comparison of different SR that use the same atomic transition and verification of the coherence of measurements from individual SR.

Additionally, keeping track of the different SR in this way should allow building sufficient confidence in these standards to steer TAI to them using conventional reference frequencies, and pave the way towards a possible redefinition of the second.

VI. DISCUSSION AND CONCLUSION

We have presented data from almost 6 years of measurements of TAI frequency by primary frequency standards (PFS), in particular Cs fountains (FO) and two secondary representations of the SI second (SR), the SYRTE-Rb fountain and the PTB Yb^+ optical standard. We have studied the impact of the recent advent of high accuracy standards (FO) on the knowledge of the frequency of TAI, and used the data to compare the standards amongst each other, with uncertainties that are comparable to the best on-site or long distance comparison campaigns.

As discussed in section III, use of the FO data has improved the uncertainty of TAI calibration by about a factor 2. There are several ways for further improvement:

- improving the uncertainties of the PFS and the time transfer
- increasing the number of measurements from PFS
- decreasing the instability of EAL.

Any one or a combination of these factors would benefit TAI and any user that demands utmost accuracy, for example a laboratory that wants to measure an atomic transition frequency without disposing of a high accuracy Cs reference.

We have studied four of the fountain PFS individually (section IV) and found good self coherence of the measurements but significant offsets between each standard and "the rest of the world", ranging from $(0.89\pm0.46)\times10^{-15}$ to $(3.5\pm0.76)\times10^{-15}$ in amplitude. Those discrepancies could be due to the time transfer (link to TAI) or the instability of EAL, but we consider this as unlikely because the corresponding uncertainties are incorporated in our comparison (via $u_{\mathrm{l/TAI}}$ and u_{Tp}) and are estimated rather conservatively. Another possibility could be an unknown or incorrectly characterised frequency bias in the PFS themselves, like for example the black body radiation shift whose "standard" evaluation has been called into question recently [10]. Nonetheless, that alone is unlikely to be sufficient to explain all the differences, indicating that there might still be some effects in (individual or all) fountain PFS that are insufficiently understood at the upper 10^{-16} or even the 10^{-15} level.

The two studied SR show good coherence of the individual measurements and good agreement with the PFS. As mentioned in section V, the latter does not allow drawing significant conclusions as the used reference frequencies (1) were derived essentially from the same measurements. Instead we consider the measurements as the first of their type that, in the long run, should allow steering of TAI to SR and pave the way towards a possible redefinition of the second. More generally, studies of the type presented here show that comparing SR to TAI via a local clock (H-maser) can allow laboratories to perform measurements of atomic transition frequencies with relatively good accuracy (potentially mid 10^{-16}) without necessarily disposing of a high accuracy Cs reference nearby. Inversely laboratories that dispose only of a SR (with a conventionally agreed reference frequency f_0) could still contribute to and improve TAI with regular measurements of their SR.

In summary, we have presented the current state of high accuracy frequency standards (fountain PFS and SR) as reported to the BIPM and discussed their contribution to TAI, and their overall performance. We hope that this study and its successors will aid the time/frequency community to make the best use of such standards and will provide valuable feedback for the groups that develop the standards themselves.

Acknowledgements

We would like to acknowledge the daily routine work of all laboratories that contribute to TAI with their clock and time transfer data, which is obviously essential to this type of study.

REFERENCES

[1] Bize S. et al., J. Phys. B: At. Mol. Opt. Phys. **38,** S449–S468, (2005). See also Chapelet F. in these proceedings.
[2] Heavner T.P., et al., Metrologia **42**, pp. 411-422, (2005).
[3] Rosenband T., et al., in these proceedings.
[5] Parker T.E. et al., Proc. IEEE FCS 2001.
[6] Richard J-Y. et al Proc. EFTF 2004.
[7] Bauch A., et al., Metrologia, **43**, 109-120, (2006).
[8] Thomas C., Wolf P., Tavella P., *Time scales*, BIPM Monograph 94/1, (1994).
[9] Azoubib J., Granveaud M., Guinot B., Metrologia **13**, 87, (1977).
[10] S. Micalizio et al., Phys. Rev. **A69**, 053401 (2004); F. Levi et al., Phys. Rev. **A70**, 033412 (2004); A. Godone et al., Phys. Rev. **A71**, 063401 (2005); S. Ulzega, et al. in these proceedings.

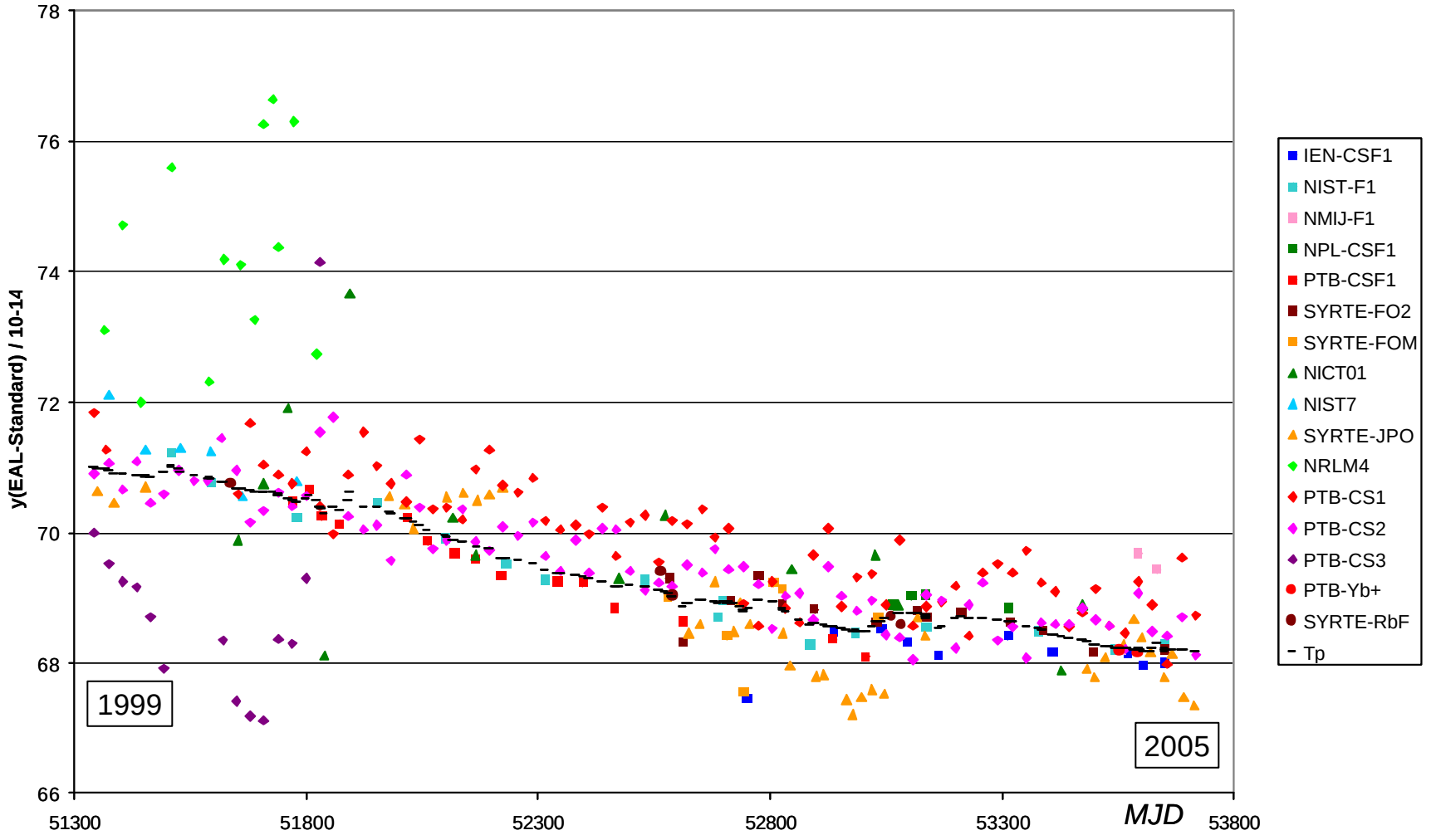

Fig. 1: All measurements of EAL frequency from PFS and the two SR (in 10^{-14}) over the period 1999 to 2005, together with the BIPM estimate (Tp) for each interval of measurement.

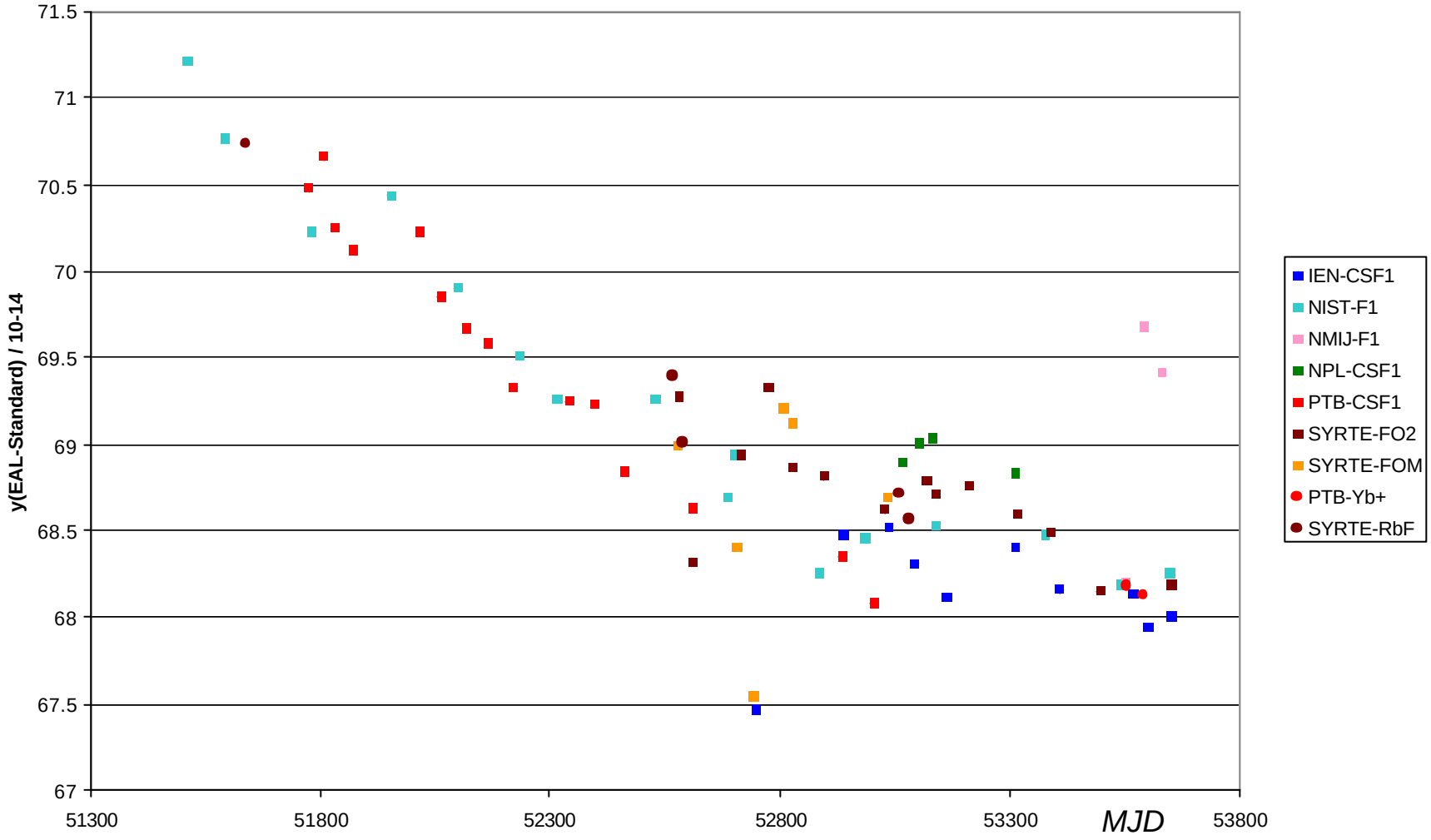

Fig. 2: Measurements of EAL frequency from Fountain PFS and the two SR (in 10^{-14}) over the period 1999 to 2005.

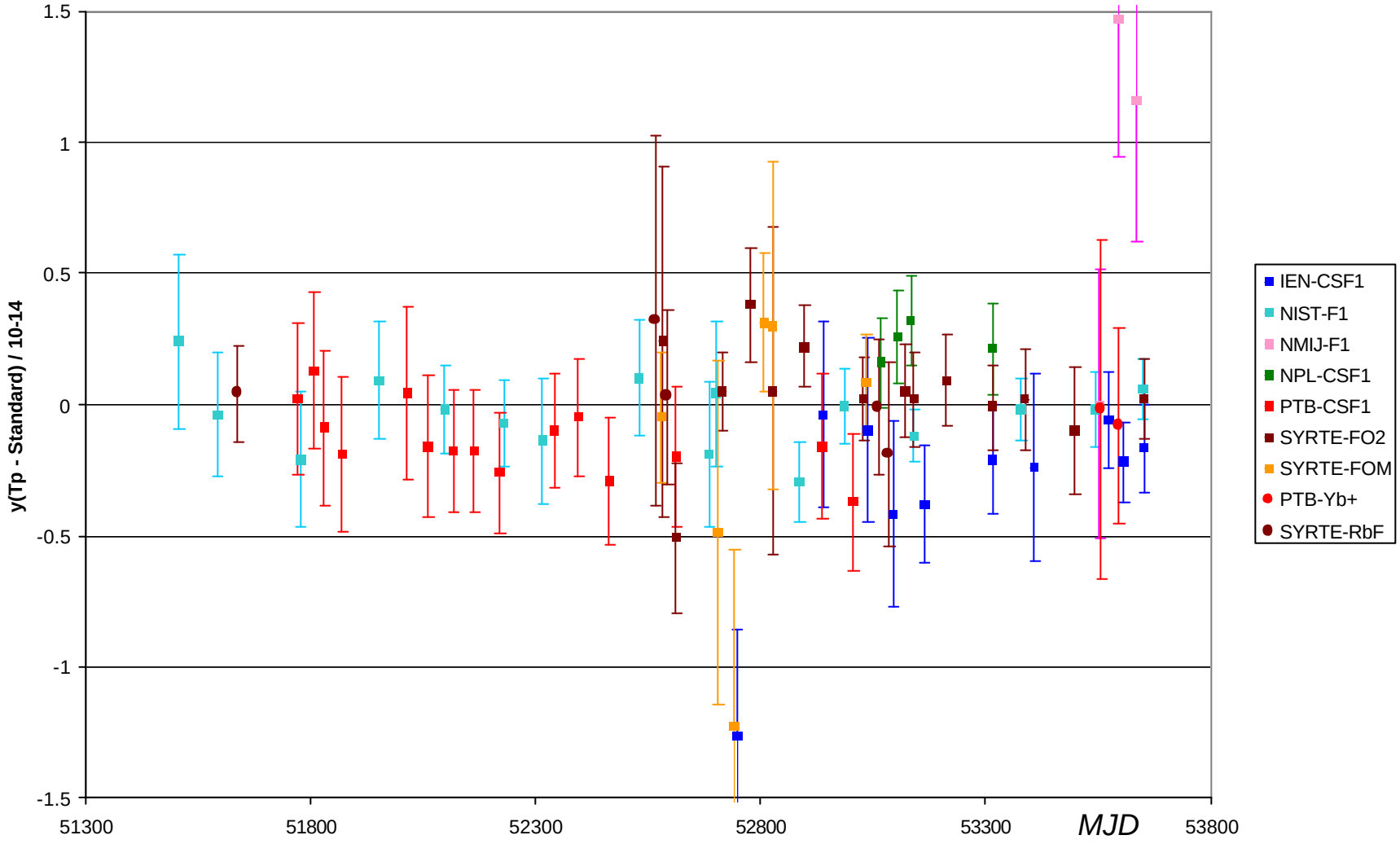

Fig. 3: Difference Tp-Standard (in 10^{-14}) for Fountain PFS and the two SR over the period 1999 to 2005.

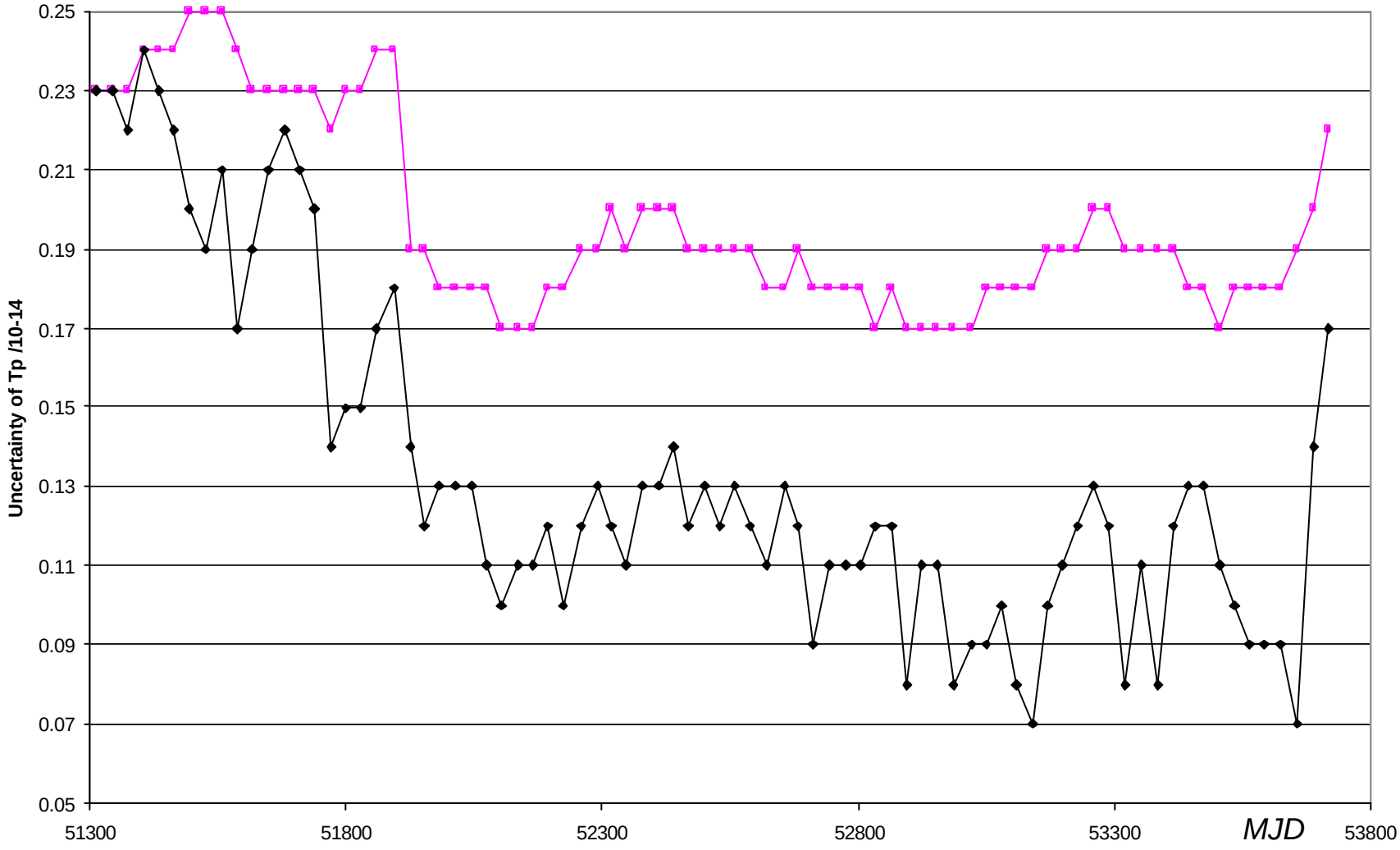

Fig. 4: Uncertainty of Tp for monthly intervals using all available PFS (lower curve), and excluding fountain PFS (upper curve).

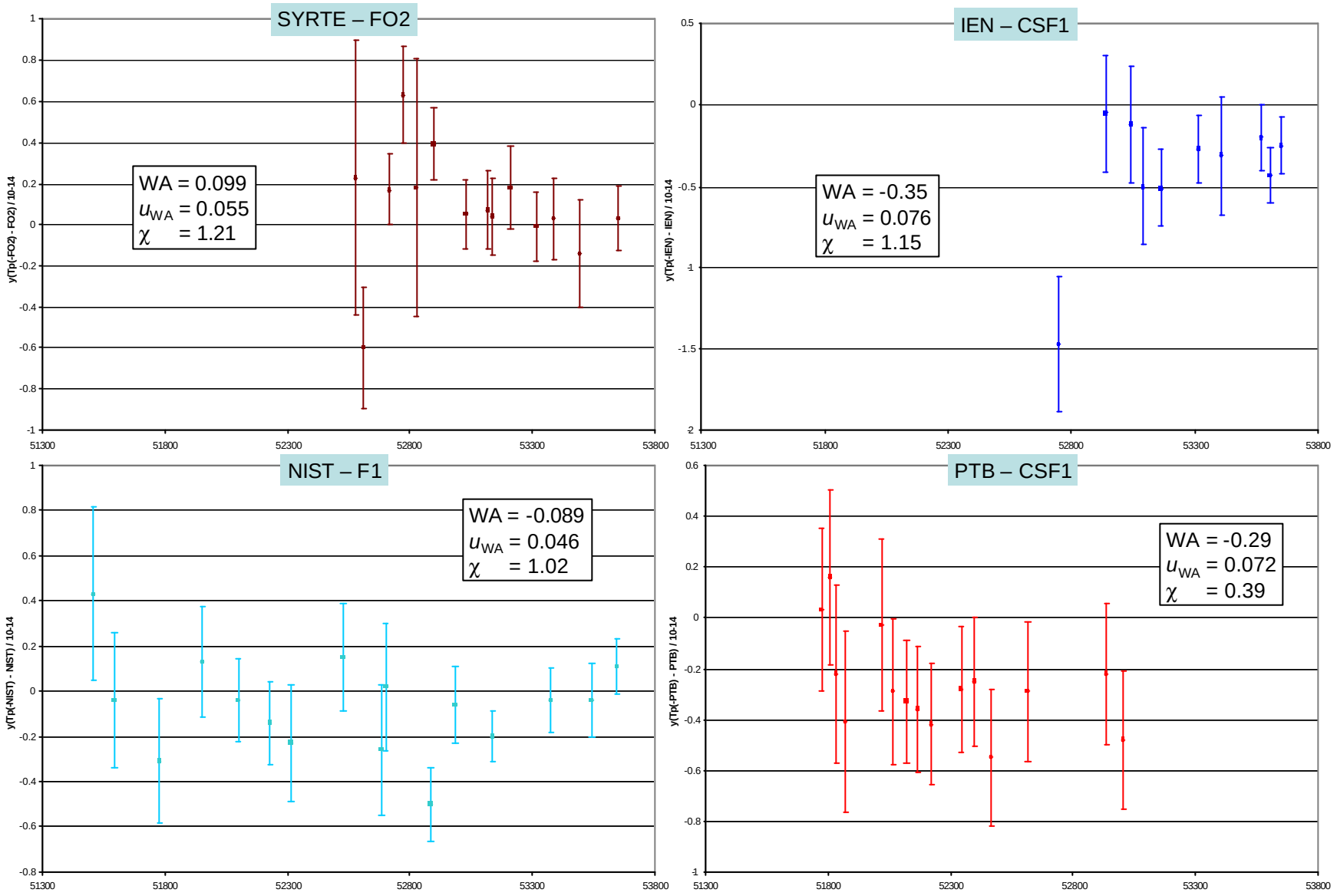

Fig. 5: Four individual PFS (see text for details).

Proceedings of the 20th EFTF, 2006

UTC(SU) steering time scale
Current status and further improvements

L. Gornaeva, N.Koshelyaevsky, E.Zagirova

Institute of Metrology for Time and Space FGUP VNIIFTRI,
Mendeleevo, Moscow region, 141570, RUSSIA
nkoshelyaevsky@imvp.ru

As it has been reported during EFTF'05 meeting on 2004, December 30 the realization of UTC(SU) – the national time scale of Russian Federation – was changed. We continue to maintain autonomous atomic time scale TA(SU) without any changes and started new realization of the steering UTC(SU). The main aim of steering time scale is to generate UTC(SU) as close as possible to the UTC and do not spoil considerably medium term time stability due to steering process.
At the moment UTC(SU) time stability relative to UTC $\sigma_x(\tau) \le 4$ ns for sample time 40 days and $\sigma_x(\tau) \le 3$ ns for TA(SU) correspondingly. This relations between time stability's looks quite natural because of time constant in steering filter about two months, so considerable stability improvement in UTC(SU) will be seen for larger sample times.

1. INTRODUCTION

As it has been reported during EFTF'05 meeting [1] on 2004, December 30 the realisation of UTC(SU) – the national time scale of Russian Federation – was changed. We continue to maintain autonomous atomic time scale TA(SU) without any changes and started new realisation of the steering UTC(SU). About one year has elapsed since that time and we would like to deliver some results regarding performances of the UTC(SU) and discuss further proposals to improve it.
The main goal of steering time scale is to generate UTC(SU) as close as possible to the UTC, following to the recommendation S5 (1993) [2], and do not spoil considerably medium term frequency stability due to steering disturbances.

II. ALGORITHM AND REALISATION

The main ideas of applied steering algorithm were quite the same as it was reported in [1] and were based on PhaseLockLoop (PLL) principles. The gained time difference was estimated and then a proper permanent for the whole month steering frequency bias was introduced to eliminate it. Steering correction to be introduced in month i+1 have been calculated in month i basing on UTC-UTC(SU) readings for the months i-2 and i-1. A linear fitting prediction model was used for time scale difference. To prevent possible abrupt frequency changes due to time link noises and keeping in mind high internal frequency stability of the atomic time scale TA(SU) based on the ensemble of H-masers a steering limit was introduced. The value of steering

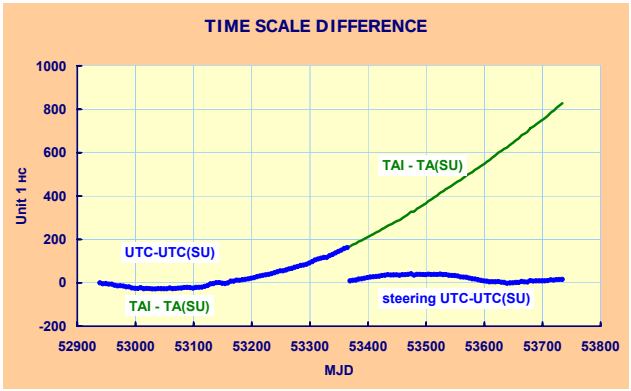

Fig.1

limit was in conformity to frequency stability and residual frequency drift of TA(SU) relative to TAI.
Such approach have been applied starting 30 December 2004 till now with steering limit 3×10^{-15} (259 ps/day) and result is depicted on Fig.1. At the start moment 2004, December 30, time difference between UTC and UTC(SU) was about 160 ns and relative frequency difference about 1.6×10^{-14}. To remove the initial time and frequency differences we introduced time step of 160 ns to the UTC(SU) but could not introduce proper frequency step into UTC(SU) but 1.0×10^{-14} only, so it takes us about half a year to equalise frequency difference. Along with it during this period additional time difference about 40 ns has been gained and we needed once more a few months to reach UTC-UTC(SU) difference in close vicinity.

III. POSSIBLE IMPROVEMENTS

A special study was made to investigate possible improvements of steering ability and compromise between time error and frequency stability deterioration.

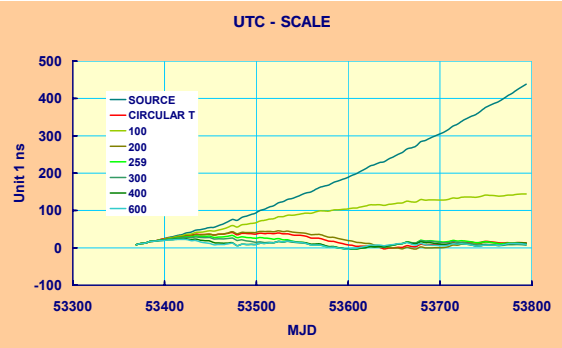

Fig.2

As a real source data for investigation purpose we used TAI - TA(SU) difference biased by 1.0×10^{-14} as it was made during UTC(SU) correction on 30 December

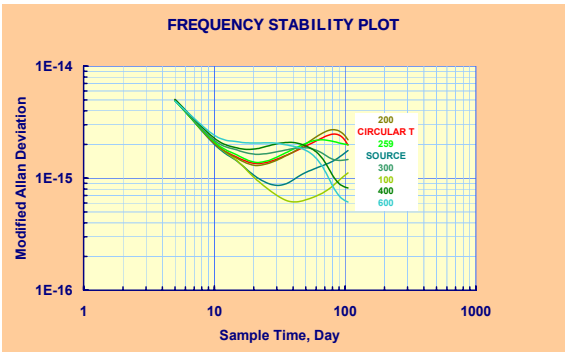

Fig.3

2004. And then apply steering algorithm with steering limit spanned from 100 ps/day to 600 ps/day. The results of the estimations are depicted on following three pictures: Fig.2 to Fig.4. Perhaps the most striking result is somewhat unexpected stability improvement to the level higher than source stability for steering limit 100 ps/day!

A possible explanation is that applied steering limit 100 ps/day$\rightarrow1.15\times10^{-15}$ is practically equivalent to estimated residual frequency change per month in TA(SU) system - 4.2×10^{-17}/day $\rightarrow1.2\times10^{-15}$/month. So in this case we revealed to full extend the potential non-deterministic level of TA(SU) stability.

Strictly speaking this is not the case. The introduced steering frequency corrections do not exceed 100 ps/day and are not equal to 100 ps/day. It's values may be some what less. So the obtained frequency stability level do not correspond exactly to that get by simple removing of visible frequency drift as a single whole.

Unfortunately tracking ability in this case is not high enough. More over the dependence of σ_y (τ) plot for steering limit 100 ps/day do not manifests stability

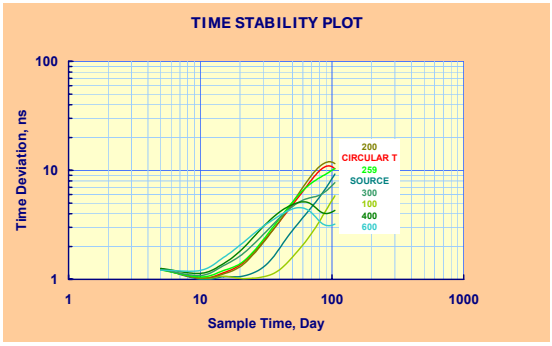

Fig.4

improvement as sample time becomes greater, so the time scale even can't be treated as steered one. For example the following table which contains extractions from figures 1-4 shows that for greater steering limits one may get rms time deviation in a few times less than for 100 ps/day.

On other hand one can't increase steering limit infinitely despite time tracking ability in this case will be better. The faster tracking inevitably produces frequency stability deterioration.

So one has to find a proper equilibrium between tracking ability and frequency stability. This compromise have to be based on application purpose of steering time scale. If the main purpose is to produce at any price time scale in closest vicinity to reference one have to introduce fast tracking.

On other hand one of the main goals of local UTC(k) is to offer user the real time realisation of the UTC because of the UTC is accessible with time lag about

	SOURCE	CIRCULAR T	100	200	259	300	400	600
MEAN DEV ns	188	20	91	21	16	13	11	10
RMS DEV ns	128	13	41	15	10	8	6	6
σ_y(10 d)$\times10^{+15}$	2.00	2.05	2.06	2.06	2.11	2.17	2.27	2.42
σ_y(30 d) $\times10^{+15}$	0.86	1.48	0.70	1.45	1.54	1.72	2.03	2.05
σ_y(60 d) $\times10^{+15}$	1.23	2.15	0.69	2.33	2.18	1.78	1.72	1.51
σ_x(10 d) ns	1.00	1.02	1.03	1.03	1.05	1.08	1.13	1.21
σ_x(30 d) ns	1.29	2.21	1.05	2.17	2.31	2.57	3.04	3.07
σ_x(60 d) ns	3.68	6.43	2.07	6.99	6.53	5.33	5.14	4.51

one and a half months. So strictly speaking user needs local UTC(k) scale for above mentioned period, after that one may get direct access to UTC.

The presented figures reflects stability estimations relative to UTC and for sample interval at least from 5 to 10 days are limited by time transfer link quality. So the influence of introduced steering corrections on stability is strongly hidden by time link resolution. This is the case for UTC-UTC(k) difference but for local

users equipped with high stable clock steering corrections may deteriorate local clock stability estimations relative to UTC(k).
We consider this problem may be somewhat soften if steering correction will be introduced not as abrupt permanent frequency step but will be done in a such way that not only time scale but at least it's derivative will be continuous in a pivot points. In this case steering corrections will be variable within month. We have just started this study and hope to finish and report it in closest future.

IV. CONCLUSIONS

For the first time in the history of Russian atomic time we developed steering coordinated time scale UTC(SU) in close vicinity to UTC. The achieved tracking ability characterised by mean time deviation |UTC-UTC(SU)| = 20 ± 13 (1σ) ns. This level is not indicative because more than half year we were forced to compensate initial frequency difference. The investigation on steering time scales will be continued and steering ability will be improved.

REFERENCES

[1] N. Koshelyaevsky, E. Zagirova, UTC(SU) Steering Time Scale Strategy. Data Stimulation and First Results, Proceeding of the 19th European Frequency and Time Forum, 21 – 24 March 2005, Besancon, France.
[2] Need to improve worldwide time coordination to UTC, Recommendation S5 (1993), Report of the Comite Consultatif pour la definition de la second (12th meeting-1993) to the Comite International des Poids et Mesures.

Proceedings of the 20th EFTF, 2006

Hardware aspects of a Real-time Software Clock

W. Klische and G. Kramer [1]
K+K Messtechnik GmbH, St.-Wendel-Str. 12, 38112 Braunschweig
Electronic address: kplusk@t-online.de
[1] *retired from* PTB

A multi-channel digital phase recorder measures the standard frequency signals of an ensemble of atomic clocks (2 hydrogen masers + 1 caesium clock) with picosecond precision, a microcomputer compares the digital phase data, calculates in real-time an optimum synthetic time scale, and automatically tunes an VCXO to represent that scale. The software is made to generate an optimally stable time scale and continue it even in the event of a sudden non-ergodic behaviour (failure) of one of the clocks.

1. INTRODUCTION

Software clock algorithms are well established, e.g. in combining stable atomic clocks – some of them scattered all around the world – to form virtual time scales (like UTC, TAI), that are normally distributed to users by bulletin in retrospect only. In contrast to such 'paper clock' approach, we have investigated the hardware requirements and actually built what we call a 'real time software clock', i.e. a device, which accepts the output signals of various stable clocks (plus possibly some bulletin information and strategic operator decisions), and from these generates an optimised output clock signal under the control of software clock algorithms.

In particular, we are currently developing a unit that combines two masers, a Caesium clock and a GPS timing receiver to form a local embodiment of UTC. The output signal, we call it PRC, the 'Primary Reference Clock', is generated by a VCXO with good short-term stability. The relative phases of all the input clock signals and of the VCXO are measured using an enhanced version of our multi-channel synchronous digital phase recorder [2], the concept of which had originally been developed for the first 'Optical Clock'[1], which was based on stabilised gas lasers and infrared molecular transitions around 30 THz and 88 THz.

From the measured phase data, the software clock algorithm derives the optimised virtual time-scale. The VCXO is then controlled by a software PLL to track this time-scale either exactly or with deliberate offset according to a operator-programmed steering function. Alternatively, instead of controlling a VCXO, a continuous digital phase shifter could be used to shift the output phase of one member of the clock ensemble accordingly. For various reasons however, in our first approach, we use the VCXO, controlled through a special high resolution (24 bit) digital-to-analogue conversion scheme.

As the resultant software clock signal is fed back into the same phase recorder, the attainable quality of the software clock output should depend on the sources only and on the proven sensitivity and stability of the phase recorder (in differential mode), which is characterised by a measurement rate of 1 kHz and a noise level below 10 ps (rms) for a single measurement. The speed and resolution characteristics of the phase recorder currently allow for relatively slow action only of the software PLL: the period of the control cycle is 0.1 s, thus calling for a good OCXO with high short- and medium-term stability.

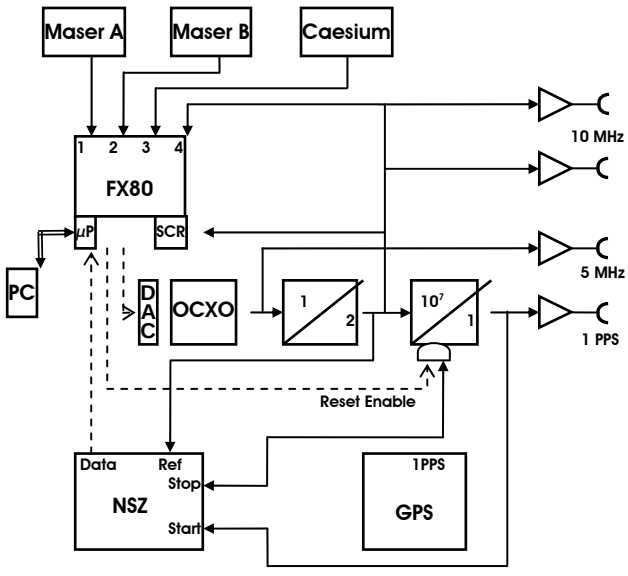

Figure 1:
Elements of the Software Clock

ENHANCED PERFORMANCE OF THE MULTI-CHANNEL PHASE RECORDERS.

The resolution of the FX-type phase recorders can be tested and demonstrated by recording the small and stable phase difference measured between two versions of the same (standard frequency) signal originating in two outputs of an isolation (buffer) amplifier. We find that logic level square waves between 10 kHz (FXE only) and 10 MHz are well suited, the two signal versions differing in the lengths of the connecting cables. The group delay of even standard RG58 appears to be stable enough, as long as short lengths of cable (~10 m) are considered.
Results for FX80 (input frequency range 4...40 MHz) have been published already [2]. The noise floor is characterised by a 10 ps (rms) scatter of the single measurement and a measurement rate of 1 kSamples/s. So at averaging times of 0.1 s the noise floor drops below 1 ps already.

In the mean time we have verified this level for FXE (with extended frequency range 4 kHz ... 65 MHz) as well. Systematic errors, i.e. errors that cannot be reduced by averaging, are mainly a residual temperature sensitivity on the order of 1...2 ps/K, reflecting either temperature gradients inside the instrument or incomplete balance of the temperature sensitivities of the components used in the nominally identical channels.
Another source of systematic error in a multi-channel instrument can be what we call 'inter-channel cross-talk'. Such cross-coupling presents a danger particularly in a software clock application, where all signals are at precise standard frequencies. The measurement of the phase difference of any two signals, applied to a pair of channels of the instrument, should by no means be influenced by signals applied to the other channels. This requires a very high degree of isolation between channels, achievement of which is complicated by the fact that the pulse length expanders forming the basic down conversion mixers of the channels should – on the other hand – be placed close together inside a common thermal shield.

In a thermally controlled laboratory environment one might consider separating the channels into different modules. Presumably this would avoid the bumps entirely.

Using our standard test method that consists of recording the pulse delay in a short length of cable, we have now applied an additional, variably phase shifted version of the same signal to a third channel in order to observe a possible interference. The result was, that in our 1st version FX80 we found the same type of 'coincidence bumps' that we had already observed as the effect of channel-to-reference coupling and which we successfully suppress to a negligible level by the method of 'reference scrambling' [2]. Scrambling the reference, however, cannot suppress channel-to-channel interference, which was found to be causing 'bumps' up to 30 ps high.

For both types of 'bumps', the dominant cross-coupling mechanism was identified as being the (linear) effect of unintentional coupling between PCB traces, in combination with the comparator non-linearity of the logic gates. It is this non-linearity that converts the superposition of an interfering waveform into phase modulation.
While such coincidence bumps are clearly a feature of our time/phase encoding, which uses short rise-time square-waves instead of sine-waves, it is interesting to note, however, that with sine-wave signalling, the stray capacitance would give rise to cross-coupling time shifts of just the same peak deviation as in the observed coincidence bumps; the main difference being that with sine-wave signalling the perturbation exist at most of the relative phases, whereas the square-waves mutually interfere in the event of near coincidence of the level transitions only.

A new, optimised PCB layout now reduces the cross-interference to a fraction of what it was before.
What we still observe as a systematic error, is an irregularly shaped cross-correlation feature, rather small (3 ps peak ; < 1ps rms, see fig. 2) deviation, to which probably a number of different types of non-linear coupling mechanisms are contributing.

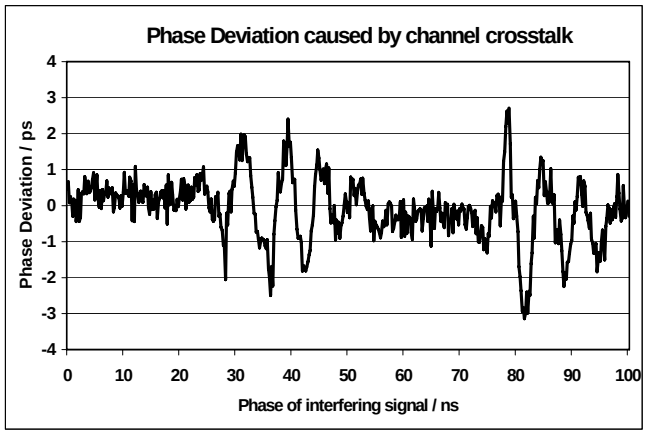

Figure 2
Correlation bumps caused by inter-channel interference

One type of unintentional coupling that we have already dealt with, is caused f. ex. by the supply current pulses drawn by the CMOS logic gates and buffers when propagating square-wave signals. The resulting noisy Vcc voltage then modulates the phase because of the supply sensitivity of the propagation delay.

It is clear that, as long as systematic errors can be made visible by any means, including signal averaging for noise reduction, they represent a challenge. Design refinement with better shielding and isolation is one approach, but it should also be noted that more sophisticated signalling formats like the use of differential signals (LVDS) and possibly PRN codes could improve the immunity to interference in a software clock system, particularly where it is based on a distributed clock ensemble.

For future applications we are also developing a new phase recorder (FXC) with still further enhanced speed/resolution characteristics. It should enable the software clock to operate a much tighter PLL, thus easing the stability requirements of the VCXO. We now found that the new design replicates an idea already published by J. Kalisz [3].

FXC already achieves the expected conversion speed (~32 µs). A further enhancement of the resolution, appearing possible because of the faster averaging, still remains to be demonstrated, however.

THE SWC COMPUTER SYSTEM

A general problem encountered when tackling time-critical real-time tasks with a standard PC, appears in the variable response time of the WINDOWS operating system. Unpredictable delays make it difficult to close real-time control loops through a PC or even to receive and store the continuous flow of data that our phase recorders generate.
The FX80 and FXE phase recorders already employ a dedicated microcomputer for handling the real-time tasks and use the standard PC for the operator interface, graphics, and file handling tasks only. Communication with the phase recorders uses a special 'hand-shake' protocol, thus ensuring that no data is lost between the 68000 type µComp and the PC. But, though not lost, data may be delayed. And wherever delayed action cannot be tolerated in a servo loop, the actions have to be carried out in the µComp.

PRESENT CONFIGURATION OF THE SWC

So far our software clock (SWC) phase-locks a quality OCXO to the mean phase of two hydrogen masers, to which a deliberate offset can be added as an operator-programmed steering function. SWC thereby assumes the additional job of an micro-phase stepper.
In another channel the software clock compares its phase to that of a commercial caesium clock.

Figures 3 and 4 show a sample recording of the control deviation (error signal) of the numerical PLL and its Allan deviation plot.

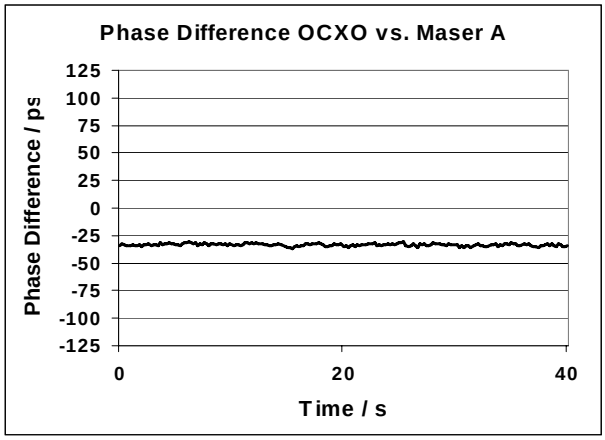

Figure 3:
Sample recording of the control deviation (error signal)

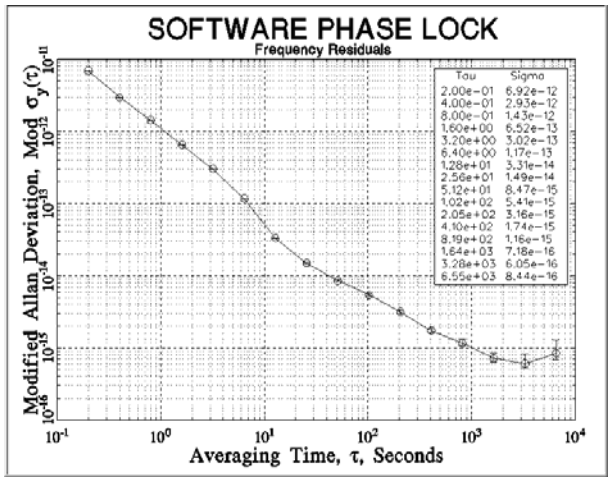

Figure 4:
Modified Allan Deviation (Noise Floor)

PRELIMINARY ROBUSTNESS RESULTS

The main advantage to be gained by employing a software clock as the Primary Reference Clock lies however not in extracting from the clock ensemble a signal with superior phase noise properties but rather in the possibility of detecting non-ergodic behaviour (failure) in one of the clocks and automatically excluding it from the ensemble that forms the primary reference.
So far we consider two failure scenarios only, and direct operator intervention.

1.) One of the maser clock signals exhibits a ***phase step*** (see fig. 5). Such would most likely be caused by a faulty connector or distribution amplifier (or by sudden bending of a connecting cable). Not only the otherwise very stable phase difference between the two maser

signals would show the step but even the VCXO with its limited intrinsic stability can serve to distinguish, which of the two maser signals is having the problem and might have to be excluded.

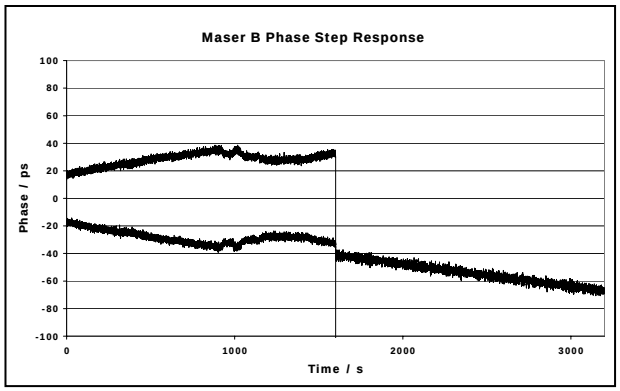

Figure 5:
PRC response to a 1 ns phase step of Maser B

2.) Identifying the faulty maser is more difficult in the case of a ***frequency step*** or slow deterioration of one of the masers.
Here we will need the caesium clock as the arbitrator. The inferior short-term stability of the caesium clock (as compared to that of a maser), calls for a long observation time, before a decision can be made, which of the two masers should be considered less reliable.

3.) ***Operator decision***, whatever information it may be based on, could also call for switching one maser temporally out of service; for maintenance or other interruption.

In all three cases, the S-W clock's PRC signal should, as precisely as possible, continue an even time scale. For that purpose the SWC continuously monitors the phases of all clocks with respect to the PRC and calculates a model track of each clock. When one clock is taken out of service, the algorithm that calculates the PRC scale will simply disregard the measured phase of that clock and replace the data with the model data, thus ensuring that the PRC continues without a step in phase or frequency.

CLOCK MODELS

For the very stable atomic clocks we consider linear interpolation models only. So the SWC software regularly (every 100 seconds) computes a linear fit of the phase data measured during the past ~5000 s (operator settable parameter). The model description has 3 parameters (x_0, y_0, t_0), where t_0 also describes the epoch of its optimal validity, i.e. where the model parameters best describe the actual behaviour. So the projected phase x(t) is described by:

$$x(t) = x_0 + y_0 \cdot (t - t_0).$$

Ergodicity monitoring / clock error detection

A rather unspecific method of detecting non-ergodic behaviour of a clock signal, that was programmed and tentatively implemented, consists of continuously calculating the Allan deviation for a number of dwell-times Tau, and comparing the (filtered) results with predetermined threshold values for every Tau. These threshold values will have to be a compromise and set so as to avoid frequent false alarms as well as excessive delay, before a warning is issued or the faulty clock is removed from the active ensemble.

When, on the other hand, a new clock is added or reintroduced into the ensemble, it will have to be monitored for a period of time in order to develop or confirm the model description before including it into the active ensemble, i.e. before using its real-time phase data in the PRC algorithm.

The model parameters are stored and can serve as a condensed log offering the possibility to tie in with prior states of the clock ensemble.

Acknowledgement

We would like to thank the staff of the PTB T&F division for the possibility to carry out the tests using PTB standard frequency signals and to borrow some of their instrumentation.

REFERENCES

[1] G. Kramer, B. Lipphardt, U. Huebner,
Joint Meeting EFTF - IEEE IFCS, 651 (1999)

[2] G. Kramer, W. Klische, Proceedings EFTF (2004)

[3] J.Kalisz, M.Pawlowski, R.Pelka, IEEE IM-35 (1986)
see also:
J. Kalisz, Review of methods for time interval measurements with picosecond resolution,
Metrologia, **41** (2004) 17-32

Proceedings of the 20th EFTF, 2006

Total deviation assessment with data preprocessing

Andrzej Dobrogowski, Michal Kasznia
Poznan University of Technology, Institute of Electronics and Telecommunications,
ul. Piotrowo 3A, 60-965 Poznan, Poland
dobrog@et.put.poznan.pl, mkasznia@et.put.poznan.pl

In the paper the time effective methods of total deviation and time total deviation calculation are described. These methods consist in the reduction of the number of data used for calculation for long observation intervals. The processes of the data reduction consisting in the creation of a new data sequence that represents the old one are described. The results of the parameters' calculations made on the raw and modified data series are presented and compared.

I. INTRODUCTION

Allan deviation ADEV and time deviation TDEV are the parameters commonly used for describing the quality of synchronization signal in the telecommunication network [1, 2, 3]. The parameters allow to assess the variations of time interval provided by the synchronization signal and recognize the type of phase noise affecting the signal. The estimates of the parameters are calculated for a series of observation intervals using the sequence of time error samples measured between two timing signals at the network interface.

The number of data necessary for the reliable estimation and the complication of the estimators' formulae may result in rather long time of the estimate calculation. Such a problem is evident in the case of the calculation performed for long observation intervals using the time error samples taken with small sampling interval. Therefore some methods enabling short ADEV and TDEV estimation were proposed [4, 5] by the authors of this paper. These methods consist in the initial preprocessing of the raw data set resulting in the reduction of the number of data used for the parameters' estimation. The data preprocessing based on the decimation (for ADEV estimation) and averaging (for TDEV estimation) is performed if the estimate is calculated for observation interval greater than specified threshold value. Such preprocessing allows to make the calculation faster (from ten to hundred times for particular observation intervals) with the relative error less than 10% for ADEV and 5% for TDEV. Such a degradation of the estimates is acceptable in the telecommunication applications.

Total approach to the parameters' estimation was proposed [6-8] in order to improve the confidence of the timing signal stability measure. It consist in the extension of the whole data sequence (in the case of total ADEV estimation) or particular data subsets of the sequence (in the case of total TDEV estimation). The number of data needed for total deviations estimation is enlarged by the extension, so we face the same problem as described above: possible long time of the parameter estimation for long observation intervals, when the time error samples were measured with small sampling interval.

In this paper the application of data preprocessing previously used for time effective ADEV and TDEV estimation, is also for total estimation of the parameters proposed. The results of calculation of total deviation and time total deviation for several data sequences with and without data preprocessing are presented and discussed. Usefulness of the total parameters in the telecommunication applications is considered.

II. ADEV AND TOTDEV ESTIMATION

The formula for the estimator of the Allan deviation ADEV takes the form:

$$\hat{ADEV}(\tau)=\sqrt{\frac{1}{2(n\tau_0)^2(N-2n)}\sum_{i=1}^{N-2n}(x_{i+2n}-2x_{i+n}+x_i)^2} \quad (1)$$

where $\{x_i\}$ is a sequence of N samples of time error function $x(t)$ taken with interval τ_0; $\tau=n\tau_0$ is an observation interval [1, 2, 3]. In order to compute the estimate of the total deviation TotDEV the extended virtual data sequence $\{x^{\#}_i\}$ is created first [6, 7, 8]. The items in the new data sequence take the values:

$$\begin{aligned} x_i^{\#} &= x_i \\ x_{1-i}^{\#} &= 2x_i - x_{1+i} \\ x_{N+i}^{\#} &= 2x_N - x_{N-i} \end{aligned} \quad (2)$$

As result, we obtain the sequence of $3N$–2 samples, indexed from 2–N till 2N–1. The formula of the total deviation estimator takes the form:

$$\hat{TOTDEV}(\tau)=\sqrt{\frac{1}{2(n\tau_0)^2(N-2)}\sum_{i=2}^{N-1}(x_{i-n}^{\#}-2x_i^{\#}+x_{i+n}^{\#})^2} \quad (3)$$

In order to reduce the calculation time for long observation intervals the modification of the time error set was proposed [4]. The modification allows reducing

the length of the time error sequence. The reduction of data consists in the creation of a new data sequence that represents the old one using the decimation of the raw time error sequence.

The first step of the reduction is made when the observation interval is greater than $300\tau_0$. In this case the number of data is ten times smaller than the number of samples in the raw data set. The second step of the reduction is performed, when the observation interval exceeds $3000\tau_0$. The number of values in the new data set in this case is hundred times smaller than the number of samples in the raw data set. The successive steps of the data reduction can be performed for the observation intervals greater than $30000\tau_0$ or $300000\tau_0$, if necessary.

III. TOTDEV COMPUTATION EXPERIMENT

The time of calculation and the accuracy of total deviation values computed with and without data preprocessing were analyzed in the experiment. Several data sequences representing different time error types were used. Two sequences were obtained from the measurement process [4, 5]. The first time error sequence (denoted as MSG, Fig. 1) was obtained from the comparison of two internal oscillators of a timing signal measurement system. The second sequence (denoted as GPS, Fig. 2) was the result of the comparison of two different oscillators controlled by the GPS signals. The time error samples were measured with the sampling interval τ_0=1/30 s during the measurement time of 4000 s.

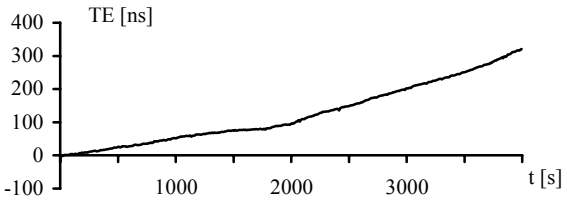

Fig. 1. Time error of the MSG signal measurement

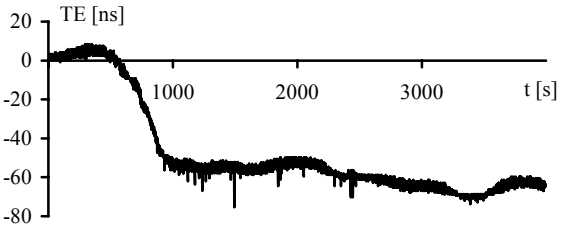

Fig. 2. Time error of the GPS signal measurement

Other sequences represent the typical noises for the timing signals: white phase modulation (WPM), flicker phase modulation (FPM), white frequency modulation (FPM), flicker frequency modulation (FFM) and random walk frequency modulation (RWFM).

In the experiment the 81 values of TotDEV estimate for the observation intervals changing from τ=0.1 s till 1000 s were computed. According to the rules of data preprocessing presented in the previous section, the calculations with data modification were performed for the observation intervals greater than 10 s (first step of modifications) and 100 s (second step).

In the Table 1 the time of TotDEV calculation for the whole range of 81 observation intervals and for the decade subranges of the whole range is presented. In the Table 2 the time of calculation for some chosen observation intervals is given. The format of the time is as follows: minutes:seconds. The PC computer with Pentium IV 3 GHz microprocessor was used for all calculations.

Table 1. Time of TotDEV calculation for the ranges of observation intervals

data	range of observation intervals τ [s]				
	[0.1-1000]	[0.1-1]	(1-10]	(10-100]	(100-1000]
raw	3:03.68	47.13	44.88	45.03	46.64
mod.	1:37.33	-	-	4.50	0.49

Table 2. Time of TotDEV calculation for chosen observation intervals

data	observation intervals τ [s]				
	0.1	1	10	100	1000
raw	2.20	2.25	2.26	2.25	2.42
mod.	-	-	-	0.22	0.02

The time of calculation with data modification is approximately ten times smaller for the observation intervals between 10 s and 100 s. It is about hundred times smaller for the intervals greater than 100 s. Thus the calculation time of the whole range of the parameter's estimate can be about two times smaller for the modified data. The time of the data extension process, necessary in the total deviation calculation, was not taken into consideration.

The results of TotDEV calculations for the MSG and GPS time error sequences are presented in the Fig. 3 and Fig. 4. The relative error of the calculations with data modification is presented in the Fig. 5.

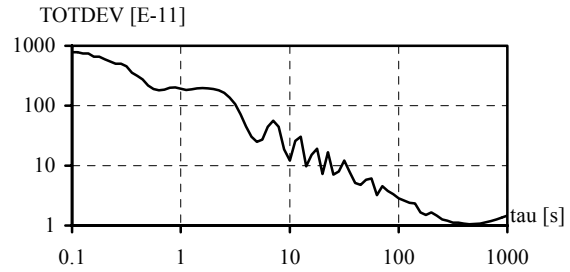

Fig. 3. TotDEV for the MSG sequence

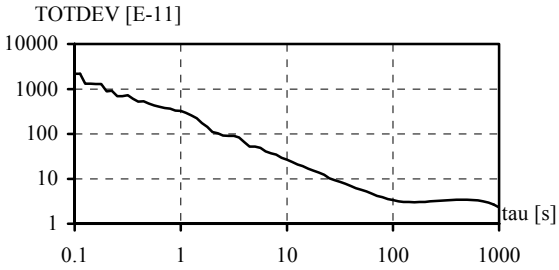

Fig. 4. TotDEV for the GPS sequence

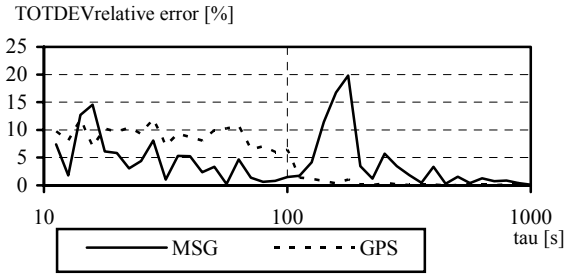

Fig. 5. TotDEV relative error for MSG and GPS sequences

The relative error of the TotDEV calculations for WPM and FPM sequences is presented in Fig. 6. The relative error for the WFM, FFM and RWFM sequences is presented in Fig. 7.

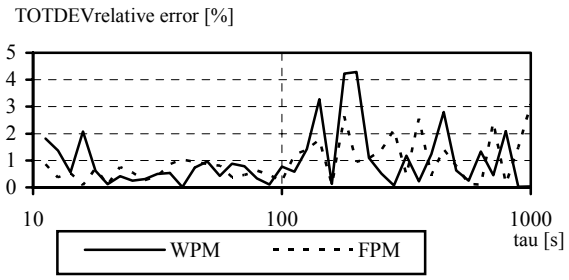

Fig. 6. TotDEV relative error for WPM and FPM sequences

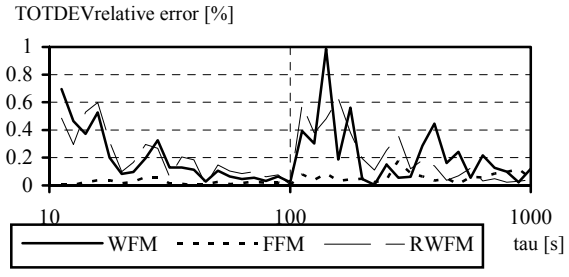

Fig. 7. TotDEV relative error for WFM, FFM, and RWFM sequences

The relative error of TotDEV calculations for MSG and GPS data sequences is rather acceptable. It does not exceed 20% for the MSG sequence and 15% for the GPS sequence. Better results were obtained for the next sequences. The relative error was less than 5% for the WPM and FPM sequences. The smallest error was obtained for the WFM, FFM, and RWFM sequences, where it is less than 1%.

IV. TDEV AND TOTAL TDEV ESTIMATION

Modified Allan deviation (MADEV) is used in order to distinguish between the WPM noise and FPM noise. Time deviation TDEV ($TDEV(\tau)=\frac{\tau}{\sqrt{3}}MADEV(\tau)$) is used in the telecommunication applications to evaluate the synchronization signals in the telecommunication network. The formula for the estimator of the time deviation TDEV takes the form:

$$\hat{TDEV}(\tau)=\sqrt{\frac{1}{6n^2(N-3n+1)}\sum_{j=1}^{N-3n+1}\left[\sum_{i=j}^{j+n-1}(x_{i+2n}-2x_{i+n}+x_i)\right]^2} \quad (4)$$

where $\{x_i\}$ is a sequence of N samples of time error function $x(t)$ taken with interval τ_0; $\tau=n\tau_0$ is an observation interval [1, 2, 3].

In order to compute the estimate of total time deviation for the observation interval $\tau=n\tau_0$, the procedure described in [8] is applied. First, a subsequence consisting $3n$ samples is chosen. Then the linear trend is removed from this data subsequence. In the next step the subsequence is extended at both ends by uninverted, even reflection. The items in the new subset take the values:

$$\begin{aligned} x_k^{\#} &= x_{3n+1-k}^{*} \\ x_{3n+k}^{\#} &= x_k^{*} \\ x_{6n+k}^{\#} &= x_{3n+1-k}^{*} \end{aligned} \quad (5)$$

where x_k^* is time error sample with linear trend removed. Working on this extended subsequence containing $9n$ samples, the average $z_j(n)$ is computed:

$$z_j(n)=\overline{x_j^{\#}}(n)-2\overline{x_{j+n}^{\#}}(n)+\overline{x_{j+2n}^{\#}}(n) \quad (6)$$

where $\overline{x_j^{\#}}(n)$ is an average over n samples starting at the index j. The formula (6) can be written in the form:

$$z_j(n)=\frac{1}{n}\sum_{k=j}^{j+n-1}\left(x_k^{\#}-2x_{k+n}^{\#}+x_{k+2n}^{\#}\right) \quad (7)$$

The square root of the average of all subestimates for each $3n$ subsequence existing in the data sequence gives us the formula of the total time deviation estimator:

$$\hat{TOTDEV}(\tau)=\sqrt{\frac{1}{6(N-3n+1)}\sum_{i=1}^{N-3n+1}\left[\frac{1}{6n}\sum_{j=i-3n}^{i+3n-1}(z_j(n))^2\right]} \quad (8)$$

The calculation of sums within the $9n$ samples subsequence can be simplified using the procedure described in [9, 10].
In order to reduce the time of calculation for long observation intervals, similar data modification, as for Allan deviation and total deviation is proposed. The data modification is performed, when the observation interval exceeds $300\tau_0$ (first step) and $3000\tau_0$ (second step), but instead of decimation the averaging of data is used [4, 5]. Therefore, in the first step of modification an item in the new data set is an average of the 10 successive samples from the raw data set, and in the second step the new data set contains the averages of the 100 successive samples from the raw data set.

V. TOTAL TDEV COMPUTATION EXPERIMENT

The same time error sequences, presented in the Section III of this paper, were used in the total time deviation calculation experiment. The assumption of the experiment was the same as in the case of total deviation: we wanted to compute 81 values of total TDEV for the observation intervals changing from 0.1 s till 1000 s (4 decades, 20 points per decade) using modified and non-modified data. Then we wanted to compare the results: time of calculation with and without modification and the obtained values of total TDEV. We changed quickly our assumption. After long lasting computation of a few first values of total TDEV we have stopped the calculation process. It turned out, that the computation of the 81 values for the whole range of observation intervals for the 4000 s data sequence should last about 40 days. Therefore we have shortened the range of observation intervals and the length of the data sequence used for calculation. Thus we computed 31 values of total time deviation for the observation intervals changing from 0.1 s till 100 s (3 decades, 10 points per decade) for the data sequences having the length of 400 s. In the Table 3 the time of total TDEV calculation for the whole range of 31 observation intervals and for the decade subranges of the whole range is presented. In the Table 4 the time of calculation for some chosen observation intervals is given. The format of the time is as follows: hours:minutes:seconds. The results of total TDEV computation for MSG and GPS sequences are presented in Fig. 8 and Fig. 9.

Table 3. Time of total TDEV calculation for the ranges of observation intervals for the 400 s data sequence

data	range of observation intervals τ [s]			
	[0.1-100]	[0.1-1]	(1-10]	(10-100]
raw	6:36:35.10	1:43.15	15:07.64	6:19:44.31
mod.	17:42.53	-	-	51.74

Table 4. Time of total TDEV calculation for chosen observation intervals for the 400 s data sequence

data	observation intervals τ [s]			
	0.1	1	10	100
raw	2.69	21.97	3:20.75	39:58.22
mod.	-	-	-	5.76

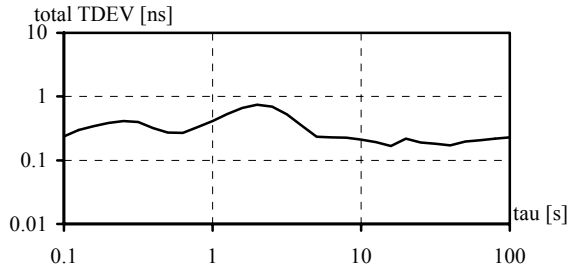

Fig. 8. Total TDEV for the MSG sequence

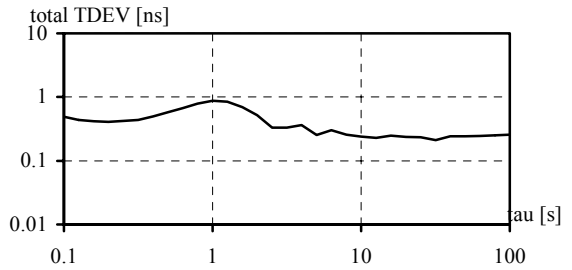

Fig. 9. Total TDEV for the GPS sequence

The comparison of time of total TDEV calculation is very promising – the data reduction causes radical shortening of the calculation time. Despite this the numerical results are unacceptable: the relative error for each data sequence exceeds 100%. The values obtained using data modification are irregular – do not fit the slopes characteristic for the particular types of noises. The examples of the computation results for the FPM and WFM time error sequences are presented in Fig. 10 and Fig. 11. The solid line presents the total TDEV obtained with data modification, and the dotted line presents the total TDEV obtained without modification.

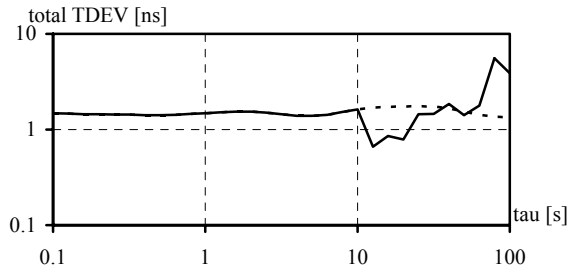

Fig. 10. Total TDEV for the 400 s FPM sequence

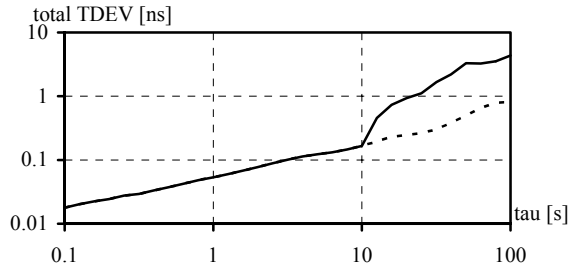

Fig. 11. Total TDEV for the 400 s WFM sequence

Because of the poor results obtained for the data sequence having the length of 400 s, the next attempt was made. The computations of total TDEV were performed for the longer time error sequences (having the length of 1000 s) expecting, that increasing the number of averaged items may improve the estimate obtained for modified data. The time of total TDEV calculation with and without data modification is presented in Table 5 (for the whole range and subranges of observation intervals) and in Table 6 (for some chosen observation intervals). The increasing of the length of the data sequence results in serious enlarging of computation time. The modification of data allows to shorten of the computation time from almost 26 hours to less than 1 hour for the whole range of observation intervals.

Table 5. Time of total TDEV calculation for the ranges of observation intervals for the 1000 s data sequence

data	range of observation intervals τ [s]			
	[0.1-100]	[0.1-1]	(1-10]	(10-100]
raw	25:53:41.36	5:06.32	47:06.03	25:01:29.01
mod.	56:12.85	-	-	3:57.50

Table 6. Time of total TDEV calculation for chosen observation intervals for the 1000 s data sequence

data	observation intervals τ [s]			
	0.1	1	10	100
raw	17.36	1:06.52	10:37.85	4:53:42.84
mod.	-	-	-	46.47

The numerical results are somewhat better, than for the shorter sequences, but there are still unacceptable. The relative error is between 60% and 100%. The obtained values are still irregular and the correct identification of the noise type is difficult. The examples of the computation results for the FPM and WFM time error sequences are presented in Fig. 12 and Fig. 13. The solid line presents the total TDEV obtained with data modification, and the dotted line presents the total TDEV obtained without modification

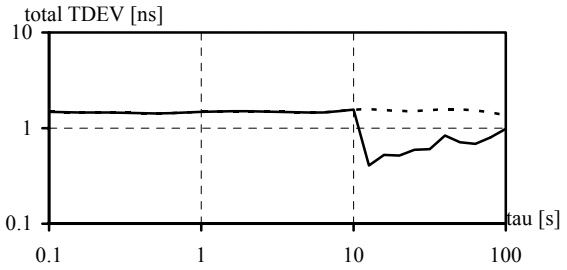

Fig. 12. Total TDEV for the 1000 s FPM sequence

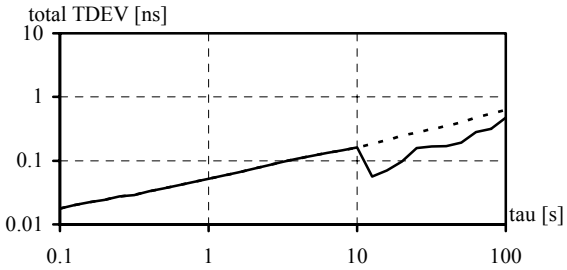

Fig. 13. Total TDEV for the 1000 s WFM sequence

VI. CONCLUSIONS

In the paper the method of data modification, previously used for time effective ADEV and TDEV assessment, were adopted for total deviation and total time deviation calculation. The decimation of data brings good results in the case of the total deviation assessment. The relative error of the result obtained with data modification was acceptable small. The computation time was from ten to hundred times shorter for the particular observation intervals. The data modification proposed will be helpful for fast TotDEV estimation, when the data sequence is an effect of long time error measurement with short sampling interval.

The data modification does not bring so good results in the case of total time deviation. The averaging of data is not an equivalent process for the data processing in the procedure of total TDEV estimation, as in the case of time deviation estimation. The data modification results in an obvious shortening of the calculation, but the degradation of the estimate is unacceptable.

Another problem is the time used for the total TDEV computation. In the telecommunication applications we often work on the long data series taken with small sampling interval in order to obtain the parameters for a wide range of observation intervals. In such a case the long time of total TDEV computation (many hours) may be unacceptable, when we need a fast evaluation of the signal analyzed. We can obtain the common time deviation within four minutes without any data modification. The total TDEV may be useful only, if we work on rather short data series.

REFERENCES

[1] ANSI T1.101-1999, Synchronization interface standard

[2] ETSI EN 300 462, Generic requirements for synchronization networks (1998).

[3] ITU-T Rec. G.810, Considerations on timing and synchronization issues (08/96).

[4] A. Dobrogowski, M. Kasznia, "Modification of the raw data set for time efficient ADEV and TDEV assessment", Proc. of the 14th EFTF, pp. 338-342, Torino 14-16 March 2000.

[5] A. Dobrogowski, M. Kasznia, "Impact of time error data preprocessing for TDEV assessment", Proc. of the 15th EFTF, pp. 463-467, Neuchatel 6-8 March 2001.

[6] D. A. Howe, "Methods of improving the estimation of long-term frequency variance", Proc. of the 11th EFTF, pp. 91-99, Neuchatel 4-6 March 1997.

[7] D. A. Howe, "The total deviation approach to long-term characterization of frequency stability", IEEE Transactions on Ultrasonics, Ferroelectrics and Frequency Control, vol. 47, No. 5, pp. 1102-1110, September 2000.

[8] D. A. Howe, T. K. Peppler, "Definitions of "total" estimators of common time-domain variances", Proc. of the 2001 International Frequency Control Symposium, pp. 127-132, Seattle, 6-8 June 2001.

[9] S. Bregni, "Synchronization of Digital Telecommunications Networks", J. Wiley & Sons, 2002

[10] M. Kasznia, "Some Approach to Computation of ADEV, TDEV and MTIE", Proc. of the 11th European Frequency and Time Forum, pp. 544-548, Neuchatel 4-6 March 1997.

Proceedings of the 20th EFTF, 2006

Applicability of Coaxial Cables at Picosecond Range Timing

K. Kalliomaki [1], J. Mannermaa [2], and T. Mansten [1]
[1)] *MIKES, FI-02150, Espoo, Finland*
[2)] *Nokia Corporation Technology Platform, FI-33100, Tre, Finland*
kalevi.kalliomaki@mikes.fi.

Timing performances of conventional coaxial cables like RG 223 and RG 58 were studied. The effects of timing pulse shape, cable bandwidth, ambient fluctuations and physical stress were as input parameters. Pulse delays and shapes were studied using a time interval counter and a fast digital oscilloscope. Delay as a function of frequency was studied with resonance method and phase delay measurements. Effects of ambient factors and physical stress were studied at a frequency of 5 MHz using a phase comparator capable of resolving 10 fs.
The results revealed that conventional tick pulse is not anymore usable below 1 ns if the cable delay has to be well known. Environmental effects may change the cable delay up to 100 ps. Therefore, as a first approximation the pulse shape has to be changed to fit the properties like bandwidth and velocity dispersion of cables. Cos^2 pulse or RF-burst may help but finally one has to use optical cables.

1. INTRODUCTION

Time and Frequency Metrology has encountered new challenges because the inaccuracy level requirements approach picosecond range. Bandwidths of conventional coaxial timing cables are limited to 100 MHz…1 GHz range depending on their length, and quality and the rise times of the PPS ticks are typically about 10 ns. Steeper pulses produce too much pulse shape changes. Moreover, the propagation velocity in cables is not constant and it is influenced by changes in temperature, in air pressure, and physical stresses due to e.g. bending. MIKES and Nokia Corporation Technology Platform have studied the impact of these phenomena on the trigger level of timing pulse. Results of the studies concerning the effects of these phenomena on the trigger level were presented in the EFTF'05 [1].
Experimental measurements were carried out to study the performance of the theoretical models and to find out, in practice, the relative short term instability of the measured value.
According to the preliminary results, e.g. the influences of air pressure changes are observed at the relative level of -5 ppm/mbar, or worse.
As conclusions, the increasing accuracy requirements of the PPS ticks can only be satisfied by the meticulous design of timing pulse shape and quality of the transmission lines. Also air pressure will effect on performance of the systems.

II. MATERIALS

The coaxial cables to be studied were RG 223 and RG 58 with BNC-connectors in different lengths up to 100 m. Most of them were in fixed installations in Time & Frequency laboratory (NMI), only short cables up to 10 m were studied separately. The reference plane for delay measurements is defined to the outer end of the dielectric insulator inside the connector.

III. MEASUREMENT METHODS AND RESULTS

Useful equations [2]

If the frequency f is high (> 1 MHz)

$$t_p \approx \sqrt{l_\infty c}\left(1+\frac{r}{2\omega l}\right)$$

$$t_g \approx \sqrt{l_\infty c}\left(1+\frac{r}{4\omega l}\right)$$

where: t_p is phase delay [s/m]
t_g is group delay [s/m]
r is the cable resistance/m
c is the cable capacitance/m
l is the nominal cable inductance/m
l_∞ is the cable inductance/m at high frequency

Cable resonance method

We have earlier used with good results resonance measurements of open and short circuited cables. By measuring all resonant frequencies up to 100 MHz, we obtain both the cable delay at fixed frequencies and the delay dispersion (and attenuation, too). Because the resonances are quite sharp, the repeatability is quite good, 0,1...0,2 % rms. of the delay for a single point. By combining all the results, we can easily go down to 100 ps level using this very simple method. The necessary instrumentation is a crystal controlled signal generator and an oscilloscope. Because we need only one end of the cable, we can measure delays of already installed cables. See Fig. 1 for results.

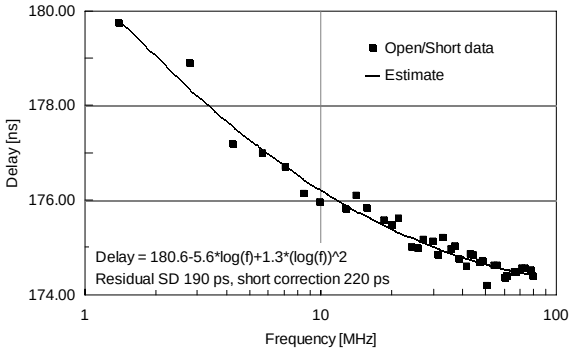

Fig. 1: Propagation delay dispersion of a 36 m cable as a function of frequency

Phase shift method

The second method we used was phase method using a crystal controlled signal generator and a two channel digital oscilloscope. We simply measured all frequencies which produced zero phase difference (modulo 2π) between the ends of the cable. In this case both ends of the cable must be available. The phase error in an oscilloscope and electrical length error of connecting cables was eliminated by interchanging the channels. Thus the dominating error is "manual" zero phase detection. The error seems to be about the same as that of the resonance method. We also used carefully calibrated Network Analyzer (Agilent PNA series) to check the delays up to 1 GHz.

Pulse delay method

Finally we tested the pulse delay method by using our automatic clock measuring system with active hydrogen maser as the main clock. After preliminary tests we had to abandon time interval methods where a separate clock was used as the pulse source because, due to random drift of a cheaper clock (like rubidium), the repeatability was worse than 100 ps.

We used the second pulse of our master clock as pulse source. The cable was simply connected/disconnected in series with our self check channel d0 and the corresponding time change was registered automatically every second. Due to the long (~ 100m) tick cable from reference clock laboratory (underground) to the time/frequency laboratory (2nd floor), the pulse shape was nicely shaped and rounded (filtered) to mach cable bandwidth, e.g. pulse shape did not change much due to the filtering effect of the cable anymore. Thus trigger point selection was not a problem and we could use our ordinary 1 V level.

Improving the accuracy of a time interval counter

To eliminate the nonlinearity of analog interpolators of the time interval counter (HP 53132A), we locked the counter time base to a frequency with an offset of $1 \cdot 10^{-9}$. This causes the counter time base to drift 1 ns/s and the 100 ns ranges of analog interpolators are covered within 100 s. Because the measurement rate of the automatic measuring system is 1/s, we obtain 100 readings in the above-defined 100 s time. After calculating the average value of those 100 readings, the nonlinearity is compensated at any time interval value (cable delay) to be measured and the random errors are decreased by one decade. We obtained 20 ps repeatability using 300 ps rms (spec.) time interval counter.

Trigger level error

The main problem is the trigger level error, which is proportional to the cable length. This can easily be 1 ns due to delay dispersion and signal attenuation. Thus the real delay in coaxial cables is a hard problem.
Fig. 2 depicts what happens in a cable due to delay dispersion. Input pulse is idealized to correspond 20 ns rise time. Output pulse is shifted left to conveniently start from the same origin. The beginning of the output pulse corresponds the contribution of high frequency (f >1 MHz) components and the remainder that of low frequency components. Naturally some low pass filtering effect (rounding-off) exists, too, but it is marginal compared to the effect of propagation dispersion.
The horizontal bar indicates the measurement error assuming that the beginning of the pulse is the "holy" point. What else could be used as the right point?
Naturally we can't set the trigger level down to zero volts to catch the right point. However, selecting a relatively low trigger level lowers the inherent error and eases the extrapolation of the pulse beginning. We have done this extrapolation job by studying the pulse shape with a fast digital oscilloscope (Tektronix TDS 2024, BW 200 MHz). This error dominates in case of "medium" and "long" cables.

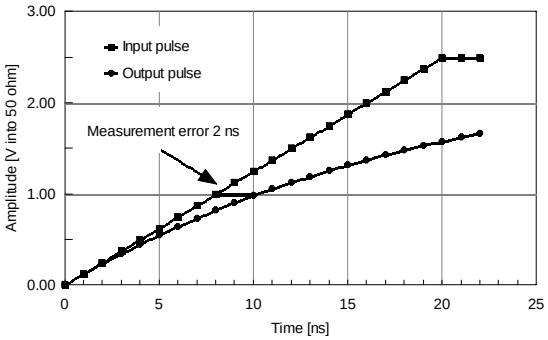

Fig. 2: The origin of measurement error

A S-shaped pulse occurs as an output pulse in long cables of bad quality, especially if the input pulse is too sharp. In this case the low pass effect is significant compared to the propagation dispersion effect. As a result of this high frequency attenuation, a low "pedestal" appears at the leading edge of the pulse. In this case the extrapolation back to the beginning of the pulse is practically impossible.
It is not necessary, however, because "pedestal" represents Fourier components outside the -3 dB boundary of the propagation media. In other words, those frequency components are not in the intended pass band. This is a good reason to omit them. The simplest way to omit the pedestal is to filter the input pulse to the cable, i.e. to use rounded pulse instead of a sharp one.

Pressure and physical stress effects

As a surprise we found very significant correlation between air pressure and cable delay. The correlation coefficient was from –5 to –10 ppm/mbar. When wondering about the explanation to this relationship, negative coefficient was difficult to understand. In later cable bending test, we collided to the same problem. The delay decreased when bending the cable. We wound 10 m cable around 25 cm (diameter) cylinder. It resulted -30..-80 ps delay change, which is mostly reversible.
Assuming that field components leak out from the cable, we submerged the cable (1.6 m long) into clean water (1.6 m) but this did not change delay significantly. In this case physical stress due to bending dominated causing up to 10 ps measurement noise.
Because group delay t_g in cables is proportional to $(l \cdot c)^{1/2}$, either inductance or capacitance has to decrease when air pressure or physical stress affects. It seems evident that capacitance is the "guilty" one. Stress may cause small air gaps between dielectric and outer conductor lowering the capacitance.

Fourier spectrum of a "tick" pulse

Fig. 3 depicts the envelope of the Fourier spectrum of a conventional tick pulse. Two essential zeros are marked up. The first one (100 kHz) corresponds pulse width τ ($f = 1/\tau$) and the second one (100 MHz) corresponds rise time tr ($f = 1/ t_r$). The actual spectra up to 50 MHz can be calculated from the well known sin(x)/x equation.
Frequency components up to 100 kHz ($f = 1/\tau$) define the basic "body" of the pulse. Components between 100 kHz and 100 MHz define the edges (rise & fall times). Because the spectrum follows 1/f –law, all components are important. The sum of those 1/f components approaches infinity when f increases without any limit. Amplitudes of frequency components after 100 MHz follow $1/f^2$-law, having only slight effect on pulse edges.

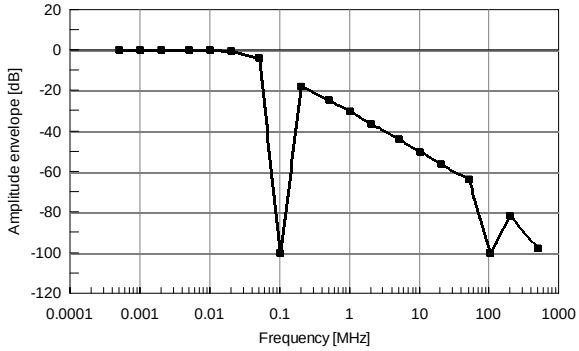

Fig. 3: Fourier Spectrum of a conventional tick pulse of 10 µs width and 10 ns rise time. Only essential zeros are marked up

IV. CONCLUSIONS

Applicability of conventional coaxial cables at picosecond range depends mostly on cable length. Cables up to 1 m in length are practically free of picosecond range problems assuming that anyone does not touch them. Touching may change the delay e.g. 10 ps and the change may not be reversible. When approaching the length of 100 m, even air pressure fluctuation may change the delay 100 ps. In fixed installations the cable movements are probably subtle and similar effects into nearby lying cables may compensate errors, when phase differences are measurement subjects. If the real cable delay is relevant, one has to be prapared to trigger level corrections. The magnitude of this correction seem to be about 30 ps/m at low (1 V) trigger levels but this correction is proportional to trigger level. Thus the above mentioned 100 m cable may cause 3 ns pulse delay error.

Final warning is, don't use too sharp pulses! Pulse spectrum must fit into –3 dB bandwidth of the cable. In case of the above mentioned RG 223 or RG58 cables, the rise time of the pulse in ns should be less than $L^2/100$, e.g. if the cable length L is 100 m the rise time should be less than 100 ns to avoid most troublesome pulse deformation effects.
To avoid dominating velocity dispersion effects, one has to use RF-pulse (e.g. 100 MHz) instead of conventional pulse. Then practically all frequency components are on the flat delay area and pulse distortion is negligible.

The use of optical cables seems to solve the above mentioned problems.

REFERENCES

[1] Kalliomäki, K., Mannermaa, J., Mansten, T., "The Effect of Counter's Trigger Level on Timing Below Nanosecond", Proceedings of the **19th** European Frequency and Time Forum (2005)
[2] L. Halme, Cable Transmission and Electromagnetic Shielding (in Finnish), pp. 170 (Otakustantamo, Espoo 1979)

Proceedings of the 20th EFTF, 2006

Time Unit Transmission for Customers

A.S.Kleiman, V.S.Solovyov, G.S.Sidorenko, S.I.Zub, S.A.Talamanov
National Scientific Center "Institute of Metrology", Mironosytskaya Str. 42, Kharkov 61002 Ukraine
Electronic address: stl@metrology.kharkov.ua

The problems of time unit transmission for customers, which one are interested with synchronization of time of computers and computer networks, are considered in the article. The results of the time server research are represented.

1. INTRODUCTION

The problem of time and frequency synchronization has gained a great interest now, because time unit is necessary for operation of many systems. Different systems apply for time and frequency unit transmission (satellite radionavigation systems (SRNS), meteoric link, television etc.), which provide high accuracy, but they have high cost. The great numbers of customers of the time-frequency information have interest in the technical accuracy (~1 ms). The transmission of time unit with such accuracy can be achieved by application of computer standard communication equipment.

II. NETWORK TIME TRANSFER TECHNOLOGIES

The computer time scale usually has an error of 5 - 15 seconds per day. Time setting of the computer is carried out by software. The information about current time transmits to the remote computer with usage of different data channels. The error of time setting is depend on a propagation time of code sending by a data channel, busy factor of system resources of the computer, resolution of an operating system on time setting, characteristics of a crystal oscillator.

There are a number of special network protocols for time transmission. Daytime protocol provides the sending format as current date (day of week, month, and number) and current time (hours, minutes of seconds). The sending format of Time protocol is time in seconds (timestamp), counted after midnight on the 1-st of January, 1900. The transmission of time is carried out on request of the client. These protocols don't provide the correction of errors, which are conditioned by transfer delay of sending on the network. Therefore their usage is effective in networks with a high transmission speed, for example in local area networks.

The most popular protocol of synchronization of time scales is the protocol NTP [1], which provides the greatest accuracy and reliability of time transmission. The synchronization accuracy (the milliseconds in local area networks and tens milliseconds in global network) is provided even at presence of different delays, which are conditioned by passing of packages through intermediate routers.

The NTP model envisions some primary time servers, which are exploited by national metrology services and are clocked under the primary standards. NTP works by hierarchical model, where small amount of servers are synchronization sources for the greater number of clients. The clients at each level or stratum are, in turn, servers are a lot of clients with higher number of stratum. The stratum numbers rise from primary servers to lower numbered stratum of a tree structure. The clients can use the information from set of servers automatically to define the best source of synchronization.

The programs performing synchronization by NTP protocol, define following values: time scale offset, complete delay from the client up to the server and back, and variation. All these values are defined relative to a time scale of the selected server. Time scale offset defines the value of time scale correction of the client, in order to their observations correspond to a standard time scale. The variation characterizes a maximum error of a local time scale relative to standard.

III. ABOUT TIME SERVER

The computer system of time-frequency information transmission is created and exploited in National Scientific Center "Institute of Metrology" [2]. The time server of this system realizes a time synchronization through telephone channels, and also by Internet with usage of NTP, Daytime, Time, TSP protocols. The server is organized on the basis of the PC Celeron and it is synchronized by a 1 PPS signal from a State primary standard of time and frequency of Ukraine. The modified kernel of operating system FreeBSD 4.10 allows realizing correction of a system scale on an external time signal which is given to one of ports. The package NTP of the version 4.2 is installed on the server. The array of time scale difference measurements of the server and State primary standard of time and frequency of Ukraine during 2 months (continuous

operation period of the server) has statistical characteristics: root-mean-square deviation of a time scale relatively a regression line is 17 mks, average change of a time scale per day is 17 ns (fig. 1). The array of relative frequency deviation values is obtained by time scale difference data of the server and State primary standard of time and frequency of Ukraine. It has statistical characteristics: root-mean square two-sample frequency deviation (Allan deviation) per day is $6 \cdot 10^{-7}$ and average relative frequency change for one day is $1 \cdot 10^{-8}$ (fig. 2).

IV. TIME TRANSFER BY TELEPHONE CHANNELS

Furthermore the described time server has the function for transmission of time unit through telephone channels. The special software which allows solving such tasks is designed.

The server waits telephone call of the client. The conversation includes registration of the client, measurement of a transfer delay from the server to the client and statistical processing of results, creation of the code of a current time in view of delay measurement result, sending this timing code to the client. On the obtained timing code the client adjusts the system time scale. Client's software is designed for an operating system Windows. The time error is defined by a transfer delay from the server to the client. The results of measurement of this value for several communication sessions are represented in the table 1

As follows from table, root-mean-square deviation of delay from a session to a session differs on hundreds microseconds, that characterizes accuracy of transmission of a unit of time.

Table 1

N	Average value of delay for a session, ms	Root-mean-square deviation of delay for a session
1	65,50	2,70
2	77,56	2,67
3	79,35	3,30
4	74,98	3,78
5	56,24	2,32

CONCLUSION

The customers of Ukraine, Russia, and other countries of CIS use the services of given time server. The application of time server with such characteristics will allow to meet the synchronization requirements of computer time scales with accuracy not worse 1 ms in a local networks and with accuracy up to 100 ms in the Internet in the presence of the channel with high capacity.

REFERENCES

[1] Mills D.L., Network Time Protocol (Version 3). Specification, Implementation and Analysis, Network Working Group Report RFC-1305, University of Delaware, 1992.

[2] Клейман А.С., Левенберг А.И., Соловьев В.С., Губин А.А. // Український метрологічний журнал. – 2003. – Вип. 2. – С. 10-19.

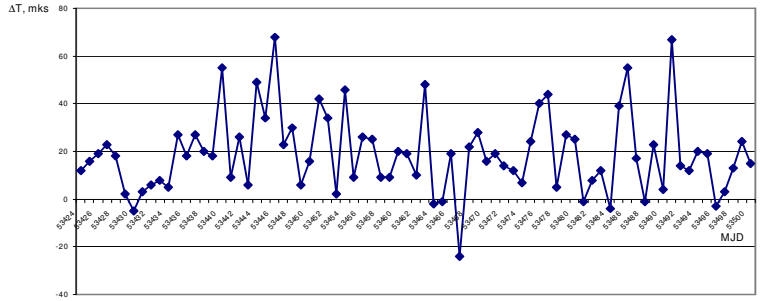

Figure 1

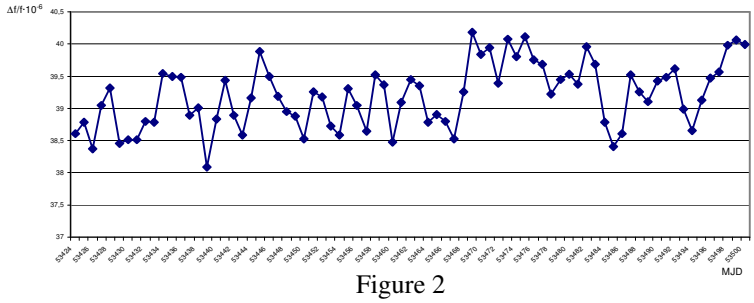

Figure 2

Proceedings of the 20th EFTF, 2006

Trusted Time Distribution Service for the Romanian Time Stamping Authorities

Anca Niculescu*, Violeta Ciociea
National Institute of Metrology, Sos. Vitan Barzesti no.11, 042122 Bucharest, Romania
**anca.niculescu@inm.ro*

The Time and frequency laboratory of the National Institute of Metrology (NIMB) is the national reference laboratory for time and frequency in Romania. This implies the assurance of measurement units for time and frequency in Romania and their traceability to SI system. The main objectives of the laboratory are to keep competence and resources for the measurement units of time, time interval and frequency, to maintain a national time scale, UTC (NIMB), traceable to the international time scale UTC and to support and supply the Romanian economy and general public with accurate references of time and frequency.
The development of electronic commerce and of the secure electronic document exchange requires trusted date and time information. To meet the requirements of the Time Stamping Authorities (TSA) that are going to be established in Romania, an experimental project was proposed by the Ministry of Communication and Information Technology. As part of this project, the National Institute of Metrology will studies a new dissemination service that provide a trusted time reference to the TSAs and for future activities that will use electronic exchange of information. TSAs must have their own time sources traceable to UTC (NIMB) within 1 second.
The approach proposed by NIMB assumes that a TSA will have already sources of data and time synchronized, e.g. GPS, in order to have the necessary redundancy. The TSA will call some times a day the NIMB trusted time service, by a secure connection, in order to have its time information traceable to UTC (NIMB). Using this solution we hope to be able to measure the rate of TSA clocks and to provide a certification of their time errors.
This paper presents the realization of the experimental project concerning the first trusted time dissemination service in Romania, based on NTP time servers, that will assure the traceability to the UTC (NIMB) for all the Romanian companies and institutions that will need this information.

1. INTRODUCTION

As a governmental institution, one of the mission of our institute, and in particular of its time and frequency laboratory is to integrate Romania in the international space – time reference system and, hence, to be able to provide precise time to Romanian official institutions, Romanian industry and private users. This implies the assurance of measurements units in Romania and the traceability or connection to the SI. The objective of time and frequency lab are to keep competence and resources for the measurement unit of time, time interval and frequency in Romania, to maintain a national time scale, UTC (NIMB), traceable to the international agreed upon official time scale UTC (Coordinated Universal Time), and to support to support and supply the Romanian industry and general public with accurate references of time and frequency.
Using the facilities of time and frequency laboratory, the MCTI has proposed an experimentally project in order to establish a time service for the distribution of data/time information, service which should be traceable to UTC NIMB).
Nevertheless this new project is affected by security problems in order to ensure integrity, authenticity, confidentiality and non repudiation of the information.

II. TIME KEEPING VIA THE INTERNET

The most established technique to realize computer time synchronization via INTERNET is the use of the NTP (Network Time Protocol) [1].
NTP is designed to work in a large, diverse INTERNET system. The best accuracy is normally obtained when the time server is located as close as possible, in terms of network delay and latency, to the inquiring clients. The main issues for good stability are, however, low network jitter and symmetric paths.
NTP is a good choice for time synchronization in a variety circumstances, especially for INTERNET environment. The flexibility of the client / server relationship and the security methods allow NTP to work well in almost any environment. NTP not only can correct the current time but, it can also keep track of consistent time variation and automatically adjust for time drift on the client. In addition, the NTP daemon can automatically adjust the time by periodic increments. NTP is also able to operate through firewalls and has a number of security features.
Today, in the world, exist more than 200 primary time servers synchronized to UTC and several thousands hosts and gateways that directly synchronize their clocks via NTP.

NTP works on a hierarchical model in which a small number of servers can give time precise time to a large number of clients. The client of each level (stratum) is, in turn, potential server to an even large numbers of clients of a higher numbered stratum. Stratum numbers increase from the primary (stratum 1) servers to the high numbered strata in the same way as the branches on a tree. Clients can use the time information receive from multiple servers to automatically determine the best source of data/time and can prevent bad time sources from corrupting this information. Figure 1 illustrates the hierarchical model of the servers used in NTP.

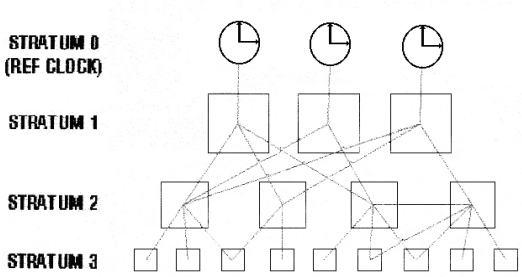

Fig.1 – Hierarchical strata model of servers used in NTP

Under good condition on a LAN (Local Area Network) without too many routers or other network delay sources, the synchronization to within a few milliseconds is normal. Anything that can adds latency, such as hubs, switches, routers, or network traffic will reduce this accuracy. The synchronization accuracy on a WAN (Wide Area Network) is typically within the range of (10-100) ms.

A server and a client can operate in three different NTP modes: procedure-call, multicast and symmetric mode.

In the procedure-call mode, the server announces its willingness to provide synchronization, but not to be synchronized itself. Such a server is a primary server that synchronizes its clock to a UTC source. The client on the other hand announces its willingness to be synchronized, but usually not to provide synchronization. The active communication between the client and the server makes it possible to estimate the time and frequency offset between their clocks and also to estimate and correct for the network path delay.

In multicast mode, the server sends periodic NTP broadcasts. The client receives these and determines the time offset on the basis of an assumed delay. The major difference between this mode and the procedure-call mode is that the path delay cannot be estimated momentarily. Instead, the path delay has to be estimated, if needed, in advance. The multicast mode is mainly intended for synchronization within local area networks, which implies short distances, constant and predictable delays and symmetric paths.

In the symmetric mode, a server announces its willingness to provide synchronization, but also to be synchronized itself, if necessary. This mode is normally used when primary servers need a back-up if the UTC source fails.

The most common source of UTC is the GPS (Global Positioning System) [2] which gives time to within 1 µs relative to UTC. Other common UTC sources are long wave radio transmitters with varying accuracy and stability. One disadvantage with these radio transmitters, as well as with GPS, is that they are out of control by the users and may be subject to changes without previous notice to the users. Other time sources are of course local time scales based on one or several atomic frequency standards.

For the INTERNET, synchronization accuracy is unpredictable, so special care is need when configuring a client to use public NTP servers.

The NTP software distribution supports the use of redundant time servers. This means that a client has the possibility to, after outlier detection and different combining techniques, choose the most trustable server or combination of servers among those inquired. Redundant time servers are especially important for time sensitive applications involving economic transactions or legal issues. These applications would also gain in reliability if a set of primary servers are available in the close vicinity, for instance within a country or region.

III. IMPLEMENTATION OF THE SYSTEM

The time and frequency laboratory of the NIMB is presently equipped with 2 clocks: 1 HP5071A caesium clock and 1 5071A Agilent caesium clock. The UTC realization UTC (NIMB) is obtained from the HP5071A clock. The time lab has been installed in a new temperature stabilized room in January this year.

The time servers system was drawing up to be fully redundant: two independent clocks, two time servers, two independent INTERNET providers and an autonomous power supply source (see Figure 3). For the clients, this system is seen as a single system with one IP address, available only for authorized ones within a Public Key Infrastructure (PKI) [3]. The PKI is composed by some Certification Authorities that manage the cryptographic keys and by the Time Stamping Authorities (TSA) to provide the necessary trusted time reference.

Redundant time servers are especially important for time sensitive applications involving economic transactions or legal issues. These applications would also gain in reliability if a set of primary time servers were available in the close vicinity (say within a country or a region).

As primary servers were used two NTS-3000 server from the company Elproma. The standard NTS-3000 network time server synchronized its clock via GPS satellite system. The company who make the system asked Elproma to add a 1PPS input to our NTS-3000 server in order to use it for connecting UTC (NIMB). The advantage of adding this 1PPS input to the time server, beside the better accuracy and the link to a national time scale, is that contrarily of our reference clock, the GPS system is out of control by the user and may be subject to changes without notice to the users. For the moment we allow a direct synchronization on the NTS-3000 from our LAN. There is also a stratum 2 server, set up at MCTI headquarters, available for time synchronization over the INTENET, it synchronizes itself on our stratum 1 time servers which in turn has two UTC sources: UTC(NIMB) and GPS.

The NTP daemon computes about every 60 seconds a mean and a standard deviation for each of the different sources available: UTC (NIMB) and GPS. The server oscillator is then steered to a value on an internal algorithm in order to minimize the time offset between UTC and the server clock.

The TSAs clocks will be synchronized by calling the NIMB trusted time server some times per day to get the certification of their time references. In case when UTC(NIMB)-Time (TSA) is less that 1 s the NIMB will confirm the TSA time and certificates its validity.

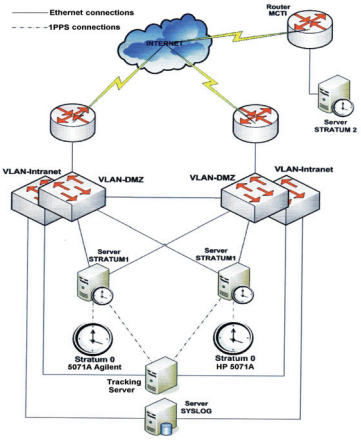

Fig. 2 - NTP servers system at NIMB

IV. PERFORMANCE TESTS

In order to evaluate the performance of the NTP service that we will offer, we must perform some tests. One of these test consist of comparison of the internal clock of NTP server with different UTC sources available: UTC(NIMB), GPS and other national laboratories time servers (for instance: Real Observatorio de la Armada - ROA).

Figure 3 shows the time offset and jitter (due to interrupt latency, processing delays and similar effects) of the time server NTS-3000 connected to UTC (NIMB) over a period of 1 day and 1 week. It can be seen from Figure 3 that the NTP daemon is able to synchronize the clock in the NTS-3000 server with a mean of few µs. On the X axes is representing CET time, not UTC because the local PC clock is not UTC synchronized. On the Y axes the deviation from zero includes the deviation form UTC of our server plus the asymmetry of the going and coming paths.

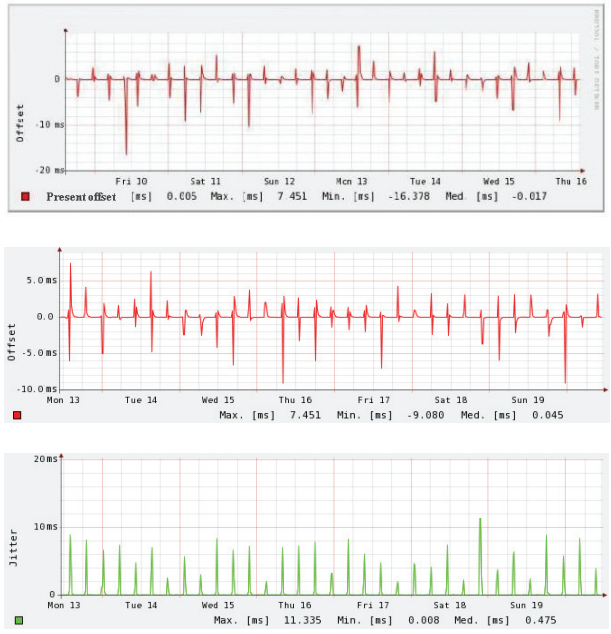

Figure 3 - Time offset and jitter between the NTS-3000 server and UTC (NIMB)

Figure 4 shows the evidence about how our time server is seen from ROA for 1 day and also 1 week. The same as in Figure 3, the X axes is representing CET time, not UTC because the local PC clock is not UTC synchronized and on the Y axes the deviation from zero includes the deviation form UTC of our server plus the asymmetry of the going and coming paths and also the deviation of the local PC WRT ntp.roa.es.

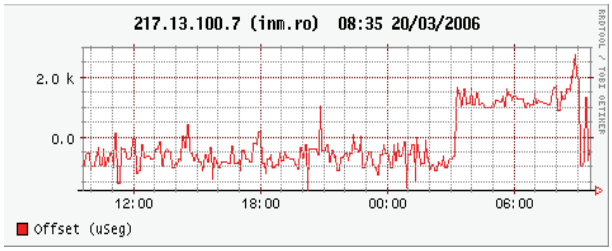

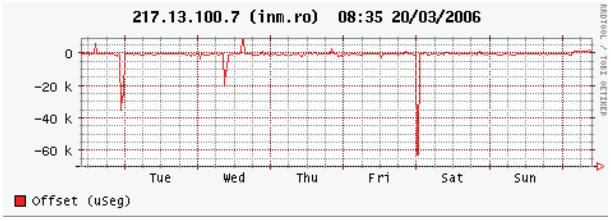

Figure 4 – Evaluation of NTS-3000 server from ROA

In future, we will make more tests in order to evaluate the time synchronization by LAN and also by INTERNET. In order to see it our time server is able to handle many request at the same time, we will simulate high traffic load condition by stressing the CPU with benchmark programs as well as by flooding the time server with millions of ping request.

V. CONCLUSIONS

We have described in this paper all the working that we carried on to implement a time server service at National Institute of Metrology of Romania, to ensure a trusty time reference source for the Time Stamping Authorities (TSA) that are going to be established in Romania.
One advantage of this system is its direct traceability to UTC via our local realization UTC (NIMB). Another advantage is the reliability of the system: we used 2 time servers, two different ways to connect to INTERNET (radio and classic cable).

Acknowledgements

We would like to thank professor Jose Palacio who most kindly allow me to use the results of the NTP survey made by the Real Observatorio de la Armada as part of EUROMRT project no.351 „Traceability of computer synchronised using Network Time Protocol to national timing centres“

REFERENCES

[1] D.L.Mills, *Internet Time Synchronization: The Network Time Protocol* (IEEE Trans. On Comm., vol.39, No. 10, pp. 1482-1493, October 1991)
[2] G.Seeber, *Satellite Geodesy* (Walter de Gruyter & Co, Berlin New York, 1993)
[3] F. Cordara, M. Mascarello, V. Pettiti, G. Vizio and R. Costa, *Trusted Time Service for the Italian Time Stamping Authorities* (14th EFTF, Torino, Italy,13-16 March 2000)

Proceedings of the 20th EFTF, 2006

Time and Frequency Transfer in an Optical Fiber Network: First Results

R. Emardson[1], P.O. Hedekvist[1,2], K. Jaldehag[1], N. Berg[1], M. Nilsson[1], S.C. Ebenhag[1], P. Jarlemark[1], C. Rieck[1], J. Johansson[1,2], L. Pendrill[1], P. Löthberg[3], H. Nilsson[1]
[1] SP Swedish National Testing and Research Institute, Borås, Sweden
[2] Chalmers University of Technology, Göteborg, Sweden
[3] STUPI, Los Altos, USA
ragne.emardson@sp.se

A technique for time and frequency transfer over an asynchronous fiber-optical TCP/IP network is being developed in Sweden by SP Measurement Technology together with STUPI. The technique is based on passive listening to existing data traffic at 10 Gbit/s in the network. Since the network is asynchronous, intermediate supporting clocks will be located and compared at each router. We detect with a specially-designed Header Recogniser high-speed optoelectronic device the frame alignment bytes of the SONET/SDH protocol as references for the supporting clock comparison. The goal of the project is to establish a time transfer system with a precision on the ns level. We have performed an assessment of the technique in a lab environment. The root mean square (rms) difference between the values measured with the fiber network technique and using GPS phase observations is approximately 40 ps. Hence, we conclude that the noise contribution from the hardware will not be a limiting factor in the time transfer system.

I. INTRODUCTION

Demand for synchronization in different fields has increased the use of the Global Positioning System (GPS) [1] for time and frequency transfer. As an alternative to the existing technique of transferring time using GPS, we are developing a time transfer system using an optical fiber network. This new transfer system is planned to be installed in the Swedish University computer Network (SUNET). Prior to deployment, an initial assessment of the technique is being performed in a lab environment. In this paper, the first results of time transfer measurements in this environment together with a description of the three corresponding experiments will be presented. The experiments are described in section 3 followed by the results from each experiment in section 4.

II. SYSTEM DESCRIPTION

Figure 1 shows the main principle of transferring time and frequency over an optical fiber network. In order to compare two clocks located at two routers in a network, we compare the clocks to the data traffic propagating along the fiber. When implemented in an asynchronous network such as SUNET, time measurement systems such as these will have to be in place at every router.

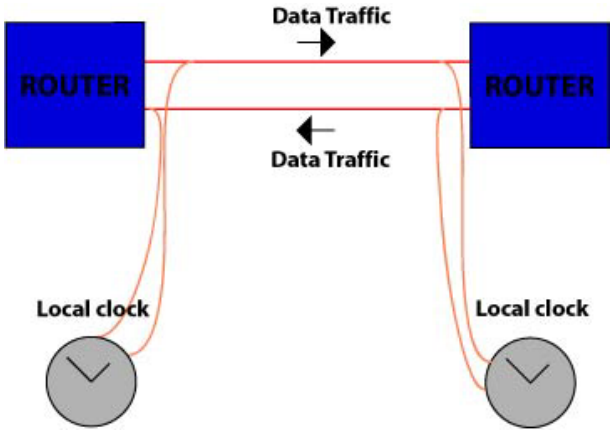

Figure 1: Main principle of transferring time over an optical fiber network.

A schematic view of the proposed setup at one router in a TCP/IP network is shown in Figure 2. About 1% of the outgoing optical power, and 10% of the incoming power, are coupled out in order to extract output and input timing signals from the traffic. The diverted optical signal is then optoelectronically (o/e) converted to an electrical signal before being fed into a specially-designed high-speed Header Recogniser[1] which generates a pulse of length 25 ns every time a sequence

[1] The three components, amplifier, opto/electric converter (o/e) and header recognizer (HR) will hereafter be referred to as Frame Start Pulse Generator (FSPG).

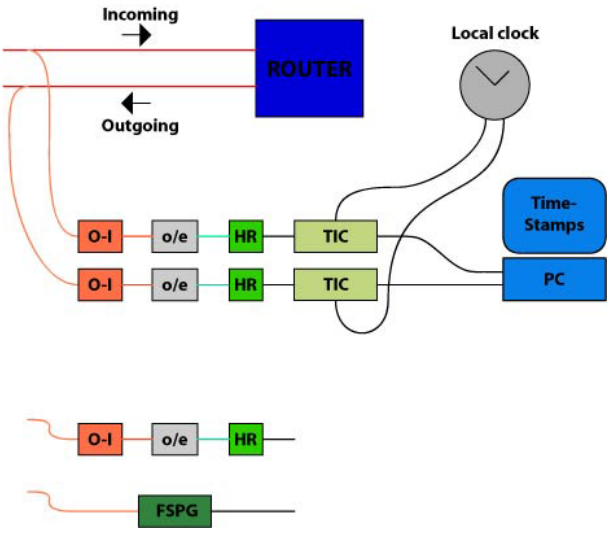

Figure 2: Technical setup at one router for the time transfer system.

of 384 bytes of the 10 Gbit/s SDH frame alignment bytes A1 and A2 is received.

By performing time interval measurements between the HR pulses and pulses from a local clock with a time interval counter (TIC) for each pair of routers, we can estimate the time difference between the local clocks at each router. Variations in the propagation delay along the fibers, which otherwise might be interpreted as clock errors, will to a large extent be cancelled by performing measurements on both outgoing and incoming fibers under the assumption that the pairs of fibers carrying traffic in these two directions are exposed to similar environmental perturbations. An assessment of fiber delay variations on system stability will not be performed as a part of this paper but will be performed in a later stage of the project. A more thorough description of the system is given in [2].

III. LAB EXPERIMENTAL SETUP

We have performed several different experiments in a lab environment in order to assess the performance of the hardware of the system. A description of the experimental setups will be given below.

a) Comparative HR card test

The specially-designed high-speed Header Recogniser and associated electronics are initially assessed in a zero baseline test [Figure 3]. The same optical signal is used as input to both FSBG's which feed the time interval counter. HR card number one is used to trigger the start

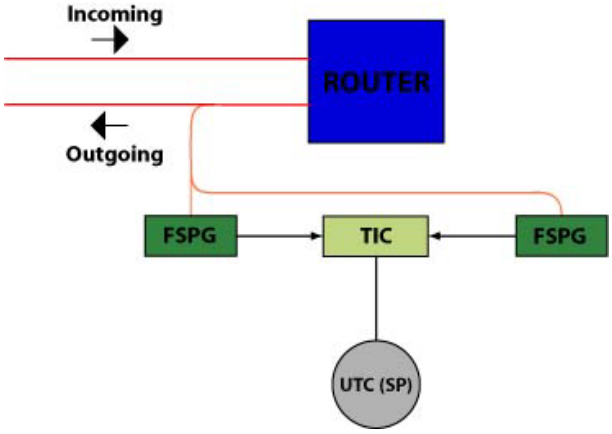

Figure 3: Experimental setup.

of the time interval measurement while the output of HR card number two is used to stop the measurement. An ideal result of such an assessment would be a measurement result equal to zero, because we feed the two systems with an identical signal. The sampling rate for this experimental setup was 8 kbit/s.

b) Zero baseline test

Figure 4 shows the setup used for this experiment which is closer to that of a final system. The pulses from the header recognizers are used to start a time interval measurement and clock pulses are used to indicate the stop the measurement. The difference from this experimental setup and a final system is that instead of a comparison between two remote clocks, we here use only one local clock. Hence we compare that clock to itself. An ideal result of such measurements would thus be zero and the results we measure indicate the noise generated within the system.

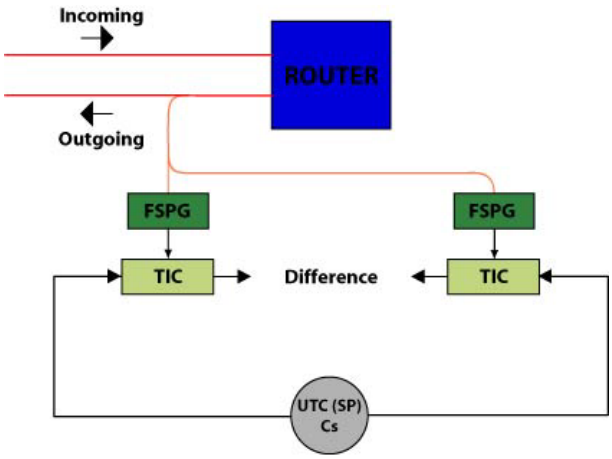

Figure 4: Stability test of the time transfer system.

c) Comparison with independent techniques

Experiment number three is a configuration substantially that of a finalized system and shown in Figure 5. We measured the time difference between the Cesium and H-maser clocks located in the lab at SP. The difference between this setup and that of a final system is that the two clocks are compared using time references from the same location on the optical fiber. Imagine that the H-maser in Figure 5 were to be compared to a reference from the optical fiber at the other end, i.e., at the router by the other end of the fiber. The difference from this setup is that the travel time and the variations in the delay of the fiber are not taken into consideration in the analysis. Hence, the result of this test indicates the precision ideally if one could cancel all delay variations in the fiber.

In this experiment, for comparison with the time difference measurements with the fiber system, we also measure the time differences using two independent techniques. These are direct TIC measurements, and using GPS. The GPS estimates are of two kinds, namely those based on code observables and those based on phase observables. The GPS estimates based on code observables are determined from standard GPS P3 [3] measurements. The GPS phase estimates will hereafter be referred to as GPS CP. The sampling intervals for the different techniques are: fiber (1 s), GPS CP (30 s), GPS P3 (16 minutes), and TIC (10 minutes).

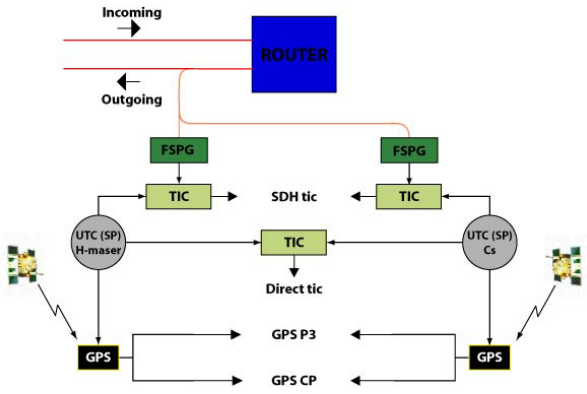

Figure 5: Experimental setup for the measurement of the time difference between the Cesium and H-maser clocks at the time and frequency lab at SP.

IV. RESULTS

In this section we present the results of the measurements described in the previous sections. The results will be presented mainly by the time series of the measurements and by corresponding stability plots where we mostly use the Time Allan Deviation (TDEV).

a) Comparative HR card test

Figure 6 shows the measured intervals between the pulses generated by the two header recognizers, see Figure 3. A constant offset of approximately 1.7 ns can be seen in the figure and is presumably due mainly to differences in cable delays to and from the two header recognizers. The rms scatter, with a mean value removed, in the time series is approximately 40 ps at 8 kbit/s sampling. This value represents the best precision that can be achieved with this system on a sample to sample basis. The precision of the counters used in this assessment is typically 100 ps and hence we assume that the precision of the time transfer system today is limited by the counters and may be improved in a future with access to a more precise counting method. Figure 7 shows the TDEV of the time intervals showed in Figure 6. The figure shows that the noise seen in Figure 6 is mainly white with some evidence of a 50 Hz component.

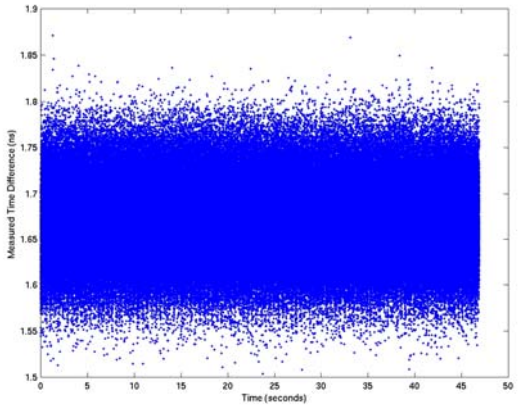

Figure 6: Measured intervals between the pulses generated by the two header recognizers.

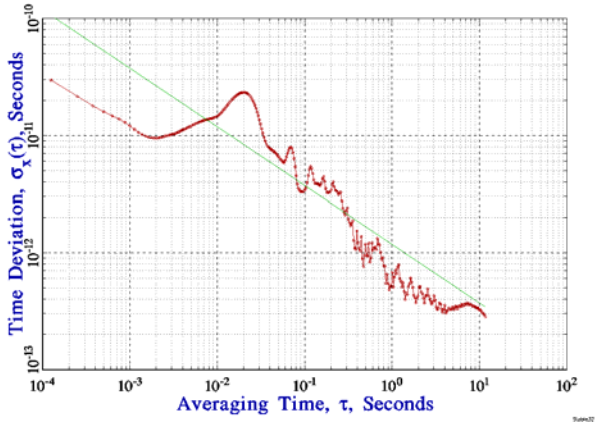

Figure 7: TDEV of the measured time differences. The green curve corresponds to a slope given by a white phase modulation.

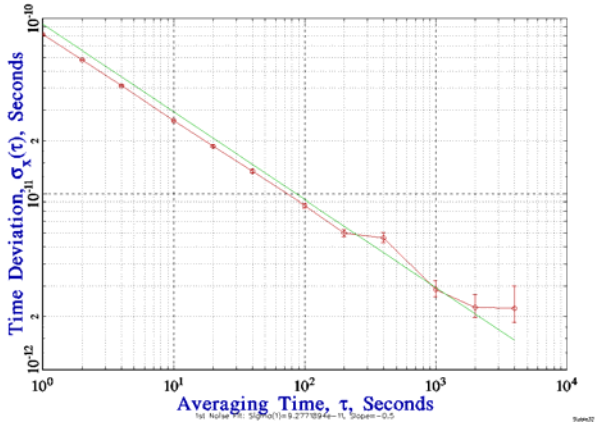

Figure 9: TDEV of the measured time differences. The green curve corresponds to a slope given by a white phase modulation.

b) Zero baseline test

Figure 8 shows the measured time differences of the Cs clock as described in Figure 4. As in the previous experiment an offset can be found in the data, this time of approximately 11.4 ns. We presume this offset is due to differences in cable delays of the setup. The rms scatter around the offset is approximately 80 ps at 1 s sampling. Figure 9 shows the TDEV of the measured time differences in Figure 8. From the figure, we can see that the measurement noise is white noise. A deviation from this statistics can be seen around an averaging time of 500 s. This deviation is still unexplained but does not affect the conclusions of this experiment. That is, that the internally generated noise in the time interval measurement of the final system is white noise.

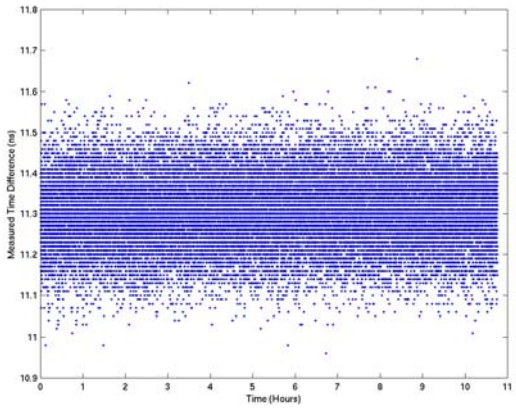

Figure 8: Measured time difference by two systems of header recognizers of the same Cesium clock.

c) Comparison with independent techniques

Figure 10 shows the measured time difference between the Cesium and H-maser clocks at the time and frequency lab at SP over a time period of almost 3 days. The different curves show the time difference measured with the different techniques described in section 2. With the curves numbered from the top they show the measurements from, (1) fiber, (2) GPS CP, (3) GPS P3, and (4) TIC. The GPS CP estimates have no absolute level and has been placed offset from the fiber measurements with 1 ns for clarity. In order to compare the fiber and GPS CP estimates, we smoothed the fiber measurements to a sampling interval of 30 s corresponding to that of the GPS CP. The rms difference between the values measured with the fiber technique and using the GPS phase observations is approximately 40 ps at the 30 s sampling.

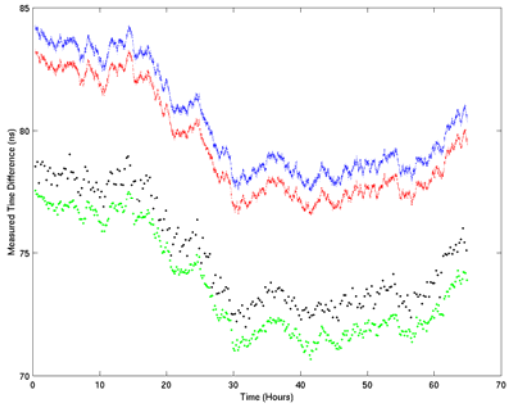

Figure 10: Measured time difference between Cs and H-maser clocks. The different curves show the time difference measured with different techniques.

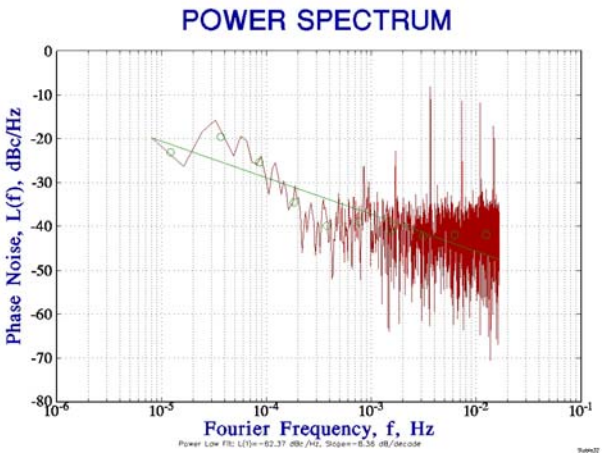

Figure 11: Power spectrum of the difference between measured time differences.

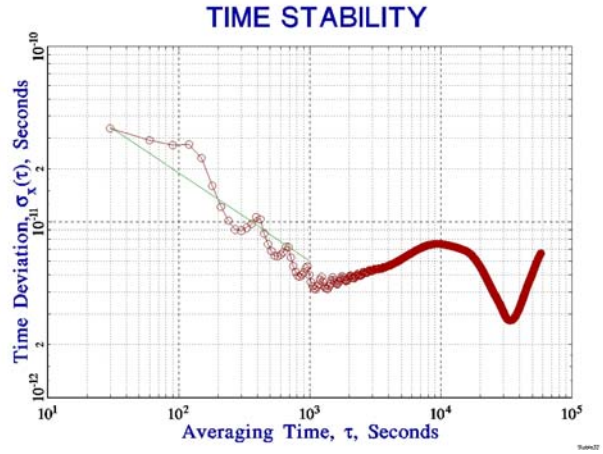

Figure 12: TDEV of the differences between fiber and GPS CP time difference measurements.

Figure 11 shows the power spectrum of the difference between the fiber and GPS CP measurements. At frequencies above 10^{-3} Hz, the difference shows behaviour similar to a white noise process. At lower frequencies, however, systematic variations seem present in the difference. This is supported also by the time Allan Deviation (TDEV), see Figure 12. This systematic is presumably due to errors in the GPS processing or temperature variations affecting the electronics in both systems.

V. DISCUSSION

We have developed a new technique for time transfer over optical fiber networks. Initial tests in a laboratory environment show that the internal precision of the measurement system, including a specially-designed high-speed optoelectronic Header Recogniser operating on 10 Gbit/s data, is well below 1 ns. Comparison with GPS estimates based on the phase observable show differences between the techniques of 40 ps over a time period of three days. This value is based on an averaging of the time measurements from 1 s data to 30 s data, i.e., by reducing the noise of a factor of a square root of 30. In a final system we anticipate the sampling rate to be 8 ksample/s. Based on the fact that noise in the time interval measurements is white noise, also for very short averaging times, we conclude that this level of noise reduction will be possible to reach even if the decimation of data will be to, for example, a 1s rate.

In a final system we will perform measurements on both outgoing and incoming fibers. Variations in the propagation delay along the fibers, which otherwise might be interpreted as clock errors, will to a large extent be cancelled by performing measurements on both outgoing and incoming fibers under the assumption that the pairs of fibers carrying traffic in these two directions are exposed to similar environmental perturbations. However, residual temperature differences and additional electronics along the signal path will presumably contribute to more noise than 50 ps. Hence, we anticipate that the delay variations in the transporting fiber will be the main error source of the future system when time transfer is performed between clocks separated in distance.

Acknowledgements

This work was supported by PTS, the Swedish National Post and Telecom Agency. We would like to thank SUNET for supporting the project with access to their network.

REFERENCES

[1] W. Lewandowski, C. Thomas, “GPS time transfer”, Proc. IEEE, 79, 991-1000, 1991.

[2] R. Emardson *et al*., Time and Frequency Transfer in an Asynchronous TCP/IP over SDH-network Utilizing Passive Listening, 2005 Joint IEEE International Frequency Control Symposium and Precise Time and Time Interval (PTTI) Systems and Applications Meeting, Vancouver, B.C. (2005).

[3] P. Defraigne, and G. Petit, Time Transfer to TAI using Geodetic Receivers, Metrologia, 40, 184-188, 2003.

Proceedings of the 20th EFTF, 2006

Fibre frequency dissemination with resolution below 10^{-17}

O. Lopez*, C. Daussy, A. Amy-Klein, C. Chardonnet
LPL, Laboratoire de Physique des Lasers, UMR753 CNRS, Université Paris 13, 99 avenue J.B. Clement, 93430 Villetaneuse France
F. Narbonneau, M. Lours, G. Santarelli,
LNE-SYRTE, Systeme de Reference Temps Espace, UMR 8630 CNRS, Observatoire de Paris, 61 avenue de l'Observatoire, 75014 Paris, France
**Electronic address:* lopez@galilee.univ-paris13.fr

In this paper we present an ultra-stable fiber optical link which allows transferring radio frequency reference signal between two research laboratories. The link is composed of two 43 km twin optical fibers of the urban telecommunications network that connect the LPL to the LNE-SYRTE. The phase/frequency stability of the transferred signal is degraded by mechanical vibrations and temperature variations along the fiber. To correct these deleterious effects we develop a compensation system who acts directly on the fiber length with a variable optical delay line.

1. INTRODUCTION

We have already demonstrated distribution of reference signal at 100 MHz over 86 km with a frequency stability of 10^{-14} at 1 s and 10^{-17} at one day integration time [1, 2]. Two frequency standards separated by 43 km, one in the IR domain (CO_2/OsO_4 at 30 THz) and the other in the microwave domain (CSO at 12 GHz) have been compared with a resolution of 3x 10^{-14} at 1s [1].
To improve the frequency stability and to further extend the distribution distance, the compensation system has been upgraded to 1 GHz and the length was increased to 86 km. In this paper we focus on the compensation system of the fiber perturbation that acts directly on the fiber length. The parasitic effects which limit the performance of the compensation have been studied and partially cancelled.

II. COMPENSATION SYSTEM

The optical compensation system is shown in Figure 1. The 86 km link is obtained cascading the two twin fibers between LPL and LNE-SYRTE. This way the two ends are collocated at LPL. At each fiber end, one designed as Local and the other as Remote, an electronic system synthesizes the RF signal to be sent to the other end, 1 GHz for the forward signal and 900 MHz for the return signal. Each RF signal modulates the beam intensity of a 20mW, DFB laser diode at 1.55µm. This modulation is detected with a fast photodiode at the other end of the fiber. The optical polarization is scrambled directly at each emitted source as discussed below. Mechanical and temperature variation along the fiber perturb the propagation delay across the fiber. In order to remove this parasitic variation we use a round trip phase correction technique.

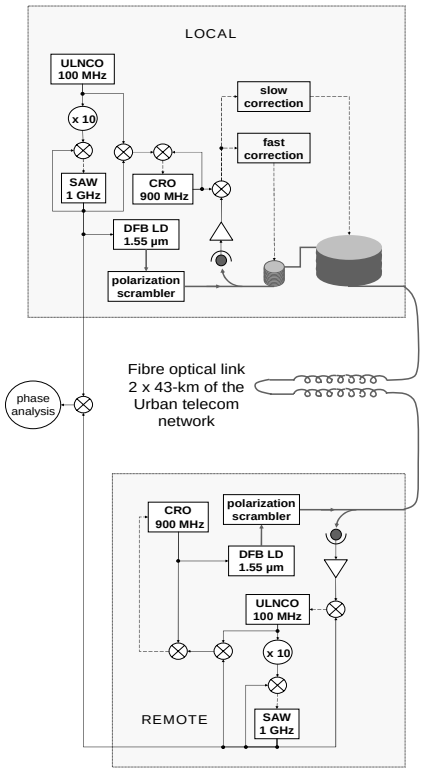

Figure 1: Block diagram of the 86 km fiber link and the optical compensation system. Both LOCAL and REMOTE functions are located in the same place.

To remove the effect of the perturbation cumulated along the link, we make a comparison between the reference phase signals at the input (LOCAL) with the phase signal after one round trip. This leads to the generation of an error signal which is processed by a

simple analog loop filter and applied to two delay lines. The delay lines at the LOCAL input of the link cancel out the variations of propagation delay. The fast and small variation corrections are applied with 15 meters of piezoelectrically stretched fiber (correction range of about 15 ps). The fiber is wrapped around a cylindrical PZT. The slow corrections are applied by heating 4 km of optical fiber wrapped around a copper wheel with 150 ps / °C and (6 ns dynamic range).

We measure relative stability of the compensated link by analyzed phase variation between the 1 GHz at local end and the 1 GHz at remote end. Figure 2 shows the relative phase noise spectral density of the compensator with 86 km link (upper trace) and without link (lower trace). The bump around 300 Hz is due to delay loop. The compensation system can potentially reach -120 dB at 1 Hz corresponding to an ADEV (Allan deviation) of 10^{-15} at 1 s integration time but the attenuation along the fibre degrades the signal to noise ratio at receiver and limits the compensation at -105 dB at 1 Hz. Figure 3 shown the ADEV calculated from the phase data measured on the compensated link and filtered with low-pass filter of 3 Hz. We obtain residual frequency stabilities of the link of $5x10^{-15}$ at 1 second integration time and $2x10^{-18}$ at one day integration time.

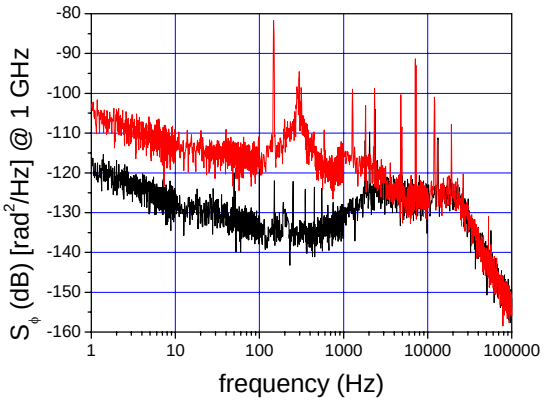

Figure 2 : residual Phase noise spectral density of the optical compensation system at 1GHz.

We use different frequencies at forward and back signals to avoid parasitic reflections due to the fiber connectors along the link. Another parasitic reflection is due to Stimulated Brillouin Scattering, SBS, which reflects noise at the same RF frequency input signal and can degrade the signal-to-noise ratio. Figure 4 shows the spectrum of the detected signal at the LOCAL end. We can see that if the received signal was at the same frequency that the emitted, 1 GHz, the signal to noise will be only of the order of 80 dB in 1 Hz Bandwidth when 100 dB is necessary for reach a relative stability of 10^{-14} at one second integration time.

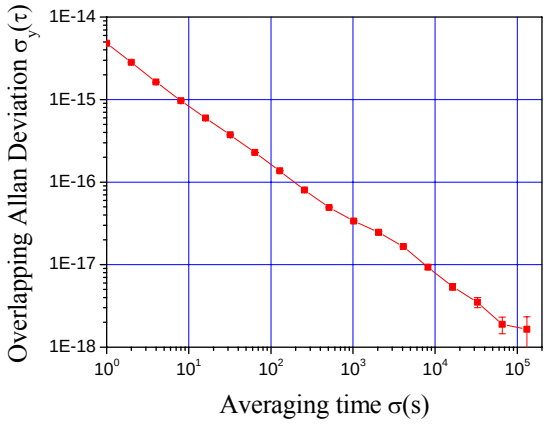

Figure 3: Fractional frequency stability of the compensated 86 km link.

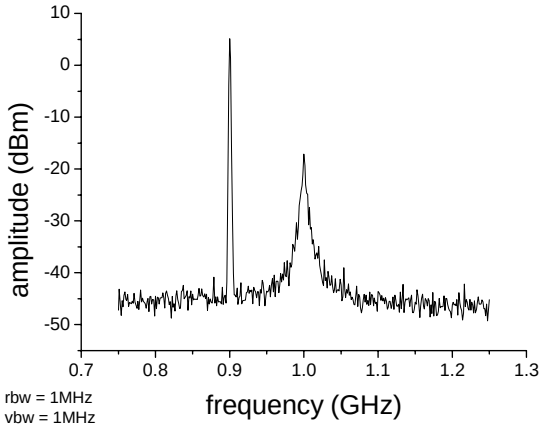

Figure 4 : RF spectrum of the detected signal at the local end. The spectrum shows clearly the SBS excess noise due to the emitted signal. The return signal at 900 MHz is not affected by this noise since the SBS spectrum is Lorentzian with a linewidth below 10 MHz.

III. PMD PARASITIC EFFECTS

During preliminary measurements, we have observed a randomly instability of the loop and large phase fluctuations on the long time. These two effects are due to the polarization mode dispersion, PMD, of the 86 km link. The PMD is induced by the birefringence of the optical fiber due to asymmetry of the core. This PMD is varying in time when the asymmetry is due to mechanical stress induced by vibrations or by temperature variations. Moreover, the direction of axis, fast and slow, of the link move randomly in the time.

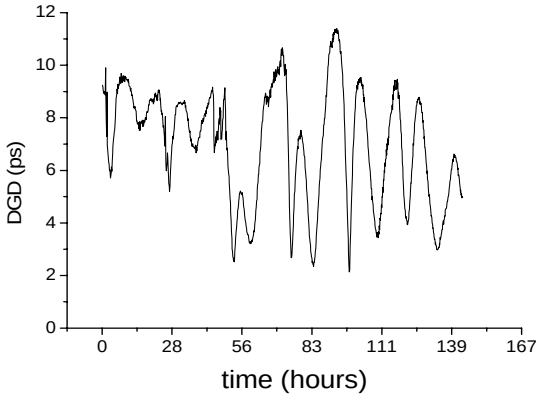

Figure 5 : Measured time variation of the DGD on 86 km link over one week.

The first order PMD is called differential group delay (DGD). We have measured time variation of the DGD on 86 km link over one week (see Figure 5). The average DGD of our link is ~7 ps which gives a PMD coefficient of ~0.75 ps/km$^{1/2}$.

A first effect of PMD on the stabilized link is to limit the short term stability. The piezoelectrically fiber stretcher indeed varies the polarization state of the transmitted signal and thus introduces a variable propagation delay which adds to the primary delay of the link.

Second effect of the PMD degrades long term stability. The slow variation in time of the DGD and direction axis of polarization of the fibre causes a random variation of the propagation delay not of same way for the propagation of forward signal and the back signal. The compensator floor is limited to a few 10^{-17} between 10^4 and 10^5 seconds integration time.

The solution used in this work is to scramble the polarization directly at the emitted source at a frequency higher than the cut off frequency loop. In this case the DGD is averaged and the effects of PMD are minimized. For that purpose we use polarization scrambler (General Photonics) which has three axes acting in a same way as a variable retardation wave plate. Each axis is excited at different resonant frequency (~60, ~100, ~130 kHz) which allows exploring all polarization states.

IV. PRELIMINARY 186 km LINK

We have explored the possibility of increasing the link length to186 km by adding 100 km of fiber spools. Two Erbium Doped Fiber Amplifiers (EDFA) were added at half distance to compensate the 20dB additional optical losses. We obtain a rather good result on long term frequency stability, better than 10^{-17} at one day integration time while the short term is severely degraded by the EDFA excess noise. Figure 6 shows the preliminary measurement of the relative frequency stability of 186 km link for the optical compensator and for an electronic compensator. This alternative compensator is described in [3] and works in a rather different way, the correction being applied directly on the RF source signal. The two systems give about the same result.

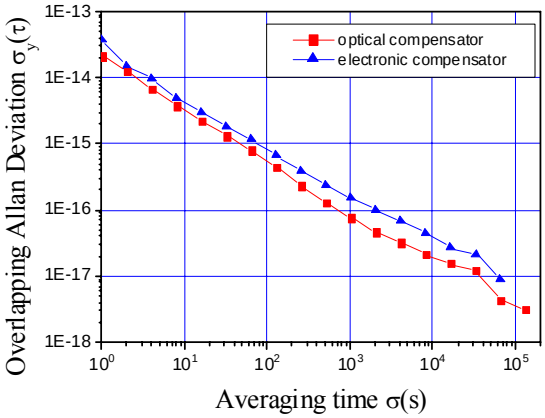

Figure 6: Preliminary relative frequency stability of a 186 km link. Triangle : electronic compensator ; square : optical compensator.

V. CONCLUSION & PERSPECTIVE

We have demonstrated an 86 km stabilized link with a frequency stability better than $5x10^{-15}$ at one second and 2-3 10^{-18} at one day integration time.

The limiting effects have been analyzed and several solutions have been carried out: two different AM frequencies for each way and fast polarization scrambling.

A preliminary stability of 10^{-17} at one day integration time has been measured on a 186 km link using EDFA.

In the aim of extending the distribution range, we will implement a 2 x 186 km link with the electronic and the optical compensator in cascade.

Further study of the PMD effects will be carried out with external modulated laser diodes (to avoid any frequency chirp). The aim is to better understand the limiting mechanism for long distance transfer.

Moreover a full evaluation of the EDFA residual phase noise and stability is in progress.

REFERENCES

[1] C. Daussy et al, *Phy. Rev. Lett.* **94,** 203904 (2005)

[2] F.Narbonneau et al, in arXiv:physics/0603125, in press *Rev. of Scient. Instr.* (2006)

[3] F.Narbonneau et al, EFTF Procedings 2005.

Proceedings of the 20th EFTF, 2006

RAPID TRANSATLANTIC TIME TRANSFER: SURVEYING THE LINK BETWEEN USNO AND IEN WITHIN THE IGS GLOBAL REAL-TIME NETWORK

G.CERRETTO[1], D.ORGIAZZI[1], P.TAVELLA[1], P.COLLINS[2], F.LAHAYE[2]
[1] *Istituto Nazionale di Ricerca Metrologica (I.N.RI.M, formerly I.E.N), Torino, Italy.*
[2] *Geodetic Survey Division, Natural Resources Canada (NRCan), Ottawa, Canada.*
cerretto@inrim.it

This paper reports on the capability of rapid time/frequency transfer, surveying the transatlantic link between timing laboratories of the U.S. Naval Observatory (USNO, Washington D.C., USA) and the Istituto Nazionale di Ricerca Metrologica (I.N.RI.M., Torino, Italy). Over a six month period, the near-real-time estimation of the UTC(USNO) to UTC(IEN) offset computed by Natural Resources Canada (NRCan) is directly compared with BIPM Circular T data and other independent synchronization techniques, such as TWSTFT.

I. INTRODUCTION

Natural Resources Canada (NRCan) computes real-time wide-area differential GPS corrections, known as GPS·C [2]. These corrections allow real-time Canadian users of GPS to reduce the errors in the broadcast satellite position and clock states and achieve improved positioning accuracy. One by-product of the estimation process is receiver clock states for all stations used in the corrections computation.

NRCan is currently testing an improved phase-based corrections algorithm with a global network of stations. These stations include a selection of those from the International GNSS Service (IGS) prototype real-time network (RTIGS), supplemented with stations from IGS Low Earth Orbiters (LEO) network to maximize satellite visibility. The selected RTIGS stations include that contributed by the Istituto Nazionale di Ricerca Metrologica, I.N.RI.M (Torino, Italy). Due to the inherent delay in the submission of the LEO data, the estimation process runs in near-real-time, which is every 15 minutes and with a delay of 2 hours, yielding satellite and station parameters at 2 seconds interval.

A preliminary assessment of the near-real-time receiver clock states estimates was performed in early 2005 [4], showing the estimates to be consistent with IGS Final clock products in terms of availability, accuracy (at ns-level) and frequency stability, but with much reduced latency. This is currently a few hours in near-real-time, but could potentially be a few minutes or less with sufficient station data available in real-time.

In this paper, we report on the capability of rapid time/frequency transfer, surveying the transatlantic link between timing laboratories of the U.S Naval Observatory (Washington D.C., USA) and I.N.RI.M. Over a 6 month period, the near-real-time estimation of the UTC(USNO) to UTC(IEN) offset is then directly compared with BIPM Circular T data and other independent synchronization techniques, such as TWSTFT, putting this new technique into perspective aiming to support the real-time institutional activities of timing laboratories.

II. REAL-TIME TIME TRANSFER

The IGS Real-Time network - The Real-Time Working Group (RTWG) was created in 2002 within the International GNSS Service (IGS). The role of the RTWG is to develop required infrastructure and processes for the real-time delivery of high-rate GNSS data to analysis centers and the dissemination of real-time GNSS products [1].

A subset of the IGS network of stations has been upgraded to allow real-time distribution of GPS data, forming a prototype real-time network (RTIGS). IGS members have shown significant support to this project and at the end of the year 2005, the participating stations was on the order of 45.

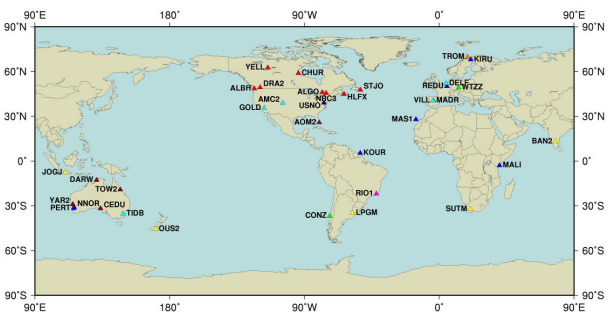

Figure 1 RTIGS network stations (red triangles) along with LEO network stations (blue triangles).

As shown in Fig. 1, several institutions involved in precise time and frequency applications contribute to the RTIGS. In particular, the Time and Frequency Department of Istituto Nazionale di Ricerca Metrologica (I.N.RI.M), Torino, Italy, has been contributing data from its "IENG" IGS station since November 2004. This station is directly referenced to the Italian realization of UTC (Universal Time Coordinated), namely UTC (IEN).

Real-Time estimation of receiver clock - Natural Resources Canada (NRCan) has been computing real-time wide-area differential GPS corrections for the last ten years. These corrections, known as GPS·C [2], allow real-time Canadian users of GPS to correct for errors in the broadcast satellite position and clock states for improved positioning capacity. NRCan's most recent development of GPS·C uses GPS code and carrier-phase observations to increase the precision of the corrections. Two by-products of the estimation process are station local zenith tropospheric delays and receiver clock offsets.

Although this code and carrier-phase based computation is run continuously from real-time station data streams to generate corrections and station parameters at 2-second interval (synchronized with the GPS even second) with a delay of a few seconds, NRCan is also testing the process in "near-real-time", taking advantage of an improved global distribution of stations. The stations include a selection of those in the RTIGS network, complemented with stations from the IGS Low Earth Orbiters (LEO) network. The real-time-ready estimation process is executed every 15 minutes in a continuous fashion with a current delay of 2 hours (allowing for the acquisition of the required LEO network data), yielding satellite and station parameters at 2-second interval.

All estimated satellite and station clock offsets are referenced to a system Virtual Reference Clock (VRC). At each solution epoch, a station is selected "on-the-fly" as a time reference and its clock offset is fixed to a value predicted from a two-state model. The choice of the reference station is based on an operator-selectable priority list as well as real-time-derived quality estimates such as detected receiver clock resets and agreement statistics between two-states clock models computed over different preset intervals. The estimated epoch corrections to the *a priori* clock offsets are then used in a timescale ensembling algorithm to generate a VRC correction that is applied to all clocks. The two-states clock models (two per station) are evaluated continuously using the real-time clock estimates and its ensemble is kept aligned to GPS time by applying common corrections as required [2,3].

The station serving as reference has its formal standard deviation set to 0. This means that the formal standard deviation of other stations results from the combination of the standard deviation of both the specific station and the reference station.

A transatlantic link survey – In an effort to evaluate the capabilities of the Real-Time technique to support real-time institutional activities, a transatlantic link was surveyed for a period of six months. Two RT stations that are operated at timing laboratories, namely USNO and INRIM, have been chosen. The RT stations located at these laboratories (USN3 and IENG) are directly referenced to the local UTC(k) realization of UTC, i.e. UTC(USNO) and UTC(IEN). The RT estimates for USN3 and IENG baseline thus represent the UTC(USNO) and UTC(IEN) time offset, plus a calibration constant (i.e., electrical delays of hardware) and this allows a direct comparison of RT estimates with those provided by both BIPM Time Section monthly Circular T [5] and other time transfer techniques, such as TWSTFT. The surveying activity covered a period of about 6 months (11th September 2005, MJD 53624, to 28th February 2006, MJD 53794) in which "near-real-time" 30 seconds spaced clock solution were analyzed.

III. CHARACTERIZATION OF REAL-TIME ESTIMATES

RT estimates availability - The preliminary assessment of the quality of station clock states, estimated in "near-real-time" by the process running at Natural Resources Canada (NRCan) [4], was able to show that RT estimates were consistent with IGS Final clock products in terms of availability.

Also in the surveying of the transatlantic link between the stations hosted in the USNO and INRIM laboratories, RT estimates availability was comparable with IGS Final ones and reached a level of 98%.

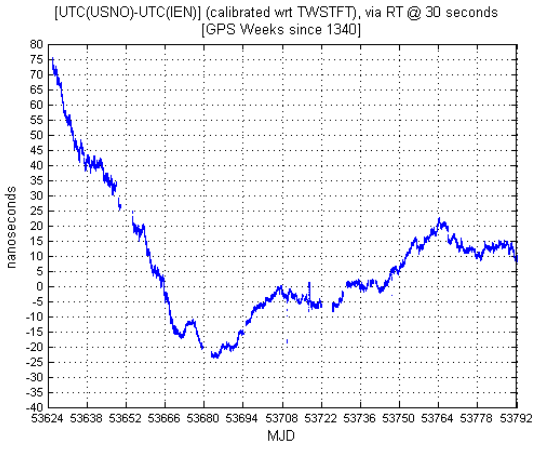

Figure 2 RT estimates for the overall surveying period.

Figure 2 shows the RT estimates for the overall surveying period.

RT estimates filtering - As mentioned above, in the RT process any station can be chosen "on-the-fly" as reference station and it is indicated by an associated formal standard deviation set to 0. The formal standard deviation of non-reference stations is normally at the level of 30 ps. However some real-time estimates are associated with larger standard deviations, indicative of anomalies. These usually result from tracking difficulties, such as loss of lock on all satellites or pseudorange-phase inconsistencies. The following Figure 3 shows an example of such anomalies reflected with high values of standard deviations for RT estimates.

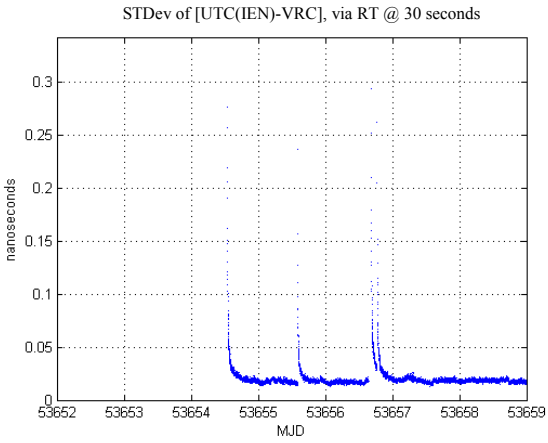

Figure 3 Example of anomalous standard deviations associated with some RT estimates.

In Figure 4, the aforementioned anomalies are shown using the Dynamic Allan Deviation (here after called as DADev) [8]. DADev is an extension of the classical Allan variance that is commonly used to evaluate the stability of atomic clocks. In particular it is a representation of the instantaneous instability of an atomic clock.

In order to remove potentially anomalous data, a preliminary "standard deviation filter" should be applied, preferably able to adapt to specific stations data noise levels. Many kinds of filter can be used, such as a simple "mean+3sigma" filter or a more robust MAD (Median of the Absolute Deviation) based filter [5,6], with an appropriate tuning process.

The consequences of a "mean+3sigma" filtering to the standard deviations estimates (with .1ns and .05ns threshold in terms of "residuals") are shown in the Figure 5 and in Figure 6 in terms of Dynamic Allan Deviation.

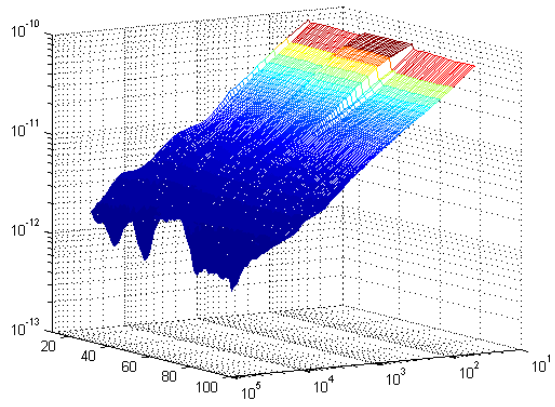

Figure 4 Anomalies of RT estimates checked using Dynamic Allan Deviation (DADev) tool.

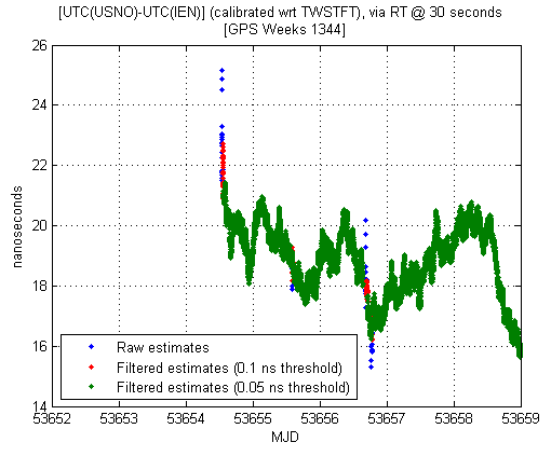

Figure 5 The effects of a "mean+3sigma" filtering applied to RT estimates.

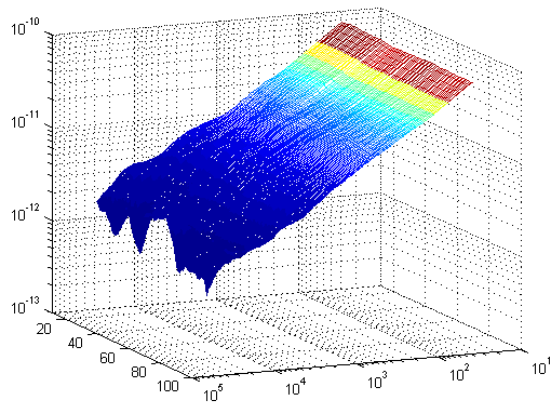

Figure 6 The effects of a "mean+3sigma" filtering applied to RT estimates using the Dynamic Allan Deviation.

IV. COMPARISON WITH TWSTFT AND BIPM CIRCULAR T

As mentioned before, the two RT stations considered in this analysis (USN3 and IENG) are operated at timing laboratories and are thus collocated with other time-transfer means. In particular a TWSTFT link is regularly operated between these timing laboratories, so a comparison between RT and TWSTFT estimates can be performed. In the following Figure 7, RT and TWSTFT estimates are shown for the entire surveying period. A calibration constant has been applied.

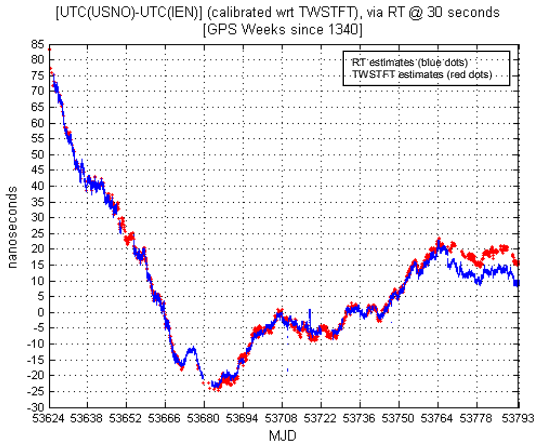

Figure 7 RT and TWSTFT estimates comparison for the overall surveying period.

It's worth mentioning that "near-real-time" estimates are 30 seconds spaced whilst the TWSTFT estimates are two hours spaced since 1st October 2005, MJD 53644 (until 30th September, they were 4 hours spaced) .

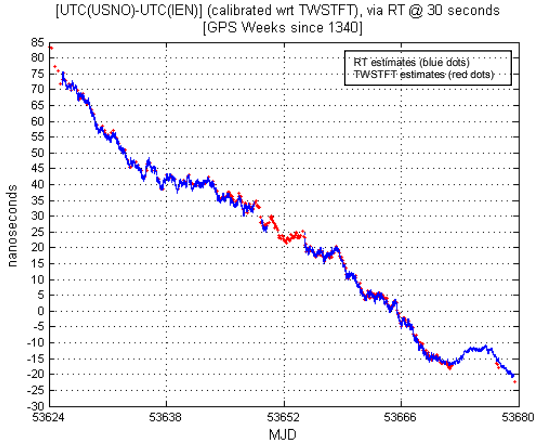

Figure 8 RT and TWSTFT estimates comparison for the MJD 53624 to 53680 period.

In Figure 8 it is possible to notice a very good agreement between the two series of estimates for the MJD 53624 to MJD 53680 period. This agreement can be much more noticed by analyzing the double differences between the RT and TWSTFT estimates for the related period, as shown in the following plot:

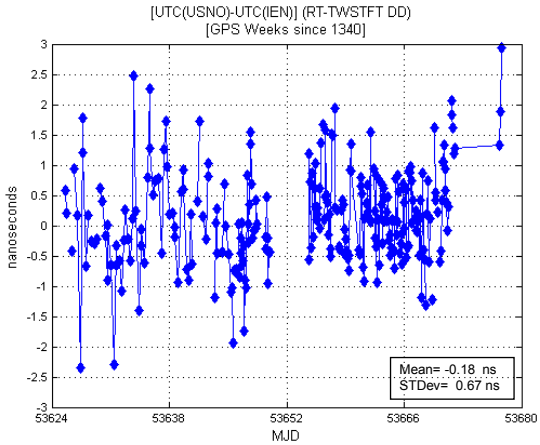

Figure 9 Double differences between RT and TWSTFT for the MJD 53624 to 53680 period.

It's worth mentioning that due to the different "sampling" of RT and TWSTFT estimates, a decimation process has to be performed in order to carry out a direct comparison between the outputs of those techniques. In detail, each RT value has been related to its corresponding TWSTFT value choosing the immediately previous and subsequent RT value and averaging them.
Other important information about the quality of RT estimates can be achieved by a frequency stability analysis (in terms of Allan deviation), as shown in the following Figure 10.

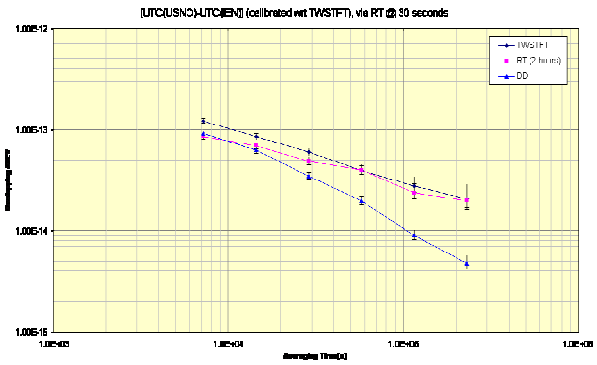

Figure 10 RT and TWSTFT estimates comparison in terms of frequency stability (Allan Deviation) for the MJD 53624 to 53680 period.

From the plot above it follows that the RT estimates standard stability is comparable with the TWSTFT one (especially in the short term) and both techniques show the UTC(IEN) inherent noise. Concerning the double differences, it's worth mentioning that they are characterized by a "white phase noise", that is the inherent noise of the two techniques.
In the following plots another portion of the overall surveying period is shown. In particular, it's referred to the period since MJD 53683 to MJD 53715.

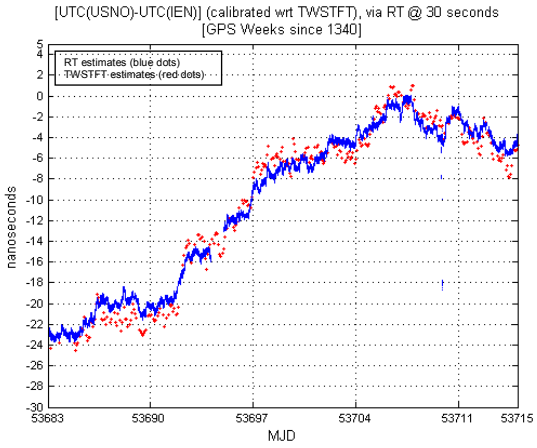

Figure 11 RT and TWSTFT estimates comparison for the MJD 535683 to MJD 53715 period.

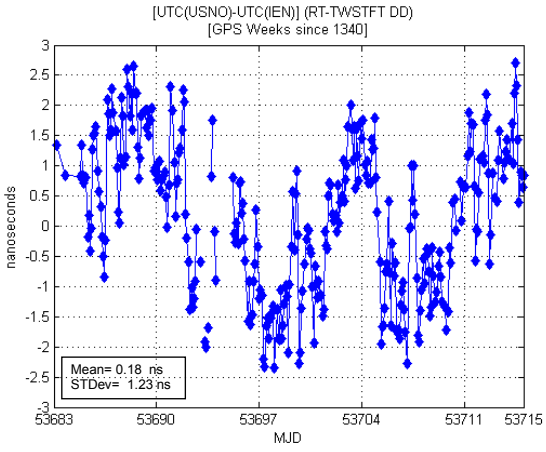

Figure 12 Double differences between RT and TWSTFT for the MJD 535683 to MJD 53715 period.

In Figure 11 and in Figure 12 it is possible to notice that the double differences between RT and TWSTFT estimates have a "cyclic" behavior. At the moment the reasons of this trend are not clear.

In Figure 13 the final portion of the analysis period is shown. In particular it's referred to the period since MJD 53743 to MJD 53793.

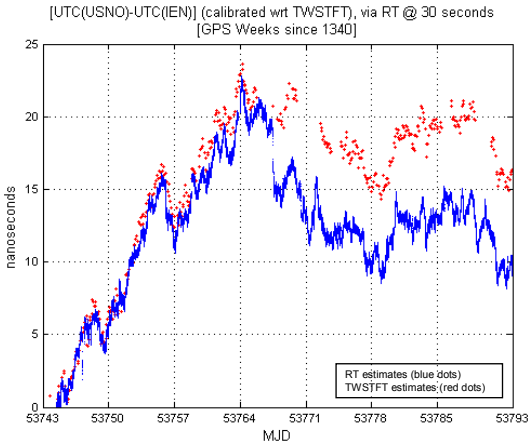

Figure 13 RT and TWSTFT estimates comparison for the MJD 535743 to MJD 53793 period.

From the plot above it's able to notice a divergence between RT and TWSTFT estimates since the day MJD 53767, when a glitch to the Ashtech receiver occurred.
This behavior is clearly evident from the plot showing the RT to TWSTFT double differences:

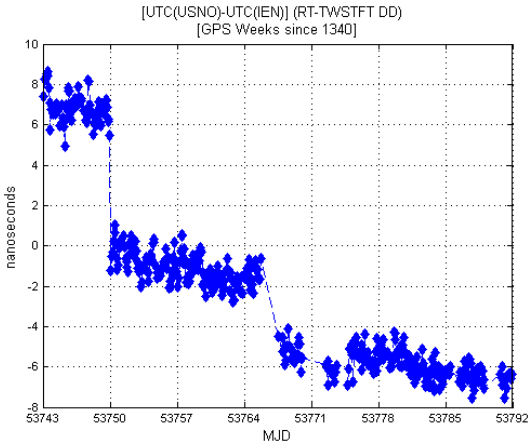

Figure 14 Double differences between RT and TWSTFT for the MJD 535743 to MJD 53793 period.

The reason for the divergence was due to an epoch where all but one of the carrier phase measurements was subject to a very small cycle slip. Some of these jumps were detected by a-posteriori residual detection, but it

appears that the statistical strength of the solution was not sufficient to trap them all.

In general, only cycle slips with a magnitude significantly larger than the noise level of the associated pseudorange can be detected in the residuals. Devising methods of detecting these marginal events in real-time remains a significant challenge.

Moreover, a direct comparison of the RT estimates with the UTC(USNO) to UTC(IEN) offset provided by BIPM Time Section in monthly Circular T can be performed, as shown in Figure 15. The results show that the RT estimates are consistent at ns-level with BIPM Circular T data, after a calibration constant application.

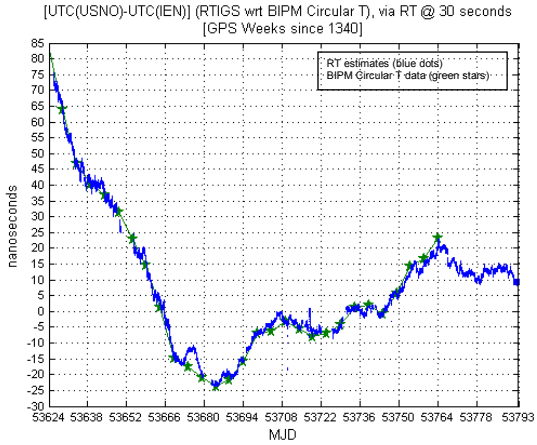

Figure 15 RT and TWSTFT estimates comparison for the overall surveying period.

V. RTIGS AS A MONITORING TOOL

The aim of this work is to evaluate the capabilities of the Real-Time time-transfer technique as a tool for the monitoring of the behavior of a time scale in order to support the real-time activities of the laboratory that will host this new tool.

During the whole surveying period, some problematic circumstances occurred. Some of these were due to glitches in the tracking of the IENG receiver which the Real Time tool was able to detect.

In Figure 16 a jump that occurred at IENG station on DOY 347/2005 (MJD 53717) is shown. From the plot it is possible to observe that the RT detected the trouble as well as the IGS clock products were are able to do, but with a shorter latency.

In Figure 17 a very steep slope in the first part of the DOY 21/2006 (MJD 53756) is shown. Also in this case the RT was able to detect this kind of problem as well as the IGS clock products were able to do.

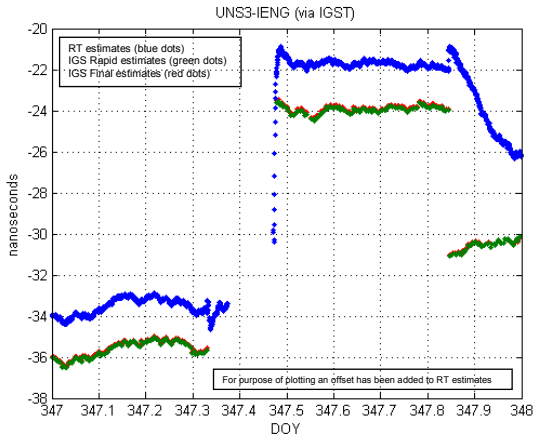

Figure 16 RT and IGS (rapid and final products) estimates comparison for the DOY 347 (year 2005), MJD 53717.

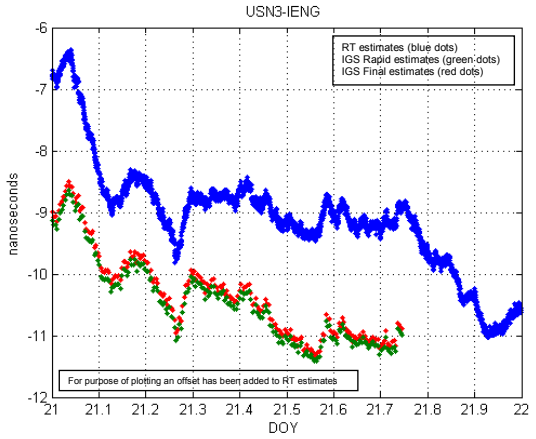

Figure 17 RT and IGS (rapid and final products) estimates comparison for the DOY 21 (year 2006), MJD 53756.

As we can see from the plots mentioned above, the RT estimates are consistent with IGS Final clock products in term of availability and accuracy (at ns-level), but with much reduced latency, currently few hours and potentially a few minutes.

In Figure 18 the “glitch” that occurred at IENG station on DOY 32/2006 (MJD 53767) is shown. Also this picture exhibits the good performance of the Real-Time

in order to detect the real behavior of a Geodetic GPS receiver.

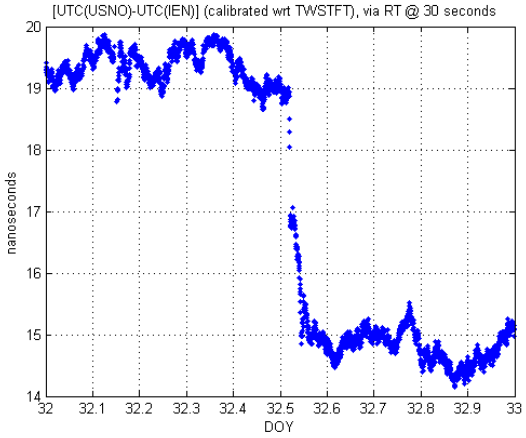

Figure 18 RT estimates for the DOY 32 (year 2006), MJD 53767.

VI. CONCLUSIONS

This work reveals that RT estimates are consistent at the ns-level with both BIPM Circular T and TWSTFT data, but providing a much reduced latency. Prior filtering of the RT clock estimates, based on computed formal standard deviations, is required to remove potentially anomalous data. Useful information can be derived from DADev if applied as real-time dynamic detector of degraded performance of station hardware or RT processing.

This work shows that the RTIGS infrastructure provides the opportunity to develop real-time applications for the timing community, such as a tool for the real-time detection of possible anomalies and the generation of a more timely local realization of UTC.

The Real-Time IGS has matured to a point where the current prototype phase will be moving into a pilot project phase [9]. This will help considerably in further understanding the feasibility of a real-time time-transfer technique for metrological purposes.

Acknowledgements

We would like to thank USNO, all International agencies and their staff for provision and support of real-time data access for the RTIGS.

REFERENCES

[1] "Real-Time Working Group Charter", IGS Central Bureau, http://igscb.jpl.nasa.gov/projects/rtwg/charter.pdf .

[2] F. Lahaye, P. Collins and J. Popelar, "The Virtual Reference Clock (VRC) Time Scale of the NRCan Real Time Wide Area GPS Correction Service (GPS·C)," in Proceedings of IVth, International Time Scales Algorithms Symposium, Sèvres, France, March 18-19, 2002.

[3] P. Collins, F. Lahaye, J. Kouba and P. Héroux, "Real-Time WADGPS Corrections from Undifferenced Carrier Phase," in Proceedings of National Technical Meeting of the Institute of Navigation (ION), Long Beach, California, USA, January 22-24, 2001, pp. 254-260.

[4] D. Orgiazzi, P. Tavella, G. Cerretto, P. Collins and F. Lahaye, "First Evaluation of a Rapid Time Transfer within the IGS Glbal Real-Time Network" in Proceedings of the 2005 Joint IEEE International Frequency Control Symposioum and Precise Time and Time Interval (PTTI) systems and Applications Meeting, August 2005, Vancouver, BC, Canada.

[5] R.K. Pearson, "Outliers in Process Modelling and Identification," in IEEE Transactions on Control Systems Technology, vol. 10, 2002, pp. 55-63.

[6] R. Costa, D. Orgiazzi, V. Pettiti, I. Sesia and P. Tavella, "Performance Comparison and Stability Characterization of Timing and Geodetic GPS Receivers at IEN," in Proceedings of the 18th European Time and Frequency Forum (EFTF), Guildford, UK, 5-7 April, 2004.

[7] ftp://62.161.69.5/pub/tai/publication/cirt.

[8] L. Galleani and P. Tavella, "The characterization of clock behaviour with dynamic Allan variance," in Proceedings of Joint Meeting European Frequency and Time Forum (EFTF) and IEEE Frequency Control Symposium (FCS), May 2003, pp.239-244.

[9] M. Caissy, RTIGS Working Group Co-Chair, RTIGS Mailing List

Proceedings of the 20th EFTF, 2006

Multipath mitigation in GPS-based time and frequency transfer

P. Defraigne,* and C. Bruyninx
Royal Observatory of Belgium
Avenue Circulaire, 3
B-1180 Brussels, Belgium
**Electronic address:* p.defraigne@oma.be

GPS-based time and frequency transfer is presently performed either with a code-only analysis (as presently done for TAI, using C/A or P codes), or with a combined analysis of code and carrier phase measurements using geodetic analysis techniques (as used for the generation of the IGS time scale).When neglecting calibration issues, the accuracy of both solutions highly depends on the noise of the GPS codes. An important part of this code noise is caused by multipath. In this paper, we use a linear combination of GPS codes and carrier phases to mitigate the effect of multipath and noise on the code measurements, and we evaluate the influence of this code noise reduction on the time transfer results. On one hand, we get a reduction of the rms of the CGGTTS results from 0.3 to 0.1 nanosecond for particular stations. On the other hand we show that the multipath/noise mitigation does not allow reducing significantly the day boundary jumps in the time transfer solutions obtained from code and carrier phase measurements.

I. INTRODUCTION

GPS is presently largely used for time scale generation (TAI, IGS time scales, local time scales) as well as for comparing precise frequency standards [1]. Two methods are generally used: a GPS code-only analysis, following the CCTF (Consultative Committee for Time and Frequency) procedure [2,3] and providing the results in CGGTTS (Common GPS GLONASS Time Transfer Standard) format, and a geodetic analysis combining GPS code and carrier phase measurements. This latter offers significantly higher time transfer precision thanks to the precision of the carrier phase measurements (about two orders of magnitude better than the code precision). However, when using the carrier phases, the code measurements are necessary to determine unambiguously the absolute clock offset; the ambiguity being intrinsic to the carrier phase measurements.
Consequently, the pseudorange noise level limits the accuracy of both GPS-based time transfer methods, beyond the problem of instrumental calibration uncertainties which are not considered here. In particular, the timing results obtained from the geodetic analysis are characterized by jumps at the day boundaries, caused by the fact that the data are analyzed in daily data batches where the absolute clock offset is determined by the mean code value during the daily data batch. The colored noise of the pseudoranges causes the jumps between the individual daily solutions. The amplitude of these jumps is highly station-dependent, but the origin of this dependence is not yet fully understood [4]; one hypothesis is the code multipath, i.e. signal reflections around the antenna.
In this paper, we go deeper into this multipath hypothesis: we apply a code noise and multipath mitigation procedure similar to the one used by the TEQC tool [5] on the RINEX observation files, and investigate the impact on time transfer for the CGGTTS analysis as well as the geodetic analysis.

II. MULTIPATH/NOISE MITIGATION

The procedure we use to correct the pseudorange observations for noise and multipath is based on the same idea as the TEQC multipath estimation. This procedure aims at mitigating both multipath and noise and no distinction between both is possible.

The measurement equation for carrier phases (Φ_{L1} and Φ_{L2}) and pseudoranges (P_1 and P_2) can be written as:

$$\Phi_{Li} = R + c(-\tau_s + \tau_r + \tau_t) - c\tau_{i,Li} + \frac{\lambda_{Li}}{2\pi}(\varphi_{LO,Li} - \varphi_{d,Li}) + N_{Li}\lambda_{Li} + mp_{\Phi Li} + n_{\Phi Li}$$

$$P_{Li} = R + c(-\tau_s + \tau_r + \tau_t) + c\tau_{i,Li} + c\tau_{d,Li} + mp_{PLi} + n_{PLi}$$

with R the geometric distance receiver-satellite, τ_s the satellite clock error, τ_r the receiver clock error, τ_t the tropospheric delay, τ_i the ionospheric delay (frequency-dependent, with $\tau_{i,L2} = \frac{f_{L1}^2}{f_{L2}^2}\tau_{i,L1} = \alpha\tau_{i,L1}$), λ the carrier wavelength, N the phase ambiguity, mp the multipath

error, τ_d the instrumental code delay, φ_d the instrumental phase shift on the carrier (receiver + satellite), φ_{L0} the initial phase error, and n the noise.

For each satellite, the code multipath can be obtained from a combination of code and phase measurements in which the phase multipath and noise, significantly smaller than the code multipath and noise, is neglected. For the code multipath/noise on L1, this relation reads:

$$MP_1 = P_{L1} - \Phi_{L1} - \frac{2}{\alpha - 1}(\Phi_{L1} - \Phi_{L2})$$

which reduces to

$$MP_1 = mp_{P_{L1}} + n_{P_{L1}} \qquad (mp + noise)$$

$$-\frac{\lambda_{L1}}{2\pi}\frac{\alpha+1}{\alpha-1}(\varphi_{LO,L1} + 2\pi N_{L1}) + \frac{\lambda_{L2}}{2\pi}\frac{2}{\alpha-1}(\varphi_{LO,L2} + 2\pi N_{L2}) \qquad (constant)$$

$$+ c\tau_{d,L1} + \frac{\lambda_{L1}}{2\pi}\frac{\alpha+1}{\alpha-1}\varphi_{d,L1} - \frac{\lambda_{L2}}{2\pi}\frac{2}{\alpha-1}\varphi_{d,L2} \qquad (constant\ or\ very\ slow\ variations)$$

Under the conditions that 1) multipath and noise have a zero-mean during a period T_m, 2) the hardware delays are constant during T_m and 3) no cycle slips occur during T_m, the multipath and noise can be obtained through the relation $mp_{PL1} \approx MP_1 - \overline{MP}_{1Tm}$, where $\overline{MP}_{1Tm}$ is the average of MP_1 over the period T_m. To satisfy the third condition, the Bernese software [6] is used to remove cycle slips from the carrier phase data prior to the multipath/noise mitigation procedure.

The multipath and noise on P2 can be obtained in a similar way from the combination

$$MP_2 = P_{L2} - \Phi_{L2} - \frac{2\alpha}{\alpha - 1}(\Phi_{L1} - \Phi_{L2})$$

From which we obtain under the same conditions $mp_{PL2} \approx MP_2 - \overline{MP}_{2Tm}$.

The results which will be presented in this paper are based on either an averaging period T_m of 40 minutes, which removes all the noise and short-term (shorter than 40 min) multipath, or on averaging over the full satellite track, which further removes long-term multipath. The first choice of 40 min is deduced from the observation that the noise reduction on pseudorange increases with increasing T_m up to 40 min, while it remains stable for T_m larger than 40 min. In that case, the data 40 min around the track were used to compute the mean *MP*. One disadvantage of this method is that it is only possible to obtain corrected pseudoranges for a particular epoch if the satellite is visible 20 minutes before and after the epoch, without tracking interruption. The number of satellites (and number of observations) is therefore reduced with respect to the full dataset. For averaging periods of 40 min, about 10% of the original observations are lost, but it mainly concerns observations at low elevations. In the second case, we use the mean *MP1* and *MP2* over the full satellite track to correct the data. The main sources of data loss are now the tracking interruptions longer than 30 second causing in addition cycle slips which are not corrected by the Bernese software. However, these tracking interruptions occur mainly at low elevations so that the reduction of observations is of the same order as for the 40 min averaging.

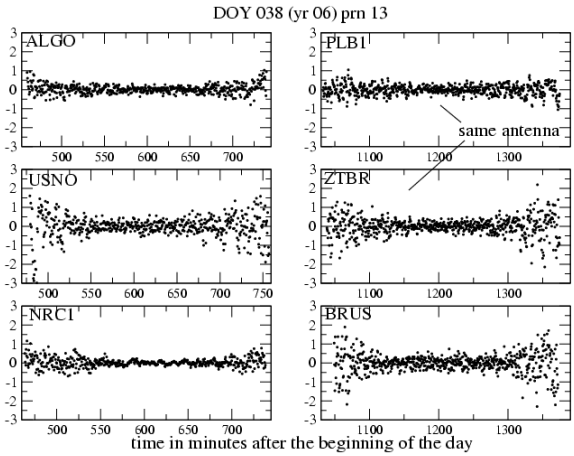

Figure 1. Estimated multipath and noise, mp_{PL1} (in meters), using an averaging period of 40 min, for different stations and receivers : ALGO and NRC1 use AOA receivers, USNO, BRUS and ZTBR use Ashtech Z-XII3T receivers, and PLB1 uses a PolaRx2 receiver.

Examples of the mp_{PL1} obtained with T_m=*40min* for several stations are shown in Figure 1. The station-dependent behavior and receiver-dependent behavior are clearly illustrated.

The maximal difference between the mp_{PL1} obtained when averaging over T_m=*40min* or over the whole visibility period is at the level of 50 centimeter, with a long-term behavior. For this reason, we do not show in the graphics the mp_{PL1} obtained with averaging on the whole visibility, as the difference is not clearly visible due to the high noise level of the multipath correction. The mean multipath/noise correction for one satellite is perfectly zero for the averaging over the full satellite track, while it is between -1 and +1 cm with T_m=*40min*; no significant offset is therefore introduced in the pseudorange measurements of one satellite when applying the multipath/noise correction. However, the effect of the multipath on the mean pseudorange during one satellite track is not accounted for in our correction. This remaining part of the multipath effect will be discussed later.

III. EFFECT ON CGGTTS RESULTS

The CGGTTS results are obtained through the CCTF procedure [2], or its modified version [3] using the ionosphere-free pseudoranges P3 from 30-second RINEX observation files. This procedure includes quadratic (in its original form) and linear fits proposed partly to mitigate the effect of multipath. The aim of the present study is therefore to investigate if the CGGTTS results are multipath-free, and if not, to determine the impact of multipath on the CGGTTS results. We compare in a first step the results obtained without the CCTF procedure (what we call the code-only clock solution STAT-IGST) and the CGGTTS results. In both cases, all the results are based on the ionosphere free combination P3 taken at a 30-second sampling rate, from which we remove the corrected geometric distance (including the station displacement due to solid earth tides and the correction for satellite antenna phase center for blocks II and IIA), the troposphere delay using the Hopfield model, the satellite clock error, and the relativistic clock correction. The code-only clock solution outputs 30-second results, while in the CCTF procedure a linear fit is applied on the 13 min tracks (= 26 points) of the BIPM tracking schedule, with 89 tracks per day, and the CGGTTS solution corresponds to the mid point of the linear fit for each of the satellites visible during that track. All the results presented in this study are based on the IGS precise satellite orbits and clocks.

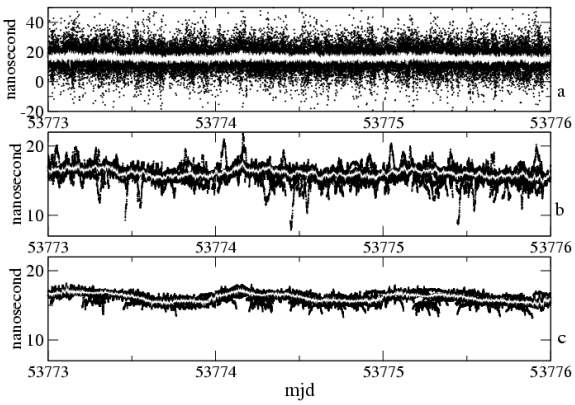

Figure 2. BRUS-IGST using code-only analysis. All satellite results are plotted as black dots, the weighted averages per epoch are plotted in white. Results have been obtained (a) from raw data, (b) from data corrected for *mp1* and *mp2* using T_m=*40min*, (c) from data corrected for mp1 and mp2 using the averaging on the full satellite track.

Figure 2 presents the code-only clock solution BRUS-IGST during 4 days, obtained from code data with and without the multipath and noise mitigation. The picture shows the results for all the visible satellites as well as the weighted average at each observation epoch, with the weighting scheme sin^2(elevation).

A clear reduction of the noise is observed when applying the multipath/noise mitigation; the rms of the averaged solutions falls down from 1.4 nanosecond (ns) for the raw data to 0.5 ns after correction (with T_m=*40min* and with averaging on the whole period of visibility). Furthermore, the long-term multipath, remaining after the correction with T_m=*40min* and clearly visible in the second graph is largely reduced in the lower graph, after correction with averaging on the whole satellite track.

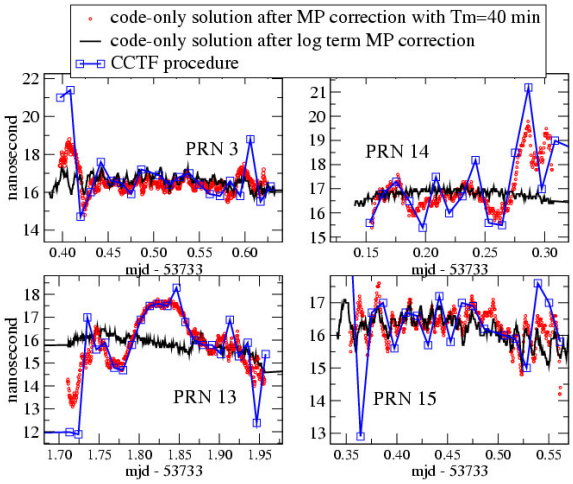

Figure 3. BRUS-IGST as obtained from different PRN's, with code-only analysis with and without multipath and noise mitigation, and with the classical CCTF procedure applied on the raw code data.

Figure 3 presents for several individual satellites the code-only analysis obtained from pseudoranges corrected for multipath and noise with T_m=*40min* or with the whole visibility period average. This picture underlines the long-term multipath remaining in the correction based on T_m=*40min,* and removed with the correction based on an averaging on the whole satellite track.

Note the large long-term multipath for PRN 13. This behaviour is cancelled by our noise-multipath mitigation procedure when averaging on the whole satellite track, while it is not certain that its origin is multipath. We could indeed find the same shape in other European stations (see Figure 4), so that it could be associated to some non-multipath effect, not yet identified to date.

Figure 3 also shows the CGGTTS results obtained from the CCTF procedure on raw data. The differences between the CCTF results on raw data and the code-only analysis obtained on the data after multipath/noise mitigation reach 7 ns in extreme cases, and such large differences occur only at low elevations. When using an elevation-dependent weighting, the low elevation results

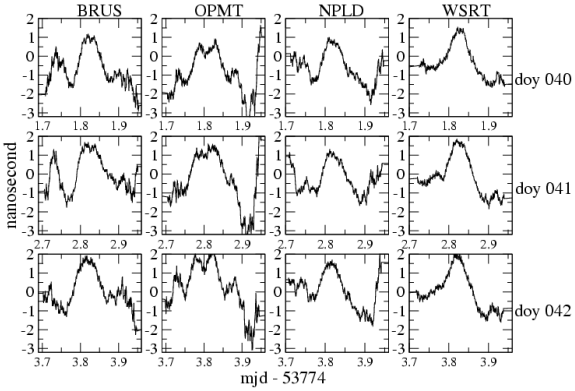

Figure 4. BRUS-IGST as obtained through PRN 13, with code-only analysis on code data corrected for multipath and noise with T_m=*40min*, in four European stations, and three consecutive days.

do not affect significantly the final clock-IGST results, so that finally the difference between the CCTF results obtained with and without noise/multipath mitigation are rarely larger than one nanosecond. This is illustrated in Figure 5 for three different stations equipped with H-masers: WSRT, BRUS and USNO. The rms of the results is clearly reduced when applying the multipath/noise mitigation on the pseudoranges, this corresponds to a reduction from 0.4 to 0.3 ns for BRUS-IGST, from 0.3 ns to 0.1 ns for USNO-IGST, and from 0.3 to 0.2 for WSRT-IGST. The maximal difference between results obtained with and without noise/multipath mitigation is 1 ns.

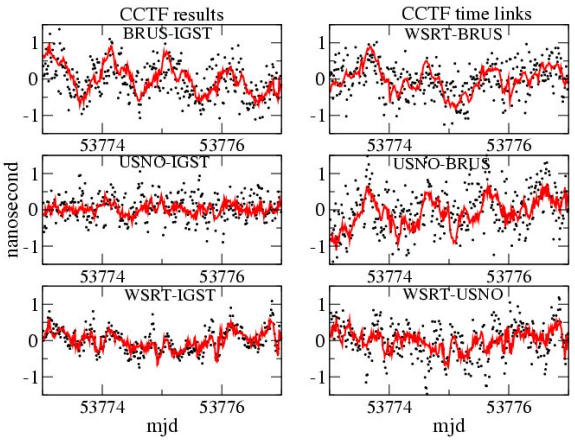

Figure 5. CCTF results (in nanosecond) obtained from raw data (dots) and from data corrected for multipath and noise using an averaging on the full period of visibility of the satellite (continuous line).

Note that a clear diurnal periodicity is present in the signal for BRUS (in the results obtained with both uncorrected and corrected pseudoranges); it is caused by a satellite-dependent phenomena not yet identified to date. As this periodicity is not observed in a close station as WSRT (290 km), this seems to be a satellite-station effect rather than a pure satellite-dependent effect. A part of this effect could be due to the impact of multipath on the mean pseudorange during the period of visibility of one satellite, which was not corrected as explained before (our procedure is based on the hypothesis of a zero mean of the multipath during the averaging period).

The time links between the three stations are also presented in Figure 5. They have been obtained using the "all-in-view" scheme used by the BIPM, i.e. differences between the solution STAT-IGST at each epoch [7], with only one difference concerning the weighting scheme which is sin^2(elevation) in our study, and $1/cos^2$(elevation) in the BIPM computations. The rms of the results for the three time links presented is reduced by the noise/multipath mitigation, from 0.4 to 0.3 ns for WSRT-BRUS, from 0.6 to 0.3 for USNO-BRUS and from 0.5 to 0.2 ns for WSRT-USNO. The maximal difference between the results obtained with and without noise/multipath mitigation of 1.6 ns.

IV. EFFECT ON GEODETIC RESULTS

As the code multipath is suspected to be responsible of part of the day boundary jumps in geodetic code/carrier phase clock solutions, we investigated also the possible reduction of these day boundary jumps induced by the mitigation of multipath and noise on the P1 and P2 pseudoranges. In the IGS clock solution the day boundary jumps show large dispersion between stations, with rms ranging from 150 ps to 1000 ps [4], reflecting the different station code performances. These rms values are higher than the expected 120 ps based on the accuracy of each clock estimate, the 1 meter precision of the code data and a 5-minute sampling. We have only investigated stations equipped with H-masers as for less stable frequency standards the clock instability dominates the day boundary jumps caused by the pseudorange noise. A part of the code variability can be associated with the variations of the instrumental delays, primarily due to temperature variations. We could in particular find a large correlation between the code-only analysis results and the temperature variations at ALGO (about 300 ps/°C), which could explain, as already pointed out in [8], the large day boundary jumps at that station especially during winter time (see Figure 6). We therefore investigated the possibility to reduce the day boundary jumps only in stations where we did not see any correlation of the code-only solutions with external temperature variations and where the internal temperature is stabilized (except for NRC1), so that the day boundary jumps where suspected to be due to code multipath.

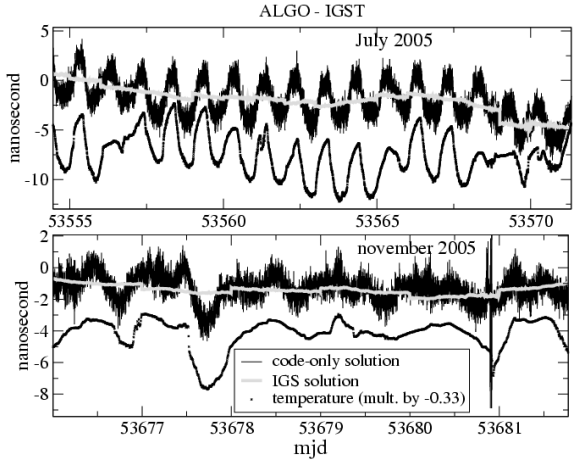

Figure 6. Correlation between the code-only clock solution for ALGO and the external temperature, which is the cause of the major part of the large day boundary jumps at that station. The temperature was multiplied by -0.33 and shifted in order to allow the comparison.

Our geodetic analysis has been performed using the Bernese 5.0 software. We only present the differential solutions, as the Bernese results for PPP (Precise Point Positioning) show day boundary jumps significantly higher than in the IGS solutions; these day boundary jumps find therefore their origin certainly in the software and could not be reduced by the multipath corrections. The differential solutions have however day boundary jumps similar to the IGS solution. Only the results obtained with multipath/noise corrections computed with an averaging period corresponding to the full satellite track are presented; our first results showed that the correction using T_m=*40min* did not affect the results of the geodetic time transfer.

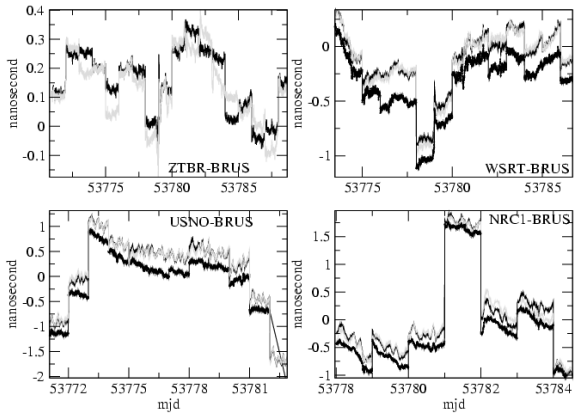

Figure 7. Comparison of code/carrier time transfer solutions computed with the Bernese 5.0 software without (black) and with (grey) correction for multipath and noise; the IGS solution is also shown (black, shifted by 0.2 ns to allow better visibility).

Figure 7 presents the effect of multipath/noise mitigation on a local setup, where the same clock is driving two similar GPS receivers Ashtech Z-XII3T named BRUS and ZTBR, connected to two separate but similar Ashetch antennae. In the clock solutions from geodetic analysis for the link ZTBR-BRUS during 2 weeks, the day boundary jumps are modified by the multipath/noise correction but in some cases they are increased while in other cases they are reduced. The differences between the day boundary jumps with and without multipath/noise correction reach maximally 150 ps.

Three other IGS stations have been analyzed; these stations were chosen because of their typical day boundary jumps as presented in [4]: WSRT and USNO for their medium-size jumps, and NRC1 for its very large jumps. The results presented in Figure 7 are also compared with the IGS solution. Similar to the local setup, the difference between the day boundary jumps obtained with and without multipath/noise mitigation is small compared to the amplitude of the day boundary jumps, with a maximum difference of 300 ps for NRC1 for one particular day boundary; but again, the correction results in both reductions and increases of the jumps.

V. CONCLUSIONS

This study investigated the effect of code multipath/noise mitigation on code- and code/carrier-based GPS time transfer. The proposed mitigation procedure is derived from a combination of L1 and L2 code and carrier-phase measurements, and is based on the hypothesis that the instrumental delays are constant and that the sum of noise and multipath has a zero average over a specified period. We used both an averaging period of 40 minutes, to remove noise and short-term multipath, as well as an averaging period corresponding to the full satellite track, removing both the short and long-term multipath.

The impact of the complete multipath/noise correction on the CGGTTS results (short and long-term) has been estimated and gives a reduction of the rms between 0.1 and 0.3 ns on the clock-IGST results as well as on the time links based on CGGTTS results. This corresponds for example to a rms reduction from 0.3 to 0.1 ns for USNO-IGST and from 0.5 to 0.2 ns for WSRT-USNO, for the period investigated here. The maximal difference between results obtained with and without noise/multipath mitigation reaches 1 ns for the clock-IGST results and 1.6 ns for the time links. The multipath impact is therefore still present in the CGGTTS results at a level of some tenths of nanoseconds.

When using the combined code-carrier phase analysis, we know that the absolute clock value is determined from the daily mean of the code data, and that the jumps between daily solutions are due to the colored code noise. We therefore investigated the impact of our multipath/noise mitigation on the day boundary jumps. The observed changes in the day boundary jumps were significantly smaller than the amplitudes of the original day boundary jumps and the size of the jumps was not necessarily reduced. It is therefore necessary to find another candidate to explain the large dispersion between day boundary jumps observed at some IGS stations [4].

A part of the day boundary jumps could however still be associated with the multipath, as we did not take into account the effect of the effect of multipath on the mean pseudorange during the satellite track, because our procedure is based on the hypothesis of a zero-mean multipath/noise during the averaging period T_m. This non-zero mean multipath could also explain a part of the diurnal periodicity observed in the CGGTTS results. This periodicity is clearly visible in the multipath/noise mitigated results for BRUS (Figure 5), and it originates from a satellite-dependent phenomena with a daily period. Some other effects on the code measurements, not yet identified, inducing jumps in the code-only solution, could also explain the day boundary jumps, and will be the subject of further investigations.

REFERENCES

[1] Bauch A., Achkar J., Bize S., Calonico D., Dach R., Hlavac R., Lorini L., Parker T., Petit G., Piester D., Szymaniec K., Uhrich P. Comparison between frequency standards in Europe and the USA at the 10-15 uncertainty level, Metrologia, 43, Tech. Suppl., 2006.

[2] Allan, D.W., Thomas, C., Technical directives for standardization of GPS time receiver software, Metrologia 31, PP. 69-79, 1994.

[3] Defraigne, P., and Petit G., Time transfer to TAI using geodetic receivers, Metrologia 40, 184-188, 2003.

[4] Ray J., and Senior K., Geodetic techniques for time and frequency comparisons using GPS phase and code measurements, Metrologia 42, 215-232, 2005.

[5] Estey LH, Meertens C, TEQC: the multi-purpose toolkit for GPS-GLONASS data. GPS Solutions, 3, No 1, 42-49, 1999.

[6] Beutler, G. and al., Bernese GPS software version 5.0 (draft), ed. Urs Hugentobler, R. Dach, P. Fridez, M. Meindl, 2006.

[7] Arias, F., Use of GPS satellites All in View technique in TAI computation, BIPM TM 134, 2004.

[8] Senior, K., and Ray., J., Accuracy and precision of GPS carrier phase clock estimates, Proc. 33rd Precise Time and Time Interval Meeting, 2001.

Proceedings of the 20th EFTF, 2006

COMBINED MULTI–SYSTEM GNSS ANALYSIS FOR TIME AND FREQUENCY TRANSFER

R. Dach*, S. Schaer†, U. Hugentobler*, T. Schildknecht*, and A. Gäde*

*Astronomical Institute, University of Bern, Sidlerstrasse 5. CH-3012 Bern, Switzerland
e-mail: rolf.dach@aiub.unibe.ch, phone: ++41–31–631 3802, fax: ++41–31–631 3869
†Federal Office of Topography (swisstopo), Switzerland

Keywords: GNSS carrier phase, time transfer, frequency transfer, GLONASS interfrequency code biases.

Abstract

The Center for Orbit Determination in Europe (CODE) is one of the Analysis Centers (AC) of the International GNSS Service (IGS). It is located at the Astronomical Institute of the University of Bern (AIUB). Since May 2003, CODE provides consistent GPS and GLONASS satellite orbits from a combined analysis using the Bernese GPS Software package. The data of about 30 stations in the IGS network that are equipped with GNSS receivers tracking GPS as well as GLONASS satellites are analyzed for that purpose together with numerous stations that only track the GPS satellites.

With the background of the experience in orbit determination for more than one satellite system, we discuss the use of both GPS and GLONASS observations in a combined analysis for geodetic time and frequency transfer using code and phase measurements. The number of satellites that can be used for time transfer is increased when adding the GLONASS observations to the analysis. This may help to improve the redundancy for the receiver clock parameters that are estimated for each station from all satellites in view.

GLONASS satellites emit the signals on individual frequencies. This may lead to frequency–dependent biases in the receivers that have been investigated, e.g., in [1]. Of course, these biases must be considered in a combined analysis of GPS and GLONASS code data. Corresponding parameters can be estimated for all GNSS receivers even if they are not connected to an external reference clock. This offers the possibility to investigate the frequency–dependent biases for all receiver types that are represented in the IGS network. The estimated biases can be interpreted as a relative "calibration" of each individual frequency used by a GLONASS satellite with respect to the GPS frequency.

The rigorous common analysis of GPS and GLONASS measurements is considered as a good preparation for including the upcoming European GALILEO system into the processing for geodetic time and frequency transfer with a maximum benefit for the solution.

1 Introduction

The Center for Orbit Determination in Europe (CODE) is one of the global Analysis Centers (AC) of the International GNSS Service (IGS). It is a collaboration between the Astronomical Institute at the University of Bern (AIUB, Switzerland), the Federal Office of Topography (swisstopo, Switzerland), the Federal Agency for Cartography and Geodesy (BKG, Germany), and the Institut Géographique National (IGN, France). It is located at AIUB. The development version of the Bernese GPS Software package [2] is used for all analyses.

Since May 2003, CODE includes not only GPS but also GLONASS satellites in all its orbit determination procedures for the submission to the different IGS product lines: the final, rapid, and even ultra–rapid products[1]. It is — at least up today — the only AC of the IGS that performs a rigorous GNSS analysis by processing the observations from different Global Navigation Satellite Systems (GNSS) together in one common parameter estimation procedure. On one hand, this strategy requires a higher computer performance because of the higher number of observations that have to be processed together and because of the higher number of parameters that have to be solved for. On the other hand, the resulting orbits for all satellites of both GNSS have the best possible consistency. Further details on the processing strategy at CODE may be found in [3].

Up to now, CODE does not include GLONASS in its final and rapid clock products. The most important reason for this is, that interfrequency biases as described and calibrated, e.g., in [4] are unknown for the GNSS receivers that are used in the IGS network. For a combined GNSS analysis they have to be considered by estimating them as unknown parameters in the processing. A summary of the results will be given in Section 3.

In addition, the number of additional observations (including the corresponding increased number of phase am-

[1]The IGS product lines are defined by their latencies between the observation and the availability of the products. The ultra–rapid products are generated four times per day and are available three hours after the last observation. The rapid products are made available at 17:00 UT for the previous day whereas the final products have a latency of about two weeks.

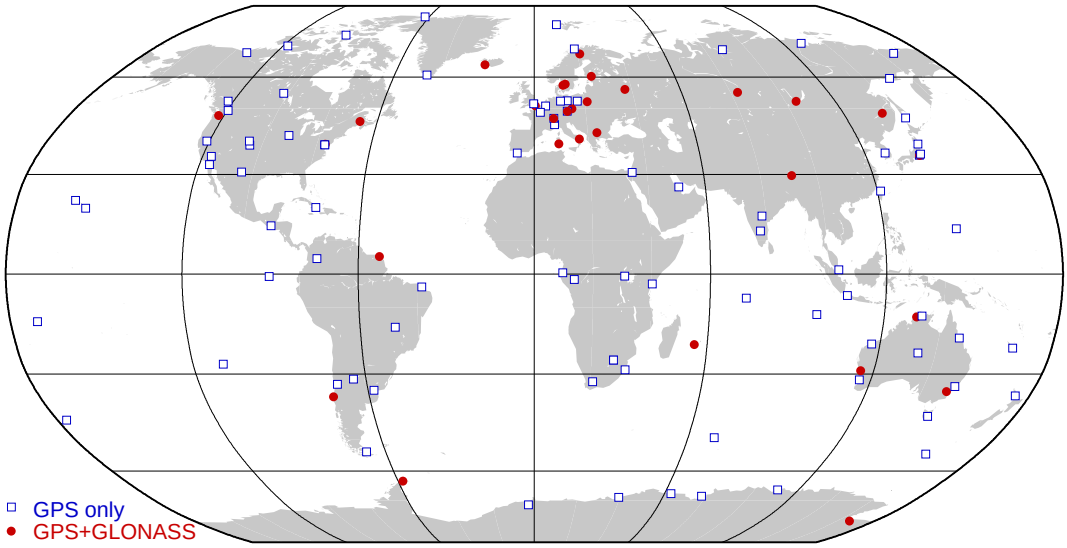

Figure 1: Location of the IGS stations included in the CODE GNSS clock processing.

biguity parameters) and the number of interfrequency bias parameters that have to be estimated as well, increases the required computing effort that is necessary to provide also satellite clocks for GLONASS satellites.

On the other hand, the stations currently providing GNSS data for GPS and GLONASS do not allow for a complete coverage of the GLONASS orbits. A few gaps remain over the Pacific Ocean and the southern part of the Atlantic Ocean and Africa. For the orbit determination these gaps can easily be bridged by dynamic orbit modeling, but for the clock products epochs with missing satellite clocks result. This sparse station distribution may effect the results when only the GLONASS satellite clocks are introduced for a precise point positioning (PPP) resp. a PPP solution needs not to be improved by adding the GLONASS to the GPS observations in a combined GNSS analysis — especially outside from Europe where most of the GNSS receivers are located in the IGS network. More details will be discussed in Section 2.

In this paper we present results of a series of test solutions set up to compute fully consistent satellite clock corrections for different GNSS. Problems and the benefit for time and frequency transfer from a combined analysis using carrier phase data from multiple GNSS are discussed in Section 4.

2 Description of the combined GNSS Analysis

To compute the GPS satellite clock corrections from the tracking network of nearly 350 IGS stations a subset of 90 stations for the rapid and 120 stations for the final products are selected for the processing at CODE. As long as no data problems are encounted the IGS stations located at timing laboratories contributing to TAI and the IGS stations equipped with H-maser clocks to support the generation of the IGS time scale ([5]) are included in the solution every day. Further IGS stations with a low noise in the code data (e.g., because of a low impact from multipath or environmental effects) are added to get a network with global coverage that allows to compute the satellite clock corrections for all satellites and epochs from the observations of at least three stations.

Today the IGS network contains about 30 stations equipped with GNSS receivers that track signals from GPS as well as from GLONASS satellites. As illustrated by Figure 1 most of them are located in Europe while the coverage of other region is very sparse. No redundancy is available (except in Europe) to cope with station outages or late data submissions. When requesting a minimum number of stations to contribute to the estimation of a satellite clock parameter it is for most GLONASS satellites not possible to provide clock corrections for all epochs (usually only for about 90%). Regions where no GLONASS satellite clock parameters can be provided due to lack of data are the Pacific Ocean and the southern part of the Atlantic ocean as well as southern Africa.

As shown in Figure 2 the GPS satellite clock corrections are computed from the data of at least ten stations. However, there are daily intervals where the GLONASS satellites are not observed by any of the GNSS receivers in the IGS network. As a consequence, independent parts in the resulting GLONASS satellite clock time series result that are not connected by continuous carrier phase data. Discontinuities analogous to day boundary discontinuities for station clocks (see, e.g., [6]) have to be expected.

Because of the lower redundancy for the estimation of GLONASS satellite clock corrections stations with a higher noise level in the code data may have a higher impact on the results because they cannot be replaced by other sites in the analysis. Figure 3 shows the Al-

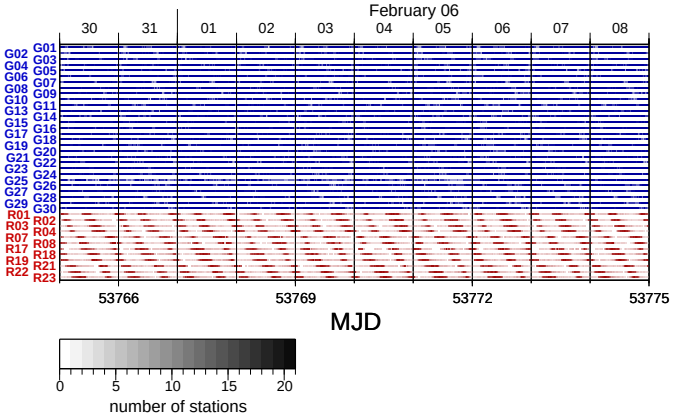

Figure 2: Number of stations that are used to compute the GNSS satellite clocks in the CODE analysis for a period of ten days. According to the RINEX convention the GPS satellites are labeled with Gxx while the GLONASS satellites are named Rxx.

lan variance of the GPS and GLONASS satellite clocks. To achieve a better comparability both the GPS and GLONASS satellite clock corrections are computed from the about thirty GNSS stations in the IGS network only. The performance of the GLONASS satellite clocks is comparable with the GPS Block II resp. IIA Cesium clocks. It is interesting to note that no improvement for clocks onboard of the new generation of GLONASS–M satellites with respect to the older GLONASS satellites can be found in the Allan variance.

For some satellites (GPS as well as GLONASS) a periodic once per revolution signal can be found. These satellites are located on different orbital planes and not all of them are eclipsing during this period. Because the periods of the different satellites are not in phase it can be ruled out that the GNSS station SPT0 (Swedish National Testing and Research Institute, Boras, Sweden) used as reference clock has introduced this disturbation.

As long as the estimated satellite clock corrections are used for a PPP such an effect does not inevitably degrade the results if fully consistent satellite orbits and clocks are used as required for the PPP in general.

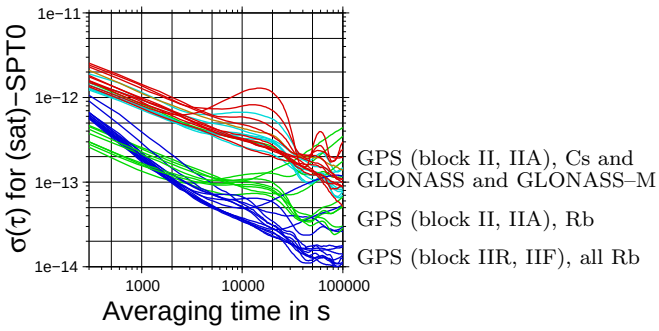

Figure 3: Allan variance of GNSS satellites computed for 10 days in February 2006.

3 Intersystem and Interfrequency Biases in GNSS Receivers

Because the orbits and clock corrections for the satellites of the different GNSS are the result of a combined analysis all these products are fully consistent. They refer to the same geodetic reference frame and to the same reference clock. That's why they can be introduced into a GNSS analysis without considering additional intersystem biases. The only remaining type of intersystem bias relevant for the users are possible receiver time resp. receiver antenna biases. Both are discussed in this section.

3.1 Receiver Antenna Model

Because of the different frequencies and signal structure of the individual GNSS the electronical characteristics of a receiver antenna (described for the processing as models of the antenna phase center variation – PCV) may be different for each satellite navigation system. Calibrations of geodetic GNSS antennas (as described, e.g., in [7, 8]) are done using observations to GPS satellites only. The question is whether these receiver antenna models can also be used for observations to GLONASS satellites or whether there are significant differences.

To generate Figure 4 the GPS derived receiver antenna model was applied for the GPS as well as for the GLONASS observations. Furthermore, from all GLONASS measurements, parameters to characterize an elevation–dependent (i.e. rotation symmetric) receiver antenna model are estimated. It is expected that these corrections are zero if the GPS derived model can also be used for GLONASS observations. The differential phase pattern was computed for five antennas that are used in the IGS network for GNSS receivers from four weeks of data.

The values for very high and low elevations can be ignored:

> **80°:** Close to the zenith only a small number of observations is available due to the satellite geometry. This leads to uncertain estimates for the corrections.

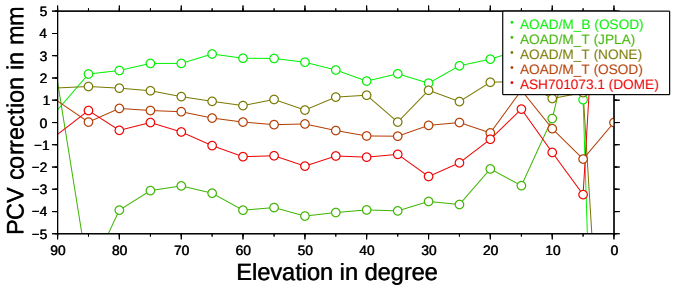

Figure 4: Parameters of an elevation–dependent receiver antenna model for five antennas that are currently used for GNSS receivers in the IGS network. The results are obtained from four weeks of data in January 2006.

$< 20°$: Close to the horizon troposphere and multipath effects result in a higher noise of the observations. Masking and elevation cutoff in addition reduces the number of observations.

After removing the estimated corrections at the extreme elevations a middle part between 20° and 80° of elevation remains. The curves can now be shifted by a few millimeters so that their mean value becomes zero. This shift corresponds to a time offset between the GPS and GLONASS observations that also can to be considered as intersystem receiver code bias as will be discussed in the following section. For the phase measurement the intersystem time bias is absorbed by the phase ambiguity parameters resp. by the phase shift parameters that have to be estimated if the ambiguities for the GLONASS observations are resolved to their integer values. As conclusion, the estimated corrections for the GLONASS receiver antenna model w.r.t. the GPS derived antenna model are in the order of 1 mm. This means that this experiment did not indicate a significant discrepancy between the antenna models for both GNSS.

3.2 Receiver Intersystem/Interfrequency Biases

The satellite clock corrections obtained in a combined analysis of the GPS and GLONASS observations refer to one and the same reference clock in the network solution. The difference in the broadcast time scales between GPS and GLONASS are, therefore, not relevant anymore. Nevertheless, an intersystem time bias within each receiver may be expected because of the different frequencies and signal structure of the individual GNSS.
Such a receiver internal time bias is only relevant for processing the code data. When analyzing the phase measurements the corresponding phase ambiguity parameters will absorb the time biases.
Because the GLONASS satellites emit their signal on individual frequencies, in addition to intersystem also interfrequency biases for the receivers are expected (they were detected already by other groups, e.g., [1, 4]). To make this study as general as possible one bias for the code measurements of each satellite (GPS and GLONASS) was setup for each station. Because the receiver and satellite clocks are also computed, two singularities have to be treated. We use to introduce a zero mean condition over all estimated corrections:

- The sum of all estimated biases for the GPS satellites of a station is zero for each day. This means that all computed satellite biases of the GLONASS satellites are relative to the biases for the GPS satellites.
- Furthermore, the sum of the biases of all stations for one and the same satellite is zero.

These zero mean conditions are equivalent to fixing all satellite biases of one receiver resp. to fixing the biases of one satellite for all receivers in the network to any value. When using the zero mean condition the reference changes from day to day according to the magnitude of the biases of the receivers contributing to the daily network solution. Nevertheless, there are two strong reasons to prefer the zero mean condition instead of fixing biases: First, there is no preference for a specific receiver or a satellite. Second, when fixing biases and the particular reference receiver resp. satellite is not available during an interval, no solution can be generated or an alternative reference must be defined. The second reason demands that a change of the reference can be considered in a way that the results remain comparable. With the same algorithm the disadvantage of the zero mean condition can be compensated.
The impact of the individual realization of the reference in the case of a zero mean condition is demonstrated in Figure 5. The upper diagram shows the satellite biases as they are computed for each day for the station ONSA (Onsala, Sweden; receiver: JPS E_GGD). There is a clear systematic pattern in the graph that is similar to all satellite biases. In addition, there are several values in the time series that look like outliers. When unifying the reference a long-term solution for the satellite biases of all stations is generated. After that the daily solutions are fitted to the long–term solution with the same zero mean conditions as in the processing. With this algorithm the daily estimated satellite biases are made comparable. The biases obtained for station ONSA after the unification of the reference are shown in the lower graph of Figure 5.
The satellite biases are constant for all stations (apart

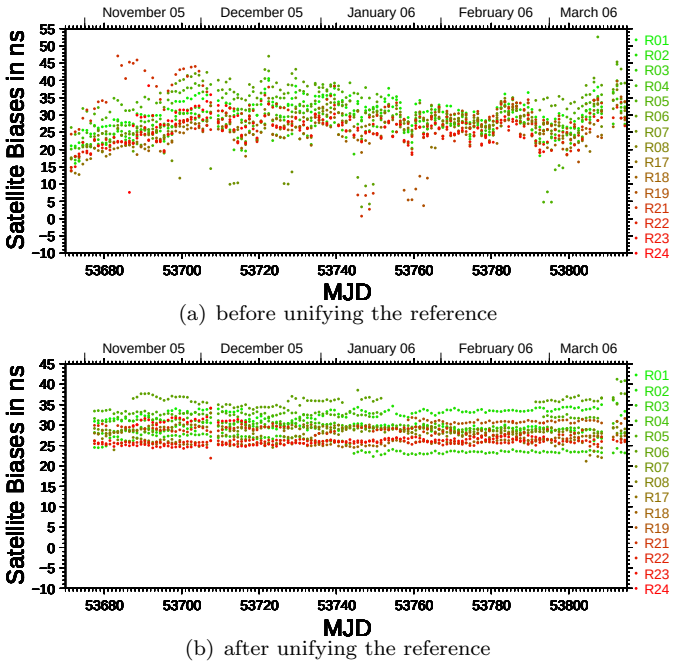

(a) before unifying the reference

(b) after unifying the reference

Figure 5: Daily estimated satellite biases for the GLONASS satellites at station ONSA (receiver: JPS E_GGD) before and after unifying the reference realized by the zero mean condition.

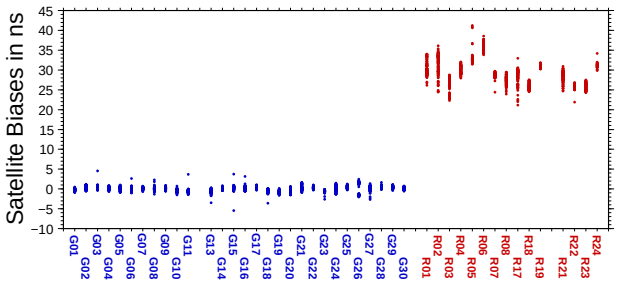

Figure 6: Daily estimated biases for all satellites at the station ONSA (receiver: JPS E_GGD). GPS satellites are named Gxx resp. GLONASS satellites Rxx.

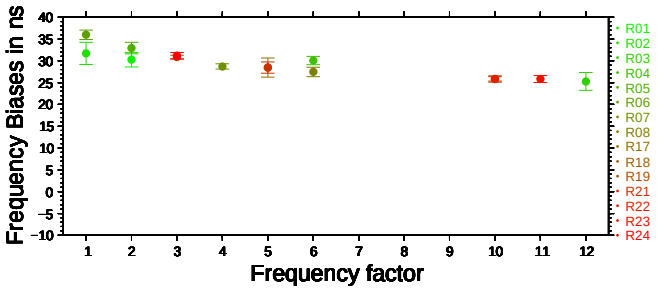

Figure 7: Mean satellite biases for the GLONASS satellites at the station ONSA (receiver: JPS E_GGD) as a function of the frequency factor of the individual satellites.

from receiver changes) over the time interval of more than four months (November 2005 to the mid of March 2006) that was processed here. No significant jumps were found even if a satellite was not available for several days. On the other hand, the repeatability of the satellite biases is very different for individual stations — but it is consistent with the mean noise level of the code data that may be found in the post–fit residuals. The use of one value for each satellite and receiver seems to be reasonable. This is also supported by Figure 6 where the biases obtained for the individual days are plotted in one column for each satellite. The satellite biases for all GPS satellites are zero within the uncertainty level. For the GLONASS satellites a mean bias w.r.t. the GPS satellites of about 30 ns is found. This can be interpreted as an intersystem bias of the receiver at ONSA. Nevertheless, a significant variation between the biases of the individual GLONASS satellites remains.

Figure 7 confirms that these variations depend on the signal frequency. Here the mean satellite biases are ordered in columns labeled with the frequency factors k that are used for the the computation of the carrier phase frequencies of the individual GLONASS satellites ($f_{Rxx} = f_0 + k_{Rxx} \cdot \Delta f$). For the receiver in ONSA as well as for the other stations no significant difference of the mean satellite biases can be found if two satellites are emitting their signal on the same frequency:

factor 1:	R02 and R06,
factor 2:	R01 and R05,
factor 3:	R19 (since Jan. 2006), R23, and R24 (until Dec. 2005),
factor 5:	R17 and R21,
factor 6:	R04 and R08,
factor 10:	R18 and R22,
factor 11:	R20, as well as
factor 12:	R03.

These results allow it to switch from satellite to interfrequency biases. This has the advantage that less unknown parameters have to be estimated. But also another problem may be reduced: Due to the sparse coverage of stations observing the GLONASS satellites it may happen that the network is decomposed into independent clusters that are not connected by simultaneous observations to each of the active GLONASS satellites. In that case, two independent references to compute the satellite biases are required to prevent singularities when resolving for the unknown parameters. If two satellites contribute to one interfrequency bias the decomposition of the network becomes less likely. Furthermore, the number of observations that contribute to the interfrequency biases is two times higher than for satellite biases which improves the uncertainty of the estimated parameters.

Figure 8 summarizes the mean interfrequency biases that are computed for all GNSS receivers in the IGS network for the period from November 2005 to March 2006. The stations are included in separated diagrams according to their receiver types. The stations equipped with ASHTECH Z18 receivers have a negative bias w.r.t. the GPS satellites whereas the JAVAD receivers show a positive bias. Obviously this is caused by the zero mean condition that was applied for computing these values. No conclusion on the real receiver quality (no significant intersystem as well as interfrequency biases are expected for a perfect receiver) can be derived. It is furthermore noticeable that the biases differ not only between the receiver types but also from station to station that are using the same receiver type (see, e.g., station MTKA for the ASHTECH Z18 receiver, or station SPT0 for the JPS LEGACY receiver).

The estimation of interfrequency biases for each GNSS station introduces a big number of additional parameters when computing GLONASS satellite clock corrections. On the other hand, biases that are computed from a certain time interval for a station can later be applied for the analysis as it is done today with the differential code biases. The interfrequency biases and the obtained satellite clocks are fully correlated. This means that, when using the satellite clocks, e.g., for a PPP of further stations, corresponding biases have also to be estimated or applied for these GNSS receivers.

When comparing these results with other calibration results, we have to keep in mind that the estimation of the frequency biases is independent from the broadcast

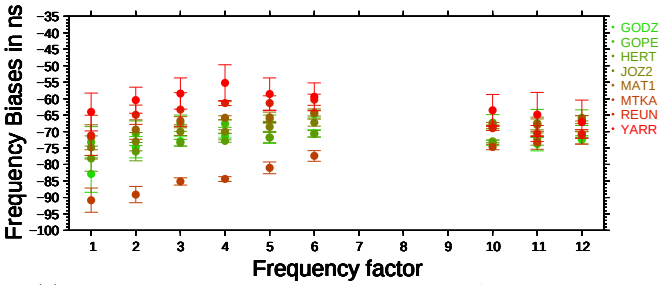

(a) Receiver inter–frequency time biases for ASHTECH Z18

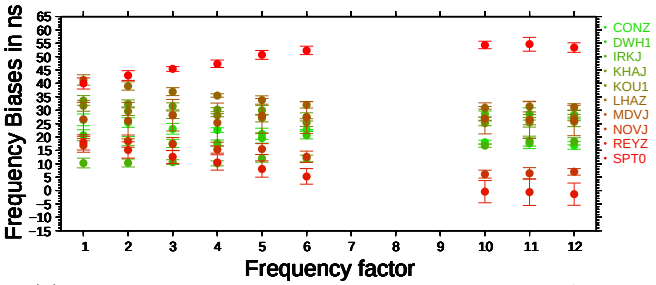

(b) Receiver inter–frequency time biases for JPS LEGACY

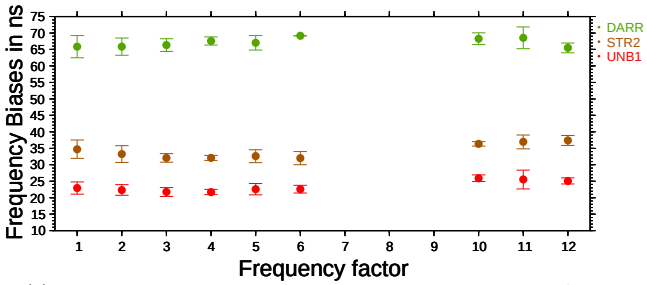

(c) Receiver inter–frequency time biases for TPS LEGACY

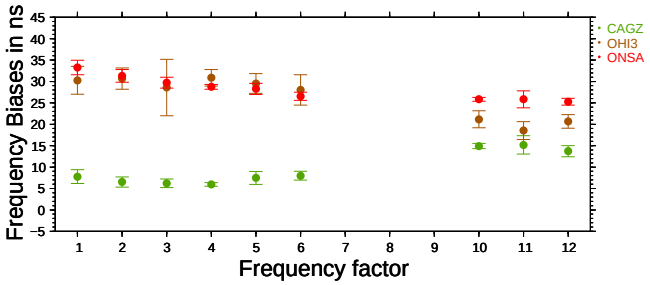

(d) Receiver inter–frequency time biases for JPS E_GGD

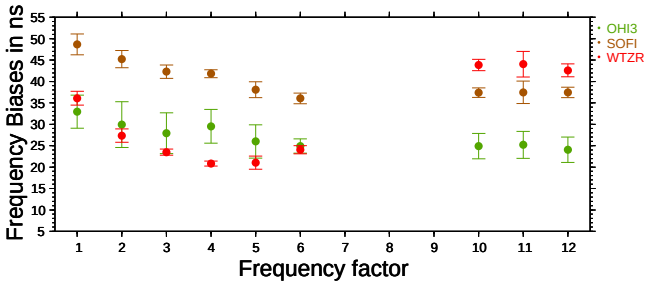

(e) Receiver inter–frequency time biases for TPS E_GGD

Figure 8: Receiver interfrequency biases for the GLONASS frequencies for five GNSS receiver types in the IGS network relative the GPS frequency. The values are computed from four month of data (as long as the observations to the corresponding GLONASS satellites are available). A zero mean condition for each GLONASS frequency was applied.

GPS and GLONASS satellite clocks. This makes sense because of their higher uncertainty. In addition, the computation of GLONASS satellite clock corrections remains independent from the availability of GLONASS broadcast messages. The solution is obtained by analyzing the ionosphere–free linear combination of the phase observations at both frequencies. Calibration results obtained for the individual frequencies of the two signals have to be transformed to make them comparable with the results from this study. Because also the satellite clock corrections are estimated when computing the interfrequency biases for the individual receivers only the differences between the biases of one frequency for different receivers can be directly compared.

It is clear that this approach is not a real calibration. It considers the interfrequency and intersystem time biases of the receivers in such a way that the corresponding code measurement can be used for a geodetic (or also for a code–only) time and frequency transfer. The advantage is that also uncalibrated receivers can be included into the network solution without degrading the quality of the estimated satellite clocks resp. the time transfer results between two calibrated GNSS receivers.

4 Multi-System GNSS Analysis for Time and Frequency Transfer

If two GNSS receivers are used for a time transfer experiment that are both calibrated with GPS (e.g., [9]) the interfrequency biases for both receivers (or at least their difference) have to be considered. Additional observations from the GLONASS satellites may then only help the frequency transfer because the interfrequency biases for the receiver(s) have to be estimated. Since they are constant in time, the additional code observations may help for the time transfer when multiple days are analyzed (even if independent daily solutions are computed accepting the day

boundary discontinuities, see [10]). Assuming that multipath effects depend on the frequency of the affected signal, the addition of an alternative GNSS (e.g., GLONASS) may help to reduce the impact of these effects on the results. This is in particular valid for the GLONASS system that has individual frequencies for each satellite and for which the satellite constellation repeats only every eight sidereal days. Assuming that the antipodal satellites emit the signal on the same frequencies, a repeated multipath situation is expected every four sidereal days instead of every single sidereal day in the case of GPS. Nevertheless, the argument for a combined GNSS analysis is mostly the increased number of observations.

Figure 9 displays the number of satellites in view for the station ONSA during 10 days as an example. During this selected period between three and five GLONASS satellites are observed whereas usually measurements to between eight and ten GPS satellites are available. By adding the measurements of the GLONASS satellites to those to the GPS vehicles in a GNSS analysis, the number of available data can be multiplied by a factor of up to 1.5 . With a full GLONASS (and later also GALILEO) constellation, this factor increases to nearly two (resp. three).

As a first rough estimate an improvement of the results of a factor $\sqrt{1.5} = 1.2$ (and in future up to $\sqrt{3} = 1.7$) may be expected from this increased number of observations. Provided that consistent products for the different GNSS (see Section 2) are introduced into the combined analysis only intersystem biases of the user's receivers have to be considered in the processing as it was discussed in Section 3. In the case of GLONASS the interfrequency biases weaken the solution because for each frequency factor (usually one pair of satellites) one additional parameter has to be solved for when the receiver and satellite clocks are computed. For that reason, the factor of 1.2 for the improvement of the combined GPS and GLONASS solution is not realistic.

Figure 10 shows the differences of the GPS resp. GLONASS solution to the combined GNSS solution for the baseline between the two GNSS stations in SPT0 and ONSA, both equipped with H-masers. The GPS and GNSS solution are equal within the 10 ps level. The difference between the GLONASS and GNSS solution reach 50 ps. This higher noise level can be assigned to the solution using only GLONASS satellites which is plausible because of the estimation of the interfrequency biases together with the clock parameters.

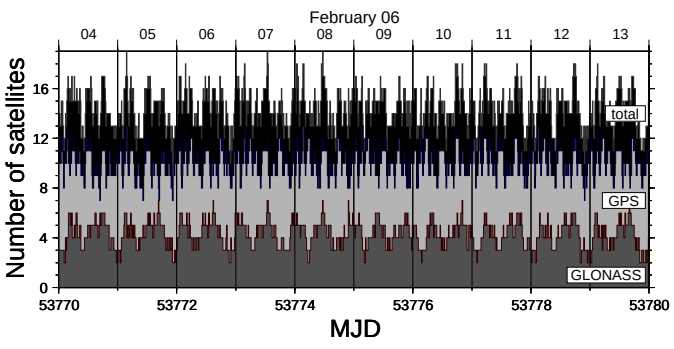

Figure 9: Number of observed satellites from the different GNSS for the station ONSA.

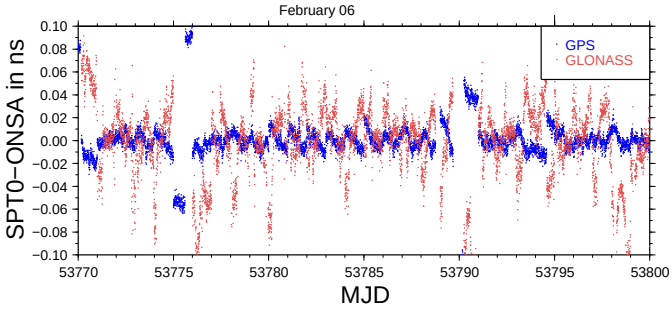

Figure 10: Receiver clock differences for the baseline ONSA→SPT0 between the solutions computed from GLONASS resp. GPS observations only and the receiver clock differences obtained from a combined GPS and GLONASS GNSS solution.

The Allan variances of the three solutions for this baseline in Figure 11 do not allow to favor either the GPS or the GNSS solution. The advantage of the additional observations is compensated by the estimation of the additional parameters, the interfrequency code biases. On the other hand, the addition of the GLONASS to the GPS satellites in the analysis does not degrade the solution. This confirms that all relevant biases are considered in the solutions.

5 Summary and Outlook

To obtain consistent products for different GNSS a rigorous combined analysis of measurements from all systems is preferable. The network may contain single system receiver as long as enough multi–system receivers can be included. At the IGS analysis center CODE, this approach is successfully applied for the combined processing of GPS and GLONASS satellite tracking data to generate consis-

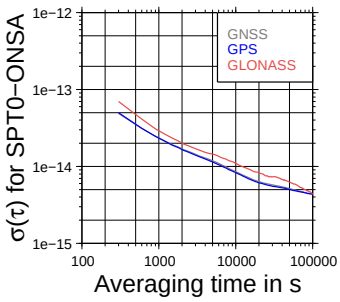

Please not that the curve for the GNSS solution is hidden by the curve for the GPS solution because the Allan variance for both resulting time series are nearly identical.

Figure 11: Allan variance for the receiver clock differences for the baseline ONSA→SPT0 computed only from GLONASS, only from GPS, and from a combined GNSS solution.

tent orbits since May 2003. First experience to extent this combined analysis to the computation of fully consistent precise GNSS satellite clocks are encouraging. The obtained GLONASS satellite clocks have a comparable accuracy to the satellite clock corrections for the GPS satellites. The performance of the GLONASS satellite clocks is comparable with the performance of the GPS block II/IIA satellites with Cs clocks.

A prerequisite for the combined analysis of different GNSS is that also the receiver intersystem biases are taken into account. One item of investigation was the verification of the validity of the GPS derived receiver antenna models also for GLONASS observations. Data from five antennas currently used at GNSS sites in the IGS network are analyzed for an interval of four week. No significant differences were detected, which means that the GPS derived receiver antenna models also can be adopted for GLONASS measurements.

Because the GLONASS satellites emit the signal on individual frequencies, GLONASS (and also GNSS) receivers are affected by interfrequency time biases. For a GNSS receiver, these interfrequency biases also act as intersystem time biases as long as the GLONASS interfrequency biases refer to the GPS frequencies. The corresponding biases have to be considered (estimated or introduced) when analyzing GLONASS code data. These biases are different for individual receivers. As long as interfrequency time biases for the GNSS receivers have to be estimated together with the receiver and satellite clock corrections, the advantage of more satellites due to a GNSS instead of GPS analysis is compensated. For carrier phase measurements these biases are absorbed by the phase ambiguity parameters. They become only relevant if ambiguities are resolved to their integer values.

The launch of further GLONASS satellites and the densification of the GNSS stations in the IGS network will improve the situation for the rigorous GNSS analysis. When adding GALILEO as third GNSS to a combined analysis, only one additional intersystem time bias for each receiver is expected (in the optimistic case, one for each receiver type).

References

[1] A. Foks, J. Nawrocki, and W. Lewandiowski, "Latest Calibration of GLONASS P-Code Time Receeivers," in *Proceedings of the* 36^{th} *Precise Time and Time Interval Systems and Application Meeting PTTI 2004*, (Washington, D.C.), pp. 99–103, December 7–9 2005.

[2] U. Hugentobler, S. Schaer, and P. Fridez, eds., *The Bernese GPS Software Version 4.2*. University of Berne: Astronomical Institute, February 2001.

[3] U. Hugentobler, M. Meindl, G. Beutler, H. Bock, R. Dach, A. Jaeggi, C. Urschl, L. Mervart, M. Rothacher, S. Schaer, E. Brockmann, D. Ineichen, A. Wiget, U. Wild, G. Weber, H. Habrich, and C. Boucher, "CODE IGS Analysis Center Technical Report 2003/2004," in *IGS 2004 Technical Reports*, (Jet Propulsion Laboratory, Pasadena, California U.S.A.), IGS Central Bureau, still in preparation 2006.

[4] W. Lewandowski, A. Foks, Z. Jiang, J. Nawrocki, and P. Ngoas, "Recent Progress in GLONASS Time Transfer," in *Proceedings of the Joint IEEE International Frequency Control Symposium and Precise Time and Time Interval (PTTI) Systems and Applications Meeting*, (Vancouver, British Columbia), pp. 728–734, August 29–31 2005.

[5] J. Ray and K. Senior, "IGS/BIPM pilot project: GPS carrier phase for time/frequency transfer and timescale formation," *Metrologica*, vol. 40, pp. 270–288, 2003.

[6] J. Ray and K. Senior, "Geodetic Techniques for Time and Frequency Comparisons Using GPS Phase and Code Measurements," *Metrologica*, vol. 42, pp. 215–232, 2005.

[7] F. Menge, G. Seeber, C. Völksen, G. Wübbena, and M. Schmitz, "Results of Absolute Field Calibration of GPS Antenna PCV," in *International Technical Meeting of the Satellite Division of the Institute of Navigation ION GPS-98, Nashville, Tennessee, 15-18. September 1998*, 1998.

[8] R. Schmid and M. Rothacher, "Estimation of elevation-dependent satellite antenna phase center variations of GPS satellites," *Journal of Geodesy*, vol. 77, no. 7–8, pp. 440–446, 2003.

[9] G. Petit, Z. Jiang, J. White, R. Beard, and E. Powers, "Absolute Calibration of an Ashtech Z12-T GPS receiver," *GPS Solutions*, vol. 4(4), pp. 41–46, 2001.

[10] R. Dach, T. Schildknecht, U. Hugentobler, L.-G. Bernier, and G. Dudle, "Continuous Geodetic Time Transfer Analysis Method," *IEEE Transactions on Ultrasonics, Ferroelectrics, and Frequency Control*, vol. accepted for publication, 2006.

Proceedings of the 20th EFTF, 2006

The T2L2 Ground Experiment
Time transfer in the picosecond range over a few kilometres

E. Samain, D. Albanese, F. Baumont, E. Cuot, R. Dalla, *P. Fridelance, **K. Gasc, **Ph. Guillemot, ***S. Léon, JF. Mangin, JL. Oneto, J. Paris, **I. Petitbon, M. Ravet, JM. Torre, P. Vrancken, J. Weick

CNRS/Gémini, Observatoire de la Côte d'Azur, Grasse, France
* Phusipus Intégration, Saint Vallier de Thiey, France
**CNES, Toulouse, France
***CNES, Paris, France

The new generation of optical time transfer (T2L2: Time Transfer by Laser Link [1]), under development at CNES (Centre National d'Etudes Spatiales) and OCA (Observatoire de la Côte d'Azur), shall allow the synchronisation of remote ultra-stable clocks and the determination of their performances over intercontinental distances. The principle is based on the propagation of light pulses between clocks to be synchronized. T2L2 is the follow-on mission to LASSO (LAser Synchronisation from Stationary Orbit) [2, 3] with performances in the picosecond range for both stability and accuracy. T2L2 is based on a space instrumentation that includes an event timer linked to the space clock, and some laser ranging stations linked to ground clocks.

In order to validate the concept and to evaluate precisely the error budget, we realized two global experiments with some prototypes of both the ground and space instrumentations. These prototypes are based on electronic event timers and photo-detection devices that we developed in the framework of T2L2 project. In 1998, we performed a first ground experiment involving two OCA's laser stations and a first prototype of the space instrumentation 2.5 km apart. Results were promising but with some limitations due to the use of a bad quartz oscillator as the space clock. A second experiment was decided in 2004 with the OCA Lunar laser ranging station and a more finalized space segment installed closed to the station. The experiment was based on a free space propagation across 10 kilometres thanks to a large corner cube placed 2.5 km away. In order to measure the noise of the link without the noise of the clocks, a third event timer was able to measure the direct phase between signal clocks of both the space and ground prototypes.

1. INTRODUCTION

The "Time Transfer by Laser Link" experiment T2L2 [1], under development at CNES (Centre National d'Etudes Spatiales) and OCA (Observatoire de la Côte d'Azur), France, will be launched in 2008 aboard the altimetric satellite Jason 2. T2L2 on Jason 2 will permit to synchronize remote ground clocks and to compare their frequency stabilities with a performance never reached before. In common view mode (i.e. two laser stations are communicating with T2L2 at the same time), T2L2 will measure the stability of remote ground clocks, itself having a time stability in the range of 1 ps over 1000 s.

The objectives of the T2L2 mission are threefold:
The first one is a technological objective concerning the validation of optical time transfer, including the validation of the experiment and of time stability and accuracy.
The second one is oriented to time and frequency metrology, fundamental physics and earth observation.
The characterization of the onboard Doris oscillator and the validation of the one-way laser ranging concept is the third and complementary objective of the mission.

In order to evaluate precisely the error budget, a comprehensive T2L2 ground experiment has been performed with some prototypes of both ground and space instrumentations.

II. T2L2 DESCRIPTION

T2L2 is a follow-on mission to LASSO [2], [3] which was proposed in 1972 and launched in 1988 on Meteosat P2. T2L2 was first proposed in 1996 to fly on the Russian space station MIR [4] as a French passenger experience. It has been accepted by CNES before being cancelled. In the meantime, it was accepted by ESA in

the framework of the ACES (Atomic Clock Ensemble in Space) program which was scheduled on the International Space Station (ISS) in 2002. T2L2 was one of the three scientific proposals of ACES, but was cancelled again for technical reasons concerning the whole ACES mission. T2L2 was then phase-A studied for a dedicated micro-satellite Myriade with CNES before being proposed and definitively accepted by CNES in 2005 to fly on Jason 2.

T2L2 is based on the propagation of light pulses between the clocks to be synchronized. The light pulses carry the temporal information from one clock to another. An ultra-stable oscillator and a time-tagging unit on the satellite are used as relay to allow time transfer between remote ground clocks. Some laser stations at ground emit asynchronous short light pulses (~ 20 ps FWHM) towards the satellite. Retro-reflecting corner-cubes located near the T2L2 payload return a fraction of the received photons back to the ground station which records, for each laser pulse, the start and return time. The T2L2 payload records the arrival time in the temporal reference frame of the on-board oscillator. These data are downloaded to the ground via a regular microwave communication link. The synchronization between the ground and space clocks is then derived a-posteriori from these data.

Figure 1 shows the synoptic of the whole T2L2 space instrument. The photo-detection unit is composed of two avalanche photo-detectors. One is working in a special "Geiger" mode for precise chronometry, the other one is in linear gain mode in order to trigger the system and to measure the received optical energy [5], [6], [7]. The time tagging unit is a dedicated design, built with a programmable logic array at 100 MHz for rough timing and a vernier for precise measurement with a resolution of 1 ps [8].

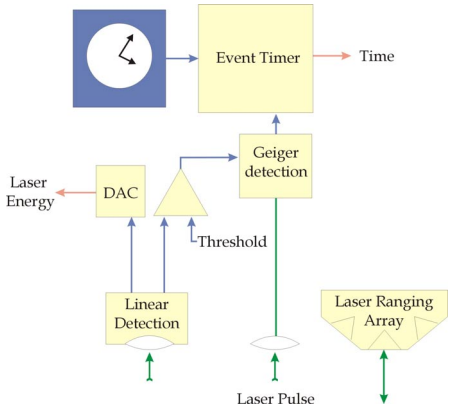

Figure 1: Synoptic of the whole T2L2 space instrument.

The T2L2 ground segment is a laser ranging station with a special instrumentation to measure accurately both the start and return time of laser pulses. There are roughly 40 laser stations in the world that range satellites and moon and roughly 25 that range JASON 1 regularly. A typical laser station includes a pulsed Nd:Yag Laser (20 to 200ps) at 10 Hz, a telescope (~ 1m) , 2 event timers or an intervalometer.

III. GROUND EXPERIMENT DESCRIPTION

The objective is to realize an experiment very close to the real space project in order to get the best estimation of the whole error budget.

A first experiment was done in 1998 at OCA between the Lunar laser ranging and the ultra-mobile stations via a prototype of the space segment (Figure 2).

Figure 2: first ground experiment at OCA in 1998.

The space segment was set at 2.5km from the stations without any direct connection. It was power supplied by a generator unit and driven with an autonomous software. Unfortunately, during the acquisition phase, the temperature control of the quartz oscillator used in space prototype was out of range. This failure degraded considerably the time stability of the whole experiment. An other experiment with only one station (figure 4) and a new prototype of the space segment has then been planned in 2004.

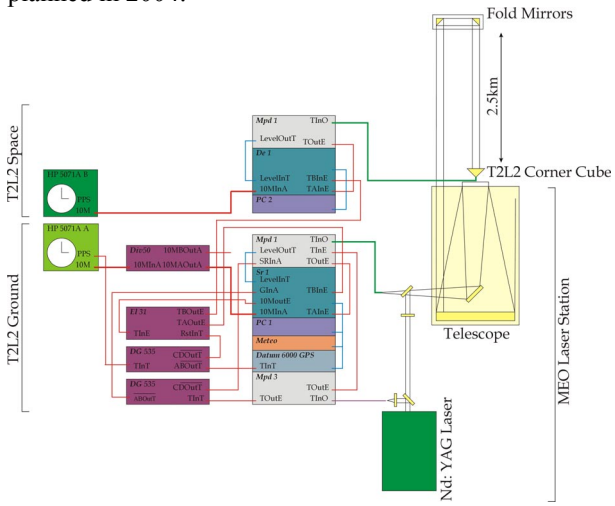

Figure 3: Experimental setup. The equivalent distance between the T2L2 space segment and the MeO laser station is 2 x 2.5km.

The space prototype is set close to the station and the beacon emitted from the laser is bent back to the station by a fold mirror (figure 3, 5, 6). The equivalent distance between the station and the prototype is 5 km (fold mirror located at 2.5 km from the laser station). The T2L2 corner cube is fixed on the secondary mirror of the telescope, in the central obstruction of the beacon.

Figure 4: MeO laser Ranging station. It is based on a 1.5 m telescope and a flash pomped Nd:YAG laser. The station has been built in 1980 to range the Moon

The main optical characteristics of the experimental setup are:

- Telescope diameter:1.5 m,
- Central obstruction 0.45 m,
- Fold mirror aperture: 30 mm,
- Fold mirror translation: 400 mm,
- T2L2 retro-reflector: a unique high index corner cube,
- T2L2 retro-reflector diameter: 100 mm.

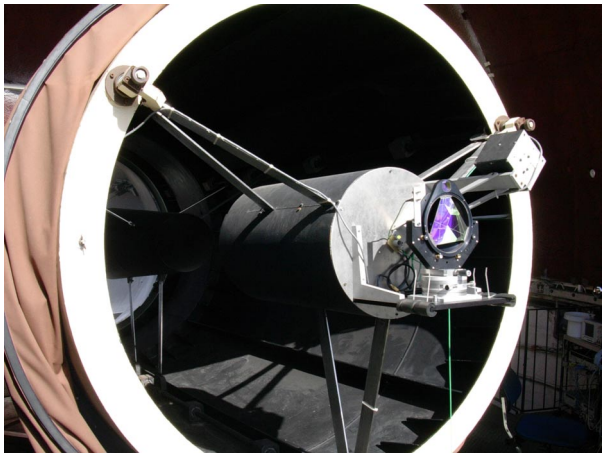

Figure 5 : MeO station telescope. The T2L2 corner cube is set on the secondary mirror, in the central obstruction of the beacon.

Two HP5071A atomic clocks are used for the experiment. The first one is connected to the laser station and the second one is connected to the space instrument prototype. The prototype of the T2L2 space instrument includes a PC, a photo-detection module and two event timers (Dassault Electronique). One of them is used to record the arrival time of the laser pulse and the other one to perform a direct phase comparison between the space and ground clocks. The phase comparison event timer is linked to the same 10 MHz space clock signal and receives a PPS (Pulse Per Second) extracted from the 10 MHz ground clock.

Figure 6: Fold mirrors. The device has an equivalent aperture of 30 mm and generate a beacon translation of 400 mm.

In order to eliminate the noise generated by the clocks one has also the possibility to connect the same clock on both the space and ground instruments (Figure 7).

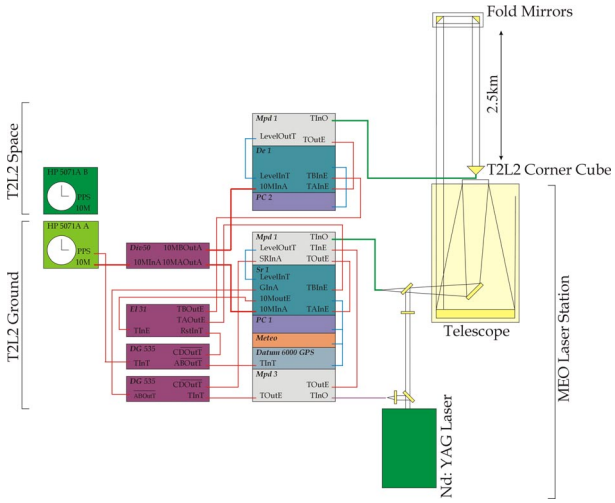

Figure 7: On the scheme, the same atomic clock is connected on both space and ground instruments. This permits to reject the noise generated by the clocks.

The photo-detection instrument is the first prototype of the T2L2 space photo-detection device (Figure 8). As compared to the real T2L2 space instrument for Jason 2, the optical configuration is a little bit different: the light pulses are sent to the instrument through an unique multi-mode optical fiber and splitted for the chrononometry and the energy measurement inside the instrument with a separator cube.

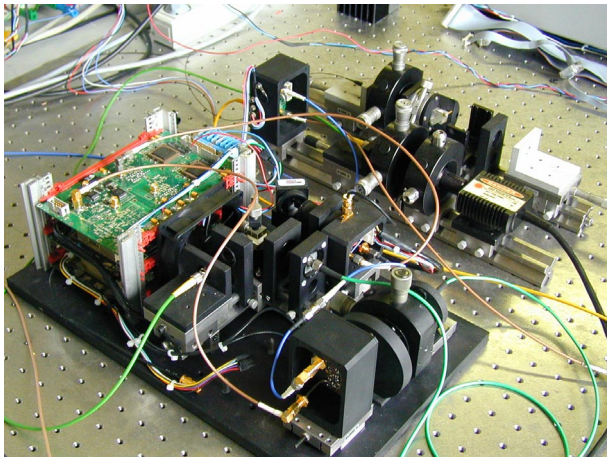

Figure 8: Prototype of the T2L2 space photo-detection module. It includes a Geiger photo-detector and a linear photo-detector for respectively the chronometry and the energy measurement.

The photo-detection for the ground segment is based on the same scheme. Since the photon number received at ground is lower than the photon number received at the satellite, the instrument uses a miniature photo-multiplier for the energy measurement instead of an avalanche photodiode. This permits a threshold of only one photon.

For some statistical reasons, the precision of the instrument depends on the photon number received. One gets roughly 40 ps rms in a single photon mode and 5 ps with 100 000 photons (Figure 9) [9].

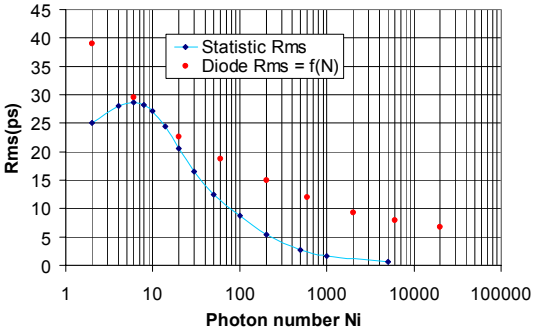

Figure 9: Precision of the T2L2 instrument versus the photons number received (dots). The photons noise statistic is illustrated on the lower curve (diamonds).

The event-timer used in this ground experiment for the space prototype was built by Dassault Electronique in 1995. It includes a frequency synthesis @ 200 MHz and two 2 verniers. Its main characteristics are:

- Precision: 5 and 2 ps,
- Dead time: 400 µs,
- Time stability: < 10 fs over 1000 s.

The event-timer uses for the ground prototype was built by OCA (Figure 10). The characteristics are the same except for the dead time that is 10 µs. This short dead time allows to get both the start and return events with the same instrument: the time-interval measured is 34 µs (4 x 2.5km). The time stability is illustrated on figure 11.

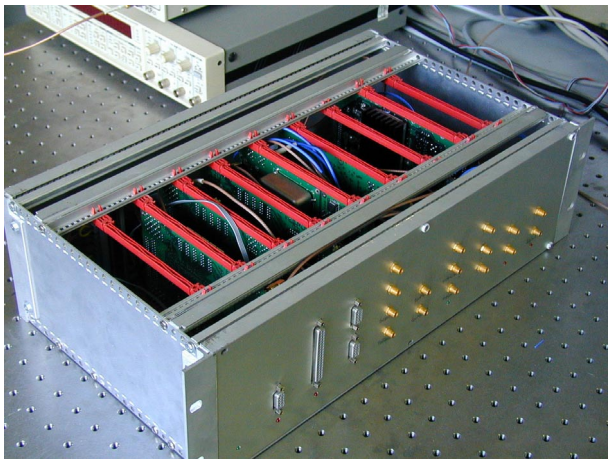

Figure 10: OCA event-timer. The T2L2 space instrument for Jason 2 is also based on this design. The event-timer has a precision better than 2 ps and a time stability of 10 fs over 1000s.

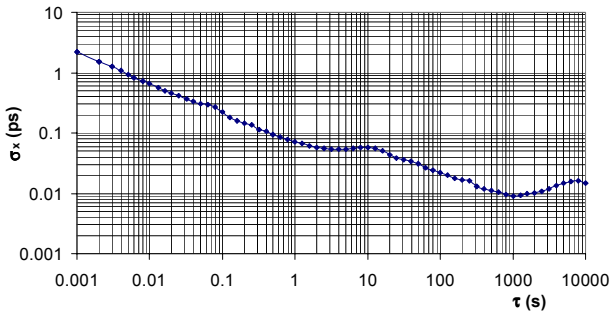

Figure 11: Time stability of the OCA event-timer. For this measurements the event-timer measures some electrical events generated from the 10 MHz clock signal.

IV. RESULTS

Data were acquired during the summer in 2004 for a T2L2 ground segment validation. The whole experiment was maintained during two weeks providing 71 observation sessions. It allowed stability measurements, noise estimations and dedicated sensitivity measurements: corner cube orientation, light energy, corner cube distance, distance between reflection and detection. The data, ground start and return times, and space arrival times with the corresponding detection levels, are treated to extract the time offset between the clocks.

The time walk of the detector is computed on a reference calibration session and removed from all the data (Figure 12). After the fit, the residual dispersion of a typical session is 13.5 ps rms.

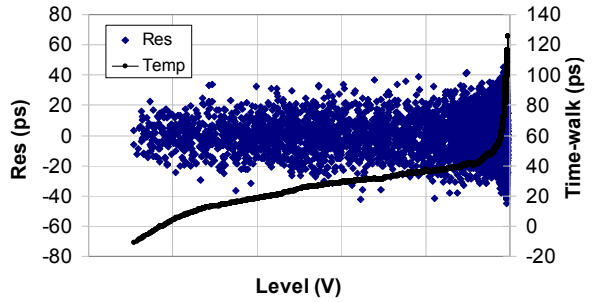

Figure 12 : Ground detector Time-walk fit versus Level (040728, session 10).

In order to evaluate the short term time stability, a continuous acquisition was made during 30 hours @ 10 Hz, with a single HP5071A clock, connected to both ground and space segments. The experimental set-up is shown on Figure 7. The ground-space offsets have a dispersion of 18 ps (Figure 13). The round trip time residuals have a dispersion of 23 ps with a drift that didn't show up the ground-space offsets. The ground-space offset time variance shows a short time stability better than 0.7 ps for half an hour measurements. The short term white phase noise is $\sigma_x = 17.10^{-12}\tau^{-1/2}$ @ $\tau_0 = 1$ ps (Figure 14).

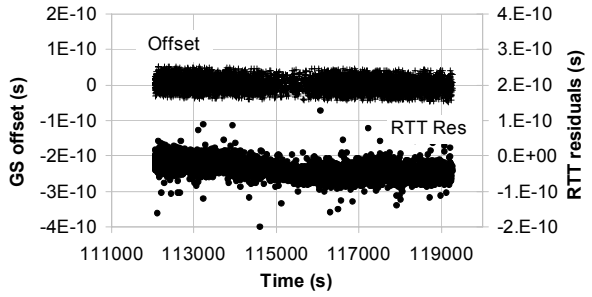

Figure 13 : Ground-Space offset and Round Trip Time residuals after removing a constant versus Time (040729, session 5).

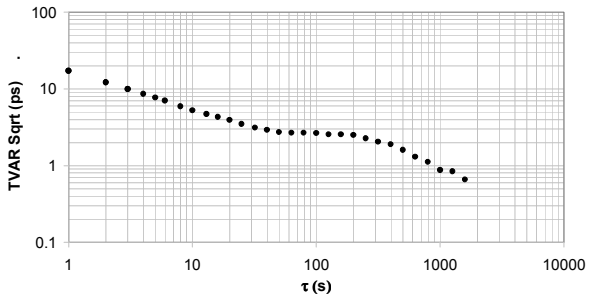

Figure 14 : Ground-Space offset Time variance versus Time (040729, session 5) with $\tau_0 = 1$ s.

An acquisition of one hour every 6 hours during 7 days was made with an unique HP5071A clock connected to the ground and the space segments. The objective is to get the mid-term time stability. A daily fluctuation can be seen on Figure 15 certainly due to thermal effects.

The dispersion of the ground-space offsets is 19 ps rms and the mid-term stability is $\sigma_x = 1.5$ ps for $\tau = 1000$ s (Figure 16).

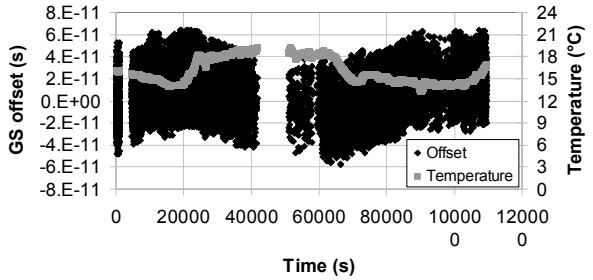

Figure 15 : Ground-Space Offset and Temperature versus Time during 33 hours (040728 session 1 to 040729 session 5).

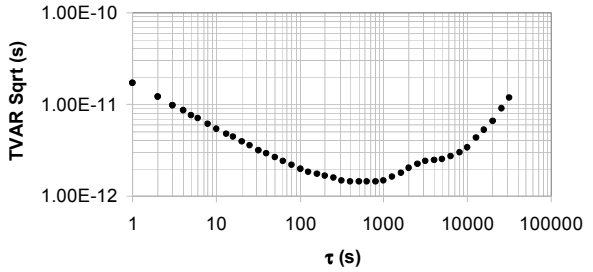

Figure 16 : Ground-Space offset Time variance versus Time during 33 hours (040728 session 1 to 040729 session 5) with $\tau_0 = 1$ s.

The data from the 28/7/04 session 1 to the 01/08/04 session 4 are used to compute a long term stability curve with $\tau_0 = 1$ s for 1 s < τ < 30000 s and $\tau_0 = 21600$ s for τ > 30000 s (Figure 17).

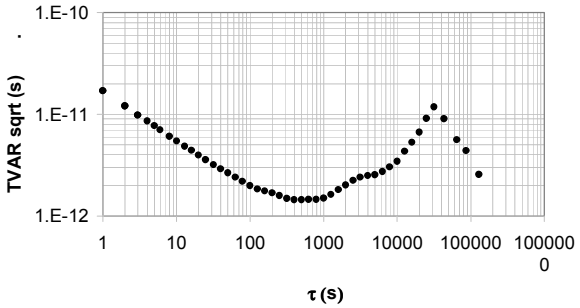

Figure 17 : Ground-Space offset long term Time variance versus Time with $\tau_0 = 21600$s.

A continuous acquisition during 8 hours @ 10 Hz between two distinct HP5071A clocks was made with an independent phase measurement. The experimental set-up is shown on Figure 3. The objective is to identify the noise that could be eliminated in common mode with an unique clock. The offset between the clocks is computed and compared to the phase (Figure 18). We can see the very good agreement between the offset and the phase: the difference of the two quantities has a

mean value lower than 0.5 ps and a dispersion of 26 ps rms.

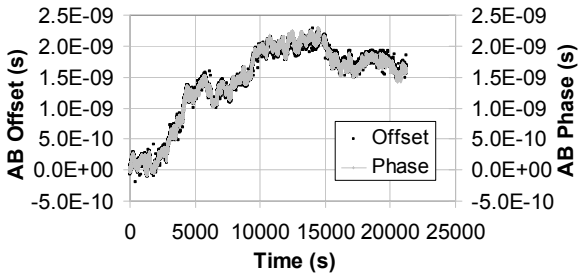

Figure 18 : AB clocks Offset and Phase versus Time during 8 hours (040802 sessions 1 to 4).

The time variance of the differences between the offset and the phase is computed (Figure 19). The short term stability, $\sigma_x = 2.10^{-11}\tau^{-1/2}$ @ $\tau_0 = 1$ ps, is very close to the time stability obtained previously with a common clock.

T2L2 measurement is sensitive to the noise $\sigma_x(\tau_{pulse})$ added by space clock (if we consider the ground clock as a reference) over an integration time equal to the time between laser pulses $\tau_{pulse} = \tau_0$. This noise is computed directly from phase data. It includes both the clock noises and the noise coming from the phase measurement. We get $\sigma_x(\tau_{pulse} = 1s) = 4ps$ that is small as compared to the global T2L2 noise. This can be seen on figure 19: the T2L2 offset noise, considered on the short term, is equal to the noise of the differences.

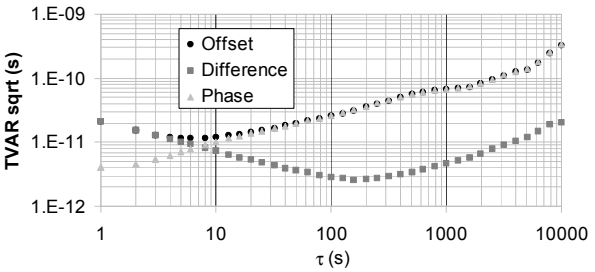

Figure 19 : AB clocks Offset Time variance and AB clocks Offset minus Phase Time variance versus Time (040802 sessions 1 to 4) with $\tau_0 = 1$ s.

An acquisition was dedicated to sensitivity to the corner cube distance. The data shows that the T2L2 time transfer performances are not affected by a variation of the space segment distance (Figure 20). The corner cube distance varies between 0 and 25 mm corresponding to a variation of the round trip time about 165 ps. The analysis shows that the offset is not varying significantly. The time stability of the mid and long term offset is not degraded (Figure 21).

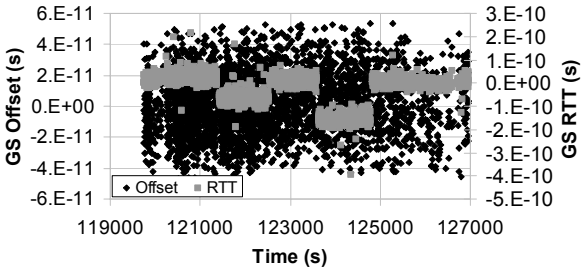

Figure 20 : Ground-Space Offset and Ground-Space Round trip time versus Time during 2 hours (040729 session 6).

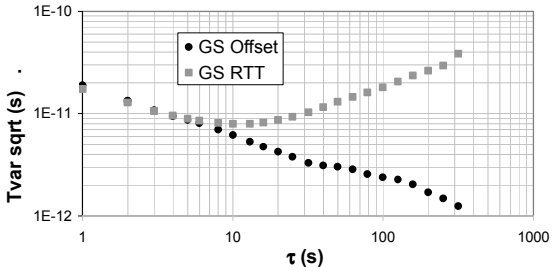

Figure 21 : Ground-Space Offset and Ground-Space Round trip time Time variance versus Time with $\tau_0 = 1$ s (040729 session 6).

V. CONCLUSIONS

This ground experiment performed in 2004 permitted to precisely evaluate the T2L2 performance. The experiment was able to reproduce an atmospheric propagation of 2 x 5 km, some observation conditions with a real laser station and some prototypes of both the T2L2 space and ground instrumentations.

As compared to the real space project, the ground experiment gave an unique opportunity to perform a comparison of the T2L2 link by eliminating the clock noises: a common clock for both the space and ground segment and also two directly connected clocks.

Time stability performances measured in this experiment are quite close to the performances specifications that were deduced from a global link budget. Data analysis showed a daily drift of the offsets that seems to be temperature related with a sensitivity in the range of 4 ps/°C and a time shift of a few hours. This sensitivity is probably linked to the thermal dilatation of the whole laser station. Even if this drift is not very large, it should be eliminated in the real space project because laser stations perform some continuous internal calibrations that will permit to correct this problem.

REFERENCES

[1] P. Fridelance, E. Samain, C. Veillet, Experimental Astronomy, 191 (1996)
[2] P. Fridelance, C. Veillet, Metrologia, **32**, 27 (1995)
[3] P. Fridelance, Thèse de doctorat de Physique de l'Université Paris 6 (1994)
[4] E. Samain, P. Fridelance, Metrologia **35**, 151 (1998)
[5] E. Samain, Applied Optics **37,** No 3, 502 (1998)
[6] I. Procazka, K. Hamal, Proceedings of the 9th International Workshop on laser ranging instrumentation **2**, 469 (1994)
[7] R.H. Kingston, *Detection of optical and infrared radiation* (Springer Verlag, Berlin, 1978)
[8] E. Samain, Proceedings of the 13th International Workshop on laser ranging instrumentation (2002)
[9] E. Samain, R. Dalla, Proceedings of the 13th International Workshop on laser ranging instrumentation (2002)

Proceedings of the 20th EFTF, 2006

Time Transfer by Laser Link : The T2L2 experiment onboard the Jason-2 space vehicle

Ph. Guillemot, I. Petitbon, K. Gasc, *E. Samain, *D. Albanese, *R. Dalla,
*M. Furia, *J. Paris, *J-F. Mangin, *J-M. Torre, *P. Vrancken, *J. Weick
CNES, Toulouse, France
*CNRS/Gémini, Observatoire de la Côte d'Azur, Grasse, France
philippe.guillemot@cnes.fr – etienne.samain@obs-azur.fr

The new generation of optical time transfer (T2L2: Time Transfer by Laser Link [1]) under development at OCA and CNES shall allow the synchronisation of remote ultra stable clocks and the determination of their performances over intercontinental distances. The principle is based on the propagation of light pulses between clocks to synchronize. T2L2 is the follow-on mission to LASSO (LAser Synchronisation from Stationary Orbit) [2] with performances improved by two orders of magnitude.

We have now the opportunity to put a T2L2 payload on the Jason-2 space vehicle, which will be launched in mid 2008 for a 5 years long mission. A preliminary performance budget and a ground experiment conducted by the OCA permit to envision a performance improvement of at least one order of magnitude as compared to the best time transfer techniques available. Expected performances are in the 100ps range for accuracy, with an ultimate stability better than 1ps over 1000s (one pass) and than 10ps over one day. Time transfer performances in a common view mode are driven by the noise of both the ground and the onboard timers whereas the performances in a non-common view configuration are limited by the onboard clock (DORIS USO). The main objectives of the T2L2 mission are technological (In-orbit functional and performance validation), scientific (Time & Frequency metrology and Fundamental physics tests) with also a contribution to the Jason-2 core mission (Evaluation of the behaviours, versus radiations, of the DORIS USO).

1. INTRODUCTION

In a few years, space will be used like a laboratory of physics with missions dedicated to extremely fine tests of the Gravitation theory. The General theory of relativity is a classical theory of which unification with the other interactions, treated within the frame of quantum physics, presents particular difficulties. All the models of unification lead to modifications of the theory with observable consequences, for example a violation of the principle of equivalence, or a variation of the fundamental constants.

The measurement of these observable, often infinitely "small", needs new extremely powerful techniques such as ultra-precise atomic clocks, inertial sensors, laser ranging or very large baseline interferometers. Precise synchronization devices for distant clocks comparison, either spatial or terrestrial, will play an major role then.

The "Time Transfer by Laser Link" experiment T2L2 [1], under development at CNES (Centre National d'Etudes Spatiales) and OCA (Observatoire de la Côte d'Azur), France, will be launched in 2008 onboard the altimetric satellite Jason 2. T2L2 on Jason 2 will permit to synchronize remote ground clocks and compare their frequency stabilities with a performance never reached before. In common view mode (i.e. two laser stations are communicating with T2L2 at the same time), T2L2 will measure the stability of remote ground clocks, itself having a time stability in the range of 1 ps over 1000 s.

The objectives of the T2L2 experiment onboard Jason-2 are threefold:

- The first one is a technological validation of optical time transfer, including the validation of the experiment, of time stability and accuracy and of one way ranging.

- The second one is the characterization of the onboard Doris oscillator needed for Jason-2 purpose and a contribution to the Jason-2 laser ranging core mission.

- The third one is aimed at various scientific applications concerning time and frequency metrology, fundamental physics, earth observation or very long baseline interferometry (VLBI).

2. T2L2 HISTORICAL ACCOUNT

T2L2 is a follow-on mission to LASSO [2], which was proposed in 1972 and launched in 1988 on Meteosat P2. A first optical time transfer had been successfully achieved in 1992 between OCA, France and Mac Donald, USA.
T2L2 was first proposed in 1996 to fly on the Russian space station MIR [3] taking the opportunity of the French PERSEUS mission but finally it could not be selected by CNES. In the meantime it was accepted by ESA in the framework of the ACES (Atomic Clock Ensemble in Space) program scheduled on the International Space Station (ISS). T2L2 was one of the three scientific proposals of ACES, but had to be descoped in 2001 for some technical reasons concerning the whole ACES mission. CNES decided to go on with the feasibility study of the instrument and to look for other flight opportunities.

A new opportunity for the T2L2 instrument appeared at the end of 2004, when NASA decided to abandon the WSAO instrument, an American contribution to the Jason-2 mission. Preliminary analysis shows that it is relevant to put the T2L2 instrument onboard the Jason-2 space vehicle, both for the T2L2 mission and the Jason-2 mission (through a synergy with the DORIS instrument). Then a new version of the T2L2 instrument was selected as a passenger on the Jason-2 mission.

3. T2L2 PRINCIPLE

T2L2 allows the synchronization of remote clocks on Earth and the monitoring of satellite clocks. The principle, shown in Figure 1, is based on the propagation of light pulses between the clocks to be synchronized. The light pulses carry the temporal information from one clock to another.

The Earth clock and the satellite clock (the ultra-stable oscillator USO of DORIS in case of Jason-2) to synchronize are linked respectively to a laser station and to the T2L2 space equipment. This equipment is constituted of a photo-detection device, a time tagging unit and a retro-reflector. The laser station emits asynchronous, short light pulses (~ 20 ps FWHM) towards the satellite. Retro-reflecting corner-cubes returns a fraction of the received photons back to the station. The station records the start (t_S) and return (t_R) time of each light pulse. The T2L2 payload records the arrival time (t_B) in the temporal reference frame of the on-board oscillator. These data are downloaded to the ground via a regular microwave communication link.

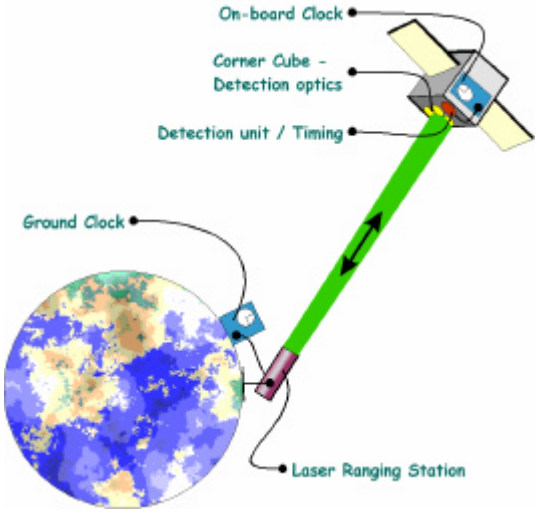

Figure 1 : T2L2 principle
The project needs laser ranging stations on ground and a specific time tagging unit on the satellite.

For a given light pulse emitted from station A, the synchronization χ_A between the ground clock A and the satellite clock can is then derived a-posteriori from these data :

$$\chi_A = \frac{t_S + t_R}{2} - t_B + \tau_{Relativity} + \tau_{Atmosphere} + \tau_{Geom}$$

For another light pulse emitted from a station B, χ_B can be also computed.

In the common view configuration, the noise of the onboard oscillator, which has to be considered over very short time, is negligible in the global error budget and time transfer between ground clocks A and B is then deduced from the difference between χ_A and χ_B. In the non-common view mode, the time walk of onboard clock between the two stations has to be taken into account and the use of a quartz crystal oscillator induces a significant degradation of the performances.

4. T2L2 INSTRUMENTATION ON JASON 2

Jason 2 is a French-American follow-on mission to Jason 1 and Topex/Poseïdon. Its goal is to study the internal structure and dynamics of ocean currents mainly by radar altimetry. It will be placed in an 1,336 km orbit with 66° inclination by a Delta launcher [4]. Jason-2 core mission consists in a dual-frequency radar altimeter Poseidon 3 , a radiometer (AMR – Advanced Microwave Radiometer) to measure the water vapor content in the troposphere and derive the appropriate radar path delay correction, a DORIS receiver and a

GPS receiver for precise determination of the orbit of the satellite, and a laser retro-reflector (LRA - Laser Ranging Array) to complete the orbit tracking.

T2L2 is a passenger instrument as well as two other payloads designed to study radiations (Carmen 2 – France – and LPT – Light Particle Telescope, Japan –). The altitude of Jason-2 will allow common views at the continental scale (~3000 km baseline), with 6 pass per day over each participating ground station. The dead time between two consecutive passes is about 120 mn, their average duration is 1000 s (for passes with a maximal elevation greater than 20°).

T2L2 will use the ultra stable oscillator of the DORIS positioning system [5], [6] as the reference clock for the onboard time tagging. The retro reflector LRA designed by JPL and already installed onboard will be used for laser ranging to reflect the light pulses (Figure 2), instead of the dedicated corner cube previously foreseen which was developed as a breadboard model tested at OCA.

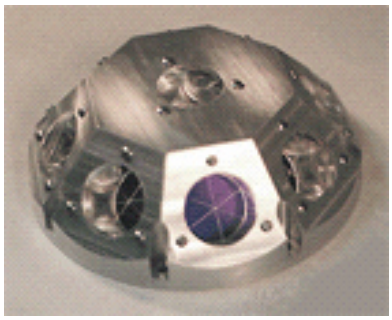

Figure 2 : The LRA (Laser Ranging Array) consists of nine 32mm diameter corner cubes.

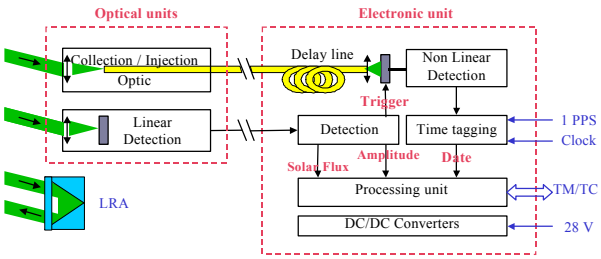

Figure 3 : Instrument architecture.

The instrument breaks up into two subsystems, an optical one and an electronic one (Figure 3) :

- Two Optical Photo Detection Units are located outside the main Jason 2 payload on the LRA boom (Figure 4). Both are composed of avalanche photo detectors. The first one is working in a special "Geiger" mode for precise chronometry (so called Non Linear Detector). The other is in linear gain mode (so called Linear Detector) in order to trigger the system and to measure the optical energy received and the solar flux [7], [8], [9]. Trigger level could be adjusted either by telecommand or from the solar flux measurement in order to optimise the false detection rate.

- The Electronic Unit, located inside the Jason-2 payload module, ensures the conversion of the laser pulse into an electronic signal and then its dating and the management of the whole instrument.

The T2L2 instrument has an estimated mass of 12 kg and a power consumption of 48 W.

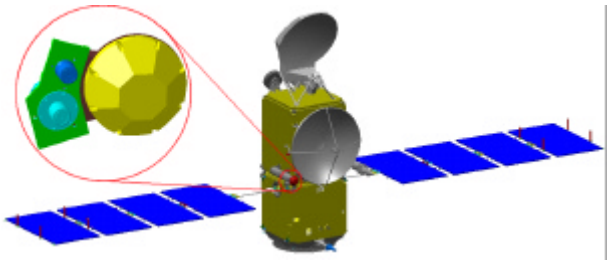

Figure 4 : Jason-2.
The LRA (yellow) and the T2L2 optical units (blue) are on the left of the Poseidon antenna.

The definition and the conception of the metrological part of the instrument is under the responsibility of OCA/GEMINI. The time tagging system is a dedicated design, based on a 54 bits counter for rough timing and a vernier for precise measurement with a resolution of 1 ps [10] (
Figure 5). A PLL provides, from the 10 MHz clock (i.e. DORIS USO), the 100 MHZ signal used to synchronized the 54 bit counter and to generate reference signals for the vernier and for internal calibrations. Internal calibrations are mandatory to monitor the behaviour of the instrument all along the mission and to compensate internal drifts due to aging or to external sensibilities.

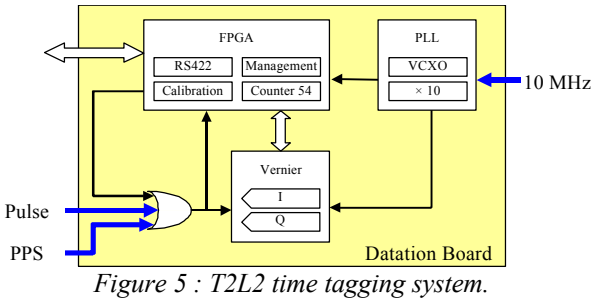

Figure 5 : T2L2 time tagging system.

The T2L2 onboard instrument will tag the arrival time of light events in the reference of the Doris OUS with a resolution of 1 ps. Figure 6 shows the precision versus the number of photons received on the Geiger photo

detector measured with a first OCA prototype of the T2L2 instrument [11], [12]. The dead time between 2 consecutive measurements must be below 20 µs. Its expected time stability is defined by:

$$\sigma_x^2(\tau)_{T2L2} \le K_1^2\tau^{-1} + K_2^2\tau$$

with :

$$K_1 = 4\times\sqrt{10} \approx 12.6 \text{ s.ps}$$
$$K_2 = 4/\sqrt{100000} \approx 12.6 \text{ fs/s}$$

Moreover, In order to see a linear phase drift between ground clocks, T2L2 must be able to measure accurately a time interval τ with an uncertainty lower than the time deviation $\sigma_{x\text{-Clock}}(\tau)$ of the clock.

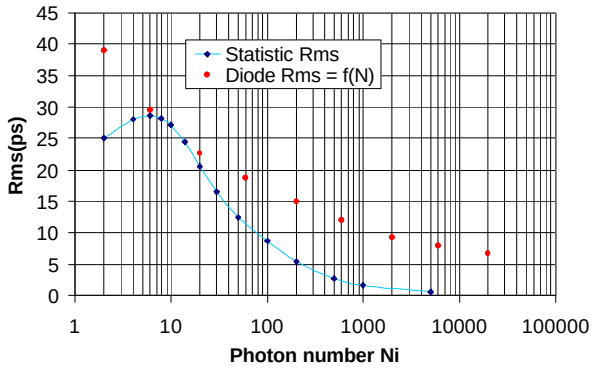

Figure 6: Precision of the T2L2 instrument versus the photon number received (dots). The photon noise statistic is illustrated on the lower curve (diamonds)

5. PRELIMINARY BUDGETS

The time transfer between a ground clock and the on-board clock is given by :

$$\chi_A = \frac{t_S + t_R}{2} - t_B + \tau_{Relativity} + \tau_{Atmosphere} + \tau_{Geom} \quad \textbf{(1)}$$

Where :

- t_S is the departure date of the light pulse from the ground station,
- t_R is the arrival date of the echo light pulse at the ground station,
- t_B is the detection date of the light pulse by the onboard instrument
- $\tau_{Relativity}$ represents all relativity delays
- $\tau_{Atmosphere}$ is the atmosphere delay
- τ_{Geom} is the geometrical delays dues to the difference of optical path between the ground station and the reflection reference point on one side and between the ground station and the timing reference point on the other side (Because of the distance between the LRA and the T2L2 optic elements).

Time Stability :

The time stability of the time transfer between a ground clock and the on-board clock is then give from (1) by :

$$\sigma^2_{x.BS}(\tau) = \frac{\sigma^2_{x.S}(\tau)}{4} + \frac{\sigma^2_{x.R}(\tau)}{4} + \sigma^2_{x.B}(\tau) + \sigma^2_{x.Geom}(\tau) + \sigma^2_{x.Atmosphere}(\tau) + \sigma^2_{Relativity}(\tau) \quad \textbf{(2)}$$

$\sigma^2_{x.S}(\tau)$ is the stability of the dating of the departure of the laser pulse from the station. With the assumption of the use of a device based on a fast linear photodiode, one has :

$$\sigma^2_{x.S}(\tau) = \left(4\times10^{-12}\times\tau^{-½}\right)^2 + \left(10\times10^{-15}\times\tau^{+½}\right)^2$$

$\sigma^2_{x.R}(\tau)$ is the time stability of the dating of the return of the laser pulse to the station. Its is dependent on the link budget. The use of the LRA places us in the most unfavourable case, with a number of photons per pulse between 0,1 and 100. For a detection based on a avalanche photodiode in its Geiger mode, we have, in a single photon mode :

$$\sigma^2_{x.R}(\tau) = \left(30\times10^{-12}\times\tau^{-½}\right)^2 + \left(10\times10^{-15}\times\tau^{+½}\right)^2$$

$\sigma^2_{x.B}(\tau)$ is the time stability of the dating of the arrival of the laser pulse onboard the satellite. It gathers instabilities due to the detection and the time tagging unit. T2L2 instrument requirement are :

$$\sigma^2_{x.S}(\tau) = \left(12.6\times10^{-12}\times\tau^{-½}\right)^2 + \left(12.6\times10^{-15}\times\tau^{+½}\right)^2$$

$\sigma^2_{x.Geom}(\tau)$ represents the noise in the restitution of the relative positions of the reflection reference point and the detection reference point. This noise breaks up into two terms: One comes from the signature of target (LRA), the other from the uncertainty on the distance between the reflection reference point and the detection reference point. The first term has been evaluated in OCA laboratory by measurements carried out with ultra mobile laser station FTLRS and based on an emulation of the LRA by 3 corner-cubes laid out with characteristic distances. Using the short term stability of the oscillator, it is possible to transform the real noise generated by this signature into a white phase noise. For the second term, by supposing a difference between these two points of 100 mm and by taking into account a noise of restitution of the attitude of 1 mRad (Jason-1 value) we obtain an RMS error of 3×10^{-13} s which is negligible. Thus one has :

$$\sigma^2_{x.Geom}(\tau) = \left(1.10^{-11}\times\tau^{-½}\right)^2$$

$\sigma^2_{x.Atmosphere}(\tau)$ is the instability related to the atmospheric fluctuations between the outward travel of the laser pulse and the return.

$$\sigma^2_{x.Atmosphère}(\tau) = \left(6.10^{-12} \times \tau^{-½}\right)^2 \text{ for } 0.1 < \tau < 10^6 \text{ s}$$

$\sigma^2_{x.Relativity}(\tau)$, which represent fluctuations of the terms related to calibration and the relativistic effects, is supposed to be negligible.

We have then from (2) the time stability for the time transfer between a ground clock and the on-board clock :

$$\sigma^2_{x.BS}(\tau) = \left(23\times10^{-12} \times \tau^{-½}\right)^2 + \left(14\times10^{-15} \times \tau^{+½}\right)^2 \quad \textbf{(3)}$$

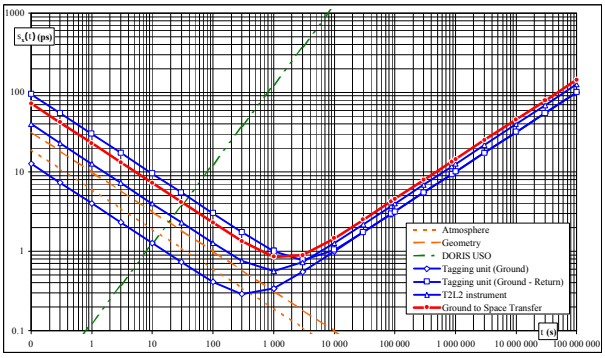

Figure 7: T2L2 ground to space stability budget : We will be able to read DORIS USO for $t > 30$ s.

Accuracy :

The uncertainty budget, at one σ, takes into account on the one hand uncertainty terms from equation (1) and on the other hand the reattachment to the local onboard or ground time frame.

We can deduce from (1) the uncertainty for the time transfer :

$$\sigma^2_{TGS} = \frac{\sigma^2_D}{4} + \frac{\sigma^2_R}{4} + \sigma^2_S + \sigma^2_{Atmosphere} + \sigma^2_{Relativity} + \sigma^2_{Geom}$$

Where :

- $\sigma^2_D = \sigma^2_{GrDet} + \sigma^2_{GrTag} + \sigma^2_{GrCal}$ is the departure date uncertainty where σ_{GrDet} is the contribution of the photo detector, σ_{GrTag} the contribution of the tagging unit and σ_{GrCal} is linked to the fluctuation of the optical path inside the instrument ;
- σ_R is the return date uncertainty, same as σ_D ;
- $\sigma^2_S = \sigma^2_{SpaceDet} + \sigma^2_{SpaceTag} + \sigma^2_{SpaceCal}$ is the onboard date uncertainty where $\sigma_{SpaceDet}$ is the contribution of the photo detector, $\sigma_{SpaceTag}$ the contribution of the tagging unit and $\sigma_{SpaceCal}$ the contribution of the calibration terms (they include vernier calibration, delays compensation due to laser pulse energy, differential transmission of linear and non linear optics …). Internal calibrations performed by the T2L2 instrument shall allow us to neglect this last term ;
- $\sigma_{Atmosphere}$: Uncertainty on the atmosphere delay compensation, due to atmospheric fluctuation between the outward propagation of the pulse and the return ;
- $\sigma_{Relativity}$ is the uncertainty on the relativistic delay compensation, which is supposed to equal to zero thanks to a high performance orbit determination (DORIS, GPS and laser ranging) ;
- σ_{Geom} is the uncertainty on the determination of the relative positions of the LRA and of the T2L2 Optical Units.

To take into account the reattachment to the local onboard or ground time frame, we have then :

$$\sigma^2_{GS} = \sigma^2_{TGS} + \sigma^2_{Groud} + \sigma^2_{Space}$$

That lead to the preliminary uncertainty budget give in Table 1. Contributions of ground tagging units come from evaluations performed by the OCA whereas it is expected values for the onboard equipment.

Item	**Uncertainty (ps)**	
	Type A	Type B
Departure Date σ_D	12.4	
s_{GrDet}	*12.0*	
s_{GrTag}	*3.0*	
s_{GrCal}		*1.0*
Return Date σ_R	40.1	
s_{GrDet}	*40.0*	
s_{GrTag}	*3.0*	
s_{GrCal}		*1.0*
Onboard Date σ_S	17.2	
$s_{SpaceDet}$	*16.9*	
$s_{SpaceTag}$	*3.0*	
$s_{SpaceCal}$	-	
Atmosphere $\sigma_{Atmosphere}$	20.0	
Relativity $\sigma_{Relativity}$	0.0	
Geométry σ_{Geom}		0.3
Time Transfer s_{TGS}	**29.5**	
Onboard reattachment s_{Space}		35.0
Ground reattachment s_{Ground}		50.0
Total Uncertainty (1 s)	**67.8**	

Table 1 : T2L2 expected ground to space uncertainty budget

Common view and non common view :

For ground to ground clocks comparisons, we have to consider the transfer between each ground clock and the space clock, $\chi_A(t_A)$ and $\chi_B(t_B)$, and the time walk of the onboard clock during $\tau_{AB} = t_B - t_A$.

In common view configuration, that is to say when the two ground stations draw at the same time on space vehicle, τ_{AB} is the dead time between to laser pulse, i.e. τ_p = 0.1 s. The onboard clock contribution has to be taken into account for this duration τ_p and we have :

$$\sigma^2_{x.AB\_CV}(\tau) = \sigma^2_{x.A}(\tau) + \sigma^2_{x.B}(\tau) + \sigma^2_{x.Clock}(\tau_p)\frac{\tau_p}{\tau} \quad \textbf{(4)}$$

With a stability of $\sigma_{x\text{-}Clock}(\tau) \approx 12\times10^{-12}\times\tau^{-½}$, the contribution of the DORIS USO is negligible over 0.1 s and we have (Figure 8) :

$$\sigma^2_{x.AB\_CV}(\tau) = \left(32\times10^{-12}\times\tau^{-½}\right)^2 + \left(20\times10^{-15}\times\tau^{+½}\right)^2$$

We can deduce from (4) the uncertainty for the time transfer :

$$\sigma^2_{TAB\_CV} = \sigma^2_A + \sigma^2_B + \sigma^2_{x.Clock}(\tau_p)$$

To take into account the reattachment to the local onboard or ground time frame, we have then (Table 2) :

$$\sigma^2_{AB\_CV} = \sigma^2_{TAB\_CV} + 2\times\sigma^2_{Ground} + \sigma^2_{Space}$$

Item	**Uncertainty (ps)**	
	Type A	Type B
Ground/Space Transfer $\sigma_{A,B}$	29.5	
Cock $\sigma_{x.Clock}(0.1s)$	0.01	
Time Transfer s_{TAB_CV}	**41.7**	
Onboard reattachment s_{Space}		35.0
Ground reattachment s_{Ground}		50.0
Total Uncertainty (1 s)	**89.3**	

Table 2 : T2L2 ground to ground uncertainty budget common view configuration

In non common view configuration, that is when there is a dead time $\Delta\tau_{AB}$ between the access of each ground station to space vehicle, the onboard clock contribution becomes significant and the larger this dead time the bigger the degradation of performances. Considering an average pass duration of 1000 s over each ground station we have for $\tau > 1000$ s :

$$\sigma^2_{x.AB\_NCV}(\tau) = \sigma^2_{x.A}(\tau) + \sigma^2_{x.B}(\tau) + \left\{\sigma^2_{x.A}(10^3) + \sigma^2_{x.B}(10^3) + \sigma^2_{x.Clock}(\tau_{AB})\right\}\frac{\tau_{AB}}{\tau} \quad \textbf{(5)}$$

That gives, for different values of $\Delta\tau_{AB}$ (Figure 8) :

$$\sigma^2_{x.AB\_300s}(\tau) = \left(0.6\times10^{-9}\times\tau^{-½}\right)^2 + \left(20\times0^{-15}\times\tau^{+½}\right)^2$$

$$\sigma^2_{x.AB\_100s}(\tau) = \left(4\times10^{-9}\times\tau^{-½}\right)^2 + \left(20\times0^{-15}\times\tau^{+½}\right)^2$$

$$\sigma^2_{x.AB\_3000s}(\tau) = \left(21\times10^{-9}\times\tau^{-½}\right)^2 + \left(20\times0^{-15}\times\tau^{+½}\right)^2$$

We can deduce from (5) the uncertainty for the time transfer :

$$\sigma^2_{TAB\_NCV} = \sigma^2_A + \sigma^2_B + \sigma^2_{x.Space}(\tau_{AB})$$

To take into account the reattachment to the local onboard or ground time frame, we have then (Table 3) :

$$\sigma^2_{AB\_NCV} = \sigma^2_{TAB\_NCV} + 2\times\sigma^2_{Ground} + \sigma^2_{Space}$$

clocks grounds starting from 1000s. **Item**	**Uncertainty (ps)**	
	Type A	Type B
Ground/Space Transfer $\sigma_{A,B}$	29.5	
Cock		
$\sigma_{x.Clock}(300s)$	37.5	
$\sigma_{x.Clock}(1000s)$	125.0	
$\sigma_{x.Clock}(3000s)$	375.0	
Time Transfer		
s_{TAB_NCV} (300s)	56.1	
s_{TAB_NCV} (1000s)	131.8	
s_{TAB_NCV} (3000s)	377.3	
Onboard reattachment s_{Space}		35.0
Ground reattachment s_{Ground}		50.0
Total Uncertainty (1 s)		
s_{AB_NCV} (300s)	**96.8**	
s_{AB_NCV} (1000s)	**153.6**	
s_{AB_NCV} (3000s)	**385.5**	

Table 3 : T2L2 ground to ground uncertainty budget non common view configuration. This budget is clearly controlled by the contribution of the oscillator.

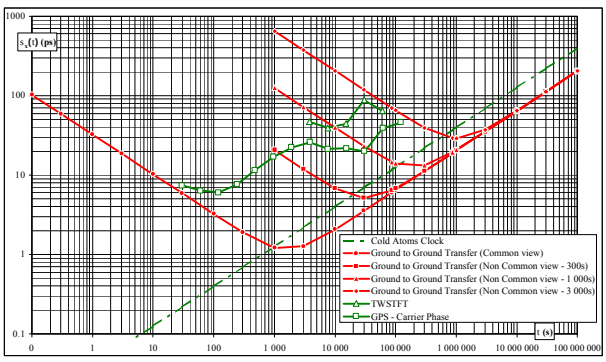

Figure 8: T2L2 ground to space stability budget : Even in non common view, with an improvement of at least on order of magnitude, T2L2 offers the capability calibrate existing RF time transfer systems [13], [14].

In common view configuration, T2L2 should reach the majority of the current atomics clock, including cold atoms microwave ones, for duration greater than 1000 s. In non common view configuration, if the T2L2 loses of its interest because of the limitation imposed by the onboard clock, Figure 8 shows that T2L2, even in this unfavourable configuration, offers an interesting alternative in calibration campaigns of radiofrequency frequency and time transfer systems based on transportable stations.

Influence of the signal to noise ratio

In order to limit the rate of false detections onboard and to optimize the signal to noise ratio, non linear detection works in a triggered mode. Release of the trigger is managed by the linear detection, when the measure of the received energy is greater than a threshold whish is adjusted according to the solar noise. At this time, linear detection then sends a polarization signal to non linear detection in order to prepare it on arrival of the laser pulse (This pulse will have been delayed by an optical delay line). However, this system is not insensitive with the photons of noise which would arrive on the linear detector the moment between the establishment of this polarization signal and the true laser pulse. Such false measurements are not filterable a priori and induce a degradation of the precision of dating. This degradation depend on the width of the spectral filter implemented on the non linear detection, of, and of solar flux :

$$\sigma_N^2 = k\left(\frac{\delta t}{2\sqrt{3}}\right)^2 + (1-k)\sigma_0^2 \text{ with } k \approx \frac{\Phi_{thv}}{hc/\lambda}$$

Where :

- σ_0^2 is the nominal precision ;
- δt is the normal time between the establishment of the signal and the arrival of the pulse (set by hardware) ;
- Φ_{thv} is the solar flux reflected by the Earth and received by the detector after the spectral filter. Φ_{thv} depends on the weather conditions (night / day, sunny / cloudy) and of the geography (sea, snow …).

With a 2 nm width spectral filter and δt set to 3 ns, k varies from 0 (night) to 0,075 (day, cloudy). That led to a degradation of the precision of a factor up to 8. It should be possible to limit this degradation to a factor for if we are able to reduce δt to 1.5 ns.

6. CURRENT STATUS

Only a proto-flight model of the optical subsystem will be manufactured. Its elements are under development by SESO company (Aix-en-Provence, France) and first measurements are envisaged during June 2006. Concerning the electronic subsystem, carried out by EREMS company (Toulouse, France), it was decided to proceed in 3 steps : Prototype boards of the metrological part, engineering model and qualification and flight model. Prototype boards have been just delivered and are under evaluation at the OCA. First results exhibit a precision of one ps in calibration mode.

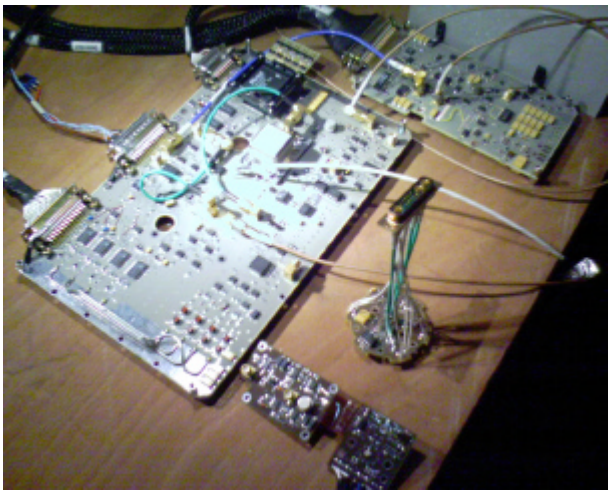

Figure 9: Prototype boards of the detection and time tagging system.

7. CONCLUSION

T2L2, because of its non all weather capacity, will never be an operational system. Nevertheless its performances, with an improvement of one order of magnitude compared to existing systems, will allow a calibration of the various existing radiofrequency time and frequency transfer systems, based on GPS or TWSTFT, and comparisons of ground cold atoms atomic clocks at level never yet reached.

Beyond first measurements on the engineering model foreseen in May 2006, next milestones are the characterization and then delivery of the flight model at the end of 2006 and the launch of Jason-2 mid-2008.

Acknowledgements

We would like to thank the whole Jason-2 and DORIS teams at CNES who make it possible to realise this project.

Thank also to Pierre Uhrich from SYRTE for very useful discussions on uncertainty budgets.

REFERENCES

[1] P. Fridelance, E. Samain and C. Veillet, "*T2L2 - Time transfer by Laser link: a new optical time transfer*

generation", Experimental Astronomy Vol.7 Num.3 Sept.97.
[2] P. Fridelance, C. Veillet, "*Operation and data analysis in the LASSO experiment*", Metrologia, 32, 27-33, 1995. [1] N. Ramsey, Phys. Rev. **78**, 695 (1950).
[3] Samain E., Fridelance P., "*Time Transfer by Laser Link (T2L2) experiment on MIR*", Metrologia, 35, pp 151-159, 1998.
[4] Y. Menard, L. Fu, F. Parisot, S. Kaki, A. Ratier, R. Cheney, "*The Jason-2 Mission: Monitoring Ocean Surface Topography from Space*", Eumetsat Science and Technology Working Group, Sept 2002.
[5] Brunet M., In Proc. 6th European Frequency and Time Forum, 125-136, 1992.
[6] Brunet M., Auriol A., Berthias J.P., Costes M., Issler J.L., Sengenes P., In Proc. 11th European Frequency and Time Forum, 311-318, 1997.
[7] Samain E., "*Timing of optical pulses by photodiode in Geiger mode*", Applied Optics, 37, No 3, pp 502-506, 1998.
[8] Procazka I., Hamal K., "*Recent achievements in solid state detector technology for laser ranging*", 2 , 469, Proceedings of the 9th International Workshop on laser ranging instrumentation, 1994.
[9] Kingston R.H. , in Detection of optical and infrared radiation, Springer - Verlag Berlin, p. 52 1978.
[10] Samain E., "*An Ultra Stable Event Timer*", Proceedings of the 13th International Workshop on laser ranging instrumentation, 2002.
[11] Samain E., Dalla R., "*Time walk compensation of an avalanche photo-diode with a linear photo-detection*", Proceedings of the 13th International Workshop on laser ranging instrumentation, 2002.
[12] Samain E., Vrancken P.,Weick J., Guillemot Ph., Petitbon I., Léon S., "*One Way Laser Ranging TIPO - Time Transfer by Laser Link T2L2*", To be issued.
[13] Delporte J., Mercier F., "*Recent improvements in GPS carrier phase frequency transfer*", Proceedings of the join IEEE-UFFC & PTTI meting, 2005.
[14] Achkar J., Uhrich P., Merck P. , and Valat D., "*Recent Time and Frequency Transfer Activities at the Observatoire de Paris*", Proceedings of the join IEEE-UFFC & PTTI meting, 2005.

Proceedings of the 20th EFTF, 2006

A GPS CV LINK EXPERIENCE BETWEEN ROA AND IREE

Héctor Esteban, Juan Palacio, Fco. Javier Galindo, Jose A Lima
Real Instituto y Observatorio de la Armada, San Fernando, Cádiz, Spain
Jan Čermák, Alexander Kuna
Institute of Radio Engineering and Electronics Czech Academy of Sciences
Prague, Czech Republic
Electronic address: hesteban@roa.es

Increasing the number of tracks per day of a TTR-6 receiver has been demonstrated to provide a good tool to reduce the uncertainty of the comparison of two clocks located at laboratories within few hundreds of kilometres after J.Palacio et al. [1]. To check the validity of the results obtained with this cheap and easy-to-implement method, it was necessary to use it in a regular way to link two long-distance separated Timing Laboratories that contribute to TAI. Thus Real Observatorio de la Armada (ROA) and the Institute of Radio Engineering and Electronics (IREE - TP), with a 2200 km baseline, have agreed to set up a computer that controls the spare TTR-6 AOA GPS receiver of IREE in order to increase the daily number of tracks.

I. INTRODUCTION

The tracking schedule for time and frequency comparisons by GPS common-view single-channel for Europe area has the disadvantage of having to track low elevation satellites both in IREE and ROA laboratories (Fig. 2, 4). In this paper it will be shown how the tracking schedule can be improved by adding a selection of new satellites to the standard schedule and thus increasing the number of observations up to the 89 daily tracks.

Fig. 1 shows the time difference between ROA and IREE reference clocks obtained from the extended schedule since MJD 53150. The excessive jumps around MJD 53700 are due to sudden malfunction of the TP reference clock.

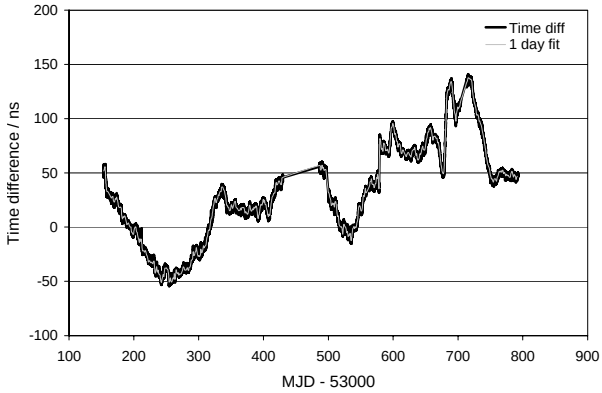

Fig. 1. Time difference between ROA and TP reference clocks.

II. THE EXTENDED SCHEDULE

The extended schedule for ROA and IREE receivers shown below allows us to make a selection of more suitable satellites with higher elevations (Fig. 3, 5). This new schedule is modified every month in order to get the best results in both laboratories.

Tracking schedule No. 45 for international time and frequency comparisons by GPS CV single-channel receivers.
Tracks added

CLASS	PRN	hour	min
EE	28	0	8
A0	28	0	24
EA	26	0	40
EE	29	0	56
18	18	1	12
EE	29	1	28
EE	26	1	44
EE	26	2	0
EE	9	2	16
EE	9	2	32
EE	5	2	48
EE	5	3	4
EE	5	3	20
EE	30	3	36
EE	30	3	52
18	14	4	8
BC	9	4	24
EE	30	4	40
EE	6	4	56
18	1	5	12
A0	2	5	28
EE	6	5	44
EE	6	6	0
EE	6	6	16
EE	6	6	32
EE	6	6	48
18	16	7	4
BC	30	7	20
EE	21	7	36
BD	30	7	52
74	16	8	8
EE	21	8	24
18	3	8	40
19	3	8	56
1A	3	9	12
EE	16	9	28
74	3	9	44
EE	16	10	0
EE	16	10	16
BC	22	10	28
EE	3	10	44
A0	18	11	0
74	19	11	16
EE	3	11	32
EE	3	11	48

CLASS	PRN	hour	min
EE	19	12	4
18	11	12	20
A0	22	12	36
BC	3	12	52
EE	19	13	8
EE	19	13	24
A0	14	13	40
BC	1	13	56
BD	1	14	12
18	24	14	28
EA	20	14	44
EE	20	15	0
A0	1	15	16
A1	1	15	32
74	24	15	48
A2	1	16	4
EA	20	16	20
BC	11	16	36
EE	24	16	52
EE	24	17	8
74	4	17	24
EE	24	17	40
EE	24	17	56
BC	20	18	12
EE	24	18	28
A0	23	18	44
A1	23	19	0
A2	23	19	16
EE	27	19	32
EE	27	19	48
A0	13	20	4
A1	13	20	20
74	10	20	36
18	29	20	52
19	29	21	8
EE	27	21	24
18	26	21	40
A0	27	21	56
74	29	22	12
EE	29	22	28
74	26	22	44
EE	29	23	0
EE	29	23	16
EE	29	23	32
EA	29	23	48

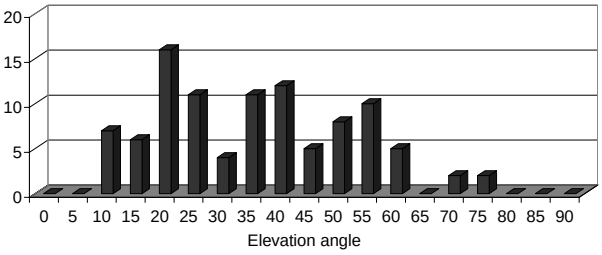

Fig. 2. Monthly elevation average of tracked satellites, following the BIPM schedule for GPS CV single channel in ROA.

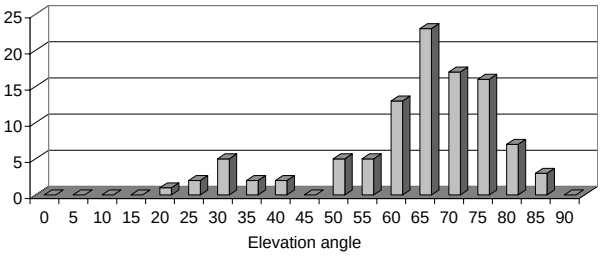

Fig. 3. Monthly elevation average of tracked satellites added to the BIPM schedule for GPS CV single channel in ROA.

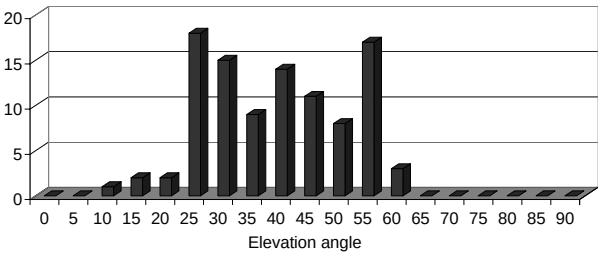

Fig. 4. Monthly elevation average of tracked satellites, following the BIPM schedule for GPS CV single channel in TP.

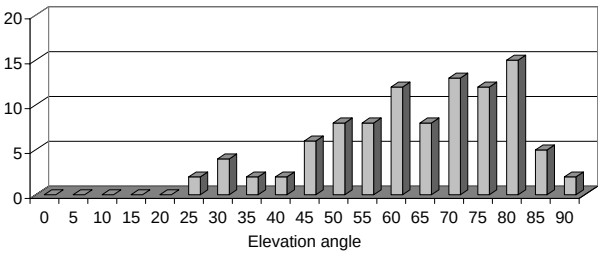

Fig. 5. Monthly elevation average of tracked satellites added to the BIPM schedule for GPS CV single channel in TP.

Due to this low elevation, the uncertainty in the determination of the ionospheric and tropospheric delays reduces severely the achievable accuracy in time and frequency transfer. Fig. 6 shows the difference of the ionospheric delay applied by the receiver and the one calculated using IONEX files, versus the satellite elevation.

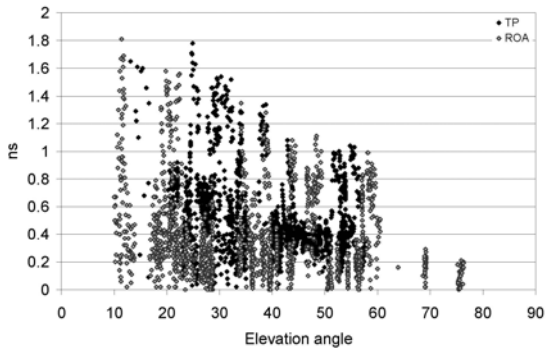

Fig. 6. Ionospheric delay errors vs. elevation angle errors.

Although the ionospheric delay can be compensated properly, the estimation of the delay caused by the troposphere is more complicated, being separated into its two components, the zenith hydrostatic delay (ZHD) and the zenith wet delay (ZWD).
The ZHD can be precisely determined by means of surface pressure measurements, whereas the ZWD (Fig. 7) can hardly be modelled due to the irregular and changing distribution of the water vapour in the atmosphere.

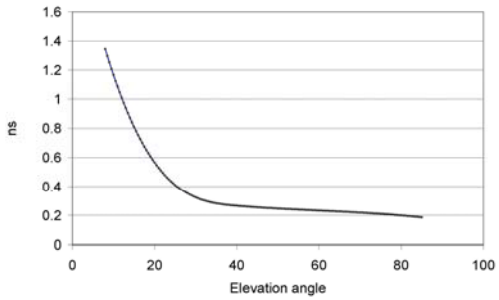

Fig. 7. Dependency of Zenit Wet Delay on the satellite elevation angle.

The important influence of the satellite elevation can be quickly observed taking into consideration the DSG value [2] which is provided by the receivers as a quality factor for individual tracks, and can be considered as a contribution to the uncertainty of the measurement (Fig. 8). Thus, we can evaluate the influence of the selection of the satellites with higher elevation in the accuracy of the comparison.
The multipath effect [3] is another important contribution to the total error, although this effect is reduced using grounded plate antenna in the ROA station (Fig. 8).

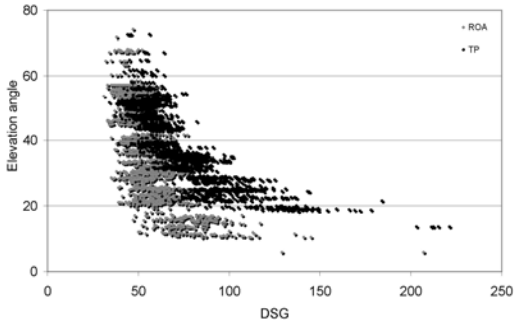

Fig. 8. Root mean square of the linear fit residuals used to produce the REFGPS common view data file.

III. DATA PROCESSING

Taking several weeks of raw data and studying separately standard and added tracks, a reduction near to 1 ns rms has been shown, as resulting from a fit and a better approximation of the resulting data from Circular T (Fig. 9). This improvement in the added data can be also shown in terms of modified Allan deviation (Fig. 10).

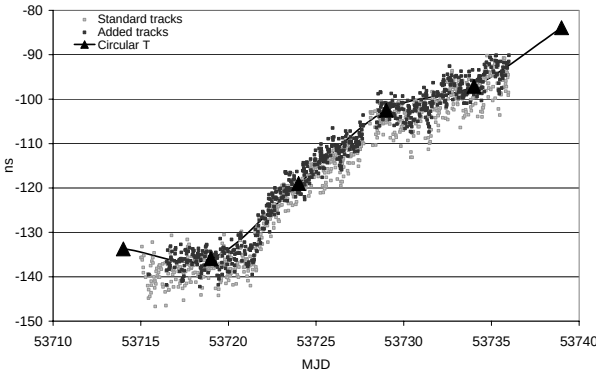

Fig. 9. Time difference between ROA and TP reference clocks for ordinary and EE class tracks.

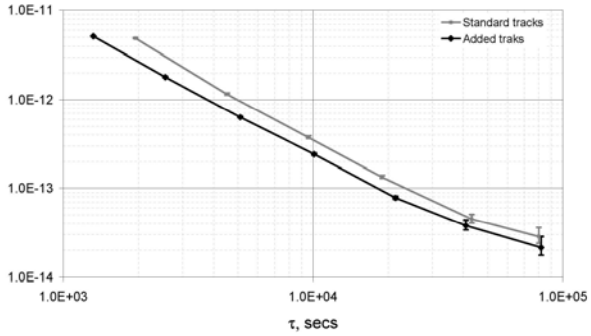

Fig. 10. Modified Allan deviation of raw data.

In order to improve the quality of observations, the data of both laboratories have been corrected by precise ephemeris and ionospheric delay. The atmospheric delay has been calculated using IONEX files, which contain the vertical TEC (VTEC) needed to estimate the first order ionospheric propagation delay.

Precise IGS orbits in the SP3 format have been used, after applying Neville algorithm [4], to estimate the biases between the precise satellite position and the result from the broadcast ephemeris contained in the RINEX navigation files.

Finally the modified and overlapping Allan deviations have been calculated (Fig. 11, 12) to confirm the improvement due to the extended schedule. In the presence of white phase noise it can be translated into a theoretical improvement in the stability of time transfer by a factor close to √2.

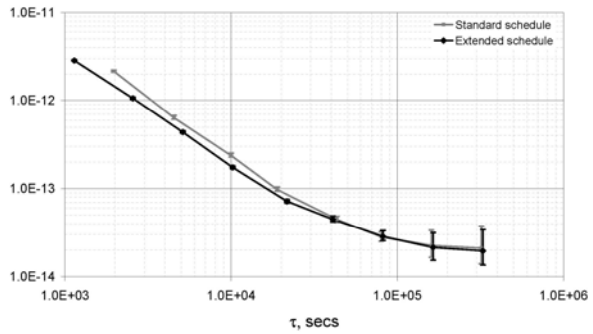

Fig. 11. Modified Allan deviation of time difference reference clocks between ROA & TP.

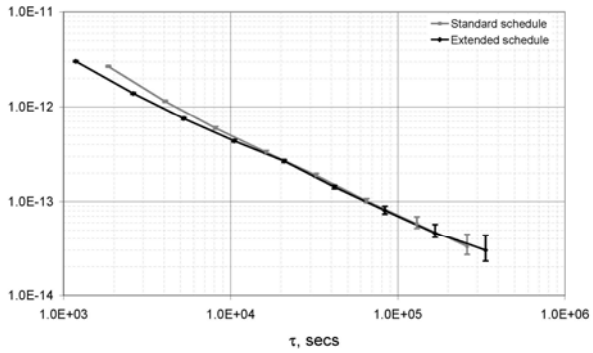

Fig. 12. Overlapping Allan deviation of time difference reference clocks between ROA & TP

IV. CONCLUSIONS

With this improvement the TTR-6 receivers can perform 89 daily tracks which represent the useful 16-minute time slots. Although the amount of data is reduced after the common-view processing, it still

remains about twice as large compared to the usual single channel schedule.

Using the raw data and only taking into account the added and standard BIPM tracks, an improvement in the uncertainty of time and frequency transfer has been shown, mainly due to the selection of high elevation satellites.

This increase in the number of observations and its theoretical improvement in the stability is in agreement with the real data results in terms of modified and overlapping Allan deviations.

REFERENCES

[1] J. Palacio et al., “A contribution for the improvement of GPS CV time transfer technique”. Proceedings of the EFTF 2004.

[2] D. Allan, C. Thomas, “Technical Directives for Standardization of GPS Time Receiver Software”, Metrologia, 1994, 31, pp. 67-79.

[3]G. J. Bishop and J. A. Klobuchar, “Multipath effects on the determination of absolute ionospheric time delay from GPS signals”. Radio Sci., vol. 20, pp. 388-396,1985.

[4] M. Schenewerk, "A brief review of basic GPS orbit interpolation strategies," GPS Solutions (2003) 6:265-267.

Proceedings of the 20th EFTF, 2006

The Comparison between TWSTFT and GPS time transfers on inter-continental baseline links

W. H. Tseng[1,*], S. Y. Lin[1], H. M. Peng[2], H. T. Lin[1], and C. S. Liao[1]
[1]*Telecommunication Laboratories, Taiwan*
[2]*Institute of Applied Mechanics, National Taiwan University*
**email:* whtseng@cht.com.tw

This study compares the results of different kinds of the precise time transfer techniques and estimates their qualities. Four laboratories equipped with the two-way satellite time and frequency transfer (TWSTFT) stations and dual frequency GPS multi-channel receivers are chosen for the representative sites of Europe, North-American and Asia. We investigate the difference between TWSTFT and different kinds of GPS data, including the continuous GPS code combined with Carrier-Phase solutions, GPS Multi-Channel C/A code, GPS P3 code Common-View and All-in-View. This study shows that TWSTFT and GPS data are in good agreement. The standard deviations of their double difference could be in the order of sub-nanosecond.

I. INTRODUCTION

The two-way satellite time and frequency transfer (TWSTFT) and GPS techniques are the major methods for the long distance time transfer. The TWSTFT data in European and North American have been used to calculate the international atomic time (TAI) since 1998 [1]. In Asia-Pacific region, several major time and frequency institutes are participating in a TWSTFT network, including the link between the NICT in Japan and TL in Taiwan. The NICT-TL TWSTFT data have also been used for the computation of TAI since January 2002 [2]. From the middle of the 2005, the multi-channel TWSTFT modems, which are developed by NICT, are formally used on the Asia-Pacific TWSTFT links. And, the TWSTFT data of more than 24 points per day are available. On the other hand, the first Asia and Europe TWSTFT link was set up between VSL and TL in 2003 [3]. In September 2005, both VSL and TL have finished the automation of their daily TWSTFT measurements and data processing. Therefore, we can compute the time difference data between TL and the laboratories in European or North American via the VSL-TL TWSTFT link.

The performance of TWSTFT was conventionally considered by the comparison with GPS Common-View (CV) method, which is widely used for the inter-national time comparison. The earlier GPS CV time transfer used the single-channel and single-frequency GPS receivers. The errors in the ionospheric correction would be present in the results of GPS CV, especially for TL that is located at tropical ionosphere latitudes [4]. The multi-channel or dual-frequency GPS receivers have progressively replaced the previous receivers, due to the advantage of the correction of the ionospheric delay [5]. Furthermore, the International GPS Service (IGS) provides more precise ephemeredes and clock offsets of the GPS satellites. A GPS All-in-View (AV) method has become realizable to perform directly time transfer between any two laboratories on the Earth [6] [7].

On the other hand, a network of the GPS stations in Europe and North America has been routinely analyzed for the continuous time transfer purposes using the carrier phase observations [8]. Since 2001, The IGS stations of "KGN0" in NICT and "TWTF" station in TL have been contributing to the IGS Time. The continuous GPS code combined with Carrier-Phase (CP) results could provide a precise time and frequency transfer data.

Remarkable advances of the time transfer method have been made in the recent years. The goal of this paper is to compare the precise time transfer techniques and to estimate their qualities.

II. TIME TRANSFER LINKS

Four laboratories equipped with TWSTFT stations and dual frequency GPS multi-channel receivers are chosen for the representative sites of Europe, North-American and Asia. They are PTB, USNO, NICT and TL. Table 1 shows the baseline lengths of each time transfer links. We investigate the difference between TWSTFT and different kinds of GPS data, including the continuous GPS CP, GPS Multi-Channel (MC) C/A code, GPS P3 code. Table 2 lists the multi-channel and dual-frequency GPS receivers of each laboratories. For computing the time transfer results, we downloaded the data of GPS MC and P3 from BIPM ftp site, except for TL's GPS

MC data that were put on TL's ftp site. And, the data of GPS CP were downloaded from IGST web site. The GPS data from MJD 53555 to 53766 were used in this study.

The TW data were downloaded from the ftp site of each laboratories. Table 3 lists the time spans of TW data used for the calculation. The kinds of TW modem are also listed.

Table 1. Baseline lengths and time transfer methods.
TW: Two-Way satellite time and frequency transfer
TW*:Calculating TW links via VSL-TL TW link
MC: GPS single-frequency Multi-Channel C/A code
P3: GPS dual-frequency multi-channel P3 code
CP: GPS code combined with Carrier-Phase solutions

Link	Distance	Method
NICT- TL	2113 km	TW, MC, P3, CP
PTB-TL	8376 km	TW*, MC, P3, CP
USNO-TL	10692 km	TW*, MC, P3, CP

Table 2. Laboratories and their GPS equipments.

Laboratory	GPS MC	GPS P3, CP
NICT	Topcon EURO 80	Ashtech Z12T
TL	Topcon EURO 80	Ashtech Z12T
PTB	AOS SRC TTS-2	Ashtech Z12T
USNO	AOS SRC TTS-2	Ashtech Z12T

Table 3. TW data used for the calculation.

Laboratory	TW modem	Data
NICT/TL	NICT/NICT	MJD 53664-53764 (24 points/day)
VSL/TL	MITREX/SATRE	MJD 53615-53766 (1 point/day)
PTB/VSL	SATRE/MITREX	MJD 53615-53645 (4 points/day)
USNO/VSL	SATRE/MITREX	MJD 53646-53766 (12 points/day)

III. COMPARSIONS

For the purpose of a direct and meaningful comparison, we averaged the GPS data over the time interval that around to the time tag of individual TW measurements. To ensure a meaningful average, we demanded that there are 9~12 points in a time interval for the most part of the GPS data. Then, we selected a time interval of ± 0.5 hours for the GPS CP data, ± 1.5 hours for GPS P3 data, and ± 2.5 hours for GPS MC data. For the GPS MC and P3 data, we computed their time transfer results between two laboratories by Common-View and All-in-View methods. In the All-in-View method, we calculated two results by using equal weight and elevation weight on different satellites. The elevation weight means that the weight of different satellites are determined according to their elevations as following.

$$\text{Weight}_j = 1/\cos^2(\text{Elevation}_j)$$

NICT-TL link

Both the NICT and TL are located in the Asia-Pacific Region. During the time span of the data that we used, the reference of NICT was based on a high performance CS clock, and the reference of TL was an active Hydrogen maser.

Since the data of TW, GPS MC and GPS P3 have been calibrated, the different values of TW-MC and TW-P3 are close to zero. The phase offset of the GPS CP has not been calibrated, and the difference between TW and GPS CP data is about 380.5 ns. Some gibbous about 4 ns can be found from MJD 53730 to 53760. The plots of the double differences for TW-CP and TW-P3 AV (elevation weight) are shown in Figures 1 and 2.

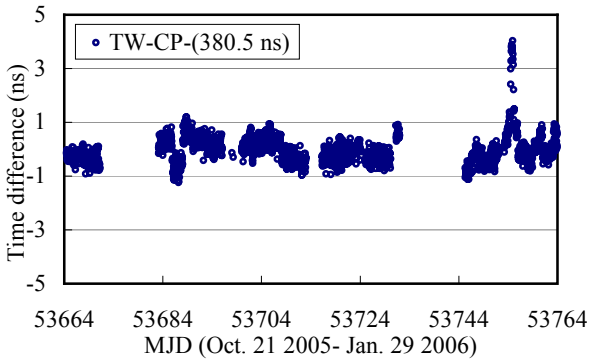

Figure 1. Double differences of TW and GPS CP for the NICT-TL link.

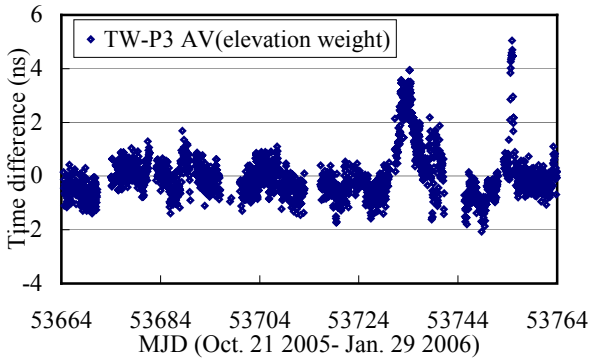

Figure 2. Double differences of TW and GPS P3 AV for the NICT-TL link.

The differences between TW and different kinds of GPS data for the NICT-TL link are listed in Table 4. The standard deviations show that the GPS CP data has the best agreement with TW. The deviation of their differences amounts to 0.558 ns over the 100 days of 1503 available data. The GPS P3 data also show a good agreement with TW. As we included the P3 data only on the period that the CP data were also available, a deviation of 0.694 ns for TW-P3 AV (elevation weight) is obtained. The AV method with elevation weight has a better agreement with TW than CV or AV with equal weight.

Table 4. Double differences of TW and GPS data for the NICT-TL link. Double differences of TW-CP means $[UTC(NICT)–UTC(TL)]_{TW}–[UTC(NICT)–UTC(TL)]_{CP}$. *: only on that the CP data are also available.

Comparison	Points	Mean (ns)	Std.Dev. (ns)
TW-MC CV	1922	-3.116	2.223
TW-MC AV (equal weight)	1922	-3.122	2.250
TW-MC AV (elevation weight)	1922	-4.010	2.053
TW-P3 CV	1892	-0.012	0.904
	*1503**	*-0.209**	*0.726**
TW-P3 AV (equal weight)	1892	0.141	0.934
	*1503**	*-0.066**	*0.749**
TW-P3 AV (elevation weight)	1892	-0.018	0.884
	*1503**	*-0.224**	*0.694**
TW-CP	1503	380.474	0.558

PTB-TL link

The TW data for PTB-TL link were computed from PTB-VSL and VSL-TL TW data. VSL and TL started to perform the daily measurements from September 2005. There are 3 sessions from 7:38 UTC to 7:48 UTC every day. The average value of these 3 sessions was taken as the single point TW result.

For the PTB-VSL TW link, there were 4 points/day before MJD 53645, and 12 points/day after MJD 53646. We took a linear fit to compute the point corresponded to the time of VSL-TL link. In order to avoid the clock error, no fitted data were used unless the data of PTB-VSL link can be obtained within ± 0.5 hours interval around the regular VSL-TL sessions. From MJD 53643, new CALR was inserted to the data of VSL-PTB link. And we compensated it for the calculation of PTB-TL link. A few data were removed due to the obvious jump compared with the adjacent points. The reference of PTB is based on a primary CS clock, and the reference of VSL is based on a high performance CS clock.

Figures 3 and 4 show the double differences TW-CP and TW-P3 AV (elevation weight). There were no TW data from MJD 53708 to 53740, because the antenna of VSL was under repair. The resumption of VSL-TL link caused a step. The TW data for VSL-TL link and CP data for PTB-TL link have not been calibrated. For the convenience of comparison, different offsets have been added to the data sets. Both plots of the TW-CP and TW-P3 AV results show obvious tilts before MJD 53741, but become flat after MJD 53741.

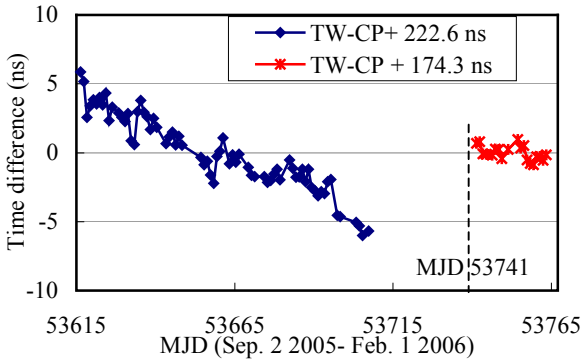

Figure 3. Double differences of TW and GPS CP for the PTB-TL link.

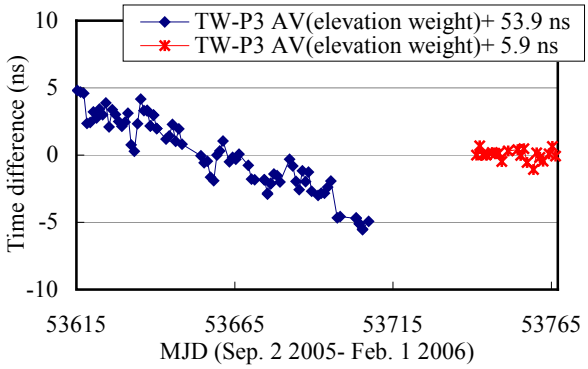

Figure 4. Double differences of TW and GPS P3 AV for the PTB-TL link.

The double differences of TW and GPS data for the PTB-TL link, before and after MJD 53741, are listed in Tables 5 and 6 respectively. One can see that the standard deviations after MJD 53741 are reduced, because the VSL-TL TW data have better quality afterward. This may due to the reinforcement of VSL's antenna structure, and then the performance of TW data was less affected by wind. Both TW-P3 AV with equal weight and elevation weight show a similar standard deviation about 0.42 ns, which is smaller than that of TW-CP.

Table 5. Double differences of TW and GPS data for the PTB-TL link from MJD 53615 to 53707.

Comparison	Points	Mean (ns)	Std.Dev. (ns)
TW-MC CV	73	-54.310	3.674
TW-MC AV (equal weight)	73	-55.085	2.787
TW-MC AV (elevation weight)	73	-54.559	2.849
TW-P3 CV	72	-53.491	2.753
TW-P3 AV (equal weight)	72	-53.490	2.701
TW-P3 AV (elevation weight)	72	-53.784	2.666
TW-CP	71	-222.638	2.730

Table 6. Double differences of TW and GPS data for the PTB-TL link from MJD 53741 to MJD 53766.

Comparison	Points	Mean (ns)	Std.Dev. (ns)
TW-MC CV	22	-1.772	2.344
TW-MC AV (equal weight)	22	-2.154	2.213
TW-MC AV (elevation weight)	22	-1.799	2.248
TW-P3 CV	20	-5.620	0.511
TW-P3 AV (equal weight)	20	-5.881	0.424
TW-P3 AV (elevation weight)	20	-5.880	0.420
TW-CP	19	-174.307	0.523

USNO-TL link

As the case of PTB-TL link, the TW data for USNO-TL link were obtained by using USNO-VSL and VSL-TL TW data. We applied the same data processing method as described in the previous section. The reference of USNO is based on a Hydrogen maser ensemble.

Figures 5 and 6 show the double differences TW-CP and TW-P3 AV (equal weight). Just as in Figures 3 and 4, both results also show tilts before MJD 53741, and become flat afterward. The double differences between TW and GPS data during different time spans are listed in Tables 7 and 8, respectively. There is no CV data here, because no common GPS satellite could be observed at the same time by USNO and TL. It is obvious that the standard deviations after MJD 53741 are better. The best standard deviation is the TW-CP result of 0.833 ns. For the TW-P3 AV results, equal weight is better than elevation weight.

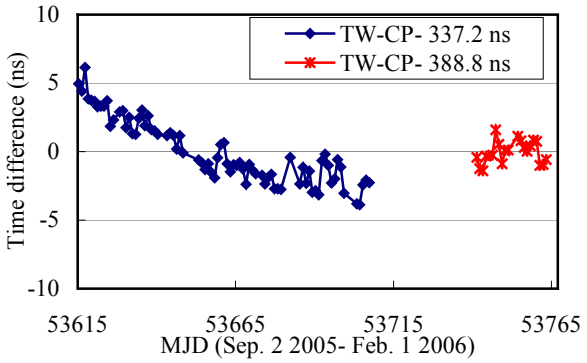

Figure 5. Double differences of TW and GPS CP for the USNO-TL link.

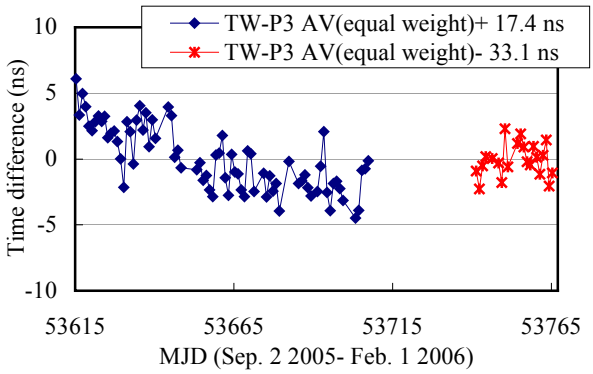

Figure 6. Double differences of TW and GPS P3 AV for the USNO-TL link.

Table 7. Double differences of TW and GPS data for the USNO-TL link from MJD 53615 to 53707.

Comparison	Points	Mean (ns)	Std.Dev. (ns)
TW-MC AV (equal weight)	77	-10.504	2.744
TW-MC AV (elevation weight)	77	-10.366	2.308
TW-P3 AV (equal weight)	76	-17.385	2.450
TW-P3 AV (elevation weight)	76	-17.440	2.820
TW-CP	78	337.198	2.338

Table 8. Double differences of TW and GPS data for the USNO-TL link from MJD 53741 to MJD 53765.

Comparison	Points	Mean (ns)	Std.Dev. (ns)
TW-MC AV (equal weight)	22	41.373	1.669
TW-MC AV (elevation weight)	22	41.416	1.793
TW-P3 AV (equal weight)	21	33.083	1.203
TW-P3 AV (elevation weight)	21	32.984	1.620
TW-CP	20	388.779	0.833

IV. SUMMARY

This paper compares the time transfer results of TWSTFT and different kinds of GPS methods, and summarizes the following.

We averaged the GPS data over the same time span of TW measurements, and then made double differences of TW and GPS data.

The comparison for NICT-TL link shows a good agreement. The standard deviations of double differences amount to 2 ns for TW-MC, 0.7 ns for TW-P3, and 0.56 ns for TW-CP over 3 months. The AV method with elevation weight has a better agreement with TW than methods of CV or AV with equal weight.

We calculated the TW data between PTB, USNO, and TL via VSL-TL TWSTFT link. For both the PTB-TL and the USNO-TL links, all the results of the TW-CP, TW-P3, and TW-MC show the obvious tilts before MJD 53741, and become flat after MJD 53741. The tilts may be caused by the system errors of TW or GPS in long-baseline time transfer. We also note that the VSL-TL TW data have a better quality after MJD 53741.

In the case of the PTB-TL link, the GPS AV data with elevation weight is better than that of equal weight. Contrarily, the equal weight is the better method for the USNO-TL link, in which the baseline distance is too long to have common observations.

In both cases of the NICT-TL and USNO-TL links, the TW-CP result shows the smallest standard deviation. But in the PTB-TL link, the standard deviation of TW-P3 AV is 0.42 ns, which is better than the results of TW-CP.

Acknowledgements

We would like to thank the colleagues of NICT, VSL, PTB, and USNO for sharing their TWSTFT and GPS data.

REFERENCES

[1] J. Azoubib, D. Kirchner, W. Lewandowski, P. Hetzel, W. Klepczynski, *et al.*, "Two-way satellite time transfer using INTELSAT 706 on a regular basis: Status and data evaluation," in *Proc. 30th PTTI*, p. 393, 1998.

[2] J. Azoubib, and W. Lewandowski, "20th BIPM TWSTFT Report," BIPM, Mar. 2002.

[3] H. T. Lin, W. H. Tseng, S. Y. Lin, H. M. Peng, C. S. Liao, G. de Jong, E. Kroon, and M. J. Brakel, "The First Two-Way Time Transfer Link between Asia and Europe," in *Proc. of 35th Annual Precise Time and Time Interval (PTTI) Meeting*, pp. 71-80, 2003.

[4] Huang, Y. N., K. Cheng, and W. T. Huang, "Seasonal and Solar Cycle Variations of Spread F at the Equatorial Anomaly Crest Zone," J. Geomag. Geoelectr., 39, pp. 639-657, 1987.

[5] P. Defraigne and G. Petit, "Time transfer to TAI using geodetic receivers," Metrologia, Vol. 40, pp. 184-188, 2003.

[6] T. Gotoh, "Improvement GPS Time Link in Asia," in *Proc. of 2005 Joint Meeting IEEE IFCS and Precise Time and Time Interval (PTTI) Meeting*, pp. 707-711, 2005.

[7] Z. Jiang and G. Petit, "Time transfer with GPS satellites all in view," in *Proc. ATF2004*, Beijing, China, Oct. 2004, pp. 236-243.

[8] R. Dach, T. Schildknecht, T. Springer; G. Dudle, and L. Prost, "Continuous time transfer using GPS carrier phase," *IEEE Trans. Ultrason., Ferroelect., Freq. Contr.*, vol. 49, no. 11, pp. 1480—1490, Nov. 2002.

Proceedings of the 20th EFTF, 2006

An experiment of GPS+GLONASS common-view time transfer using new multi-system receivers

J. Nawrocki*, W. Lewandowski**, P. Nogaś*, A. Foks*, D. Lemański*
*Space Research Centre, Borowiec, 62-035 Kórnik, Poland,
e-mail: nawrocki@cbk.poznan.pl
**Bureau International des Poids et Mesures, Sèvres

In this paper we report a new experiment of the combined use of GPS and GLONASS for international time and frequency transfer using TTS-3 multi-channel multisystem receivers. The investigation was carried out on a baseline of about 1400 km between the Astrogeodynamical Observatory (AOS) in Poland and Bureau International des Poids et Mesures (BIPM) in Sèvres. Unlike GPS, almost every GLONASS satellite works at a different basic frequency. In order to study the effects of these different frequencies on the common-view links, the investigations were carried out for every individual satellite. The results confirm that a combined use of GPS and GLONASS is feasible, despite the differences between the two systems. The use of two systems in multi-channel mode increases the number of observations by a factor of 28 in comparison to a single-channel-one-system mode, resulting in improved time and frequency comparisons.

1. INTRODUCTION

For the twenty five years the common-view time transfer for TAI calculation has been carried out using GPS, meanwhile the estimated uncertainty of GLONASS time transfer is comparable. The major obstacle to using GLONASS is operability of the system, at the time of experiment the number of satellites was 17 (included 13 operating) instead of 24.
A new experiment of the combined use of GPS and GLONASS for international time and frequency transfer was carried out on a baseline of about 1400 km between the Astrogeodynamic Observatory (AOS) in Poland and Bureau International des Poids et Mesures (BIPM) in Sèvres using the new *TTS-3* multi-channel multisystem receivers.

II. GLONASS FREQUENCIES CALIBRATION

The problems that appear when combining signals from both systems are results of substantial differences in time and space references and signal structure. The discrepancy in time scales vanish in the common-view time transfer, the different reference frames are aligned by transformation parameters in the receiver software, only the problem of different frequencies used by GLONASS satellites remains and leads to the necessity of receivers calibration for each GLONASS frequency.

In March 2006 the *TTS-3* receiver from BIPM was calibrated in AOS, the results of GLONASS frequency biases application are shown below.

SAT	FR	Obs.	bias	σ	bias	σ	bias	σ
			C/A		L1 P		L2 P	
102	1	218	1,36	0,69	1,27	0,69	5,24	0,74
106	1	185	*0,00*	0,64	0,67	0,55	3,71	0,78
105	2	154	6,33	0,52	5,50	0,51	7,90	0,64
119	3	204	5,70	0,70	4,25	0,68	5,13	0,64
107	4	91	8,03	0,27	6,42	0,36	3,83	0,26
117	5	214	6,75	0,71	7,42	0,72	6,77	0,71
121	5	75	6,20	0,76	7,38	0,69	6,26	0,90
104	6	207	7,17	0,56	7,75	0,56	6,89	0,75
108	6	216	7,60	0,67	8,00	0,56	5,82	0,50
118	10	188	8,14	1,03	7,95	1,03	6,61	0,89
122	10	212	8,54	0,68	8,47	0,71	6,64	0,62
103	12	195	8,23	0,73	9,22	0,76	6,41	0,99

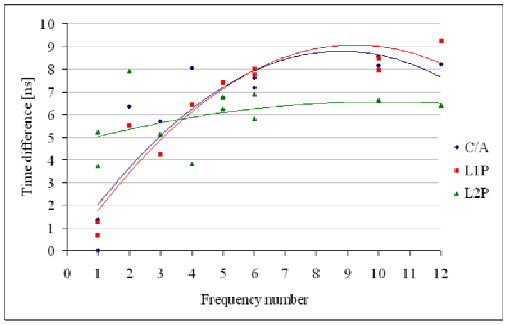

Table 1., fig. 1. GLONASS frequency biases between rec. *TTS-3* sn.12 (BIPM) and *TTS-3* sn. 02 (AOS) with respect to frequency No. 1.

Removing the frequency biases, which reach even 9 ns, allows one-site comparisons with an accuracy of 1 ns.

MJD	C/A	C/A cal.	1P	1P cal.	2P	2P cal.
53801	2,8	1,1	3,1	1,0	1,6	1,0
53802	2,9	1,0	3,0	1,0	1,6	1,0
53803	3,0	1,4	3,2	1,3	1,9	1,5
53804	3,2	1,7	3,4	1,6	2,4	2,1
53805	3,2	1,4	3,3	1,3	1,9	1,4
53806	2,6	1,0	2,9	1,0	1,5	0,9
53807	2,6	0,9	2,9	0,9	1,6	1,0
53808	2,7	1,1	2,9	1,0	1,6	1,0

Table 2. Standard deviations [ns] of one-site time comparisons by *TTS-3* sn. 12 and *TTS-3* sn. 02 multichannel GLONASS common-view before and after calibration.

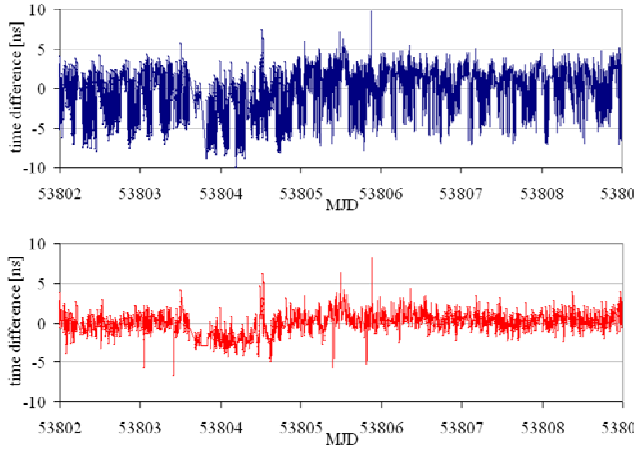

Fig. 2. One-site comparisons at the AOS: GLONASS C/A code multichannel and GLONASS C/A code multichannel with frequency biases removed (below).

III. TTS3 – MULTICHANNEL MULTISYSTEM RECEIVER

The experiment was carried out using a new 20-channel TTS-3 receivers which integrate observations of all available navigation satellites: GPS, GLONASS, WAAS and EGNOS, and use GPS and GLONASS C/A-code, GLONASS P-code, GPS reconstruted P-code and P3 mode. The receiver hardware, the treatment of the observations, and the output data fulfil the recommendations of the CCTF Group on GNSS Time Transfer Standards (CGGTTS).

IV. AOS/BIPM CV TIME LINK

On average six to seven GPS and three GLONASS satellites were observed at the same time in AOS and BIPM, which gives 19 simultaneous observations by GPS (C/A, P1, P2) multichannel method and 28 observations by GPS+GLONASS.

The use of two systems in multi-channel mode increases the number of daily observations by a factor of 28 in comparison to a single-channel-one-system mode, from 89 for the one-channel GPS link to 2451 for the GPS+GLONASS multichannel link.

Method	average number of			
	sat in c-v	obs.	sat.in c-v	obs.
	at the same time		per day	
GPS C/A single channnel	1	1	89,3	89,3
GPS C/A	6,6	6,6	574,4	574,4
GPS L1P	6,2	6,2	535,0	535,0
GPS L2P	6,2	6,2	535,0	535,0
GPS multichannnel	6,6	18,8	574,4	1644,4
GLONASS C/A	3,1	3,1	272,4	272,4
GLONASS L1P	3,1	3,1	266,9	266,9
GLONASS L2P	3,1	3,1	266,9	266,9
GLONASS multich	3,1	9,3	272,4	806,2
GPS+GLONASS multich	9,7	28,2	846,8	2450,6

Table 3. Number of observations by different methods for [*UTC (AOS) – BIPM clock*] comparison.

The following figures present the results of time transfer between AOS and BIPM over the same period by different possible methods using TTS-3 on both sides. For the GPS+GLONASS multichannel link we applied a constant to the GLONASS data to bring it in line with GPS. The linear trend is removed.

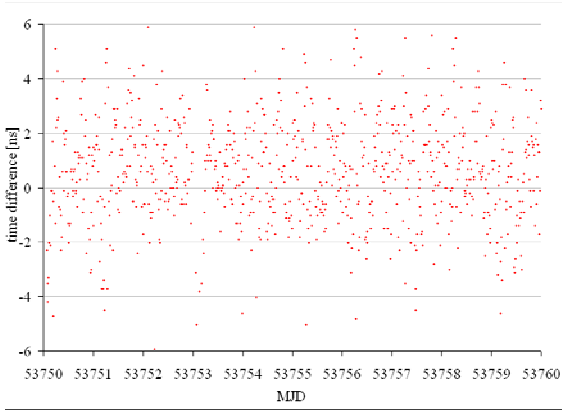

Fig. 3. [*UTC (AOS) - BIPM clock*] by single-channel GPS C/A common-view.

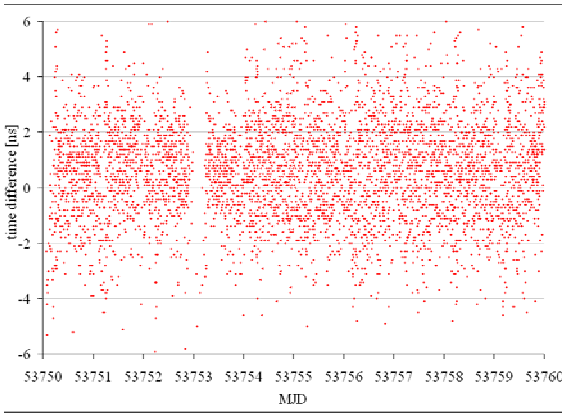

Fig. 4. [*UTC (AOS) - BIPM clock*] by multichannel GPS C/A common-view.

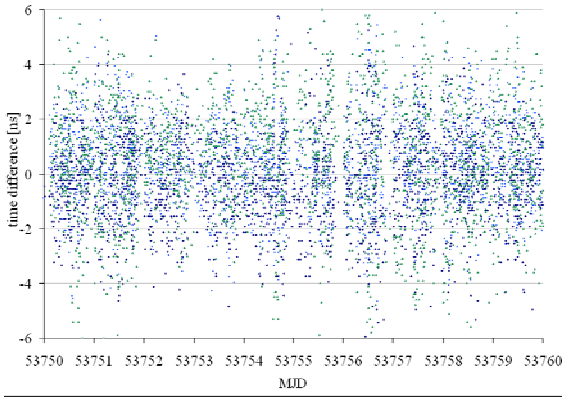

Fig. 5. [*UTC (AOS) - BIPM clock*] by multichannel GLONASS C/A and P common-view.

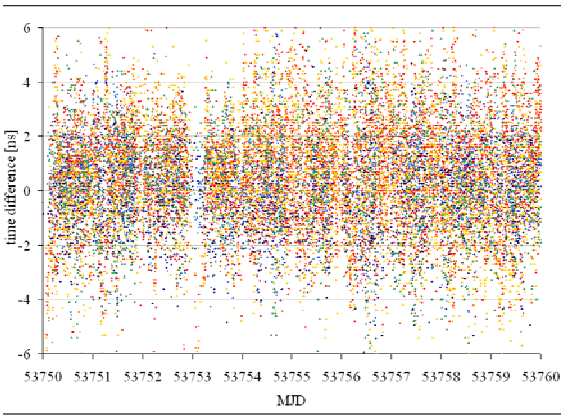

Fig. 6. [*UTC (AOS) - BIPM clock*] by multichannel GPS+ GLONASS common-view.

Figure 7 shows the TDEV of CV time transfer using GLONASS multichannel C/A (a), GPS multichannel C/A (b) and GPS+GLONASS method (c). The observations were not corrected for ionosphere observations and precise orbits.

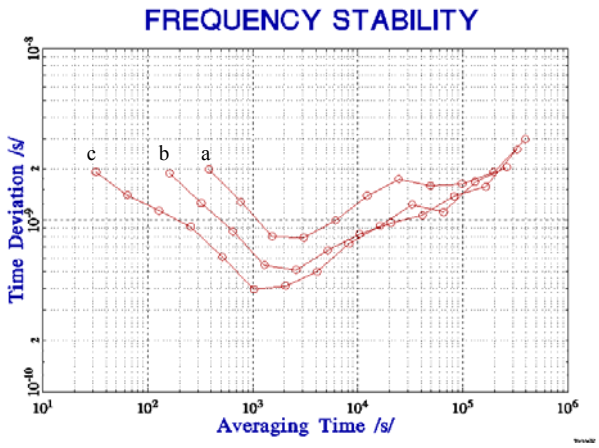

Fig. 7. Time deviation of [*UTC (AOS) - BIPM clock*] as given by multichannel GLONASS C/A (a), by multichannel GPS C/A (b) and multichannel GPS+GLONASS (c) observations.

All data presented, for averaging period of half a day and more, are affected by a noise. This noise might be due to the short period of UTC(AOS) steering, but it requires further investigation calling for more data.

V. CONCLUSION

The results confirm that a combined use of GPS and GLONASS is feasible, despite the differences between the two systems.

A significant increase of daily multichannel GPS + GLONASS common-views in comparison with the single-channel GPS link improves the reliability of the time transfer. A theoretical gain in stability is of (847/89)1/2=3,1.

Investigation reported in this paper demonstrates that GLONASS and GPS+GLONASS time links might be considered by the BIPM, initially as back-up links for TAI calculation, and later as possible official time links.

REFERENCES

[1] W. Lewandowski, J. Azoubib, G. de Jong, J. Nawrocki, J. Danaher, *A New Approach to International Satellite Time and Frequency Comparisons: 'All-in-View' Multi-Channel GPS + GLONASS Observations*, Proc. ION-GPS, 1997, pp. 1085-1091.

[2] W. Lewandowski, J. Azoubib, A.G. Gevorkyan, P.P. Bogdanov, J. Danaher, G. de Jong, J. Hahn, 1996, *First Results from GLONASS Common-View Time Comparisons Realized*

According to the BIPM International Schedule, Proc. 28th PTTI, 357-366.

[3] J. Azoubib and W. Lewandowski, 2000, *Test of GLONASS precise-code time transfer,* Metrologia, **37**, 55-59.

[4] A. Foks, W. Lewandowski, J. Nawrocki, *Frequency biases calibration of GLONASS P-code time receivers*, Proc. 19th EFTF, 2005, Besancon, France.

EUROMET project 529: Results of the 2004 GPS receiver calibration campaign

Proceedings of the 20th EFTF, 2006

Juan Palacio [1],* Fco. Javier Galindo [1], Hector Esteban [1], Jose A. Lima [1], Gerrit de Jong [2], Erik Kroon [2], Dirk Piester [3], Jean-Yves Richard [4], and David Valat [4]

[1] *Real Instituto y Observatorio de la Armada (ROA), San Fernando, Spain*
[2] *NMi Van Swinden Laboratorium (VSL), Delft, The Netherlands*
[3] *Physikalisch-Technische Bundesanstalt (PTB), Braunschweig, Germany and*
[4] *LNE-SYRTE (Système de Références Temps-Espace-OP), Paris, France*

The goal of the EUROMET Project 529 is to extend the GPS receiver calibrations performed by the BIPM to all the European Laboratories that contribute with their data to the computation of the TAI. During 2004 a TTR6-AOA GPS receiver from ROA has been sent to selected European Laboratories with some expertise in former GPS calibration trips, to elaborate a procedure valid within Europe.

A relevant result of the experience is that the pilot laboratories, ROA and VSL, have gained a valuable experience allowing to increase the performance of the 'traveling standard' and have confidence in the results.

In this paper the results of the year 2004 calibration trip are exposed including the expression of the considered uncertainties well below ten nanoseconds.

I. INTRODUCTION

The circulation of a traveling receiver led by BIPM, has allowed participated timing laboratories to calibrate their Common View GPS links. The effort done by the BIPM Time Section is recognized and a corresponding effort from the time laboratories is required to extend the calibration results to other laboratories not visited in the past. According to the spirit of the MRA, the traceability of the Regional Metrological Organization laboratories must be an issue of the concern of the members. In Europe, the laboratories that participated in the past GPS calibration trips were chosen from those ones which in the time of the trip were equipped with a TWSTFT station. These are only 10 of a total of 28 European laboratories that participate to TAI. Thus, there is a need for such a work to be performed. The EUROMET Time and Frequency Technical Committee approved during the annual meeting held at Torino in the year 2000, to carry out a Cooperation Project to circulate a NBS GPS time receiver to extend the calibration to all laboratories participating to TAI.

II. THE TRAVELING SET

All the components of the setup were transported in a single box, subdivided in compartiments. The receiver, a TTR-6 AOA model s/n 419, is a single channel GPS receiver, specially designed for time transfer. The original power supply unit of the receiver was changed on Februry 15^{th} 2002 after it failed; all other components of the receiver remain original. The original antenna, s/n 527, was modified to allow it to be mounted on a metal ground plate to reduce the multipath. The length of the IF and LO cables was chosen to fit the maximum distance between the roof and the measurement room of the visited laboratories. So a one hundred meters pair of cable was prepared and calibrated at ROA. No measurements of the cables were required nor requested to be done in each visited laboratory. A temperature sensor was also included to store the temperature near the antenna during the calibration, and the temperature inside the box during the transport. Unfortunately, temperature data recorded during the trip were missed due to a communication failure of the device. A personal computer was prepared to control the functioning of the receiver and to increase the number of tracks per day up to 90, as explained in [1]

III. THE CALIBRATION TRIP

The receiver setup was completed at ROA on December 30^{th} 2003, and it was installed in the environmental controlled room and the results were stored in the hard disk of the computer. As the master GPS receiver at the laboratory and the traveling one were controlled by an external computer, a mean of 80 tracks per day were available for common-view.

On February 03^{rd} 2004, MJD 53038, all parts were tidily packed in a box as seen in Figure 1 and the box was sent for the calibration trip to VSL, PTB and OP, and afterwards back to ROA. The traveling receiver was operated in parallel to the local reference GPS receiver in a common clock experiment.

In the Table I, the days the receiver collected data at each laboratory, the total number of tracks performed by the traveling receiver, and the number of tracks used for the CV are shown.

One inmediate conclusion is that the traveling receiver collected more data than the local ones, and

*Electronic address: jpalacio@roa.es

FIG. 1: Box ready for the travel.Ground plate at the top .

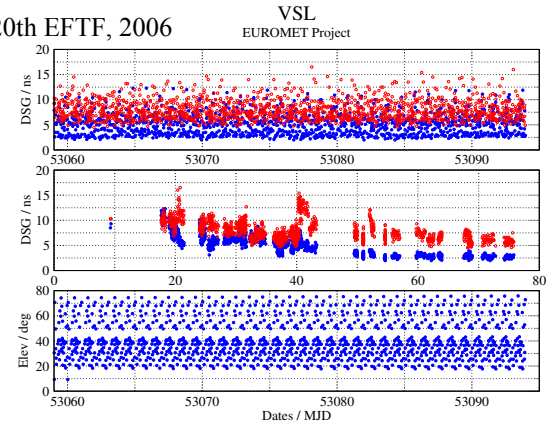

FIG. 2: DSG values and elevation of tracks at VSL.

TABLE I: Campaign schedule.

Lab	Interval Days	Total tracks	Used tracks	Perc.
ROA	53003 - 53037	2813	2694	96%
VSL	53059 - 53093	2722	1522	56%
PTB	53109 - 53128	1578	871	55%
OP	53135 - 53156	1775	943	53%
ROA	53164 - 53191	2881	2170	74%

thus only the 56 per cent of them were usefull for CV, because the local receiver was working as originally programmed.

IV. ANALYSIS OF THE DATA

To analyze the quality of the stored data, we studied the DSG columm provided by the standard format. This value (Data Sigma) corresponds to the Root-mean-square of the residuals to the linear fit of the 52 points after obtained the quadratic fit [2]. We analyzed the DSG values with respect to the elevation, to perceive the origin of unexpected high data scattering that appeared at some sites. In the following graphs the red (brigth) triangles correspond to the data from the traveling receiver and the solid blue (dark) dots are from the local one.

A. VSL

Refer to FIG. 2. VSL's receiver is the least noisy of the involved local GPS. It is an original NBS design s/n VSL01, constructed at VSL. The traveling receiver shows higher noise in all the elevations compared to the local one, but particularly around 40 and 50 degrees, probably due to the surrounding elements on the roof around the antenna. Most of the tracks are allocated between 20 and 40 degrees of elevations, which is a limiting factor for the comparison due to the high DSG values obtained for these elevations.

B. PTB

While the receiver was traveling from VSL to PTB the BIPM issued a new tracking schedule to be uploaded to the receivers at MJD 53097. A new extended schedule table was issued to cover the gaps of the BIPM's table and uploaded to the computer before connecting it to the traveling receiver. The effect of the new schedule was accompanied by a concentration of the tracked satellites with elevations around 40 degrees, in contrast with the concentration on two differentiated elevations observed at VSL.
The local GPS receiver unit was a TTR-5 AOA model s/n 156.

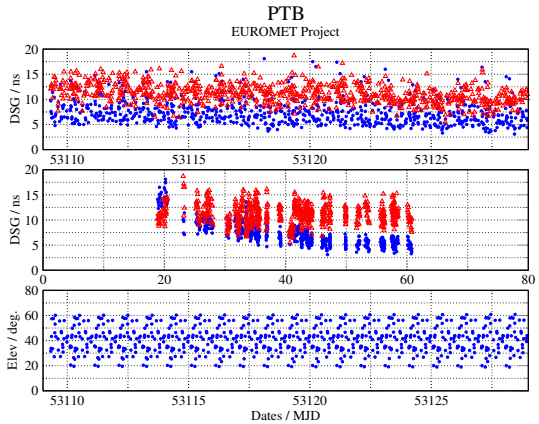

FIG. 3: DSG values and elevation of tracks at PTB.

Refer to FIG.3. A slight increase in the mean of the DSG values of the tracks performed by the traveling receiver is detected at PTB, as observed in the DSG vs elevation graph and comparing it to what obtained at VSL. Also, the DSG values remain mostly constant for

all the elevations, against what it is expected, lower DSG values for higher elevation satellites.

C. OP

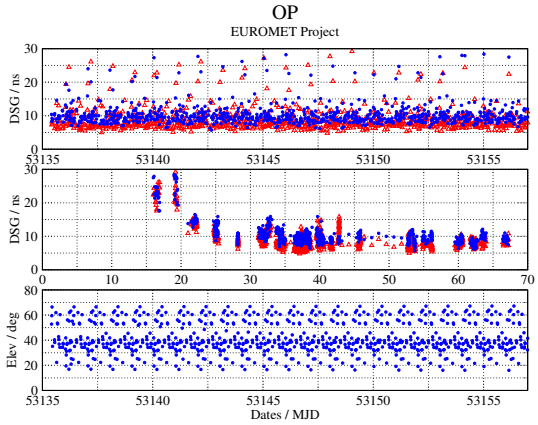

FIG. 4: DSG values and elevation of tracks at OP.

At OP the DSG values for the traveling receiver was lower than those of the local receiver, which is mainly due to the effect of the ground plate that eliminates rebounds of signals on elements of the roof close the antenna. See FIG 4. The site for the antenna at OP is surrounded by high buildings preventing the tracking of satellites below 30 degrees of elevation; in the graph some satellites below 30 degrees of elevation are shown, corresponding to the azimuths with open sky. However, larger DSG values were observed compared to low elevation satellite trackings at other sites.
The local GPS receiver unit was a TTR-5 AOA receiver, designated as AOA51.

D. ROA

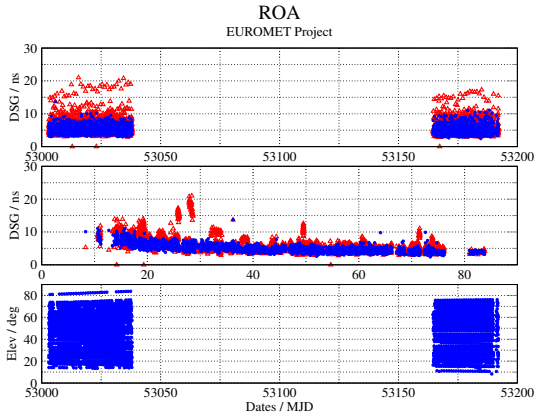

FIG. 5: DSG values and elevation of tracks at ROA.

In FIG 5 two different zones are shown in the graph, corresponding to the period of time before the departure and after the arrival. We observe that the traveling receiver obtains lower DSG values by the end of the trip, due to change of the tracking schedule that selects higher elevation satellites shortly after the changing date. This situation degrades with time and some satellites are going slowly to low elevation, having the effect of increasing the noise of the track.
The change of the tracking schedule table has no considerable effect in density of the elevation of the tracked satellites (lower graph), because the extended schedule table selects the higher elevation satellites for the common view measurements in the European region.
The local GPS receiver was a TTR-6 AOA model s/n 253.

V. RESULTS

To obtain the results of the comparison, the data are subtracted to get the Ref $_{laboratory}$ - Ref $_{traveling}$ differences. A 3σ filter is applied to the results, to eliminate those differences whose residuals with respect to the mean are greater than three times 'sigma'. The DSG values of each corresponding track are combined to get a common DSG value ($DSG_{total} = \sqrt{DSG_{Lab}^2 + DSG_{Trav}^2}$). The raw differences are plotted and also the histogram of the data is displayed. Then one point per day is obtained running a weighted average window over a period of time of a complete day, using the inverse of the squared combined DSG as the weighting factor. The program also produces the standard deviation of the mean of the data included inside the one day window.
The intermediate results obtained in each laboratory are shown in pictures 6 - 9 and Table II sumarizes the results.

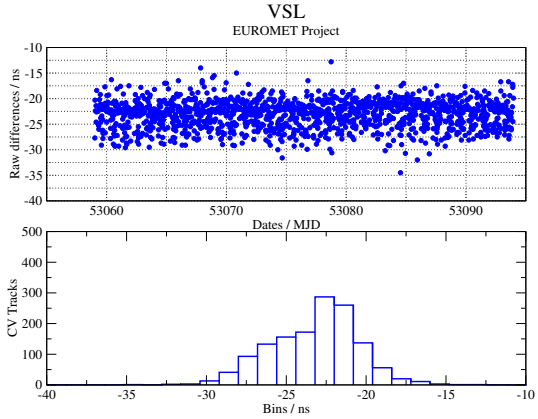

FIG. 6: Mean phase differences between VSL and traveling receiver

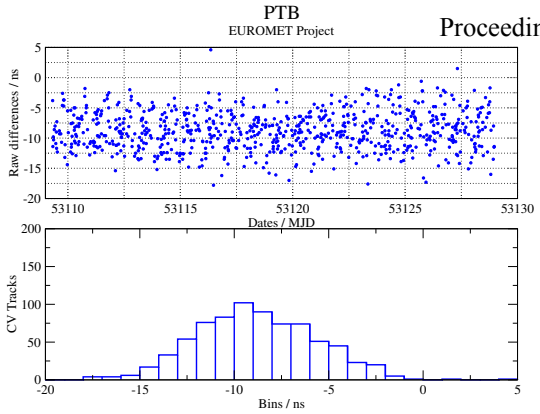

FIG. 7: Mean phase differences between PTB and traveling receiver

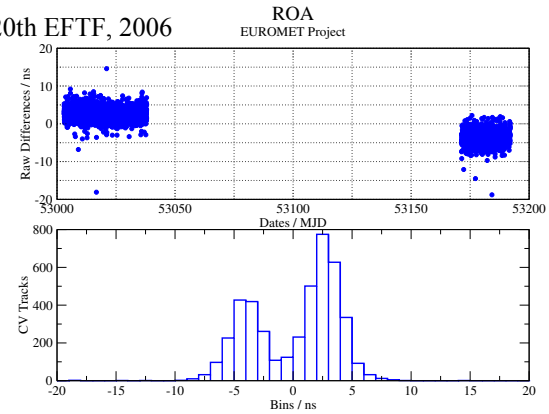

FIG. 9: Mean phase differences between ROA and traveling receiver

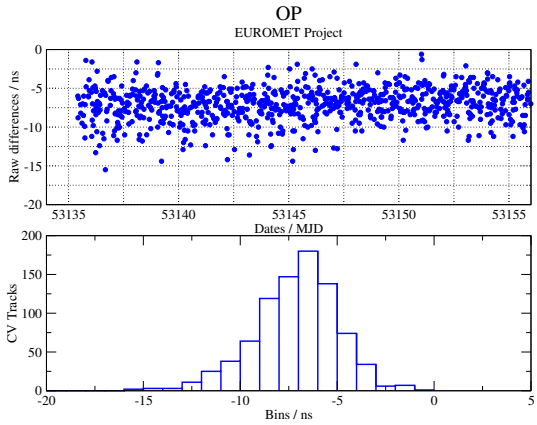

FIG. 8: Mean phase differences between OP and traveling receiver

The histogram at VSL shows an accumulation around the -22.5 nanoseconds bin but most of them are closed in an interval of 5 nanoseconds centered at this value.
The dispersion of the data is larger at PTB. They are centered around the -9 nanoseconds bin, but the interval is 7 nanoseconds.
At OP, the values are centered around the -7 nanoseconds bin, with an interval centered in this bin of 5 nanoseconds.
When looking at the graph corresponding to ROA, FIG 9, one can see that there are two zones of concentration: one around the +2.5 nanoseconds bin and the other around the -4 nanoseconds bin. They correspond respectively to the days previous to the trip and the days after the arrival. A jump in phase was detected when the receiver was back, but no indication about its nature was found.

TABLE II: Results of the raw differences. Units ns

Lab	Mean difference	σ	Mean tracks/day
ROA	2.71	0.17	77
VSL	-23.12	0.43	43
PTB	-8.79	0.60	43
OP	-6.86	0.59	43
ROA	-3.92	0.18	77

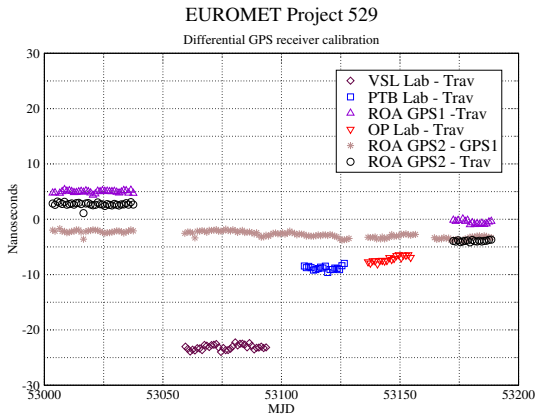

FIG. 10: Daily mean

The source of this jump could be either the traveling receiver or the local receiver at ROA. To discriminate between both of them, a third receiver, a TTR-5 receiver (s/n E63) that acts as a spare at the laboratory, was included in the analysis.
Figure 10 shows the differences obtained following the procedure previously described, including the spare receiver at ROA (named ROA GP1) . Observing the graph, the 'star' symbols show that the differences between the receivers at ROA (GP2 - GP1) is nearly constant during the whole campaign. So we must conclude that the source of the jump was the traveling receiver.

We have forced the receiver at ROA with series of power off and on cycles according to the calibration

TABLE III: Results of the calibration. Units: ns

Lab	Diff.	$u_{A(1\sigma)}$	$\varepsilon_{closure}$	u_{ε}	y	$U_{(k=2)}$
ROA	2.71	0.17	6.63	0.25	2.7	7.2
VSL	-23.12	0.43	6.63	0.25	-23.1	7.6
PTB	-8.79	0.60	6.63	0.25	-8.8	7.9
OP	-6.86	0.59	6.63	0.25	-6.9	7.9
ROA	-3.92	0.18	6.63	0.25	-3.9	7.2

trip practice in wich the receiver is shipped between different laboratories, to quantify the maximun error of the jumps we expect to have. After several cycles, we have not detected significant quantities.

The difference between the initial value at ROA and the value obtained when the receiver returned is -6.63 ns and its uncertainty (1σ) 0.25 ns. Assuming this figure as the closure error, combining the uncertainties and using a covering factor k=2 in the uncertainty budget, we have the results for the calibration trip in Table III.

VI. CONCLUSIONS

- EUROMET has demonstrated to be prepared to extend the past GPS CV calibration trips carried out by BIPM within the area of its responsability.
- For calibration purposes it is preferred to select high elevation satellites to avoid the multipath effect and reduce the DSG values of the individual tracks residual. This can be successfully achieved using external computers to drive the SC GPS receiver.
- Using two receivers at the pilot laboratory can avoid misinterpretations of phases jumps observed during the experience.
- The use of a ground plate can decrease the effect of multipath.
- The selection of the site for the antenna of the traveling standard is not trivial, the presence of obstacles, reflecting parts, etc., should be considered. The coordinates of the site should be determined using the same reference frame as the local GPS antenna point.
- Using an external PC to drive the SC NBS GPS receivers can extend the performance of the receivers and the quality of the comparison. When both receivers, the local and the traveling, are managed in this way, the standard deviation of the results are reduced in a range going from 30 to 50 per cent.
- For the next calibration trips, an additional computer will be included to increase the number of high elevation satellites tracks.

[1] J. Palacio et al. *A contribution for the improvement of GPS CV time transfer technique.* **Proceedings of the** 18^{th} **EFTF**, 140, 5-7 April 2004, Guilford (2005)

[2] D.W Allan, C. Thomas, *Metrologia* **31**, 69 - 79, (1994)

Proceedings of the 20th EFTF, 2006

Research and Application of Multi-channel GPS Common-view Receiver in NIM

Zhang Aimin and Gao Xiaoxun
National Institute of Metrology, Beijing,China
zhangam@nim.ac.cn, gaoxx@nim.ac.cn

Abstract

GPS Common-view is a very important and widely used technology for time and frequency transfer. The multi-channel GPS common-view receiver has been developed successfully in NIM China. This receiver is composed of a VP ONCORE engine made by Motorola company and a .high precision time interval counter（TIC）developed by our staff. the resolution of the TIC is 50ps. The software is accordant with standardization guide for data process software of GPS common-view method. Compared with single channel receiver, this multi-channel receiver has more friendly interface, it is more convenient to operate and also has a stronger ability to analyze and process data. The experimental result shows the time transfer uncertainty of the multi-channel GPS receiver is less than 4ns in the condition of common-clock on zero base line. As for the complicated circumstance in NIM China, Some experiments have been done in order to decrease the effect of the circumstance. The multi-channel receiver has been used in the International Atomic Time Comparison System of NIM China, and also been used in domestic remote time and frequency calibration service. Some detail will be described in this paper.

1． Introduction

GPS Common-view is a very important and widely used technology for time and frequency transfer. The multi-channel GPS common-view receiver has been developed successfully in NIM China. In this paper we introduce the principle and the performance of the multi-channel GPS common-view receiver. As for the complicated circumstance in NIM China, Some experiments have been done in order to decrease the effect of the circumstance. The multi-channel receiver has been used in the International Atomic Time Comparison System of NIM China and report the data to BIPM, and also been used in domestic remote time and frequency calibration service.

2. NIM multi-channel GPS common-view receiver

Time links from UTC(NIM) to UTC was based on single-channel GPS common view receiver since 90's. In order to improve the link, and also to establish remote time and frequency calibration service system in China, a multi-channel GPS common view receiver has been developed in NIM. This receiver is composed of a VP ONCORE engine made by Motorola company and a .high precision time interval counter（TIC）

The TIC card is developed by our staff, The resolution is 50ps. it satisfies CCTF recommendation for hardware of GPS common view receiver.

The principle of this TIC is as follows

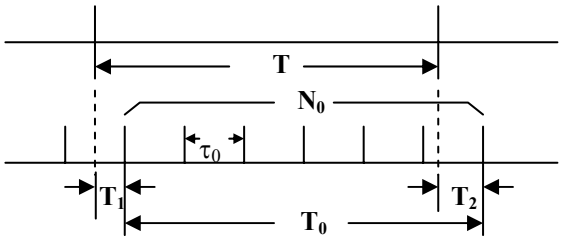

Fig.1 Principle of TIC

T is the time interval to be measured:

$$T = T_0 + T_1 - T_2$$

N_0 is the integer number of the pulse measured, and $T_0 = N_0\tau_0$

T_0 can be measured accurately, and if we can measure T_1 and T_2 accurately then the ±1 errors can be eliminated.

We enlarge T_1 and T_2 first, then measure them by time base τ_0.

Suppose we enlarge T_1 and T_2 2000 times. and we can get pulse data which are N1 and N2, then we can get the following formula.

$$T = \left(N_0 + \frac{N_1}{2000} - \frac{N_2}{2000} \right) \tau_0 \pm \delta T$$

$$\delta T \le \pm \frac{2}{2000} \tau_0$$

If time base is 10 MHz, then $\tau_0 = 0.1\mu s, \delta T \le 0.1ns$.

VP ONCORE Engine is composed of an antenna and a metal-sealed PCB，provided with one RS232 serial port. We choose Motorola Binary Format for data transfer protocol. By sending commands to VP ONCORE GPS Engine, we can receive corresponding response messages. And we also can get GPS 1pps signal.

1pps from Local atomic clock and 1pps from VP ONCORE GPS engine are used as start and stop signal of TIC.

Fig 2 TIC card integrated with Vponcore engine

The software for NIM GPS Multi-channel GPS receiver consists of 3 parts:

(1) communication between the computer and VP ONCORE GPS engine

(2) communication between the computer and TIC

(3) data process according to the standardization guide for data process software of GPS common-view method published by CCTF.

The software add some functions that single channel receiver could not have, such as: automatically position，Input of known antenna coordinates，compensation of 1pps antenna cable delay，compensation of GPS receiver delay，selection for GPS satellites mask angle，etc.

Some experiments were carried out with 3 GPS receivers(2 single channel GPS receivers and the NIM multi-channel GPS receiver) under the condition of zero baseline, common clock and common view. With this measurement setup, the common errors caused by satellites ephemeris, ionospheric delay, tropospheric delay and antenna position etc. were all cut off. By comparing the common uncertainty of each 2 receivers, we can get each receiver's uncertainty. Through the experiment results, we deduced the uncertainty of the NIM multi-channel GPS receiver is 3.54ns when the elevation is more than 40 degrees.

And also we carried out the experiments with 2 NIM multi-channel GPS receiver under the condition of zero baseline, 2 different local clock and common view. From the experiment results, we can see that relative frequency difference of two atomic clocks measured by 2 Multi-channel GPS receivers is very close to the relative frequency difference directly measured by 2 atomic clocks. It indicates that the performance of NIM multi-channel GPS receiver is credible.

3. Experiments to decrease the effect of the circumstance.

The GPS antennas are set on the top of our building, but the top is also an EMC open field. The reflection affects the GPS common view result. In order to obtain good results for GPS common view and time measurement,

two ways were taken. First, a chock ring was installed on the top of GPS antenna, which reduces the reflection of GPS signal from feild close to the antenna. Fig.3 shows the data before and after the chock ring was installed, it is obviously that after the chock ring was installed, the data is more stable.

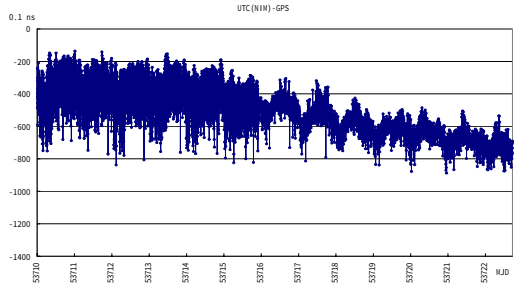

Fig.3 comparison before and after the chock ring was installed

Another way is a new 1PPS distribution amplifier was implemented in the system, this amplifier has good driving capacity for long distance, it also has good isolation and keeps sharp rising edge of 1PPS signal from output of the clock.

4. Application of the NIM multi-channel GPS receiver

Recently, more and more Hydrogen masers have been used in different fields in China, because of the difficulties in transiting this device to the metrology institute and the need to keep it traceable to UTC(NIM) , the method of GPS common view is introduced, it is also called remote calibration method. The NIM multi-channel GPS receivers are used in the remote calibration of the Hydrogen masers. NIM makes the common view time schedule, then NIM(place A) and the customer(place B) all use the NIM multi-channel GPS receiver to measured the time difference between their 1pps signal and GPS 1pps signal simultaneously according the schedule, NIM executed the calculation and get the relative frequency difference of the Hydrogen maser under test, the averaging time was 1 day or 10 days.

Suppose ΔT_{AG} and ΔT_{BG} are average time difference between GPS time and local clock on place A and place B respectively, then $\Delta T_{AB} = \Delta T_{AG} - \Delta T_{BG}$ is the time difference of place A and B, and the fractional frequency difference of the Hydrogen maser under test is:

$$y(\tau) = \frac{\Delta f}{f_0} = \frac{\Delta T_{AB2} - \Delta T_{AB1}}{\tau}$$

ΔT_{AB1} and ΔT_{AB2} are the average time difference of place A and B on the first and second day respectively, and τ = 1 day = 86400×10^9ns. The uncertainty is less than 1×10^{-13}.

If τ =10 days, ΔT_{AB1} and ΔT_{AB2} are the average time difference of place A and B on the first and 11th day respectively. The uncertainty is less than 1×10^{-14}.

With the development of GPS time transfer technology, the remote calculation will be a more and more popular way of time and frequency calibration.

5. References

[1]Gerard Petit, Claudine Thomas, Philippe MoussayJohn A. Davis, Mihran Miranian ,Juan Palacio Multi-channel GPS common view time transfer experiments: first results and uncertainty study[J]

[2] D.W.Allan and C.Thomas. Technical Directives for Standardization of GPS Time Receiver Software[J]. Metrologia,1994,31：69-79

6. Acknowledgments

We would like to thank Mr. Gao Yuan, Ms. Zhang Yue, Mr. Wang Weibo and all the colleagues in the Time and Frequency Group who have contributed to the development of the multi-channel GPS receiver.

Proceedings of the 20th EFTF, 2006

Establishment of a TWSTFT link between Asia and Europe connecting NICT and PTB

H. Maeno[1], M. Fujieda[1], D. Piester[2], A. Bauch[2] , M. Aida[1], Q. T. Lam[1], T. Gotoh[1], and Y. Takahashi[1]

[1]*National Institute of Information and Communications Technology*
4-2-1 Nukuikita-machi, Koganei, Tokyo 184-8795 JAPAN
[2]*Physikalisch-Technische Bundesanstalt*
Bundesallee 100, 38116 Braunschweig, Germany

Electronic address: maeno@nict.go.jp

In this contribution we report on the installation of a two-way satellite time and frequency transfer link (TWSTFT) between NICT and PTB and discuss first observation results. Specific features of the architecture of the Earth stations are the use of the multi-channel time-transfer modems developed by NICT, which are also in operation in the Asia-Pacific TWSTFT network, and optical fiber connections for radio frequency transmission between indoor and outdoor equipment. Especially at PTB a distance of 1 km has to be bridged by that way. We have performed time transfer alternatively with two different reference sources, caesium standard based realizations of UTC and hydrogen masers (HM) at both sites, NICT and PTB. First results show Allan standard deviations at 10^4 s of $1x10^{-13}$ and $5x10^{-14}$, respectively. This represents a significant improvement compared to the GPS based comparisons made hitherto. In a first approach towards an improvement of the TWSTFT stability we study the causes of diurnal variations appearing in the measurements.

1. INTRODUCTION

Two-way satellite time and frequency transfer (TWSTFT) is the leading technique for intercontinental comparisons of time scales. At present, two networks employing TWSTFT exist worldwide, the Asia-Pacific net which is operated by NICT and the Europe-USA net [1]. Following first TWSTFT experiments between Asia and Europe [2], a link between NICT and PTB was established to connect both networks by means of TWSTFT.

After a description of the installed hardware and the operation parameters we show first results of clock comparisons between NICT and PTB using TWSTFT. We investigated the stability of the link by using different frequency sources at both sites, caesium standards or hydrogen masers. Thereafter, routine operation was started comparing the local realizations of UTC at each laboratory. An analysis of four months data recording is presented. In a first approach to improve the stability of the link we investigate diurnal effects.

II. HARDWARE AND OPERATION

In addition to the existing TWSTFT systems for clock comparisons between institutes in the Pacific-Rim region [3], NICT initiated the establishment of a TWSTFT link between Asia and Europe. Two earth stations were designed and hardware was initially tested to be installed thereafter at PTB and NICT. Both stations consist of standard telecommunication up- and down-converters (UC, DC), solid state power amplifiers (SSPA), low noise amplifiers (LNA), and antennae. The modem is a 8-receive-channel modem developed at NICT [4]. In Fig. 1 a block diagram of the hardware is shown, and in Fig. 2 the earth stations of PTB and NICT for communication with the PAS-4 satellite is depicted. At both sites the modems, UC, and DC are located indoors in temperature stabilized environment (temperature variations < 1 K). Only SSPAs, LNAs and antennae are installed outdoors. The LNAs are mounted in temperature stabilized boxes. At PTB and NICT 2.4 m diameter Cassegrain and offset antennae have been installed, respectively. RF frequencies are transmitted from indoors to outdoors and vice versa via 40 m coaxial cables at NICT. At PTB the antenna is located at a distance of about 1 km from the time laboratory. To transmit the RF frequencies over that distance an optical fibre cable with electro-optical (E/O) and optical-electrical (O/E) converters have been installed indoors and outdoors. The separation in longitude between both sites is quite large which implies low elevation angles. Fortunately, the PAS-4 satellite is positioned such that a rather symmetrical signal path with elevation angles of 8^o at PTB and 9^o at NICT is feasible. At present, we use up- and down-link frequencies of 14.265000 GHz and 12.678250 GHz (14.426250 GHz and 11.465000 GHz) at NICT (PTB), respectively. The occupied bandwidth is 2.5 MHz.

After an initial performance evaluation and an up link access test (UAT), the first observation succeeded on July 22nd in 2005. Tentative operation started on that day. During August and September 2006 different test measurements were carried out (see Section III). The transponder frequency was changed to avoid interference problems on 18 October 2005. Regular operation started on 26 October 2005. Starting from 1 January 2006, data formatted according to the relevant ITU-R recommendation [5] are submitted to the BIPM on a weekly basis.

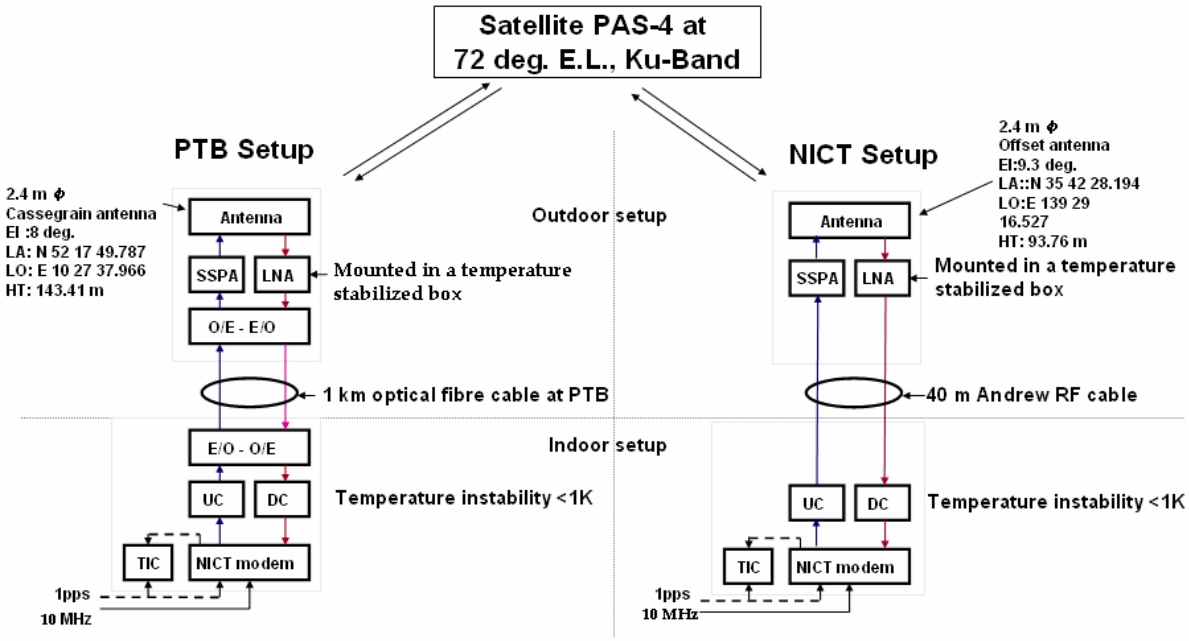

Figure 1. Block diagram of NICT-PTB Link

PTB Antenna of 2.4m

Equipment in PTB

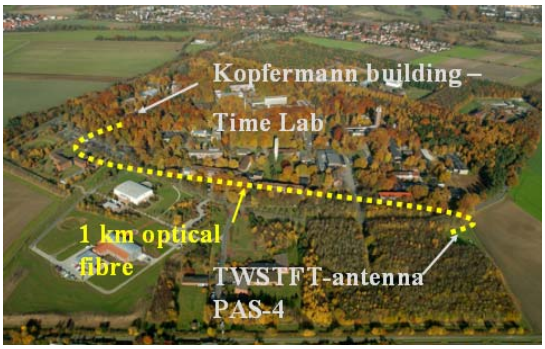

Optical fibre cable in PTB

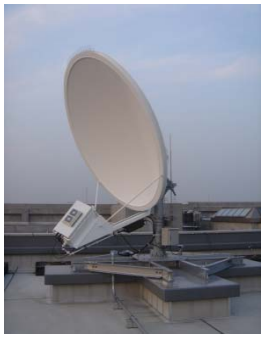

NICT Antenna of 2.4m

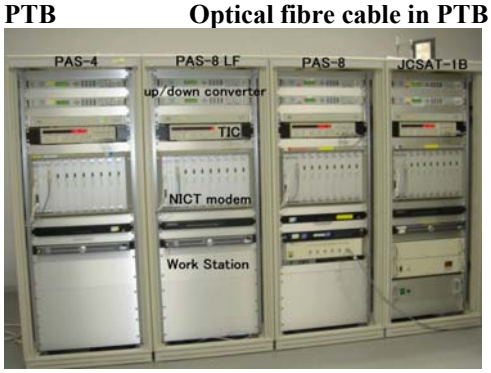

Equipment in NICT

Figure 2. Earth station for PAS-4 satellites of PTB and NICT

III. Short Term Stability

During the first operation phase we changed the frequency references from caesium standards based local realization of UTC (CS) to hydrogen masers (HM) of the modems to investigate the achievable short term frequency stability. Two measurement series were recorded, one with CS connected to the modems and the other with HM as the source for the frequency reference. The series consist of six and nine days continuous recordings of one second measurements UTC(NICT) – UTC(PTB) and HM(NICT) – HM(PTB), respectively. In Fig. 3a and b the results of Allan standard deviation analysis are shown for both cases, respectively (dots). The slope reveals white phase noise up to $\tau = 10^4$ s, and values of 1×10^{-13} and 5×10^{-14} at $\tau = 10^4$ s are reached. Reducing measurement noise by reducing the one-second-data to 5 minute averages results in a lower noise level (line). The dominant noise type changes to white frequency noise for CS, proving that 5 minutes averaging is sufficient. However, in the case of HM the noise type at 5 min is still white phase and a small bump at about $\tau = 4 \times 10^4$ s may indicate diurnal effects superposed to the time transfer information.

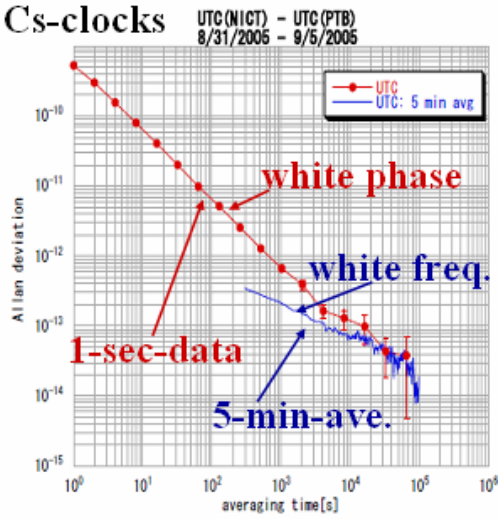

Figure 3a. Frequency stability of time transfer UTC(NICT) – UTC(PTB).

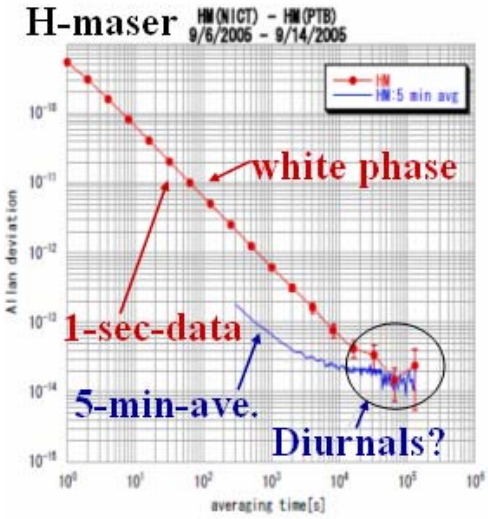

Figure 3b. Frequency stability of time transfer HM(NICT) – HM(PTB).

IV. FOUR MONTH OBSERVATION RESULTS

Since Nov 2005 the TWSTFT link is routinely operated. The one second data are reduced to one value per hour. The first 300 data points taken every hour are fitted with a quadratic function, and the midpoint is reported in the file format according to the well-known ITU-R recommendation [5]. Additionally, the link was calibrated using GPS P3 time transfer data provided by the BIPM [7]. The estimated uncertainty for a time comparison is thus $u_B = 5.0$ ns due to the uncertainty of the GPS link calibration. A comparison of the TWSTFT and the GPS P3 link is shown in Fig. 4. The red line represents GPS P3 data while the blue line represents the TWSTFT measurements. The course of both time series data show good agreement. In Fig. 5 the corresponding Allan deviations are displayed in the same colors. TWSTFT shows a significant improvement of the time-transfer stability compared to GPS P3. The noise level and slope of the Allan deviation plot at long averaging times is typical for Cs standards which were the frequency sources connected to the modems during this period of time. A change of the UTC(NICT) generation from a CS clock ensemble to a HM steered in frequency happened on 7 Feb 2006. Data taken afterwards (black crosses) reveal a reduced noise, and one can see the typical shot-noise limited frequency stability of PTB's primary standard CS2. Additionally, the Allan deviation of one year (starting in Feb 2005) CircT data are shown as black dots.

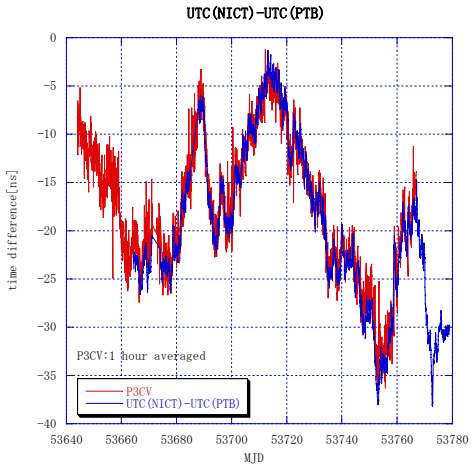

Figure 4. Time difference of UTC(NICT)-UTC (PTB)

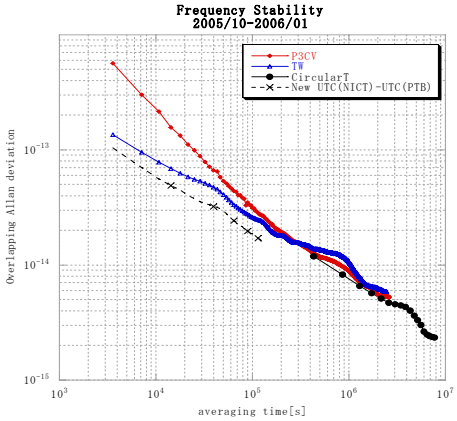

Figure 5. Frequency stability.

V. DIURNAL EFFECTS

A small bump in the Allan deviation at $\tau \approx$ ½ day visible in Fig. 5 indicates a diurnal effect superimposed to the time transfer. These variations were also observed by BIPM [6]. The correlation of these diurnals to the outdoor temperatures at both earth stations is analysed in the following. In Fig. 6, a five-days excerpt of the double differences GPS P3 - TWSTFT from the data shown in Fig. 4 is displayed together with records of the outdoor temperatures at PTB (upper graph) and NICT (lower graph). The GPS P3 analysis shows clear diurnals, so we attribute most of the effect visible in the double differences to the TWSTFT link. The correlation coefficient between the temperature records at PTB and NICT and the double differences are 0.26 and -0.57, respectively. The diurnal variation seems to be related to the temperature at NICT. In fact, the course of the temperature at NICT shows a strong day-to-day periodicity, which makes an analysis of the correlation much easier than in case of PTB. The main difference between the NICT setup and the PTB setup is the use of optical fibres at PTB instead of coaxial cables at NICT to connect indoor and outdoor equipment. However, the E/O and O/E mounted in an outdoor box have only minor temperature coefficients (overall < 25 ps/K) of the group delay. The source of the diurnals should be analysed in more detail in future investigations.

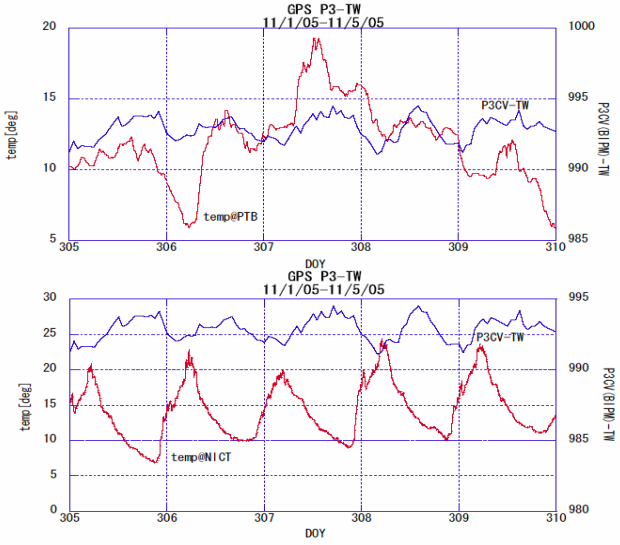

Figure 6. Double difference (ns) between P3CV and TWSTFT (blue) and local temperature (°C) at PTB (upper graph) and NICT (lower graph).

VI. CONCLUSION

On initiative of NICT, a TWSTFT link between NICT and PTB was established. This link has a baseline of about 10,000 km. This is the longest baseline in the world wide network of TWSTFT links used in the production of TAI. The time transfer is regularly performed and hourly data are reported to the BIPM. The observed diurnal variations are an important issue to be understood and its analysis will continue. Furthermore, in a cooperation between NICT, TL, USNO, and NIST a construction of an earth station at Hawaii is planned to expand the Asia-Pacific TWSTFT network to USA. Once this project is completed, an around the world TWSTFT network will be in operation.

Acknowledgements

We would like to express our thanks to T. Leder, C. Richter, J. Becker, and T. Polewka in PTB, and T&F members in NICT for their support during the installation of the link.

REFERENCES

[1] B. Guinot and E. F. Arias: "Atomic time-keeping from 1955 to the present"; *Metrologia*, Vol. **42**, No. 3, pp. S20-S30, 2005.
[2] H. T. Lin, W. H. Tseng, S. Y. Lin, H. M. Peng, C. S. Liao, G. de Jong, E. Kroon, M. J. Brakel: "The first two-way time transfer link between Asia and Europe"; *Proc. 35th PTTI*, 2-4 Dec 2003, San Diego, USA, pp. 71-79 (2004).
[3] H. Maeno, M. Fujieda, M. Aida, L. Q. Tung, R. Tabuchi, F. Nakawa, T. Suzuvama, Y. Takahashi: "TWSTFT plans for the Pacific-Rim region and Europe link"; *Proc. EFTF 2005*, pp. 459-463 , 2006.
[4] M. Imae, T. Suzuyama, T. Gotoh, Y. Shibuya, F. Nakagawa, Y. Shimizu and N. Kurihara: "Two Way Satellite Time and Frequency Transfer"; *Journal of the NICT*, Vol. **50**, No. 1/2, pp. 125-133, 2003.
[5] Recommendation ITU-R TF.1153-2: "The operational use of two-way satellite time and frequency transfer employing PN time codes"; Geneva, last update 2003.
[6] Z. Jiang and G. Petit, "BIPM first analysis of NICT-PTB TW link and comparison with GPS CV-AV P3 links BIPM"; *TM144*, 2006.
[7] Z. Jiang: private communication

Proceedings of the 20th EFTF, 2006

The Use of Ambiguity Resolution for Continuous Real-Time Frequency Transfer by Filtering GNSS Carrier Phase Observations

Carsten Rieck,* Per Jarlemark, and Kenneth Jaldehag
SP Swedish National Testing and Research Institute, Box 857, S-501 15 Borås, Sweden, Phone +46 33 165440, Fax +46 33 125038

We have studied the influence of phase ambiguities and their resolution on the quality of the station clock parameter when filtering real-time GNSS carrier phase observations. Especially the benefits of fixed integer phase parameters are discussed in this paper. An earlier work [1] describes a continuous real-time GPS carrier phase processing software based on Kalman filtering of common view satellite observations. In this processing carrier phase ambiguities were handled by estimating separate initial L3 phase parameters for each observed satellite. In such an approach the frequency estimation suffers from mapping of differential station coordinate errors into these non-integer start phase estimates. Most of the phase parameters are initialized with a biased error due to the fact that the orientation of satellite passes is unequally distributed, which in turn accumulates into the estimated station clock parameters. This introduces a constant error in the frequency estimation of the station clocks. Fixed integer phase parameters are one solution to the problem described.
The paper describes how to resolve integer phase ambiguities on single differences from a real-time data stream. At startup, at any time a new satellite is included to the computation and at any cycle slip occasion, the differential phase ambiguities are resolved ahead of the filtering process. In such a way the initial phase parameters do not need to be estimated by the filter and leaks of position errors into the clock parameters are minimized, i.e. they do not bias the estimated frequency. Aditionally, the Kalman filter is less computational demanding, which allows higher throughput and more stations to be computed at the same time. Even though the approach was only tested on GPS carrier phase observables, the method is generally applicable for any multi-frequency GNSS carrier signal.
Continuous real-time frequency estimations are very useful for precise system critical oscillator monitoring as for example in real-time interferometry applications (VLBI).

I. INTRODUCTION

In the following we consider GPS as an example of a generic multi-carrier-frequency GNSS system.
We have studied the influence of phase ambiguities and their resolution on the quality of the station clock parameter when filtering real-time GNSS carrier phase (CP) observations. In an earlier work [1] we describe a continuous real-time GPS common view carrier phase (L3) processing software based on Kalman filtering, that estimates station clock differences, tropospheric delays and constant non-integer float phase ambiguities ($F3$), in the following also called start phase or initial phase. All station positions are fixed and assumed to be accurately known with an uncertainty of a couple of mm. Such small systematic station coordinate errors have the potential to bias the initial phase estimates. Due to the fact that the orientation of the satellite passes is unequally distributed, it exhibits a dominant West-East orientation, every time a new satellite is allowed to contribute data to the filtering, the respective start phase is estimated with a systematic bias. Both the ambiguous start phase parameters and the station clock differences are described with a similar partial derivative that has no elevation dependence. This makes it difficult to distinguish between station clock drift and initial phase. Figure 1 shows how a typical GPS visibility at the Borås site evolves over the course of a day. In this case new satellites appear in the Western/Northern part of the sky and together with the dominant West-East orientation of the satellite passes create always a similar error in the start phase estimate if baseline errors exist. Thus the clock solution is mostly sensitive to errors in the East-West component of the station coordinate. Figure 2 summarizes the results of a few clock solutions estimated for the SP-PTB baseline. By applying deliberate East-West baseline errors the clock solutions comprise frequency errors, here visible as differences to a reference solution. A typical value is about 20ps/day per mm East-West coordinate error. Even other position component errors (i.e. North and Up) result in frequency offsets, but to a lesser degree. Table I lists approximate frequency error values for the SP-PTB baseline, that appear also to be valid for other (smaller) baselines. Also systematic tropospheric model errors at low elevation angles could cause the start phase to be wrongly estimated. As a result the frequency estimates of the stations clock differences are always biased, it is not possible to avoid this effect in our type of processing using $F3$ estimates. In order to overcome the described problem we have introduced integer ambiguity resolution in the real-time processing. Even though the created frequency offset errors are very small, these errors are apparent in comparison with the accuracy of todays

*Electronic address: carsten.rieck@sp.se

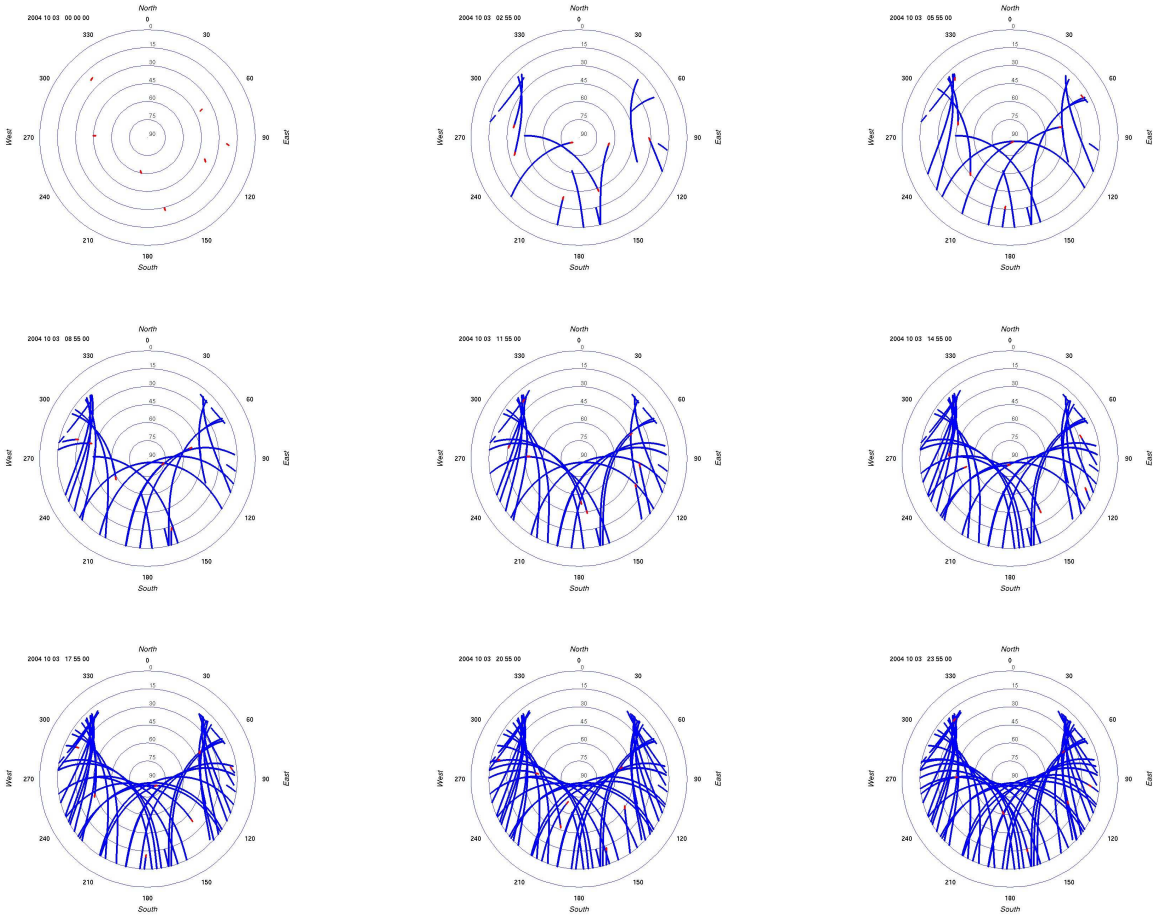

FIG. 1: Dominant West-East GPS satellite passes: visibility plots for 3rd of October 2004, Borås, Sweden; the majority of satellites pass from West to East. The current satellite positions are marked red.

atomic oscillators. Figure 3 shows a 65 day long continuous real-time CP processing in comparison with a time series derived from TWSTFT measurements, which we assume to have a zero mean frequency error. The frequency error seen in the graph can be translated to a 2 mm East-West baseline error.

II. PROBLEM DESCRIPTION

Forming L3 observables directly from L1 and L2, in case of GPS, has the advantage of eliminating the ionospheric delay with mm accuracy, but destroys the natural integer ambiguity relation of the two carrier signals by introducing non-integer ambiguities. These are estimated as L3 float start phase parameters ($F3$) by the real-time filter. But the estimates do not necessarily correspond to the right combination of L1, L2 ambiguities ($N1, N2$) due to unmodeled components in the observables, thus introducing an ambiguity error. In order to synchronize new satellite observations to a set of existing ones, it would be necessary to convert all phase parameters to a concurrent set of $N1$ and $N2$, which is generally difficult. Figure 4 pictures possible relations of arbitrary phase ambiguities between $N1$, $N2$ and the float area of the estimated $F3$. No distinction between the different values of a float area is possible because a float area can be mapped to an infinite number of $N1, N2$ combinations. A $F3$ ambiguous float area is a small area around a mapped $(N1, N2) -> \mathrm{F3}$ start phase estimate, which matches the noise level of the filtering. The small systematic errors introduced, by for example station coordinate errors, create an inconsistent set of phase parameters.

TABLE I: Frequency offsets due to station position errors in common view CP processing with float ambiguities.

Error Component	Absolute Δf	Relative Δf
East-West	20ps/day·mm	$2.3 \cdot 10^{-16}$/mm
North-South	3.5ps/day·mm	$4.1 \cdot 10^{-17}$/mm
Up	0.2ps/day·mm	$2.3 \cdot 10^{-18}$/mm

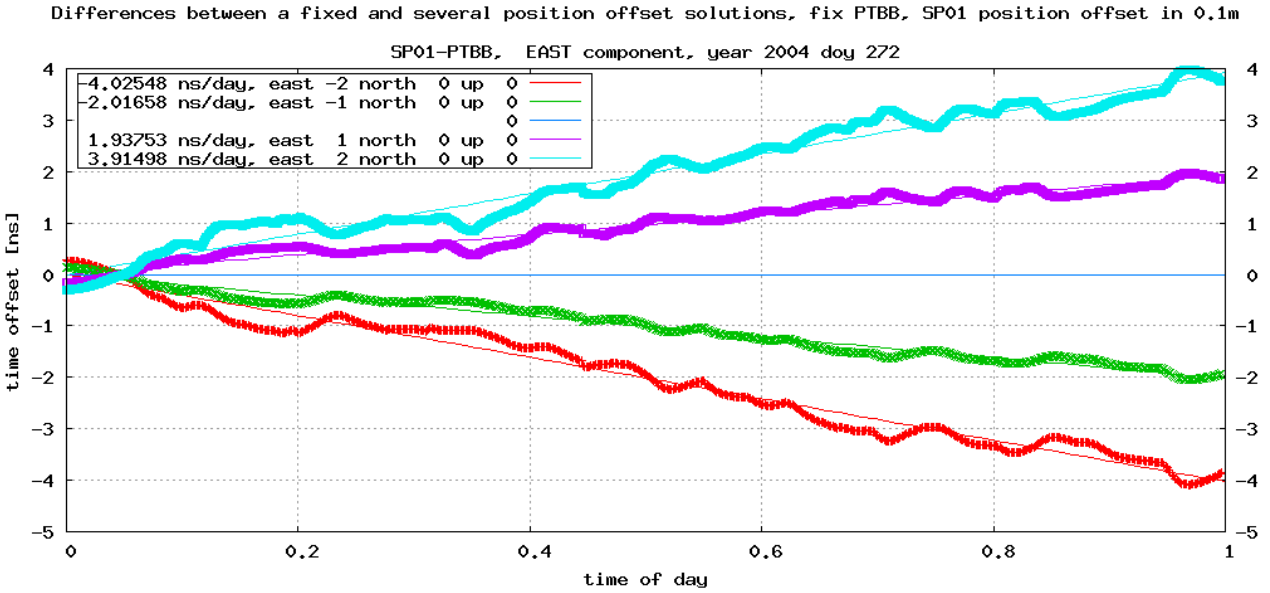

FIG. 2: Processed GPS carrier phase data PTBB-SP01: frequency offset error of the clock solution due to deliberate station coordinate offsets of SP01. The east components is especially sensitive because of the West-East dominance of the satellite passes. A 0.1m East offset causes a frequency offset error of about $2.3 \cdot 10^{-14}$

Thus it is desirable to determine $N1, N2$ before combining to L3. However, errors in the observables, mainly unmodeled tropospheric delay, unmodeled ionospheric delay and distance errors due to orbits can prevent the $N1, N2$ resolution at low elevation angles.

In order to illustrate the difference between **float estimation** and **integer determination** a very simplified satellite system is introduced in Figure 5. Imagine a single frequency $f = c/\lambda$ and two dimensional GNSS system. All the satellite clocks are perfect and exhibit no relative drift. Any of the max three satellites that are visible at any time are always measured in three well defined positions A, B and C. The receiving antenna is offset from its known position x_0 by Δx causing the observables to differ by $(-\epsilon, 0, \epsilon)$ for satellite measurements at (A, B, C), which are otherwise perfectly modeled (i.e. no atmosphere, perfect orbits, etc.). ϵ is a function of Δx, e.g. $\epsilon = -\cos\alpha \cdot \Delta x$, with α being the elevation angle to a satellite in position A or C. N_x defines the delay caused by the phase ambiguity of the respective measurement. This kind of error contribution also ensures a perfect receiver clock but the filter software does not assume this fact in its processing. For the following discussion it should be noted that no differences are considered, which does not limit the validity of the examples below. Table II describes some steps in the clock estimation for the two methods. A total of four satellites rise sequentially, passing positions A, B, C and disappear from sight after six time units t_0. In this limited model a measurement M_s to satellite s is defined as :

$$M_s(t) = A_s + C_s(t) \qquad (1)$$

where A_s defines the over the course of a satellite pass constant phase ambiguity of the carrier signal and C the station clock parameter.

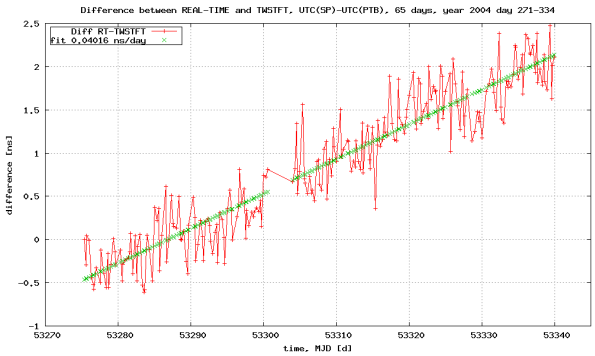

FIG. 3: Comparison between a GPS real-time clock solution and results from Two Way Satellite Time and Frequency Transfer (TWSTFT) of the baseline SP-PTB 623km. The calculated frequency offset can be translated to about a 2mm error in the East component of the baseline.

- Initially, no previous clock estimate exists at $t = 1$, thus the **FLOAT** method assumes the clock parameter C_1 to be zero. Since there are no other parameters to be estimated (Eq. 1) the filter sets the initial phase value A_1 to the value of the measurement M_1. At $t = 2$ A_1 is kept

constant and C_1 starts to accumulate an error which is caused by the assumption that all relevant effects are perfectly modeled. As the second satellite comes into view the filters best estimate about the new measurements's clock contribution C_2, is that it is equal to that of measurement 1, C_1, since the same receiver clock governs all channels of the receiver. In turn, also the initial phase A_2 is wrongly estimated. This error propagates through the entire processing and causes the averaged clock parameter C to exhibit a drift of:

$$\lim_{t\to\infty} \mathrm{FLOAT}\,(f,\epsilon) = \frac{\epsilon}{t_0} \qquad (2)$$

with t_0 defining the sampling interval.

- The **FIXAMB** method assumes that $\epsilon >> \lambda$ and thus can determine $A_1 = N_1$ at $t = 1$ by rounding the measurement M_1/λ. The error ϵ is entirely absorbed by the clock parameter C_1. At $t = 2$ and any subsequent sampling times the determined carrier phase ambiguity A_1 is still valid and used to determine the measurement's clock contribution C_1. Any new satellite is treated independently from each other reflecting that the filter allows model errors in the measurements. This causes the clock parameter $C = \mathrm{mean}(C_1 ... C_n)$ to be wrong at the beginning and at the end of the time series. For long observations times the clock drift is essentially zero:

$$\lim_{t\to\infty} \mathrm{FIXAMB}\,(f,\epsilon) = 0\ . \qquad (3)$$

It can be seen that the float solution in presence of a coordinate error estimates the station clock with a frequency error, whereas the integer ambiguity solution does not introduce such an error.

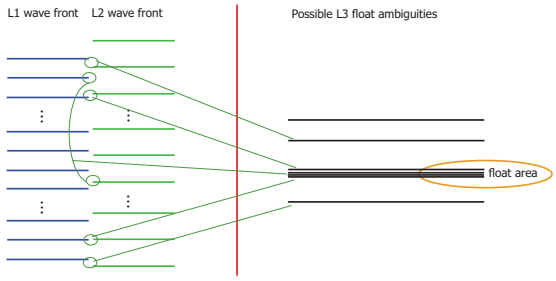

FIG. 4: GPS L3 float ambiguities (F3) and L1,L2 integer ambiguities: distinct integer $N1$, $N2$ ambiguities are mapped via the linear ionospheric free combination to arbitrary close float values. The float area matches the noise level of the filtering.

III. METHOD

The real-time processing can be simplified with three steps. Raw data Φ at time t and a troposphere delay estimate T from the previous step $t-1$ is fed to the *model reduction routine* that removes all estimated and modeled contributions from the raw measurement of the carrier phase observables at two frequencies f_1 and f_2. The reduced measurements ϕ are used to determine N_{f_1} and N_{f_2} with the *ambiguity resolution routine*. N_{f_1}, N_{f_2} and ϕ are then used by the *filter* to form L3 observables and to estimate clock and troposphere delays.

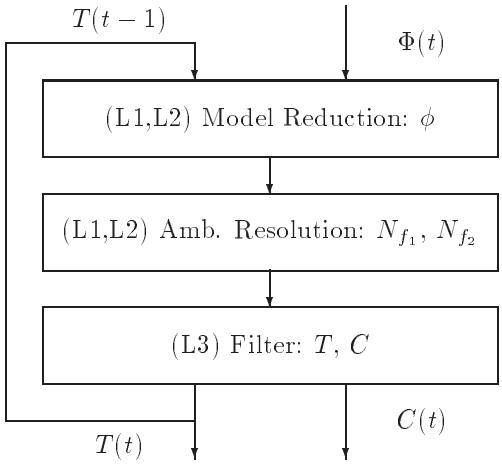

The following is a generally valid description of the model reduction and ambiguity determination process, which excludes the final filtering as pictured above.
If we define Φ_f to be a raw measurement at carrier frequency f directly extracted from a carrier phase GNSS receiver, see e.g [2], then the measurement ϕ_f presented to the ambiguity resolution routine is

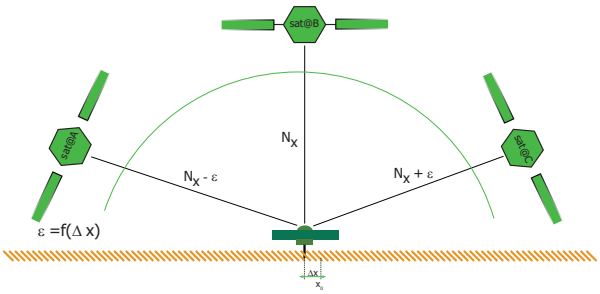

FIG. 5: A very simplified two-dimensional navigation system. Maximal three satellites are visible at any time and those are always measured at three well defined points A, B and C. No differences, no atmosphere and perfectly modeled satellite clocks and orbits.

TABLE II: Simulation of the very simplified GPS filtering according to Figure 5, with the error in the observable due to a position offset. The upper table shows the solution based on estimation of float ambiguities. A constant frequency offset of ϵ/t_0 is visible. The lower table depicts the the same steps but uses fixed integer ambiguity resolution. The clock solution is noisy but exhibits no frequency offset for long time series.

SAT	FLOAT	$t=1$	2	3	4	5	6
1	Measurement M_1	$-\varepsilon + N_1\lambda$	$0 + N_1\lambda$	$+\varepsilon + N_1\lambda$			
	Initial Phase A_1	$-\varepsilon + N_1\lambda$	$-\varepsilon + N_1\lambda$	$-\varepsilon + N_1\lambda$			
	Clock C_1	0^a	ε^b	2ε			
2	M_2		$-\varepsilon + N_2\lambda$	$0 + N_2\lambda$	$+\varepsilon + N_2\lambda$		
	A_2		$-2\varepsilon + N_2\lambda$	$-2\varepsilon + N_2\lambda$	$-2\varepsilon + N_2\lambda$		
	C_2		ε^b	$2\varepsilon^c$	3ε		
3	M_3			$-\varepsilon + N_3\lambda$	$0 + N_3\lambda$	$+\varepsilon + N_3\lambda$	
	A_3			$-3\varepsilon + N_3\lambda$	$-3\varepsilon + N_3\lambda$	$-3\varepsilon + N_3\lambda$	
	C_3			$2\varepsilon^c$	$3\varepsilon^d$	4ε	
4	M_4				$-\varepsilon + N_4\lambda$	$0 + N_4\lambda$	$+\varepsilon + N_4\lambda$
	A_4				$-4\varepsilon + N_4\lambda$	$-4\varepsilon + N_4\lambda$	$-4\varepsilon + N_4\lambda$
	C_4				$3\varepsilon^d$	4ε	5ε
	Clock_{Mean} C	0	ε	2ε	3ε	4ε	5ε

SAT	AMBFIX[e]	$t=1$	2	3	4	5	6
1	Measurement M_1	$-\varepsilon + N_1\lambda$	$0 + N_1\lambda$	$+\varepsilon + N_1\lambda$			
	Phase Ambig. A_1	$N_1\lambda$	$N_1\lambda$	$N_1\lambda$			
	$M_{reduced}$ $M_{\overline{A_1}}$	$-\varepsilon$	0	ε			
	Clock C_1	$-\varepsilon$	0	ε			
2	M_2		$-\varepsilon + N_2\lambda$	$0 + N_2\lambda$	$+\varepsilon + N_2\lambda$		
	A_2		$N_2\lambda$	$N_2\lambda$	$N_2\lambda$		
	C_2		$-\varepsilon$	0	ε		
3	M_3			$-\varepsilon + N_3\lambda$	$0 + N_3\lambda$	$+\varepsilon + N_3\lambda$	
	A_3			$N_3\lambda$	$N_3\lambda$	$N_3\lambda$	
	C_3			$-\varepsilon$	0	ε	
4	M_4				$-\varepsilon + N_4\lambda$	$0 + N_4\lambda$	$+\varepsilon + N_4\lambda$
	A_4				$N_4\lambda$	$N_4\lambda$	$N_4\lambda$
	C_4				$-\varepsilon$	0	ε
	Clock_{Mean} C	ε	$\frac{1}{2}\varepsilon$	0	0	$\frac{1}{2}\varepsilon$	ε

[a] initial clock estimate is zero at $t = 1$
[b] use estimate of $\text{Clock}_1(t = 2)$ to initialize Clock_2 at $t = 2$
[c] use estimate of $\text{Clock}_2(t = 3)$ to initialize Clock_3 at $t = 3$
[d] use estimate of $\text{Clock}_3(t = 4)$ to initialize Clock_4 at $t = 4$
[e] assumes $\epsilon << \lambda$ in order to robustly estimate A

simply defined as:

$$\phi_f = \Phi_f - \rho - T - I_f^{model} \quad (4)$$

where ρ defines the modeled distance to the satellite. ρ includes the satellite orbits derived from broadcast ephemerides and IGS ultra rapid orbit predictions, see [3], [4] as well as a simple earth tide model and feed rotation corrections. T denotes the tropospheric delay estimated using Niell's mapping function [5]. This delay consists of a standard atmospheric value (mainly hydrostatic delay) and the atmospheric delay derived by the real-time filter that comprises the biased dynamic part of the tropospheric delay (mainly wet delay). I_f^{model} is an ionospheric model derived from the Klobuchar coefficients [6] found in the GPS broadcast message.

In a typical situation both ρ and T can be derived with sufficient accuracy in order to allow a robust ambiguity resolution. I_f^{model} is transparent to the determination process, but by removing the "known" ionospheric delay it allows the ambiguity resolution method to use a limited search range.

Consider in the following an epoch t and observables from two different receivers k and l with observations of a satellite i at frequency f that can be written as :

$$ {}_k\phi_f^i = c_f^i + {}_kI_f^i + {}_kc_f + \lambda_f \cdot {}_kN_f^i + {}_k\epsilon_f^i \ , \quad (5)$$

$$ {}_l\phi_f^i = c_f^i + {}_lI_f^i + {}_lc_f + \lambda_f \cdot {}_lN_f^i + {}_l\epsilon_f^i \quad (6)$$

comprising of the satellite clock c_f^i, the station clocks ${}_kc_f$ and ${}_lc_f$, the remaining unmodeled ionospheric delays ${}_kI_f^i$ and ${}_lI_f^i$, the phase ambiguities ${}_kN_f^i$ and ${}_lN_f^i$ with their respective wavelengths λ_f, and residuals ${}_k\epsilon_f^i$ and ${}_l\epsilon_f^i$ that have contribution from unmodeled errors and measurement noise. Assuming ideally aligned measurement epochs (t) for both observations one can form a single difference ϕ_f^i as:

$$\phi_f^i \equiv {}_k\phi_f^i - {}_l\phi_f^i = I_f^i + c_f + \lambda_f \cdot N_f^i + \epsilon_f^i \quad (7)$$

where the components for the ionospheric delay I_f^i, the station clock c_f, the phase ambiguity N_f^i and the residual ϵ_f^i are differences of the respective receiver observable components for k and l. A convenient effect of differencing is that the satellite clock c_f^i becomes a common clock and is canceled in the equation. Especially from a real-time filter point of view it is easier to process GNSS data without the difficult to predict satellite clocks. Equation 7 still contains the station clock difference c_f between j and k, which is an unknown that needs to be removed from the equation in order to determine the right phase ambiguity N_f^i. One could either use the filter estimate in order to get rid of this contribution, or, in a more correct way, form a double difference, ϕ_f^{ij} where i and j denote the two different satellites used:

$$\phi_f^{ij} \equiv \phi_f^i - \phi_f^j = I_f^{ij} + \lambda_f \cdot N_f^{ij} + \epsilon_f^{ij} \ . \quad (8)$$

Now, left in the equation are only double differenced: ionospheric delay I_f^{ij}, the phase ambiguity N_f^{ij} and the model residual ϵ_f^{ij}. Let us introduce two carriers at frequencies f_1 and f_2 for Eq. 8. Assuming that the residual ϵ_f^{ij} is small enough, then it is possible to determine the phase ambiguity by using the fact that during normal ionospheric activity the ionospheric delay on the carrier frequency f_1 is a down-scaled version of the delay on carrier frequency f_2 with $f_1 > f_2$:

$$I_{f_1}^{ij} = \frac{f_2^2}{f_1^2} \cdot I_{f_2}^{ij} \ . \quad (9)$$

At elevation angles $\alpha_{Ncut} > 30$ degrees the tropospheric model error is on a level of a few mm, and for baselines < 1000km satellite orbit predictions as well result in differential distance errors of a few mm. If the accumulated model errors ϵ_f^{ij} are below a certain threshold $\epsilon_f << \lambda_f$, e.g 1cm, the ionospheric rule can be used in order to find a right combination of $N_{f_1}^{ij}, N_{f_2}^{ij}$, provided that the search window for N_f^{ij} is small enough. The algorithm searches in real-time for a suitable combination that minimizes the ionospheric residual:

$$\min_{\mathcal{N}_{f_1}, \mathcal{N}_{f_2}} \left(\mathrm{abs} \left(\phi_{f_1}^{ij}(N_{f_1}^{ij}) - \phi_{f_2}^{ij}(N_{f_2}^{ij}) \cdot \frac{f_1^2}{f_2^2} \right) \right) \quad (10)$$

where $\mathcal{N}_{f_1}, \mathcal{N}_{f_2}$ define the search range of $N_{f_1}^{ij}$ and $N_{f_2}^{ij}$ respectively. The search range is usually set to about $\pm 3 \ldots 4$ cycles for each carrier frequency f around an initial estimate of $\check{N}_f^{ij}$

$$\check{N}_f^{ij} = \mathrm{round} \left(\frac{\phi_f^{ij}}{\lambda_f} \right) \ . \quad (11)$$

A new set of $(N_{f_1}^{ij}, N_{f_2}^{ij})$ is only accepted if the ionospheric residual for $(N_{f_1}^{ij}, N_{f_2}^{ij})$ in Equation 10 is smaller than a certain threshold, e.g. 1cm. The double differences ϕ_f^{ij} are calculated between all satellites i and j from the valid set of satellites at the current epoch t with elevation angles $\alpha > \alpha_{Ncut}$, where j denotes a reference satellite, which is chosen as the satellite with the highest elevation α. This reference satellite has also to have a valid set of (N_f^j) for $(t-1)$, setting $\left(N_{f_1}^j(t), N_{f_2}^j(t)\right) = \left(N_{f_1}^j(t-1), N_{f_2}^j(t-1)\right)$ in order to bind the current epoch t to all the previous epochs. This will ensure a set of compatible ionospheric delays for the two frequencies. If this requirement is not met or no trusted combination is found the procedure indicates this fact. In order to find the single difference phase ambiguities $N_f^i(t)$ the reference ambiguity $N_f^j(t)$ has to be added to the double difference phase ambiguity $N_f^{ij}(t)$ for every i:

$$N_f^i = N_f^{ij} + N_f^j \ . \quad (12)$$

The procedure applies some further rules of when to accept and release phase ambiguities to and from the

valid set in order to ensure a robust filtering. In addition the real-time Kalman filter is now capable of handling any combination of integer and float ambiguities, which allows the determination process to reject uncertain phase ambiguities without compromising the number of observations available to the filter.

IV. RESULTS

Our algorithm removes the sensitivity to small errors, on the cm level, in the station positions. We have made several experiments on short baselines.

- *Zero-clock and very short baseline, Figure 6:*
  A clock is connected to two carrier phase receivers, which each in turn is connected to its own antenna that are separated by a very short baseline (30m). The station coordinates are known and fixed. Any correct clock solution should produce a zero-mean clock difference. The differential atmospheric delay is basically zero. The turquoise graph represents the standard clock solution using estimated float start phase parameters. It can be seen that even with a reasonable well known baseline the solution exhibits a clock drift corresponding to an East station coordinate error of about 7.5mm. All other graphs have additional East-component baseline errors introduced. Both the clock differences based on float start phase estimates (blue and pink) show the expected additional clock offset of about 20ps/(day·mm) East coordinate error. The two solutions based on fixed integer phase ambiguities (green and red) behave according to the theory explained above. The solutions were processed with a differential East baseline error of 15mm, but they still maintain a zero clock drift. In addition, the green graph is produced by a special mode that deliberately uses only one fixed integer ambiguity at any epoch and estimates all others as floats (in green). This single fixed ambiguity maintained the right clock difference as much as a solution based on the maximal number of fixed integer ambiguities (in red).
- *Short Baseline SP01-ONSA, Figure 7:*
  On the 67km long baseline between SP and the Onsala Space Observatory (OSO) we have tested a more relevant setup. The two graphs represent the differences between two 5mm East station coordinate offset-ed clock solutions,
  left graph: using float ambiguity estimates and
  right graph: fixed integer ambiguities.
  The float based solutions differ by 20ps/(day·mm), whereas the integer ambiguity fixed solutions differ insignificantly. The scatter between the clock estimates in the *right graph* relates to the amount of the coordinate error imposed between the two solutions. This might not prove that the fix ambiguity solutions have a zero mean frequency error but the difference shows that both solution agree despite the imposed baseline error. Currently, no alternative and independent time link exists between OSO and SP.

V. CONCLUSIONS AND DISCUSSIONS

We have shown that the real-time estimation of carrier phase ambiguities increases the robustness of the real-time filter and that the frequency offsets, mainly caused by differential position errors, are removed from the clock solution. This works well for short and very short baselines, however longer baselines, e.g. SP-PTB (622km) need a more fine-tuning of the estimation algorithm due to the tropospheric disturbances at low elevation angles. During future work we will generalize the algorithm for use with any multi-frequency GNSS system (Glonass, Galileo).

Acknowledgments

We would like to thank our colleagues at SP for discussions and the OpenSource Community for all the magic tools and all the beautiful software around.

[1] Rieck et al. *"Real-Time Time and Frequency Transfer using GPS Carrier Phase Observations"* (Proceedings of the 35th Annual PTTI System and Applications Meeting, 2003)
[2] B Hofmann-Wellenhof, H. Lichtenegger, and J. Collins, *"GPS: Theory and Practice"* 5th ed. (Springer Verlag, 2001)
[3] International GNSS Service IGS, web-site *http://igscb.jpl.nasa.gov/*
[4] G. Beutler, M. Rothacher, S. Schaer, T.A. Springer, J. Kouba, and R.E. Neilan, *"The International GPS Service (IGS): An Interdisciplinary Service in Support of Earth Sciences"* (Adv. Space Res. Vol. 23, No. 4, pp. 631-635, 1999)
[5] A.E. Niell, *"Global Mapping Functions for the Atmosphere Delay at Radio Wavelengths"* (J. Geophys. Res., 101, 3227-3246, 1996)
[6] J. A. Klobuchar, *"Ionospheric Time-Delay Algorithm for Single-Frequency GPS Users"* (IEEE Transactions on Aerospace and Electronic Systems, 23(3), 332-338, 1987)

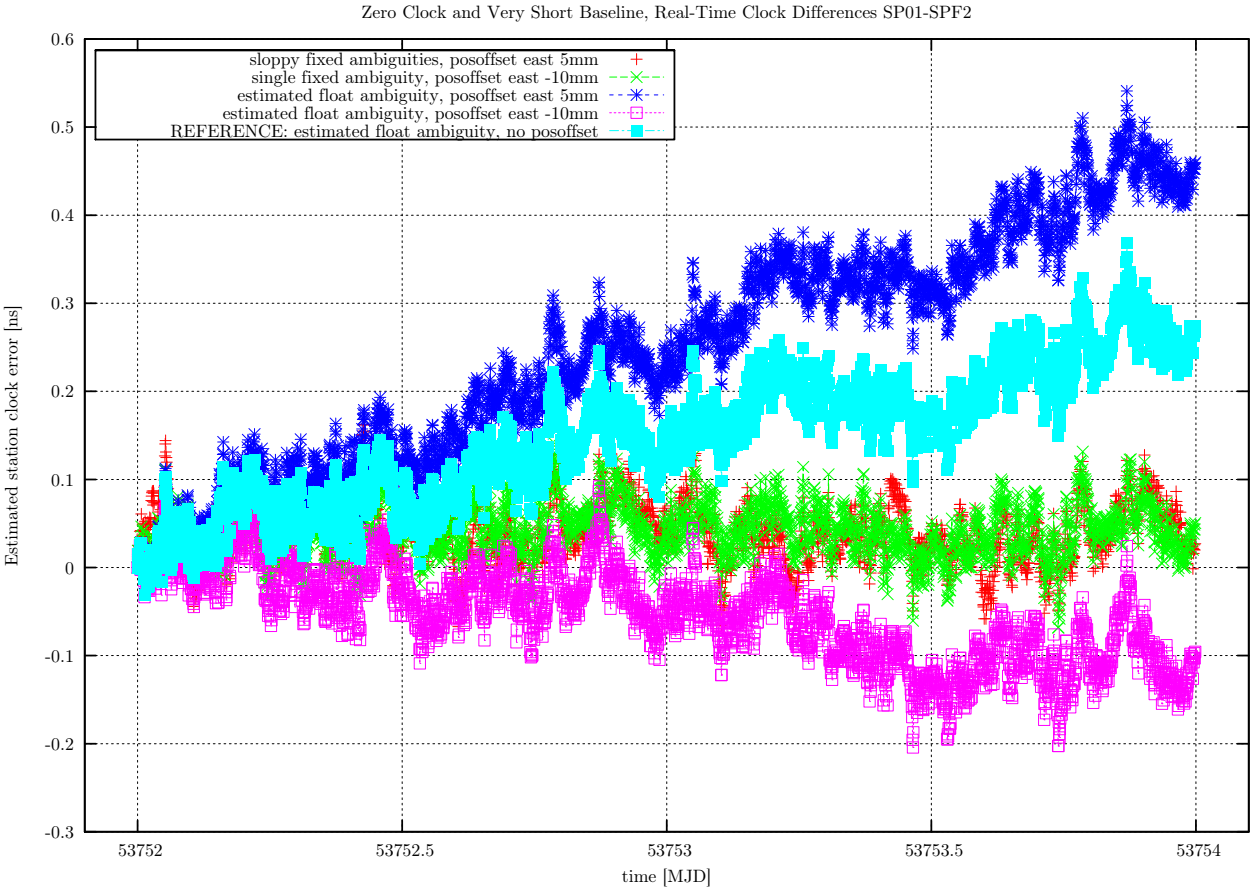

FIG. 6: Zero-Clock, very short baseline (30m) experiment: the plot shows several different station clock solutions derived from two days of GPS carrier phase data. Due to that both receivers (SP01, SPF2) use the same clock the clock difference should be zero. Due to deliberate station position offsets the solutions based on L3 float ambiguities clearly show frequency offsets (100ps/day for 5mm east component). Both position-offset integer ambiguity solution are close to zero mean in frequency.

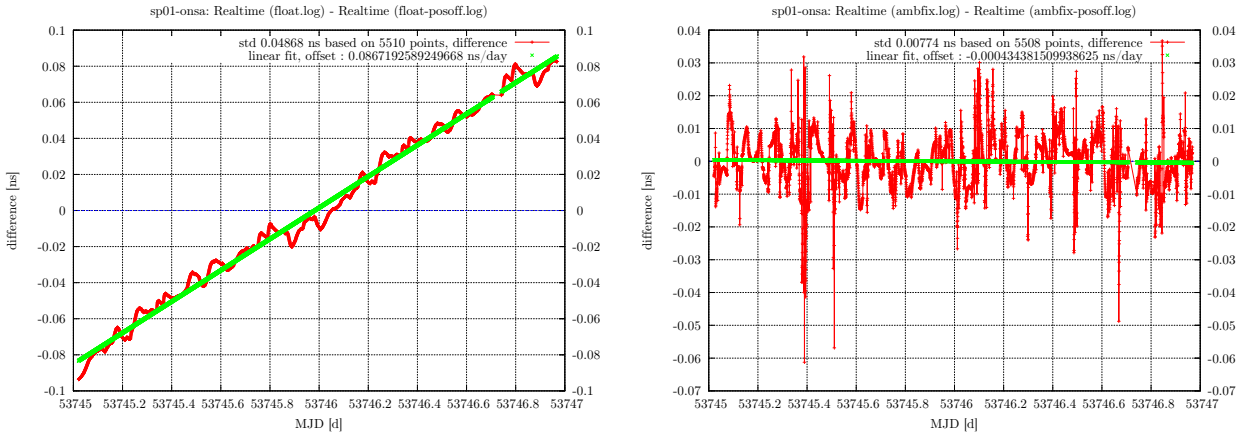

FIG. 7: Short baseline SP01-ONSA (67km) experiment: a two day data set was processed with float ambiguities and fixed integer ambiguities, both with and without a station offset of 5mm East component resulting in four clock solutions. The left graph shows the difference between the two float solutions revealing a frequency offset of about 90ps/day. On the contrary the difference of the two fixed integer ambiguity solutions on the right side show an insignificant frequency offset of about 0.4ps/day.

List of Exhibitors

Aeroflex	http://www.aeroflex.com
EFG GmbH	http://www.efg-berlin.de
hwl Scientific Instruments GmbH	http://www.hwlscientific.com
Kolinker Industrial Equipments Ltd.	http://www.kolinker.com
Lange-Electronic GmbH	http://www.lange-electronic.de
Meinberg Funkuhren GmbH & Co. KG	http://www.meinberg.de
Menlo Systems GmbH	http://www.menlosystems.com
Microsystemes	http://www.microsystemes.com
Pendulum Instruments	http://www.pendulum-instruments.com
ppm GmbH	http://www.ppmgmbh.com
Quartzlock	http://www.quartzlock.com
Sacher Lasertechnik GmbH	http://www.sacher-laser.com
Symmetricom	http://www.symmetricom.com
Temex Time SA	http://www.temextime.com
TimeTech GmbH	http://www.timetech.de
Toptica Photonics	http://www.toptica.com

List of Participants

Participant	Institute
Abgrall, Michel	BNM-SYRTE-Systèmes de Référence Temps-Espace, France
Abramzon, Igor	Magic Crystal Ltd., Russian Federation
Addouche, Mahmoud	CNRS / FEMTO-ST, France
Akil, Mariam	ENSMM-LCEP, France
Ansorge, Erik	Otto-von-Guericke Universität Magdeburg, Germany
Arias, Elisa Felicitas	Bureau International des Poids et Mesures, France
Baillard, Xavier	Observatoire Paris, France
Barillet, Roland	Observatoire Paris, France
Barragan, Francisco J. R.	ESA - European Space Agency ESTEC, Netherlands
Barwood, Geoffrey	National Physical Laboratory, United Kingdom
Bauch, Andreas	Physikalisch-Technische Bundesanstalt, Germany
Baumont, Francoise	Observatoire de la Cote d'Azur, France
Becker, Thomas	Max-Planck Institut für Quantenoptik, Germany
Bedrich, Stefan	Kayser-Threde GmbH, Germany
Belloni, Marco	Galileo Avionica, Italy
Belyaev, Alexandr	Vremya-CH ISC, Russian Federation
Ben-Aroya, Ido	Technion, Israel
Benmessai, Karim	CNRS / FEMTO-ST, France
Bennett, Stacey	Symmetricom, United States
Bergquist, Jim	National Institute of Standards and Technology, United States
Bernier, Laurent-Guy	Bundesamt für Metrologie und Akkreditierung Schweiz, Switzerland
Berthoud, Patrick	Observatoire Cantonal de Neuchâtel, Switzerland
Besson, Raymond	ENSMM-LCEP, France
Beuret Mallaby, Sarah	Temex Neuchâtel Time, Switzerland
Bigler, Emmanuel	ENSMM-LCEP, France
Bize, Sebastien	BNM-SYRTE-Systèmes de Référence Temps-Espace, France
Blas, Luciano S.	Instituto Nacional de Tecnologia Industrial, Argentina
Bonafede, Laura	SEPA Sistemi Ellettronici Per Automazione, Italy
Bourga, Christophe	Alcatel Alenia Space, France
Bourquin, Roger	ENSMM-LCEP, France
Boy, Jean-Jacques	ENSMM-LCEP, France
Boyd, Martin	JILA, NIST and the University of Colorado, United States
Bradaczek, H.-A.	EFG GmbH, Germany
Bragagnini, Luigi	Consorzio Torino Time, Italy
Brendel, Rémi	CNRS / FEMTO-ST, France
Buchleitner, Anton	Tele Filter GmbH, Vectron Internat., Germany
Burnicki, Martin	Meinberg GmbH & Co KG, Germany
Butorac, Josip	University of Zagreb, Croatia
Capetti, Paola	SEPA Sistemi Ellettronici Per Automazione, Italy
Cereja, Francis	Microsystemes, France
Cerretto, Giancarlo	IEN Galileo Ferraris, Italy
Chapelet, Frédéric	BNM-SYRTE-Systèmes de Référence Temps-Espace, France
Chaubet, Michel	Centre National d'Etudes Spatiales, France
Chen, Jingbiao	Peking University, China
Cordara, Franco	IEN Galileo Ferraris, Italy
Costanzo, Giovanni A.	Politecnico di Torino, Italy
Crane, Scott	US Naval Observatory, United States
Dach, R.	University of Bern, Switzerland
Dannull, Frank	Meinberg GmbH & Co KG, Germany
De Vicente, Javier	European Space Agency (ESA), Germany
de Vos, Jean-Pierre	Symmetricom GmbH, Germany
Defraigne, Pascale	Observatoire Royal de Belgique, Belgium
DeGiovanni, Guillaume	AEROFLEX, France

Demidov, Nikolay	KVARZ, IEM, Russian Federation
Dimarcq, Noel	BNM-SYRTE-Systèmes de Référence Temps-Espace, France
Doberstein, Sergei	ONIIP, Russian Federation
Domnin, Yu.S.	Institute of Metrology for Time and Space FGUP VNIIFTRI, Russian Federation
Donati, Alessandro	Kayser Italia SRL, Italy
Droz, Fabien	Temex Neuchâtel Time, Switzerland
Du Burck, Frederic	Laboratoire de Physique des Lasers, Université Paris 13 - IG, France
Dudle, Gregor	Bundesamt für Metrologie und Akkreditierung Schweiz, Switzerland
Dulmet, Bernard	ENSMM-LCEP, France
Dumke, Rainer	Max Planck Forschungsgruppe f. Optik Information u. Photonik, Germany
Earley, Donald N.	NATO Maintenance and Supply Agency, Luxembourg
Ecabert, Marcel	FSRM, Switzerland
Eikema, Kjeld	Laser Centre Vrije Universiteit, Netherlands
Eisele, Christian	Heinrich Heine Universität Düsseldorf, Germany
Eisenstein, Gadi	Technion, Israel
Ernsting, Ingo	Heinrich Heine Universität Düsseldorf, Germany
Ertmer, Wolfgang	Universität Hannover, Germany
Eskelinen, Pekka	Helsinki University of Technology, Finland
Esnault, Francois-Xavier	BNM-SYRTE-Systèmes de Référence Temps-Espace, France
Esteban Pinillos, Hector	Real Instituto y Observatorio de la Armada, Spain
Fischer, Marc	Menlo Systems GmbH, Germany
Föckersperger, Stefan	Kayser-Threde GmbH, Germany
Friebe, Jan	Universität Hannover, Germany
Friederich, Michael	AEROFLEX, France
Gachon, Dorian	CNRS / FEMTO-ST, France
Galindo, Francisco Javier	Real Instituto y Observatorio de la Armada, Spain
Galliou, Serge	ENSMM-LCEP, France
Gao, Xiaoxun	National Institute of Metrology, China
Garvey, Michael	Symmetricom, United States
Geissler, Stefan	ppm GmbH, Germany
Gerginov, Vladislav	National Institute of Standards and Technology, United States
Gerstung, Heiko	Meinberg GmbH & Co KG, Germany
Getz, Andreas	Symmetricom GmbH, Germany
Gill, Patrick	National Physical Laboratory, United Kingdom
Giordano, Vincent	CNRS / FEMTO-ST, France
Gozemba, Erik	Symmetricom GmbH, Germany
Grain, Christophe	Physikalisch-Technische Bundesanstalt, Germany
Grosche, Gesine	Physikalisch-Technische Bundesanstalt, Germany
Guena, Jocelyne	Observatoire Cantonal de Neuchâtel, Switzerland
Guillemot, Philippe	Centre National d'Etudes Spatiales, France
Günther, Christoph	DLR, Institute of Communications and Navigation, Germany
Guyennon, Nicolas	Observatoire Royale Bruxelles, Belgium
Hamid, Ramiz	National Metrology Institute UME, Turkey
Hammesfahr, Jens	DLR, Institute of Communications and Navigation, Germany
Helmcke, Jürgen	Physikalisch-Technische Bundesanstalt, Germany
Hermann, Virgile	Thales Electron Devices, France
Hlavac, Roman	Galileo Industries GmbH, Germany
Horstjann, Markus	Sacher Lasertechnik GmbH, Germany
Hosokawa, Mizuhiko	National Inst. of Information and Communications Technology, Japan
Hoyt, Chad W.	National Institute of Standards and Technology, United States
Huang, Guilong	Wuhan Institute of Physics and Mathematics, China
Ikegami, Takeshi	National Metrology Institute of Japan, Japan
Imlau, Helmut	Deutsche Telekom - T-Com, Germany
Jaduszliwer, Bernardo	The Aerospace Corporation, United States
Jaldehag, Kenneth	SP Swedish National Testing and Research Institute, Sweden

Jefferts, Steven R.	National Institute of Standards and Technology, United States
Jiang, Zhiheng	Bureau International des Poids et Mesures, France
Johansson, Staffan	Pendulum Instruments AB, Sweden
Jurcevic, Marko	University of Zagreb, Croatia
Kajita, Masatoshi	National Inst. of Information and Communications Technology, Japan
Kalliomaki, Kalevi	MIKES (Centre for Metrology and Accredittion), Finland
Karl, Gerhard	Quartzlock UK Ltd., United Kingdom
Kasjanenko, Sergejs	Latvian National Metrology Centre Ltd., Latvia
Kastowsky, Manfred	EFG GmbH, Germany
Kasznia, Michal	Poznan University of Technology, Poland
Kazakov, Georgy	St. Petersburg State Polytechnic University, Russian Federation
Klepczynski, William	US Naval Observatory, United States
Klische, Wolfgang	K+K Messtechnik GmbH, Germany
Knight, David	DK Research, United Kingdom
Koshelyaevsky, Nicholas	Institute of Metrology for Time and Space FGUP VNIIFTRI, Russian Federation
Kramer, G.	Physikalisch-Technische Bundesanstalt, Germany
Krempl, Peter	AVL List GmbH, Austria
Külz, Uwe	HWL Scientific Instruments GmbH, Germany
Kunze, Hans J.	KLA Global, United States
Lämmerzahl, Claus	University of Bremen, Germany
Lange, Werner R.	Lange Electronic GmbH, Germany
Laurent, Philippe	Observatoire Paris, France
Le, Trong Thao	Philips Semiconductors, France
Lee, Arthur	Kolinker Industrial Equipments Ltd., Hong Kong
Legero, Thomas	Physikalisch-Technische Bundesanstalt, Germany
Lemanski, Darinsz	Polish Academy of Sciences, Astrogeodynamical Observatory, Poland
Lemonde, Pierre	BNM-SYRTE-Systèmes de Référence Temps-Espace, France
Leschiutta, Sigfrido	IEN Galileo Ferraris, Italy
Levi, Filippo	IEN Galileo Ferraris, Italy
Lewandowski, W.	Bureau International des Poids et Mesures, France
Li, Mingshou	National Institute of Metrology, China
Ligeret, Vincent	Thales Research and Technology, France
Lin, Pingwei	National Institute of Metrology, China
Lin, Calvin	Telecommunication Laboratories, Taiwan
Lipphardt, Burghard	Physikalisch-Technische Bundesanstalt, Germany
Liu, Tao	Max Planck Forschungsgruppe f. Optik Information u. Photonik, Germany
Lopez, Olivier	Laboratoire de Physique des Lasers, Université Paris 13 - IG, France
Ma, Longesheng	Bureau International des Poids et Mesures, France
Maeno, Hideo	National Inst. of Information and Communications Technology, Japan
Maleki, Lute	Jet Propulsion Laboratory, United States
Mallaby, Reuben	Temex Neuchâtel Time, Switzerland
Malocha, Donald	University of Central Florida, United States
Mannermaa, Jari	Finland
Mansten, Tapio	MIKES (Centre for Metrology and Accredittion), Finland
Mateescu, Irina	National Institute of Materials Physics, Romania
Matsakis, Demetrios	US Naval Observatory, United States
Mehlstäubler, Tanja E.	Universität Hannover, Germany
Meinberg, Werner	Meinberg GmbH & Co KG, Germany
Mellberg, Kristoffer	Pendulum Instruments AB, Sweden
Messina, Filippo	Cagliari Astronomical Observatory, Italy
Mileti, Gaetano	Observatoire Cantonal de Neuchâtel, Switzerland
Minchev, Gencho	Bulgarian Academy of Sciences, Bulgaria
Mirsaitov, F. N.	Kazan State Technical University, Russian Federation
Miskinis, Rimantas	Semiconductor Physics Institute, Lithuania

Moldenhauer, Karsten	Universität Hannover, Germany
Mozhaev, Vladimir	Moscow State University, Russian Federation
Much, Rudolf	ESA - European Space Agency ESTEC, Netherlands
Mueller, Tobias	Universität Hannover, Germany
Müller, Holger	Stanford University, United States
Nawrocki, Jerzy	Polish Academy of Sciences, Astrogeodynamical Observatory, Poland
Nazarova, Tatiana	Physikalisch-Technische Bundesanstalt, Germany
Nevsky, Alexander	Heinrich Heine Universität Düsseldorf, Germany
Nicolas, Jacques	FPS Economy-Metrology Division (SMD), Belgium
Niculescu, Anca	National Institute of Metrology, Romania
Niemeier, Wolfgang	Technische Universität Braunschweig, Germany
Niessner, Anton	BEV, Austria
Nogas, Pawel	Polish Academy of Sciences, Astrogeodynamical Observatory, Poland
Oates, Chris	National Institute of Standards and Technology, United States
Oneto, Jean Louis	Observatoire de la Cote d'Azur, France
Ovchinnikov, Yuri	National Physical Laboratory, United Kingdom
Pal'chikov, Vitaly	Institute of Metrology for Time and Space FGUP VNIIFTRI, Russian Federation
Palacio Rodriguez, Juan	Real Instituto y Observatorio de la Armada, Spain
Parker, Thomas	National Institute of Standards and Technology, United States
Partanen, Juho	Helsinki University of Technology, Finland
Pawlitzki, Alexander	Time Tech GmbH, Germany
Peier, Ulrich	Dr.U.R.Peier Engineering, Switzerland
Peik, Ekkehard	Physikalisch-Technische Bundesanstalt, Germany
Peil, Steven	US Naval Observatory, United States
Pendrill, Leslie	SP Swedish National Testing and Research Institute, Sweden
Petit, Gérard	Bureau International des Poids et Mesures, France
Piester, Dirk	Physikalisch-Technische Bundesanstalt, Germany
Pietropaoli, Tommaso	Istituto Superiore C.T.I., Italy
Poli, Nicola	Universita ' di Firenze, Dipartimento di Fisica, Italy
Posthumus, Jan	TOPTICA Photonics AG, Germany
Pouytes, Jean-Claude	Microsystemes, France
Puranen, Mikko	Helsinki University of Technology, Finland
Rasel, E. M.	Universität Hannover, Germany
Ratier, Nicolas	CNRS / FEMTO-ST, France
Richard, Jean-Yves	BNM-SYRTE-Systèmes de Référence Temps-Espace, France
Rieck, Carsten	SP Swedish National Testing and Research Institute, Sweden
Riedmann, Matthias	Universität Hannover, Germany
Riehle, Fritz	Physikalisch-Technische Bundesanstalt, Germany
Rivas, Manuel	Instituto Nacional de Tecnologia Industrial, Argentina
Robertsson, Lennart	Bureau International des Poids et Mesures, France
Rosenband, Till	National Institute of Standards and Technology, United States
Rosenbusch, Peter	BNM-SYRTE-Systèmes de Référence Temps-Espace, France
Rost, Michael	Physikalisch-Technische Bundesanstalt, Germany
Roth, Hartmut	Symmetricom GmbH, Germany
Rubiola, Enrico	CNRS / FEMTO-ST, France
S'ramar, Jaroslav	Krystaly, Hradee Kra'love, a.S., Czech Republic
Sacher, Joachim	Sacher Lasertechnik GmbH, Germany
Safonova, Ekaterina	Kazan State Technical University, Russian Federation
Salomon, Christophe	Département de physique de l'Ecole Normale Supérieure, France
Salzenstein, Patrice	CNRS / FEMTO-ST, France
Santarelli, Giorgio	BNM-SYRTE-Systèmes de Référence Temps-Espace, France
Sarikaya, Dilek	Time Tech GmbH, Germany
Sauter-Koeder, Beate	TOPTICA Photonics AG, Germany
Sautter, Eike	Quartzlock UK Ltd., United Kingdom

Schaefer, Wolfgang	Time Tech GmbH, Germany
Schiller, Stephan	Heinrich Heine Universität Düsseldorf, Germany
Schlueter, Bernard	Privat, Switzerland
Schlüter, Wolfgang	BKG-Fundamentalstation Wettzell, Germany
Schnatz, Harald	Physikalisch-Technische Bundesanstalt, Germany
Schweda, Hartmut	Observatoire Cantonal de Neuchâtel, Switzerland
Sesia, Ilaria	IEN Galileo Ferraris, Italy
Seydel, Eberhard	Privat, Germany
Siccardi, Marco	SKK Electronics, Italy
Sonn, Nico	EADS Astrium GmbH, Germany
Stejskal, Alois	Max Planck Forschungsgruppe f. Optik Information u. Photonik, Germany
Sterr, Uwe	Physikalisch-Technische Bundesanstalt, Germany
Strauss, Nadine	Heinrich Heine Universität Düsseldorf, Germany
Sultanov, Farkhat I.	Kazan State Technical University, Russian Federation
Svehla, Drazen	Technische Universität München, Germany
Szymaniec, Krzysztof	National Physical Laboratory, United Kingdom
Talamanov, Sergei	National Scientific Center "Institute of Metrology", Ukraine
Tamm, Christian	Physikalisch-Technische Bundesanstalt, Germany
Tauser, Florian	TOPTICA Photonics AG, Germany
Tavella, Patrizia	IEN Galileo Ferraris, Italy
Thomann, Pierre	Observatoire Cantonal de Neuchâtel, Switzerland
Tobar, Michael	University of Western Australia, School of Physics, Australia
Tuckey, Philip	BNM-SYRTE-Systèmes de Référence Temps-Espace, France
Udem, Thomas	Max-Planck Institut für Quantenoptik, Germany
Ulzega, Simone	University of Fribourg, Switzerland
Underhill, Micheal J.	Underhill Research, United Kingdom
Unverdross, Rainer	Unverdross Technik, Germany
Vogt, Felix	Physikalisch-Technische Bundesanstalt, Germany
Vorokhovsky, Yokov	Morton Inc., Russian Federation
Waller, Pierre	ESA - European Space Agency ESTEC, Netherlands
Wang, Lijun	Max Planck Forschungsgruppe f. Optik Information u. Photonik, Germany
Wang, Yanhui	Max Planck Forschungsgruppe f. Optik Information u. Photonik, Germany
Watabe, Ken-ichi	National Metrology Institute of Japan, Japan
Webster, Stephen A.	National Physical Laboratory, United Kingdom
Weiss, Carl-Otto	Physikalisch-Technische Bundesanstalt, Germany
Wendrich, Thijs	Universität Hannover, Germany
Weyers, Stefan	Physikalisch-Technische Bundesanstalt, Germany
Wicht, Andreas	Heinrich Heine Universität Düsseldorf, Germany
Wickard, Tim	Vectron International, United States
Wolf, Peter	Bureau International des Poids et Mesures, France
Wolf, Michael	Time Tech GmbH, Germany
Wong, Eric	Kolinker Industrial Equipments Ltd., Hong Kong
Wynands, Robert	Physikalisch-Technische Bundesanstalt, Germany
Yanagimachi, Shinya	National Metrology Institute of Japan, Japan
Zhang, Shougang	National Time Service Center, China
Zhang, Aimin	National Institute of Metrology, China
Zhao, Yanning. N.	Max Planck Forschungsgruppe f. Optik Information u. Photonik, Germany
Zholnerov, Vadim	The Russian Institute of Radionavigation and Time, Russian Federation
Zucco, Massimo	Bureau International des Poids et Mesures, France

Index